Disease Markers

Body Fluid Biomarkers in Chronic Diseases

Lead Guest Editor: Yi Shao
Guest Editors: Wen-Qing Shi, Ting Su, Zhang hong, Jing Zhong, and Fei Dong

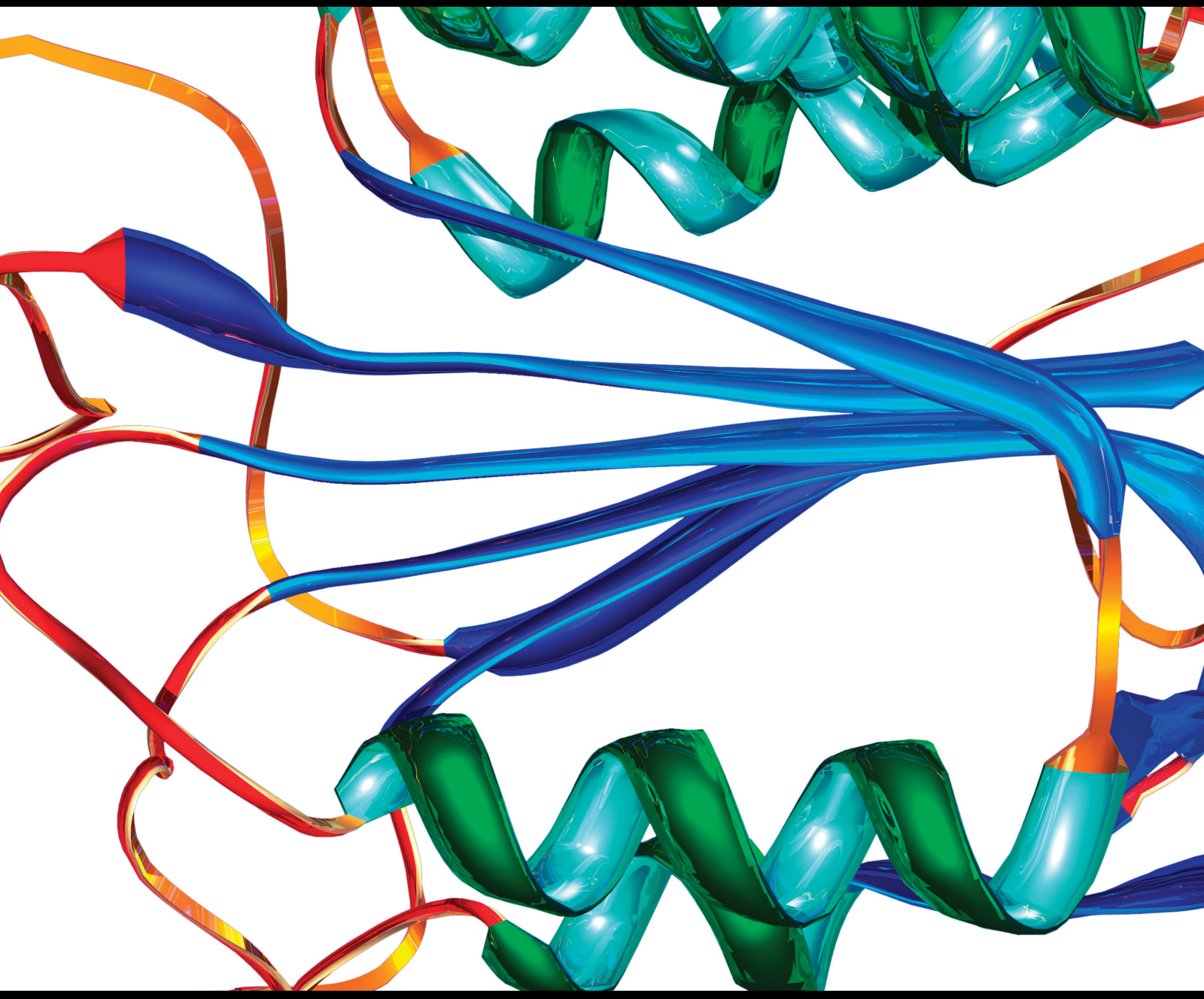

Body Fluid Biomarkers in Chronic Diseases

Disease Markers

Body Fluid Biomarkers in Chronic Diseases

Lead Guest Editor: Yi Shao
Guest Editors: Wen-Qing Shi, Ting Su, Zhang hong, Jing Zhong, and Fei Dong

Contents

Retracted: The Correlation between Functional Connectivity of the Primary Somatosensory Cortex and Cervical Spinal Cord Microstructural Injury in Patients with Cervical Spondylotic Myelopathy
Disease Markers
Retraction (1 page), Article ID 9879526, Volume 2023 (2023)

Retracted: Effects of Medium-Term Soft Contact Lens Fitting on Dry Eye: Analyses Using Ultra-High Resolution Optical Coherence Tomography and Digital Slit-Lamp Biomicroscopy
Disease Markers
Retraction (1 page), Article ID 9813896, Volume 2023 (2023)

RhoA with Associated TRAb or FT3 in the Diagnosis and Prediction of Graves' Ophthalmopathy
Sidi Zhao, Shuangshuang Shi, Wanchen Yang, Hanqing Wang, Tianming Jian, Qing He, Yang Liu, Xiaoming Huang, and Tong Wu
Research Article (14 pages), Article ID 8323946, Volume 2022 (2022)

Galectin-3 Is a Crucial Immunological Disease Marker in Patients with Fungal Keratitis
Yichen Xiao, Jiahui Yang, Zhenyuan Fu, Dalian He, Naiyang Li, and Jin Yuan
Research Article (10 pages), Article ID 1380560, Volume 2022 (2022)

Exploring the Potential Mechanisms of *Melilotus officinalis* (L.) Pall. in Chronic Muscle Repair Patterns Using Single Cell Receptor-Ligand Marker Analysis and Molecular Dynamics Simulations
Yisheng Chen, Zhiwen Luo, Jinrong Lin, Beijie Qi, Yaying Sun, Fangqi Li, Chenyang Guo, Weiwei Lin, Xueran Kang, Xinyi He, Qian Wang, Shiyi Chen, and Jiwu Chen
Research Article (11 pages), Article ID 9082576, Volume 2022 (2022)

Screening Biomarkers and Constructing a Predictive Model for Symptomatic Urinary Tract Infection and Asymptomatic Bacteriuria in Patients Undergoing Cutaneous Ureterostomy: A Metagenomic Next-Generation Sequencing Study
Qian Yuan, Rong Huang, Liping Tang, Lijuan Yuan, Li Gao, Yang Liu, and Ying Cao
Research Article (16 pages), Article ID 7056517, Volume 2022 (2022)

Efficacy of Navigated Laser Photocoagulation for Chronic Central Serous Chorioretinopathy: A Retrospective Observational Study
Fen Zhou, Jin Yao, Qin Jiang, and Weihua Yang
Research Article (8 pages), Article ID 7792291, Volume 2022 (2022)

Inhibition of Galectin-3 Impairs Antifungal Immune Response in Fungal Keratitis
Yichen Xiao, Jiahui Yang, Zhenyuan Fu, Zhile Xiong, Chao Zhang, Dalian He, Zhenwen Zhou, Naiyang Li, and Jin Yuan
Research Article (11 pages), Article ID 8316004, Volume 2022 (2022)

Identification and Validation of Immune Cells and Hub Genes in Gastric Cancer Microenvironment
Huan Wang, Jianfang Rong, Qiaoyun Zhao, Conghua Song, Rulin Zhao, Sihai Chen, and Yong Xie
Research Article (18 pages), Article ID 8639323, Volume 2022 (2022)

Abdominal Obesity: An Independent Influencing Factor of Visuospatial and Executive/Language Ability and the Serum Levels of Aβ40/Aβ42/Tau Protein
Xin Fan, Yun Zhong, Lingling Zhang, Jiaqi Li, Fei Xie, and Zhiyuan Zhang
Research Article (13 pages), Article ID 3622149, Volume 2022 (2022)

[Retracted] Effects of Medium-Term Soft Contact Lens Fitting on Dry Eye: Analyses Using Ultra-High Resolution Optical Coherence Tomography and Digital Slit-Lamp Biomicroscopy
Yuzhou Wang, Zhiqiang Xu, Shuangjiao Chen, Yangyang Xu, Linzhi Wei, Fan Lu, and Liang Hu
Research Article (14 pages), Article ID 7220706, Volume 2022 (2022)

HuR Promotes the Progression of Gastric Cancer through Mediating CDC5L Expression
Jing Cui, Nanjing Cao, Guochao Wang, Fuhua Wang, Bin Yang, Jian Wang, Yongqiang Lv, Yunqing Chen, and Feng Li
Research Article (12 pages), Article ID 5141927, Volume 2022 (2022)

The Role of Symptom Duration and Serologic Factors in the Relapse of IgG4-Related Ophthalmic Disease following Surgery: A Retrospective Cohort Study
Siyu Liu, Zifan Yue, Chengcheng Zeng, Xiao Huang, Jian Li, Jiale Diao, Xinxin Chen, Ruili Wei, and Weihua Yang
Research Article (9 pages), Article ID 5651506, Volume 2022 (2022)

Elevated Thyroid Autoantibodies Aggravate Stroke Severity in Euthyroidism with Acute Ischemic Stroke
Jingyi Li, Shoulong Hu, Fang Liu, Dapeng Wu, Wei Song, and Miao Hui
Research Article (5 pages), Article ID 8741058, Volume 2022 (2022)

The Microbiome of Meibomian Gland Secretions from Patients with Internal Hordeolum Treated with Hypochlorous Acid Eyelid Wipes
Shu Yang, Bing-Cheng Wu, Zhe Cheng, Lan Li, Yuan-Ping Zhang, Hui Zhao, Han-Mei Zeng, Dong-Fang Qi, Zi-Yao Ma, Jian-Guo Li, Rui Han, Fang-Zhou Qu, Yan Luo, Yi Liu, Xiao-Lei Chen, and Hong-Mei Dai
Research Article (8 pages), Article ID 7550090, Volume 2022 (2022)

Exosomal hsa_circ_0008925 from Urine Is Related to Chronic Renal Fibrosis
Yuhan Cao, Yuanhui Shi, Yuwei Wang, Yanlang Yang, Wenjun Guo, Cuifeng Zhang, Wenjun Pei, and Cong Fu
Research Article (10 pages), Article ID 1899282, Volume 2022 (2022)

Serum and Cerebrospinal Fluid Testing in Optic Neuropathy Patients with Malignant Tumors
Chuan-bin Sun, Geng-hao Liu, Qing Xiao, Yi-nv Zhao, and Qian Ren
Research Article (12 pages), Article ID 7076385, Volume 2022 (2022)

Contents

Polyphenol Extracts from Grape Seeds and Apple Can Reactivate Latent HIV-1 Transcription through Promoting P-TEFb Release from 7SK snRNP
Cong Wang, Huiru Wang, Zhenrui Pan, Jun Wu, Yafei Guo, Jing Zhang, Zixun Xiang, Wei Lu, and Yuhua Xue
Research Article (8 pages), Article ID 6055347, Volume 2022 (2022)

Cytokine Changes in the Aqueous Humor in Rubella-Related Fuchs Heterochromic Iridocyclitis
Yi Mao, Sijie Lin, Chengfang Zhu, Xiaodong Liu, Huping Wu, and Shangkun Ou
Research Article (6 pages), Article ID 8906752, Volume 2022 (2022)

Identification of the Relationship between Hub Genes and Immune Cell Infiltration in Vascular Endothelial Cells of Proliferative Diabetic Retinopathy Using Bioinformatics Methods
Jing Huang and Qiong Zhou
Research Article (21 pages), Article ID 7231046, Volume 2022 (2022)

Age of Rats Affects the Degree of Retinal Neuroinflammatory Response Induced by High Acute Intraocular Pressure
Shuhan Meng, Dan Wen, Jingge Xiao, Qianyue Zhang, Weizhou Fang, Xiao Xue, Tu Hu, and Xiaobo Xia
Research Article (10 pages), Article ID 9404977, Volume 2022 (2022)

[Retracted] The Correlation between Functional Connectivity of the Primary Somatosensory Cortex and Cervical Spinal Cord Microstructural Injury in Patients with Cervical Spondylotic Myelopathy
Guoshu Zhao, Chenlei Zhang, Yaru Zhan, and Laichang He
Research Article (16 pages), Article ID 2623179, Volume 2022 (2022)

Decreased Adiponectin Levels Are a Risk Factor for Cognitive Decline in Spinal Cord Injury
Fan-jie Liu, Hong-hao Xu, Ying Yin, Yuan-zhen Chen, Liang-yu Xie, Hua-zhong Li, Dan-dan Wang, and Bin Shi
Research Article (6 pages), Article ID 5389162, Volume 2022 (2022)

Evaluation of Meibomian Gland Function after Therapy of Eyelid Tumors at Palpebral Margin with Super Pulse CO_2 Laser
Songjiao Zhao, Jueni Duan, Jing Zhang, and Lan Gong
Research Article (6 pages), Article ID 8705436, Volume 2022 (2022)

Identification of Hub Genes Associated with Immune Infiltration in Cardioembolic Stroke by Whole Blood Transcriptome Analysis
Qiaoqiao Li, Xueping Gao, Xueshan Luo, Qingrui Wu, Jintao He, Yang Liu, Yumei Xue, Shulin Wu, and Fang Rao
Research Article (23 pages), Article ID 8086991, Volume 2022 (2022)

Crosslinking-Induced Corneal Endothelium Dysfunction and Its Protection by Topical Ripasudil Treatment
Xuemei Wang, Yanlin Zhong, Minghui Liang, Zhirong Lin, Huping Wu, and Cheng Li
Research Article (12 pages), Article ID 5179247, Volume 2022 (2022)

Hypochlorous Acid Can Be the Novel Option for the Meibomian Gland Dysfunction Dry Eye through Ultrasonic Atomization
Zhiyuan Li, Haiyan Wang, Mo Liang, Zhenghua Li, Yvliang Li, Xiaoping Zhou, and Guoping Kuang
Research Article (12 pages), Article ID 8631038, Volume 2022 (2022)

Outcomes of a Foldable Capsular Vitreous Body Implantation: A Retrospective Study
Xiangzhong Xu, Huimin Ge, Jiajun Li, Weihong Shang, Yuke Ji, Weihua Yang, and Keran Li
Research Article (8 pages), Article ID 6575195, Volume 2021 (2021)

MiR-126-HMGB1-HIF-1 Axis Regulates Endothelial Cell Inflammation during Exposure to Hypoxia-Acidosis
Jinxue Liu, Eileen Wei, Jianqin Wei, Wei Zhou, Keith A. Webster, Bin Zhang, Dong Li, Gaoxing Zhang, Yidong Wei, Yusheng Long, Xiuyu Qi, Qianhuan Zhang, and Dingli Xu
Research Article (14 pages), Article ID 4933194, Volume 2021 (2021)

Comprehensive Analysis to Identify Key Genes Involved in Advanced Atherosclerosis
Tian-ming Huo and Zhi-wei Wang
Research Article (25 pages), Article ID 4026604, Volume 2021 (2021)

Discovery and Validation of Novel Methylation Markers in *Helicobacter pylori*-Associated Gastric Cancer
Huan Wang, Nian-Shuang Li, Cong He, Chuan Xie, Yin Zhu, Nong-Hua Lu, and Yi Hu
Research Article (11 pages), Article ID 4391133, Volume 2021 (2021)

Septicemic Melioidosis Detection Using Support Vector Machine with Five Immune Cell Types
Ke Xu, Fang Lian, Yunfan Quan, Jun Liu, Li Yin, Xuexia Li, Shen Tian, Hua Pei, and Qianfeng Xia
Research Article (9 pages), Article ID 8668978, Volume 2021 (2021)

A Novel Predictive Nomogram including Serum Lipoprotein a Level for Nonsentinel Lymph Node Metastases in Chinese Breast Cancer Patients with Positive Sentinel Lymph Node Metastases
Zeng Fang, Ruizhi Wang, Ciqiu Yang, Dong Wang, Wanna Chen, Bo Lin, Dongsheng Gong, Songqi Li, Jiadong Liang, Xiaoli Liang, Chunxian Zeng, Jie Li, Kun Wang, and Weiming Lv
Research Article (10 pages), Article ID 7879508, Volume 2021 (2021)

The Prognostic Value of the Albumin to Gamma-Glutamyltransferase Ratio in Patients with Hepatocellular Carcinoma Undergoing Radiofrequency Ablation
Wenfeng Liu, Feng Zhang, Bing Quan, Miao Li, Shenxin Lu, Jinghuan Li, Rongxin Chen, and Xin Yin
Research Article (10 pages), Article ID 3514827, Volume 2021 (2021)

PKM2 Is a Potential Diagnostic and Therapeutic Target for Retinitis Pigmentosa
Peiwen Zhu, Qian Yang, Gang Li, and Qing Chang
Research Article (10 pages), Article ID 1602797, Volume 2021 (2021)

Contents

The Ocular Surface Characteristics in Prostate Cancer Patients Treated with Androgen Deprivation Therapy
Weina Li, Xiaofeng Li, Feilun Cui, Zhipeng Xu, Nuo Dong, and Cheng Li
Research Article (6 pages), Article ID 5390195, Volume 2021 (2021)

The Roles of Liver Inflammation and the Insulin Signaling Pathway in PM2.5 Instillation-Induced Insulin Resistance in Wistar Rats
Zhihua Zhang, Shujun Hu, Ping Fan, Ling Li, Shanshan Feng, Huabing Xiao, and Lingyan Zhu
Research Article (11 pages), Article ID 2821673, Volume 2021 (2021)

The Metabolome of Carbapenem-Resistant Klebsiella pneumoniae Infection in Plasma
Zhongwei Wen, Mei Liu, Dong Rui, Xiaoxiao Liao, Rui Su, Zhenming Tang, Zhineng Wen, and Zhougui Ling
Research Article (9 pages), Article ID 7155772, Volume 2021 (2021)

Whole Blood Transcriptome Analysis Reveals the Correlation between Specific Immune Cells and Septicemic Melioidosis
Ke Xu, Dahua Xu, Hua Pei, Yunfan Quan, Jun Liu, Li Yin, Xuexia Li, ShenTian, Kongning Li, and Qianfeng Xia
Research Article (13 pages), Article ID 6166492, Volume 2021 (2021)

OATP1B1 Plays an Important Role in the Transport and Treatment Efficacy of Sorafenib in Hepatocellular Carcinoma
Jinhua Wen and Menghua Zhao
Research Article (13 pages), Article ID 9711179, Volume 2021 (2021)

Hindawi
Disease Markers
Volume 2023, Article ID 9879526, 1 page
https://doi.org/10.1155/2023/9879526

Retraction

Retracted: The Correlation between Functional Connectivity of the Primary Somatosensory Cortex and Cervical Spinal Cord Microstructural Injury in Patients with Cervical Spondylotic Myelopathy

Disease Markers

Received 20 June 2023; Accepted 20 June 2023; Published 21 June 2023

This article has been retracted by Hindawi following an investigation undertaken by the publisher [1]. This investigation has uncovered evidence of one or more of the following indicators of systematic manipulation of the publication process:

(1) Discrepancies in scope

(2) Discrepancies in the description of the research reported

(3) Discrepancies between the availability of data and the research described

(4) Inappropriate citations

(5) Incoherent, meaningless and/or irrelevant content included in the article

(6) Peer-review manipulation

The presence of these indicators undermines our confidence in the integrity of the article's content and we cannot, therefore, vouch for its reliability. Please note that this notice is intended solely to alert readers that the content of this article is unreliable. We have not investigated whether authors were aware of or involved in the systematic manipulation of the publication process.

Wiley and Hindawi regrets that the usual quality checks did not identify these issues before publication and have since put additional measures in place to safeguard research integrity.

We wish to credit our own Research Integrity and Research Publishing teams and anonymous and named external researchers and research integrity experts for contributing to this investigation.

The corresponding author, as the representative of all authors, has been given the opportunity to register their agreement or disagreement to this retraction. We have kept a record of any response received.

References

[1] G. Zhao, C. Zhang, Y. Zhan, and L. He, "The Correlation between Functional Connectivity of the Primary Somatosensory Cortex and Cervical Spinal Cord Microstructural Injury in Patients with Cervical Spondylotic Myelopathy," *Disease Markers*, vol. 2022, Article ID 2623179, 16 pages, 2022.

Hindawi
Disease Markers
Volume 2023, Article ID 9813896, 1 page
https://doi.org/10.1155/2023/9813896

Retraction

Retracted: Effects of Medium-Term Soft Contact Lens Fitting on Dry Eye: Analyses Using Ultra-High Resolution Optical Coherence Tomography and Digital Slit-Lamp Biomicroscopy

Disease Markers

Received 20 June 2023; Accepted 20 June 2023; Published 21 June 2023

This article has been retracted by Hindawi following an investigation undertaken by the publisher [1]. This investigation has uncovered evidence of one or more of the following indicators of systematic manipulation of the publication process:

(1) Discrepancies in scope

(2) Discrepancies in the description of the research reported

(3) Discrepancies between the availability of data and the research described

(4) Inappropriate citations

(5) Incoherent, meaningless and/or irrelevant content included in the article

(6) Peer-review manipulation

The presence of these indicators undermines our confidence in the integrity of the article's content and we cannot, therefore, vouch for its reliability. Please note that this notice is intended solely to alert readers that the content of this article is unreliable. We have not investigated whether authors were aware of or involved in the systematic manipulation of the publication process.

Wiley and Hindawi regrets that the usual quality checks did not identify these issues before publication and have since put additional measures in place to safeguard research integrity.

We wish to credit our own Research Integrity and Research Publishing teams and anonymous and named external researchers and research integrity experts for contributing to this investigation.

The corresponding author, as the representative of all authors, has been given the opportunity to register their agreement or disagreement to this retraction. We have kept a record of any response received.

References

[1] Y. Wang, Z. Xu, S. Chen et al., "Effects of Medium-Term Soft Contact Lens Fitting on Dry Eye: Analyses Using Ultra-High Resolution Optical Coherence Tomography and Digital Slit-Lamp Biomicroscopy," *Disease Markers*, vol. 2022, Article ID 7220706, 14 pages, 2022.

Hindawi
Disease Markers
Volume 2022, Article ID 8323946, 14 pages
https://doi.org/10.1155/2022/8323946

Research Article

RhoA with Associated TRAb or FT3 in the Diagnosis and Prediction of Graves' Ophthalmopathy

Sidi Zhao,[1] Shuangshuang Shi,[1] Wanchen Yang,[2] Hanqing Wang,[1] Tianming Jian,[1] Qing He,[3] Yang Liu,[4] Xiaoming Huang,[5] and Tong Wu[1,5]

[1]*Tianjin Key Laboratory of Retinal Functions and Diseases, Tianjin Branch of National Clinical Research Center for Ocular Disease, Eye Institute and School of Optometry, Tianjin Medical University Eye Hospital, Tianjin 300384, China*
[2]*Department of Ophthalmology, First Hospital of Qinhuangdao, Qinhuangdao, 066000 Hebei Province, China*
[3]*Department of Endocrinology, Tianjin Medical University General Hospital, Tianjin 300041, China*
[4]*Research and Development Department, Microsensor Labs, Chicago, IL 60602, USA*
[5]*Sichuan Eye Hospital, AIER Eye Hospital Group, Chengdu, Sichuan Province, China*

Correspondence should be addressed to Xiaoming Huang; hxm@tmu.edu.cn and Tong Wu; victorwutong@163.com

Received 17 December 2021; Revised 18 May 2022; Accepted 1 July 2022; Published 29 July 2022

Academic Editor: Ting Su

During Graves' disease (GD) treatment, Graves' ophthalmopathy (GO) is often ignored because only mild ocular symptoms are present in early GD. Therefore, we performed isobaric tags for relative and absolute quantification (iTRAQ) analysis and measured relevant endocrine hormones to identify predisposing factors of GO. Serum samples from 3 patients with mild GD and GO and 3 patients with GD but without GO were analyzed by iTRAQ. Based on their clinical data, 60 patients with GD were divided into the GO-free and GO groups. All patients were followed up for 7 months. Their eye conditions and changes in related biochemical indexes were recorded. The iTRAQ results showed that RhoA expression was upregulated and correlated significantly with the tight junction pathway and immunity. The changes in FT3 and RhoA from baseline to 7 months, the FT3 and RhoA baseline levels, and the TRAb titer levels in patients with GD significantly differed between the groups. ELISA and western blotting for RhoA, TRAb, and FT3 in the serum samples from GO patients showed significant upregulation, as well as elevated serum RhoA and TRAb levels in the mild stage of GO. At 7 months, the serum RhoA and FT3 levels were elevated. RhoA is a potential biomarker for mild GO. In GD patients, if an elevated serum RhoA level is accompanied by an elevated TRAb or FT3 level, GO is highly likely to occur, even when obvious ocular symptoms are absent.

1. Introduction

Graves' disease (GD) is an autoimmune thyroid disease and the main cause of hyperthyroidism in adults. Incidence rates are approximately 3% for females and 0.5% for males [1, 2]. Graves' ophthalmopathy (GO) is the most common extrathyroidal manifestation. Approximately 25%-50% of GD patients have ocular involvement [3, 4]. Most GO patients have hyperthyroidism, though a small number of cases may be hypo- or euthyroid [5–7]. Approximately 90% of GO patients display symptoms of eyelid retraction, which is an initial symptom and sign of early disease [8, 9]. Approximately 3% to 5% of GO patients will develop severe disease, which involves severe inflammation, eye pain, and vision-threatening corneal ulcers or compressive optic neuropathy (CON) [3, 4, 10, 11]. The appearance of GO is often ignored due to the presence of only mild ocular symptoms in the early stage.

Proteomics is a large-scale, high-throughput, and systematic study of the composition and function of all proteins in a certain type of cell, tissue, or body fluid. High-quality protein separation and identification technology combined with full utilization of bioinformatics reflects changes in the composition and expression level of proteins as a whole, which helps to identify those related to the formation and development of diseases and to explore the process of disease occurrence and development. Biological mechanisms and clinically related research as well as research and

development of new drug targets, among others, have been widely employed [12–14]. In recent years, high-throughput mass spectrometry has been implemented and used in the study of screening serum proteins, revealing many molecules with biomarker values.

In the past few decades, the incidence of GO has shown an increasing trend. GO severely affects vision, leading to blindness and depression in most patients. Therefore, treatment early in the mild stage of the disease is likely to result in a better prognosis. The purpose of this study was to determine risk factors leading to the onset of GO, which is very important for its early diagnosis. We observed changes in levels of endocrine hormones in GD patients and discovered possible markers for early diagnosis of GO through proteomics, with a view toward early diagnosis of CON and prevention of visual impairment caused by it. We sought to provide new ideas for improving the diagnosis and treatment of GO and for evaluating prognosis.

2. Materials and Methods

2.1. Subjects. We collected clinical data and serum samples for GD patients admitted to the Tianjin Medical University General Hospital from June 2018 to October 2019. We randomly collected venous blood from 3 patients in the mild stage who were first diagnosed with GO complicated with GD (experimental group) and 3 diagnosed with GD without GO (control group) treated at the Tianjin Medical University Eye Hospital from January 2020 to October 2020. The present study was approved by the Tianjin Medical University Eye Hospital Foundation Institutional Review Board (REC No. 2020KY(L)-01) and followed the principles of the Declaration of Helsinki. Written informed consent was obtained from all study subjects. The study participants were not financially compensated.

Diagnostic criteria of GD were as follows [1, 2]: (1) clinical diagnosis of hyperthyroidism, (2) diffuse thyroid enlargement (confirmed by palpation and B-ultrasound), with some cases lacking goiter, (3) exophthalmos and other infiltrating eye signs, (4) anterior tibial mucin edema, and (5) TRAb, TSAb, and TPOAb positivity. Of the above criteria, items (1) and (2) were essential for diagnosis, and items (3), (4), and (5) were auxiliary factors for diagnosis.

GO diagnostic criteria were as follows [5]: (1) Mild GO usually involves one or more of the following symptoms: mild eyelid retraction (<2 mm), mild soft tissue damage, exophthalmos < 3 mm of the same population and sex, no diplopia or intermittent diplopia, and corneal exposure which can be improved by a lubricant, and (2) Moderate to severe GO usually has the following two or more symptoms: eyelid retraction ≥ 2 mm, moderate or severe soft tissue damage, exophthalmos ≥ the same population and sex normal value 3 mm, and persistent or intermittent diplopia.

The inclusion criteria for the experimental group were as follows: (1) initial diagnosis of GD with ophthalmopathy, (2) ophthalmopathy diagnosed as mild GO, (3) oral methimazole prescribed for GD treatment, and (4) no treatment for ophthalmopathy.

The inclusion criteria for the control group were as follows: (1) initial diagnosis of GD without ophthalmopathy and (2) oral methimazole prescribed for GD treatment.

Exclusion criteria were as follows: (1) hyperthyroidism caused by nodular goiter, thyroid cancer, high-functioning adenoma, and thyroiditis, (2) thyroidectomy, (3) primary hypothyroidism, (4) orbital inflammatory pseudotumors, orbital cellulitis, and orbital granuloma, among others, and (5) pregnancy.

The patients were divided into two groups based on changes to the eye condition: a GO-free (36 cases) group and a GO (24 cases) group. All patients were given methimazole for GD. According to EUGOGO [5], all patients in the GO group were evaluated according to the CAS. No patient scored higher than 3. Therefore, none of the patients were considered in the active disease phase. Because these patients were first diagnosed in the Endocrine Department, ocular manifestations of the disease may not have been obvious.

2.2. Isobaric Tags for Relative and Absolute Quantification (iTRAQ) Protein Spectrum Analysis. Peripheral venous blood was collected from patients with GO and GO-free disease and centrifuged as soon as possible to separate the serum, which was immediately stored at -80°C. High-abundance proteins were removed according to the instructions of the ProteoMiner™ kit (Bio-Rad Laboratories, USA). Protein quantification was carried out according to the BCA method, and SDS-PAGE was performed. The samples were reduced, alkylated, and enzymatically hydrolyzed. The isotope mass label iTRAQ reagent was used for labeling and high pH reverse-phase fractionation. Finally, the protein samples were analyzed using a nanoupgraded reverse-phase chromatography-TripleTOF™ 5600.

2.3. ELISA. Using a serum separator tube, the blood samples were allowed to clot for two hours at room temperature or overnight at 4°C before centrifugation for 20 minutes at 1000 × g. Freshly prepared serum was assayed immediately or stored in aliquots at -20°C or -80°C for later use. Experiments were performed according to the manufacturer's protocol of the FT3 ELISA kit (LEVELOP, Wuxi, China) and TRAb ELISA kit (GTX, Shanghai, China).

2.4. Western Blotting. Whole blood samples were centrifuged at 4°C 3000 × g for 20 minutes. The serum samples were added to serum protein extracts and centrifuged at 14,000 × g at 4°C for 10 minutes. Proteins (30 μg) were separated by SDS-PAGE and transferred to polyvinylidene fluoride (PVDF) membranes (Bio-Rad Laboratories, USA). The membranes were washed for 1-2 minutes in 0.1% Tween-20 (TBST) (Solarbio, Beijing, China), blocked (5% skimmed milk powder) at 37°C for 1 hour, and incubated with a primary antibody against RhoA (1 : 5000, Abcam, UK), overnight at 4°C. After rinsing with TBST three times, the membrane was incubated with a rabbit/mouse secondary antibody at room temperature for 1 hour and exposed.

2.5. Biochemical Index Detection. Blood was drawn from fasting patients in the morning. Chemiluminescence immunoassays using Abbott reagents and instruments were used

to measure free thyroid function. Chemiluminescence immunoassays using German Siemens reagents and instruments were employed for TPOAb and TgAb detection. Electrochemiluminescence immunoassays using Roche reagents and instruments were used to detect TRAb. The reference value range was 2.63~5.70 pmol/L for FT3, 9.01~19.05 pmol/L for FT4, 0.350~4.940 μU/L for TSH, 0.00~1.75 IU/L for TRAb, 0.00~35.00 IU/mL for TPOAb, and 0.00~40.00 IU/mL for TgAb. Because the measurement range for TPOAb was 10~1000 IU/mL, a level ≥ 1000 IU/mL was considered to be 1000 IU/mL, similarly, as the range for TgAb was 20~3000 IU/mL, a level ≥ 3000 IU/mL was considered to be 3000 IU/mL.

2.6. Data Collection. We conducted a 7-month follow-up to record patient serum samples and clinical data from June 2018 to October 2019. Age, sex, treatment of thyroid disease, history of hyperthyroidism, and monthly levels of thyroid-related hormones (FT3, FT4, TSH, TRAb, TPOAb, and TgAb) were collected, related biochemical indexes and the time of occurrence of various eye signs were measured.

2.7. Statistical Analysis. Analyses were performed using SPSS version 23.0 and GraphPad Prism version 8.0 for Windows. All numerical data conforming to a normal distribution are expressed as the mean ± SD. Data not conforming to a normal distribution are presented as medians (interquartile ranges), and enumeration data are given as percentages. The Mann–Whitney U test was used for comparison of age. Two-tailed Fisher's exact tests were applied to compare enumeration data. Mauchly's test and the Greenhouse-Geisser correction method were utilized to determine significant differences in thyroid hormone levels of continuous data between the groups. Spearman's rank correlation coefficient was used to determine whether different hormone or antibody titer levels of the two groups correlated with the occurrence of GO. ROC curves were drawn to assess whether hormone or antibody levels predict GO pathogenesis at certain cutoff levels. The area under the ROC curve (AUC) was evaluated for diagnostic value. $P < 0.05$ was considered statistically significant.

3. Results

3.1. Demographic and Ophthalmological Data. The GO and GO-free groups were similar in age at diagnosis and sex (Supplementary Table 1).

3.2. Results of iTRAQ. We randomly collected venous blood from 3 GO with GD patients (experimental group) and 3 GD patients without GO (control group) with matching sex and age and performed iTRAQ protein profile analysis. As Pearson coefficients between the control group and the experimental group samples were greater than 0.86, the data were significant and repeatable.

In the principal component analysis of the protein quantitative results, the control group and the experimental group aggregated obviously into different clusters, indicating that protein expression in the experimental group was significantly different from that in the control group (Figure 1(a)).

We detected 1552 proteins. Compared with the control group, the experimental group showed 229 differential proteins with expression difference > 1.5. Among these, 129 proteins were upregulated and 100 downregulated in the experimental group. Among them, the most significantly upregulated proteins were YBX3, RAB3GAP2, APOC3, GCA, and CSRP2, the most significantly downregulated proteins were POLA1, SMAP, ETFB, RNMT, and MAGED4 (Figures 1(b) and 1(c)).

To better investigate the biochemical process of the occurrence and development of GO, we conducted Gene Ontology analysis of differential proteins, mainly from three aspects: cell component, molecular function, and biological process. GO analysis was performed on upregulated proteins. The functions of these targeted proteins in cell components mainly involved focal adhesions and cell substrate joints. Molecular function terms largely were cell adhesion molecule binding and actin binding. In terms of biological process, enrichment in such processes as actin polymerization and depolymerization, cell adhesion, and neutrophil-mediated immunity was observed. For downregulated differential proteins (Figure 1(e)), cell composition terms were mostly the cytoplasm and extracellular matrix. Molecular function mainly involved antigen binding and serine endopeptidase activity, and biological process terms were the protein activation cascade, complement activation, and acute inflammation.

Through KEGG analysis (Figures 1(f) and 1(g)), upregulated differential proteins participate in signaling pathways such as actin cytoskeleton regulation, platelet activation, pathogenic *Escherichia coli* infection, tight junctions, and transendothelial migration of leukocytes. Downregulated proteins are mainly involved in the complement and coagulation cascade, *Staphylococcus aureus* infection, and prion diseases. We also performed gene set enrichment analysis ($P < 0.05$, FDR < 0.25) on the quantitative data for differential proteins (Figures 2(a) and 2(b)). The results showed tight junction signaling pathways to be enriched and upregulated in GO, consistent with the KEGG results. The main enriched proteins were also similar to the KEGG results, including YBX3, TJP2, RhoA, RAC1, MYL12A, MYH9, F11R, and CTTN. These proteins are all upregulated in GO.

Pearson correlation analysis revealed a high correlation of expression of proteins involved in the GSEA tight junction pathway (Figure 2(c)). High correlations, such as for RhoA, RAC1, F11R, and TJP2, suggest that these proteins may be similar in function. Furthermore, protein-protein interaction analysis of differential proteins related to tight junctions showed that RhoA is at the center of the interaction (Figure 2(d)). Next, we used western blotting to detect RhoA in serum samples from the two groups (Figure 2(e)) and calculated the grayscale value (Figure 2(g)). ELISA was applied to detect FT3 and TRAb (Figure 2(f)). The results showed that RhoA, FT3, and TRAb levels were significantly higher in the GO group than in the GO-free group.

3.3. Changes in RhoA, FT3, FT4, and TSH Levels. In the GO-free group, 24 patients (66.7%) developed hypothyroidism, with reversion to normal thyroid function levels occurring

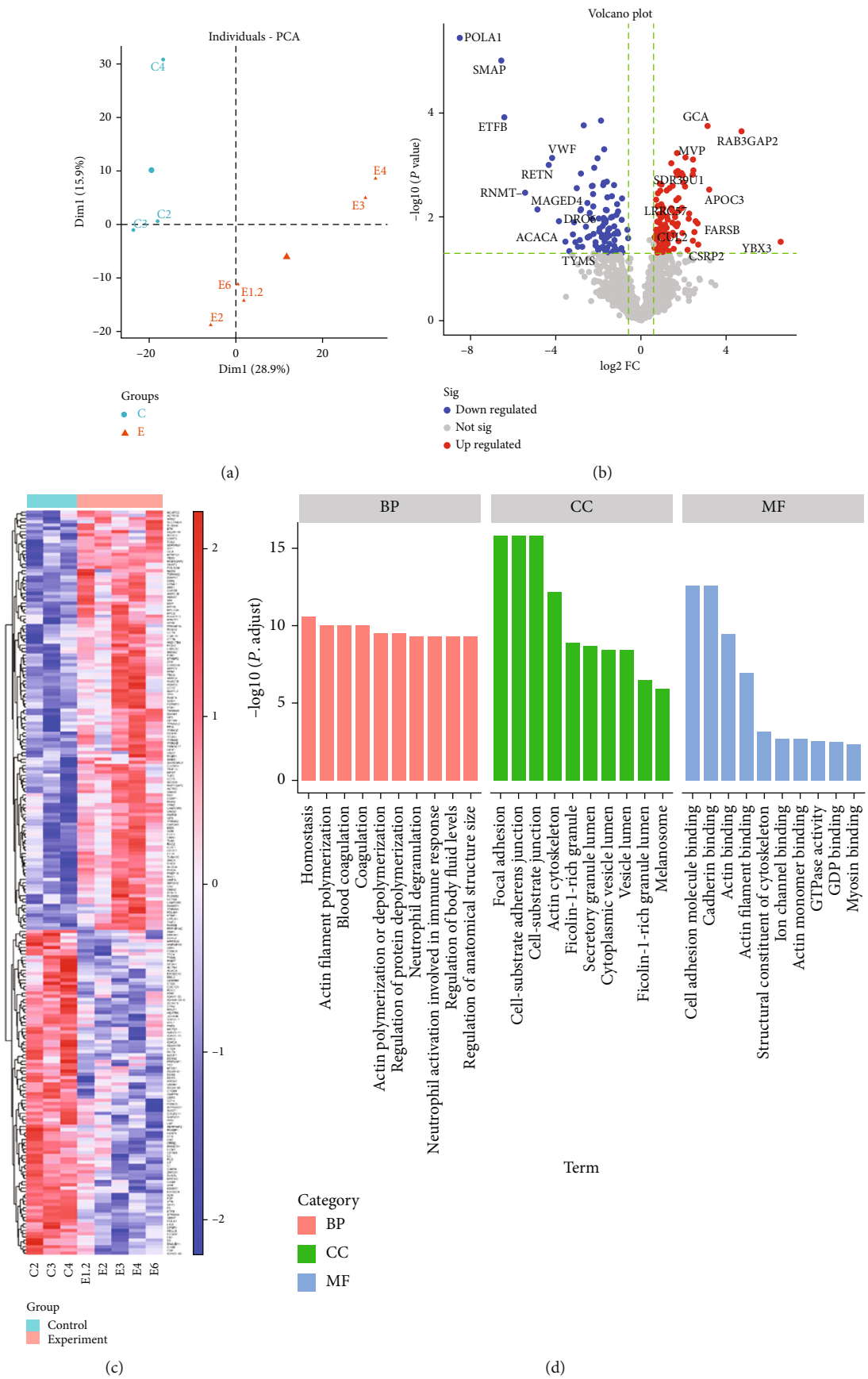

Figure 1: Continued.

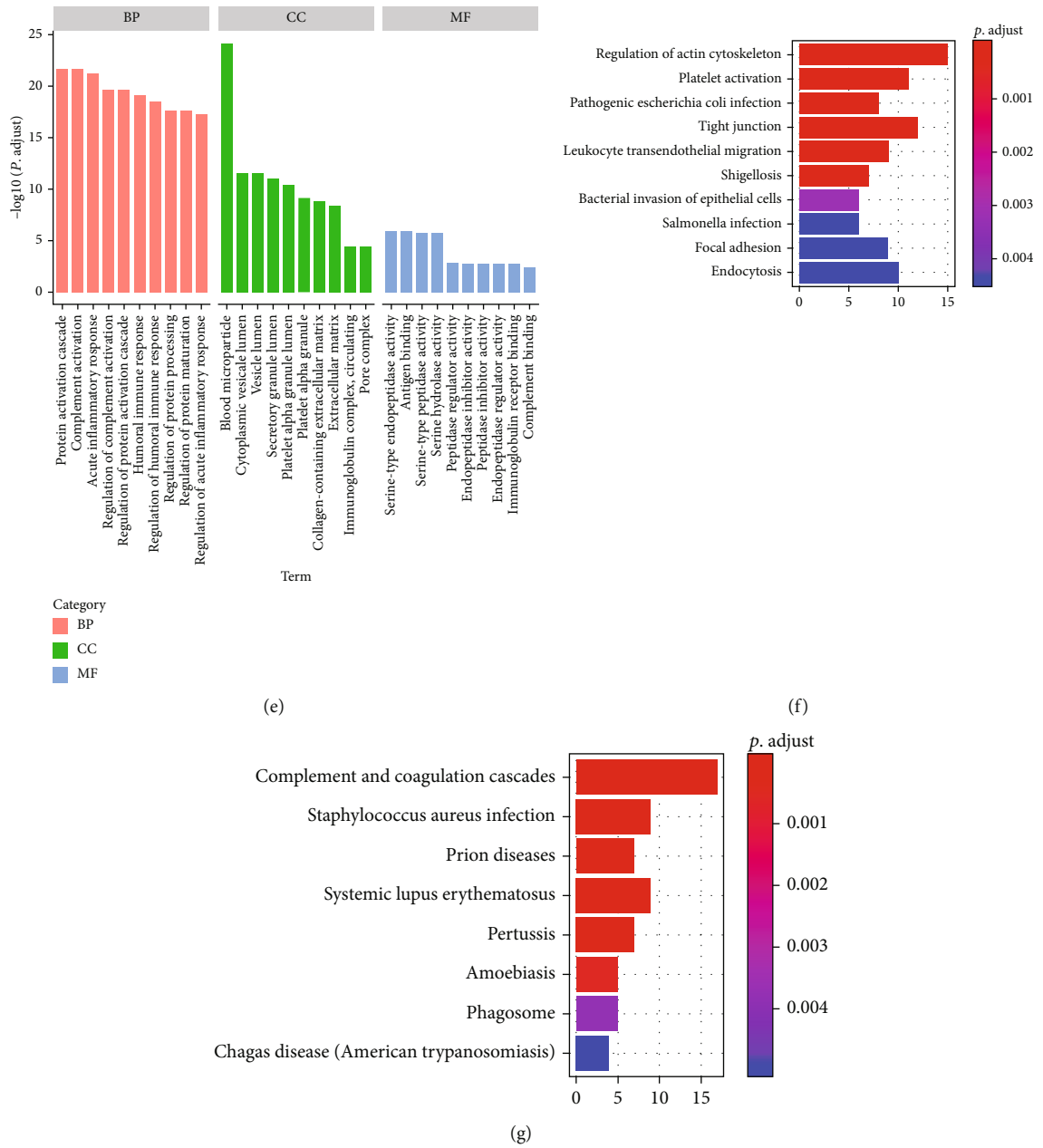

Figure 1: iTRAQ results. (a) Protein quantitative results were analyzed by principal component analysis. The control group and the experimental group aggregated significantly into different clusters. Blue: control group; red: experiment group. Heatmap (b) and volcano plots (c) protein expression between the control and experimental groups (fold change > 1.5 and adjusted P value < 0.05). Red: upregulated; blue: downregulated. (d) GO enrichment analysis was performed for upregulated proteins. The results showed that the upregulated proteins are mainly involved in actin filament polymerization, focal adhesion, and actin binding. (e) GO enrichment analysis was performed for downregulated proteins. The results showed that the downregulated proteins are mainly involved in the protein activation cascade, blood microparticles, and antigen binding. (f) KEGG pathway analysis was performed for upregulated proteins. The results showed that the upregulated proteins are mainly involved in the regulation of actin cytoskeleton, platelet activation, pathogenic Escherichia coli infection, and tight junction. (g) KEGG pathway analysis was performed for downregulated proteins. The results showed that the downregulated proteins are mainly involved in complement and coagulation cascades, Staphylococcus aureus infection, prion disease, and systemic lupus erythematosus.

in 12 (33.3%). In the GO group, 20 patients (83.3%) had hypothyroidism, and 4 experienced reversions to normal thyroid function levels (16.7%). Overall, changes in the thyroid hormone levels of the two groups of patients were recorded for 7 consecutive months (Figures 3(b)–3(d)), and serum RhoA levels were assessed by ELISA (Figure 3(a)). We performed repeated-measurement data analysis of variance for FT3, FT4, TSH, and RhoA at different time points. Mauchly's test of sphericity was performed on factors in each group, however, the data did not satisfy

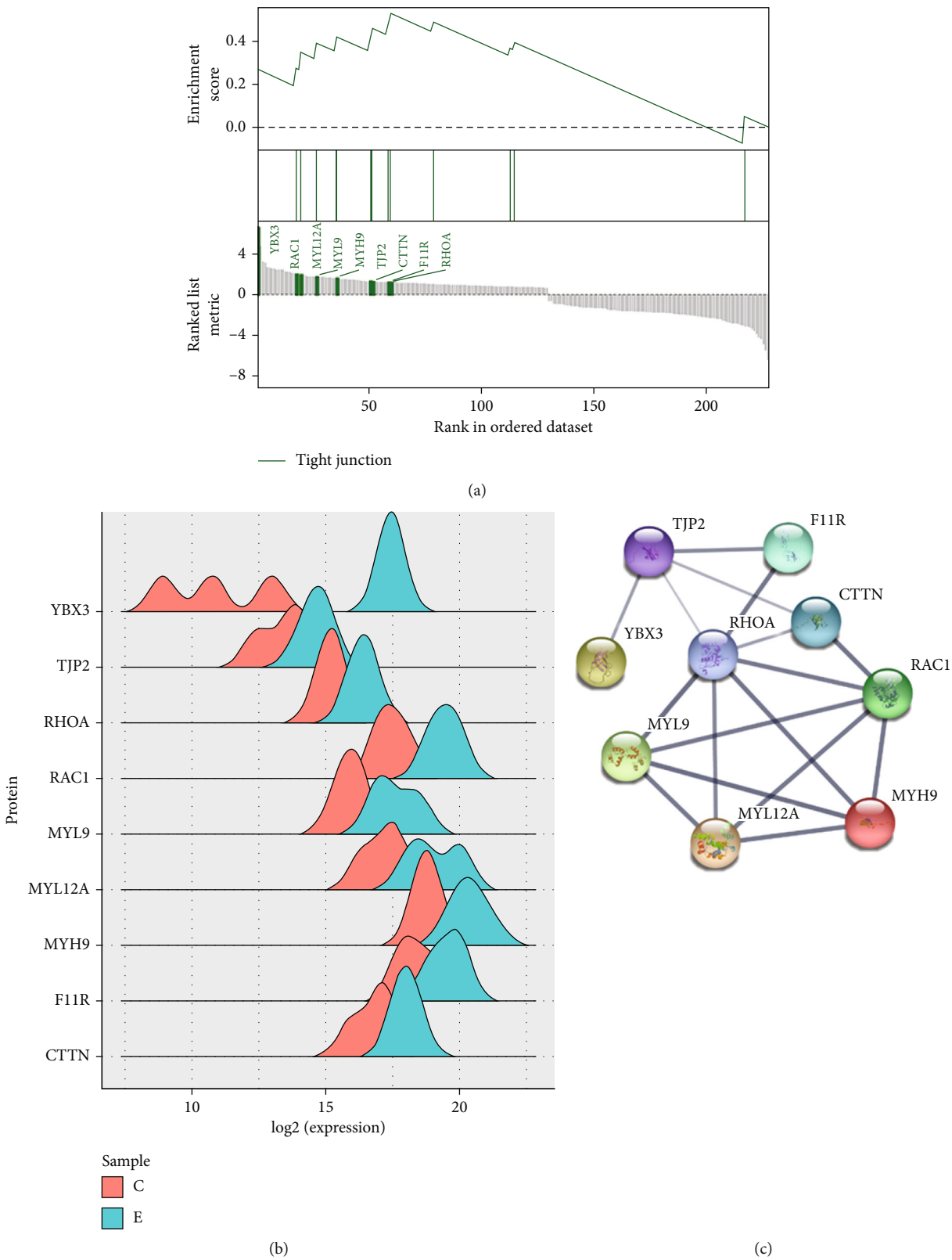

Figure 2: Continued.

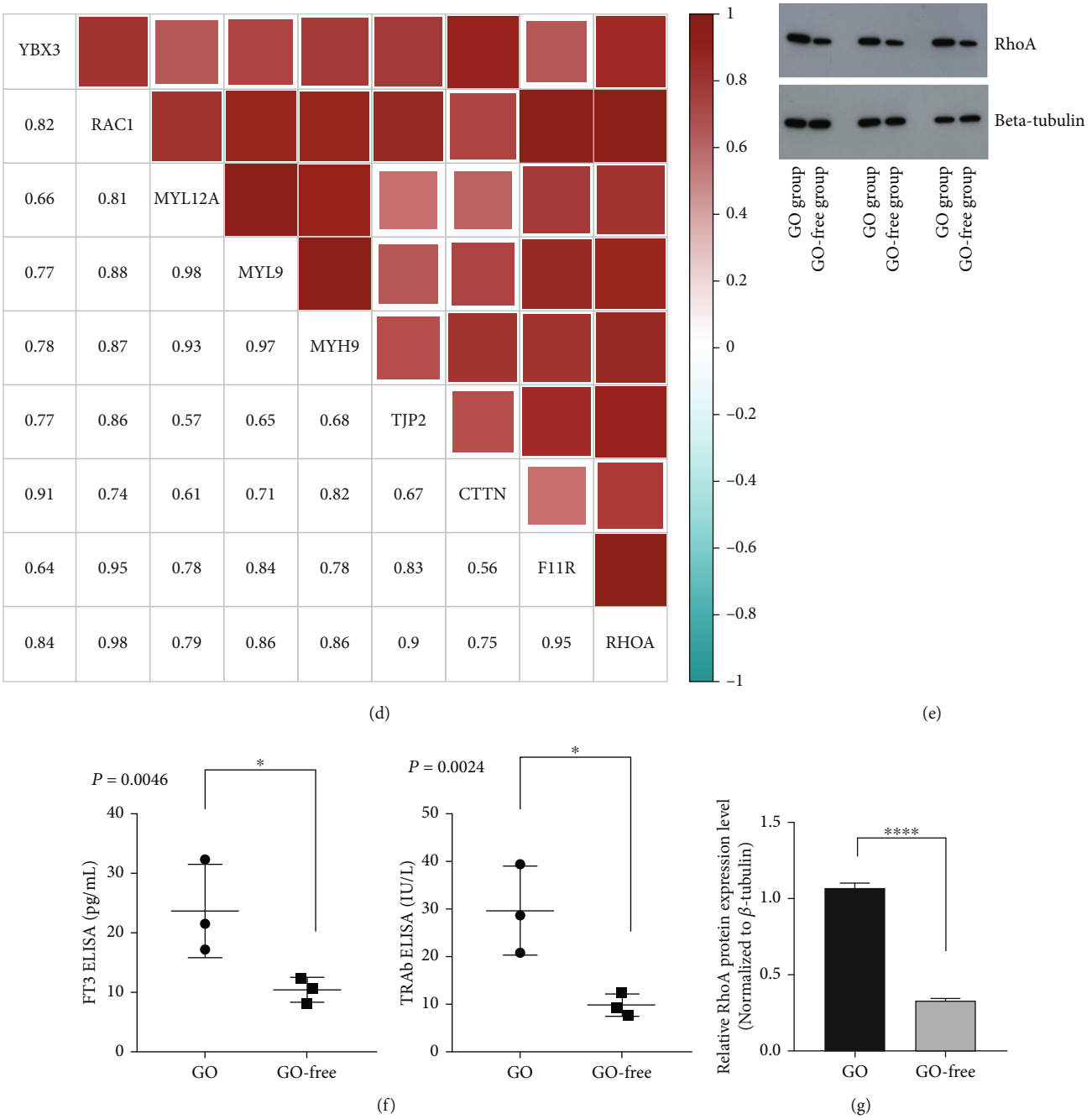

Figure 2: Results of bioinformatics analysis and results of ELISA and western blotting. (a) GSEA analyses of gene sets for tight junctions. (b) Ridge plot reflecting protein expression of the experimental group and the control group. Blue: experimental group; red: control group. (c) Perform protein-protein interaction analysis on differential proteins related to tight junctions, and RhoA is at the center of the interaction. (d) Pearson correlation analysis was performed on proteins involved in the tight junction pathway of GSEA. Serum samples from 3 patients with newly diagnosed GO complicated with GD (experimental group) and 3 with GD without GO (control group). These serum samples were detected by WB and ELISA. (e) Western blotting for RhoA. (f) Results of FT3 ELISA and results of TRAb ELISA. (g) The grayscale value of the RhoA band ($P < 0.0001$).

the sphere hypothesis ($P < 0.05$, Supplementary Table 2). Hence, the values were adjusted using the Greenhouse-Geisser correction method (Supplementary Tables 2 and 3). A correlation between repeated measurements of FT3, FT4, TSH, and RhoA data was detected. After eliminating the interaction of hormones and time, FT3, FT4, and RhoA levels in the GO-free and GO groups were statistically significant, though there were no significant differences in TSH. Nevertheless, monthly FT3, FT4, and RhoA levels were higher in the GO group than in the GO-free group.

3.4. Changes in Basal Levels, Endpoint Values, and Differences in Thyroid-Related Hormone and RhoA Levels. For the two groups, we calculated differences in hormone

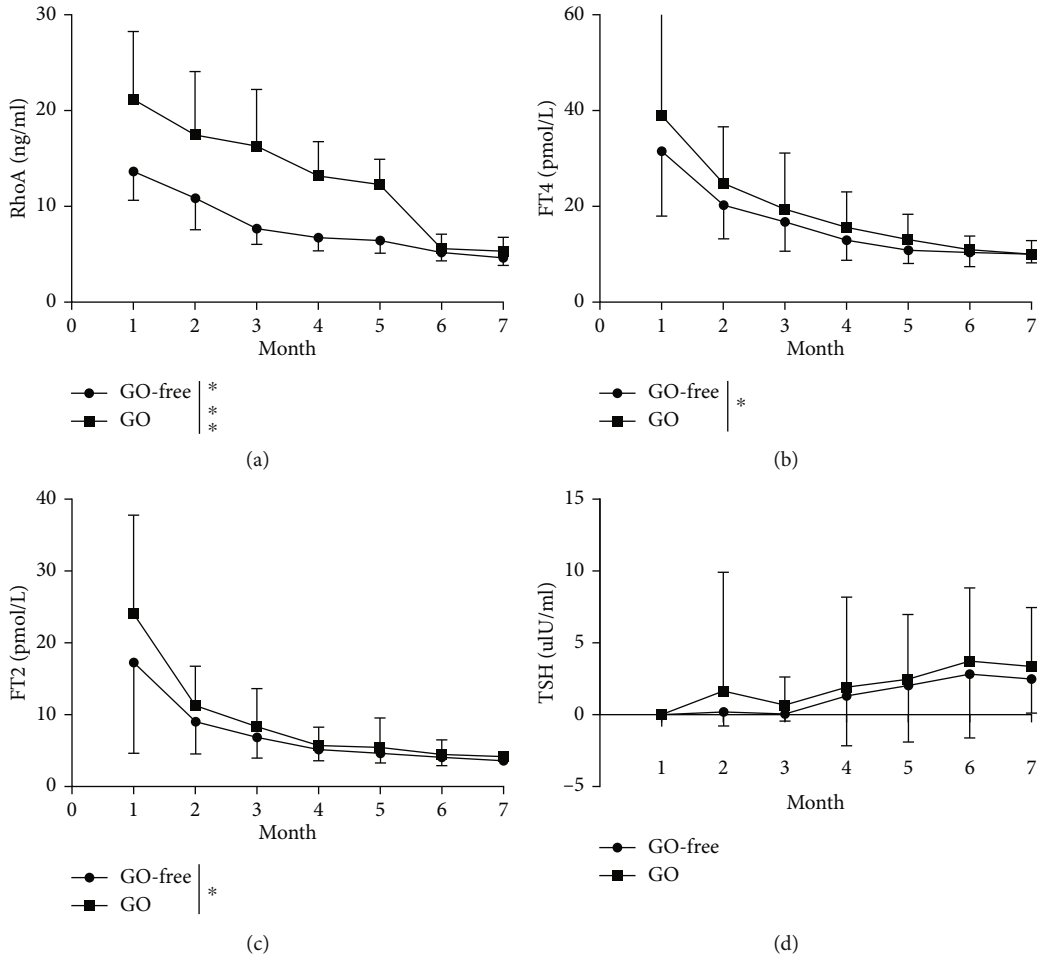

Figure 3: RhoA, FT3, FT4, and TSH levels in patients in the GO-free and GO groups over a 7-month follow-up period. (a–c) After eliminating the interaction between hormones and time by the Greenhouse-Geisser correction method, monthly RhoA, FT4, and FT3 levels in the GO group were higher than those in the GO-free group. (d) After eliminating the interaction of hormones and time by the Greenhouse-Geisser correction method, no significant differences in TSH levels were observed between the GO-free and GO groups.

and RhoA levels between baseline and the follow-up endpoint to evaluate fluctuations (Table 1). Numerical data in accordance with a normal distribution are expressed as the mean ± SD, and the parameter *t*-test was used. Data that did not conform to a normal distribution are presented as the median (range of quartiles), and the Mann–Whitney *U* test was used. The difference between basal levels and endpoint values was statistically significant for RhoA and FT3 levels but not for FT4 or TSH.

3.5. Changes in Thyroid Antibody Titer at the First Diagnosis of GD. Because TRAb levels change slightly during short-term treatment and TPOAb and TgAb are not affected by antithyroid drugs, we compared antibody titers of the two groups of patients at first diagnosis of GD using the Mann–Whitney *U* test. The difference in TRAb titer ($P = 0.004$) was statistically significant (Figure 4(a)), whereas that for TPOAb and TgAb titers ($P = 0.973$, $P = 0.929$) was not (Figures 4(b) and 4(c)).

3.6. Correlation Analysis of Thyroid Hormone and Related Antibodies with GO. Thyroid hormone levels, antibody titers, and RhoA levels were analyzed using Spearman rank correlation analysis, revealing that basal RhoA levels correlated positively with the incidence of GO. In addition, the higher the basal RhoA level was, the more likely the patient was to develop GO. Moreover, the difference between the RhoA endpoint value and basal level correlated negatively with the incidence of GO. As the absolute value was greater when there was a smaller difference between the RhoA endpoint value and the basal level, such patients were likely to develop GO. In addition, basal FT3 levels correlated positively with GO incidence, where the greater the basal FT3 level was, the more prone the patient was to developing GO. The difference between the FT3 endpoint value and basal level correlated negatively, with a smaller difference between the FT3 endpoint value and basal level indicating a greater absolute value and likely GO development. TRAb titers at first diagnosis of GD also correlated positively with the incidence of GO, and patients with a large TRAb value were prone to develop GO. Conversely, FT4, TSH, TPOAb, and TgAb levels did not correlate with GO onset (Table 2).

3.7. Diagnostic Significance of RhoA, FT3, FT4, TSH, and Related Antibodies in Onset of GO. We used specificity as the horizontal axis and sensitivity as the vertical axis to

Table 1: Comparison of FT3\FT4\TSH endpoint values and baseline values between the two groups of patients.

Parameters	GO-free	GO	*P* value
Basal RhoA level	13.63 ± 2.99	25.09 (14.77, 26.11)	**<0.001**
Endpoint RhoA level	5.16 ± 0.86	5.59 ± 1.50	0.1643
RhoA difference	−8.47 ± −15.59	-18.03 (-20.69, -10.95)	**<0.001**
Basal FT3 level	13.00 (8.81, 17.17)	21.82 (12.35, 36.38)	**0.027**
Endpoint of FT3	3.89 (3.36, 4.71)	3.97 (3.60, 4.92)	0.407
FT3 difference	-9.35 (-13.28, -5.17)	-17.45 (-31.18, -8.93)	**0.036**
Basal FT4 levels	28.08 (23.24, 33.60)	30.72 (25.38, 43.33)	0.215
Endpoint of FT4	10.38 (8.87, 11.24)	10.29 (8.27, 12.91)	0.979
FT4 difference	-17.83 (-24.84, -12.58)	-21.52 (-33.59, -15.25)	0.130
Basal TSH levels	0.004 (0.004, 0.004)	0.004 (0.004, 0.004)	0.960
Endpoint of TSH	0.442 (0.142, 3.889)	2.425 (0.048, 5.209)	0.581
TSH difference	0.440 (0.100, 3.878)	2.425 (0.045, 5.203)	0.546

RhoA difference: difference between the RhoA endpoint value and the basal level. FT3 difference: difference between the FT3 endpoint value and the basal level. FT4 difference: difference between the FT4 endpoint value and basal level. TSH difference: difference between the TSH endpoint value and basal level. Statistically significant results are in bold.

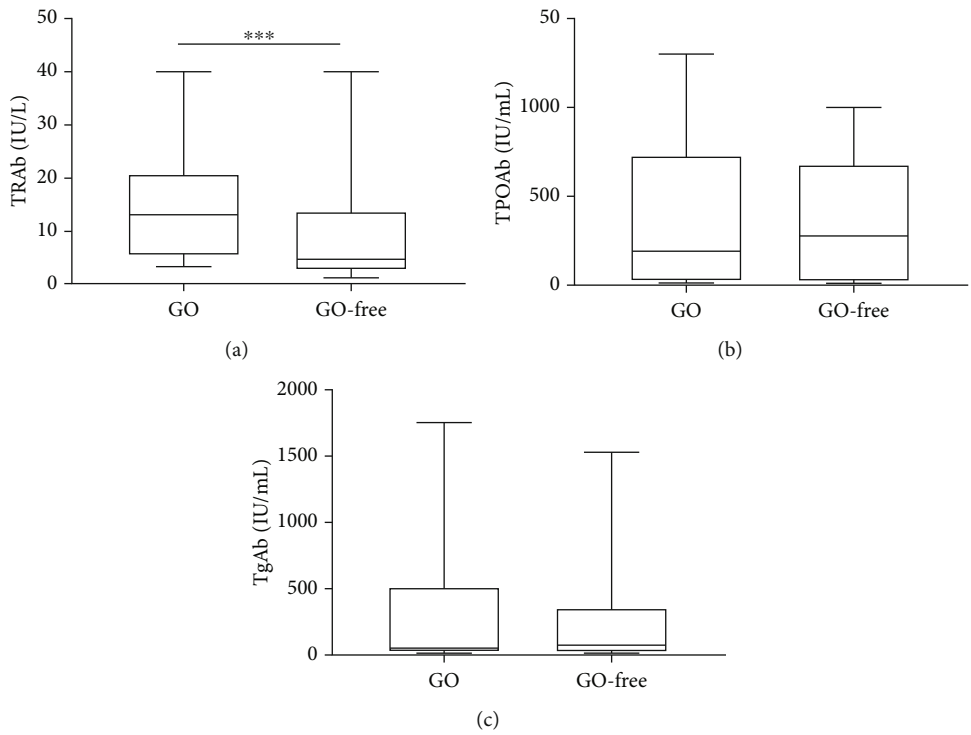

Figure 4: Differences in thyroid antibody titer at first diagnosis of GD. (a) The difference in TRAb titer levels was statistically significant ($P = 0.004$). (b, c) TPOAb ($P = 0.972$) and TgAb ($P = 0.929$) titer levels were not statistically significant. Median (line), interquartile range (box), and total range (whiskers) for TRAb, TPOAb, and TgAb titers between the GO-free group and the GO group when the two groups of patients were diagnosed with GD.

generate a ROC curve to evaluate the diagnostic significance of thyroid hormones, RhoA, and related antibodies. The results demonstrated that basal FT3 levels, basal RhoA levels, and the difference between basal FT3 levels and FT3 endpoint values and the difference between basal RhoA and RhoA endpoint values had diagnostic values (the difference indicates the absolute value) (Figure 5(a)). When patients were diagnosed with GD, TRAb titers also had diagnostic values and were superior to FT3. However, FT4, TSH, TPOAb, and TgAb levels exhibited no diagnostic value (Figure 5(b) and Table 2).

4. Discussion

GO is an autoimmune disease and a common orbital disease that affects vision eye movement and appearance. GO is seriously detrimental to quality of life. The incidence rate of GO is approximately 16 females and 3 males per 100,000 people

Table 2: Correlation coefficients and diagnostic significance of thyroid hormone and related antibodies with GO incidence for the two groups.

Parameters	r	P value	Area under the curve (AUC)	P value	Confidence interval of 0.95	
					Lower bound	Upper bound
Basal RhoA levels	0.501	**0.001**	0.795	**0.001**	0.652	0.938
Endpoint RhoA levels	0.197	0.130	0.616	0.129	0.459	0.774
RhoA difference	-0.527	**0.001**	0.811	**0.001**	0.676	0.945
Basal FT3 levels	0.287	**0.026**	0.669	**0.028**	0.526	0.812
Endpoint value of FT3	0.109	0.407	0.564	0.402	0.417	0.711
FT3 difference	-0.272	**0.035**	0.660	**0.037**	0.513	0.807
Basal FT4 levels	0.163	0.213	0.596	0.210	0.445	0.747
Endpoint value of FT4	0.004	0.976	0.502	0.976	0.346	0.658
FT4 difference	-0.198	0.129	0.617	0.128	0.469	0.764
Basal TSH levels	0.019	0.886	0.508	0.922	0.358	0.657
Endpoint value of TSH	0.073	0.581	0.543	0.577	0.388	0.697
TSH difference	0.080	0.545	0.547	0.541	0.393	0.700
TRAb	0.372	**0.003**	0.719	**0.004**	0.592	0.846
TPOAb	0.005	0.970	0.497	0.970	0.346	0.648
TgAb	0.012	0.926	0.507	0.928	0.349	0.665

Statistically significant results are in bold.

[11]. Most patients with GD are overlooked due to the mild ocular symptoms, and treatment tends to focus on GD, delaying the diagnosis and treatment of GO. Hence, we aimed to identify biomarkers for early GO diagnosis through iTRAQ analysis. We investigated GD patients with new-onset GO to determine predisposing factors influencing the occurrence of GO. We used iTRAQ and WB and identified that expression of RhoA was significantly increased in GO, as verified in 60 patients and found that expression of RhoA was significantly higher in the GD with GO group than in the GD group at the initial stage (basal level = 25.09, $P < 0.001$).

Ras homolog family member A (RhoA) is a low-molecular-weight G protein, and serine/threonine kinase Rho-associated kinase (ROCK) is one of the main downstream effectors of RhoA [15]. Studies have shown that RhoA plays important roles in cell adhesion, migration, and transformation, which is consistent with the results of our KEGG analysis. For example, Wei et al. [16] studied an in vitro model of GO and found that RhoA is involved in these processes. The RhoA/ROCK signaling pathway is also involved in the differentiation of myofibroblasts induced by TGF-β. And in the pathogenesis of GO, orbital fibroblasts are the central target of the immune response and are involved in the process of inflammation and remodeling of orbital connective tissue and extraocular muscles. GO is caused by an autoimmune reaction of shared antigens between the thyroid and the orbit, mainly involving the connective tissue behind the bulb and extraocular muscles. Based on immunohistochemical experiments of orbital tissues of patients with GO [17, 18], Weetman et al. [19] reported infiltration of a large number of lymphocytes, neutrophils, serum cells, and mucopolysaccharide deposits, mainly in fat cells and intermuscular spaces, and that the lymphocytes were T cells. It has also been found that the Th1/Th2 balance participates in the progression of GO, with a shift toward Th1 dominance in the later stage [20]. RhoA is a ubiquitously expressed cytoplasmic protein belonging to the small GTPase family and plays a key regulatory role in innate and adaptive immunity. For example, many scientists have shown that Th0 cells differentiate into one of four main subgroups (Th1, Th2, Th17, and Treg) to perform functions when the initial T lymphocytes entering the periphery are activated by the dual signals of antigen-presenting cells [21–23]. Tregs play the most important role in regulating self-reactive T cells and in preventing an excessive immune reaction, which is harmful to the host [21]. RhoA is one of the core proteins for T cell migration [23], and studies on T cell-specific knockout RhoA mice show that RhoA is vital for T cell proliferation, activation, and migration. Therefore, we speculate that RhoA affects the balance of Th1/Th2 cells by interrupting Th0 cell differentiation, which promotes GO pathogenesis.

With the gradual development of GO, severe exophthalmos can lead to incomplete eyelid closure, dry exfoliation of the corneal epithelium, exposure keratitis, corneal ulcers, and even corneal perforation. Hypertrophic extraocular muscles oppress the optic nerve, which can lead to optic neuropathy and even vision loss. ROCK inhibitors have been shown to promote corneal cell proliferation and repair [24, 25]. Okumura et al. [26] found that apoptosis can activate phosphorylation within the Rho/ROCK signaling pathway in corneal endothelial cells, and the loss of cell adhesion can induce apoptosis. ROCK inhibitors can counteract the loss of cell adhesion by activating the focal adhesion complex. Inhibition of the Rho/ROCK pathway can also promote axonal regeneration and functional repair of the central nervous system. Yu et al. [27] established a rabbit model of optic nerve injury and administered the Rho/ROCK inhibitor fasudil. The state of retinal ganglion cells was better in the model group than in the saline group or the dexamethasone group, suggesting that inhibition of the Rho/ROCK signaling pathway can promote optic nerve

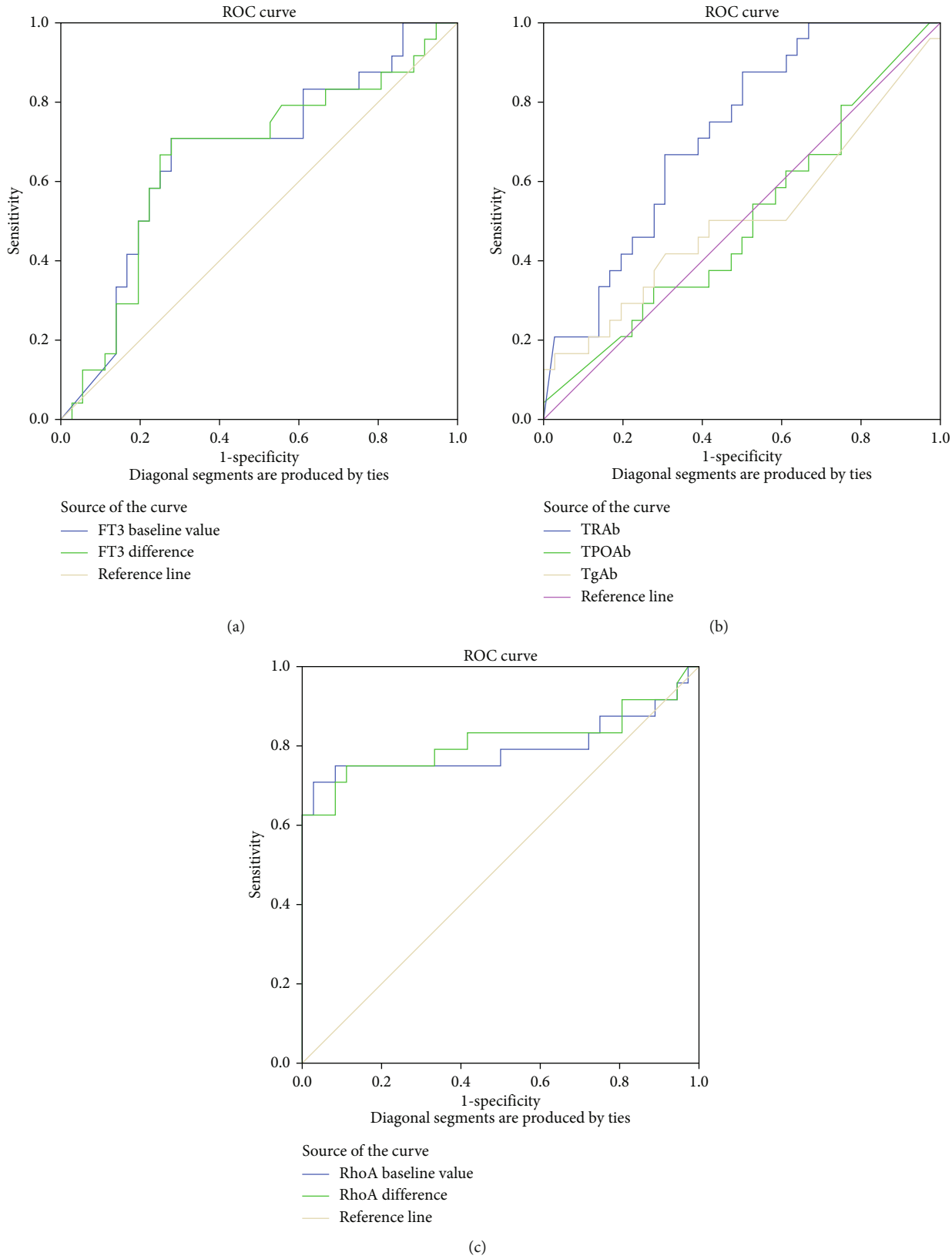

Figure 5: Receiver operating characteristic (ROC) curves were generated to evaluate the diagnostic significance of RhoA, FT3, FT4, TSH, TPOAb, and TgAb for onset of GO. (a) The area under the ROC curve (AUC) refers to the area formed by the ROC curve and the x -axis, (1, 0) -(1, 1). The basal FT3 level and difference between the basal FT3 level and endpoint value had diagnostic value. (b) TRAb titer also had diagnostic value and was superior to FT3. FT4, TSH, TPOAb, and TgAb titers had no diagnostic value. (c) The basal RhoA level and difference between the basal RhoA level and endpoint value had diagnostic value.

repair to some extent. Furthermore, we observed increases in TRAb in 60 patients with GD and GO compared with GD patients. GD is characterized by the presence of antibodies against TSHR [28–30]. TSH-receptor antibodies (TRAbs) are divided into thyroid-stimulating (TSAbs), thyroid-blocking (TBAbs), and neutral (neutral Abs) antibodies. Studies have demonstrated a close clinical and temporal relationship between GD and GO, which suggests a common pathogenic antigen in the thyroid and orbit [4, 5, 31]. As TRAb is an autoantibody that causes GD [32], TRAb levels may have a certain clinical value in determining the relationship between GD and GO [33]. In our study, the average TRAb titer in the GO-free group at first diagnosis of GD was 4.58 (IU/L), whereas the titer in patients in the GO group was 13.07 (IU/L), indicating diagnostic significance for GO (Figures 2(c) and 3(b)). Our findings are consistent with those of several published studies [34, 35]. It has also been shown that levels of TSAb and TBII may be related to the incidence and severity of GO, with more significance for the former [34, 36]. At present, it is believed that a lack of CD28 on the surface of CD4+ and CD8+ T cell subsets in the peripheral blood is the reason that patients are prone to immune-mediated diseases [37, 38]. The amount of CD28 in the serum of patients with GD is higher than that of normal subjects, and levels of endogenous IFN-γ and IL-6 cytokines in patients with GD with GO are higher than those in GO-free patients, with a positive correlation with TRAb [37–41].

TSH is the most sensitive indicator for thyroid function. As T3 and T4 levels are usually affected by binding proteins and albumin, FT3 and FT4 can well reflect thyroid function. During the 7-month follow-up, we found that basal FT3 levels and the difference between basal levels and endpoint values had diagnostic values for GO, based on Mann–Whitney U test results (AUC = 0.669, $P = 0.028$; AUC = 0.660, $P = 0.037$). Nonetheless, there were no statistically significant differences between the endpoints of FT4 and TSH and their basal levels. Thus, a true representation of thyroid function should be evaluated using serum FT4 levels instead of serum FT3 levels. However, in our study, FT3 levels in the serum of GO patients showed a positive result that was significantly different from that for the serum of GO-free patients, which may be because FT3 is more sensitive than FT4 during the early stages. We collected patient serum during the early stages of GD, and FT3 might be more easily overactivated than FT4. Hence, patients with GD with significantly elevated FT3 during the early stages were more likely to develop GO, therefore, such an increase in FT3 was easy to detect.

Based on our study, we speculate that RhoA is a potential biomarker for GO and may play an important role in the differentiation and migration of T cells and promote the pathogenesis of GO. We also found that GD patients with a significant increase in TRAb and FT3 in the early stage were more likely to develop GO. TRAb is an autoantibody that is highly expressed in the adipose tissue of GO patients and correlates positively with the secretion of endogenous INF-γ and IL-6 cytokines [42]. Therefore, we speculate that RhoA and TRAb promote the development of GO at the immune level, but whether there is a direct relationship between them requires more detailed evidence

5. Limitation

Relatively few patients met the inclusion criteria, and some patients were excluded because of loss to follow-up, poor compliance, and the use of other oral drugs. These factors may have affected the results of the experiment. Therefore, the study was limited by the inadequate sample size, which we will aim to expand by continuing to collect relevant medical records. At the same time, the conclusions we reached based on the current sample size are consistent with those drawn by others, indicating that the results of this experiment are credible despite the limitations.

6. Conclusion

RhoA is a potential biomarker in the mild stage of GO. If elevation of RhoA in the serum of GD patients is accompanied by elevation of TRAb or FT3, GO is highly likely to occur, even in the absence of obvious ocular symptoms. Our study provides a new biomarker for early diagnosis of GO, and we hope that it will allow patients with GO to be diagnosed and treated in a timelier manner in the future.

Data Availability

The data used to support the findings of this study are available from the corresponding authors upon request.

Conflicts of Interest

The authors declare that there are no conflicts of interest.

Authors' Contributions

Sidi Zhao, Shuangshuang Shi, and Wanchen Yang contributed equally to this work and share first authorship.

Acknowledgments

This study was supported by the Science and Technology Project of Tianjin Municipal Education Commission (NO. 2020KJ176), Science and Technology Project of Tianjin Binhai New Area Health Care Committee (NO. 2019BWKZ009), and Chengdu Medical Scientific Research Project of Chengdu Municipal Health Commission.

Supplementary Materials

Supplementary Table 1: demographic and ophthalmological data of the study participants, i.e., GO-free and GO groups. Supplementary Table 2: Mauchly's sphericity test of thyroid hormone levels in the two groups. Supplementary Table 3: analysis of variance of repeated-measurement data for the two groups. *(Supplementary Materials)*

References

[1] L. Bartalena, "Diagnosis and management of Graves disease: a global overview," *Nature Reviews Endocrinology*, vol. 9, no. 12, pp. 724–734, 2013.

[2] D. S. Ross, H. B. Burch, D. S. Cooper et al., "2016 American Thyroid Association guidelines for diagnosis and management of hyperthyroidism and other causes of thyrotoxicosis," *Thyroid*, vol. 26, no. 10, pp. 1343–1421, 2016.

[3] L. Wang, F.-S. Wang, and M. E. Gershwin, "Human autoimmune diseases: a comprehensive update," *Journal of Internal Medicine*, vol. 278, no. 4, pp. 369–395, 2015.

[4] E. Şahlı and K. Gündüz, "Thyroid-associated ophthalmopathy," *Türk Oftalmoloji Dergisi*, vol. 47, no. 2, pp. 94–105, 2017.

[5] L. Bartalena, L. Baldeschi, K. Boboridis et al., "The 2016 European Thyroid Association/European Group on Graves' orbitopathy guidelines for the management of Graves' orbitopathy," *European Thyroid Journal*, vol. 5, no. 1, pp. 9–26, 2016.

[6] E. Piantanida, M. L. Tanda, A. Lai, L. Sassi, and L. Bartalena, "Prevalence and natural history of Graves' orbitopathy in the XXI century," *Journal of Endocrinological Investigation*, vol. 36, no. 6, pp. 444–449, 2013.

[7] M. Leo, F. Menconi, R. Rocchi et al., "Role of the underlying thyroid disease on the phenotype of Graves' orbitopathy in a tertiary referral center," *Thyroid*, vol. 25, no. 3, pp. 347–351, 2015.

[8] G. B. Bartley and C. A. Gorman, "Diagnostic criteria for Graves' ophthalmopathy," *American Journal of Ophthalmology*, vol. 119, no. 6, pp. 792–795, 1995.

[9] G. H. Milbratz, D. M. Garcia, F. C. Guimarães, and A. A. V. Cruz, "Multiple radial midpupil lid distances: a simple method for lid contour analysis," *Ophthalmology*, vol. 119, no. 3, pp. 625–628, 2012.

[10] R. S. Bahn and A. E. Heufelder, "Pathogenesis of Graves' ophthalmopathy," *The New England Journal of Medicine*, vol. 329, no. 20, pp. 1468–1475, 1993.

[11] R. S. Bahn, "Graves' ophthalmopathy," *New England Journal of Medicine*, vol. 362, no. 8, pp. 726–738, 2010.

[12] S. Sun, R. T. P. Poon, N. P. Lee et al., "Proteomics of hepatocellular carcinoma: serum vimentin as a surrogate marker for small tumors (≤2 cm)," *Journal of Proteome Research*, vol. 9, no. 4, pp. 1923–1930, 2010.

[13] N. Li, Y. Long, X. Fan et al., "Proteomic analysis of differentially expressed proteins in hepatitis B virus-related hepatocellular carcinoma tissues," *Journal of Experimental & Clinical Cancer Research*, vol. 28, no. 1, p. 122, 2009.

[14] V. Ignjatovic, P. E. Geyer, K. K. Palaniappan et al., "Mass spectrometry-based plasma proteomics: considerations from sample collection to achieving translational data," *Journal of Proteome Research*, vol. 18, no. 12, pp. 4085–4097, 2019.

[15] H.-B. Tan, Y.-S. Zhong, Y. Cheng, and X. Shen, "Rho/ROCK pathway and neural regeneration: a potential therapeutic target for central nervous system and optic nerve damage," *International Journal of Ophthalmology*, vol. 4, no. 6, pp. 652–657, 2011.

[16] Y.-H. Wei, S.-L. Liao, S.-H. Wang, C.-C. Wang, and C.-H. Yang, "Simvastatin and ROCK inhibitor Y-27632 inhibit myofibroblast differentiation of Graves' ophthalmopathy-derived orbital fibroblasts via RhoA-mediated ERK and p38 signaling pathways," *Frontiers in Endocrinology*, vol. 11, 2021.

[17] T. J. Smith and J. A. M. J. Janssen, "Insulin-like growth factor-I receptor and thyroid-associated ophthalmopathy," *Endocrine Reviews*, vol. 40, no. 1, pp. 236–267, 2019.

[18] T. J. Smith, "Challenges in orphan drug development: identification of effective therapy for thyroid-associated ophthalmopathy," *Annual Review of Pharmacology and Toxicology*, vol. 59, no. 1, pp. 129–148, 2019.

[19] A. P. Weetman, S. Cohen, K. C. Gatter, P. Pells, and B. Shine, "Immunohistochemical analysis of the retrobulbar tissues in Graves' ophthalmopathy," *Clinical and Experimental Immunology*, vol. 75, no. 2, pp. 222–227, 1989.

[20] N. Xia, S. Zhou, Y. Liang et al., "CD4+ T cells and the Th1/Th2 imbalance are implicated in the pathogenesis of Graves' ophthalmopathy," *International Journal of Molecular Medicine*, vol. 17, no. 5, pp. 911–916, 2006.

[21] M. Bros, K. Haas, L. Moll, and S. Grabbe, "RhoA as a key regulator of innate and adaptive immunity," *Cells*, vol. 8, no. 7, p. 733, 2019.

[22] N. Gagliani and S. Huber, *Basic Aspects of T Helper Cell Differentiation*, Springer New York, New York, NY, 2017.

[23] J. Zhu and W. E. Paul, "Peripheral CD4+ T-cell differentiation regulated by networks of cytokines and transcription factors," *Immunological Reviews*, vol. 238, no. 1, pp. 247–262, 2010.

[24] A. V. Ljubimov and M. Saghizadeh, "Progress in corneal wound healing," *Progress in Retinal and Eye Research*, vol. 49, pp. 17–45, 2015.

[25] Z. A. Syed and C. J. Rapuano, "Rho kinase (ROCK) inhibitors in the management of corneal endothelial disease," *Current Opinion in Ophthalmology*, vol. 32, no. 3, pp. 268–274, 2021.

[26] N. Okumura, K. Fujii, T. Kagami et al., "Activation of the rho/rho kinase signaling pathway is involved in cell death of corneal endothelium," *Investigative Ophthalmology & Visual Science*, vol. 57, no. 15, pp. 6843–6851, 2016.

[27] J. Yu, L. Lin, X. Luan, X. Jing, and Maierab, "Impacts of rho kinase inhibitor fasudil on rho/ROCK signaling pathway in rabbits with optic nerve injury," *International Journal of Clinical and Experimental Pathology*, vol. 8, no. 11, pp. 14717–14724, 2015.

[28] F. Träisk, L. Tallstedt, M. Abraham-Nordling et al., "Thyroid-associated ophthalmopathy after treatment for Graves' hyperthyroidism with antithyroid drugs or iodine-131," *The Journal of Clinical Endocrinology & Metabolism*, vol. 94, no. 10, pp. 3700–3707, 2009.

[29] D. Y. Chen, P. F. Schneider, X. S. Zhang, X. Y. Luo, Z. M. He, and T. H. Chen, "Changes in Graves' ophthalmopathy after radioiodine and anti-thyroid drug treatment of Graves' disease from 2 prospective, randomized, open-label, blinded end point studies," *Experimental and Clinical Endocrinology & Diabetes*, vol. 122, no. 1, pp. 1–6, 2014.

[30] E. Fröhlich and R. Wahl, "Thyroid autoimmunity: role of anti-thyroid antibodies in thyroid and extra-thyroidal diseases," *Frontiers in Immunology*, vol. 8, 2017.

[31] L. Bartalena, L. Baldeschi, A. Dickinson et al., "Consensus statement of the European Group On Graves' Orbitopathy (EUGOGO) on management of GO," *European Journal of Endocrinology*, vol. 158, no. 3, pp. 273–285, 2008.

[32] X. Chen, F. Huang, Y. Qi et al., "Serum and thyroid tissue level of Let-7b and their correlation with TRAb in Graves' disease," *Journal of Translational Medicine*, vol. 16, no. 1, p. 188, 2018.

[33] S. Y. Jang, D. Y. Shin, E. J. Lee, Y. J. Choi, S. Y. Lee, and J. S. Yoon, "Correlation between TSH receptor antibody assays and clinical manifestations of Graves' orbitopathy," *Yonsei Medical Journal*, vol. 54, no. 4, pp. 1033–1039, 2013.

[34] A. K. Eckstein, M. Plicht, H. Lax et al., "Thyrotropin receptor autoantibodies are independent risk factors for Graves' ophthalmopathy and help to predict severity and outcome of the disease," *The Journal of Clinical Endocrinology & Metabolism*, vol. 91, no. 9, pp. 3464–3470, 2006.

[35] D. E. Williams, S. N. Le, M. Godlewska, D. E. Hoke, and A. M. Buckle, "Thyroid peroxidase as an autoantigen in Hashimoto's disease: structure, function, and antigenicity," *Hormone and Metabolic Research*, vol. 50, no. 12, pp. 908–921, 2018.

[36] I. Subekti, A. Boedisantoso, N. D. Moeloek, S. Waspadji, and M. Mansyur, "Association of TSH receptor antibody, thyroid stimulating antibody, and thyroid blocking antibody with clinical activity score and degree of severity of Graves ophthalmopathy," *Acta Medica Indonesiana*, vol. 44, no. 2, pp. 114–121, 2012.

[37] A. H. Sharpe and G. J. Freeman, "The B7-CD28 superfamily," *Nature Reviews Immunology*, vol. 2, no. 2, pp. 116–126, 2002.

[38] B. Salomon and J. A. Bluestone, "Complexities of CD28/B7: CTLA-4 costimulatory pathways in autoimmunity and transplantation," *Annual Review of Immunology*, vol. 19, no. 1, pp. 225–252, 2001.

[39] Z. Sun, L. Yi, H. Tao et al., "Clinical immunology enhancement of soluble CD28 levels in the serum of Graves' disease," *Central European Journal of Immunology*, vol. 2, no. 2, pp. 216–222, 2014.

[40] S. Kumar, R. Schiefer, M. J. Coenen, and R. S. Bahn, "A stimulatory thyrotropin receptor antibody (M22) and thyrotropin increase interleukin-6 expression and secretion in Graves' orbital preadipocyte fibroblasts," *Thyroid*, vol. 20, no. 1, pp. 59–65, 2010.

[41] F. Eliana, P. Suwondo, A. Asmarinah et al., "The role of cytotoxic T-lymphocyte-associated protein 4 (CTLA-4) gene, thyroid stimulating hormone receptor (TSHR) gene and regulatory T-cells as risk factors for relapse in patients with Graves disease," *Acta Medica Indonesiana*, vol. 49, no. 3, pp. 195–204, 2017.

[42] T. K. Khoo and R. S. Bahn, "Pathogenesis of Graves' ophthalmopathy: the role of autoantibodies," *Thyroid*, vol. 17, no. 10, pp. 1013–1018, 2007.

Hindawi
Disease Markers
Volume 2022, Article ID 1380560, 10 pages
https://doi.org/10.1155/2022/1380560

Research Article

Galectin-3 Is a Crucial Immunological Disease Marker in Patients with Fungal Keratitis

Yichen Xiao,[1] **Jiahui Yang**,[1] **Zhenyuan Fu**,[1] **Dalian He**,[1] **Naiyang Li**,[2] **and Jin Yuan**[1]

[1]*State Key Laboratory of Ophthalmology, Zhongshan Ophthalmic Center, Sun Yat-Sen University, Guangdong Provincial Key Laboratory of Ophthalmology and Visual Science, Guangzhou 510060, China*
[2]*Eye Center, Zhongshan Hospital of Sun Yat-Sen University, Zhongshan, Guangdong, China*

Correspondence should be addressed to Jin Yuan; yuanjincornea@126.com

Received 24 November 2021; Revised 18 May 2022; Accepted 1 June 2022; Published 8 July 2022

Academic Editor: Shih-Ping Hsu

Fungal keratitis, one of the most common infectious eye diseases in China, often results in a poor prognosis due to a delayed diagnosis and the insufficiency of effective therapy. There is an urgent need to identify specific biomarkers for the disease. In this study, we screened out tear proteins in patients with fungal keratitis by microsphere-based immunoassay analysis. Levels of cytokine expression were determined in both human corneal epithelial cell models in vitro and the corneas of patients by western blot, quantitative polymerase chain reaction (qPCR), and immunofluorescence analysis. Neutrophil activation was examined by flow cytometry analysis. The relationship between the cytokine expression and neutrophils was evaluated by immunofluorescence costaining and correlation analysis. These results demonstrated that the galectin-3 expression level was increased in both cell model and patient samples at the early and late stages of fungal keratitis. The neutrophils were significantly activated during the disease course of fungal keratitis. Meanwhile, colocalization and a positive correlation between galectin-3 and neutrophils were observed, suggesting that galectin-3 may play a crucial role in the recruitment of neutrophils and immune regulation of fungal keratitis. In conclusion, galectin-3 could be a key disease marker implying a beneficial immune response in the pathogenesis of fungal keratitis, which might be a target of therapeutic strategy in the future.

1. Introduction

Fungal keratitis (FK), also known as mycotic keratitis, is a severe corneal infection that often results in permanent blindness and vision loss. It is estimated that there are 1051787 new FK cases each year worldwide, with the highest incidence rates in Asia and Africa. The incidence of FK in China is more common than in other regions [1]. The immune responses of fungal keratitis include both anti-infection responses and immune disorders after pathogen invasion. Our previous study demonstrated that triggering receptors expressed on myeloid cells-1 (TREM-1) and dendritic cell-associated C-type lectin-1 (Dectin-1), the vital pattern recognition receptors (PRRs) in the innate immune response, initiated the whole anti-infection process, positively participated in the pathogenesis of ocular fungal infection, and provided the foundation of the adaptive immune response [2–4]. However, the mechanism of innate immune response in FK remains unveiled to a great extent [5].

On the ocular surface, where the battlefield of FK is, the inherent corneal epithelial cells, together with macrophages, neutrophils, and T effective immune cells recruited from the systemic immune system, fight against invading pathogens [6]. Galectin-3 is a soluble mammalian lectin that positively modulates the immune response against pathogenic microorganisms, including bacteria and fungi [7, 8]. It is implicated that galectin-3 can activate chitin-responsive pattern recognition receptors and regulate signal transduction, thereby playing a vital role in initiating an anti-infection inflammation cascade in the host immune system [9, 10]. The fungal infection leads to an inflammatory cascade of signal transduction events, including infiltration of

inflammatory cells like neutrophils and inflammatory cytokines necessary to initiate adaptive immunity and to kill and clear the invading fungi [11]. The activation and recruitment of neutrophils run throughout the whole antifungal defense, and neutrophils are the main force fighting against fungal invasion as well as responders to proinflammatory cytokines [2]. Since galectin-3 functions as a regulatory molecule in acute and chronic inflammation, it is well-accepted that it acts as an amplifier of the inflammatory cascade with its accelerative role in neutrophil chemotaxis. However, its role in fungal keratitis and its potential synergetic mechanism with neutrophils remain unknown [7, 12, 13]. We deemed that further studies on the innate immune system should be performed to discover more potential immunological targets to unveil and enrich the pathogenesis of fungal keratitis.

This study was aimed at identifying potential disease markers of FK by evaluating the levels of tear cytokines, validating the candidate biomarker in both fungal infection cell model and tissue biospecimens obtained from FK patients, and confirming its role in the blood sample and focal corneal tissue. Our findings provide a new biomarker for the prediction of the development of FK and the regulation of immune responses in FK. The current study will also shed light on the development of a novel therapeutic strategy against FK.

2. Materials and Methods

2.1. Patient and Tissue Specimens. The tissue samples were collected from patients who had clinically diagnosed fungal keratitis by corneal scraping culture and received corneal transplantation from May 2020 to May 2021 at the Zhongshan Ophthalmic Center. This study was approved by the Zhongshan Ophthalmic Center Medical Science Research Ethics Committee (protocol number: 2020KYPJ115). All participants in this study provided written consent. The infected corneal tissues were collected from the corneal transplantation surgery. Tears and peripheral blood specimens were collected from the Department of Cornea and Ocular Surface Disease at Zhongshan Ophthalmic Center. Normal donor corneas were obtained from the Guangdong Eye Bank. Samples were quickly stored in a cryogenic refrigerator at -80°C. All medical records, clinical signs, anterior segment photography, and follow-up data were complete. The patients were divided into two groups based on the severity of the ulcer: 9 cases with the partially infiltrated cornea and no anterior chamber empyema in the early stage group and 22 cases with total corneal infiltration or anterior chamber empyema in the late stage group. The severity of fungal keratitis was graded on a scale ranging from 0 to 12 according to a scoring system developed by Zhou et al. [14]. Four clinical scores were calculated by aspects: diameter of corneal ulcer (0-3), infiltrating depth (0-3), corneal edema (0-3), and the response of the anterior chamber (0-3).

In this study, a patient with clinical symptoms of suppurative keratitis was considered to be a case of FK if the patient met one or more than one of the following criteria at the initial visit: (1) grown fungal organism from a corneal scrape or biopsy sample in one or more culture media, or featured fungal elements shown in light microscopy of corneal scrape samples, and (2) fungal elements identified by in vivo confocal microscopy (IVCM). Subjects were excluded if they had (1) coexistence of bacteria organism determined by culture results, (2) presence of corneal endophthalmitis and specific perforation on the day that cultures were taken, (3) presence of immune disorders, autoimmune diseases, allergic diseases (such as Mooren's corneal ulcer), and (4) not willing to participate, pregnancy, or breastfeeding.

2.2. Microsphere-Based Immunoassay Analysis. To measure the minimal concentrations of tear cytokines, we performed a microsphere-based immunoassay analysis with a multifunctional liquid suspension chip system from Luminex to test different cytokine levels simultaneously. The patients' tear samples were collected in a quiet room at 17 : 00 each day. With no epithelial anesthetics, sterile capillary tubes were used to collect fluid tear samples from the edge of the lower eyelid under a slit lamp. 2 μL fluid tear samples of involved patients were collected from each eye and immediately stored in a cryogenic refrigerator at -80°C to avoid repeated freezing and thawing. We used the Luminex 200™ system (Luminex, Austin, TX, USA) to detect cytokine levels in tear samples, including galectin-3, IL-1β, IL-18, and TNF-α, and three replicate analyses were performed. Luminex 200 IS V2.1 software was applied to obtain the concentration value from the mean fluorescence intensity (MFI). After a standard curve was generated concerning cytokine gradient concentration, the concentrations of the cytokines listed above in the tear samples were calculated according to the standard curve.

2.3. In Vitro Cell Model. The corneal epithelial cell line HCEC (human corneal epithelial cell) used in this study was purchased from Cyto-Biotech. HCECs were seeded into flasks and put into a humidified incubator with 5% carbon dioxide (CO2) at 37°C. The cell culture medium is made up of Dulbecco's modified Eagle's medium (DMEM)/F12 cell culture medium (Gibco, Grand Island) containing 1% sodium pyruvate, 10% fetal bovine serum, 1% human epidermal growth factor, 1% streptomycin, and penicillin that were added to the culture medium. Confluent cells were subcultured every 2–3 days by trypsinization with a 0.5% trypsin/EDTA solution. An in vitro model of fungal keratitis was established by treating corneal epithelial cells with zymosan, a yeast polysaccharide (100 mg/mL) for 24 h [2, 15, 16]. Total proteins or RNA was extracted from cells after treatment for further examination.

2.4. Immunofluorescence Staining. Immunofluorescence staining was performed in both human corneal epithelial cell line and corneal tissues from patients with fungal keratitis to detect the expression of cytokeratin 12 (CK12), CD11b, and galectin-3. After being stimulated by yeast polysaccharide (100 mg/mL) for 24 h, cell cultures were cooled at 4°C, then washed with PBS, and fixed overnight with methanol at −20°C. After treatment with acetone for 1 minute, the cells were dried in the open air. The cells were rehydrated in

IMF buffer (0.1% Triton X-100, 0.15 mol/L NaCl, 5 mmol/L EDTA, 20 mmol/L HEPES, and 0.02% NaN3) and incubated at 4°C overnight with a mixture of mouse anti-CK-12 (rabbit, Bioss, bs-4625R; 1 : 50) or mouse anti-CD11b (rabbit, Bioss, bs-1014R; 1 : 50) and rabbit anti-galectin-3 (mouse, ThermoFisher, 395100; 1 : 25) antibodies. The cells were then washed and incubated for 1 h at room temperature with secondary antibodies Dy-Light 594 goat anti-mouse IgG (Vector Laboratories, DI-1094; 1 : 200) and streptavidin-FITC (Southern Biotech, 7100-02; 1 : 50) in HEPES solution for more than 1 hour at room temperature, followed by rinsing with PBS. Nuclei were freshly stained with DAPI (Millipore Sigma), and tissue sections were covered with a set of coverslips. Images were acquired with a BZ-X700 all-in-one fluorescence microscope (Keyence).

The corneal tissues of patients with fungal keratitis were prepared by frozen sectioning techniques. After washing with distilled water, tissue sections were blocked with a 3% BSA blocking solution, according to the reagent instructions (Abcam). Sections were incubated with primary antibodies for a mixture of CK12 (rabbit, Bioss, bs-4625R; 1 : 100) or CD11b (rabbit, Bioss, bs-1014R; 1 : 100) and galectin-3 (mouse, ThermoFisher, 395100; 1 : 200) in HEPES solution and then supplemented with 2.5% horse serum overnight at 4°C. After careful washing, tissue sections were incubated with the secondary antibody (1 : 200). The subsequent operation is the same as the cell slide treatment.

2.5. Flow Cytometry Analysis. Flow cytometry was performed to determine the proportion of neutrophils in peripheral blood at different stages of fungal keratitis. Cell blood samples were washed twice at 1000 rpm for 5 min at 4°C in PBS. The cell suspension was resuspended in Thermo lysing buffer for 60s to eliminate red blood cells out of cell suspension, and it was centrifuged again at 1000 rpm for 5 min at 4°C in PBS and then stained with antibodies in the dark. Fc receptors were blocked for 15 min at RT with anti-mouse or anti-human CD16/32 antibody (e-Bioscience 16-0161-81) followed by incubation with FITC tagged anti-CD11b antibody and PE tagged anti-CD66b antibody (Biolegend, 127613, Bio-legend, 561650, 0.5 μg added to 1×10^6 cell suspension in 100 μL). After two washes in FACS buffer (1% FBS in PBS), the cells were fixed in 0.5% PFA, then washed, resuspended in flow cytometry staining buffer and analyzed by flow cytometry on a FACs Aria (BD Biosciences). Data were analyzed using BD FACSDiva software.

2.6. Western Blot Analysis. To measure the protein level of galectin-3 in both corneal epithelial cells and tissues from patients with fungal keratitis, cellular and tissue lysates were prepared by lysing samples in ice-cold RIPA buffer (25 mM Tris-HCl pH 7.6, 0.15 M NaCl, 1% IGEPAL CA-630, 1% sodium deoxycholate, 0.1% SDS) containing 1%PMSF. Protein extraction was precisely performed using a Pierce BCA Protein Assay Kit (Tiangen, Beijing, China). For each sample, 40 μg of protein was loaded into each well. Sodium dodecyl sulfate-polyacrylamide gel electrophoresis (SDS-PAGE) was performed with 12% gels to separate proteins. Proteins were transferred to a polyvinylidene difluoride (PVDF) membrane (Invitrogen, USA), which was then blocked for 2 h with 5% bovine serum albumin (BSA). The membrane was then incubated with rat anti-mouse galectin-3 mAbs (Abcam, UK) overnight at 4°C. On the next day, the membrane was washed and incubated with anti-rat or peroxidase-conjugated secondary antibodies (Abcam, UK) for 1 h. Immuno-reactive bands were visualized in an Odyssey Infrared Imaging System (LI-COR Biosciences, Frederick, MD) according to the supplier's instructions. GAPDH was used as the loading control. The integrated density of bands in the obtained results was further quantitatively analyzed by ImageJ.

2.7. Quantitative RT-PCR. To examine galectin-3 mRNA expression in fungal keratitis patients, we used a Qiagen RNA extraction kit to extract total RNA from the corneas of fungal keratitis patients, according to the instructions. RNA reverse transcription was performed with the TaKaRa Reverse Transcription Kit on a PCR machine. Transcripts were quantified with SYBR Green qPCR reagents on an IQ Thermocycler (Bio-Rad) or ABI Quant Studio Design v1.3. PCR primers were purchased from Invitrogen, and their sequences are shown below:

(i) Galectin-3: forward: 5′-GCTTATCCTGGCCCAACTGC-3′, reverse: 5′-CCCCGCTGGACCACTGACGG-3′

(ii) GAPDH: forward: 5′-TGTGGGCATCAATGGATTTGG-3′, reverse: 5′-ACACCATGTATTCCGGGTCAAT-3′

2.8. Statistical Methods. Normally distributed data (such as age and disease course) were analyzed by mean ± SD and an independent *t*-test. Qualitative data, including gender and the number of the affected eyes, were compared using the chi-square test. Paired *t*-tests were utilized to analyze the differences in the cytokine levels and cell proportion in normal vs. affected eyes and the early vs. late stage of fungal keratitis. Spearman's tests were used for correlation analysis between the levels of galectin-3 in tears and neutrophils in peripheral blood of patients with fungal keratitis. Statistical analyses were performed using SPSS for Windows (version 22.0; International Business Machines Corporation). Graphs were generated by GraphPad Prism 7 for Windows (version 7.04; GraphPad Software). *P* values were considered significant when less than 0.05.

3. Results

3.1. Galectin-3 Significantly Expressed in Tears of Patients with Fungal Keratitis. Thirty-one fungal keratitis patients with a mean age of 61.30 ± 2.55 years (males 33.33%, females 67.67%) in the early stage and 62.05 ± 1.47 (males 40.91%, females 59.09%) in the late stage were recruited into the study. Right eye data and left eye data counted for 67.7% and 33.3%. The data of fellow eyes of disease patients without systemic immune disease were collected as the control group. Patients were divided into 2 groups, 9 patients in

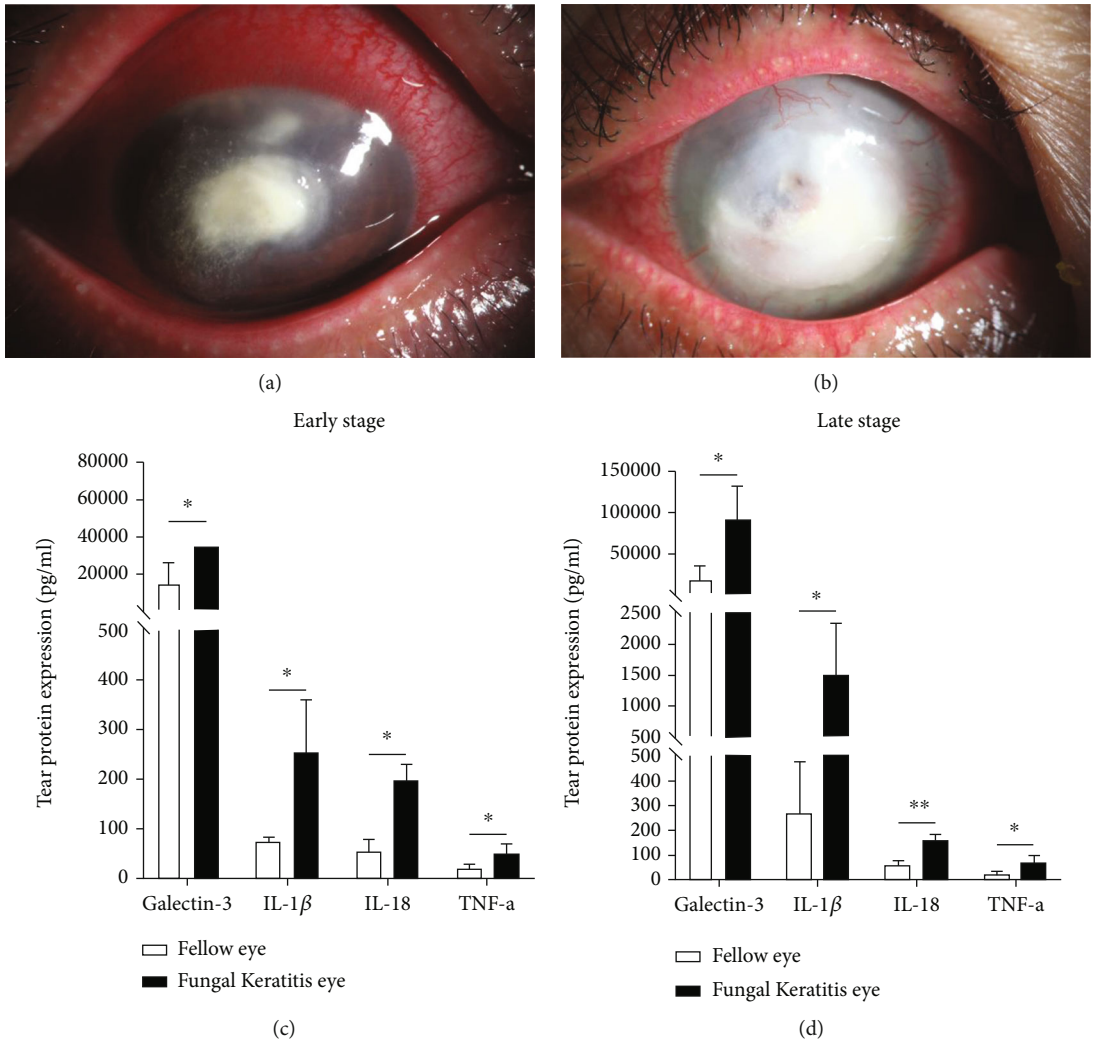

Figure 1: Morphology of human fungal keratitis in the early (a, $n = 9$) and late (b, $n = 22$) stages (tear protein levels were measured with more than 3 repeats). Samples of each patient were collected 3 times repetitively. Protein levels of galectin-3 and related inflammatory factors IL-1β, IL-18, and TNF-α in tears of patients with fungal keratitis. The expression of these factors was increased in both the early (c) and late stages (d) compared to the fellow eyes. $*$: $P < 0.05$; $**$: $P < 0.01$; $***$: $P < 0.001$; NS: no statistical difference.

the early stage group and 22 patients in the late stage group. Figure 1(a) showed the patients in the early stage had typical signs such as localized infiltration of inflammatory cells, fungal pseudopodia, and corneal conjunctival hyperemia. While in the late stage (Figure 1(b)), the infiltration was further aggravated to hypopyon, with ulcers involving the whole anterior chamber. The average disease score of the early stage group is 9.90 ± 1.05, while of the late stage is 37.41 ± 4.04 ($P < 0.001$). The peak incidence of severe symptoms and signs is significantly higher in late stage patients, resulting in a higher average clinical score.

To further investigate the possible key disease markers in the pathogenesis of fungal keratitis, the levels of tear cytokines, which were found to be different between the early and late stages in fungal keratitis patients, were tested with microsphere-based immunoassay analysis. Through the analysis of tear cytokines, four cytokines were found to have statistically significant differences, including IL-18, IL-1β, galectin-3, and TNF-α. The expression of these inflammatory factors increased in the early and late stages compared with the fellow eyes. The expression levels of four factors in the tears of patients with fungal keratitis in the early stage are as follows: galectin-3, 36107.60 ± 6116.71 pg/mL ($P < 0.05$); IL-1β, 242.76 ± 105.73 pg/mL ($P < 0.05$); IL-18, 194.57 ± 29.45 pg/mL ($P < 0.05$); and TNF-α, 49.91 ± 17.57 pg/mL ($P < 0.05$) (Figure 1(c)) while galectin-3, 87507.08 ± 31474.39 pg/mL ($P < 0.05$); IL-1β, 1526.30 ± 766.98 pg/mL ($P < 0.05$); IL-18, 148.11 ± 28.99 pg/mL ($P < 0.01$); and TNF-α, 70.29 ± 27.73 pg/mL ($P < 0.05$) in the late stage (Figure 1(d)), respectively. The results also showed that the expression levels of IL-1β, galectin-3, IL-18, and TNF-α were higher than the healthy control. Both in the early and the late stages, galectin-3 increased most significantly among these proinflammatory cytokines. It is noteworthy that the expression level of galectin-3 was the highest in both early and late stages among detected cytokines, suggesting that it may play an important role in fungal keratitis.

3.2. Galectin-3 Expressed Highly in Both Cell Model In Vitro of Fungal Keratitis and the Corneas of Patients with Fungal Keratitis. To further investigate the role of galectin-3 in fungal keratitis, we determined the expression of galectin-3 in cell model in vitro of fungal keratitis and in corneal tissues collected from patients with fungal keratitis. In the cell model, human corneal epithelial cells were treated with zymosan (a yeast polysaccharide) for 24 h. The western blot data showed that the expression of galectin-3 in zymosan-treated cells was significantly higher than that in the control group, which was proved by the relativity analysis of the integrated density (HCEC vs. HCEC+zymosan: 0.63 ± 0.05 vs. 0.87 ± 0.05, $P < 0.01$) (Figures 2(a)). Immunofluorescence results showed that galectin-3 signals (red fluorescence) were primarily localized on the plasma membrane of the corneal epithelial cells labeled CK12 (green fluorescence), and the galectin-3 expression was significantly increased after the zymosan treatment (Figure 2(b)).

Next, we analyzed galectin-3 expression in corneal tissues collected from corneal transplantation surgery of patients with fungal keratitis. Real-time PCR analysis (Figure 3(a)) showed that the expression of galectin-3 RNA was significantly upregulated in corneas infected by fungus, with a 4-fold increase in the early stage (6.20 ± 1.31) ($P < 0.01$) and a 10-fold increase in the late stage (12.00 ± 3.61) ($P < 0.01$) compared to normal controls (1.03 ± 0.25). Western blot also showed that the levels of integrated density of galectin-3 expression increased gradually during the course of disease (healthy people vs. FK early stage: 0.92 ± 0.04 vs. 1.12 ± 0.05, $P < 0.01$; healthy people vs. FK late stage: 0.92 ± 0.04 vs. 1.27 ± 0.05, $P < 0.001$; FK early stage vs. FK late stage: 1.12 ± 0.05 vs. 1.27 ± 0.05, $P < 0.05$) (Figure 3(b)), consistent with the PCR results. Together, the results from both in vitro cell-based and human corneal tissue-based studies indicate that galectin-3 is significantly upregulated in fungal keratitis, and the expression is positively correlated with the disease progression, suggesting that galectin-3 may play an important role in fungal keratitis.

3.3. Galectin-3 Recruited Neutrophils from the Peripheral Blood in Fungal Keratitis Patients. To explore the immune mechanisms underlying galectin-3 in the regulation of fungal keratitis, we first analyzed neutrophils, which play a significant role in the innate immunity of keratitis, at different stages of the disease. Flow cytometry was used to analyze the proportion of neutrophils in peripheral blood samples of fungal keratitis patients. The results showed that the cell frequency of neutrophils (CD66b, CD11b) significantly increased with the progression of the disease. The proportions of CD11b positive neutrophils in the CD66b positive group were $73.63 \pm 7.19\%$ at the early stage and $82.73 \pm 3.75\%$ at the late stage, both of which were significantly higher than that of the normal controls ($53.67 \pm 5.90\%$) ($P < 0.05$) (Figures 4(a)–4(c)). The results indicated that neutrophils play a vital role in the pathogenesis of fungal keratitis.

Next, we analyzed the potential correlation between the expression of galectin-3 and neutrophil activation in peripheral blood samples of patients with fungal keratitis. The results showed that galectin-3 expression was positively correlated with the proportion of neutrophil frequency in peripheral blood samples ($Y = 0.00028x + 70.48$, $R = 0.9643$, $P < 0.01$) (Figure 4(d)). To confirm this, frozen corneal tissue sections were collected from patients after corneal transplantation. The relationship between the expression of galectin-3, human corneal epithelium-labeled protein CK12, and neutrophil-labeled protein CD11b was determined by immunofluorescence costaining. We observed that galectin-3 (green fluorescence) is mainly expressed in the corneal stromal layer and the corneal epithelium layer (CK12, red fluorescence), and CD11b (red fluorescence) is also expressed in both two layers (Figure 4(d)). Galectin-3 and CK12 were co-expressed in the corneal epithelium, while galectin-3 and CD11b were aggregated near the corneal ulcer. Elevated expression of galectin-3 and its localization to the corneal epithelium and stroma suggested that galectin-3 may play an important immune regulatory function by recruiting and activating neutrophils in fungal keratitis.

4. Discussion

Fungal keratitis is an ocular infection disease. Its pathogenic mechanism mainly emphasizes chronic inflammation and immune dysregulation [17]. Our results demonstrate that galectin-3, an essential immunological marker, participated in the immune responses and increased obviously in different stages of fungal keratitis. Moreover, neutrophils were intensely activated in the course of fungal keratitis, and the positive correlation and colocation of galectin-3 and neutrophils suggested that galectin-3 may play an immune regulatory role by recruiting neutrophils in the early and late stages of fungal keratitis.

The role of galectin-3 in fungal keratitis has not been studied previously. Our finding of a significant increase of galectin-3 in tear samples of patients with fungal keratitis suggests that galectin-3 might be an indicator of the initiation of immune reactions in human fungal keratitis. The expression of galectin-3 in the HCEC cell model infected by zymosan, the specific antigen of fungi, suggests that human corneal epithelial cells secrete galectin-3 after recognizing the fungi invasion. It has been reported that the recruitment of neutrophils to the site of infection is critical for the clearance of the invading fungi, although other factors governing the host response are responsible for sensing the fungal invasion [18]. Galectin-3 has been reported as a markedly upregulated factor in mice fungi pulmonary infection. It possibly regulates fungal clearance mainly by promoting neutrophil activation migration in the lung fungal infection mice model [19, 20]. This research agrees with our data on the correlation between neutrophils and galectin-3 in FK. In the innate immune system responses to fungal infection, both the inherent corneal epithelial cells and neutrophils are recruited from the systemic immune system to fight together against invading pathogens [5]. Increased expression of galectin-3 in both tear samples and the cell model of FK supports the hypothesis that galectin-3 participates in the activation of inherent HCEC cells.

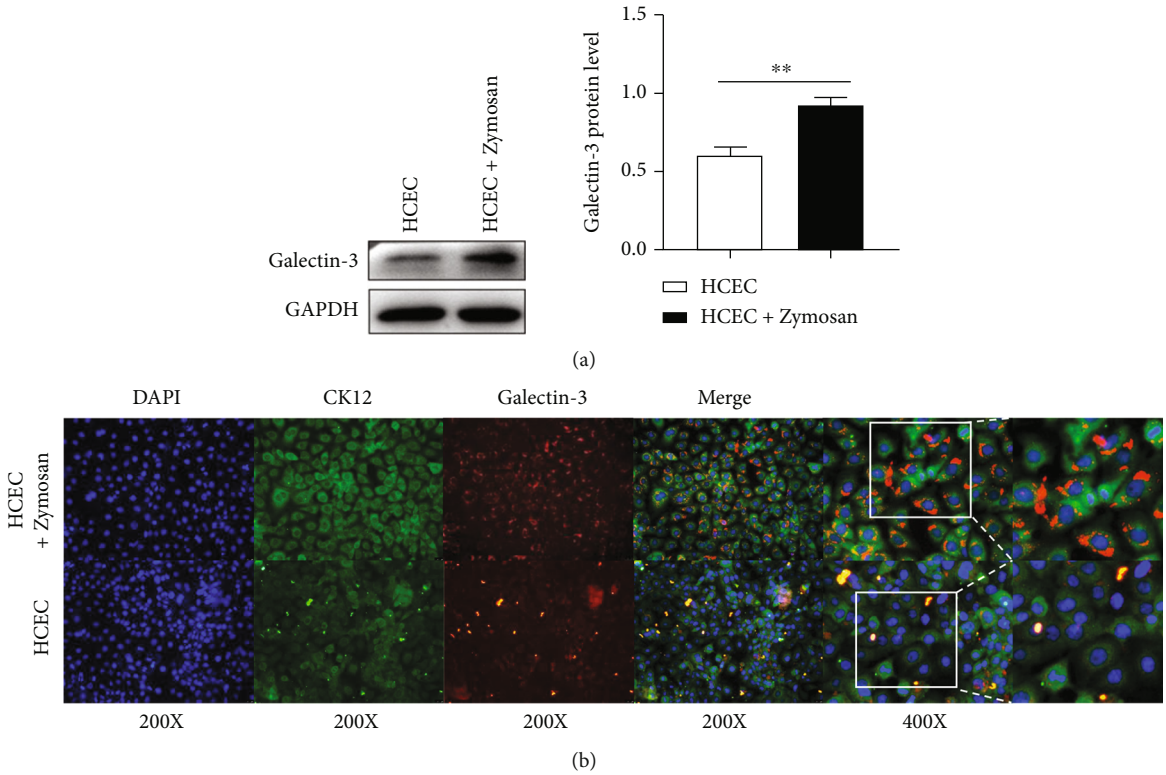

Figure 2: The expression of galectin-3 protein determined by western blots and statistical difference in galectin-3 expression of WB results of corneal epithelial cells increased in the presence or absence of zymosan (a). Colocalization of CK12 and galectin-3 expression in corneal epithelial cells was determined by immunofluorescence analysis (b). There were more than 3 repetitive samples of each group. $*$: $P < 0.05$; $**$: $P < 0.01$; $***$: $P < 0.001$; NS: no statistical difference.

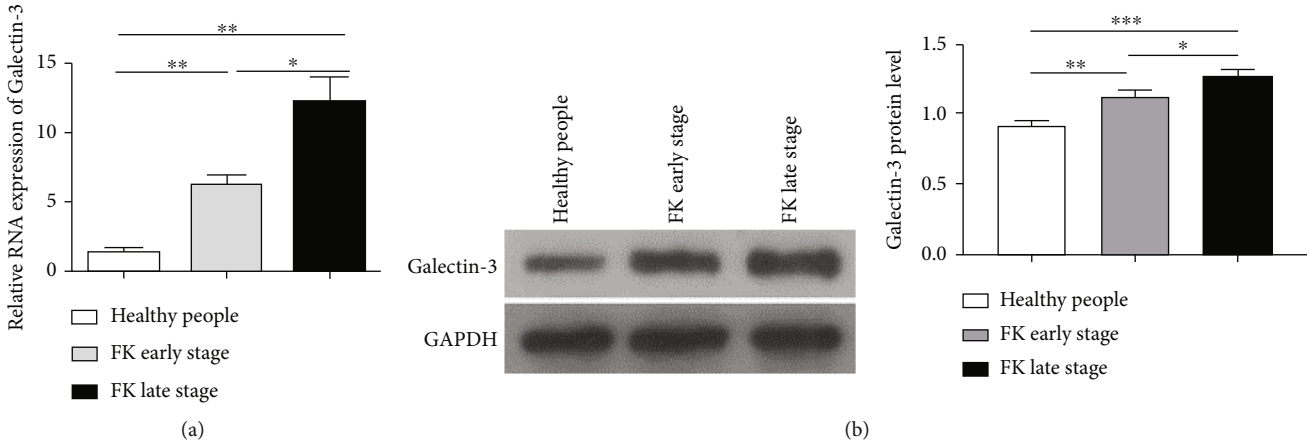

Figure 3: The expression of galectin-3 at the mRNA and protein level in the cornea of patients with fungal keratitis in early and late stages increased significantly, which was determined by qPCR (a) and western blot (b), respectively. There were more than 3 repetitive samples in each group. $*$: $P < 0.05$; $**$: $P < 0.01$; $***$: $P < 0.001$; NS: no statistical difference.

Speaking of bacterial keratitis and viral keratitis, there is no specific research on galectin-3 in animal models of the viral keratitis or the bacterial keratitis, but in the human epithelial cell models, galectin-3 is produced and expressed [21]. Galectin-3 contributes to maintaining innate barrier function and supports its physical defense [22]. Galectin-3 reduced the combined efficiency of virus and bacterial infections, such as HSV-1 and P. aeruginosa [23]. Galectin-3 participates in the mechanism of viral infections, such as human immunodeficiency virus (HIV) and influenza virus infections in viral binding, replication, budding, and transmission [24]. Some studies have revealed a direct antimicrobial effect of galectin-3 on the bacteria for galectin-3-binding caused bacterial cell death and bacterial growth suppression [25–27]. A protective role of extracellular galectin-3 against S. pneumoniae infection was proved in a bacterial infection model. For the reason that galectin-3 is involved in key immune cell subtypes in inflammatory responses, including

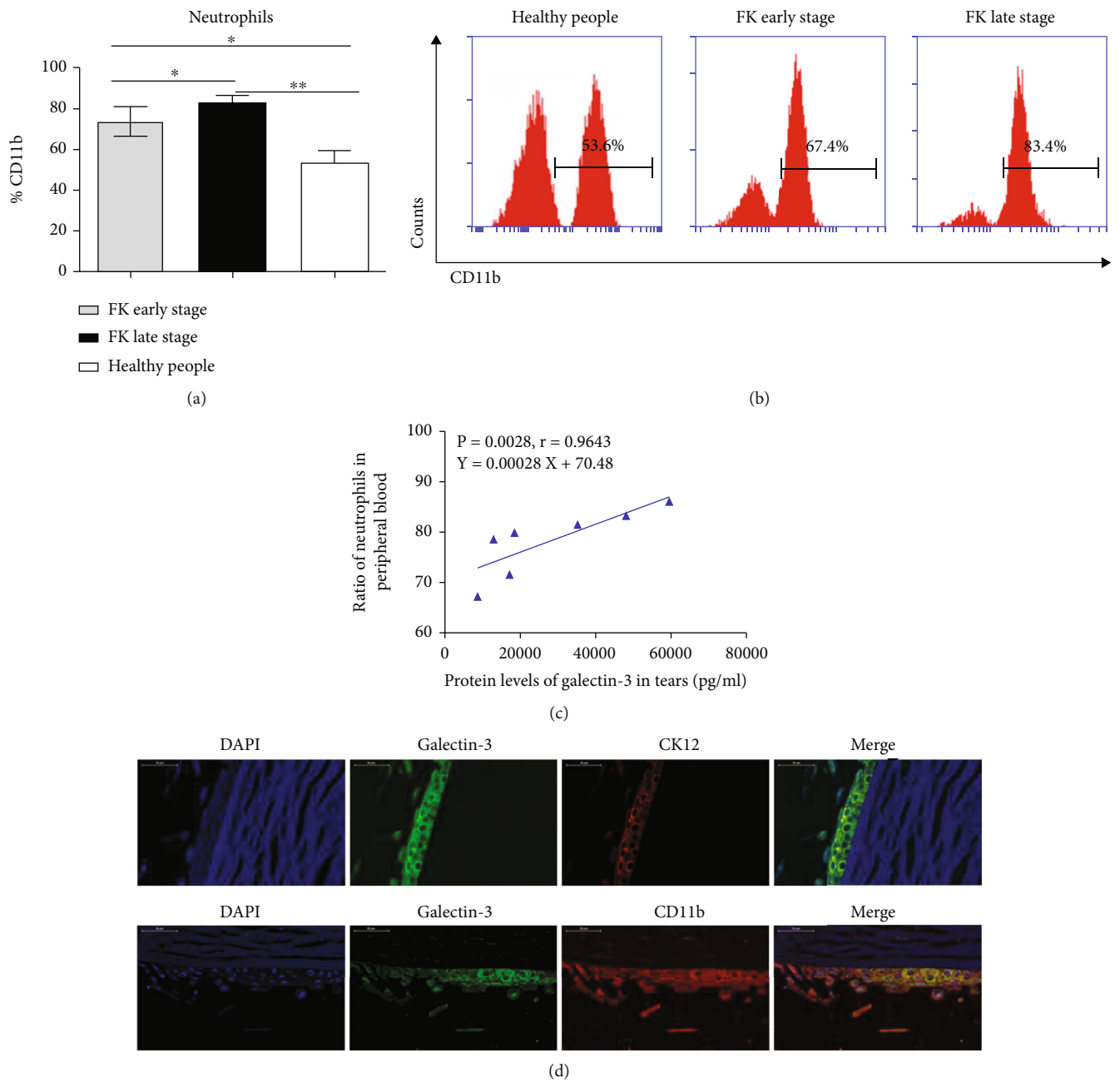

Figure 4: Analysis of neutrophil activation (CD11b) in peripheral blood at both the early and late stages of fungal keratitis and its correlation with the expression of galectin-3. The proportion of neutrophil activation increased gradually with the prolongation of the disease course (a and b). Correlation analysis (c) as well as immunofluorescence costaining (d) of galectin-3 (green fluorescence) and corneal epithelial cells (CK12, red fluorescence) or neutrophil (CD11b, red fluorescence) indicated that galectin-3 and neutrophil recruitment were highly correlated. There were more than 3 repetitive samples in each group. $*$: $P < 0.05$; $**$: $P < 0.01$; $***$: $P < 0.001$; NS: no statistical difference.

neutrophil activation and adhesion [28], such as chemoattraction of monocytes and macrophages [29] and opsonization of apoptotic neutrophils [30], galectin-3 is vital in the immunological mechanism of inflammatory diseases.

On the other hand, our data on FK patient peripheral blood samples confirmed that the increased tendency of neutrophils is significantly elevated compared to healthy patients both at the early and late stages. The co-location expression results of galectin-3 and the typical markers of neutrophils (CD11b), and HCECs (CK12) reveal the co-resistance of galectin-3 and neutrophils in fungal keratitis lesions. Even though the blood-eye barrier limits the frequent recruitment of immune cells, the certain correlation between galectin-3 and neutrophils implies that targeting galectin-3 could be a promising alternative for FK treatment during the different courses. It is reported that members of the galectin family are able to crosslink cell-surface glycoconjugates with β-galactoside, resulting in the regulation of

signaling, adhesion, and cell survival of immune cells such as neutrophils [7]. A specific alternative spliced form of galectin-3 has been reported to contain a predicted transmembrane-spanning domain. The neutrophils play a key role in immune responses caused by fungi infection. For the well-recognized key pathogenic role of neutrophils in FK, a novel role in host defense against fungal infections of ocular disease is found. The elevated galectin-3 expression might be an indicator of the inflammatory response against fungal infection. Thus, a decreased galectin-3 expression might be a "red light" signal of immunosuppressive drug abuse. Galectin-3 can serve as a sensitive biomarker for clinicians to make adjustments for better drug therapy [31, 32]. Besides, the increased levels of proinflammatory cytokines (IL-18, IL-1β, and TNF-α) in tear samples of FK patients, suggesting NLRP3 inflammasome activation, also contributes orchestration of neutrophil recruitment depending upon TLR-induced inflammatory cascade [33, 34].

It is controversial that it is whether the yeasts or hyphae are the certain forms of the pathogen to cause corneal infections; it is reported that yeasts are likely to activate immune response [35], while hyphae can activate the immune response and cause corneal stroma melting and corneal perforation at the same time; the expression levels of inflammatory factors could be affected by the forms of fungi [35]. With accumulating evidence, hyphae form is an essential pathogen agent in fungal infectious diseases. In a recent study, for gut fungal infection, the transition between yeast and invasive hyphae is crucial to fungal toxicity. The master regulator of hyphae-specific markers regulated the disease-causing potential of the pathogen. The formation of yeast-to-hyphae is essential for its pathogenesis [36]. It is also reported that fungi tended to provoke inflammatory responses only upon morphological transformation to their hyphal appearance [37]. Moreover, in skin lesions of fungal infection, the presence of hyphae is correlated with the intense production of proinflammatory cytokines [38]. We assumed that yeasts may exist in the early stage of disease and scar healing stage, but fungi thrive and grow robustly in the stage of disease progression, so the forms of fungi in this stage would be mixed. It could be a factor of the reason why the levels of inflammatory factors in tears are different from the early stage to the late stage, which is the reason why the form of fungi in the progression stage is mixed (both yeasts and hyphae). It could be a factor to affect inflammatory factor expression in tear samples in the early stage and the late stage.

In this study, for microsphere-based immunoassay analysis protein examination in tear samples, 9 patients with fungal keratitis in the early stage and 22 patients with fungal keratitis in the late stages were recruited. However, more patients could be recruited in future studies. For the limited quantity and size of corneal tissues taken from corneal transplantation surgeries, the RNA and protein expression of key disease markers were examined, while the expression levels of other markers remained to be done. With more accumulated corneal samples of fungal keratitis patients, future research should be undertaken to explore more essential biomarkers using RNA-seq, CO-IP, LC-MS, and so on.

There is accumulating evidence that galectin-3 regulates TLR activation and PAMPs at the beginning of host defense and inflammatory cascades [32]. Innate immune responses, including antigen-presenting, cell survival, ROS production, macrophage phagocytosis, cytokine production, and the microbial killing neutrophil generation take place sequentially in the pathogenesis of fungal keratitis [39, 40]. Our finding indicates the interactions between neutrophils and galectin-3. It has not been reported that galectin-3 regulates neutrophil functions, including recruitment, killing, and response to immune-modulatory cytokines in the fungal keratitis model in vivo. We intend to explore this mechanism in detail in the near future.

5. Conclusion

Conclusively, our results demonstrated that galectin-3 could be a significant and promising disease marker in fungal keratitis, and the galectin-3 modulation correlated with neutrophils in fungal keratitis at the early and late stages. In other words, galectin-3 might be a promising target for fungal keratitis therapeutic strategy in the future, which will shed some light on fungal keratitis patients, who are first to care.

Data Availability

The data and materials used to support the findings of this study are available from the corresponding author upon request.

Conflicts of Interest

The authors declare no competing financial interests.

Authors' Contributions

Jin Yuan guided the project. Yichen Xiao and Jiahui Yang conceived the project. Yichen Xiao and Jiahui Yang designed the experiments. Yichen Xiao, Jiahui Yang, Zhenyuan Fu, and Dalian He carried out the experiments. Yichen Xiao, Jiahui Yang, Zhenyuan Fu, and Dalian He analyzed the data. Yichen Xiao and Jiahui Yang wrote the manuscript draft. Jin Yuan revised the manuscript. All the authors have read and approved the submission for publication. Yichen Xiao Jiahui Yang contributed equally to this work and co-first author of this manuscript.

Acknowledgments

This work was supported by the National Natural Science Foundation of China (Nos. 81870633 and 82101086).

References

[1] L. Brown, A. K. Leck, M. Gichangi, M. J. Burton, and D. W. Denning, "The global incidence and diagnosis of fungal keratitis," *The Lancet Infectious Diseases*, vol. 21, no. 3, pp. e49–e57, 2021.

[2] L. Peng, J. Zhong, Y. Xiao et al., "Therapeutic effects of an anti-IL-6 antibody in fungal keratitis: macrophage inhibition and T

cell subset regulation," *International Immunopharmacology*, vol. 85, p. 106649, 2020.

[3] J. Zhong, W. Huang, Q. Deng et al., "Inhibition of TREM-1 and Dectin-1 alleviates the severity of fungal keratitis by modulating innate immune responses," *PLoS One*, vol. 11, no. 3, article e0150114, 2016.

[4] C. Pasare and R. Medzhitov, "Toll-like receptors: linking innate and adaptive immunity," *Microbes and Infection*, vol. 6, no. 15, pp. 1382–1387, 2004.

[5] S. M. Leal Jr., K. G. Rodino, W. C. Fowler, and P. H. Gilligan, "Practical guidance for clinical microbiology laboratories: diagnosis of ocular infections," *Clinical Microbiology Reviews*, vol. 34, no. 3, p. e0007019, 2021.

[6] R. Medzhitov, "Recognition of microorganisms and activation of the immune response," *Nature*, vol. 449, no. 7164, pp. 819–826, 2007.

[7] G. A. Rabinovich, L. G. Baum, N. Tinari et al., "Galectins and their ligands: amplifiers, silencers or tuners of the inflammatory response?," *Trends in Immunology*, vol. 23, no. 6, pp. 313–320, 2002.

[8] R. Lakshminarayan, C. Wunder, U. Becken et al., "Galectin-3 drives glycosphingolipid-dependent biogenesis of clathrin-independent carriers," *Nature Cell Biology*, vol. 16, no. 6, pp. 595–606, 2014.

[9] C. P. Rezende, P. K. Martins Oliveira Brito, A. M. Pessoni, T. A. da Silva, G. H. Goldman, and F. Almeida, "Altered expression of genes related to innate antifungal immunity in the absence of galectin-3," *Virulence*, vol. 12, no. 1, pp. 981–988, 2021.

[10] V. P. Mysore, Z. W. Zhou, C. Ambrogio et al., "A structural model of a Ras-Raf signalosome," *Nature Structural & Molecular Biology*, vol. 28, no. 10, pp. 847–857, 2021.

[11] Y. Zhang, J. Wu, Z. Xin, and X. Wu, "Aspergillus fumigatus triggers innate immune response via NOD1 signaling in human corneal epithelial cells," *Experimental Eye Research*, vol. 127, pp. 170–178, 2014.

[12] Y. Uchino, A. M. Woodward, J. Mauris et al., "Galectin-3 is an amplifier of the interleukin-1β-mediated inflammatory response in corneal keratinocytes," *Immunology*, vol. 154, no. 3, pp. 490–499, 2018.

[13] A. Romero and H. J. Gabius, "Galectin-3: is this member of a large family of multifunctional lectins (already) a therapeutic target?," *Expert Opinion on Therapeutic Targets*, vol. 23, no. 10, pp. 819–828, 2019.

[14] P. Zhou, M. C. Sieve, J. Bennett et al., "IL-12 prevents mortality in mice infected with Histoplasma capsulatum through induction of IFN-gamma," *Journal of Immunology*, vol. 155, no. 2, pp. 785–795, 1995.

[15] N. Nomi, K. Kimura, and T. Nishida, "Release of interleukins 6 and 8 induced by zymosan and mediated by MAP kinase and NF-kappaB signaling pathways in human corneal fibroblasts," *Investigative Ophthalmology & Visual Science*, vol. 51, no. 6, pp. 2955–2959, 2010.

[16] W. Huang, S. Ling, X. Jia et al., "Tacrolimus (FK506) suppresses TREM-1 expression at an early but not at a late stage in a murine model of fungal keratitis," *PLoS One*, vol. 9, no. 12, article e114386, 2014.

[17] Y. Acharya, B. Acharya, and P. Karki, "Fungal keratitis: study of increasing trend and common determinants," *Nepal Journal of Epidemiology*, vol. 7, no. 2, pp. 685–693, 2017.

[18] E. A. Machala, B. P. McSharry, B. T. Rouse, A. Abendroth, and B. Slobedman, "Gal power: the diverse roles of galectins in regulating viral infections," *The Journal of General Virology*, vol. 100, no. 3, pp. 333–349, 2019.

[19] B. D. Snarr, G. St-Pierre, B. Ralph et al., "Galectin-3 enhances neutrophil motility and extravasation into the airways during aspergillus fumigatus infection," *PLoS Pathogens*, vol. 16, no. 8, article e1008741, 2020.

[20] S. Sehrawat and M. Kaur, "Galectin-3 as a modifier of antimicrobial immunity: unraveling the unknowns," *Glycobiology*, vol. 30, no. 7, pp. 418–426, 2020.

[21] U. Schlötzer-Schrehardt, S. André, C. Janko et al., "Adhesion/growth-regulatory galectins in the human eye: localization profiles and tissue reactivities as a standard to detect disease-associated alterations," *Graefe's Archive for Clinical and Experimental Ophthalmology*, vol. 250, no. 8, pp. 1169–1180, 2012.

[22] P. Argüeso, A. Guzman-Aranguez, F. Mantelli, Z. Cao, J. Ricciuto, and N. Panjwani, "Association of cell surface mucins with galectin-3 contributes to the ocular surface epithelial barrier," *The Journal of Biological Chemistry*, vol. 284, no. 34, pp. 23037–23045, 2009.

[23] A. M. Park, S. Hagiwara, D. K. Hsu, F. T. Liu, and O. Yoshie, "Galectin-3 plays an important role in innate immunity to gastric infection by Helicobacter pylori," *Infection and Immunity*, vol. 84, no. 4, pp. 1184–1193, 2016.

[24] A. M. Woodward, J. Mauris, and P. Argueso, "Binding of transmembrane mucins to galectin-3 limits herpesvirus 1 infection of human corneal keratinocytes," *Journal of Virology*, vol. 87, no. 10, pp. 5841–5847, 2013.

[25] S. L. Farnworth, N. C. Henderson, A. C. MacKinnon et al., "Galectin-3 reduces the severity of pneumococcal pneumonia by augmenting neutrophil function," *The American Journal of Pathology*, vol. 172, no. 2, pp. 395–405, 2008.

[26] M. F. Ferrer, E. Scharrig, N. Charo et al., "Macrophages and galectin 3 control bacterial burden in acute and subacute murine leptospirosis that determines chronic kidney fibrosis," *Frontiers in Cellular and Infection Microbiology*, vol. 8, p. 384, 2018.

[27] E. M. Feeley, D. M. Pilla-Moffett, E. E. Zwack et al., "Galectin-3 directs antimicrobial guanylate binding proteins to vacuoles furnished with bacterial secretion systems," *Proceedings of the National Academy of Sciences of the United States of America*, vol. 114, no. 9, pp. E1698–E1706, 2017.

[28] I. Kuwabara and F. T. Liu, "Galectin-3 promotes adhesion of human neutrophils to laminin," *Journal of Immunology*, vol. 156, no. 10, pp. 3939–3944, 1996.

[29] H. Sano, D. K. Hsu, L. Yu et al., "Human galectin-3 is a novel chemoattractant for monocytes and macrophages," *Journal of Immunology*, vol. 165, no. 4, pp. 2156–2164, 2000.

[30] A. Karlsson, K. Christenson, M. Matlak et al., "Galectin-3 functions as an opsonin and enhances the macrophage clearance of apoptotic neutrophils," *Glycobiology*, vol. 19, no. 1, pp. 16–20, 2009.

[31] S. Sciacchitano, L. Lavra, A. Morgante et al., "Galectin-3: one molecule for an alphabet of diseases, from A to Z," *International Journal of Molecular Sciences*, vol. 19, no. 2, p. 379, 2018.

[32] K. Di Gregoli, M. Somerville, R. Bianco et al., "Galectin-3 identifies a subset of macrophages with a potential beneficial role in atherosclerosis," *Arteriosclerosis, Thrombosis, and Vascular Biology*, vol. 40, no. 6, pp. 1491–1509, 2020.

[33] K. Futosi, S. Fodor, and A. Mócsai, "Neutrophil cell surface receptors and their intracellular signal transduction pathways," *International Immunopharmacology*, vol. 17, no. 3, pp. 638–650, 2013.

[34] A. A. A. Silveira, V. M. Dominical, C. B. Almeida et al., "TNF induces neutrophil adhesion via formin-dependent cytoskeletal reorganization and activation of β-integrin function," *Journal of Leukocyte Biology*, vol. 103, no. 1, pp. 87–98, 2018.

[35] J. N. Witchley, P. Penumetcha, N. V. Abon, C. A. Woolford, A. P. Mitchell, and S. M. Noble, "Candida albicans morphogenesis programs control the balance between gut commensalism and invasive infection," *Cell Host & Microbe*, vol. 25, no. 3, pp. 432–443, 2019.

[36] O. Rogiers, D. Frising, D. S. A. Kucharíková et al., "Candidalysin crucially contributes to Nlrp3 inflammasome activation by Candida albicans hyphae," *MBio*, vol. 10, no. 1, p. e02221-18, 2019.

[37] I. M. Siqueira, R. J. A. de Castro, L. C. D. M. Leonhardt et al., "Modulation of the immune response by Fonsecaea pedrosoi morphotypes in the course of experimental chromoblastomycosis and their role on inflammatory response chronicity," *PLoS Neglected Tropical Diseases*, vol. 11, no. 3, p. e0005461, 2017.

[38] M. C. Almeida, D. Antunes, B. Silva et al., "Early interaction of Alternaria infectoria conidia with macrophages," *Mycopathologia*, vol. 184, no. 3, pp. 383–392, 2019.

[39] F. Almeida, J. M. Wolf, T. A. Da Silva et al., "Galectin-3 impacts Cryptococcus neoformans infection through direct antifungal effects," *Nature Communications*, vol. 8, no. 1, pp. 1–13, 2017.

[40] N. C. Henderson and T. Sethi, "The regulation of inflammation by galectin-3," *Immunological Reviews*, vol. 230, no. 1, pp. 160–171, 2009.

Hindawi
Disease Markers
Volume 2022, Article ID 9082576, 11 pages
https://doi.org/10.1155/2022/9082576

Research Article

Exploring the Potential Mechanisms of *Melilotus officinalis* (L.) Pall. in Chronic Muscle Repair Patterns Using Single Cell Receptor-Ligand Marker Analysis and Molecular Dynamics Simulations

Yisheng Chen,[1] Zhiwen Luo,[1] Jinrong Lin,[1] Beijie Qi,[1] Yaying Sun,[1] Fangqi Li,[1] Chenyang Guo,[2] Weiwei Lin,[3] Xueran Kang,[4] Xinyi He,[5] Qian Wang,[6] Shiyi Chen,[1] and Jiwu Chen[2]

[1]*Department of Sports Medicine, Huashan Hospital, Fudan University, Shanghai, China*
[2]*Department of Orthopedics, Shanghai General Hospital, Shanghai Jiao Tong University School of Medicine, Shanghai Jiao Tong University, Shanghai 200080, China*
[3]*Department of Neurosurgery, Second Affiliated Hospital of Zhejiang University School of Medicine, Zhejiang University, 88 Jiefang Road, Hangzhou, 310009 Zhejiang, China*
[4]*Shanghai Jiao Tong University, Shanghai 200080, China*
[5]*State Key Laboratory of Genetics Engineering, Collaborative Innovation Center for Genetics and Development, School Life Sciences and Human Phenome Institute, Fudan University, Shanghai, China*
[6]*Postdoctoral Workstation, Department of Central Laboratory, The Affiliated Taian City Central Hospital of Qingdao University, Taian 271000, China*

Correspondence should be addressed to Qian Wang; qianqianwangxi@163.com, Shiyi Chen; cshiyi@163.com, and Jiwu Chen; jeevechen@gmail.com

Received 17 December 2021; Revised 28 February 2022; Accepted 26 April 2022; Published 1 June 2022

Academic Editor: Alexander Berezin

Information regarding the function of *Melilotus officinalis* (L.) Pall. in skeletal muscles is still unknown. In this study, we explored the possible regulatory targets of M. (L.) Pall. that affects the repair patterns in chronic muscle injury. We analyzed the potential target genes and chemical composition of M. (L.) Pall. and constructed a "drug-component-disease target genes" network analysis. Five active ingredients and 87 corresponding targets were obtained. Muscle-tendon junction (MTJ) cells were used to perform receptor-ligand marker analysis using the CellphoneDB algorithm. Targets of M. (L.) Pall. were screened further for the cellular ligand-receptor protein action on MTJs. Enrichment analysis suggests that those protein-associated ligand receptors may be associated with a range of intercellular signaling pathways. Molecular docking validation was then performed. Five proteins (CCL2, VEGFA, MMP2, MET, and EGFR) may be regulated by the active ingredient luteolin and scoparone. Finally, molecular dynamics simulations revealed that luteolin can stably target binding to MMP2. M. (L.) Pall. influences skeletal muscle repair patterns by affecting the fibroblast interactions in the muscle-tendon junctions through the active ingredients luteolin and scoparone.

1. Introduction

Melilotus officinalis (L.) Pall. (M. (L.) Pall.) is a traditional Chinese medicine that is widely distributed and has broad prospects for development and utilization [1]. M. (L.) Pall. has antiedema, antioxidant, and hepatoprotective properties [1–3]. In ancient China, M. (L.) Pall. was used to treat a variety of chronic diseases [4]. M. (L.) Pall. is often used to reduce postoperative edema and promote early recovery after clinical orthopedic and sports medicine procedures. However, the function of M. (L.) Pall. in chronic skeletal muscle injury is unproven.

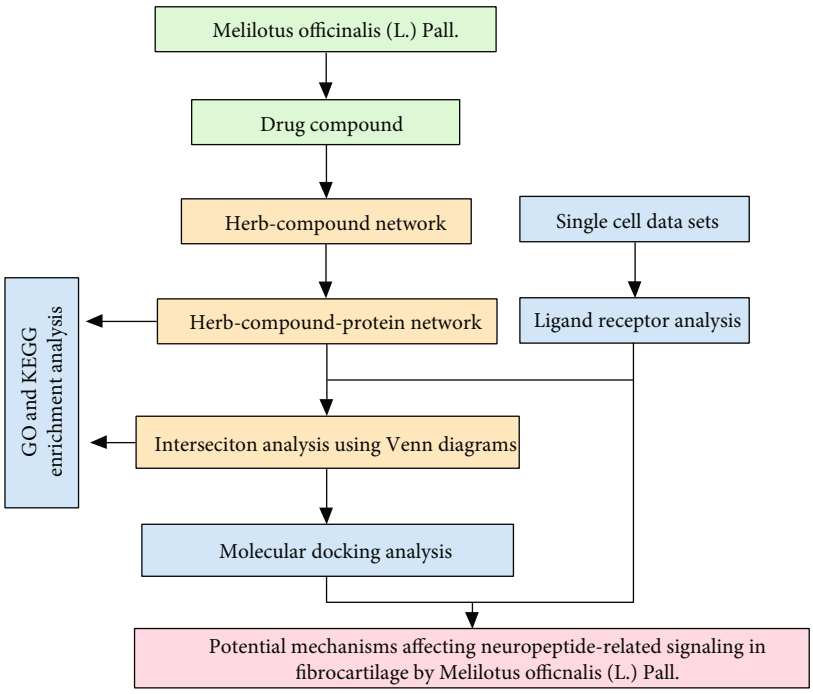

Figure 1: Research flow chart.

Skeletal muscle injuries are one of the most common sports injuries, accounting for approximately 40% of sports-related injuries in older people [5]. Muscles can be damaged by external forces, biological factors, and chemical factors [6, 7]. Excessive chronic injuries will lead to scar formation and fat infiltration [8, 9]. Therefore, understanding the factors influencing muscle repair can help promote skeletal muscle repair [10, 11]. Recent topical studies have explored the spatial-positional interactions of skeletal muscle regeneration and their underlying mechanisms to find new ways to improve the repair potential of skeletal muscles [12, 13]. Recent studies have found that the positional information driving limb muscle patterns are contained in the fibroblasts of the connective tissues [14]. Our previous studies have annotated and functionally analyzed these cells [15]. These cells have extensive intercellular interactions via the ligand-receptor pathway.

Liu et al. isolated 29 compounds from M. (L.) Pall. alcoholic extracts. They have good antioxidant activity and play an important role in anti-inflammatory and antioxidant functions [16]. Recent studies have also found that M. (L.) Pall. promotes wound repair [17]. This study provides a new way to explore these effects of M. (L.) Pall. in skeletal muscles by targeting the ligand-receptor pathway, which is important for drug function [18, 19]. Studying the effects of M. (L.) Pall. in the skeletal muscle fibroblasts allows us to explore its potential mechanisms in muscle repair patterns.

In this study, network pharmacology and molecular docking approaches have been used to predict the possible regulatory targets of M. (L.) Pall. in muscle repair patterns, to reveal the potential molecular mechanisms of this compound in regulating muscle repair patterns and provide new ideas for the treatment of skeletal muscle injury.

Table 1: Six active ingredients of M. (L.) Pall. were screened.

Molecule name	Molecule ID	OD	Drug-likeness
Scoparone	MOL001999	74.75	0.09
Ferulic acid	MOL000360	39.56	0.06
Soyasapogenol E	MOL003651	37.64	0.75
Beta-sitosterol	MOL000358	36.91	0.75
Luteolin	MOL000006	36.16	0.25
Salicylic acid	MOL001801	32.13	0.03

2. Materials and Methods

2.1. Screening for Active Ingredients and Targets of M. (L.) Pall. The active ingredients of M. (L.) Pall. were obtained from previous research results [16]. The active ingredients of M. (L.) Pall. were screened from the Traditional Chinese Medicine Systems Pharmacology Database and Analysis Platform (TCMSP) [20] database using the following conditions: oral bioavailability (OB) ≥ 30% and drug – likeness (DL) ≥ 0.1820 . Potential target genes of M. (L.) Pall. were obtained by converting the screened active ingredients into corresponding targets through the UniProt database (http://www.uniprot.org/).

2.2. "Drug-Component-Target" Network Construction. A "drug-component-target" network structure was constructed with the active ingredient and corresponding target genes of M. (L.) Pall. using the Cytoscape (version 3.7.2) software [21]. Each node and edge in the network was analyzed to determine the relationship between the diseases and drug actions.

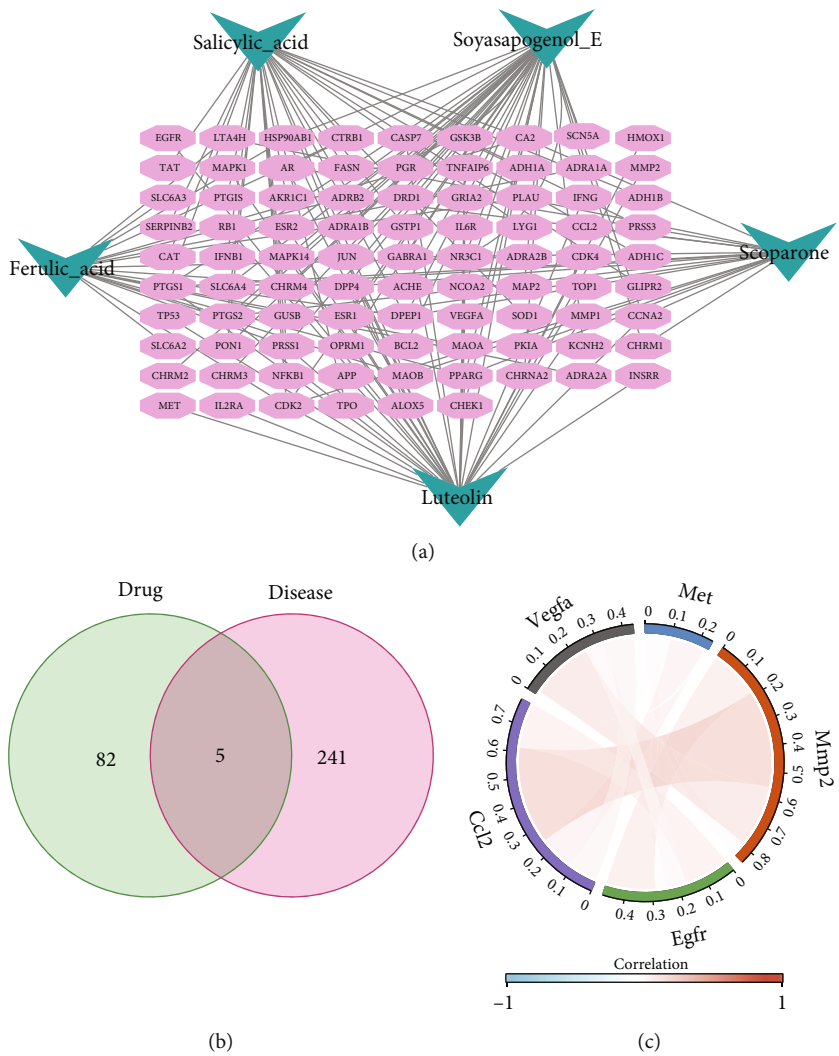

Figure 2: Potential role of M. (L.) Pall. (a) "drug-component-disease target genes" network; (b) drug target-MTJ ligand-receptor Venn diagram; (c) correlation analysis of five receptor-ligand-related genes (CCL2, EGFR, MMP2, MET, and VEGFA) demonstrated by the chord diagram.

2.3. Single-Cell Dataset-Based Receptor-Ligand Marker Analysis. Seurat results from our previous study of single-cell data analysis were used to perform ligand-receptor maker analysis [15]. Muscle-tendon junction (MTJ) cells were obtained from the GEO dataset of GSE168153 [14]. GSE168153 is a single-cell dataset describing fibroblasts in muscle tendon junctions. Receptor-ligand marker analysis of the MTJ cells was performed using the CellphoneDB algorithm (v2.1.2), to analyze the cellular interactions in MTJ regions [22]. After filtering with $P < 0.05$, key intercellular interactions were identified. The results were visualized using the dot_plot function in the CellphoneDB and the R software.

2.4. Screening and Molecular Docking Validation for the M. (L.) Pall. Cellular Action Targets in MTJs. R language and VennDiagram packages were used to obtain the M. (L.) Pall. targets on the MTJ cells [23]. The active ingredients of the drug were pretreated as shown in the following: screening of key targets and active ingredients in "drug-component-target," downloading 3D structures of active ingredients (mol2 format) from PubChem database, hydrogenation, charge addition, root detection of ligands, search and definition of rotatable bonds, etc. [24]. The 3D structure of the target protein was downloaded from the Protein Data Bank, all hydrogen atoms were added, Gasteiger charges were calculated, and nonpolar hydrogens were combined and saved in the pdbqt format using the AutoDock software [25]. The parameter exhaustiveness was set to 20, and other parameters were set to default values. AutoDock Vina 1.1.2 was used for molecular docking, and PyMOL was used for plotting [26].

2.5. Molecular Dynamics Simulation. To perform molecular dynamics simulations (MD), the force field parameters of luteolin were generated in this study using ACPYPE Server, an online tool [25, 27, 28]. Protein force fields are described by CHARMM [29]. TIP3P is for water modeling. The simulation was performed after a slow increase in system temperature from 0 K to 307 K. MD simulations were performed

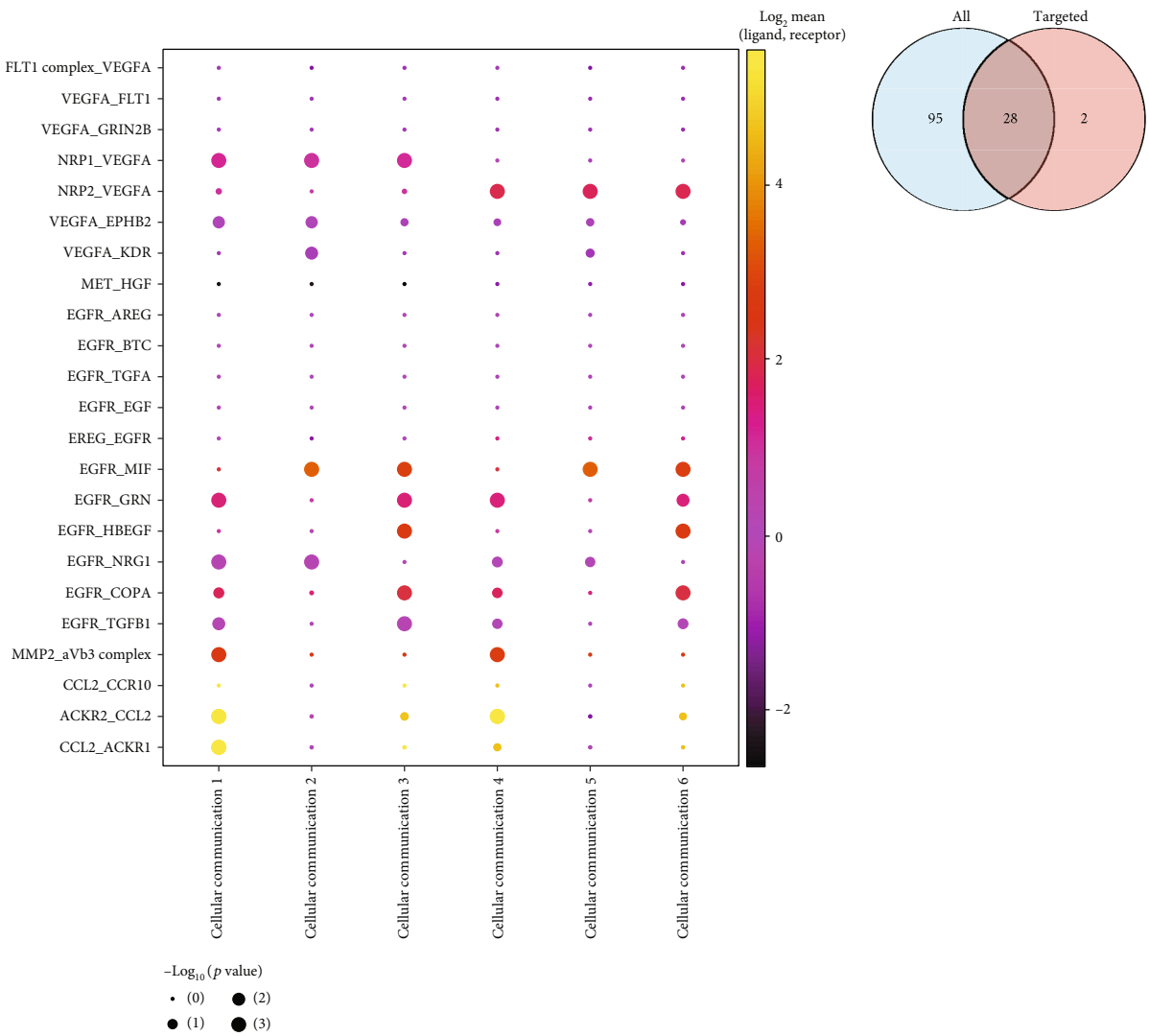

(a) (b)

Figure 3: Continued.

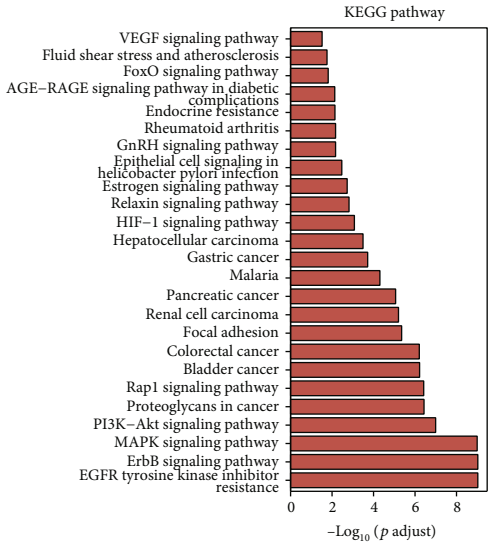

(c)

Figure 3: Ligand receptor analysis of MTJs targeted by M. (L.) Pall. (a) The key intercellular ligand-receptor interactions in MTJs, the vertical coordinate is the type of receptor-ligand linkage, and the horizontal coordinate is the corresponding cell-cell interaction; (b) "drug-component-disease target genes" network-MTJ ligand receptor-related pathway intersection analysis, "ALL" represents targets that M. (L.) Pall. may target, and "targeted" represents ligand-receptor-associated genes in (a); (c) enriched KEGG pathways.

using the GROMACS software under constant temperature and pressure conditions as shown in previous studies. Visualization of the results of molecular dynamics simulations was done using PyMOL [26, 29, 30].

2.6. Gene Ontology (GO) Functional Enrichment Analysis and Kyoto Encyclopedia of Genes and Genomes (KEGG) Pathway Enrichment Analysis. The study species was *homo sapiens*, and molecular function (MF), biological process (BP), and cellular component (CC) were used for GO enrichment analysis as previous researches [31–33]. The significance of the KEGG pathway was set at $P < 0.05$ to search for the major functional and in vivo pathways significantly enriched by the active ingredient targets. Bar graphs of the pathways in the GO and KEGG pathway enrichment analysis were plotted using the clusterProfiler toolkit in R and ggplot [19, 34].

2.7. Statistical Analysis. Statistical analyses were performed using the R software (version 3.6.3), and differences were significant at $P < 0.05$. Spearman's method was used for correlation analysis, and the results of the analysis were presented as chord plots using the circlize package of the R software (version 0.4.12) [35].

3. Results

3.1. Screening for Potentially Active Compounds in M. (L.) Pall. Figure 1 depicts the research flow of this study. The active ingredients of M. (L.) Pall. are based on previous research results [16]. Six active ingredients were screened according to the following conditions: OB ≥ 30% and DL ≥ 0.18 (Table 1).

3.2. Potential M. (L.) Pall. Targets of on the MTJ Cells. Five of the six active ingredients had 87 corresponding targets (after excluding duplicates). The "herbal-active-component-disease target gene" regulatory network was constructed (Figure 2(a)). The red oval in the diagram represents the gene corresponding to the target protein. The green triangle represents the active ingredient. MTJ cells from the GSE168153 dataset were used for ligand-receptor analysis. All 246 potential ligand-receptor key genes were extracted. Cross-talk analysis revealed that M. (L.) Pall. might regulate the proteins of five genes (Figure 2(b)). Correlation analysis revealed that the expressions of CCL2, VEGFA, MET, MMP2, and EGFR were positively correlated with each other (Figure 2(c)).

3.3. Potential Effects of M. (L.) Pall. on MTJ Cells. As previously described, the data and cellular annotations for ligand-receptor maker analysis were obtained from GSE168153 database and our previous study, respectively. The receptor-ligand marker analysis of the MTJ cells was performed using the CellphoneDB algorithm (v2.1.2) (Figure 3(a)). The intersection analyses between the target enrichment pathways of M. (L.) Pall. and ligand receptor-related pathways of MTJs are shown in Figure 3(b). These target genes were found to be enriched in 28 KEGG pathways (EGFR tyrosine kinase inhibitor resistance, cancer-related pathway, epithelial cell signaling in *Helicobacter pylori* infection, rheumatoid arthritis, endocrine resistance; ErbB, MAPK, PI3K−Akt, Rap1, HIF−1, relaxin, estrogen, GnRH, and AGE−RAGE signaling pathways in diabetic complications; and so on). This suggests that M. (L.) Pall. may target some intercellular signaling pathways, such as neuropeptide-related, tumor-related, and stress direction-

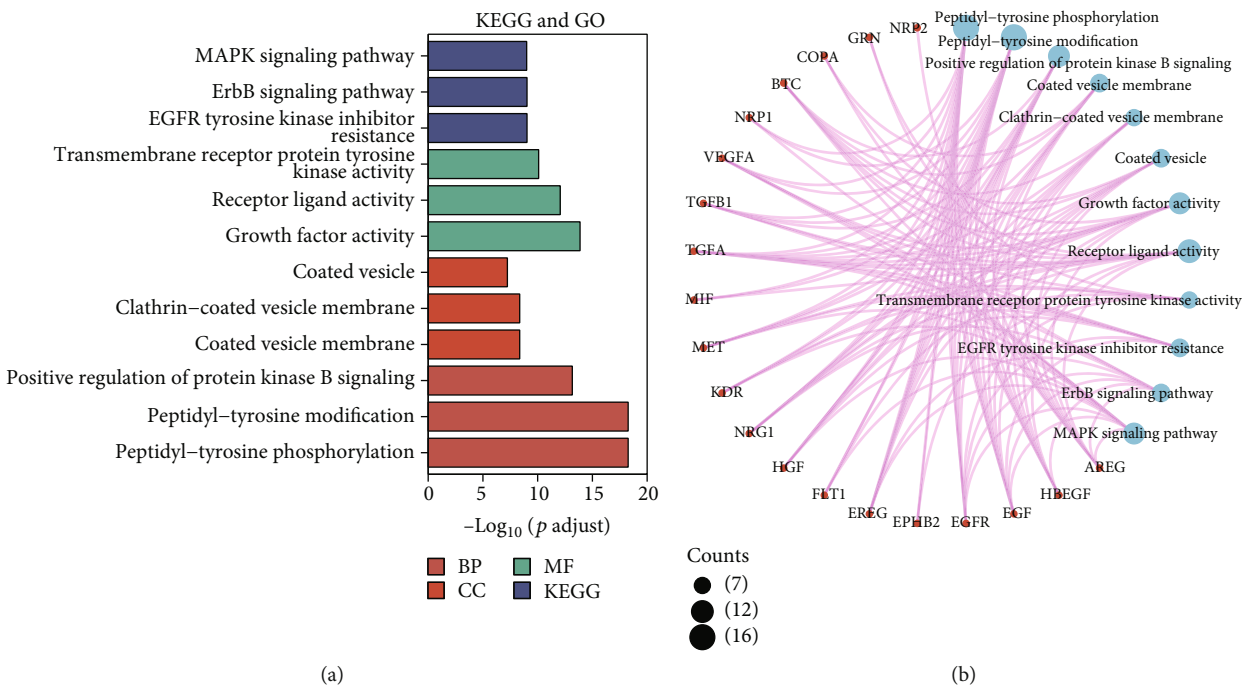

Figure 4: Enrichment analysis of core target proteins of M. (L.) Pall. (a) GO and KEGG enrichment analyses of core target proteins. (b) Distribution of the proteins in (a) from the GO and KEGG pathways.

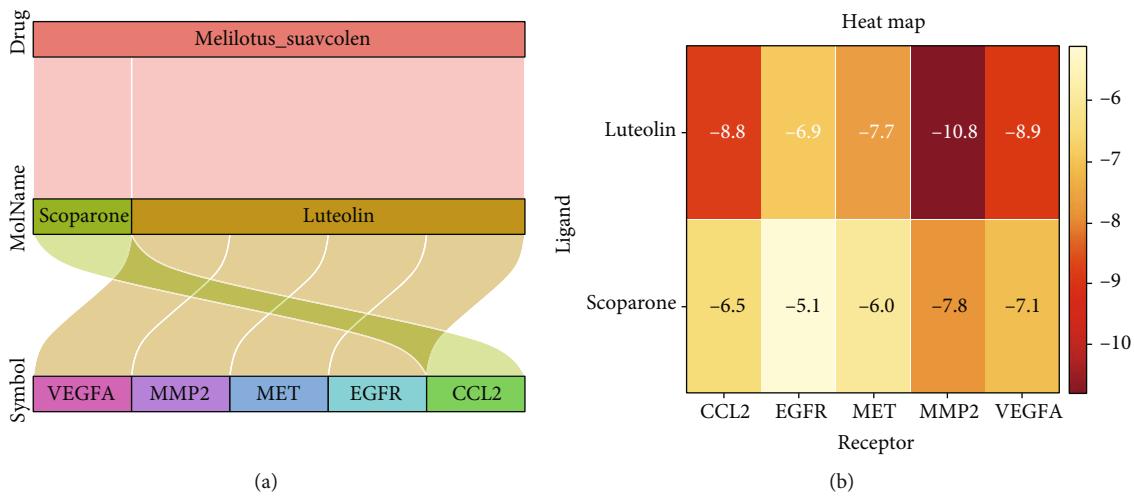

Figure 5: M. (L.) Pall. active ingredient-target protein regulatory relationships. (a) The Sankey diagram suggests that scoparone, the active ingredient of M. (L.) Pall. targets CCL2 and luteolin targets VEGFA, MMP2, MET, and EGFR. (b) Heat map showing the minimum binding energy of scoparone and luteolin to dock with target proteins CCL2, VEGFA, MMP2, MET, and EGFR.

related pathways (Figures 2(b) and 2(c)). These genes were also enriched in metabolic functions (MF), including transmembrane receptor protein tyrosine kinase, receptor-ligand, and growth factor activities. Moreover, these genes were found to be enriched in cellular functions (CC), including coated vesicle, clathrin-coated vesicle membrane, and coated vesicle membrane. In biological processes (BP), these genes are enriched in the positive regulation of protein kinase B signaling, peptidyl-tyrosine modification, and peptidyl-tyrosine phosphorylation (Figures 4(a) and 4(b)).

3.4. Regulatory Relationship and Molecular Docking Analysis of Active Ingredient-Target Proteins of M. (L.) Pall. Pharmacological database analysis suggests that scoparone, the active ingredient of M. (L.) Pall. targets CCL2 and luteolin targets VEGFA, MMP2, MET, and EGFR (Figure 5(a)). CCL2, VEGFA, MMP2, MET, and EGFR were molecularly docked to the two key pharmacodynamic components (scoparone, luteolin) of M. (L.) Pall. The lowest docking binding energy is shown in Figure 5(b). These molecular dockings are visualized in Figures 6(a)–6(e). The hydrogen bonds

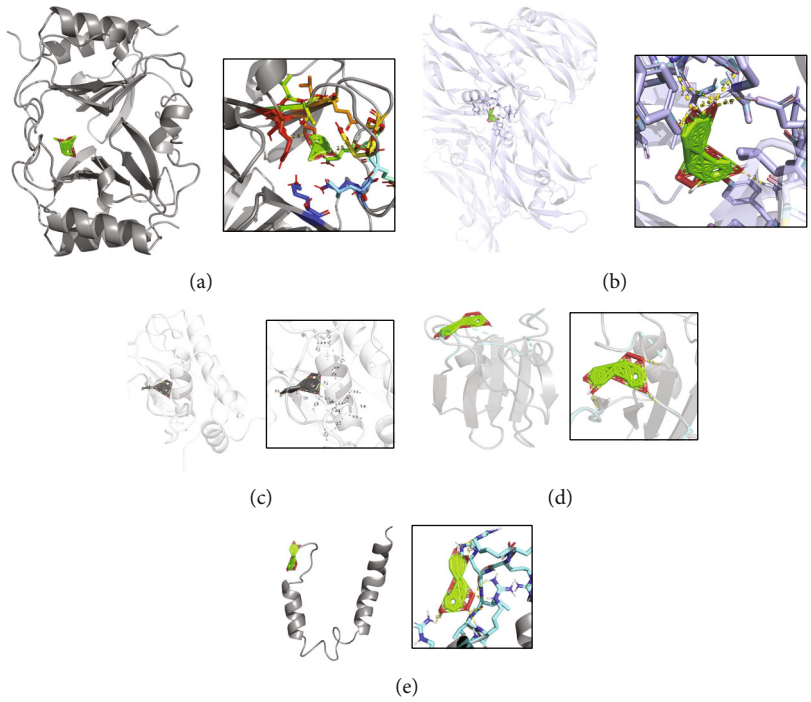

Figure 6: Schematic representation of molecular docking of target proteins with the active ingredients of M. (L.) Pall. (a) Interaction of scoparone with target CCL2 protein. (b) Interaction of luteolin with the target VEGFA protein. (c) Interaction of luteolin with the target MMP2 protein. (d) Interaction of luteolin with the target MET protein. (e) Interaction of luteolin with target EGFR protein. The dashed line indicates the hydrogen bond and marks the distance between the hydrogen bond and the compound.

are indicated using dashed lines, and the distances between the hydrogen bonds and the compounds are also marked. The scoparone target binding CCL2 protein has a free energy of -6.5 kJ/mol. The free energies of luteolin target binding energy for VEGFA, MMP2, MET, and EGFR proteins are -8.9, -10.8, -7.7, and -6.9 kJ/mol, respectively. The minimum binding energies of these two key components to CCL2, VEGFA, MMP2, MET, and EGFR were less than -5.0 kJ/mol suggesting that M. (L.) Pall. exerts its effects mainly by targeting these components through scoparone and luteolin.

3.5. Molecular Dynamics Simulations of MMP2 and Luteolin. In the above molecular docking analysis, MMP2 and luteolin had the minimum binding free energy. The free energy of luteolin target binding energy for MMP2 is -10.8 kJ/mol. To further assess the binding efficacy of MMP2 and luteolin, MD simulations were performed (Figure 7(a)). Due to the interaction between MMP2 and luteolin, the root mean square displacement (RMSD) was found to increase at first and then stabilise (Figure 7(b)). The radius of gyration (Rg) of the MMP2-lutelin complex was also found to stabilise with the time passing (Figure 7(c)). In addition, the number of hydrogen bonds formed by MMP2 with luteolin remained in a relatively stable range (Figure 7(d)). The overall free energy in the system was also found to be stable (Figure 7(e)). Finally, MD simulations revealed that luteolin can stably target binding to MMP2.

4. Discussion

To the best of our knowledge, this study is the first to assess the impact of M. (L.) Pall. on the musculotendinous junction. According to the TCMSP database, M. (L.) Pall. has five active ingredients (OB ≥ 30% and DL ≥ 0.18) potentially acting on 87 targets. Therefore, the "herb-active ingredient-disease target gene" network was constructed. We found that M. (L.) Pall. influences the interaction of fibroblasts in muscle-tendon junctions and affects muscle repair patterns through the modulation of five ligand receptor-related proteins (CCL2, VEGFA, MMP2, MET, and EGFR) using the active ingredients luteolin and scoparone. And MD simulations revealed that luteolin can stably target binding to MMP2.

Scoparone is a naturally occurring coumarin found in green plants. It is purified from a lipid-lowering herb that reduces the proliferation of human peripheral blood mononuclear cells, scavenges reactive oxygen species, inhibits tyrosine kinase, and enhances the production of prostaglandins [36]. Recent studies have confirmed that scoparone has various biological activities such as antifibrosis, antioxidant, and fat differentiation inhibition [37–39]. Scoparone was also found to inhibit high-glucose-induced activation of the ERK1/2 signaling pathway in thylakoid cells and played an active role in inhibiting the accumulation of extracellular matrix in the high-glucose microenvironment [40]. In this study, scoparone was found to target CCL2. CCL2 is a ligand for CCR2. Inhibition of CCR2 after injury promotes skeletal muscle

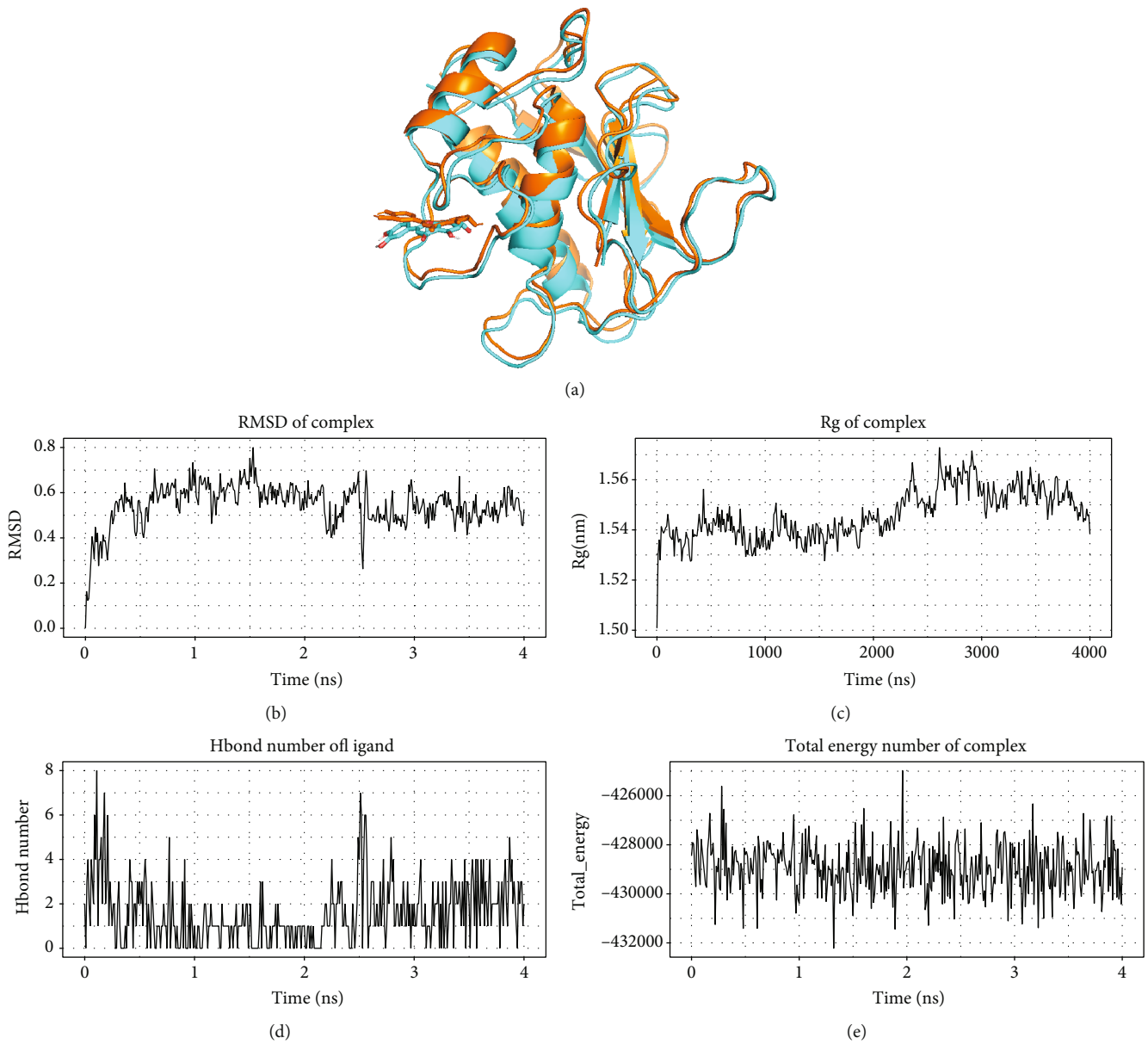

Figure 7: Molecular dynamics simulations of MMP2 and luteolin. (a) Conformational changes of the complex before and after MD, brown indicates before MD, and blue indicates after MD. (b) Variation of the root mean square displacement (RMSD) of the MMP2-lutelin complex. (c) Variation of the radius of gyration (Rg) of the MMP2-lutelin complex with time. (d) Variation of the number of hydrogen bonds formed between MMP2 and luteolin with time. (e) The free energy of binding between the small molecule ligand and the protein over time.

regeneration and function recovery [41, 42]. Our study suggests that scoparone may inhibit the function of CCR2 by binding to CCL2, and this may be a potential mechanism for M. (L.) Pall. to promote skeletal muscle regeneration.

Recent studies have found that luteolin protects skeletal muscles from attrition caused by inflammation and downregulates the expression of proteins associated with muscle catabolism [43]. Luteolin increased muscle strength in fatigued subjects and improved skeletal muscle contraction during ischemia and reperfusion [44]. In this study, luteolin targeted VEGFA, MMP2, MET, and EGFR. Luteolin inhibits VEGFA and affects microvascular networks formed during neovascularization in mice [45]. In tumors, luteolin inhibits MMP2 and MET [46–48]. Luteolin also inhibits downstream signaling molecules activated by EGFR, especially the Akt and MAPK signaling pathways [49].

Luteolin was found to target MMP2 in MD simulations. Elevated levels of MMP2 expression are associated with insulin resistance due to extracellular matrix (ECM) remodelling in skeletal muscle [50]. This suggests that luteolin targeting of MMP2 may have the potential to improve insulin resistance due to ECM. MMP2 has been found to be widespread in skeletal muscle, and therefore, the study of its function is important for exploring the repair of skeletal muscle after injury

[51]. For example, both exogenous hydrogen sulphide and electroacupuncture treatments can improve skeletal muscle injury and reduce skeletal muscle fibrosis by downregulating MMP2 and related pathways [5, 52]. In the present study, luteolin was found to target MMP2, which may contribute to skeletal muscle injury repair.

This study provides new data supporting the treatment of sports injuries using M. (L.) Pall. and provides a theoretical basis for clinical application. All the core components of M. (L.) Pall. were screened and docked successfully with their key targets. The core components of M. (L.) Pall. have good binding activities to their key targets, suggesting that they can effectively treat skeletal muscles. However, more Chinese medicine databases need to be used, and target prediction databases need to be improved. This study did not directly examine the chronic muscle injury dataset, but rather by examining the MTJ fibroblastic dataset, which may be biased. Furthermore, more in vivo and ex vivo clinical studies are also needed to validate the mechanisms of action M. (L.) Pall. in the treatment of chronic skeletal muscle injury.

5. Conclusion

In summary, this study demonstrates that M. (L.) Pall. can skeletal muscle injury by acting on CCL2, VEGFA, MMP2, MET, and EGFR, through luteolin and scoparone. They are the key active ingredients of M. (L.) Pall. and affect intercellular signaling, such as neuropeptide-related, tumor-related, and stress-related pathways. M. (L.) Pall. may influence the interaction of fibroblasts in muscle tendon junctions to affect muscle repair patterns. Molecular docking analysis validated some of the network pharmacology results and confirmed the multicomponent, multitarget, and multipathway characteristics of M. (L.) Pall. in the treatment of skeletal muscle injury.

Data Availability

Muscle tendon junction (MTJs) cells are from the GEO dataset in the GSE168153 database.

Conflicts of Interest

The authors declare that they have no conflicts of interest.

Authors' Contributions

Yisheng Chen, Zhiwen Luo, Jinrong Lin, and Beijie Qi contributed equally to this work.

Acknowledgments

Thanks are due to all those who worked on this study. This study was supported by grants from the National Natural Science Foundation of China (Nos. 82102634, 81972062, and 81772419) and the Medical and Health Science and Technology Development Project of Shandong Province (2018WS147). This work was also supported by the Project of the Key Clinical Medicine Center of Shanghai (No. 2017ZZ01006), the Sanming Project of Medicine in Shenzhen (No. SZSM201612078), the Development Project of Shanghai Peak Disciplines-Integrative Medicine (No. 20180101), and the Shanghai Committee of Science and Technology (No. 19441901600). We thank Bullet Edits Limited for the linguistic editing and proofreading of the manuscript.

References

[1] M. Ilhan, Z. Ali, I. A. Khan, H. Taştan, and E. Küpeli Akkol, "The regression of endometriosis with glycosylated flavonoids isolated from Melilotus officinalis (L.) Pall. in an endometriosis rat model," *Taiwanese Journal of Obstetrics & Gynecology*, vol. 59, no. 2, pp. 211–219, 2020.

[2] G. Paun, E. Neagu, C. Albu, S. Savin, and G. L. Radu, "In vitro evaluation of antidiabetic and anti-inflammatory activities of polyphenolic-rich extracts from Anchusa officinalis and Melilotus officinalis," *ACS Omega*, vol. 5, no. 22, pp. 13014–13022, 2020.

[3] I. W. Southon, J. Buckingham, F. A. Bisby, and J. B. Harborne, *Phytochemical Dictionary of the Leguminosae*, Chapman and Hall/CRC, 1994.

[4] China Ministry of Health, *People's Republic of China Ministry of Health Drug Standard Tibetan Medicine. Volume 1. in 65*, Chemical Industry Press, 1995.

[5] H. Han, M. Li, H. Liu, and H. Li, "Electroacupuncture regulates inflammation, collagen deposition and macrophage function in skeletal muscle through the TGF-β1/Smad3/p38/ERK1/2 pathway," *Experimental and Therapeutic Medicine*, vol. 22, no. 6, p. 1457, 2021.

[6] T. A. H. Järvinen, T. L. N. Järvinen, M. Kääriäinen et al., "Muscle injuries: optimising recovery," *Best Practice & Research. Clinical Rheumatology*, vol. 21, no. 2, pp. 317–331, 2007.

[7] Y. Chen, Y. X. Cai, X. R. Kang et al., "Predicting the risk of sarcopenia in elderly patients with patellar fracture: development and assessment of a new predictive nomogram," *PeerJ*, vol. 8, article e8793, 2020.

[8] M. L. Bayer, M. Hoegberget-Kalisz, R. B. Svensson et al., "Chronic sequelae after muscle strain injuries: influence of heavy resistance training on functional and structural characteristics in a randomized controlled trial," *The American Journal of Sports Medicine*, vol. 49, no. 10, pp. 2783–2794, 2021.

[9] S. Mannava, J. F. Plate, P. W. Whitlock et al., "Evaluation of in vivo rotator cuff muscle function after acute and chronic detachment of the supraspinatus tendon: an experimental study in an animal model," *Journal of Bone and Joint Surgery*, vol. 93, no. 18, pp. 1702–1711, 2011.

[10] S. Corti, S. Strazzer, R. del Bo et al., "A subpopulation of murine bone marrow cells fully differentiates along the myogenic pathway and participates in muscle repair in the mdx dystrophic mouse," *Experimental Cell Research*, vol. 277, no. 1, pp. 74–85, 2002.

[11] Z. Luo, Y. Sun, B. Qi et al., "Human bone marrow mesenchymal stem cell-derived extracellular vesicles inhibit shoulder stiffness via let-7a/Tgfbr1 axis," *Bioactive Materials*, vol. 17, pp. 344–359, 2022.

[12] A. L. Mackey and M. Kjaer, "Connective tissue regeneration in skeletal muscle after eccentric contraction-induced injury," *Journal of Applied Physiology*, vol. 122, no. 3, pp. 533–540, 2017.

[13] X. Yin, T. Yu, B. Chen et al., "Spatial distribution of motor endplates and its adaptive change in skeletal muscle," *Theranostics*, vol. 9, no. 3, pp. 734–746, 2019.

[14] J. Esteves de Lima, C. Blavet, M. A. Bonnin et al., "Unexpected contribution of fibroblasts to muscle lineage as a mechanism for limb muscle patterning," *Nature Communications*, vol. 12, no. 1, p. 3851, 2021.

[15] Y. Chen, C. Chen, X. Xiao, Z. Huang, X. Huang, and W. Yao, "TNF-α induces neutrophil apoptosis delay and promotes intestinal ischemia- reperfusion-induced lung injury through activating JNK/FoxO3a pathway," *Oxidative Medicine and Cellular Longevity*, vol. 2021, 13 pages, 2021.

[16] Y.-T. Liu, P. H. Gong, F. Q. Xiao et al., "Chemical constituents and antioxidant, anti-inflammatory and anti-tumor activities of Melilotus officinalis (Linn.) Pall," *Molecules*, vol. 23, no. 2, p. 271, 2018.

[17] M. Shahrousvand, V. Haddadi-Asl, and M. Shahrousvand, "Step-by-step design of poly (ε-caprolactone) /chitosan/Melilotus officinalis extract electrospun nanofibers for wound dressing applications," *International Journal of Biological Macromolecules*, vol. 180, pp. 36–50, 2021.

[18] P. De Benedetti and F. Fanelli, "Ligand-receptor communication and drug design," vol. 10, no. 2, pp. 186–193, 2009.

[19] J. W. Peng, "Communication breakdown: protein dynamics and drug design," *Structure*, vol. 17, no. 3, pp. 319-320, 2009.

[20] J. Ru, P. Li, J. Wang et al., "TCMSP: a database of systems pharmacology for drug discovery from herbal medicines," *Journal of Cheminformatics*, vol. 6, no. 1, p. 13, 2014.

[21] P. Shannon, A. Markiel, O. Ozier et al., "Cytoscape: a software environment for integrated models of biomolecular interaction networks," *Genome Research*, vol. 13, no. 11, pp. 2498–2504, 2003.

[22] M. Efremova, M. Vento-Tormo, S. A. Teichmann, and R. Vento-Tormo, "CellPhoneDB: inferring cell-cell communication from combined expression of multi-subunit ligand-receptor complexes," *Nature Protocols*, vol. 15, no. 4, pp. 1484–1506, 2020.

[23] H. Chen and P. C. Boutros, "VennDiagram: a package for the generation of highly-customizable Venn and Euler diagrams in R," *BMC Bioinformatics*, vol. 12, no. 1, p. 35, 2011.

[24] S. Kim, "Getting the most out of PubChem for virtual screening," *Expert Opinion on Drug Discovery*, vol. 11, no. 9, pp. 843–855, 2016.

[25] O. Trott and A. J. Olson, "AutoDock Vina: improving the speed and accuracy of docking with a new scoring function, efficient optimization, and multithreading," *Journal of Computational Chemistry*, vol. 31, no. 2, pp. NA–461, 2009.

[26] D. Seeliger and B. L. de Groot, "Ligand docking and binding site analysis with PyMOL and AutoDock/Vina," *Journal of Computer-Aided Molecular Design*, vol. 24, no. 5, pp. 417–422, 2010.

[27] S. Kim, A. Gindulyte, J. Zhang, P. A. Thiessen, and E. E. Bolton, "PubChem periodic table and element pages: improving access to information on chemical elements from authoritative sources," *Chemistry Teacher International*, vol. 3, no. 1, pp. 57–65, 2021.

[28] A. W. Sousa da Silva and W. F. Vranken, "ACPYPE - AnteChamber PYthon Parser interfacE," *BMC Research Notes*, vol. 5, no. 1, p. 367, 2012.

[29] M. J. Abraham, T. Murtola, R. Schulz et al., "GROMACS: high performance molecular simulations through multi-level parallelism from laptops to supercomputers," *SoftwareX*, vol. 1-2, pp. 19–25, 2015.

[30] Y. Zhang, J. Zhang, C. Sun, and F. Wu, "Identification of the occurrence and potential mechanisms of heterotopic ossification associated with 17-beta-estradiol targeting MKX by bioinformatics analysis and cellular experiments," *PeerJ*, vol. 9, article e12696, 2022.

[31] Y. Chen, X. R. Kang, Z. H. Zhou et al., "MiR-1908/EXO1 and MiR-203a/FOS, regulated by scd1, are associated with fracture risk and bone health in postmenopausal diabetic women," *Aging*, vol. 12, no. 10, pp. 9549–9584, 2020.

[32] W.-W. Lin, L.-T. Xu, Y.-S. Chen, K. Go, C. Sun, and Y.-J. Zhu, "Single-cell transcriptomics-based study of transcriptional regulatory features in the mouse brain vasculature," *BioMed Research International*, vol. 2021, Article ID 7643209, 15 pages, 2021.

[33] J. Wu, J. Qin, L. Li et al., "Roles of the immune/methylation/autophagy landscape on single-cell genotypes and stroke risk in breast cancer microenvironment," *Oxidative Medicine and Cellular Longevity*, vol. 2021, Article ID 5633514, 32 pages, 2021.

[34] G. Yu, L.-G. Wang, Y. Han, and Q.-Y. He, "clusterProfiler: an R package for comparing biological themes among gene clusters," *Integrative Biology*, vol. 16, no. 5, pp. 284–287, 2012.

[35] Z. Gu, L. Gu, R. Eils, M. Schlesner, and B. Brors, "Circlize implements and enhances circular visualization in R," *Bioinformatics*, vol. 30, no. 19, pp. 2811-2812, 2014.

[36] J. R. Hoult and M. Payá, "Pharmacological and biochemical actions of simple coumarins: natural products with therapeutic potential," *General Pharmacology*, vol. 27, no. 4, pp. 713–722, 1996.

[37] B. Fu, Y. Su, X. Ma, C. Mu, and F. Yu, "Scoparone attenuates angiotensin II-induced extracellular matrix remodeling in cardiac fibroblasts," *Journal of Pharmacological Sciences*, vol. 137, no. 2, pp. 110–115, 2018.

[38] J.-R. Noh, Y. H. Kim, J. H. Hwang et al., "Scoparone inhibits adipocyte differentiation through down-regulation of peroxisome proliferators-activated receptor γ in 3T3-L1 preadipocytes," *Food Chemistry*, vol. 141, no. 2, pp. 723–730, 2013.

[39] L. Lyu, J. Chen, W. Wang et al., "Scoparone alleviates Ang II-induced pathological myocardial hypertrophy in mice by inhibiting oxidative stress," *Journal of Cellular and Molecular Medicine*, vol. 25, no. 6, pp. 3136–3148, 2021.

[40] Y. Wang, M. Wang, B. Chen, and J. Shi, "Scoparone attenuates high glucose-induced extracellular matrix accumulation in rat mesangial cells," *European Journal of Pharmacology*, vol. 815, pp. 376–380, 2017.

[41] R. S. Blanc, J. G. Kallenbach, J. F. Bachman, A. Mitchell, N. D. Paris, and J. V. Chakkalakal, "Inhibition of inflammatory CCR2 signaling promotes aged muscle regeneration and strength recovery after injury," *Nature Communications*, vol. 11, no. 1, p. 4167, 2020.

[42] J. G. Tidball, "Inflammatory processes in muscle injury and repair," *American Journal of Physiology. Regulatory, Integrative and Comparative Physiology*, vol. 288, no. 2, pp. R345–R353, 2005.

[43] T. Chen, B. Li, Y. Xu, S. Meng, Y. Wang, and Y. Jiang, "Luteolin reduces cancer-induced skeletal and cardiac muscle atrophy in a Lewis lung cancer mouse model," *Oncology Reports*, vol. 40, no. 2, pp. 1129–1137, 2018.

[44] M. Gelabert-Rebato, J. C. Wiebe, M. Martin-Rincon et al., "Mangifera indica L. leaf extract in combination with luteolin or quercetin enhances VO2peak and peak power output, and preserves skeletal muscle function during ischemia-reperfusion in humans," *Frontiers in Physiology*, vol. 9, p. 740, 2018.

[45] Y. Dai, H. Zheng, Z. Liu, Y. Wang, and W. Hu, "The flavonoid luteolin suppresses infantile hemangioma by targeting FZD6 in the Wnt pathway," *Investigational New Drugs*, vol. 39, no. 3, pp. 775–784, 2021.

[46] H. Liu, Z. Zeng, S. Wang et al., "Main components of pomegranate, ellagic acid and luteolin, inhibit metastasis of ovarian cancer by down-regulating MMP2 and MMP9," *Cancer Biology & Therapy*, vol. 18, no. 12, pp. 990–999, 2017.

[47] X. Yao, W. Jiang, D. Yu, and Z. Yan, "Luteolin inhibits proliferation and induces apoptosis of human melanoma cells in vivo and in vitro by suppressing MMP-2 and MMP-9 through the PI3K/AKT pathway," *Food & Function*, vol. 10, no. 2, pp. 703–712, 2019.

[48] W. Masraksa, S. Tanasawet, P. Hutamekalin, T. Wongtawatchai, and W. Sukketsiri, "Luteolin attenuates migration and invasion of lung cancer cells via suppressing focal adhesion kinase and non-receptor tyrosine kinase signaling pathway," *Nutrition Research and Practice*, vol. 14, no. 2, pp. 127–133, 2020.

[49] D. M. Anson, R. M. Wilcox, E. D. Huseman et al., "Luteolin decreases epidermal growth factor receptor-mediated cell proliferation and induces apoptosis in glioblastoma cell lines," *Basic & Clinical Pharmacology & Toxicology*, vol. 123, no. 6, pp. 678–686, 2018.

[50] C. S. Tam, R. Chaudhuri, A. T. Hutchison, D. Samocha-Bonet, and L. K. Heilbronn, "Skeletal muscle extracellular matrix remodeling after short-term overfeeding in healthy humans," *Metabolism*, vol. 67, pp. 26–30, 2017.

[51] X. Ren, G. D. Lamb, and R. M. Murphy, "Distribution and activation of matrix metalloproteinase-2 in skeletal muscle fibers," *American Journal of Physiology-Cell Physiology*, vol. 317, no. 3, pp. C613–C625, 2019.

[52] L. Zhao, X. Liu, J. Zhang, G. Dong, W. Xiao, and X. Xu, "Hydrogen sulfide alleviates skeletal muscle fibrosis via attenuating inflammation and oxidative stress," *Frontiers in Physiology*, vol. 11, article 533690, 2020.

Hindawi
Disease Markers
Volume 2022, Article ID 7056517, 16 pages
https://doi.org/10.1155/2022/7056517

Research Article

Screening Biomarkers and Constructing a Predictive Model for Symptomatic Urinary Tract Infection and Asymptomatic Bacteriuria in Patients Undergoing Cutaneous Ureterostomy: A Metagenomic Next-Generation Sequencing Study

Qian Yuan,[1,2] **Rong Huang**,[1,2] **Liping Tang**,[1,2] **Lijuan Yuan**,[3] **Li Gao**,[3] **Yang Liu**,[4] **and Ying Cao**[1,2]

[1]*Department of Nursing, The First Affiliated Hospital of Nanchang University, Nanchang 330006, China*
[2]*Nursing School, Nanchang University, Nanchang 330006, China*
[3]*Genskey Medical Technology Co. Ltd., Beijing 102206, China*
[4]*Department of Clinical Microbiology, The First Affiliated Hospital of Nanchang University, Nanchang 330006, China*

Correspondence should be addressed to Yang Liu; 13576091584@163.com and Ying Cao; xymz339436@126.com

Received 16 December 2021; Accepted 2 April 2022; Published 28 April 2022

Academic Editor: Jing Zhong

Objectives. To investigate the clinical diagnostic value of differential flora as biomarkers in patients with symptomatic urinary tract infection (UTI) and asymptomatic bacteriuria (ASB) undergoing cutaneous ureterostomy based on metagenomic next-generation sequencing and construct predictive models to provide a scientific reference for clinical diagnosis and treatment. *Material and Methods*. According to standard procedures, samples were taken from each patient for routine tests (urine, ureteral stent, and skin swab around the stoma). Cytokine levels in the blood were also detected. Urinary microflora were measured by mNGS, and potential biomarkers for distinguishing UTI and ASB were identified by differential flora. Finally, we generated the predictive models for ASB and UTI using the Lasso method and cytokine levels. *Results*. Urine culture was performed for 50 patients with cutaneous ureterostomy; 44 of these patients developed bacteriuria. The incidence of symptomatic bacteriuria was 54.55%. Biomarker analysis showed that *Propionimicrobium lymphophilum*, *Staphylococcus haemolyticus*, *Stenotrophomonas maltophilia*, *Ralstonia insidiosa*, and *Aspergillus sydowii* all had good predictive performance and were combined in a single model. The predictive model exhibited good prediction performance (area under the curve (AUC) = 0.8729, sensitivity = 80%, specificity = 83.3%, and cutoff = 1.855). We also identified a significant negative correlation between the weight sum of the abundance for these five characteristic pathogens (Sum_weighted_Reads) and levels of the cytokine IL-6 and IL-1β ($P < 0.05$). *Conclusion*. mNGS had a higher positive detection rate for pathogens in urine samples. The selected differential bacteria can be used as biomarkers of ASB and UTI, and the prediction model has good predictive performance. Analysis also showed that the occurrence of symptoms was related to individual immunity. Combined with the Sum_weighted_Reads cutoff and cytokine levels (IL-6 and IL-1β) of differential flora, it was possible to judge the severity of symptoms in cutaneous ureterostomy patients with bacteriuria and provide new insights for the treatment and intervention of ASB and UTI.

1. Introduction

Bladder cancer, with an estimated 573,000 new cases and 213,000 deaths in 2020, is the tenth most diagnosed cancer worldwide and is more common in men than in women [1]. Radical cystectomy (RC) with urinary diversion (UD) is the gold standard for the treatment of muscle-invasive bladder cancer (MIBC) and high-risk nonmuscle invasive bladder cancer (NMIBC) [2]. Cutaneous ureterostomy (CU) is one of the effective ways of performing UD and has a wide range of indications, involves relatively simple surgery, is associated with faster postoperative recovery,

and is a reliable choice for older and frail populations [3]. However, a previous study showed that patients undergoing RC had the highest 30-day readmission rate among all urological oncological diseases; 14% of these readmitted cases were due to infection [4].

The most common postoperative infection types in CU patients are urinary tract infection (UTI) and asymptomatic bacteriuria (ASB); the latter is relatively common among older patients [5]. The clinical presentation of ASB and UTI shows distinct variations. Indwelling ureteral stents have been associated with a high incidence of bacteriuria and the incidence of chronic indwelling stent bacterial colonization, and bacteriuria has been reported to be 100%; these factors complicate the diagnosis of ASB and symptomatic UTI in patients with CU [6]. Globally, infection is a huge problem and associated with a high recurrence rate; these infections can lead to bacteremia, acute, and chronic renal insufficiency and can even become life-threatening [7].

Currently, the diagnosis of bacteriuria is mainly based on urine culture; however, this is a nonspecific laboratory test [8, 9]. According to the traditional viewpoint, the urine of normal and healthy subjects is sterile; positive and negative urine culture tests are usually regarded as the basis to distinguish whether an infection exists or not. However, routine urine culture methods are associated with certain limitations [10]. The urinary tract of normal and healthy controls is not "sterile;" rather, it possesses a core urinary microbiome. Approximately two thirds of these core bacteria are difficult to detect by traditional culture methods [11]. The intravesical instillation of some *Escherichia coli* strains have even been shown to prevent recurrent bacterial interference infection [12]. Therefore, the existence of bacteriuria does not necessarily imply infection. The detection of bacteria in urine does not in itself distinguish between symptomatic UTI and ASB. At present, in the unique group of patients undergoing radical cystectomy and urinary diversion, there is no clear criteria with which to distinguish UTI from ASB [13]. Rather, differential diagnosis mainly depends on urinary tract symptoms; UTI without obvious symptoms may be diagnosed as ASB, a condition that is relatively common in the elderly, those with cognitive impairment, and patients in an immunosuppressive state [14]. Therefore, it is vital that we develop novel and specific biomarkers that can reliably distinguish UTI from ASB.

Over time, it has become evident that asymptomatic bacteriuria, although classified as severe in terms of bacterial load, can no longer be considered an infection. Rather, such conditions are more like colonization, or in some cases, a risk factor; therefore, treatment is often unnecessary and may even be harmful [15, 16]. ASB does not require treatment, except for pregnant women and those undergoing invasive genitourinary surgery. However, in clinical practice, antibiotics are used empirically to treat bacteriuria and patients with ASB are often treated with antibiotics [17, 18]. Inaccurate and inadequate treatment coverage may lead to the acquisition of multidrug-resistant organisms, increased health care costs, and reduced patient satisfaction. Being able to distinguish between ASB and UTI is very important if we are to avoid unnecessary treatment in patients with ASB. At present, there is no clinically useful biomarker for the differential diagnosis of ASB and UTI in patients with CU.

Metagenomic next-generation sequencing (mNGS), as a new form of methodology, is rapidly being translated to clinical laboratories to permit the analysis of microorganisms and host genetic material in patient samples and can also be used for the unbiased detection of pathogens. mNGS has been applied to the pathogenic detection of infectious diseases and even the etiological diagnosis of some infectious diseases [19]. With the rapid development of mNGS technology, it has not only been confirmed that the urinary tract of healthy subjects has its own structure of unique flora but can also provide more comprehensive data relating to the microenvironment of an individual patient's urinary tract than traditional culture methods. This allows us to locate the microorganisms that may cause symptoms in a more accurate manner and thus helps us to move towards a model of precision medicine [20]. The flora of human urine is often associated with the occurrence of symptoms [21]. Moreover, there is a relationship between urinary microflora and a therapeutic response to urinary tract infection [22, 23]. Some studies have indicated that the diversity index of the bladder microbiome may eventually become a useful biomarker to distinguish ASB colonization from impending symptomatic UTI [24].

In the present study, we investigated the distributions of pathogens and factors related to bacteriuria in patients with CU. We also used mNGS and bioinformatics technology to identify potential biomarkers in the differential urinary flora of patients with ASB and UTI. Next, we used this information to build a predictive model to provide a reference for the differentiation of ASB and UTI in patients with CU. Finally, the model was combined with the weight sum of the abundance for these five characteristic pathogens (Sum_weighted_Reads) and cytokine levels to provide a scientific basis for the prevention of bacteriuria and the administration of antibiotics.

2. Materials and Methods

2.1. Patient Selection. All patients who were diagnosed with bladder cancer according to the bladder cancer diagnosis and treatment guidelines of the National Comprehensive Cancer Network (NCCN) [25] and underwent CU between December 1st, 2020 and January 31st, 2021 were selected as subjects for this study. We excluded patients who had been using steroids and immunosuppressants over the long term or those with infections other than in the urinary system or those who had received antibiotic treatment within the previous 14 days. Fifty patients undergoing CU were selected and urine samples were collected for urinary culture and mNGS tests; samples were removed from analysis if they were suspected of being contaminated or if they contained too few sequences.

Patients undergoing CU with bacteriuria were included according to their urinary test results. The diagnostic criteria for bacteriuria is mainly based on a positive urine culture: a bacterial count of ≥10^5 colony-forming units (CFU)/mL

[26, 27]. ASB is defined as the presence of at least one type of bacterial growth in urine with a bacterial count ≥ 10^5 CFU/mL irrespective of whether pyuria is present or not and if there are no symptoms or signs attributable to UTI according to the guidelines published by the Infectious Diseases Society of America (IDSA) [28]. The US Preventive Services Task Force (USPSTF) recommends that the diagnosis for ASB should be the presence of bacteria in the urine without any signs or symptoms of UTI [29]. The European Association of Urology (EAU) guidelines on urological infections define ASB as a midstream sample of urine showing bacterial growth ≥ 10^5 CFU/mL without urinary tract symptoms. Published reports define UTI by urinalysis, bacteriuria, and clinical symptoms (fever, flank pain, and changes in the color, character, and smell of the urine) [30, 31].

A total of 44 CU patients with bacteriuria were included in this study. The included patients were divided into two groups by considering the clinical characteristics of their infection: a symptomatic UTI group (bacteriuria with clinical symptoms) and an ASB group (isolation of a bacterial organism with a count of at least 10^5 CFU/mL in a urine specimen from a patient without UTI symptoms).

2.2. Sample Collection. Ureteral stents and skin swabs around the stoma were collected and cultured according to standard procedures [32]. Cytokine levels in the blood were also detected. All samples were analyzed immediately after collection. Samples for mNGS were frozen in a refrigerator at −80°C and sent out to Genskey for central analysis. This study was approved by the ethics committee of the First Affiliated Hospital of Nanchang University, and all patients participating in this study signed an informed consent form. The protocol used for data collection in this study is in line with the Declaration of Helsinki.

2.3. Urinary Testing. Urinalysis was carried out with a AX4030 automatic urine dry chemical analyzer (ARKRAY Company of Japan). Urinary bacterial count and white blood cell count were determined with a UF1000i urine tangible component analyzer (Sysmex Company, Japan); all operating procedures were performed in strict accordance with the manufacturer's instructions. For urine culture, 1 μL of clean midstream urine was inoculated onto a Columbia blood plate and a McConkey medium plate (Oxoid Company, UK); isolated bacteria were counted after culture at 37°C for 48 hours.

2.4. The Detection of Cytokine Levels. In total, twelve cytokine levels (including IFN-α, IL-1β, IL-6, IFN-γ, IL-10, IL-12P70, IL-17, IL-2, IL-4, IL-5, IL-8, and TNF-α) of each sample were detected by flow immunofluorescence photoluminescence with multiple microspheres using a kit from Qingdao Raiscare Biotechnology Co. Ltd. and a BD FACSCalibur flow cytometer.

2.5. DNA Extraction, Library Preparation, and mNGS Sequencing. Urine samples (5 mL) were collected using sterile screw freezing tubes. Then, 800 μL was absorbed from the liquefied sample, transferred to a centrifuge tube, and centrifuged at 13,600 g for 5 min. Next, the supernatant was discarded and the precipitate was used for extraction. DNA was extracted with a Genskey Micro DNA Kit (1901, Genskey, Tianjin) in accordance with the manufacturer's instructions. The total mass of the extracted DNA, as determined by a Qubit dsDNA HS Assay Kit, needed to exceed 5 ng.

DNA libraries were constructed by DNA enzyme digestion (200-300 bp), end repair, A-tailing, adapter ligation, and PCR amplification using an NGS library construction kit (2012B, Genskey, Tianjin). Prior to sequencing, we used an Agilent 2100 Biological Analyzer (Agilent Technologies, Santa Clara, USA) to determine the quality of the DNA libraries in conjunction with qPCR to test the adapters. The concentration of the constructed DNA library needed to exceed 1 Nmol/L.

Finally, all of the sample DNA libraries were mixed in the form of DNA nanospheres; these were created by adding single-stranded circular DNA in 2–3 quantitative sets. The DNA nanospheres were loaded onto a sequencing chip and sequenced by the MGISEQ-2000 sequencing platform (MGI, Shenzhen, China). In each sequencing run, environmental control samples were used to monitor microbial DNA signals and microbial DNA signals generated by the background during batch processing; different ID spike variants were used to monitor for contamination between samples.

2.6. Bioinformatic Analysis of mNGS Data. Raw reads were quality filtered by fastp (version 0.19.5) [33] and Komplexity version 0.3.6 [34]; in particular, we evaluated data for adapter contamination, low-quality reads, and low-complexity reads. Reads that mapped to the human reference assembly GRCh38 were removed with bowtie2 version 2.3.4.3 [35]. Next, reads were aligned to a microorganism database consisting of approximately 12,000 genomes with SNAP version 1.0beta.18 [36], as described previously [37]. The mapped reads were classified based on the NCBI taxonomy assignment of the reference genomes. After filtering false-positive organisms, we then determined the species or genus abundance with Perl scripts.

Based on genera profiles, we also calculated the within-sample (α) diversity using the Shannon index and the Simpson index to estimate the richness of samples by QIIME2 [38]. Principal component analysis (PCA) was performed using the FactoMineR package in R software and a heat map was generated by the pheatmap package in R software, SVG scripts, and GraphPad Prism 8.

2.7. Statistical Analysis. The Wilcoxon test was used to compare differences across subgroups. Data analysis was performed using GraphPad Prism 8 software and R software. $P < 0.05$ was considered statistically significant.

3. Results

3.1. Demographic Characteristics. In total, 44 subjects (age range: 56–82 years) were included in this study. Of these 44 patients with CU, 36 patients were males (81.82%) and 8 patients were females (18.18%). There were 20 patients with ASB and 24 patients with symptomatic UTI (Table 1

Table 1: Patients' baseline characteristics.

Patients characteristics	ASB ($n = 20$)	UTI ($n = 24$)	P value	Normal range
Gender			0.6339	
Male	17 (85.0%)	19 (79.2%)		
Female	3 (15.0%)	5 (20.8%)		
Age (years)	66.45 (56–78)	67.79 (57–82)	0.524	
Hypertension			0.615	
Yes	6 (30.0%)	12 (50.0%)		
No	14 (70.0%)	12 (50.0%)		
Diabetes			0.111	
Yes	0 (0.0%)	3 (12.5%)		
No	20 (100%)	21 (87.5%)		
Ureterostomy type			0.093	
Double ureterostomy	11 (55.0%)	19 (79.2%)		
Unilateral ureterostomy	9 (45.0%)	5 (20.8%)		
Ureteral type			0.228	
Double ureter	17 (85.0%)	23 (95.8%)		
Single ureter	3 (15.0%)	1 (4.2%)		
IFN-α (pg/mL)	1.81 (0.78–3.08)	1.69 (0.83–2.92)	0.487	0–8.5
0–8.5	20 (100%)	24 (100%)		
>8.5	0 (0)	0 (0)		
IL-1β (pg/mL)	10.51 (0–73.67)	4.26 (0–31.2)	0.033*	0–12.4
0–12.4	17 (85.0%)	15 (62.5%)		
>12.4	3 (15.0%)	9 (37.5%)		
IL-6 (pg/mL)	10.17 (0.25–30.95)	4.64 (1.07–19.1)	0.025*	0–5.4
0–5.4	14 (70.0%)	12 (50.0%)		
>5.4	6 (30.0%)	12 (50.0%)		
IFN-γ (pg/mL)	5.55 (2.51–8.71)	7.64 (0.44–21.08)	0.248	0–23.1
0–23.1	20 (100%)	24 (100%)		
>23.1	0 (0)	0 (0)		
IL-10 (pg/mL)	0.86 (0.3–2.44)	0.94 (0.32–4.23)	0.888	0–12.9
0–12.9	20 (100%)	24 (100%)		
>12.9	0 (0)	0 (0)		
IL-12P70 (pg/mL)	0.02 (0–0.3)	0.2 (0–2.1)	0.063*	0–3.4
0–3.4	20 (100%)	24 (100%)		
>3.4	0 (0)	0 (0)		
IL-17 (pg/mL)	1.74 (0.92–3.73)	2.16 (0.97–14.62)	0.229	0–21.4
0–21.4	20 (100%)	24 (100%)		
>21.4	0 (0)	0 (0)		
IL-2 (pg/mL)	0.7 (0–1.99)	0.82 (0–2.99)	0.396	0–7.5
0–7.5	20 (100%)	24 (100%)		
>7.5	0 (0)	0 (0)		
IL-4 (pg/mL)	0.6 (0–0.83)	0.64 (0.51–1.34)	0.981	0–8.56
0–8.56	20 (100%)	24 (100%)		
>8.56	0 (0)	0 (0)		
IL-5 (pg/mL)	2.17 (0–4.83)	2.27 (0.54–6.91)	0.934	0–3.1
0–3.1	20 (100%)	24 (100%)		
>3.1	0 (0)	0 (0)		
IL-8 (pg/mL)	11.23 (0–80.96)	7.08 (0.64–35.41)	0.352	0–20.6
0–20.6	19 (95.0%)	21 (90.0%)		

Table 1: Continued.

Patients characteristics	ASB ($n = 20$)	UTI ($n = 24$)	P value	Normal range
>20.6	1 (5.0%)	3 (10.0%)		
TNF-α (pg/mL)	1.27 (0–3.65)	1.6 (0–7.36)	0.502	0–16.5
0–16.5	20 (100%)	24 (100%)		
>16.5	0 (0)	0 (0)		
Nitrite (NIT)	0.22 (0–1)	0.06 (0–1)	0.206	Negative (−)
Negative (−)	15 (75.0%)	14 (58.3%)		
Positive (+)	1 (5.0%)	4 (16.7%)		
NULL	4 (20.0%)	6 (25.0%)		
Leukocyte esterase (LE)	2.06 (0–4)	1.91 (0–3)	0.760	Negative (−)
Negative (−)	2 (10.0%)	1 (4.2%)		
Suspective (±)	1 (5.0%)	2 (8.3%)		
Positive (+)	13 (33.3%)	15 (62.5%)		
NULL	4 (20.0%)	6 (25.0%)		
Bacteria count (U_BACT) (number/μL)	2,714.71 (26.6––22,218.4)	1724.76 (52.1–7822.6)	0.800	0–32.8
0–32.8	0 (0.0%)	1 (4.2%)		
>32.8	15 (75.0%)	15 (62.5%)		
NULL	5 (25.0%)	8 (33.3%)		
Red blood cell count (RBC) (number/μL)	1,051.36 (0.1–9,840.5)	824.05 (4.1–5,596.7)	0.711	0.2–13.8
<0.2	0 (0.0%)	1 (4.2%)		
0.2–13.8	3 (15.0%)	4 (16.7%)		
>13.8	12 (60%)	11 (45.8%)		
NULL	5 (25.0%)	8 (33.3%)		
White blood cell count (WBC) (number/μL)	1,276.02 (87.1–4,670.7)	3,610.14 (7.5–36,212.4)	0.626	0–7.1
0–7.1	0 (0.0%)	0 (0.0%)		
>7.1	15 (75.0%)	16 66.73%)		
NULL	5 (25.0%)	8 (33.3%)		

Data are presented as n (%) or means (range).

and Supplementary Table S1). There was no significant difference between the ASB and UTI groups with regard to the age and gender. Most of the patients (in both groups) were elderly. Differential analysis between the two groups showed that patients with bilateral CU was more likely to have symptoms of infection than patients with unilateral CU, although the difference was not very significant ($P = 0.093$). There were differences between the two groups in terms of inflammatory cytokines (IL-6, IL-1β, and IL-12P70); only the levels of IL-6 ($P = 0.025$) and IL-1β ($P = 0.033$) were significantly different. There were no significant differences between the ASB and UTI groups with regard to other cytokines (Table 1).

3.2. Distribution of Pathogenic Bacteria in Urinary Cultures. Urinary analysis of samples from the 44 patients isolated 23 strains of pathogenic bacteria, most of which were bacteria (Figure 1 and Supplementary Table S1).

The main pathogens of infection in patients with a positive urine culture were Gram-negative bacilli: *Klebsiella pneumoniae* (ASB: 4 strains; UTI: 8 strains), *Escherichia coli* (ASB: 6 strains; UTI: 3 strains), *Morganella mortis* (ASB: 3 strains; UTI: 4 strains), *Proteus mirabilis* (ASB: 2 strains; UTI: 4 strains) and Gram-positive bacteria: *Staphylococcus aureus* (ASB: 3 strains; UTI: 3 strains), and *Enterococcus faecalis* (ASB: 3 strains; UTI: 2 strains). These six species of bacteria accounted for 57.69% (45/78) of the pathogens identified in urine cultures. These findings were consistent with the existing literature [39]. More than 2–4 different types of bacteria were cultured in the urine samples from 26 patients, including *Morganella* and mucinous *Neisseria*, *Klebsiella pneumoniae*, and *Escherichia coli*. Only one sample (S17) produced a fungus (*Candida auricularis*). *Klebsiella pneumoniae*, *Staphylococcus aureus, Proteus mirabilis*, and *Morganella* were detected more frequently in the UTI group than in the ASB group. The main pathogens (*Escherichia coli* and *Enterococcus faecalis*) were detected more frequently in the ASB group than in the UTI group. *Escherichia coli* accounted for 30% (6/20) of patients with ASB and 12.5% (3/24) of patients with symptomatic UTI.

3.3. Analysis of the Factors Affecting the Occurrence of Bacteriuria. In this study, while urine culture was carried out, skin swabs around the stoma and ureteral stents were also collected for bacterial culture. From the Ven diagram of the culture results of each sample, culture species of pathogen showed a decreasing trend from the skin to urine to ureteral stents. A total of 14 species are identical, including

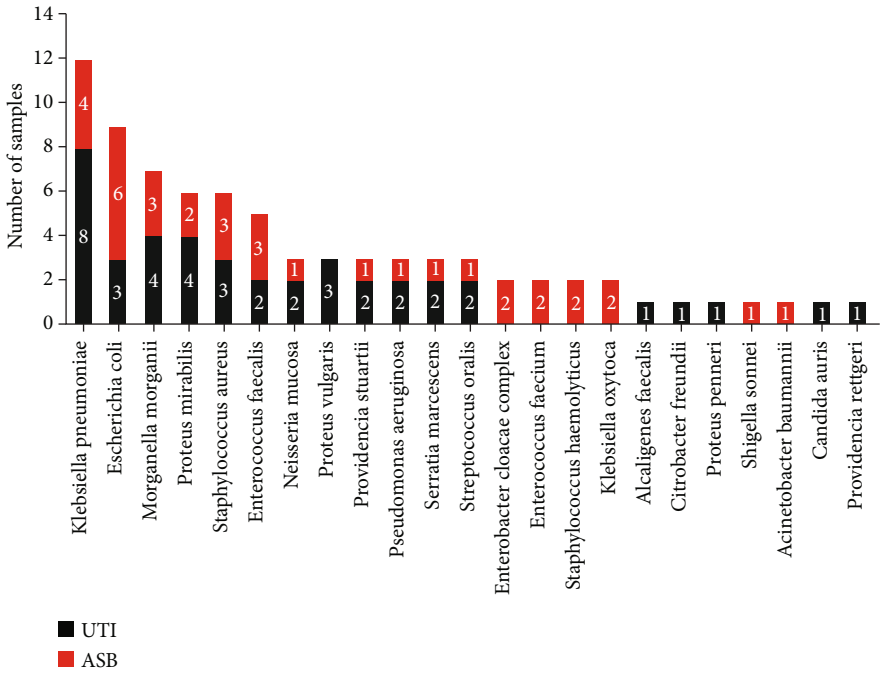

Figure 1: Urine culture pathogen detection spectrum and frequency.

6 pathogens frequently detected in the UTI group: *Klebsiella pneumoniae*, *Proteus mirabilis*, *Escherichia coli*, *Morgan*, *Staphylococcus aureus*, *and Enterococcus faecium* (Figure 2).

A heat map was made for the detection of these 14 bacteria in 44 patients (Figure 3). It can be seen from the chart that 63.6% (28/44) of patients could detect the same kind of bacteria from two or more kinds of samples at the same time and 47.7% (21/44) could detect the same kinds of bacteria from three kinds of samples at the same time. In addition, the culture results of all UTI and ASB groups were consistent with those of urine culture alone. The detection frequency of *Klebsiella pneumoniae*, *Staphylococcus aureus*, *Proteus mirabilis*, and *Morganella mortis* in the UTI group was higher than that in the ASB group. The first pathogen of infection in the ASB group was *Escherichia coli*, 35% (7/20) of the patients in the ASB group were cultured with *Escherichia coli*, and 33.33% (8/24) of the patients in the UTI group were cultured with *Escherichia coli*, which were higher than those cultured in urine alone. *Escherichia coli* can be cultured in stents or the skin in patients when *Escherichia coli* was cultured in urine (Supplementary Table S1). Therefore, it can be inferred that the pathogenic agents of infection in urine may come from the skin, stents, and other closely related external environments. Therefore, the longer stent placement time or numbers of stent placement were one risk factor affecting urinary tract infection, which is consistent with the results reported in other literature [40].

In addition, it has been reported that diabetes mellitus was a risk factor for urinary tract infection [30]. In this study, 3 patients (S18, S14, and S22) were complicated with diabetes, all of which were symptomatic urinary tract infections (Supplementary Table S1). It is suggested that diabetes may be one of the risk factors for the aggravation of bacteriuria in CU patients.

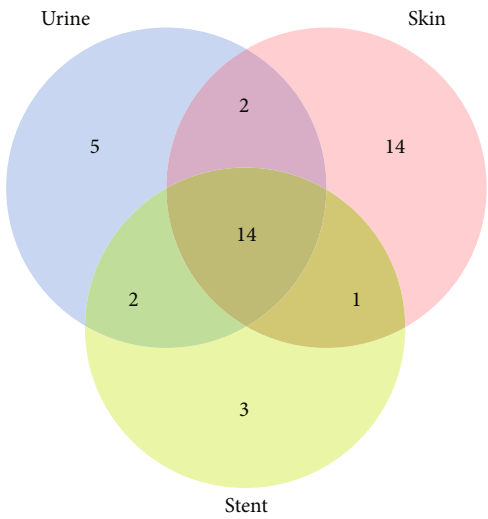

Figure 2: Ven diagram of cultured species of different kinds of samples. The 14 overlapping species of three groups (urine, skin, and stent) were *Candida auris*, *Enterococcus faecium*, *Enterobacter cloacae complex* sp., *Proteus vulgaris*, *Providencia stuartii*, *Proteus mirabilis*, *Morganella morganii*, *Enterococcus faecalis*, *Staphylococcus aureus*, *Escherichia coli*, *Klebsiella pneumoniae*, *Klebsiella oxytoca*, *Serratia marcescens*, and *Streptococcus oralis*.

3.4. The Detection Performance of Urinary mNGS. Compared with the bacteria results from traditional urinary culture, the mNGS showed 97.44% consistency (Table 2). In total, 78 pathogens were identified by mNGS from urine samples; 76 of these samples were consistent with the results derived from urinary culture. Only two of the mixed infections were inconsistent between the two detection methods. The first case, S40 in the ASB group, was positive for *Enterococcus faecium* and *Staphylococcus haemolyticus* in the

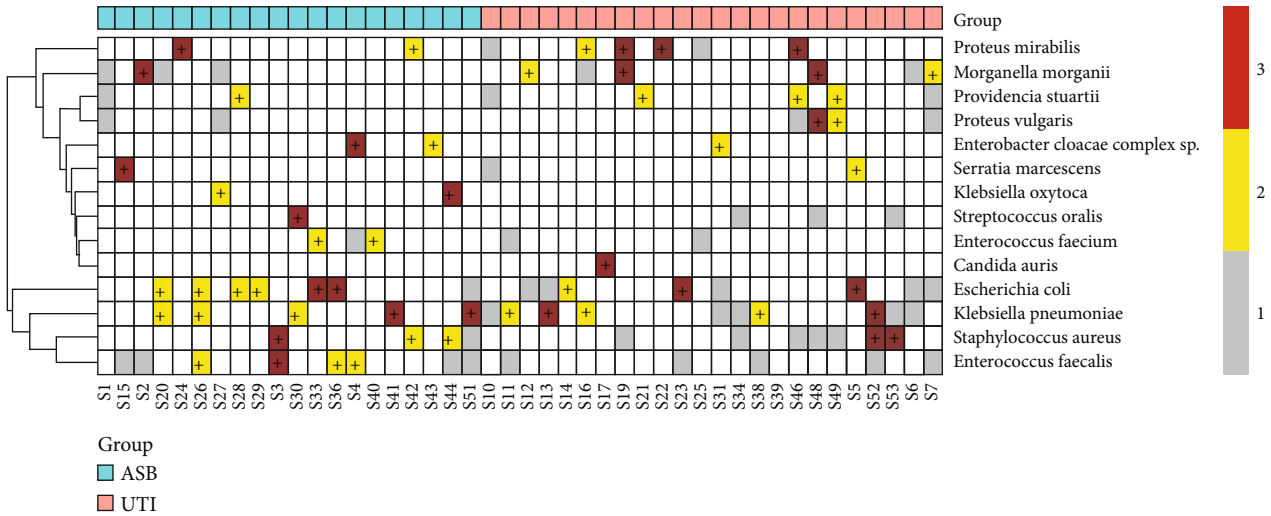

Figure 3: Heatmaps of detection frequencies for 14 species.

Table 2: Consistency comparison between urine culture and mNGS.

Group	UTI	ASB	ALL
Urine_culture	42	36	78
Group	41	35	76
Consistency rate	97.62%	97.22%	97.44%

urinary cultures; mNGS did not detect *Staphylococcus haemolyticus*. In the second case, S31 in the UTI group, the urinary cultures were positive for *Klebsiella pneumoniae* and *Citrobacter freundii*; however, mNGS detected the sequence of *Citrobacter youngae*. mNGS was superior to urinary culture in terms of identifying bacterial species at a molecular level; therefore, the false-negative detection by mNGS in the second case may have been caused by incorrect identification at the species level in the urinary culture method. With regard to identifying bacteriuria, the positive rate of mNGS for ASB was the same as that for UTI; irrespective of whether cases were symptomatic or asymptomatic, the detection performance of mNGS was unaffected.

The mNGS detection spectrum is known to be more extensive than traditional culture methods [41]. Pathogens with a higher abundance and frequency in the mNGS results were selected to create pathogen spectra (Figure 4). mNGS was able to detect bacteria (including *Enterococcus faecalis*, *Klebsiella pneumoniae*, *Morganella morganii*, *Pseudomonas aeruginosa*, *Escherichia coli*, *Proteus mirabilis*, *Streptococcus pneumoniae*, *Veillonella parvula*, *Staphylococcus aureus*, *and Citrobacter youngae*), fungi *(Candida albicans, Candida tropicalis*), and viruses (*Human gamma herpes virus 4* and *Human polyomavirus 2*).

3.5. Analysis of Microflora Diversity. Shannon and Simpson indices demonstrated that the diversity index for the ASB group was higher than that of the UTI group (Shannon: $P = 0.075$; Simpson: $P = 0.13$) (Figures 5(a) and 5(b)). The species diversity in the UTI group was lower than that in the ASB group, although there was no statistical significance, proving that the species structure was significantly similar when compared between the two groups of patients. Principal coordinate analysis (PCoA) further showed that there was a trend for separation between the UTI group and the ASB group (Figures 5(c) and 5(d)) and that the separation effect was better than that of unweighted PCoA, thus indicating that the effect of species abundance change was higher than that of species change. Therefore, the diversity of microflora was shown to decrease with the severity of infection in both the UTI and ASB groups. Furthermore, the species abundance could reflect the severity of infection. When the infection was serious, the abundance and diversity of the microflora changed; these results were consistent with the existing literature [42].

Sequencing reads from the 44 samples were greater than those from conventionally sequenced 20 million (Supplementary Table S2). All reads from the mNGS pathogens were normalized by equation (1).

$$\text{Pathgeon}_{\text{reads}} * \frac{20\ \text{million}}{\text{Total}_{\text{reads}}}. \quad (1)$$

Once the data had been normalized, we identified differences in the bacterial species between the UTI and ASB groups. Of all the pathogens detected by mNGS, 19 pathogens were significantly different when compared between the UTI and ASB groups (Table 3 and Supplemental Figure S1). Only the abundance of *Burkholderia cepacia* and *nematophilus* pathogenic bacteriashowed a significant increase in the symptomatic UTI group. The abundance of the 17 other bacterial species showed a significantly higher abundance in the ASB group, particularly Enterococcus faecalis, *Moraxella osloensis*, *Cutibacterium acnes*, *Stenotrophomonas maltophilia*, *Staphylococcus haemolyticus*, *Ralstonia insidiosa*, and *Propionimicrobium lymphophilum* (normalized abundance

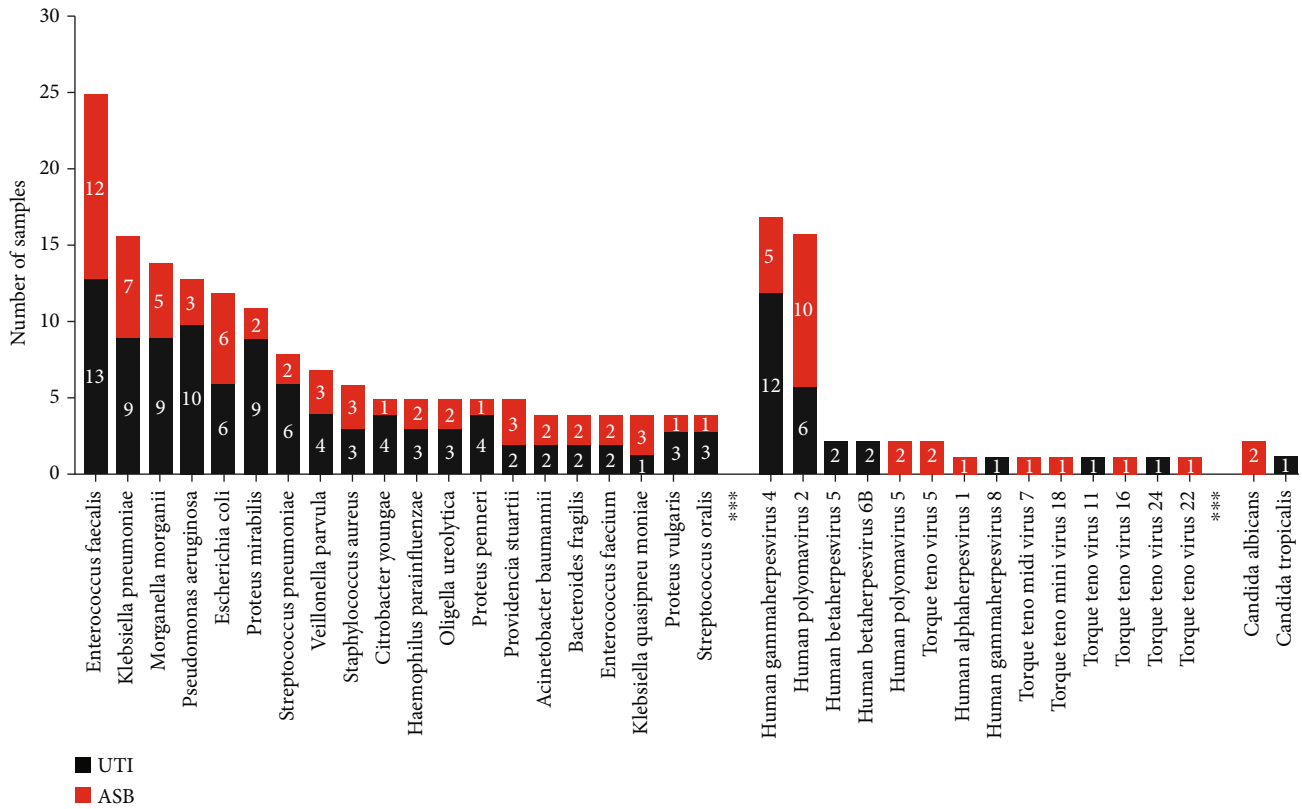

Figure 4: mNGS pathogen detection spectrum and frequency. Only twenty top species of bacteria by frequency were displayed.

was >20 and the occurrence frequency was ≥50% in the ASB group). Of these, *Enterococcus faecalis* and *Stenotrophomonas maltophilia* were common opportunistic pathogens; *Moraxella osloensis* and *Cutibacterium acnes* were common colonization pathogens.

3.6. Generation of a Prediction Model for ASB and UTI. Next, the 19 species showing differential abundance between the two groups were investigated by Lasso regression; this led to the identification of five characteristic species and five characteristic weight coefficients (Table 4).

Then, we use these five characteristic species and weight coefficients to calculate the weight sum of the abundance for these five characteristic pathogens (Sum_weighted_Reads) and used this value as the final index to distinguish ASB from UTI. The formula for calculating the Sum_weighted_Reads is given in equation (2).

$$\mathrm{Sum}_{\mathrm{weighted}_{\mathrm{reads}}} = \sum_{1}^{5}\left(\frac{\mathrm{Pi(reads)}}{\mathrm{total\ reads}} * 20\ \mathrm{million}\right) * \mathrm{weight}_{\mathrm{coefficient}}. \tag{2}$$

In equation (2), P represents pathogen, i represents the serial number of the characteristics, and Weight_coefficient represents the weight coefficient of the characteristics in this model.

Next, a ROC curve was generated to determine the accuracy (AUC = 0.8729; Figure 6); the sensitivity was 80%, the specificity was 83.3%, and the classification effect was good. According to a cutoff of 1.855 for this index, it follows that samples with an index < 1.855 are more likely to be classified as a UTI.

3.7. Correlation Analysis of Cytokine Levels. We also performed correlation analysis on the levels of key clinical cytokines. Analysis showed that the levels of IL-6 and IL-1β in the UTI group were significantly higher than those in the ASB group; the increase in IL-6 was the most significant (Figures 7(a) and 7(b)).

IL-6 is a key mediator that plays an important role in inflammation and anti-inflammation during the process of wound repair. The expression levels of IL-6 can effectively reflect the severity of tissue and cell damage and can be used as the serological index for the clinical diagnosis of acute and chronic inflammation [43]. A sharp rise in the levels of IL-6 represents a red flag and has been widely recognized. IL-1β is an important inflammatory factor derived from the peripheral and central nervous systems [44].

The severity of infection is known to be associated with the levels of IL-6 and IL-8, at least to some extent. The levels of serum IL-6 and IL-1β in the acute stage of severe infection were previously shown to be significantly higher than those in the convalescent stage of severe infection and the acute stage of *Streptococcus pneumoniae* infection, while the abundance of *Streptococcus pneumoniae* in the acute stage was significantly higher than that in the convalescent stage ($P < 0.05$) [45].

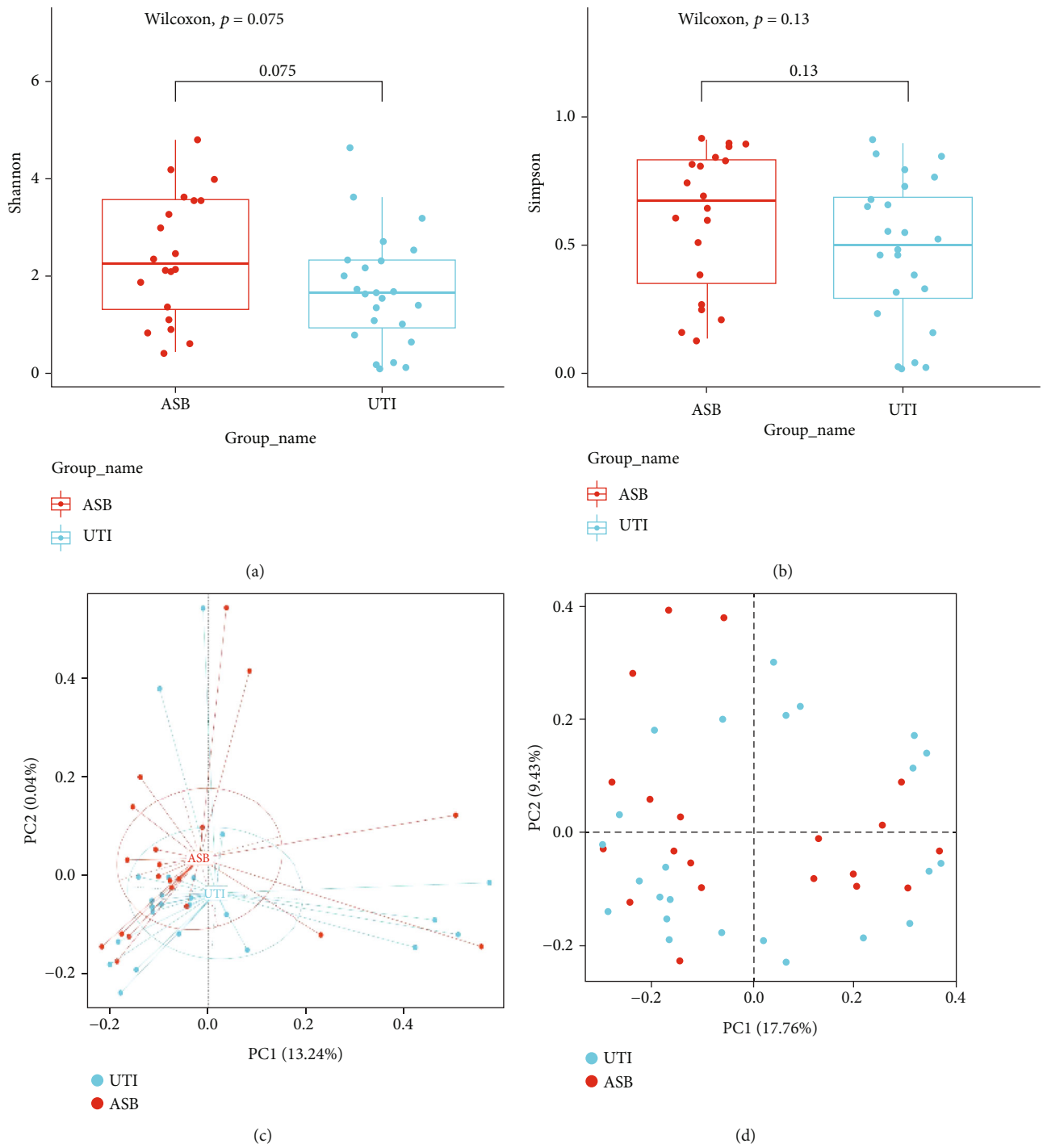

Figure 5: Metagenomic microbial diversity analysis. (a) Shannon α index diversity analysis. (b) α diversity Simpson index analysis. (c) Weighted PCoA using Bray-Curtis distance. (d) Unweighted PCoA.

Patients in the UTI group may have had immune dysfunction, thus leading to a significant increase in the serum levels of IL-1β and IL-6. Consequently, these levels can be used as reference indices to evaluate the severity of infection. The higher the levels of IL-1β and IL-6, the more serious the infection may be.

Next, we investigated the correlation between Sum_weighted_Reads and cytokine levels and found that Sum_weighted_Reads was negatively correlated with both IL-1β and IL-6 levels ($P < 0.05$). We found that this index exhibited a significant negative correlation with IL-1β levels; this was consistent with the reduction in abundance and species diversity in the UTI group (Figures 7(c) and 7(d)). These results suggested that we can combine the cutoff for the Sum_weighted_Reads for IL-1β and IL-6 to predict the severity of symptoms in patients with bacteriuria and thus identify appropriate forms of prophylactic medication in advance.

Table 3: Statistics of 19 different species between ASB and UTI groups.

Different pathogens	ASB_mean	UTI_mean	*P* value	ASB_num (*n*%)	UTI_num (*n*%)
Enterococcus faecalis *	12404.9	3495.8	0.0400	19 (95%)	19 (79.2%)
Moraxella osloensis *	22.9	9.0	0.0371	17 (85%)	15 (62.5%)
Burkholderia cenocepacia *	0.0	0.6	0.0342	0 (0%)	5 (20.8%)
Pandoraea norimbergensis	2.5	2.2	0.0337	7 (35%)	2 (8.3%)
Xenorhabdus nematophila *	0.8	1.7	0.0309	1 (5%)	8 (33.3%)
Cutibacterium acnes *	122.3	58.4	0.0283	20 (100%)	24 (100%)
Eikenella corrodens	293.7	0.0	0.0248	4 (20%)	0 (0%)
Neomicrococcus aestuarii	1.1	0.0	0.0248	4 (20%)	0 (0%)
Staphylococcus warneri	1.4	0.0	0.0248	4 (20%)	0 (0%)
Paraburkholderia fungorum	3.8	1.0	0.0149	11 (55%)	5 (20.8%)
Aspergillus sydowii	0.8	0.2	0.0136	10 (50%)	4 (16.7%)
Malassezia globosa	4.2	0.8	0.0094	16 (80%)	14 (58.3%)
Stenotrophomonas maltophilia *	56.2	1.0	0.0064	14 (70%)	9 (37.5%)
Legionella drozanskii	0.5	0.0	0.0047	6 (30%)	0 (0%)
Acidovorax sp. KKS102	5.5	3.8	0.0033	15 (75%)	6 (25%)
Staphylococcus haemolyticus *	44.2	0.0	0.0020	7 (35%)	0 (0%)
Desulfocarbo indianensis	5.2	0.3	0.0018	9 (45%)	1 (4.2%)
Ralstonia insidiosa *	56.9	1.4	0.0002	14 (70%)	6 (25%)
Propionimicrobium lymphophilum *	807.6	0.0	0.0001	10 (50%)	0 (0%)

*For pathogens with normalized abundance > 20 and occurrence frequency ≥ 50% in ASB, indicating higher abundance in UTI.

Table 4: Weight coefficients of five characteristics.

No.	Pathogens	Weight coefficient
1	Propionimicrobium_lymphophilum	0.016094976
2	Staphylococcus_haemolyticus	0.038285169
3	Stenotrophomonas_maltophilia	0.063515774
4	Ralstonia_insidiosa	0.170320578
5	Aspergillus_sydowii	0.462107080

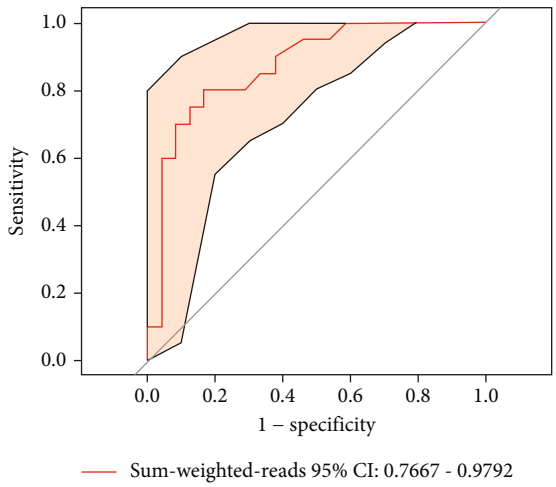

Figure 6: ROC curve of the prediction model.

4. Discussion

This is the first study to use mNGS to identify biomarkers and construct a prediction model for UTI and ASB in patients undergoing CU. In this study, urine culture was performed in 50 patients with CU; of these, 44 patients developed bacteriuria. Consequently, there was a high incidence of bacteriuria in CU patients. The distribution of pathogenic bacteria in urinary cultures showed that the main pathogen associated with bacteriuria was Gram-negative bacilli, followed by Gram-positive cocci; these findings concurred with the general etiological characteristics of UTI. Furthermore, 2–4 different types of bacteria were cultured in the urine samples from 26 patients. The main risk factors for bacteriuria are the time and number of indwelling ureteral stents and diabetes mellitus. mNGS had a higher positive detection rate for pathogens in urine samples. Shannon and Simpson index analysis showed that the diversity index for the ASB group was higher than that for the UTI group. Thus, the identified differential bacteria (*Propionimicrobium lymphophilum*, *Staphylococcus haemolyticus*, *Stenotrophomonas maltophilia*, *Ralstonia insidiosa*, and *Aspergillus sydowii*) can be used as biomarkers for ASB and UTI. The generated prediction model showed good predictive performance. Furthermore, it is possible to judge the severity of symptoms of bacteriuria by combining the model with the cutoff of Sum_weighted_Reads and cytokines (IL-1β and IL-6) for differential flora.

The total incidence of bacteriuria in CU patients was 88%; 54.55% were diagnosed with UTI and 45.45% were diagnosed with ASB. ASB is common in many populations,

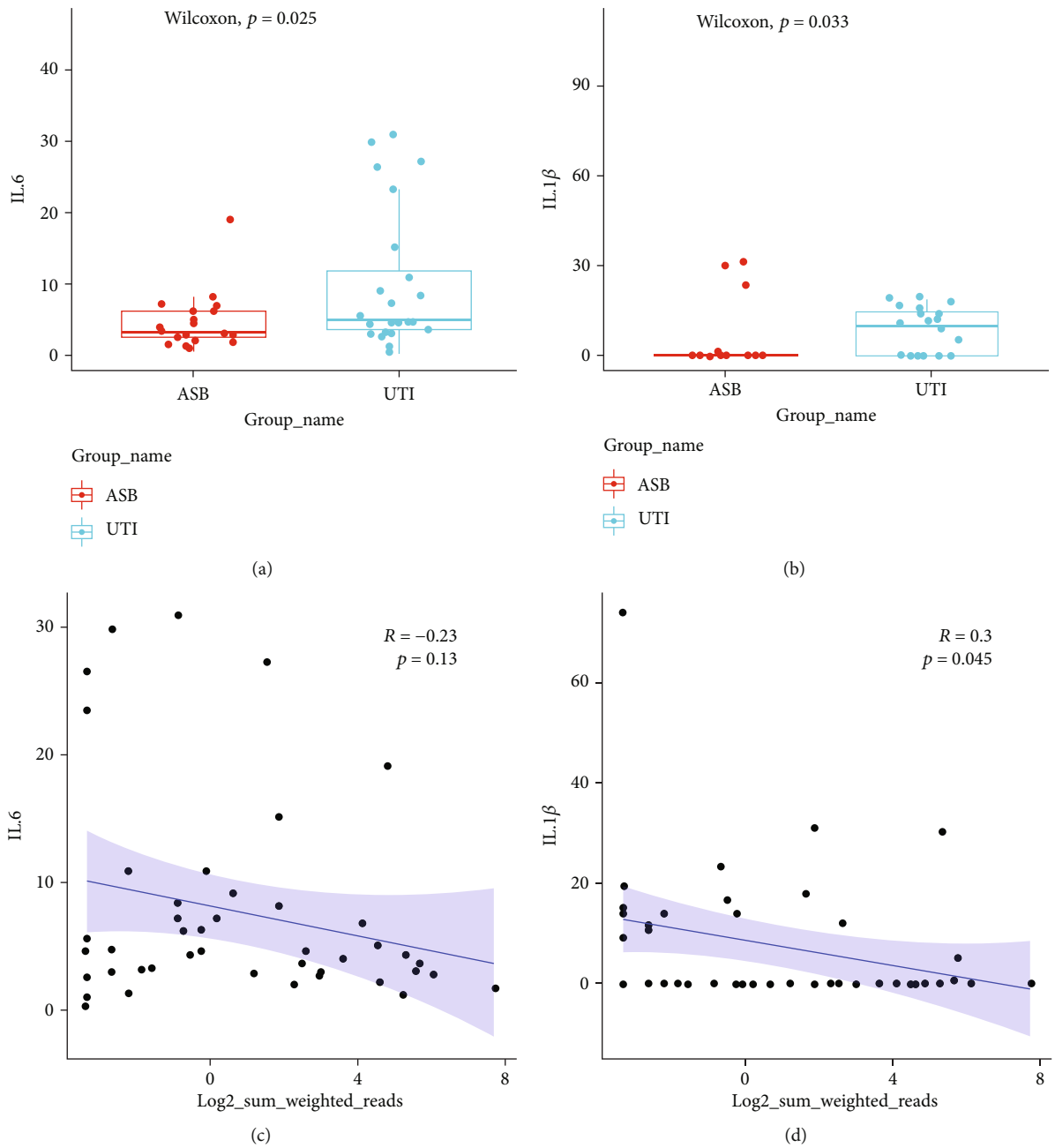

Figure 7: Association analysis of inflammatory factors. (a) Differential analysis of the inflammatory factor IL-6 between the ASB and UTI groups, (b) differential analysis of the inflammatory factor IL-1β between the ASB and UTI groups, (c) correlation analysis between Sum_weighted_Reads and IL-6 levels, and (d) correlation analysis between Sum_weighted_Reads and IL-1β levels.

although the prevalence is highly variable [46]. The incidence of ASB is 3.6% to 19% in older men and 40% in renal transplant recipients during the first month after surgery but can be as high as 100% in patients with chronic indwelling catheters [47]. In view of the large differences in the incidence of UTI and ASB reported in the literature, it is very important to define UTI and ASB in a specific manner if we are to better describe the real incidence of UTI in patients [48–50]. Most UTIs are caused by the ascending pathway, and the first step in its pathogenesis is the colonization of urinary tract pathogens in the tissue around the urethra. Second, urological pathogens may enter the urethra, thus leading to the occurrence of UTI or ASB; some pathogens may even reach the kidneys through the ureters [51]. In this study, the incidence of bacteriuria in CU patients was very high. After radical cystectomy and CU, the inevitable changes in the physiological structure can interfere with the normal barriers of the urinary system; this means that urinary reflux is common [52]. The implantation of ureteral stents can increase the risk of bacteriuria and bacterial colonization [53]. Therefore, ir is necessary to improve our understanding and monitor bacteriuria in patients with CU. The early identification of ASB and UTI is the premise of effective treatment, although there is no objective

laboratory diagnostic index for ASB and UTI in patients with CU. Therefore, there is an urgent need to identify reliable biomarkers for differential diagnosis.

In total, 23 strains of pathogenic bacteria were isolated in this study, most of which were bacteria; only one sample produced a fungus (*Candida auricularis*). *Klebsiella pneumoniae*, *Staphylococcus aureus*, *Proteus mirabilis*, and Morgan were detected more frequently in the UTI group than in the ASB group. The main pathogens detected in the ASB patients were *Escherichia coli* and *Enterococcus faecalis*. A previous retrospective analysis of 1,133 patients after RC showed that the most common pathogens associated with UTI were *Escherichia coli*, *Enterococcus faecalis*, and *Klebsiella pneumoniae*; these findings concurred with those of the present study [53]. Gram-negative bacteria are known to be dominant in the microbiology of infection after RC (65–91% of isolates) [49]. Lipopolysaccharide (LPS) is expressed by Gram-negative bacteria and may interact with host cells such as leukocytes in the urinary system and uroepithelial cells. Although bacteria and/or LPS are present in the urine of both ASB and UTI patients, they seem to cause inflammation in UTI but not in ASB [54]. Perturbation of the urinary microbiome may indicate the development of a UTI. These pathogens existed in both ASB and UTI patients; therefore, we speculated that these populations would change and cause UTI when immunity was low or when there was a disruption in the balance of flora. Only one sample produced a fungus; the underlying causes for this may include different patient characteristics and the use of perioperative antibiotics. More than 2–4 different types of bacteria were cultured in the urine of some patients with bacteriuria. Most of the pathogenic bacteria arise from the commensal human urinary tract bacteria. Pathogenicity arises due to an imbalance in the relative abundance of pathogenic bacteria. Therefore, we speculate that there is a certain relationship between the production of bacteriuria and changes in the urinary flora, although the specific mechanisms involved need to be investigated further.

The etiology of UTI is also affected by host-related factors, such as age, diabetes, or catheterization [55]. The difference in age and gender between the ASB group and UTI group in the present study was not significant. Most patients in both groups were elderly. Bacteriuria is common in elderly patients, and its incidence is known to increase with age. In this study, because the patients undergoing CU surgery were elderly and frail, there was a lack of controls for different age groups. The female gender is known to be the main risk factor for the occurrence of bacteriuria [56]. Due to the fact that bladder cancer is more prevalent in males and because our sample size was limited, the results showed that males had a higher risk of bacteriuria. Furthermore, urine culture, ureteral stents, and skin swabs around the stoma were also collected for routine culture tests and we need to consider that ureteral stents are usually inserted after CU in patients with bladder cancer to prevent complications such as ureteral stricture. Bilateral CU is more likely to be associated with infection symptoms than unilateral ureterostomy; patients with positive *E. coli* urinary cultures can grow *E. coli* in both stents or the skin. Therefore, we inferred that the pathogens in urine may arise from the skin, stents, and the closely related external environment and that the main risk factors for UTI are the placement time or number of stents. In a previous study, Kehinde et al. investigated a large consecutive case series of 250 patients and concluded that the duration of stenting over 30 days correlated strongly with stent and stent tip culture results [57]. Other studies have shown that when ureteral stents were inserted for more than 6 weeks, there was a sharp increase in the abundance of bacteria in the urine [58]. Therefore, ureteral stents should be replaced in good time. Furthermore, it is important to maintain stents on a daily basis. Previous research has demonstrated an association between diabetes and the risk of UTI after RC and urinary diversion; this is consistent with the fact that diabetes is one of the risk factors for UTI in the normal population [59, 60]. Thus, targeted intervention according to the related factors of bacteriuria can effectively prevent and reduce the occurrence of bacteriuria.

According to the traditional viewpoint, the detection of urinary microorganisms is mainly based on standard urine culture in a clinical microbiology laboratory. However, urinary culture has some limitations; for example, these tests only allow the detection of aerobic bacteria and the rapid growth of a limited number of bacteria, such as *E. coli*. Metagenomic analysis using next-generation sequencing can provide information relating to microbial populations and help identify undetected microorganisms [61]. Previous studies have shown that mNGS has higher levels of sensitivity than traditional culture for certain types of sample such as blood, cerebrospinal fluid, and bronchoalveolar lavage fluid [62, 63]. Only a few reports have compared this new technology with traditional urinary culture. In this study, compared with conventional urinary culture, mNGS showed a consistency of 97.44%; only one bacterial result in each of the two cultures of mixed bacteria was inconsistent. We believe that there are specific reasons for this inconsistency. For example, mNGS is superior to clinical culture for the identification of species at the molecular level; therefore, the false-negative detection by mNGS in this case may be due to errors in the identification of specific species by the culture method. With regard to the identification of bacteriuria, the positive rates of detection for mNGS and urine culture were the same. Irrespective of whether a case was symptomatic or asymptomatic, the detection performance of mNGS remained unaffected. The detection spectrum for mNGS is more extensive than culture methods; in addition to bacteria, mNGS can also detect fungi and viruses. However, due to the high cost of mNGS detection, it may be a long time before this technology is widely used in clinical practice. As the cost of sequencing gradually decreases, the application of mNGS for urinary microbes is expected to be further developed.

The species diversity index for the ASB group was higher than that for the UTI group, although there was no significant difference, thus proving that the species structures of ASB and UTI were similar. According to the guidelines published by the Infectious Diseases Society of America (IDSA), ASB does not require screening and treatment except for pregnant women and patients undergoing invasive

genitourinary surgery; this is because the effect of treatment cannot be improved [29]. A previous study showed that the frequency of UTI in patients with ASB was increased, although it was not clear whether symptomatic UTI develops from ASB; this needs further investigation [47]. PCoA analysis showed that the effect of species abundance change was higher than that of species change. When comparing the UTI and ASB groups, we found that the diversity of microflora decreased with the severity of infection and that the species abundance could reflect the severity of infection. When the infection was serious, the abundance and diversity of microflora changed; these findings were consistent with the literature [43].

Among all of the pathogens detected by mNGS, 19 pathogens were significantly different when compared between the UTI and ASB groups. The abundance of *Burkholderia cepacia* and nematophilus pathogenic bacteria was significantly higher in the UTI group. These are important pathogens. The abundance of the other 17 types of differential bacteria was significantly higher in the ASB group. Of the seven species of bacteria with significantly increased abundance in the ASB group, *Enterococcus faecalis* and *Stenotrophomonas maltophilia* were the most common opportunistic pathogens, while *Moraxella osloensis* and *Cutibacterium acnes* were the most common colonization pathogens. When the body has low resistance or in cases where there has been unreasonable use of antibiotics, opportunistic pathogenic bacteria can break through the protective barrier of the body, thus resulting in infection [46]. ASB is one of the main risk factors for the development of UTI [64], although individual immunity is also involved. Therefore, we inferred that a reduction in the abundance of beneficial bacteria and an increase in the abundance of pathogenic bacteria may lead to the occurrence of UTI although this requires further investigation.

Biomarkers are usually used to monitor and diagnose the pathological status of diseases. At present, biomarkers play an important role in the differential diagnosis and prediction of disease progression [65]. Therefore, it is of great significance to identify biomarkers with high accuracy to distinguish ASB and UTI so that we can improve the effective use of antibiotics and the prediction of infection progression. With the rapid development of bioinformatics and sequencing technology, a series of biomarkers had emerged. Some studies have shown that Akt and CD9 in urinary exosomes can be used as biomarkers to distinguish UTI from ASB [14]. However, it is technically difficult to measure the number of urinary exosomes because of the presence of outer membrane vesicles (OMVs) whose size and density are similar to that of exosomes; furthermore, exosomes that express Akt may not always express CD9. Recent studies have shown that there is a certain correlation between microflora and the production of symptoms. Important microflora could be used as diagnostic markers to distinguish ASB from UTI. Compared with existing indices, this strategy us simple and allows efficient intervention. Based on the use of mNGS to identify differences in the microflora as potential biomarkers, our current data show that *Propionimicrobium lymphophilum*, *Staphylococcus haemolyticus*, *Stenotrophomonas maltophilia*, *Ralstonia insidiosa*, and *Aspergillus sydowii* all performed well.

At present, most of the predictive models for urinary tract infection are based on the retrospective analysis of clinical data and the construction of predictive models according to risk factors. A previous retrospective analysis identified the characteristics of pathogens associated with catheter-related UTI by reviewing and analyzing relevant data from patients, including demographic, clinical, and microbiological data; the authors then constructed a predictive model with a sensitivity of <40% and a specificity of >90%. The sensitivity of this model for clinical prediction was low; therefore, it is necessary to develop more refined and sensitive tools [66]. The accuracy (AUC) of the predictive model developed in the present study was 0.8729, the sensitivity was 80%, the specificity was 83.3%, and the classification effect was good. According to an index cutoff of 1.855, it follows that when the index is <1.855, the sample is more likely to be diagnosed as a UTI. According to our predictive model, ASB and UTI can be identified effectively. However, in the future, it is necessary to expand the sample size and optimize the prediction performance of this model.

As a family of cytokines, interleukin plays an important role in regulating the immune response of infection and mediates the production of proinflammatory and anti-inflammatory signals [67]. During the acute stage of infection, both IL-6 and IL-1β are known to be expressed [46]. IL-6 is secreted by white blood cells and urothelial cells; these not only cause an acute response; they also lead to specific cellular and humoral immune responses. Therefore, IL-6 is an important inflammatory regulatory cytokine that acts in both the acute response and chronic response phases [67]. IL-1β is an important inflammatory factor from both peripheral and central nervous sources and can induce the production and release of many inflammatory factors, such as IL-8 and macrophage inflammatory protein 1 [45].

In the present study, we found that the levels of IL-6 and IL-1β in the UTI group were significantly higher than those in the ASB group and that the increase in IL-6 levels was the most significant. Related studies have shown that IL-6 is a highly sensitive and specific biomarker for UTI [67]. IL-6 and IL-1β play a certain role in inflammatory stress caused by clinical infection and the immune regulation of patients and are known to possess positive clinical significance in the postoperative tissue trauma repair of bladder cancer [68]. Inflammation is related to the migration of white blood cells to damaged tissue, thus destroying or challenging inflammatory triggers. Inflammation is a natural defense mechanism of the body. The initial stage of acute inflammation is caused by infectious and allergic inducement; this has a beneficial effect to a certain extent although persistent acute inflammation will lead to chronic inflammation and eventually lead to tissue damage [69]. It can be inferred that the patients in our UTI group also had immune dysfunction and the serum levels of IL-1β and IL-6 were significantly increased. These factors can be used as reference indices to evaluate the severity of infection. The higher the IL-1β and IL-6 levels, the more serious the infection.

Finally, we investigated the correlation between differential flora Sum_weighted_Reads and cytokine levels and found that Sum_weighted_Reads was negatively correlated with both IL-1β and IL-6. We found that this index showed a significant negative correlation with IL-1β, which was consistent with the observed reduction in UTI abundance and species diversity. These results suggest that we can combine the cutoff, IL-1β and IL-6 levels, and the Sum_weighted_Reads for specific bacteria to predict the severity of symptoms in patients with bacteriuria and thus provide prophylactic medication in advance.

5. Conclusion

Bacteriuria is relatively common among CU patients and may lead to significant morbidity. There were differences in species diversity and abundance between ASB and UTI. There are many potential consequences of microflora changes which may be important for generation of symptoms. mNGS has a higher pathogen-positive detection rate in urine samples. The selected differential bacteria can be used as biomarkers of ASB and UTI, and the prediction model has good predictive performance. The occurrence of symptoms is related to individual immunity. Combined with the cutoff of differential flora Sum_weighted_Reads and cytokines IL-1β and IL-6, the severity of symptoms in CU patients with bacteriuria can be judged, which provides a new perspective for the treatment and intervention of ASB and UTI. In general, we think that the findings of this study are of great significance because they provide a new insight into the occurrence, development, diagnosis, and treatment of cutaneous ureterostomy urinary tract infection.

5.1. Study Limitations. We are aware that there are some limitations in the statistical analysis of 44 cases in this study: the relatively small number of samples and the failure to dynamically monitor the changes in the composition of microflora in different periods may underestimate the accuracy of microbial diversity and relative abundance in our findings and reduce the performance of the prediction model. In the future, it is necessary to expand the sample size, monitor the dynamic changes of flora, and explain the possible pathogenicity of these specific bacteria, in order to evaluate their potential as new biomarkers and optimize the performance of the prediction model.

Data Availability

Sequencing data from the 50 samples (with human reads removed) are available in NCBI Sequence Read Archive (SRA) with the BioProject identifier PRJNA779226.

Conflicts of Interest

The authors declare that there are no potential conflicts of interest.

Authors' Contributions

Qian Yuan, Rong Huang, and Liping Tang contribute equally to this work.

Acknowledgments

This study was partly funded by the Science and Technology Department Foundation of Jiangxi Province (no. 20202BBGL73090).

Supplementary Materials

Supplementary Table S1: clinic characteristics of patients included in this study. Supplementary Table S2: data production of 44 samples. *(Supplementary Materials)*

References

[1] H. Sung, J. Ferlay, R. L. Siegel et al., "Global cancer statistics 2020: GLOBOCAN estimates of incidence and mortality worldwide for 36 cancers in 185 countries," *CA: A Cancer Journal for Clinicians*, vol. 71, no. 3, pp. 209–249, 2021.

[2] N. J. Farber, I. Faiena, V. Dombrovskiy et al., "Disparities in the use of continent urinary diversions after radical cystectomy for bladder cancer," *Bladder Cancer*, vol. 4, no. 1, pp. 113–120, 2018.

[3] J. A. Witjes, H. M. Bruins, R. Cathomas et al., "European Association of Urology guidelines on muscle-invasive and metastatic bladder cancer: summary of the 2020 guidelines," *European Urology*, vol. 79, no. 1, pp. 82–104, 2021.

[4] K. Kaczmarek, A. Lemiński, A. Bańcarz, A. Zakrzewska, and M. Słojewski, "Post-operative infections among patients undergoing radical cystectomy at a tertiary center," *Surgical Infections*, vol. 19, no. 4, pp. 451–458, 2018.

[5] N. W. Cortes-Penfield, B. W. Trautner, and R. L. P. Jump, "Urinary tract infection and asymptomatic bacteriuria in older adults," *Infectious Disease Clinics of North America*, vol. 31, no. 4, pp. 673–688, 2017.

[6] D. S. Kaufman, W. U. Shipley, and A. S. Feldman, "Bladder cancer," *The Lancet*, vol. 374, no. 9685, pp. 239–249, 2009.

[7] V. D. Rosenthal, H. Bijie, D. G. Maki et al., "International nosocomial infection control consortium (INICC) report, data summary of 36 countries, for 2004-2009," *American Journal of Infection Control*, vol. 40, no. 5, pp. 396–407, 2012.

[8] L. Grigoryan, B. W. Trautner, and K. Gupta, "Diagnosis and management of urinary tract infections in the outpatient setting," *JAMA*, vol. 312, no. 16, p. 1677, 2014.

[9] C. M. Chu and J. L. Lowder, "Diagnosis and treatment of urinary tract infections across age groups," *American Journal of Obstetrics and Gynecology*, vol. 219, no. 1, pp. 40–51, 2018.

[10] A. J. Wolfe, E. Toh, N. Shibata et al., "Evidence of uncultivated bacteria in the adult female bladder," *Journal of Clinical Microbiology*, vol. 50, no. 4, pp. 1376–1383, 2012.

[11] M. J. Drake, N. Morris, A. Apostolidis, M. S. Rahnama'I, and J. R. Marchesi, "The urinary microbiome and its contribution to lower urinary tract symptoms; ICI-RS 2015," *Neurourology and Urodynamics*, vol. 36, no. 4, pp. 850–853, 2017.

[12] G. Godaly, I. Ambite, and C. Svanborg, "Innate immunity and genetic determinants of urinary tract infection susceptibility,"

Current Opinion in Infectious Diseases, vol. 28, no. 1, pp. 88–96, 2015.

[13] T. G. Clifford, B. Katebian, C. M. van Horn et al., "Urinary tract infections following radical cystectomy and urinary diversion: a review of 1133 patients," *World Journal of Urology*, vol. 36, no. 5, pp. 775–781, 2018.

[14] K. Mizutani, K. Kawakami, K. Horie et al., "Urinary exosome as a potential biomarker for urinary tract infection," *Cellular Microbiology*, vol. 21, no. 7, p. e13020, 2019.

[15] M. Grabe, R. Bartoletti, T. E. Bjerklund Johansen et al., *EAU Guidelines on Urological Infections*, 2015.

[16] T. Cai, S. Mazzoli, N. Mondaini et al., "The role of asymptomatic bacteriuria in young women with recurrent urinary tract infections: to treat or not to treat?," *Clinical Infectious Diseases*, vol. 55, no. 6, pp. 771–777, 2012.

[17] L. Grigoryan, A. D. Naik, D. Horwitz et al., "Survey finds improvement in cognitive biases that drive overtreatment of asymptomatic bacteriuria after a successful antimicrobial stewardship intervention," *American Journal of Infection Control*, vol. 44, no. 12, pp. 1544–1548, 2016.

[18] M. J. Lee, M. Kim, N. Kim et al., "Why is asymptomatic bacteriuria overtreated?: a tertiary care institutional survey of resident physicians," *BMC Infectious Diseases*, vol. 15, no. 1, p. 289, 2015.

[19] M. R. Wilson, S. N. Naccache, E. Samayoa et al., "Actionable diagnosis of neuroleptospirosis by next-generation sequencing," *New England Journal of Medicine*, vol. 370, no. 25, pp. 2408–2417, 2014.

[20] M. Dixon, M. Stefil, M. McDonald et al., "Metagenomics in diagnosis and improved targeted treatment of UTI," *World Journal of Urology*, vol. 38, no. 1, pp. 35–43, 2020.

[21] F. Sorrentino, R. Cartwright, G. A. Digesu et al., "Associations between individual lower urinary tract symptoms and bacteriuria in random urine samples in women," *Neurourology and Urodynamics*, vol. 34, no. 5, pp. 429–433, 2015.

[22] M. M. Pearce, M. J. Zilliox, A. B. Rosenfeld et al., "The female urinary microbiome in urgency urinary incontinence," *American Journal of Obstetrics and Gynecology*, vol. 213, no. 3, pp. 347.e1–347.e11, 2015.

[23] K. J. Thomas-White, E. E. Hilt, C. Fok et al., "Incontinence medication response relates to the female urinary microbiota," *International Urogynecology Journal*, vol. 27, no. 5, pp. 723–733, 2016.

[24] D. Horwitz, T. McCue, A. C. Mapes et al., "Decreased microbiota diversity associated with urinary tract infection in a trial of bacterial interference," *Journal of Infection*, vol. 71, no. 3, pp. 358–367, 2015.

[25] T. W. Flaig, P. E. Spiess, N. Agarwal et al., "Bladder cancer, version 3.2020, NCCN clinical practice guidelines in oncology," *Journal of the National Comprehensive Cancer Network*, vol. 18, no. 3, pp. 329–354, 2020.

[26] CFDC Prevention, *Urinary tract infection (catheter associated urinary tract infection [CAUTI]) and non-catheter associated urinary tract infection [UTI] and other urinary system infection (USI) events*.

[27] L. Nicolle, "Symptomatic urinary tract infection or asymptomatic bacteriuria? Improving care for the elderly," *Clinical Microbiology and Infection*, vol. 25, no. 7, pp. 779–781, 2019.

[28] L. E. Nicolle, K. Gupta, S. F. Bradley et al., "Clinical practice guideline for the management of asymptomatic bacteriuria: 2019 Update by the Infectious Diseases Society of Americaa," *Clinical Infectious Diseases*, vol. 68, no. 10, pp. e83–e110, 2019.

[29] D. K. Owens, K. W. Davidson, A. H. Krist et al., "Screening for asymptomatic bacteriuria in adults: US Preventive Services Task Force recommendation statement," *JAMA*, vol. 322, no. 12, pp. 1188–1194, 2019.

[30] T. C. Horan, M. Andrus, and M. A. Dudeck, "CDC/NHSN surveillance definition of health care-associated infection and criteria for specific types of infections in the acute care setting," *American Journal of Infection Control*, vol. 36, no. 5, pp. 309–332, 2008.

[31] National Health and Family Planning Commission of the People's Republic of China, *Laboratory diagnosis of urinary tract infections*, 2016, WS/T 489-2016.

[32] Health industry standard of the People's Republic of China, *Collection and transport of clinical microbiology test specimens*, 2018, WS/T640-2018.

[33] S. Chen, Y. Zhou, Y. Chen, and J. Gu, "fastp: an ultra-fast all-in-one FASTQ preprocessor," *Bioinformatics*, vol. 34, no. 17, pp. i884–i890, 2018.

[34] E. L. Clarke, L. J. Taylor, C. Zhao et al., "Sunbeam: an extensible pipeline for analyzing metagenomic sequencing experiments," *Microbiome*, vol. 7, no. 1, p. 46, 2019.

[35] B. Langmead and S. L. Salzberg, "Fast gapped-read alignment with bowtie 2," *Nature Methods*, vol. 9, no. 4, pp. 357–359, 2012.

[36] M. Zaharia, W. J. Bolosky, K. Curtis et al., *Faster and More Accurate Sequence Alignment with SNAP*, p. 2011, 2011.

[37] C. Jing, H. Chen, Y. Liang et al., "Clinical evaluation of an improved metagenomic next-generation sequencing test for the diagnosis of bloodstream infections," *Clinical Chemistry*, vol. 67, no. 8, pp. 1133–1143, 2021.

[38] M. Hall and R. G. Beiko, "16S rRNA gene analysis with QIIME2," in *Methods in Molecular Biology*, Humana Press, New York, NY, 2018.

[39] Y. Yang, Y. Zhang, J. Liu et al., "Clinical characteristics of patients with asymptomatic bacteriuria and symptomatic urinary tract infection," *Chinese Journal of Nosocomiology*, vol. 28, no. 14, p. 4, 2018.

[40] S. Wang, H. Liu, S. Zuo, Y. Qi, W. Li, and M. Su, "Analysis of risk factors and preventive measures for urinary tract infection in patients of ureterocutaneostomy," *Chinese Journal of Disinfection*, vol. 35, no. 11, p. 3, 2018.

[41] S. L. Mitchell and P. J. Simner, "Next-generation sequencing in clinical microbiology: are we there yet?," *Clinics in Laboratory Medicine*, vol. 39, no. 3, pp. 405–418, 2019.

[42] E. Shrestha, J. R. White, S. Yu et al., "Profiling the urinary microbiome in men with positive versus negative biopsies for prostate cancer," *Journal of Urology*, vol. 199, no. 1, pp. 161–171, 2018.

[43] C. A. Hunter and S. A. Jones, "Correction: corrigendum: IL-6 as a keystone cytokine in health and disease," *Nature Immunology*, vol. 18, no. 11, p. 1271, 2017.

[44] R. Li, D. Li, N. Liu, H. Yan, and H. Li, "Expression of IL-1β in astrocyte after traumatic brain injury," *Chinese Journal of Anatomy*, vol. 39, no. 3, p. 4, 2016.

[45] X. Han, H. Huang, and X. Wei, "Serum TNF-α, IL-1β and IL-6 expression levels and significance of children with severe pneumococcal infection," *International Journal of Laboratory Medicine*, vol. 39, no. 9, p. 4, 2018.

[46] L. Nicolle, "The paradigm shift to non-treatment of asymptomatic bacteriuria," *Pathogens*, vol. 5, no. 2, p. 38, 2016.

[47] W. Parapiboon, A. Ingsathit, S. Jirasiritham, and V. Sumethkul, "High incidence of bacteriuria in early post-kidney transplantation; results from a randomized controlled study," *Transplantation Proceedings*, vol. 44, no. 3, pp. 734–736, 2012.

[48] A. Ghoreifi, C. M. van Horn, W. Xu et al., "Urinary tract infections following radical cystectomy with enhanced recovery protocol: a prospective study," *Urologic Oncology: Seminars and Original Investigations*, vol. 38, no. 3, pp. 75.e9–75.e14, 2020.

[49] R. Mano, J. Baniel, H. Goldberg, Y. Stabholz, D. Kedar, and O. Yossepowitch, "Urinary tract infections in patients with orthotopic neobladder," *Urologic Oncology: Seminars and Original Investigations*, vol. 32, no. 1, pp. 50.e9–50.e14, 2014.

[50] P. G. Abril, J. S. Ríos, L. M. Suárez et al., "Urinary Tract Infection as the Main Cause of Admission in Cystectomized Patients," *Actas Urológicas Españolas (English Edition)*, vol. 45, no. 4, pp. 247–256, 2021.

[51] S. E. Geerlings, R. Meiland, and A. I. M. Hoepelman, "Pathogenesis of bacteriuria in women with diabetes mellitus," *International Journal of Antimicrobial Agents*, vol. 19, no. 6, pp. 539–545, 2002.

[52] W. P. Parker, A. Toussi, M. K. Tollefson et al., "Risk factors and microbial distribution of urinary tract infections following radical cystectomy," *Urology*, vol. 94, pp. 96–101, 2016.

[53] B. C. Ozgur, M. Ekıcı, C. N. Yuceturk, and O. Bayrak, "Bacterial colonization of double J stents and bacteriuria frequency," *The Kaohsiung Journal of Medical Sciences*, vol. 29, no. 12, pp. 658–661, 2013.

[54] U. Dobrindt, B. Wullt, and C. Svanborg, "Asymtomatic bacteriuria as a model to study the coevolution of hosts and bacteria," *Pathogens*, vol. 5, no. 1, p. 21, 2016.

[55] A. Ronald, "The etiology of urinary tract infection: traditional and emerging pathogens," *Disease-a-Month*, vol. 49, no. 2, pp. 71–82, 2003.

[56] J. Coussement, A. Scemla, J. Hougardy et al., "Prevalence of asymptomatic bacteriuria among kidney transplant recipients beyond two months post-transplant: a multicenter, prospective, cross-sectional study," *PLoS One*, vol. 14, no. 9, article e221820, 2019.

[57] E. O. Kehinde, V. O. Rotimi, K. A. Al-Awadi et al., "Factors predisposing to urinary tract infection after j ureteral stent insertion," *Journal of Urology*, vol. 167, no. 3, pp. 1334–1337, 2002.

[58] S. L. Chen, S. L. Jackson, and E. J. Boyko, "Diabetes mellitus and urinary tract infection: epidemiology, pathogenesis and proposed studies in animal models," *Journal of Urology*, vol. 182, no. 6S, pp. S51–S56, 2009.

[59] T. Wilke, B. Boettger, B. Berg et al., "Epidemiology of urinary tract infections in type 2 diabetes mellitus patients: an analysis based on a large sample of 456,586 German T2DM patients," *Journal of Diabetes and its Complications*, vol. 29, no. 8, pp. 1015–1023, 2015.

[60] T. Ishihara, N. Watanabe, S. Inoue et al., "Usefulness of next-generation DNA sequencing for the diagnosis of urinary tract infection," *Drug Discoveries & Therapeutics*, vol. 14, no. 1, pp. 42–49, 2020.

[61] N. Liu, J. Kan, W. Cao et al., "Metagenomic next-generation sequencing diagnosis of peripheral pulmonary infectious lesions through virtual navigation, radial EBUS, ultrathin bronchoscopy, and ROSE," *Journal of International Medical Research*, vol. 47, no. 10, pp. 4878–4885, 2019.

[62] T. A. Blauwkamp, S. Thair, M. J. Rosen et al., "Analytical and clinical validation of a microbial cell-free DNA sequencing test for infectious disease," *Nature Microbiology*, vol. 4, no. 4, pp. 663–674, 2019.

[63] A. M. Macejko and A. J. Schaeffer, "Asymptomatic bacteriuria and symptomatic urinary tract infections during pregnancy," *Urologic Clinics of North America*, vol. 34, no. 1, pp. 35–42, 2007.

[64] M. Buoli, A. Caldiroli, C. Cumerlato Melter, M. Serati, J. de Nijs, and A. C. Altamura, "Biological aspects and candidate biomarkers for psychotic bipolar disorder: a systematic review," *Psychiatry and Clinical Neurosciences*, vol. 70, no. 6, pp. 227–244, 2016.

[65] W. S. Oh, J. Hur, E. S. Kim et al., "Factors associated with specific uropathogens in catheter-associated urinary tract infection: developing a clinical prediction model," *Journal of International Medical Research*, vol. 42, no. 6, pp. 1335–1347, 2014.

[66] W. Yang, P. Liu, Y. Zheng et al., "Transcriptomic analyses and experimental verification reveal potential biomarkers and biological pathways of urinary tract infection," *Bioengineered*, vol. 12, no. 1, pp. 8529–8539, 2021.

[67] G. Kaplanski, V. Marin, F. Montero-Julian, A. Mantovani, and C. Farnarier, "IL-6: a regulator of the transition from neutrophil to monocyte recruitment during inflammation," *Trends in Immunology*, vol. 24, no. 1, pp. 25–29, 2003.

[68] C. Zuoliang, L. Shuanglin, Y. Jindong et al., "Immune state and inflammatory mediators of patients with urinary tract infections after bladder cancer operation," *Chinese Journal of Nosocomiology*, vol. 28, no. 11, p. 4, 2018.

[69] S. Kaur, Y. Bansal, R. Kumar, and G. Bansal, "A panoramic review of IL-6: Structure, pathophysiological roles and inhibitors," *Bioorganic & Medicinal Chemistry*, vol. 28, no. 5, p. 115327, 2020.

Hindawi
Disease Markers
Volume 2022, Article ID 7792291, 8 pages
https://doi.org/10.1155/2022/7792291

Research Article

Efficacy of Navigated Laser Photocoagulation for Chronic Central Serous Chorioretinopathy: A Retrospective Observational Study

Fen Zhou, Jin Yao, Qin Jiang, and Weihua Yang

Nanjing Medical University Affiliated Eye Hospital, China

Correspondence should be addressed to Jin Yao; dryaojin@126.com, Qin Jiang; jqin710@vip.sina.com, and Weihua Yang; benben0606@139.com

Received 5 December 2021; Accepted 9 March 2022; Published 20 April 2022

Academic Editor: Wen-Qing Shi

Background. No consensus has been reached regarding the management of central serous chorioretinopathy (CSCR). We aimed to investigate the efficacy of navigated laser treatment for chronic CSCR and changes in the morphology of the retinal pigment epithelium (RPE). In this retrospective observational study, 19 patients with subjective symptoms admitted to the Nanjing Medical University Affiliated Eye Hospital were included between January 2021 and August 2021. All patients underwent visual acuity and optical coherence tomography (OCT) examination during follow-up. Fluorescein angiography (FA) was performed at baseline and at the final follow-up to confirm the dye leakage sites. The mean logMAR BCVA at baseline and at the end of follow-up was 0.49 ± 0.24 and 0.24 ± 0.15, respectively. The mean logMAR BCVA 3 months after treatment was significantly better than that before treatment ($p = 0.002$). Significant improvements were observed in central macular thickness (CMT) and subfoveal choroidal thickness (SFCT) after navigated laser photocoagulation ($p < 0.0001$). Subretinal fluid was completely resolved in 13 (68%) of 19 eyes at 3 months. RPE lesions on OCT images showed RPE detachment in 17 eyes (61.5%), small protrusion of the RPE layer in 5 eyes (7.5%), and a rough RPE layer in 4 eyes (31%). After laser treatment, 9 points (35%) showed retinal detachment, and 10 (38.5%) regions showed an irregular RPE layer. An irregularly protruded RPE layer was also observed in different regions of the leakage spot in 5 (19%) eyes, and RPE defects were seen in 2 (7.5%) eyes. Navigated laser photocoagulation for chronic CSCR can achieve substantial anatomical and visual improvement. OCT outcomes may provide new information to facilitate understanding of the mechanism of chronic CSCR. Navigated laser photocoagulation should be chosen as an optimal treatment option in patients with chronic CSCR who cannot afford photodynamic therapy.

1. Introduction

Central serous chorioretinopathy (CSCR) is one of the most common retinal diseases characterized by fluid leakage. CSCR is a main cause of vision loss among middle-aged males due to photoreceptor and retinal pigment epithelium (RPE) atrophy [1]. However, the pathogenesis of CSCR remains poorly understood. Fluorescein angiography (FA) shows single or multiple spots of fluorescein leakage at the level of the RPE. Dysfunction in RPE activity and increased vascular choroidal hyperpermeability are considered important factors in fluid collection. RPE dysfunction cannot prevent diffusion of fluid into the subretinal space. Complete resolution of subretinal fluid (SRF) should be the principal target of CSCR therapy, as prolonged SRF can result in permanent damage to the photoreceptors [2]. SRF is a common hallmark of CSCR. The principal monitoring device of SRF is optical coherence tomography (OCT). The volume of SRF can be quantified by OCT. A higher SRF volume may be closely related to poorer best-corrected visual acuity (BCVA) [3]. SRF absorption is an important prognostic indicator in patients with CSCR. If SRF resolves quickly, patients with CSCR have good outcomes. The RPE can be not only impaired by SRF but also damaged by underlying multifocal

Table 1: Patient characteristics.

Case	Age	Gender	Eye	Leakage pattern	Leak point	OCT-ophthalmoscope	VA	CMT (μm)	SFCT (μm)
1	50	M	L	Inkblot	1	Protrusion-protrusion	0.15	663	700
2	52	F	R	Smokestack	1	Rough RPE-protrusion	0.3	466	632
3	54	M	R	Smokestack	2	Rough RPE-protrusion PED-rough RPE	0.12	374	550
4	33	M	L	Inkblot	1	PED-protrusion	0.15	570	546
5	39	M	L	Inkblot	1	PED-PED	0.6	389	398
6	37	M	L	Inkblot	1	Protrusion-rough RPE	0.4	455	455
7	31	F	R	Inkblot	2	PED-PED PED-rough RPE	0.5	598	757
8	38	M	R	Inkblot	1	Rough RPE-RPE defect	0.1	361	326
9	65	F	R	Inkblot	1	Rough RPE-rough RPE	0.4	372	377
10	50	M	L	Inkblot	1	PED-rough RPE	0.3	422	487
11	43	M	R	Inkblot	1	PED-PED	0.2	399	565
12	40	F	R	Inkblot	1	PED-protrusion	0.5	287	465
13	63	M	R	Inkblot	1	PED-PED	0.2	302	482
14	49	M	R	Inkblot	2	PED-PED PED-PED	0.6	546	554
15	38	M	L	Inkblot	2	PED-PED PED-PED	0.8	374	500
16	43	M	R	Inkblot	4	Rough RPE-rough RPE (3) PED-rough RPE (1)	0.6	410	634
17	57	M	R	Inkblot	1	PED-rough RPE	0.4	438	439
18	64	M	L	Inkblot	1	Rough RPE-RPE defect	0.15	500	354
19	49	M	R	Inkblot	1	PED-PED	0.6	508	328

choroidal vascular dysfunction without the presence of SRF [4, 5]. Changes in central macular thickness (CMT) appear to be associated with a decrease in SRF [6].

To date, there is no consensus regarding the management of CSCR. Treatment options include pharmacology, an intravitreal injection of anti-vascular endothelial growth factor (VEGF) antibodies, and laser photocoagulation. Conventional lasers, subthreshold lasers, photodynamic therapy, and transpupillary thermotherapy are available for laser photocoagulation [7, 8]. CNV secondary to CSCR was treated with the use of anti-VEGF therapy or with the use of PDT [9, 10]. Laser photocoagulation was the first-line treatment in CSCR.

It can be challenging to perform conventional laser photocoagulation for leaks in CSCR. It can be a difficult task to determine the exact location on the live fundus view of the leaky spot among the network of blood vessels on a moving eye. To improve the accuracy and predictability of retinal laser photocoagulation for CSCR, the NAVILAS® laser system (OD-OS GmbH, Teltow, Germany) provides the option to plan the treatment beforehand directly on the early fluorescein angiogram. The angiogram is imported into the laser device, superimposed, and continuously aligned with the live image using an eye tracking system, so that physicians can perform more precise targeted treatments than conventional manually directed laser photocoagulation in CSCR.

The difficulty is alleviated by using a navigated laser device when seeking the leaky spot on the live inverted fundus view through the slit-lamp laser device. Several advantages exist for the NAVILAS® laser system, including identifying the exact location of the leak, eye tracking, and laser planning abilities of the laser system on fluorescein angiograms. In addition, navigated laser photocoagulation is a shorter procedure than conventional laser treatments and is less painful for patients. However, direct observation of precise morphologic changes in the RPE after navigated laser treatment in patients with CSCR has not been conducted. Therefore, this study aimed to evaluate the efficacy of navigated laser treatment for CSCR and to assess morphological changes in the RPE during treatment.

2. Materials and Methods

2.1. Ethics Statements. This study was approved by the Nanjing Medical University Affiliated Eye Hospital institutional review board and conducted in accordance with the Declaration of Helsinki (1964). Informed consent was obtained from all patients.

2.2. Study Design and Patients. In our retrospective observational study, we included 19 eyes of 19 patients with serous retinal detachment who were diagnosed with chronic CSCR.

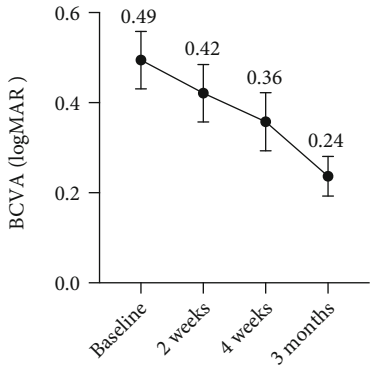

Figure 1: Variation of best-corrected visual acuity (logMAR) during follow-up expressed as mean and standard deviation. The comparison between different time points was evaluated. We found a time-dependent increase in BCVA. The mean logMAR BCVA was 0.42 ± 0.21 and 0.36 ± 0.22 at 2-week and at 4-week follow-up, respectively. There was no statistically significant difference compared to baseline ($p = 0.4192$, $p = 0.1403$). There was a sharp increase at 3-month follow-up. LogMAR BCVA at 3-month follow-up was higher than at baseline. The difference was significant ($p = 0.002$).

All patients received navigated laser photocoagulation therapy between January 2021 and August 2021 at our hospital. Diagnosis of CSCR was based on fundus examination, FA, and indocyanine green angiography (ICGA). Patients were excluded if diagnosed with intraocular inflammation, retinal vascular occlusive disease (RVO), or neovascular maculopathies such as age-related macular degeneration (AMD) and polypoidal choroidal vasculopathy (PCV). All patients underwent ophthalmic examinations, including slit-lamp microscope examination, measurement of BCVA, Goldmann tonometry, spectral-domain OCT (Spectralis HRA+OCT, Heidelberg Spectralis, Heidelberg Engineering GmbH, Heidelberg, Germany) of the macula, and FA (Spectralis HRA+OCT, Heidelberg Spectralis, Heidelberg Engineering GmbH).

2.3. Treatment. Before laser photocoagulation using the NAVILAS® laser system (532 nm double-pulsed YAG laser, OD-OS GmbH), an image of the posterior pole was captured. The physician planned treatment by using the early images of FA that showed a leaking spot, and then, the same physician performed the laser treatment. To determine the parameters for the laser shots, an initial test burn away from the macular region was performed. Laser parameters were set as follows: grayish white burn, energy 50-80 mW; spot size, 100-150 μm; and pulse duration, 70-100 ms. One to ten laser spots of 100-150 μm per leaking point were marked on the superimposed image together with a protection shield for the fovea and optic nerve. After laser treatment, all patients underwent color fundus photography. The laser software provided an additional feedback window that showed the immediate laser effect captured at the end of the pulse. Treatment was repeated if focal leakage of the same lesion was visible on FA at the 1-month follow-up. If patients developed a new leaking point on FA distant from the previous lesion, they also received additional laser treatment. This was considered as a second treatment of the same eye.

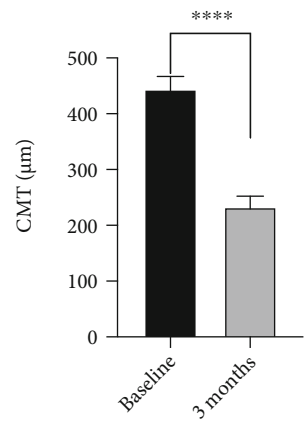

Figure 2: The mean CMT value at the 3-month follow-up was higher than at baseline. The deference was significant. $^{****}p < 0.0001$.

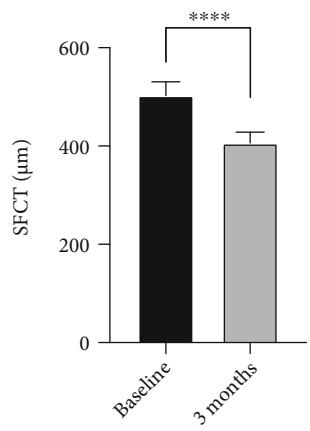

Figure 3: The mean SFCT value at the 3-month follow-up was higher than at baseline. The deference was significant. $^{****}p < 0.0001$.

2.4. Follow-Up and Analysis. Comprehensive eye examinations were performed during every follow-up visit, such as OCT and FA. All patients were examined at 2 weeks, 4 weeks, and 3 months after laser treatment. Data regarding BCVA, subfoveal choroidal thickness (SFCT), and CMT were collected from the records of the patients in this study. At baseline, CMT was measured from the inner surface of the neurosensory retina to the inner portion of the RPE at the fovea. SFCT was measured via subfoveal localization using enhanced depth imaging [11].

2.5. Statistical Analysis. Each variable involved calculation of descriptive statistics. Data were expressed as the mean $\pm$ SD. Normal distribution was checked by using the Shapiro-Wilk test. Paired t-test were used to analyze the changes in BCVA at baseline and follow-up at 2 weeks, 4 weeks, and 3 months. CMT and SFCT differences between baseline and 3-month follow-up were also calculated by

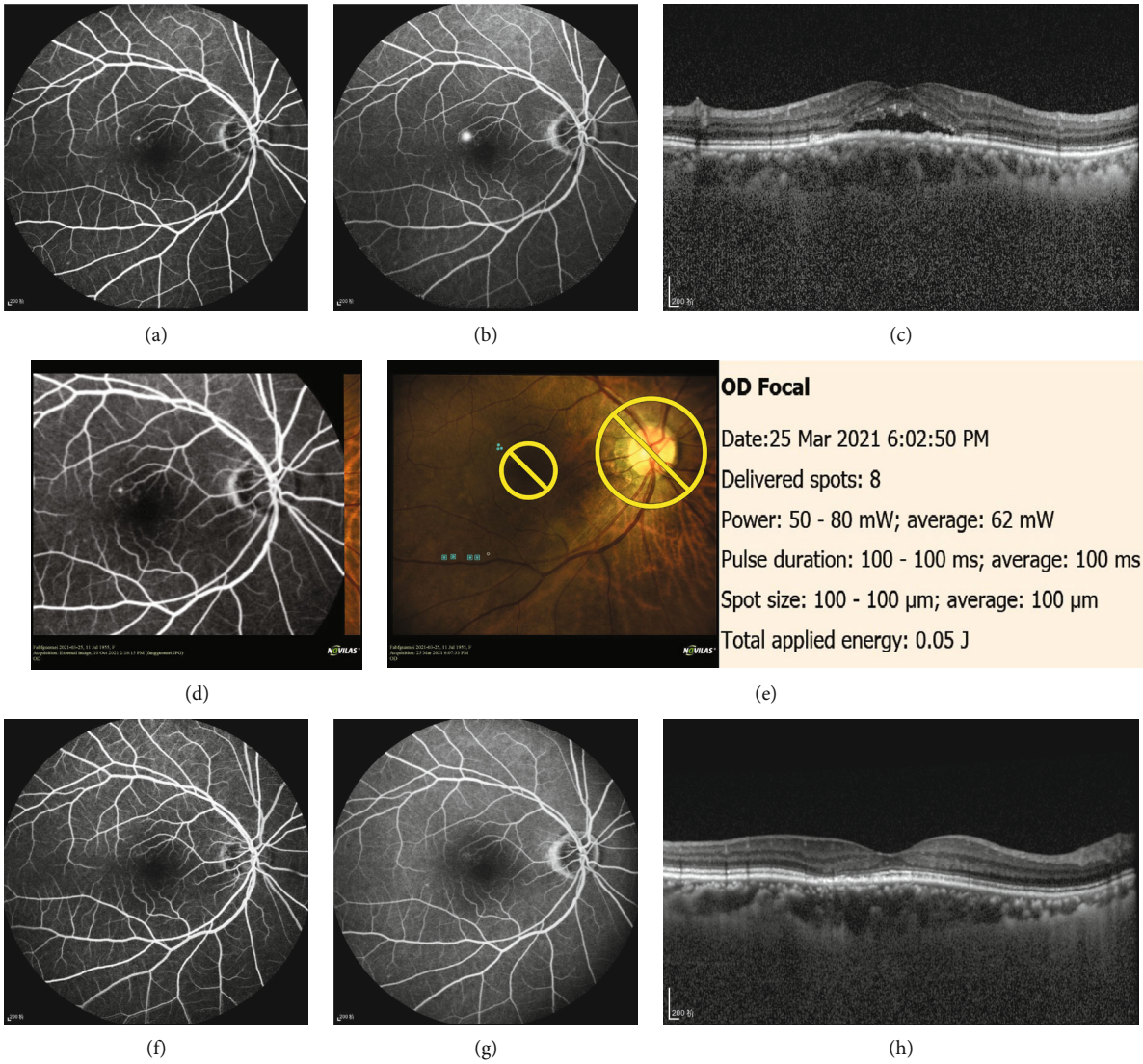

Figure 4: Images of a 65-year-old woman with chronic CSC for 48 months. (a) FA showed early hyperfluorescence representing a leak. (b) The hyperfluorescence was increased in the late phase. (c) OCT showed obvious subretinal fluid and irregular RPE. (d) The selected FA image showing the focal leakage was imported and automatically superimposed on the color fundus photograph. (e) NAVILAS® laser photocoagulation was programmed on the actual image to three single laser spots on the leak and performed with the following parameters: spot size: 100 μm; power: 50–80 mW; and pulse duration: 100 ms. (f) At the 3-month follow-up, focal leakage in the early stage on FA has disappeared. (g) The focal leakage in the late stage on FA has also disappeared. (h) OCT showed no serous pigment epithelial detachment.

paired t-test. Statistical analysis was performed using SPSS Statistics version 22 (IBM, Armonk, NY). Statistical significance was set at $p < 0.05$.

3. Results

3.1. Patients. Table 1 shows the patient characteristics. In total, 19 eyes of 19 patients (15 men (78.9%) and 4 women (21.1%); mean age, 41.7 ± 8.6 years; age range, 31–65 years) were enrolled in this study. The mean duration of symptoms was 13 ± 15 months (range, 3 months to 4 years). Thirteen eyes (74%) had one point of focal leakage, four eyes (21%) showed two points of leakage, and one eye (5%) showed four points of leakage. Dye leakage was observed in all patients on FA. Seventeen and two patients presented with inkblot and smokestack leakages on FA, respectively. Two eyes had previously received treatment with a subthreshold micropulse laser (SML), and four eyes had a history of CSCR in the fellow eye.

3.2. Visual Acuity. The mean logMAR BCVA at baseline was 0.49 ± 0.24. At the final visit, the mean logMAR BCVA was 0.24 ± 0.15. The mean logMAR BCVA at 2 weeks and 4 weeks was 0.42 ± 0.21 and 0.36 ± 0.22, respectively (Figure 1).

3.3. Findings of Optical Coherence Tomography. Figures 2 and 3 show the outcome parameters. At baseline and at the 3-month follow-up, the mean CMT values were 443.9 ± 79.5 μm and 232.9 ± 48.4 μm, respectively, while the mean SFCT

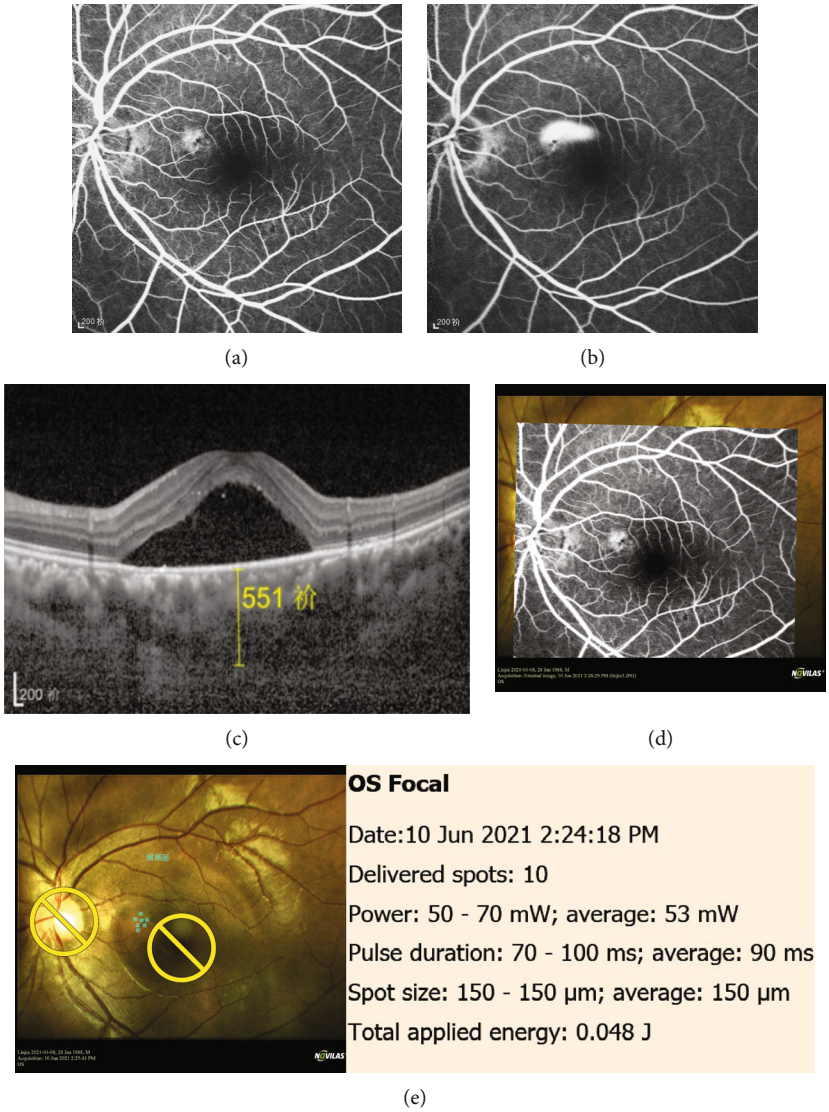

Figure 5: Images of a 40-year-old male patient with recurrent and chronic central serous chorioretinopathy for 4 months. (a) FA showed focal leakage in the early stage. (b) FA showed more obvious focal leakage in the late stage. (c) OCT showed conspicuous serous pigment epithelium detachment and the thickness of choroid was 551 μm. (d) The selected FA image showing the focal leakage was imported and automatically superimposed on the color fundus photograph. (e) NAVILAS® laser photocoagulation was programmed on the actual image to seven single laser spots on the leak and performed with the following parameters: spot size: 150 μm; power: 50–70 mW; and pulse duration: 70–100 ms.

values were $502.6 \pm 96.6\,\mu$m and $406.3 \pm 79.7\,\mu$m, respectively. Figures 4(a)–4(h) show a representative case.

3.4. Changes in Subretinal Fluid during the Follow-Up. SRF was completely resolved in 13 (68%) of 19 eyes at 3 months. However, 6 leaky points (23%) among 26 leakage sites were also detected in 6 eyes. Extensive SRF was present and involved the macula. Figures 5(a)–5(d) show a representative case.

3.5. Changes in the Retinal Pigment Epithelium during the Follow-Up. Among the 26 leakage sites in 19 eyes, 16 (61.5%) showed RPE detachment (PED), and 8 (31%) showed an irregular RPE layer. An irregularly protruded RPE layer was also observed in different regions from the leakage spot in two eyes (7.5%). After laser treatment, 9 points (35%) showed PED, and 10 (38.5%) regions showed an irregular RPE layer. The irregularly protruded RPE layer was also observed in different regions from the leakage spot in five (19%) eyes, and RPE defects were observed in two (7.5%) eyes. Figures 6(a)–6(h) show a representative case.

4. Discussion

Although there are various available treatment options for CSCR, laser-related RPE atrophy and choroidal neovascularization cannot be ignored [12, 13]. Navigated laser photocoagulation may be an optimal option, especially during

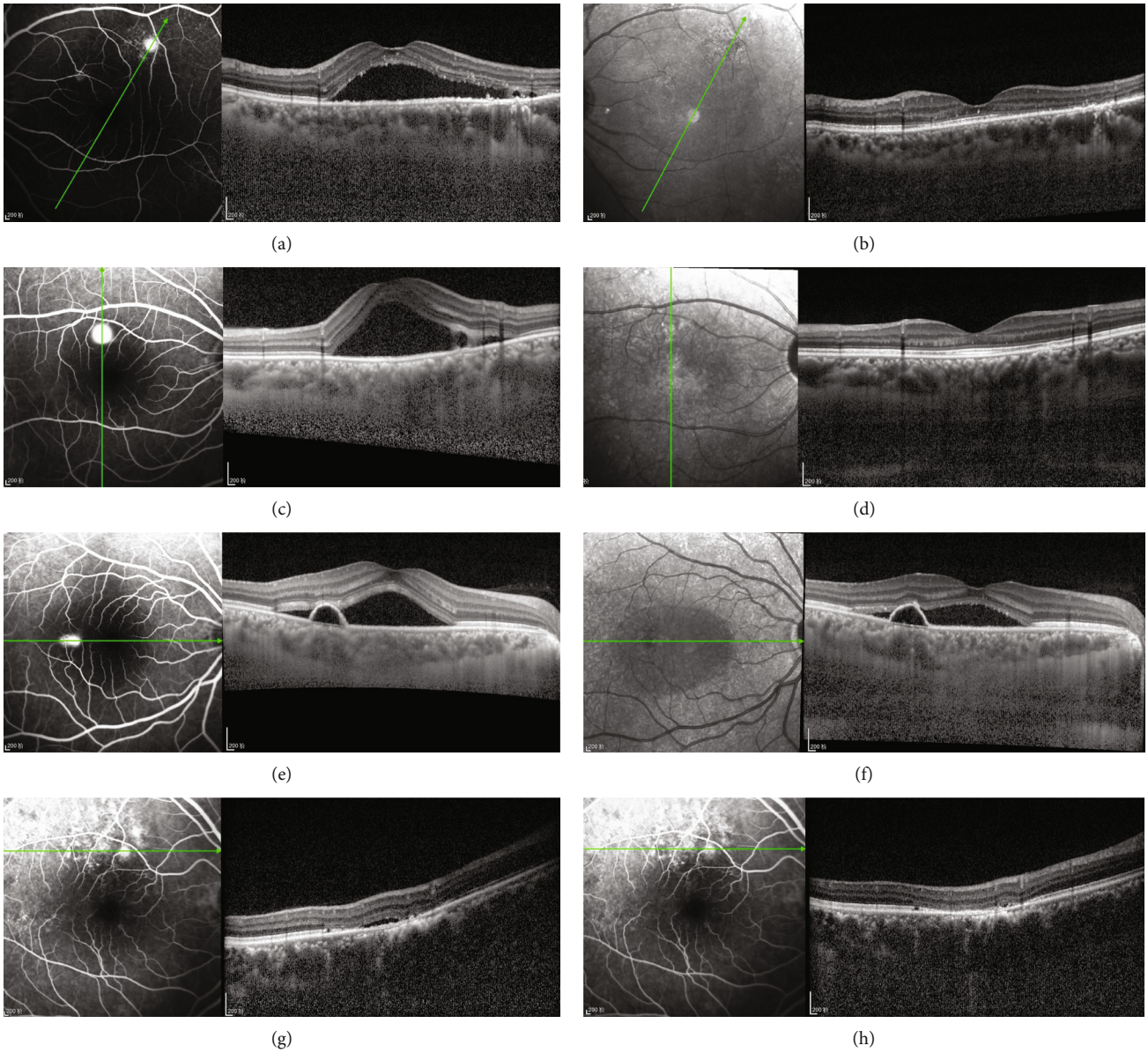

Figure 6: (a) OCT image showed SRF and irregular RPE. (b) OCT image shows an RPE defect and complete absorption of SRF after 3 months. (c) OCT image showed the retina dipping above the irregular RPE with slight fibrin. (d) After 3 months of NAVILAS® laser photocoagulation, OCT image shows an RPE defect and complete absorption of SRF. (e) OCT image showed SRF and PED at the dye leakage spot. (f) OCT image after 3 months of NAVILAS® laser photocoagulation showed decreased SRF, but PED remains. (g) OCT image showed irregular RPE changes. (h) After 3 months of NAVILAS® laser photocoagulation, OCT image also showed irregular RPE changes but complete absorption of SRF.

the coronavirus disease pandemic. A previous report showed that navigated laser photocoagulation was safe and more accurate (92%) than a conventional laser (72%) in the treatment of diabetic retinopathy microaneurysms [14]. Recently, resolution of SRF and minimum iatrogenic damage was achieved through navigated laser photocoagulation in CSCR [15]. Therefore, it was deemed an effective and safe alternative therapy for patients with chronic CSCR [16].

Half-dose photodynamic therapy is superior to SML for treating CSCR regarding the complete resolution of SRF and functional improvement. At 6–8 weeks after treatment, resolution of SRF was achieved in 51.2% and 13.8% of patients, respectively [17]. In our study, the outcomes were also favorable. The mechanism of SRF resolution after laser photocoagulation treatment is yet unknown. In previous studies, some mechanisms like stimulating the pump function of RPE cells near the leak, sealing focal defects in the RPE, promoting a healing response, and recruiting healthy RPE cells have been proposed [18–21]. In CSCR, the prolonged presence of SRF can cause decreased vision and irreversible RPE damage. Our study showed an improvement in BCVA from 0.37 to 0.62 after NAVILAS® laser photocoagulation treatment by follow-up at 3 months. Similar BCVA

outcomes were reported by Müller et al. in 32 previously untreated eyes after 3 months [16]. SRF can be used as an important biomarker of CSCR, and we found that navigated laser photocoagulation could induce complete resolution of SRF in 68% of patients with CSCR in the short term.

The pathological mechanism of CSCR includes enhanced permeability of choroidal capillaries and increased hydrostatic pressure, which leads to abnormal morphology and decreased function of the RPE and damage to its barrier function, leading to the infiltration of plasma and other substances in choroidal capillaries into the retinal neuroepithelium [1, 22, 23]. The mechanism of CSCR can be better understood with OCT, especially the changes in the RPE layer [24, 25].

To the best of our knowledge, this is the first report to draw attention to RPE morphological changes after navigated laser photocoagulation treatment in CSCR. Our study showed OCT images of leaky spots at the level of the RPE. Before laser photocoagulation treatment, RPE changes were found in the leaky regions of affected eyes with PED, an irregular RPE, a protruding RPE, and RPE defects. OCT images of leakage points showed PED in 16 leaky points (61.5%), small protrusion of the RPE layer at 2 leaky points (7.5%), and a rough RPE layer at 8 leaky points (31%). Mitarai et al. reported similar RPE changes [26]. PED may be the most common RPE abnormality at the leaky point in eyes with CSCR. Hirami et al. reported that RPE abnormalities within areas of choroidal vascular hyperpermeability were observed [27]. Dysfunction of the underlying choroid is likely to impair barrier function. Fluid can pass from the sub-RPE to the subretinal area due to a defect in the RPE layer. Thermal photocoagulation of the leaking site or region of RPE dysfunction may seal the leaky points and stimulate the neighboring RPE cells covering the coagulated area. Our study showed OCT changes in the RPE after thermal photocoagulation. PED was significantly reduced, and RPE morphology changed to an irregular RPE and a protruded RPE. This suggests that laser photocoagulation therapy is helpful for the gradual recovery of the morphology and function of the RPE. However, nine points (35%) showed retinal PED in seven eyes. Repeated laser treatment was performed in six patients with six leaky points, although RPE morphological change consisted of PED in five leaky points. This emphasized the importance of maintaining RPE integrity against increasing pressure from the choroid capillaries.

Eight regions (31%) showed an irregular RPE layer before the laser treatment. When a defect occurs in abnormal RPE regions, a new leakage spot will be observed. After laser treatment, an irregular RPE will change to an irregular and protruded RPE with RPE defects. In our study, an irregularly protruded RPE layer was also observed in different regions from the leakage site in two eyes (7.5%). The protruded RPE changed to an irregular and protruded RPE. This result shows that laser photocoagulation could promote the absorption of SRF; however, localized RPE defects and irregular RPE changed to an abnormal RPE morphology, indicating repair of functional damage of the RPE. Therefore, maintaining the integrity of RPE morphology is very important to resist the increased hydrostatic pressure of choroid capillaries during CSCR treatment.

Choroidal hyperpermeability at the location of the RPE leakage can be observed in ICGA. An enhanced-depth imaging model (EDI) of the choroid is another aspect of this study. Studies have revealed that there will be a reduction in SFCT with the resolution of the disease [28, 29]. Our study showed that the median value of SFCT was 502.6 mm (range, 326-757 mm) at baseline. After navigated laser photocoagulation, the SFCT decreased to 406.3 mm. This suggests that choroidal thickness may play an important role in the pathophysiology of CSCR.

The limitations of our study are its retrospective design, small sample size, and no control group. To study the efficacy of navigated laser photocoagulation in CSCR would require further studies with a longer follow-up.

5. Conclusions

In conclusion, after laser treatment, SRF absorption takes time. This finding draws attention to the development of best practice guidelines for treating CSCR. Navigated laser photocoagulation is a reliable treatment choice for sealing exudative lesions and allowing the resolution of SRF in some patients with chronic CSCR. OCT also provides a better understanding of RPE changes in this disease.

Data Availability

The article can be obtained from the corresponding author six months after publication.

Conflicts of Interest

The authors declare that there is no conflict of interest regarding the publication of this paper.

Acknowledgments

This research was funded by the National Natural Science Foundation (grant number 82070983), the Nanjing Enterprise Expert Team Project and the Medical Science, and Technology Development Project Fund of Nanjing (grant no. YKK21262).

References

[1] A. Daruich, A. Matet, A. Dirani et al., "Central serous chorioretinopathy: recent findings and new physiopathology hypothesis," *Progress in Retinal and Eye Research*, vol. 48, pp. 82–118, 2015.

[2] J. I. Lim, A. R. Glassman, L. P. Aiello, U. Chakravarthy, C. J. Flaxel, and R. F. Spaide, "Collaborative retrospective macula society study of photodynamic therapy for chronic central serous chorioretinopathy," *Ophthalmology*, vol. 121, no. 5, pp. 1073–1078, 2014.

[3] U. Nair, S. Ganekal, M. Soman, and K. Nair, "Correlation of spectral domain optical coherence tomography findings in acute central serous chorioretinopathy with visual acuity," *Clinical Ophthalmology*, vol. 6, pp. 1949–1954, 2012.

[4] R. Ranjan, G. Manayath, S. Karandikar, V. Shah, V. Saravanan, and V. Narendran, "Central serous chorioretinopathy: Current

update on management," *Oman Journal of Ophthalmology*, vol. 11, no. 3, pp. 200–206, 2018.

[5] M. Ratanasukon, K. Thongthong, P. Bhurayanontachai, and P. Jirarattanasopa, "Photoreceptor disruption in central serous chorioretinopathy treated by half-dose photodynamic therapy," *Clinical Ophthalmology*, vol. 7, pp. 87–92, 2013.

[6] S. R. Singh, C. Iovino, D. Zur et al., "Central serous chorioretinopathy imaging biomarkers," *The British Journal of Ophthalmology*, vol. 106, p. 553, 2022.

[7] T. J. van Rijssen, E. H. C. van Dijk, S. Yzer et al., "Central serous chorioretinopathy: towards an evidence-based treatment guideline," *Progress in Retinal and Eye Research*, vol. 73, p. 100770, 2019.

[8] J. B. Mao, C. Y. Zhang, C. Y. Liu et al., "Comprehensive evaluation of intravitreal conbercept versus half-dose photodynamic therapy for chronic central serous chorioretinopathy," *International Journal of Ophthalmology*, vol. 14, no. 5, pp. 719–724, 2021.

[9] E. Peiretti, G. Caminiti, R. Serra, L. Querques, R. Pertile, and G. Querques, "Anti-vascular endothelial growth factor therapy versus photodynamic therapy in the treatment of choroidal neovascularization secondary to central serous chorioretinopathy," *Retina*, vol. 38, no. 8, pp. 1526–1532, 2018.

[10] E. Smretschnig, S. Hagen, C. Glittenberg et al., "Intravitreal anti-vascular endothelial growth factor combined with half-fluence photodynamic therapy for choroidal neovascularization in chronic central serous chorioretinopath," *Eye*, vol. 30, no. 6, pp. 805–811, 2016.

[11] O. Yalcinbayir, O. Gelisken, B. Akova-Budak, G. Ozkaya, S. Gorkem Cevik, and A. A. Yucel, "Correlation of spectral domain optical coherence tomography findings and visual acuity in central serous chorioretinopathy," *Retina*, vol. 34, no. 4, pp. 705–712, 2014.

[12] Z. Michalewska, K. Dulczewska, and J. Nawrocki, "Choroidal neovascularization in central serous chorioretinopathy—a new clinical entity," *Spektrum Augenheilkd*, vol. 31, no. 6, pp. 251–256, 2017.

[13] G. I. Lee, A. Y. Kim, S. W. Kang et al., "Risk factors and outcomes of choroidal neovascularization secondary to central serous chorioretinopathy," *Scientific Reports*, vol. 9, no. 1, p. 3927, 2019.

[14] I. Kozak, S. F. Oster, M. A. Cortes et al., "Clinical evaluation and treatment accuracy in diabetic macular edema using navigated laser photocoagulator NAVILAS," *Ophthalmology*, vol. 118, no. 6, pp. 1119–1124, 2011.

[15] J. Chhablani, P. K. Rani, A. Mathai, S. Jalali, and I. Kozak, "Navigated focal laser photocoagulation for central serous chorioretinopathy," *Clinical Ophthalmology*, vol. 8, pp. 1543–1547, 2014.

[16] B. Müller, J. Tatsios, J. Klonner, D. Pilger, and A. M. Joussen, "Navigated laser photocoagulation in patients with non-resolving and chronic central serous chorioretinopathy," *Graefe's Archive for Clinical and Experimental Ophthalmology*, vol. 256, no. 9, pp. 1581–1588, 2018.

[17] E. H. C. van Dijk, S. Fauser, M. B. Breukink et al., "Half-dose photodynamic therapy versus high-density subthreshold micropulse laser treatment in patients with chronic central serous chorioretinopathy: the PLACE trial," *Ophthalmology*, vol. 125, no. 10, pp. 1547–1555, 2018.

[18] M. Büttner, on behalf of the SRT Study Group, B. Luger et al., "Selective retina therapy (SRT) in patients with therapy refractory persistent acute central serous chorioretinopathy (CSC): 3 months functional and morphological results," *Graefe's Archive for Clinical and Experimental Ophthalmology*, vol. 259, no. 6, pp. 1401–1410, 2021.

[19] L. Verma, R. Sinha, P. Venkatesh, and H. K. Tewari, "Comparative evaluation of diode laser versus argon laser photocoagulation in patients with central serous retinopathy: a pilot, randomized controlled trial [ISRCTN84128484]," *BMC Ophthalmology*, vol. 4, no. 1, p. 15, 2004.

[20] C. Klatt, M. Saeger, T. Oppermann et al., "Selective retina therapy for acute central serous chorioretinopathy," *The British Journal of Ophthalmology*, vol. 95, no. 1, pp. 83–88, 2011.

[21] R. Kaye, S. Chandra, J. Sheth, C. J. F. Boon, S. Sivaprasad, and A. Lotery, "Central serous chorioretinopathy: an update on risk factors, pathophysiology and imaging modalities," *Progress in Retinal and Eye Research*, vol. 79, p. 100865, 2020.

[22] L. A. Yannuzzi, "Central serous chorioretinopathy: a personal perspective," *American Journal of Ophthalmology*, vol. 149, no. 3, pp. 361–363.e1, 2010.

[23] B. Nicholson, J. Noble, F. Forooghian, and C. Meyerle, "Central serous chorioretinopathy: update on pathophysiology and treatment," *Survey of Ophthalmology*, vol. 58, no. 2, pp. 103–126, 2013.

[24] H. Fujimoto, F. Gomi, T. Wakabayashi, M. Sawa, M. Tsujikawa, and Y. Tano, "Morphologic changes in acute central serous chorioretinopathy evaluated by Fourier-domain optical coherence tomography," *Ophthalmology*, vol. 115, no. 9, pp. 1494–1500.e2, 2008.

[25] M. Ho, S. H. W. Kwok, A. C. Y. Mak et al., "Fundus autofluorescence and optical coherence tomography characteristics in different stages of central serous chorioretinopathy," *Journal of Ophthalmology*, vol. 2021, Article ID 6649064, 9 pages, 2021.

[26] K. Mitarai, F. Gomi, and Y. Tano, "Three-dimensional optical coherence tomographic findings in central serous chorioretinopathy," *Graefe's Archive for Clinical and Experimental Ophthalmology*, vol. 244, no. 11, pp. 1415–1420, 2006.

[27] Y. Hirami, A. Tsujikawa, M. Sasahara et al., "Alterations of retinal pigment epithelium in central serous chorioretinopathy," *Clinical & Experimental Ophthalmology*, vol. 35, no. 3, pp. 225–230, 2007.

[28] C. Brandl, H. Helbig, and M. A. Gamulescu, "Choroidal thickness measurements during central serous chorioretinopathy treatment," *International Ophthalmology*, vol. 34, no. 1, pp. 7–13, 2014.

[29] A. Arrigo, E. Aragona, A. Bordato et al., "Acute central serous chorioretinopathy subtypes as assessed by multimodal imaging," *Translational Vision Science & Technology*, vol. 10, no. 13, p. 6, 2021.

Hindawi
Disease Markers
Volume 2022, Article ID 8316004, 11 pages
https://doi.org/10.1155/2022/8316004

Research Article

Inhibition of Galectin-3 Impairs Antifungal Immune Response in Fungal Keratitis

Yichen Xiao,[1] **Jiahui Yang**,[1] **Zhenyuan Fu**,[1] **Zhile Xiong**,[2] **Chao Zhang**,[2] **Dalian He**,[1] **Zhenwen Zhou**,[2] **Naiyang Li**,[3] **and Jin Yuan**[1]

[1]*State Key Laboratory of Ophthalmology, Zhongshan Ophthalmic Center, Sun Yat-sen University, Guangdong Provincial Key Laboratory of Ophthalmology and Visual Science, Guangzhou 510060, China*
[2]*Clinical Laboratory, Guangzhou Women and Children's Medical Center, Guangzhou Medical University, Guangzhou, Guangdong 510623, China*
[3]*Eye Center, Zhongshan Hospital of Sun Yat-sen University, Zhongshan, Guangdong, China*

Correspondence should be addressed to Jin Yuan; yuanjincornea@126.com

Received 14 December 2021; Accepted 7 February 2022; Published 9 April 2022

Academic Editor: Wen-Qing Shi

Galectin-3 is one of the galectin family members which are master regulators of immune homeostasis, especially in infectious diseases. However, its mechanism of immune regulation in fungal keratitis has not been thoroughly studied. Our study is aimed at clarifying the role of galectin-3 in the fungal keratitis mouse model in vivo, thereby providing a new biomarker of antifungal therapy. In our study, aspergillus, the most common pathogenic fungi of fungal keratitis, was identified and isolated by corneal tissue fungus culture. Then, the RNA expression levels of galectin family members in corneas of the mouse model with aspergillus fumigatus keratitis were screened by transcriptome sequencing (RNA-seq). The expression of the galectin-3 was detected by quantitative real-time Polymerase Chain Reaction (qPCR), enzyme-linked immunosorbent assay (ELISA), and immunofluorescence in the corneal tissue of the fungal keratitis mouse model. Recruitment of neutrophils and the co-immunofluorescence of galectin-3 and related markers in corneal tissue were determined by flow cytometry analysis and immunofluorescence staining. The regulatory role of galectin-3 for proinflammatory cytokines and neutrophils was validated by the knockout mouse model. Galectin-3 knockout deteriorated the condition for the inhibition of galectin-3 was benefecial for fungi to survive and thrive in corneal lesions. These results demonstrated that in the ocular fungal infection, galectin-3 is capable of regulating the pathogenesis of fungal keratitis by modulating neutrophil recruitment. The deterioration of fungal keratitis and increased fungal load in corneal lesions of galectin-3 knockout mice proved the regulatory role of galectin-3 in fungal keratitis. In conclusion, galectin-3 is going to be an essential target to modulate neutrophil recruitment and its related antifungal immune response in fungal keratitis.

1. Introduction

The human body, an intricate system protecting us from microbial attacks and invasions. Microbes live on/inside our body and play key roles in human physiology turbulence, and immune disorders [1]. Fungal keratitis (FK), one of the most detrimental ocular diseases caused by a fungal infection, loomed so large to be a key health issue of great importance [2, 3]. There are at least 100,000 known species of fungi. However, fewer than 500 have been proved to cause disease in animals, including human beings. The incidence rate of aspergillus is the highest among the pathogenic fungi, according to epidemiologic studies [4–6]. The immunological mechanism of microbial infectious disease includes both pathogen clearance and anti-infection immune response [7]. The microbial ocular disease has been of great interest to us for over a decade [8, 9].

Galectins as a family are characterized by a galactose-specific carbohydrate-binding domain interacting with galactose moieties located at glycoproteins on the surface of the lipid bilayer of cell membranes [10–12]. The galectin group consists of 15 different galectins which have already

been identified structurally and functionally [12–14]. The members of this family play different roles in immune homeostasis regulation [15]. Galectin-1 triggers homeostatic signals to turn off T-cell effector functions, galectin-9 promotes pro-inflammatory cytokines release by the signal of Toll-like receptors down-regulation, and galectin-7 and galectin-12 have effects on apoptosis. Galectin-3 always behaves as the amplifier of the inflammatory cascade, thereby playing a key role in inflammatory diseases [16–19]. Galectin-3, the only member containing carbohydrate recognition domain with an extended N-terminus, behaves as a regulator to amplify the process of the inflammatory cascade [20]. Accumulating evidence showed that galectin-3 is instrumental to many biological and pathobiological functions. Galectin-3 could regulate immune responses in infectious diseases such as fungal nephropathy, streptococcus pneumonia, and HSC virus infection by controlling immune cell activation, recruitment, and differentiation [15, 21–27].

It is worth noting that galectin-3 plays a central role in innate immune cell homeostasis, especially for neutrophils, which are the primary inflammatory cells during the disease course of fungal keratit [28]. Galectin-3 enhances the adherence between neutrophils and monolayers consisting of endothelial cells as well as the matrix proteins and fibronectins in vitro [29, 30]. The role of galectin-3 in immune cell regulation remains to be unveiled which contributes most to the antipathogen immune response in infectious diseases, especially the regulation of neutrophils. The current accumulation of new information depicts a future scenario where galectin-3 could be used as a potential anti-inflammatory mediator and a specific modulator of the immune response in inflammatory and infectious disease, possibly by regulating neutrophils and other related immune responses. However, its role in regulating ocular fungal infection remains unknown.

This study aims to explore potential target and the underlying mechanism of fungal keratitis caused by the typical strain of pathogenic fungi with high incidence. The fungal infection mouse model would be established, and the correlation between key immune cells and biomarkers would be explored. This study is designed and aimed at providing evidence to support the vital role of galectin-3 in fungal keratitis immune disorders, pointing out the key disease marker. Targeting galectin-3 for antifungal therapy based on the emerging findings of biology and pathology related to galectin-3 is coming of age. Therefore, it is going to shed some light on patients with fungal keratitis all over the world.

2. Methods

2.1. Patient and Tissue Specimens. The tissue samples, ocular image, periodic acid-Schiff Stain (PAS), and microbial culture results were collected from patients who were clinically diagnosed with fungal keratitis by corneal scraping culture and received corneal transplantation from May 2020 to May 2021 at the Zhongshan Ophthalmic Center. This study was approved by the Zhongshan Ophthalmic Center Medical Science Research Ethics Committee (protocol number: 2020KYPJ115). All participants in this study provided written consent. The infected corneal tissues were collected during corneal transplantation surgery and quickly stored in a cryogenic refrigerator at -80°C.

2.2. Preparation of Aspergillus Fumigatus Spores. The typical fungal strain was cultured on Potato dextrose agar (PDA) or Sabouraud dextrose agar (SDA, Difco, Detroit, Michigan, USA) at 30°C. The presence of fungal stain in the corneas of patients was confirmed by the characteristic branching hyphae and granular spores of Aspergillus under the microscope. The strain of Aspergillus fumigatus used in this investigation was AS 3.1320,purchased from the Guang Dong Microbiological Culture Collection Center, Gouangzhou, China. The Aspergillus fumigatus strain was grown on Sabouraud dextrose agar (Difco, Detroit, MI) at 30°C for 4 days. After washing the dishes in phosphate-buffered saline with 0.1% Tween 20 (PBST), the spore suspension was harvested by washing in sterile phosphate-buffered saline (PBS). All spore solutions were diluted to a 5×10^5 colony-forming units (CFU)/mL concentration with a cell counting chamber. The preparation of Aspergillus fumigatus spores was completed in the Laboratory of Guangzhou Women and Children's Medical Centre (Guangzhou, China).

2.3. Experimental Animals. 150 female C57BL/6N mice (6-8 weeks old), weighing 18-21 g, were purchased from Beijing Vital River Laboratory Animal Technology Co. Ltd., and the construction of galectin-3 complete knockout mice was commissioned by Saiye Biology (Strain name: C57BL/6N-Lgals3em1cyagen, strain number: KOCMP-16854-Lgals3-B6N-VA). The mice were divided into four groups: wild type group, wild type fungal keratitis group, galectin-$3^{-/-}$ group, and galectin-$3^{-/-}$ fungal keratitis group. Animal breeding and experiments were carried out in the Specific Pathogen-Free (SPF) animal room of the Experimental Animal Center of Sun Yat-sen University Zhongshan Ophthalmic Center. All animals were treated following the guidelines provided by the Ophthalmology and Vision Research Animal Use Vision and Ophthalmology Research Association and were approved by the Zhongshan Ophthalmic Center Institutional Review Committee (ethics number: 2020-011). All laboratory animal use followed the Association for Research in Vision and Ophthalmology (ARVO) requirements.

2.4. Animal Model In Vivo. To establish the fungal keratitis model in vivo, C57BL/6N mice or galectin-$3^{-/-}$ mice were anesthetized intraperitoneally with sodium pentobarbital (1%) and lidocaine hydrochloride (0.5%) was applied to the eye surface twice or more for corneal anesthesia. First, a 30-gauge needle was used to form a tunnel in the corneal stroma of the right eye. Then, we used a 33-gauge syringe to puncture through the tunnel and injected 5 μL spore solution (5×10^5CFU/mL) into the corneal stroma until the corneal stroma turned into a uniform white color. The untreated left eye of each mouse was regarded as a control for the disease course of fungal keratitis. After the mice were

sacrificed with an overdose of anesthesia, the corneal tissues were harvested.

To illustrate disease progression, mouse corneas were photographed to determine clinical scores at 5 days postinfection (dpi). The severity of fungal keratitis was graded on a scale ranging from 0 to 12 according to a scoring system developed by Wu et al. [31]. The clinical scores were calculated by three aspects: area of corneal opacity (0-4), density of corneal opacity (0-4), and corneal surface regularity (0-4).

2.5. RNA-seq and Data Analysis. RNA samples were extracted from corneas of the mouse model with fungal keratitis at 5 dpi ($n = 3$/group/time point) following the procedure as instructed by RNeasy Plus Mini Kit (Qiagen, Valencia, CA, USA). RNA-seq library construction and computer sequencing were completed by Annoyoda Biotechnology Co. Ltd., and trimmomatic software was applied to remove the adapter sequence from the original data, low-quality bases, and low-quality reads. We used Hisat2 software to compare valid reads to the human GRCh38 reference genome and RSEM software to calculate the TPM value of each sample. R package DESeq2 was used to analyze differentially expressed genes. Differential gene expression was defined as log2-fold change > 1 and p value < 0.05. R package cluster profiler was used to perform GO BP and KEGG enrichment analysis for differential genes. p value cutoff of 0.01 and q value cutoff of 0.05 were thresholds to filter significantly enriched GO terms.

2.6. Quantitative Real-Time Polymerase Chain Reaction (qRT-PCR). To examine galectin-3 mRNA expression in fungal keratitis mice and compare the expression of C-X-C Motif Chemokine Ligand 1 (CXCL1) and Interleukin-1β (IL-1β) mRNA between wild type and fungal keratitis mice, fungal keratitis mice, and Galectin-3 knock-out fungal keratitis mice, we first used Qiagen RNA extraction kit to extract total RNA from the corneas of fungal keratitis mice, according to the instructions and TaKaRa Reverse Transcription Kit to perform RNA reverse transcription in a PCR machine. Transcripts were quantified via SYBR Green qPCR performed an iQ Thermocycler (Bio-Rad) or ABI using Quant Studio Design v1.3. Relative expression of RNA was normalized, and the data were analyzed using the $2-\Delta\Delta Ct$ method. All qRT-PCR experiments were repeated three times. The primers were purchased from Invitrogen, and their sequences are shown as follows:

(1) Galectin-3: forward, 5′-GCTTATCCTGGCCCAACTGC-3′; reverse: 5′-CCCCGCTGGACCACTGACGG-3′

(2) IL-1β: forward, 5′-TGTCGGACCCATATGAGCTG-3′; reverse: 5′-TCCTTTGAGGCCCAAGGCCA-3′

(3) CXCL-1: forward, 5′-CAAACCGAAGTCATAGCCAC-3′; reverse, 5′-TGGGGACACCTTTTAGCATC-3′

(4) GAPDH: forward, 5′-CTCATGACCACAGTCCATGC-3′; reverse, 5′-TTCAGCTCTGGGATGACCTT-3′

2.7. Enzyme-Linked Immunosorbent Assay (ELISA). The protein levels of galectin-3 and CXCL1 were selectively tested using ELISA kits (R&D Systems). Corneal samples of fungal keratitis mice were individually collected at 5 dpi and homogenized in 0.5 mL PBS containing 0.1% Tween-20. All samples were centrifuged for 5 minutes, and then, the supernatant was assayed under the manufacturer's instructions.

2.8. Flow Cytometry Analysis. To determine the proportion of neutrophils in different stages of fungal keratitis mice, infected corneas were harvested at 5 dpi and cut into pieces (about 1 mm^3) under the microscope. According to the manufacturer's instructions, each tube was added with 60 U/mL Liberase TL (Roche Diagnostics, USA) and 1 mL serum-free 1640 medium and placed in a 37°C incubator for lysis for about 45 minutes, shaking several times every 15 minutes. The digested tissue and its suspension were filtered with a 70 μm nylon mesh to form a single cell suspension in 10% 1640 medium for staining. After that, cells were blocked with unconjugated anti-CD32/anti-CD16 mAbs for 15 min in FACS buffer (2% fetal bovine serum in PBS). Next, cells were treated with FITC-conjugated CD45 antibody, PE-conjugated Ly6G antibody, and BV 421-conjugated CD11b antibody for 30 min on ice. The cells were then resuspended in flow cytometry staining buffer and analyzed in a Cyto-FLEX S flow cytometer (Beckman, USA).

2.9. Immunofluorescence Staining. To detect the expression of Cytokeratin 12 (CK12), galectin-3, and CD11b in fungal keratitis, immunofluorescence staining in mouse corneas of fungal keratitis was performed. Corneal tissues were fixed with 4% paraformaldehyde for 10 minutes. The mouse cornea tissues were then equilibrated in 30% sucrose solution overnight for cryoprotection, embedded in OCT media, and sectioned using a Cryostat set at 10 μm per section. Slides of corneal tissues were saturated with 0.5% Triton X-100 in PBS for 60 minutes and blocked with 3% BSA for 30 minutes. The slides and cells were incubated with primary antibodies specific for CK12 (1 : 200, Abcam, UK), galectin-3 (1 : 200, Abcam, UK), and CD11b (1 : 500, Abcam, UK) for one hour at room temperature. After washing 5 minutes, 3 times in PBS, slides were incubated with respective secondary antibodies of Alexa Fluor 594-conjugated IgG (1 : 300, Abcam, UK) or Alexa Fluor 488-conjugated IgG (1 : 300, Abcam, UK) for one hour at room temperature, and the nucleus was stained with 4′,6-diamidino-2-phenylindole (DAPI) for 10 minutes. Fluorescence images were acquired by a laser confocal fluorescence microscope (LSM800; Carl Zeiss Microscopy, White Plains, NY, USA).

2.10. Hematoxylin-Eosin (HE) Staining. To determine the pathological changes of fungal keratitis, the entire eyeballs of fungal keratitis mice ($n = 3$/group/time point) were harvested at 5 dpi, fixed with 4% formaldehyde overnight. Then,

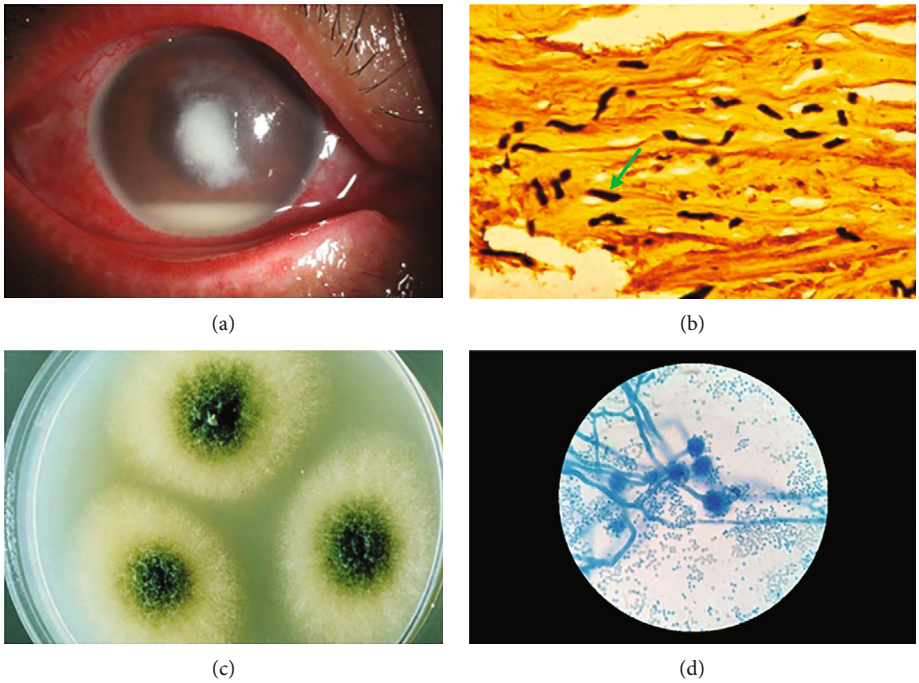

Figure 1: The cornea samples of the patients with fungal keratitis with the typical anterior segment photographic appearance (a) and corneal PAS staining results (b) were collected to culture fungi. Aspergillus fumigatus was isolated from the culture flora (c). It was lactic acid phenol cotton orchid stained to reveal the typical aspergillus morphology under the microscope, including branching hyphae and granular spores (d).

the corneal tissues were dehydrated through a graded ethanol series (70–99%), embedded in paraffin, cut into sections (5 μm thick), and stained with HE.

2.11. Two-Photon Microscopy (TPM). To detect the existence of hyphae in vivo, we performed cornea imaging of both FK mice and galectin-3 knockout FK mice using a custom-built TPM system. Corneal scraping was performed to obtain the corneal sample for imaging. TPM used a Ti-Sapphire femtosecond laser (Chameleon Ultra II; Coherent, Inc., Santa Clara, CA) as a light source. A ×20 objective lens [XLUMPlanFLN, ×20, 1.0 numerical aperture (NA), water immersion; Olympus] was used. The imaging field of view and imaging speed was approximately $300 \times 300\,\mu$m in the transverse x-y plane consisting of 512×512 pixels and 0.1 frame/s, respectively. The excitation wavelength was 780 nm for both intrinsic contrast and moxifloxacin-based imaging. Autofluorescence and SHG signals were collected in two detection channels by separating emission light with a 430 long-pass dichroic mirror. Then, ImageJ was used to form the color fungal hypha image.

2.12. Fungal Load Counting. Infected mouse corneas ($n = 3$/group/time point) were harvested at 5 dpi, then washed, and homogenized in 1000 μL of normal sterile saline. Serial dilutions were made accordingly to achieve a proper number of colonies on each plate. A total of 100 μL of corneal tissue suspensions were dropped on respective PDA plates and evenly spread with a spreader. CFU counting was calculated after 18–24 h incubation at 37°C. Aspergillus fumigatus loads were expressed as CFU/mL. Petri dishes that were only exposed to the clean bench for 10 s were regarded as a negative control.

2.13. Statistical Methods. The results are presented as the mean ± standard error of the mean (SEM) values. Statistical analyses were performed using SPSS for Windows (version 22.0; International Business Machines Corporation). An independent t-test was used to compare the differences between the two groups. One-way analysis of variance (ANOVA) with Dunnett's test for multiple comparisons was performed to assess the significance of experimental groups versus the control group. The images were generated by GraphPad Prism 7 for Windows (version 7.04; GraphPad Software). p values less than 0.05 were considered significant.

3. Results

3.1. Aspergillus Was One of the Most Common Pathogenic Fungi of Fungal Keratitis. Aspergillus was one of the most common pathogenic fungi of fungal keratitis, and Figure 1(a) shows a representative fungal keratitis typical clinical signs like corneal inflammatory ulcer and corneal tissue PAS staining showing the presence of a large number of fungi (green arrow) in the stroma (Figures 1(a) and 1(b)). To detect the main pathogenic microorganism in the cornea of patients, the corneal tissue was extracted and cultured fungi. Then, the fungi with the highest proportion screened by the laboratory department were further cultured, which showed the characteristic cotton-like aspergillus appearance (Figure 1(c)). The lactic acid phenol cotton orchid staining

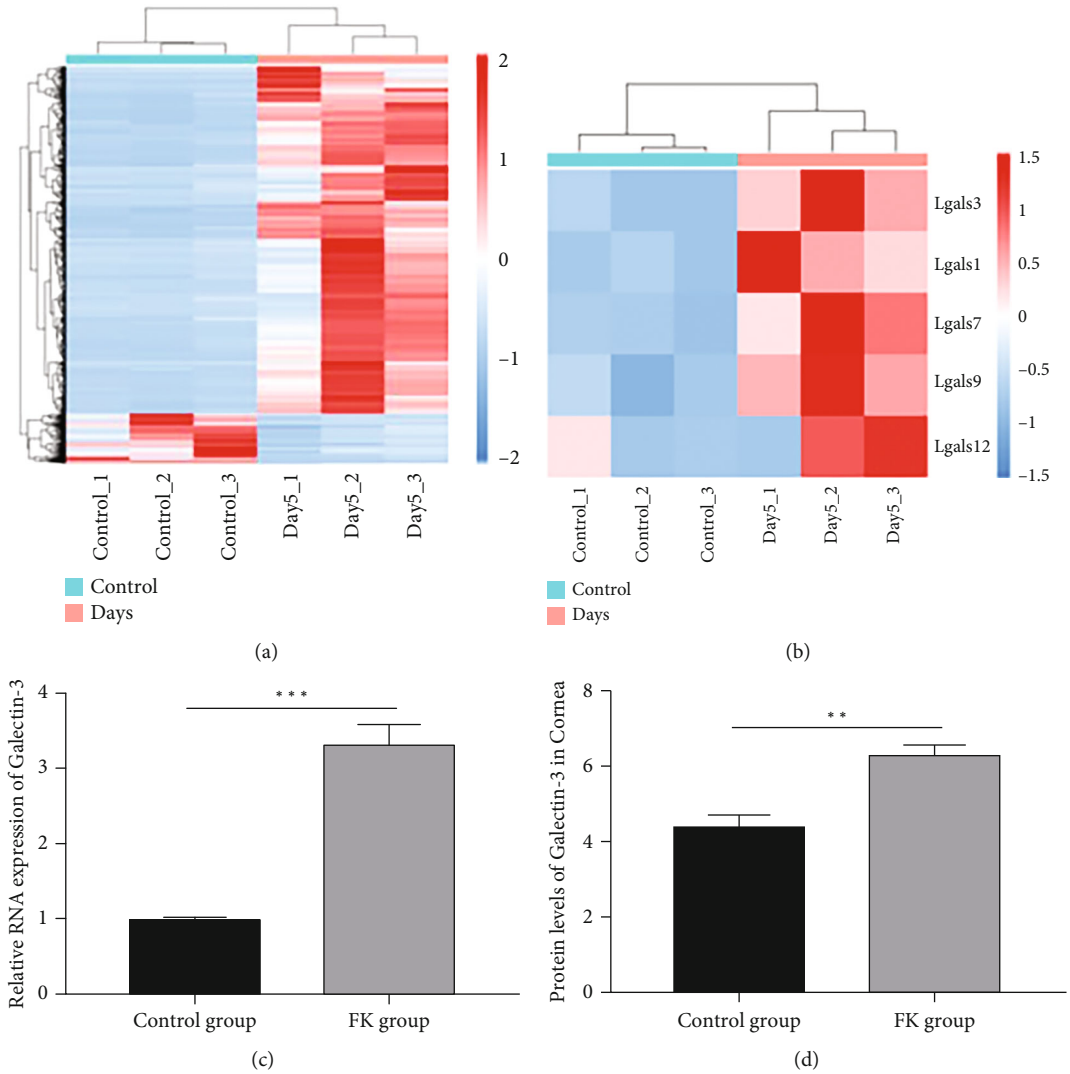

Figure 2: Analysis of RNA-seq in the cornea of a mouse model of fungal keratitis was used to screen the targets in the disease. (a) was the number of differential genes between the mode and the control groups. The log2-fold change sequencing screened out highly expressed genes in the galectin family, galectin-3 expressing obviously (b). Meanwhile, qPCR (c) results in mouse cornea or ELISA (d) in corneas verified the upregulated expression of galectin-3 in fungal keratitis. $^{*}p < 0.05$; $^{**}p < 0.01$; $^{***}p < 0.001$; NS: no statistical difference.

of the fungi revealed dendritic hyphae and scattered granular spores under the microscope, proving typical characteristics of aspergillus (Figure 1(d)).

3.2. The Expression of Galectin-3 was Significantly Increased in the Corneal Lesions of the Fungal Keratitis Model. RNA-seq sequencing analysis was performed in the extracted corneas of the mouse model to screen out the key target of fungal keratitis. Among the detected genes, 3025 upregulated and 2654 downregulated genes were found on the fifth day after being infected, which was the peak of the disease (Figure 2(a)). Meanwhile, the galectin family was significantly expressed in the upregulated gene spectrum, which aroused our attention, and we further analyzed them. The results showed that the expression of galectin-3 increased most significantly among the galectin family members. (Figure 2(b)). In addition, the RNA expression of galectin-3 (3.32 ± 0.26, $p < 0.001$) (Figure 2(c)) or the protein expression level of galectin-3 (Figure 2(d)) in corneas (6.40 ± 0.14 ng/mL, $p < 0.01$) also showed that galectin-3 was significantly increased in the disease model compared to the normal group. It suggested that galectin-3 may play an important role in fungal keratitis.

3.3. Galectin-3 and Neutrophils were Colocalized during the Disease Development of Fungal Keratitis. The mouse model of fungal keratitis was established to further verify the high expression of galectin-3 in fungal keratitis and its potential regulatory mechanism. We calculated the changes in the levels of neutrophil activation during disease by flow cytometry analysis. Figure 3(a) shows that neutrophils (CD45+ ly6G+ CD11b+) were activated obviously during the course of the disease ($37.80 \pm 1.87\%$, $p < 0.001$) in corneas, indicating neutrophils to be the primary functional cell subtype in antifungal immune responses. Meanwhile, the results of immunofluorescence showed that galectin-3 (green

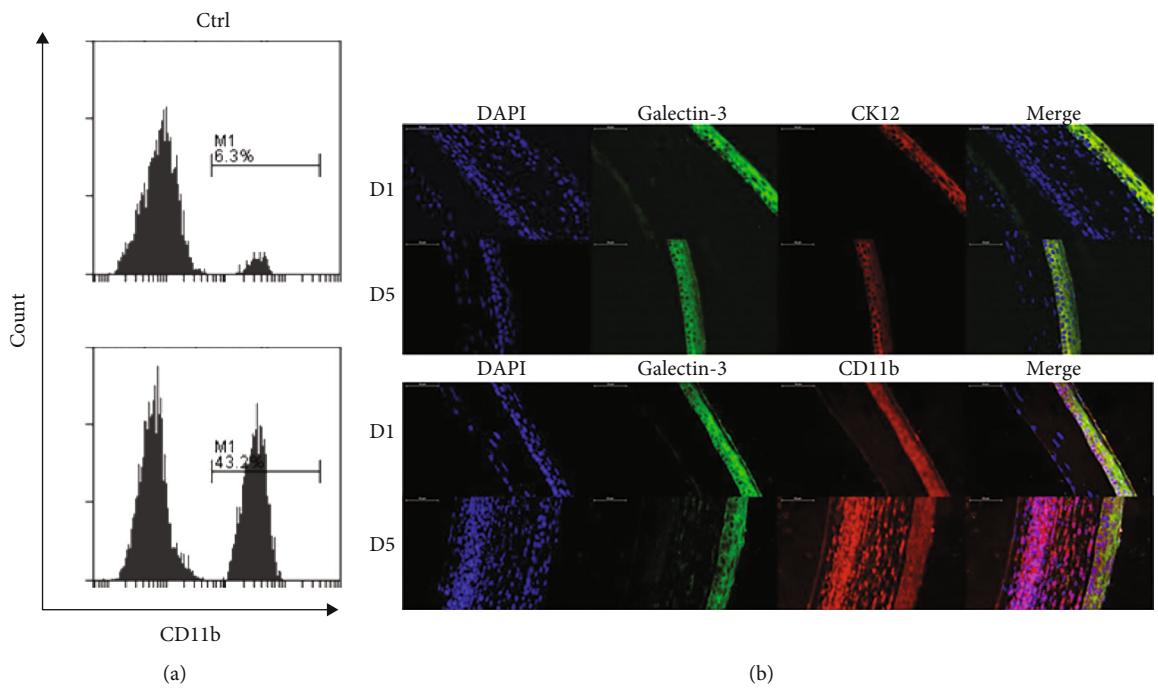

Figure 3: The cell frequency rate of neutrophil (a) detected by flow cytometry analysis at the 5 days post-infection. Immunofluorescence co-staining (b) of galectin-3 (green fluorescence) and cornea (CK12, red fluorescence) or neutrophil (CD11b, red fluorescence) indicated that galectin-3 and neutrophil activation were highly correlated at one day postinfection and 5 days postinfection. $^{*}p < 0.05$; $^{**}p < 0.01$; $^{***}p < 0.001$; NS: no statistical difference.

fluorescence) was coexpressed in corneal epithelial cell layer with corneal epithelial cell marker CK12 (red fluorescence), which indicated galectin-3 was located in corneal epithelium. Moreover, galectin-3 and neutrophil marker CD11b were coexpressed in corneal epithelial cells and stroma layer, suggesting galectin-3 and neutrophils were correlated in immune responses of the fungal keratitis (Figure 3(b)). It was implied that the expression of galectin-3 has a positive effect on neutrophil recruitment in fungal keratitis.

3.4. Galectin-3 Knockout Significantly Affected the Progression of Fungal Keratitis. To further study the regulation of galectin-3 in fungal keratitis, we established the mouse model of the wild type mice and galectin-3 knockout (galectin-$3^{-/-}$) mice to evaluate the effect on the course of the disease. Anterior segment photography (Figure 4(a)) and clinical scores (galectin-$3^{-/-}$ FK vs. wild type FK D1: 5.60 ± 0.15 vs. 5.50 ± 0.10; D3: 8.70 ± 0.20 vs. 10.60 ± 0.25; D5: 11.50 ± 0.20 vs. 11.90 ± 0.10) (Figure 4(b)) showed that compared with the wild type FK group, the condition of galectin-$3^{-/-}$ FK group aggravated rapidly on the third day after infection, mainly caused by increased perforation rate (galectin-$3^{-/-}$ FK vs. wild type FK D1: 1.33 ± 0.58 vs. 1.67 ± 0.58; D3: 2.33 ± 0.58 vs. 3.67 ± 0.58; D5: 3.33 ± 0.58 vs. 4.00 ± 0.00) (Figure 4(e)). While the trend of corneal edema (galectin-$3^{-/-}$ FK vs. wild type FK D1: 1.00 ± 0.00 vs. 1.33 ± 0.58; D3: 2.33 ± 0.58 vs. 2.67 ± 0.58; D5: 3.33 ± 0.58 vs. 4.00 ± 0.00) and ulcer coverage (galectin-$3^{-/-}$ FK vs. wild type FK D1: 1.33 ± 0.58 vs. 1.33 ± 0.58; D3: 2.33 ± 0.58 vs. 3.67 ± 0.57; D5: 3.33 ± 0.58 vs. 3.67 ± 0.58) was similar between the two groups (Figures 4(c) and 4(d)). It implied that the antifunal immune function of inflammatory cells to fight off fungal attacks was damaged by galectin-3 knockout. Pathological sections also showed that the are of inflammation and corneal edema severity in the mouse model of galectin-$3^{-/-}$ fungal keratitis group were significantly increased than those in wild type FK group, and the depth of inflammatory cell infiltration gradually increased (Figure 4(f)), which was consistent with the disease scores.

Moreover, the effects of galectin-3 on anti-fungal activity were verified in this study. Two-photon microscopy was used to observe the number and morphology of fungal mycelia in corneas of wild type FK mice and galectin-$3^{-/-}$ FK mice on day 5 after infection. It was found that the mycelium in the corneas of galectin-$3^{-/-}$ FK mice was significantly denser than that in the normal mice (Figure 4(g)). Corresponding to this, the results of corneal fungal load (CFU) (Figure 4(h)) showed that on day 5 after infection, the CFU of wild type FK mice and galectin-$3^{-/-}$ FK mice was $45.00 \pm 5.78 * 10^4$ and 90.67 ± 2.19 ($P < 0.01$), which mean the fungi in the galectin-$3^{-/-}$ model grew well and vigorously. The results above suggested that galectin-3 may prevent and/or inhibit the fungal keratitis progression and positively regulate the fungal clearance of inflammatory cells.

3.5. Galectin-3 Knockout Impaired the Recruitment of Neutrophils in the Mouse Model of Fungal Keratitis. To illustrate the effect of galectin-3 on immune cells in the mouse model of fungal keratitis, we first examined neutrophils' levels under different conditions. Flow cytometry analysis showed that neutrophils (CD45+ ly6G+ CD11b+) were

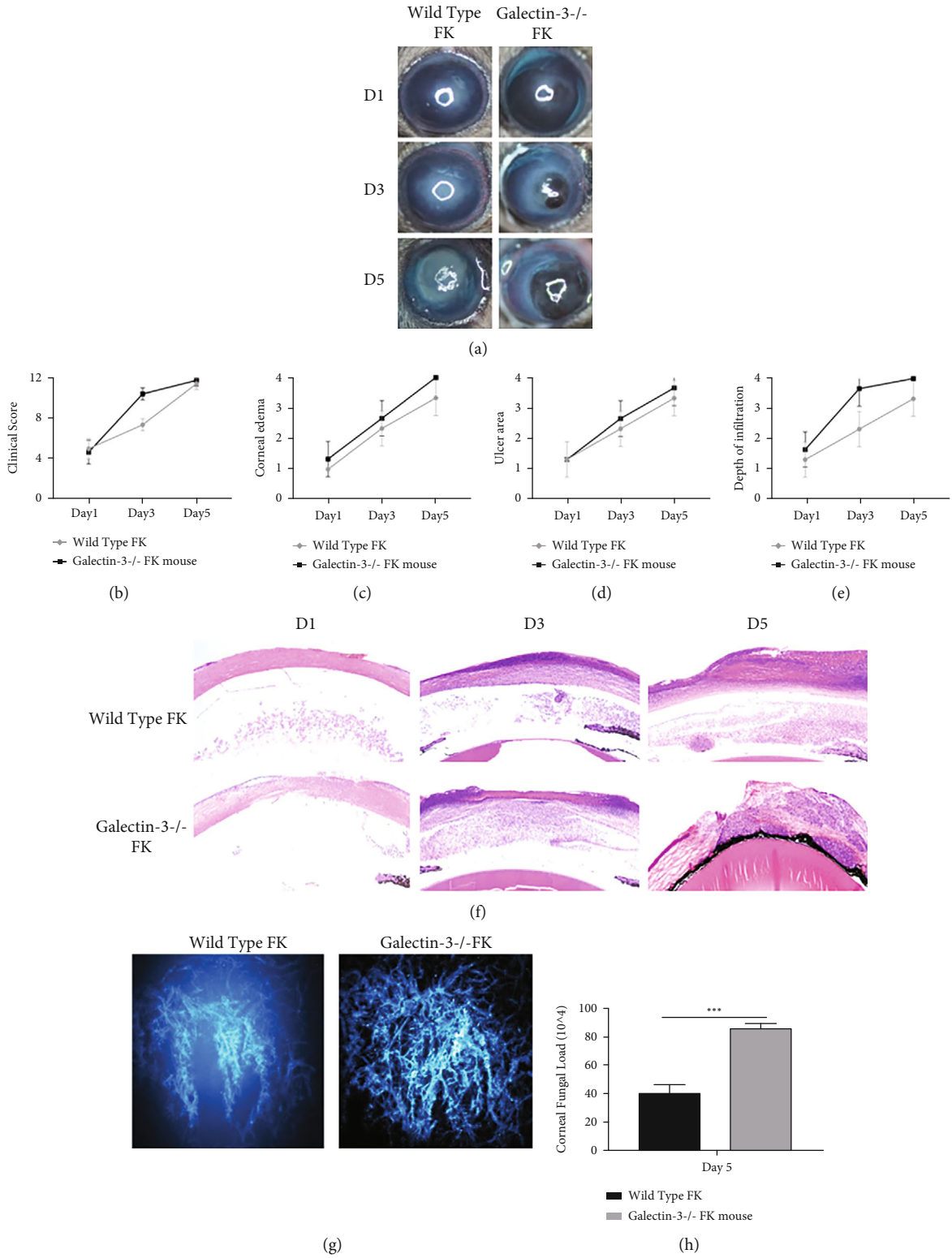

Figure 4: The model of fungal keratitis was established in galectin-3 knockout mice and wild type mice, and anterior segment imaging (a), clinical score (b–d), HE staining (e), two-photon microscopy (TPM) observation (g), and corneal fungal load (CFU) (h) detection were performed. The condition of galectin-$3^{-/-}$ mice deteriorated rapidly on the third day after infection compared with the control group. Meanwhile, the number of fungal mycelia in corneas of C57 mice was much more than that of galectin-$3^{-/-}$ mice. Magnification: photographic 16 times, HE 100 times. $^{*}p < 0.05$; $^{**}p < 0.01$; $^{***}p < 0.001$; NS: no statistical difference.

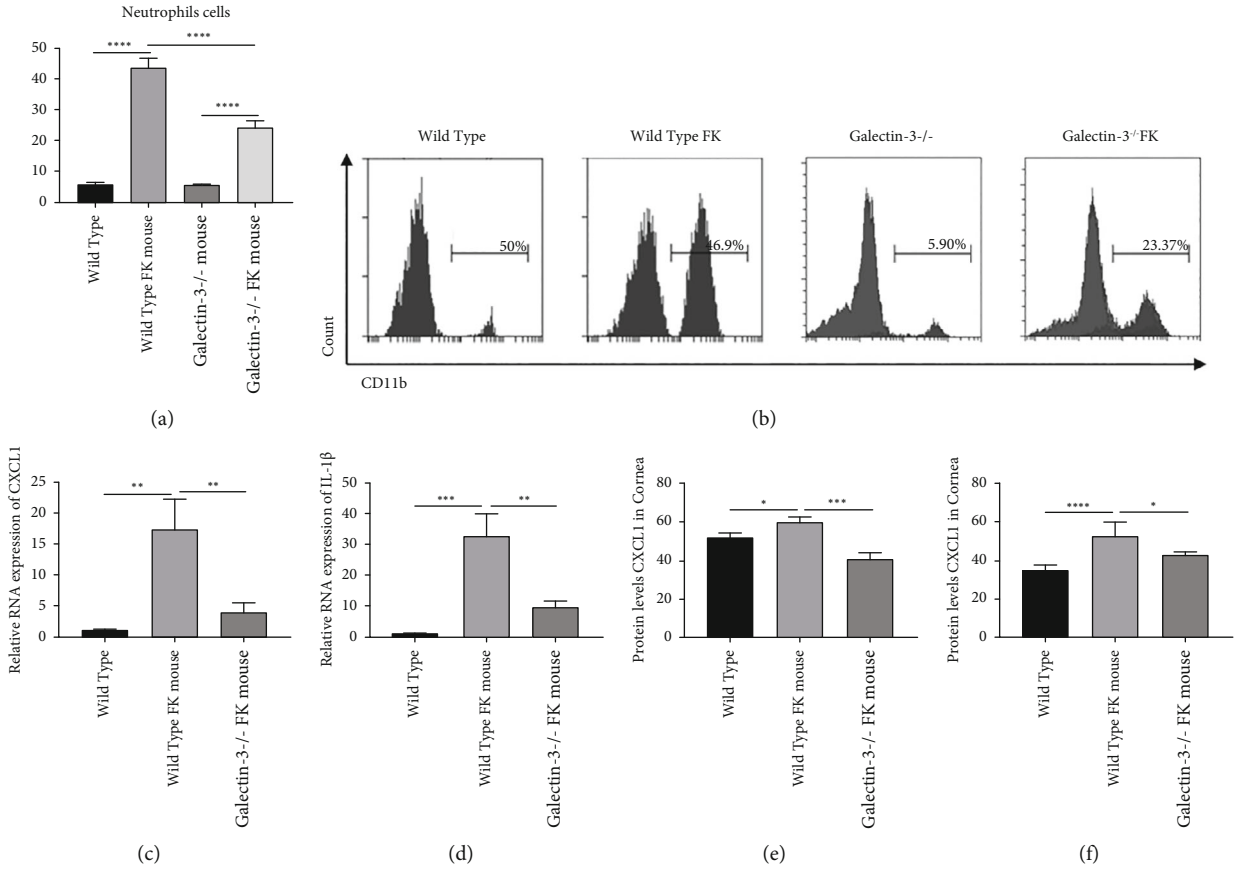

Figure 5: The levels of the activation of neutrophils in corneas (a, b) and the expression levels of CXCL1 (c, e, f) and IL-1β (d) in normal C57 mice, C57 model, galectin-3$^{-/-}$wild type mice, and galectin-3$^{-/-}$ model were detected. The deletion of galectin-3 significantly inhibited the neutrophil activation and the expression of the related chemokines CXCL1 and IL-1β. $^{*}p < 0.05$; $^{**}p < 0.01$; $^{***}p < 0.001$; NS: no statistical difference.

significantly activated in corneas in the normal mice with fungal keratitis. At the same time, this phenomenon was inhibited in galectin-3$^{-/-}$ disease model (wild type vs. wild type model: 5.78 ± 0.39 vs.$43.57 \pm 1.83\%$, $p < 0.001$; wild type model vs. galectin-3$^{-/-}$ model: 5.69 ± 0.13 vs.$24.19 \pm 1.28\%$, $p < 0.001$) (Figures 5(a) and 5(b)).

In addition, corneas of mice were collected 5 days after infection to detect the RNA and protein levels of neutrophil chemokine CXCL1 and IL-1β. The results showed that the RNA levels of CXCL1 were increased in normal mice and decreased in knockout mice (wild type vs. wild type FK: 1.07 ± 0.07 vs.17.27 ± 2.86, $p < 0.01$; wild type FK vs. galectin-3$^{-/-}$ FK: 17.27 ± 2.86 vs.3.87 ± 0.87, $p < 0.05$) (Figure 5(c)), and the protein levels in the corneas showed the same trend (wild type vs. wild type FK: 51.56 ± 1.24 vs.59.98 ± 1.03 ng/mL, $p < 0.01$; wild type vs. galectin-3$^{-/-}$ FK: 59.98 ± 1.03 vs.40.27 ± 1.98, $p < 0.001$) (Figure 5(e)) as well as in the lymph nodes (wild type vs. wild type FK: 34.11 ± 3.13 vs.51.79 ± 7.74 ng/mL, $p < 0.001$; wild type FK vs. galectin-3$^{-/-}$ FK: 51.79 ± 7.74 vs.42.25 ± 1.92, $p < 0.05$) (Figure 5(f)). The expression trend of IL-1β in the levels of protein (wild type vs. wild type FK: 1.07 ± 0.12 vs. 32.53 ± 7.47, $p < 0.01$; wild type FK vs. galectin-3$^{-/-}$ FK: 32.53 ± 7.47 vs.9.53 ± 1.78, $p < 0.01$) (Figure 5(d)) was similar to CXCL1 with statistical differences. These data above implied that galectin-3 played an immune role by promoting the activation of neutrophils in fungal keratitis. Furthermore, decreased activity of neutrophils, which are responsible for fungus control and antigen presentation, also explains the faster corneal perforation in the galectin-3$^{-/-}$ mice of fungal keratitis.

4. Discussion

Galectin-3 is a master regulator of infectious disease. This study demonstrated that galectin-3 might play an important antifungal role in immunological responses to fight against fungal invasion by neutrophil recruitment in the FK mouse model. It was verified that galectin-3 knockout mice suffered a much more severe onset of FK with higher clinical scores of corneal lesion depth, area, and corneal edema degree compared to the wild-type mice. Lower levels of neutrophils and pro-inflammatory cytokines were found in the galectin-3 knockout mice group compared to the wild-type mouse model group, which indicates the regulatory role of galectin-3 in immune responses in vivo. The fungal load

and fungal morphological activity were much higher in the galectin-3 knockout group than in the model group as well. These data suggested that galectin-3 might be a necessary regulatory biomarker in immunological responses to fight off fungal invasion on the ocular surface, and galectin-3 knockout could impair the antifungal immune response to a great extent.

Galectin-3 plays a pivotal role in microbial infection, such as bacteria, fungi, viruses, and parasites [32–34]. The mainstream points of view on galectin-3 in infectious disease pathogenesis support it to be beneficial. For example, In virus infectious diseases, galectin-3 tended to affect viruses such as HIV-1 (human immunodeficiency virus-1), MV-Mp (Minute virus of mouse protoparvovirus), and EV71 (Enterovirus 71), such as viral combination, replication, budding, and transmission, followed by infection-associated inflammation, and endogenous galectins as cellular factors by regulating viral infection interacting with cellular components under viral hijacking or inflammation led by virus replication [35]. Galectin-3 was recognized as a target to regulate viral immune response to modulate virus infection. In bacterial infection, the majority of researches on bacterial infection showed that streptococcus in galectin-3 knockout mice had a higher bacterial burden and enhanced nephritis and renal dysfunction in comparison with wild-type mice [36, 37]. Many studies demonstrated that galectin-3 appears to mediate neutrophil migration and recruitment in bacteria-caused infection animal models [37]. Our study was in agreement that galectin-3 knockout is detrimental to infectious disease recovery, leading to severe disease development and even corneal perforation. It is assumed that galectin-3 might fulfil its immunological regulation by recruiting key immune cells subtypes of FK pathogenesis, especially neutrophil recruitment.

Galectin-3 is important for both the activation and recruitment of neutrophils in the immune response of infectious diseases [20]. Neutrophils reacted positively in response to fungi invasion, killing and clearing foreign pathogens through phagocytosis. Studies on the galectin-3 receptors on neutrophils reported that adhesion between the neutrophils and inherent endothelial cells increased, so did the expression level of proinflammatory cytokines [37]. The recruitment and activation effect of galectin-3 on neutrophils demonstrated that inhibition of galectin-3 could be the reason of the down-regulation of innate immune responses in inflammatory disorders, especially infectious diseases. Recent studies showed that galectin-3 knockout mice show an elevated number of neutrophils in the primary focus of infection and reduced fungal loads in the fungal pneumonia lesions and peritoneal cavity caused by fungal infection [30]. Protective effects of galectin-3 deficiency in fungal keratitis proved the regulatory role of galectin-3 of neutrophil cell subtypes; thereby, our data hints at the importance of galectin-3 for innate immunity in fungal infection. Together, the current study supported the regulatory role of galectin-3 in the activation and recruitment of neutrophils in inflammatory diseases, especially infectious diseases. Our study proved the regulatory role of galectin-3 for key immune subtypes in antifungal inflammation. Speaking of galectin-3 involved immune-mediated cytokines, we also testified downstream cytokines in the inflammatory cascade; the expression levels of protein like CXCL1 and IL-1β were increased apparently. These are positively correlated with neutrophils in inflammatory responses. CXCL1 is an upstream signaling site for active migration of monocytes and neutrophils to gather timely in corneal lesion tissue. IL-1β contributes to the inflammatory cascades under the regulation of NLRP3 inflammasome, a hub protein complex that senses and cleaves cytokines into functioning forms.

Once the innate immune system recognizes pathogens, the barrier of the ocular surface will be the first line force to fight against fungal invasion. The ocular surface barrier consists of corneal epithelial cells, conjunctival cells, and so on [29]. Galectin-3 promotes barrier function at the vessel mucosa, skin layer, and ocular surface to protect the internal system from interaction to microbe everywhere. Galectin-3 is reported to be effective in controlling infection extension in bacterial lung infection and renal fungi infection [37, 38]. The barrier function of HCE in the human ocular surface contributes to the healthy microenvironment to protect inner cells from detrimental factors like oxidative stress, physical trauma and overstressed vision working load. It is assumed that ocular barrier function might be important to keep pathogens from settlement and generation [39, 40]. Our data showed that the knockout of galectin-3 intensifies the ocular barrier's damage in the fungal invasion. The lack of galectin-3 might do evil in fungal clearance, for the better growing status in corneal tissue under the observation of a two-photon microscope. Our data suggested that galectin-3 might regulate the barrier function to prevent tissue damage from the beginning of the inflammatory disease in fungal infectious disease, which indicated the key role of galectin-3 in infectious disease in a larger field.

In our study, it was shown that galectin-3 inhibition decreased neutrophils in the FK mouse model. The antifungal immune response occurs due to tissue infection and/or barrier function damage. Antifungal immune response aims at removing the invaders and rebalance local homeostasis. Galectin-3 regulates the anti-infection immune signaling pathway in fungal keratits. It is a process that is crucial to the host immune system in which neutrophils are activated and recruited. Therefore, targeting galectin-3 in anti-infection immune response would be a potential therapeutic alternative for fungal keratitis. With a better understanding of the molecular and cellular mechanism of galectin-3, it is pertinent to provide a new antifungal therapy for patients with fungal keratitis, and/or patients suffering from other fungal infectious diseases.

Data Availability

The data and materials used to support the findings of this study are available from the corresponding author upon request.

Conflicts of Interest

The authors declare no competing financial interests.

Authors' Contributions

Jin Yuan guided the project. Yichen Xiao and Jiahui Yang conceived the project. Yichen Xiao and Jiahui Yang designed the experiments. Yichen Xiao, Jiahui Yang, Zhenyuan Fu, Zhile Xiong, Chao Zhang, and Dalian He carried out the experiments. Yichen Xiao, Jiahui Yang, Zhenyuan Fu, and Dalian He analyzed the data. Yichen Xiao and Jiahui Yang wrote the manuscript draft. Jin Yuan revised the manuscript. Yichen Xiao and Jiahui Yang are co-first authors.

Acknowledgments

This work was supported by the National Natural Science Foundation of China (No. 81870633 and No. 82101086).

References

[1] S. Yurist-Doutsch, M. C. Arrieta, S. L. Vogt, and B. B. Finlay, "Gastrointestinal microbiota-mediated control of enteric pathogens," *Annual Review of Genetics*, vol. 48, no. 1, pp. 361–382, 2014.

[2] M. L. Durand, M. B. Barshak, and J. Chodosh, "Infectious keratitis in 2021," *JAMA*, vol. 326, no. 13, pp. 1319-1320, 2021.

[3] L. Brown, A. K. Leck, M. Gichangi, M. J. Burton, and D. W. Denning, "The global incidence and diagnosis of fungal keratitis," *The Lancet Infectious Diseases*, vol. 21, no. 3, pp. e49–e57, 2021.

[4] G. D. Brown and D. Wilson, "Mammalian innate immunity to fungal infection," *Seminars in Cell & Developmental Biology*, vol. 89, pp. 1-2, 2019.

[5] A. E. Barber, T. Sae-Ong, K. Kang et al., "*Aspergillus fumigatus* pan-genome analysis identifies genetic variants associated with human infection," *Nature Microbiology*, vol. 6, no. 12, pp. 1526–1536, 2021.

[6] G. Suleyman and G. J. Alangaden, "Nosocomial fungal infections: epidemiology, infection control, and prevention," *Infectious Disease Clinics of North America*, vol. 30, no. 4, pp. 1023–1052, 2016.

[7] M. L. Durand, "Bacterial and fungal endophthalmitis," *Clinical Microbiology Reviews*, vol. 30, no. 3, pp. 597–613, 2017.

[8] L. Peng, J. Zhong, Y. Xiao et al., "Therapeutic effects of an anti-IL-6 antibody in fungal keratitis: macrophage inhibition and T cell subset regulation," *International Immunopharmacology*, vol. 85, p. 106649, 2020.

[9] J. F. Huang, J. Zhong, G. P. Chen et al., "A hydrogel-based hybrid theranostic contact lens for fungal keratitis," *ACS Nano*, vol. 10, no. 7, pp. 6464–6473, 2016.

[10] G. A. Rabinovich and M. A. Toscano, "Turning 'sweet' on immunity: galectin-glycan interactions in immune tolerance and inflammation," *Nature Reviews. Immunology*, vol. 9, no. 5, pp. 338–352, 2009.

[11] D. Laaf, P. Bojarova, L. Elling, and V. Křen, "Galectin-carbohydrate interactions in biomedicine and biotechnology," *Trends in Biotechnology*, vol. 37, no. 4, pp. 402–415, 2019.

[12] L. Johannes, R. Jacob, and H. Leffler, "Galectins at a glance," *Journal of Cell Science*, vol. 131, no. 9, 2018.

[13] F. T. Liu and G. A. Rabinovich, "Galectins as modulators of tumour progression," *Nature Reviews. Cancer*, vol. 5, no. 1, pp. 29–41, 2005.

[14] K. H. Mayo, *From Carbohydrate to Peptidomimetic Inhibitors of Galectins, Galectins and Disease Implications for Targeted Therapeutics*, American Chemical Society, 2012.

[15] M. A. Toscano, V. C. Martinez Allo, A. M. Cutine, G. A. Rabinovich, and K. V. Mariño, "Untangling galectin-driven regulatory circuits in autoimmune inflammation," *Trends in Molecular Medicine*, vol. 24, no. 4, pp. 348–363, 2018.

[16] H. Y. Chen, Y. F. Wu, F. C. Chou et al., "Intracellular galectin-9 enhances proximal TCR signaling and potentiates autoimmune diseases," *Journal of Immunology*, vol. 204, no. 5, pp. 1158–1172, 2020.

[17] A. Cao, N. Alluqmani, F. H. M. Buhari et al., "Galectin-9 binds IgM-BCR to regulate B cell signaling," *Nature Communications*, vol. 9, no. 1, p. 3288, 2018.

[18] N. V. Sewgobind, S. Albers, and R. J. Pieters, "Functions and inhibition of galectin-7, an emerging target in cellular pathophysiology," *Biomolecules*, vol. 11, no. 11, p. 1720, 2021.

[19] L. Wan, R. Y. Yang, and F. T. Liu, "Galectin-12 in cellular differentiation, apoptosis and polarization," *International Journal of Molecular Sciences*, vol. 19, no. 1, p. 176, 2018.

[20] G. A. Rabinovich, L. G. Baum, N. Tinari et al., "Galectins and their ligands: amplifiers, silencers or tuners of the inflammatory response?," *Trends in Immunology*, vol. 23, no. 6, pp. 313–320, 2002.

[21] C. Villanueva, A. Albillos, J. Genesca et al., "Bacterial infections adversely influence the risk of decompensation and survival in compensated cirrhosis," *Journal of Hepatology*, vol. 75, no. 3, pp. 589–599, 2021.

[22] A. I. Lim, T. Mcfadden, V. M. Link et al., "Prenatal maternal infection promotes tissue-specific immunity and inflammation in offspring," *Science*, vol. 373, no. 6558, 2021.

[23] R. C. Gilson, S. D. Gunasinghe, L. Johannes, and K. Gaus, "Galectin-3 modulation of T-cell activation: mechanisms of membrane remodelling," *Progress in Lipid Research*, vol. 76, p. 101010, 2019.

[24] R. Mu, Y. Zhang, L. Yan et al., "A "bridge-building" glycan scaffold mimicking microbial invasion for in situ endothelialization," *Advanced Materials*, vol. 33, no. 42, article e2103490, 2021.

[25] P. Bieniasz-Krzywiec, R. Martin-Perez, M. Ehling et al., "Podoplanin-expressing macrophages promote lymphangiogenesis and lymphoinvasion in breast cancer," *Cell Metabolism*, vol. 30, no. 5, pp. 917–936.e10, 2019.

[26] A. J. Brown, N. A. Gow, A. Warris, and G. D. Brown, "Memory in fungal pathogens promotes immune evasion, colonisation, and infection," *Trends in Microbiology*, vol. 27, no. 3, pp. 219–230, 2019.

[27] D. W. Denning and A. Chakrabarti, "Pulmonary and sinus fungal diseases in non-immunocompromised patients," *The Lancet Infectious Diseases*, vol. 17, no. 11, pp. e357–e366, 2017.

[28] C. F. Urban and J. E. Nett, "Neutrophil extracellular traps in fungal infection," *Seminars in Cell & Developmental Biology*, vol. 89, pp. 47–57, 2019.

[29] M. Sundqvist, A. Welin, J. Elmwall et al., "Galectin-3 type-C self-association on neutrophil surfaces; the carbohydrate recognition domain regulates cell function," *Journal of Leukocyte Biology*, vol. 103, no. 2, pp. 341–353, 2018.

[30] B. D. Snarr, G. St-Pierre, B. Ralph et al., "Galectin-3 enhances neutrophil motility and extravasation into the airways during Aspergillus fumigatus infection," *PLoS Pathogens*, vol. 16, no. 8, article e1008741, 2020.

[31] T. G. Wu, K. R. Wilhelmus, and B. M. Mitchell, "Experimental keratomycosis in a mouse model," *Investigative Ophthalmology & Visual Science*, vol. 44, no. 1, pp. 210–216, 2003.

[32] S. Sehrawat and M. Kaur, "Galectin-3 as a modifier of antimicrobial immunity: unraveling the unknowns," *Glycobiology*, vol. 30, no. 7, pp. 418–426, 2020.

[33] A. A. Da Silva, T. L. Teixeira, S. C. Teixeira et al., "Galectin-3: a friend but not a foe during Trypanosoma cruzi experimental infection," *Frontiers in Cellular and Infection Microbiology*, vol. 7, p. 463, 2017.

[34] J. Garcia-Revilla, T. Deierborg, J. L. Venero, and A. Boza-Serrano, "Hyperinflammation and fibrosis in severe COVID-19 patients: galectin-3, a target molecule to consider," *Frontiers in Immunology*, vol. 11, p. 2069, 2020.

[35] A. Hara, M. Niwa, K. Noguchi et al., "Galectin-3 as a next-generation biomarker for detecting early stage of various diseases," *Biomolecules*, vol. 10, no. 3, p. 389, 2020.

[36] M. F. Ferrer, E. Scharrig, N. Charo et al., "Macrophages and galectin 3 control bacterial burden in acute and subacute murine leptospirosis that determines chronic kidney fibrosis," *Frontiers in Cellular and Infection Microbiology*, vol. 8, p. 384, 2018.

[37] S. C. Chen and P. L. Kuo, "The role of galectin-3 in the kidneys," *International Journal of Molecular Sciences*, vol. 17, no. 4, p. 565, 2016.

[38] S. Sato, N. Ouellet, I. Pelletier, M. Simard, A. Rancourt, and M. G. Bergeron, "Role of galectin-3 as an adhesion molecule for neutrophil extravasation during streptococcal pneumonia," *Journal of Immunology*, vol. 168, no. 4, pp. 1813–1822, 2002.

[39] Y. Uchino, J. Mauris, A. M. Woodward et al., "Alteration of galectin-3 in tears of patients with dry eye disease," *American Journal of Ophthalmology*, vol. 159, no. 6, pp. 1027–1035.e3, 2015.

[40] Y. Uchino, "The ocular surface glycocalyx and its alteration in dry eye disease: a review," *Investigative Ophthalmology & Visual Science*, vol. 59, no. 14, pp. DES157–DES162, 2018.

Hindawi
Disease Markers
Volume 2022, Article ID 8639323, 18 pages
https://doi.org/10.1155/2022/8639323

Research Article

Identification and Validation of Immune Cells and Hub Genes in Gastric Cancer Microenvironment

Huan Wang,[1,2] Jianfang Rong,[1,2] Qiaoyun Zhao,[2] Conghua Song,[2] Rulin Zhao,[1] Sihai Chen,[1] and Yong Xie[1]

[1]*The First Affiliated Hospital of Nanchang University, Nanchang, 330006 Jiangxi Province, China*
[2]*Medical College of Nanchang University, Nanchang, 330006 Jiangxi Province, China*

Correspondence should be addressed to Yong Xie; xieyong_tfahoncu@163.com

Received 15 November 2021; Accepted 24 February 2022; Published 5 April 2022

Academic Editor: Ting Su

Gastric cancer (GC) is the most common malignant tumor in the digestive system, traditional radiotherapy and chemotherapy are not effective for some patients. The research progress of immunotherapy seems to provide a new way for treatment. However, it is still urgent to predict immunotherapy biomarkers and determine novel therapeutic targets. In this study, the gene expression profiles and clinical data of 407 stomach adenocarcinoma (STAD) patients were downloaded from The Cancer Genome Atlas (TCGA) portal, and the abundance ratio of immune cells in each sample was obtained via the "Cell Type Identification by Estimating Relative Subsets of RNA Transcripts (CIBERSORT)" algorithm. Five immune cells were obtained as a result of abundance comparison, and 295 immune-related genes were obtained through differential gene analysis. Enrichment, protein interaction, and module analysis were performed on these genes. We identified five immune cells associated with infiltration and 20 hub genes, of which five genes were correlated with overall survival. Finally, we used Real-time PCR (RT-PCR) to detect the expression differences of the five hub genes in 18 pairs of GC and adjacent tissues. This research not only provides cellular and gene targets for immunotherapy of GC but also provides new ideas for researchers to explore immunotherapy for various tumors.

1. Introduction

As a common malignant tumor, the GC has a high incidence of concealment and a high recurrence rate, which is the second cause of cancer death after lung cancer [1]. Approximately 990,000 people are diagnosed with GC each year worldwide, and most patients are already in a stage of local progression at the time of diagnosis, resulting in high mortality [2]. Traditional treatments such as chemotherapy, radiotherapy, and surgery are difficult for most patients with advanced GC to completely remove the tumor, and the 5-year survival rate of advanced GC treated with traditional methods is always on the low side [3, 4].

In recent years, with the understanding of tumor microenvironment and immune targets, immunotherapy has gradually become a new therapeutic method. Immunotherapy can reduce the pain of patients, improve the quality of life, and even prolong the survival time. Tumor immunotherapy mainly uses the body's natural defense mechanism to kill tumor cells, thereby enhancing antitumor immunity [5, 6]. At present, tumor immunotherapy mainly includes immune checkpoint inhibitors, adoptive cellular immunity, and immune vaccines. Immunotherapy is a new type of antitumor therapy, which has achieved certain results in the treatment of GC [7–9]. However, due to the complexity of human immune mechanisms, tumor-induced immune escape is a widespread phenomenon. There are still many problems that need to be addressed in GC immunotherapy, especially in predicting immunotherapy biomarkers and finding new effective therapeutic targets.

Cancer immunotherapy mainly cooperates with some important proteins to enhance or restore the function of immune cells in the tumor microenvironment. Therefore, we first studied the immune cells related to the degree of

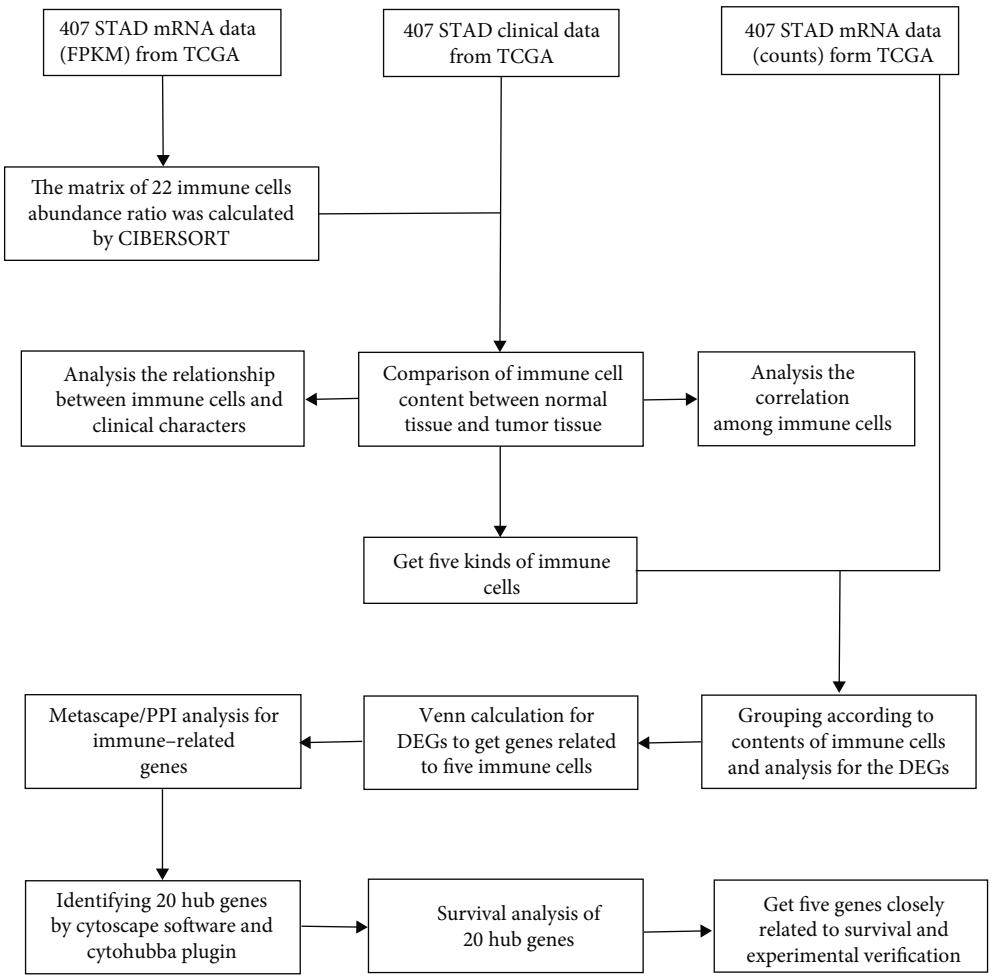

Figure 1: Flowchart of data acquisition and analysis process. TCGA: The Cancer Genome Atlas (https://portal.gdc.cancer.gov/). FPKM and counts are two different mRNA data formats in TCGA databases. CIBERSORT is a network tool that uses gene expression data to estimate the abundance ratio of member cell types in a mixed cell population. DEGs: differentially expressed genes. Metascape is a web-based portal designed to provide a comprehensive gene list annotation and analysis resource for experimental biologists. PPI: protein-protein interactions. Cytoscape is a network processing software, and the Cytohubba is a plugin in Cytoscape.

infiltration in STAD, then investigated the genes that are crucial to the level of infiltration of immune cells, and performed experiments to verify the results. Our study provides ideas and clues for the immunotherapy of STAD, and the identified cells and genes can be considered biomarkers for the prognosis or target of STAD therapy. In addition, this study also provides a new way for immunotherapy researchers to explore cellular and gene targets of immunotherapy.

2. Materials and Methods

2.1. Data Source and Preprocessing. Download RNA-Seq gene expression profiles of 407 STAD patients (including 375 tumor samples and 32 normal samples) from the TCGA database, including FPKM and COUNT formats. Clinical data such as gender, age, tumor grade, clinical stage, and survival time were downloaded from the Genomic Data Commons (GDC) which was retrieved from the TCGA (https://tcga-data.nci.nih.gov/tcga/) database. Then, the R software was used to extract and sort the data to obtain the gene expression matrix and clinical data. This was followed by an analysis, and all the analytical processes are shown in Figure 1.

2.2. Identifying Immune-Related Cells. The CIBERSORT (https://cibersort.stanford.edu/) is an analytical tool developed by Newman that uses gene expression data to estimate the abundance ratio of member cell types in a mixed cell population [10]. To quantify the proportion of immune cells in STAD specimens, we used the CIBERSORT method and the LM22 gene signature [10]; the latter contains 547 genes, which can be highly sensitive and specific for the recognition of 22 human hematopoietic cell phenotypes (including B cells, T cells, natural killer cells, macrophages, dendritic cells, and myeloid subpopulations). The CIBERSORT uses the Monte Carlo sampling to derive a P value for the deconvolution of each sample, providing a measure of confidence in the results. At the threshold of $P < 0.05$, the results of the inferred part of the immune cell population produced by the CIBERSORT were considered accurate [11]. 164 samples

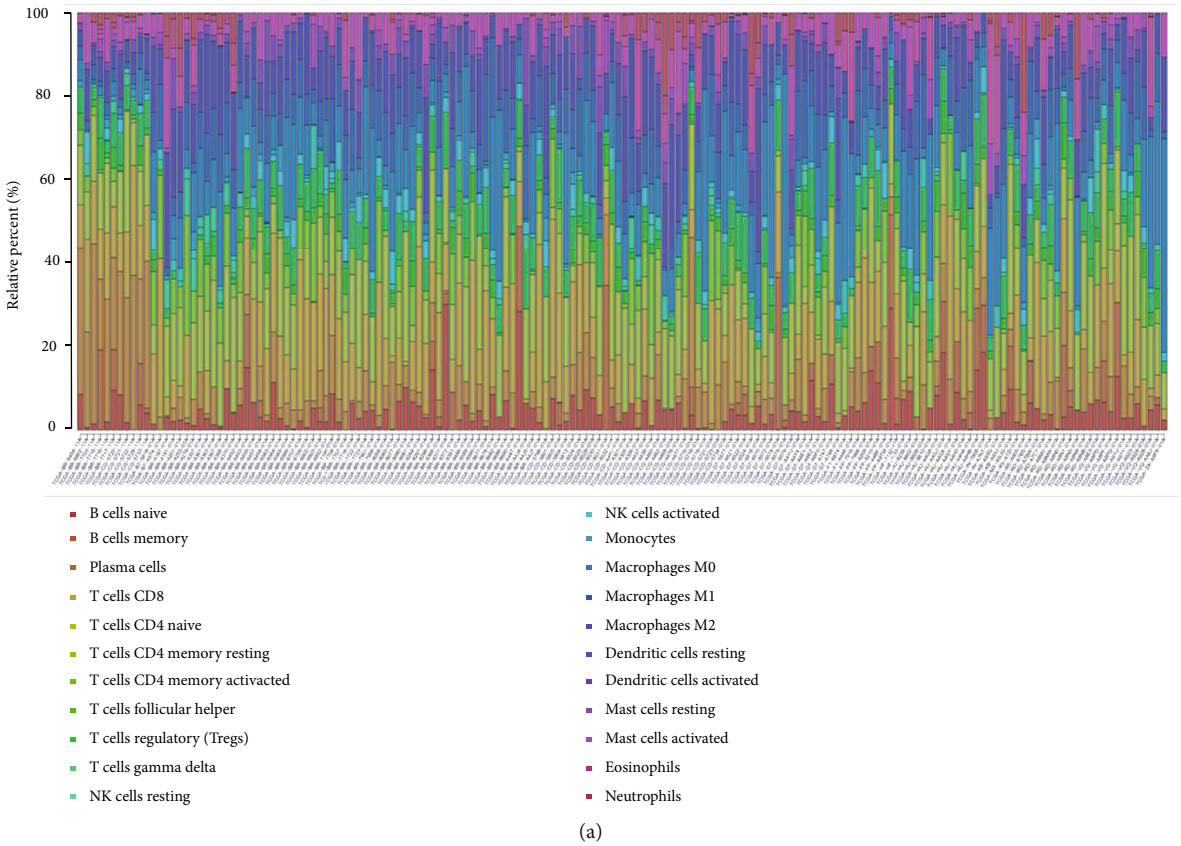

(a)

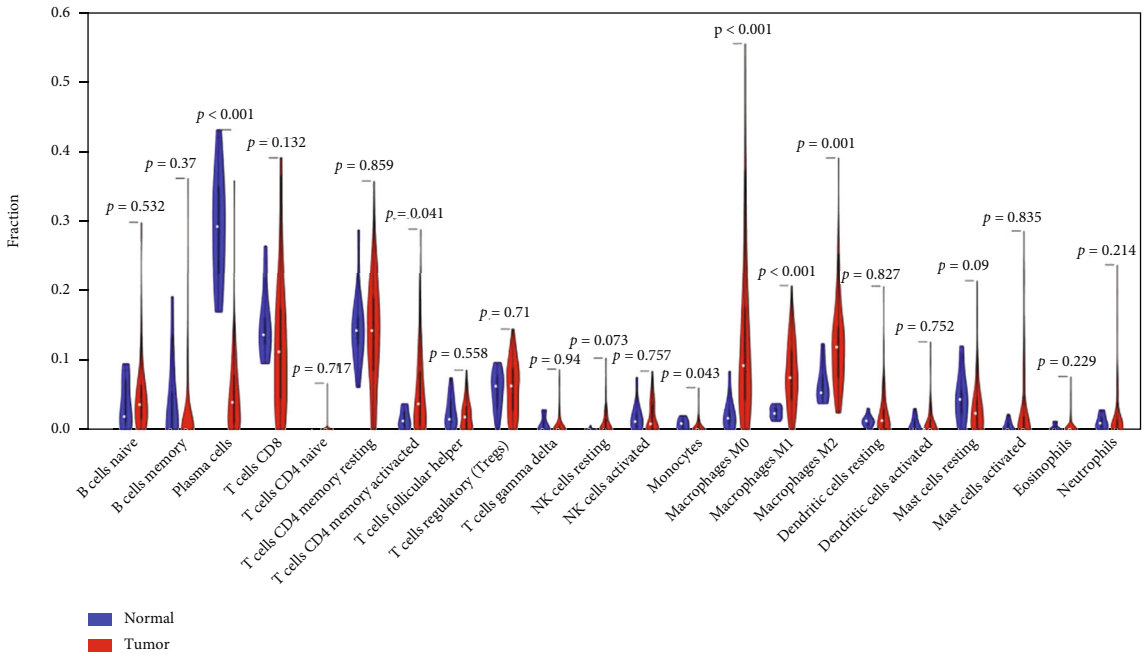

(b)

Figure 2: Continued.

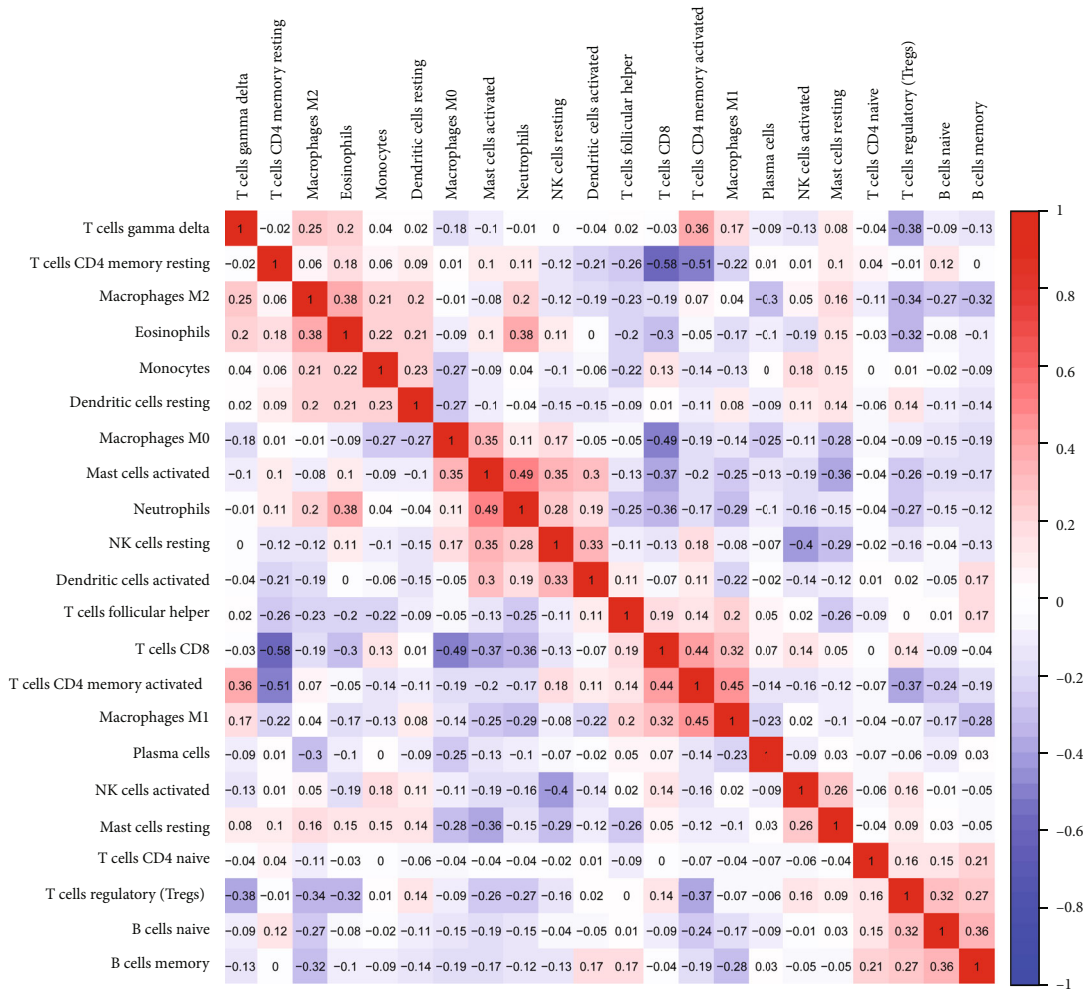

(c)

Figure 2: Identifying immune cells in GC. (a) The abundance ratio of immune cells in 164 samples. Each column represents a sample, and different colors and heights of each column represent the abundance ratio of immune cells in the sample. (b) Abundance ratio of 22 immune cells in cancer ($n = 153$) and normal ($n = 11$) samples. Blue represents normal samples, red represents tumor samples. (c) The relationship between abundance ratios of 22 immune cells. The value represents the relevant value. Red represents positive correlation, blue represents negative correlation.

(including 153 tumor samples and 11 normal samples) were selected by $P < 0.05$ for subsequent analysis. The Wilcoxon test was used to analyze the difference in the proportion of 22 immune cells in tumor samples and normal samples, and the cells with a significantly higher infiltration degree in tumor samples were identified as immune-related cells.

2.3. Clinical Relationship with Immune-Related Cells. Combined with the immune cell abundance ratio and clinical characteristics of 153 tumor samples, the relationship between immune cell abundance ratio and tumor grade, clinical stage, T-stage, and N-stage was analyzed by the independent samples t-test.

2.4. Identifying Immune-Related Genes. The STAD samples were grouped (high abundance group and low abundance group) according to the median abundance of the five immune cells identified in Section 2.2, by using the edgeR R software package and controlling | log FC | >1 and $P < 0.05$ to identify the differentially expressed genes (DEGs). An R package Venn diagram was used to generate these immune-related genes.

2.5. Enrichment Analysis of Immune-Related Genes. In order to elucidate the potential gene functional annotation and pathway enrichment associated with the 295 DEGs, Gene Ontology (GO) [12, 13] terms and Kyoto Encyclopedia of Genes and Genomes (KEG) [14–16] pathways were performed using the Metascape (http://metascape.org) [17]. These genes were assigned to functional groups according to molecular functions, biological processes, and specific pathways.

2.6. Protein-Protein Interaction Network Construction, Hub Genes, and Module Analysis. To assess the interactions among DEGs, the 295 immune-related genes were submitted to the String database (https://string-db.org/), a network tool

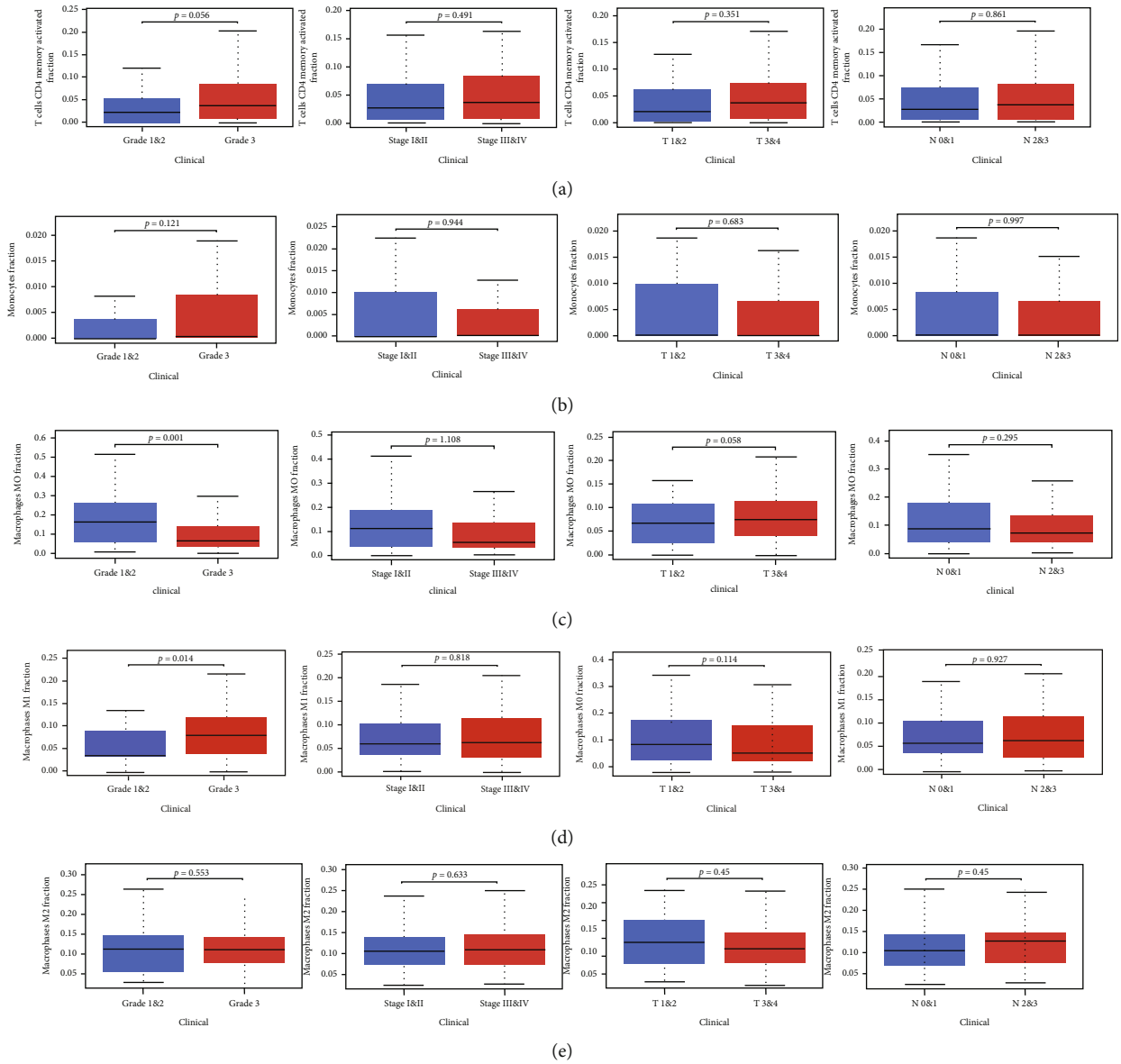

Figure 3: The relationship between the abundance ratio of immune cells and clinical characteristics. (a–e) The relationship between the abundance ratio of each immune cell and tumor grade, clinical stage, T-stage, and N-stage. The upper and lower sides of the boxplot are 75% and 25% quantiles. The line in the middle of the box indicates the median.

for studying protein-protein interactions (PPI), and the comprehensive score was set to ≥0.4 [18]. An interactive network consisting of 148 nodes and 142 edges was obtained. The network was reconstructed by Cytoscape software (cytoscape.org) and a module analysis of the network was performed using the "MCODE" plugin [19] to search subnetworks of the PPI network. At the same time, important nodes in the network were predicted by the "Cytohubba" plugin [20], and the top 20 genes generated by Maximal Clique Centrality (MCC) were screened and identified as hub genes. Finally, we selected the module with the highest score from MCODE for enrichment analysis through the Metascape.

2.7. Survival Analyses of Hub Genes. Overall survival analyses of hub genes were performed using the GEPIA2 [21](http://gepia2.cancer-pku.cn/).

2.8. Patients and Tissue Specimens. Human gastric tissue samples (18 pairs of GC and adjacent samples) were collected from GC patients who underwent gastrectomy at the First Affiliated Hospital of Nanchang University. The diagnoses of GC were confirmed based on histology. All subjects provided informed consent for obtaining the study specimens. The study protocol was approved by the Clinical Research Ethics Committee of the First Affiliated Hospital of Nanchang University. All included cases were recorded in the Human Genetic Resources Center of the First Affiliated Hospital of Nanchang University.

2.9. Real-Time Quantitative PCR Analysis of the Five Hub Genes. TRIzol (Invitrogen) was then used to extract total tissue RNA, after which SYBR® Premix Ex Taq (TaKaRa) was used for RT–PCR. The primers used for the detection of

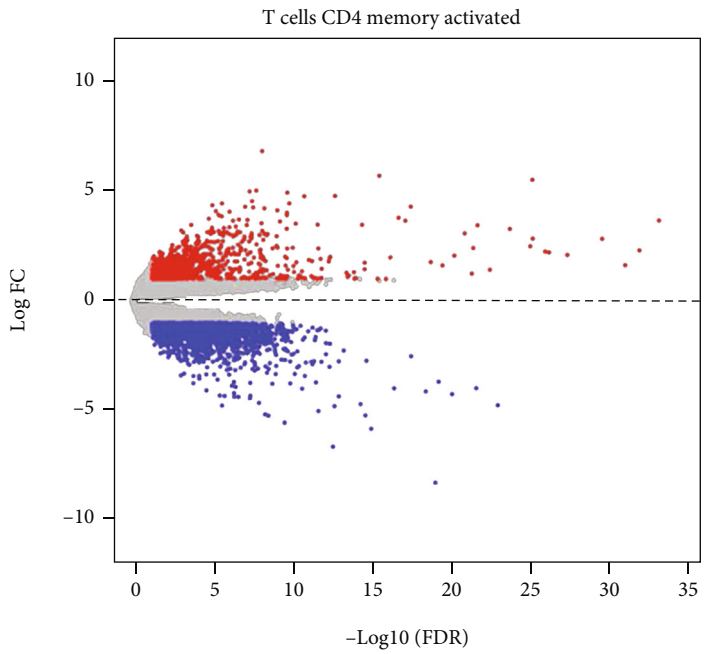

(a)

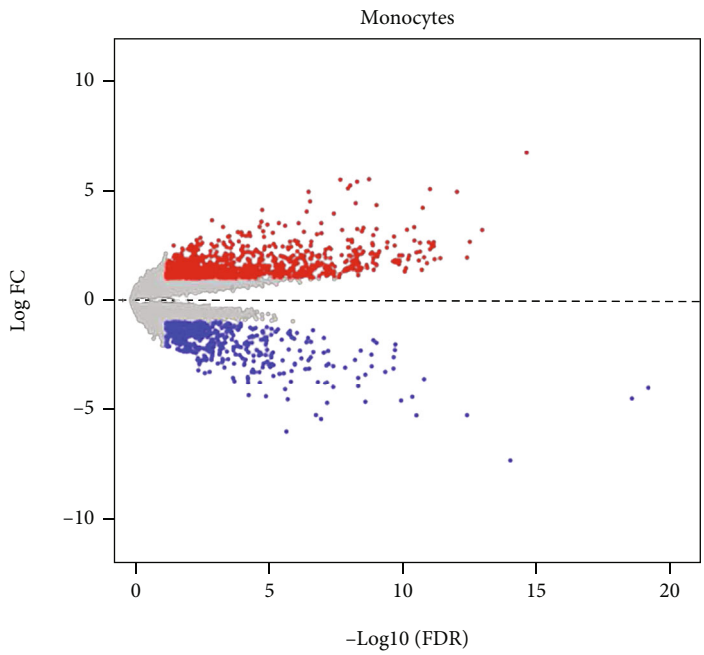

(b)

Figure 4: Continued.

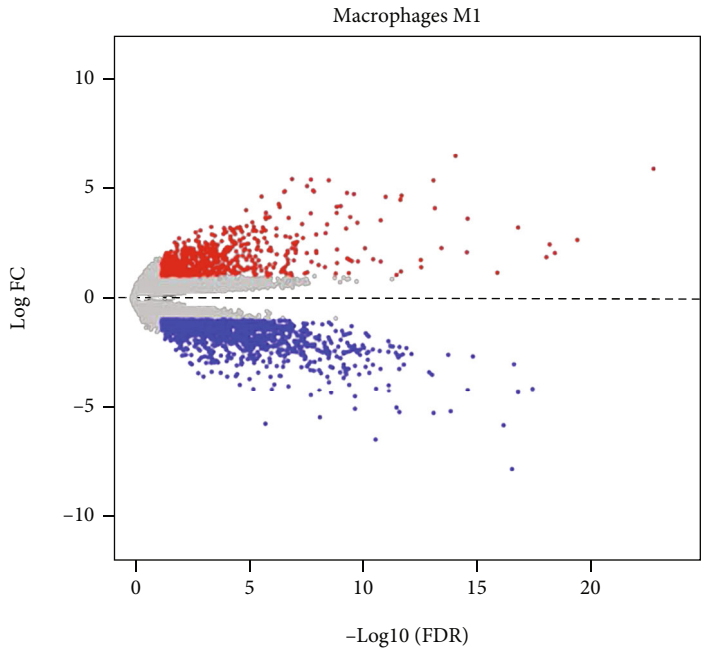

(c)

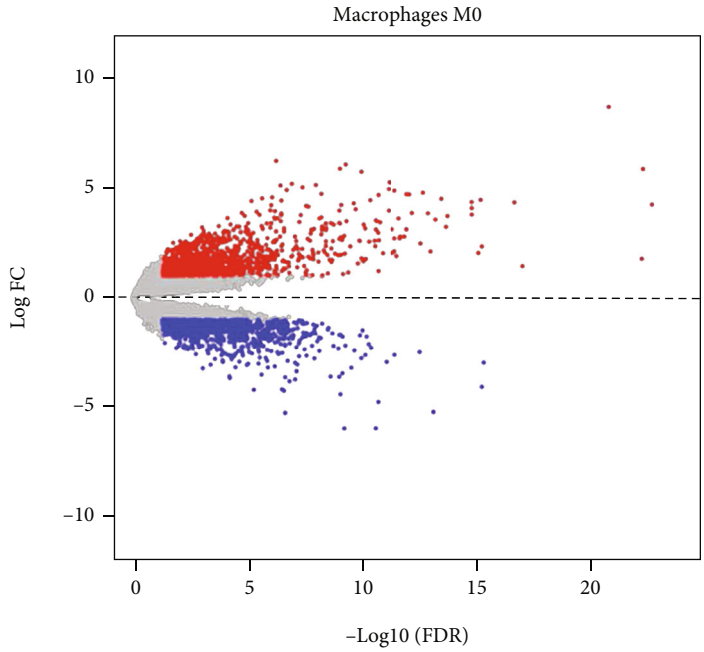

(d)

Figure 4: Continued.

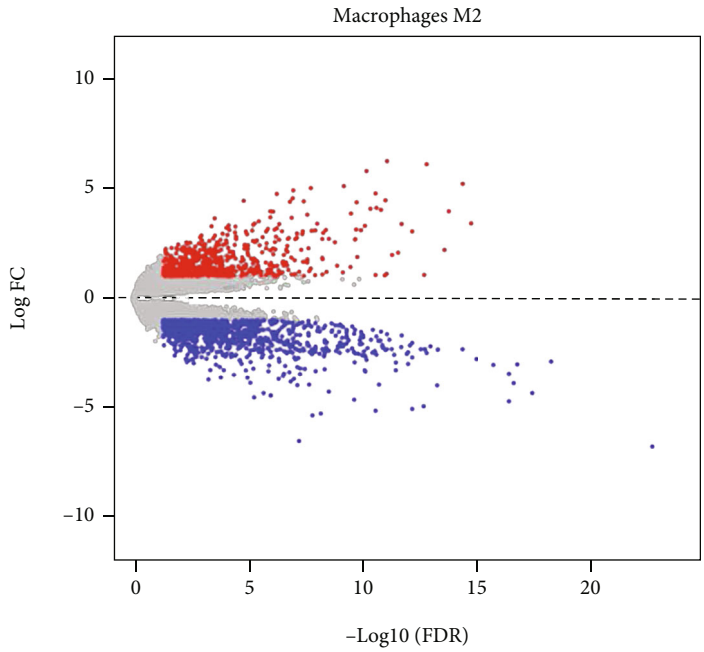

(e)

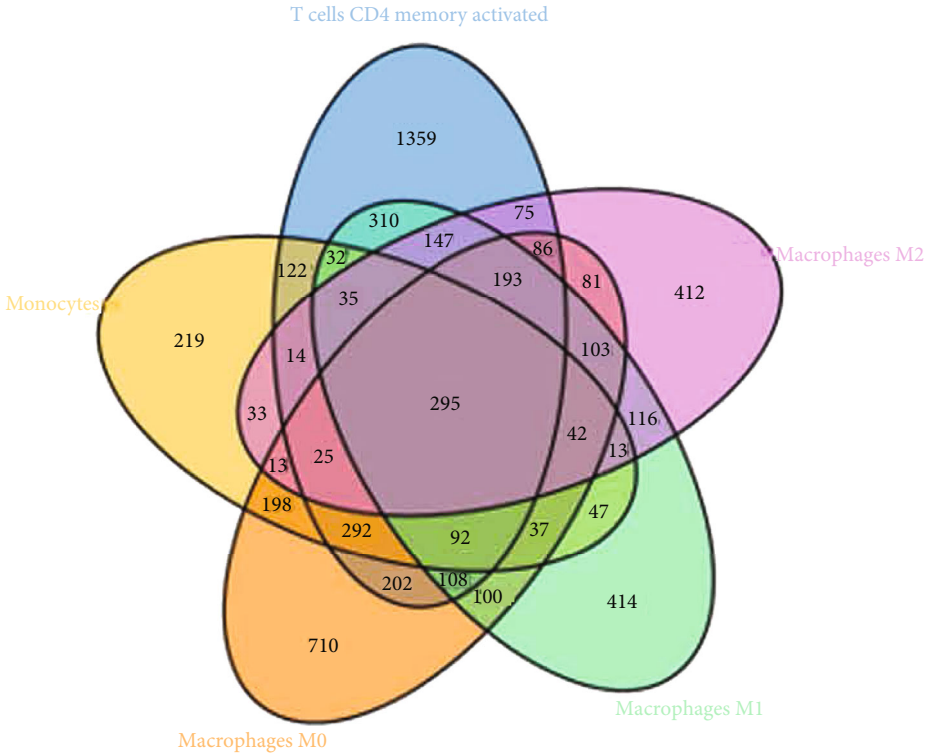

(f)

Figure 4: Identification of DEGs associated with immune cells. (a–e) Volcano plots of the GC gene expression profiles grouping by T cell CD4 memory activated, monocytes, macrophages M0, macrophages M1, and macrophages M2. Red represents upregulated genes, blue represents downregulated genes. $|\text{Log}\,2\,\text{FC}| > 1$ and P value < 0.05. (f) Venn calculation results using an online tool to obtain genes involved in the infiltration of five immune cells. The numbers in different color blocks represent the number of genes related to immune cell infiltration. A total of 295 genes are related to the five immune cells.

human specimens are as follows: β-actin forward primer 5′-TGACGTGGACATCCGCAAAG-3′ and reverse primer 5′-CTGGAAGGTGGACAGCGAGG-3′; ADRA1B, forward primer 5′-CTTTCACGAGGACACCCTTAGC-3′ and reverse primer 5′-GCCCAACGTCTTAGCTGCTT-3′; BRS3 forward primer 5′-CTGCGTCTGGATCGTGTCTAT-3′

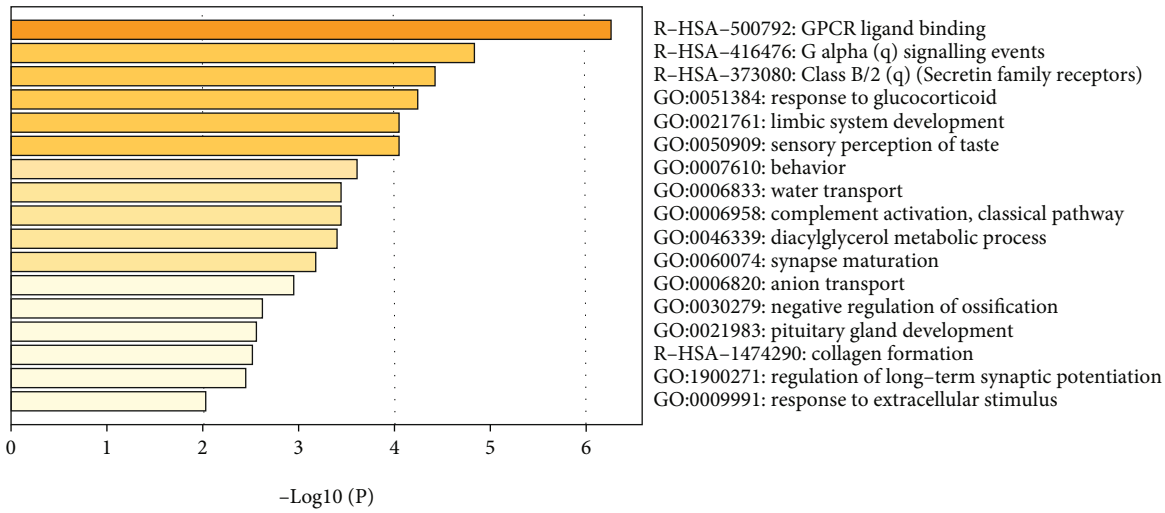

(a)

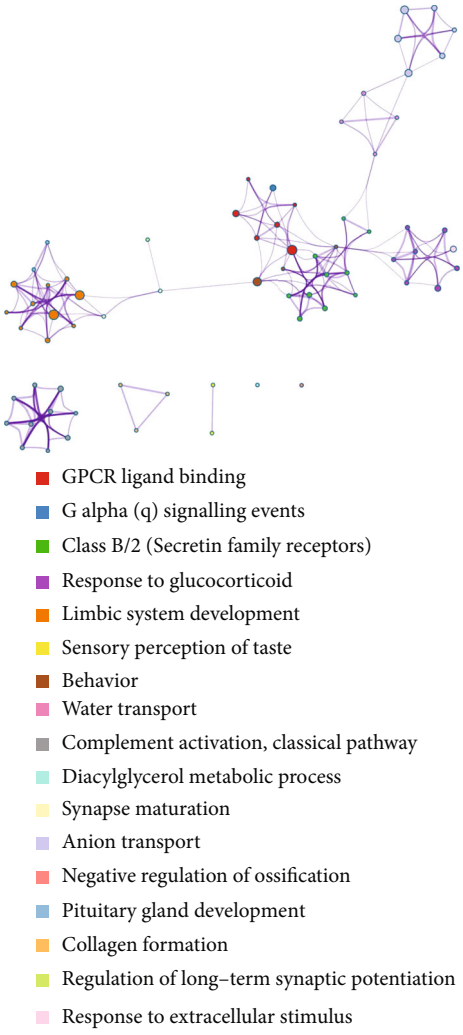

(b)

Figure 5: Metascape analysis. (a) Bar graph of enriched terms across input gene lists, colored by *P* values. (b) Network of enriched sets colored by cluster ID, where nodes that share the same cluster ID are typically close to each other.

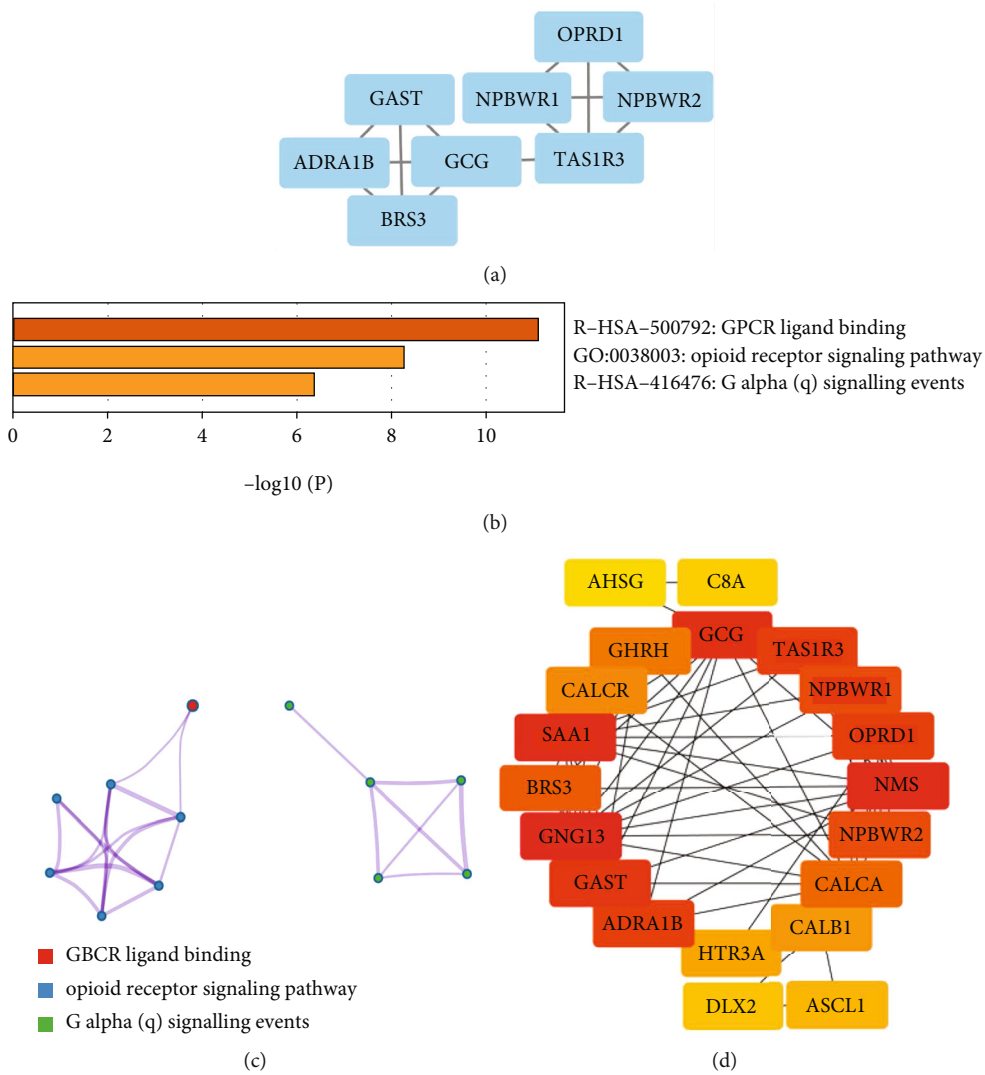

Figure 6: PPI network construction and module analysis. (a) The module with the highest score obtained using the MCODE plugin. (b and c) Metascape analysis. (d) Top 20 genes selected based on MCC methods. The darker the color of the node, the higher the score.

and reverse primer 5′-AGGGTCCTAGCAATCAAGGAAT-3′; CALCA, forward primer 5′-AAGCGGTGCGGTAATC TGAG-3′ and reverse primer 5′-GGGGAACGTGTGAAAC TTGTTG-3′; CALCR forward primer 5′-CCTATCCAACA ATAGAGCCCAAG-3′ and reverse primer 5′-TGCATTCG GTCATAGCATTTGTA-3′; OPRD1 forward primer 5′-CG TCCGGTACACTAAGATGAAGA-3′ and reverse primer 5′-GCCACGTCTCCATCAGGTA-3′. Student's t-test was used for comparison between the two groups. $P < 0.05$ was considered statistically significant.

3. Results

3.1. Data Source and Preprocessing. The RNA-Seq (including FPKM and counts) and clinical data of the 407 patients with STAD were obtained from the TCGA. Figure 1 flowchart shows the process of data acquisition and subsequent analysis.

3.2. Identifying Immune Cells in GC. By using the CIBERSORT, the abundance ratio of 22 immune cells in 164 STAD samples and the difference of the abundance ratios in cancer and normal samples were analyzed, as shown in Figures 2(a) and 2(b). The abundance ratio of plasma cell in normal samples ($n = 11$) was significantly higher than in cancer tissues ($n = 153$), while the contents of T cell CD4 memory activated, monocytes, macrophages M0, macrophages M1, and macrophages M2 in normal samples were significantly lower than that of tumor tissues. Besides, we also analyzed the correlation between the 22 immune cells. As shown in Figure 2(c), T cell CD4 memory resting was negatively correlated with T cell CD8 and T cell CD4 memory activated, while neutrophils and mast cells activated were significantly correlated. From the above results, it can be seen that the abundance ratios of T cell CD4 memory activated, monocytes, macrophages M0, macrophages M1, and macrophages M2 in GC were significantly higher than that of normal tissue.

Table 1: Functional roles of the 20 hub genes.

NO.	Gene	Full name	Function
1	ADRA1B	Adrenoceptor alpha 1B	G protein-coupled receptor activity, alpha1-adrenergic receptor activity, and protein binding
2	AHSG	Alpha 2-HS glycoprotein	Cysteine-type endopeptidase inhibitor activity and endopeptidase inhibitor activity
3	ASCL1	Achaete-scute family bHLH transcription factor 1	DNA-binding transcription factor activity and DNA-binding transcription factor activity
4	BRS3	Bombesin receptor subtype 3	G protein-coupled receptor activity and bombesin receptor activity
5	C8A	Complement C8 alpha chain	Encodes the alpha subunit of C8
6	CALB1	Calbindin 1	Calcium ion binding and protein binding
7	CALCA	Calcitonin-related polypeptide alpha	Calcitonin receptor binding and hormone activity
8	CALCR	Calcitonin receptor	G protein-coupled peptide receptor activity and contributes to amylin receptor activity
9	DLX2	Distal-less homeobox 2	DNA-binding transcription activator activity and RNA polymerase II-specific
10	GAST	Gastrin	Hormone activity and protein binding
11	GCG	Glucagon	Glucagon receptor binding and hormone activity
12	GHRH	Growth hormone-releasing hormone	Growth hormone-releasing hormone activity and neuropeptide hormone activity
13	GNG13	G protein subunit gamma 13	G-protein beta-subunit binding and GTPase activity
14	HTR3A	5-hydroxytryptamine receptor 3A	Neurotransmitter receptor activity and protein binding
15	NMS	Neuromedin S	G protein-coupled receptor binding
16	NPBWR1	Neuropeptides B and W receptor 1	G protein-coupled receptor activity and neuropeptide binding
17	NPBWR2	Neuropeptides B and W receptor 2	G protein-coupled receptor signaling pathway and neuropeptide signaling pathway
18	OPRD1	Opioid receptor delta 1	G protein-coupled receptor activity and enkephalin receptor activity
19	SAA1	Serum amyloid A1	G protein-coupled receptor binding and chemoattractant activity
20	TAS1R3	Taste 1 receptor member 3	G protein-coupled receptor activity and signaling receptor activity

3.3. Clinical Relationship with Immune-Related Cells. According to the clinical characteristics, 153 tumor samples were grouped to analyze the relationship between the abundance of five immune cells and the clinical characteristics (including T-stage, N-stage, clinical stage, and tumor grade), so as to determine the influence of the abundance ratio of immune cells on the clinical characteristics of STAD. As shown in Figure 3, the abundance ratio of macrophages M0 in the high-grade samples (Grades 1 and2) was significantly lower than that in the low-grade group (Grade 3). The abundance of macrophages M1 increased with the increase of tumor grade. Although the difference was not significant, with the increase of tumor grade, clinical stage, T-stage, and N-stage, the abundance of T cell CD4 memory activation and monocytes increased (Figures 3(a) and 3(b)). In addition, the abundance of macrophages M2 in the N2&N3 group was slightly higher than that of the N1&N2 group (Figure 3(e)).

3.4. Identification of DEGs Related to Immune Cells. In order to identify immune-related DEGs, the STAD samples were grouped (high abundance group and low abundance group) according to the median abundance of the five immune cells. We found that there were 475 DEGs in T cell CD4 memory activation, 269 genes with downregulated expression, and 206 genes with upregulated expression. In monocytes, there were 360 DEGs, including 173 genes were downregulated and 187 genes were upregulated. There were 488 DEGs, 139 downregulated genes and 349 upregulated genes in macrophages M0. There were 511 DEGs in macrophages M1, with 313 downregulated genes and 198 upregulated genes. 440 DEGs were identified in macrophages M2, including 272 downregulated genes and 169 upregulated genes. Volcano graphs were used to show the results in Figures 4(a) and 4(e). The Venn diagram analysis shown in Figure 4(f) revealed 295 DEGs related to immune cells.

3.5. Enrichment Analysis of Genes Related to Immune Cells. In order to investigate the functions of the 295 immune-related DEGs, enrichment analysis was performed by using the Metascape. The Metascape analysis shows the top 17 clusters of enriched sets (Figure 5). These genes were enriched in the biological process (BP) categories response to glucocorticoid, limbic system development, sensory perception of taste, and so on. The KEGG pathway data were enriched in GPCR ligand binding, G alpha (q) signaling events, Class B/2 (Secretin family receptors), etc.

3.6. PPI Network Construction, Module Analysis, and Identification of Hub Genes. In order to explore the correlation of the 295 immune-related genes and obtain hub genes,

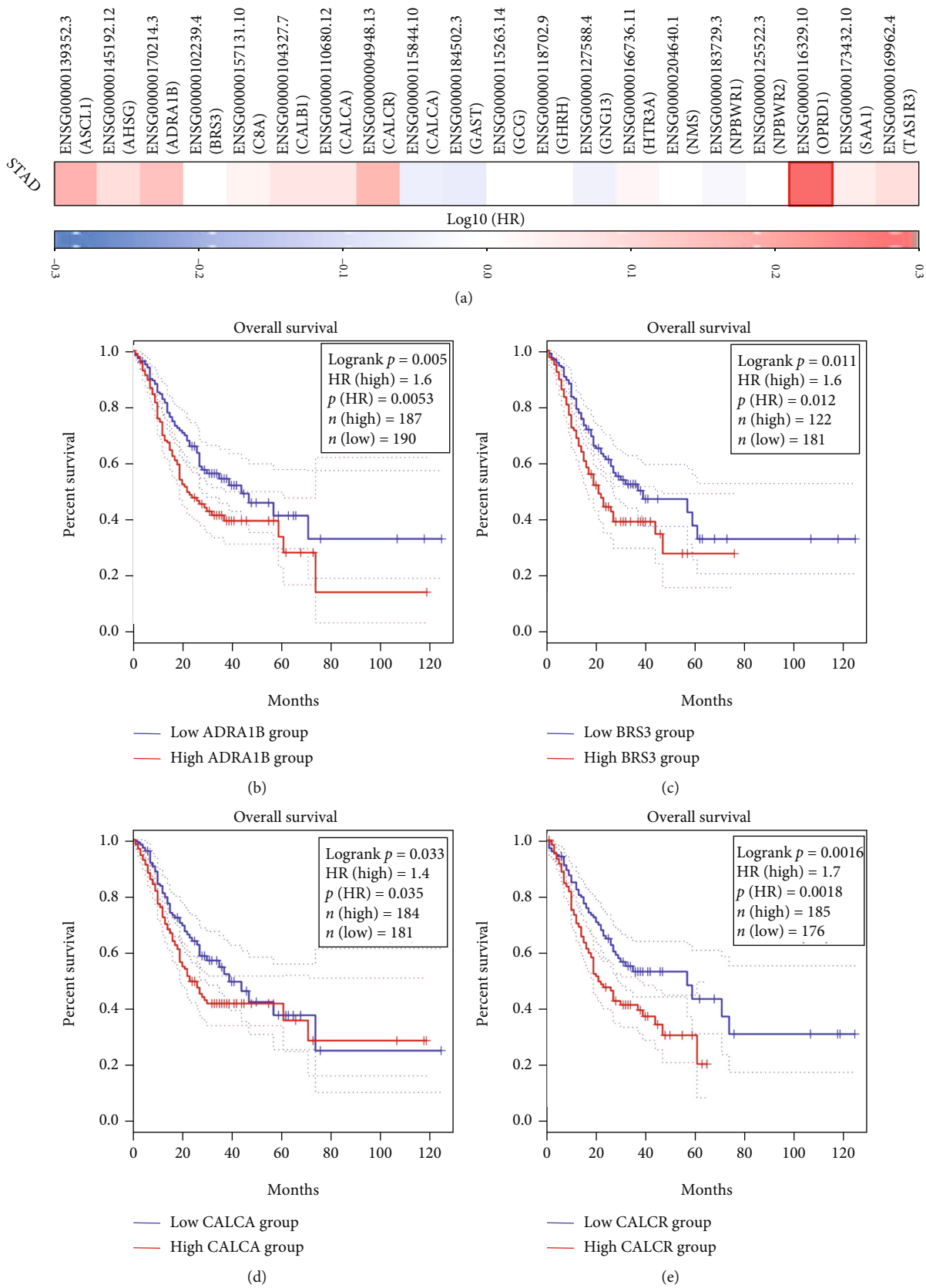

Figure 7: Continued.

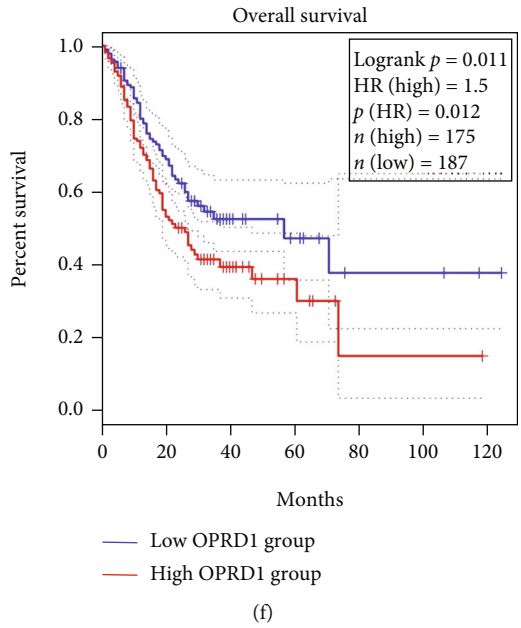

Figure 7: Survival analysis of the hub genes. (a) Survival map of 20 hub genes obtained through the online tool GEPIA2. Red means positive correlation, blue means negative correlation. (b–f) The five genes closely related to survival of STAD. The red line indicates the group with high gene expression, and the blue line indicates the group with low gene expression.

PPI and module analysis were conducted. The module with the highest score was shown in Figure 6(a). To explore the function of this module, we conducted an enrichment analysis by using the Metascape and the results showed the genes were enriched in the BP categories opioid receptor signaling pathway. For KEGG pathway, these genes showed enrichment in GPCR ligand binding and G alpha (q) signaling events (Figures 6(b) and 6(c).

The hub genes were determined by the PPI network by using the Cytohubba plugin. The MCC methods were performed to calculate the top 20 genes, which were considered as hub genes, as shown in Figure 6(d). Table 1 shows the information of 20 hub genes, including complete gene names and main functions.

3.7. Survival Analysis of Hub Genes. These 20 hub genes are potential immunotherapy targets, and their relationship with prognosis of GC is of great value for further immune-related research. Figure 7(a) is a survival map of 20 hub genes obtained through the online tool GEPIA2. Figures 7(b)–7(f) show the five hub genes significantly related to overall survival of STAD, namely, ADRA1B, BRS3, CALCA, CALCR, and OPRD1.

3.8. Validation of the Five Hub Genes. For validating the five hub genes related to survival, we detected the expression difference of these five genes in 18 pairs of cancer and adjacent tissues by RT-PCR, and the results showed that the expression of ADRA1B mRNA in the adjacent tissues was higher than that in the adjacent tissues, while the expression of BRS3, CALCA, and CALCR mRNA in the cancer tissues was significantly higher than that in the adjacent tissues. In addition, the expression of OPRD1 in cancer tissues was also higher than that in adjacent tissues, with an insignificant difference (Figure 8).

4. Discussion

GC is the most common malignant tumor in the digestive system. Traditional radiotherapy and chemotherapy are not effective for some patients, so it is imperative to seek new treatment. In recent years, with the development of immunotherapy in multiple cancers, PD-1 inhibitors have received widespread attention in the treatment of GC [22–24]. However, not all patients can get a considerable curative effect, so it is particularly important to look for biomarkers with predictive value and screen the beneficiary population. The purpose of the study was to screen and identify immune cells and genes closely related to immune and clinical outcomes in the STAD microenvironment. This study has not only identified the potential cells and gene targets of STAD immunotherapy but also provided new research ideas for the other tumor immunotherapy.

In the study, we found T cell CD4 memory activated, monocytes, macrophages M0, macrophages M1, and macrophages M2 were highly infiltrated in tumor samples. CD4+ memory T cells play an important role in the occurrence and development of tumors [25]. CD4+ central memory T (TCM) cells maintain immune memory and play a protective role in tumor metastasis [26, 27]. CD4+ effector memory T (TEM) cells express adhesion molecules and chemokine receptors, which perform rapid functions [28]. Both of them play an important role in antitumor immunity. In the peripheral blood of patients with advanced cancer, the proportion of TCM cells decreased and TEM cells increased, showing a typical state of T cell exhaustion [29]. In this

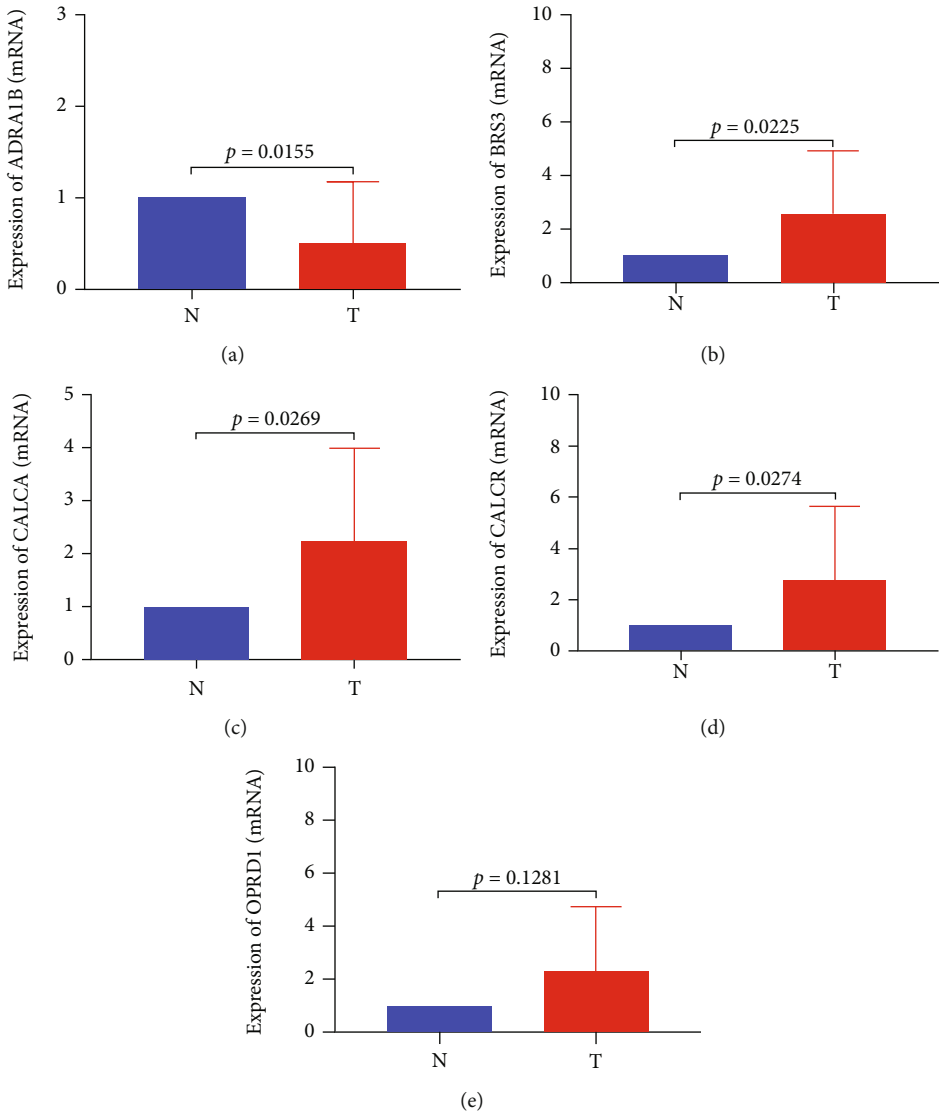

Figure 8: Validation of the five hub genes. (a–e) RT-PCR detected the expression of ADRA1B, BRS3, CALCA, CALCR, and OPRD1 in 18 pairs of cancer and adjacent tissues. *N* represents 18 cases of adjacent tissues, and *T* represents 18 cases of cancerous tissues.

study, it was found that the content of T cell CD4 memory activated in tumor tissue was significantly increased. Monocytes appear to be recruited to tumor tissue throughout the tumor progression, including the early stages of tumor growth [30, 31] and the establishment of distant metastasis [32, 33], under the influence of the tumor microenvironment, it can differentiate into tumor-related macrophages, thus promoting tumor growth and metastasis [34]. This study showed that the content of monocytes in tumor samples increased significantly, which further proved the role of monocytes in promoting tumor development. Macrophages can be divided into classic macrophages M1 and alternative macrophages M2 according to their functions [35]. Macrophages M1 is involved in inflammation and antitumor immunity, while macrophages M2 have the characteristics of promoting tumor development [36, 37]. Macrophages M0 are formed by monocytes and have not been polarized to M1 or M2 macrophage subtypes in tumors [38]. In the initial stage of tumor formation, monocytes in peripheral blood gather around the tumor and are mainly polarized to macrophages M1, which plays an antitumor immune role. However, once the tumor has formed, under tumor microenvironment conditions of partial hypoxia and partial acid, macrophages are polarized to M2 type, which has the role of promoting tumor growth, invasion, and angiogenesis and suppressing the immune response [39, 40]. This explains that the infiltration of macrophages M0, M1, and M2 in tumor samples was higher than that in normal samples. In summary, the five cells identified in this study are most likely to play an important role in tumor immune infiltration and GC immunotherapy, confirming the credibility of cell-based immune-related gene analysis.

Enrichment analysis of immune-related genes shows that these genes are mainly related to G protein-coupled receptors (GPCRs) ligand binding. GPCR, which represents the largest gene family in the human genome, plays a vital

role in various physiological functions as well as tumor growth and metastasis [41]. Crosstalk between different receptors, including GPCRs, triggers related biological functions of normal and tumor cells [42]. It has been reported that many GPCRs activate many signaling pathways that interact with other plasma membrane receptors [42]. For example, crosstalk between acetylcholine muscarinic receptors (mAChRs), epidermal growth factor (EGFR), and platelet-derived growth factor (PDGFR) receptors leads to the activation of mitotic pathway, which mediates cell proliferation, differentiation, and survival [43]. Some GPCR ligands, such as bradykinin (BK), LPA, gastrin-releasing peptide (GRP), and bombesin (BN), activate EGFR and then induce stimulation in different types of tumors, such as prostate cancer, breast cancer, and pancreatic adenocarcinoma [44] Besides, studies have shown that leukocytes, including neutrophils, T cells, and dendritic cells, mainly perceive signals of movement, migration, chemotaxis, and localization through GPCRs and induce intracellular premigration response through the combination of agonists [45, 46]. These studies indicate that GPCR is closely related to the tumor immune microenvironment.

A total of 20 hub genes were finally identified, five of which were related to survival, namely, ADRA1B, BRS3, CALCA, CALCR, and OPRD1. Studies have shown that these genes are related to the occurrence of certain tumors. ADRA1B is a member of the GPCRs, and it has been reported that this gene is closely related to the prognosis of thyroid papillary carcinoma [47]. Studies have shown that the methylation of ADRA1B plays a key role in the occurrence and development of GC [48, 49]. Our study showed that the expression of ADRA1B in GC tissues was lower than that in adjacent tissues, which may be related to methylation. BRS3 is a G protein-coupled membrane receptor that binds bombesin-like peptides, it is widely distributed in the peripheral tissues and central nervous system, as well as some tumors [50, 51]. It has been reported that BRS3 activation promotes metastasis formation and drug resistance in small cell lung cancer cells [52]. In addition, studies have shown that relative to normal tissue, primary neuroendocrine tumor expression of BRS3 was increased by 13-fold [53]. Similarly, our study also showed that BRS3 expression in GC tissues was significantly higher than that in adjacent tissues. CALCA encodes a peptide hormone that plays a key role in maintaining serum calcium levels and the regulation of T and B cells in some cancers, which are often methylated in many types of cancer [54, 55]. Multiple studies have shown that the level of CALCA methylation in GC tissue is significantly higher than that of normal gastric tissue [56–58]. However, our study suggested that CALCA was highly expressed in cancer tissues, which may need to be further verified by relevant experiments. As a member of GPCRs, CALCR binds to its ligand and calcitonin and regulates a variety of downstream signaling pathways, thus regulating bone metabolism, calcium flux, and cancer cell proliferation [59, 60]. It has been reported that CALCR expression is significantly upregulated in non-small-cell lung cancer and positively correlated with tumor invasion [61]. And another analysis also showed that CALCR is closely linked to the survival of GC, which is consistent with the results of this study [62]. OPRD1 encodes the delta opioid receptor, which is a member of the opioid GPCRs [63], and plays an important role in potassium homeostasis [64, 65] and glucose metabolism [66]. In order to satisfy the needs of rapid proliferation of energy and biosynthesis, tumor cells use aerobic glycolysis to rapidly supply energy [67]. Compared with adjacent tissues, OPRD1 expression was slightly increased in GC tissues in our study. Therefore, there is an energy competition between tumor cells and immune cells, and OPRD1 may act as a regulatory role.

In summary, we identified five immune cells and 20 hub genes, five of which were shown to be related to the overall survival of STAD patients and were significantly associated with some immune cell infiltration. These cells and genes can be considered biomarkers for prognosis as well as markers for STAD therapy, which may be a focus of STAD immunotherapy. However, the evidence from bioinformatics and RT-PCR alone seems to be insufficient, and more relevant experiments such as flow cytometry should be used to verify the results. The potential relationship between tumor microenvironment, STAD immunotherapy, and prognosis can be rerecognized through the in-depth study of these cells and genes.

Data Availability

Publicly available datasets were analyzed in this study, these can be found in The Cancer Genome Atlas (https://tcga-data.nci.nih.gov/tcga/).

Ethical Approval

The human gastric tissue samples (18 pairs of GC and adjacent samples) were collected from GC patients undergoing gastrectomy at the First Affiliated Hospital of Nanchang University. The diagnoses of GC were all histologically confirmed and all subjects provided informed consent for obtaining the study specimens. The study protocol was approved by the Clinical Research Ethics Committee of the First Affiliated Hospital of Nanchang University.

Consent

The authors consent to the publication of this paper.

Conflicts of Interest

The authors declare that they have no conflicts of interest.

Authors' Contributions

The study conception and design were performed by YX and HW. Material preparation, data collection, and analysis were performed by HW, JFR, SHC, and QYZ. HW, CHS, QYZ, RLZ, and YX contributed to the manuscript writing and revision. HW conducted the experiments. All authors commented on previous versions of the manuscript. All authors read and approved the final manuscript.

Acknowledgments

We acknowledge the TCGA, CIBERSORT, Metascape, and GEPIA2 databases for the free use. This work was supported by National Key Research and Development Program of China (No. 2016YFC1302201), National Natural Science Foundation of China (No. 81970502, No. 81860107, and No. 81460115), and Leading Talent Training Plan of the Gan-PO Outstanding Talents 555 Project of Jiangxi Province (2010-3-61).

References

[1] A. Jemal, F. Bray, M. M. Center, J. Ferlay, E. Ward, and D. Forman, "Global cancer statistics," *CA: a Cancer Journal for Clinicians*, vol. 61, no. 2, pp. 69–90, 2011.

[2] J. Ferlay, H. R. Shin, F. Bray, D. Forman, C. Mathers, and D. M. Parkin, "Estimates of worldwide burden of cancer in 2008: GLOBOCAN 2008," *International Journal of Cancer*, vol. 127, no. 12, pp. 2893–2917, 2010.

[3] C. Fitzmaurice, D. Dicker, A. Pain et al., "The global burden of cancer 2013," *JAMA Oncology*, vol. 1, no. 4, pp. 505–527, 2015.

[4] K. Yamaguchi, K. Yoshida, T. Tanahashi et al., "The long-term survival of stage IV gastric cancer patients with conversion therapy," *Gastric Cancer*, vol. 21, no. 2, pp. 315–323, 2018.

[5] P. N. Tran, S. Sarkissian, J. Chao, and S. J. Klempner, "PD-1 and PD-L1 as emerging therapeutic targets in gastric cancer: current evidence," *Gastrointest Cancer*, vol. 7, pp. 1–11, 2017.

[6] Z. W. Myint and G. Goel, "Role of modern immunotherapy in gastrointestinal malignancies: a review of current clinical progress," *Journal of Hematology & Oncology*, vol. 10, no. 1, p. 86, 2017.

[7] A. Ribas and J. D. Wolchok, "Cancer immunotherapy using checkpoint blockade," *Science*, vol. 359, no. 6382, pp. 1350–1355, 2018.

[8] M. Kim, S. Pyo, C. H. Kang et al., "Folate receptor 1 (FOLR1) targeted chimeric antigen receptor (CAR) T cells for the treatment of gastric cancer," *PLoS One*, vol. 13, no. 6, article e198347, 2018.

[9] J. A. Ajani, J. Randolph Hecht, L. Ho et al., "An open-label, multinational, multicenter study of G17DT vaccination combined with cisplatin and 5-fluorouracil in patients with untreated, advanced gastric or gastroesophageal cancer: the GC4 study," *Cancer: Interdisciplinary International Journal of the American Cancer Society*, vol. 106, no. 9, pp. 1908–1916, 2006.

[10] A. M. Newman, C. L. Liu, M. R. Green et al., "Robust enumeration of cell subsets from tissue expression profiles," *Nature Methods*, vol. 12, no. 5, pp. 453–457, 2015.

[11] H. R. Ali, L. Chlon, P. D. Pharoah, F. Markowetz, and C. Caldas, "Patterns of immune infiltration in breast cancer and their clinical implications: a gene-expression-based retrospective study," *PLoS Medicine*, vol. 13, no. 12, article e1002194, 2016.

[12] M. Ashburner, C. A. Ball, J. A. Blake et al., "Gene ontology: tool for the unification of biology," *Nature Genetics*, vol. 25, no. 1, pp. 25–29, 2000.

[13] The Gene Ontology Resource, "The gene ontology resource: 20 years and still GOing strong," *Nucleic Acids Research*, vol. 47, no. D1, pp. D330–D338, 2019.

[14] M. Kanehisa, Y. Sato, M. Furumichi, K. Morishima, and M. Tanabe, "New approach for understanding genome variations in KEGG," *Nucleic Acids Research*, vol. 47, no. D1, pp. D590–D595, 2019.

[15] M. Kanehisa and S. Goto, "KEGG: Kyoto encyclopedia of genes and genomes," *Nucleic Acids Research*, vol. 28, no. 1, pp. 27–30, 2000.

[16] M. Kanehisa, M. Furumichi, M. Tanabe, Y. Sato, and K. Morishima, "KEGG: new perspectives on genomes, pathways, diseases and drugs," *Nucleic Acids Research*, vol. 45, no. D1, pp. D353–D361, 2017.

[17] S. Tripathi, M. O. Pohl, Y. Zhou et al., "Meta- and orthogonal integration of influenza "OMICs" data defines a role for UBR4 in virus budding," *Cell Host & Microbe*, vol. 18, no. 6, pp. 723–735, 2015.

[18] D. Szklarczyk, J. H. Morris, H. Cook et al., "The STRING database in 2017: quality-controlled protein-protein association networks, made broadly accessible," *Nucleic Acids Research*, vol. 45, no. D1, pp. D362–D368, 2017.

[19] G. D. Bader and C. W. Hogue, "An automated method for finding molecular complexes in large protein interaction networks," *BMC Bioinformatics*, vol. 4, no. 1, article 2, 2003.

[20] C. H. Chin, S. H. Chen, H. H. Wu, C. W. Ho, M. T. Ko, and C. Y. Lin, "cytoHubba: identifying hub objects and sub-networks from complex interactome," *BMC Systems Biology*, vol. 8, no. 4, pp. 1–7, 2014.

[21] Z. Tang, B. Kang, C. Li, T. Chen, and Z. Zhang, "GEPIA2: an enhanced web server for large-scale expression profiling and interactive analysis," *Nucleic Acids Research*, vol. 47, no. W1, pp. W556–W560, 2019.

[22] Y. Y. Janjigian, J. Bendell, E. Calvo et al., "CheckMate-032 study: efficacy and safety of nivolumab and nivolumab plus ipilimumab in patients with metastatic esophagogastric cancer," *Journal of Clinical Oncology*, vol. 36, no. 28, pp. 2836–2844, 2018.

[23] Y. K. Kang, N. Boku, T. Satoh et al., "Nivolumab in patients with advanced gastric or gastro-oesophageal junction cancer refractory to, or intolerant of, at least two previous chemotherapy regimens (ONO-4538-12, ATTRACTION-2): a randomised, double-blind, placebo- controlled, phase 3 trial," *Lancet*, vol. 390, no. 10111, pp. 2461–2471, 2017.

[24] C. S. Fuchs, T. Doi, R. W. Jang et al., "Safety and efficacy of pembrolizumab monotherapy in patients with previously treated advanced gastric and gastroesophageal junction cancer: phase 2 clinical KEYNOTE-059 trial," *JAMA Oncology*, vol. 4, no. 5, article e180013, 2018.

[25] F. Sallusto, D. Lenig, R. Forster, M. Lipp, and A. Lanzavecchia, "Two subsets of memory T lymphocytes with distinct homing potentials and effector functions," *Nature*, vol. 401, no. 6754, pp. 708–712, 1999.

[26] B. Ludewig, S. Oehen, F. Barchiesi, R. A. Schwendener, H. Hengartner, and R. M. Zinkernagel, "Protective antiviral cytotoxic T cell memory is most efficiently maintained by restimulation via dendritic cells," *Journal of Immunology*, vol. 163, pp. 1839–1844, 1999.

[27] E. J. Wherry, V. Teichgräber, T. C. Becker et al., "Lineage relationship and protective immunity of memory CD8 T cell subsets," *Nature Immunology*, vol. 4, no. 3, pp. 225–234, 2003.

[28] N. van Panhuys, R. Perret, M. Prout, F. Ronchese, and G. Le Gros, "Effector lymphoid tissue and its crucial role in

protective immunity," *Trends in Immunology*, vol. 26, no. 5, pp. 242–247, 2005.

[29] C. A. Klebanoff, L. Gattinoni, and N. P. Restifo, "CD8+ T-cell memory in tumor immunology and immunotherapy," *Immunological Reviews*, vol. 211, no. 1, pp. 214–224, 2006.

[30] R. A. Franklin, W. Liao, A. Sarkar et al., "The cellular and molecular origin of tumor-associated macrophages," *Science*, vol. 344, no. 6186, pp. 921–925, 2014.

[31] K. Movahedi, D. Laoui, C. Gysemans et al., "Different tumor microenvironments contain functionally distinct subsets of macrophages derived from Ly6C(high) monocytes," *Cancer Research*, vol. 70, no. 14, pp. 5728–5739, 2010.

[32] B. Z. Qian, J. Li, H. Zhang et al., "CCL2 recruits inflammatory monocytes to facilitate breast-tumour metastasis," *Nature*, vol. 475, no. 7355, pp. 222–225, 2011.

[33] R. N. Hanna, C. Cekic, D. Sag et al., "Patrolling monocytes control tumor metastasis to the lung," *Science*, vol. 350, no. 6263, pp. 985–990, 2015.

[34] C. Li, X. Luo, Y. Lin et al., "A higher frequency of CD14+ CD169+ monocytes/macrophages in patients with colorectal cancer," *PLoS One*, vol. 10, no. 10, article e141817, 2015.

[35] T. Chanmee, P. Ontong, K. Konno, and N. Itano, "Tumor-associated macrophages as major players in the tumor microenvironment," *Cancers*, vol. 6, no. 3, pp. 1670–1690, 2014.

[36] I. Rhee, "Diverse macrophages polarization in tumor microenvironment," *Archives of Pharmacal Research*, vol. 39, no. 11, pp. 1588–1596, 2016.

[37] X. Liu, S. Wu, Y. Yang, M. Zhao, G. Zhu, and Z. Hou, "The prognostic landscape of tumor-infiltrating immune cell and immunomodulators in lung cancer," *Biomedicine & Pharmacotherapy*, vol. 95, pp. 55–61, 2017.

[38] R. D. Bense, C. Sotiriou, M. J. Piccart-Gebhart et al., "Relevance of tumor-infiltrating immune cell composition and functionality for disease outcome in breast cancer," *Journal of the National Cancer Institute*, vol. 109, no. 1, p. djw192, 2017.

[39] M. N. Petruzzi, K. Cherubini, F. G. Salum, and M. A. de Figueiredo, "Role of tumour-associated macrophages in oral squamous cells carcinoma progression: an update on current knowledge," *Diagnostic Pathology*, vol. 12, no. 1, p. 32, 2017.

[40] A. M. Monjazeb, A. E. Zamora, S. K. Grossenbacher, A. Mirsoian, G. D. Sckisel, and W. J. Murphy, "Immunoediting and antigen loss: overcoming the Achilles heel of immunotherapy with antigen non-specific therapies," *Frontiers in Oncology*, vol. 3, p. 197, 2013.

[41] R. Lappano and M. Maggiolini, "GPCRs and cancer," *Acta Pharmacologica Sinica*, vol. 33, no. 3, pp. 351–362, 2012.

[42] V. Almendro, S. Garcia-Recio, and P. Gascon, "Tyrosine kinase receptor transactivation associated to G protein-coupled receptors," *Current Drug Targets*, vol. 11, no. 9, pp. 1169–1180, 2010.

[43] L. M. Luttrell, "'Location, location, location': activation and targeting of MAP kinases by G protein-coupled receptors," *Journal of Molecular Endocrinology*, vol. 30, no. 2, pp. 117–126, 2003.

[44] R. Lappano and M. Maggiolini, "G protein-coupled receptors: novel targets for drug discovery in cancer," *Nature Reviews. Drug Discovery*, vol. 10, no. 1, pp. 47–60, 2011.

[45] D. F. Legler and M. Thelen, "New insights in chemokine signaling," *F1000Research*, vol. 7, article 95, 2018.

[46] B. A. Zabel, A. Rott, and E. C. Butcher, "Leukocyte chemoattractant receptors in human disease pathogenesis," *Annual Review of Pathology*, vol. 10, no. 1, pp. 51–81, 2015.

[47] L. K. Zhong, X. X. Gan, X. Y. Deng et al., "Potential five-mRNA signature model for the prediction of prognosis in patients with papillary thyroid carcinoma," *Oncology Letters*, vol. 20, no. 3, pp. 2302–2310, 2020.

[48] H. Noda, Y. Miyaji, A. Nakanishi, F. Konishi, and Y. Miki, "Frequent reduced expression of alpha-1B-adrenergic receptor caused by aberrant promoter methylation in gastric cancers," *British Journal of Cancer*, vol. 96, no. 2, pp. 383–390, 2007.

[49] T. Wang, Y. Qin, H. Lai et al., "The prognostic value of ADRA1 subfamily genes in gastric carcinoma," *Oncology Letters*, vol. 18, no. 3, pp. 3150–3158, 2019.

[50] T. W. Moody, S. A. Mantey, P. Moreno et al., "ML-18 is a non-peptide bombesin receptor subtype-3 antagonist which inhibits lung cancer growth," *Peptides*, vol. 64, pp. 55–61, 2015.

[51] I. Ramos-Álvarez, P. Moreno, S. A. Mantey et al., "Insights into bombesin receptors and ligands: highlighting recent advances," *Peptides*, vol. 72, pp. 128–144, 2015.

[52] X. Hou, L. Wei, A. Harada, and K. Tatamoto, "Activation of bombesin receptor subtype-3 stimulates adhesion of lung cancer cells," *Lung Cancer*, vol. 54, no. 2, pp. 143–148, 2006.

[53] S. K. Sherman, J. C. Carr, D. Wang, M. S. O'Dorisio, T. M. O'Dorisio, and J. R. Howe, "Gastric inhibitory polypeptide receptor (GIPR) is a promising target for imaging and therapy in neuroendocrine tumors," *Surgery*, vol. 154, pp. 1206–1214, 2013.

[54] V. A. Paixão, D. O. Vidal, O. L. Caballero et al., "Hypermethylation of CpG island in the promoter region of CALCA in acute lymphoblastic leukemia with central nervous system (CNS) infiltration correlates with poorer prognosis," *Leukemia Research*, vol. 30, no. 7, pp. 891–894, 2006.

[55] M. Brait, S. Begum, A. L. Carvalho et al., "Aberrant promoter methylation of multiple genes during pathogenesis of bladder cancer," *Cancer Epidemiology, Biomarkers & Prevention*, vol. 17, no. 10, pp. 2786–2794, 2008.

[56] A. Chu, J. Liu, Y. Yuan, and Y. Gong, "Comprehensive analysis of aberrantly expressed ceRNA network in gastric cancer with and withoutH.pyloriinfection," *Journal of Cancer*, vol. 10, no. 4, pp. 853–863, 2019.

[57] D. Yao, J. Shi, B. Shi et al., "Quantitative assessment of gene methylation and their impact on clinical outcome in gastric cancer," *Clinica Chimica Acta*, vol. 413, no. 7-8, pp. 787–794, 2012.

[58] C. A. Eads, R. V. Lord, K. Wickramasinghe et al., "Epigenetic patterns in the progression of esophageal adenocarcinoma," *Cancer Research*, vol. 61, no. 8, pp. 3410–3418, 2001.

[59] B. W. Purdue, N. Tilakaratne, and P. M. Sexton, "Molecular pharmacology of the calcitonin receptor," *Receptors & Channels*, vol. 8, pp. 243–255, 2002.

[60] E. W. Robbins, E. A. Travanty, K. Yang, and K. A. Iczkowski, "MAP kinase pathways and calcitonin influence CD44 alternate isoform expression in prostate cancer cells," *BMC Cancer*, vol. 8, no. 1, article 260, 2008.

[61] T. He and F. Ling, "CALCR knockdown inhibits the development and progression of non-small-cell lung cancer," *Carcinogenesis*, vol. 42, no. 11, pp. 1390–1398, 2021.

[62] K. Nie, L. Shi, Y. Wen et al., "Identification of hub genes correlated with the pathogenesis and prognosis of gastric cancer via

bioinformatics methods," *Minerva Medica*, vol. 111, no. 3, pp. 213–225, 2020.

[63] P. Cruz-Gordillo, O. Fedrigo, G. A. Wray, and C. C. Babbitt, "Extensive changes in the expression of the opioid genes between humans and chimpanzees," *Brain, Behavior and Evolution*, vol. 76, no. 2, pp. 154–162, 2010.

[64] D. Chao, D. F. Donnelly, Y. Feng, A. Bazzy-Asaad, and Y. Xia, "Cortical delta-opioid receptors potentiate K+ homeostasis during anoxia and oxygen-glucose deprivation," *Journal of Cerebral Blood Flow and Metabolism*, vol. 27, no. 2, pp. 356–368, 2007.

[65] D. Chao, Q. Wang, G. Balboni, G. Ding, and Y. Xia, "Attenuating ischemic disruption of K+ homeostasis in the cortex of hypoxic-ischemic neonatal rats: DOR activation vs. acupuncture Treatment," *Molecular Neurobiology*, vol. 53, no. 10, pp. 7213–7227, 2016.

[66] M. C. Olianas, S. Dedoni, A. Olianas, and P. Onali, "δ-Opioid receptors stimulate the metabolic sensor AMP-activated protein kinase through coincident signaling with Gq/11-coupled receptors," *Molecular Pharmacology*, vol. 81, no. 2, pp. 154–165, 2012.

[67] E. M. Palsson-McDermott and L. A. O'Neill, "The Warburg effect then and now: from cancer to inflammatory diseases," *BioEssays*, vol. 35, no. 11, pp. 965–973, 2013.

Hindawi
Disease Markers
Volume 2022, Article ID 3622149, 13 pages
https://doi.org/10.1155/2022/3622149

Research Article

Abdominal Obesity: An Independent Influencing Factor of Visuospatial and Executive/Language Ability and the Serum Levels of Aβ40/Aβ42/Tau Protein

Xin Fan,[1] **Yun Zhong**,[2] **Lingling Zhang**,[3] **Jiaqi Li**,[3] **Fei Xie**,[1] **and Zhiyuan Zhang**[1]

[1]*Department of Otolaryngology Head and Neck Surgery, The First Affiliated Hospital of Nanchang University, Nanchang 330000, China*
[2]*The First Clinical Medical College of Nanchang University, Nanchang 330000, China*
[3]*School of Stomatology, Nanchang University, Nanchang 330000, China*

Correspondence should be addressed to Zhiyuan Zhang; zzyent@126.com

Received 15 December 2021; Accepted 17 March 2022; Published 1 April 2022

Academic Editor: Jing Zhong

Background. Although obesity affects human health and cognitive function, the influence of abdominal obesity on cognitive function is still unclear. *Methods*. The MoCA scale was used to evaluate the overall cognitive function and the function of each subitem of 196 subjects, as well as the SDMT and TMT-A scales for evaluating the attention and information processing speed. In addition, radioimmunoassay was used to detect the serum levels of Aβ40, Aβ42, and tau protein in 45 subjects. Subjects were divided into abdominal and nonabdominal obesity groups. Before and after correcting confounding factors, the differences in cognitive scale evaluation indexes and three protein levels between the two groups were compared. We also explore further the correlation between various cognitive abilities and the waist circumference/levels of the three proteins. Linear regression was used to identify the independent influencing factors of various cognitive functions and three protein levels. *Results*. After correcting for multiple factors, we observed the lower scores of visuospatial function, execution, and language in the MoCA scale, as well as higher levels of Aβ40 and tau protein in the abdominal obesity group, supported by the results of correlation analysis. Abdominal obesity was identified as an independent negative influencing factor of MoCA visual space, executive power, and language scores and an independent positive influencing factor of Aβ40, Aβ42, and tau protein levels. *Conclusion*. Abdominal obesity may play a negative role in visuospatial, executive ability, and language function and a positive role in the Aβ40, Aβ42, and tau protein serum levels.

1. Introduction

The pathological manifestations caused by excessive fat content or abnormal fat distribution in the human body are called obesity. Obesity is becoming more and more common worldwide. Between 1980 and 2015, the number of obese children and adults in 73 countries doubled [1]. In 2016, more than 1.9 billion adults, 18 years and older, were overweight. Of these, over 650 million were obese [2]. Projections for 2022 are that the prevalence of obesity may reach 24.8% [3]. The China Health and Nutrition Survey (CHNS) showed that between 1993 and 2009, the prevalence of adult overweight/obesity increased from 13.4% to 26.4%, and the prevalence of adult abdominal obesity increased from 18.6% to 37.4%, which reveals that the prevalence of abdominal obesity is increasing faster than overweight/obesity [4]. Related studies have also found that the body fat distribution of Asian populations is more inclined to abdominal obesity [5].

Obesity is a recognized risk factor for various chronic physical health diseases, including metabolic syndrome, hypertension, cardiovascular disease, diabetes, stroke, and

cancer [6–9]. Compared with general obesity, abdominal obesity has a stronger connection with these chronic diseases [10, 11]. These chronic diseases caused by abdominal obesity have complex and diverse causes, high prevalence, and a long course of the disease, which have also produced a huge burden of disease. Abdominal obesity has become one of the public problems that Chinese adults urgently need to solve.

In addition, obesity is also inextricably linked with neurodegenerative diseases. But the results of research on the effects of obesity on these diseases appear to be ambiguous. For example, some studies have found that obesity can lead to cognitive dysfunction [12, 13], and have identified obesity as an independent influence factor of cognitive function [14]. Studies have also found that obesity is associated with an increased risk of dementia [15]. However, some recent studies failed to find evidence that obesity increases the risk of dementia [16, 17]. Other studies have even found that underweight people are at greater risk, thus intuitively regard obesity as a protective factor for dementia [18, 19]. At present, the measurement effect of body mass index (BMI) on obesity has been proven to be inferior to waist circumference (WC) and waist-to-hip ratio (WHR) by more and more studies [20]. Chelsea et al. also believe that BMI is not a highly sensitive measurement method because it cannot distinguish between fat mass and lean body mass nor does fat distribution. As an alternative measure of obesity, WC can be used to define abdominal obesity and be used in future research related to cognitive function [21]. Therefore, the divergent conclusions about the influence of obesity on cognitive function may be caused by the widespread use of BMI to define obesity. At the same time, the excessive dependence on cross-sectional design and the lack of specificity in assessing the basic areas also contributed to the mixed findings of the impact of obesity on cognition [22]. A few studies have found that abdominal obesity defined by the WHR cut-off value is significantly associated with the risk of cognitive impairment [23, 24]. However, related research on abdominal obesity defined by WC is still lacking.

Alzheimer disease (AD) is a chronic neurodegenerative disease. Its main symptoms include gradual memory decline, cognitive function, and behavioral disorders such as learning, language, and spatial orientation [25]. The typical pathological features of AD are the accumulation of amyloid β-protein (Aβ) outside the cell and excessive tau protein, which leads to amyloid plaques, neurofibrillary tangles, and neuronal apoptosis [26]. Eventually, these lead to cognitive dysfunction. At present, various literature reports have confirmed that Aβ42 in the cerebrospinal fluid of AD patients is increased, and the phosphorylated tau protein is increased. Similarly, Mild Cognitive Impairment (MCI), as a transitional precursor stage from normal aging to dementia [27], has also been linked to the pathological damage mechanism of Aβ and tau protein in many studies. Although obesity is considered an influencing factor of AD [28], there are currently few human studies on the relationship between abdominal obesity/cognitive function of patients with abdominal obesity and Aβ and tau protein [29–31].

Chinese-Beijing Version of Montreal Cognitive Assessment (MoCA-C) is a widely used method to measure cognitive function in Chinese [32]. The Symbol Digit Modalities Test (SDMT) [33, 34] and Trail Making Test-Part A (TMT-A) [35, 36] are two representative tools for assessing general cognitive function. This study is aimed at exploring the effects of abdominal obesity on cognitive function indexes assessed by the MoCA-C, SDMT, and TMT-A scale and the serum levels of Aβ40, Aβ42, and tau protein and the correlation among the three and finally exploring the potential mechanism of action between them.

2. Methods

2.1. Ethical Approval and Participants. This study was approved by the ethics committee of the First Affiliated Hospital of Nanchang University (approval number: 2019-05-051) and was carried out following the Declaration of Helsinki. Subjects were informed of the general content of the study before taking the test, followed the principle of voluntariness, and signed the informed consent form. The inclusion and exclusion criteria of participants are as follows:

Inclusion criteria: (1) the age group being 18-72 years old, (2) the number of years of education ≥ 5 years, (3) being able to fully understand and sign the informed consent form voluntarily, and (4) being able to independently complete tests of various cognitive scales.

Exclusion criteria: (1) having a history of cardiovascular complication severely affecting the body (such as heart failure, severe cerebral infarction, and myocardial infarction), (2) having a history of mental or neurological diseases or a history of psychotropic drug dependence, (3) recently affected the history of neurological brain drugs, (4) drinking alcoholic beverages within 24 hours before receiving relevant tests, (5) being unable to cooperate with the research due to various reasons, (6) missing or incomplete data, (7) pregnant or breastfeeding women, (8) recent major surgery, (9) having the history of participating in clinical research on weight loss or any other weight loss therapy in the past three months, (10) other diseases or reasons unable to cooperate with the research.

2.2. Basic and Human Data Collection. Subject's basic information (gender and age), disease history (diabetes and hypertension), smoking history, and alcohol intake history were collected.

Height, weight, neck circumference (NC), waist circumference (WC), hip circumference (HC), and BMI are measured and assigned readings by the same professional researchers using the same measuring equipment (tape measure, automatic height and weight instrument), based on the WHO standard method. According to the criteria for determining abdominal obesity of Chinese adults: WC ≥ 90 cm for men and WC ≥ 85 cm for women [37].

To reduce the influence of obstructive sleep apnea-hypopnea syndrome (OSAHS) on the final result, Polysomnography (PSG) from professional measurement was always performed at 10 PM and concluded at 6 AM the following day. apnea-hypopnea index (AHI), oxygen-desaturation

index (ODI), lowest oxygen saturation (LSpO2) obtained by PSG were used in this study. According to the standards set by the American Sleep Medicine Association, AHI ≥30 is defined as severe OSAHS [38, 39].

2.3. Cognitive Data Collection. Participants in the study are not allowed to drink strong tea, wine, and coffee within 24 hours and must not have a history of taking sedatives and hypnotic drugs soon. All research results are conducted under the same standard guidance by the same professionally trained personnel. After completing the assessment, the same person analyzes each field's scores and total scores according to the same standards.

Cognitive data can be used for the following neuropsychological tests:

(1) Epworth Sleepiness Scale (ESS): it was used to assess subjective sleepiness [40]

(2) MoCA-C: it includes seven areas of visuospatial and executive, naming, attention, language, abstraction, delayed recall, and orientation [32]

(3) SDMT: referring to a key at the top of the page to translate nonverbal symbols to an alpha-numeric digit, participant filled in boxes (written version) or verbalized the correct digit for each symbol on this timed test. Total correct responses within 90 seconds were measured [33, 34]

(4) TMT-A: this requires an individual to sequence numbers within the format of a visual motor task. This measures processing speed [35, 36].

2.4. Blood Collection, Processing, and Protein Level Determination. After the PSG monitoring, 5 ml of peripheral fasting venous blood was drawn from the subject and centrifuged at 3000 r/min for 10 min within 60 min. The separated serum was stored in a cryotube and immediately frozen at -80°C until a batch determination was performed. Radioimmunoassay (RIA) was used to detect the levels of Aβ40, Aβ42, and tau protein. The operation was carried out in strict accordance with the instructions of the kit (Shanghai Haling Biological Technology Co., Ltd.).

2.5. Statistical Analysis. Use SPSS22.0 software to perform statistical analysis on the data. The measurement data is expressed in terms of $X \pm S$, and the counting data is expressed in frequency and/or percentage. Continuous variables (baseline data such as gender, PSG indicators such as ODI between the two groups of abdominal obesity) used Mann-Whitney U test or t-test according to the distribution characteristics. When comparing the cognitive function assessment indicators and the three protein levels between the two groups, the Mann-Whitney U test or t-test was used when no factor was corrected. The covariance analysis was used when multiple factors were corrected. The corresponding mulberry diagram is drawn by GraphPad prism 9.0.0 (GraphPad Software, La Jolla, California, USA). Categorical variables (including gender, smoking, alcohol consumption history, etc.) use the Chi-square test/Fisher's exact test. Use multiple linear regression analysis to determine the factors affecting cognitive function and the level of each protein content. Spearman's rank correlation analysis between WC and various cognitive function scores, between WC and Aβ40, Aβ42, and tau protein levels, and between various cognitive functions and Aβ40, Aβ42, and tau protein levels, were all based on R software 4.0.3 (R Foundation for Statistical Computing, Vienna, Austria). $P < 0.05$ is considered statistically different.

3. Results

3.1. Association between Abdominal Obesity and MoCA Scores

3.1.1. Comparison of Basic and Human Body Data. After screening by the eligibility criteria, 196 qualified subjects completed the MoCA-C test. The subjects were divided into abdominal obesity ($n = 156$) and nonabdominal obesity ($n = 40$) groups.

In terms of baseline data, the percentages of age, BMI, NC, WC, HC and the proportion of hypertension in the abdominal obesity group were significantly higher than those in the nonabdominal obesity group ($P < 0.05$) (Table 1). There were no significant differences between gender, the proportion of severe OSAHS, the proportion of diabetes, the proportion of smoking, the proportion of alcohol consumption, the years of education, and the ESS score between the two groups ($P \geq 0.05$) (Table 1). In terms of PSG indicators, the AHI and ODI indexes of the obesity group were significantly higher than those of the nonabdominal obesity group, while the LSpO2 of the abdominal obesity group was significantly lower ($P < 0.05$) (Table 1).

3.1.2. Comparison of Each Item Score in MoCA. When no factors are corrected, the visuospatial and executive ability, language, and total MoCA scores of the abdominal obesity group were significantly lower than those of the nonabdominal obesity group (3.85 ± 1.02 vs. 4.45 ± 0.68, $P = 0.001$; 1.99 ± 0.68 vs. 2.43 ± 0.68, $P \leq 0.001$; and 24.53 ± 2.68 vs. 25.65 ± 2.36, $P = 0.030$, respectively). No significant difference was found between the two groups in naming, attention, abstraction, delayed recall, and orientation score ($P \geq 0.05$) (Table 1). After correcting for gender, age, years of education, ESS, severe OSAHS, smoking and alcohol consumption, there were still significant differences in visuospatial and executive ability, and language scores between the two groups ($P^1 = 0.008$ and $P^1 = 0.004$, respectively). And no significant differences in naming, attention, abstraction, delayed recall, orientation total and MoCA scores between the two groups were observed ($P^1 \geq 0.05$) (Table 1).

3.1.3. Correlation between WC and the Various Items Scores of MoCA. These results imply that abdominal obesity is associated with cognitive function. Therefore, we further analyzed the correlation between WC and various cognitive functions. The high negative correlation between WC and visuospatial and executive, and language scores further supports the previous conclusions (Figure 1). But unfortunately, only the language score shows significance ($P < 0.05$).

Table 1: Comparison of baseline characteristics, PSG indicators, and MoCA scores between the nonabdominal obesity and the abdominal obesity groups.

	Nonabdominal obesity ($n = 40$)	Abdominal obesity ($n = 156$)	P	P^1
Gender (female/male)	36/4	137/19	0.085	—
Age (years)	39.75 ± 14.00	43.58 ± 11.36	0.048	—
BMI (kg/m^2)	23.40 ± 2.14	27.86 ± 3.63	0	—
Neck circumference (cm)	37.34 ± 2.50	41.00 ± 3.39	0	—
Waist circumference (cm)	83.04 ± 6.81	99.99 ± 9.15	0	—
Hip circumference (cm)	95.38 ± 4.51	102.71 ± 10.08	0	—
Severe OSAHS, no. (%)	19 (47.5%)	100 (64.1%)	0.055	—
Hypertension, no. (%)	5 (12.5%)	50 (32.1%)	0.014	—
Diabetes, no. (%)	0 (0.0%)	7 (4.5%)	0.348	—
Smoking, no. (%)	18 (45.0%)	75 (48.1%)	0.728	—
Alcohol consumption, no. (%)	23 (57.5%)	73 (46.8%)	0.227	—
Education (years)	12.15 ± 3.77	10.98 ± 3.65	0.055	—
ESS score	9.15 ± 4.59	10.60 ± 5.32	0.102	—
PSG indicator				
AHI	29.47 ± 22.11	44.46 ± 27.60	0.002	—
ODI	25.35 ± 22.80	44.65 ± 30.41	0	—
LSpO2	80.98 ± 9.86	73.54 ± 13.61	0.003	—
MoCA score				
Visuospatial and executive	4.45 ± 0.68	3.85 ± 1.02	0.001	0.008
Naming	2.90 ± 0.30	2.92 ± 0.31	0.45	0.322
Attention	5.87 ± 0.56	5.88 ± 0.51	0.674	0.698
Language	2.43 ± 0.68	1.99 ± 0.68	0	0.004
Abstraction	1.63 ± 0.54	1.49 ± 0.74	0.553	0.947
Delayed recall	2.48 ± 1.41	2.55 ± 1.45	0.85	0.136
Orientation	5.90 ± 0.30	5.85 ± 0.41	0.605	0.667
Total score	25.65 ± 2.36	24.53 ± 2.68	0.03	0.374

P value: comparison of baseline characteristics, PSG indicators, and MoCA scores, without correcting any factors; P^1 value: comparison of the various items and total scores of MoCA score, correcting for the factors of gender, age, years of education, ESS, severe OSAHS, smoking, and alcohol consumption. BMI: body mass index; OSAHS: obstructive sleep apnea-hypopnea syndrome; ESS: Epworth Sleepiness Scale; PSG: polysomnography; AHI: apnea-hypopnea index; ODI: oxygen-desaturation index; LSpO2: lowest oxygen saturation; MoCA: Montreal Cognitive Assessment.

3.1.4. Identification of the Influencing Factors of Some Items Scores in MoCA. Linear regression analysis based on visuospatial and executive, language and total scores, and various potential factors were performed to identify the independent influencing factors of these cognitive functions. Factors used in the linear regression included severe OSAHS, abdominal obesity, gender, age, ESS, smoking, alcohol consumption, and years of education (Table 2).

The independent influencing factors of visuospatial and executive score included abdominal obesity (beta = −0.159, $P = 0.008$) and years of education (beta = −0.523, $P < 0.001$). The only independent influencing factors of language scores was abdominal obesity (beta = −0.201, $P = 0.004$). In addition, severe OSAHS (beta = −0.180, $P = 0.002$), age (beta = −0.261, $P < 0.001$) and years of education (beta = 0.454, $P < 0.001$) were identified as independent influencing factors of the MoCA total score. All the results are shown in Table 2.

3.2. Association between Abdominal Obesity and SDMT/TMT Indicators

3.2.1. Comparison of Basic and Human Body Data. In the SDMT and TMT tests, 161 subjects were qualified. The subjects were divided into abdominal obesity ($n = 126$) and nonabdominal obesity ($n = 35$) groups.

In terms of baseline data, the percentages of BMI, NC, WC, HC, and the proportion of hypertension in the abdominal obesity group were significantly higher than those in the nonabdominal obesity group ($P < 0.05$) (Table 3). However, gender, age, the proportion of severe OSAHS, the proportion of diabetes, the proportion of smoking, the proportion of alcohol consumption, years of education, and ESS score were not significantly different between the two groups ($P \geq 0.05$) (Table 3). In terms of PSG indicators, the AHI and ODI indicators of the abdominal obesity group were significantly higher than those of the nonabdominal obesity group, while

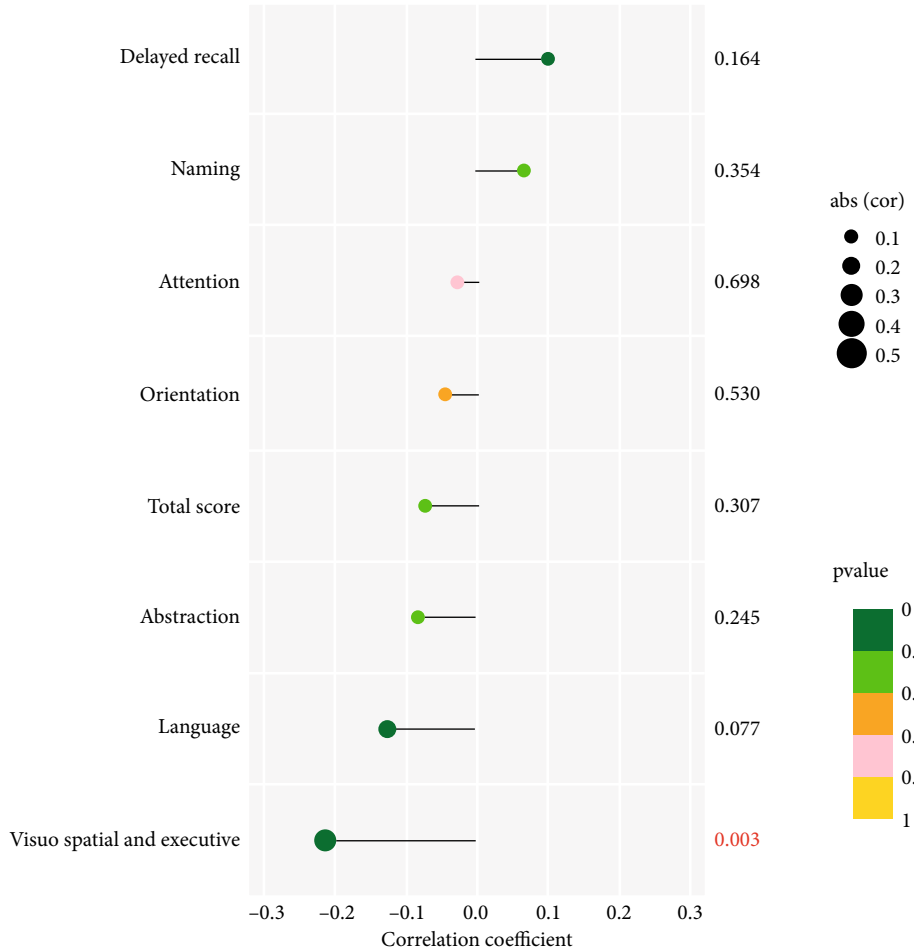

Figure 1: The correlation between WC and the various items of MoCA. The number closely connected to the label of each lollipop shows the corresponding *P* value displayed in different colors. The different sizes of each lollipop ball represent different correlation coefficients.

Table 2: Linear regression analysis based on various potential influencing factors and MoCA scores of some items.

		Severe OSAHS	Abdominal obesity	Gender	Age	ESS	Smoking	Alcohol consumption	Education
Visuospatial and executive	Beta	-0.070	-0.159	-0.032	-0.063	-0.029	0.014	-0.003	0.523
	P	0.265	0.008	0.618	0.305	0.643	0.837	0.962	<0.001
Language	Beta	-0.048	-0.201	-0.092	-0.141	-0.092	-0.004	-0.050	0.140
	P	0.506	0.004	0.223	0.051	0.213	0.961	0.526	0.071
Total score	Beta	-0.180	-0.050	-0.073	-0.261	-0.044	-0.047	-0.040	0.454
	P	0.002	0.374	0.225	<0.001	0.462	0.471	0.537	<0.001

ESS: Epworth Sleepiness Scale.

the LSpO2 of the abdominal obesity group was significantly lower than that of the nonabdominal obesity group ($P < 0.05$) (Table 3).

3.2.2. Comparison of SDMT/TMT Indicators. When no factors were corrected, there was no significant difference in SDMT and TMT indicators between the two groups (both $P \geq 0.05$) (Table 3). After correcting for gender, age, years of education, ESS, severe OSAHS, smoking and alcohol consumption, there was still no significant difference in SDMT and TMT indicators between the two groups ($P^1 > 0.05$) (Table 3).

3.2.3. Correlation between WC and SDMT/TMT Indicators. Although no significant difference was found, the correlation between WC and SDMT/TMT indicators was still further

Table 3: Comparison of baseline characteristics, PSG indicators, SDMT, and TMT between nonabdominal obesity and abdominal obesity groups.

	Nonabdominal obesity ($n = 35$)	Abdominal obesity ($n = 126$)	P	P^1
Gender (female/male)	32/3	109/17	0.569	—
Age (years)	40.71 ± 14.80	43.44 ± 11.56	0.171	—
BMI (kg/m^2)	22.48 ± 2.08	27.93 ± 3.66	0	—
Neck circumference (cm)	36.69 ± 2.43	41.07 ± 3.40	0	—
Waist circumference (cm)	81.71 ± 7.15	99.75 ± 9.01	0	—
Hip circumference (cm)	93.83 ± 5.27	102.43 ± 10.63	0	—
Severe OSAHS, no. (%)	17 (48.6%)	81 (64.3%)	0.092	—
Hypertension, no. (%)	1 (2.9%)	30 (23.8%)	0.005	—
Diabetes, no. (%)	0 (0.0%)	2 (1.6%)	1	—
Smoking, no. (%)	17 (48.6%)	69 (54.8%)	0.516	—
Alcohol consumption, no. (%)	19 (54.3%)	51 (40.5%)	0.145	—
Education (years)	11.13 ± 3.67	10.13 ± 3.33	0.126	—
ESS score	9.26 ± 4.38	10.71 ± 4.87	0.091	—
PSG indicator				
AHI	28.89 ± 21.92	45.03 ± 28.43	0.003	—
ODI	23.30 ± 23.13	45.38 ± 31.70	0	—
LSpO2	81.97 ± 10.37	73.51 ± 13.22	0.001	—
Attention and information processing speed				
SDMT (correct number)	48.46 ± 12.62	44.99 ± 15.28	0.256	0.808
TMT (time consumption)	42.26 ± 13.36	49.11 ± 21.66	0.144	0.467

P value: compare baseline characteristics and PSG, SDMT, and TMT indicators, without correcting any factors; P^1 value: comparing SDMT and TMT indicators, correcting for the gender, age, years of education, ESS, severe OSAHS, smoking, and alcohol consumption factors. BMI: body mass index; OSAHS: obstructive sleep apnea-hypopnea syndrome; ESS: Epworth Sleepiness Scale; PSG: polysomnography; AHI: apnea-hypopnea index; ODI: oxygen-desaturation index; LSpO2: lowest oxygen saturation; MoCA: Montreal Cognitive Assessment; SDMT: Symbol Digit Modalities Test; TMT: Trail Making Test.

analyzed. Unfortunately, we still have not observed a significant result ($P \geq 0.05$, Figure 2).

3.3. Association between Aβ40, Aβ42, and Tau Protein Levels and Abdominal Obesity

3.3.1. Comparison of Basic and Human Body Data. The subjects ($n = 45$) were divided into abdominal obesity ($n = 34$) and nonabdominal obesity ($n = 11$). In terms of baseline data, the BMI, NC, WC, and HC of the abdominal obesity group were significantly higher (all $P < 0.05$) (Table 4). However, the proportion of gender, age, the proportion of gender severe OSAHS, the proportion of gender hypertension, the proportion of gender alcohol consumption, the proportion of gender smoking, years of education, and ESS score were not significantly different between the two groups (P both ≥0.05) (Table 4). In terms of PSG indicators, AHI, ODI and LSpO2 were not significantly different between the two groups ($P \geq 0.05$) (Table 4).

3.3.2. Comparison of the Levels of Aβ40, Aβ42, and Tau Protein. Before and after correcting gender, age, years of education, ESS score, severe OSAHS, smoking and alcohol consumption, the levels of Aβ40, Aβ42, and tau protein in the abdominal obesity group were significantly higher than those in the non-to-moderate OSAHS group (279.47 ± 108.93 vs. 166.98 ± 94.56, $P = 0.004$, $P^1 = 0.001$; 203.44 ± 86.52 vs. 141.62 ± 77.18, $P = 0.048$, $P^1 = 0.006$; and 32.62 ± 16.08 vs. 17.29 ± 14.26, $P = 0.008$, $P^1 = 0.004$, respectively) (Figures 3(a)–3(c)).

3.3.3. Correlation between WC and Aβ40, Aβ42, and Tau Protein Levels. In Figure 4(c), a significant positive correlation between tau protein level and WC can be observed. Although not significant, a positive correlation trend can still be observed between WC and Aβ40 and Aβ42 protein levels (both $P \geq 0.05$, Figures 4(a) and 4(b)).

3.3.4. Identification of the Influencing Factors of Aβ40, Aβ42, and Tau Protein Levels. Table 5 shows all results of multiple linear regression based on Aβ40, Aβ42, and tau protein levels and various potential factors. Independent influencing factors of Aβ40 protein level include severe OSAHS (beta = −0.355, $P = 0.011$), abdominal obesity (beta = 0.481, $P = 0.001$) and alcohol consumption (beta = −0.430, $P = 0.013$). Abdominal obesity (beta = 0.410, $P = 0.006$) and smoking (beta = 0.395, $P = 0.045$) were identified as independent influencing factors of Aβ42 protein level. The only independent factor influencing tau protein level was abdominal obesity (beta = 0.450, $P = 0.004$). Surprisingly, abdominal obesity has been identified as an independent factor affecting the levels of all three proteins.

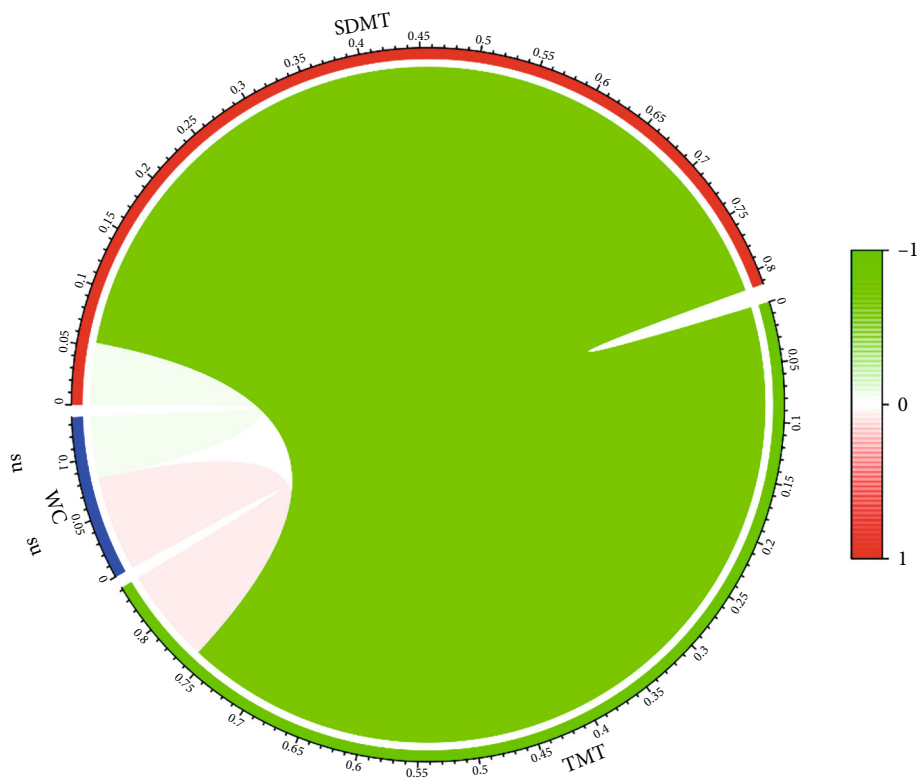

Figure 2: The correlation between WC and SDMT/TMT indicators. The legend of the circle graph shows the correlation coefficients corresponding to different colors. Above the circle: ns: no significance.

3.4. Association between Aβ40, Aβ42 and Tau Protein Levels and Cognitive Functions. To verify the close correlation between cognitive functions and Aβ40, Aβ42 and tau protein levels, we reran the correlation analysis between them. Unfortunately, only significant negative correlations were observed between Aβ40/Aβ42 protein level and language scores (Figure 5). Even though the other results did not show significance, they still provided a lot of valuable information. Except for naming and TMT, the level of Aβ40 protein is negatively correlated with other project indicators. Except for naming, orientation and TMT, the level of Aβ42 protein is also negatively associated with other project indicators. In addition, TMT indicator has been observed positively correlated with the three protein levels. The opposite results were found in the SDMT indicator.

4. Discussion

Cognition is the intelligent process of body recognition and knowledge acquisition. It involves a series of psychological and social behaviors, such as learning, memory, language, thinking, spirit, and emotion. Executive function refers to a person's ability to respond adaptively to situations and successfully engage in independent, purposeful, and self-service behaviors, the foundation of many cognitive, social, and emotional skills [41].

Because obesity is closely related to OSAHS [42], about 40% to 70% of obese people are diagnosed with OSAHS [43, 44]. Obesity is considered one of the most critical risk factors for OSAHS [45]. In addition, through a meta-analysis of previous research systems, Bucks et al. found that most studies support OSAHS patients' deficits in attention/alertness, delayed long-term visual and language memory, visuospatial/structural abilities, and deficits in executive function [46]. Therefore, it is necessary to correct OSAHS, an important factor of cognitive function. To reduce the impact of other potential influencing factors on the research results, we also performed corrections for cognitive impairment risk factors (including age, gender, abdominal obesity, smoking, alcohol consumption, years of education, and ESS score) [47].

Before and after correcting the related influencing factors, lower visual space and execution and language scores were found in the abdominal obesity group, which was also supported by the negative correlation between WC and these two MoCA scores in our study. Conversely, Aβ40, Aβ42, and tau protein levels in the abdominal obesity group were higher than those in the nonabdominal obesity group, also supported by the corresponding correlation results. Not only that, abdominal obesity has also been identified as an independent negative factor of visual space and execution and language scores, as well as an independent positive factor of Aβ40, Aβ42, and tau protein levels in further regression analysis. The above results all imply that abdominal obesity may significantly negatively affect the visual space and execution and language ability of the subject and increase the Aβ40, Aβ42, and tau protein levels of the subject. Our regression analysis also found that age negatively affects

Table 4: Comparison of baseline characteristics, PSG indicator, and protein levels between nonabdominal obesity and abdominal obesity groups.

	Nonabdominal obesity ($n = 11$)	Abdominal obesity ($n = 34$)	P	P^1
Gender (female/male)	8/3	26/8	1	—
Age (years)	48.18 ± 18.79	40.27 ± 13.51	0.161	—
BMI (kg/m^2)	22.44 ± 2.61	29.31 ± 3.91	0	—
Neck circumference (cm)	36.14 ± 2.65	40.82 ± 3.49	0	—
Waist circumference (cm)	81.96 ± 6.92	100.12 ± 11.97	0	—
Hip circumference (cm)	90.64 ± 7.72	102.00 ± 18.12	0	—
Severe OSAHS, no. (%)	3 (27.3%)	16 (47.1%)	0.309	—
Hypertension, no. (%)	0 (0.0%)	7 (20.6%)	0.168	—
Diabetes, no. (%)	0 (0.0%)	0 (0.0%)	—	—
Smoking, no. (%)	7 (63.6%)	14 (41.2%)	0.194	—
Alcohol consumption, no. (%)	7 (63.6%)	11 (32.4%)	0.086	—
Education (years)	7.64 ± 4.06	9.82 ± 3.86	0.118	—
ESS score	10.18 ± 4.02	10.71 ± 4.09	0.73	—
PSG indicator				
AHI	20.53 ± 23.71	35.86 ± 33.06	0.154	—
ODI	19.55 ± 24.45	35.54 ± 35.76	0.166	—
LSpO2	81.16 ± 14.62	75.24 ± 14.99	0.149	—
Protein level				
Aβ40	166.98 ± 94.56	279.47 ± 108.93	0.004	0.001
Aβ42	141.62 ± 77.18	203.44 ± 86.52	0.048	0.006
Tau	17.29 ± 14.26	32.62 ± 16.08	0.008	0.004

P value: compare baseline characteristics, PSG indicator, and Aβ40, Aβ42, and tau protein levels, without correcting any factors; P^1 value: compare protein levels, correcting for gender, age, years of education, ESS, severe OSAHS, smoking, and alcohol consumption factors. BMI: body mass index; OSAHS: obstructive sleep apnea-hypopnea syndrome; ESS: Epworth Sleepiness Scale; PSG: polysomnography; AHI: apnea-hypopnea index; ODI: oxygen-desaturation index; LSpO2: lowest oxygen saturation.

delayed recall, overall cognitive attention, and information processing speed. The years of education have also been found to be a positive factor in visual space and execution, abstraction, overall cognition, attention, and information processing speed capabilities.

Few studies focus on the relationship between obesity and cognitive function. It is generally believed that obese subjects usually exhibit deficits in memory, learning, and executive function in the previous study. Moreover, various indicators of obesity, including BMI, WHR, and WC, have also been shown to impair overall cognitive function, learning, memory, and language ability [48]. This study explored the influence of abdominal obesity judged by WC on the cognitive field, which has carried out a deeper exploration in related fields. The worse visual space and executive and language skills observed in the abdominal obesity group supported the views in the literature. In addition to obesity and OSAHS, normal human aging can also change some areas of cognition, such as processing speed, attention, context, and working memory, and rarely affects language ability and recognition memory [49]. Our results are also consistent with previous research results. With age, performance in the areas of delayed recall, overall cognition, attention, and information processing speed decreases.

At present, inflammation, gut-brain axis, and insulin resistance are considered the main mechanisms of obesity in impairing cognitive function. Inflammation is the ultimate common pathway of these mechanisms [26, 50]. First, a long-term high-fat diet can cause increased proinflammatory and inflammatory cytokines in the blood [51]. These factors can increase blood-brain barrier penetration and transport dysfunction [52]. The lesions of the blood-brain barrier directly affect the lateral hypothalamic nucleus and the preoptic area to produce behavioral and mental abnormalities [53] and affect the dorsal hippocampus to cause learning and memory decline [54]. After inflammatory factors enter the brain through the blood-brain barrier, they can further induce a series of inflammatory damage and apoptosis of different types of nerve cells to affect cognitive function [55]. The brain-gut axis mainly affects cognitive function through immune activation, intestinal permeability, intestinal endocrine, and neural signal pathways. Dietary saturated fatty acids can activate Toll-like receptors (TLR) expressed in the intestinal epithelium and innate immune cells [56]. TLR2 activates the conduction cascade to amplify the inflammatory response [57, 58], and TLR4 activates the upregulation of proinflammatory cytokines to trigger brain inflammation [59]. Intestinal flora imbalance may also affect brain development and

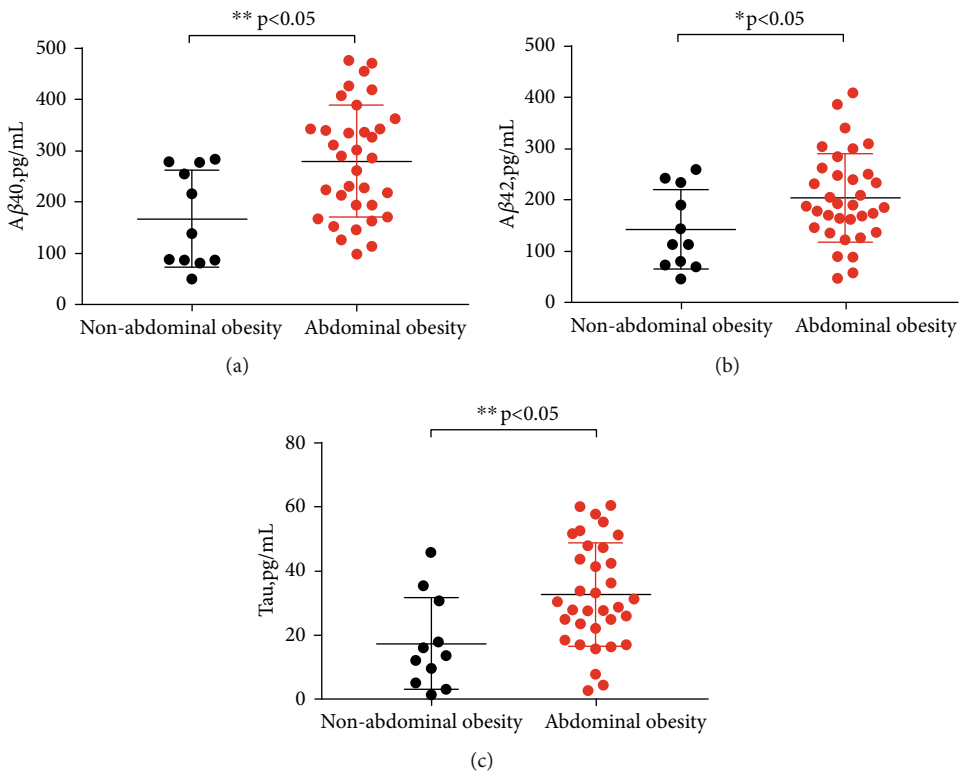

Figure 3: Comparison of Aβ40, Aβ42, and tau protein levels between nonabdominal obesity and abdominal obesity groups, respectively. (a) Aβ40. (b) Aβ42. (c) Tau. Before P: $*$ means $P < 0.05$; $**$ means $P < 0.01$.

plasticity by affecting neurotrophins (BDNF) and neurotransmitters (5HT, GABA, etc.), thereby impairing cognitive functions such as memory. Finally, insulin plays an active role in cognition and memory as a neuromodulator and neuroprotective agent in the brain [60, 61]. Excessive free fatty acids in obesity can increase the release of proinflammatory cytokines in the blood [62]. These cytokines not only activate the phosphorylation of insulin receptor substrate (insulin receptor substrate-1 (IRS-1)) at the serine site (normally the tyrosine site) but also activates other inflammation-related negative regulators (such as inhibitors of cytokine signal transduction) in the IRS protein to inhibit cell insulin signal transduction in target organs and cause insulin resistance [63]. In addition, obesity-induced oxidative stress and hyperglycemia lead to mitochondrial dysfunction, generating peripheral insulin resistance [64, 65]. Peripheral insulin resistance can also induce brain inflammation, oxidative stress, and insulin resistance through ceramide production in the liver, leading to neurodegeneration and cognitive impairment [66]. These potential biological processes may explain the worse visual space, execution, and language ability in subjects with abdominal obesity.

Tau protein, a kind of microtubule-associated protein, is necessary for normal neuronal activity [19]. However, under pathological conditions, certain phosphorous sites of tau protein can bind to phosphoric acid and undergo abnormal hyperphosphorylation to form p-tau protein. The p-tau protein makes the microtubule-binding region self-associate and causes abnormal entanglement of microtubule spiral filaments, forming neurofibrillary tangles [18]. The function of Aβ is to maintain neuron growth, synaptic activity, and survival at low levels [20]. However, at sufficiently high levels, Aβ forms aggregates. Eventually, nerve fiber plaques are formed [22]. The systemic inflammation of obesity can promote the production of Aβ, which may be one of the pathogenesis of AD. Peripheral insulin resistance and hyperinsulinemia will increase peripheral free fatty acid levels, and peripheral and central TNF-α levels will also increase, thereby reducing and clearing Aβ through the liver, leading to increased peripheral Aβ levels [67, 68]. High levels of Aβ in plasma interfere with the transfer of Aβ from the brain to the periphery, thereby increasing its transfer to the brain. As a result, the release of Aβ from nerve cells is inhibited. The decrease in insulin-degrading enzyme levels in obese individuals also aggravated the deposition of Aβ in neurons. Therefore, accumulation results from a variety of pathological mechanisms, such as increased Aβ production, peripheral clearance dysfunction, and increased brain inflammation, may lead to memory deficits and even AD. Perhaps these underlying processes can explain the upregulation of Aβ40, Aβ42, and tau protein levels in subjects with abdominal obesity and the negative correlation between various cognitive functions and these protein levels observed in our research.

Although not many significant results have been found, there is no doubt that we have expanded the few researches in the relevant fields. Considering that our research is based on large sample testing, highly sensitive and specific protein detection technology (RIA), and multiple and complex analysis methods, the results obtained have a high degree of credibility. But unfortunately, the limited number of blood samples could

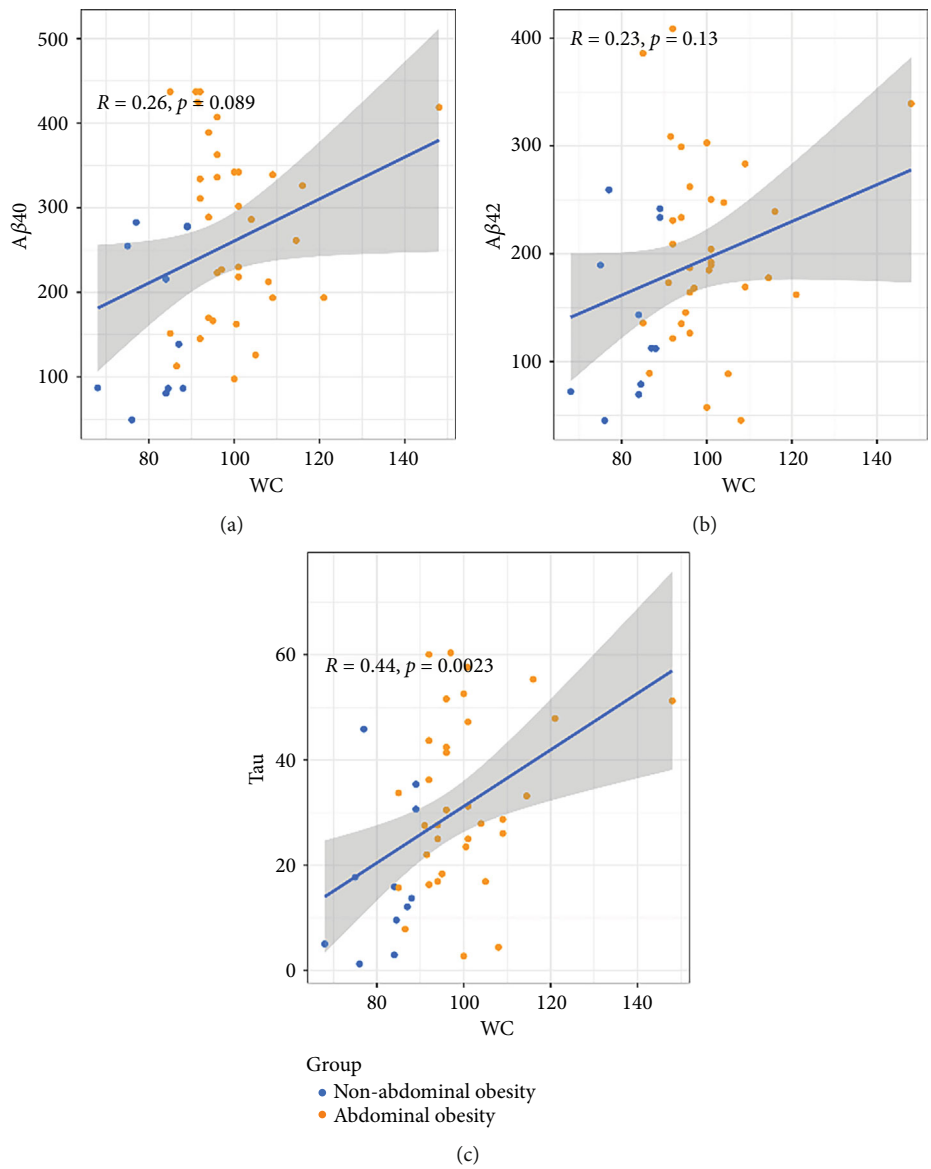

Figure 4: The correlation between WC and Aβ40, Aβ42, and tau protein levels, respectively. (a) Aβ40. (b) Aβ42. (c) Tau. *R* represents the coefficient of correlation.

Table 5: Linear regression analysis based on Aβ40, Aβ42, and tau protein levels and various potential influencing factors.

		Severe OSAHS	Abdominal obesity	Gender	Age	ESS	Smoking	Alcohol consumption	Education
Aβ40	Beta	-0.355	0.481	-0.316	0.149	-0.149	0.343	-0.43	-0.074
	P	0.011	0.001	0.06	0.294	0.279	0.058	0.013	0.621
Aβ42	Beta	-0.198	0.41	-0.236	0.222	-0.047	0.395	-0.27	-0.099
	P	0.176	0.006	0.191	0.154	0.753	0.045	0.141	0.546
Tau	Beta	-0.09	0.45	-0.288	0.308	0.058	0.042	-0.222	-0.154
	P	0.547	0.004	0.123	0.058	0.703	0.831	0.238	0.36

ESS: Epworth Sleepiness Scale.

easily amplify the chance of type II error and lead to inaccurate results. The shortcomings of the cross-sectional study and the limited data sources may cause some deficiencies in this study. As a commonly used scale, MoCA still has many shortcomings, such as limited cognitive domains and poor specificity and sensitivity, leading to deviations in our results. Although many subjects were recruited in our study, more significant and reliable results still require a larger sample size to support. Although

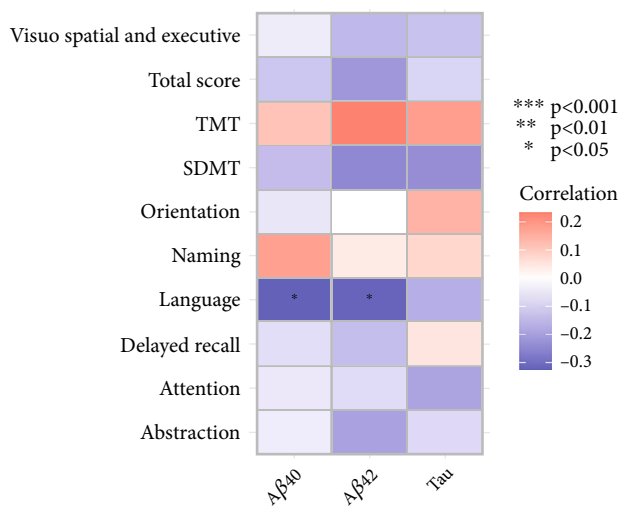

Figure 5: The correlation between Aβ40, Aβ42, and tau protein levels and various cognitive function indicators.

some factors that may affect cognitive function have been adjusted, it is difficult for us to correct the interference of other confounding factors, such as APOE4 genotype and tester's experience. Due to the limitations of clinical conditions, this study failed to collect more sensitive cerebrospinal fluid to determine related protein levels. Limited experimental conditions also limit us to explore deeper mechanisms combined with more basic experiments.

Abbreviations

CHNS: The China Health and Nutrition Survey
WC: Waist circumference
WHR: Waist-to-hip ratio
AD: Alzheimer disease
Aβ: Amyloid β-protein
MCI: Mild cognitive impairment
NC: Neck circumference
HC: Hip circumference
OSAHS: Obstructive sleep apnea-hypopnea syndrome
PSG: Polysomnography
AHI: Apnea-hypopnea index
ODI: Oxygen-desaturation index
LSpO2: Lowest oxygen saturation
ESS: Epworth Sleepiness Scale
MoCA-C: Chinese-Beijing Version of Montreal Cognitive Assessment
SDMT: Symbol Digit Modalities Test
TMT-A: Trail Making Test-Part A
RIA: Radioimmunoassay
TLR: Toll-like receptors
DAMPs: Damage-related molecular patterns
BDNF: Neurotrophins.

Data Availability

The data in this study were from the Department of Otolaryngology Head and Neck Surgery, The First Affiliated Hospital of Nanchang University.

Conflicts of Interest

The authors declare that there is no conflict of interest.

Authors' Contributions

Xin Fan and Zhiyuan Zhang designed the research. Xin Fan prepared the figures and drafted the manuscript. Xin Fan analyzed the data, Xin Fan contributed analytic tools and finalized the manuscript. Xin Fan, Yun Zhong, Lingling Zhang, Jiaqi Li, Fei Xie, and Zhiyuan Zhang participated in the writing of the manuscript. All authors have read and approved the final manuscript.

Acknowledgments

The authors sincerely thank all the participants and acknowledge the support from the Research Fund Project of Jiangxi Provincial Department of Education (180017).

References

[1] The GBD 2015 Obesity Collaborators, "Health effects of overweight and obesity in 195 countries over 25 years," *The New England Journal of Medicine*, vol. 377, no. 1, pp. 13–27, 2017.

[2] World Health Organization, "Obesity and overweight," December 2020, https://www.who.int/en/newsroom/fact-sheets/detail/obesity-and-overweight.

[3] P. N. Gondim, P. V. Rosa, D. Okamura et al., "Benefits of fish oil consumption over other sources of lipids on metabolic parameters in obese rats," *Nutrients*, vol. 10, no. 1, p. 65, 2018.

[4] L. Hu, X. Huang, C. You et al., "Prevalence of overweight, obesity, abdominal obesity and obesity-related risk factors in southern China," *PLoS One*, vol. 12, no. 9, article e0183934, 2017.

[5] R. M. Harper, R. Kumar, P. M. Macey, M. A. Woo, and J. A. Ogren, "Affective brain areas and sleep-disordered breathing," *Progress in Brain Research*, vol. 209, pp. 275–293, 2014.

[6] P. G. Kopelman, "Obesity as a medical problem," *Nature*, vol. 404, no. 6778, pp. 635–643, 2000.

[7] V. J. Lawrence and P. G. Kopelman, "Medical consequences of obesity," *Clinics in Dermatology*, vol. 22, no. 4, pp. 296–302, 2004.

[8] G. A. Bray, "Medical consequences of obesity," *The Journal of Clinical Endocrinology and Metabolism*, vol. 89, no. 6, pp. 2583–2589, 2004.

[9] T. J. Oh, J. H. Moon, S. H. Choi et al., "Body-weight fluctuation and incident diabetes mellitus, cardiovascular disease, and mortality: a 16-year prospective cohort study," *The Journal of Clinical Endocrinology and Metabolism*, vol. 104, no. 3, pp. 639–646, 2019.

[10] J. P. Reis, C. A. Macera, M. R. Araneta, S. P. Lindsay, S. J. Marshall, and D. L. Wingard, "Comparison of overall obesity and body fat distribution in predicting risk of mortality," *Obesity*, vol. 17, no. 6, pp. 1232–1239, 2009.

[11] R. Anari, R. Amani, S. M. Latifi, M. Veissi, and H. Shahbazian, "Association of obesity with hypertension and dyslipidemia in type 2 diabetes mellitus subjects," *Diabetes and Metabolic Syndrome: Clinical Research and Reviews*, vol. 11, no. 1, pp. 37–41, 2017.

[12] A. Rolls, D. Colas, A. Adamantidis et al., "Optogenetic disruption of sleep continuity impairs memory consolidation," *Proceedings of the National Academy of Sciences of the United States of America*, vol. 108, no. 32, pp. 13305–13310, 2011.

[13] S. Naismith, V. Winter, H. Gotsopoulos, I. Hickie, and P. Cistulli, "Neurobehavioral functioning in obstructive sleep apnea: differential effects of sleep quality, hypoxemia and subjective sleepiness," *Journal of Clinical and Experimental Neuropsychology*, vol. 26, no. 1, pp. 43–54, 2004.

[14] J. L. Tartar, C. P. Ward, J. T. McKenna et al., "Hippocampal synaptic plasticity and spatial learning are impaired in a rat model of sleep fragmentation," *The European Journal of Neuroscience*, vol. 23, no. 10, pp. 2739–2748, 2006.

[15] D. E. Barnes and K. Yaffe, "The projected effect of risk factor reduction on Alzheimer's disease prevalence," *The Lancet*, vol. 10, no. 9, pp. 819–828, 2011.

[16] A. K. D. Aslan, J. M. Starr, A. Pattie, and I. Deary, "Cognitive consequences of overweight and obesity in the ninth decade of life?," *Age and Ageing*, vol. 44, no. 1, pp. 59–65, 2015.

[17] E. Albanese, B. Davis, P. V. Jonsson et al., "Overweight and obesity in midlife and brain structure and dementia 26 years later: the AGES-Reykjavik study," *American Journal of Epidemiology*, vol. 181, no. 9, pp. 672–679, 2015.

[18] B. S. Aribisala, M. C. Valdés Hernández, N. A. Royle et al., "Brain atrophy associations with white matter lesions in the ageing brain: the Lothian Birth Cohort 1936," *European Radiology*, vol. 23, no. 4, pp. 1084–1092, 2013.

[19] A. Harada, K. Oguchi, S. Okabe et al., "Altered microtubule organization in small-calibre axons of mice lacking *tau* protein," *Nature*, vol. 369, no. 6480, pp. 488–491, 1994.

[20] M. S. Parihar and G. J. Brewer, "Amyloid-β as a modulator of synaptic plasticity," *Journal of Alzheimer's Disease*, vol. 22, no. 3, pp. 741–763, 2010.

[21] A.-A. Baril, J. Carrier, A. Lafrenière et al., "Biomarkers of dementia in obstructive sleep apnea," *Sleep Medicine Reviews*, vol. 42, pp. 139–148, 2018.

[22] M. A. Daulatzai, "Evidence of neurodegeneration in obstructive sleep apnea: relationship between obstructive sleep apnea and cognitive dysfunction in the elderly," *Journal of Neuroscience Research*, vol. 93, no. 12, pp. 1778–1794, 2015.

[23] L. Xie, H. Kang, Q. Xu et al., "Sleep drives metabolite clearance from the adult brain," *Science*, vol. 342, no. 6156, pp. 373–377, 2013.

[24] Y.-E. S. Ju, S. J. Ooms, C. Sutphen et al., "Slow wave sleep disruption increases cerebrospinal fluid amyloid-β levels," *Brain*, vol. 140, no. 8, pp. 2104–2111, 2017.

[25] "2021 Alzheimer's disease facts and figures," *Alzheimer's & Dementia*, vol. 17, no. 3, pp. 327–406, 2021.

[26] M. Solas, F. I. Milagro, M. J. Ramírez, and J. A. Martínez, "Inflammation and gut-brain axis link obesity to cognitive dysfunction: plausible pharmacological interventions," *Current Opinion in Pharmacology*, vol. 37, pp. 87–92, 2017.

[27] Y. H. Jung, S. Park, H. Jang et al., "Frontal-executive dysfunction affects dementia conversion in patients with amnestic mild cognitive impairment," *Scientific Reports*, vol. 10, no. 1, p. 772, 2020.

[28] C. Coisne and B. Engelhardt, "Tight junctions in brain barriers during central nervous system inflammation," *Antioxidants & Redox Signaling*, vol. 15, no. 5, pp. 1285–1303, 2011.

[29] E. Smith, P. Hay, L. Campbell, and J. N. Trollor, "A review of the association between obesity and cognitive function across the lifespan: implications for novel approaches to prevention and treatment," *Obesity Reviews*, vol. 12, no. 9, pp. 740–755, 2011.

[30] M. Loef and H. Walach, "Midlife obesity and dementia: meta-analysis and adjusted forecast of dementia prevalence in the United States and China," *Obesity*, vol. 21, no. 1, pp. E51–E55, 2013.

[31] W. L. Xu, A. R. Atti, M. Gatz, N. L. Pedersen, B. Johansson, and L. Fratiglioni, "Midlife overweight and obesity increase late-life dementia risk: a population-based twin study," *Neurology*, vol. 76, no. 18, pp. 1568–1574, 2011.

[32] X. Chen, R. Zhang, Y. Xiao, J. Dong, X. Niu, and W. Kong, "Reliability and validity of the Beijing version of the Montreal Cognitive Assessment in the evaluation of cognitive function of adult patients with OSAHS," *PLoS One*, vol. 10, no. 7, 2015.

[33] S. Aaron, *Symbol Digit Modalities Test (SDMT)*, Western psychological services, LA, USA, 1982.

[34] H. S. Levin, X. Li, S. R. McCauley, G. Hanten, E. A. Wilde, and P. Swank, "Neuropsychological outcome of mTBI: a principal component analysis approach," *Journal of Neurotrauma*, vol. 30, no. 8, pp. 625–632, 2013.

[35] C. R. Bowie and P. D. Harvey, "Administration and interpretation of the Trail Making Test," *Nature Protocols*, vol. 1, no. 5, pp. 2277–2281, 2006.

[36] M. A. R. Hodge, D. Siciliano, P. Withey et al., "A randomized controlled trial of cognitive remediation in schizophrenia," *Schizophrenia Bulletin*, vol. 36, no. 2, pp. 419–427, 2010.

[37] "Chinese guidelines on prevention and treatment of dyslipidemia in adults," *Zhonghua Xin Xue Guan Bing Za Zhi*, vol. 35, no. 5, pp. 390–419, 2007.

[38] R. K. Malhotra, D. B. Kirsch, D. A. Kristo et al., "Polysomnography for obstructive sleep apnea should include arousal-based scoring: an American Academy of Sleep Medicine position statement," *Journal of Clinical Sleep Medicine*, vol. 14, no. 7, pp. 1245–1247, 2018.

[39] R. B. Berry, R. Budhiraja, D. J. Gottlieb, D. Gozal, C. Iber, V. K. Kapur et al., "Rules for scoring respiratory events in sleep: update of the 2007 AASM Manual for the Scoring of Sleep and Associated Events. Deliberations of the Sleep Apnea Definitions Task orce of the American Academy of Sleep Medicine," *Journal of Clinical Sleep Medicine*, vol. 8, pp. 597–619, 2012.

[40] A. Alterki, S. Joseph, T. A. Thanaraj et al., "Targeted metabolomics analysis on obstructive sleep apnea patients after multilevel sleep surgery," *Metabolites*, vol. 10, no. 9, p. 358, 2020.

[41] T. Saunamäki, S.-L. Himanen, O. Polo, and M. Jehkonen, "Executive dysfunction in patients with obstructive sleep apnea syndrome," *European Neurology*, vol. 62, no. 4, pp. 237–242, 2009.

[42] A. S. Gami, S. M. Caples, and V. K. Somers, "Obesity and obstructive sleep apnea," *Endocrinology and Metabolism Clinics of North America*, vol. 32, no. 4, pp. 869–894, 2003.

[43] T. Young, L. Finn, P. E. Peppard et al., "Sleep disordered breathing and mortality: eighteen-year follow-up of the Wisconsin sleep cohort," *Sleep*, vol. 31, no. 8, pp. 1071–1078, 2008.

[44] P. P. Lopez, B. Stefan, C. I. Schulman, and P. M. Byers, "Prevalence of sleep apnea in morbidly obese patients who presented for weight loss surgery evaluation: more evidence for routine screening for obstructive sleep apnea before weight loss surgery," *The American Surgeon*, vol. 74, no. 9, pp. 834–838, 2008.

[45] C. E. Ievers-Landis and S. Redline, "Pediatric sleep apnea: implications of the epidemic of childhood overweight," *American Journal of Respiratory and Critical Care Medicine*, vol. 175, no. 5, pp. 436–441, 2007.

[46] R. S. Bucks, M. Olaithe, and P. Eastwood, "Neurocognitive function in obstructive sleep apnoea: a meta-review," *Respirology*, vol. 18, no. 1, pp. 61–70, 2013.

[47] C. Lal, C. Strange, and D. Bachman, "Neurocognitive impairment in obstructive sleep apnea," *Chest*, vol. 141, no. 6, pp. 1601–1610, 2012.

[48] J. Gunstad, A. Lhotsky, C. R. Wendell, L. Ferrucci, and A. B. Zonderman, "Longitudinal examination of obesity and cognitive function: results from the Baltimore longitudinal study of aging," *Neuroepidemiology*, vol. 34, no. 4, pp. 222–229, 2010.

[49] A. Mathieu, S. Mazza, A. Décary et al., "Effects of obstructive sleep apnea on cognitive function: a comparison between younger and older OSAS patients," *Sleep Medicine*, vol. 9, no. 2, pp. 112–120, 2008.

[50] S.-J. Leigh and M. J. Morris, "Diet, inflammation and the gut microbiome: mechanisms for obesity-associated cognitive impairment," *Biochimica et Biophysica Acta - Molecular Basis of Disease*, vol. 1866, no. 6, 2020.

[51] M. L. Alosco and J. Gunstad, "The negative effects of obesity and poor glycemic control on cognitive function: a proposed model for possible mechanisms," *Current Diabetes Reports*, vol. 14, no. 6, p. 495, 2014.

[52] B. Obermeier, R. Daneman, and R. M. Ransohoff, "Development, maintenance and disruption of the blood-brain barrier," *Nature Medicine*, vol. 19, no. 12, pp. 1584–1596, 2013.

[53] J. P. Thaler, C.-X. Yi, E. A. Schur et al., "Obesity is associated with hypothalamic injury in rodents and humans," *The Journal of Clinical Investigation*, vol. 122, no. 1, pp. 153–162, 2012.

[54] S. E. Kanoski and H. J. Grill, "Hippocampus contributions to food intake control: mnemonic, neuroanatomical, and endocrine mechanisms," *Biological Psychiatry*, vol. 81, no. 9, pp. 748–756, 2017.

[55] J. C. Moraes, A. Coope, J. Morari et al., "High-fat diet induces apoptosis of hypothalamic neurons," *PLoS One*, vol. 4, no. 4, p. e5045, 2009.

[56] D. H. Hwang, J.-A. Kim, and J. Y. Lee, "Mechanisms for the activation of Toll-like receptor 2/4 by saturated fatty acids and inhibition by docosahexaenoic acid," *European Journal of Pharmacology*, vol. 785, pp. 24–35, 2016.

[57] J. H. Hayward and S. J. Lee, "A decade of research on TLR2 discovering its pivotal role in glial activation and neuroinflammation in neurodegenerative diseases," *Experimental Neurobiology*, vol. 23, no. 2, pp. 138–147, 2014.

[58] V. Kumar, "Toll-like receptors in the pathogenesis of neuroinflammation," *Journal of Neuroimmunology*, vol. 332, pp. 16–30, 2019.

[59] O. Guillemot-Legris and G. G. Muccioli, "Obesity-induced neuroinflammation: beyond the hypothalamus," *Trends in Neurosciences*, vol. 40, no. 4, pp. 237–253, 2017.

[60] E. Blázquez, E. Velázquez, V. Hurtado-Carneiro, and J. M. Ruiz-Albusac, "Insulin in the brain: its pathophysiological implications for states related with central insulin resistance, type 2 diabetes and Alzheimer's disease," *Frontiers in Endocrinology*, vol. 5, 2014.

[61] M. Soto, W. Cai, M. Konishi, and C. R. Kahn, "Insulin signaling in the hippocampus and amygdala regulates metabolism and neurobehavior," *Proceedings of the National Academy of Sciences of the United States of America*, vol. 116, no. 13, pp. 6379–6384, 2019.

[62] O. Osborn and J. M. Olefsky, "The cellular and signaling networks linking the immune system and metabolism in disease," *Nature Medicine*, vol. 18, no. 3, pp. 363–374, 2012.

[63] E. D. Werner, J. Lee, L. Hansen, M. Yuan, and S. E. Shoelson, "Insulin resistance due to phosphorylation of insulin receptor substrate-1 at serine 302," *The Journal of Biological Chemistry*, vol. 279, no. 34, pp. 35298–35305, 2004.

[64] G. Boden, "Obesity, insulin resistance and free fatty acids," *Current Opinion in Endocrinology, Diabetes, and Obesity*, vol. 18, no. 2, pp. 139–143, 2011.

[65] Y. Peng, J. Liu, L. Shi et al., "Mitochondrial dysfunction precedes depression of AMPK/AKT signaling in insulin resistance induced by high glucose in primary cortical neurons," *Journal of Neurochemistry*, vol. 137, no. 5, pp. 701–713, 2016.

[66] J. Górski, "Ceramide and insulin resistance: how should the issue be approached?," *Diabetes*, vol. 61, no. 12, pp. 3081–3083, 2012.

[67] O. Busquets, M. Ettcheto, M. Pallàs et al., "Long-term exposition to a high fat diet favors the appearance of β-amyloid depositions in the brain of C57BL/6J mice. A potential model of sporadic Alzheimer's disease," *Mechanisms of Ageing and Development*, vol. 162, pp. 38–45, 2017.

[68] M. V. Lourenco, J. R. Clarke, R. L. Frozza et al., "TNF-α mediates PKR-dependent memory impairment and brain IRS-1 inhibition induced by Alzheimer's β-amyloid oligomers in mice and monkeys," *Cell Metabolism*, vol. 18, no. 6, pp. 831–843, 2013.

Hindawi
Disease Markers
Volume 2023, Article ID 9813896, 1 page
https://doi.org/10.1155/2023/9813896

Retraction

Retracted: Effects of Medium-Term Soft Contact Lens Fitting on Dry Eye: Analyses Using Ultra-High Resolution Optical Coherence Tomography and Digital Slit-Lamp Biomicroscopy

Disease Markers

Received 20 June 2023; Accepted 20 June 2023; Published 21 June 2023

This article has been retracted by Hindawi following an investigation undertaken by the publisher [1]. This investigation has uncovered evidence of one or more of the following indicators of systematic manipulation of the publication process:

(1) Discrepancies in scope

(2) Discrepancies in the description of the research reported

(3) Discrepancies between the availability of data and the research described

(4) Inappropriate citations

(5) Incoherent, meaningless and/or irrelevant content included in the article

(6) Peer-review manipulation

The presence of these indicators undermines our confidence in the integrity of the article's content and we cannot, therefore, vouch for its reliability. Please note that this notice is intended solely to alert readers that the content of this article is unreliable. We have not investigated whether authors were aware of or involved in the systematic manipulation of the publication process.

Wiley and Hindawi regrets that the usual quality checks did not identify these issues before publication and have since put additional measures in place to safeguard research integrity.

We wish to credit our own Research Integrity and Research Publishing teams and anonymous and named external researchers and research integrity experts for contributing to this investigation.

The corresponding author, as the representative of all authors, has been given the opportunity to register their agreement or disagreement to this retraction. We have kept a record of any response received.

References

[1] Y. Wang, Z. Xu, S. Chen et al., "Effects of Medium-Term Soft Contact Lens Fitting on Dry Eye: Analyses Using Ultra-High Resolution Optical Coherence Tomography and Digital Slit-Lamp Biomicroscopy," *Disease Markers*, vol. 2022, Article ID 7220706, 14 pages, 2022.

Hindawi
Disease Markers
Volume 2022, Article ID 7220706, 14 pages
https://doi.org/10.1155/2022/7220706

Research Article

Effects of Medium-Term Soft Contact Lens Fitting on Dry Eye: Analyses Using Ultra-High Resolution Optical Coherence Tomography and Digital Slit-Lamp Biomicroscopy

Yuzhou Wang,[1,2] **Zhiqiang Xu**,[1,2] **Shuangjiao Chen**,[1,2] **Yangyang Xu**,[1,2] **Linzhi Wei**,[1,2] **Fan Lu**,[1,2] **and Liang Hu**[1,2]

[1]*School of Ophthalmology and Optometry, Eye Hospital, Wenzhou Medical University, Wenzhou, Zhejiang, China*
[2]*National Clinical Research Center for Ocular Diseases, Wenzhou, Zhejiang, China*

Correspondence should be addressed to Fan Lu; lufan62@mail.eye.ac.cn and Liang Hu; liang_hu@live.cn

Received 13 December 2021; Accepted 12 February 2022; Published 18 March 2022

Academic Editor: Ting Su

Purpose. This study aimed to evaluate the medium-term fit of soft contact lenses (SCLs) and its effects on dry eye by using ultra-high-resolution optical coherence tomography (UHR-OCT) and digital slit-lamp biomicroscopy (DSLB) and identify factors indicating a better contact lens fit. *Methods.* A total of 14 participants (7 men, 7 women; mean age, 23.1 years) were recruited. Temporal lag and conjunctival coverage were imaged by UHR-OCT. DSLB was used to assess lens decentration and blink-induced movement. In addition, dry eye indices, including ocular surface disease index (OSDI), tear break-up time (TBUT), and Schirmer I test scores, were measured at baseline and 1 day, 1 week, 1 month, 3 months, and 6 months after wearing. *Results.* Good repeatability was found in the assessments of lens fit characteristics by two researchers and in the assessments by one researcher at different follow-up times. There were no significant differences in lens fit characteristics, TBUT and Schirmer I test scores at each checkpoint ($P > 0.05$). However, the OSDI was significantly higher than baseline after wearing ($P < 0.05$). Changes in the temporal lag were positively correlated with changes in TBUT ($r = 0.544$, $P = 0.044$) and negatively correlated with changes in OSDI ($r = -0.629$, $P = 0.016$). Changes in blink-induced movement were positively correlated with changes in OSDI, Schirmer I test scores, and TBUT ($P < 0.05$). *Conclusions.* UHR-OCT and DSLB can be used to comprehensively and quantitatively evaluate SCL fit. Both the contact lenses and ocular surface conditions are almost stable within 6 months of SCL wear. Temporal lag and blink-induced movement have a strong correlation with dry eye parameters in SCL wearers.

1. Introduction

Over the last 40 years, contact lenses (CLs) have become increasingly popular in correcting refractive errors. At present, about 140 million people worldwide use CLs [1]. Several studies have indicated that approximately 30%-50% of lens wearers report dry eye and discomfort that prevents them from wearing CLs continuously [2, 3], and 25% of wearers will permanently cease wearing CLs as a result [4]. Numerous factors are associated with CL-induced dry eye, such as lens material, design, care systems, and replacement frequencies [5]. In addition, poor lens fit also plays an important part in the discomfort caused by lens wearing and the subsequent discontinuation [6]. Lens mobility is generally believed to be correlated with tear exchange [7]. Proper lens fit facilitates tear exchange underneath the lens and the removal of debris, inflammatory cells, and dead cells, which can improve the safety and comfort of CL wear and also extend the life cycle of CLs [4, 8].

In clinical practice, assessments of soft CL (SCL) fit are limited to evaluation of lens centration and corneal coverage, movement, surface wettability, and subjective comfort [7]. Although this approach is more intuitive, it still has some limitations. First, it is highly subjective and requires long-

term clinical experience of the fitting physicians. Moreover, the assessments may be inadequate due to the lack of static landmarks and quantification of movement at the micrometer level [9]. In addition, this approach only assesses the overall fit, and the edge-fitting properties remain unknown. The interaction between the ocular surface and the lens edge may play a significant role in wearing comfort and in the health of the ocular surface [10]. Therefore, it is necessary to characterize the edge fitting of SCLs, which can improve our understanding of the relationship between lens properties and the ocular surface.

A number of studies have attempted to evaluate SCL fit to date. Young [11] measured lens centration, blink-induced lens movement, and lag using a slit-lamp microscope fitted with an eyepiece graticule. The results confirmed that most of the characteristics were poorly predictive of lens fit when used alone. However, this study involved multiple types of SCLs and used relatively rough measurement methods. Wolffsohn et al. [12] performed a comprehensive objective evaluation of lens fit in primary and multiple other positions of gaze by using DSLB providing 6× magnification (JAI C-S2300; resolution, 767 × 569 pixels), showing that movement on blink in up-gaze, horizontal lag, and push-up recovery speed were the key metrics to independently characterize SCL mobility. Belda-Salmerón et al. [7] used the same apparatus to assess objectively SCL fit characteristics and demonstrated that objective image analysis allowed an accurate, reliable, and repeatable assessment.

Because of the lack of suitable tools, there is very little published evidence that quantitatively characterizes the edge-fitting properties of SCLs. Wang et al. [13] successfully observed tear distribution and dynamics in CL wearers using ultra-high-resolution optical coherence tomography (UHR-OCT) for the first time, which suggested that UHR-OCT might yield new ways of evaluating CL fit. On the basis of this finding, Shen et al. [10] attempted to characterize lens edge fitting through UHR-OCT and proposed the concept of conjunctival coverage. The percentage of the lens edge covered by the conjunctiva was categorized by an analog ranking scale of 0%, 25%, 50%, 75%, and 100%. Turhan [14] measured the angle of conjunctival indentation and determined the effect of lens power on the lens fit characteristics by using the RTVue OCT system. To the best of our knowledge, this was the first study to demonstrate quantitative assessment of conjunctival indentation. Cui et al. [15] compared the horizontal lag and blink-induced lens movement of four different types of soft CLs using UHR-OCT. They found that the horizontal lag in nasal gaze and temporal gaze showed good correlation and consistency. In addition, the study visualized the footprint of SCLs in micrometer dimensions for the first time, providing additional information on the amount of movement that resulted from blinking.

However, most of the SCL fit studies are methodological studies. The interaction between fit properties and dry eye indicators has not been analyzed. It is also unknown how these indicators change over time in medium-term wearers. The purpose of this study was to evaluate the fit characteristics of SCLs and study the changes in indices included after medium-term SCL wearing.

2. Subjects and Methods

2.1. Subjects and CLs. Eighteen subjects from Eye Hospital of Wenzhou Medical University participated in the present study; three subjects dropped out at 1 month and one subject dropped out at 3 months because of work-related stress. Finally, 14 subjects (14 right eyes) were included in this study. The study group consisted of seven men and seven women (age, 23.1 ± 1.6 years [mean ± SD]). None of the subjects had a history of SCLs wearing or ocular surgery or any current ocular or systemic diseases other than refractive errors. The study was approved by the Human Sciences Ethical Committee of The Eye Hospital of Wenzhou Medical University (approval no. of ethics committee: KYK-2018-23) and followed the tenets of the Declaration of Helsinki. The study was registered on the Chinese Clinical Trial Registry (registration number: ChiCTR1800018001). Written informed consent was obtained from all subjects after receiving a full explanation of the content and possible consequences of the study. BAUSCH+LOMB SoftLens 59 (Hilafilcon b, 59% water content, 8.6 mm base curve, 14.2 mm diameter) was used in this study. All the subjects wore SCLs according to the degree of subjective refraction and corneal curvature for 6 months on a full-time, daily wear basis (minimum 8 h/day; minimum 5 days per week). CL fit characteristics and dry eye-related indices were measured at 1 day, 1 week, 1 month, 3 months, and 6 months after the subjects started wearing the SCLs.

2.2. Dry Eye Examination. Subjective questionnaire: ocular surface disease index was used to evaluate the subjective sensation related to dry eyes. The larger the value, the more obvious the ocular surface discomfort.

After a drop of normal saline, a single fluorescein strip (Jingming, Tianjin, China) was gently placed on the lower eyelid conjunctiva to measure TBUT. The subjects were asked to blink three times and then open their eyes wide. The time of the first corneal black spot on the stained tear film was measured and repeated three times to take the average value.

Schirmer I test was performed by folding the Schirmer paper strip (Jingming, Tianjin, China) at the notch and hooking the folding end to the lateral third of the lower lid margin without topical anesthesia. The score is the wetted length measured from the notch after 5 minutes.

2.3. Lens Fit Characteristics. A custom-built UHR-OCT unit with a resolution of approximately 3 μm was used to image each contact lens on the eyes. The accuracy and repeatability of the instrument have been confirmed in a previous study [10, 16]. All images were taken in a laboratory under controlled temperature (15°C–25°C) and humidity (30%–50%) [17]. Each subject was scheduled to be examined after 10 am to avoid the corneal edema and tear film alterations caused by sleep [18, 19].

Subjects were instructed to look straight at the fixation target first, which was placed in the front of the eye for primary gaze, and the OCT detector was moved 45° to the temporal side of the right eye to image the temporal lag and conjunctival coverage. Then, the subject looked at the

fixation target placed 45° nasally, and the lens edge at the temporal side was imaged. Using the ending of Bowman's layer at the limbus and the lens edge as reference points, temporal lag was defined as the difference between the linear distances measured while gazing forward and nasally (Figure 1). Conjunctival coverage was defined as the vertical linear distance between the lens edge and anterior surface of the cornea (h). Commercial software (MATLAB R2015b, The MathWorks, Inc; ImageJ, ver. 1.51w) was used to perform image processing and determine the temporal lag and conjunctival coverage.

A slit-lamp biomicroscope (SLM-4ER; KANGHUA, Chongqing City, China) equipped with a digital camera (60D; Canon, Tokyo, Japan) was used to capture images of SCLs when subjects looked straight ahead. The eyelids were not pulled to avoid changing the lens position. Three continuous high-definition images were obtained, and ImageJ software was used to quantitatively analyze the lens eccentricity (Figure 2). A circle was drawn along the edge of the pupil and lens, respectively, and the coordinate parameters of the two centers were obtained. The differences in the X- and *y*-axes were the amount of eccentricity in the horizontal and vertical directions, respectively. Total decentration was calculated using the Pythagoras theorem. A ruler was imaged through the same slit-lamp and camera system, and calibration was performed by considering 1 pixel as equivalent to 0.004 mm.

Videos were captured to visualize lens movement induced by blinking using the same DSLB providing 10x magnification (resolution 640 x 480 pixels, frame rate 60 Hz). Subjects were asked to look straight ahead during the open-eye period and immediately after every blink. The lower eyelid was pulled down a little if the lower edge of the lens was not fully exposed. Using specific software to convert the videos into images and trace the footprint of the lower lens edge, blink-induced movement was assessed by determining the changes in vertical lens position relative to the lower corneal margin from the first video frame after the blink until the lens had stabilized. A ruler was imaged under the same shooting conditions, and calibration was performed by considering 1 pixel to be equivalent to 0.032 mm. All parameters were measured three times and averaged. The data of the four lens fit indicators for 1 day, 1 week, and 1 month after wearing SCLs were independently processed by two researchers, and inter-researcher repeatability was evaluated. One researcher repeated the image processing two weeks later, and intra-researcher repeatability was evaluated.

2.4. Statistical Analysis. SPSS version 23.0 (SPSS Inc., Chicago, IL) was used for statistical analysis. All of the data were presented as mean ± standard deviation (SD) values. The inter- and intra-researcher differences in assessments of temporal lag, conjunctival coverage, decentration, and blink-induced movement were plotted versus the average on Bland–Altman plots for comparison. The Shapiro-Wilk test was used to evaluate the normality of the data distribution. The inter-researcher and intra-researcher differences were assessed by means of an independent t-test or Wilcoxon signed-rank test. Repeated measures analysis of variance (ANOVA) was used to compare the changes in the values of each index at different follow-up times. Pearson correlation or Spearman correlation was used to analyze the correlation between these indicators. The results were considered statistically significant when the *p* value was less than 0.05.

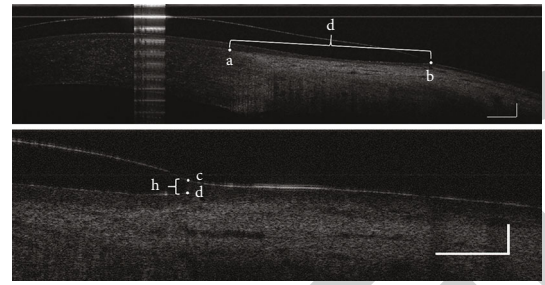

Figure 1: Ultra-high-resolution OCT images of temporal lag and conjunctival coverage. Two landmarks were used in image processing. One was the ending of the Bowman's layer at the limbus (a), and the other was the contact lens edge (b). Lens location was defined as the linear distance (d) between "a" and "b," which was different in primary gaze and nasal gaze. This difference represented the temporal lag. The vertical distance from the edge of the contact lens (c) to the surface of the cornea (d) represents the conjunctival coverage. Bars = 500 μm.

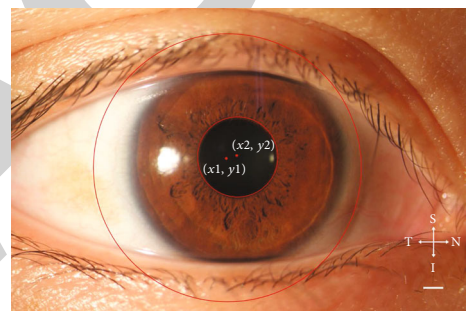

Figure 2: Digital slit-lamp biomicroscopic images of decentration. The two red circles are the edges of the lens and the pupil, and the two red dots are the center of the lens and the pupil. The difference (x1-x2) in the *x*-axis is the amount of eccentricity in the horizontal direction, and the difference (y1-y2) in the *y*-axis is the amount of eccentricity in the vertical direction. S, upper; I, lower; T, temporal side; N, nasal side. Bars = 1 mm.

3. Results

3.1. Methodological Repeatability Analysis. The inter- and intra-researcher differences in the four CL fitting characteristics at different follow-up periods showed no statistical significance (Table 1, Table 2). Bland–Altman plots are shown in Figures 3–8.

3.2. Changes in Fitting Characteristics after Wearing CLs. Temporal lag, conjunctival coverage, decentration, and blink-induced movement at different time points after wearing CLs showed no significant differences (Table 3).

Table 1: The repeatability of four contact lens fitting characteristics between two researchers.

Variables	Post 1 day			Post 1 week			Post 1 month		
	Mean difference	SD of the difference	P	Mean difference	SD of the difference	P	Mean difference	SD of the difference	P
Temporal lag (mm)	0.004	0.119	0.900	-0.010	0.123	0.770	-0.004	0.074	0.975
Conjunctival Coverage (mm)	-0.003	0.010	0.484	0.004	0.014	0.343	-0.000	0.005	0.836
Decentration (mm)	-0.054	0.114	0.062	-0.029	0.131	0.245	0.018	0.079	0.418
Blink-induced Movement (mm)	0.002	0.007	0.465	0.001	0.008	0.863	-0.003	0.025	0.865

SD: standard deviation.

Table 2: The repeatability of the four fitting characteristics between two time periods.

Variables	Post 1 day			Post 1 week			Post 1 month		
	Mean difference	SD of the difference	P	Mean difference	SD of the difference	P	Mean difference	SD of the difference	P
Temporal lag (mm)	-0.019	0.061	0.262	0.011	0.055	0.482	-0.005	0.074	0.778
Conjunctival Coverage (mm)	0.002	0.010	0.609	0.002	0.006	0.194	0.002	0.006	0.275
Decentration (mm)	-0.053	0.096	0.062	-0.013	0.056	0.638	-0.006	0.052	0.674
Blink-induced Movement (mm)	0.001	0.003	0.414	0.000	0.007	0.608	-0.001	0.005	0.273

SD: standard deviation.

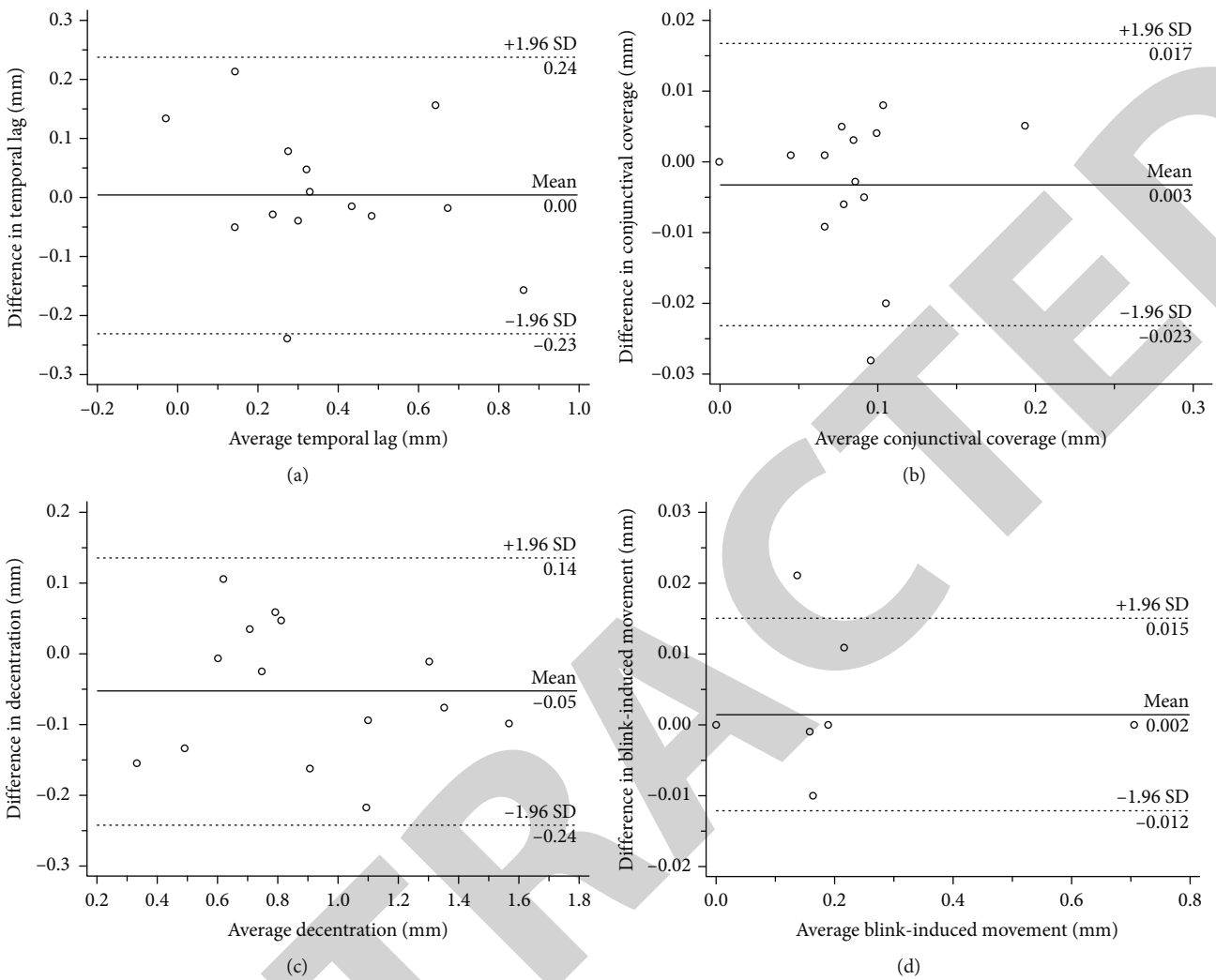

Figure 3: Bland–Altman plots of inter-observer repeatability for the four contact lens fit characteristics after lens wearing for 1 day. Solid line = mean, dashed lines = 95% confidence interval, N = 14 eyes.

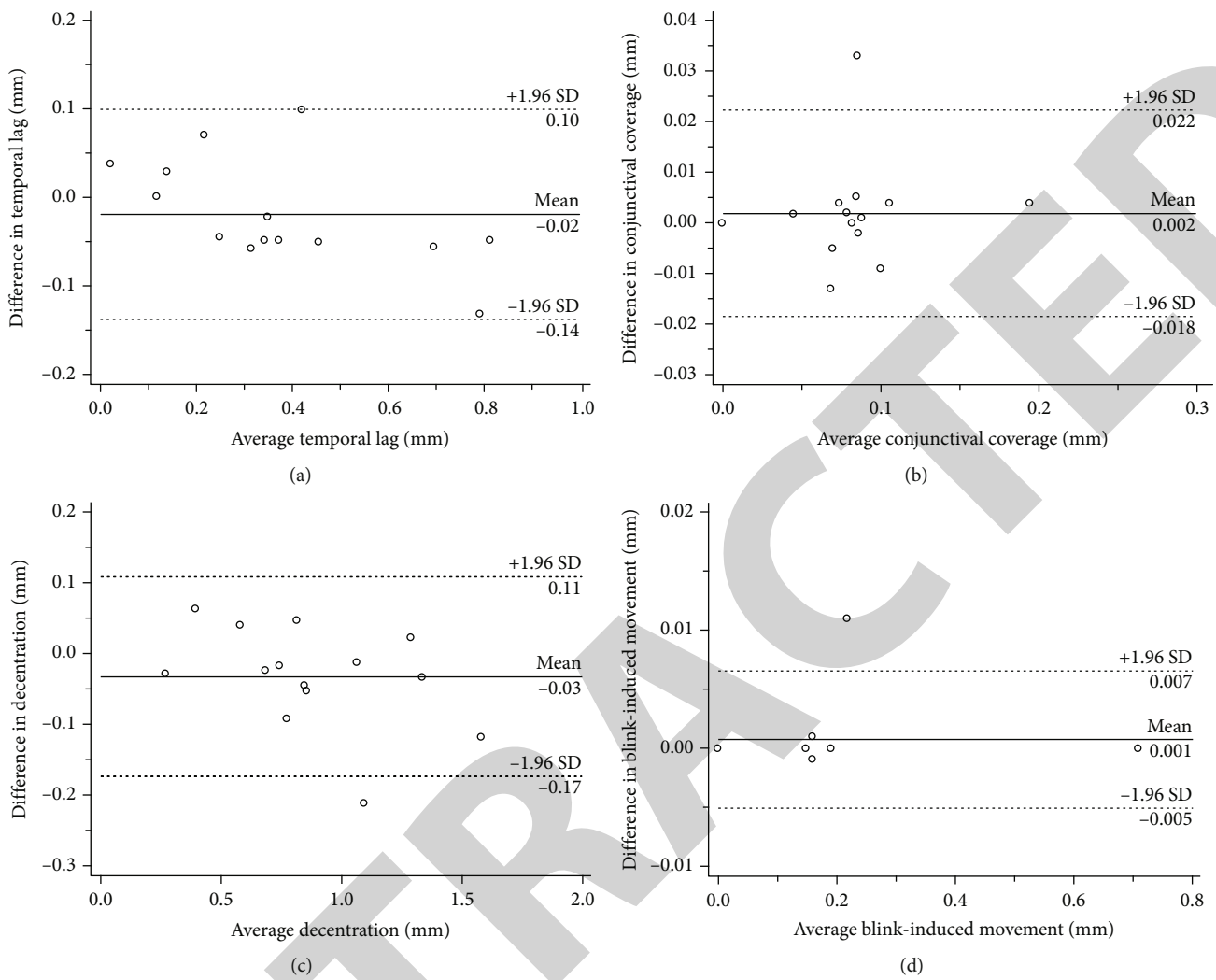

Figure 4: Bland–Altman plots of intra-observer repeatability for the four contact lens fit characteristics after lens wearing for 1 day. Solid line = mean, dashed lines =95% confidence interval, N =14 eyes.

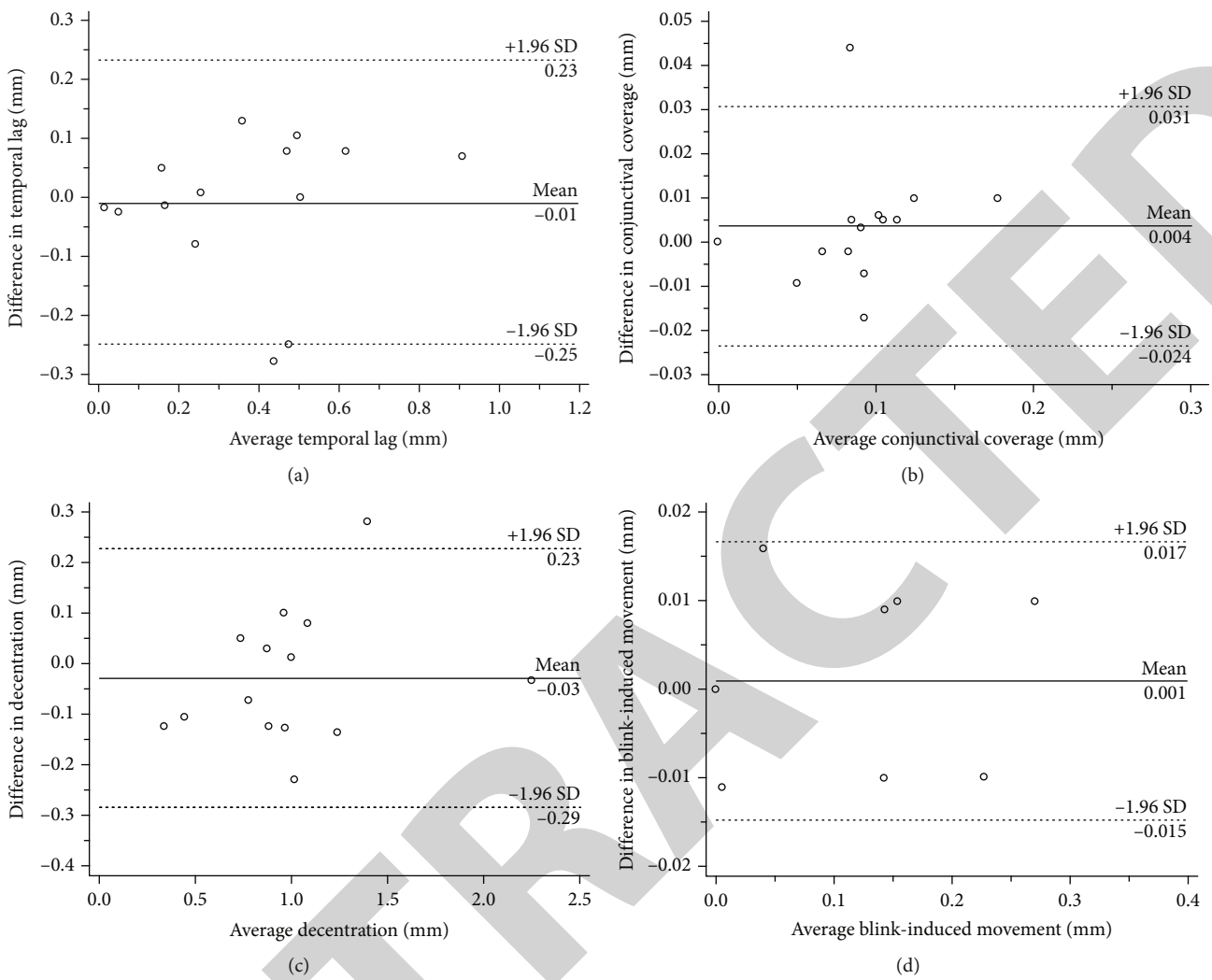

Figure 5: Bland–Altman plots of inter-observer repeatability for the four contact lens fit characteristics after lens wearing for 1 week. Solid line = mean, dashed lines = 95% confidence interval, N = 14 eyes.

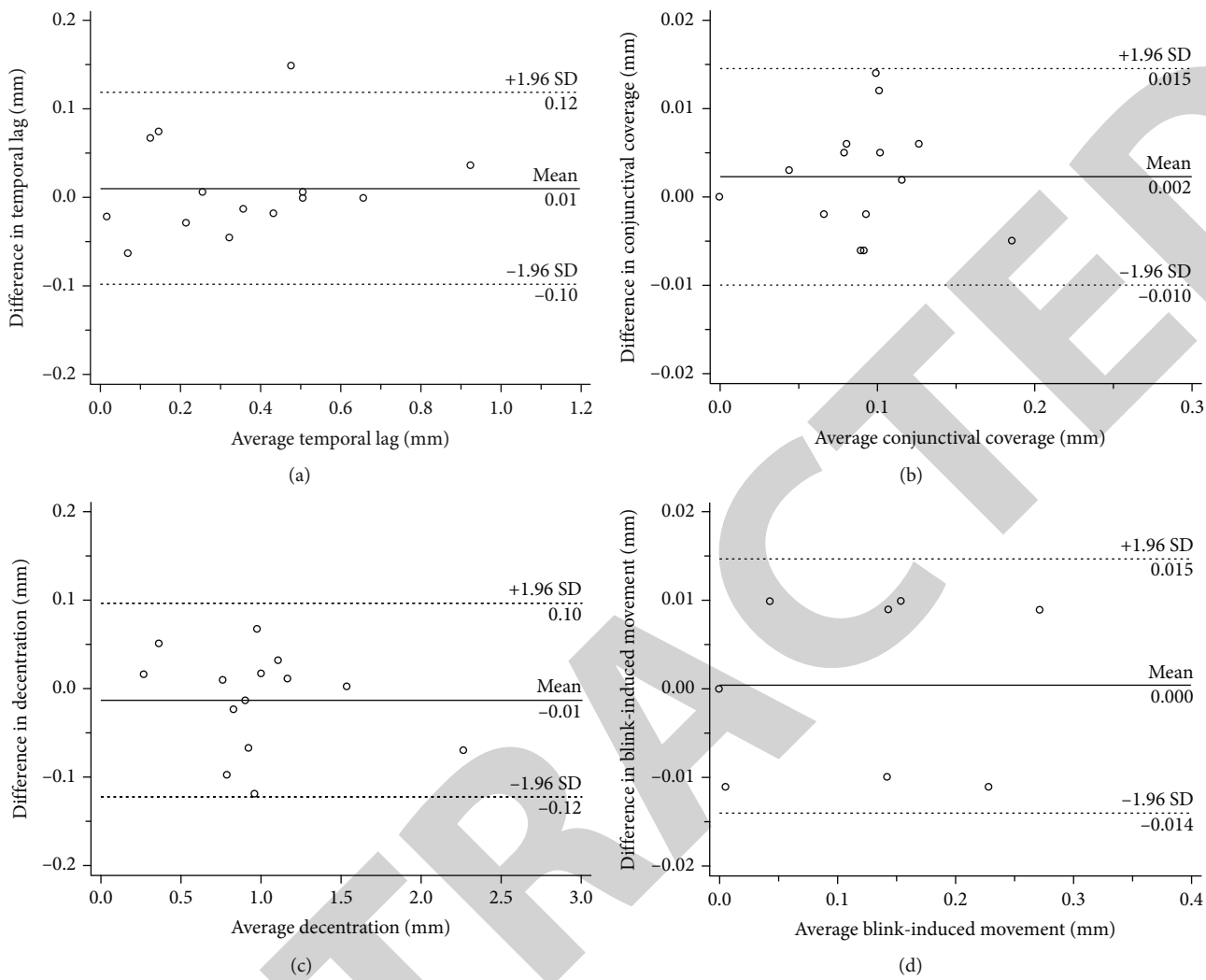

Figure 6: Bland–Altman plots of intra-observer repeatability for the four contact lens fit characteristics after lens wearing for 1 week. Solid line = mean, dashed lines =95% confidence interval, N =14 eyes.

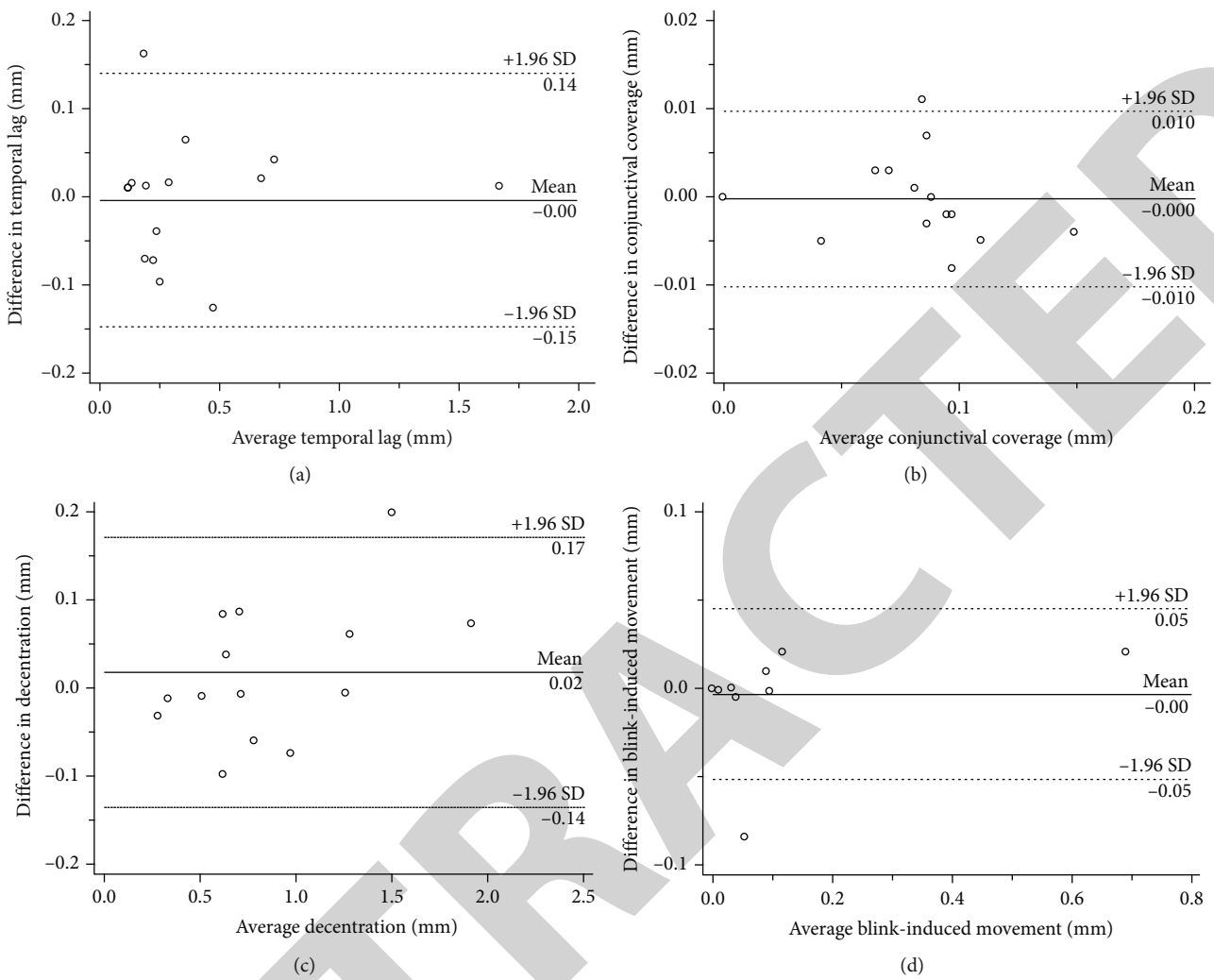

Figure 7: Bland–Altman plots of inter-observer repeatability for the four contact lens fit characteristics after lens wearing for 1 month. Solid line = mean, dashed lines =95% confidence interval, N =14 eyes.

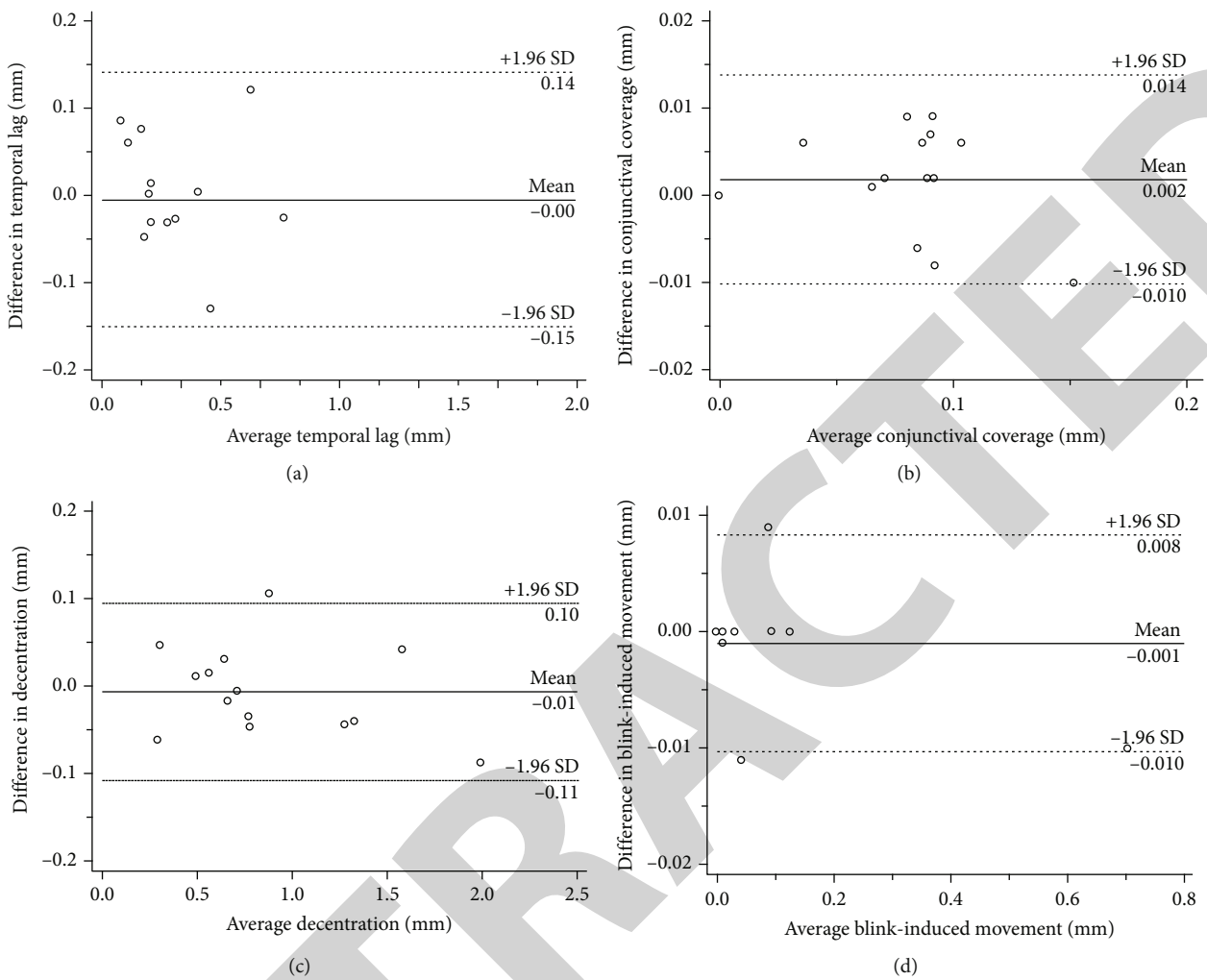

Figure 8: Bland–Altman plots of intra-observer repeatability for the four contact lens fit characteristics after lens wearing for 1 month. Solid line = mean, dashed lines =95% confidence interval, N =14 eyes.

Table 3: Comparison of the four contact lens fitting characteristics at different time points.

Variables	After wearing contact lens					F value	P value
	1 day	1 week	1 month	3month	6month		
Temporal lag (mm)	0.367 ± 0.225	0.365 ± 0.255	0.410 ± 0.413	0.262 ± 0.217	0.233 ± 0.135	1.570	>0.05
Conjunctival Coverage (mm)	0.084 ± 0.042	0.093 ± 0.042	0.082 ± 0.033	0.083 ± 0.036	0.083 ± 0.024	0.792	>0.05
Decentration (mm)	0.864 ± 0.349	0.986 ± 0.475	0.876 ± 0.486	0.745 ± 0.282	0.763 ± 0.267	2.143	>0.05
Blink-induced Movement (mm)	0.114 ± 0.193	0.071 ± 0.098	0.079 ± 0.184	0.200 ± 0.346	0.036 ± 0.099	1.539	>0.05

Values are mean ± SD.

3.3. Changes in Dry Eye Indices after Wearing CLs. The OSDI values at different time points after wearing CLs showed significant differences in comparison with the baseline results. Schirmer I test scores and TBUT at baseline and different time points after wearing CLs showed no significant differences (Table 4).

3.4. Correlation of Dry Eye Indices and CL Fitting Characteristics. Changes in the temporal lag three months after wearing CLs were positively correlated with changes in TBUT ($P < .05$; Table 5). Changes in the temporal lag 6 months after wearing CLs were negatively correlated with changes in OSDI ($P < .05$; Table 5). Changes in the blink-induced movement one week after wearing CLs were positively correlated with changes in OSDI, Schirmer I test scores, and TBUT ($P < .05$; Table 5). Changes in the blink-induced movement 6 months after wearing CLs were positively correlated with changes in OSDI and TBUT ($P < .05$; Table 5). There were no correlations between changes in conjunctival coverage and dry eye indices at any time points

Table 4: Comparison of three dry eye indices at different time points.

Variables	Before and after wearing contact lens						F value	P value
	Baseline	1 day	1 week	1 month	3month	6month		
OSDI	8.4 ± 1.9	22.6 ± 4.4	24.3 ± 3.1	26.3 ± 3.9	24.6 ± 4.8	24.8 ± 3.5	6.118	<0.001
Schirmer I test (mm)	15.4 ± 12.2	14.0 ± 10.5	12.4 ± 10.6	13.4 ± 10.1	16.0 ± 12.7	17.0 ± 11.9	1.364	>0.05
TBUT (s)	5.3 ± 1.1	3.7 ± 0.5	3.8 ± 0.7	4.4 ± 1.3	4.0 ± 0.7	3.5 ± 0.5	0.848	>0.05

OSDI = ocular surface disease index; TBUT = tear break-up time. Values are mean ± SD.

Table 5: The correlation of dry eye indices and CL fitting characteristics at different time points.

	Temporal lag△1w		Conjunctival coverage△1w		Decentration △1w		Blink-induced movement△1w	
	r	p	r	p	r	p	r	p
OSDI△1w	-0.473	0.088	0.139	0.636	0.178	0.543	0.614	0.020∗
Schirmer I test △1w	-0.306	0.288	-0.129	0.661	-0.388	0.171	0.570	0.033∗
TBUT△1w	-0.073	0.805	-0.317	0.269	-0.374	0.187	0.730	0.003∗
OSDI△1 m	-0.481	0.082	0.484	0.08	0.423	0.131	0.233	0.422
Schirmer I test △1 m	-0.202	0.488	0.258	0.373	0.131	0.655	0.167	0.569
TBUT△1 m	-0.324	0.259	-0.410	0.146	-0.137	0.642	0.150	0.608
OSDI△3 m	-0.407	0.148	0.140	0.633	0.461	0.097	0.119	0.686
Schirmer I test △3 m	-0.345	0.228	0.087	0.768	-0.051	0.861	-0.170	0.560
TBUT△3 m	0.544	0.044∗	-0.259	0.372	0.164	0.575	-0.027	0.928
OSDI△6 m	-0.629	0.016∗	0.130	0.658	0.450	0.106	0.577	0.031∗
Schirmer I test △6 m	-0.172	0.555	-0.134	0.648	-0.033	0.911	0.061	0.836
TBUT△6 m	-0.246	0.396	0.207	0.478	0.177	0.546	0.533	0.050∗

OSDI = ocular surface disease index; TBUT = tear break-up time. △value of dry eye indices: the difference between baseline and each time point. △value of CL fitting characteristics: the difference between 1 day and each time point. Pearson correlation coefficient (r) was used to analyze the associations between variables. ∗: P <0.05.

after wearing CLs, nor were there any correlations between changes in decentration and dry eye indices (Table 5).

4. Discussion

Poor-fitting SCLs are commonly associated with discomfort and dry eye and have a negative impact on ocular physiology. Therefore, assessment of contact lens fit is crucial to clinical practice. Unlike gas-permeable lenses, SCLs cannot be evaluated by determining the pattern of fluorescein staining under the lens because of permanent staining of the lens surface. Thus, the development of comprehensive and objective lens fit assessment methods may contribute to better understanding of the fitting characteristics. The validity and repeatability of blink-induced movement and decentration assessed by using a DSLB has been confirmed [7]. Studies have shown that UHR-OCT is feasible to evaluate horizontal excursion lag [15], and conjunctival coverage can be used to characterize SCL edge fitting [10]. However, the relationship between SCL fit characteristics and dry eye indices and changes in these parameters over time after wearing SCLs have not been confirmed.

In the present study, we quantified conjunctival coverage and combined edge-fitting and overall fit characteristics to adequately describe SCL fit. The temporal lag, decentration, and blink-induced movement were within the ranges reported by others [7, 15]. The inter- and intra-researcher repeatability of measurements of the four main lens fit variables was good at different follow-up times. The four fit characteristics did not change significantly with the CL wearing time, which indicated that both the CL and the shape of the ocular surface had relatively stabilized within 6 months. However, it is generally believed that the lens needs time to adapt and it would dehydrate after being worn for a relatively long time. Hence, the inconsistent shooting time of each follow-up might have some impact on the results of fit characteristics, which needs to be improved in follow-up experiments.

OSDI changed obviously after wearing SCLs and remained steady over 6 months. This result suggested that wearing SCLs would lead to some discomfort in comparison with non-wearing. Objective dry eye indices, which included Schirmer I test scores and TBUT, remained relatively stable during the follow-up period, suggesting that the ocular surface condition of subjects had not changed significantly within 6 months of wearing SCLs.

We considered that a higher level of conjunctival coverage around the lens edge might reduce tear exchange beneath the lens. In this scenario, a subject with greater conjunctival coverage might have more serious dry eye

symptoms. However, the results of our study did not find any correlations between conjunctival coverage and dry eye indices. Turhan [14] demonstrated that lens power might have no significant influence on the conjunctival indentation exerted by the lens edge. Therefore, differences in diopter values of SCLs might not affect conjunctival coverage. Sorbara et al. [20] found an optical displacement artefact when imaging a contact lens on two rigid continuous surfaces with UHR-OCT. They concluded that the displacement at the intersection of the CL edge and the conjunctiva was likely a manifestation of both the artefact and compression of the conjunctiva. Therefore, conjunctival coverage might cannot adequately represent SCL fit characteristics, which might explain the absence of significant correlations between conjunctival coverage and dry eye indices.

In contrast to our presumption that more decentration with a looser lens fit would cause less discomfort, lens centration had no significant impact on the dry eye symptoms induced by SCLs. Lens centration might be affected by lid tension and lens gravity since most of the lenses in this study were centered slightly inferior relative to the limbus. Wolffsohn et al. [12] demonstrated that horizontal lag was more predictive of overall lens movement than vertical lag. Cui et al. [15] reported that temporal and nasal lags were similar to and correlated with each other. Hence, we only assessed the temporal lag in the present study. We found that the temporal lag was positively correlated with TBUT and negatively correlated with OSDI. This finding was in agreement with our assumption that a smaller temporal lag indicated a tighter CL.

In our study, blink-induced movement was positively correlated with changes in OSDI, Schirmer I test scores, and TBUT. Sufficient movement of the CL during blinking may facilitate the exchange of the tears under and around the lens and the removal of debris [4, 8]. As a consequence, objective dry eye assessment indices were positively associated with blink-induced movement of SCLs. However, excessive lens movement is also likely to increase the friction between the contact lens front surface and eyelid, giving rise to a certain degree of subjective discomfort [21]. Confirmation of these hypotheses needs to be elucidated in further studies.

There were some limitations in the present study. A larger sample size and longer follow-up period will be needed to verify the accuracy of the results obtained in our study. However, even with the small sample size, significant correlations between ocular comfort and lens fit interactions were evident. The software for determining the values of fit indices was semi-automated. More precise and convenient measurements and devices may further enhance the method for routine clinical application. The detailed quantitative relationships between dry eye indices and CL fit characteristics should be fully investigated in further studies, which can provide guidance for clinical practitioners.

In summary, this was the first study to demonstrate the correlations between fit properties and dry eye indices and changes in these parameters over time within 6 months after wearing SCLs. Our results suggest that UHR-OCT and DSLB can be combined to quantitatively evaluate SCL fit characteristics. The semi-automated image analysis method allows an accurate, reliable, and repeatable assessment of SCL fit characteristics, serving as a useful tool for research and optimization of lens fit in clinical practice. Both the CL and ocular surface conditions are almost stabilized after SCL wear for a relatively long time. Temporal lag and blink-induced movement shows better correlation with dry eye symptoms than conjunctival coverage and decentration.

Data Availability

The data used to support the findings of this study are available from the corresponding author upon request.

Conflicts of Interest

No conflicting relationship exists for any author.

Authors' Contributions

Yuzhou Wang and Zhiqiang Xu contributed equally to this study as first authors.

Acknowledgments

Key Projects in Scientific Research Foundation of National Health Commission and Medical Science and Technology Program of Zhejiang Province (WKJ-ZJ-1930); Wenzhou Science and Technology Project; Social Development in Medicine and Health (ZY2020010); National Natural Science Foundation of China (82070933).

References

[1] H. D. R. D. Cavanagh, W. M. Petroll, and J. V. Jester, "Castroviejo lecture 2009: 40 years in search of the perfect contact lens," *Cornea*, vol. 29, no. 10, pp. 1075–1085, 2010.

[2] J. J. Nichols, C. Ziegler, G. L. Mitchell, and K. K. Nichols, "Self-reported dry eye disease across refractive modalities," *Investigative Ophthalmology & Visual Science*, vol. 46, no. 6, pp. 1911–1914, 2005.

[3] C. Riley, G. Young, and R. Chalmers, "Prevalence of ocular surface symptoms, signs, and uncomfortable hours of wear in contact lens wearers: the effect of refitting with daily-wear silicone hydrogel lenses (senofilcon a)," *Eye & Contact Lens*, vol. 32, no. 6, pp. 281–286, 2006.

[4] A. Muntz, L. N. Subbaraman, L. Sorbara, and L. Jones, "Tear exchange and contact lenses: A review," *Journal of Optometry*, vol. 8, no. 1, pp. 2–11, 2015.

[5] G. Young, J. Veys, N. Pritchard, and S. Coleman, "A multi-Centre study of lapsed contact lens wearers," *Ophthalmic & Physiological Optics*, vol. 22, no. 6, pp. 516–527, 2002.

[6] G. Young, "Why one million contact lens wearers dropped out," *Contact Lens and Anterior Eye*, vol. 27, no. 2, pp. 83–85, 2004.

[7] L. Belda-Salmerón, T. Drew, L. Hall, and J. S. Wolffsohn, "Objective analysis of contact lens fit," *Contact Lens and Anterior Eye*, vol. 38, no. 3, pp. 163–167, 2015.

[8] M. N. NA, K. A. Polse, R. J. Brand, A. D. Graham, J. S. Chan, and M. K. CD, "Tear mixing under a soft contact lens: effects

Hindawi
Disease Markers
Volume 2022, Article ID 5141927, 12 pages
https://doi.org/10.1155/2022/5141927

Research Article

HuR Promotes the Progression of Gastric Cancer through Mediating CDC5L Expression

Jing Cui,[1] Nanjing Cao,[2,3] Guochao Wang,[4] Fuhua Wang,[3] Bin Yang,[5] Jian Wang,[5] Yongqiang Lv,[6] Yunqing Chen,[5] and Feng Li[3]

[1]*Department of Biochemistry and Molecular Biology, Basic Medical College, Shanxi Medical University, Taiyuan 030001, China*
[2]*Department of Clinical Laboratory, Xi'an Da Xing Hospital, No. 353, North Labor Road, Xi'an 710016, China*
[3]*Department of Cell Biology, Shanxi Cancer Hospital, Affiliated Cancer Hospital of Shanxi Medical University, Taiyuan 030012, China*
[4]*Radiation Oncology Center, Shanxi Cancer Hospital, Affiliated Cancer Hospital of Shanxi Medical University, Taiyuan 030012, China*
[5]*Surgical VIP, Shanxi Cancer Hospital, Affiliated Cancer Hospital of Shanxi Medical University, Taiyuan 030012, China*
[6]*Shanxi Cancer Hospital, Affiliated Cancer Hospital of Shanxi Medical University, Taiyuan 030012, China*

Correspondence should be addressed to Yunqing Chen; chenmao1965@sina.com and Feng Li; lifenglover@sina.com

Received 17 December 2021; Revised 9 February 2022; Accepted 11 February 2022; Published 12 March 2022

Academic Editor: Jing Zhong

Background and Objectives. Gastric cancer (GC) is one of the common gastrointestinal tumors and the third in the mortality rate among tumors. Studies have shown that the human antigen receptor (HuR) is associated with the malignant degree of GC. *Methods*. We performed qRT-PCR, cell cycle assay, cell migration, and mouse transplantation model analysis in our experiments. It has been clarified that HuR and microRNAs (miRNAs) have important interplays in the regulation of tumor progression. *Results*. This study found microRNA-133b (miR-133b), as a HuR-sponged miRNA in GC cells. Downregulation of HuR can promote the expression of miR-133b and further affect the downstream cyclin CDC5L. The expressions of miR-133b were slightly lower in GC tissues than adjacent normal tissues. *Conclusion*. Our studies suggest that HuR and miR-133b are involved in the development and pathological process of GC cells.

1. Introduction

Gastric cancer (GC) is one of the most common gastrointestinal tumors. In China, the diagnosis and treatment rates of early GC are less than 10%. The 5-year survival rate is about 30% after radical resection of advanced [1]. Clinical statistics show that the incidence and death rate of GC is high, but the early diagnosis rate and 5-year survival rate are low. The pathogenesis of GC has yet to clear, but the diagnosis of 80% ~ 90% of progression has spread to the lymph nodes and even distant metastasis over time. Lymph node metastasis of GC, nearly 20%, is the main route of GC metastasis. Studies have shown that lymphatic metastasis of GC is an important factor affecting the prognosis of early GC [2]. Therefore, it is of great clinical significance to explore the related factors of GC metastasis, early prediction of the risk of lymph node metastasis to improve the survival rate of patients.

Human antigen receptor (HuR) belongs to the RNA binding protein family, embryonic lethal abnormal vision (ELAV). It is known as the class embryonic death abnormal visual, widely expressed in mammalian cells [3]. HuR was first detected in the serum from lung cancer patients in 1990. In 1996, Ma et al. [4] applied the polymerase chain reaction (PCR) technology identifying and cloning HuR. HuR includes four members: HuB, HuC, HuD, and HuR. The first three members are mainly expressed in neural tissues and reproductive organs and related to neural development. HuR can be connected with multiple regulatory factors such as Von Hippel Lindau tumor suppressor

(VHL), cyclooxygenase 2 (cox-2) [5], cyclin A, and matrix metallopeptidase-9 (MMP-9) [6] and participate in various cell responses and inflammatory tumor formation. In recent years, increasing studies have found that HuR is associated with the occurrence, invasion, metastasis, and prognosis of oesophageal squamous cell carcinoma [7], glioma [8], breast cancer [9], lung cancer [10], and colorectal cancer [11].

MicroRNA (miRNA) is a kind of short RNAs, which are nonprotein coding and mainly regulate the expression of target mRNA at the transcriptional or posttranscriptional level. Many studies have confirmed that miRNA plays an essential role in cell proliferation, differentiation, apoptosis, and metabolism and participates in the regulation of various signals in the process of tumorigenesis [12]. Different types of miRNAs with abnormal expression have been detected in multiple malignant tumors. They are related to the occurrence, development, treatment, and prognosis of tumors. A single miRNA can regulate one or more invasion-related genes, and multiple miRNAs can control a single invasion-related gene simultaneously [13]. In the early stage, we conducted miRNA microarray analysis on GC tissues. We found that the expression of many miRNAs was upregulated or downregulated, among which miR-133b was most significantly downregulated in GC tissues. In other tumors, overexpressed miR-133b can inhibit the proliferation and induce apoptosis of tumor cells, suggesting that it has a classical pattern of regulating miRNA target genes. Then, we will study the interaction between HuR and miR-133b as posttranscriptional regulators.

2. Materials and Methods

2.1. Clinical Specimens and Cell Culture. GC tissue and paired adjacent normal tissue samples from 80 patients were collected from Shanxi Cancer Hospital/Institute. GC tissue microarrays were from Shanghai Qiagen Biotech (China). The ethical board approved the experiment by the Shanxi Cancer Hospital/Institute. GC tissues were obtained with the patient's informed content and were confirmed by clinical.

GC cell lines BGC-823, MKN-45, MGC-803, SGC-7901, and AGS were obtained from the ATCC. GC cells were grown in a 5% CO_2 culture incubator with 10% FBS DMEM (Hyclone, Utah) at 37°C. Mycoplasma detected cell lines according to the verification recommendations of the ATCC.

2.2. RNA Isolation and qRT-PCR Analysis. Total RNA was extracted from the cultured cells using TRIzol reagent (Invitrogen, CA, USA). RNA isolation and quantitative real-time PCR (qPCR) analysis were conducted with the Vii7 Q-PCR system (ABI, USA) in the Thermal Cycler Dice Real-time System (Takara). The qPCR primers are listed in Table 1.

2.3. Oligonucleotide. Cells were transfected (100 nM) with HuR (si-HuR) and control siRNA (si-control) using Lipofectamine TM 2000 (Invitrogen, USA). The results were measured relative to light units per luciferase activity by qRT-PCR.

2.4. Cell Proliferation and Migration. In cell proliferation, si-HuR and si-control transfected GC cells were seeded in 96-well plates at 2000 cells per well. The assay was evaluated by 10% CCK-8 (DOJINDO) diluted on a microtiter plate reader (Spectra Rainbow, Tecan) after 1, 2, 3, and 4 days posttransfection. Proliferation rates were determined under the manufacturer's recommended protocol.

In wound-healing assays, GC cells were transfected with si-HuR and si-control on 6-well plates. Linear scratch wounds were created after 1 day of transfection in a serum-free medium. The degree of convergence was obtained at every 24 h. Each group had three duplicate holes.

2.5. Colony Formation Assays. Transfected cells were growing in 24-well plates at 1×10^3 cells per well. Cells treated with trypsin were maintained in an incubator for 7-10 days. Then, the cells were washed with PBS, fixed with formalin, and stained with methyl violet. The number of colonies was counted using a microscope (Olympus IX-7, Japan) [35].

2.6. Cell Cycle Assay. Si-HuR and si-control transfected GC cells were seeded at 3×10^5 cells per well in 6-well plates. The cells were maintained in complete medium for 2 days. By using precooling, 1 × PBS contained EDTA washing cells twice, suspending cells, blending, and washing cells. The cell cycle of GC cells was examined after treatment with si-HuR or si-control and staining with PI.

2.7. Luciferase Assay. After 48 h of cell transfection, the old culture medium was sucked off and washed twice with PBS. PLB (Passive Lysis Buffer) of 100 μL was added to each cell hole. Then, it was shaken gently for 10-15 minutes and collected the cell lysate. Then, we added 100 μL LAR II working fluid to each sample, mixed it immediately and read the value 2 s, added 100 μL Stop & Glo® Reagent, mixed it quickly, and put it into the luminescent detector to read the value 2 s.

2.8. Tumorigenicity Assay In Vivo. Animal experiment was conducted according to the guide for the Care and Use of Laboratory Animals (NIH publications nos. 80–23, revised 1996) and the institutional ethical guidelines for animal experiments. si-control and si-HuR transduced GC cells (1×10^7) with 100 μL of PBS were placed into one side of the posterior flank of the nude mouse at 5-6 weeks of age. Tumor growth was examined and tumor volume (V) was monitored with the width (W) and length (L) ($V = (L \times W^2) \times 0.5$).

2.9. Immunoblotting Analysis. GC cells were cultured in 8-well chamber slides (Thermo Scientific), then fixed, washed, incubated (0.01% NaAzide, 3% BSA, TBS pH 7.8, 1% Triton X-100, 1% normal goat serum), and stained. At last, they were incubated with an IgG-antibody (Life Technologies) and captured images by Zeiss microscope.

2.10. Immunohistochemistry and H&E Staining. In H&E staining, GC tissues were embedded, sectioned, dewaxed, and hydrated. Then, tissues were incubated with antibodies,

Table 1: Primers used for qRT-PCR.

Name		Sequence (5′-3′)
CDC5L	Forward	GAGAGCTCTCAAGTGAAGCTTA
	Reverse	TCTTCTTTTCCATCTTTGCAGC
BCAS2	Forward	ACCGACCTACTAAGAACTACCT
	Reverse	ATTCTTGCCATGCAGTAATGTC
PTBP1	Forward	TCTACTTGTGTCACTAACGGAC
	Reverse	TGAACTTCTTGCTGTCATTTCC
TRA2B	Forward	GCAGGTCTTACAGTCGAGATTA
	Reverse	ACAAAGGCAAATCCTCTTGAAC
SRSF3	Forward	TTGAATTTGAAGATCCCCGAGA
	Reverse	AGAATCACTTGAACCCAGTAGG
SF3B1	Forward	ACATGCAAACTGAAGATCGAAC
	Reverse	TTGCTCTTCTGGACTAAGTGTT
SF3A1	Forward	CTGCTCCAGATGAGTATCTTGT
	Reverse	GCTTCAAGCTGCTCTCAATATC
HNRNPC	Forward	ACAGATCCTCGCTCCATGAACTCC
	Reverse	TTCTGCCATCCTCTCCTGCTACAG
PLRG1	Forward	TCTGACCGTCCACAGCCTACAG
	Reverse	TCCAGGTTCCACAGCAATACATCG
HuR	Forward	AAGCCTGTTCAGCAGCATTG
	Reverse	CTTCGCGGTCACGTAGTTCA
GAPDH	Forward	TCAACGACCACTTTGTCAAGCTCA
	Reverse	GCTGGTGGTCCAGGGGTCTTACT
miR-133b mimics	Forward	UUUGGUCCCCUUCAACCAGCUA
	Reverse	GCUGGUUGAAGGGGACCAAAUU
miR-133b nc	Forward	UUCUCCGAACGUGUCAGGUTT
	Reverse	ACGUGACACGUUGGGAGAATT

stained with hematoxylin and eosin (H&E), and observed with a microscope finally. For immunohistochemistry, 0.3% H_2O_2 was incubated for 15 minutes and antigen was extracted from 0.01 M sodium citrate-hydrochloric acid buffer. HuR (Proteintech) and GAPDH (Cell Signaling Technology) antibodies were used for immunohistochemical analysis. Cells were viewed and photographed with a Zeiss UV LSM confocal microscope.

3. Results

3.1. Abnormal Expression of HuR in Human Cell Lines and GC Tissues. To determine the expression of HuR (ELAVL1, ELAV like RNA binding protein 1) in GC, 80 pairs of clinic GC tissues and matched adjacent normal tissues were analyzed with quantitative PCR (qPCR). Results show that the expression of mRNA in 66 cases (82.5%) was rising in tumor tissues compared with their normal tissues, while only 14 cases (17.5%) showed a reduced level in GC (Figure 1(a)). Therefore, the overall expression of HuR in GC tissues was upregulated significantly (Figure 1(b), $p < 0.001$, GC vs. normal). To further study the relationship between the expression of HuR and the development of GC, we analyzed the relationship between metastatic and nonmetastatic of GC and the level of HuR statistically (nonparametric test). We found that a high HuR level was associated with the pM stage (Figure 1(c), $p < 0.001$, metastasis vs. nonmetastasis) in GC patients. However, there was no significant difference between HuR and other clinicopathological features such as Borrmann typing, age, position, gender, and venous invasion. Besides, overall survival and disease-free survival were significantly worse in GC patients with high HuR expression (Figure 1(d)).

For further determination, we examined HuR protein levels in 6 pairs of GC samples. In parallel with mRNA expression changes, the HuR protein levels were escalated significantly in GC tissues (>1.7-fold) compared with normal tissues (Figure 1(e)). Moreover, we used five GC cell lines (MKN-45, SGC-7901, AGS, BGC-823, and MGC-803) and normal cells to analyze the expression of the protein. It was shown that HuR was also elevated in GC cell lines in comparison with normal cells (Figure 1(f)). These results indicated that HuR was a potential oncogene in GC tumorigenesis.

3.2. HuR Promotes GC Cell Proliferation and Migration. Upregulated HuR expression in GC tissues was reminded us to explore the function of HuR in GC tumorigenesis. We selected SGC-7901 and MGC-803 cell lines to disclose the role of HuR in the pathogenesis of GC, in which the

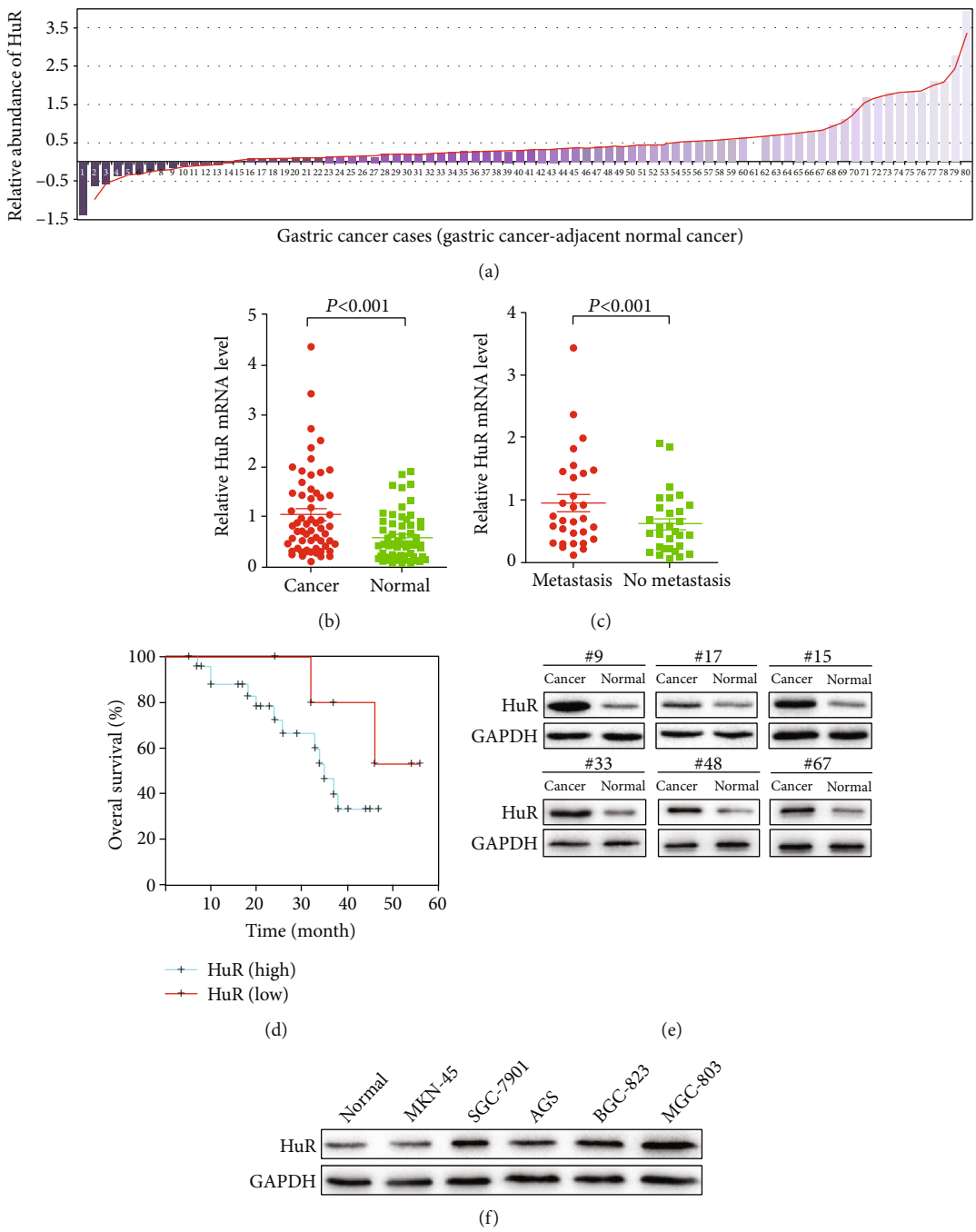

Figure 1: Expression of HuR in GC tissues and cell lines. (a) Relative abundance of HuR was detected in 80 pairs of GC cancers and adjacent normal cancers by RT-qPCR. (b) Scatter plots show the relative HuR mRNA level between cancer tissues and normal tissues. (c) The statistical analysis of the association between the HuR level and pM stage (metastasis and no metastasis). (d) Statistical analysis of survival probability of HuR high- ($n = 26$) and low-expressing ($n = 6$) GC patients using Kaplan–Meier analysis. Statistical analysis is described in the Materials and Methods. (e) Immunoblotting analysis of HuR proteins in 6 pairs of GC samples. GAPDH was used as a loading control. The HuR expression level was normalized to loading control. (f) Levels of HuR protein in GC cell lines (MKN-45, SGC-7901, AGS, BGC-823, and MGC-803) relative to one normal control sample. For all qPCR results, the data are presented as the mean ± SEM, and the error bars represent the standard deviation obtained from three independent experiments. $^{*}p < 0.05$; $^{**}p < 0.01$.

HuR expression was higher than other cells (Figure 1(f)). After transfecting si-HuR into SGC-7901 and MGC-803 cells, we confirmed the efficiency of low HuR expression. Compare with the empty vector si-control, the level of HuR protein was reduced in SGC-7901 and MGC-803 cells treated with si-HuR (Figure 2(a)). Then, we used propidium iodide staining assay to assess the effect of si-HuR on the cell cycle. As expected, the percentage of S-phase cells reduced markedly after being treated with si-HuR in SGC-7901 and MGC-803 cells (Figure 2(b)). Accordingly, the low

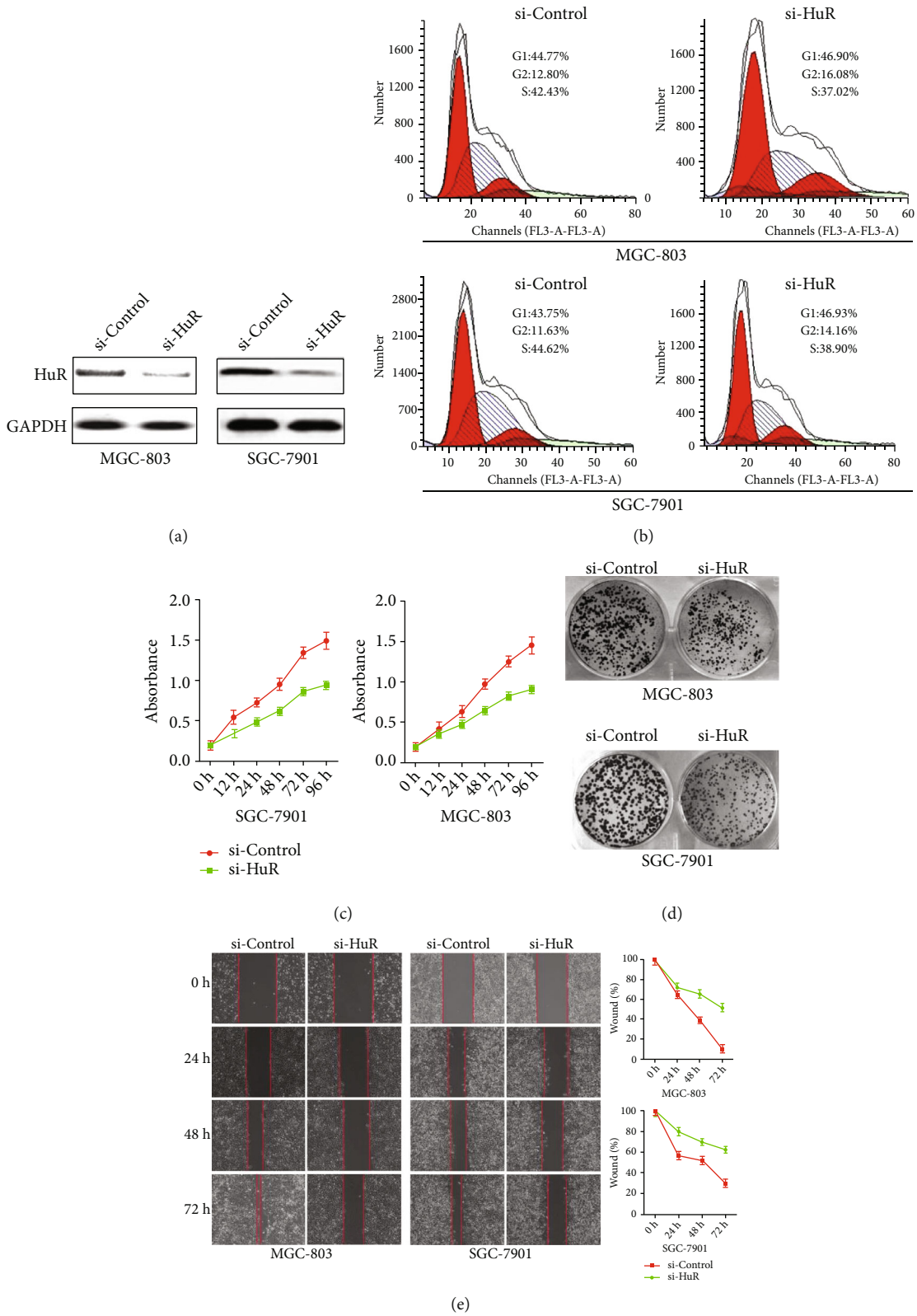

Figure 2: Functional analysis of HuR in GC cells. (a) HuR levels were detected in SGC-7901 and MGC-803 cells after treatment with si-HuR or si-control by immunoblotting. (b) Flow cytometry was conducted to examine the cell cycle of SGC-7901 and MGC-803 cells after treatment with si-HuR or si-control and staining with PI. (c) Cell proliferation assay of SGC-7901 and MGC-803 cells after treatment with si-HuR or si-control using CCK-8. (d) Wound healing assays of SGC-7901 and MGC-803 cells after treatment with si-HuR or si-control. The relative ratio of wound closure per field is shown in the right. (e) Clone formation assay of SGC-7901 and MGC-803 cells after treatment with si-HuR or si-control. For all qPCR results, the data are presented as the mean ± SEM, and the error bars represent the standard deviation obtained from three independent experiments. $^{*}p < 0.05$; $^{**}p < 0.01$.

expression of HuR pointed to more sluggish proliferation rate than controls after CCK-8 assay (Figure 2(c)). Moreover, clonogenic tests were indicated a noticeable decline in cell proliferation after si-HuR transfection into both SGC-7901 and MGC-803 cells (Figure 2(d)).

Based on the communication between HuR expression and GC tumorigenesis, we suggested that the protein might regulate some cell functions of GC cells. To verify this hypothesis, we performed cell migration assays in SGC-7901 and MGC-803 cells with si-HuR or si-control treated. To compare with the si-control, the wound healing degree was decreased in si-HuR GC cells (Figure 2(e)). The above results vouched that HuR may act as an oncogene by promoting cell migration and proliferation, as well as promoting the cell cycle in GC cells.

3.3. HuR Promotes Tumor Cell Growth and Metastasis In Vivo. We further validated these findings in mouse models by subcutaneous injection of (s.c.) si-HuR or si-control lentivirus MGC-803 cells on the posterior flank of nude mice. The animals were sacrificed after six weeks. Low HuR expression was suppressed tumor growth significantly compared with the control group (Figure 3(a)). The mean final tumor volume was 217 mm^3 and 355 mm^3, respectively (Figure 3(b)). Final tumor weights were 2207 mg and 3446 mg, respectively. Similarly, immunohistochemistry showed that HuR staining was increased clearly in GC tissues (Figure 3(d)). Hematoxylin and eosin (H&E) staining was illustrated more metastatic nodules in GC tissues with high expression of HuR compared with adjacent normal tissues (Figure 3(d)). Thus, HuR may mediate tumorigenesis by promoting the degree of migration and proliferative in GC cells. The findings above reminded us that the HuR was played a visible role in tumor oncogenes in GC cells.

3.4. HuR Regulates the Expression of miR-133b in GC Cells. Recent work by Qin et al. has revealed that the appearance of HuR could mediate the miR-133b level in oesophageal squamous cell carcinoma [7]. Furthermore, the changes of contents of miR-133b were revealed in other human cancers, including glioma [8], colorectal [9], and lung cancers [10]. After that, we used MGC-803 cells with a high endogenous HuR level through si-HuR transfection to detect how HuR has regulated the expression of miR-133b in GC cells. miRNA array was performed to confirm the changes in HuR gene level leading to changes in miRNA (Figure 4(a)). In MGC-803 cells, si-HuR was considerably increased in miR-133b mRNA levels compared with si-control (Figure 4(a)). We determined significant enrichment of the HuR group and control group for normalizing expression. Biological replicates were analyzed by statistical methods showed a strong correlation. (Figure 4(b)). Luciferase reporter assay verified that the HuR was reduced in luciferase expression of miR-133b compared to NC (Figures 4(c) and 4(d)). Our data implied that HuR and miR-133b were a very close relationship in GC cells.

3.5. miR-133b Functions as a Tumor Suppressor in GC. Based on the above findings, we selected 60 case tissues to study the mysterious effect of miR-133b. QPCR showed that the levels of miR-133b in normal tissues were increased compared with the cancer tissue cells (Figure 5(a)). To confirm the weakening effects of miR-133b on GC development, the known expression miRNAs were used as control (Figure 5(b)). Compared with high miR-133b expression GC patients, the low miR-133b expression had markedly worse overall (Figure 5(c)). We also found that a high miR-133b level impacted GC progression (Figure 5(d)), $p < 0.001$, nonmetastasis vs. metastasis) in GC patients. The CCK-8 proliferation assay in MGC-803 and SGC-7901 cells showed that cell growth was suppressed more severely after transfection with miR-133b mimics (Figure 5(e)). Moreover, clonogenic assays indicated an uncommon reduction in cell proliferation after miR-133b mimics transfection into SGC-7901, MGC-803, and BGC-823 cells (Figure 5(f)). These findings tell us that miR-133b had a tumor suppressor role in GC cells.

3.6. HuR and miR-133b Affect the Expression of CDC5L in GC Cells. GO analysis (string analysis) revealed that most of the interacting genes were splicing factors and transcriptional regulatory genes, especially CDC5L (cell division cycle 5-like protein), acted as a transcription activator (Figure 6(a)). We compared the expression of CDC5L between GC cell lines and normal cells (Figure 6(b)) and selected MGC-803 and BGC-823 for candidate cells. As shown in Figure 6(c), CDC5L displayed the obvious lessen upon HuR knockdown. Given its oncogenic roles in some cancers, colorectal [14] and hepatocellular [15] cancers, we selected CDC5L for western blot analysis. Western blot analysis confirmed that HuR and miR-133b were upstream of CDC5L in MGC-803 and BGC-823 cells (Figure 6(d)).

The introduction of si-HuR into MGC-803 cells would weaken the expression of CDC5L and BCL2. However, we also detected the opposite changes in Cyclin B, P53, and caspase-3 protein expression after knockdown HuR expression in MGC-803 cells. Consistent with the reduced HuR levels in MGC-803 cells, the CDC5L level was markedly lower in BGC-823 cells compared with that in si-control (Figure 6(d)). Therefore, the novel miR-133b-HuR-CDC5L axis was present in GC cells (Figure 6(e)).

4. Discussion

GC, the third most lethal tumor, is a common gastrointestinal cancer worldwide, especially in some countries in East Asia and Eastern Europe [16]. GC is often diagnosed at the advanced stage, accompanied by malignant cell growth and metastasis. In recent years, considerable progress has been made in the clinical treatment of GC, but the survival rate of patients with GC is still not satisfactory [17–19]. Although scientists have identified several related oncogenes or tumor suppressor genes that are identified as crucial regulators of GC, few have been recognized or treated for early clinical screening [20]. Therefore, it is of great significance for clinical treatment to research new markers of GC and explore the related mechanism. In this study, we confirmed an RNA-binding protein, HuR, which is upregulated in GC

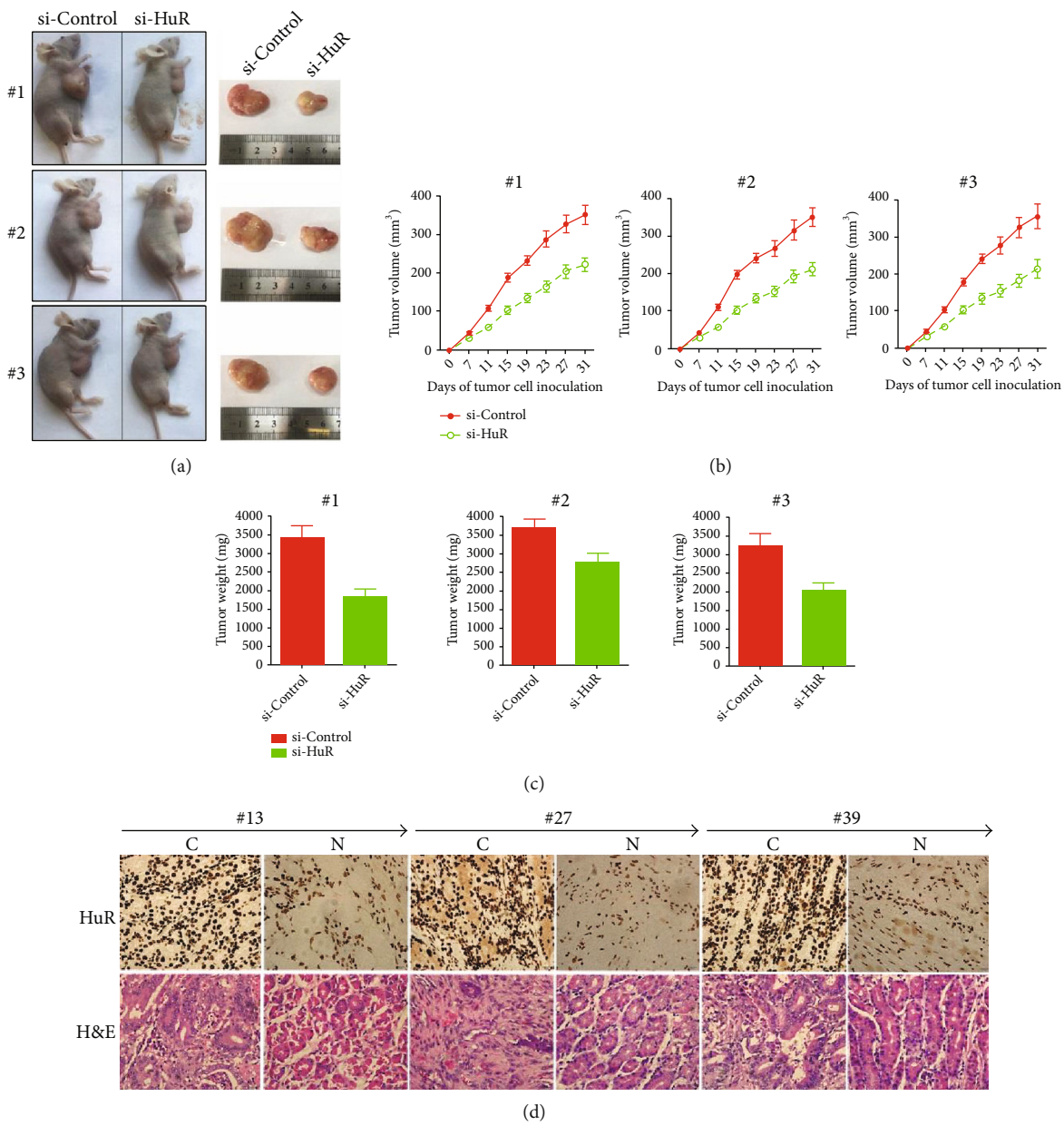

Figure 3: HuR promotes GC cell growth in vivo. (a) Xenograft model in nude mice. si-HuR or si-control transfected MGC-803 cells were injected s.c. into the posterior flank of nude mice. The graph is representative of tumors in mice at five weeks after inoculation. The right photo is representative of excised tumors from killed mice. (b) Tumor volume was calculated and all data are shown as the mean ± SD. (c) Tumor weight was calculated and all data are shown as the mean ± SD. (d) Pathology analysis of tumor sections from GC tissues and adjacent normal tissues. Immunohistochemistry, H&E staining, and labeling with HuR were performed. Bars: 20 μm. $^{*}p < 0.05$; $^{**}p < 0.01$.

patients. The reduced expression of HuR could inhibit the occurrence and development of GC, providing a new strategy for the treatment of GC.

Human antigen receptor (HuR) belongs to the RNA binding protein family and embryonic lethal abnormal vision (ELAV). Moreover known as the class embryonic death abnormal visual, widely expressed in mammalian cells [3]. It has been found to affect mRNA translation [21], cell responses [22], and inflammatory tumor formation [6]. In recent years, more studies have found that HuR is associated with the occurrence and prognosis of different carcinoma, glioma [8], breast cancer [9], lung cancer [10], and colorectal cancer [11]. The HuR regulated COX-2 has been shown to promote the progression of nonsmall cell lung carcinoma [23]. HuR also regulates E-cadherin expression and barrier function [24]. Additionally, HuR regulates AKT phosphorylation level through the PI3K/AKT/NF-B signaling pathway [25]. Although numerous studies have strongly demonstrated that HuR promotes the progression of many cancers [26], the targets and functional mechanisms are only beginning. We established the axis between HuR miR-133b in GC in the study.

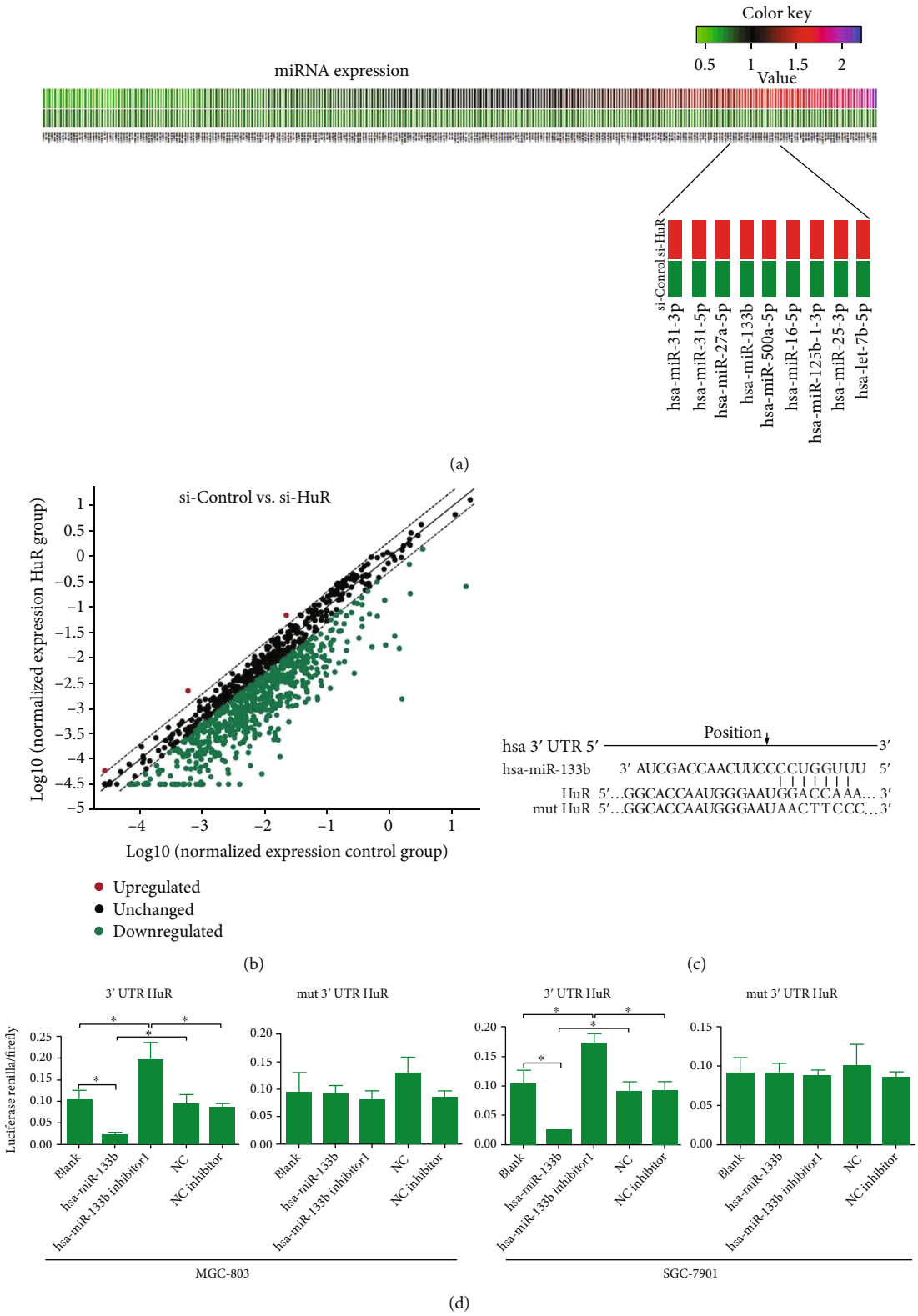

Figure 4: HuR regulates the expression of miR-133b in GC cells. (a) Relative expression of miR-133b and total miRNA in HuR knockdown cells as described. (b) Enrichment of HuR group and control group for normalized expression. (c) Luciferase reporter assay was conducted with HuR and mut-HuR. (d) Luciferase reporter assay detected the changes in fluorescence activity of mir-133b group and blank group in transfected 3′UTR HuR gene or mut 3′UTR HuR gene. Statistical analysis using Kaplan–Meier analysis. Statistical analysis is described in Materials and Methods. $^{*}p < 0.05$; $^{**}p < 0.01$.

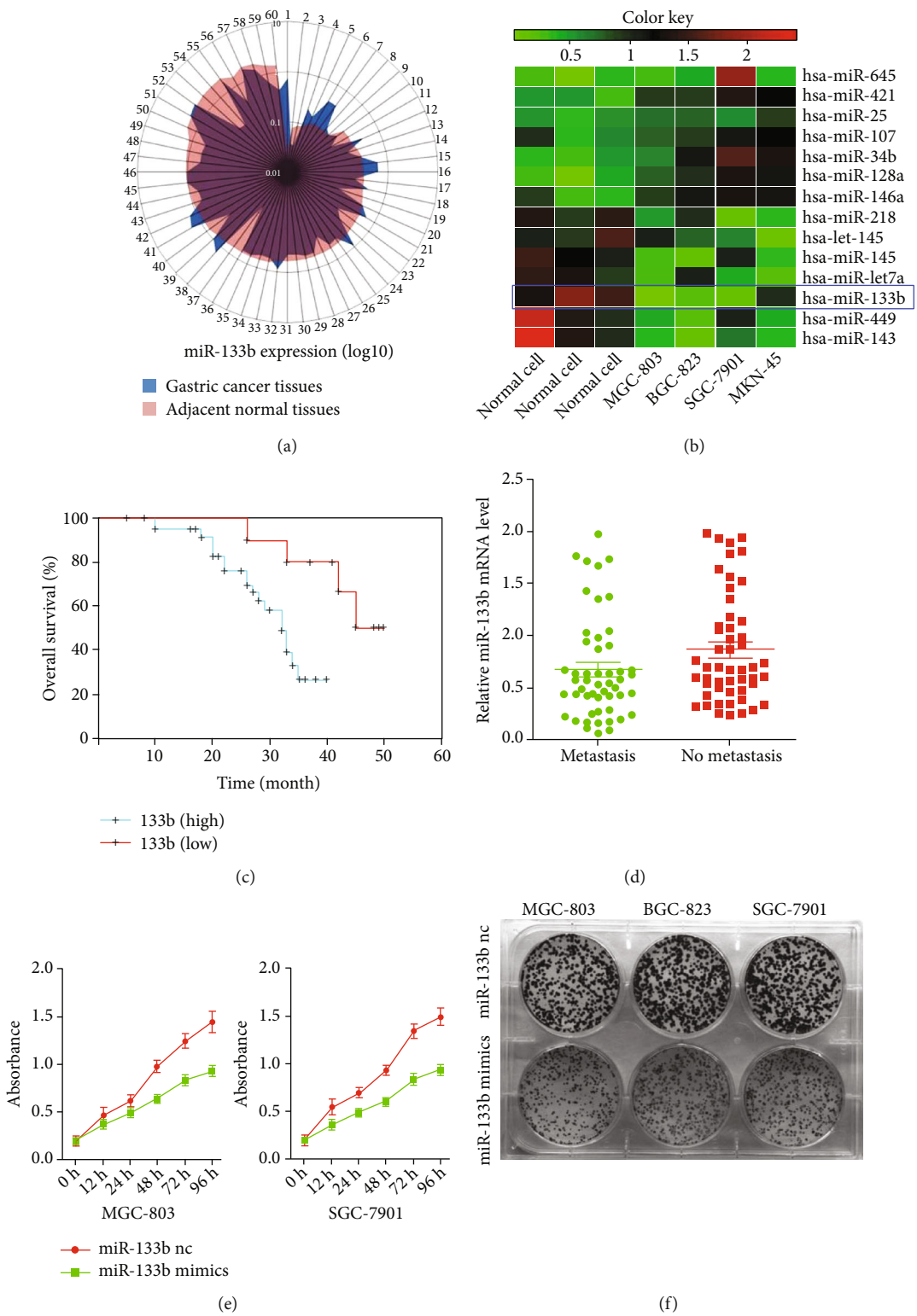

Figure 5: Functional analysis of miR-133b in GC cells. (a) miR-133b levels were detected in 60 pairs of GC tissues and adjacent normal regions by RT-qPCR. (b) Heat maps show the expression of miR-133b and known miRNAs in normal cells and GC cell lines. (c) Statistical analysis of survival probability of miR-133b high- ($n = 10$) and low-expressing ($n = 40$) GC patients using Kaplan–Meier analysis. Statistical analysis is described in the Materials and Methods. (d) The statistical analysis of the association between miR-133b level and pM stage (metastasis and no metastasis). (e) Cell proliferation assay of SGC-7901 and MGC-803 cells after treatment with miR-133b mimics or miR-133b nc using CCK-8. (f) Clone formation assay of SGC-7901 and MGC-803 cells after treatment with miR-133b mimics or miR-133b nc. For all qPCR results, the data are presented as the mean ± SEM, and the error bars represent the standard deviation obtained from three independent experiments. $^{*}p < 0.05$; $^{**}p < 0.01$.

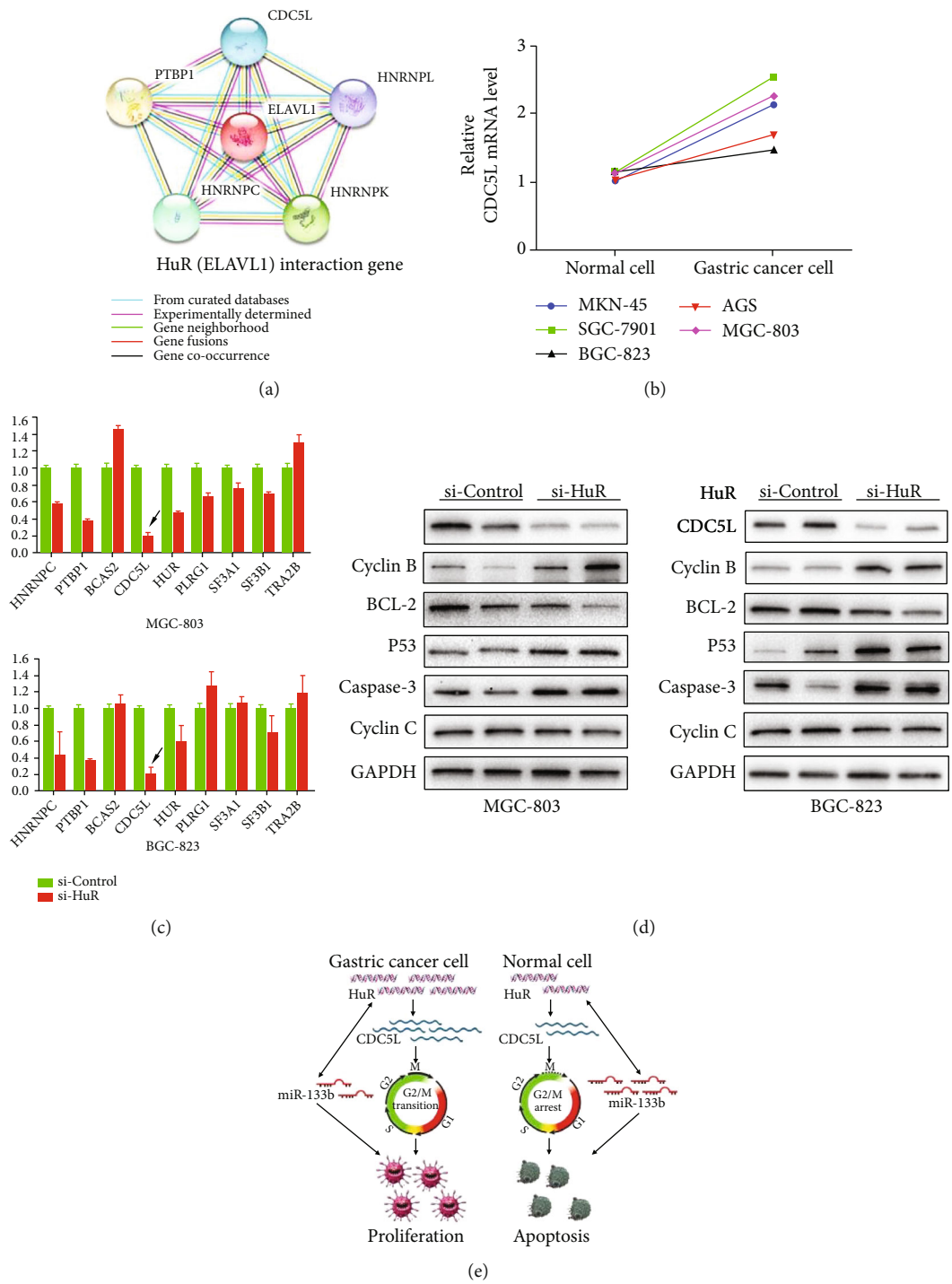

Figure 6: HuR and miR-133b coregulate the progression in GC cells. (a) String analysis reveal that most of the interacting genes between HuR and other genes. (b) Compared with the expression of the CDC5L between GC cell lines and normal cells. (c) CDC5L displayed the significant reduction changes upon HuR knock-down in MGC-803 and BGC-823 cells. (d) Western blots analysis and confirmed the function of HuR and miR-133b on the upstream of the CDC5L in MGC-803 and BGC-823 cells. (e) The axis diagram shows the relationship between HuR and miR-133b with the progression of GC.

Recently, Xue et al. reported that microRNA-133b (miR-133b) plays a suppressor role in several human cancers, as well as glioma [8], colorectal cancer [11]. MicroRNAs (miRNAs) are small noncoding RNAs that bind to mRNAs and regulate gene expression at the posttranscriptional level [5–7]. There are a lot of evidence revealing that miRNAs' expression is maladjusted in many cancers, but more studies are needed to confirm how it affects tumorigenesis and metastasis. miRNAs can act as oncogenes or tumor suppressors to regulate the occurrence and development of tumors. For example, miR-218 [27], miR-129 [28], miR-148 [29], and miR-7a [30] were considered as tumor suppressor.

However, miR-21 [31], miR-221 [32], miR-214 [33], miR-34b [34], and miR-532 [35] were considered as oncogenes in GC [31–35]. In this study, we aimed to study the clinical diagnostic value of HuR and miR-133b in GC.

Abbreviations

GC: Gastric cancer
HuR: Human antigen receptor
VHL: Von Hippel Lindau tumor suppressor
cox-2: Cyclooxygenase 2
MMP-9: Matrix metallopeptidase-9
miRNA: MicroRNA.

Data Availability

You can request the data by contacting the author's email address: lifenglover@sina.com

Additional Points

Statistics. All experiments were repeated at least three times. Statistical analyses were evaluated by the two-tailed t-test and one-way ANOVA. Statistically significance was set at $p < 0.05$ using SPSS program (SPSS 15.0, USA).

Conflicts of Interest

The authors disclose no potential conflicts of interest.

Authors' Contributions

Jing Cui, Nanjing Cao, and Guochao Wang contributed equally to this work.

Acknowledgments

Feng Li designed and performed the experiments, interpreted data, and wrote the manuscript; Jing Cui and Nanjing Cao performed bioinformatics analysis; Guochao Wang and Fuhua Wang provided the experimental material of gastric cancer patients and healthy donors; Bin Yang and Jian Wang helped collect the samples and perform partial experiments. Yunqing Chen and Yongqiang Lv designed the study, directed the experiments, and wrote the manuscript. All authors read and approved the manuscript. This work was supported by grants from the Key Research and Development (R&D) Projects of Shanxi Province (201803D31166 to Feng Li), the Science and Technology Department Basic Research Project of Shanxi (201801D121303 to Feng Li), the PhD Foundation of Shanxi Cancer Hospital/Institute (2017A07 to Feng Li), the scientific research of Health Commission of Shanxi Province (2019062 to Yunqing Chen), and the scientific research and innovation team construction project of Shanxi Cancer Hospital (2020 to Feng Li).

References

[1] Z. Zhu, H. Huiqin, and X. Wang, "Advances in the application of tumor autoantibodies in early diagnosis and screening of gastric cancer," *Guangdong Medical Journal*, vol. 37, no. 15, pp. 2358–2360, 2016.

[2] O. Yangxi and T. Hao, "Lymph node micrometastasis in gastric cancer: research advances," *Chinese Journal of General Surgery*, vol. 24, no. 4, pp. 589–592, 2015.

[3] H. H. Kim, K. Abdelmohsen, A. Lal et al., "Nuclear HuR accumulation through phosphorylation by Cdk1," *Genes & Development*, vol. 22, no. 13, pp. 1804–1815, 2008.

[4] W. J. Ma, S. Cheng, C. Campbell, A. Wright, and H. Furneaux, "Cloning and characterization of HuR, a ubiquitously expressed Elav-like protein," *The Journal of Biological Chemistry*, vol. 271, no. 14, pp. 8144–8151, 1996.

[5] J. Mrena, J. P. Wiksten, A. Kokkola, S. Nordling, A. Ristimäki, and C. Haglund, "COX-2 is associated with proliferation and apoptosis markers and serves as an independent prognostic factor in gastric cancer," *Tumour Biology*, vol. 31, no. 1, pp. 1–7, 2010.

[6] Y.-H. Cui, Q.-Y. Feng, and Q. Liu, "Posttranscriptional regulation of MMP-9 by HuR contributes to IL-1β-induced pterygium fibroblast migration and invasion," *Journal of Cellular Physiology*, vol. 11, no. 6, 2019.

[7] Y. Qin, Y. Zhang, Q. Tang, L. Jin, and Y. Chen, "SQLE induces epithelial-to-mesenchymal transition by regulating of miR-133b in esophageal squamous cell carcinoma," *Acta biochimica et biophysica Sinica*, vol. 49, no. 2, pp. 138–148, 2017.

[8] K. Xue, J. Yang, J. Hu, J. Liu, and X. Li, "MicroRNA-133b expression associates with clinicopathological features and prognosis in glioma," *Artificial Cells, Nanomedicine, and Biotechnology*, vol. 46, no. 4, pp. 815–818, 2018.

[9] I. Grammatikakis, K. Abdelmohsen, and M. Gorospe, "Posttranslational control of HuR function," *RNA*, vol. 8, no. 1, 2017.

[10] J. Y. Pan, C. C. Sun, Z. Y. Bi et al., "miR-206/133b cluster: a weapon against lung cancer?," *Molecular Therapy-Nucleic Acids*, vol. 8, no. 8, pp. 442–449, 2017.

[11] K. M. Xiang and X. R. Li, "miR-133b acts as a tumor suppressor and negatively regulates TBPL1 in colorectal cancer cells," *Asian Pacific Journal of Cancer Prevention*, vol. 15, no. 8, pp. 3767–3772, 2014.

[12] M. Masè, M. Grasso, L. U. Avogaro et al., "Upregulation of miR-133b and miR-328 in patients with atrial dilatation: implications for stretch-induced atrial fibrillation," *Frontiers in Physiology*, vol. 10, no. 10, p. 1133, 2019.

[13] L. Lv, Q. Li, S. Chen et al., "miR-133b suppresses colorectal cancer cell stemness and chemoresistance by targeting methyltransferase DOT1L," *Experimental Cell Research*, vol. 385, no. 1, article 111597, 2019.

[14] J. Li, N. Zhang, R. Zhang et al., "CDC5L promotes hTERT expression and colorectal tumor growth," *Cellular Physiology and Biochemistry*, vol. 41, no. 6, pp. 2475–2488, 2017.

[15] H. Qiu, X. Zhang, W. Ni et al., "Expression and clinical role of Cdc5L as a novel cell cycle protein in hepatocellular carcinoma," *Digestive Diseases and Sciences*, vol. 61, no. 3, pp. 795–805, 2016.

[16] A. Zulueta, A. Caretti, P. Signorelli, and R. Ghidoni, "Resveratrol: a potential challenger against gastric cancer," *World Journal of Gastroenterology: WJG*, vol. 21, no. 37, pp. 10636–10643, 2015.

[17] Q. Zhao, Y. Li, J. Wang et al., "Concurrent neoadjuvant chemoradiotherapy for Siewert II and III adenocarcinoma at gastroesophageal junction," *The American Journal of the Medical Sciences*, vol. 349, no. 6, pp. 472–476, 2015.

[18] A. Tozzi, C. Iftode, L. Cozzi et al., "Neoadjuvant chemoradiotherapy with volumetric-modulated arc therapy for medium-distal oesophageal and gastro-oesophageal junction carcinoma," *Anticancer Research*, vol. 35, no. 7, pp. 4109–4116, 2015.

[19] L. Lowenfeld, J. Datta, R. S. Lewis et al., "Multimodality treatment of T4 gastric cancer in the United States: utilization trends and impact on survival," *Annals of Surgical Oncology*, vol. 22, Supplement 3, pp. 863–872, 2015.

[20] F. Li, P. Yi, J. Pi et al., "QKI5-mediated alternative splicing of the histone variant macroH2A1 regulates gastric carcinogenesis," *Oncotarget*, vol. 7, no. 22, pp. 32821–32834, 2016.

[21] W. Eberhardt, U. Nasrullah, and K. Haeussler, "Inhibition of caspase-2 translation by the mRNA binding protein HuR: a novel path of therapy resistance in colon carcinoma cells?," *Cell*, vol. 8, no. 8, pp. 797–818, 2019.

[22] D. Ostareck and A. Ostareck-Lederer, "RNA-binding proteins in the control of LPS-induced macrophage response," *Frontiers in Genetics*, vol. 10, no. 31, 2019.

[23] C. Giaginis, P. Alexandrou, N. Tsoukalas et al., "Hu-antigen receptor (HuR) and cyclooxygenase-2 (COX-2) expression in human non-small cell lung carcinoma: associations with clinicopathological parameters, tumor proliferative capacity and patients' survival," *Tumour*, vol. 36, no. 1, pp. 315–327, 2015.

[24] T. Xiyu, B. Lingu, J. Kaiyan et al., "CUGBP1 and HuR regulate E-cadherin translation by altering recruitment of E-cadherin 2 mRNA to processing bodies and modulate epithelial barrier function," *American Journal of Physiology. Cell Physiology*, vol. 310, no. 1, pp. 54–65, 2016.

[25] M. J. Kang, B. K. Ryu, M. G. Lee et al., "NF-kappaB activates transcription of the RNA-binding factor HuR, via PI3K-AKT signaling, to promote gastric tumorigenesis," *Gastroenterology*, vol. 135, no. 6, pp. 2030–2042.e3, 2008.

[26] J. Wei, Z. Wang, Z. Wang et al., "MicroRNA-31 function as a suppressor was regulated by epigenetic mechanisms in gastric cancer," *BioMed Research International*, vol. 2017, Article ID 5348490, 11 pages, 2017.

[27] M. Deng, C. Zeng, X. Lu et al., "miR-218 suppresses gastric cancer cell cycle progression through the CDK6/cyclin D1/E2F1 axis in a feedback loop," *Cancer Letters*, vol. 403, no. 403, pp. 175–185, 2017.

[28] C. Lu, Z. Shan, C. Li, and L. Yang, "MiR-129 regulates cisplatin-resistance in human gastric cancer cells by targeting P-gp," *Biomedicine & Pharmacotherapy*, vol. 86, pp. 450–456, 2017.

[29] Y. Song, J. Sun, Y. Xu et al., "Microarray analysis of long noncoding RNAs related to microRNA-148b in gastric cancer," *Neoplasma*, vol. 64, no. 2, pp. 199–208, 2017.

[30] B. M. Kim, J. Woo, C. Kanellopoulou, and R. A. Shivdasani, "Regulation of mouse stomach development and Barx1 expression by specific microRNAs," *Development*, vol. 138, no. 6, pp. 1081–1086, 2011.

[31] P. Zheng, L. Chen, X. Yuan et al., "Exosomal transfer of tumor-associated macrophage-derived miR-21 confers cisplatin resistance in gastric cancer cells," *Journal of Experimental & Clinical Cancer Research*, vol. 36, no. 1, p. 53, 2017.

[32] T. Ning, H. Zhang, X. Wang et al., "miR-221 and miR-222 synergistically regulate hepatocyte growth factor activator inhibitor type 1 to promote cell proliferation and migration in gastric cancer," *Tumour Biology*, vol. 39, no. 6, p. 1010428317701636, 2017.

[33] X. Wang, H. Zhang, M. Bai et al., "Exosomes serve as nanoparticles to deliver anti-miR-214 to reverse chemoresistance to cisplatin in gastric cancer," *Molecular Therapy*, vol. 26, no. 3, pp. 774–783, 2018.

[34] K. Yu, "The Rs4938723 polymorphism reduces expression of microRNA-34b and increases the risk of recurrence after endoscopic dissection in early gastric cancer," *Cellular Physiology and Biochemistry*, vol. 43, no. 3, pp. 1235–1246, 2017.

[35] S. Hu, Q. Zheng, H. Wu, C. Wang, T. Liu, and W. Zhou, "miR-532 promoted gastric cancer migration and invasion by targeting NKD1," *Life Sciences*, vol. 177, no. 177, pp. 15–19, 2017.

Hindawi
Disease Markers
Volume 2022, Article ID 5651506, 9 pages
https://doi.org/10.1155/2022/5651506

Research Article

The Role of Symptom Duration and Serologic Factors in the Relapse of IgG4-Related Ophthalmic Disease following Surgery: A Retrospective Cohort Study

Siyu Liu,[1,2] Zifan Yue,[1] Chengcheng Zeng,[1] Xiao Huang,[1] Jian Li,[1] Jiale Diao,[1] Xinxin Chen,[1] Ruili Wei,[1] and Weihua Yang[3,4]

[1]*Department of Ophthalmology, Changzheng Hospital of Naval Medicine University, Shanghai, China 200003*
[2]*Department of Ophthalmology, Naval Medical Center of PLA, Shanghai, China 200050*
[3]*The Affiliated Eye Hospital of Nanjing Medical University, Nanjing, Jiangsu, China 210029*
[4]*The Laboratory of Artificial Intelligence and Bigdata in Ophthalmology, 210029, China*

Correspondence should be addressed to Ruili Wei; ruiliwei@smmu.edu.cn and Weihua Yang; benben0606@139.com

Received 11 December 2021; Accepted 10 January 2022; Published 26 February 2022

Academic Editor: Wen-Qing Shi

IgG4-related disease (IgG4-RD) affects multiple organs and is characterized by immune-mediated inflammation and fibrosis; IgG-RD affecting orbital tissue is known as IgG4-related ophthalmic disease (IgG4-ROD). This research is aimed at exploring whether symptom duration and common serologic factors, such as IgG, IgE, and eosinophils, are potential risk factors for IgG4-ROD patient relapse after surgery and identifying possible causes of the positive correlation between symptom duration and relapse. This retrospective cohort study included 40 IgG4-ROD patients after surgery. Auxiliary inspection results were obtained before surgery and during follow-up, and relapse risk factors were identified based on previous studies. We used the Spearman rank correlation test to reveal the relationship between symptom duration and relapse time and identified the optimal cutoff value for symptom duration by X-tile. Then, we divided the patients into the long-duration and short-duration groups. Kaplan–Meier survival analyses and log-rank tests were performed to identify the relationship between symptom duration and relapse using X-tile software. Finally, we studied the relationship between previously studied relapse risk factors and symptom duration. The survival curves of the long-duration and short-duration groups were obviously different, and the baseline serum IgG, IgE, and eosinophil levels and asthma concomitant rate were significantly different between the long-duration and short-duration groups. Furthermore, the baseline serum IgG ($r = 0.485$, $P = 0.002$), IgE ($r = 0.350$, $P = 0.037$), and eosinophil ($r = 0.6535$, $P < 0.0001$) levels were positively correlated with symptom duration. Our study shows that IgG4-ROD symptom duration is significantly positively correlated with relapse rate and negatively correlated with relapse time. Symptom duration was positively correlated with serum baseline IgG4, IgE, and eosinophil levels and asthma history, which were potential risk factors for disease relapse. We recommended that IgG4-ROD patients with symptom durations greater than 96 months continue to receive maintenance steroid therapy longer than 1 year postsurgery to reduce the relapse rate.

1. Introduction

IgG4-related disease (IgG4-RD) is an immune-mediated inflammatory disorder with fibrosis that can affect multiple organs, and the affected organs can have tumor-like lesions and even failure [1]. The histopathological characteristics of IgG4-RD are abundant IgG4-positive plasma cell infiltration, numerous lymphocyte and plasma cell infiltration, phlebitis obliterans, and mat-pattern fibrosis [2], and the gold standard for the diagnosis of IgG4-RD is its characteristic histopathology accompanied by a significant infiltration of IgG4+ plasma cells [3]. IgG4-RD can affect multiple organs of the human body, including the lacrimal glands, salivary glands, aorta, bile ducts, pancreas, lungs, kidneys, liver, and dura mater. The clinical features of IgG4-RD include autoimmune pancreatitis, Mikulitz disease, retroperitoneal fibrosis,

orbital inflammatory pseudotumor, autoimmune cholangitis, hypertrophic dura meningitis, and interstitial pneumonia [4]. IgG-RD that affects orbital tissue is also known as IgG4-related ophthalmic disease (IgG4-ROD).

More and more attention paid to the diagnosis and treatment of this infrequent autoimmune disease since the publication of diagnostic criteria for IgG4-RD [5]. In 2015, the first international consensus guidance statement which provided standardized management and treatment of IgG4-RD was published [6]. The statement called for all active IgG4-RD and IgG4-ROD patients to receive treatment, and the first-line drug for remission induction is glucocorticoids. For patients whose disease progression cannot be controlled by glucocorticoid monotherapy, a combination of glucocorticoid and immunosuppressant therapy is required, and B cell depletion therapy and surgery are also reasonable treatment options. However, each treatment method is accompanied by different degrees of relapse [7, 8], and the pattern of disease relapse is still unpredictable [9]. How to maintain treatment to avoid relapse is still an urgent problem to be solved, and a better understanding of risk factors for relapse plays an important role in disease management and relapse monitoring. The risk factors for relapse of IgG4-RD include an increase in serum IgE, mast cells, eosinophils, and a history of asthma [10, 11]. However, due to the heterogeneity and rarity of the disease, there are still few studies on the influencing factors of IgG-ROD relapse, especially in patients who have undergone surgical treatment.

Our study is a retrospective cohort study that included 40 IgG4-ROD patients after surgery. Our study describes the clinical characteristics and differences in serological indicators of each patient, explores and analyses whether symptom duration and serologic factors, such as serum IgE and IgG4, are potential risk factors for IgG4-ROD patient relapse after surgery, and tries to identify possible causes of the positive correlation between the duration of symptoms and relapse. We hope that this study will provide reliable predictors of relapse for IgG4-ROD and new recommendations for the rational treatment of IgG4-ROD.

2. Materials and Methods

2.1. Cohort Conduction and Patient Selection. This research was permitted by the Ethics Committee of Changzheng Hospital affiliated with Naval Military Medical University. All the patients enrolled in the study signed an informed consent form, and all of our procedures for experimental implementation complied with the Declaration of Helsinki. We included all IgG4-ROD patients who met the inclusion criteria treated in Changzheng Hospital from March 2013 to July 2020 in the cohort ($n = 40$), and 4 patients were excluded from our cohort due to loss of follow-up. We diagnosed 21 (58.3%), 4 (11.1%), and 11 (30.6%) patients with definite, probable, and possible IgG4-ROD, respectively, according to the 2015 IgG4-ROD diagnostic criteria [12]. The inclusion criteria were patients undergoing surgical treatment, and the postoperative follow-up time was more than 1 year. The patients included in the cohort had no history of other autoimmune diseases.

2.2. Auxiliary Inspection Results. Auxiliary inspections, which included serologic factor analysis, imaging examinations, other laboratory tests, and histological examinations, were conducted before surgery and during follow-up. The indices detected included complete blood cell counts, serum IgE levels, serum IgG and IgG subclass levels, serum eosinophil concentrations and ratios, and other necessary test results. All patients received imaging examinations, such as computed tomography (CT), ultrasound scanning (US), and magnetic resonance imaging (MRI). All tissues removed after surgery underwent pathological biopsy.

2.3. Assessing Duration of Symptoms and Disease Relapse. We determined the time of onset during detailed medical history inquiry and diagnosis and treatment records provided by the patient. The time of onset was defined as the time when positive symptoms or signs appeared or when clinically significant auxiliary examination results appeared. After the operation, the patients went to the ophthalmology clinic of Changzheng Hospital for related examinations and follow-up at 1 month and 6 months later. Afterward, we sent questionnaires to the patients to investigate the relapse situation every year. The relapse time is defined as the reappearance of positive symptoms and signs, as well as the reappearance of diagnostic laboratory tests and imaging findings. An increase in serum IgG4 concentration alone cannot be considered a disease relapse. We determined the time from onset to treatment as the duration of symptoms.

X-tile was used to identify the optimal cutoff value, and the statistical significance index was $P < 0.05$ [13]. The obtained cutoff value was used as the basis for grouping the long-duration group and the short-duration group. Kaplan–Meier survival analyses and log-rank tests were performed to identify the relationship between the duration of symptoms and relapse using X-tile software.

2.4. Confirmation of Potential Predictors of Disease Relapse. The predictors screened in this experiment to predict disease relapse include some common clinical features of IgG4-ROD, past medical history, and serological indicators, like gender ratio, the rates of having a history of asthma, baseline serum IgG4, IgE, IgG, and eosinophil counts, which have been suggested by previous studies to be predictors of IgG4-RD relapse [8, 10, 11, 14, 15].

2.5. Statistical Analysis. All patient clinical data were gathered and are listed in the tables and supplementary materials of this article. We present distributed normally distributed quantitative variables as the means ± SDs and present nonnormally distributed features as the medians (IQRs). We compared continuous variables using the Mann–Whitney test. The Spearman rank correlation test was used to quantify the correlations. We used the chi-square test to compare categorical variables. Then, we generated all figures with GraphPad Prism version 8.1.1 (GraphPad Software, Inc., La Jolla, CA, USA) and performed all statistical analyses with SPSS Statistics version 24.0 (IBM Corp., Armonk, NY, USA).

3. Results

3.1. Baseline Features of the Patients Enrolled in This Cohort. We enrolled 40 patients in our cohort. After excluding 4 patients who were missing the follow-up, 36 patients remained, and their clinical and demographic baseline features are shown in Table 1. The average age at onset was 52.86 years, and the sex ratio was 3.5, with male patients accounting for the majority of the cohort. In addition, the average follow-up time was 40.64 months. Notably, the average time from onset to treatment was 64.22 months, and the relapse rate after surgery was 38.9%.

According to the clinical characteristics, eyelid swelling (77.8%) and exophthalmos (52.8%) were the most common clinical symptoms in IgG4-ROD patients, and the lacrimal gland was the most commonly affected organ/anatomical site (88.9%). The proportion of asthma history was 36.1%.

3.2. Survival Analysis Construction and Cutoff Value Identification. The Spearman rank correlation test was used to reveal the relationship between the duration of symptoms and the relapse time, and the results are presented in Figure 1. The Spearman rank correlation test shows that there is a negative correlation between the duration of symptoms and the relapse time ($r = -0.526$, $P < 0.05$). We performed Kaplan–Meier survival analyses and log-rank tests to identify the potential relationship between the duration of symptoms and relapse. Based on the cutoff value calculated by X-tile (duration of symptoms = 96 months, the result is shown in Figure 2); we divided the 36 patients into a long-duration group ($n = 10$) and a short-duration group ($n = 26$). The survival curves of the IgG4-ROD patients in the long-duration group and short-duration group are shown in Figure 3. The log-rank test results revealed that the survival curves of the long-duration group and short-duration group were significantly different ($P < 0.05$), and the relative risk (RR) was 2.6 (95% CI 1.225-5.516), which indicates that symptom duration is strongly correlated with the disease relapse rate.

3.3. Differences in Clinical Features between the Long-Duration Group and the Short-Duration Group. A comparison of the baseline clinical characteristics between the patients in the two groups is presented in Table 2. According to the results, we found that the probability of asthma history was higher in the long-duration group, which means that patients with a long duration of symptoms had a higher probability of having asthma. The difference in the relapse rate of IgG4-ROD between the patients in the long-duration group and short-duration group was also statistically significant, and the long-duration group had a higher relapse rate. There were no significant differences in other clinical indicators, including the rates of eyelid swelling, exophthalmia, vision decrease, eyelid hyperemia, and diplopia, between the patients in the long-duration group and short-duration group.

There are differences in serological indicators between the long-duration group and the short-duration group. Mann–Whitney tests were performed to analyze whether there were significant differences in serological indicators, including serum IgG4, IgG, IgE, eosinophil, and globulin levels, between the long-duration group and short-duration group. The results are presented in Table 3 and Figure 4.

According to the results, we found that the levels of serum IgE, IgG, and eosinophils were significantly different between the long-duration group and short-duration group, which means that patients with a long duration of symptoms have higher baseline serum IgE, IgG, and eosinophil levels.

3.4. Identification of the Relationship between Risk Factors for Relapse and Duration of Symptoms. We used the Spearman

Table 1: Baseline clinical characteristics of patients with IgG4-related ophthalmic disease ($n = 36$).

Variables	Value
Age (mean ± SD), years	52.9 ± 16.4
Sex (male/female)	28/8
Laterality (unilateral/bilateral)	13/23
Duration of symptoms, median (IQR), months	42 (9-96)
IgG4-ROD diagnosis (definite/probable/possible)	21/4/11
Orbital lesion	
Lacrimal glands (%)	32 (88.9)
Extraocular muscles (%)	14 (38.9)
Orbital fat (%)	4 (11.1)
Optic nerve (%)	3 (8.3)
Trigeminal nerve (%)	9 (25.0)
Clinical symptoms	
Eyelid hyperemia (%)	13 (36.1)
Diplopia (%)	9 (25.0)
Eyelid swelling (%)	28 (77.8)
Exophthalmia (%)	19 (52.8)
Decreased vision (%)	4 (11.1)
Paranasal sinusitis (%)	28 (77.8)
Asthma (%)	13 (36.1)

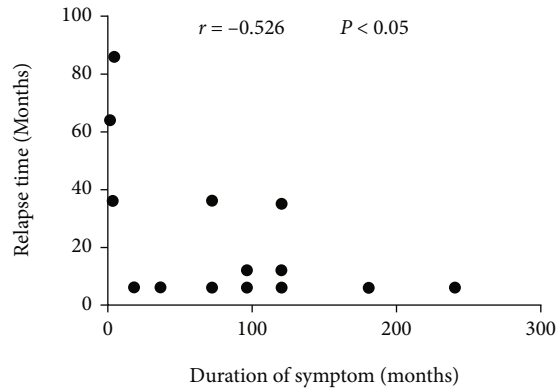

Figure 1: Comparison of the duration of symptoms and the relapse time by Spearman rank correlation tests. P values < 0.05 were considered significant.

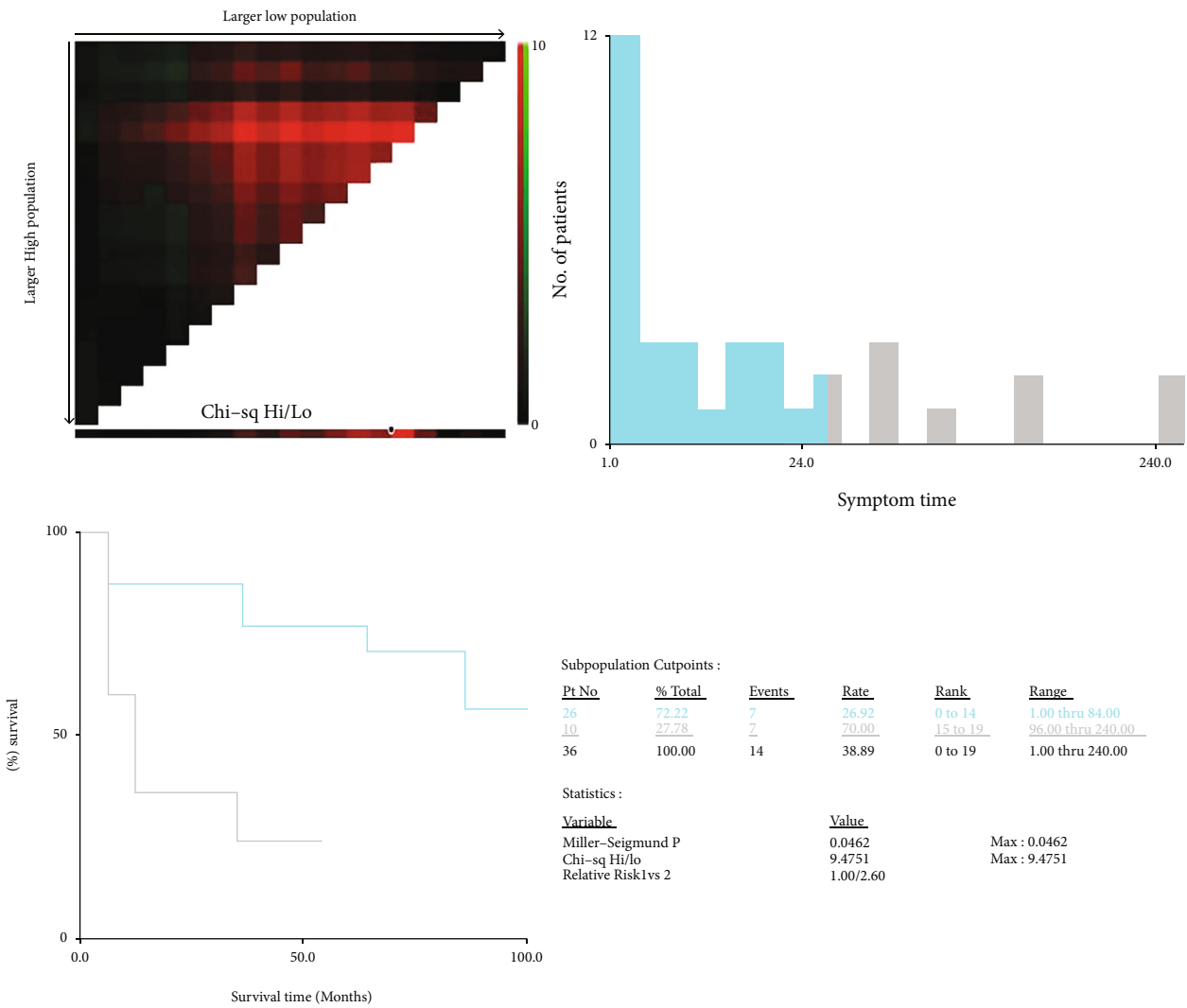

Figure 2: Identification of the cutoff value by X-tile software according to the duration of symptoms and the disease relapse time and rate. Each graph contains the X-tile plot, a histogram, the K-M curve, and the data related to the optimal cutoff point.

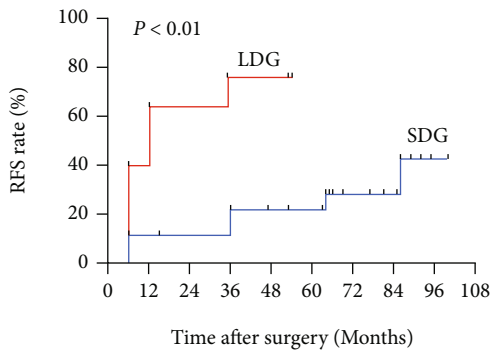

Figure 3: Survival curves of patients in the long-duration group (LDG) and the short-duration group (SDG). The relapse rate (RFS rate) of the long-duration group was higher than that of the short-duration group ($P < 0.001$).

rank correlation test to identify the relationships between baseline serum IgE and eosinophil levels and symptom duration, and chi-square tests were conducted to verify the relationship between the duration of symptoms and the history of associated asthma. The results are presented in Figure 5. Specifically, the results showed that serum IgE ($r = 0.350$, $P = 0.037$) and eosinophil ($r = 0.654$, $P < 0.0001$) levels were positively correlated with the duration of symptoms, and the chi-square test results between the long-duration group and short-duration group were also significantly different. This suggests a longer symptom duration along with higher serum IgE and eosinophil levels, and patients with a longer symptom duration are more likely to suffer from asthma.

4. Discussion

IgG4-related ophthalmic disease is a fibroinflammatory disease mostly characterized by $IgG4^+$ plasma cell invasion. The lacrimal gland is the most common anatomical site of IgG4-ROD involvement [16, 17], and eyelid swelling, exophthalmos, and diplopia were the most common clinical symptoms [18]; our research results were consistent with these previous findings. In addition, IgG4-ROD can also affect

Table 2: Baseline clinical characteristics of patients in the short- and long-duration groups.

Variables	Short symptom duration	Long symptom duration	*P* value	Variables	Short symptom duration	Long symptom duration	*P* value
Gender			0.397	Lacrimal glands			0.305
Male	19 (73.1%)	9 (90.0%)		Yes	24 (92.3%)	8 (80.0%)	
Female	7 (26.9%)	1 (10.0%)		No	2 (7.7%)	2 (20.0%)	
Laterality			0.270	Extraocular muscles			0.462
Unilateral	11 (42.3%)	2 (20.0%)		Yes	9 (34.6%)	5 (50.0%)	
Bilateral	15 (57.7%)	8 (80.0%)		No	17 (65.4%)	5 (50.0%)	
Smoking history			0.179	Orbital fat			0.057
Yes	4 (15.4%)	4 (40.0%)		Yes	1 (3.9%)	3 (30.0%)	
No	22 (84.6%)	6 (60.0%)		No	25 (96.2%)	7 (70.0%)	
Diplopia			0.686	Optic nerve			0.181
Yes	6 (23.1%)	3 (30.0%)		Yes	1 (3.9%)	2 (20.0%)	
No	20 (76.9%)	7 (70.0%)		No	25 (96.2%)	8 (80.0%)	
Eyelid hyperemia			1.000	Trigeminal nerve			0.226
Yes	9 (34.6%)	4 (40.0%)		Yes	5 (19.2%)	4 (40.0%)	
No	17 (65.4%)	6 (60.0%)		No	21 (80.8%)	6 (60.0%)	
Decreased vision			0.057	Paranasal sinusitis			0.397
Yes	1 (3.9%)	3 (30.0%)		Yes	19 (73.1%)	9 (90.0%)	
No	25 (96.2%)	7 (70.0%)		No	7 (26.9%)	1 (10.0%)	
Eyelid swelling			0.076	Asthma			**0.018**
Yes	18 (69.2%)	10 (100.0%)		Yes	6 (23.1%)	7 (70.0%)	
No	8 (30.8%)	0 (0.0%)		No	20 (76.9%)	3 (30.0%)	
Exophthalmia			0.274	Recurrence			**0.026**
Yes	12 (46.2%)	7 (70.0%)		Yes	7 (26.9%)	7 (70.0%)	
No	14 (53.9%)	3 (30.0%)		No	19 (73.1%)	3 (30.0%)	

[a]Continuous correction chi-square test. [b]Fisher exact test.

Table 3: Baseline serological test in the short- and long-symptom-duration groups.

Variables	Short symptom duration	Long symptom duration	*P* value
Serum IgG (g/L)	16.42 ± 5.90	23.74 ± 9.45	0.030
Serum IgG4 (g/L)	9.27 ± 10.74	10.37 ± 7.68	0.417
Serum IgG4/IgG (%)	0.48 ± 0.36	0.46 ± 0.25	0.972
Serum IgM (g/L)	0.98 ± 0.42	1.01 ± 0.76	0.536
Serum IgE (IU/mL)	457.22 ± 636.89	1864.70 ± 2210.19	0.011
Serum IgA (g/L)	1.79 ± 0.71	1.68 ± 0.71	0.724
Serum eosinophilia ($\times 10^9$/L)	0.31 ± 0.25	0.58 ± 0.24	0.004

Normal ranges: IgG 7-16 g/L; IgG4 <1.35 g/L; IgM 0.5-2.5 g/L; IgE <165 IU/mL; IgA 0.85-3 g/L; eosinophilia 0.02-0.52 ($\times 10^9$/L).

eyelids, extraocular muscles, orbital adipose tissue, the optic nerve, conjunctiva, the trigeminal nerve, orbital bone, the lacrimal sac, sclera, choroid, and other ocular accessory tissues and adjacent orbital tissues [19, 20] and can cause symptoms, such as diplopia, orbital pain, restrictive eye movement disorder, decreased vision, tearing, and conjunctival congestion [18].

IgG4-ROD is a chronic illness, and the development of this disease involves a process of remission-relapse-remission [21]. How to effectively reduce the relapse rate has become a major problem in the treatment of IgG4-related ophthalmic disease, and identification of the risk factors could improve the management and probably decrease the relapse rate of IgG4-ROD. Regarding therapeutic methods, glucocorticoids are the first-line treatment for most patients with IgG4-ROD. In particular, systemic glucocorticoid therapy should be the first choice for patients with

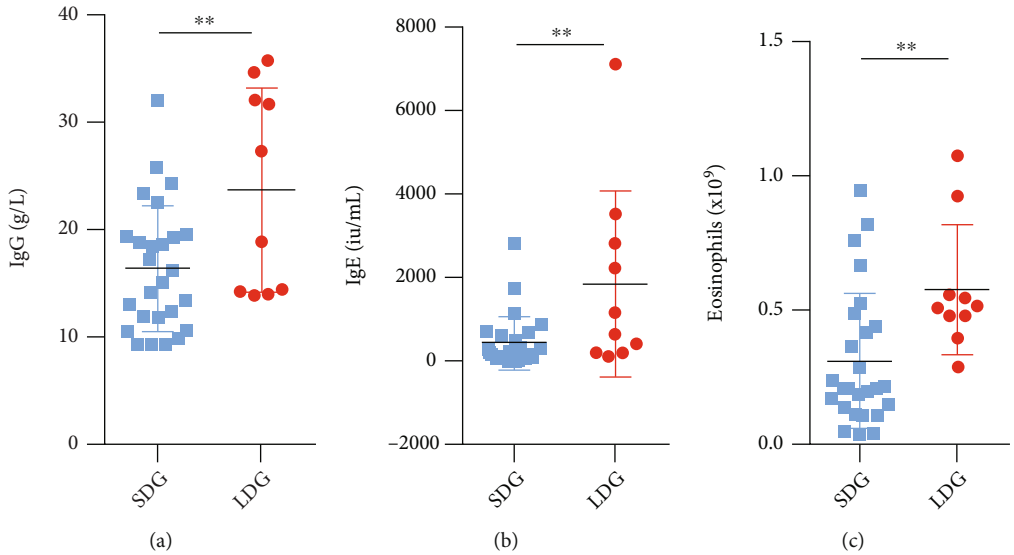

Figure 4: Comparison of baseline serum IgG, IgE, and eosinophil levels between patients in the long-duration group and the short-duration group. The horizontal bars represent the standard errors of the means. P values < 0.05 were considered significant. (a) Patients in the long-duration group and short-duration group presenting with elevated serum IgG levels. (b) Patients in the long-duration group and short-duration group presenting with elevated serum IgE levels. (c) Patients in the long-duration group and short-duration group presenting with elevated serum eosinophils levels.

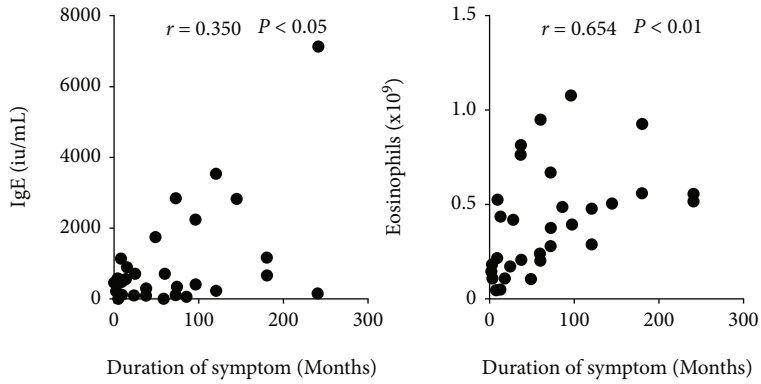

Figure 5: Comparison of eosinophil counts and serum IgE levels by Spearman rank correlation tests. P values < 0.05 were considered significant.

active IgG4-ROD [19]. However, glucocorticoid therapy has a high relapse rate. Ebbo et al. [22] found that 68.4% of IgG4-ROD patients relapsed after a first course of glucocorticoids in their cohort, and Karim found that including IgG4-ROD, approximately 62% of IgG4-RD patients relapsed in their cohort [23]. Furthermore, glucocorticoid therapy does not respond particularly well to many hormone-intolerant patients and elderly people, and the cycle of glucocorticoid therapy is also relatively long. Tacelli et al. revealed that maintenance steroid therapy lasting longer than 1 year could reduce the risk of relapse [24]. Surgical treatment as an alternative treatment for IgG-ROD has been shown to have a lower relapse rate than glucocorticoid therapy [25]. All the IgG4-ROD patients in our cohort had a relapse rate of 38.9%, and in particular, those in the short-duration group had a relapse rate of 26.9%; these findings confirmed the results of previous studies, suggesting that surgical treatment for IgG4-ROD likely has a lower relapse rate than glucocorticoid treatment. This provides a new direction of rational treatment for IgG4-ROD patients, especially those with glucocorticoid intolerance and elderly people. In addition, researchers found that low-dose steroid maintenance therapy significantly reduced the relapse rate [1, 2]. However, long-term glucocorticoid treatment has many complications, such as Cushing's syndrome, osteoporosis, hypertension, and diabetes [26, 27]. If doctors can correctly identify patients at high risk of relapse and target them with low-dose steroid, maintenance therapy could lead to more rational treatment strategies for IgG4-ROD.

From our survival analysis results, we realized that there was a potential relationship between symptom duration and disease relapse: as the duration of symptoms increased, the relapse time was earlier, and the relapse rate also increased. Liu et al. [8] found that the duration from diagnosis to

treatment was an independent risk factor for relapse in IgG4-RD patients. However, there is no previous independent study on the relationship between IgG4-ROD and the duration of symptoms. Our research proves that the duration of symptoms is a risk factor for disease relapse and provides theoretical support for the rationality of early diagnosis and treatment of IgG4-ROD.

To further explore the reasons for the high relapse rate of IgG-ROD due to the long duration of symptoms, we conducted a study on the relationships between common serological and clinical indicators and the duration of symptoms. The results show that a longer symptom duration causes higher serum IgE and eosinophil baseline levels, and patients with a longer symptom duration were more likely to develop asthma. Interestingly, serum baseline levels of IgE and eosinophils and history of asthma are all risk factors for IgG4-ROD relapse. Wallace et al. [15] found that baseline elevations in both serum IgE and blood eosinophil concentrations independently predict IgG4-RD, including IgG4-ROD relapses. Zhou et al. [11] found that IgG4-RD patients (including IgG4-ROD patients) with high serum IgE levels at baseline were more likely to have higher disease activity and higher disease relapse rates. Liu et al. [8] found that the risk factors for IgG4-ROD relapse required a longer duration from diagnosis to treatment and a history of allergy. Della Torre et al. [14] found that increased serum IgE and eosinophil levels are independent of atopic disease history, revealing that these factors reflect mechanisms inherent to the immune response driving IgG4-RD; they also found that T-helper type 2 (Th2) cells play crucial roles in IgG4-RD pathogenesis [14] and proved that the IgG4-RD Th2-polarized immune state is related to antecedent atopic disease rather than disease activity [28]. We speculated that the serum IgE and eosinophil levels might reflect the different immune statuses of the body. Patients with high serum indexes are more sensitive to the immune response, which makes the disease more likely to relapse. Furthermore, Th2 cells can secrete specific cytokines, such as IL-13, IL-5, and IL-4, to cause asthma and immune abnormalities [29], and the presence of asthma can increase the number of circulating Th2 memory cells, which increases atopy and enhances Th2 responses, such as increasing serum IgE and eosinophil levels, in IgG4-RD [28, 30]; this phenomenon explains why the relapse rate of patients with a history of asthma is increased. In addition, our research verified the positive correlation between serum baseline levels of IgG, IgE, eosinophils, history of asthma, and symptom duration in IgG4-ROD patients, indicating that as the duration of symptoms increases, serum baseline levels of IgE and eosinophils accumulate in the body and are more likely to accompany asthma. These factors induce IgG4-ROD relapse and suggest that patients with IgG4-ROD should undergo surgery as soon as possible to reduce the duration of symptoms to reduce the relapse rate. This is probably due to the increasing number of circulating Th2 memory cells with prolonged symptom duration because Th2 memory cells secrete a large number of cytokines, such as IL-4 and IL-13, which leads to the accumulation of serum IgE and eosinophils and the occurrence of asthma. However, whether the above high-concentration serological indicators and high asthma concomitant rate are the cause of disease relapse still needs follow-up prospective studies and animal experiments for verification.

5. Limitations

Our research was retrospective, selection bias and recall bias probably occurred, and measurement bias may exist in different patients due to the different testing times and personnel of serological indicators. Furthermore, the sample size of the research is small and does not conform to the normal distribution, so many reasonable statistical methods cannot be performed. Whether the duration of symptoms is indeed an independent risk factor for relapse still needs to be further explored by expanding the sample size and using Cox regression analysis and other more convincing statistical methods. Moreover, due to the scarcity of IgG4-ROD patients and the limitations of retrospective studies, the experiment did not adopt 1 : 1 grouping. The patient's disease relapse time may not be completely accurate due to the limitation of the follow-up period. The duration of symptoms completely depended on patient self-report; consequently, the possibility of memory bias existed, although we carefully verified symptom duration. We plan to further explore whether the duration of symptoms is indeed an independent risk factor for relapse by expanding the sample size and using more convincing statistical methods in our future research.

6. Conclusions

In conclusion, our research used the largest known cohort of patients undergoing surgical treatment for IgG4-ROD and for the first time explored the relationship between the duration of symptoms and the relapse of IgG4-ROD. Our study provides novel information about risk factors for IgG4-ROD relapse and found that the duration of symptoms of IgG4-ROD has a significant positive correlation with relapse of the disease. As the duration of symptoms increases, the relapse time becomes earlier, and the relapse rate also increases. The duration of symptoms is positively correlated with serum baseline levels of IgE, eosinophils, and asthma history, which are risk factors for disease relapse, suggesting that the prolonged duration of symptoms may lead to the accumulation of risk factors for the relapse of the abovementioned diseases and lead to relapse. For these reasons, we recommended that IgG4-ROD patients with symptom durations greater than 96 months continue to receive maintenance steroid therapy longer than 1 year after surgery to reduce the relapse rate. Our research provides theoretical support for advocating early treatment of IgG4-ROD and for the reasonable selection of treatment options; additionally, our study provides new directions and ideas for follow-up studies on the prevention of IgG4-ROD relapse and the identification of potential serologic biomarkers for predicting disease relapse.

Data Availability

All of our research data can be found in the supplementary data we uploaded.

Conflicts of Interest

The authors declare that there is no conflict of interest regarding the publication of this paper.

Authors' Contributions

Siyu Liu, Zifan Yue, and Chengcheng Zeng contributed equally to this work and share first authorship.

Acknowledgments

We thank all authors who submitted their work for this research. We are deeply indebted to the patients who agreed to participate in this research. This study was funded by grants from the National Natural Science Foundation of China (grant numbers 81770959 and 81570885).

References

[1] T. Kamisawa, Y. Zen, S. Pillai, and J. H. Stone, "IgG4-related disease," *The Lancet*, vol. 385, no. 9976, pp. 1460–1471, 2015.

[2] J. H. Stone, Y. Zen, and V. Deshpande, "IgG4-related disease," *The New England Journal of Medicine*, vol. 366, no. 6, pp. 539–551, 2012.

[3] V. Deshpande, Y. Zen, J. K. Chan et al., "Consensus statement on the pathology of IgG4-related disease," *Modern Pathology*, vol. 25, no. 9, pp. 1181–1192, 2012.

[4] H. Umehara, K. Okazaki, Y. Masaki et al., "A novel clinical entity, IgG4-related disease (IgG4RD): general concept and details," *Modern Rheumatology*, vol. 22, no. 1, pp. 1–14, 2012.

[5] H. Umehara, K. Okazaki, Y. Masaki et al., "Comprehensive diagnostic criteria for IgG4-related disease (IgG4-RD), 2011," *Modern Rheumatology*, vol. 22, no. 1, pp. 21–30, 2012.

[6] A. Khosroshahi, Z. S. Wallace, J. L. Crowe et al., "International consensus guidance statement on the management and treatment of IgG4-related disease," *Arthritis & Rhematology*, vol. 67, no. 7, pp. 1688–1699, 2015.

[7] N. Andrew, D. Kearney, and D. Selva, "IgG4-related orbital disease: a meta-analysis and review," *Acta Ophthalmologica*, vol. 91, no. 8, pp. 694–700, 2013.

[8] Y. Liu, Q. Zeng, L. Zhu et al., "Relapse predictors and serologically unstable condition of IgG4-related disease: a large Chinese cohort," *Rheumatology (Oxford)*, vol. 59, no. 8, pp. 2115–2123, 2020.

[9] M. Yamamoto, H. Takahashi, K. Ishigami et al., "Relapse patterns in IgG4-related disease," *Annals of the Rheumatic Diseases*, vol. 71, no. 10, p. 1755, 2012.

[10] E. L. Culver, R. Sadler, A. C. Bateman et al., "Increases in IgE, eosinophils, and mast cells can be used in diagnosis and to predict relapse of IgG4-related disease," *Clinical Gastroenterology and Hepatology*, vol. 15, no. 9, pp. 1444–1452.e6, 2017.

[11] J. Zhou, Y. Peng, L. Peng et al., "Serum IgE in the clinical features and disease outcomes of IgG4-related disease: a large retrospective cohort study," *Arthritis Research & Therapy*, vol. 22, no. 1, p. 255, 2020.

[12] H. Goto, M. Takahira, and A. Azumi, "Diagnostic criteria for IgG4-related ophthalmic disease," *Japanese Journal of Ophthalmology*, vol. 59, no. 1, pp. 1–7, 2015.

[13] R. L. Camp, M. Dolled-Filhart, and D. L. Rimm, "X-tile," *Clinical Cancer Research*, vol. 10, no. 21, pp. 7252–7259, 2004.

[14] E. Della Torre, H. Mattoo, V. S. Mahajan, M. Carruthers, S. Pillai, and J. H. Stone, "Prevalence of atopy, eosinophilia, and IgE elevation in IgG4-related disease," *Allergy*, vol. 69, no. 2, pp. 269–272, 2014.

[15] Z. S. Wallace, H. Mattoo, V. S. Mahajan et al., "Predictors of disease relapse in IgG4-related disease following rituximab," *Rheumatology (Oxford)*, vol. 55, no. 6, pp. 1000–1008, 2016.

[16] W. Cheuk, H. K. Yuen, S. Y. Chu, E. K. W. Chiu, L. K. Lam, and J. K. C. Chan, "Lymphadenopathy of IgG4-related sclerosing disease," *The American Journal of Surgical Pathology*, vol. 32, no. 5, pp. 671–681, 2008.

[17] L. D. Cornell, S. L. Chicano, V. Deshpande et al., "Pseudotumors due to IgG4 immune-complex tubulointerstitial nephritis associated with autoimmune pancreatocentric disease," *The American Journal of Surgical Pathology*, vol. 31, no. 10, pp. 1586–1597, 2007.

[18] W. Cheuk and J. K. Chan, "IgG4-related sclerosing disease," *Advances in Anatomic Pathology*, vol. 17, no. 5, pp. 303–332, 2010.

[19] A. Khosroshahi, Z. S. Wallace, J. L. Crowe et al., "International consensus guidance statement on the management and treatment of IgG4-related disease," *Arthritis & Rheumatology*, vol. 67, no. 7, pp. 1688–1699, 2015.

[20] A. Wu, N. H. Andrew, A. A. McNab, and D. Selva, "IgG4-Related ophthalmic disease: pooling of published cases and literature review," *Current Allergy and Asthma Reports*, vol. 15, no. 6, p. 27, 2015.

[21] C. S. Lee, G. J. Harocopos, C. L. Kraus et al., "IgG4-associated orbital and ocular inflammation," *Journal of Ophthalmic Inflammation and Infection*, vol. 5, no. 1, p. 15, 2015.

[22] M. Ebbo, M. Patient, A. Grados et al., "Ophthalmic manifestations in IgG4-related disease," *Medicine (Baltimore)*, vol. 96, no. 10, p. e6205, 2017.

[23] A. F. Karim, R. D. Bansie, S. M. Rombach et al., "The treatment outcomes in IgG4-related disease," *The Netherlands Journal of Medicine*, vol. 76, no. 6, pp. 275–285, 2018.

[24] M. Tacelli, C. Celsa, B. Magro et al., "Risk factors for rate of relapse and effects of steroid maintenance therapy in patients with autoimmune pancreatitis: systematic review and meta-analysis," *Clinical Gastroenterology and Hepatology*, vol. 17, no. 6, pp. 1061–1072.e8, 2019.

[25] J. Ominato, T. Oyama, H. Cho et al., "The natural course of IgG4-related ophthalmic disease after debulking surgery: a single-centre retrospective study," *BMJ Open Ophthalmology*, vol. 4, no. 1, article e000295, 2019.

[26] G. Mazziotti, A. M. Formenti, S. Frara, F. Maffezzoni, M. Doga, and A. Giustina, "Diabetes in Cushing disease," *Current Diabetes Reports*, vol. 17, no. 5, p. 32, 2017.

[27] P. Chotiyarnwong and E. V. McCloskey, "Pathogenesis of glucocorticoid-induced osteoporosis and options for treatment," *Nature Reviews. Endocrinology*, vol. 16, no. 8, pp. 437–447, 2020.

[28] H. Mattoo, E. Della-Torre, V. S. Mahajan, J. H. Stone, and S. Pillai, "Circulating Th2 memory cells in IgG4-related disease are restricted to a defined subset of subjects with atopy," *Allergy*, vol. 69, no. 3, pp. 399–402, 2014.

[29] A. S. Paller, J. M. Spergel, P. Mina-Osorio, and A. D. Irvine, "The atopic march and atopic multimorbidity: many trajectories, many pathways," *The Journal of Allergy and Clinical Immunology*, vol. 143, no. 1, pp. 46–55, 2019.

[30] J. Punnonen, G. Aversa, B. G. Cocks et al., "Interleukin 13 induces interleukin 4-independent IgG4 and IgE synthesis and CD23 expression by human B cells," *Proceedings of the National Academy of Sciences of the United States of America*, vol. 90, no. 8, pp. 3730–3734, 1993.

Hindawi
Disease Markers
Volume 2022, Article ID 8741058, 5 pages
https://doi.org/10.1155/2022/8741058

Research Article

Elevated Thyroid Autoantibodies Aggravate Stroke Severity in Euthyroidism with Acute Ischemic Stroke

Jingyi Li,[1] **Shoulong Hu**,[2] **Fang Liu**,[3] **Dapeng Wu**,[3] **Wei Song**,[3] **and Miao Hui**[3]

[1]*The Department of Endocrinology, Beijing United Family Hospital, Beijing, China*
[2]*The Department of Ophthalmology, Beijing Children's Hospital, Capital Medical University, Beijing, China*
[3]*The Department of Neurology, The First Affiliated Hospital, Tsinghua University, Beijing, China*

Correspondence should be addressed to Jingyi Li; doctorlijingyi@163.com

Received 19 November 2021; Accepted 1 February 2022; Published 26 February 2022

Academic Editor: Ting Su

Introduction. Studies have indicated that immune reactions contribute to endothelial dysfunction and atherosclerosis. It is unclear whether thyroid dysfunction or elevated thyroid autoantibodies are associated with atherosclerosis. Therefore, we investigated the influence of thyroid autoimmunity related to elevated thyroid autoantibodies on functional outcome in euthyroidism with acute ischemic stroke (AIS). *Methods*. All patients with AIS underwent tests for thyroid function and thyroid antibodies (thyroid peroxidase antibody and thyroglobulin autoantibody). We divided the patients suffering from euthyroidism and AIS into positive thyroid autoantibody and negative thyroid autoantibody groups. Demographic profiles, risk factors, and functional outcomes were compared between the two groups. *Results*. Out of the total 422 patients, 50 (11.8%) were included in the positive thyroid autoantibody group. The National Institutes of Health Stroke Scale (NIHSS) score at admission and discharge was higher in the positive thyroid autoantibody group than the negative thyroid autoantibody group ($P < 0.05$). In addition, there was significant difference in the mortality during hospitalizations between the two groups ($P < 0.01$). *Conclusion*. This study showed that thyroid autoantibodies aggravate stroke severity in euthyroidism with AIS. We speculate that vascular damage related to thyroid autoimmunity may aggravate the increased risk of unfavorable outcomes, independent of thyroid function.

1. Introduction

Ischemic stroke is one of the leading causes of morbidity and mortality worldwide, and endothelial dysfunction and arteriosclerosis are its primary etiologies. Several factors such as age, smoking, obesity, hypertension, diabetes, and dyslipidemia have been recognized as aggravating the progress of arteriosclerosis. In addition, in recent years, some studies have highlighted that the immune responses are profoundly involved in the progression of endothelial dysfunction and arteriosclerosis [1]. Several cases have provided evidence for the association between thyroid diseases and arterial damage [2, 3]. A study showed the correlation between hyperthyroidism and intracranial arterial stenosis in stroke patients [4]. In addition, thyroid dysfunction and positive thyroid autoantibodies were shown in pediatric patients with moyamoya disease [5]. It is unclear whether thyroid dysfunction or positive thyroid autoantibodies were associated with vascular diseases. Therefore, we retrospectively analyzed our AIS patients with euthyroidism and compared the stroke severity between the two groups with or without elevated thyroid peroxidase antibody (TPO-Ab) and thyroglobulin autoantibody (Tg-Ab) in China.

2. Methods

2.1. Patient Selection. We followed the methods of Cho et al. [6]. We retrospectively analyzed our AIS patients with euthyroidism admitted to the First Affiliated Hospital of Tsinghua University from January 2017 to December 2018 and compared the stroke severity between these patients with or without elevated TPO-Ab and Tg-Ab. The protocols of our study had been approved by the Tsinghua University ethics committee. The inclusion criteria were AIS confirmed

by magnetic resonance imaging (MRI) within 3 days of symptom onset, and the results of thyroid function, TPO-Ab, and Tg-Ab were available. Patients with an overt history of thyroid disease or diagnosed with thyroid disorder during admission; those with immunological, infectious, and toxic diseases; those undergoing thrombolytic treatment; and those on immunosuppressant drugs or immunomodulators were excluded. Thyroid function was considered based on thyroid-stimulating hormone (TSH) level. Of the initial 469 patients, 47 were excluded because of hyperthyroidism (TSH < 0.27 mU/L, $n = 6$, 1.28%) and hypothyroidism (TSH > 4.2 mU/L, $n = 41$, 8.74%). Finally, a total of 422 (TSH 0.27–4.2 mU/L, 89.98%) patients with normal thyroid function were eligible for inclusion in this study.

2.2. Assessment of Clinical Courses. The baseline demographics and some vascular risk factors were collected. We especially paid more attention to the effects of aspirin. Patients were considered as being on aspirin therapy if they regularly took the drug within the 3-month period before admission. The patients were diagnosed with diabetes mellitus if the fasting blood glucose was elevated (≥7.0 mmol/L) at least 2 times or if patients were on regular hypoglycemic agents. Patients were diagnosed with hypertension if their blood pressure was elevated (systolic: ≥140 mmHg or diastolic: ≥90 mmHg) or if they were on regular antihypertensive medication. The patients were diagnosed with hyperlipidemia if their fasting serum total cholesterol (≥6.2 mmol/L) or low-density lipoprotein cholesterol (≥4.1 mmol/L) was elevated, or if they were on regular lipid-lowering medication. Patients were considered smokers if they smoked at least one cigarette per day within the 3-month period before admission.

Laboratory tests included blood glucose, blood lipid profile, erythrocyte sedimentation rate, high-sensitivity C-reactive protein, fibrinogen, homocysteine, thyroid function, TPO-Ab, and Tg-Ab in consecutive patients with AIS presenting within 3 days of symptom onset. The fasting blood samples were collected in the morning after admission. The thyroid functions were evaluated by measuring the serum levels of total triiodothyronine (TT3), free triiodothyronine (FT3), total thyroxine (TT4), free thyroxine (FT4), and thyroid- stimulating hormone (TSH). The reference ranges for TT3, FT3, TT4, FT4, and TSH, respectively, were 1.3–3.1 nmol/L, 2.8–7.1 pmol/L, 66–181 nmol/L, 12–22 pmol/L, and 0.27–4.2 mU/L. For the assessment of thyroid autoimmunity, the serum concentrations of the TPO-Ab and Tg-Ab were checked using electrochemiluminescence with a commercial kit (Roche, Basel, Switzerland). We divided the AIS patients into two groups according to the levels of the thyroid autoantibodies. The positive thyroid autoantibody (PTA) group was defined as either $\mathrm{TPO-Ab} > 34\,\mathrm{IU/mL}$ and/or $\mathrm{Tg-Ab} > 115\,\mathrm{IU/mL}$ in accordance with the manufacturer's reference. The negative thyroid autoantibody (NTA) group was defined as $\mathrm{TPO-Ab} \leq 34\,\mathrm{IU/mL}$ and $\mathrm{Tg-Ab} \leq 115\,\mathrm{IU/mL}$.

Stroke severity was assessed according to the National Institutes of Health Stroke Scale (NIHSS) score at admission and discharge. In addition, the mortality during hospitalizations and hospitalization time were used to evaluate the unfavorable outcome.

Table 1: Comparison of demographic features in AIS and euthyroidism with and without elevated thyroid autoantibodies.

	PTA ($n = 50$)	NTA ($n = 372$)	P value
Age, years	72.8 ± 10.9	76.4 ± 14.0	0.518
Female, n (%)	25 (50.0)	113 (30.4)	$P < 0.01^{**}$
Hypertension, n (%)	46 (92.0)	332 (89.2)	0.550
Diabetes, n (%)	29 (58.0)	197 (53.0)	0.503
Hyperlipidemia, n (%)	29 (58.0)	234 (62.9)	0.502
Cigarette smoking, n (%)	11 (22.0)	115 (30.9)	0.192
Aspirin therapy, n (%)	11 (22.0)	97 (26.1)	0.529

Data presented as mean ± standard deviation or percentage. Abbreviations: AIS: acute ischemic stroke; PTA: positive thyroid autoantibody; NTA: negative thyroid autoantibody. $^{*}P < 0.05$ and $^{**}P < 0.01$.

2.3. Statistical Analysis. Data were expressed as the mean ± standard deviation or percentage. Statistical analysis was performed with SPSS (version 20.0; IBM Corporation, Armonk, NY, USA) between the two groups using independent sample two-tailed t-test and chi-square test. $P < 0.05$ was considered to indicate statistically significant differences.

3. Results

Out of the included 422 patients, 50 (11.8%) were included in the PTA group. Both the TPO-Ab and Tg-Ab were elevated in 22 patients in the PTA group. There was no significant difference on the prevalence of the positive TPO-Ab and the positive Tg-Ab ($n = 37$ [8.8%] vs. $n = 34$ [8.1%], $P = 0.509$).

The baseline demographics (Table 1) and all the laboratory results including the risk factors related to the intracranial stenosis (Table 2) and the clinical features including the thyroid function (Table 3) of the PTA and NTA groups were shown in detail. Table 1 shows that more female patients had elevated thyroid autoantibodies ($n = 25$ [50.0%] vs. $n = 113$ [30.4%], $P < 0.01$) compared to the NTA group. The age and vascular risk factors were not significantly different between the two groups ($P > 0.05$). Furthermore, the rate of aspirin therapy was not significantly different between the two groups ($P > 0.05$) in Table 1. Even though the protective high-density lipoprotein cholesterol was higher in the PTA group than the NTA group ($P < 0.01$) in Table 2, the higher NIHSS scores at admission were observed in the PTA group than the NTA group ($P < 0.05$). The duration of hospital stay was similar between the two groups ($P = 0.523$). The NIHSS at discharge was evaluated again. Higher NIHSS scores at discharge could be used to predict poor prognosis and severity of AIS patients early in the PTA group than the NTA group in Table 3. Overall, seven patients died (four patients in the PTA group [8%] and three patients in the NTA group [0.8%] ($P < 0.01$)). Therefore, there was significant difference

Table 2: Comparison of the risk factors related to the intracranial stenosis in AIS and euthyroidism with and without elevated thyroid autoantibodies.

	PTA ($n = 50$)	NTA ($n = 372$)	P value
Blood pressure at admission			
Systolic blood pressure (mmHg)	151.4 ± 19.2	149.2 ± 21.5	0.482
Diastolic blood pressure (mmHg)	86.7 ± 12.6	85.0 ± 13.8	0.408
Blood lipid profile			
Total cholesterol (mmol/L)	4.57 ± 1.06	4.31 ± 1.07	0.118
Triglycerides (mmol/L)	1.47 ± 1.1	1.54 ± 1.02	0.626
High-density lipoprotein cholesterol (mmol/L)	1.33 ± 0.41	1.18 ± 0.32	$P < 0.01^{**}$
Low-density lipoprotein cholesterol (mmol/L)	3.0 ± 1.02	2.9 ± 1.27	0.571
Blood glucose profile			
Fasting plasma glucose (mmol/L)	7.21 ± 3.44	6.78 ± 2.6	0.296
Glycosylated hemoglobin (%)	7.0 ± 2.3	6.6 ± 1.6	0.238
Erythrocyte sedimentation rate (mm/h)	10.6 ± 8.4	8.7 ± 11.9	0.33
High-sensitivity C-reactive protein (mg/L)	10.31 ± 17.8	9.97 ± 21.71	0.92
Fibrinogen (g/L)	3.18 ± 0.77	3.23 ± 0.81	0.685
Homocysteine (umol/L)	16.26 ± 12.67	17.33 ± 14.08	0.618

Data presented as mean ± standard deviation or percentage. Abbreviations: AIS: acute ischemic stroke; PTA: positive thyroid autoantibody; NTA: negative thyroid autoantibody. $^{*}P < 0.05$ and $^{**}P < 0.01$.

Table 3: Comparison of thyroid function and clinical features in AIS and euthyroidism with and without elevated thyroid autoantibodies.

	PTA ($n = 50$)	NTA ($n = 372$)	P value
Thyroid function test			
TT3 (pmol/L)	1.67 ± 0.33	1.62 ± 0.35	0.350
FT3 (pmol/L)	3.83 ± 0.54	4.02 ± 0.74	0.025^{*}
TT4 (pmol/L)	99.86 ± 17.14	96.39 ± 21.94	0.288
FT4 (pmol/L)	16.33 ± 2.6	16.54 ± 4.71	0.753
TSH (mU/L)	1.76 ± 1.17	1.68 ± 0.92	0.632
NIHSS score at admission	5.3 ± 5.4	3.9 ± 3.9	0.025^{*}
NIHSS score at discharge	3.9 ± 4.2	2.8 ± 3.1	0.023^{*}
Mortality, n (%)	4 (8%)	3 (0.8)	$P < 0.01^{**}$
Duration of hospital stay (days)	14.3 ± 7.1	14.8 ± 7.1	0.523

Data presented as mean ± standard deviation or percentage. Abbreviations: AIS: acute ischemic stroke; PTA: positive thyroid autoantibody; NTA: negative thyroid autoantibody; TT3: total triiodothyronine; FT3: free triiodothyronine; TT4: total thyroxine; FT4: free thyroxine; TSH: thyroid-stimulating hormone; NIHSS: National Institutes of Health Stroke Scale score. $^{*}P < 0.05$ and $^{**}P < 0.01$.

in the mortality between the PTA group and NTA group in this study.

Table 3 shows that even though the mean values of TSH, TT3, TT4, FT3, and FT4 were all within the normal reference range, the FT3 level was significantly lower in AIS patients with elevated thyroid autoantibodies ($P < 0.05$).

4. Discussion

This study indicated that TPO-Ab and Tg-Ab aggravate stroke severity in euthyroidism with AIS, independent of thyroid function. In our study sample, we evaluated the possible influence of thyroid autoimmunity related to elevated TPO-Ab and Tg-Ab on functional outcome in euthyroidism with AIS in China. Some previous studies have indicated that autoimmune reactions were related to the occurrence of intracranial arterial stenosis in stroke patients with hyperthyroidism [4]. Hyperthyroidism was investigated as a risk factor for vascular damages related to poor functional outcome [7]. A case report detailed the intracranial stenosis and damages noticed in Graves' disease, which were relieved after glucocorticoid treatment and plasmapheresis [8]. The above several studies have shown that abnormal thyroid function may involve short- and long-term cardiovascular and cerebrovascular bad effects. However, it is unclear whether the autoimmunity related to elevated TPO-Ab or Tg-Ab was associated with the severity of AIS. To exclude the effects of thyroid dysfunction on stroke functional outcome, we reviewed 422 patients with normal thyroid function and AIS. Some researchers have shown that male sex, diabetes, dyslipidemia, hypertension, smoking, and hyperhomocystinemia are the key risk factors of intracranial stenosis and damages in AIS patients [9, 10]. High-density lipoprotein cholesterol is one of the protective factors of atherosclerosis in ischemic stroke patients [11]. In addition, aspirin is the most commonly used antiplatelet drug and may provide greater protection against the ischemic stroke. We focused our attention on the effects of aspirin and removed the interference of aspirin therapy between the two groups. All the vascular risk factors were excluded. We

found that stroke was still more serious in the PTA group, despite elevated levels of high-density lipoprotein cholesterol, which further suggested and illustrated the possible specific effects of autoimmunity related to elevated TPO-Ab or Tg-Ab on stroke severity in euthyroid state. Although the precise mechanism related to the poor functional outcome is not discussed in this study, the most likely and reasonable speculation is that the vascular damage associated with inappropriate autoimmune response may aggravate stroke severity by contributing to endothelial dysfunction and atherosclerosis [12]. The previous research reported the impairment of endothelial-dependent arterial dilatation in autoimmune thyroiditis patients with euthyroidism, indicating that thyroid autoimmunity may cause endothelial dysfunction [13]. In addition, the endothelial dysfunction was a marker of atherosclerosis risk [14]. Furthermore, brain perfusion in patients with autoimmune thyroiditis was decreased, which suggested the possible relationship between elevated thyroid autoantibodies and unfavorable brain perfusion in AIS [15]. Now that the endothelial dysfunction is recognized as an important early event in atherogenesis, further studies may be needed to clarify the relationship between the thyroid autoantibodies and endothelial dysfunction in AIS patients with normal thyroid function states.

Our study revealed more female than male patients in the group with positive thyroid autoantibodies in China, which was consistent with a previous study that indicated a clear female preponderance with a high prevalence of thyroid autoantibodies in the general population [16–19]. The ratio of female and male ranged from 1.8 : 1 to 4.4 : 1 in the above studies. Our study showed the ratio of female and male was 1 : 1 in the PTA group; however, the ratio of female and male was 1 : 2.3 in the NTA group. This significant difference between the two groups highlighted an obvious female preponderance. These monoclonal antibodies specific to estrogen receptors and progesterone receptors were present in the thyroid gland tissues [20]. Hence, there could be an association between thyroid autoimmunity reactions and sex hormone receptors. A study showed an independent association of elevated TPO-Ab with intracranial large artery damages in younger stroke patients with normal thyroid function. However, in that case, the independent relationship of elevated Tg-Ab on intracranial large artery stenosis could not be found [21]. The levels of Tg-Ab and TPO-Ab increase independently in response to thyroglobulin and thyroid peroxidase, respectively. The prevalence of positive TPO-Ab ranges from 3.4% to 13.4% in the general population. In our study, the prevalence of elevated TPO-Ab and elevated Tg-Ab was 8.8% and 8.1%, respectively. To investigate thyroid autoimmunity, we included both thyroid autoantibodies to elucidate their effects on functional outcome in patients with AIS.

Our data suggested that lower FT3 values within the normal reference range on admission in the elevated thyroid autoantibodies group may predict a poor functional outcome in AIS patients. Low T3 syndrome is known as euthyroid sick syndrome, which shows a reduction of serum T3 without the elevation of serum TSH [22]. In our study, the mean values of TSH, TT3, TT4, FT3, and FT4 were all within the euthyroid reference range. However, the lower FT3 has been described as being consistent with worse AIS severity. FT3 is generally more sensitive than TT3. The change trend of FT3 can still predict the stroke severity in AIS, even though FT3 is in the normal range.

The limitations of our study include the retrospective nature of our study and the limitation of a single academic institution. We need to further carry out large-scale prospective and multicenter studies to validate our findings.

5. Conclusions

Our results indicate that the elevated thyroid autoantibodies aggravate stroke severity in euthyroidism with AIS in Chinese patients. Our findings remind us that we need to further evaluate the role of the autoimmune factors in the pathogenesis of AIS, independent of thyroid function.

Data Availability

The data used to support the findings of this study are included within the article.

Conflicts of Interest

The authors declare that there are no conflicts of interest regarding the publication of this paper.

References

[1] Y. Yoshida, T. Hiwasa, and T. Machida, "Elevation of autoantibody in patients with ischemic stroke," *Neurologia Medico-Chirurgica (Tokyo)*, vol. 58, no. 7, pp. 303–310, 2018.

[2] B. Gini, L. Lovato, R. Cianti et al., "Novel autoantigens recognized by CSF IgG from Hashimoto's encephalitis revealed by a proteomic approach," *Journal of Neuroimmunology*, vol. 196, no. 1-2, pp. 153–158, 2008.

[3] K. Moodley, J. Botha, D. M. Raidoo, and S. Naidoo, "Immunolocalisation of anti-thyroid antibodies in adult human cerebral cortex," *Journal of the Neurological Sciences*, vol. 302, no. 1-2, pp. 114–117, 2011.

[4] X. Zhang, Z. Chen, Z. Shi, and M. Lou, "Correlation between thyroid autoantibodies and intracranial arterial stenosis in stroke patients with hyperthyroidism," *Journal of the Neurological Sciences*, vol. 318, no. 1-2, pp. 82–84, 2012.

[5] H. Li, Z. S. Zhang, Z. N. Dong et al., "Increased thyroid function and elevated thyroid autoantibodies in pediatric patients with moyamoya disease: a case-control study," *Stroke*, vol. 42, no. 4, pp. 1138-1139, 2011.

[6] H. J. Cho, S. S. Kim, S. M. Sung, and D. S. Jung, "Impact of thyroid autoantibodies on functional outcome in patients with acute ischemic stroke," *Journal of Stroke and Cerebrovascular Diseases*, vol. 23, no. 7, pp. 1915–1920, 2014.

[7] F. A. Wollenweber, V. Zietemann, A. Gschwendtner, C. Opherk, and M. Dichgans, "Subclinical hyperthyroidism is a risk factor for poor functional outcome after ischemic stroke," *Stroke*, vol. 44, no. 5, pp. 1446–1448, 2013.

[8] U. Utku, T. Asil, Y. Celik, and D. Tucer, "Reversible MR angiographic findings in a patient with autoimmune Graves disease," *AJNR. American Journal of Neuroradiology*, vol. 25, no. 9, pp. 1541–1543, 2004.

[9] F. Z. Caprio and F. A. Sorond, "Cerebrovascular disease: primary and secondary stroke prevention," *The Medical Clinics of North America*, vol. 103, no. 2, pp. 295–308, 2019.

[10] S. G. Chrysant and G. S. Chrysant, "The current status of homocysteine as a risk factor for cardiovascular disease: a mini review," *Expert Review of Cardiovascular Therapy*, vol. 16, no. 8, pp. 559–565, 2018.

[11] X. Zheng, N. Zeng, A. Wang et al., "Elevated C-reactive protein and depressed high-density lipoprotein cholesterol are associated with poor function outcome after ischemic stroke," *Current Neurovascular Research*, vol. 15, no. 3, pp. 226–233, 2018.

[12] A. Katsargyris, S. Tsiodras, S. Theocharis et al., "Toll-like receptor 4 immunohistochemical expression is enhanced in macrophages of symptomatic carotid atherosclerotic plaques," *Cerebrovascular Diseases*, vol. 31, no. 1, pp. 29–36, 2011.

[13] G. Xiang, Y. S. He, L. S. Zhao, J. Hou, L. Yue, and H. J. Xiang, "Impairment of endothelium-dependent arterial dilation in Hashimoto's thyroiditis patients with euthyroidism," *Clinical Endocrinology*, vol. 64, no. 6, pp. 698–702, 2006.

[14] S. Sitia, L. Tomasoni, F. Atzeni et al., "From endothelial dysfunction to atherosclerosis," *Autoimmunity Reviews*, vol. 9, no. 12, pp. 830–834, 2010.

[15] M. Piga, A. Serra, L. Deiana et al., "Brain perfusion abnormalities in patients with euthyroid autoimmune thyroiditis," *European Journal of Nuclear Medicine and Molecular Imaging*, vol. 31, no. 12, pp. 1639–1644, 2004.

[16] M. Kabelitz, K. P. Liesenkötter, B. Stach et al., "The prevalence of anti-thyroid peroxidase antibodies and autoimmune thyroiditis in children and adolescents in an iodine replete area," *European Journal of Endocrinology*, vol. 148, no. 3, pp. 301–307, 2003.

[17] J. G. Hollowell, N. W. Staehling, W. D. Flanders et al., "Serum TSH, T (4), and thyroid antibodies in the United States population (1988 to 1994): National Health and Nutrition Examination Survey (NHANES III)," *The Journal of Clinical Endocrinology*, vol. 87, no. 2, pp. 489–499, 2002.

[18] K. Kasagi, N. Takahashi, G. Inoue, T. Honda, Y. Kawachi, and Y. Izumi, "Thyroid function in Japanese adults as assessed by a general health checkup system in relation with thyroid-related antibodies and other clinical parameters," *Thyroid*, vol. 19, no. 9, pp. 937–944, 2009.

[19] Y. Li, D. Teng, Z. Shan et al., "Antithyroperoxidase and antithyroglobulin antibodies in a five-year follow-up survey of populations with different iodine intakes," *The Journal of Clinical Endocrinology*, vol. 93, no. 5, pp. 1751–1757, 2008.

[20] S. R. Money, W. Muss, W. L. Thelmo et al., "Immunocytochemical localization of estrogen and progesterone receptors in human thyroid," *Surgery*, vol. 106, no. 6, pp. 975–8; discussion 979, 1989.

[21] Z. Shi, X. Zhang, Z. Chen, D. S. Liebeskind, and M. Lou, "Elevated thyroid autoantibodies and intracranial stenosis in stroke at an early age," *International Journal of Stroke*, vol. 9, no. 6, pp. 735–740, 2014.

[22] L. J. De Groot, "Dangerous dogmas in medicine: the nonthyroidal illness syndrome," *The Journal of Clinical Endocrinology*, vol. 84, no. 1, pp. 151–164, 1999.

Hindawi
Disease Markers
Volume 2022, Article ID 7550090, 8 pages
https://doi.org/10.1155/2022/7550090

Research Article

The Microbiome of Meibomian Gland Secretions from Patients with Internal Hordeolum Treated with Hypochlorous Acid Eyelid Wipes

Shu Yang,[1] Bing-Cheng Wu,[1] Zhe Cheng,[2] Lan Li,[3] Yuan-Ping Zhang,[4] Hui Zhao,[5] Han-Mei Zeng,[1] Dong-Fang Qi,[1] Zi-Yao Ma,[1] Jian-Guo Li,[1] Rui Han,[1] Fang-Zhou Qu,[1] Yan Luo,[6] Yi Liu,[7] Xiao-Lei Chen,[8] and Hong-Mei Dai[1]

[1]*Department of Ophthalmology, The First Hospital of Kunming, Kunming, 650011 Yunnan Province, China*
[2]*Eye institute of Xiamen University, Xiamen, Fujian, China*
[3]*Department of Ophthalmology, The Calmette Affiliated Hospital of Kunming Medical University, Kunming, China*
[4]*Department of Ophthalmology, The Second Affiliated Hospital of Kunming Medical University, Kunming, China*
[5]*Department of Ophthalmology, Shanghai General Hospital (Shanghai First People's Hospital), Shanghai 200080, China*
[6]*Department of Pediatrics, The First Hospital of Kunming, Kunming, 650011 Yunnan Province, China*
[7]*Department of Otorhinolaryngology, The First Hospital of Kunming, Kunming, 650011 Yunnan Province, China*
[8]*Department of Endocrinology, The First Hospital of Kunming, Kunming, 650011 Yunnan Province, China*

Correspondence should be addressed to Hong-Mei Dai; dhm0428@163.com

Received 29 October 2021; Revised 13 February 2022; Accepted 15 February 2022; Published 24 February 2022

Academic Editor: Wen-Qing Shi

Objective. The aims of our experiment were to compare the microorganisms in meibomian gland secretions from patients with internal hordeolum before and after treatment using hypochlorous acid eyelid wipes, to elucidate the mechanism underlying hypochlorous acid eyelid wipe treatment of internal hordeolum. *Methods.* This was a prospective, matched-pair study. A total of eight patients with internal hordeolum who attended the ophthalmology clinic of our hospital from April to August 2020 were included. Meibomian gland secretions were collected from subjects before treatment (Group A) and from patients cured after eyelid cleaning with hypochlorous acid eyelid wipes for 7 days (Group B). Samples were submitted to 16S rRNA high-throughput sequencing, and the resulting data were analyzed to compare the differences in the structure and composition of meibomian gland secretion microbial flora before and after treatment of internal hordeolum. *Results.* A total of 2127 operational taxonomic units were obtained from the two groups of samples, and there was no significant difference in alpha diversity before and after eyelid cleaning. At the phylum level, there was no significant difference between the two groups. The predominant phyla in Group A included the following: *Firmicutes* (32.78% ± 20.16%), *Proteobacteria* (26.73% ± 7.49%), *Acidobacteria* (10.58% ± 11.45%), *Bacteroidetes* (9.05% ± 6.63%), *Actinobacteria* (8.48% ±1.77%), and *Chloroflexi* (3.15% ± 3.12%), while those in Group B were the following: *Proteobacteria* (31.86% ± 9.69%), *Firmicutes* (29.07% ± 24.20%), *Acidobacteria* (11.33% ± 7.53%), *Actinobacteria* (7.10% ± 1.98%), *Bacteroidetes* (5.39% ± 5.17%), and *Chloroflexi* (3.89% ± 3.67%). Starting from the class level, significant differences in microbial communities were detected before and after eyelid cleaning ($P < 0.05$). Linear discriminant analysis effect size analysis showed the core flora in Group A microbiome comprising *Actinobacteria*, *Staphylococcus*, *Staphylococcaceae*, *Staphylococcus aureus*, *Ruminococcacea UCg-014*, *Ruminococcacea-UCG-014*, *Halomonadaceae*, *Neisseria, Methylobacterium, Frankiales, and Neisseria sicca*, *while those in Group B microbial* were *Streptococcus* sp., *Blautia*, *Bifidobacterium pseudocatenulatum*, *Subdoligranulum*, *Subdoligranulum variabile*, *Faecalibacterium*, and *Faecalibacterium prausnitzii*. *Conclusion.* Eyelid cleaning with hypochlorous acid eyelid wipes does not change the biodiversity in the meibomian gland secretions of patients with internal hordeolum. Hypochlorous acid eyelid wipes may affect the internal hordeolum through broad-spectrum antibacterial action to effectively reduce the relative abundance of symbiotic pathogens, such as *Staphylococcus*, *Neisseria*, *Actinomycetes*, and *Ruminococcus* and increase that of *Faecalibacterium prausnitzi*i and other symbiotic probiotics with anti-inflammatory effects.

1. Introduction

A hordeolum is an acute suppurative reaction within the eyelid glands that is usually staphylococcal in origin. According to different disease sites, hordeolum can be medically divided into external (Zeis gland or Moll gland) and internal (meibomian gland) types [1, 2]. This study focuses solely on the internal hordeolum. The clinical manifestations of internal hordeolum are a swollen red eyelid with a painful lump that appears spontaneously within a few days and purulent inflammation of the meibomian glands [3–5]. Lederman et al. reported that internal hordeolum pathogenesis was caused by the infection of the glands with *Staphylococcus* (*Staphylococcus epidermidis* or *Staphylococcus aureus*) [3, 4]. *Staphylococcus* is an opportunistic pathogen in the internal hordeolum, therefore reducing pathogen invasion is the key to treatment.

Nonsurgical treatments for internal hordeolum include hot compresses and topical or systemic antibiotics. Commonly used antibiotics include levofloxacin eye drops [5], ofloxacin eye ointment, and tobramycin eye drops plus dexamethasone eye ointment, among others [4, 6]. Although these antibiotics are effective for treatment of the disease, they have many limitations, including bacterial resistance [7], insufficient drug concentration of eye drops in the meibomian glands, ointment affecting patient visual perception, and side effects caused by long-term use of tobramycin dexamethasone eye ointment, such as increased intraocular pressure [8]. To address these problems, ophthalmologists have focused on hypochlorous acid, which has good bactericidal, anti-inflammatory, and wound healing effects [9–12], and is used as an antimicrobial agent for disinfection and treatment of diabetic feet [13], bedsores [14], and sinusitis [15], as well as skin disinfection [16, 17] and oral irrigation [18], providing a sufficient theoretical rationale for use of hypochlorous acid in treatment of blepharitis. Many studies have confirmed that hypochlorous acid eye cleansing wipes can effectively reduce the amount of bacteria on the skin around the eyes [19]. Furthermore, studies by our team have shown that hypochlorous acid eyelid wipes have a good effect on blepharitis (including hordeolum); however, the mechanism by which hypochlorous acid acts in the treatment of blepharitis has yet to be clarified. Based on knowledge of the pathogenesis of internal hordeolum and the pharmacological characteristics of hypochlorous acid, we hypothesized that hypochlorous acid eyelid wipes exert their therapeutic function by changing the microbiome of the internal hordeolum, and that understanding the mechanisms involved in hypochlorous acid treatment of internal hordeolum by studying the microbiome could provide new ideas for the application of hypochlorous acid in the field of ophthalmology.

2. Methods

2.1. Study Population. This study recruited eight patients (2 males and 6 females) with internal hordeolum, who attended the ophthalmology clinic of The First Hospital of Kunming (Southern District) from April 2020 to August 2020. Samples were collected from the subjects before (Group A, 8 samples) and after (Group B, 8 samples) treatment with hypochlorous acid eyelid wipes for 7 days. Microorganisms collected on swabs of secretions from meibomian gland orifices of the two groups were analyzed.

Inclusion criteria were as follows: (1) presented with a painful red lump in one eyelid that appeared spontaneously within 5 days and consented to undergo a complete slit lamp biomicroscope ophthalmic examination; (2) monocular internal hordeolum was diagnosed by the ophthalmologist based on a swollen red eyelid with a painful lump in one eye, bulbar conjunctival hyperemia, telangiectasia, thickening, or irregularity of the eyelid margins, or meibomian gland orifice suppuration [20] (Figure 1(a)). The condition disappeared after 7 days of treatment with hypochlorous acid eyelid wipes (Figure 1(b)); (3) had not received treatment since the onset of the illness, including no use of antibiotics or other drugs and no use of hot or cold compresses or other treatments; and (4) Demodex examination was negative. The exclusion criteria were as follows: (1) lactating or pregnant women, (2) contact lens wearers, (3) combination with other acute ocular inflammation or infection, (4) obvious scarring or keratinization of the eyelid margin, (5) had received eye surgery or eyelid surgery within the past 6 months, (6) use of punctal plugs, (7) Follow-up time exceeded the predetermined time by more than one week, (8) diabetes, glaucoma, and other ocular or systemic diseases that affect the health of the ocular surface, and (9) discrepancies discovered after the start of the experiment (so that the participant met the exclusion criteria). All participants signed the informed consent before participating in the study. This study was approved by The First Hospital of Kunming Institutional Review Board (No. YLS2020-29), and all methods adhered to the principles of the Declaration of Helsinki.

2.2. Use of Hypochlorous Acid Eyelid Wipes. All subjects consented to an ophthalmic slit lamp examination when they attended our ophthalmology clinic and then cleaned the eyelid margins with hypochlorous acid eyelid wipes (Xiamen Xinruize, China) once a day for 7 consecutive days. The eyelid margin cleaning method was as follows: wipe the eyelid margin with the convex surface of the wet wipe 10 times, particularly suppuration of the meibomian gland orifices, and then attach the concave surface to the eyelid until the wet wipe dries. Seven days later, the subjects attended the ophthalmology clinic and data were collected from selected cured patients before and after treatment. After topical anesthesia (Santen, Osaka, Japan), pharyngeal swabs were used to collect secretions from the meibomian gland orifices after meibomian gland massage and expression.

2.3. Microbiome Analysis. The 16S rDNA gene exists in the genomes of all bacteria and is highly conserved. The sequence contains 9 hypervariable regions and 10 conserved regions. A sequence of a certain hypervariable region (V4 region or V3-V4 region) is amplified by PCR and then sequenced to obtain a sequence of about 1500 bp. The method is as follows: (1) Use DNA extraction kit (MN NucleoSpin 96 Soi) to extract sample DNA;

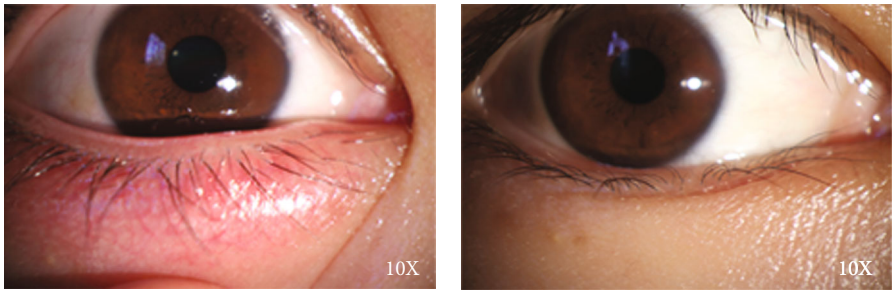

(a) (b)

Figure 1: Anterior segment photographs of subjects. (a) Clinical manifestations pretherapy (Group A). (b) Clinical manifestations posttherapy (Group B).

(2) use the following primers (338F 5′-ACTCCTACGGG AGGCAGCA-3′; 806R 5′- GGACTACHVGGGTWTCTA AT-3′) to amplify bacterial 16S V3 + V4 region; (3) microbial diversity library construction and sequencing is as follows: a two-step library construction method, the first step uses DNA as a template, and primers with adapters are designed for PCR, and the second step uses the PCR product of the first step as a template PCR; and (4) microbial diversity analysis: analyze the species composition and diversity change characteristics of the two groups of sample communities through sequencing data quality assessment, OUT analysis, and diversity analysis [21–23].

2.4. Statistical Methods. Venn diagrams were used to illustrate the number of common and unique features among samples. The Wilcoxon matched-pairs signed rank test was used to evaluate differences in alpha diversity index between treatment groups. Mothur software and R language tools were used to draw Shannon diversity index dilution curves (the Shannon index reflects the microbial diversity in the sample) for each sample at different sequencing depths. Our experiment included two paired groups of small sample size (where a number of samples ≤20 is defined as a small sample) and the significance of differences between them was analyzed by Wilcoxon rank-sum test. $P < 0.05$ indicated a statistically significant difference. Linear discriminant analysis effect size (LEfSe) analysis was implemented using LEfSe software.

3. Results

3.1. Taxonomic Assignment. A total of eight patients with internal hordeolum (2 males and 6 females) were enrolled in this study, and a total of 16 samples were collected before and after eyelid cleaning with hypochlorous acid eyelid wipes, to generate pretherapy (Group A) and posttherapy (Group B) group samples, respectively. Meibomian gland orifice secretion samples were submitted for OTU biodiversity and sample difference analyses before and after treatment (Table 1). The numbers of OTUs in groups A and B were plotted in a Venn diagram, which showed that, of a total of 2127 OTUs, the samples in Group A included 1925 OTUs, and those in Group B 1857 OTUs. (Figure 2).

3.2. There is no Significant Change in Bacterial Alpha Diversity of with Internal Hordeolum before and after Treatment with Hypochlorous Acid Eye Cleansing Wipes. Alpha diversity index analysis was performed on the two groups of samples. Evaluation indicators included the Shannon, Simpson, ACE, and Chao1 indices. Comparisons between the two groups showed no significant difference in any of the indices. This indicates that the microbial diversity was not changed between internal hordeolum onset and cured by the hypochlorous acid eye cleansing wipes. ($P > 0.05$; Table 2; Figure 3).

3.3. Microbial Communities from Patients with Internal Hordeolum before and after Treatment. We detected the relative abundance of OTUs in microbial communities from the patients with internal hordeolum before and after treatment with a hypochlorous acid eyelid wipe. The major phyla detected before treatment included *Firmicutes* (32.78% ± 20.16%), *Proteobacteria* (26.73% ± 7.49%), *Acidobacteria* (10.58% ± 11.45%), *Bacteroidetes* (9.05% ± 6.63%), *Actinobacteria* (8.48% ± 1.77%), and *Chloroflexi* (3.15% ± 3.12), and those after treatment were as follows: *Proteobacteria* (31.86% ± 9.69%), *Firmicutes* (29.07% ± 24.20%), *Acidobacteria* (11.33% ± 7.53%), *Actinobacteria* (7.10% ± 1.98%), *Bacteroidetes* (5.39% ± 5.17%), and *Chloroflexi* (3.89% ± 3.67%). There was no significant difference between the two groups at this level (Figure 4).

Significant differences in bacterial communities were detected between the two groups at the class level. At the genus level, compared with Group B, Group A had a significantly higher abundance of *Staphylococcus* (1.58% ± 3.5% vs. 0.17% ± 0.19%; $P < 0.05$), *Ruminococcaceae_UCG014* (0.88% ± 0.82% vs. 0.21% ± 0.37%; $P < 0.05$), *Neisseria* (0.37% ± 0.45% vs. 0.13% ± 0.36%; $P < 0.05$), *Methylobacterium* (0.35% ± 0.32% vs. 0.07% ± 0.05%; $P < 0.05$), *Massilia* (0.29% ± 0.20% vs. 0.18% ± 0.23%; $P < 0.05$), with lower abundances of *Pantoea* (0.05% ± 0.12% vs. 0.14% ± 0.17%; $P < 0.05$), *Subdoligranulum* (0.03% ± 0.04% vs. 0.50% ± 0.85%; $P < 0.05$), and *Ruminococcaceae_UCG-002* (0.02% ± 0.04% vs. 0.04% ± 0.09%; $P < 0.05$) (Figure 4). This shows that the differences of the microorganisms between the onset and the cure to internal hordeolum start from the class level.

Table 1: Summary sequencing data from the two paired group.

Group	Subject	Subject no.	Age	Sex	Reads	High quality reads	Average read length (bp)	OTUs
Pretherapy group (group A)	StOD0d2	1	32	Female	80180	65539	417	316
	StOD0d3	2	24	Female	80068	62882	417	319
	StOS0d4	3	28	Female	79539	64427	418	311
	StOD0d5	4	29	Male	79610	65553	420	233
	StOD0d11	5	29	Female	79995	76296	418	1193
	StOD0d12	6	26	Female	79687	75793	418	1231
	StOD0d13	7	23	Male	80347	76903	418	1197
	StOD7d3	8	36	Female	80185	63218	419	191
Posttherapy group (group B)	StOD7d4	1	32	Female	79660	65596	417	220
	StOD7d2	2	24	Female	79922	67809	417	268
	StOS7d1	3	28	Female	79731	65019	421	203
	StOD7d8	4	29	Male	79845	76476	418	1194
	StOD7d6	5	29	Female	80154	76856	418	1200
	StOD7d7	6	26	Female	80396	73965	421	1302
	StOD7d5	7	23	Male	79834	76891	418	1234
	StOD2m1	8	36	Female	80875	76929	418	1184

*St indicates staphylococcal blepharitis, which is equivalent to internal hordeolum in this study. OD, right eye; OS, left eye; 0d/7d3, Pretherapy group (Group A); 7d/2 m1, Posttherapy group (Group B); no., serial number.

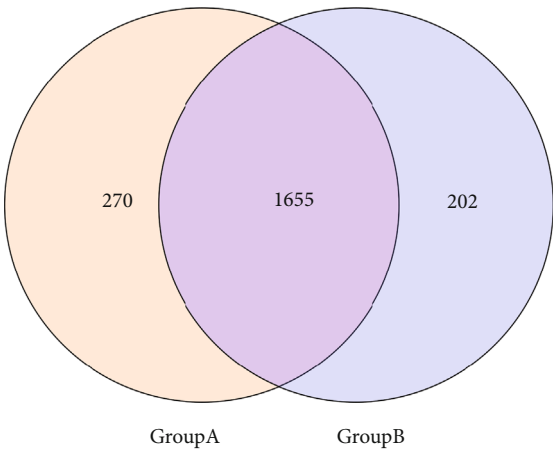

Figure 2: Number of OTUs shared between the two groups.

Table 2: Comparison of differences in α diversity index between the two groups.

Alpha diversity	Group A	Group B	P value
Shannon	7.521[6.879,9.036]	7.935[6.540,8.987]	$P > 0.05$
Simpson	0.992[0.983,0.996]	0.988[0.980,0.996]	$P > 0.05$
ACE	656.6[344.4,1238]	1214[244.2,1259]	$P > 0.05$
Chao1	408.2[307.3,1290]	1257[263.1,1302]	$P > 0.05$

3.4. Pathogens such as Staphylococcus and Neisseria are Reduced after Treatment; Faecalibacterium prausnitzii and other Probiotics are Increased Compared to Pretherapy Group. LEfSe software was used for multilevel species discrimination of high-dimensional biomarkers for internal hordeolum and analysis of genomic characteristics before and after treatment, and significant differences were detected ($P < 0.05$). Linear discriminant analysis (effect size) indicated that the core flora in the Group A microbial community were *c-Actinobacteria*, *f-Staphylococcaceae*, *g-Staphylococcus*, *s-S. aureus*, *g-Ruminococcacea-UCG-014*, *s-Ruminococcacea-UCG-014*, *f-Halomonadaceae*, *g-Neisseria*, *f-Methylobacterium*, *o-Frankiales*, and *s-Neisseria sicca*, whereas those in Group B were *s-Streptococcus* sp., *g-Blautia*, *s-Bifidobacterium pseudocatenulatum*, *g-Subdoligranulum*, *s-Subdoligranulum variabile*, *g-Faecalibacterium*, and *s-Faecalibacterium prausnitzii*. It is speculated that hypochlorous acid eye cleansing wipes in the treatment of hordeolum can be effective by reducing the relative abundance of pathogenic bacteria and increasing the relative abundance of probiotics. (prefix explanation: *c-* means class level; *o-* means order level; *f-* means family level; *g-* means genus level; and *s-* means specie level.)

4. Discussion

The significance of the ocular microbiome in eye health has become a research focus in ophthalmology in recent years, primarily concerned with the ocular surface microbiome (OSM) [24]. Many studies have reported significant differences in the microbiomes of patients with ocular surface diseases such as blepharitis, (including internal hordeolum), meibomian gland dysfunction, dry eye, and keratitis, compared with healthy people [25–29]; however, there has been a lack of comparative studies of microorganisms in these diseases before and after treatment, and investigating the changes in microbial communities will be helpful in understanding the pathogenesis of internal hordeolum, as well as prevention and treatment methods.

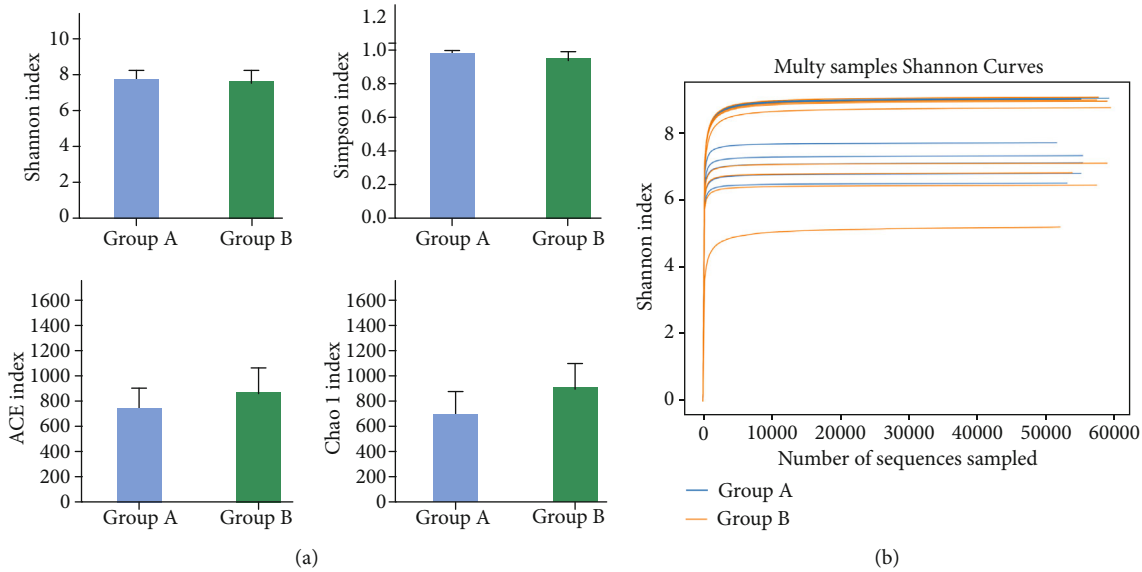

Figure 3: Alpha diversity indices of individual samples. (a) Alpha diversity indices, including Shannon, Simpson, ACE, and Chao1, did not differ significantly between the two groups. (b) All rarefaction curves of individual samples from the internal hordeolum before and after treatment reached the saturation platform, indicating that the sequencing data size was reasonable.

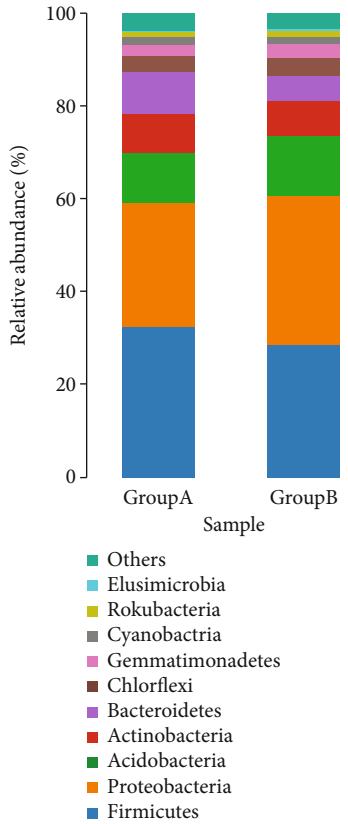

Figure 4: The relative abundances of core phyla before and after treatment. (A) The relative abundances of the top 10 most abundant phyla. There was no significance between the two groups at the phylum level ($P > 0.05$).

The biodiversity and relative abundance of organisms in the ocular surface microbiome are affected by age, sex, geographic differences, and microbial habitat [30–32]. The mean age of the subjects in this study was 28.38 ± 4.24 years old. A paired sample test method was used to collect secretions from the meibomian glands before and after treatment for microbial high-throughput sequencing, which avoided the influence of other factors on the study results. In groups A and B, 1955 and 1857 OTUs were identified, respectively. There was no significant difference in OTUs before and after treatment for internal hordeolum with hypochlorous acid eyelid wipes. The Shannon index was used to draw a dilution curve to analyze the complexity of the two sets of samples, and the results, that its, platform curve, showed that the coverage depth was >99%, indicating that the sequencing data reflected microorganism diversity information relatively completely.

We found no significant differences in alpha diversity between the two groups, according to the analysis of the Shannon, Simpson, ACE, and Chao1 indices ($P > 0.05$), indicating that the microbial communities in the two groups were highly similar and that the composition of the microbiome did not alter before and after treatment. Moreover, we detected no significant difference in flora before and after treatment at the phylum level. The major phyla in patients with internal hordeolum before treatment included *Firmicutes* (32.78% ± 20.16%), *Proteobacteria* (26.73% ± 7.49%), *Acidobacteria* (10.58% ± 11.45%), *Bacteroidetes* (9.05% ± 6.63%), *Actinobacteria* (8.48% ± 1.77%), and *Chloroflexi* (3.15% ± 3.12%), while after treatment the major phyla were as follows: *Proteobacteria* (31.86% ± 9.69%), *Firmicutes* (29.07% ± 204.20%), *Acidobacteria* (11.33% ± 7.53%), *Actinobacteria* (7.10% ± 1.98%), *Bacteroidetes* (5.39% ± 5.17%), and *Chloroflexi* (3.89% ± 3.67%). Dong et al. demonstrated that, among healthy people, the core flora are *Proteobacteria* (64%), *Actinomycetes* (19.6%), and *Firmicutes* (3.9%) [33], while Delbeke conducted a review of all current research data after calculation and integration and found that 16S

rRNA detection from ocular surface core bacteria in healthy people included mainly *Actinomycetes* (53%), followed by Proteobacteria (39%) and *Firmicutes* (8%) [34]. The core flora types detected at the phylum level in this study are consistent with the findings described above; however, the relative abundance ratio differed, indicating that changes in the relative abundance of organisms in the OSM are part of internal hordeolum pathogenesis, and restoration of OSM to a healthy state is key to treatment. Combined with our results showing that treatment with hypochlorous acid eyelid wipes did not change the bacterial diversity of meibomian gland secretions before and after treatment, and the differences in the dominant flora before and after treatment, our data support this hypothesis.

There were statistically significant differences in the relative abundances of bacterial communities between groups A and B beginning at the class level. LEfSe analysis was used to identify dominant species with significant differences in abundance between the two groups. The dominant flora in Group A were *c-Actinobacteria*, *f-Staphylococcaceae*, *g-Staphylococcus*, *s-S. aureus*, *g-Ruminococcacea-UCG-014*, *s-Ruminococcacea-UCG-014*, *f-Halomonadaceae*, *g-Neisseria*, *f-Methylobacterium*, *o-Frankiales*, and *s-Neisseria sicca.* Previous studies have proven that the purulent reaction in the internal hordeolum is caused by *S. epidermidis* or *S. aureus,* invasion of the meibomian glands [3], which is consistent with our results; however, in addition to *Staphylococcus*, we also found that the abundance levels of *Neisseria*, *Actinomycetes*, and *Ruminococcus* were also decreased after treatment, which has not been reported in previous studies. Overall, our results suggest the following two points: (1) Other microorganisms may be involved in the occurrence of internal hordeolum. Hypochlorous acid eyelid wipes have a therapeutic effect by reducing the relative abundance of the abovementioned symbiotic pathogens. At present, the drugs most routinely used in ophthalmology are quinolone antibiotics; however, the first choice for the treatment of *Neisseria* is β-lactam antibiotics such as penicillin [35]. Our results likely explain the frequent occurrence of drug resistance in the clinic. Hypochlorous acid can inactivate microorganisms by oxidizing ATP hydrolases and synthetases to prevent the production of energy-providing ATP [36]. The results of this study also support that this ingredient can effectively kill a variety of pathogenic bacteria that cause internal hordeolum. (2) The reason for our detection of novel commensal pathogenic bacteria may be related to advances in the detection method. Previous studies of ophthalmic microorganisms have been limited to the use of the culture detection method, which can only detect bacteria grown in standardized laboratories. It is estimated that most bacteria cannot be cultured in the laboratory; however, high-throughput sequencing methods can detect more of the microbiome. High-throughput sequencing studies have found that the core microbiome of the ocular surface is very different from that detected using traditional culture methods and contains numerous bacteria that had never been described previously [30, 34, 37], consistent with the results of this study.

The dominant flora in Group B were *s-Streptococcus* sp., *g-Blautia*, *s-Bifidobacterium pseudocatenulatum*, *g-Subdoligranulum*, *s-Subdoligranulum variabile*, *g-Faecalibacterium*, and *s-F. prausnitzii*. In other studies, no prominent indications of these types of probiotic organisms have been reported in meibomian gland secretions from healthy people, indicating that the meibomian glands analyzed in the treated state may contain different microbes from those found in healthy people. It is worth paying attention that the relative abundance of *F. prausnitzii* increased after the disease is cured in our study for the first time. Since there is no healthy control group in this paper, and there are no researches reported on hypochlorous acid regulating the relative abundance of *F. prausnitzii*, it is indeed impossible to determine whether the changes of bacteria are caused by the self-healing process of the human body or induced by hypochlorous acid. However, we speculate that there is a possibility that hypochlorous acid regulates the relative abundance of *F. prausnitzii* increased to treat the disease. The reasons are as follows: (1) *F. prausnitzii* is a major component of the intestinal flora and has been confirmed by numerous studies as a biological indicator of human health. *F. prausnitzii* produces energy and anti-inflammatory metabolites that can support host health. This bacterium is among the most important butyrate-producing microbes in the human colon [38]. Its metabolites, butyrate, and salicylic acid block NFkB signal transduction, which is a regulator of inflammation [39]. Decreases in the *F. prausnitzii* population promote inflammatory processes [40], and some studies have shown that the relative abundance of *F. prausnitzii* in dry eye and keratitis is lower than healthy people [41]. There are studies showed that the relative abundance of F. prausnitzii has increased after treatment with tacrolimus and other therapeutic drugs, which suggest that the *F. prausnitzii* are changed after the treatment of the disease [42, 43]. This indicates that the relative abundance of *F. prausnitzii* may be induced to increase in the process of drug treatment to play an anti-inflammatory role.(2) In addition to the broad-spectrum sterilization effect, hypochlorous acid can also reduce the levels of inflammatory factors [11]. There may be some potential connection between these changes. In summary, our results suggest that increasing the relative abundance of probiotics, such as *F. prausnitzii*, is potentially related to the anti-inflammatory effects of hypochlorous acid.

In conclusion, the core microbiome in the internal hordeolum includes *Firmicutes*, *Proteobacteria*, *Acidobacteria*, *Bacteroidetes*, *Actinobacteria*, and *Chloroflexi* consistent with the organisms found in the OSM, albeit at different relative abundances. Hypochlorous acid eyelid wipes do not change the microbial diversity of meibomian gland secretions before and after eyelid margin cleaning. The potential mechanism underlying the effects of hypochlorous acid eyelid wipes could be reduction of the relative abundance of commensal pathogenic bacteria, such as *Staphylococcus, Neisseria, Actinomycetes,* and *Ruminococcus* in patients with internal hordeolum via its broad-spectrum antibacterial effects, leading to increases in the relative abundance of *F. prausnitzii* and other probiotics, to mediate anti-inflammatory therapy for internal hordeolum. Considering the small sample size of this study and in order to ensure the

accuracy of the research, subsequent studies with increased sample size and adding control group were necessary to make a solid conclusion about the mechanism of hypochlorous acid eyelid wipes on internal hordeolum.

Data Availability

The 16S rRNA high-throughput sequencing of meibomian gland secretions from patients with internal hordeolum used to support the findings of this study is available from the corresponding author upon request.

Conflicts of Interest

This was not an industry-supported study. The authors report no conflicts of interest in this work.

Acknowledgments

This study is supported by the 2020 Kunming Xishan District Science and Technology Plan Project (Xike Zi No. 27).

References

[1] C. McAlinden, M. González-Andrades, and E. Skiadaresi, "Hordeolum: acute abscess within an eyelid sebaceous gland," *Cleveland Clinic Journal of Medicine*, vol. 83, no. 5, pp. 332–334, 2016.

[2] K. J. Bragg, P. H. Le, and J. K. Le, *Hordeolum*, StatPearls, Treasure Island (FL), 2021.

[3] C. Lederman and M. Miller, "Hordeola and chalazia," *Pediatrics in Review*, vol. 20, no. 8, pp. 283-284, 1999.

[4] K. Lindsley, J. J. Nichols, K. Dickersin, and Cochrane Eyes and Vision Group, "Non-surgical interventions for acute internal hordeolum," *Cochrane Database of Systematic Reviews*, vol. 2017, no. 1, 2017.

[5] K. Tajima, T. Miyake, N. Koike et al., "*In vivo* challenging of polymyxins and levofloxacin eye drop against multidrug-resistant *Pseudomonas aeruginosa* keratitis," *Journal of Infection and Chemotherapy*, vol. 20, no. 6, pp. 343–349, 2014.

[6] X. M. Yan, X. G. Sun, H. P. Xie, J. Hong, and Z. C. Wang, "Effects of tobramycin dexamethasone eye ointment for blepharitis: multi-center clinical trial," *Zhonghua Yan Ke Za Zhi*, vol. 49, no. 1, pp. 16–21, 2013.

[7] T. F. Bernardes and A. A. Bonfioli, "Blepharitis," *Seminars in Ophthalmology*, vol. 25, no. 3, pp. 79–83, 2010.

[8] K. Duncan and B. H. Jeng, "Medical management of blepharitis," *Current Opinion in Ophthalmology*, vol. 26, no. 4, pp. 289–294, 2015.

[9] S. J. Klebanoff, A. J. Kettle, H. Rosen, C. C. Winterbourn, and W. M. Nauseef, "Myeloperoxidase: a front-line defender against phagocytosed microorganisms," *Journal of Leukocyte Biology*, vol. 93, no. 2, pp. 185–198, 2013.

[10] A. Day, A. Alkhalil, B. C. Carney, H. N. Hoffman, L. T. Moffatt, and J. W. Shupp, "Disruption of biofilms and neutralization of bacteria using hypochlorous acid solution: an in vivo and in vitro evaluation," *Advances in Skin & Wound Care*, vol. 30, no. 12, pp. 543–551, 2017.

[11] J. Q. Del Rosso and N. Bhatia, "Status report on topical hypochlorous acid: clinical relevance of specific formulations, potential modes of action, and study outcomes," *The Journal of Clinical and Aesthetic Dermatology*, vol. 11, no. 11, pp. 36–39, 2018.

[12] M. H. Gold, A. Andriessen, A. C. Bhatia et al., "Topical stabilized hypochlorous acid: the future gold standard for wound care and scar management in dermatologic and plastic surgery procedures," *Journal of Cosmetic Dermatology*, vol. 19, no. 2, pp. 270–277, 2020.

[13] D. G. Armstrong, G. Bohn, P. Glat et al., "Expert recommendations for the use of hypochlorous solution: science and clinical application," *Ostomy/Wound Management*, vol. 61, no. 5, pp. S2–S19, 2015.

[14] D. Joachim, "Wound cleansing: benefits of hypochlorous acid," *Journal of Wound Care*, vol. 29, no. Sup10a, pp. S4–S8, 2020.

[15] H. J. Cho, H. J. Min, H. J. Chung et al., "Improved outcomes after low-concentration hypochlorous acid nasal irrigation in pediatric chronic sinusitis," *Laryngoscope*, vol. 126, no. 4, pp. 791–795, 2016.

[16] J. Fisher, "Commentary on: comparison of skin antiseptic agents and the role of 0.01% hypochlorous acid," *Aesthetic Surgery Journal*, vol. 41, no. 10, pp. 1176–1178, 2021.

[17] A. Q. Tran, N. Topilow, A. Rong et al., "Comparison of skin antiseptic agents and the role of 0.01% hypochlorous acid," *Aesthetic Surgery Journal*, vol. 41, no. 10, pp. 1170–1175, 2021.

[18] D. M. Castillo, Y. Castillo, N. A. Delgadillo et al., "Viability and effects on bacterial proteins by oral rinses with hypochlorous acid as active ingredient," *Brazilian Dental Journal*, vol. 26, no. 5, pp. 519–524, 2015.

[19] D. W. Stroman, K. Mintun, A. B. Epstein et al., "Reduction in bacterial load using hypochlorous acid hygiene solution on ocular skin," *Clinical Ophthalmology*, vol. Volume 11, p. 707, 2017.

[20] K. Lindsley, J. J. Nichols, and K. Dickersin, "Interventions for acute internal hordeolum," *Cochrane Database of Systematic Reviews*, vol. 4, article CD007742, 2013.

[21] R. C. Edgar, "UPARSE: highly accurate OTU sequences from microbial amplicon reads," *Nature Methods*, vol. 10, no. 10, pp. 996–998, 2013.

[22] N. A. Bokulich, S. Subramanian, J. J. Faith et al., "Quality-filtering vastly improves diversity estimates from Illumina amplicon sequencing," *Nature Methods*, vol. 10, no. 1, pp. 57–59, 2013.

[23] C. Quast, E. Pruesse, P. Yilmaz et al., "The SILVA ribosomal RNA gene database project: improved data processing and web-based tools," *Nucleic Acids Research*, vol. 41, no. Database issue, pp. D590–D596, 2013.

[24] J. A. P. Gomes, L. Frizon, and V. F. Demeda, "Ocular surface microbiome in health and disease," *Asia-Pacific Journal of Ophthalmology*, vol. 9, no. 6, pp. 505–511, 2020.

[25] K. M. Cavuoto, S. Banerjee, and A. Galor, "Relationship between the microbiome and ocular health," *The Ocular Surface*, vol. 17, no. 3, pp. 384–392, 2019.

[26] F. Petrillo, D. Pignataro, M. A. Lavano et al., "Current evidence on the ocular surface microbiota and related diseases," *Microorganisms*, vol. 8, no. 7, p. 1033, 2020.

[27] S. H. Lee, D. H. Oh, J. Y. Jung, J. C. Kim, and C. O. Jeon, "Comparative ocular microbial communities in humans with and without blepharitis," *Investigative Ophthalmology & Visual Science*, vol. 53, no. 9, pp. 5585–5593, 2012.

[28] X. Dong, Y. Wang, W. Wang, P. Lin, and Y. Huang, "Composition and diversity of bacterial community on the ocular

surface of patients with meibomian gland dysfunction," *Investigative Ophthalmology & Visual Science*, vol. 60, no. 14, pp. 4774–4783, 2019.

[29] X. Zhang, M. Vimalin Jeyalatha, Y. Qu et al., "Dry eye management: targeting the ocular surface microenvironment," *International Journal of Molecular Sciences*, vol. 18, no. 7, p. 1398, 2017.

[30] J. Ozkan and M. D. Willcox, "The ocular microbiome: molecular characterisation of a unique and low microbial environment," *Current Eye Research*, vol. 44, no. 7, pp. 685–694, 2019.

[31] H. J. Thiel and U. Schumacher, "Über die Standortflora der menschlichen Bindehaut: Untersuchungen von 135 Personen unterschiedlichen Alters," *Klinische Monatsblätter für Augenheilkunde*, vol. 205, no. 12, pp. 348–357, 1994.

[32] Y. Zhou, M. J. Holland, P. Makalo et al., "The conjunctival microbiome in health and trachomatous disease: a case control study," *Genome Medicine*, vol. 6, no. 11, p. 99, 2014.

[33] Q. Dong, J. M. Brulc, A. Iovieno et al., "Diversity of bacteria at healthy human conjunctiva," *Investigative Ophthalmology & Visual Science*, vol. 52, no. 8, pp. 5408–5413, 2011.

[34] H. Delbeke, S. Younas, I. Casteels, and M. Joossens, "Current knowledge on the human eye microbiome: a systematic review of available amplicon and metagenomic sequencing data," *Acta Ophthalmologica*, vol. 99, no. 1, pp. 16–25, 2021.

[35] B. Shaskolskiy, E. Dementieva, I. Kandinov et al., "Resistance of Neisseria gonorrhoeae isolates to beta-lactam antibiotics (benzylpenicillin and ceftriaxone) in Russia, 2015-2017," *PLoS One*, vol. 14, no. 7, article e0220339, 2019.

[36] A. Ulfig and L. I. Leichert, "The effects of neutrophil-generated hypochlorous acid and other hypohalous acids on host and pathogens," *Cellular and Molecular Life Sciences*, vol. 78, no. 2, pp. 385–414, 2021.

[37] A. Grzybowski, P. Brona, and S. J. Kim, "Microbial flora and resistance in ophthalmology: a review," *Graefe's Archive for Clinical and Experimental Ophthalmology*, vol. 255, no. 5, pp. 851–862, 2017.

[38] R. Balamurugan, E. Rajendiran, S. George, G. V. Samuel, and B. S. Ramakrishna, "Real-time polymerase chain reaction quantification of specific butyrate- producing bacteria, Desulfovibrio and Enterococcus faecalis in the feces of patients with colorectal cancer," *Journal of Gastroenterology and Hepatology*, vol. 23, 8 Part1, pp. 1298–1303, 2008.

[39] Z. Wei, S. Cao, S. Liu et al., "Could gut microbiota serve as prognostic biomarker associated with colorectal cancer patients' survival? A pilot study on relevant mechanism," *Oncotarget*, vol. 7, no. 29, pp. 46158–46172, 2016.

[40] C. V. Ferreira-Halder, A. V. S. Faria, and S. S. Andrade, "Action and function of Faecalibacterium prausnitzii in health and disease," *Best Practice & Research. Clinical Gastroenterology*, vol. 31, no. 6, pp. 643–648, 2017.

[41] R. Jayasudha, S. K. Chakravarthy, G. S. Prashanthi et al., "Alterations in gut bacterial and fungal microbiomes are associated with bacterial keratitis, an inflammatory disease of the human eye," *Journal of Biosciences*, vol. 43, no. 5, pp. 835–856, 2018.

[42] J. R. Lee, T. Muthukumar, D. Dadhania et al., "Gut microbiota and tacrolimus dosing in kidney transplantation," *PLoS One*, vol. 10, no. 3, article e0122399, 2015.

[43] Y. Guo, C. M. Crnkovic, K. J. Won et al., "Commensal gut bacteria convert the immunosuppressant tacrolimus to less potent metabolites," *Drug Metabolism and Disposition*, vol. 47, no. 3, pp. 194–202, 2019.

Hindawi
Disease Markers
Volume 2022, Article ID 1899282, 10 pages
https://doi.org/10.1155/2022/1899282

Research Article

Exosomal hsa_circ_0008925 from Urine Is Related to Chronic Renal Fibrosis

Yuhan Cao,[1,2,3] **Yuanhui Shi**,[1] **Yuwei Wang**,[1] **Yanlang Yang**,[1] **Wenjun Guo**,[2,4] **Cuifeng Zhang**,[2] **Wenjun Pei**,[5] **and Cong Fu**[2,3,6]

[1]*Department of Nephrology, Yijishan Hospital Affiliated to Wannan Medical College, Wuhu, China*
[2]*Anesthesia Laboratory and Training Center of Wannan Medical College, Wuhu, China*
[3]*Key Laboratory of Non-coding RNA Transformation Research of Anhui Higher Education Institution (Wannan Medical College), Wuhu, China*
[4]*Department of Anesthesiology, Yijishan Hospital Affiliated to Wannan Medical College, Wuhu, China*
[5]*Anhui Province Key Laboratory of Biological Macromolecules Research (Wan Nan Medical College), Wuhu, China*
[6]*Department of Cardiology, Yijishan Hospital Affiliated to Wannan Medical College, Wuhu, China*

Correspondence should be addressed to Cong Fu; fucong7706@163.com

Received 9 December 2021; Revised 28 January 2022; Accepted 4 February 2022; Published 18 February 2022

Academic Editor: Wen-Qing Shi

At present, there is no noninvasive biomarker of renal fibrosis. The potential diagnostic value of urinary exosome-derived circRNAs from glomerular disease patients for renal fibrosis is still uncertain. Here, we first detected the expression of hsa_circ_0008925 in TGF-β1-cultured HK-2 cell-derived exosomes. Secondly, we collected urine samples from 95 biopsy-proven glomerular disease patients and 34 healthy controls. The expression of hsa_circ_0008925 was analyzed, and the correlation with renal function and pathological changes was calculated. The receiver operating characteristic (ROC) curve for the diagnosis of renal fibrosis was performed. The results showed that in exosomes derived from TGF-β1-cultured HK-2 cells, the expression of hsa_circ_0008925 was increased compared with normal cultured. Further, the expression level of hsa_circ_0008925 was increased in urinary exosomes from renal fibrosis patients and correlated with serum creatinine, blood urea nitrogen (BUN), estimated glomerular filtration rate, and cystatin C. The level of hsa_circ_0008925 was furthermore correlated with the score of tubulointerstitial fibrosis (TIF) and the score of glomerular sclerosis. The ROC curve showed that hsa_circ_0008925 can diagnose renal fibrosis at a cut-off value of 0.093 with a sensitivity of 52.2% and specificity of 96.4%. In summary, we indicated that urinary exosomal hsa_circ_0008925 could be acted as a noninvasive biomarker for renal fibrosis in glomerular diseases patients.

1. Introduction

Chronic kidney disease (CKD) is a major medical problem in China and around the world. A cross-sectional survey revealed that the morbidity of CKD in China is 10.8% [1]. Glomerular disease is a common type of CKD. Glomerular disease includes many pathological types. Renal fibrosis (RF) which is defined as glomerulosclerosis and tubulointerstitial fibrosis (TIF) is a common outcome of all pathological types [2]. RF is a typical manifestation of end-stage renal disease. Renal biopsy is the golden standard for the diagnosis of renal fibrosis. Renal biopsy is a risky procedure that cannot be used as a routine examination in glomerular disease patients. Previous studies have found that urine-containing molecules have the potential to serve as noninvasive biomarkers for RF [3, 4]. So far, there is still no method for the noninvasive and dynamic detection of RF that can be applied in clinical practice.

The biological information contained in urine as well as urinary exosomes has great potential to become biomarkers for glomerular disease and renal fibrosis. Real-time quantitative polymerase chain reaction- (qPCR-) based urinary RNA detection has been found as a novel method for detection of biomarkers of kidney disease [5, 6]. Recently, noncoding

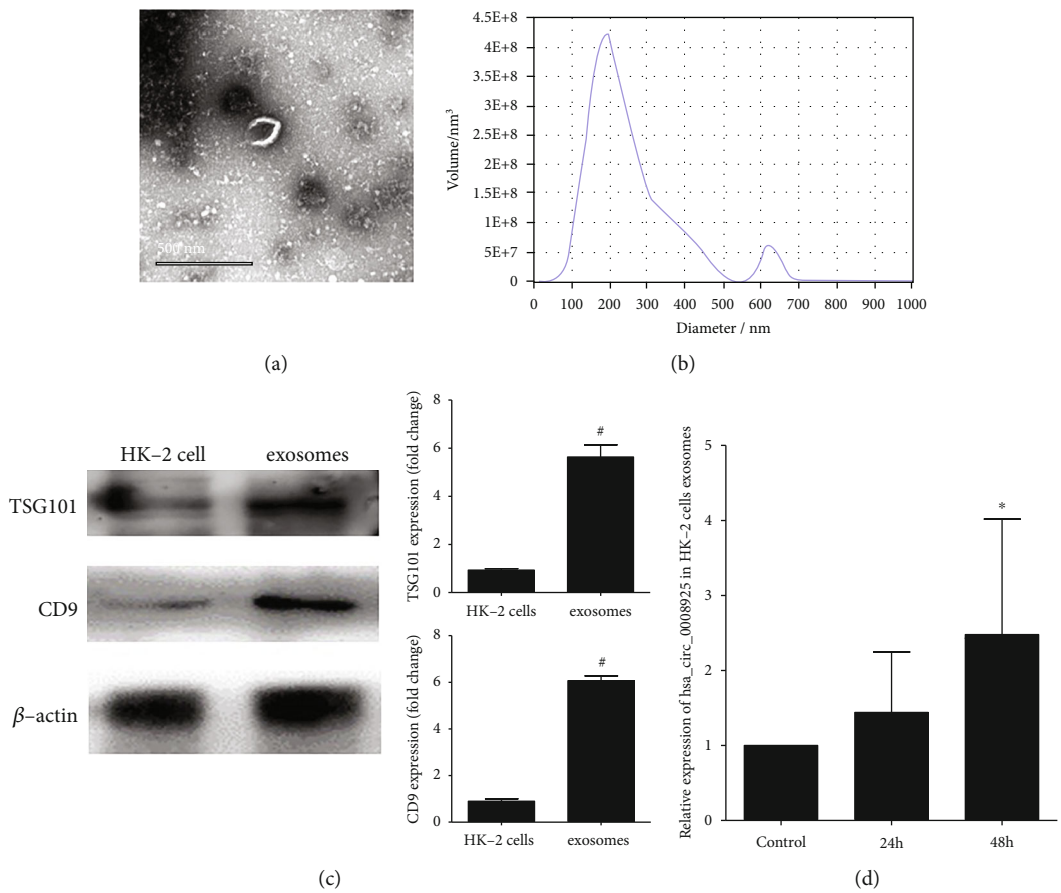

Figure 1: HK-2 cell-derived exosomes and hsa_circ_0008925 expression. (a) TEM image of exosomes. (b) NTA analysis of exosomes. (c) Western blot showed that exosomes from HK-2 cells expressed CD9 and TSG101. Histogram showed that the fold change of CD9 and TSG101 protein expression was normalized to β-actin ($^{\#}P < 0.05$ vs. HK-2 cells). (d) RT-PCR showed that coculture with 100 ng/mL for 48 h significantly increased the expression of hsa_circ_0008925 in HK-2 cell-derived exosomes ($^{*}P < 0.001$ vs. 24 h).

RNA such as circRNAs showed great aptitude as biomarkers of kidney disease progression [7–9]. Urine also contained exosomes [10]. And exosomes contained proteins and RNA, from the cytoplasm of the cells [11, 12]. Urinary exosome secretion and their content, especially mRNAs, miRNAs, and circRNAs, were considered the potential candidates for novel biomarkers of kidney disease. Recently, sec63 has been found correlated with renal interstitial inflammation [13]. sec is the symbol of hsa_circ_0008925. However, it is still uncertain if urinary exosomal circRNAs, especially has_circ_0008925, have the potential to act as renal fibrosis biomarkers. In this study, we aimed to identify the potential candidate biomarkers of RF through the detection of urinary exosomes and further explore the relationship of urinary exosomal has_circ_0008925 with histological changes in glomerular disease patients with RF.

2. Methods

2.1. Cell Culture and Treatment. To determine if TGF-β1-treated HK-2 cell could secrete exosomal has_circ_0008925, HK-2 cells were cultured with Dulbecco's modified Eagle medium (DMEM)/F12 medium (Gibco) supplemented with 10% fetal bovine serum (FBS, Gibco, USA), 100 U/mL penicillin (Gibco), and 100 μg/mL streptomycin (Gibco, USA) in a humidified incubator with 5% CO_2 at 37°C. HK-2 cells were purchased from the National Collection of Authenticated Cell Cultures (Shanghai). The 1×10^7 HK-2 cells were exposed to 100 ng/mL recombinant TGF-β1 protein (Sino Biological, China) for 24 and 48 hours. The cell supernatants were collected. After centrifugation in 300 g at 4°C for 10 min, the supernatants were collected and further centrifuged in 2000 g at 4°C for 20 min. Then, the supernatants were collected and centrifuged in 100000 g at 4°C for 70 min. The precipitates were collected as exosomes.

2.2. Exosomes from Cell Supernatants Identification. The exosomes from cell supernatants were identified by transmission electron microscope. In brief, a 10 μL exosome sample was dropped on the copper net for precipitation for 1 min, and the filter paper absorbs the floating liquid. Then uranyl acetate 10 μL is added to the copper net for precipitation for 1 min, and the floating liquid is absorbed by the filter paper and dried at room temperature for several minutes. The exosomes were imaged by transmission electron microscope (TEM, Hitachi, HT-7700) at 100 kV. Nanoparticle tracking analysis (NTA) (Particle Metrix, ZetaView) was performed to confirm the particle size. Isolated exosome

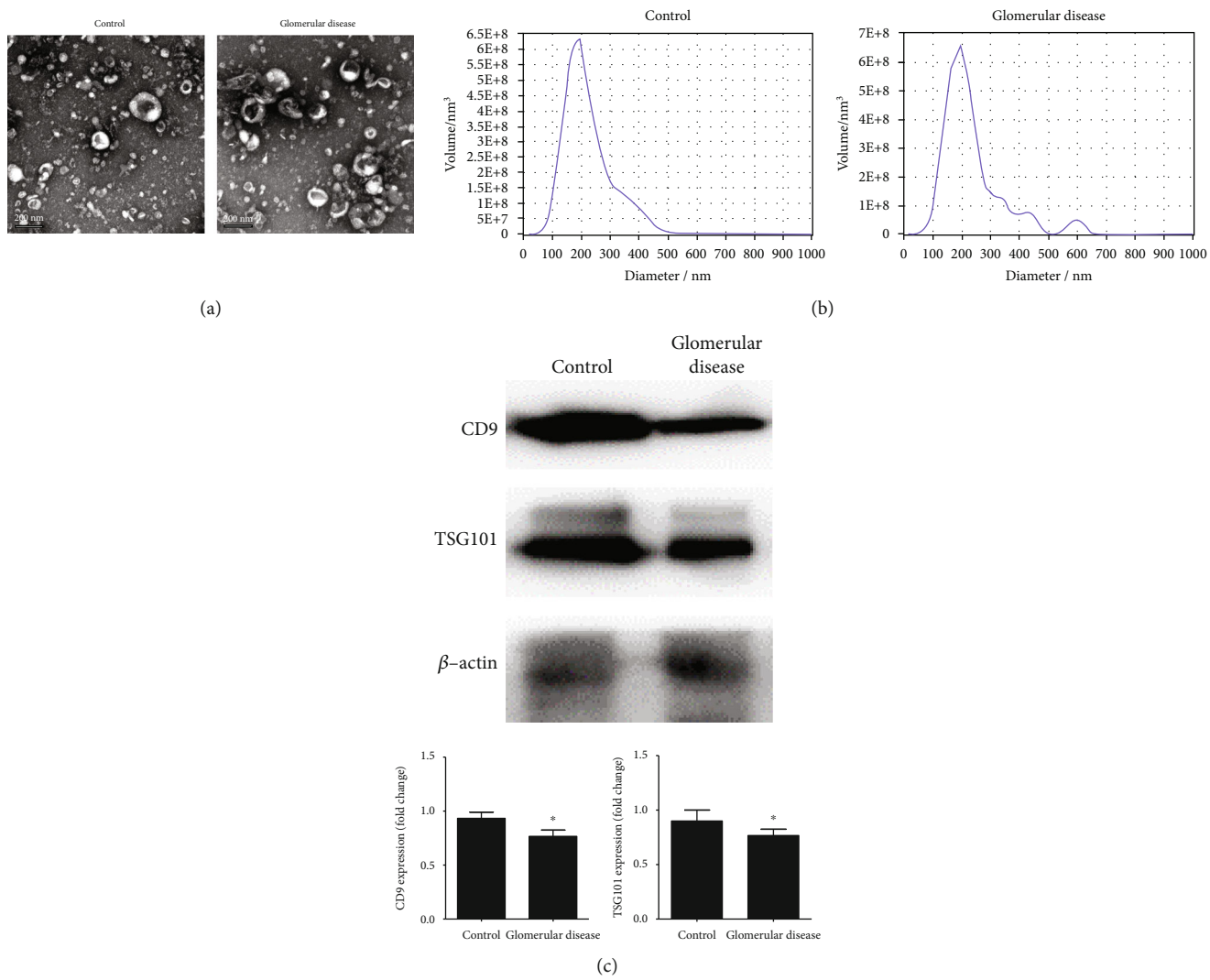

Figure 2: Urine-derived exosomes from healthy control and patients' identification. (a) TEM image of exosomes. (b) NTA analysis of exosomes. (c) Western blot showed that urinary exosomes expressed CD9 and TSG101. Histogram showed that the fold change of CD9 and TSG101 protein expression was normalized to β-actin ($^{*}P > 0.05$ vs. control).

Table 1: Clinical characteristics of glomerular disease patients and healthy controls.

	Glomerular disease ($n = 95$)	Control ($n = 34$)	P value
Age (years)	44.5 ± 14.6	43.6 ± 15.5	0.756
Gender (male/female)	51/44	25/9	0.067
24 h proteinuria (g/day)	2.190 (0.080-21.580)	/	/
Scr (mmol/L)	107.9 ± 92.0	62.3 ± 7.0	0.005
BUN (mmol/L)	7.1 ± 4.1	4.4 ± 1.1	<0.001
Cystatin C (mg/L)	1.39 ± 0.86	0.67 ± 0.10	<0.001
eGFR (mL/min per 1.73 m^2)	84.1 ± 36.0	121.0 ± 22.8	<0.001
Score of TIF	30 (0-91)	/	/
Score of glomerular sclerosis	1.0 (0-4.0)	/	/
Exosomal hsa_circ_0008925	0.085 (0.035-0.511)	0.058 (0.033-0.093)	/ 0.001

Abbreviations: Scr: serum creatinine; eGFR: estimated glomerular filtration rate; BUN: blood urea nitrogen.

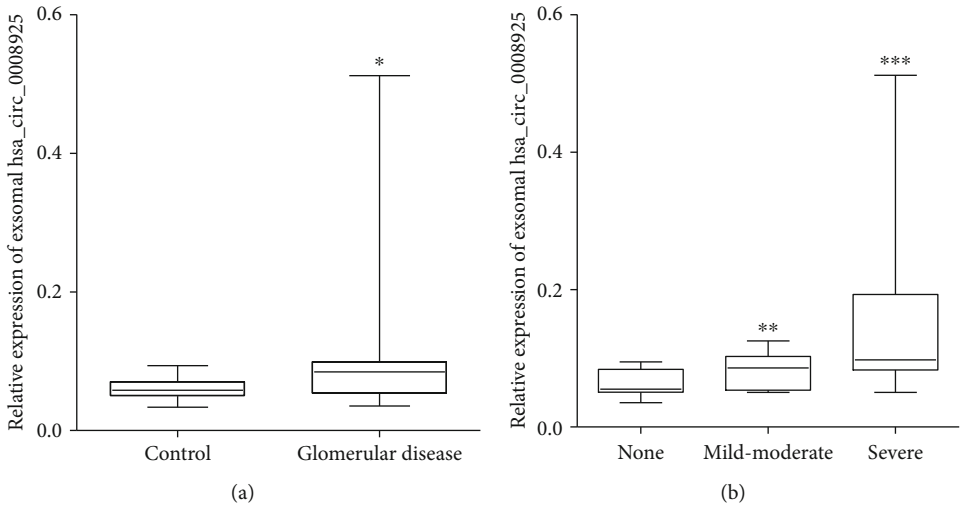

Figure 3: hsa_circ_0008925 expression in urinary exosomes from glomerular disease patients and healthy control. (a) Expression of hsa_circ_0008925 was significantly increased in glomerular disease patients compared to healthy controls. (b) In glomerular disease patients, urinary exosome hsa_circ_0008925 expression was significantly increased in mild-moderate and severe renal fibrosis patients compared to no fibrosis ($^{*}P < 0.001$ vs. control; $^{**}P = 0.002$ vs. no fibrosis; $^{***}P = 0.0038$ vs. mild-moderate).

Table 2: Clinical and pathological characteristics of glomerular disease patients.

	None ($n = 28$)	Mild-moderate ($n = 39$)	Severe ($n = 28$)	P value
Age (y)	42.9 ± 18.2	41.7 ± 12.2	49.9 ± 12.6	0.061
Sex (M/F)	11/17	21/18	19/9	0.100
Scr (μmol/L)	83.5 ± 37.1	88.6 ± 73.0	159.2 ± 129.4	0.002
BUN (mmol/L)	7.1 ± 4.2	5.6 ± 3.0	9.1 ± 4.7	0.002
Cystatin C (mg/L)	1.19 ± 0.63	1.06 ± 0.54	2.05 ± 1.07	<0.001
eGFR (mL/min per 1.73 m^2)	94.2 ± 35.8	98.6 ± 31.1	54.0 ± 22.8	<0.001
24 h proteinuria (g/day)	2.130 (0.080-9.160)	1.290 (0.100-21.580)	2.810 (0.220-13.210)	0.227
hsa_circ_0008925	0.055 (0.035-0.095)	0.086 (0.051-0.125)	0.098 (0.050-0.512)	<0.001
Score of TIF (%)	0	30 (10-45)	70 (52-91)	<0.001
Score of glomerular sclerosis	0.6 (0-1.0)	1.0 (0-2.4)	2.3 (1.0-4.0)	<0.001

Abbreviations: Scr: serum creatinine; eGFR: estimated glomerular filtration rate; BUN: blood urea nitrogen.

samples were appropriately diluted using PBS to measure the particle size and concentration. NTA measurement was recorded and analyzed at 11 positions. The ZetaView system was calibrated using 110 nm polystyrene particles. Temperature was maintained around 23°C and 30°C. Western blot was performed to confirm the expression of exosomes specific marker CD9 and TSG101 using rabbit CD9 antibody, rabbit TSG101 antibody (ProteinTech, USA) and HRP-labeled goat anti-rabbit IgG (H+L) (Beyotime, China). β-Actin was used as a loading control (Biosharp, China).

2.3. Detection of hsa_circ_0008925 in Exosomes from Cell Supernatants. The whole RNA in exosomes was isolated using TRIzol-LS (Invitrogen, USA) according to the manufacturer's protocol. The concentration and purity of RNA were assessed using the relative absorbance ratio at 260/280 in a NanoDrop 2000 (Thermo, USA). The reverse transcription was performed using THE PrimeScript™ RT Reagent Kit (TAKARA, Japan) according to the manufacturer's protocol. RT-PCR was performed using the TB Green Premix Ex Taq Kit (TAKARA, Japan). The primers was as follows: hsa_circ_0008925 primers (sense: 5′-TTATGGCTGTCCTTGGGAGTTT-3′; antisense: 5′-GGTATTCTCGGTCTGTTTTGGA-3′) and U6 primers (sense: 5′-GCTTCGGCAGCACATATACTAAAAT-3′; antisense: 5′-CGCTTCACGAATTTGCGTGTCAT-3′). The hsa_circ_0008925 expression was normalized to U6 and calculated as $2^{-\Delta\Delta Ct}$.

2.4. Study Population. To determine if urinary exosomes displayed a high-level expression of hsa_circ_0008925 in glomerular disease patients, a total of 95 biopsy-proven glomerular disease patients were selected from the Department of Nephrology, Yijishan Hospital, Wannan Medical College. The pathological types of 95 glomerular disease patients concluded IgA nephropathy ($n = 34$), membranous nephropathy ($n = 27$), minimal-change glomerulonephritis ($n = 16$), focal segmental glomerulosclerosis ($n = 2$), diabetic

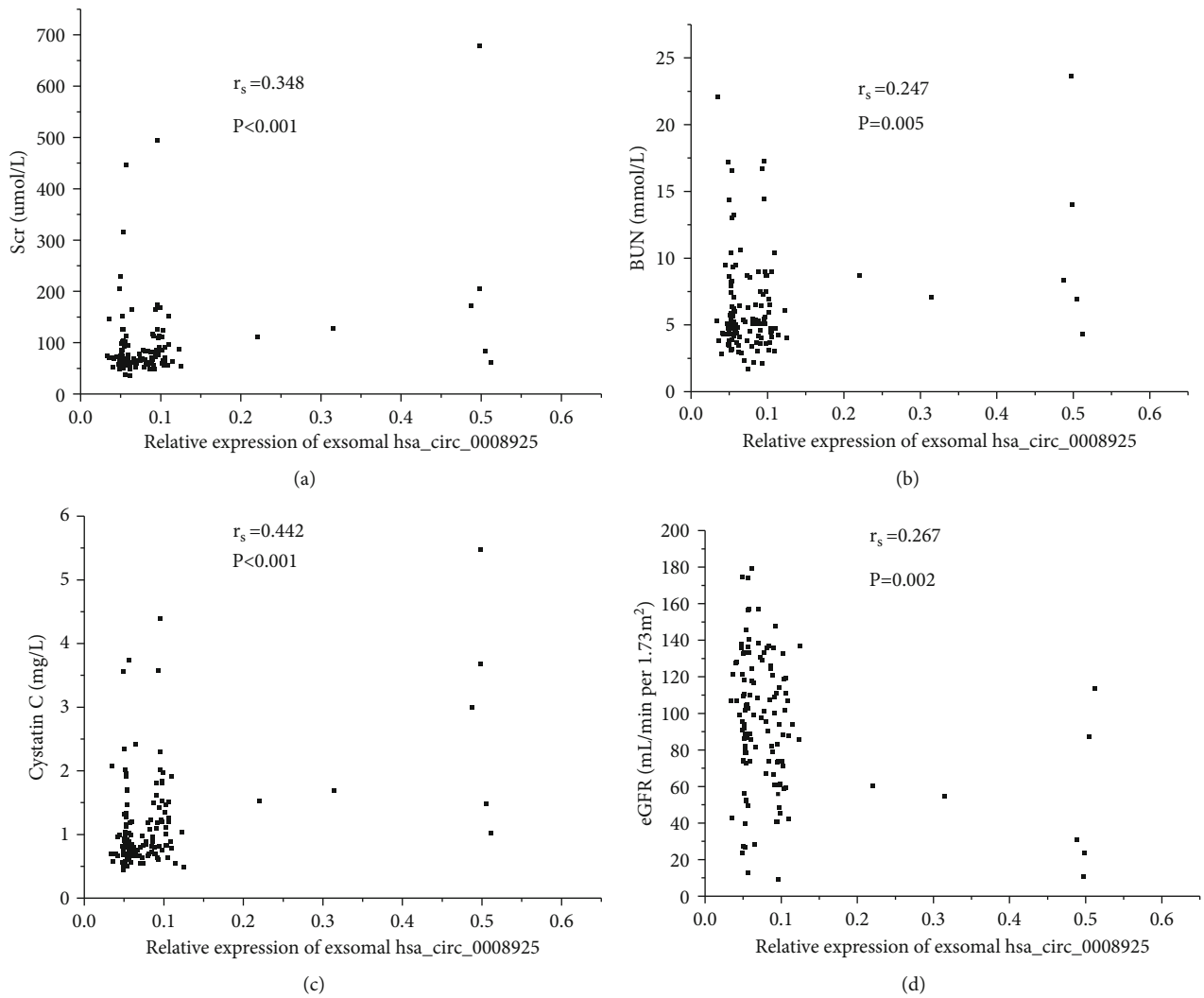

Figure 4: Correlation between urinary exosomal hsa_circ_0008925 expression and kidney function. (a) Spearman's correlation between hsa_circ_0008925 and Scr ($r_s = 0.348$, $P < 0.001$). (b) Spearman's correlation between hsa_circ_0008925 and BUN ($r_s = 0.247$, $P = 0.005$). (c) Spearman's correlation between hsa_circ_0008925 and cystatin C ($r_s = 0.442$, $P < 0.001$). (d) Spearman's correlation between hsa_circ_0008925 and eGFR ($r_s = -0.267$, $P = 0.002$).

nephropathy ($n = 3$), hypertensive nephropathy ($n = 4$), intracapillary proliferative glomerulonephritis ($n = 1$), mesangial proliferative glomerulonephritis ($n = 3$), membranoproliferative glomerulonephritis ($n = 1$), crescentic glomerulonephritis ($n = 2$), and lupus nephritis ($n = 2$). The exclusion criteria were as follows: patients younger than 18 years old or older than 80 years old; patients with chronic liver disease, urinary tract infection, cancer, or organ transplantation; glomerular disease patients with severe complications: cardiovascular disorder; or the use of steroids or immunosuppressive medications. The results of the laboratory examination were collected. Age- and gender-matched healthy volunteers ($n = 54$) also enrolled who were defined with the absence of abnormalities on a routine urinalysis and normal renal function (estimated glomerular filtration rate (eGFR) > 90 mL min/1.73 m^2).

2.5. Collection of Urine Samples and Exosomes. The whole-stream early-morning urine specimens were collected after hospitalization. 100 mL urine sample was centrifuged at 3000 g for 30 min at 4°C. Then, the supernatants were centrifuged at 13500 g for 30 min at 4°C. The sediments were discarded, and the supernatants were centrifuged at 100000 g for 70 min at 4°C. The sediments were suspended in 100 μL phosphate buffer saline (PBS) as urinary exosomes. Exosomes were identified as described above.

2.6. Detection of hsa_circ_0008925 in Urinary Exosomes. The RNA from exosomes was isolated as described above. The reverse transcription and RT-PCR were performed as described above.

2.7. Assessment of Renal Fibrosis. Analysis of renal fibrosis was performed on paraffin-embedded sections stained with periodic acid-Schiff and Masson trichrome. Serial 3 μm sections were acquired from each paraffin block. Two experienced pathologists who were blinded to the results of molecular studies subjectively scored the severity of renal

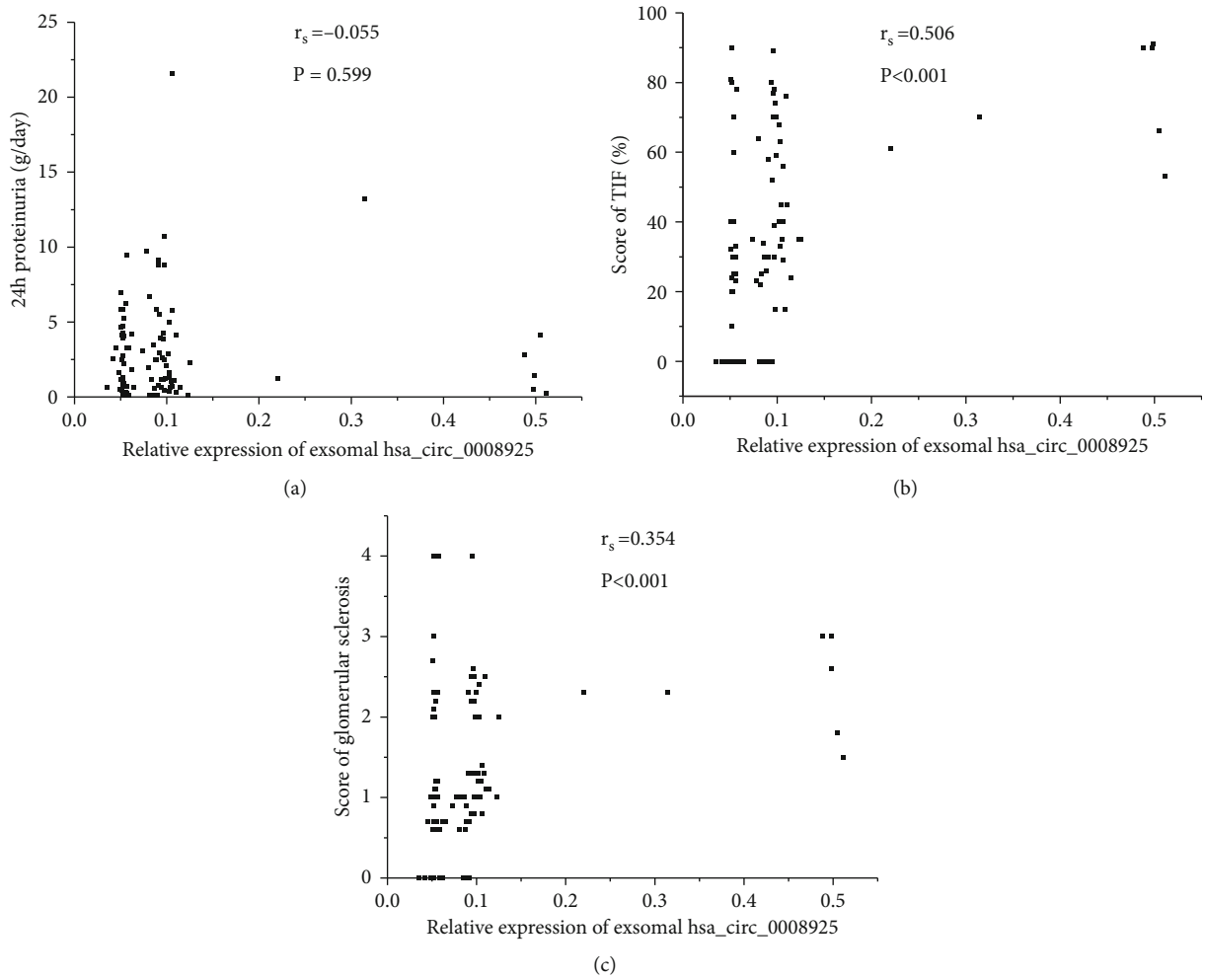

Figure 5: Correlation between urinary exosomal hsa_circ_0036649 expression and 24 h proteinuria, renal fibrosis pathological score. (a) Spearman's correlation between hsa_circ_0008925 and 24 h proteinuria ($r_s = -0.055$, $P = 0.599$). (b) Spearman's correlation between hsa_circ_0008925 and the score of TIF ($r_s = 0.506$, $P < 0.001$). (c) Spearman's correlation between hsa_circ_0008925 and the score of glomerular sclerosis ($r_s = 0.354$, $P < 0.001$).

Table 3: Multivariate logistic regression analysis of selected variables for renal fibrosis.

	OR	95% CI	*P* value
hsa_circ_0008925	1.517	1.178-1.954	0.001
Scr	1.027	0.993-1.063	0.116
BUN	0.800	0.611-1.046	0.103
Cystatin C	0.660	0.104-4.189	0.660
eGFR	0.996	0.969-1.024	0.784
24 h proteinuria	1.093	0.889-1.343	0.400

Abbreviations: Scr: serum creatinine; eGFR: estimated glomerular filtration rate; BUN: blood urea nitrogen; OR: odds ratio; CI: confidence interval.

fibrosis. The degree of renal fibrosis for glomerular disease patients was evaluated, and the score of TIF and glomerular sclerosis performed on Masson-stained sections was calculated according to the previous study [3]. No fibrosis was considered 0 of the renal interstitium fibrosis. Mild-moderate fibrosis was considered ≤50%. Severe was considered >50%.

2.8. Western Blot. The protein in exosomes from cell supernatants and urine were collected using RIPA lysis buffer (Beyotime, China). Protein concentration was determined using a BCA kit (Beyotime, China). The CD9 and TSG101 protein expressions were determined by western blot. Rabbit anti-human CD9 antibody (ProteinTech, USA) and rabbit anti-human TSG101 antibody (ProteinTech, USA) were used. HRP-labeled goat anti-rabbit IgG (Beyotime, China) was used as the secondary antibody. β-Actin was used as a loading control (Biosharp, China).

2.9. Statistical Analysis. SPSS 17.0 was used for data analysis. The method of calculating the relative expression of circRNA was described in the previous study. Statistical comparison of different types of data, the correlation coefficient, logistic regression, and receiver operating characteristic (ROC) curves were calculated according to a previous study described [3]. Relative changes in gene expression were calculated using the $\Delta\Delta$Ct (threshold cycle) method: ΔCt = Ct gene of interest − Ct internal control, while $\Delta\Delta$Ct = Ct gene of interest − Ct internal control sample − Ct gene of interest

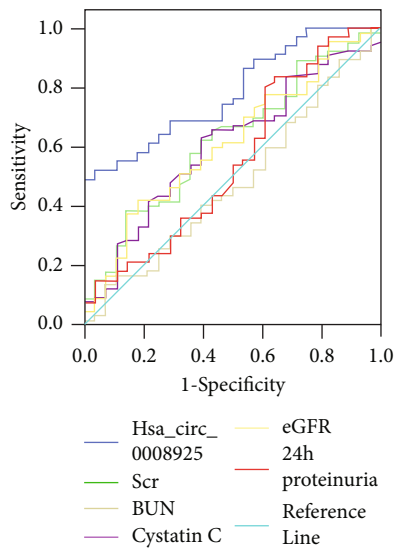

Figure 6: The receiver operating characteristic (ROC) curve showed the diagnostic value of the urinary exosomal hsa_circ_0008925 for renal fibrosis. ROC curve showed the urine exosomes hsa_circ_0008925-distinguished renal fibrosis (AUC of 0.782, 95% CI: 0.690-0.874; $P < 0.001$).

− Ct internal control. Fold change = target gene expression level of sample/target gene expression level of control = $2^{-\Delta\Delta Ct}$. Normal distribution and equal variance data were expressed as mean ± standard deviation and compared using Student's t-test. Variance inequality or nonnormal distribution data were expressed as median (min, max). A Mann–Whitney test was used for variance inequality or nonnormal distribution data. Spearman's rank-order correlation coefficient was used to assess associations between gene expression levels and clinical parameters. Stepwise multivariate logistic regression analysis was used to assess the predictors for renal fibrosis. The diagnostic performance of biomarkers was evaluated using receiver operating characteristic (ROC) curves. The diagnostic threshold for maximum sensitivity and specificity was calculated. All P values were two-tailed, and $P < 0.05$ was considered statistically significant.

3. Results

3.1. Elevated Expression of hsa_circ_0008925 in Cell Supernatant-Derived Exosomes. To identify the change of exosome release in TGF-β1-treated HK-2 cell, we isolated, characterized, and quantified exosomes from cell supernatants using transmission electron microscopy (TEM), western blotting (using CD9 and TSG101 as exosome markers), and ZetaView nanoparticle tracking analysis (NTA). Figure 1(a) showed the TEM image of exosomes. The NTA is shown in Figure 1(b). Exosomes purified from cell culture supernatants showed the typical size and shape. The western blot exhibited that exosomes expressed specific protein markers CD9 and TSG101 compared to HK-2 cells (Figure 1(c)). RT-PCR showed that after coculture with 100 ng/mL TGF-β1 for 24 h and 48 h, the hsa_circ_0008925 expression in cell-derived exosomes was significantly increased compared to normal cultured (Figure 1(d)).

3.2. Identification of Urinary Exosomes from Healthy and Glomerular Disease Patients. The TEM images and ZetaView nanoparticle tracking analysis of urinary exosomes are shown in Figure 2. Exosomes purified from urine exhibited the typical size and shape. The western blot of CD9 and TSG101 (Figure 2(c)) identified that exosomes expressed specific protein markers CD9 and TSG101.

3.3. Baseline Characters of Patients. The clinical characters of the involved subjects are shown in Table 1. There were no significant differences in age and gender between glomerular disease patients and controls. The glomerular disease patients showed high levels of Scr, BUN, and cystatin C and low estimated glomerular filtration rate (eGFR) compared with controls. eGFR was calculated by modified MDRD equations [14]. The relative expression level of hsa_circ_0008925 was significantly increased in the glomerular disease patients (median expression 0.085 in glomerular disease vs. 0.058 in healthy controls, $P < 0.001$ vs. control, Figure 3(a)).

The 95 glomerular disease patients included 28 patients without renal fibrosis, 39 patients with mild-moderate renal fibrosis, and 28 patients with severe renal fibrosis. As shown in Table 2, there were no significant differences in age, gender, and 24 h proteinuria among these 3 groups. The relative expression level of urinary exosomal hsa_circ_0008925 was significantly higher in the mild-moderate group and severe group compared to the no fibrosis group (Median expression 0.086 in mild-moderate vs. 0.055 in the no fibrosis group, $P = 0.002$; mild-moderate vs. 0.098 in severe, $P = 0.038$; Figure 3(b)).

3.4. Correlation between Urinary Exosomal hsa_circ_0008925 and Clinical Parameters as well as Pathological Parameters. Urinary exosomal hsa_circ_0008925 correlated with Scr ($r_s = 0.348$, $P < 0.001$), BUN ($r_s = -0.215$, $P = 0.005$), cystatin C ($r_s = 0.442$, $P < 0.001$), and eGFR ($r_s = -0.267$, $P = 0.002$; Figure 4). In glomerular disease patients, urinary exosomal hsa_circ_0008925 correlated with the score of TIF ($r_s = 0.506$, $P < 0.001$) and the score of glomerular sclerosis ($r_s = 0.354$, $P < 0.001$; Figure 5). However, urinary exosomal hsa_circ_0008925 did not correlate with 24 h proteinuria ($r_s = -0.055$, $P = 0.599$).

The stepwise multivariate logistic regression analysis further showed that the relative expression of urinary exosomal hsa_circ_0008925 significantly correlated with renal fibrosis (Table 3, OR: 1.517; 95% CI: 1.178-1.954; $P = 0.001$). In addition, Scr, BUN, cystatin C, eGFR, and 24 h proteinuria had no statistical significance in the correlation with renal fibrosis by the stepwise multivariate logistic regression analysis (Table 3).

3.5. Diagnostic Value of Urinary Exosomal hsa_circ_0008925 for Renal Fibrosis. The results showed that urinary exosomal hsa_circ_0008925 could effectively distinguish renal fibrosis from no fibrosis, with the largest AUC of 0.782 (95% CI: 0.690-0.874; $P < 0.001$) higher than that of Scr (AUC of 0.625; 95% CI: 0.504-0.760; $P = 0.055$), BUN (AUC of 0.479; 95% CI: 0.351-0.606; $P = 0.744$), cystatin C (AUC of

0.606; 95% CI: 0.484-0.729; $P = 0.103$), eGFR (AUC of 0.612; 95% CI: 0.489-0.734; $P = 0.087$), and 24 h proteinuria (AUC of 0.555; 95% CI: 0.421-0.688; $P = 0.403$). Urinary exosomal hsa_circ_0008925 displayed a sensitivity of 52.2% and specificity of 96.4% at the optimal cut-off value of 0.093 (Figure 6).

4. Discussion

In this study, we found that tubular epithelial cell-derived exosomes contained a high level of hsa_circ_0008925 in the renal fibrosis model in vitro. In addition, we found that the urinary exosomal hsa_circ_0008925 expression level was increased in glomerular disease patients. Furthermore, within glomerular disease patients, patients with renal fibrosis showed a higher urinary exosomal hsa_circ_0008925 expression level than patients with no fibrosis, which suggested the potential of urinary exosomal hsa_circ_0008925 to become a noninvasive biomarker for renal fibrosis.

Noninvasive and repeatable detection of renal fibrosis is the key for early monitoring and prevention of glomerular disease progression. Additionally, biomarkers often play an important role in the occurrence and development of diseases and are major molecules to reveal the pathogenesis of diseases. However, renal biopsy is incapable of the advantages of being noninvasive and repeatable. Noninvasive markers and detection methods of renal fibrosis are necessary in clinical practice. In 2001, Li et al. first established a noninvasive approach to diagnose acute renal rejection of allografts by isolating and quantifying RNA of specific genes in urine sediments [5]. Subsequently, many studies found that the RNA contained in urinary sediment cells is related to a variety of kidney diseases and has the application value of biomarkers [3, 14–17]. Urinary sediment contains different types of cells, including renal intrinsic cells. The difference in mRNA expression in urinary sediment cannot accurately reflect the state of renal disease.

Pisitkun et al. first found exosomes in urine [10]. Urine exosomes are produced by the fusion of MVB with renal epithelial cells which can reflect the pathological changes of the kidney [18]. Previous studies have found that protein, mRNA, and miRNA in urinary exosomes can be used as biomarkers for the diagnosis of CKD [4, 19, 20]. Exosomes contained abundant circRNAs [21]. Ma et al. reported that 89 circRNAs were significantly differentially expressed in idiopathic membranous nephropathy patients' urine exosomes and MUC3A could be considered a potential diagnostic biomarker of idiopathic membranous nephropathy [9]. In our study, we found that HK-2 cell-derived exosomes contained a high level of hsa_circ_0008925 in the fibrotic microenvironment in vitro. That strongly indicated that in renal fibrosis, renal tubular epithelial cells secrete a large number of circRNAs carried by exosomes. Urinary exosomal hsa_circ_0008925 expression level correlated with renal function and pathological changes, which may show the potential of the ability to diagnose renal fibrosis.

Tubular epithelial cells play an important role in renal fibrosis. A previous study showed that the metabolic state of tubular epithelial cells and excessive accumulation of the extracellular matrix are important factors which may influence renal fibrosis [22, 23]. There are a few studies on whether circular RNA in tubular epithelial cells is involved in renal fibrosis. Peng et al. found that the circRNA_010383 expression level was markedly downregulated in tubular epithelial cells cultured in high-glucose conditions. Loss of circRNA_010383 promoted proteinuria and renal fibrosis in DN by acting as a sponge for miRNA-135a [24]. Wen et al. reported that circACTR2 regulated high glucose-induced pyroptosis, inflammation, and fibrosis in proximal tubular cells. circACTR2 was defined as a novel circular RNA-regulated high glucose-induced fibrosis [25]. Cui et al. revealed that circZNF609 is involved in the pathogenesis of focal segmental glomerulosclerosis [26]. Xu et al. further found that circEIF4G2 aggravates renal fibrosis in mouse models and rat cell lines [27]. These researches indicated that in CKD that progressed to renal fibrosis, circRNAs played a key role in the progression of the disease. In our research, we first suggested that the expression level of hsa_circ_0008925 increased in TGF-β1-cultured HK-2 cell-derived exosomes. The elevated level of hsa_circ_0008925 in urinary exosomes was probably from tubular epithelial cells. So far, there was no relevant research that revealed the biological function of hsa_circ_0008925. hsa_circ_0008925 originated from chr6:108222573-108246136, and the gene symbol was sec63. Ishikawa et al. found that the loss of sec63 promoted spliced XBP1 which alleviated renal interstitial inflammation [13]. In this study, our data strongly suggested that hsa_circ_0008925 participated in the progression of renal fibrosis and indicated that hsa_circ_0008925 might be used as a noninvasive biomarker of renal fibrosis.

Our study also has some limitations. First, this study did not focus on the specific pathological types of glomerular disease. Whether the urinary exosomal hsa_circ_0008925 can be used as renal fibrosis biomarkers in different pathological types still needs to be further determined by large sample size research. Second, subsequent cell and animal studies are needed in the future research to determine the mechanism of hsa_circ_0008925 in renal fibrosis. Additionally, whether hsa_circ_0008925 will affect the prognosis of patients with renal fibrosis is uncertain and still needs to be further studied.

5. Conclusion

Patients with renal fibrosis showed a higher urinary exosomal hsa_circ_0008925 expression level than patients with no fibrosis, which suggested the potential of urinary exosomal hsa_circ_0008925 to become a noninvasive biomarker for renal fibrosis.

Data Availability

The datasets used and/or analyzed in the current study are available from the corresponding author on reasonable request.

Ethical Approval

The Ethical Committee of Yijishan Hospital, Wannan Medical College, approved all studies (approval number: 2017LSY No.18).

Consent

Written informed consents were obtained from all subjects. The research was conducted ethically in accordance with the World Medical Association Declaration of Helsinki.

Disclosure

The sponsors played no role in the preparation of data or the manuscript.

Conflicts of Interest

The authors have no conflicts of interest to declare.

Authors' Contributions

Yuhan Cao and Yuanhui Shi contributed equally to this work.

Acknowledgments

This research is financially supported by the National Natural Science Foundation of China (81702092 to Yuhan Cao, 81700265 to Cong Fu).

References

[1] L. Zhang, F. Wang, L. Wang et al., "Prevalence of chronic kidney disease in China: a cross-sectional survey," *Lancet*, vol. 379, no. 9818, pp. 815–822, 2012.

[2] Y. Liu, "Cellular and molecular mechanisms of renal fibrosis," *Nature Reviews. Nephrology*, vol. 7, no. 12, pp. 684–696, 2011.

[3] Y. Cao, Y. Wang, N. Peng, J. Xiao, S. Wang, and C. Fu, "The ratio of urinary TREM-1/TREM-2 mRNA expression in chronic kidney disease and renal fibrosis," *Annals of Medicine*, vol. 53, no. 1, pp. 1010–1018, 2021.

[4] Y. Feng, L. L. Lv, W. J. Wu et al., "Urinary exosomes and exosomal CCL2 mRNA as biomarkers of active histologic injury in IgA nephropathy," *The American Journal of Pathology*, vol. 188, no. 11, pp. 2542–2552, 2018.

[5] B. Li, C. Hartono, R. Ding et al., "Noninvasive diagnosis of renal-allograft rejection by measurement of messenger RNA for perforin and granzyme B in urine," *The New England Journal of Medicine*, vol. 344, pp. 947–954, 2001.

[6] M. Suthanthiran and T. Muthukumar, "Urinary-cell mRNA and acute kidney-transplant rejection," *The New England Journal of Medicine*, vol. 369, pp. 1860-1861, 2013.

[7] J. Jin, H. Sun, C. Shi et al., "Circular RNA in renal diseases," *Journal of Cellular and Molecular Medicine*, vol. 24, no. 12, pp. 6523–6533, 2020.

[8] M. Kölling, H. Seeger, G. Haddad et al., "The circular RNA ciRs-126 predicts survival in critically ill patients with acute kidney injury," *Kidney International Reports*, vol. 3, no. 5, pp. 1144–1152, 2018.

[9] H. Ma, Y. Xu, R. Zhang, B. Guo, S. Zhang, and X. Zhang, "Differential expression study of circular RNAs in exosomes from serum and urine in patients with idiopathic membranous nephropathy," *Archives of Medical Science*, vol. 15, no. 3, pp. 738–753, 2019.

[10] T. Pisitkun, R. F. Shen, and M. A. Knepper, "Identification and proteomic profiling of exosomes in human urine," *Proceedings of the National Academy of Sciences*, vol. 101, no. 36, pp. 13368–13373, 2004.

[11] C. Théry, L. Zitvogel, and S. Amigorena, "Exosomes: composition, biogenesis and function," *Nature Reviews. Immunology*, vol. 2, no. 8, pp. 569–579, 2002.

[12] A. V. Vlassov, S. Magdaleno, R. Setterquist, and R. Conrad, "Exosomes: current knowledge of their composition, biological functions, and diagnostic and therapeutic potentials," *Biochimica et Biophysica Acta*, vol. 1820, no. 7, pp. 940–948, 2012.

[13] Y. Ishikawa, S. Fedeles, A. Marlier et al., "Spliced XBP1 rescues renal interstitial inflammation due to loss of sec63 in collecting ducts," *Journal of the American Society of Nephrology*, vol. 30, no. 3, pp. 443–459, 2019.

[14] Y. H. Cao, L. L. Lv, X. Zhang et al., "Urinary vimentin mRNA as a potential novel biomarker of renal fibrosis," *American Journal of Physiology. Renal Physiology*, vol. 309, pp. F514–F522, 2015.

[15] Y. Cao, Y. Wang, Y. Liu et al., "Decreased expression of urinary mammalian target of rapamycin mRNA is related to chronic renal fibrosis in IgAN," *Disease Markers*, vol. 2019, Article ID 2424751, 10 pages, 2019.

[16] M. Zheng, L. L. Lv, Y. H. Cao et al., "Urinary mRNA markers of epithelial-mesenchymal transition correlate with progression of diabetic nephropathy," *Clinical Endocrinology*, vol. 76, pp. 657–664, 2012.

[17] M. Zheng, L. L. Lv, J. Ni et al., "Urinary podocyte-associated mRNA profile in various stages of diabetic nephropathy," *PLoS One*, vol. 6, article e20431, 2011.

[18] P. Gonzales, T. Pisitkun, and M. A. Knepper, "Urinary exosomes: is there a future?," *Nephrology, Dialysis, Transplantation*, vol. 23, no. 6, pp. 1799–1801, 2008.

[19] P. G. Moon, J. E. Lee, S. You et al., "Proteomic analysis of urinary exosomes from patients of early IgA nephropathy and thin basement membrane nephropathy," *Proteomics*, vol. 11, no. 12, pp. 2459–2475, 2011.

[20] T. Chen, C. Wang, H. Yu et al., "Increased urinary exosomal microRNAs in children with idiopathic nephrotic syndrome," *eBioMedicine*, vol. 39, pp. 552–561, 2019.

[21] Y. Li, Q. Zheng, C. Bao et al., "Circular RNA is enriched and stable in exosomes: a promising biomarker for cancer diagnosis," *Cell Research*, vol. 25, no. 8, pp. 981–984, 2015.

[22] H. M. Kang, S. H. Ahn, P. Choi et al., "Defective fatty acid oxidation in renal tubular epithelial cells has a key role in kidney fibrosis development," *Nature Medicine*, vol. 21, no. 1, pp. 37–46, 2015.

[23] L. Zhang, L. Liu, M. Bai et al., "Hypoxia-induced HE4 in tubular epithelial cells promotes extracellular matrix accumulation and renal fibrosis via NF-κB," *The FASEB Journal*, vol. 34, no. 2, pp. 2554–2567, 2020.

[24] F. Peng, W. Gong, S. Li et al., "circRNA_010383 acts as a sponge for miR-135a and its downregulated expression contributes to renal fibrosis in diabetic nephropathy," *Diabetes*, vol. 70, no. 2, pp. 603–615, 2020.

[25] S. Wen, S. Li, L. Li, and Q. Fan, "circACTR2: a novel mechanism regulating high glucose-induced fibrosis in renal tubular cells via pyroptosis," *Biological & Pharmaceutical Bulletin*, vol. 43, no. 3, pp. 558–564, 2020.

[26] X. Cui, J. Fu, J. Luan et al., "Circ ZNF609 is involved in the pathogenesis of focal segmental glomerulosclerosis by sponging miR-615-5p," *Biochemical and Biophysical Research Communications*, vol. 531, no. 3, pp. 341–349, 2020.

[27] B. Xu, Q. Wang, W. Li et al., "Circular RNA circEIF4G2 aggravates renal fibrosis in diabetic nephropathy by sponging miR-218," *Journal of Cellular and Molecular Medicine*, 2020.

Hindawi
Disease Markers
Volume 2022, Article ID 7076385, 12 pages
https://doi.org/10.1155/2022/7076385

Research Article

Serum and Cerebrospinal Fluid Testing in Optic Neuropathy Patients with Malignant Tumors

Chuan-bin Sun,[1] **Geng-hao Liu**,[1] **Qing Xiao**,[1] **Yi-nv Zhao**,[1] **and Qian Ren**[2]

[1]*Eye Center, Second Affiliated Hospital of Zhejiang University School of Medicine, Hangzhou 310009, China*
[2]*Department of Ophthalmology, Shijiazhuang People's Hospital, Shijiazhuang 050011, China*

Correspondence should be addressed to Chuan-bin Sun; sunshine2012@zju.edu.cn and Qian Ren; renqian010602@hotmail.com

Received 17 December 2021; Accepted 8 February 2022; Published 17 February 2022

Academic Editor: Yi Shao

Purpose. To evaluate the value of serum and cerebrospinal fluid (CSF) testing in optic neuropathy (ON) patients with malignant tumors. *Methods*. Fourteen patients clinically diagnosed as ON with malignant tumors but without intracranial or orbital mass in MRI were included in this study. Detailed medical records including medical history, complete ophthalmic examination, colour fundus photography, visual field test, orbital MRI examination, serum and CSF testing data were collected and analyzed. The diagnosis of paraneoplastic optic neuropathy (PON) based on the 2004 recommended criteria of the paraneoplastic syndrome-Euronetwork consortium for paraneoplastic neurological disorders, and current adaption for neuropathies. All patients underwent serum tests for pathogens and autoantibodies including antinuclear antibodies, anticardiolipin antibodies, antineutrophil cytoplasmic antibodies, AQP4-Ab and MOG-Ab, as well as CSF tests for malignant cells under microscope. Serum paraneoplastic antibodies were detected in PON patients. Monkey cerebellar tissue-based assay was used to detect unknown serum anti-neuron antibodies in PON patients with negative paraneoplastic antibody testing results. *Results*. Fourteen ON patients were classified as four groups based on their clinical and MRI characteristics, as well as serum and CSF testing results: [1] definite PON, 6 cases (11 eyes); [2] possible PON, 3 case (5 eyes); [3] meningeal carcinomatosis-associated optic neuropathy (MCON), 4 cases (6 eyes); [4] infiltrative optic neuropathy (ION), 2 cases (2 eyes). Malignant cells were found under microscope in CSF samples from MCON and ION patients, contrast to no malignant cells in CSF samples from PON cases. All 14 ON patients with malignant tumors showed negative results in serum tests for pathogens and autoantibodies. Serum paraneoplastic antibodies were tested in PON patients, anti- CV2, anti-Yo, and anti- amphiphysin were detected positive in 2, 1, and 1 case, respectively, in definite PON group, whereas no serum paraneoplastic antibody detected in possible PON group. Two unknown serum antineuronal antibodies (an anti- Purkinje cell antibody and an anti-granular cell antibody) were detected using monkey cerebellar tissue-based assay in 2 of 5 PON patients with negative paraneoplastic antibody test results. *Conclusions*. Serum and CSF tests are of great importance in differentiating different subtypes of ON with malignant tumors. Current diagnosis of PON still depends on combination of clinical and MRI manifestations, as well as serum and CSF tests. Tissue-based assay may help to detect new biomarkers for ON etiology and diagnosis.

1. Introduction

Optic neuropathy (ON) such as papilloedema secondary to intracranial metastasis is not uncommon in patients with malignant tumors, however, other optic neuropathies such as paraneoplastic optic neuropathy (PON), infiltrative optic neuropathy, and demyelinating optic neuritis, are rare in malignant tumor patients, and their early diagnosis is quite challenging in clinical practice [1–4].

PON, also called paraneoplastic optic neuritis, is a rare but blindness-causing inflammatory disease [1–5]. PON is believed to be caused by the immune-mediated cross-

reaction between the malignant tumor and the retina and (or) optic nerve which share same antigens, rather than by an infiltration or metastasis of a malignant tumor. PON should be considered as a possible diagnosis in any cancer patient with optic disc edema and subacute bilateral visual loss, especially when there is no evidence of intracranial or orbital metastasis [1–3].

However, it is really difficult and challenging to distinguish PON from other optic neuropathies including infiltrative optic neuropathy (ION), meningeal carcinomatosis-associated optic neuropathy (MCON), and demyelinating optic neuritis in malignant tumor cases because of many overlapping clinical manifestations [1–6]. We herein evaluated the serum and cerebrospinal fluid (CSF) testing in ON patients with malignant tumors but without intracranial or orbital mass in MRI examination.

2. Materials and Methods

2.1. Patients. Fourteen patients clinically diagnosed as ON with malignant tumors but without intracranial or orbital mass in MRI from May, 2017 to November, 2021 in Second Affiliated Hospital of Zhejiang University School of Medicine and Shijiazhuang People's Hospital were included in this study. Detailed medical records including medical history, complete ophthalmic examination, colour fundus photography, visual field test, orbital or cranial MRI examination, serum and CSF testing data were collected and analyzed. This study was conducted according to the tenets of the Declaration of Helsinki. Informed consents were obtained from all patients. Institutional review board approvals were obtained from Second Affiliated Hospital of Zhejiang University School of Medicine and Shijiazhuang People's Hospital.

The inclusion criteria were as follows: (1) definite ON diagnosis based on the typical ophthalmic manifestations: (a) acute or subacute visual loss, or blurred vision, (b) swollen optic disc, or occasionally normal optic disc, (c) exclusion of severe cataract, glaucoma, and toxic, compressive, traumatic, or hereditary optic neuropathy; (2) at least one malignant tumor diagnosed before, during or after ON occurrence; (3) serum autoantibody tests including IgM or IgG antibodies to pathogens, antinuclear antibodies, anticardiolipin antibodies, antineutrophil cytoplasmic antibodies, aquaporin 4-IgG antibody (AQP4-Ab), and myelin oligodendrocyte glycoprotein-IgG antibody (MOG-Ab); (4) serum paraneoplastic autoantibody tests in suspected PON patients; (5) at least 6 months follow-up.

The exclusion criteria were: (1) positive serum IgM or IgG antibodies of pathogens including treponema, mycobacterium tuberculosis, herpes viruses, hepatitis viruses, or HIV, which indicating infectious ON; (2) positive serum autoantibodies including antinuclear antibodies, anticardiolipin antibodies, antineutrophil cytoplasmic antibodies, and instant excellent therapeutic response to steroid which supporting a diagnosis of typical inflammation-related ON; (3) concurrent uveitis or retinopathy probably not related to paraneoplastic syndrome; (4) one or more intracranial or orbital mass in MRI.

The diagnosis of PON was based on the 2004 recommended criteria of the paraneoplastic syndrome (PNS)-Euronetwork consortium for paraneoplastic neurological disorders, and the adaption for neuropathies suggested by Antoine et al. Briefly, definite PON was diagnosed based on (1) a direct pathogenic link between the tumor and ON was demonstrated, with or without positive serum paraneoplastic antibodies; (2) well-established PNS but no identified paraneoplastic antibodies, (3) ON unequivocally improved by tumor treatment provided that it has no spontaneous tendency to recovery. Any other ON occurring within 2 years of a cancer was a possible paraneoplastic disorder [1, 2]. ION was defined as optic nerve infiltration by metastatic malignant tumors such as leukemia and lymphoma, or inflammation near optic nerve. MCON was defined as swollen optic disc secondary to meningeal metastasis of malignant tumors such as leukemia, lymphoma, lung and breast cancer. ION can occur alone or accompanied by MCON.

2.2. Ophthalmic Examination. All patients underwent best corrected visual acuity (BCVA), complete ophthalmic examination, colour fundus photography, and visual field test was tested using a Snellen chart. Colour fundus photography was taken using Canon CX-1 (Canon Company, Japan), visual field was tested using 30 program for Octopus 900 (HAAG-STREIT Diagnostics, Swissland) perimeter, low vision program was used for patients with BCVA lower than 20/200, but better than hand motion.

2.3. Orbital/Cranial MRI Examination. At presentation, all patients underwent orbital or cranial MRI examination using T2-weighted imaging sequence with fat suppression and fluid attenuated inversion recovery sequence, and T1-weighted imaging sequence with fat suppression sequence and gadolinium-enhancement.

2.4. Serum and CSF Testing. All patients underwent serum tests including T-spot test, serum IgM or IgG antibodies to pathogens including treponema, mycobacterium tuberculosis, herpes viruses, hepatitis viruses, and HIV, antinuclear antibodies including antinuclear antibody, antidouble-stranded DNA, anti-Sjogren syndrome A or Sjogren syndrome B, anticardiolipin antibodies, antineutrophil cytoplasmic antibodies, serum AQP4-Ab and MOG-Ab tested using cell-based assay. Serum paraneoplastic antibodies were detected using different test panels commercially available predominantly including anti-Hu, anti-Yo, anti-Ri, anti-CV2/CRMP5, anti-Ma2/TA, anti-amphiphysin, anti-Tr, anti- Zic4, and anti-recoverin, in PON patients using indirect immunofluorescence testing and western blotting. Monkey cerebellar tissue -based assay was used to detect unknown serum antineuronal antibodies in PON patients with negative paraneoplastic antibody test results. CSF tests for malignant cells under microscope were performed in all patients.

3. Results

3.1. Clinical and MRI Characteristics of ON Patients with Malignant Tumors. Table 1 showed the clinical and MRI characteristics, as well as serum and CSF testing results of

Table 1: Clinical and MRI characteristics, and serum and CSF test results of optic neuropathy patients with malignant tumors.

No.	Sex	Age	Eye	BCVA Initial	BCVA Final	Ophthalmic examination	Visual field	Orbital/cranial MRI	MCs in CSF test	PA in serum test	ON type	Malignant tumor type	Follow-up (months)
1	M	54	R	20/100	20/25	Swollen disc	Tunnel vision	Optic nerve enlargement and enhancement	No	No	dPON	Lung cancer	17
			L	20/40	20/20	Swollen disc	Arcuate scotoma						
2	M	58	R	CF	NLP	Normal disc	Generalized depression	Normal	No	Anti-Amphiphysin	dPON	Lung cancer	10
			L	HM	LP								
3	F	62	R	20/200	20/60	Swollen disc	Generalized depression	Optic nerve enlargement and enhancement	No	Anti-CV2	dPON	Lung cancer	14
			L	CF	20/100								
4	M	62	R	20/25	20/200	Normal disc	Ring scotoma	Optic nerve enlargement and enhancement	No	Anti-CV2	dPON	Lung cancer	6
			L	20/400	NLP	Swollen disc	Tunnel vision						
5	M	61	R	HM	20/125	Swollen disc	Generalized depression	Optic nerve enlargement and enhancement	No	Anti-Yo	dPON	Prostate cancer	8
			L	20/60	20/40	Swollen disc	Tunnel vision						
6	F	48	R	20/60	20/32	Swollen disc	Peripheral defect	Normal	No	No	dPON	Ovarian cancer	49
7	M	61	R	20/200	20/40	Swollen disc	Altitudinal hemiscotosis	Normal	No	No	pPON	Gastric cancer	55
			L	20/100	20/32	Swollen disc	Large cental scotoma						
8	M	54	R	20/100	20/32	Swollen disc	Generalized depression	Normal	No	No	pPON	Lung cancer	20
			L	CF	20/200								
9	F	64	L	CF	20/125	Swollen disc	Generalized depression	Optic nerve enlargement and enhancement	No	No	pPON	Lung cancer	16
10	M	59	R	20/20	20/20	Swollen disc	Normal	Normal optic nerve, focal meningeal enhancement	Yes	N.A.	MCON	Gastric cancer	15
			L	20/20	20/20								
11	F	52	L	20/20	20/20	Swollen disc and lateral rectus palsy	Normal	Enlarged optic nerve sheath space with sheath enhancement, enlarged cavernous sinus with meningeal enhancement	Yes	N.A.	MCON CSS	Lung cancer	6

Table 1: Continued.

No.	Sex	Age	Eye	BCVA Initial	BCVA Final	Ophthalmic examination	Visual field	Orbital/cranial MRI	MCs in CSF test	PA in serum test	ON type	Malignant tumor type	Follow-up (months)
12	F	57	R	20/50	20/40	Swollen disc Enlarged SOV	Normal	Enlarged optic nerve sheath space with sheath enhancement, enlarged cavernous sinus with meningeal enhancement	Yes	N.A.	MCON CSS	Nasopharyngeal carcinoma	48
			L	20/40	20/32								
13	M	37	L	20/20	20/20	Swollen disc	Normal	Enlarged optic nerve sheath space with sheath enhancement, focal meningeal enhancement	Yes	N.A.	MCON	Leukemia	36
			R	20/40	NLP	Swollen disc CRAO	N.A.	Optic nerve enlargement with sheath enhancement, focal meningeal enhancement	Yes	N.A.	ION		
14	M	49	R	NLP	NLP	Swollen disc CRAO	N.A.	Optic nerve enlargement with sheath enhancement	Yes	N.A.	ION	Lymphoma	15

BCVA: best corrected visual acuity; R: right; L: left; MCs: malignant cells; CSF: cerebrospinal fluid; PA: paraneoplastic antibody; ON: optic neuropathy; CF: counting fingers; HM: hand motion; LP: light perception; NLP: no light perception; PON: paraneoplastic optic neuropathy; dPON: definite PON; pPON: possible PON; MCON: meningeal carcinomatosis-associated optic neuropathy; CSS: cavernous sinus syndrome; SOV: superior ophthalmic vein; ION: infiltrative optic neuropathy; CRAO: central retinal artery occlusion; N.A.: not applicable.

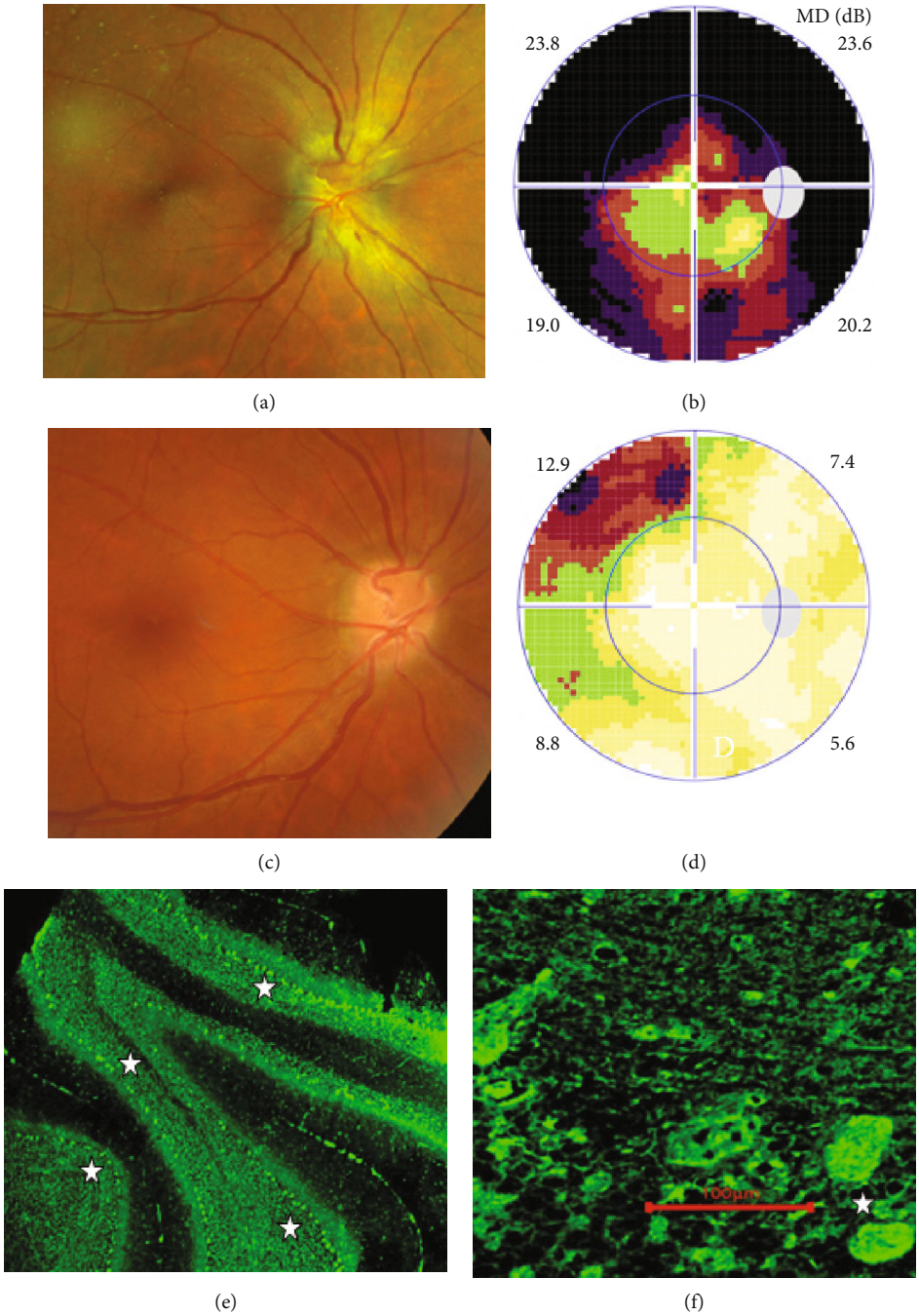

Figure 1: Ophthalmic examination and tissue-based assay of definite paraneoplastic optic neuropathy with lung cancer in Case1. Fundus photograph showed swollen optic disc (a), visual field test showed tunnel vision (b) in the right eye. 2 months after chemotherapy, the edema of optic disc greatly resolved (c) and only small peripheral visual field loss left (d). Unknown serum antineuronal antibody bound to monkey cerebellar Purkinje cells (star, E, F) was detected by tissue-based assay in this patient whose paraneoplastic antibody test result was negative.

fourteen ON patients (24 eyes) with malignant tumors but without intracranial or orbital mass in MRI, including nine males and five females. The mean age was 55.6 (range from 37 to 64) years, mean follow-up was 22.5 (range from 6 to 55) months. The concurrent malignant tumors included lung cancer, gastric cancer, prostate cancer, ovarian cancer, nasopharyngeal carcinoma, leukemia, and lymphoma in 7, 2, 1, 1, 1, 1, 1case, respectively. Malignant tumours were treated with at least one of the following: surgery, chemotherapy, radiotherapy, and targeted therapy with biologic agents. Eleven patients with malignant tumors were cured or kept stable at last follow-up, whereas three cases (Case 3, 4, 5) died of relapsed or metastasized malignant tumors.

Fourteen ON patients were classified as four groups based on their clinical and MRI characteristics, as well as serum and CSF testing results: (1) definite PON, 6 cases

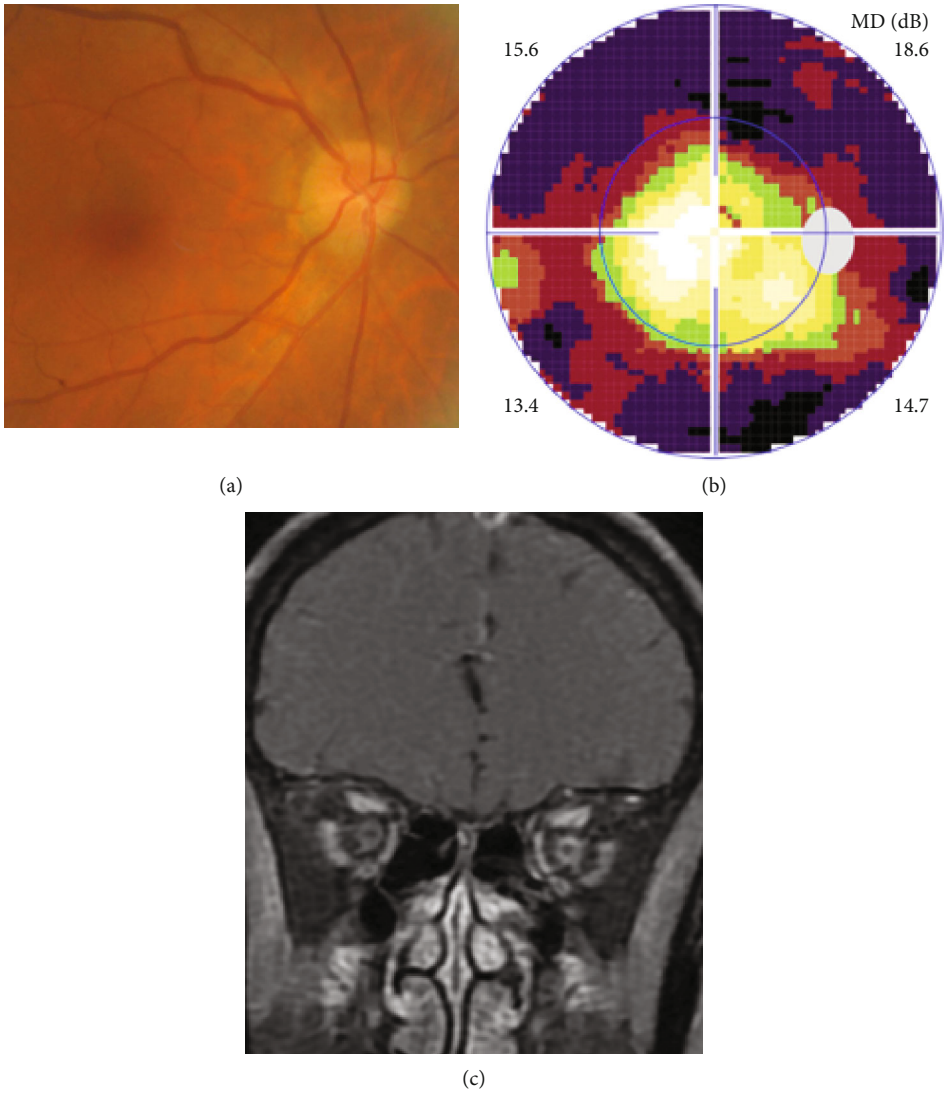

Figure 2: Ophthalmic and MRI examination of definite paraneoplastic optic neuropathy with gastric cancer in Case 4. Fundus photograph showed normal optic disc (a), visual field test showed ring scotoma (b), MRI showed optic nerve enlargement with sheath enhancement in both eyes, more evident in the lfet eye (c).

(11 eyes); (2) possible PON, 3 case (5 eyes); (3) MCON, 4 cases (6 eyes); (4) ION, 2 cases (2 eyes) (Table 1). Nine ON patients (Case 1 to Case 9) were classified as PON based on the direct pathogenic link between the tumor and neuropathy, and ON totally or partially improved after tumor treatment during long-term observation. However, 3 of above 9 PON patients (Case 7 to Case 9) underwent concurrent short-term steroid pulse therapy continued by tapered oral steroid when their ON occurred. More over, these 3 cases were negative for serum paraneoplastic antibody tests. Hence, they were classified as possible PON.

Definite PON presented as subacute (9/11) or acute (2/11) visual loss, mostly bilaterally invovled (5/6). The median of BCVA was 20/200 (range from hand motion to 20/25) and 20/100 (range from no light perception to 20/20) at presentation and final follow-up, respectively. Seven eyes showed visual improvement whereas 4 eyes visual deterioration at last follow-up. Definite PON predominantly appeared as swollen optic disc (9/11), normal optic disc (2/11) was rare in definite PON patients. Visual field test revealed generalized depression, tunnel vision, ring scotoma, arcuate scotoma, and peripheral defect in 5, 3, 1, 1, and 1 eye, respectively (Figures 1, 2). MRI showed optic nerve enlargement with gadolinium enhancement in 8 eyes, whereas normal MRI in the other 3 eyes (Figure 2). Three of 6 definite PON patients were reported dead at last telephone follow-up.

Possible PON also presented as subacute (4/5) or acute (1/5) visual loss, also mostly bilaterally invovled (2/3). All possible PON appeared as swollen optic disc, visual field test revealed generalized depression, altitudinal hemiscotosis, and large cental scotoma in 3, 1, and 1 eye, respectively. MRI showed optic nerve enlargement with gadolinium enhancement in one eye, whereas normal MRI in the other 4 eyes (Figure 3). (Table 1).

MCON (4 cases, 6 eyes) generally presented as slightly blurred vision, although BCVA and visual field test results

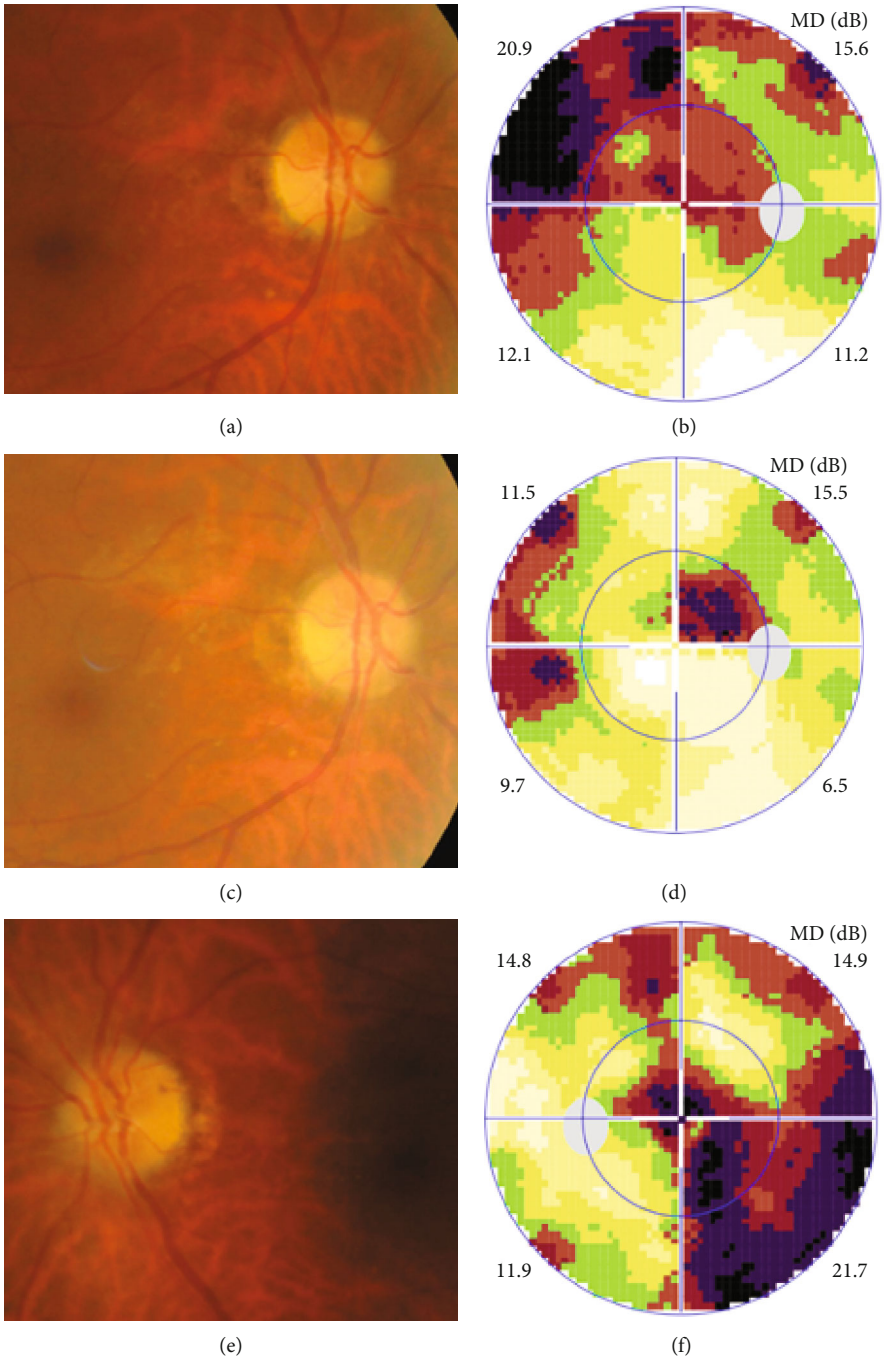

Figure 3: Continued.

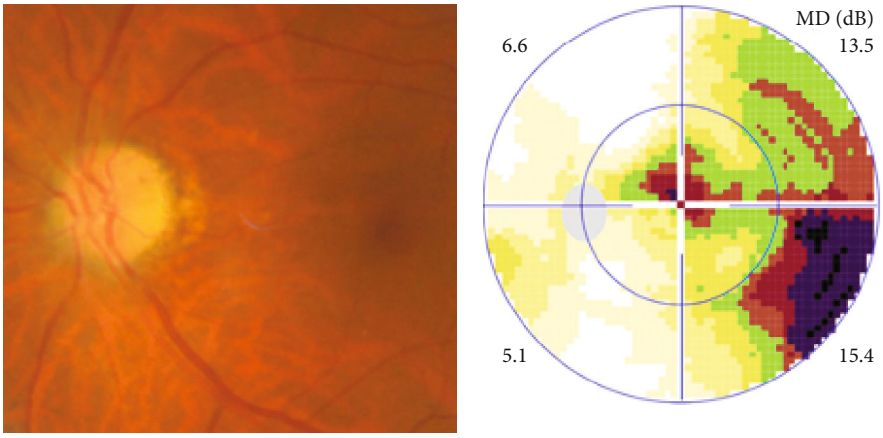

(g) (h)

Figure 3: Ophthalmic examination of possible paraneoplastic optic neuropathy with gastric cancer in Case 7. Fundus photographs showed swollen optic disc in both eyes (A, E), visual field test showed altitudinal hemiscotosis (B) and large cental scotoma (F) in the right and left eye. 6 months after surgery and steroid therapy, both eyes appeared as pale temporal disc (C, G), visual field test showed small centrocecal (D) and cental scotoma (H) in the right and left eye, respectively.

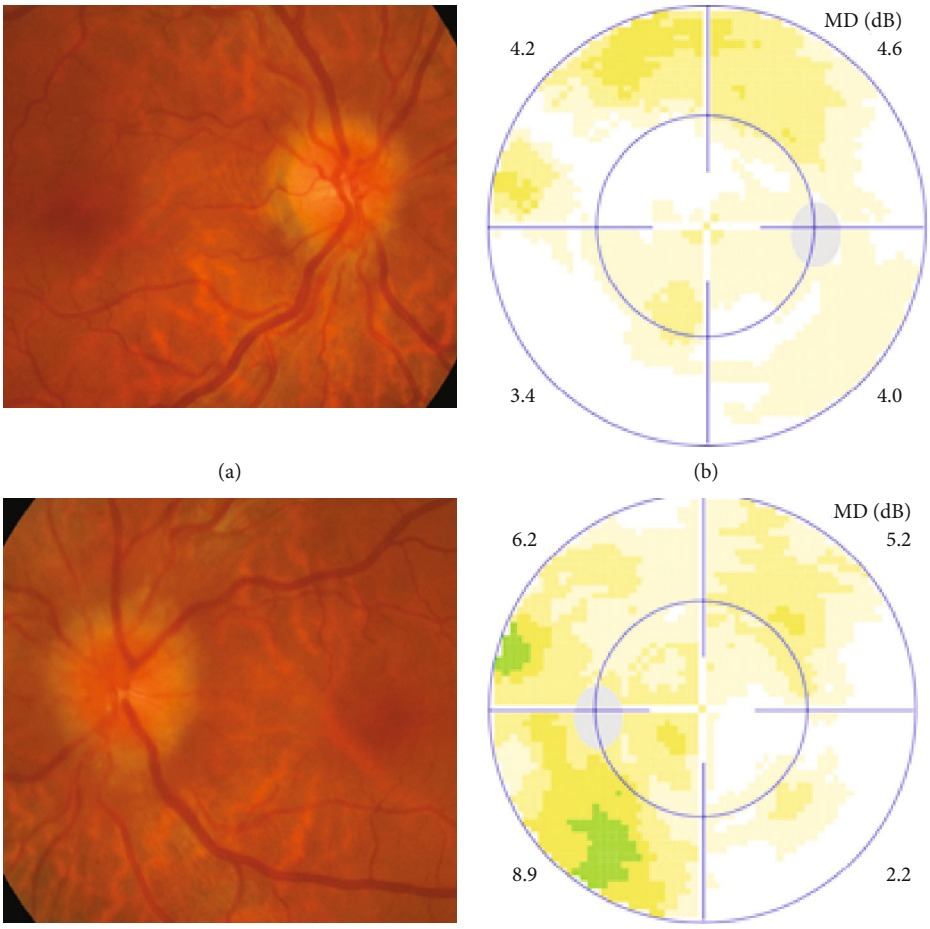

(a) (b)

(c) (d)

Figure 4: Ophthalmic examination of meningeal carcinomatosis-associated optic neuropathy with gastric cancer in Case10. Fundus photographs showed swollen optic disc (A, C), visual field test was normal (B, D) in both eyes.

are usually normal. Patients with MCON (Case 10 to Case 13) all appeared as swollen optic disc (Figures 4, 5), whereas diplopia due to lateral rectus palsy and enlarged superior ophthalmic vein in B type ultrasound were found in Case 11, and Case 12, respectively. Malignant cell-related cavernous sinus syndrome was found in

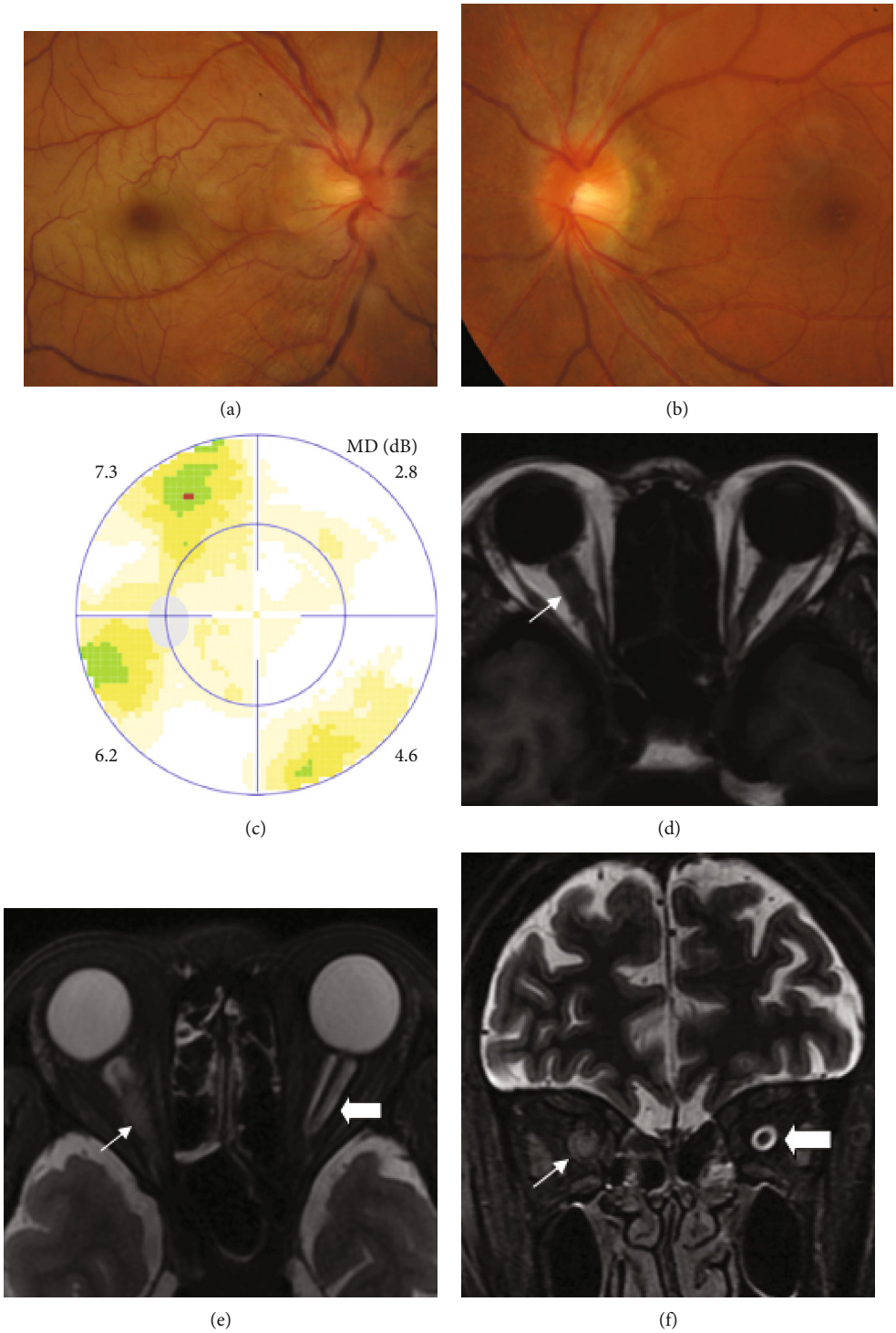

Figure 5: Continued.

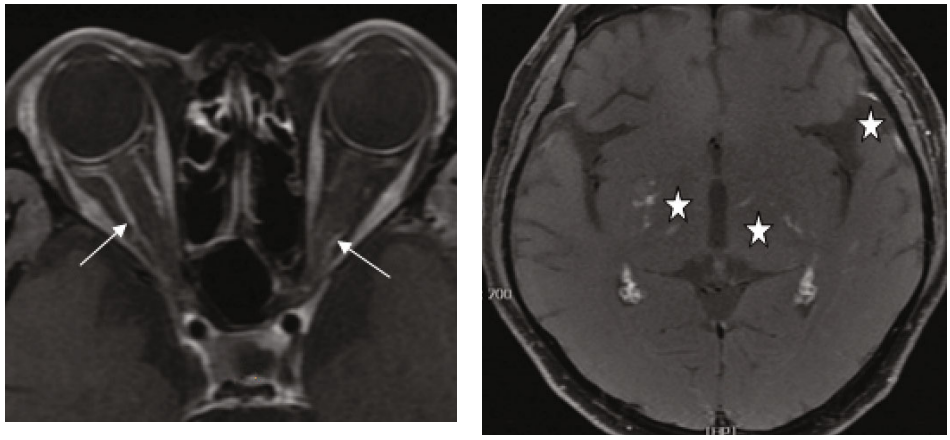

(g) (h)

Figure 5: Ophthalmic and MRI examination of infiltrative optic neuropathy (right eye) and meningeal carcinomatosis-associated optic neuropathy (left eye) with leukemia in Case 13. Fundus photographs showed moderate swollen optic disc and posterior retinal edema with macular cherry red in the right eye (A), and mild swollen optic disc in the left eye (B). Visual field test was normal in the left eye (C). MRI showed enlarged optic nerve (short arrow, D, E, F) with sheath enhancement (long arrow, G) in the right eye, enlarged optic nerve sheath space (arrowhead, E, F) with sheath enhancement (long arrow, G) in the left eye. Focal linear enhancement of the meninge, and spotty and linear lesions with enhancement in basal ganglia (star, H) which supporting meningeal carcinomatosis found in T1-weighted MRI with contrast enhancement.

two cases (Case 11, 12). MRI revealed normal, enlarged optic nerve sheath space and sheath enhancement with or without enlarged cavernous sinus in 2, 3, 1 eye, respectively (Figure 5). However, focal linear enhancement of the meninge which indicating meningeal carcinomatosis was found in T1-weighted MRI with contrast enhancement in all MCON cases (Figure 5).

ION usually presented as subacute progressive visual loss starting from peripheral visual defect, but acute visual loss could also occur when central retinal artery occlusion secondary to ION developed. Patients with ION (Case 13and Case 14) both manifested swollen optic disc, and diffuse posterior retinal edema and cherry-red macular when central retinal artery occlusion occurred. Optic nerve enlargement with sheath enhancement were typical MRI finding of ION (Figure 5).

3.2. Serum and CSF Tests of ON Patients with Malignant Tumors. Malignant cells consistent to their primary tumors were found under microscope in CSF samples from MCON and ION patients, although negative results might appear in the first CSF testing. Whereas there was no malignant cells found in CSF samples from PON cases.

All 14 ON patients with malignant tumors included in this study showed negative results in serum tests for pathogens and autoantibodies including antinuclear antibodies, anticardiolipin antibodies, antineutrophil cytoplasmic antibodies, AQP4-Ab and MOG-Ab. Serum paraneoplastic antibodies were tested in PON patients, anti- CV2, anti-Yo, and anti- amphiphysin were detected positive in 2, 1, and 1 case, respectively, in definite PON group, whereas no serum paraneoplastic antibodies detected in possible PON group.

Two unknown serum antineuronal antibodies (an anti-Purkinje cell antibody in Case 1, and an anti-granular cell antibody in Case 8) were detected by monkey cerebellar tissue-based assay in 2 of 5 PON patients with negative paraneoplastic antibody test results (Figure 1).

4. Discussion

Ophthalmic involvement including PON and cancer associated retinopathy is common in PNS, even presenting as the initial clinical manifestation of PNS in some cases with malignant tumors [1–4, 7–8]. However, many other optic neuropathies should be excluded before PON was diagnosed in malignant tumor patients with optic nerve involved, which including ischemic anterior ON, papilloedema due to intracranial metastasis, MCON, ION, compressive ON, toxic or malnutritional ON, and demyelinating optic neuritis [1–4, 6–8]. Therefore, early diagnosis of PON is challenging in clinical practice.

Anterior ischemic ON was characterized by mild to moderate visual loss, swollen optic disc spontaneously resolving in 6 to 8 weeks, persistent quadrant or altitudinal hemiscotosis in visual field test, and normal MRI, which could easily differentiated from PON. Toxic or malnutritional ON occurred only after chemotherapy, which could be relieved when chemotherapy stopped.

Papilloedema and compressive ON caused by intracranial or orbital metastasis of malignant tumors could be diagnosed based on one or mass found in MRI. However, early-staged MCON might present as mere swollen disc with no visual defect and normal MRI, at this instance, CSF test for malignant cells was crucial for its diagnosis. Unfortunately, several tests were needed in some cases to find malignant cells in CSF samples.

It was challenging to differentiate PON from ION and demyelinating optic neuritis, because they shared many similar ophthalmic manifestations including acute or

subacute visual loss, central or peripheral visual field defect, and optic nerve enlargement with enhancement in MRI [1–6]. CSF test for malignant cells was crucial to exclude ION, and serum autoantibody tests for AQP4-Ab and MOG-Ab were important to exclude AQP4-Ab positive optic neuritis and MOG-Ab related optic neuritis, which was further supported by our results in this study [1–9].

Currently, there still lacks of generally acknowledged criteria for PON diagnosis. The PNS Euronetwork defined six antibodies (anti-Hu, Yo, CV2/CRMP-5, Ri, Ma2 and amphiphysin) as "well characterized onconeural antibodies", and five antibodies (anti-Tr, ANNA3, PCA2, Zic4, and mGluR1) as "partially characterised onconeural antibodies", which could confirm or support the diagnosis of PNS [1–3, 10–16]. However, the seropositivity of paraneoplastic antibodies in PON patients is still under evaluation due to lack of enough volume of PON patients [1–4, 8, 10–16]. In our study, serum paraneoplastic antibodies were detected in only 44.4% (4/9) PON patients. The explanation may exist as follows: (1) presently, there is no generally acknowledged technique standards used in serum paraneoplastic antibody testing, seropositivity of paraneoplastic antibodies may differ between agencies supplying commercial testing; (2) maybe there exist other paraneoplastic antibodies responsible for PON still not recognized in laboratory or clinical practice, or tested in paraneoplastic antibody assay kits currently commercially available [17]. Therefore, critical analysis of the causation between the malignant tumor and ON is still of great importance in the diagnosis of PON.

In this study, two unknown serum antineuronal antibodies (an anti-Purkinje cell antibody and an anti-granular cell antibody) were detected by monkey cerebellar tissue-based assay in 2 of 5 PON patients with negative paraneoplastic antibody test results, indicating tissue-based assay may help to detect current or new biomarkers for ON etiology and diagnosis.

There are some limitations in our study. Firstly, the sample size is small, which is common in PNS studies, since PON and PNS are rare in clinical practice. Secondly, the structural characteristics and physiochemical features of two serum anti- neuron antibodies detected by tissue-based assay in PON patients with negative paraneoplastic antibodies test results are still unknown, more workup needs to be done for further understanding the value of these new biomarkers in etiology and diagnosis of optic neuropathies.

Data Availability

The data used to support the findings of this study are included within the article.

Conflicts of Interest

The authors declare that they have no competing interests.

Acknowledgments

This study was supported in part by Ophthalmology Star Program (QMX2019-01-001). The funding organization does not have any role in the design or conduct of this study.

References

[1] F. Graus, J. Y. Delattre, J. C. Antoine et al., "Recommended diagnostic criteria for paraneoplastic neurological syndromes," *Journal of Neurology, Neurosurgery, and Psychiatry*, vol. 75, no. 8, pp. 1135–1140, 2004.

[2] J. C. Antoine and J. P. Camdessanché, "Paraneoplastic neuropathies," *Current Opinion in Neurology*, vol. 30, no. 5, pp. 513–520, 2017.

[3] Q. Xu, W. Du, H. Zhou et al., "Distinct clinical characteristics of paraneoplastic optic neuropathy," *The British Journal of Ophthalmology*, vol. 103, no. 6, pp. 797–801, 2019.

[4] L. Gordon and M. Dinkin, "Paraneoplastic syndromes in neuro-ophthalmology," *Continuum (Minneap Minn).*, vol. 25, no. 5, pp. 1401–1421, 2019.

[5] J. L. Bennett, "Optic neuritis," *Continuum (Minneap Minn).*, vol. 25, no. 5, pp. 1236–1264, 2019.

[6] Y. Wang, J. Fu, H. Song, Q. Xu, H. Zhou, and S. Wei, "Differences of the involved sites of different types of demyelinating optic neuritis in traditional MRI examination: a systemic review and meta-analysis," *Advances in Ophthalmology Practice and Research.*, vol. 1, article 100019, 2021.

[7] D. A. Cohen, R. Gise, and E. D. Gaier, "Serum biomarkers in neuro-ophthalmology: when to test," *Seminars in Ophthalmology*, vol. 36, no. 4, pp. 322–328, 2021.

[8] E. Rahimy and D. Sarraf, "Paraneoplastic and non-paraneoplastic retinopathy and optic neuropathy: evaluation and management," *Survey of Ophthalmology*, vol. 58, no. 5, pp. 430–458, 2013.

[9] R. Bernard-Valnet, A. Cobo-Calvo, A. Siegfried et al., "Paraneoplastic neuromyelitis optica and ovarian teratoma: a case series," *Multiple Sclerosis and Related Disorders*, vol. 31, pp. 97–100, 2019.

[10] C. Lee, S. Y. Oh, K. A. Park, G. I. Lee, and S. Y. Oh, "A case of paraneoplastic optic neuropathy in pancreatic adenocarcinoma," *Neurological Sciences*, vol. 42, no. 5, pp. 2123–2127, 2021.

[11] J. Y. Yap, W.-H. W. HItam, S. A. Halim, and N. A. Masnon, "Paraneoplastic optic neuropathy secondary to adenocarcinoma of the lung," *BML Case Reports*, vol. 14, no. 5, article e242082, 2021.

[12] M. Nakajima, A. Uchibori, Y. Ogawa et al., "CV2/CRMP5-antibody-related paraneoplastic optic neuropathy associated with small-cell lung cancer," *Internal Medicine*, vol. 57, no. 11, pp. 1645–1649, 2018.

[13] S. Y. Shukla, J. H. Pula, S. Khan, and J. M. Lee, "Paraneoplastic optic neuropathy and pineal Germinoma with Collapsin response-mediating protein antibodies," *Journal of Neuro-Ophthalmology*, vol. 38, no. 2, pp. 198-199, 2018.

[14] J. A. Micieli and E. A. Margolin, "Paraneoplastic optic neuropathy associated with Purkinje cell Antibody-2 in a patient with small cell lung cancer," *Journal of Neuro-Ophthalmology*, vol. 37, no. 1, pp. 53–55, 2017.

[15] S. D. Schoenberger, S. J. Kim, and P. Lavin, "Paraneoplastic optic neuropathy from cutaneous melanoma detected by

positron emission tomographic and computed tomographic scanning," *Archives of Ophthalmology*, vol. 130, no. 9, pp. 1223–1225, 2012.

[16] G. Carboni, G. Forma, A. D. Bond, G. Adamus, and A. Iannaccone, "Bilateral paraneoplastic optic neuropathy and unilateral retinal compromise in association with prostate cancer: a differential diagnostic challenge in a patient with unexplained visual loss," *Documenta Ophthalmologica*, vol. 125, no. 1, pp. 63–70, 2012.

[17] A. Gadoth, Y. Segal, Y. Paran, O. Aizenstein, and Y. Alcalay, "The importance of tissue-based assay in the diagnosis of autoimmune encephalitis," *Journal of Neurology*, 2022.

Hindawi
Disease Markers
Volume 2022, Article ID 6055347, 8 pages
https://doi.org/10.1155/2022/6055347

Research Article

Polyphenol Extracts from Grape Seeds and Apple Can Reactivate Latent HIV-1 Transcription through Promoting P-TEFb Release from 7SK snRNP

Cong Wang,[1,2] Huiru Wang,[3] Zhenrui Pan,[1] Jun Wu,[1] Yafei Guo,[1] Jing Zhang,[1] Zixun Xiang,[1] Wei Lu,[4] and Yuhua Xue[1]

[1]*School of Pharmaceutical Sciences and Fujian Provincial Key Laboratory of Innovative Drug Target Research, Xiamen University, Xiamen, Fujian 361005, China*
[2]*Medical Center of Hematology, The Second Affiliated Hospital, Army Medical University, Chongqing, China*
[3]*Department of Pharmacology, Baotou Medical College, Baotou, Inner Mongolia 014040, China*
[4]*Rehabilitation Hospital of Huishan, Wuxi, Jiangsu 214181, China*

Correspondence should be addressed to Wei Lu; luweikaoshi@sina.com and Yuhua Xue; xueyuhua@xmu.edu.cn

Received 19 November 2021; Accepted 6 January 2022; Published 7 February 2022

Academic Editor: Wen-Qing Shi

The principal barrier for the eradication of HIV/AIDS is the virus latency. One of the effective strategies so called "shock and kill" is to use latency-reversing agents (LRAs) to activate the latent HIV reservoirs and then combine them with the highly active antiretroviral therapy (HAART) to eradicate the virus. However, most of the current LRAs are too toxic; therefore, they have not been used clinically. Our preliminary data indicated that polyphenols from grape seeds can activate HIV in latently infected Jurkat T cells. Owing to a lot of food containing polyphenols and based on a reasoning whether all of these kinds of polyphenols contain the latency-reversing function, in this study, we screened 22 fruits/vegetables to see whether polyphenols from these can reactivate latent HIV-1 transcription. We finally proved that the polyphenols from grape seeds, apple, pomegranate, and bilberry can reactivate latent HIV-1 transcription. The activation of which can be detected on the level of protein and mRNA. The activation of which is in a dose- and time-dependent manner, while the activated polyphenol extracts have the effects to stimulate Tat-independent HIV-1 transcription. The mechanism shows that polyphenol extracts from grape seeds and apple can stimulate P-TEFb's release from 7SK snRNP to induce HIV gene transcription. These results indicate that using a few food of high-content polyphenols as latent activators and combining HARRT may be of great use for the treatment of HIV/AIDS in the future.

1. Introduction

HIV which was first isolated in 1983 will attack T cells, disable the immune system, and eventually lead to HIV/AIDs [1–3]. The emergence of HIV has been a threat to public health, and it is a big challenge for human to eliminate virus because of HIV pathogenesis [4]. An important breakthrough in the area of HIV treatment is the highly active antiretroviral therapy (HAART) which has been used to reduce the levels of plasma HIV RNA below the limits of detection.

However, the treatments must be maintained for life, which can lead to serious chronic consequences and extraordinary financial constraint on the overburdened health care system [5–7]. Moreover, the interruption of HAART inevitably causes a rapid rebound of viremia [8]. This is because various cellular reservoirs, with memory CD4+ T cells being the most well-defined one, harbor integrated and transcriptionally silent proviruses, which remain replication-competent despite extended HAART [9–11]. Clearly, the HAART-mediated viral suppression alone cannot eradicate HIV, and novel approaches must be designed to eliminate the latent reservoirs.

For making up for the shortfall, several new methods urgently need to be designed to address HIV infection [12–14]. One of the potential therapeutic approaches which

was called "shock and kill" showed up. The "shock" phase is aimed at reactivating the latent viral reservoirs in chronically infected individuals. Next, in the "kill" phase, the highly active antiretroviral therapy (HAART), immune system, and viral cytopathogenicity are used for destroying the infection [7, 15–17]. If the "shock and kill" strategy can be applied successfully, a critical step is to screen potential compounds to reactivate latent HIV expression [18]. Up to now, some reported latency-reversing agents such as JQ1 [19], prostratin [20], AV6 [21], PKC activators [22], and positive transcription elongation factor (P-TEFb) inducers [23] play a role in different ways. However, not only do these agents have strong toxicity and side effects but also a majority of them cannot be administered effectively for the human body [16]. Hence, we need to focus on some novel and safe latency activators to attend the process of HIV/AIDS eradication.

It is well known that a major rate-limiting step controlling HIV viral gene expression is promoter proximal pausing of initiated RNA polymerase II (Pol II) on integrated HIV proviral DNA in the elongation phase [19, 24–26]. To overcome this restriction, the HIV-encoded specific Tat protein recruits the human Super Elongation Complex (SEC) to paused Pol II through forming a multicomponent complex that also contains P-TEFb, ELL2, the TAR RNA, and a stem-loop structure located at the $5'$ end of all nascent HIV transcripts [25, 27]. Once recruited to the viral promoter by Tat and TAR, P-TEFb and ELL2 synergistically activate Pol II elongation to produce full-length HIV transcripts by different mechanisms. Active P-TEFb can phosphorylate Ser2 of Pol II CTD and two negative elongation factors NELF and DSIF to stimulate transcription elongation. And ELL2 can directly stimulate the processivity of Pol II through suppressing its transient pausing. Therefore, depending on Tat to deliver P-TEFb to the paused Pol II is an essential part for HIV gene transcription [25, 28, 29].

With the development of pharmaceutical industry, dietary therapy [30, 31] as a novel method attracts the general public's attention. Nowadays, dietary therapy not only has been used in the treatment of the disease but also gives rise to the application of some health care products because this method has provided great benefits for human health [32–34]. Previously, our laboratory proved that procyanidin C-13,$3'$,$3''$-tri-O-gallate (named as REJ-C1G3) from *Polygonum cuspidatum* Sieb. et Zucc which belongs to polyphenols can activate HIV transcription in latently infected Jurkat T cells [26]. And in recent years, great attention is focused on the research of polyphenols including epigallocatechin-3-gallate, quercetin, resveratrol, and myricetin in the academic field, regarding their different functions such as anticancer and antioxidant [35]. Outcomes of some researches have indicated that often taking in polyphenol-rich food like fruits has a powerful role in strengthening the human body's ability to prevent disease [36, 37]. According to the above contents and based on a reasoning whether all of these kinds of polyphenols contain the latency-reversing function, this present article points out that the polyphenols from grape seeds [35, 36, 38] possess the activation which can be proven on the level of protein and mRNA though treating different cell lines. What is more, we proved that other such similar polyphenol-rich foods, like apple polyphenols [39, 40], pomegranate polyphenols [41], and bilberry polyphenols [42, 43], show a consistent result compared with polyphenols from grape seeds. All the results indicate that in combination with a few food of high-content polyphenols as latent activators and HARRT, it may be a promising strategy formed by dietary therapy and chemotherapeutics in curing HIV/AIDS and of great use for public health in the future.

2. Materials and Methods

2.1. Extract Materials. Polyphenol extracts from grape seeds, pomegranate, bilberry (GNC, USA), and apple polyphenols (Yuanye Biology Company, Shanghai, China) and the other polyphenolic extracts (Changyue Biology Company, Xi'an, China) were purchased from commercial resources. These polyphenol-rich extracts were dissolved with DMSO in the process of experiments.

2.2. Antibodies. The anti-GFP (RLM3124; Ruiying Biological) and anti-α-tubulin (T6074; Sigma-Aldrich) were used in the western blotting.

2.3. Flow Cytometry for Activity Screening. J-Lat A2 cells [44] were treated with polyphenol extracts from grape seeds, apple, pomegranate, bilberry, and other foods at the indicated concentrations and times in the figure or figure legends. After the treatment, cells were harvested at 2000 rpm for 5 min, washed in cold phosphate-buffered saline (PBS) and centrifuged at the same centrifugal condition, and resuspended and filtered in PBS. The outcomes were determined by flow cytometry (FACS) (Beckman Coulter, Miami, FL, USA). 2D10 cells [45] were treated and analyzed like J-Lat A2 cells.

2.4. Quantitative PCR. The reactions were treated with the Applied Biosystems Real-Time PCR System and CWBIO Ultra SYBR Mixture RT-PCR reagents according to the manufacturers' instructions. The sequences of the primers used in PCR are as follows: EGFP-F: CAGTGCTTCAG CCGCTACCC; EGFP-R: AGTTCACCTTGATGCCGTT CTT; GAPDH-F: GCACCACCAACTGCTTAGC; and GAPDH-R: GGCATGGACTGTGGTCATG. PCR conditions included an initial denaturing step at 95°C for 10 min and then 40 cycles of amplification. Each cycle consisted of 15 sec at 95°C and 1 min at 62°C. The values were normalized to those of GAPDH to obtain the relative folds of induction [26].

2.5. Luciferase Assay. For the luciferase assay, the HeLa-based NH1 cells [19, 26] containing an integrated HIV-1 LTR-luciferase reporter construct but expressing no Tat, as well as its derivative NH2 cells [26], which also harbor an integrated Tat-HA expression vector, were used. Cells were then treated with different concentrations of extracts for 24 h and subjected to the luciferase assay using kit E1501 from Promega and following the manufacturer's instructions. Lysates were prepared from an approximately equal number of cells and normalized based on their contained α-tubulin levels among all the samples.

2.6. Cell Viability. Measurement of cell viability was performed with the Promega CellTiter-Glo kit according to the manufacturer's instructions. Cells were seeded at 5000 cells/well in a 96-well plate (3 wells/sample) and then treated or untreated. The measurements were taken to track cell proliferation during the course of the treatment.

3. Results

3.1. Polyphenol Extracts from Grape Seeds, Apple, Pomegranate, and Bilberry Facilitate Latent HIV Transcription. To screen agents which make latent HIV reactivation, the J-Lat A2 cell line generated by the Verdin Laboratory has been used [44]. This cell line was created by transducing an HIV vector expressing Tat-Flag and the enhanced green fluorescent protein (GFP) HIV vector under the control of the viral 5′-LTR and an internal ribosome entry site (IRES) placed in between Tat and GFP (LTR-Tat-Flag-IRES-EGFP) in human Jurkat T cells [19, 44]. In the context of activation, transcription will be performed, followed by testing GFP though flow cytometry, and we can detect whether they contain the activity. J-Lat A2 cells were incubated individually with these agents for 24 h as shown in Table 1. On the basis of results obtained by FACS, polyphenol extracts from grape seeds, pomegranate, bilberry, and apple were found to cause HIV LTR-driven GFP production in these experiments.

According to Table 1, it is important that the same consequence of these products was detected in the 2D10 cell line [19, 45], another Jurkat-based postintegrative latency cell model, which consisted of almost all the HIV genome encoding a partially attenuated Tat variant H13L and the short-lived d2EGFP protein in place of the nef gene.

To evaluate the antiproliferative activity of these compounds against J-LatA2 cells, we took cell viability assays to measure the activity. The result indicated that these compounds showed the antiproliferative activity against J-Lat A2 cells and HeLa cells treated with 200 μM as indicated in Figure 1. Since these compounds' treatment exceeded 200 μM in all the experiments performed in the current study, we concluded that the effect of these compounds on proviral activation is not due to any significant change to cell growth and viability that may result from long-term exposure to these compounds.

3.2. Polyphenol Extracts from Grape Seeds, Apple, Pomegranate, and Bilberry Facilitate Latent HIV Transcription Indicated by HIV-1 LTR-Driven EGFP Expression Levels in a Dose- and Time-Dependent Manner. To test the activities of polyphenol extracts from grape seeds, apple, pomegranate, and bilberry, we treated J-Lat A2 cells with increasing concentrations of these compounds and also for different time periods. The percentage of EGFP-positive cells increased in a dose- and time-dependent manner (Figure 2(a)). Importantly, the same stimulatory effect of these compounds was also found in the Jurkat-based postintegrative latency model 2D10 (Figure 2(b)), which is another well-characterized latency model harboring almost the complete HIV genome with only the nef gene replaced by that encoding EGFP.

Table 1: Polyphenol extracts from grape seeds, apple, pomegranate, and bilberry facilitate latent HIV transcription.

Agents (200 μM)	GFP-positive cells (%) (J-Lat A2 cells)	GFP-positive cells (%) (2D10 cells)
DMSO	0.6	7.5
Litchi extract	1.2	8.4
Garlic extract	1.0	9.6
Chinese yam extract	1.3	7.5
Grape seed polyphenolic extract	29.6	56.4
Mulberry extract	1.3	6.5
Cinnamon extract	1.4	8.1
Bitter gourd extract	1.6	7.7
Hawthorn extract	1.5	6.3
Apple polyphenolic extract	24.8	60.7
Broccoli extract	1.4	8.9
Pomegranate polyphenolic extract	10.2	30.1
Chrysanthemum extract	1.6	7.0
Chinese date extract	1.6	10.6
Emblic leafflower fruit extract	1.6	11.2
Wolfberry extract	1.8	8.1
Mushroom extract	1.7	8.1
Mint extract	1.7	7.5
Walnut extract	1.6	7.8
Papaya extract	2.0	8.0
Kelp extract	1.8	9.5
Ginger extract	1.6	28.2
Bilberry polyphenolic extract	12.5	15.8
Prostratin-2.5 μM	58.7	93.7

To make sure whether the results measured by FACS were on account of the GFP expression, quantitative RT-PCR with primers that hybridize to a distal portion of the GFP gene and western blotting with anti-GFP were performed in J-Lat A2 and 2D10 cells, as indicated in Figures 2(c) and 2(d)). Utilizing these two experimental methods could attain the consistent points that these four compounds reverse latent HIV provirus at the protein and mRNA levels.

3.3. Polyphenol Extracts from Grape Seeds, Apple, Pomegranate, and Bilberry Predominantly Have the Effects Which Stimulate Tat-Independent HIV-1 Transcription. To confirm that these four agents' stimulation of the production of GFP mRNA and protein in latently infected Jurkat cells merely relied on the activation of the HIV 5′-LTR, but not any other unrelated viral or nonviral sequences in the integrated HIV elements, we inspected the function of these four agents that were treated in the NH1 cell line including an

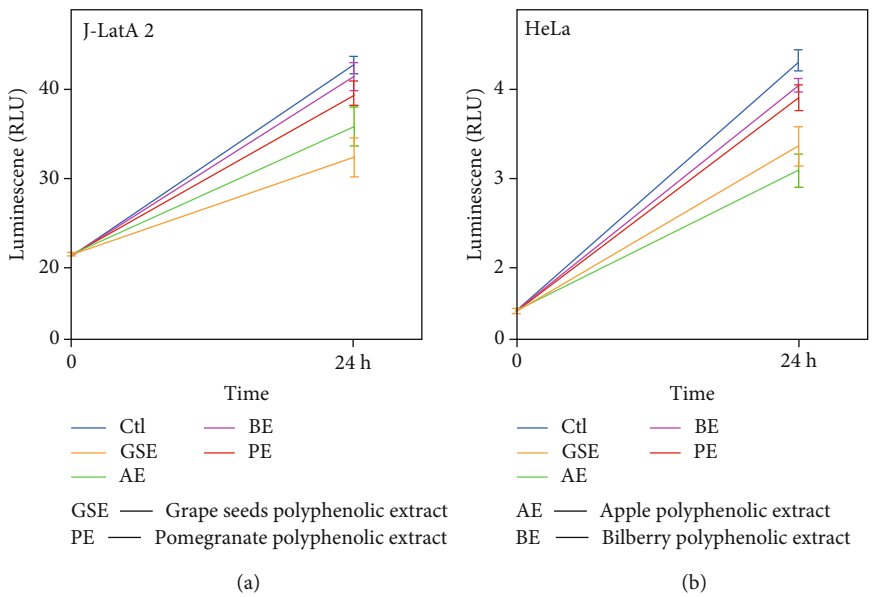

Figure 1: Polyphenol extracts from grape seeds, apple, pomegranate, and bilberry impact on cell viability. J-Lat A2 (a) and HeLa cells (b) were exposed to these agents (200 μM) for 24 hours and then assayed for cell viability. The error bars represent mean ± SD from three independent experiments.

integrated luciferase reporter gene that is driven solely by the HIV 5′-LTR [19, 26]. The results in Figure 3(a) show that polyphenol extracts from grape seeds, apple, pomegranate, and bilberry (200 μM for 24 h) increased the LTR-driven luciferase expression in NH1 cells (2.4-, 2.7-, 1.9-, and 1.5-fold). Besides, in the NH2 cell line, another HeLa-based cells expressing the HIV-1 Tat protein were stably transfected into these cells; four agents were found to activate the HIV LTR more potently in this isogenic cell line (4.0-, 3.9-, 1.5-, and 1.6-fold; Figure 3(b)). Together, these data prove that these four agents worked through the HIV-1 5′-LTR and had synergetic effects with Tat in HIV-1 transcription.

3.4. Polyphenol Extracts from Grape Seeds and Apple Promote the Release of P-TEFb from 7SK snRNP. P-TEFb plays a key role in HIV-1 transcription, and its sequestration in the inactive 7SK snRNP has been proposed to contribute to viral latency. To confirm whether polyphenol extracts may affect the level of P-TEFb present in 7SK snRNP, we chose polyphenol extracts from grape seeds and apple and performed anti-CDK9 immunoprecipitation in HeLa cells that were treated with polyphenol extracts from grape seeds and apple. Then, we examined the association of CDK9 with two signature 7SK snRNP components HEXIM1 and LARP7 in the immunoprecipitates through western blotting. As shown in Figure 4, reduced amounts of HEXIM1 and LARP7 were found to bind to CDK9 upon the treatment with polyphenol extracts from grape seeds and apple. These results indicated that the treatment caused the disassociation of P-TEFb from the 7SK snRNP.

4. Discussion

Up to now, HIV/AIDS is still difficult to overcome for human health. Although HARRT has been regarded as the most effective way to treat HIV infection and extend the patients' lives, it was unable to eliminate the latent HIV reservoirs and the high cost of HARRT cannot but make us face a reality. Under the circumstances, a novel strategy, called "shock and kill" which combined effective latency-reversing agents without significantly impacting the host cell growth and function with HARRT, was proposed to cure infected patients of HIV/AIDS [8, 15–17]. Unfortunately, the currently available latency activators have all shown high toxicity and/or poor clinical outcomes [46].

Nowadays, dietary therapy has been used not only in the treatment of the disease but also in the application of some health care products which has provided great benefits for human health. If dietary therapy and chemotherapy are together used in the treatment of HIV infection, it is perhaps an effective way. To achieve this goal, we found that polyphenol extracts from grape seeds, apple, pomegranate, and bilberry have been identified and shown to facilitate latent HIV transcription and predominantly have synergetic effects with Tat protein. In addition to four extracts, the other similar polyphenol-rich agents as indicated in Table 1 have a light increase in the LTR-driven GFP expression in J-Lat A2 cells. However, ginger extraction put up a strong activity, and others have little effect on 2D10 cells.

It is unknown what kind of mechanism these polyphenol extracts work, and combining them with chemotherapeutics to be utilized in a clinical setting is still poorly investigated. The efficiency of extracts which are in combination with HARRT is subjected to evaluation in the treatment of HIV/AIDS because food can also affect the drugs' absorption and the polyphenolic content of these extracts is not very high, so that it also forms a facing problem. Although not all the polyphenolic extraction contains an activity that reverses HIV latency and they may not necessarily be the eventual drug used clinically for waking up latent proviruses

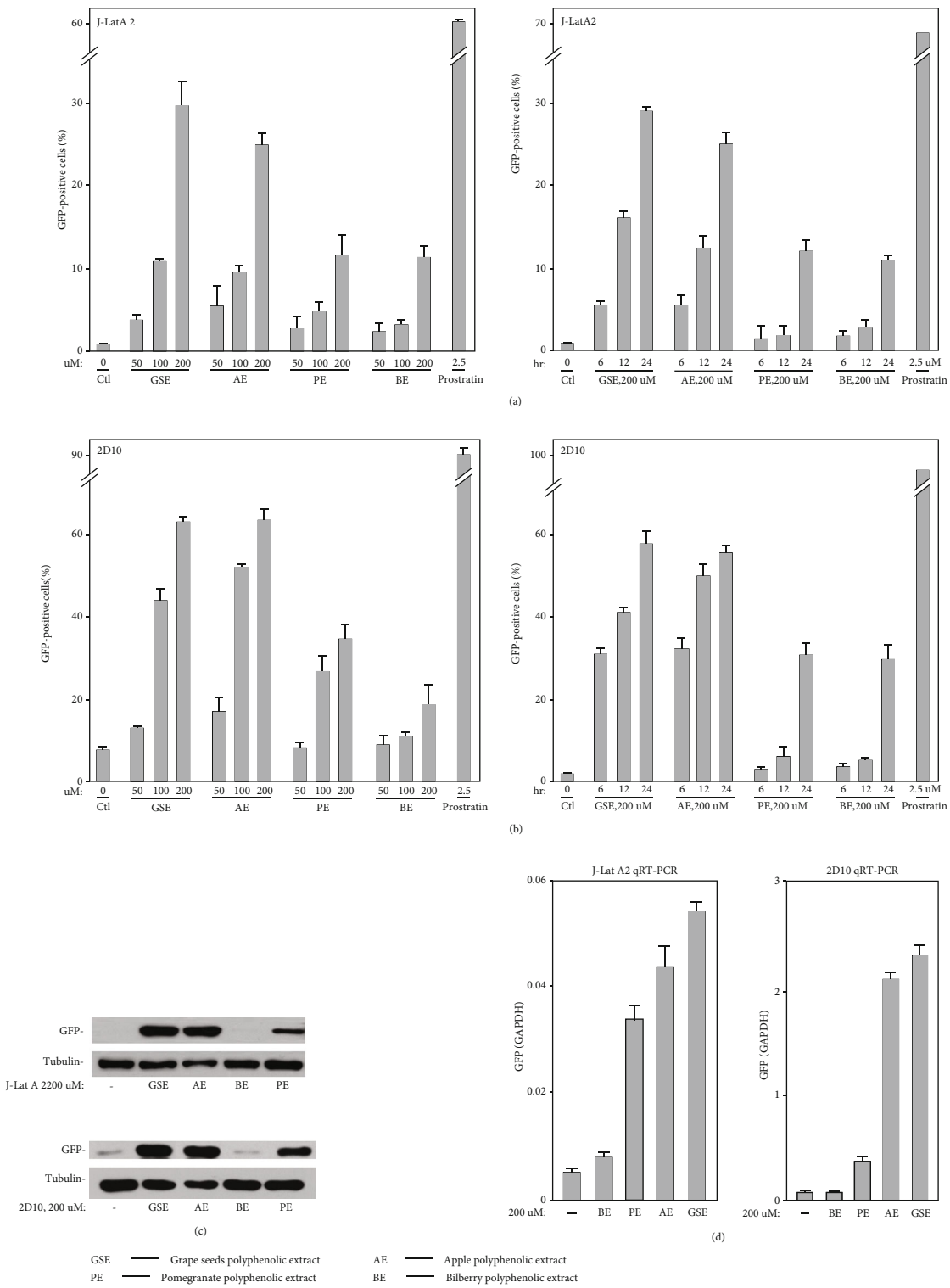

Figure 2: Polyphenol extracts from grape seeds, apple, pomegranate, and bilberry facilitate latent HIV transcription indicated by HIV-1 LTR-driven GFP expression levels in a dose- and time-dependent manner. (a, b) J-Lat A2 cells/2D10 cells were treated with 50 μM, 100 μM, and 200 μM and for increasing time periods (6, 12, and 24 h) as indicated. Polyphenol extracts from grape seeds, apple, pomegranate, and bilberry and 2.5 μM prostratin as a positive control for 24 h. The GFP-positive cells were detected by flow cytometry (FACS), and the percentages of GFP-expressing cells in the entire population were indicated. (c) WCE (whole cell extracts) of J-Lat A2 cells/2D10 cells incubated with 200 μM of polyphenol extracts from grape seeds, apple, pomegranate, and bilberry for 24 h were analyzed by western blotting to test the content of GFP protein. (d) J-Lat A2 cells/2D10 cells were treated with the same indicated concentrations and for indicated time periods. The ratios of the GFP/GAPDH mRNA levels in treated J-Lat A2 cells/2D10 cells were determined by quantitative RT-PCR (qRT-PCR). The error bars in all panels represent mean ± SD from three independent experiments.

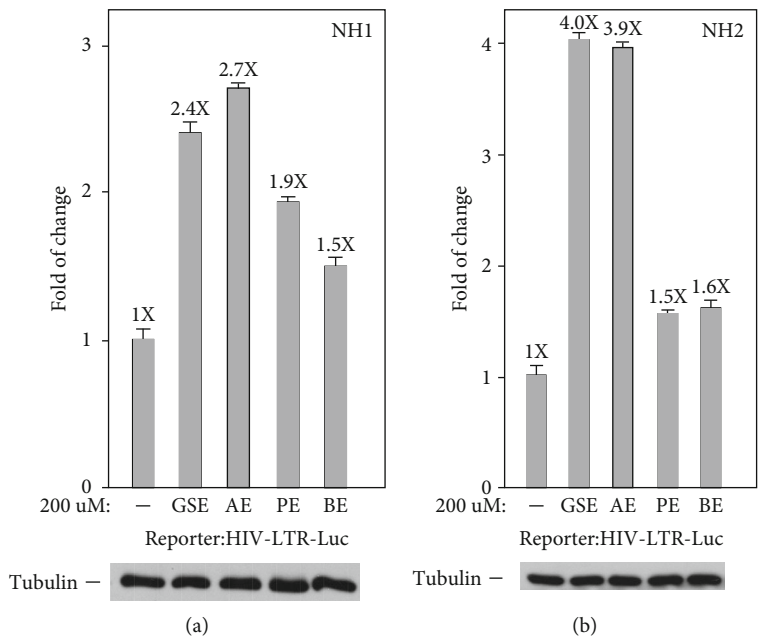

Figure 3: Polyphenol extracts from grape seeds, apple, pomegranate, and bilberry predominantly have the effects which stimulate Tat-independent HIV-1 transcription. The HeLa-based NH1 cells expressing no Tat (a) and NH2 cells stably expressing Tat-HA (b), with both containing an integrated HIV LTR-luciferase construct, were treated with polyphenol extracts from grape seeds, apple, pomegranate, and bilberry for 24 h. Whole cell extracts (WCE) were examined for the contained luciferase activities and cell tubulin protein as a reference by western blotting. The error bars in all panels represent mean ± SD from three independent experiments.

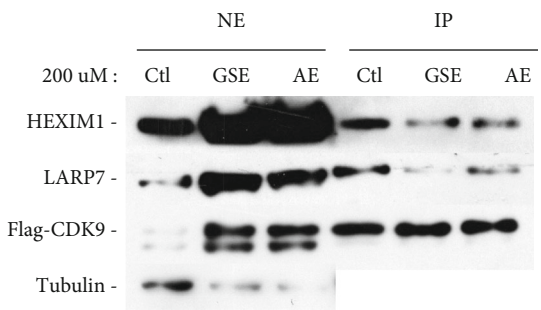

Figure 4: Polyphenol extracts from grape seeds and apple promote the release of P-TEFb from 7SK snRNP. HeLa-based cells that were either untreated (−) or treated (+) with polyphenol extracts from grape seeds and apple (200 μM) were analyzed by western blotting for the indicated proteins. Anti-Flag immunoprecipitates (IP) derived from NE were tested by western blotting for the presence of the indicated proteins.

and curing HIV/AIDS, their identification and characterization in the present study serve as an important proof of concept that dietary therapy may be joined in the combinatorial treatment.

Data Availability

The research data used to support the findings of this study are included within the article.

Conflicts of Interest

The authors declare that they have no competing financial interests.

Authors' Contributions

Y.X. and W.L. conceived the project, analyzed the data, and wrote the paper. Z.P. and C.W. performed the experiments. Z.P., C.W., H.W., J.W., Y.G., J.Z., and Z.X. analyzed the data. All authors reviewed the manuscript. Cong Wang, Huiru Wang, and Zhenrui Pan contributed equally to this work.

Acknowledgments

This work is supported by the National Key R&D Program of China (2020YFA0908100 and 2018YFA0107303) and the National Natural Science Foundation of China (81672955).

References

[1] W. Abbas and G. Herbein, "Molecular understanding of HIV-1 latency," *Advances in Virology*, vol. 2012, Article ID 574967, 14 pages, 2012.

[2] F. Barré-Sinoussi, J. C. Chermann, F. Rey et al., "Isolation of a T-lymphotropic retrovirus from a patient at risk for acquired immune deficiency syndrome (AIDS)," *Science*, vol. 220, no. 4599, pp. 868–871, 1983.

[3] Centers for Disease Control and Prevention (CDC), "Pneumocystis pneumonia–Los Angeles. 1981," *Morbidity & Mortality Weekly Report*, vol. 45, no. 34, pp. 729–733, 1996.

[4] J. Rubaihayo, N. M. Tumwesigye, J. Konde-Lule, H. Wamani, E. Nakku-Joloba, and F. Makumbi, "Frequency and distribution patterns of opportunistic infections associated with HIV/AIDS in Uganda," *BMC Research Notes*, vol. 9, no. 1, p. 501, 2016.

[5] U. Pittl, D. I. Keller, C. A. Kaiser, M. Battegay, M. E. Pfisterer, and A. Linka, ""HAART-attack" in young female HIV-patient," *Internist (Berl)*, vol. 47, no. 9, pp. 939–943, 2006.

[6] T. P. Brennan, J. O. Woods, A. R. Sedaghat, J. D. Siliciano, R. F. Siliciano, and C. O. Wilke, "Analysis of human immunodeficiency virus type 1 viremia and provirus in resting CD4+ T cells reveals a novel source of residual viremia in patients on antiretroviral therapy," *Journal of Virology*, vol. 83, no. 17, pp. 8470–8481, 2009.

[7] K. M. Barton and S. E. Palmer, "How to define the latent reservoir: tools of the trade," *Current HIV/AIDS Reports*, vol. 13, no. 2, pp. 77–84, 2016.

[8] G. Darcis, B. Van Driessche, and C. Van Lint, "HIV latency: should we shock or lock?," *Trends in Immunology*, vol. 38, no. 3, pp. 217–228, 2017.

[9] R. Lorenzo-Redondo, H. R. Fryer, T. Bedford et al., "Persistent HIV-1 replication maintains the tissue reservoir during therapy," *Nature*, vol. 530, no. 7588, pp. 51–56, 2016.

[10] C. Xia, D. Luo, X. Yu, S. Jiang, and S. Liu, "HIV-associated dementia in the era of highly active antiretroviral therapy (HAART)," *Microbes and Infection*, vol. 13, no. 5, pp. 419–425, 2011.

[11] W. Zou, Y. Liu, J. Wang, H. Li, and X. Liao, "Traditional Chinese herbal medicines for treating HIV infections and AIDS," *Evidence-based Complementary and Alternative Medicine*, vol. 2012, Article ID 950757, 8 pages, 2012.

[12] M. H. Kim, S. Ahmed, and E. J. Abrams, "Pediatric HIV: progress on prevention, treatment, and cure," *Current Pediatrics Reports*, vol. 3, no. 3, pp. 219–229, 2015.

[13] C. Katlama, S. G. Deeks, B. Autran et al., "Barriers to a cure for HIV: new ways to target and eradicate HIV-1 reservoirs," *The Lancet*, vol. 381, no. 9883, pp. 2109–2117, 2013.

[14] D. D. Richman, D. M. Margolis, M. Delaney, W. C. Greene, D. Hazuda, and R. J. Pomerantz, "The challenge of finding a cure for HIV infection," *Science*, vol. 323, no. 5919, pp. 1304–1307, 2009.

[15] A. Savarino, A. Mai, S. Norelli et al., ""Shock and kill" effects of class I-selective histone deacetylase inhibitors in combination with the glutathione synthesis inhibitor buthionine sulfoximine in cell line models for HIV-1 quiescence," *Retrovirology*, vol. 6, no. 1, p. 52, 2009.

[16] D. C. Cary, K. Fujinaga, and B. M. Peterlin, "Molecular mechanisms of HIV latency," *The Journal of Clinical Investigation*, vol. 126, no. 2, pp. 448–454, 2016.

[17] S. G. Deeks, "Shock and kill," *Nature*, vol. 487, no. 7408, pp. 439-440, 2012.

[18] E. Gallastegui, B. Marshall, D. Vidal et al., "Combination of biological screening in a cellular model of viral latency and virtual screening identifies novel compounds that reactivate HIV-1," *Journal of Virology*, vol. 86, no. 7, pp. 3795–3808, 2012.

[19] Z. Li, J. Guo, Y. Wu, and Q. Zhou, "The BET bromodomain inhibitor JQ1 activates HIV latency through antagonizing Brd4 inhibition of Tat-transactivation," *Nucleic Acids Research*, vol. 41, no. 1, pp. 277–287, 2013.

[20] S. A. Williams, L. F. Chen, H. Kwon et al., "Prostratin antagonizes HIV latency by activating NF-κB∗," *Journal of Biological Chemistry*, vol. 279, no. 40, pp. 42008–42017, 2004.

[21] S. Micheva-Viteva, Y. Kobayashi, L. C. Edelstein et al., "High-throughput screening uncovers a compound that activates latent HIV-1 and acts cooperatively with a histone deacetylase (HDAC) inhibitor∗," *The Journal of Biological Chemistry*, vol. 286, no. 24, pp. 21083–21091, 2011.

[22] A. L. Remoli, G. Marsili, A. Battistini, and M. Sgarbanti, "The development of immune-modulating compounds to disrupt HIV latency," *Cytokine & Growth Factor Reviews*, vol. 23, no. 4-5, pp. 159–172, 2012.

[23] J. Finley, "Oocyte activation and latent HIV-1 reactivation: AMPK as a common mechanism of action linking the beginnings of life and the potential eradication of HIV-1," *Medical Hypotheses*, vol. 93, pp. 34–47, 2016.

[24] M. Ott, M. Geyer, and Q. Zhou, "The control of HIV transcription: keeping RNA polymerase II on track," *Cell Host & Microbe*, vol. 10, no. 5, pp. 426–435, 2011.

[25] H. Lu, Z. Li, Y. Xue, and Q. Zhou, "Viral-host interactions that control HIV-1 transcriptional elongation," *Chemical Reviews*, vol. 113, no. 11, pp. 8567–8582, 2013.

[26] C. Wang, S. Yang, H. Lu et al., "A natural product from Polygonum cuspidatum Sieb. Et Zucc. promotes Tat-dependent HIV latency reversal through triggering P-TEFb's release from 7SK snRNP," *PLoS One*, vol. 10, no. 11, article e0142739, 2015.

[27] S. Y. Kao, A. F. Calman, P. A. Luciw, and B. M. Peterlin, "Antitermination of transcription within the long terminal repeat of HIV-1 by *tat* gene product," *Nature*, vol. 330, no. 6147, pp. 489–493, 1987.

[28] N. He, M. Liu, J. Hsu et al., "HIV-1 Tat and host AFF4 recruit two transcription elongation factors into a bifunctional complex for coordinated activation of HIV-1 transcription," *Molecular Cell*, vol. 38, no. 3, pp. 428–438, 2010.

[29] U. Schulze-Gahmen, H. Upton, A. Birnberg et al., "The AFF4 scaffold binds human P-TEFb adjacent to HIV Tat," *eLife*, vol. 2, article e00327, 2013.

[30] B. M. Fisaha Haile, "Outcome of ready to use food therapy among patients on HIV/AIDS care in Mekelle Hospital, northern Ethiopia: retrospective cohort study," *Journal of AIDS & Clinical Research*, vol. 5, no. 1, 2014.

[31] The Cochrane Collaboration, S. S. N. Mahlungulu, L. Grobler, M. M. E. Visser, and J. Volmink, "Nutritional interventions for reducing morbidity and mortality in people with HIV," *Cochrane Database of Systematic Reviews*, vol. 2, no. 3, article CD004536, 2007.

[32] B. Doerfler, P. Bryce, I. Hirano, and N. Gonsalves, "Practical approach to implementing dietary therapy in adults with eosinophilic esophagitis: the Chicago experience," *Diseases of the Esophagus*, vol. 28, no. 1, pp. 42–58, 2015.

[33] L. González-González, J. G. Pérez-Cortéz, M. Flores-Aldana, N. Macías-Morales, and C. Hernández-Girón, "Antioxidant use as dietary therapy in patients with multiple sclerosis," *Medwave*, vol. 15, no. 1, pp. e6065–e6065, 2015.

[34] P. Zou, "Traditional Chinese medicine, food therapy, and hypertension control: a narrative review of Chinese literature," *The American Journal of Chinese Medicine*, vol. 44, no. 8, pp. 1579–1594, 2016.

[35] M. Chen and S. Yu, "Lipophilized grape seed proanthocyanidin derivatives as novel antioxidants," *Journal of Agricultural and Food Chemistry*, vol. 65, no. 8, pp. 1598–1605, 2017.

[36] Z. Pons, M. Margalef, F. I. Bravo, A. Arola-Arnal, and B. Muguerza, "Chronic administration of grape-seed polyphenols attenuates the development of hypertension and improves other cardiometabolic risk factors associated with the metabolic syndrome in cafeteria diet-fed rats," *The British Journal of Nutrition*, vol. 117, no. 2, pp. 200–208, 2017.

[37] K. P. Devi, T. Rajavel, M. Daglia, S. F. Nabavi, A. Bishayee, and S. M. Nabavi, "Targeting miRNAs by polyphenols: novel therapeutic strategy for cancer," in *Seminars in cancer biology*, pp. 146–157, Elsevier, 2017.

[38] L. Porcelli, R. M. Iacobazzi, A. E. Quatrale et al., "Grape seed extracts modify the outcome of oxaliplatin in colon cancer cells by interfering with cellular mechanisms of drug cytotoxicity," vol. 8, Article ID 50845, 2017.

[39] K. E. Lee, J. K. Youm, W. J. Lee, S. Kang, and Y. J. Kim, "Polyphenol-rich apple extract inhibits dexamethasone-induced sebaceous lipids production by regulating SREBP1 expression," *Experimental Dermatology*, vol. 26, no. 10, pp. 958–960, 2017.

[40] L. Wang, T. Fumoto, S. Masumoto et al., "Regression of atherosclerosis with apple procyanidins by activating the ATP-binding cassette subfamily A member 1 in a rabbit model," *Atherosclerosis*, vol. 258, pp. 56–64, 2017.

[41] E. Turrini, L. Ferruzzi, and C. Fimognari, "Potential effects of pomegranate polyphenols in cancer prevention and therapy," *Oxidative Medicine & Cellular Longevity*, vol. 2015, article 938475, pp. 1–19, 2015.

[42] G. Aichinger, G. Pahlke, L. J. Nagel, W. Berger, and D. Marko, "Bilberry extract, its major polyphenolic compounds, and the soy isoflavone genistein antagonize the cytostatic drug erlotinib in human epithelial cells," *Food & Function*, vol. 7, no. 8, pp. 3628–3636, 2016.

[43] O. C. Bujor, C. le Bourvellec, I. Volf, V. I. Popa, and C. Dufour, "Seasonal variations of the phenolic constituents in bilberry (*Vaccinium myrtillus* L.) leaves, stems and fruits, and their antioxidant activity," *Food Chemistry*, vol. 213, pp. 58–68, 2016.

[44] A. Jordan, D. Bisgrove, and E. Verdin, "HIV reproducibly establishes a latent infection after acute infection of T cells in vitro," *EMBO Journal*, vol. 22, no. 8, pp. 1868–1877, 2003.

[45] R. Pearson, Y. K. Kim, J. Hokello et al., "Epigenetic silencing of human immunodeficiency virus (HIV) transcription by formation of restrictive chromatin structures at the viral long terminal repeat drives the progressive entry of HIV into latency," *Journal of Virology*, vol. 82, no. 24, pp. 12291–12303, 2008.

[46] X. Contreras, M. Schweneker, C. S. Chen et al., "Suberoylanilide hydroxamic acid reactivates HIV from latently infected cells∗," *The Journal of Biological Chemistry*, vol. 284, no. 11, pp. 6782–6789, 2009.

Hindawi
Disease Markers
Volume 2022, Article ID 8906752, 6 pages
https://doi.org/10.1155/2022/8906752

Research Article

Cytokine Changes in the Aqueous Humor in Rubella-Related Fuchs Heterochromic Iridocyclitis

Yi Mao,[1,2] **Sijie Lin**,[1,2] **Chengfang Zhu**,[1,2] **Xiaodong Liu**,[1,2] **Huping Wu**,[1,2] **and Shangkun Ou**[1,2]

[1]*Eye Institute and Affiliated Xiamen Eye Center of Xiamen University, School of Medicine, Xiamen University, Xiamen, Fujian 361002, China*
[2]*Fujian Key Laboratory of Ocular Surface and Corneal Diseases, Xiamen University, Xiamen 361002, China*

Correspondence should be addressed to Huping Wu; wuhuping123@163.com and Shangkun Ou; shangkun_ou@126.com

Received 27 November 2021; Accepted 27 January 2022; Published 7 February 2022

Academic Editor: Wen-Qing Shi

This retrospective study is aimed at determining the correlation between cytokine levels and virus status in the aqueous humor of 38 patients with Fuchs heterochromic iridocyclitis (FHI) with/without a viral presence between May 2017 and January 2020. The levels of cytokines were analyzed in the groups with and without virus-related FHI. Among the patients, 50% had rubella virus, 5.26% had cytomegalovirus, and 2.63% had herpes simplex virus infections. The expression of interleukin-6 (IL-6) and IL-8 was significantly higher, and that of basic fibroblast growth factor (bFGF) was significantly lower in the virus-positive group than in the virus-negative group ($P = 0.015$, $P = 0.001$, and $P = 0.001$, respectively). Although there was no significant difference in the mean expression of vascular cell adhesion protein 1 (VCAM-1), IL-10, and vascular endothelial growth factor (VEGF), that of VCAM-1 and IL-10 was higher ($M = 1338$ and $M = 1390$, respectively; $M = 6.225$ and 10.600, respectively) and that of VEGF was lower ($M = 134.5$ and $M = 38.70$, respectively) in the virus-positive group than in the virus-negative group. Similar findings were observed for the expressions of IL-6, IL-8, and bFGF in the rubella-positive and rubella-negative groups. Viral presence was highly related to FHI, especially that of the rubella virus. High levels of inflammatory cytokines and low levels of neovascularization-related factors are involved in rubella-related FHI. These study findings could be helpful in the diagnosis and treatment of FHI.

1. Introduction

Fuchs heterochromic iridocyclitis (FHI) is a chronic, usually unilateral, nongranulomatous uveitis of insidious onset. It is characterized by iris depigmentation, accounting for approximately 0.5–7% of all cases with uveitis [1–3]. However, FHI is commonly misdiagnosed because of its easily neglected and diverse manifestations [4]. The typical characteristics of FHI are keratic precipitates (KPs), iris atrophy, nonpersistent inflammatory manifestations, vitreous infiltration, lens opacification, and secondary glaucoma with symptoms such as blurred vision [4]. Medium- or star-shaped KPs could be distributed in the cornea of the triangle area, pupil area, or diffusely posterior in patients with FHI. Ocular examination can also show light anterior chamber flare, a small number of aqueous cells, iris depigmentation, or iris atrophy. FHI patients are prone to have Koeppe nodules, posterior capsule opacification, ocular hypertension, opacity, and cells in the anterior vitreous. In addition, clinical manifestations such as abnormal corneal spots or corneal endothelium, abnormal blood–humor barrier, and nonpersistent inflammation can be found in FHI [5–11].

At present, the complex and varied symptoms of FHI make it difficult to diagnose. Misdiagnosis can result in unnecessary corticosteroid treatment or misinformed expectations about the progress of the condition. Many risk factors for FHI, including inflammation, tumor, trauma, surgery, congenital syndromes, nerve dysfunction, autoimmunity, and infection, have been studied [12]. However, viral pathogens are more regarded as potential causes of FHI; these include the herpes simplex virus (HSV and VZV) [13], cytomegalovirus (CMV) [14, 15], and rubella

[16–18]. The predominant mechanisms involved in viral anterior uveitis are chronic inflammatory processes, [19] which are accompanied by changes in cytokine levels [20] and immunopathology [21].

Rubella virus infection highly correlates with FHI [16–18], with 68% of FHI patients infected with the rubella virus [22]. Rubella virus, a member of the *Riboviriad* family, *Matonaviridae* [23, 24], is the etiologic agent of rubella, which can induce congenital birth defects, miscarriage, and stillbirth via transplacental transmission [24–26]. Rubella occurs worldwide during epidemics [27]. Although the global incidence of rubella has decreased with the development of vaccines, the number of congenital rubella syndrome cases is approximately 100,000 every year [28]. Rubella virus can persistently infect the eye for years [17].

In the eyes of those with Fuchs' uveitis syndrome, significantly higher levels of inflammatory factors (IL-6, IL-8, and IL-10) than those in senile cataract-affected eyes were detected because immune mediators are crucial to specific viral intraocular inflammation [22]. IL-6 and IL-8 have the potential to act as markers of inflammation in the aqueous humor in FHI.

The role of the intraocular presence of rubella during the development of FHI is controversial [18, 29] and the mechanism of rubella infection in FHI is not clear. In this study, we aimed to investigate the viruses involved in FHI, such as CMV, HSV, VZV, and rubella, and determine the correlation between cytokine levels and virus status in the aqueous humor of patients with FHI, especially in the case of rubella.

2. Materials and Methods

2.1. Study Design and Participants. The clinical data of 38 patients with FHI treated at the Xiamen Ophthalmology Hospital affiliated with Xiamen University between May 2017 and January 2020 were retrospectively analyzed. Ethical approval was obtained from the Institutional Review Board of Xiamen Ophthalmology Hospital affiliated with Xiamen University. The study procedures were performed in accordance with the principles of the Declaration of Helsinki. The diagnosis of FHI was based on the Standardization of Uveitis Nomenclature (SUN) classification criteria [30]: (1) heterochromia or unilateral diffuse iris atrophy; (2) characteristic KPs, anterior chamber cells, or anterior chamber inflammation; (3) unilateral uveitis; (4) no evidence of active retinitis; and (5) neither endotheliitis nor nodular, coin-shaped endothelial cell. Informed consent was obtained from patients or their guardians with FHI before collecting aqueous humor samples. A tenth of a milliliter of the aqueous humor was aspirated using a 30-gauge needle via limbal paracentesis after local anesthesia using the proparacaine hydrochloride eyedrop (ALCAINE 5 mg/mL, Alcon, USA). Table 1 summarizes the demographic characteristics of the patients.

2.2. Aqueous Humor Virus Detection. The method has been described previously [29]. Briefly, the presence of rubella virus, CMV, HSV, and VZV in the aqueous humor was confirmed using an ELISA microplate reader (Biotek ELx 800).

Table 1: Demographics and clinical characteristics of FHI patients.

Case		38
	Female	24 (63.16%)
	Male	14 (36.84%)
Age (years), median (range)		38 (14-19)
Eye number		38
	Left eye	19 (50%)
	Right eye	19 (50%)

Table 2: The rate of virus involved FHI.

Case		38
Negative		16 (42.11%)
Positive		22 (57.89%)
	Rubella	19 (50%)
	CMV	2 (5.26%)
	HSV	1 (2.63%)
	VZV	0 (0%)

CMV: cytomegalovirus; HSV: herpes simplex virus-1; VZV: herpes simplex virus-2.

For viral quantification in samples, a software program was used to generate a four-parameter sigmoidal curve. The levels of CMV-IgG > 9 U/mL, HSV-IgG > 9 U/mL, HZV-IgG > 16 U/mL, and rubella-IgG > 10 U/mL indicated a positive result.

2.3. Assessment of Aqueous Humor Cytokine Levels. Flow cytometry was used to analyze the expression of vascular endothelial growth factor (VEGF), basic fibroblast growth factor (bFGF), IL-6, IL-8, IL-10, and vascular cell adhesion protein 1 (VCAM-1) using the BD CBA Human Soluble Protein Master Buffer Kit (BD, 558264). Results were analyzed using the FCAP Array™ software program.

2.4. Statistical Analysis. The parameters were compared using the Mann–Whitney U test between the FHI groups with and without viral infection. Continuous variables are presented as mean (M) and standard error of the mean for normally distributed variables and as median value and interquartile range for variables with skewed distribution. SPSS Statistics (version 22.0) was used to perform statistical analyses, and the threshold for statistical significance was set at $P < 0.05$.

3. Results

Aqueous humor specimens were collected from 38 patients whose conditions were diagnosed as FHI based on the SUN classification criteria; the patients had no other eye or systemic diseases. Twenty-four patients (63.16%) were women, and 14 (36.84%) were men. The mean age was 38 years (range, 14–69 years). The left and right eyes each accounted for 50% ($n = 19$) of the cases. The demographics and clinical information of patients with FHI are shown in Table 1.

Table 3: Cytokines levels in all measured aqueous humor.

Cytokines	Negative group ($n = 7$)	Positive group ($n = 5$)	P value
VEGF (pg/mL), median (Std)	34.500 (1.153)	38.700 (11.879)	0.200
bFGF (pg/mL), median (Std)	27.325 (6.749)	1.100 (0.173)	0.001*
IL6 (pg/mL), median (Std)	41.375 (8.4318)	145.767 (57.988)	0.015*
IL8 (pg/mL), median (Std)	30.333 (9.616)	185.100 (15.839)	0.001*
IL10 (pg/mL), median (Std)	6.225 (2.968)	10.600 (3.536)	0.530
VCAM (pg/mL), median (Std)	1338.333 (369.656)	1390.133 (438.769)	0.268

*$P < 0.05$. VEGF: vascular endothelial growth factor; bFGF: basic fibroblast growth factor; IL: interleukin; VCAM: vascular cell adhesion molecule.

Test results of the presence of intraocular viruses and antibody values of rubella virus, CMV, HSV, and VZV in the aqueous humor are shown in Table 2. Among 38 patients, 16 (42.11%) tested negative and 22 (57.89%) tested positive for the virus; 50% ($n = 19$) of the patients tested rubella positive, 5.26% ($n = 2$) tested CMV positive, 2.63% ($n = 1$) tested HSV positive, and none tested VZV positive. The presence of intraocular rubella virus infection was confirmed, consistent with the fact that most FHI patients were seropositive for this entity.

We divided the 11 patients who underwent measurements of the expression of cytokine levels in the aqueous humor into two groups (Table 3). The positive group ($n = 5$) had higher levels of IL-6 (M 145.767, SD 57.988) and IL-8 (M 185.100, SD 15.839) than the negative group ($n = 7$) (M 41.375, SD 8.432 and M 30.333, SD 9.616, respectively). The expression levels of VEGF, IL-10, and VCAM did not differ significantly between the two groups. However, the virus-positive group had a lower bFGF level (M 1.1, SD 0.17) than the virus-negative group (M 27.325, SD 6.749). Furthermore, we focused on cytokine changes in the aqueous humor of rubella-involved FHI patients, considering that half of the FHI patients had high intraocular antibody levels against rubella. IL-6 and IL-8 levels were significantly higher in the positive group than in the negative group (Figure 1). The bFGF expression was downregulated in the rubella-positive group, similar to that observed in the virus-positive group.

4. Discussion

FHI is a unilateral chronic nongranulomatous uveitis that is difficult to diagnose based on clinical manifestations alone, especially in the Chinese population. This is because these people generally do not have a different iris color of two eyes when iris depigmentation occurs owing to high pigment concentration, resulting in additional differential diagnoses. FHI is generally not detected until it causes secondary affection with late symptoms such as blurred vision and dark shadows that affect vision. In this study, we discovered the changes in inflammatory cytokines and virus antibody expression levels in aqueous humor specimens to yield strong evidence for FHI diagnosis.

HSV, VZV, and CMV are the predominant pathogens in a chronic inflammatory process with the involvement of viral anterior uveitis. However, less than 8% of patients with FHI tended to have an increased level of viral antibody expression (Table 1). Recent studies showed that rubella virus infection is a possible etiological agent of FHI [31]. This led us to hypothesize that active rubella virus infection is related to FHI, and the rubella antibody in the aqueous humor of these patients can help diagnose FHI. Rubella virus is associated with the pathogenesis of Fuchs' heterochromic uveitis, and nearly all European cases had active antibodies against the rubella virus in the aqueous humor [32]. The incidence of FHI has decreased after the introduction of vaccination against the rubella virus [31]. Several researchers have suggested that the presence of the rubella virus in the eye is not a prerequisite for the development of FHI. We carried out this study to ascertain the association between rubella virus infection and FHI by detecting the production of intraocular antibodies and to confirm the presence of the active rubella virus antibody in the aqueous humor of FHI patients.

Furthermore, we detected the levels of several proinflammatory cytokines, including IL-6, IL-8, IL-10, bFGF, VEGF, and VCAM, in the aqueous humor of FHI patients who underwent the examination. Immunoassays have been used to identify the distinct patterns of cytokines associated with both clinical disease and the cellular infiltrates present. First, VEGF, bFGF, and VCAM are all suggested as key regulators of vasculogenesis, and they can stimulate vascularization under inflammation in any type of disease. Reportedly, bFGF can improve leukocyte recruitment and endothelial cell adhesion molecule expression during inflammation [33]. In our study, we observed an obvious decrease in the level of bFGF in the aqueous humor in the virus-positive group compared with the virus-negative group, while there was no significant difference in VEGF or VCAM levels. There has been no relevant literature on the relationship between FHI and bFGF until now, as neovascularization in the iris in FHI cases has rarely been documented. The expression of bFGF in the aqueous humor could be a new observation index for FHI.

Bioinformatics plays a significant role in the pathogenesis of uveitis. There was a positive correlation between IL-6 and IL-8 levels and the number of neutrophils present in patients with uveitis aqueous humor associated with Fuchs' heterochromic cyclitis [34]. In our study, high concentrations of IL-6 and IL-8 were measured in the aqueous humor samples of patients with FHI, indicating that the anterior chambers of these patients had an increased number of

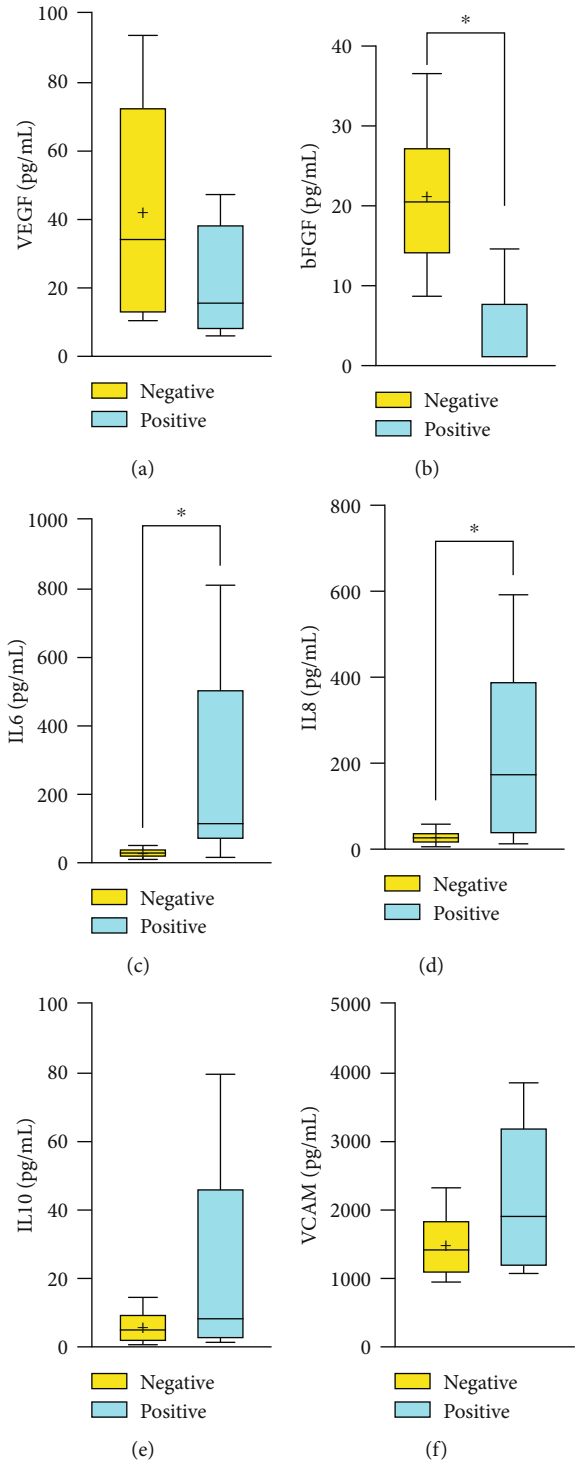

Figure 1: The cytokine changes of aqueous humor in rubella-related FHI. VEGF was high in rubella-related FHI than the virus negative group (a). BFGF was significantly lower in rubella-related FHI (b). The IL6 (c) and IL8 (d) were significantly higher in the positive group. Although there was no significance in the IL10 (e) and VCAM (f), they were higher in the positive group than the negative group ($^{*}P < 0.05$).

neutrophils. A previous study found that the levels of IL-2, interferon-gamma, IL-10, and other cytokines are significantly higher in vitreous humor-derived T cells, and Fuchs' heterochromic cyclitis patients produce high levels of IL-10, which might help downregulate the inflammatory response, resulting in benign clinical outcomes [35]. However, two groups of patients with FHI having the same level of IL-10 suggested no significant difference in the accumulation of T cells in the aqueous humor. As expected, FHI patients with rubella had downregulated expressions of

bFGF and upregulated expressions of IL-6 and IL-8, similar to that observed in the virus-positive group. If patients had high expression levels of IL-6 and IL-8 and negative results for bFGF in the aqueous humor, we would be more certain when diagnosing virus-related FHI on the basis of suggested symptoms.

The presence of the rubella virus in the aqueous humor stimulates inflammation in patients with FHI (classic FHI phenotype). With the detection of an increased level of proinflammatory cytokines and a decreased expression of bFGF preventing vasculogenesis and the local persistence of the rubella virus, we obtained a new direction in the investigation of the pathomechanism and development of a treatment against the etiology of FHI.

The presence of the virus was highly associated with the classic phenotype of FHI, especially that of the rubella virus. This presence constantly causes inflammatory stimulation in the aqueous humor, resulting in significantly increased levels of proinflammatory cytokines, such as IL-6 and IL-8, and low levels of neovascularization-related factors like bFGF. The persistence of viruses and inflammatory cytokine levels in the aqueous humor of patients with FHI could help investigate the pathomechanism of FHI and develop cause-specific treatments.

However, it is unclear whether the virus detected and isolated from aqueous humor in the FHI patient was from acute infection, reinfection, or reactivation of latent virus. Further investigations should include the isolation and characterization of rubella virus strains associated with FHI. What is more, the correlation of symptoms and the rubella-related FHI should be confirmed in the future.

Data Availability

The data used to support the findings of this study are included within the article.

Disclosure

The funders had no role in the study design, data collection and analysis, publishing decision, or preparation of the manuscript.

Conflicts of Interest

The authors declare that there is no conflict of interest regarding the publication of this paper.

Acknowledgments

We thank the Research Square for presenting an early version of this manuscript as a preprint for peer review (https://www.researchsquare.com/article/rs-1095345/v1) [36]. This study was supported by the National Natural Science Foundation of China (grant number 82101084), China Postdoctoral Science Foundation (grant number 2021M69898), and Xiamen Science and Technology Program for Public Wellbeing (grant number 3502Z20209183).

References

[1] V. T. Tran, C. Auer, Y. Guex-Crosier, N. Pittet, and C. P. Herbort, "Epidemiological characteristics of uveitis in Switzerland," *International Ophthalmology*, vol. 18, no. 5, pp. 293–298, 1994.

[2] H. Goto, M. Mochizuki, K. Yamaki, S. Kotake, M. Usui, and S. Ohno, "Epidemiological survey of intraocular inflammation in Japan," *Japanese Journal of Ophthalmology*, vol. 51, no. 1, pp. 41–44, 2007.

[3] P. Yang, W. Fang, H. Jin, B. Li, X. Chen, and A. Kijlstra, "Clinical features of Chinese patients with Fuchs' syndrome," *Ophthalmology*, vol. 113, no. 3, pp. 473–480, 2006.

[4] N. Bouchenaki and C. P. Herbort, "Fuchs' uveitis: failure to associate vitritis and disc hyperfluorescence with the disease is the major factor for misdiagnosis and diagnostic delay," *Middle East African Journal of Ophthalmology*, vol. 16, no. 4, pp. 239–244, 2009.

[5] P. Yang, W. Zhang, Z. Chen et al., "Development of revised diagnostic criteria for Fuchs' uveitis syndrome in a Chinese population," *The British Journal of Ophthalmology*, 2021.

[6] W. Zhang, Z. Chen, H. Zhang et al., "Detection of Fuchs' uveitis syndrome from slit-lamp images using deep convolutional neural networks in a Chinese population," *Frontiers in Cell and Development Biology*, vol. 9, article 684522, 2021.

[7] M. D. Ozer, F. Kebapci, M. Batur, E. Seven, and S. Tekin, "In vivo analysis and comparison of anterior segment structures of both eyes in unilateral Fuchs' uveitis syndrome," *Graefe's Archive for Clinical and Experimental Ophthalmology*, vol. 257, no. 7, pp. 1489–1498, 2019.

[8] Z. Szepessy, G. Tóth, Á. Barsi, K. Kránitz, and Z. Z. Nagy, "Anterior segment characteristics of Fuchs uveitis syndrome," *Ocular Immunology and Inflammation*, vol. 24, no. 5, pp. 594–598, 2016.

[9] K. Norrsell and L. Sjödell, "Fuchs' heterochromic uveitis: a longitudinal clinical study," *Acta Ophthalmologica*, vol. 86, no. 1, pp. 58–64, 2008.

[10] Q. Mohamed and E. Zamir, "Update on Fuchs' uveitis syndrome," *Current Opinion in Ophthalmology*, vol. 16, no. 6, pp. 356–363, 2005.

[11] B. R. Tabbut, H. H. Tessler, and D. Williams, "Fuchs' heterochromic iridocyclitis in blacks," *Archives of Ophthalmology*, vol. 106, no. 12, pp. 1688–1690, 1988.

[12] J. S. Harthan, D. L. Opitz, S. R. Fromstein, and C. E. Morettin, "Diagnosis and treatment of anterior uveitis: optometric management," *Clinical optometry*, vol. 8, pp. 23–35, 2016.

[13] I. S. Barequet, Q. Li, Y. Wang, T. P. O'Brien, J. J. Hooks, and W. J. Stark, "Herpes simplex virus DNA identification from aqueous fluid in Fuchs heterochromic iridocyclitis," *American Journal of Ophthalmology*, vol. 129, no. 5, pp. 672-673, 2000.

[14] M. Wong, D. A. Goldstein, and H. H. Tessler, "Presumed Fuchs heterochromic iridocyclitis and Posner-Schlossman syndrome: comparison of cytomegalovirus-positive and -negative eyes," *American Journal of Ophthalmology*, vol. 147, no. 6, pp. 1106-1107, 2009, author reply 1107-1108.

[15] R. N. Van Gelder, "Idiopathic no more: clues to the pathogenesis of Fuchs heterochromic iridocyclitis and glaucomatocyclitic crisis," *American Journal of Ophthalmology*, vol. 145, no. 5, pp. 769–771, 2008.

[16] Y. Liu, H. L. Takusagawa, T. C. Chen, and L. R. Pasquale, "Fuchs heterochromic iridocyclitis and the rubella virus,"

International Ophthalmology Clinics, vol. 51, no. 4, pp. 1–12, 2011.

[17] J. A. Gonzales, A. Hinterwirth, J. Shantha et al., "Association of ocular inflammation and rubella virus persistence," *JAMA Ophthalmol*, vol. 137, no. 4, pp. 435–438, 2019.

[18] C. D. Quentin and H. Reiber, "Fuchs heterochromic cyclitis: rubella virus antibodies and genome in aqueous humor," *American Journal of Ophthalmology*, vol. 138, no. 1, pp. 46–54, 2004.

[19] S. Zandi, B. Bodaghi, and J. G. Garweg, "Review for disease of the year: treatment of viral anterior uveitis: a perspective," *Ocular Immunology and Inflammation*, vol. 26, no. 7, pp. 1135–1142, 2018.

[20] A. Jad, T. Céline, B. Bahram, L. Phuc, and C. Nathalie, "Fuchs' heterochromic cyclitis: a post-infectious manifestation of ocular toxoplasmosis?," *International Ophthalmology*, vol. 33, no. 2, pp. 189–194, 2013.

[21] J. D. F. De Groot-Mijnes, A. S. Y. Chan, S. P. Chee, and G. Verjans, "Immunopathology of virus-induced anterior uveitis," *Ocular Immunology and Inflammation*, vol. 26, no. 3, pp. 338–346, 2018.

[22] H. Wang and Y. Tao, "Relationship between the higher inflammatory cytokines level in the aqueous humor of Fuchs uveitis syndrome and the presence of cataract," *BMC Ophthalmology*, vol. 21, no. 1, p. 108, 2021.

[23] P. D. Parkman, E. L. Buescher, and M. S. Artenstein, "Recovery of rubella virus from army recruits," *Proceedings of the Society for Experimental Biology and Medicine*, vol. 111, no. 1, pp. 225–230, 1962.

[24] C. Swan, A. L. Tostevin, and G. H. Black, "Final observations on congenital defects in infants following infectious diseases during pregnancy, with special reference to rubella," *The Medical Journal of Australia*, vol. 2, no. 26, pp. 889–908, 1946.

[25] L. Z. Cooper, "The history and medical consequences of rubella," *Reviews of Infectious Diseases*, vol. 7, Supplement_1, pp. S2–10, 1985.

[26] N. M. Gregg, "Congenital cataract following German measles in the mother," *Transactions ophthalmology society*, vol. 3, p. 35, 1941.

[27] W. J. Edmunds, N. J. Gay, M. Kretzschmar et al., "The prevaccination epidemiology of measles, mumps and rubella in Europe: implications for modelling studies," *Epidemiology and Infection*, vol. 125, no. 3, pp. 635–650, 2000.

[28] N. Lambert, P. Strebel, W. Orenstein, J. Icenogle, and G. A. Poland, "Rubella," *The Lancet*, vol. 385, no. 9984, pp. 2297–2307, 2015.

[29] P. C. Ruokonen, S. Metzner, A. Ücer, N. Torun, J. Hofmann, and U. Pleyer, "Intraocular antibody synthesis against rubella virus and other microorganisms in Fuchs' heterochromic cyclitis," *Graefe's Archive for Clinical and Experimental Ophthalmology*, vol. 248, no. 4, pp. 565–571, 2010.

[30] D. A. Jabs, R. B. Nussenblatt, J. T. Rosenbaum, and Standardization of Uveitis Nomenclature (SUN) Working Group, "Standardization of uveitis nomenclature for reporting clinical data. Results of the First International Workshop," *American Journal of Ophthalmology*, vol. 140, no. 3, pp. 509–516, 2005.

[31] J. Suzuki, H. Goto, K. Komase et al., "Rubella virus as a possible etiological agent of Fuchs heterochromic iridocyclitis," *Graefe's Archive for Clinical and Experimental Ophthalmology*, vol. 248, no. 10, pp. 1487–1491, 2010.

[32] J. C. E. M. ten Berge, P. L. A. van Daele, and A. Rothova, "Rubella virus-associated anterior uveitis in a vaccinated patient: a case report," *Ocular Immunology and Inflammation*, vol. 24, no. 1, pp. 113-114, 2016.

[33] S. I. Zittermann and A. C. Issekutz, "Endothelial growth factors VEGF and bFGF differentially enhance monocyte and neutrophil recruitment to inflammation," *Journal of Leukocyte Biology*, vol. 80, no. 2, pp. 247–257, 2006.

[34] S. J. Curnow, F. Falciani, O. M. Durrani et al., "Multiplex bead immunoassay analysis of aqueous humor reveals distinct cytokine profiles in uveitis," *Investigative ophthalmology & visual science*, vol. 46, no. 11, pp. 4251–4259, 2005.

[35] M. Muhaya, V. L. Calder, H. M. Towler, G. Jolly, M. McLauchlan, and S. Lightman, "Characterization of phenotype and cytokine profiles of T cell lines derived from vitreous humour in ocular inflammation in man," *Clinical and Experimental Immunology*, vol. 116, no. 3, pp. 410–414, 1999.

[36] O. Shangkun, Y. Mao, S. Lin, C. Zhu, X. Liu, and H. Wu, "Cytokine changes in the aqueous humor in rubella-related Fuchs heterochromic iridocyclitis," *Research Square*, 2022.

Hindawi
Disease Markers
Volume 2022, Article ID 7231046, 21 pages
https://doi.org/10.1155/2022/7231046

Research Article

Identification of the Relationship between Hub Genes and Immune Cell Infiltration in Vascular Endothelial Cells of Proliferative Diabetic Retinopathy Using Bioinformatics Methods

Jing Huang and Qiong Zhou

Department of Ophthalmology, The First Affiliated Hospital of Nanchang University, Jiangxi Center of National Ocular Disease Clinical Research Center, Nanchang, 330006 Jiangxi, China

Correspondence should be addressed to Qiong Zhou; qiongzd06@126.com

Received 1 October 2021; Revised 19 December 2021; Accepted 3 January 2022; Published 3 February 2022

Academic Editor: Elisa Belluzzi

Background. Diabetic retinopathy (DR) is a serious ophthalmopathy that causes blindness, especially in the proliferative stage. However, the pathogenesis of its effect on endothelial cells, especially its relationship with immune cell infiltration, remains unclear. *Methods*. The dataset GSE94019 was downloaded from the Gene Expression Omnibus (GEO) database to obtain DEGs. Through aggregate analyses such as Gene Ontology (GO) and Kyoto Encyclopedia of Gene and Genome (KEGG) pathway enrichment analysis, a protein-protein interaction (PPI) network was constructed to analyze the potential function of DEGs. Weighted gene coexpression network analysis (WGCNA) and Cytoscape software including molecular complex detection (MCODE) and cytoHubba plug-ins were used to comprehensively analyze and determine the hub genes. ImmuCellAI analysis was performed to further study the relationship between samples, hub genes, and 24 types of immune cell infiltration. Finally, gene-set enrichment analysis (GSEA) was employed to identify the enrichment of immune cell infiltration and endothelial cell phenotype modifications in GO biological processes (BP) based on the expression level of hub genes. *Results*. 2393 DEGs were identified, of which 800 genes were downregulated, and 1593 genes were upregulated. The results of functional enrichment revealed that 1398 BP terms were significantly enriched in DEGs. Three hub genes, EEF1A1, RPL11, and RPS27A, which were identified by conjoint analysis using WGCNA and Cytoscape software, were positively correlated with the number of CD4 naive T cells and negatively correlated with the numbers of B cells. The number of CD4 naive T cells, T helper 2 (Th2) cells, and effector memory T (Tem) cells were significantly higher while CD8 naive T cells and B cells significantly were lower in the diabetic group than in the nondiabetic group. *Conclusions*. We unearthed the DEGs and Hub genes of endothelial cells related to the pathogenesis of PDR: EEF1A1, RPL11, and RPS27A, which are highly related to each other and participate in the specific biological process of inflammation-related immune cell infiltration and endothelial cell development, chemotaxis, and proliferation, thus providing new perspectives into the diagnosis of and potential "killing two birds with one stone" targeted therapy for PDR.

1. Introduction

According to the latest digital information from the International Diabetes Federation, there were an estimated 463 million diabetics among adults aged between 20 and 79 worldwide in 2019, and the number is expected to reach 642 million by 2040, with the pervasiveness rate increasing from 8.8% to 10.4%. In 2019, half (50.1%) of diabetics do not know they have the disease [1]. Diabetic retinopathy (DR) and DR-related blindness occur in 34.6% and 2.6%, respectively, among the total population of diabetic patients [2]. DR, especially proliferative diabetic retinopathy (PDR), makes a relatively minor contribution to vision deprivation or blindness in working-age people in developed countries [3], and its prevalence has been increasing in some developing countries with large populations [4, 5]. This has caused a

heavy economic burden on all countries and has imposed serious obstacles to the development of global economic productivity [6].

DR is a neurovascular disease caused by the destruction of retinal neurovascular unit (NVU) due to diabetes, in which the lesions of intraocular microvessels are still dominant [7]. Chronic progressive diabetes leads to retinal microvascular leakage and occlusion and a series of secondary fundus lesions, such as microhemangioma, rigid exudation, cotton spots, neovascularization, vitreous proliferation, macular edema, and even retinal detachment [8]. The main risk factors for DR are the course of diabetes and blood glucose levels. Other important risk factors include HbA1c levels, blood pressure, serum total cholesterol, and low-density lipoprotein [8]. According to the pathogenesis of DR, nonproliferative diabetic retinopathy (NPDR) and PDR are the two major stages of DR observed in the clinic [9]. NPDR can be subdivided as mild, moderate, or severe based on fundus examination findings [9]. Approximately 16% of patients with moderate NPDR will progress to PDR within 5 years [10]. For very severe NPDR patients, the risk of developing PDR within one year is about 75% [11]. Once the disease progresses to PDR, the eye is 4.0 times more likely than an eye with mild NPDR to become blind within 2 years of DR diagnosis [12]. The main treatment methods are intravitreal injection of antiangiogenic drugs, macular and pan-retinal laser photocoagulation, and vitrectomy [13]. Antineovascularization therapies, mainly aimed at vascular endothelial growth factor (VEGF) and its receptors, have been the focus of DR treatment for many years. However, a considerable number of patients cannot benefit from these treatments [14], so there is an urgent need for new molecular targets and target-specific therapies.

Many studies have confirmed that hyperglycemia is the central precipitating factor in diabetic retinopathy [15–17]. Chronic injury and pathological changes to vascular endothelial cells are the core histopathological changes in DR injury [18, 19]. The effect of a hyperglycemic state on retinal vascular endothelial cells is multilayered and multifaceted. Retinal vascular endothelial cell function is affected by disrupting transmembrane glucose transport [20], extracellular matrix metabolism [21], protein transcription, and posttranscriptional regulation as well as cells' translation and posttranslational modification [22–24]. Abnormal function of vascular endothelial cells has been detected in the early stage of DR, and the damage is further aggravated by increased blood glucose [25]. In PDR, due to the breakdown of immune privilege and the destruction of the blood-retinal barrier (BRB), circulating immune cells will pass from retinal endothelial cells and infiltrate the retina and vitreous, causing retinal blood vessel damage which is characterized by chronic microvascular inflammation and neuronal damage [26–28]. Retinal vascular endothelial cells are the first vital station of circulating immune cell infiltration, and the overall immune infiltration situation is still unknown.

RNA sequencing (RNA-seq) is a technology that utilizes second-generation sequencing transcriptomics research methods to reveal a snapshot of the presence and quantity of RNA in a genome at a given moment [29]. It has been applied extensively as a powerful tool for exploring molecular mechanisms of diseases and identifying genome expression profiles [29]. The overall aim of this study was to use gene analysis technology to gain novel insights into the pathogenesis, diagnosis, prognosis, and treatment of DR. To achieve this aim, we adopted an RNA-seq dataset to determine differentially expressed genes (DEGs), filtrate potential biomarkers, analyze GO and KEGG pathways, and identify hub genes and their related immune cell infiltration abundances using the ImmuCellAI algorithm [30].

2. Materials and Methods

2.1. GEO Dataset Processing. The GEO database (https://www.ncbi.nlm.nih.gov/geo/) [31] was searched using "diabetic retinopathy, endothelial cell" as the subject term, yielding a total of 18 datasets. These data were filtered by selecting "expression profiling by high-throughput sequencing" as a study type and "Homo sapiens" as the organism, after which two datasets remained. After studying the specific details of the two datasets, dataset that did not meet the study criteria was discarded; we chose and downloaded GSE94019 which is based on the GPL11154 Illumina HiSeq 2000 (Homo sapiens) platform. The dataset GSE94019 contains a total of 13 human eye vascular endothelial cell samples, of which nine are from the fibrovascular membrane of patients with proliferative diabetic retinopathy, and four are from the retinas of people without diabetes. All samples were extracted, the data of each sample were preprocessed, and the average value at which the gene corresponded to multiple probes was recorded.

2.2. Analysis of Differential Expression. R software (version 4.1.0; https://www.r-project.org/) coupled with the Bioconductor package (http://www.bioconductor.org/) were implemented to correct and analyze the original data. RNA-seq data processing and normalization were performed using the edgeR package with trimmed-mean of M values (TMM) modus [32]. Criteria for statistical significance were logFC (fold change) > 2 and false discovery rate (FDR) < 0.05. DEGs, which are identified as genes that meet the screening criteria, were visualized on a heatmap by utilizing the pheatmap package and on a volcano plot by applying the EnhancedVolcano package.

2.3. Functional Enrichment Analysis. GO functional annotation and KEGG enrichment analysis were conducted on the DEGs, and results were visualized by implementing the R packages clusterProfiler, org.hs.eg.db, and enrichplot. The GO enrichment analysis consists mainly of biological processes (BPs), cellular components (CCs), and molecular functions (MFs). For the purposes of the present study, BP, which is the most important part of GO, was used for screening and analysis. The statistical significance criterion was set as adjust value of $p < 0.05$.

2.4. Coexpression Network Construction. The weighted gene coexpression network analysis (WGCNA) R package was used, and the gene expression profiles of all 17233 genes were occupied to reveal DR-related modules. Raw data were downloaded from the sample obtained from the GEO database. The edgeR package was used to process the data, and

the upper quantile normalization modus was introduced for background amendment and standardization. Genes with standard deviation less than 0.5 times that of samples in the integrated dataset were eliminated, and other screened genes were introduced into WGCNA. To ensure that the network was scale-free, the pickSoftThreshold function was used to calculate the soft threshold of adjacency. The topological overlap matrix (TOM) was constructed after the adjacency matrix was transformed. By hierarchical clustering and use of a dynamic tree cutting function detection module, the genes with analogical expression portraits were allocated into several gene modules based on TOM dissimilitude measurement with the minimal unit of the gene tree dendrogram at 50, and the cutHeight value at 0.9. Module member (MM) and gene significance (GS) were calculated to reveal clinically related attributes. Each step of the above construction process is visualized by WGCNA and its related R packages. The genes and information contained in the module were retained for further analysis.

2.5. PPI Network Construction. A PPI network diagram of DEGs was developed using the STRING database (https://string-db.org/) with the maximum confidential interaction score of 0.99. Cytoscape software was used to optimize visualization of the network, and the MCODE plug-in was employed to analyze the PPI network including all DEGs to obtain the key clusters of the most closely interrelated genes. The network analyzer was used to calculate and analyze the score of each point in a multidimensional approach for the entire undirected network. In the MCODE plug-in setting, the original parameters (degree cutoff ≥ 2, node score cutoff ≥ 2, $K-\text{core} \geq 2$, maximum depth $= 100$) were introduced to calculate and detect the key gene network model with intensive protein-protein relationship. All eleven algorithms including MCC, DMNC, MNC, Degree, EPC, EcCentricity, Closeness, Radiality, Betweenness, Stress, and BottleNeck in the CytoHubba plug-in were applied, and the intersection of the top 100 nodes from each method was recorded to identify the latent gene clusters. The gene cluster in the key module of WGCNA was intersected with the gene clusters obtained by MCODE and CytoHubba plug-ins in Cytoscape to obtain the final hub genes.

2.6. Immune Cell Infiltration Analysis. Immune Cell Abundance Identifier (ImmuCellAI) was used to estimate abundance of 24 immune cell types from RNA-seq digital gene expression data and obtain the immune cell infiltration matrix [30]. The landscapes of immune cell infiltration in retinal endothelial cells (RECs) from nondiabetic retinal tissue and fibrovascular membrane endothelial cells (FVMs) from PDR tissue were downloaded. The proportion of each immune cell subtype was extracted from the sample. A heatmap including the 24 immune cell types was created using the pheatmap package. A heatmap showing correlations between immune cells was plotted using the R package PerformanceAnalytics. The beanplot package was used to compare the distributions of the 24 immune cells between the REC and FVM groups. Lollipop plots showing the correlations between hub genes and immune cells, were created using the ggplot2 package, and the correlations were measured using the Pearson method.

Table 1: Datasets implemented for analysis.

Dataset	Gene number	Platform	Case samples	Control samples
GSE941019	17233	GPL11154	9	4
GSE102485	14108	GPL18573	22	3
GSE142025	17184	GPL20301	21	9

2.7. GSEA of Hub Genes. The GSEA program was used to analyze genome-wide expression profiles from microarray data. Within this program, two reference database index files (c2.cp.kegg.v7.3.symbols.gmt and c5.go.bp.v7.3.symbols.gmt) were used to generate GSEA image sets. The multi-GSEA images in the BP of GO were redrawn using the clusterProfiler package in R [33]. Criteria for statistical significance were $p < 0.05$ and FDR $q < 0.25$.

2.8. Verification of Hub Genes. The software package pROC in R was used to analyze and assess the diagnostic value of hub genes using receiver-operating characteristic (ROC) curves. Criteria for hub genes were area under the ROC curve (AUC) greater than 0.80 and Wilcoxon test $p < 0.05$. The details of the datasets used for analysis in this study were presented in Table 1.

2.9. Statistical Analysis. All statistical analyses were calculated using R software (4.1.0) and associated packages as explained above.

3. Results

3.1. Identification of DEGs. Using the EdgeR package, a total of 2393 DEGs were identified, of which 1593 genes were upregulated and 800 were downregulated. DEGs were filtered and rendered at a set threshold and visualized by heatmap and volcano plot, in which heatmap illustrated the first 50 upregulated and downregulated genes (Figure 1(a)), while volcano map demonstrated the top 20 upregulated and downregulated genes (Figure 1(b)).

3.2. GO and KEGG Enrichment Analysis of DEGs. The functional enrichment results showed that 1398 BP terms, 178 CC terms and 130 MF terms were significantly enriched in DEGs. The BP of DEGs is mainly related to the activation and degranulation of neutrophil-related immune response, the initiation of protein translation, and the location of organelle assembly. Cell-substrate junction and focal adhesion are the two most abundant items in CC, while cadherin binding, actin binding, and enzyme inhibitory activity were the most abundant terms in MF (Figure 1(c)). In KEGG terms, in addition to some chronic and infectious disease pathways, diabetes mellitus and its complications and DR-related pathways such as tumor necrosis factor (TNF) signaling pathway, antigen processing and presentation, phototransduction, IL-17 signaling pathway, and AGE-RAGE signaling pathway in diabetic complications were significantly highly enriched. The results

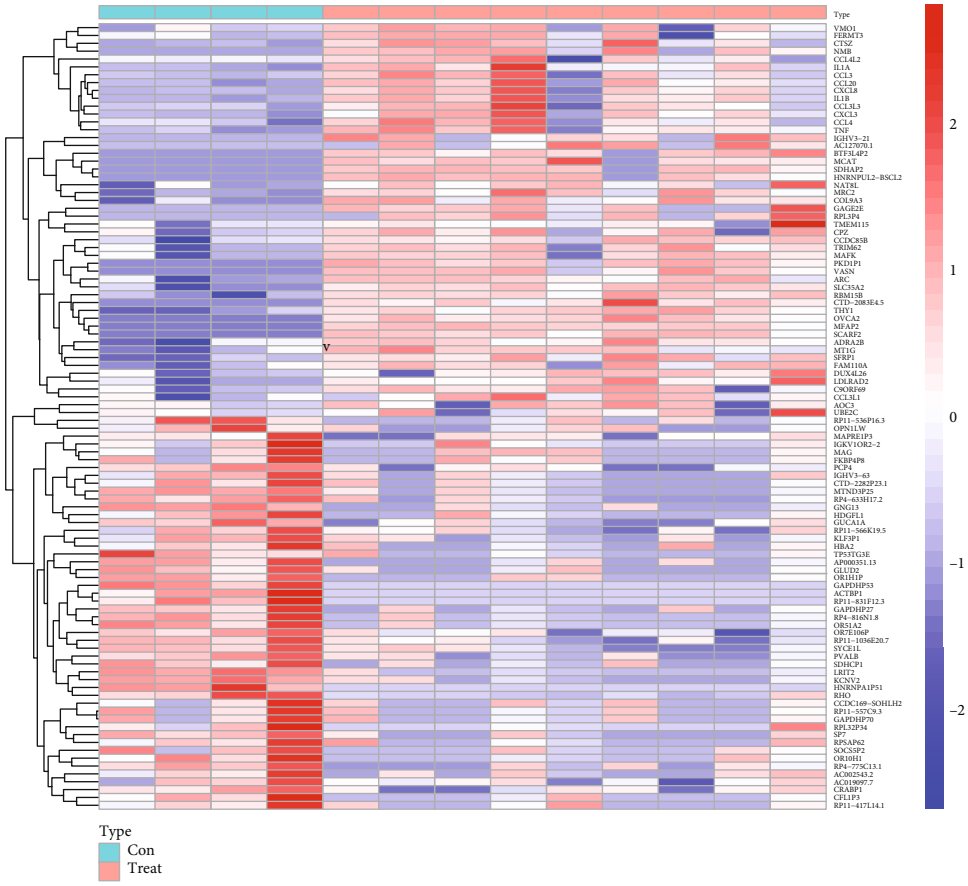

(a)

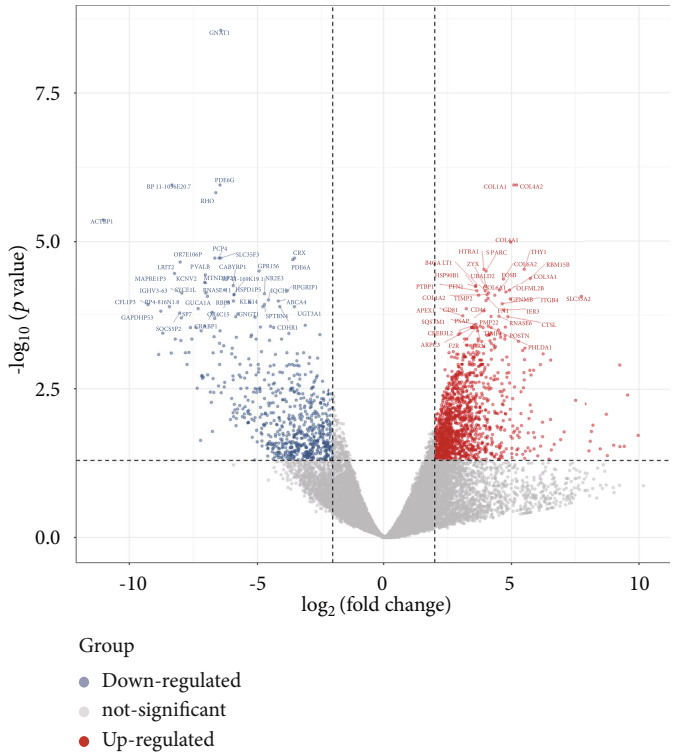

(b)

Figure 1: Continued.

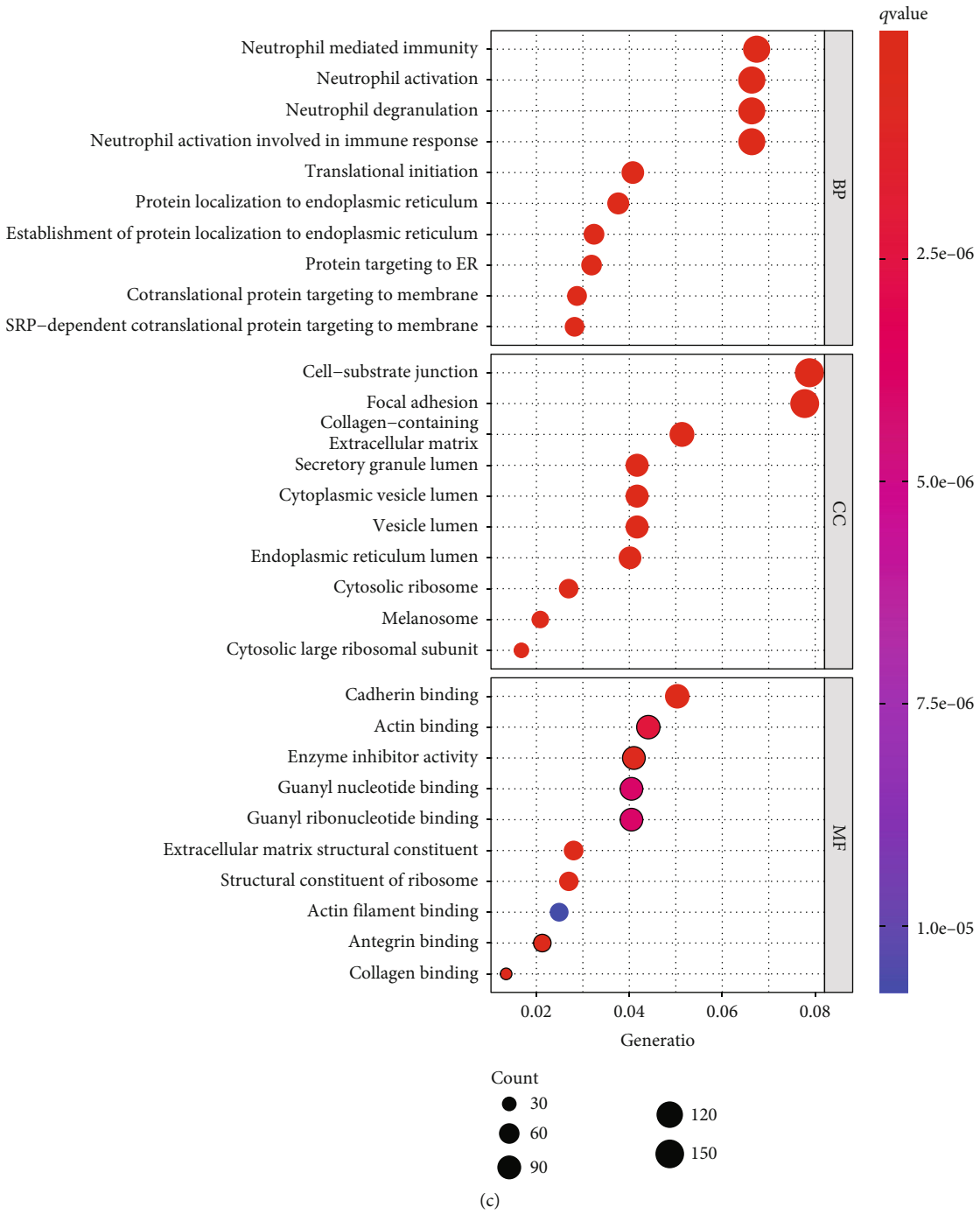

(c)

Figure 1: Continued.

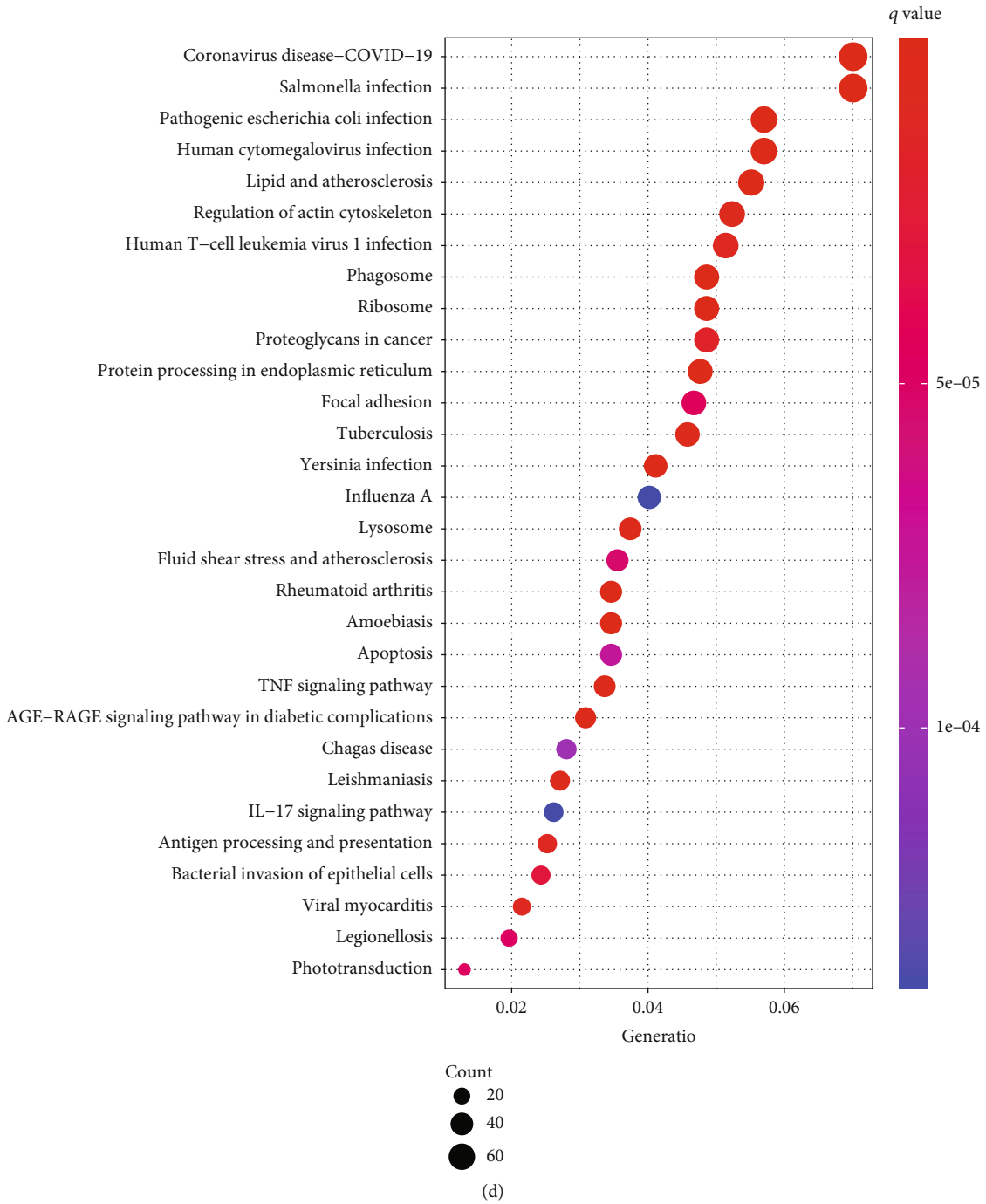

Figure 1: (a) DEG heatmap. The top 50 upregulated (red) and top 50 downregulated (blue) DEGs are shown, in order of FDR value from low to high. (b) DEG volcano plot showing the 20 most upregulated and downregulated genes. (c) GO bubble chart showing the top 10 terms manifested from the BP, CC, and MF directories. (d) KEGG bubble chart. Top 30 KEGG enrichment terms are shown.

also illustrated significant enrichment in pathways in cellular processes such as phagosome, lysosome, regulation of actin cytoskeleton, focal adhesion, apoptosis, and pathways in genetic information processing such as ribosome, protein processing in endoplasmic reticulum (Figure 1(d)).

3.3. Gene Coexpression Web Development and Fundamental Module Recognition. When constructing the sample dendrogram, there were no outlier specimens, so no specimen was removed (Figure 2(a)). Through the analysis of sample gene expression distribution, it could be seen that the baseline distribution of sample gene expression was uniform and at the same level (Figure 2(b)). Using the pickSoftThreshold function, the optimal soft threshold was automatically set at 13, which makes the evaluation coefficient R^2 of scale-free network run up to 0.9 for the first time (Figure 2(c)). After

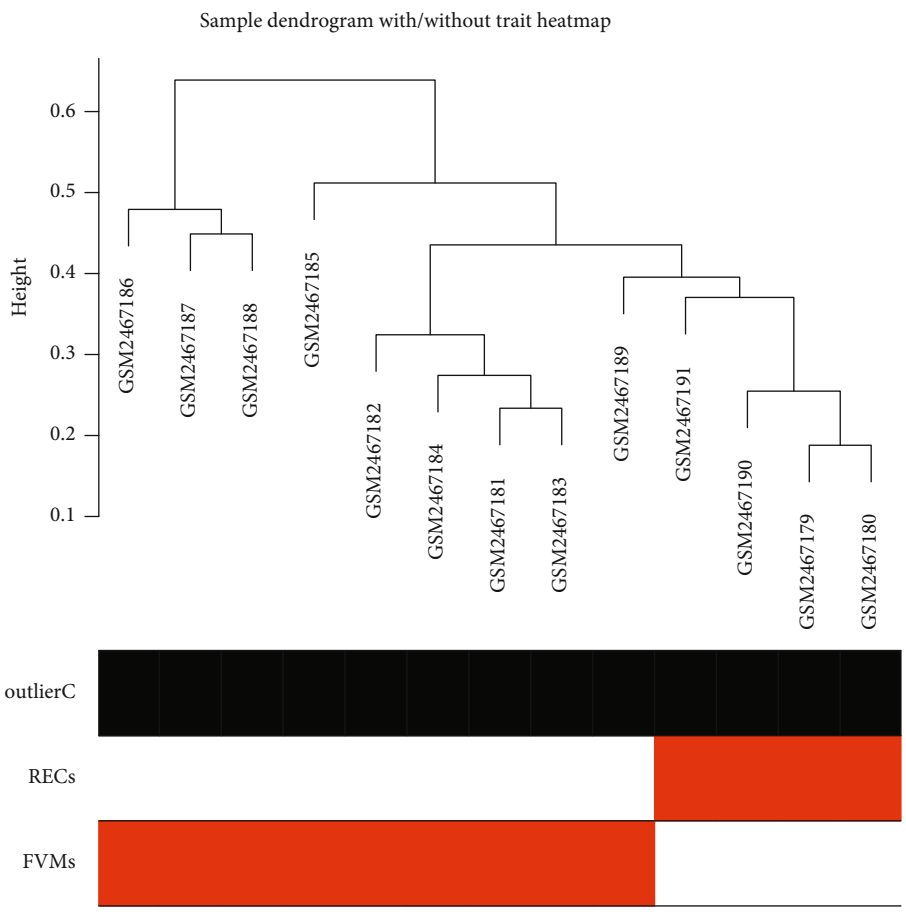

(a)

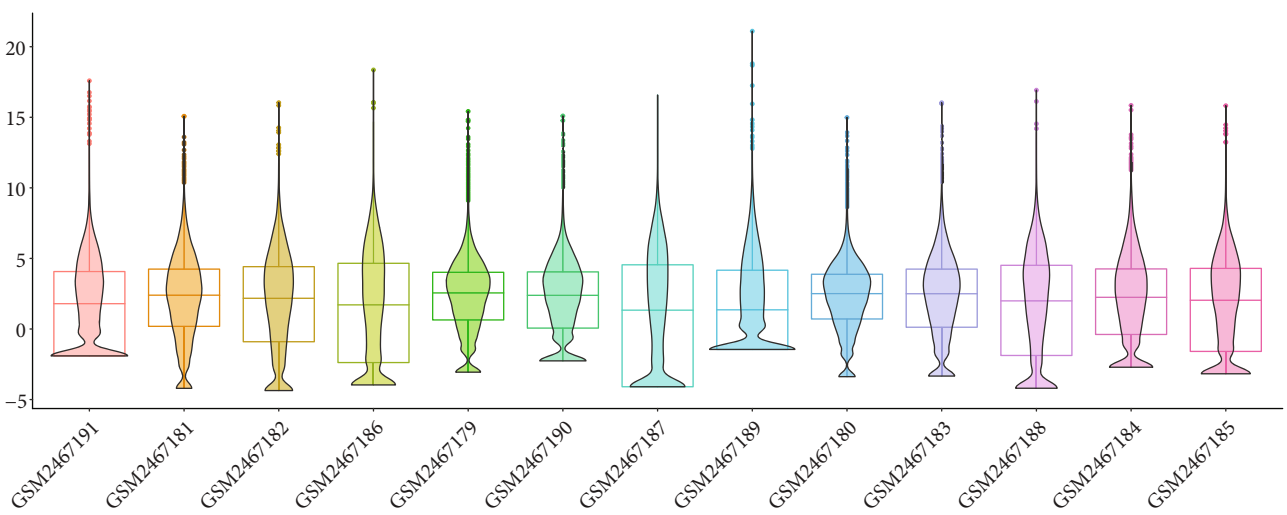

(b)

Figure 2: Continued.

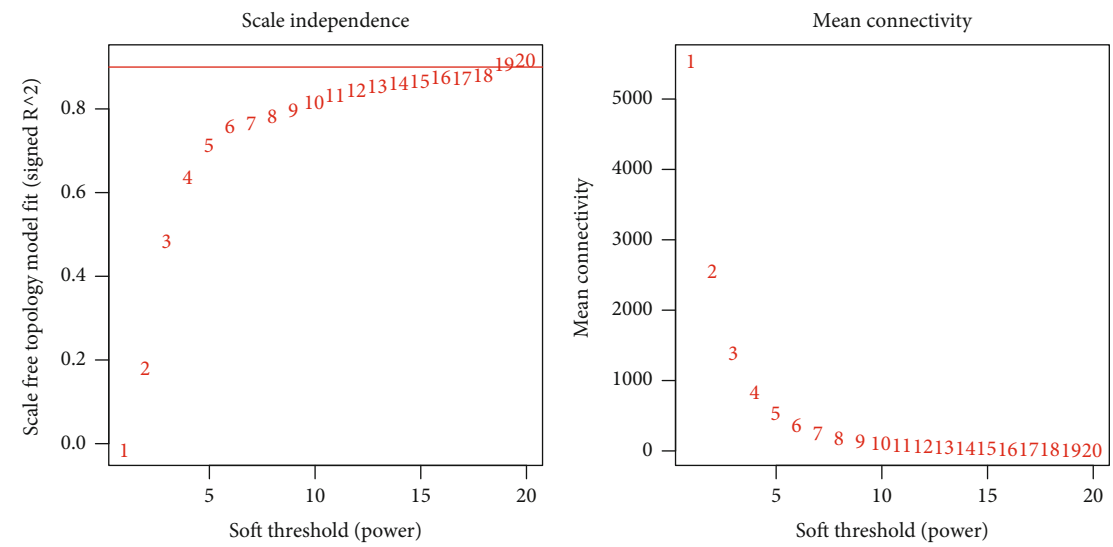

(c)

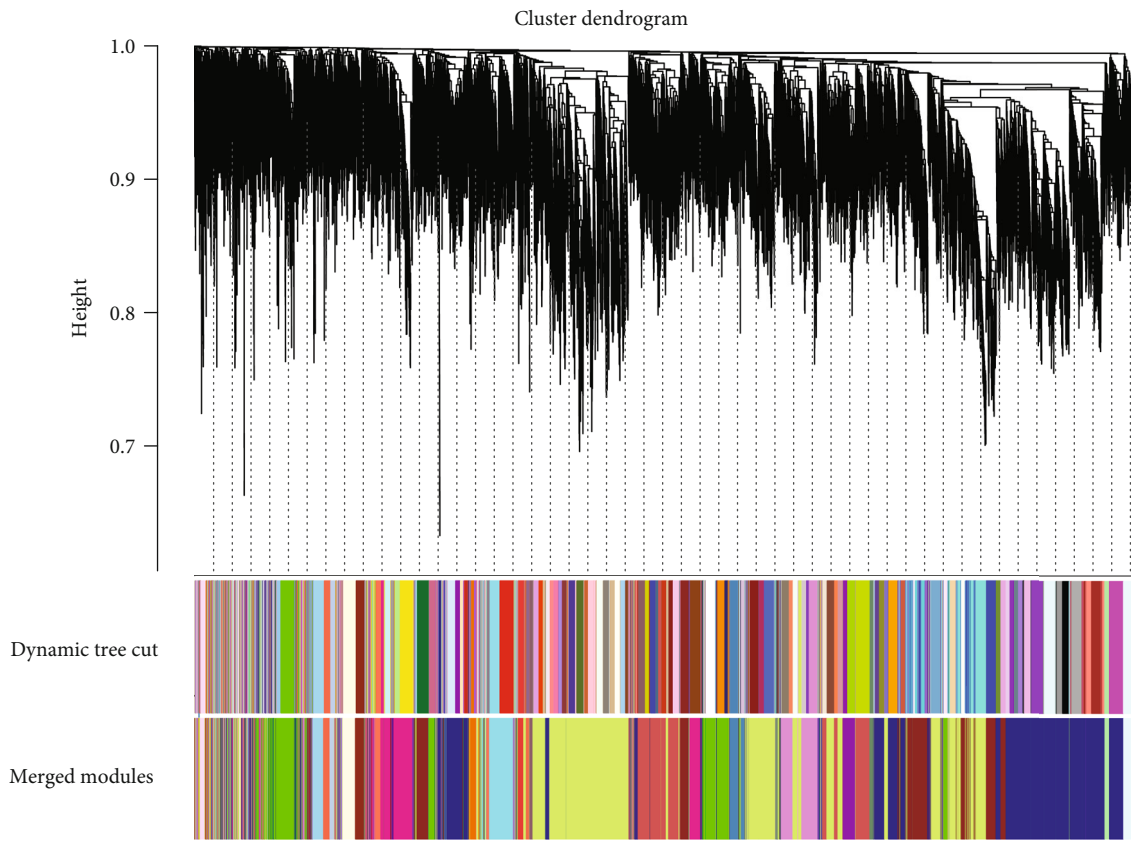

(d)

Figure 2: Continued.

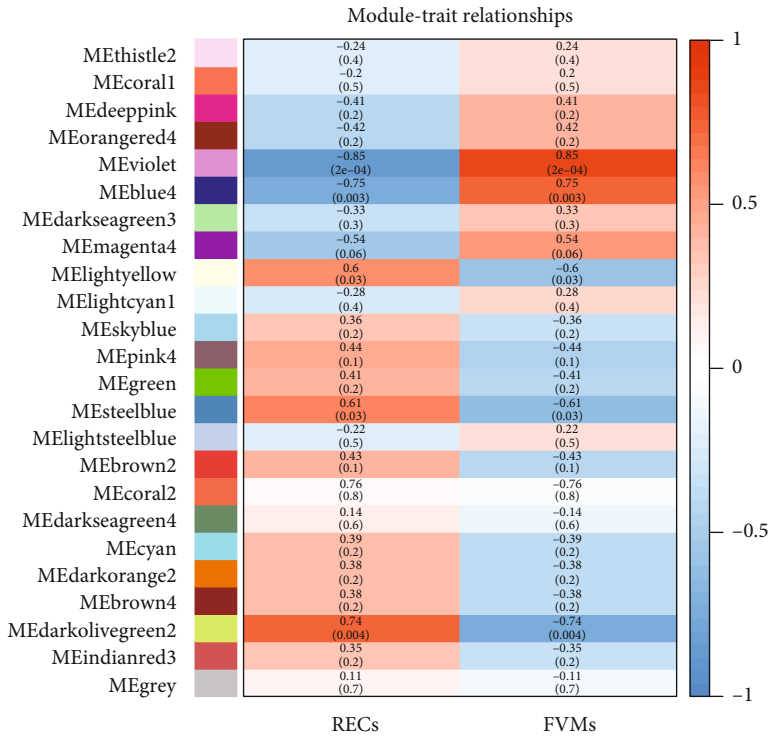

(e)

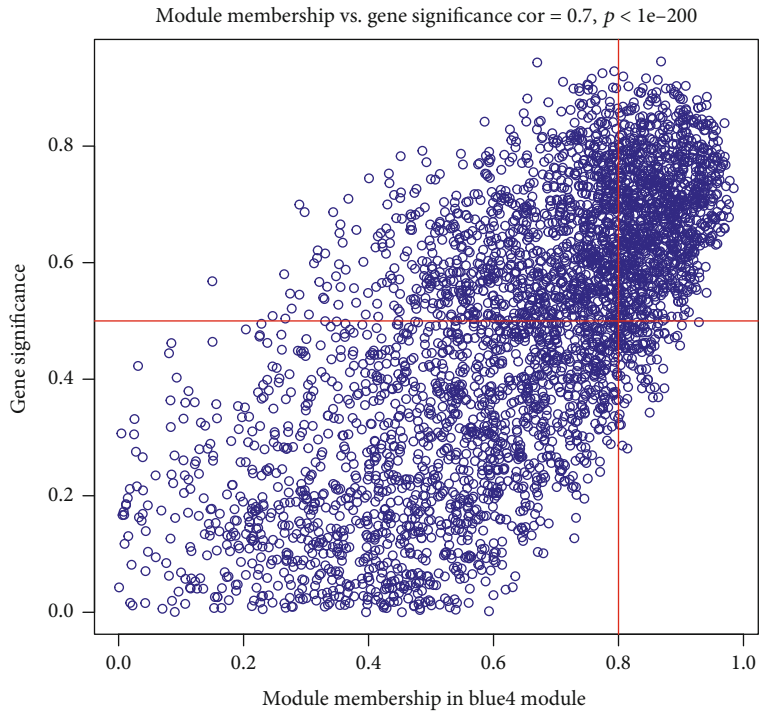

(f)

Figure 2: Continued.

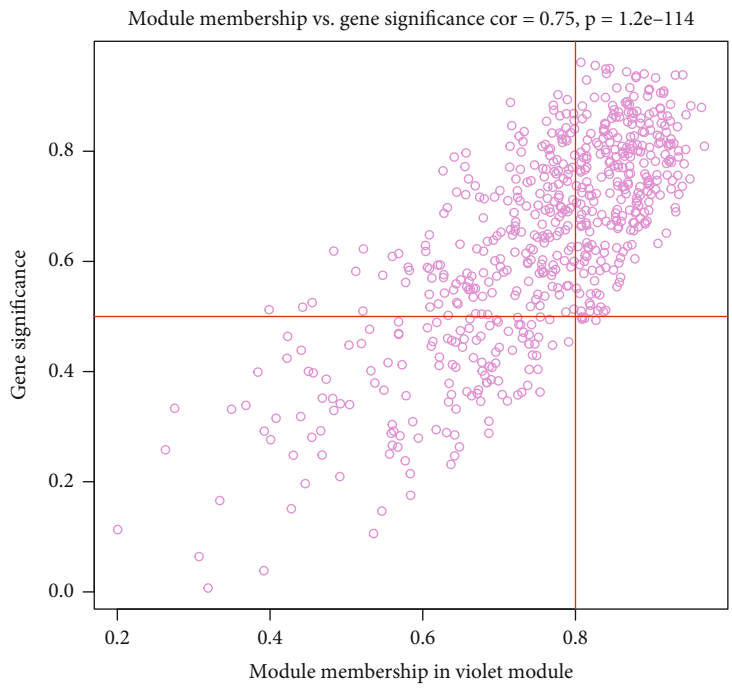

(g)

Figure 2: (a) Clustering of samples was executed to check outliers. All samples were subsumed in the cluster and were well classified, and no sample contains outliers. (b) Violin box plots show the expression profile distributions of all samples. (c) The soft threshold was calculated and determined using the pickSoftThreshold function. (d) A hierarchical clustering dendrogram was used to analyze coexpressed gene clusters, with each color representing a coexpression module. (e) Heatmap of the clinical distinguishing feature relevance of eigengenes, showing for each coexpression module gene cluster the correlation between the REC and FVM groups. (f, g) Scatter plots showing the correlations between MM and GS in the blue4 and violet modules.

merging similar modules in the cluster tree with a cutting height of 0.3, 48 modules of genes with similar coexpression specificities were identified from the coexpression network (Figures 2(d) and 2(e)). The module eigengene (ME) in the violet module ($r = -0.85$; $p = 2e - 4$) displayed the highest negative correlation, while the ME in the blue4 module ($r = -0.75$; $p = 0.003$) showed the second highest negative correlation. These two modules were top two modules which were significantly correlated with clinical traits. Both the violet (cor = 0.75, $p = 1.2e - 114$) and blue4 (cor = 0.7, $p < 1e - 200$) modules showed significant positive correlations between MM and GS of the target gene (Figures 2(f) and 2(g))). Therefore, violet module and blue4 module were recognized as key modules.

3.4. PPI Network and Identification of Hub Genes. After screening with a filter score of 0.99, the highest available in the string database, a network containing 789 nodes and 2755 edges was created using the cytoscape software. In the MCODE plug-in results, a total of 39 core networks were obtained, of which the three with the highest scores (48.208, 8.250, and 7.250) were extracted separately and visualized using Betweenness scores (Figures 3(a)–3(c)). The first of these with a score far exceeding other networks and the top 100 genes obtained by the eleven algorithms in CytoHubba were intersected using the upsetR method, and ultimately, a total of four candidate hub genes were obtained (Figure 3(d)). Intersection of these four genes with the gene sets of the two most critical modules obtained from WGCNA showed that two genes (EEF1A1, RPL11) were in the blue4 module and one gene (RPS27A) is in the violet module. After repeated screening, three genes, EEF1A1, RPL11, and RPS27A, were identified as hub genes.

3.5. Immune Cell Infiltration in RECs and FVMs. The ImmuCellAI algorithm was used to predict immune cell infiltration in the RECs and FVMs groups. Bar chart and heatmap show the relative percentage proportion of 24 immune cell types within the sample (Figures 4(a) and 4(b)). Absolute score differences between the two immune cell subgroups show that CD4 naïve cells, Th2 cells, and Tem cells in the FVMs group were significantly more advanced than in the RECs group, while the converse was true for CD8 naive cells and B cells, with significantly more cells in the RECs group than in FVMs group (Figure 4(d)). A significant correlation was found between DC and the other 11 types of immune cells; CD4 naïve cells, Tr1 cells, and CD4 T cells were significantly related to the other 10 types of immune cells; nTreg cells was significantly related to the other nine types of immune cells; Tfh cells, Tcm cells, Monocyte, NK cells, and CD8 T cells were significantly related to the other eight types of immune cells (Figure 4(c)). These correlations mean that one third or more of immune cell types were cross-correlated and may be considered as potential core immune cells with close links to the manifestation and improvement of diabetic retinopathy.

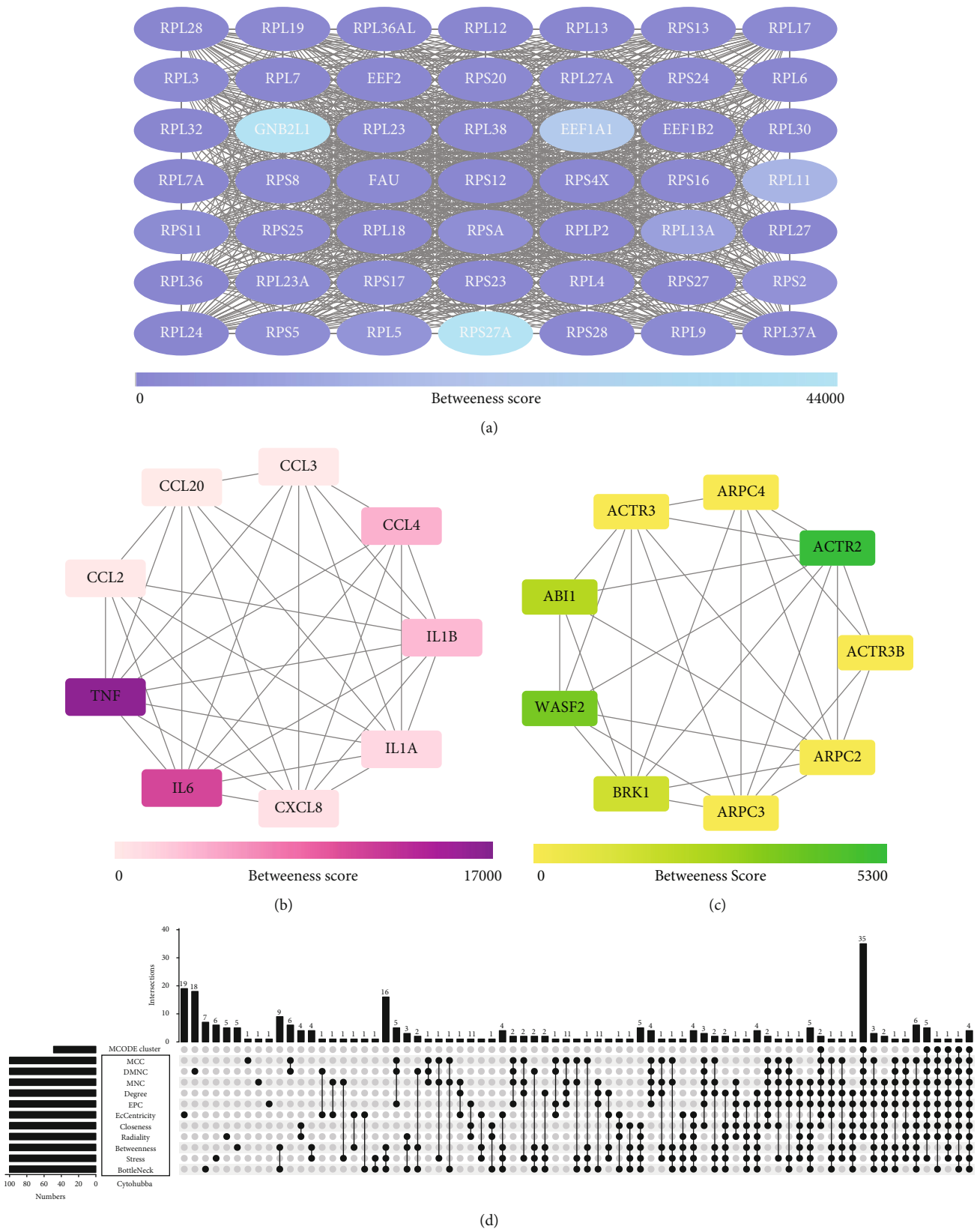

Figure 3: (a–c) Key gene modules predicted by MCODE. The top 3 key gene clusters calculated by the MCODE algorithm plug-in are uncovered, and their scores in the plug-in are 48.208, 8.250, and 7.250, respectively. The color in the figure from light to dark displayed how much the Betweenness Centrality score of each gene is. (d) The UpsetR plot unfurled the details of the number of overlapping genes obtained by the MCODE algorithm plug-in and the CytoHubba algorithm plug-in which 11 algorithms are employed.

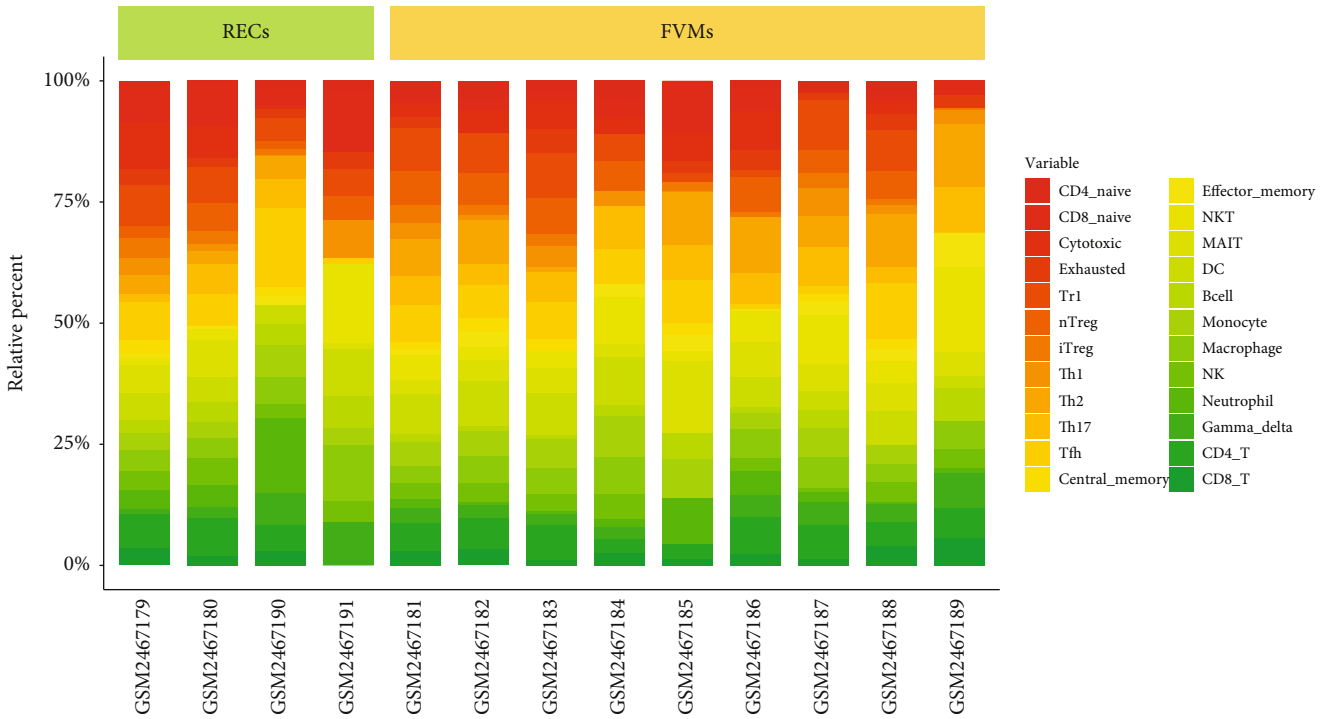

(a)

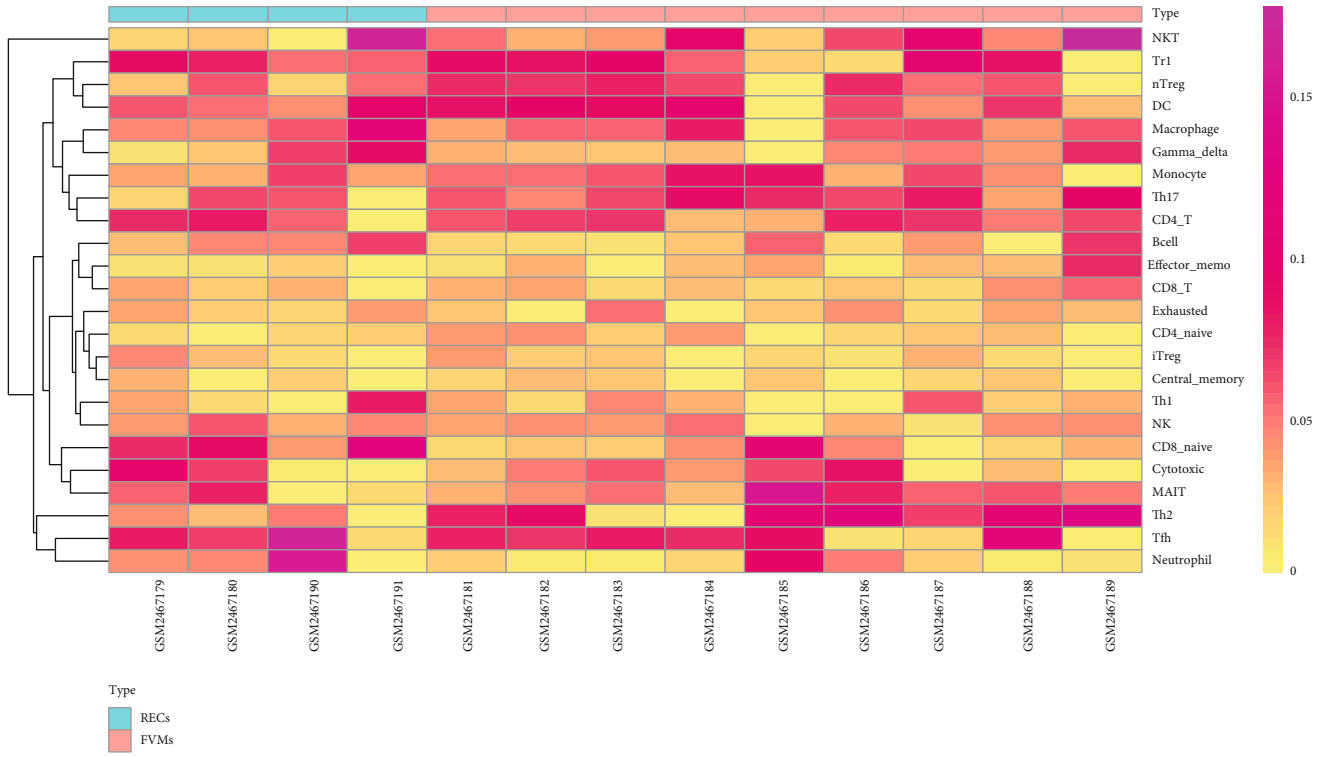

(b)

Figure 4: Continued.

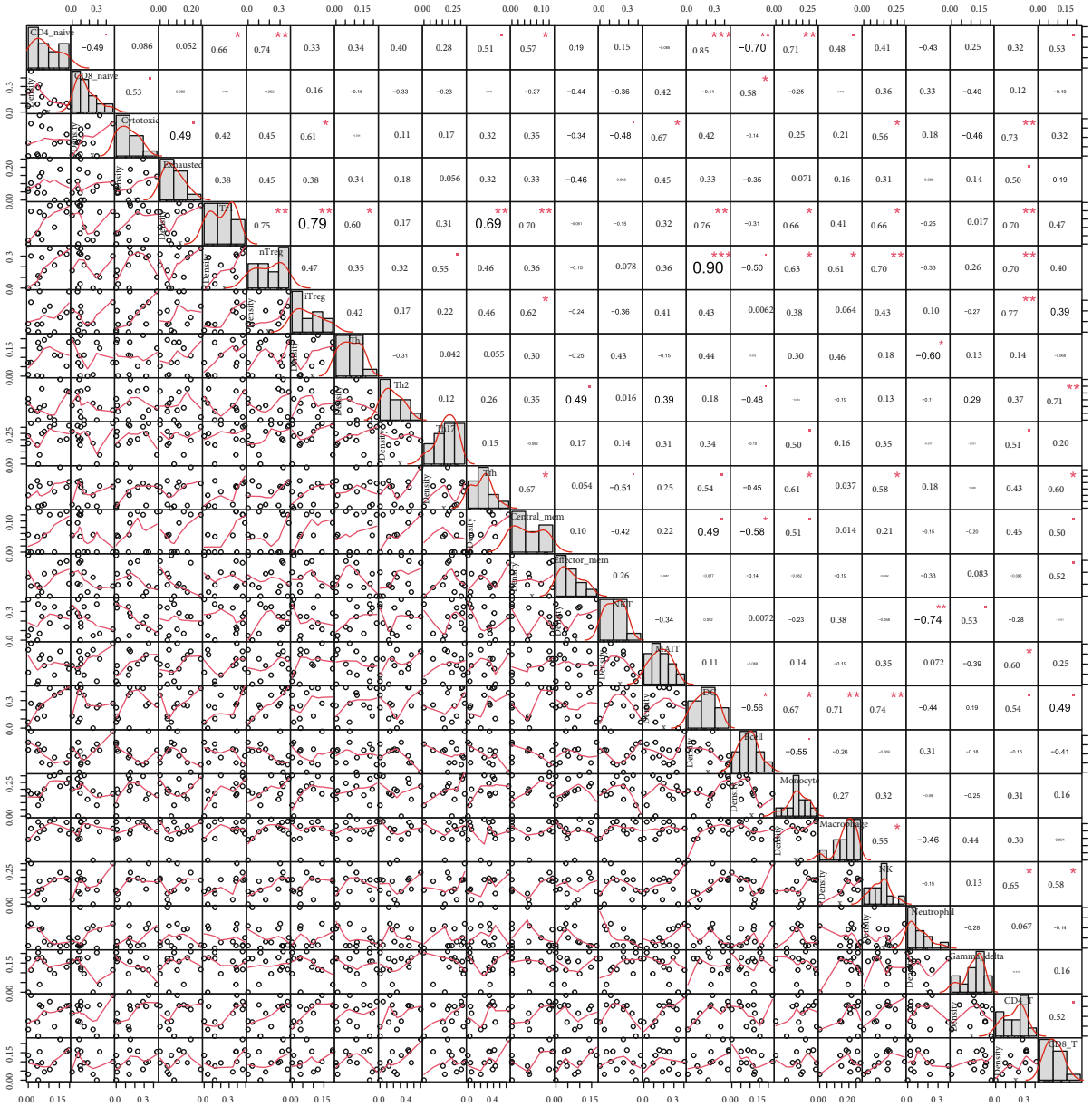

(c)

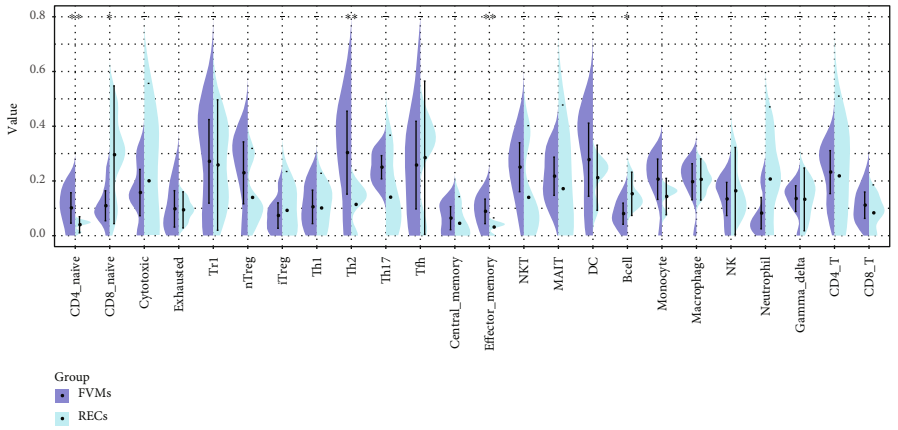

(d)

Figure 4: Continued.

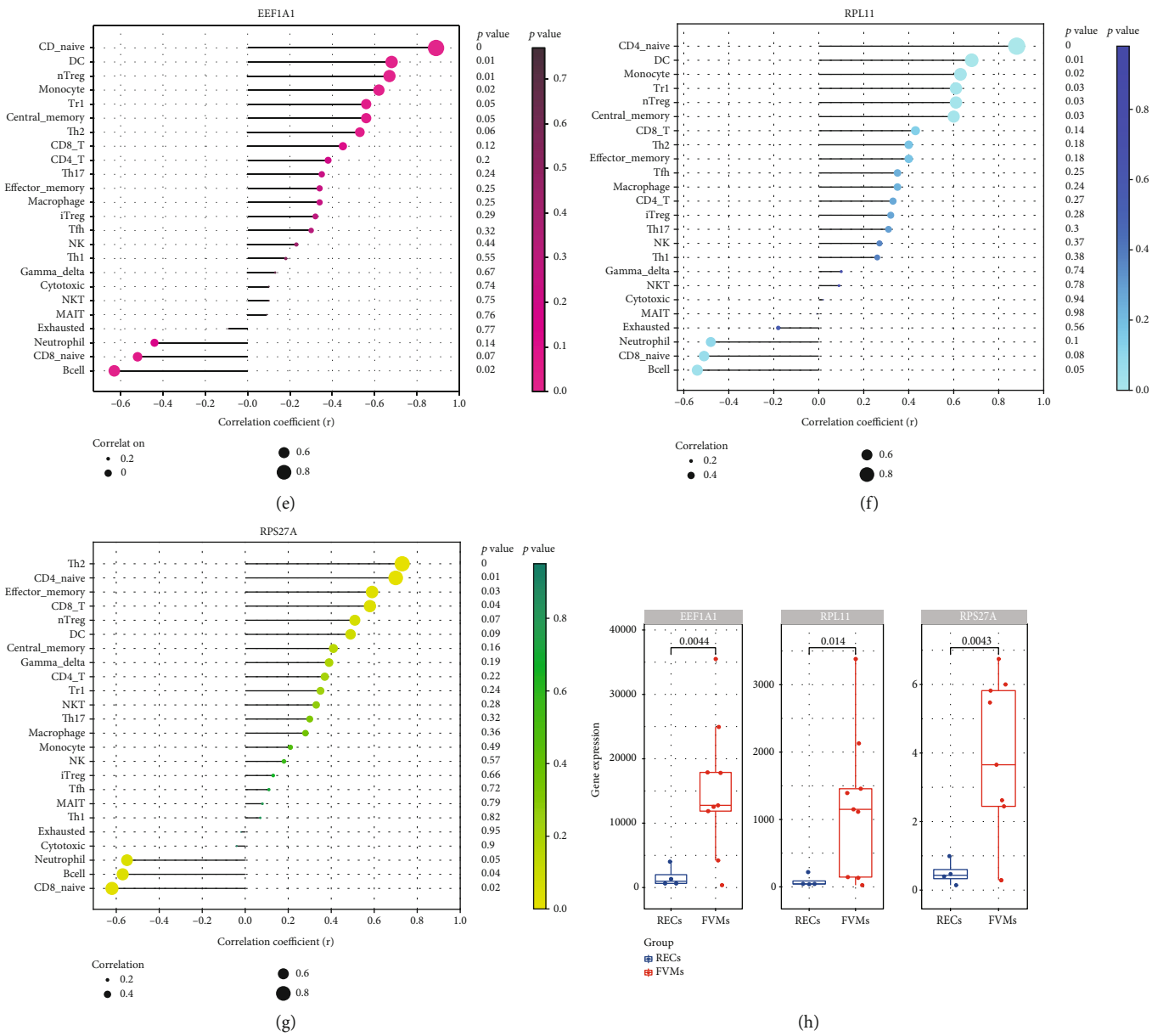

Figure 4: (a, b) Bar plot and heatmap of percentage distribution involved in 24 immune cell infiltrations in all samples. The upper part of the figure revealed the grouping of RECs and FVMs with square bars in different colors. (c) Correlation heatmap of 24 immune cells. The bottom left of the figure depicted the correlation distribution and linear regression between each immune cell subtype and all samples, and the top right described the correlation coefficient value and the value of p (* means $p < 0.05$, ** reveals $p < 0.01$, *** exhibits $p < 0.001$). (d) Bean plot. The distribution discrepancies of 24 kinds of immune cell subtypes between RECs and FVMs are exposed. ** in the figure indicated a significant increase in the FVMs group compared with the RECs group, and * implied a significant increase in the RECs group compared with the FVMs group ($p < 0.05$). (e–g) Lollipop chart. Correlation between the hub genes EEF1A1, RPL11, and RPS27A and 24 kinds of immune cells are, respectively, unshrouded. The size of the dot represented the correlation coefficient between the hub gene and immune cells, and intensity of dot color represents the p value. (h) Box plot. Reflected the grouped expression of hub genes EEF1A1, RPL11, and RPS27A in the samples. The bar at the top of the diagram illustrated the p value of the difference between groups.

Furthermore, three hub genes, the expression of which were considerably more advanced in the FVMs than the RECs group (EEF1A1, $p = 0.0044$; RPL11, $p = 0.014$; RPS27A, $p = 0.0043$) (Figure 4(h)), showed strong and significant positive correlation with CD4 naive, and a similar level of negative correlation with B cells (Figures 4(e)–4(g)). Thus, correlations exist between hub genes EEF1A1, RPL11, RPS27A, and immune cells, as well as between the different immune cell types.

3.6. GSEA Analysis Based on the Expression of Hub Genes. Correlation analysis indicated that hub genes in this study have a strong relevance (Figure 5(a)), so when conducting GSEA analysis, the hub gene expression level was divided into two groups to observe any similarities and differences in the KEGG and GO analysis results under different gene expression levels, and the overlapping results are displayed (Figure 5(b)). GSEA analysis shows that for 47 of the 3

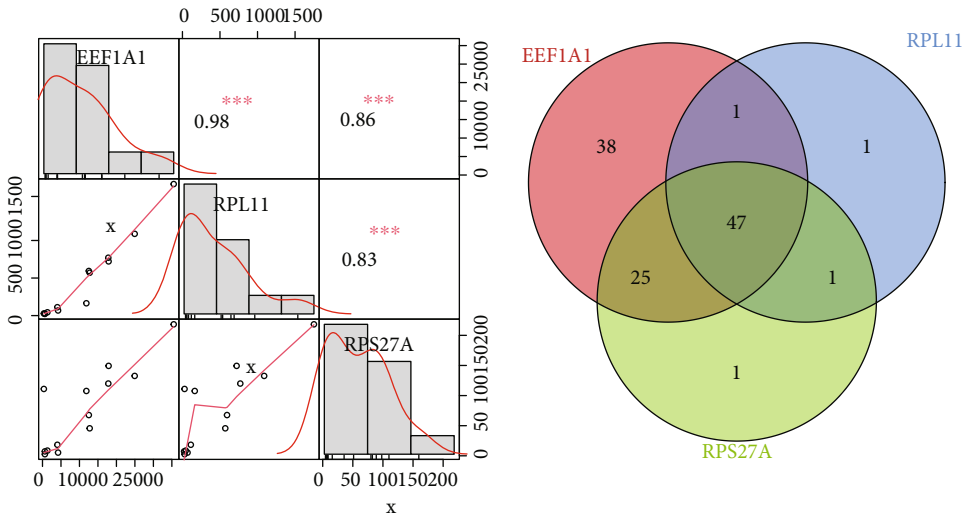

(a) (b)

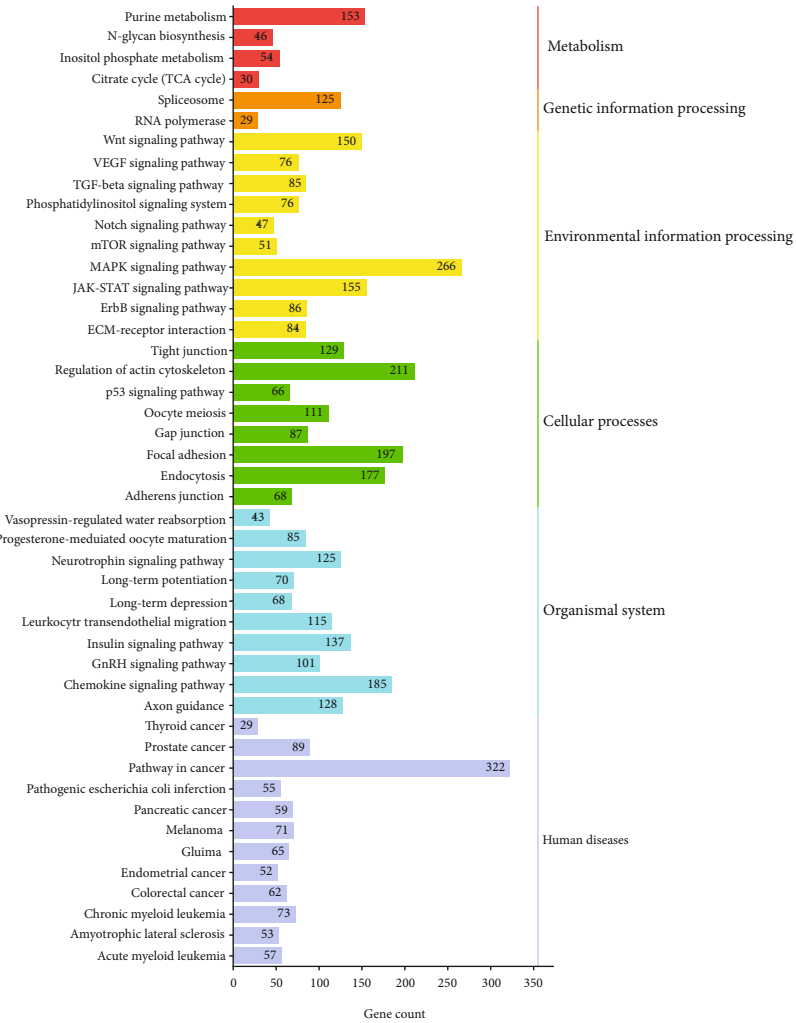

(c)

Figure 5: Continued.

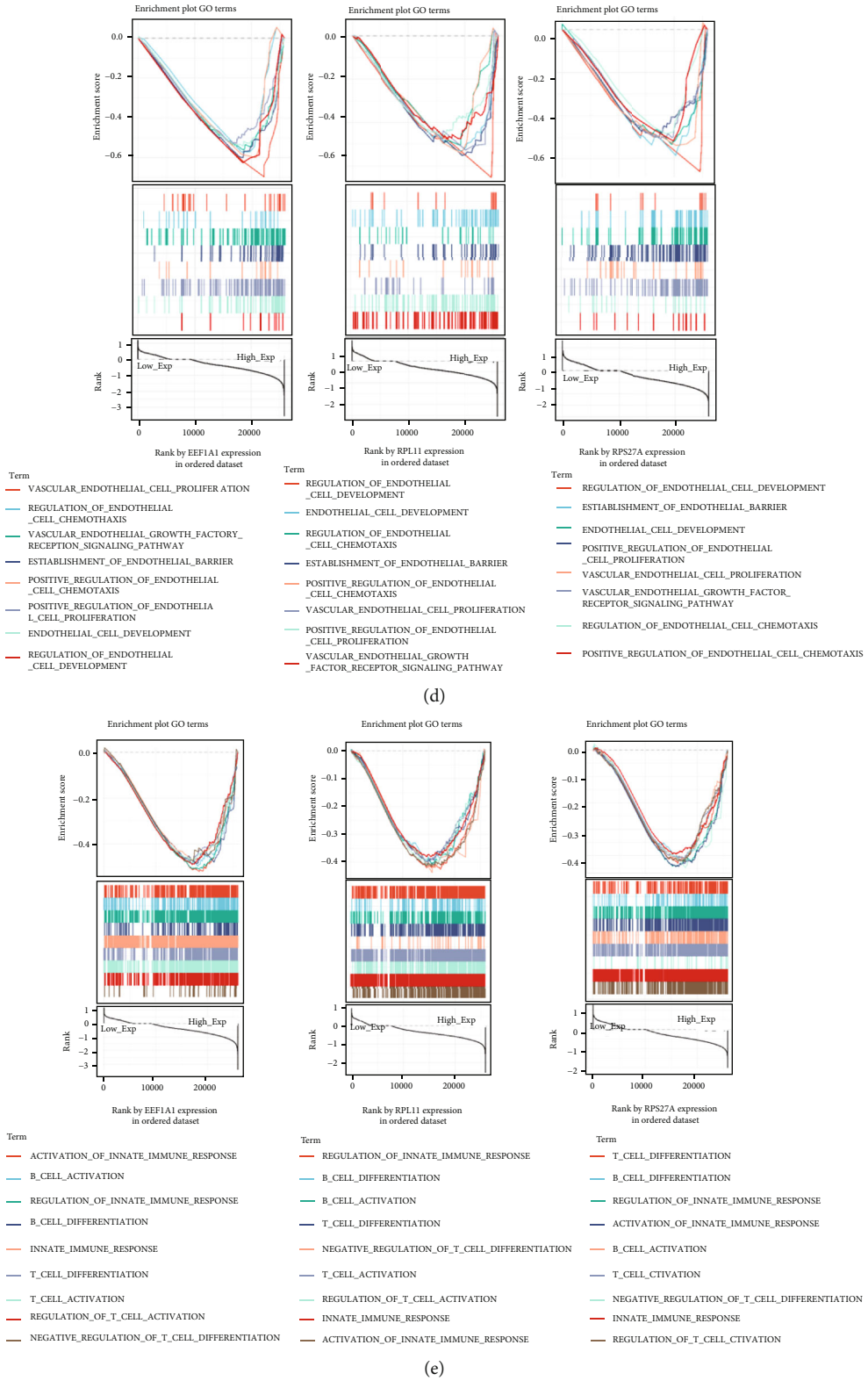

Figure 5: (a) The correlation heatmap of the hub genes EEF1A1, RPL11, and RPS27A. *** means $p < 0.001$. (b) Venn diagram. The intersection of KEGG terms of hub genes EEF1A1, RPL11, and RPS27A was manifested, including 47 common intersection items. (c) KEGG bar graph. The related terms are rearranged and classified according to the six classifications of KEGG pathways, and the length of the bar represented the number of gene count. (d, e) Multiple GSEA plot classified by the amount of hub gene expression. The former illustrated the enrichment of biological process pathways of GO related to endothelial cell phenotypic modifications, while the latter demonstrated the enrichment mode of endothelial cells participating in innate immunity and adaptive immunity.

hub gene KEGG pathways were significantly more enriched in the high expression than low expression group ($p < 0.05$). Based on the KEGG pathway database, 47 important pathways were subdivided into six functional categories (Figure 5(c)). Some key pathways such as TGF-beta signaling, MAPK signaling, JAK-STAT signaling, VEGF signaling, citrate cycle (TCA cycle), and insulin signaling pathways have been indexed from the KEGG disease database to be closely related to diabetic retinopathy. Other pathways such as Wnt signaling, Notch signaling, mTOR signaling, ErbB signaling, ECM-receptor interaction, and GnRH signaling pathways require further research into interaction with the three hub genes. Research on the biological functions of GO analysis using GSEA has found that three hub genes are significantly and highly enriched in endothelial cell development and regulation, positive chemotaxis and regulation, proliferation and positive regulation, establishment of barrier, and VEGF receptor pathways in the high expression group (Figure 5(d)). Similarly, they are also highly enriched in the endothelial cell-related immune response pathways, such as the activation, differentiation, regulation of B cells and T cells, coupled with the activation as well as regulation of innate immune responses (Figure 5(e)).

3.7. Verification of Hub Genes Using GEO Database. The AUC of the training set GSE94019 and the validation set GSE102485 used in this study were both over 0.8, the AUC of the set GSE142025 exceeding 0.9 (Figure 6). These results show that the three hub genes have potential for high differentiation between RECs and FVMs and have good diagnostic value.

4. Discussion

While recent studies increasingly indicate that chronic low-grade inflammation and neurodegeneration of the retina are early manifestations of DR and play a role in its development, microangiopathy remains a dominant factor in this condition [34]. Endothelial dysfunction dominates the pathophysiology of microangiopathy in the diabetic retina and includes leukocyte adhesion, basement membrane thickening and pericyte loss, BRB damage, and neovascularization [35]. An increasing body of evidence illustrates that immune mechanisms are key to DR pathogenesis [34, 36]. Therefore, it is particularly important to fully understand the regulation of neovascularization and immune infiltration of vascular endothelial cells in DR.

Through annotation and functional enrichment analysis of DEGs, we found that DEGs are closely connected with immunoreaction and inflammatory signals, such as the innate immune response involving neutrophils, chemokine signal pathways, protein localization and transport and translation, cell-substrate adhesion, cell-mediated immunity, and apoptosis signaling pathways. During development of DR, increased retinal blood flow, abnormal leukocyte stasis, neutrophil as well as macrophage infiltration, alexine coupled with microglia activation, upregulation of cytokines, elevated vascular permeability and tissue edema, and the pathological manifestations of chronic retinal inflammation have been confirmed in animal models and DR patients [37, 38]. These objective findings are in accordance with the results of GO assay. Similarly, via KEGG analysis, we can clearly see that phagosomes, lysosomes, TNF signaling pathway, AGE-RAGE signaling pathway in diabetic complications, apoptosis, IL-17 signaling pathway, and others are also relevant to the chronic inflammatory pathological process of DR. Some studies have shown that photoreceptor cells are the source of diabetic retinal inflammatory proteins, and the release of soluble mediators can lead to the apoptosis of retinal endothelial cells [39], which is also consistent with the pathways obtained by KEGG.

After a series of complex model constructions and operation verifications, reliable hub genes EEF1A1, RPL11, and RPS27A were obtained. EEF1A1 gene, which encodes the same type of α subunit of complex named elongation factor-1, is responsible for aminoacyl tRNA enzymic transmission to ribosomes. EEF1A1 not only plays the leading role in protein translation prolongation, but also promotes cell growth and proliferation and inhibits apoptosis [40]. Studies have found that it also presides over protein posttranslational modification, protein degradation, and regulation of the cytoskeleton [41–43]. In the present study, the cytoscape plug-in MCODE showed that the gene cluster encoding ribosomal subunits in DEGs has the highest score, far exceeding that of other clusters, and contains 49 genes or their related genes. The RPL11 gene encodes 60s ribosome protein L11, which is an element of the 60s subunit and is related to the L5P ribosome proteins family. The RPS27A gene encodes 40s ribosome protein S27A, which is a constituent of the ribosomal 40s subunit and is a member of the S27AE ribosome protein family. Controlled alterations in ribosomal heterogeneity can upregulate or downregulate specific genetic networks [44]. When ribosomal proteins are reduced or eliminated, ribosomal biosynthesis is reduced or blocked, and in turn, the biosynthesis process is accelerated or increased [45]. The three hub genes identified in the present study are involved in the process of cellular translation including initiation, extension, termination, and posttranslation. They differ significantly between the two groups compared here, so they merit special attention and further investigation in the pathophysiological process of PDR.

Considering the importance of chronic inflammation and leukocyte stasis in the pathogenesis of PDR, ImmuCellAI was used to look for differences in distribution of immune cells between RECs and FVMs groups. The result is partly consistent with the results observed by Obasanmi et al. [46] and El Asrar et al. [47]. The immune cells with significant differences between the two groups are also core immune cells, which correlate strongly with most other immune cells. At or prior to the NPDR stage, one of the early events of diabetic retinal inflammation is leukocyte adhesion to the microvascular system. Increased leukocyte adhesion leads to the loss of endothelial cells and the destruction of the BRB [48, 49]. In the present study, neutrophils associated with vascular endothelial cells were lower in the FVMs group than in the RECs group, while other studies have shown that the level of neutrophils from blood in circumambient circulation was significantly higher in PDR

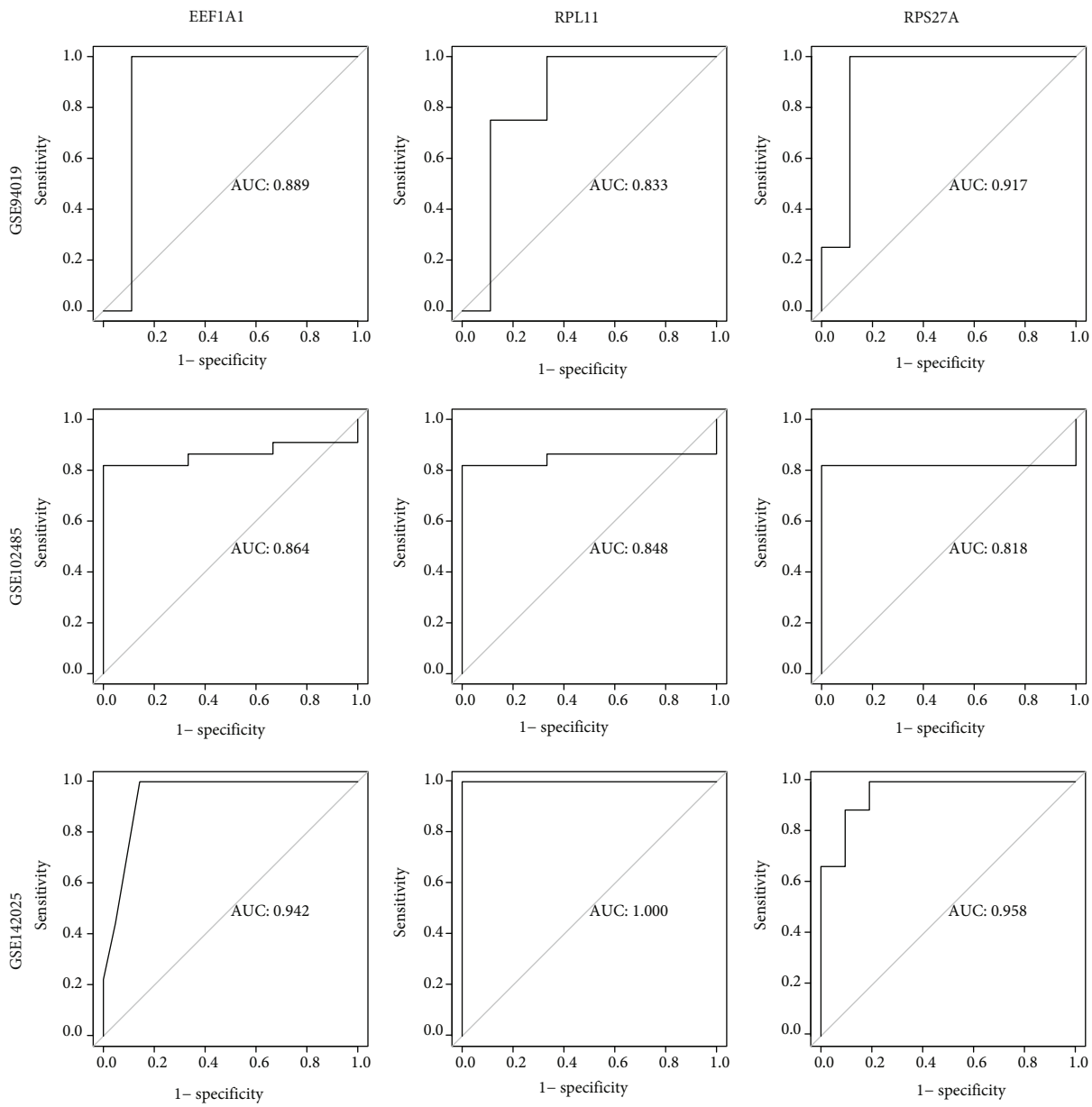

Figure 6: The ROC curve was applied to verify accurateness of hub genes. The corresponding hub gene name was presented at the top of the figure, and the GEO dataset number was manifested on the left side of the figure, where GSE941019 is the training set and GSE102485 and GSE142025 are the verification sets. The AUC of GSE941019 and GSE102485 was both greater than 0.8 and the AUC of GSE142025 was greater than 0.9.

than in a nondiabetic group [46, 50]. It has been demonstrated that the diseased vasculature releases a secretome that attracts neutrophils and triggers the production of neutrophil extracellular traps (NETs), which can clear diseased endothelial cells and reshape unhealthy blood vessels [51, 52]. In the PDR stage, especially in the inactive phase, due to the removal of neutrophils in the earlier stage, the abnormal intraocular endothelial cells were terminated, and the vascular remodeling was completed. The secretome of the abnormal vascular system was decreased, leading to a decrease in NETs, leading in turn to reduced attraction of neutrophils. At this point, the absolute number of vascular endothelial cells decreased, so the degree of neutrophil infiltration around the residual vascular endothelial cells decreased compared with the nondiabetic group. The significant downward regulation of B cells in the FVMs group compared with the RECs group may be due to the fact that most of the samples were in the inactive phase of PDR [53]. However, changes to several T cell subtypes require further investigation due to a lack of previous research data. We also found that correlations between the highly expressed genes EEF1A1, RPL11, RPS27A, and 24 immune cell types as well as the numbers of immune cell subtypes agreed with the differences in immune cell infiltration between the two groups. The above findings indicate that the three hub genes may be involved in the chronic inflammation and immune processes of PDR development.

Pathological retinal neovascularization and proliferation of endothelial cells are important features of PDR. The disorder of retinal metabolism and immune regulation in patients with diabetes induces glial cells to secrete a variety of inflammatory cytokines. Activated inflammatory mediators invoke more chemokines to act directly on endothelial cells through cascade amplification, which can not only participate in the expression of leukocyte recruitment but also be used as angiogenesis inducers of cytokines, chemokines, proinflammatory factors, and other factors [54]. Endothelial cells are affected by cytokines [55]. Upregulated proinflammatory cytokines may directly induce angiogenesis by binding to endothelial cells or indirectly induce angiogenesis by prompting endothelial cells to generate proangiogenic transmitter substances [56, 57]. In DR, retinal inflammation and vascular injury promote and regulate each other, resulting in the destruction of vascular structure and dissolution of the basement membrane, which eventually leads to destruction of the blood-retinal barrier. Endothelial injury induced by high glucose is mainly caused by cytokines released by endothelial cells, especially IL-1 β, TNF-α, and IFN-γ [58]. These cytokines can induce the expression of cytokines IL-8, MCP-1, and VEGF originated from endothelial cells [59]. Retinal ischemia and hypoxia has a strong stimulatory effect on endothelial cells [60]. Hypoxia is the most characteristic factor to promote expression of the VEGF gene [61]. When VEGF-A binds to VEGF-R2, it can promote the proliferation and exudation of vascular endothelial cells [62]. After VEGF-R2 is activated, the processes of tyrosine kinase receptor increases, leading to the activation of a variety of downstream signaling pathways and damage to the internal and external retinal barriers, important pathological mechanisms in the pathogenesis of diabetic macular edema (DME) [63]. In the present study, GSEA grouped by hub gene expression showed that the high-expression groups of three hub genes were highly enriched in biological processes such as the VEGF-R signaling pathway, endothelial cell development, chemotaxis, proliferation, and their respective regulation (chemotaxis and proliferation showed positive regulation). These findings are consistent with the pathological process and phenotypic transformations of endothelial cells in PDR, suggesting that high expression of the three hub genes was closely correlated with endothelial cell dysfunction and pathological alterations.

Our research has some limitations. First, although the study implemented WGCNA combined with Cytoscape software to conduct gene expression profiling on the RNA-seq dataset, the sample size was limited. Second, due to the lack of sufficient clinical information, including disease phenotypes and disease activity status, it was not possible to estimate the relationship between immune cells and disease severity. Thirdly, no in vivo experiments were conducted to verify these results. In future research, a large sample size combined with detailed clinical information is required for classification, and detailed studies of in vivo and in vitro pathogenesis at the molecular biology level will be required to verify our findings.

5. Conclusion

Using comprehensive bioinformatics analysis, we determined the differences in biological function of retinal vascular endothelial cells between PDR patients and normal samples. We found correlations between hub genes, EEF1A1, RPL11, and RPS27A and the immune response and infiltration of chronic inflammation of endothelial cells in PDR, as well as pathophysiological processes such as development, chemotaxis, and proliferation. These outcomes expand knowledge of the molecular mechanisms of endothelial cells in PDR and demonstrate their potential as new therapeutic targets for PDR.

Data Availability

The datasets analyzed during the current study are available in Gene Expression Omnibus (https://www.ncbi.nlm.nih.gov/geo/).

Conflicts of Interest

All authors declare no conflicts of interest.

Acknowledgments

This study was supported by the Key Research and Development Project in Jiangxi Province (nos. 20192BBGL70033 and 20203BBG73058) and the Central Government Guides Local Science and Technology Development Foundation (no. 20211ZDG02003).

References

[1] P. Saeedi, I. Petersohn, P. Salpea et al., "Global and regional diabetes prevalence estimates for 2019 and projections for 2030 and 2045: Results from the International Diabetes Federation Diabetes Atlas, 9th edition," *Diabetes research and clinical practice*, vol. 157, article 107843, 2019.

[2] J. B. Jonas and C. Sabanayagam, *Epidemiology and risk factors for diabetic retinopathy. Diabetic retinopathy and cardiovascular disease*, Karger Publishers, 2019.

[3] P. H. Scanlon, "The contribution of the English NHS Diabetic Eye Screening Programme to reductions in diabetes-related blindness, comparisons within Europe, and future challenges," *Acta Diabetologica*, vol. 58, no. 4, pp. 521–530, 2021.

[4] P. Song, J. Yu, K. Y. Chan, E. Theodoratou, and I. Rudan, "Prevalence, risk factors and burden of diabetic retinopathy in China: a systematic review and meta-analysis," *Journal of global health*, vol. 8, no. 1, 2018.

[5] R. Raman, K. Ramasamy, R. Rajalakshmi, S. Sivaprasad, and S. Natarajan, "Diabetic retinopathy screening guidelines in India: all India Ophthalmological Society diabetic retinopathy task force and Vitreoretinal Society of India Consensus Statement," *Indian Journal of Ophthalmology*, vol. 69, no. 3, p. 678, 2021.

[6] A. P. Marques, J. Ramke, J. Cairns et al., "Global economic productivity losses from vision impairment and blindness," *EClinicalMedicine*, vol. 35, article 100852, 2021.

[7] I. M. Nawaz, S. Rezzola, A. Cancarini et al., "Human vitreous in proliferative diabetic retinopathy: characterization and translational implications," *Progress in retinal and eye research*, vol. 72, article 100756, 2019.

[8] C. J. Flaxel, R. A. Adelman, S. T. Bailey et al., "Diabetic retinopathy preferred practice pattern®," *Ophthalmology*, vol. 127, no. 1, pp. P66–P145, 2020.

[9] Group ETDRSR, "Fundus photographic risk factors for progression of diabetic retinopathy: ETDRS report number 12," *Ophthalmology*, vol. 98, no. 5, pp. 823–833, 1991.

[10] A. Moshfeghi, V. Garmo, D. Sheinson, A. Ghanekar, and I. Abbass, "Five-year patterns of diabetic retinopathy progression in US clinical practice," *Clinical Ophthalmology*, vol. 14, p. 3651, 2020.

[11] Group ETDRSR, "Early photocoagulation for diabetic retinopathy: ETDRS report number 9," *Ophthalmology*, vol. 98, no. 5, pp. 766–785, 1991.

[12] C. C. Wykoff, R. N. Khurana, Q. D. Nguyen et al., "Risk of blindness among patients with diabetes and newly diagnosed diabetic retinopathy," *Diabetes Care*, vol. 44, no. 3, pp. 748–756, 2021.

[13] S. E. Mansour, D. J. Browning, K. Wong, H. W. Flynn Jr., and A. R. Bhavsar, "The evolving treatment of diabetic retinopathy," *Clinical Ophthalmology*, vol. 14, p. 653, 2020.

[14] M. Porta and E. Striglia, "Intravitreal anti-VEGF agents and cardiovascular risk," *Internal and emergency medicine*, vol. 15, no. 2, pp. 199–210, 2020.

[15] G. Giurdanella, G. Lupo, F. Gennuso et al., "Activation of the VEGF-A/ERK/PLA2 axis mediates early retinal endothelial cell damage induced by high glucose: new insight from an in vitro model of diabetic retinopathy," *International Journal of Molecular Sciences*, vol. 21, no. 20, p. 7528, 2020.

[16] T.-T. Wan, X.-F. Li, Y.-M. Sun, Y.-B. Li, and Y. Su, "Recent advances in understanding the biochemical and molecular mechanism of diabetic retinopathy," *Biomedicine & pharmacotherapy*, vol. 74, pp. 145–147, 2015.

[17] U. M. Kinuthia, A. Wolf, and T. Langmann, "Microglia and inflammatory responses in diabetic retinopathy," *Frontiers in Immunology*, vol. 11, 2020.

[18] D. Tao, N. Ni, T. Zhang et al., "Accumulation of advanced glycation end products potentiate human retinal capillary endothelial cells mediated diabetic retinopathy," *Molecular medicine reports*, vol. 20, no. 4, pp. 3719–3727, 2019.

[19] Y. Takeda, K. Matoba, K. Sekiguchi et al., "Endothelial dysfunction in diabetes," *Biomedicines*, vol. 8, no. 7, p. 182, 2020.

[20] H. Sone, B. K. Deo, and A. K. Kumagai, "Enhancement of glucose transport by vascular endothelial growth factor in retinal endothelial cells," *Investigative ophthalmology & visual science*, vol. 41, no. 7, pp. 1876–1884, 2000.

[21] M. R. Hayden, J. R. Sowers, and S. C. Tyagi, "The central role of vascular extracellular matrix and basement membrane remodeling in metabolic syndrome and type 2 diabetes: the matrix preloaded," *Cardiovascular diabetology*, vol. 4, no. 1, pp. 1–20, 2005.

[22] A. S. Bharadwaj, B. Appukuttan, P. A. Wilmarth et al., "Role of the retinal vascular endothelial cell in ocular disease," *Progress in retinal and eye research*, vol. 32, pp. 102–180, 2013.

[23] C. Yang, S. Kelaini, R. Caines, and A. Margariti, "RBPs play important roles in vascular endothelial dysfunction under diabetic conditions," *Frontiers in Physiology*, vol. 9, p. 1310, 2018.

[24] I. Stein, A. Itin, P. Einat, R. Skaliter, Z. Grossman, and E. Keshet, "Translation of vascular endothelial growth factor mRNA by internal ribosome entry: implications for translation under hypoxia," *Molecular and cellular biology*, vol. 18, no. 6, pp. 3112–3119, 1998.

[25] H. Kawano, T. Motoyama, O. Hirashima et al., "Hyperglycemia rapidly suppresses flow-mediated endothelium-dependent vasodilation of brachial artery," *Journal of the American College of Cardiology*, vol. 34, no. 1, pp. 146–154, 1999.

[26] Y. Liu, Z. Yang, P. Lai et al., "Bcl-6-directed follicular helper T cells promote vascular inflammatory injury in diabetic retinopathy," *Theranostics*, vol. 10, no. 9, p. 4250, 2020.

[27] W. W. Pan, F. Lin, and P. E. Fort, "The innate immune system in diabetic retinopathy," *Progress in Retinal and Eye Research*, vol. 100940, 2021.

[28] A. Cantón, E. M. Martinez-Cáceres, C. Hernández, C. Espejo, J. García-Arumí, and R. Simó, "CD4-CD8 and CD28 expression in t cells infiltrating the vitreous fluidin patients with proliferative diabetic retinopathy: a flow cytometric analysis," *Archives of Ophthalmology*, vol. 122, no. 5, pp. 743–749, 2004.

[29] R. Stark, M. Grzelak, and J. Hadfield, "RNA sequencing: the teenage years," *Nature Reviews Genetics*, vol. 20, no. 11, pp. 631–656, 2019.

[30] Y. R. Miao, Q. Zhang, Q. Lei et al., "ImmuCellAI: a unique method for comprehensive T-cell subsets abundance prediction and its application in cancer immunotherapy," *Advanced Science*, vol. 7, no. 7, p. 1902880, 2020.

[31] E. Clough and T. Barrett, "The Gene Expression Omnibus Database," in *Statistical genomics*, pp. 93–110, Springer, 2016.

[32] M. D. Robinson, D. J. McCarthy, and G. K. Smyth, "edgeR: a Bioconductor package for differential expression analysis of digital gene expression data," *Bioinformatics*, vol. 26, no. 1, pp. 139-140, 2010.

[33] J. Reimand, R. Isserlin, V. Voisin et al., "Pathway enrichment analysis and visualization of omics data using g:Profiler, GSEA, Cytoscape and EnrichmentMap," *Nature protocols*, vol. 14, no. 2, pp. 482–517, 2019.

[34] J. V. Forrester, L. Kuffova, and M. Delibegovic, "The role of inflammation in diabetic retinopathy," *Frontiers in Immunology*, vol. 11, 2020.

[35] F. S. Sorrentino, S. Matteini, C. Bonifazzi, A. Sebastiani, and F. Parmeggiani, "Diabetic retinopathy and endothelin system: microangiopathy versus endothelial dysfunction," *Eye*, vol. 32, no. 7, pp. 1157–1163, 2018.

[36] H. Xu and M. Chen, "Diabetic retinopathy and dysregulated innate immunity," *Vision Research*, vol. 139, pp. 39–46, 2017.

[37] S. Vujosevic and R. Simó, "Local and systemic inflammatory biomarkers of diabetic retinopathy: an integrative approach," *Investigative ophthalmology & visual science*, vol. 58, no. 6, p. BIO68-BIO75, 2017.

[38] H. Zhang, L. Liang, R. Huang, P. Wu, and L. He, "Comparison of inflammatory cytokines levels in the aqueous humor with diabetic retinopathy," *International Ophthalmology*, vol. 40, no. 10, pp. 2763–2769, 2020.

[39] D. Tonade, H. Liu, and T. S. Kern, "Photoreceptor cells produce inflammatory mediators that contribute to endothelial cell death in diabetes," *Investigative ophthalmology & visual science*, vol. 57, no. 10, pp. 4264–4271, 2016.

[40] A. Mills and F. Gago, "On the need to tell apart fraternal twins eEF1A1 and eEF1A2, and their respective outfits," *International Journal of Molecular Sciences*, vol. 22, no. 13, p. 6973, 2021.

[41] A. B. Meriin, N. Zaarur, and M. Y. Sherman, "Association of translation factor eEF1A with defective ribosomal products generates a signal for aggresome formation," *Journal of cell science*, vol. 125, no. 11, pp. 2665–2674, 2012.

[42] T. Jank, Y. Belyi, C. Wirth et al., "Protein glutaminylation is a yeast-specific posttranslational modification of elongation factor 1A," *Journal of Biological Chemistry*, vol. 292, no. 39, pp. 16014–16023, 2017.

[43] S. R. Gross and T. G. Kinzy, "Translation elongation factor 1A is essential for regulation of the actin cytoskeleton and cell morphology," *Nature structural & molecular biology*, vol. 12, no. 9, pp. 772–778, 2005.

[44] K. Norris, T. Hopes, and J. L. Aspden, *Ribosome heterogeneity and specialization in development*, no. article e1644, 2021Wiley interdisciplinary reviews: RNA, 2021.

[45] M. Penzo, L. Montanaro, D. Treré, and M. Derenzini, "The ribosome biogenesis—cancer connection," *Cell*, vol. 8, no. 1, p. 55, 2019.

[46] G. Obasanmi, N. Lois, D. Armstrong et al., "Circulating leukocyte alterations and the development/progression of diabetic retinopathy in type 1 diabetic patients-a pilot study," *Current eye research*, vol. 45, no. 9, pp. 1144–1154, 2020.

[47] A. M. A. El Asrar, D. Maimone, P. H. Morse, S. Gregory, and A. T. Reder, "Cytokines in the vitreous of patients with proliferative diabetic retinopathy," *American journal of ophthalmology*, vol. 114, no. 6, pp. 731–736, 1992.

[48] C. G. Fresta, A. Fidilio, G. Caruso et al., "A new human blood–retinal barrier model based on endothelial cells, pericytes, and astrocytes," *International journal of molecular sciences*, vol. 21, no. 5, p. 1636, 2020.

[49] S. S. Joy and K. Siddiqui, "Molecular and pathophysiological mechanisms of diabetic retinopathy in relation to adhesion molecules," *Current diabetes reviews*, vol. 15, no. 5, pp. 363–371, 2019.

[50] R.-t. Wang, J.-r. Zhang, Y. Li, T. Liu, and K.-j. Yu, "Neutrophil–lymphocyte ratio is associated with arterial stiffness in diabetic retinopathy in type 2 diabetes," *Journal of Diabetes and its Complications*, vol. 29, no. 2, pp. 245–249, 2015.

[51] F. Binet, G. Cagnone, S. Crespo-Garcia et al., "Neutrophil extracellular traps target senescent vasculature for tissue remodeling in retinopathy," *Science*, vol. 369, no. 6506, 2020.

[52] L. Wang, X. Zhou, Y. Yin, Y. Mai, D. Wang, and X. Zhang, "Hyperglycemia induces neutrophil extracellular traps formation through an NADPH oxidase-dependent pathway in diabetic retinopathy," *Frontiers in immunology*, vol. 9, p. 3076, 2019.

[53] M. Urbančič, Š. Štunf, A. MilutinovićŽivin, D. Petrovič, and M. GlobočnikPetrovič, "Epiretinal membrane inflammatory cell density might reflect the activity of proliferative diabetic retinopathy," *Investigative ophthalmology & visual science*, vol. 55, no. 12, pp. 8576–8582, 2014.

[54] S. Rangasamy, P. G. McGuire, and A. Das, "Diabetic retinopathy and inflammation: novel therapeutic targets," *Middle East African journal of ophthalmology*, vol. 19, no. 1, p. 52, 2012.

[55] G. J. Mahler, E. J. Farrar, and J. T. Butcher, "Inflammatory cytokines promote mesenchymal transformation in embryonic and adult valve endothelial cells," *Arteriosclerosis, thrombosis, and vascular biology*, vol. 33, no. 1, pp. 121–130, 2013.

[56] R. B. Nahomi, A. Palmer, K. M. Green, P. E. Fort, and R. H. Nagaraj, "Pro-inflammatory cytokines downregulate Hsp27 and cause apoptosis of human retinal capillary endothelial cells," *Biochimica et Biophysica Acta (BBA)-Molecular Basis of Disease*, vol. 1842, no. 2, pp. 164–174, 2014.

[57] J. H. Yun, S. W. Park, K. J. Kim et al., "Endothelial STAT3 activation increases vascular leakage through downregulating tight junction proteins: implications for diabetic retinopathy," *Journal of cellular physiology*, vol. 232, no. 5, pp. 1123–1134, 2017.

[58] K. Harkness, J. Sussman, G. Davies-Jones, J. Greenwood, and M. Woodroofe, "Cytokine regulation of MCP-1 expression in brain and retinal microvascular endothelial cells," *Journal of Neuroimmunology*, vol. 142, no. 1-2, pp. 1–9, 2003.

[59] H. Noma, T. Mimura, K. Yasuda, R. Motohashi, O. Kotake, and M. Shimura, "Aqueous humor levels of soluble vascular endothelial growth factor receptor and inflammatory factors in diabetic macular edema," *Ophthalmologica*, vol. 238, no. 1-2, pp. 81–88, 2017.

[60] Y. Manavski, T. Lucas, S. F. Glaser et al., "Clonal expansion of endothelial cells contributes to ischemia-induced neovascularization," *Circulation research*, vol. 122, no. 5, pp. 670–677, 2018.

[61] E. Alizadeh, P. Mammadzada, and H. André, "The different facades of retinal and choroidal endothelial cells in response to hypoxia," *International journal of molecular sciences*, vol. 19, no. 12, p. 3846, 2018.

[62] Z. Yang, H. Wang, Y. Jiang, and M. E. Hartnett, "VEGFA activates erythropoietin receptor and enhances VEGFR2-mediated pathological angiogenesis," *The American journal of pathology*, vol. 184, no. 4, pp. 1230–1239, 2014.

[63] C. S. Melincovici, A. B. Boşca, S. Şuşman et al., "Vascular endothelial growth factor (VEGF)-key factor in normal and pathological angiogenesis," *Romanian Journal of Morphology and Embryology*, vol. 59, no. 2, pp. 455–467, 2018.

Hindawi
Disease Markers
Volume 2022, Article ID 9404977, 10 pages
https://doi.org/10.1155/2022/9404977

Research Article

Age of Rats Affects the Degree of Retinal Neuroinflammatory Response Induced by High Acute Intraocular Pressure

Shuhan Meng,[1,2,3] **Dan Wen**,[1,2,3] **Jingge Xiao**,[4] **Qianyue Zhang**,[4] **Weizhou Fang**,[1,2,3] **Xiao Xue**,[4] **Tu Hu**,[1,2,3] **and Xiaobo Xia**[1,2,3]

[1]*Eye Center of Xiangya Hospital, Central South University, Changsha, Hunan, China 410008*
[2]*Hunan Key Laboratory of Ophthalmology, Changsha, Hunan, China 410008*
[3]*National Clinical Research Center for Geriatric Disorders, Xiangya Hospital, Central South University, Changsha, Hunan, China 410008*
[4]*Xiangya Medical School, Central South University, Changsha, Hunan, China 410013*

Correspondence should be addressed to Tu Hu; hutu1986@csu.edu.cn and Xiaobo Xia; xbxia21@csu.edu.cn

Received 27 November 2021; Accepted 8 January 2022; Published 29 January 2022

Academic Editor: Liu Jinhui

Purpose. To investigate whether retinal neuroinflammatory response was affected by aging in a rat model of acute glaucoma. *Methods*. Young adult and aged rats were randomly assigned into normal control, 45 mmHg, 60 mmHg, and 90 mmHg groups. Intraocular pressure (IOP) of rats was acutely elevated to 45 mmHg, 60 mmHg, and 90 mmHg, respectively. Three days after high IOP treatment, loss of retinal ganglion cells (RGCs), formation of proinflammatory microglia/macrophages and neurotoxic astrocytes, and deposition of complement C3 in the retina were detected by immunofluorescence. ELISA was used to assess the protein levels of proinflammatory cytokines TNF and IL-1β in the retina. *Results*. Compared with young adult retinae, (1) loss of RGCs was more severe in aged retinae under the same IOP treatment, (2) microglia/macrophages were more prone to adopt proinflammatory phenotype in aged retinae in response to elevated IOP, (3) high IOP treatment induced astrogliosis, formation of neurotoxic astrocytes, and deposition of complement C3 more easily in aged retinae, and (4) aged retinae induced higher levels of proinflammatory cytokines TNF and IL-1β under the same IOP treatment. *Conclusion*. Our data indicated that aging affects the degree of retinal neuroinflammatory response initiated by ocular hypertension, which may contribute to the age-related susceptibility of RGCs to elevated IOP.

1. Introduction

Glaucoma is an age-related neurodegenerative disease and the leading cause of irreversible blindness worldwide [1]. It is marked by the degeneration of retinal ganglion cell (RGC) axons, soma, and synapses [2]. Clinical studies have clearly established that increased intraocular pressure (IOP) is the major risk factor in glaucoma [3]. By now, therapeutic strategy for all types of glaucoma is limited to the reduction of elevated IOP, which does not completely stop the progression of glaucomatous neurodegeneration and visual field defects [4]. Besides IOP, age is another main risk factor of glaucoma [5, 6]. A body of studies has demonstrated that the prevalence of glaucoma increases markedly with advancing age across all populations [1, 7, 8].

Consistent with these findings, we previously identified the existence of the age-related susceptibility of rat retinae to increased IOP [9]. Other reports suggested that age-related mitochondria dysfunction and accumulation of oxidative damage make RGCs more vulnerable to damage in the progression of glaucomatous neurodegeneration [10, 11]. Moreover, chronic exposure of tissue stress (oxidized lipoproteins and free radicals) triggered the low-grade inflammation (parainflammation) in aged retinae [12]. A physiological level of parainflammation was critical for maintaining the retinal homeostasis, but when injuries occurred, dysregulated parainflammation developed into detrimental inflammatory response which exacerbates the glaucomatous neurodegeneration [13]. Similar to other neurodegenerative diseases, resident microglia and astrocytes as

well as infiltrated macrophages participated in the retinal neuroinflammatory response in glaucoma [14]. These immune cells could recognize and respond to various stimuli including glaucoma-related stress and damage-associated molecular patterns (DAMPs) arising from stressed or damaged RGCs [15]. Recent studies have well established that microglia/macrophages and astrocytes can be activated by these stimuli and transform into the proinflammatory/neurotoxic phenotype [16–19]. In glaucoma, these proinflammatory microglia/macrophages and neurotoxic astrocytes produced proinflammatory cytokines (e.g., tumor necrosis factor (TNF), interleukin-1β (IL-1β), IL-6, and IL-12), chemokines (e.g., C-C motif chemokine ligand 2 (CCL2), C-X-C motif chemokine ligand 2 (CXCL2), and CXCL10), complement component (e.g., C1q, C3, and C4), reactive oxygen species (ROS), and nitric oxide (NO) to directly induce RGC death or amplify the retinal neuroinflammatory response [16].

Recent evidence hinted that some microglia and astrocytes lose their ability to maintain homeostasis and adopt a more proinflammatory or "primed" phenotype as a result of the aging process [20–22]. Compared to the resting microglia and astrocytes, these "primed" microglia and astrocytes were more sensitive to inflammatory cues and displayed the more robust inflammatory response, as the higher expression of proinflammatory cytokines/chemokines and complement component [23, 24]. Our previous results showed that high IOP treatment induces the more evident activation of microglia/macrophages (characterized by the more IBA1- (ionized calcium-binding adapter molecule 1-) positive cells and IBA1-positive stained area) in aged retinae than young adult retinae [9]. However, the proinflammatory features of microglia/macrophages have not been identified in this scenario.

In the present study, we detected the formation of proinflammatory microglia/macrophages and neurotoxic astrocytes, deposition of complement C3, and production of proinflammatory cytokines (TNF and IL-1β) in the rat glaucoma model we previously used [9]. These findings raised the possibility that retinal neuroinflammatory response may contribute to the age-related vulnerability of RGCs in glaucoma.

2. Materials and Methods

2.1. Animal and Grouping. Thirty-six young adult (aged 2 months, 200–250 g) and thirty-six aged (aged 15 months, 300-350 g) female Sprague-Dawley rats were supplied from Central South University, Changsha, Hunan Province, People's Republic of China. All rats were housed under controlled environmental conditions on a 12 h light/dark cycle with ad libitum access to food and water. All experiments were approved by the animal ethics committee in the Xiangya Hospital of Central South University. Young adult and aged rats were randomly divided into normal control ($n = 9$; $n = 3$, 6 eyes for retinal whole mounts; $n = 3$, 6 eyes for retinal cross-sections; and $n = 3$, 6 eyes for ELISA test), 45 mmHg ($n = 9$; $n = 3$, 6 eyes for retinal whole mounts; $n = 3$, 6 eyes for retinal cross-sections; and $n = 3$, 6 eyes for ELISA test), 60 mmHg ($n = 9$; $n = 3$, 6 eyes for retinal whole mounts; $n = 3$, 6 eyes for retinal cross-sections; and $n = 3$, 6 eyes for ELISA test), and 90 mmHg ($n = 9$; $n = 3$, 6 eyes for retinal whole mounts; $n = 3$, 6 eyes for retinal cross-sections; and $n = 3$, 6 eyes for ELISA test) groups. IOP of rats in 45 mmHg, 60 mmHg, and 90 mmHg groups was increased acutely to 45 mmHg, 60 mmHg, and 90 mmHg, respectively. All rats were sacrificed with an i.p. overdose of pentobarbital at 3 days after high IOP treatment.

2.2. Acute IOP Model. The animal model was prepared following the reported method [9, 25]. Briefly, under anesthesia of 2% pentobarbital (40 mg/kg), a 30-gauge infusion needle connected to the installation instrument filled with sterile saline was inserted into the anterior chamber of rats. The IOP was raised to 45 mmHg, 60 mmHg, or 90 mmHg for 60 min. After maintenance of 60 min, the 90 mmHg of IOP was decreased through 80 mmHg for 5 min, 70 mmHg for 5 min, 60 mmHg for 5 min, and 30 mmHg for 5 min. For the condition of 45 mmHg and 60 mmHg of IOP, the IOP was directly decreased to 30 mmHg after maintenance of 60 min.

2.3. Retinal Tissue Preparation. After anesthetizing, rats were transcardially perfused with ice-cold 0.9% saline followed by ice-cold 4% paraformaldehyde. The eyeballs were enucleated, and the corneas, lenses, and vitreous bodies were removed. For retinal cross-sections, the remaining eye cups were postfixed overnight in 4% paraformaldehyde at 4°C, placed into 30% sucrose for cryoprotection, and embedded in OCT compound (Tissue-Tek). The 20 μm tissue sections were prepared with a Leica cryostat. For retinal whole mounts, the remaining eye cups were postfixed in 4% paraformaldehyde for 1 h, and the whole retinas were dissected and processed as described previously [26].

For ELISA, rats were transcardiac perfused with ice-cold 0.9% saline. The eyeballs were enucleated and retinae were collected. Then retinae were homogenized by sonication on ice in a digestion buffer containing protease inhibitors (Sigma). The homogenates were treated with centrifugation, protein concentration determination, and denaturation.

2.4. Immunofluorescence. Retinal whole mounts and cross-sections were blocked with PBS containing 5% BSA and 0.3% Triton X-100 for 1 h at room temperature and incubated with primary antibodies diluted in PBS containing 5% BSA and 0.1% Triton X-100 overnight at 4°C (rabbit anti-rat RBPMS (RNA-binding protein with multiple splicing), GeneTex, GTX118619, 1 : 500; rabbit anti-rat IBA1, Wako, 019-19741, 1 : 200; mouse anti-rat CD68, Abcam, ab31630, 1 : 200; mouse anti-rat MHC-II (major histocompatibility complex class II), Abcam, ab23990, 1 : 200; mouse anti-rat GFAP (glial fibrillary acidic protein), Cell Signaling Technology, #3670, 1 : 2000; and rabbit anti-rat C3, Abcam, ab200999, 1 : 200). Then the retinal whole mounts and cross-sections were incubated with secondary antibodies labeled with fluorescent dyes (1 : 1000, Jackson ImmunoResearch) for 2 h at room temperature followed by nuclei staining with DAPI (Vector Laboratories). As negative controls,

an adjacent series of sections were processed in parallel without the primary antibodies.

2.5. Enzyme-Linked Immunosorbent Assay Analysis (ELISA). The levels of secreted TNF and IL-1β in the retinal supernatants were detected by rat TNF (#CSB-E11987r, CUSABIO, China) and IL-1β (#CSB-E08055r, CUSABIO, China) ELISA kits. Briefly, the testing sample and standard sample were added in duplicates to plates precoated with the primary antibody and incubated for 2 h at 37°C. Next, the biotin-labeled secondary antibody was added and incubated for 1 h at 37°C. After incubation, HRP-conjugate reagent was added followed by repeat incubation. Then, tetramethylbenzidine enzyme-substrate (TMB) was added and incubated for 30 min at 37°C. Finally, stop solution was added for stopping the reaction, and the absorbance (OD450) of all BSA Standards and samples were recorded within 5 min.

2.6. Cell Counting and Data Analysis. The central and peripheral regions of the rat retina were defined as previously described [27]. For each retinal whole mount, twelve images from the central and peripheral region of the retina were taken under 20x magnification, respectively, using the Leica DM6000 fluorescence microscope. RBPMS-labeled RGCs in each 20x field were counted. A total RBPMS$^+$ cell number of 12 fields per region were averaged to represent RGC density in the central and peripheral retinae, respectively.

Three sections from each eye for CD68/IBA1, MHC-II/IBA1, and GFAP/C3 double staining were chosen. The proinflammatory microglia/macrophages were defined by colabeling of IBA1 (microglia/macrophages marker) and CD68 (phagocytic marker)/MHC-II (antigen presenting molecular). The neurotoxic astrocytes were defined by colabeling of GFAP (astrocyte marker) and complement C3. Two images from the central region for each retinal cross-section were randomly captured under 40x magnification using the Zeiss LSM780 confocal microscope. The number of CD68$^+$IBA1$^+$ and MHC-II$^+$IBA1$^+$ cells in captured images of the inner retina (including nerve fiber layer, ganglion cell layer, and inner plexiform layer) was blindly counted, respectively. Relative mean gray value and relative positive area of GFAP and C3 staining in the inner retina were measured by ImageJ.

All data were presented as mean ± standard deviation (mean ± SD). Two-way analysis of variance (ANOVA) followed by Tukey's multiple comparisons test was used to assess the statistical significance. Assessments with $p < 0.05$ were considered significant.

3. Results

3.1. The Same High IOP Caused More Serious Loss of RGCs in Aged Retinae than in Young Adult Retinae. Loss of RGCs is the major pathological hallmark of glaucoma [27]. Here, we assessed the RGC loss by counting the number of RBPMS- (a specific marker of RGC in the retina) labeled cells in retinal whole mounts of aged and young adult rats 3 days after IOP treatment of 45 mmHg, 60 mmHg, and 90 mmHg (Figure 1). Two-way ANOVA analysis showed that aging exacerbates the loss of RGCs after IOP treatment ($F(1, 40) = 198.97$, $p < 0.0001$, for central; $F(1, 40) = 110.26$, $p < 0.001$, for peripheral). Moreover, increased IOP also exerted effects on RGC loss ($F(3, 40) = 181.65$, $p < 0.0001$, for central; $F(3, 40) = 84.70$, $p < 0.001$, for peripheral). Compared with the normal aged retinae (Figures 1(e) and 1(m)), the number of RGCs in central and peripheral regions of aged retinae was significant decreased since IOP of 45 mmHg compared with the normal aged retinae (Figures 1(f), 1(h), 1(q), 1(n)–1(p), and 1(r)). However, significant loss of RGCs in central and peripheral retinae of young adult rats could not be detected until at 90 mmHg (Figures 1(d), 1(q), 1(l), and 1(r)). Of note, RGC loss was more evident in aged retinae than young adult retinae at each IOP treatment (Figures 1(q) and 1(r)). These results were consistent with our previous data [9], indicating that aged retinae are more vulnerable to increased IOP compared to young adult retinae.

3.2. Microglia/Macrophages of Aged Retinae Were More Prone to Exhibit Proinflammatory Phenotype than That of Young Adult Retinae after High IOP Treatment. In glaucoma, activated microglia/macrophages could adopt proinflammatory phenotype that contributes to neuronal death by releasing neurotoxic factors [28]. These proinflammatory microglia/macrophages might upregulate CD68, a lysosomal marker indicative of phagocytic activity of microglia/macrophages, and antigen presentation molecule MHC-II [16]. Here, we detected the proinflammatory microglia/macrophages in the inner retina by double immunostaining of IBA1 and CD68/MHC-II (Figure 2). Two-way ANOVA analysis showed that aging significantly increases the number of CD68$^+$IBA1$^+$ and MHC-II$^+$IBA1$^+$ cells 3 days after IOP treatment ($F(1, 40) = 116.72$, $p < 0.001$, for CD68^{+-}IBA1$^+$ cells; $F(1, 40) = 156.89$, $p < 0.001$, for MHC-II$^+$IBA1$^+$ cells). IOP treatment also significantly increased the number of CD68$^+$IBA1$^+$ and MHC-II$^+$IBA1$^+$ cells ($F(3, 40) = 250.13$, $p < 0.001$, for CD68$^+$IBA1$^+$ cells; $F(3, 40) = 190.03$, $p < 0.001$, for MHC-II$^+$IBA1$^+$ cells). The significant increases in CD68$^+$IBA1$^+$ and MHC-II$^+$IBA1$^+$ cells were detected in aged retinae since IOP of 60 mmHg (Figures 2(g), 2(h), 2(q), 2(o), 2(p), and 2(r)) and in young adult retinae at 90 mmHg (Figures 2(d), 2(q), 2(l), and 2(r)). The number of CD68$^+$IBA1$^+$ and MHC-II$^+$IBA1$^+$ cells in aged retinae was significantly higher than that of young adult retina at 60 and 90 mmHg (Figures 2(q) and 2(r)). These findings suggested that increased IOP induces the proinflammatory activation of microglia/macrophages more easily in aged retinae than young adult retinae.

3.3. Aged Retinae Were More Prone to Induce Astrogliosis and C3 Deposition than Young Adult Retinae in Response to Increased IOP. We previously found that no significant difference of astrogliosis (quantified by the relative mean gray value of reactive astrocyte marker GFAP) exists between young adult and aged retinae under the same high IOP treatment [9]. In the present study, we assessed the astrogliosis represented as the relative mean gray value of

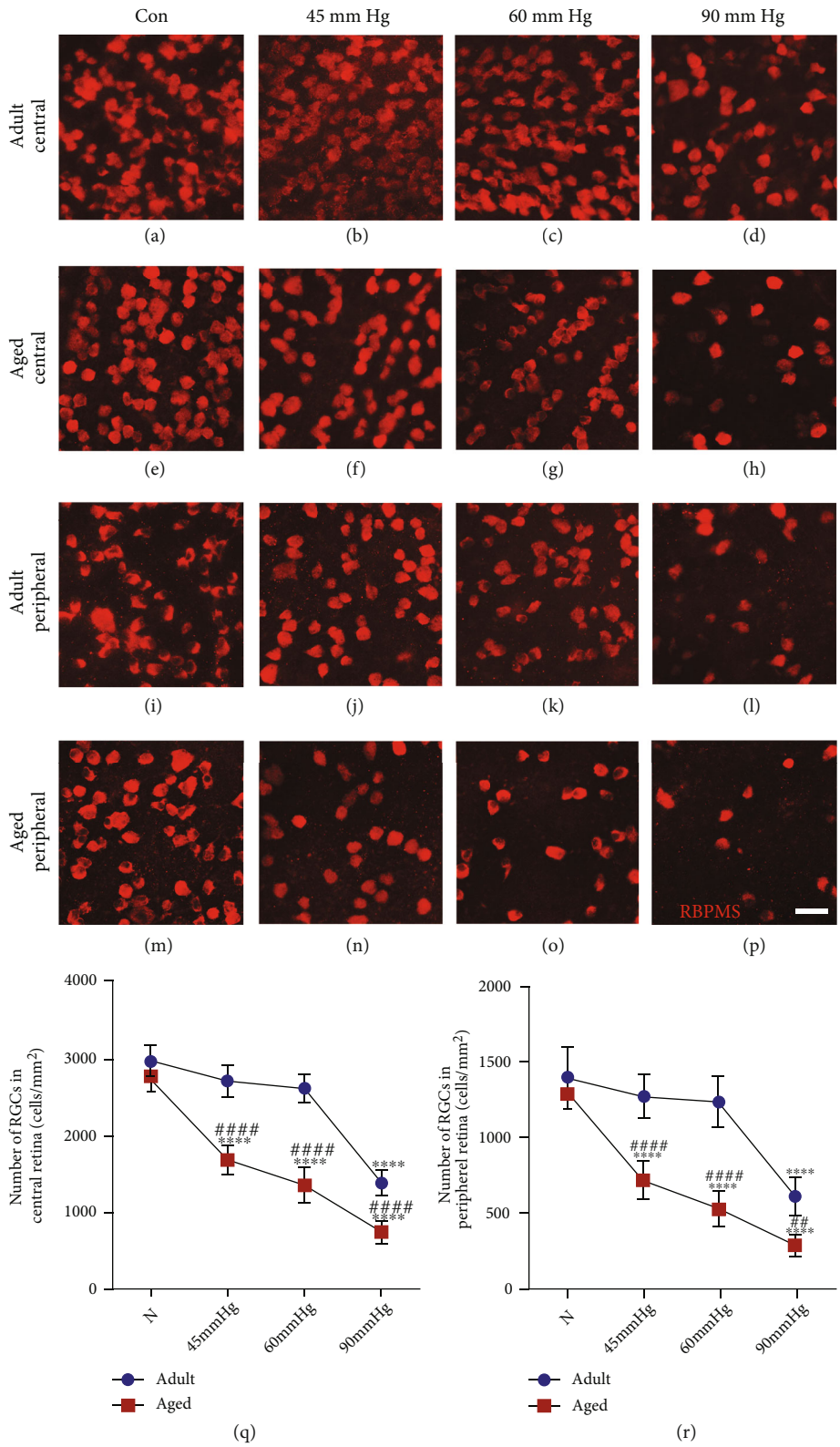

Figure 1: RGCs of aged retinae were more vulnerable to increased IOP than that of young adult retinae. Compared with the age-matched normal control (i, m), IOP treatment of 90 mmHg was sufficient to induce significant loss of RGCs in central (d, q) and peripheral regions (l, r) of young adult retina 3 days after treatment. Since IOP of 45 mmHg, the aged retina showed significant loss of RGCs in central (f–h, q) and peripheral regions (n–p, r). RGC loss in aged retinae was significantly higher than that of young adult retinae at each IOP treatment (q, r) ($^{****}p < 0.0001$ versus age-matched control; $^{\#\#}p < 0.01$, $^{\#\#\#\#}p < 0.0001$ versus matched part of young adult retina at the same IOP treatment. Scale bar: 100 μm).

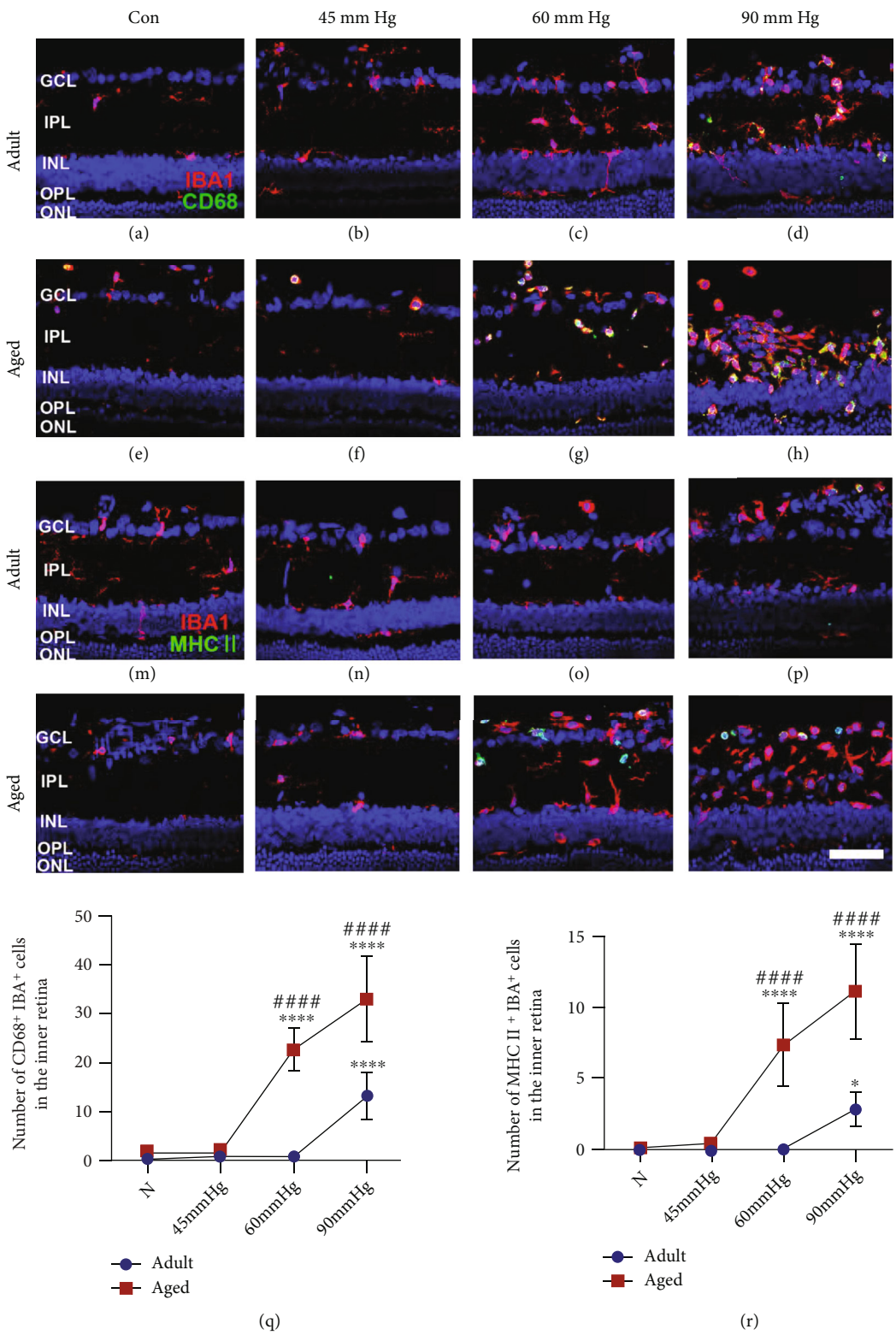

Figure 2: Microglia/macrophages were more prone to exhibit proinflammatory phenotype in aged retinae than that of young adult retinae after IOP treatment. Significant increase in $CD68^{+}IBA1^{+}$ (d, q) and $MHC\text{-}II^{+}IBA1^{+}$ cells (l, r) was observed in young adult retinae at IOP of 90 mmHg. Aged retinae showed dramatic increase in $CD68^{+}IBA1^{+}$ (g–h, q) and $MHC\text{-}II^{+}IBA1^{+}$ cells (o–p, r) since IOP of 60 mmHg. Compared with the young adult retinae, aged retinae induced more $CD68^{+}IBA1^{+}$ (q) and $MHC\text{-}II^{+}IBA1^{+}$ cells (r) at 60 and 90 mmHg 3 days after IOP treatment (GCL: ganglion cell layer; IPL: inner plexiform layer; INL: inner nuclear layer; OPL: outer plexiform layer; ONL: outer nuclear layer. $^{*}p < 0.05$, $^{****}p < 0.0001$ versus age-matched control; $^{\#\#\#\#}p < 0.0001$ versus matched part of young adult retina at the same IOP treatment. Scale bar: 50 μm).

GFAP and relative GFAP$^+$ area in the inner retinae (Figure 3). Two-way ANOVA analysis showed that IOP treatment significantly increases the relative mean gray value of GFAP ($F(3, 40) = 39.64$, $p < 0.0001$). However, aging shows no effects on the relative mean gray value of GFAP in the inner retina after IOP treatment ($F(1, 40) = 0.13$, $p = 0.7213$) (Figure 3). Of note, we found that aging affects the positive staining area of GFAP after IOP treatment ($F(1, 40) = 13.61$, $p = 0.0007$). Moreover, IOP treatment significantly increased the GFAP$^+$ area in the inner retinae ($F(3, 40) = 27.18$, $p < 0.0001$). Significant increase in the GFAP$^+$ area in the young adult retinae was not detected until at IOP of 90 mmHg (Figures 3(a)–3(d), YB). The GFAP$^+$ area in aged retinae was increased since IOP of 60 mmHg (Figures 3(e)–3(h), YB). Additionally, the GFAP$^+$ area in aged retinae was significantly higher than young adult retinae at 60 mmHg (Figure 3, YB). These results suggested that strong astrogliosis is induced more easily in aged retinae than young adult retinae.

Reactive astrocytes might adopt neurotoxic phenotype in glaucoma to drive neurodegenerative process [29]. These neurotoxic astrocytes are marked by the production of complement C3 [30]. Recent studies identified that retinal deposition of C3 contributes to glaucomatous neurodegeneration [31]. We saw the upregulation of C3 within astrocytes in both aged and young adult retinae in response to elevated IOP (Figures 3(q)–3(t) and 3(u)–3(x)). Further, we assessed the C3 deposition in the inner retinae by measurement of the relative mean gray value of C3 and C3$^+$ areas (Figure 3, ZA and ZB). We found that aging affects the relative mean gray value ($F(1, 40) = 11.05$, $p = 0.0019$) and positive staining area ($F(1, 40) = 28.24$, $p < 0.0001$) of C3. In addition, IOP treatment dramatically increased the relative mean gray value ($F(3, 40) = 47.58$, $p < 0.0001$) and positive area ($F(3, 40) = 33.37$, $p < 0.0001$) of C3. We found that the relative mean gray value and positive area of C3 in aged retinae are not different from that of young adult retinae at the normal control (Figures 3(i) and 3(m), ZA and ZB). The increase in the relative mean gray value of C3 was detected in aged retinae since IOP of 45 mmHg, whereas the C3$^+$ area was increased at 60 and 90 mmHg (Figures 3(n)–3(p), ZA and ZB). However, significant increase in the relative mean gray value and C3$^+$ area could not be detected in young adult retinae until at IOP of 90 mmHg (Figure 3(l), ZA and ZB). Moreover, aged retinae showed significantly higher levels of the relative mean gray value of the C3 at 60 mmHg and C3$^+$ area at 60 and 90 mmHg than young adult retinae (Figure 3, ZA and ZB). These results suggested that reactive astrocytes may be more primed to adopt neurotoxic phenotype in aged retinae than in young adult retinae, which is characterized by the higher levels of C3 deposition in the inner part of retinae.

3.4. High IOP Treatment Induced Higher Production of Proinflammatory Cytokines in Aged Retinae than in Young Adult Retinae. Proinflammatory microglia/macrophages and neurotoxic astrocytes produced various proinflammatory cytokines such as TNF and IL-1β to mediate neuroinflammatory response [28, 32]. Here, we detected the protein levels of TNF and IL-1β in rat retinae by ELISA (Figures 4(a) and 4(b)). Two-way ANOVA results suggested that aging seriously affects the TNF and IL-1β protein levels after IOP treatment ($F(1, 40) = 320.48$, $p < 0.0001$, for TNF; $F(1, 40) = 60.71$, $p < 0.0001$, for IL-1β). Moreover, IOP treatment significantly increased the TNF and IL-1β protein levels ($F(3, 40) = 100.43$, $p < 0.0001$, for TNF; $F(3, 40) = 73.58$, $p < 0.0001$, for IL-1β). We saw that TNF protein levels are dramatically increased in aged retinae since IOP of 45 mmHg (Figure 4(a)). The increase in TNF protein levels in young adult retinae could not be detected until at IOP of 90 mmHg (Figure 4(a)). The protein levels of IL-1β in aged retinae were significantly elevated since IOP of 60 mmHg (Figure 4(b)). Young adult retinae showed modest but not statistically significant increase in IL-1β levels at 90 mmHg ($p = 0.3323$) (Figure 4(b)). The protein levels of TNF in aged retinae were significantly higher than that of young adult retinae at each IOP treatment (Figure 4(a)). Aged retinae also showed higher degree of IL-1β protein levels than that of young adult retinae since IOP of 60 mmHg (Figure 4(b)). Collectively, these data indicated that high IOP treatment induces stronger neuroinflammatory response in aged retinae compared to young adult retinae.

4. Discussion

The purpose of this study was to investigate if age of rats affects the retinal neuroinflammatory response in acute rat glaucoma. Here, we demonstrated that compared to young adult retinae, (1) RGCs in aged retinae are more susceptible to acute IOP elevation, (2) microglia/macrophages are more prone to adopt the proinflammatory phenotype in response to IOP elevation in aged retinae, (3) astrogliosis and C3 deposition are induced more easily in aged retinae, and (4) high IOP treatment induces higher levels of proinflammatory cytokines in aged retinae. These results supported that aged retinae induce more severe neuroinflammatory response than young adult retinae in acute glaucoma.

Loss of RGCs was the main pathological hallmark of glaucomatous degeneration [33]. In our previous study, loss of neurons at ganglion cell layer (GCL) after high IOP treatment was measured by counting the number of NeuN$^+$ cells in retinal cross-sections. Here, we quantified the loss of RGCs by counting RBPMS$^+$ (a specific marker of RGC in retina) cells in retinal whole mounts. The results of RGC loss in this study were consistent with the findings we have previously reported [9], which indicates the existence of age-related susceptibility of RGC to elevated IOP.

In glaucoma, microglia/macrophages might transform into "ameboid" morphology and upregulate phagocytosis-associated protein CD68, antigen presentation molecule MHC-II, and other neurotoxic molecules, displaying the proinflammatory and phagocytic phenotypes [34, 35]. In the present study, we saw the upregulation of CD68 and MHC-II in IBA1$^+$ microglia/macrophages of the retina after high IOP treatment. We found that significant increase in CD68$^+$IBA1$^+$ and MHC-II$^+$IBA1$^+$ cells could not be detected in young adult retinae until IOP of 90 mmHg. However,

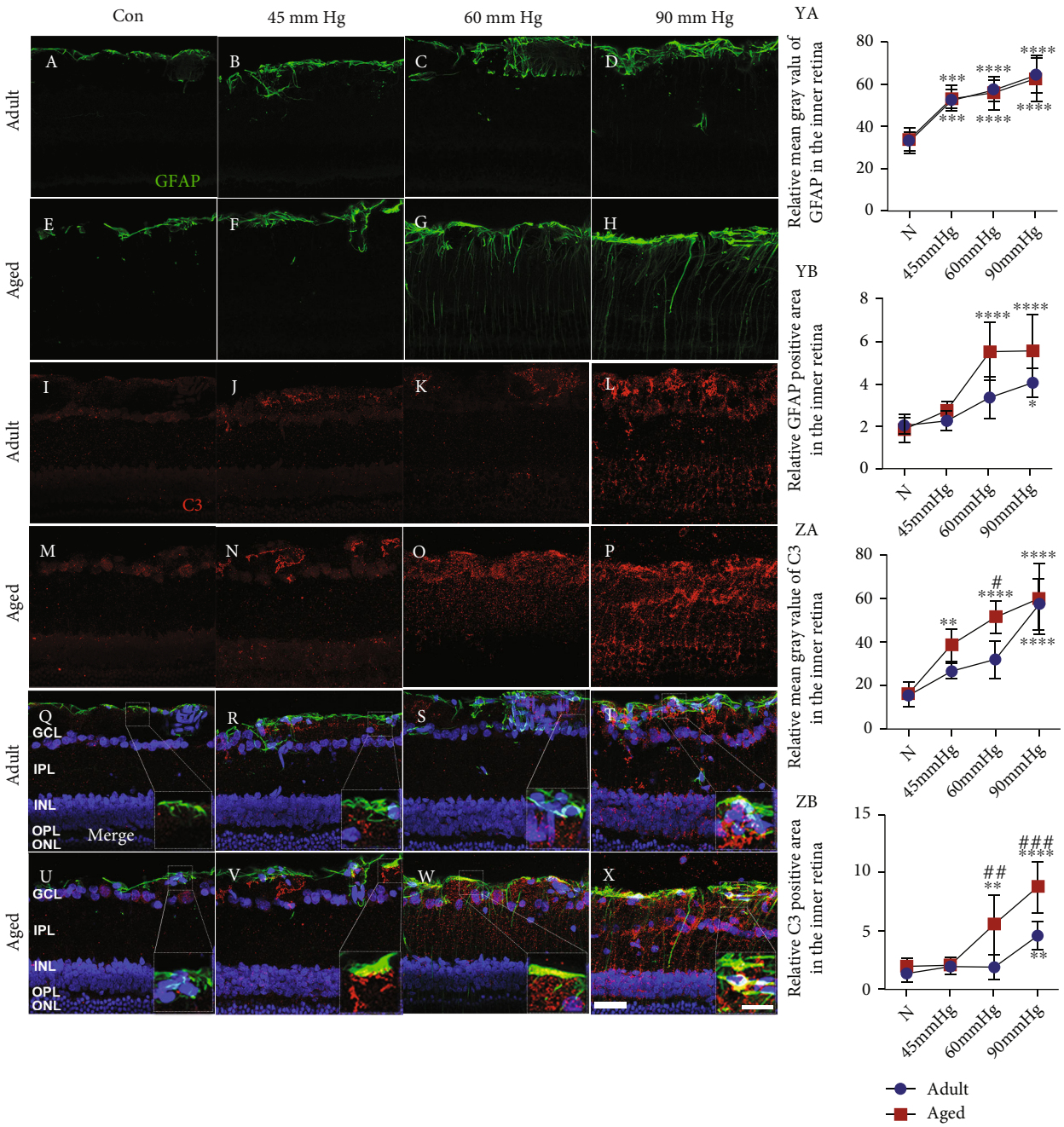

Figure 3: High IOP treatment induced astrogliosis and C3 deposition more easily in aged retinae than in young adult retinae. High IOP treatment induced the increase in GFAP and C3 staining in young adult (a–d, i–l) and aged retinae (e–h, m–p). Merged images showed colocalization (yellow) of C3 and GFAP staining, suggesting the formation of neurotoxic astrocytes in young adult (q–t) and aged retinae (u–x) 3 days after treatment. Quantification of GFAP and C3 expression in the inner retina was presented as the relative mean gray value and relative positive area (YA-YB, ZA-ZB) (GCL: ganglion cell layer; IPL: inner plexiform layer; INL: inner nuclear layer; OPL: outer plexiform layer; ONL: outer nuclear layer. $^{*}p < 0.05$, $^{**}p < 0.01$, $^{***}p < 0.001$, $^{****}p < 0.0001$ versus age-matched control; $^{\#}p < 0.05$, $^{\#\#}p < 0.01$, $^{\#\#\#\#}p < 0.0001$ versus matched part of young adult retina at the same IOP treatment. Scale bar: 50 μm, zoom: 20 μm).

aged retinae increased $CD68^{+}IBA1^{+}$ and $MHC\text{-}II^{+}IBA1^{+}$ cells at 60 mmHg and more as IOP increased. Moreover, the number of $CD68^{+}IBA1^{+}$ and $MHC\text{-}II^{+}IBA1^{+}$ cells in aged retinae was significantly higher than young adult retina at 60 and 90 mmHg. These findings indicated that microglia/macrophages are more prone to adopt proinflammatory phenotype in aged retinae in response to elevated IOP. Recent studies discovered several factors contribute to the age-related proinflammatory changes in retinal microglia, including the altered metabolism and reduced immunoregulatory signaling (e.g., CX3CL1-CX3CR1 and CD200-CD200R signaling) from the retinal neurons [11]. In addition, Tang et al. unraveled that epigenetic modification may induce the aged-related proinflammatory alterations

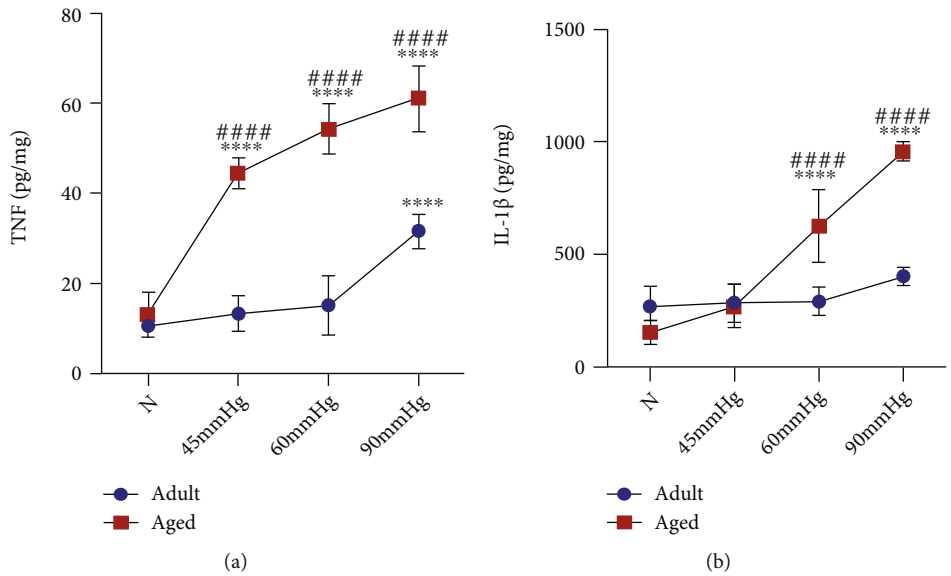

Figure 4: Aged retinae induced higher production of proinflammatory cytokines than young adult retinae after high IOP treatment. TNF levels were significantly increased in young adult retinae at IOP of 90 mmHg and in aged retinae since IOP of 45 mmHg (a). The protein levels of TNF in aged retinae were significantly higher than in young adult retinae at each IOP treatment (a). IL-1β levels were dramatically increased in aged retinae since IOP of 60 mmHg, while no significant increase in IL-1β was detected in young adult retinae after IOP treatment (b). IL-1β production in aged retinae was significantly higher than young adult retinae since IOP of 60 mmHg (b) ($^{****}p < 0.0001$ versus age-matched control; $^{\#\#\#\#}p < 0.0001$ versus matched part of young adult retina at the same IOP treatment).

in microglia [36]. In their reports, decreased expression of histone demethylases Jumonji domain-containing protein 3 (Jmjd3) and increased levels of Tri-methylation lysine 27 of histone H3 (H3K27me3) were detected in the midbrain of aged mice, which is accompanied by the upregulation of proinflammatory microglia markers (TNF, IL-6, and nitric oxide synthase 2 (NOS2)) and downregulation of anti-inflammatory microglia marker Arginase-1 (Arg-1) [36].

Recent studies identified that neurotoxic astrocytes were major effectors to drive glaucomatous neurodegeneration [29, 37]. However, the detailed mechanisms underlying how these neurotoxic astrocytes contribute to the damage of retinal neurons remained unclear. As the specific marker of neurotoxic astrocytes, complement C3 was tightly associated with neuroinflammation [30]. Lian et al. found that astrocyte-released C3 impaired dendritic morphology and network functions of cortical neurons through neuronal C3aR (C3a receptor) [38]. On the other hand, astrocyte-derived C3 could induce the proinflammatory activation of microglia via triggering the microglial C3aR [39]. In the present study, we firstly detected the degree of astrogliosis by immunostaining of reactive astrocyte marker GFAP. We found that high IOP treatment induces the increase in $GFAP^+$ area more easily in aged retinae than in young adult retinae. The obvious GFAP-positive processes in the inner plexiform layer were observed in aged retinae at IOP of 60 mmHg, while the $GFAP^+$ area in young adult retinae was limited to the ganglion cell layer under the same IOP. These findings implied that astrocytes in aged retinae may be more sensitive to increased IOP.

Next, we found upregulation of C3 within astrocytes in both young adult and aged retinae in response to increased IOP, suggesting the formation of neurotoxic astrocytes. Recent studies have identified that C3 contributes to glaucomatous neurodegeneration [31]. Here, we showed higher degree of C3 deposition in aged retinae than in young adult retinae since IOP of 60 mmHg. These findings might provide evidence for the existence of age-related proinflammatory changes in retinal astrocytes. In fact, recent studies unraveled that normal aging can induce the proinflammatory changes of astrocytes in the mouse brain, which is characterized by the upregulation of genes involved in complement, inflammatory cytokines, and antigen presentation pathways [24]. Of note, it was identified that aging-induced proinflammatory changes of astrocytes is mediated by microglia-released inflammatory signal (TNF, IL-1β, and C1q) factors. This indicated that aging-induced alterations of microglia and astrocytes may be a coordinative process [24].

Proinflammatory microglia/macrophages and neurotoxic astrocytes were the main source of proinflammatory cytokines such as TNF and IL-1β in the context of glaucoma [40]. Several studies revealed that TNF/TNF receptor 1 (TNFR1) signaling can directly induce RGC death via proteolytic caspase cascade, mitochondrial dysfunction, and oxidative damage [41–43]. On the other hand, TNF and IL-1β could promote the proinflammatory activation of microglia/macrophages and astrocytes in the autocrine or amacrine manner, which further amplifies the neuroinflammatory response [44]. Thus, we detected the TNF and IL-1β protein levels to evaluate the degree of retinal neuroinflammatory response after different IOP treatments. We found that significant increase in TNF protein levels cannot be detected in young adult retinae until IOP of 90 mmHg. In addition, young adult retinae showed a slight but not

statistically significant increase in IL-1β at 90 mmHg. However, aged retinae upregulate TNF and IL-1β levels at IOP of from 45 to 90 mmHg. Besides, upregulation of TNF and IL-1β in aged retinae was significantly higher than that of young adult retina under the same IOP. These findings indicated that elevated IOP might induce a more severe neuroinflammatory response in aged retinae than young adult retinae.

Taken together, our findings highlighted that aging can seriously affect the degree of retinal neuroinflammatory response in acute rat glaucoma. This might explain the age-related vulnerability of RGCs to increased IOP. Further studies should identify the molecular mechanisms that drive the age-related proinflammatory changes within microglia/macrophages and astrocytes, which may provide the promising target for glaucoma treatment.

Data Availability

The data used to support the findings of this study are available from the corresponding author upon request.

Conflicts of Interest

The authors declare no conflicts of interest.

Acknowledgments

This work was funded by the National Natural Science Foundation of China (No. 81900890, No. 81670858, and No. 81974134), Provincial Natural Science Foundation of Hunan, China (No. 2021JJ40991, No. 2021JJ70147), and China Postdoctoral Science Foundation (No. 2018M643004).

References

[1] H. Quigley and A. Broman, "The number of people with glaucoma worldwide in 2010 and 2020," *The British Journal of Ophthalmology*, vol. 90, no. 3, pp. 262–267, 2006.

[2] S. Syc-Mazurek and R. Libby, "Axon injury signaling and compartmentalized injury response in glaucoma," *Progress in Retinal and Eye Research*, vol. 73, article 100769, 2019.

[3] R. Casson, G. Chidlow, J. Wood, J. Crowston, and I. Goldberg, "Definition of glaucoma: clinical and experimental concepts," *Clinical & Experimental Ophthalmology*, vol. 40, no. 4, pp. 341–349, 2012.

[4] R. Re, D. Messenio, G. Marano et al., "Monitoring the haemodynamic response to visual stimulation in glaucoma patients," *Scientific Reports*, vol. 11, no. 1, p. 13567, 2021.

[5] G. Guedes, J. C. Tsai, and N. A. Loewen, "Glaucoma and aging," *Current Aging Science*, vol. 4, no. 2, pp. 110–117, 2011.

[6] S. Philip, A. Najafi, A. Tantraworasin, L. Pasquale, and R. Ritch, "Nailfold capillaroscopy of resting peripheral blood flow in exfoliation glaucoma and primary open-angle glaucoma," *JAMA Ophthalmology*, vol. 137, no. 6, pp. 618–625, 2019.

[7] P. Dimitrov, B. Mukesh, C. McCarty, and H. Taylor, "Five-year incidence of bilateral cause-specific visual impairment in the Melbourne Visual Impairment Project," *Investigative Ophthalmology & Visual Science*, vol. 44, no. 12, pp. 5075–5081, 2003.

[8] K. Nouri-Mahdavi, D. Hoffman, A. L. Coleman et al., "Predictive factors for glaucomatous visual field progression in the Advanced Glaucoma Intervention Study," *Ophthalmology*, vol. 111, no. 9, pp. 1627–1635, 2004.

[9] C. Tan, T. Hu, M. C. Peng et al., "Age of rats seriously affects the degree of retinal damage induced by acute high intraocular pressure," *Current Eye Research*, vol. 40, no. 3, pp. 300–306, 2015.

[10] Y. Takihara, M. Inatani, K. Eto et al., "In vivo imaging of axonal transport of mitochondria in the diseased and aged mammalian CNS," *Proceedings of the National Academy of Sciences of the United States of America*, vol. 112, no. 33, pp. 10515–10520, 2015.

[11] M. Chen, C. Luo, J. Zhao, G. Devarajan, and H. Xu, "Immune regulation in the aging retina," *Progress in Retinal and Eye Research*, vol. 69, pp. 159–172, 2019.

[12] H. Xu, M. Chen, and J. Forrester, "Para-inflammation in the aging retina," *Progress in Retinal and Eye Research*, vol. 28, no. 5, pp. 348–368, 2009.

[13] C. Baudouin, M. Kolko, S. Melik-Parsadaniantz, and E. Messmer, "Inflammation in glaucoma: from the back to the front of the eye, and beyond," *Progress in Retinal and Eye Research*, vol. 83, article 100916, 2021.

[14] M. Bariş and G. Tezel, "Immunomodulation as a neuroprotective strategy for glaucoma treatment," *Current Ophthalmology Reports*, vol. 7, no. 2, pp. 160–169, 2019.

[15] G. Tezel, "Molecular regulation of neuroinflammation in glaucoma: current knowledge and the ongoing search for new treatment targets," *Progress in Retinal and Eye Research*, no. - article 100998, 2021.

[16] X. Wei, K. Cho, E. Thee, M. Jager, and D. Chen, "Neuroinflammation and microglia in glaucoma: time for a paradigm shift," *Journal of Neuroscience Research*, vol. 97, no. 1, pp. 70–76, 2019.

[17] C. Luo, X. Yang, A. Kain, D. Powell, M. Kuehn, and G. Tezel, "Glaucomatous tissue stress and the regulation of immune response through glial Toll-like receptor signaling," *Investigative Ophthalmology & Visual Science*, vol. 51, no. 11, pp. 5697–5707, 2010.

[18] G. Howell, D. Macalinao, G. Sousa et al., "Molecular clustering identifies complement and endothelin induction as early events in a mouse model of glaucoma," *The Journal of Clinical Investigation*, vol. 121, no. 4, pp. 1429–1444, 2011.

[19] V. Haage, N. Elmadany, L. Roll et al., "Tenascin C regulates multiple microglial functions involving TLR4 signaling and HDAC1," *Brain, Behavior, and Immunity*, vol. 81, pp. 470–483, 2019.

[20] N. Habib, C. McCabe, S. Medina et al., "Disease-associated astrocytes in Alzheimer's disease and aging," *Nature Neuroscience*, vol. 23, no. 6, pp. 701–706, 2020.

[21] S. Krasemann, C. Madore, R. Cialic et al., "The TREM2-APOE pathway drives the transcriptional phenotype of dysfunctional microglia in neurodegenerative diseases," *Immunity*, vol. 47, no. 3, pp. 566–81.e9, 2017.

[22] S. M. O'Neil, K. Witcher, D. McKim, and J. Godbout, "Forced turnover of aged microglia induces an intermediate phenotype but does not rebalance CNS environmental cues driving priming to immune challenge," *Acta Neuropathologica Communications*, vol. 6, no. 1, p. 129, 2018.

[23] S. Patterson, "Immune dysregulation and cognitive vulnerability in the aging brain: Interactions of microglia, IL-1β, BDNF and synaptic plasticity," *Neuropharmacology*, vol. 96, no. Part A, pp. 11–18, 2015.

[24] L. Clarke, S. Liddelow, C. Chakraborty, A. Münch, M. Heiman, and B. Barres, "Normal aging induces A1-like astrocyte reactivity," *Proceedings of the National Academy of Sciences of the United States of America*, vol. 115, no. 8, pp. E1896–E1905, 2018.

[25] C. Dan, T. Jian-Bin, W. Hui et al., "Synaptophysin expression in rat retina following acute high intraocular pressure," *Acta Histochemica et Cytochemica*, vol. 41, no. 6, pp. 173–178, 2008.

[26] A. Triviño, R. De Hoz, J. Salazar, A. Ramírez, B. Rojas, and J. Ramírez, "Distribution and organization of the nerve fiber and ganglion cells of the human choroid," *Anatomy and Embryology*, vol. 205, pp. 417–430, 2002.

[27] T. Hu, S. Wang, L. Zeng, K. Xiong, D. Chen, and J. Huang, "Regional expression of act-MMP3 contributes to the selective loss of neurons in ganglion cell layers following acute retinal ischemia/reperfusion injury," *Current Eye Research*, vol. 45, no. 5, pp. 591–603, 2020.

[28] M. Madeira, R. Boia, P. Santos, A. Ambrósio, and A. Santiago, "Contribution of microglia-mediated neuroinflammation to retinal degenerative diseases," *Mediators of Inflammation*, vol. 2015, Article ID 673090, 15 pages, 2015.

[29] K. Guttenplan, B. Stafford, R. N. el-Danaf et al., "Neurotoxic reactive astrocytes drive neuronal death after retinal injury," *Cell Reports*, vol. 31, no. 12, article 107776, 2020.

[30] S. Liddelow, K. Guttenplan, L. Clarke et al., "Neurotoxic reactive astrocytes are induced by activated microglia," *Nature*, vol. 541, no. 7638, pp. 481–487, 2017.

[31] A. Bosco, S. Anderson, K. Breen et al., "Complement C3-targeted gene therapy restricts onset and progression of neurodegeneration in chronic mouse glaucoma," *Molecular Therapy*, vol. 26, no. 10, pp. 2379–2396, 2018.

[32] G. Tezel, X. Yang, C. Luo, J. Cai, and D. Powell, "An astrocyte-specific proteomic approach to inflammatory responses in experimental rat glaucoma," *Investigative Ophthalmology & Visual Science*, vol. 53, no. 7, pp. 4220–4233, 2012.

[33] Y. Abdul, N. Akhter, and S. Husain, "Delta-opioid agonist SNC-121 protects retinal ganglion cell function in a chronic ocular hypertensive rat model," *Investigative Ophthalmology & Visual Science*, vol. 54, no. 3, pp. 1816–1828, 2013.

[34] F. Walker, M. Nilsson, and K. Jones, "Acute and chronic stress-induced disturbances of microglial plasticity, phenotype and function," *Current Drug Targets*, vol. 14, no. 11, pp. 1262–1276, 2013.

[35] B. Rojas, B. Gallego, A. Ramírez et al., "Microglia in mouse retina contralateral to experimental glaucoma exhibit multiple signs of activation in all retinal layers," *Journal of Neuroinflammation*, vol. 11, no. 1, p. 133, 2014.

[36] Y. Tang, T. Li, J. Li et al., "Jmjd3 is essential for the epigenetic modulation of microglia phenotypes in the immune pathogenesis of Parkinson's disease," *Cell Death and Differentiation*, vol. 21, no. 3, pp. 369–380, 2014.

[37] J. Sterling, M. Adetunji, S. Guttha et al., "GLP-1 receptor agonist NLY01 reduces retinal inflammation and neuron death secondary to ocular hypertension," *Cell Reports*, vol. 33, no. 5, article 108271, 2020.

[38] H. Lian, L. Yang, A. Cole et al., "NFκB-Activated Astroglial Release of Complement C3 Compromises Neuronal Morphology and Function Associated with Alzheimer's Disease," *Neuron*, vol. 85, no. 1, pp. 101–115, 2015.

[39] A. Litvinchuk, Y. Wan, D. Swartzlander et al., "Complement C3aR Inactivation Attenuates Tau Pathology and Reverses an Immune Network Deregulated in Tauopathy Models and Alzheimer's Disease," *Neuron*, vol. 100, no. 6, pp. 1337–1353, 2018.

[40] G. Tezel, L. Li, R. Patil, and M. Wax, "TNF-alpha and TNF-alpha receptor-1 in the retina of normal and glaucomatous eyes," *Investigative Ophthalmology & Visual Science*, vol. 42, no. 8, pp. 1787–1794, 2001.

[41] G. Tezel and M. Wax, "Increased production of tumor necrosis factor-alpha by glial cells exposed to simulated ischemia or elevated hydrostatic pressure induces apoptosis in cocultured retinal ganglion cells," *The Journal of Neuroscience*, vol. 20, no. 23, pp. 8693–8700, 2000.

[42] G. Tezel and X. Yang, "Caspase-independent component of retinal ganglion cell death, in vitro," *Investigative Ophthalmology & Visual Science*, vol. 45, no. 11, pp. 4049–4059, 2004.

[43] X. Yang, C. Luo, J. Cai et al., "Neurodegenerative and inflammatory pathway components linked to TNF-α/TNFR1 signaling in the glaucomatous human retina," *Investigative Ophthalmology & Visual Science*, vol. 52, no. 11, pp. 8442–8454, 2011.

[44] L. Han, D. Zhang, T. Tao et al., "The role of N-glycan modification of TNFR1 in inflammatory microglia activation," *Glycoconjugate Journal*, vol. 32, no. 9, pp. 685–693, 2015.

Hindawi
Disease Markers
Volume 2023, Article ID 9879526, 1 page
https://doi.org/10.1155/2023/9879526

Retraction

Retracted: The Correlation between Functional Connectivity of the Primary Somatosensory Cortex and Cervical Spinal Cord Microstructural Injury in Patients with Cervical Spondylotic Myelopathy

Disease Markers

Received 20 June 2023; Accepted 20 June 2023; Published 21 June 2023

This article has been retracted by Hindawi following an investigation undertaken by the publisher [1]. This investigation has uncovered evidence of one or more of the following indicators of systematic manipulation of the publication process:

(1) Discrepancies in scope

(2) Discrepancies in the description of the research reported

(3) Discrepancies between the availability of data and the research described

(4) Inappropriate citations

(5) Incoherent, meaningless and/or irrelevant content included in the article

(6) Peer-review manipulation

The presence of these indicators undermines our confidence in the integrity of the article's content and we cannot, therefore, vouch for its reliability. Please note that this notice is intended solely to alert readers that the content of this article is unreliable. We have not investigated whether authors were aware of or involved in the systematic manipulation of the publication process.

Wiley and Hindawi regrets that the usual quality checks did not identify these issues before publication and have since put additional measures in place to safeguard research integrity.

We wish to credit our own Research Integrity and Research Publishing teams and anonymous and named external researchers and research integrity experts for contributing to this investigation.

The corresponding author, as the representative of all authors, has been given the opportunity to register their agreement or disagreement to this retraction. We have kept a record of any response received.

References

[1] G. Zhao, C. Zhang, Y. Zhan, and L. He, "The Correlation between Functional Connectivity of the Primary Somatosensory Cortex and Cervical Spinal Cord Microstructural Injury in Patients with Cervical Spondylotic Myelopathy," *Disease Markers*, vol. 2022, Article ID 2623179, 16 pages, 2022.

Hindawi
Disease Markers
Volume 2022, Article ID 2623179, 16 pages
https://doi.org/10.1155/2022/2623179

Research Article

The Correlation between Functional Connectivity of the Primary Somatosensory Cortex and Cervical Spinal Cord Microstructural Injury in Patients with Cervical Spondylotic Myelopathy

Guoshu Zhao, Chenlei Zhang, Yaru Zhan, and Laichang He

First Affiliated Hospital of Nanchang University, Nanchang 330006, China

Correspondence should be addressed to Laichang He; laichang_he@163.com

Received 10 October 2021; Accepted 17 December 2021; Published 19 January 2022

Academic Editor: Ting Su

Objectives. To explore functional connectivity reorganization of the primary somatosensory cortex, the chronic microstructure damage of the cervical spinal cord, and their relationship in cervical spondylotic myelopathy (CSM) patients. *Methods*. Thirty-three patients with CSM and 23 healthy controls (HCs) were recruited for rs-fMRI and cervical spinal cord diffusion tensor imaging (DTI) scans. Six subregions (including leg, back, chest, hand, finger and face) of bilateral primary somatosensory cortex (S1) were selected for seed-based whole-brain functional connectivity (FC). Then, we calculated the apparent diffusion coefficient (ADC) and fractional anisotropy (FA) values of the cervical spinal cord. Correlation analysis was conducted between FC values of brain regions and DTI parameters of cervical spinal cord (ADC, FA), and their relationship with each other and clinical parameters. *Results*. Compared with the HC group, the CSM group showed decreased FC between areas of the left $S1_{hand}$, the left $S1_{leg}$, the right $S1_{chest}$, and the right $S1_{leg}$ with brain regions. The mean FA values of the cervical spinal cord in CSM patients were positively correlated with JOA scores. Especially, the FA_{pos} values of bilateral posterior funiculus were positively correlated with JOA scores. The ADC and FA values of bilateral posterior funiculus in the cervical spinal cord were also positively correlated with the FC values. *Conclusions*. There was synchronization between chronic cervical spinal cord microstructural injury and cerebral cortex sensory function compensatory recombination. DTI parameters of the posterior cervical spinal cord could objectively reflect the degree of cerebral cortex sensory function impairment to a certain extent.

1. Introduction

Cervical spondylotic myelopathy (CSM) is the most common disorder that causes sensory and motor function impairment in the upper and lower limbs [1]. The long-term compression of the cervical spinal cord can cause the degeneration of the anterior horn and motor neurons, even the lateral and posterior funiculus axons demyelination [2]. Since there is an extensive functional and structural coupling between the spinal cord and the somatosensory cortex of the brain, however, the relationship between cervical spinal cord and brain remains unclear.

At present, MRI is the most commonly used imaging examination method to diagnose CSM. Compared with conventional MRI, diffusion tensor imaging (DTI) has higher sensitivity and specificity for the detection of CSM. Particularly, the apparent diffusion coefficient (ADC) and fractional aniostropy (FA) can detect white matter lesions before the high signal of T2 weighted image (T2WI), and FA can be a biomarker for the severity of myelopathy and for subsequent surgical outcome [3]. However, most of the current studies have not taken into account the anatomical factors of the spinal cord, such as the distribution of gray matter and white matter in the spinal cord and the distribution of sensory and motor fibers in the anterior, posterior, and lateral funiculus [4–6]. As a special spinal cord injury, CSM still needs more detailed studies on the cervical spinal cord, especially on DTI of dorsal column tracts (fasciculus gracilis and fasciculus cuneatus).

Recently, functional MRI (fMRI) could be used to assess neurological function and provide information on predicting potential neurological recovery or new experimental

treatment strategies in patients with spinal cord injury [7–9]. A number of neuroimaging studies have clarified cortical reorganization in CSM patients [10–12]. Our previous study found that alterations of intrinsic functional plasticity within the sensorimotor network in CSM patients [13]. Besides, Zhou et al. [14] also analyzed the amplitude of low-frequency fluctuations (ALFF) within sensorimotor network and its association with impaired spinal segment in CSM patients and then found that the increased ALFF values in the right posterior central gyrus was associated with decreased FA values at the C2 level. Besides, Cao et al. [15] found the altered functional topological organization of sensory-motor regions in CSM patients. However, these studies offered some clues of brain functional reorganization in CSM patients, changes in functional connectivity of the posterior central gyrus, namely, the primary somatosensory cortex (S1), and have not been thoroughly explored. Actually, different body surface regions such as the chest, back, hand, finger, face, and leg have corresponding projection areas in S1, which are related to sensory fineness and sensitivity. CSM patients existed sensory disorders, but not all surface parts of the body suffered from sensory disorders. In view of this, the present study divided S1 into six sensory subregions: chest, back, finger, hand, leg, head and face, namely, $S1_{chest}$, $S1_{back}$, $S1_{finger}$, $S1_{hand}$, $S1_{leg}$, $S1_{head}$, and $S1_{face}$ [16–19].

As we all know, the somatosensory cortex of brain can be divided into the primary somatosensory cortex (S1) and the secondary somatosensory cortex (S2). Studies on spinal cord injury have found reduced gray matter volume of S1 [20–22]. Therefore, the reduction of ascending sensory fibers after spinal cord injury causes structural changes in S1. However, it is unclear whether the functional reorganization of S1 caused by sensory impairment in CSM patients is related to the reduction of afferent sensory impulses caused by varying degrees of spinal cord compression.

Based on this, this study is aimed at exploring the changes of cerebral functional connectivity in the primary somatosensory cortex and DTI in cervical spinal cord, as well as their correlation in CSM patients. We intend to (1) perform functional connectivity (FC) analysis by seed-based whole-brain functional connectivity in CSM patients, (2) use the DTI technique to obtain the microstructural parameters of cervical spinal cord, and (3) analyze the correlation between FC values of brain regions and cervical spinal cord DTI parameters, as well as their correlation with clinical scale scores.

2. Methods

This study was approved by the Institutional Review Board of the First Affiliated Hospital of Nanchang University. Written informed consent was obtained from each subject before the study.

2.1. Participants. There were 33 CSM patients (14 males and 19 females; mean age 48.15 ± 7.12 years; disease duration from 24.5 ± 3 months) from the First Affiliated Hospital of Nanchang University and 23 HCs of level-matched age, sex, and education (10 males and 13 females; mean age 46.75 ± 7.65 years; range 30 to 59 years) and were recruited in our study from December 2015 to August 2017. The gold diagnosis standard of CSM [23] is as follows: (1) clinical manifestations of cervical spinal cord injury; (2) radiographically confirmed spinal cord compression; and (3) no amyotrophic lateral sclerosis, intramedullary tumors, secondary adhesion arachnoiditis, multiple peripheral neuritis, or spinal cord injury. Besides, patients should meet these following inclusions: (1) volunteer to enroll in the study; (2) clear evidence of cord compression on a cervical spine MRI, such as an ossified posterior longitudinal ligament, herniated discs, and demyelination with hyperintensity of the cord on T2WI; and (3) no medication therapy or decompression surgery. Exclusion criteria included (1) other neurological disorders such as multiple sclerosis, (2) a history of psychiatric disorders, and (3) claustrophobia or poor cooperation during image scanning. All patients should complete Japanese Orthopaedic Association (JOA) Scores and Neck Disability Index (NDI) assessment [24, 25].

2.2. MRI Data Acquisition. All participants performed 3.0 T MRI (Siemens Trio Tim, Erlangen, Germany) scan with a 4-channel cervical coil and an 8-channel head coil. Before the scan, subjects were asked to stay awake without intense mental activity, close their eyes, and lie comfortably on the examination bed. Sagittal and axial images of the brain and cervical spinal cord were collected, including conventional T1WI, T2WI, and fluid attenuated inversion recovery T2WI. Conventional MR scan was performed to diagnose and exclude brain disorders (such as tumor, cerebral infarction, hemorrhage, encephalomalacia foci) and cervical spinal cord disease (such as multiple sclerosis, amyotrophic lateral sclerosis, and intramedullary tumors). (1) High-resolution anatomic images of brain were acquired by 3D T1-weighted spoiled gradient recall sequence with the following parameters: repetition time (TR) = 1900 ms, echo time (TE) = 2.26 ms, flip angle = 9°, field of view (FOV) = 256 × 256 mm, matrix = 256 × 256, slice thickness = 1 mm, number of slices = 176, voxel size = 1.0 × 1.0 × 1.0 mm^3, and interslice gap = 0.5 mm. (2) Gradient-recalled echo-planar imaging (GRE-EPI) sequence parameters of brain were as followed: TR/TE = 2000 ms/30 ms, flip angle = 90°, FOV = 200 × 200 mm, matrix = 64 × 64, number of slices = 30, slice thickness = 4 mm, interslice gap = 1.2 mm, voxel size = 3.0 × 3.0 × 4.0 mm^3, and 240 time points (8 min 6 s). (3) C1-C7 cervical spinal cord DTI parameters were acquired by single-shot spin echo echo-planar image (SS-SE-EPI): TR = 5000 ms, TE = 111 ms, FOV = 109 × 109 mm, number of excitations (NEX) = 2, matrix = 128 × 124, slice thickness = 7 mm, voxel size = 0.7 × 0.7 × 7 mm, and diffusion encoding occurred in 20 noncollinear and noncoplanar diffusion directions, with $b = 600\ s/mm^2$.

2.3. Data Preprocessing. The brain fMRI preprocessing was performed by Data Processing Assistant for Resting-State 5.0 (DPABI, http://www.restfmri.net) [26]. The procedures included (1) removal of the first 10 time points; (2) slice timing and head motion correction; (3) coregistration of

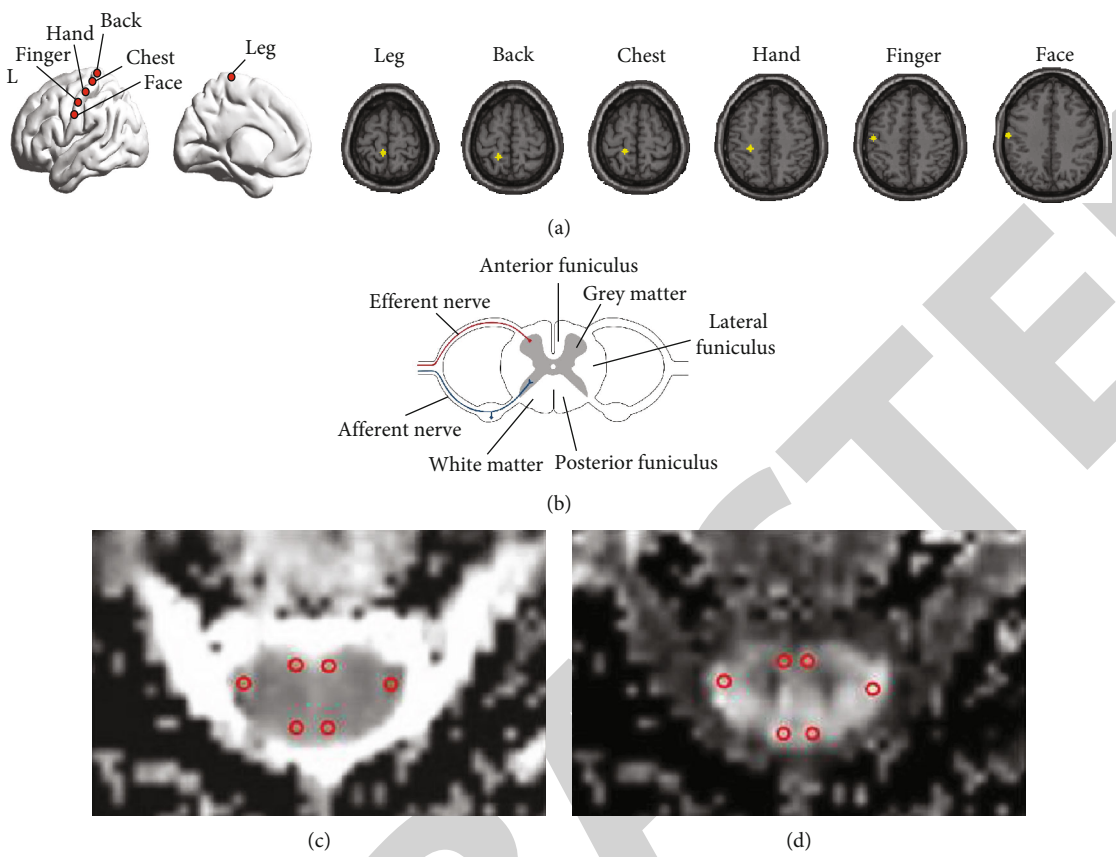

Figure 1: (a) ROI diagram of primary sensory cortex: according to the projection characteristics of sensory fibers, the posterior central gyrus was divided into different parts of the body surface. (b) Sketch of spinal cord anatomy. ROIs were manually selected on ADC (c) and FA (d) images, and 6 ROIs were selected at each segment and placed on the left and right anterior, posterior, and lateral funiculus, respectively.

functional data to the structural T1-weighted image and normalization into the Montreal Neurological Institute (MNI) space with a resampling voxel size of $3\,\text{mm} \times 3\,\text{mm} \times 3\,\text{mm}^3$; (4) removal of linear trends and nuisance covariate regression (cerebrospinal fluid signals, white matter signals, and Friston-24 head motion parameters); (5) band-pass filtering (0.01~0.08 Hz) to reduce the impact of physiological noises such as heartbeat and breathing rhythm; and (6) smooth (6 mm full-width half-maximum Gaussian Kernel).

2.4. Seed-Based Whole-Brain Functional Connectivity and Statistical Analysis. We divided each side of S1 into 6 subregions (chest, back, hand, finger, face, and leg) according to references [16–19]. According to the MNI coordinates of above six subregions of bilateral S1, 12 spherical regions of interest (ROIs) with radius of 4 mm were made (Figure 1(a)). The MNI coordinates were as follows: the face (±60, -14, 40), chest (±18, -36, 64), back (±18, -44, 64), hand (±28, -30, 50), and finger (±50, -16, 50). Then, we extracted the average fMRI signal of the above ROIs and further calculated Pearson's correlation coefficients with the whole brain. FC map was constructed, and then Fisher Z transformation was performed on the correlation coefficients to conform to the normal distribution. Finally, the two-sample t-test was used to compare the FC map between CSM group and HC group (FDR correction with $p < 0.05$, cluster voxel ≥ 10).

2.5. Processing of Cervical Spinal Cord DTI Parameters. After DTI scanning, the original data of cervical spinal cord DTI were transmitted to the postprocessing workstation of Siemens to automatically generate ADC, FA values, and FA color images. Image registration was carried out for each parameter image, and ROIs were manually selected on ADC and FA images. Six ROIs were selected for each segment and placed on the cervical spinal cord, respectively (Figures 1(b)–1(d)), with an area of 3mm^2. Cerebrospinal fluid, central canal, and gray matter were avoided, and ADC and FA values were directly measured. In the CSM group, ROIs were placed on the main compression level segments for measurement (for multisegment compression, the segment with the most obvious compression was selected) and calculated the average values of measured 6 ROI values. The total mean value of 6 ROI represented in the whole section of spinal cord, and the ROIs of posterior funiculus were calculated separately. In the HC group, the ROI was placed on each segment from C2/3 to C6/7 cross-section, and the total mean value of each segment was calculated. The data were measured twice by two researchers, and their average values were final taken. The intraclass correlation coefficient was used to test intra observer and interobserver

Table 1: Demographic and clinical characteristics of the subjects.

Clinical variables	CSM ($n = 33$)	HC ($n = 23$)	p value
Age	48.15 ± 7.12[a]	46.57 ± 7.656[a]	0.43[c]
Gender (%)			
Male	14	10	0.938[d]
Female	19	13	
Duration of symptoms (month)	24.4 ± 3[a]	NA	—
NDI scores (%)	27.64 ± 15.350[a]	NA	—
JOA scores	12.24 ± 2.077[a]	NA	—
Motor function	6 (4, 6)[b]	NA	—
Upper limb movement	3 (2, 3)[b]	NA	—
Lower limb movement	3 (2, 3)[b]	NA	—
Sensory function	4 (3, 4)[b]	NA	—
Upper limb sensation	1 (1, 1)[b]	NA	—
Lower limb sensation	1 (1, 2)[b]	NA	—
Trunk sensation	2 (1, 2)[b]	NA	—

Abbreviations: CSM: cervical spondylotic myelopathy; HC: healthy control; NDI: Neck Disability Index; JOA: Japanese Orthopedic Association; [a]the measurement data conforming to normal distribution, expressed as mean ± standard deviation; [b]the measurement data that did not conform to normal distribution, expressed as median (interquartile spacing); [c]the p value obtained by the two-sample t-test; [d]the p value obtained by χ^2 test.

consistency. SPSS 24.0 software (IBM) was used for statistical analysis, and the Kolmogorov-smirnov test was used to test the normality of ADC and FA values. ADC and FA values were expressed as mean ± standard deviation. The ADC and FA values of different cervical spinal cord segments in the HC group were compared by one-way ANOVA, and least significant difference test (LSD test) was used for pairwise comparison. The two-sample t-test was used to compare the ADC and FA values of cervical spinal cord between the CSM group and the HC group, and $p < 0.05$ was considered statistically significant.

2.6. Clinical Correlation Statistical Analysis. The SPSS 24.0 software (IBM) was used for statistical analysis, and the Kolmogorov-Smirnov test was used to test the normality of continuous quantitative data such as age and clinical scores. The difference in categorical variables between groups was tested and compared using a chi-squared test, while that between continuous variables was evaluated using a two-sample t-test. FC values of abnormal brain regions were extracted by ROI Signal Extractor of DPABI. Then, SPSS 24.0 software was used to analyze the correlation between FC values and JOA scores (including motor function and sensory function) and NDI scores (Pearson correlation or Spearman correlation analysis). Pearson correlation or Spearman correlation analysis was used to analyze the correlation between mean ADC and mean FA values of cervical spinal cord, ADC_{pos} and FA_{pos} values of posterior funiculus and JOA scores (including motor function of upper limbs and lower limbs, sensory function of upper limbs, lower limbs, and trunk), and NDI scores in the CSM group.

2.7. Correlation Analysis between FC Values of Brain Regions and DTI Parameters of the Cervical Spinal Cord. Pearson correlation analysis was performed to analyze the correlation between FC values of brain regions extracted by DPABI and mean ADC, mean FA, ADC_{pos}, and FA_{pos} values.

3. Results

3.1. Demographics and Clinical Characteristics. There was no significant difference in sex and age between CSM patients and HCs. CSM patients had a mean symptom duration of 24.5 ± 3 months, mean JOA score of 12.24 ± 2.007, and mean NDI score of 27.64 ± 15.350 (Table 1).

3.2. Analysis of Functional Connectivity Based on Bilateral Primary Somatosensory Cortex (S1). We used the seed-based correlation analysis to construct the whole brain FC maps of CSM and HC group with each sensory subregion of bilateral S1 as ROIs (SFigure 1-6). The main brain regions were as follows: (1) bilateral postcentral; (2) bilateral frontal lobe, which were consisted of precentral gyrus (PreCG), superior frontal gyrus (SFG), middle frontal gyrus (MFG), and inferior frontal gyrus (IFG); (3) bilateral temporal lobe, which were consisted of superior temporal gyrus (STG), middle temporal gyrus (MTG), and inferior temporal gyrus (ITG); (4) bilateral parietal lobe, which were consisted of superior parietal lobule (SPG) and inferior parietal lobule (IPG); (5) bilateral occipital lobe, which were consisted of inferior occipital gyrus (IFG); (6) limbic system, which were consisted of hippocampus (HIP) and parahippocampal gyrus (PHG), anterior cingulate gyrus (ACG) and posterior cingulate gyrus (PCG), and bilateral insular (INS); (7) bilateral cerebellar posterior lobe; and (8) right rolandic operculum (ROL). Single sample t-test was performed for both groups ($p < 0.001$, FDR corrected). The spatial distribution of FC maps in two groups was similar.

3.2.1. Comparison of Functional Connectivity between the CSM Group and HC Group. Compared with the HC group,

Table 2: Regions showing abnormal FC of S1 in CSM patients as compared with HC.

S1 ROIs	Brain regions	BA	MNI coordinates			Cluster size (voxels)	Peak T-scores
			X	Y	Z		
Left S_{hand}	Left ANG	39	-51	-66	39	31	-4.8343
	Left ITG	20	-60	-39	-21	20	-5.2222
	Right MTG	21	69	-39	-6	16	-4.6923
Left S_{leg}	Left ANG	39	-42	-60	24	14	-4.3113
Right S_{chest}	Left ANG	39	-45	60	24	163	-5.4478
	Left SFG	11	-24	48	-9	50	-4.7124
	Left SFGmed	32	-9	21	42	14	-3.9029
	Left MFG	6	-36	6	60	34	-4.7087
	Left MTG	20	-60	-39	-21	27	-4.3648
	Right ANG	40	45	-57	30	20	-3.6271
	Right SFG	8	18	27	54	22	-4.4711
	Right cerebellar posterior lobe	_	42	-60	-39	59	-4.5236
Right S_{leg}	Left ANG	39	-42	-60	24	20	-4.3852

Abbreviations: ROI: regions of interest; BA: Brodmann area; MNI: Montreal Neurological Institute space; T-scores: positive value represents enhanced functional connection, and negative value represents reduced functional connection ($p < 0.05$, FDR corrected). ANG: angular gyrus; ITG: inferior temporal gyrus; MTG: middle temporal gyrus; SFG: superior frontal gyrus; SFGmed: superior frontal gyrus, medial; MFG : middle frontal gyrus.

CSM patients showed (1) reduced FC between the left $S1_{hand}$ and left angular gyrus (ANG), left STG, and right MTG; (2) reduced FC between the left $S1_{leg}$ and left ANG; (3) reduced FC between the right $S1_{chest}$ and left ANG, left SFG/MFG, left superior frontal gyrus, medial (SFGmed), left MTG/IFG, right ANG, right SFG, and right cerebellar posterior lobe; and (4) reduced FC between the right $S1_{leg}$ and left ANG ($p < 0.05$, FDR corrected, Table 2, Figure 2). However, there was no significant difference between the bilateral $S1_{finger}$, bilateral $S1_{back}$, bilateral $S1_{head}$, left $S1_{chest}$, right $S1_{hand}$, and the whole brain after FDR correction.

3.2.2. Correlation Analysis of FC Value and Clinical Parameters in the CSM Group. Normality test confirmed that FC values of abnormal brain regions in S1 sensory subareas, JOA scores, and NDI scores of CSM patients showed normal distribution. Pearson's test was used to analyze the correlation between FC values and JOA scores, FC values, and NDI scores of CSM patients separately. The results showed that the FC value between the left $S1_{hand}$ and left ANG was negatively correlated with NDI score ($r = -0.377$, $p = 0.031$) (Table 3, Figure 3). The JOA scores of motor function, upper limbs movement, lower limbs movement, sensory function, upper limbs sensation, lower limbs sensation, and trunk sensation of CSM patients did not conform to normal distribution. Therefore, the Spearman test was used to analyze the correlation between FC values and JOA scores (motor function, upper limbs movement, lower limbs movement, sensory function, upper limbs sensation, lower limbs sensation, and trunk sensation), FC values, and NDI scores of CSM patients separately. The results showed that the FC value between the left $S1_{hand}$ and left ITG was positively correlated with JOA score of upper limbs sensation ($r = 0.353$, $p = 0.044$) (Table 3, Figure 3). The results showed that the FC value between the right $S1_{leg}$ and left ANG was positively correlated with JOA score of lower limb sensation ($r = 0.406$, $p = 0.019$) (Table 3, Figure 3).

3.3. DTI Analysis of the Cervical Spinal Cord

3.3.1. Comparison of ADC Value and FA Value in the HC Group and CSM Group. The intraclass correlation coefficient of the DTI data showed good levels of reliability (ADC: ICC = 0.826, $p < 0.001$; FA: ICC = 0.924, $p < 0.001$). ADC values and FA values at C2/3 to C6/7 level of cervical spinal cord in the HC group were shown in supplemental materials (STable 1). From C2/3 to C6/7, ADC values increased, while FA values decreased (ADC: $F = 19.471$, $p \leq 0.001$; FA: $F = 38.710$, $p \leq 0.001$) (supplemental materials, SFigure 7). The ADC values of C2/3 were significantly lower than those of C3/4, C4/5, C5/6, and C6/7. The ADC values of C3/4 were significantly lower than those of C5/6 and C6/7. The ADC values of C4/5 and C5/6 were significantly lower than those of C6/7 ($p < 0.05$). However, the FA values of C2/3 were significantly higher than those of C3/4, C4/5, C5/6 and C6/7. The FA values of C3/4 were significantly higher than those of C4/5, C5/6, and C6/7. The FA values of C4/5 and C5/6 were significantly higher than those of C6/7 ($p < 0.05$). There were no significant differences in ADC values and FA values between C4/5 and C5/6 levels ($p > 0.05$) (supplemental materials, STable 2). Since there was no significant difference at C4/5 and C5/6 levels in the HC group, and about 81.82% (27/33) of patients in the CSM group had the most obvious cervical spinal cord compression at C4/5 and C5/6 levels, the average values of ADC and FA of C4/5 and C5/6 levels in the HC group were taken as the final reference.

The comparison of ADC and FA values of cervical spinal cord in the CSM and HC groups was shown in supplemental materials, STable 3. Compared with the HC group, the ADC values of the CSM group increased, while the FA values decreased.

3.3.2. Correlation Analysis of Mean ADC Value, Mean FA Value, ADC_{pos} Value, FA_{pos} Value, and Clinical Parameters

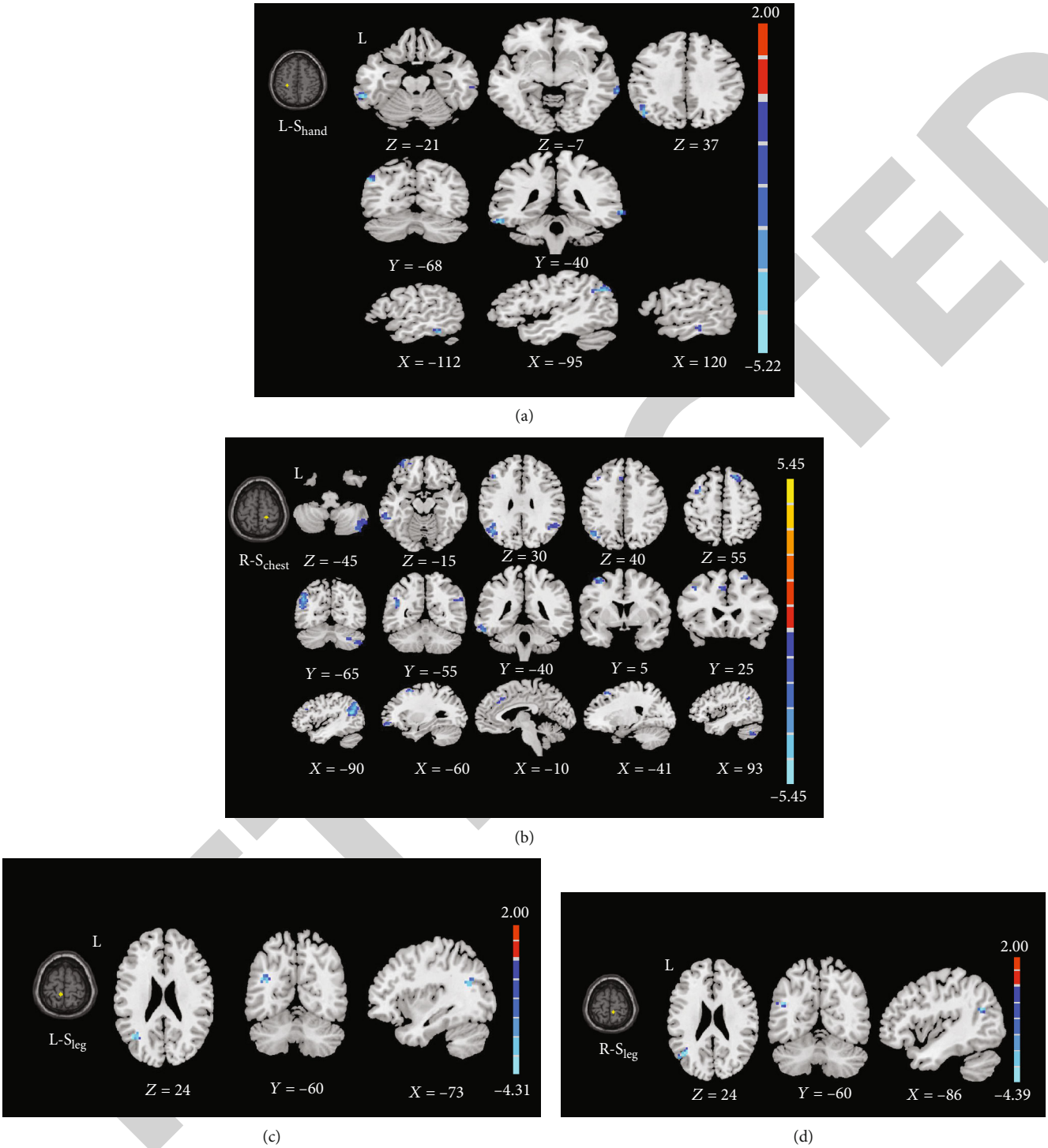

Figure 2: (a) Abnormal functional connectivity brain regions of left $S1_{hand}$ in cervical spondylotic myelopathy patients compared to healthy controls. (b) Abnormal functional connectivity brain regions of right $S1_{chest}$. (c) Abnormal functional connectivity brain regions of left $S1_{leg}$. (d) Abnormal functional connectivity brain regions of right $S1_{leg}$($p < 0.05$, FDR corrected, cluster voxels ≥ 10). Yellow-red and cyan-blue colors denote increased and decreased FC in CSM patients, respectively.

in the CSM Group. According to the normality test results, Pearson's test and Spearman correlation test were performed, respectively. The results showed that mean FA values of cervical spinal cord in CSM patients were positively correlated with JOA scores and JOA scores of motor function and lower limb motor function (Figures 4(a)–4(c)). However, there was no significant correlation between the mean ADC values and clinical parameters of CSM patients (Table 4).

In addition, correlation analysis was conducted between the ADC_{pos} values and FA_{pos} values of bilateral posterior funiculus and clinical parameters of CSM patients. The

Table 3: Correlation analysis of FC values and clinical parameters in the CSM group(r/p).

Abnormal brain regions	JOA	Motor function	Upper limb movement	Lower limb movement	Sensory function	Upper limb sensation	Lower limb sensation	Trunk sensation	NDI
Left S_{hand}-left ANG	0.210/ 0.241	0.136/ 0.449	0.153/ 0.396	0.094/ 0.603	0.223/ 0.212	0.006/ 0.972	0.109/ 0.544	0.211/ 0.239	-0.377/ 0.031*
Left S_{hand}-left ITG	0.103/ 0.569	0.040/ 0.827	0.096/ 0.596	-0.005/ 0.978	0.224/ 0.21	0.353/ 0.044*	0.052/ 0.776	-0.006/ 0.973	-0.170/ 0.344
Left S_{hand}-right MTG	-0.051/ 0.777	-0.186/ 0.301	-0.228/ 0.201	-0.082/ 0.652	0.176/ 0.327	0.154/ 0.393	0.019/ 0.915	0.045/ 0.805	0.240/ 0.178
Left S_{leg}-left ANG	0.054/ 0.765	-0.112/ 0.553	-0.161/ 0.37	-0.051/ 0.776	0.281/ 0.114	0.243/ 0.172	0.135/ 0.453	0.180/ 0.316	0.196/ 0.274
Right S_{chest}-left ANG	-0.069/ 0.701	0.012/ 0.949	0.003/ 0.986	0.051/ 0.779	-0.117/ 0.516	-0.124/ 0.492	≤0.001 1	-0.054/ 0.764	0.052/ 0.775
Right S_{chest}-left SFG	-0.001/ 0.997	0.062/ 0.732	0.075/ 0.677	-0.107/ 0.554	0.054/ 0.764	0.152/ 0.397	-0.064/ 0.25	-0.213/ 0.234	0.120/ 0.505
Right S_{chest}-left SFGmed	0.118/ 0.513	0.080/ 0.656	0.125/ 0.489	0.057/ 0.753	0.204/ 0.254	-0.032/ 0.86	0.225/ 0.207	0.174/ 0.332	-0.021/ 0.907
Right S_{chest}-left MFG	0.039/ 0.828	-0.124/ 0.492	0.007/ 0.971	-0.144/ 0.424	0.214/ 0.231	0.143/ 0.428	0.328/ 0.062	-0.066/ 0.714	-0.066/ 0.717
Right S_{chest}-left MTG	-0.205/ 0.251	-0.193/ 0.281	-0.211/ 0.238	-0.152/ 0.392	-0.170/ 0.344	0.107/ 0.552	-0.270/ 0.128	-0.092/ 0.609	0.135/ 0.454
Right S_{chest}-right ANG	-0.074/ 0.681	-0.018/ 0.923	0.004/ 0.981	-0.031/ 0.865	-0.028/ 0.878	0.163/ 0.363	-0.064/ 0.722	-0.054/ 0.764	0.036/ 0.84
Right S_{chest}-right SFG	0.102/ 0.574	0.084/ 0.641	0.161/ 0.37	0.026/ 0.885	0.006/ 0.974	0.014/ 0.939	0.206/ 0.25	-0.150/ 0.405	-0.108/ 0.549
Right S_{chest}-right cerebellar posterior lobe	0.071/ 0.693	0.015/ 0.933	0.073/ 0.687	0.029/ 0.871	0.051/ 0.777	-0.061/ 0.738	0.019/ 0.915	0.065/ 0.719	-0.152/ 0.397
Right S_{leg}-left ANG	0.188/ 0.295	0.131/ 0.467	0.055/ 0.759	0.207/ 0.249	0.231/ 0.197	-0.116/ 0.521	0.406/ 0.019*	0.100/ 0.582	0.101/ 0.576

Abbreviations: FC: functional connection; CSM: cervical spondylotic myelopathy; NDI: Neck Disability Index; JOA: Japanese Orthopedic Association; ANG: angular gyrus; ITG: inferior temporal gyrus; MTG: middle temporal gyrus; SFG: superior frontal gyrus; SFGmed: superior frontal gyrus, medial; MFG: middle frontal gyrus; *the difference was statistically significant.

results showed that FA_{pos} values of bilateral posterior funiculus were positively correlated with JOA scores and JOA scores of sensory function and lower limb sensory function (Figures 4(d)–4(f)). However, there was no significant correlation between the ADC_{pos} values and clinical parameters of CSM patients (Table 5).

3.3.3. Correlation Analysis of FC Value and Mean ADC Value, Mean FA Value, ADC_{pos} Value, and FA_{pos} Value in the CSM Group. The correlation analysis of FC values and mean ADC values, mean FA values, ADC_{pos} values, and FA_{pos} values in the CSM group was performed, and then the coefficient was obtained by statistical analysis. The results showed that the ADC_{pos} values of bilateral posterior funiculus were positively correlated with the FC value between the left $S1_{leg}$ and left ANG, the FC value between the right $S1_{chest}$, and MTG ($r = 0.373$, $p = 0.032$; $r = 0.376$, $p = 0.031$) (Figure 5). The FA_{pos} values of bilateral posterior funiculus were positively correlated with the FC value between the right $S1_{chest}$ and right cerebellar posterior lobe ($r = 0.345$, $p = 0.049$) (Figure 5). However, there was no significant correlation between the FC values and mean ADC values and mean FA values.

4. Discussion

Our study used resting-state fMRI to explore the FC between the whole brain and the primary somatosensory cortex (S1) by seed-based analysis in CSM patients. We finally found that the abnormal FC between sensory subregion of bilateral S1 and other brain regions. Then, we found the FC of abnormal brain regions were related to JOA score. These might suggest that there was relationship between the spinal cord injury and brain function. Besides, we calculated the ADC and FA value at different segments of cervical spinal cord to find the evidence of spinal cord directly. We further found the relationship between the mean FA value of cervical spinal cord and JOA score. Finally, we explored the relationship between the ADC_{pos} value of bilateral posterior funiculus and the FC value of abnormal brain regions, which could better offer evidence of the relationship between the spinal cord injury and brain function.

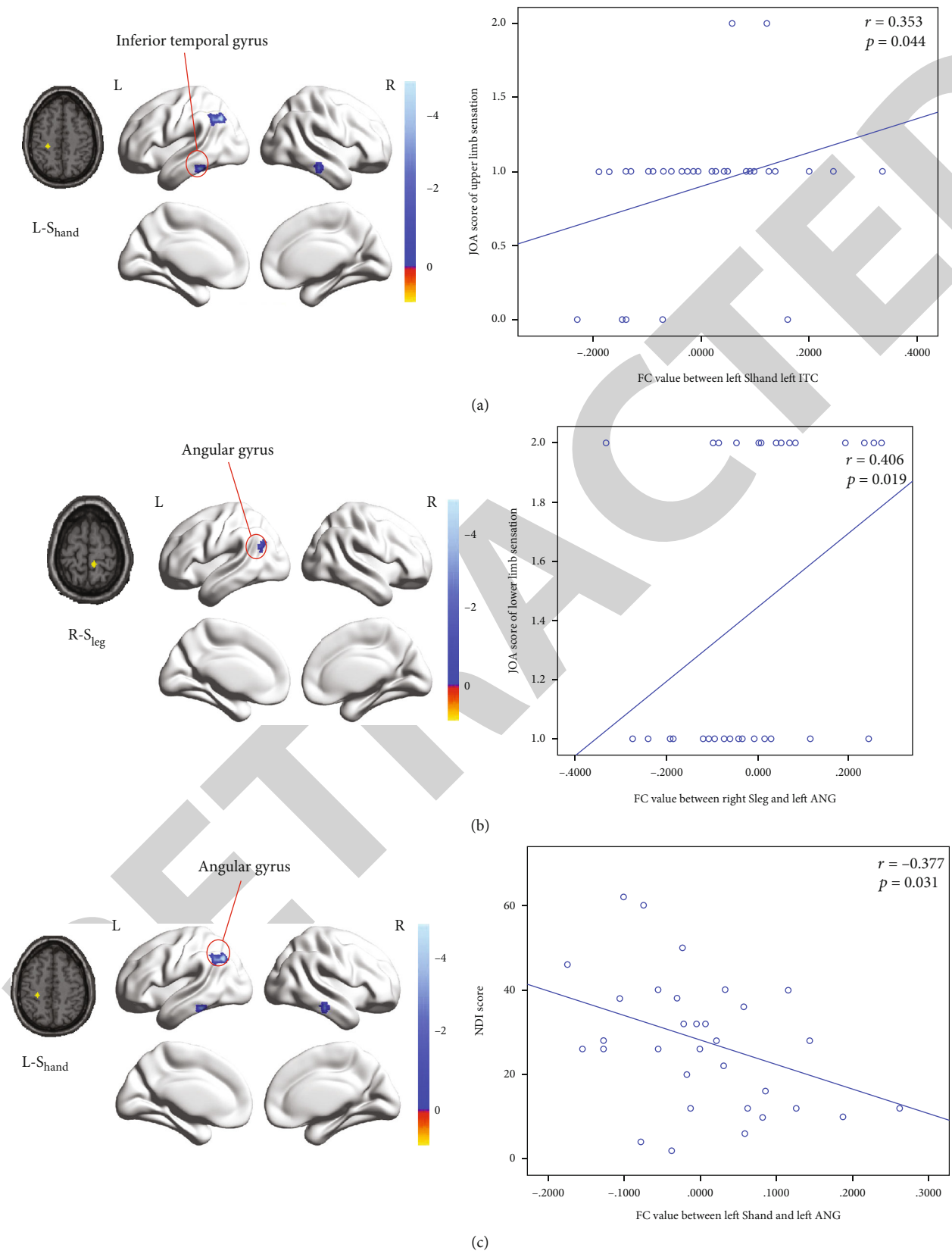

Figure 3: (a) The FC value between the left $S1_{hand}$ and left inferior temporal gyrus was positively correlated with JOA score of upper limb sensation. (b) The FC value between the right $S1_{leg}$ and left angular gyrus was positively correlated with JOA score of lower limb sensation. (c) The FC value between the left $S1_{hand}$ and left angular gyrus was negatively correlated with NDI score.

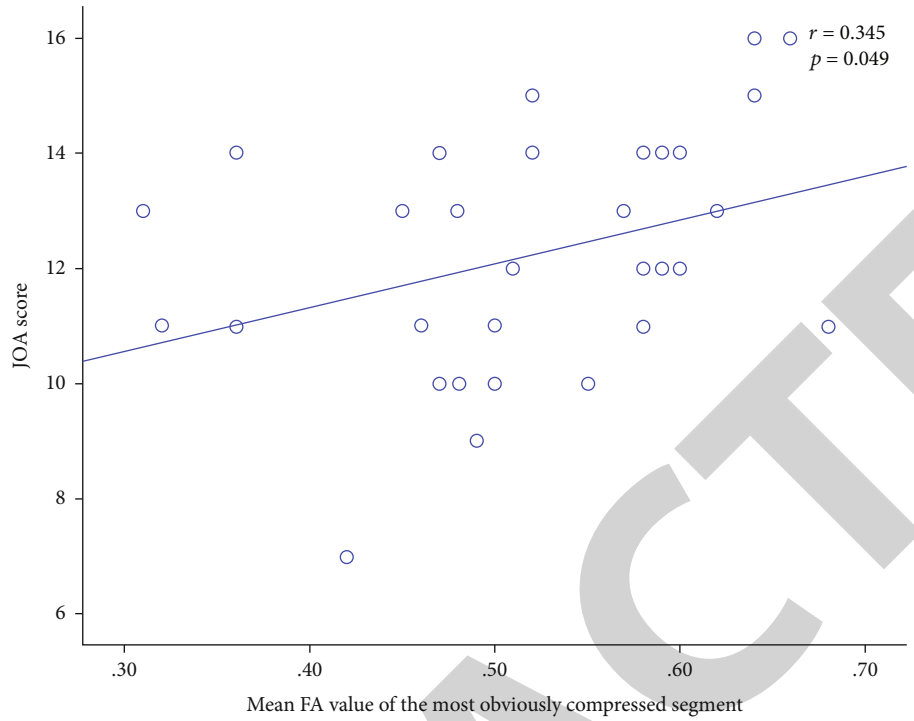

(a)

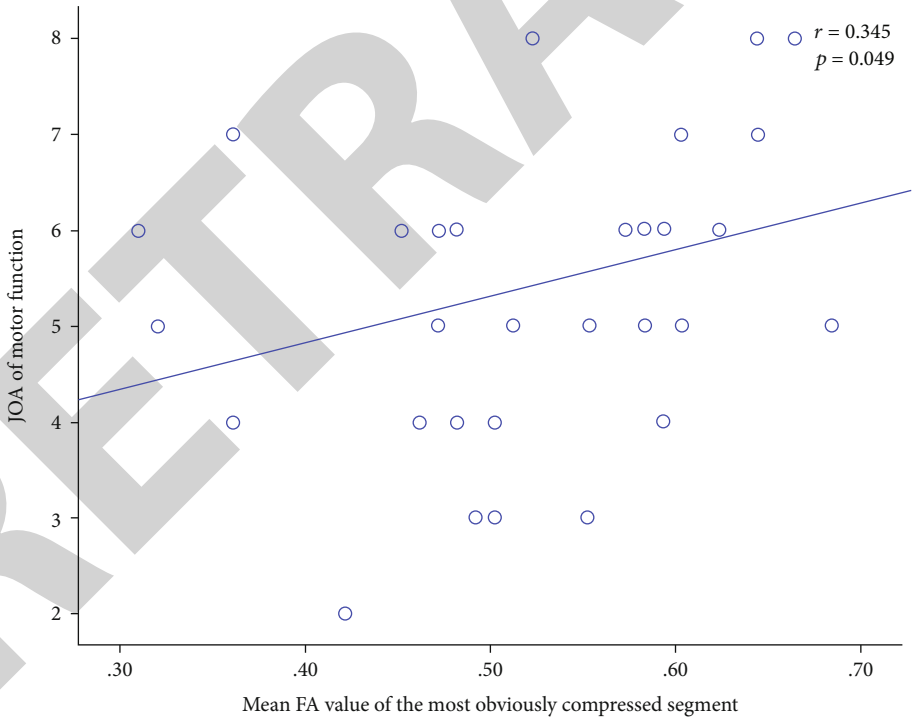

(b)

Figure 4: Continued.

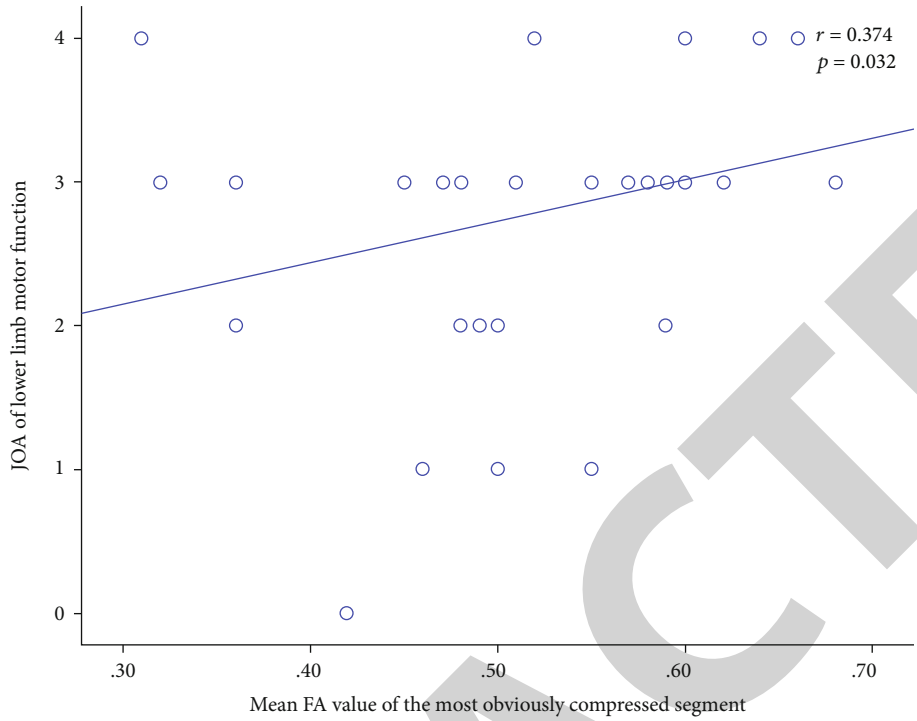

(c)

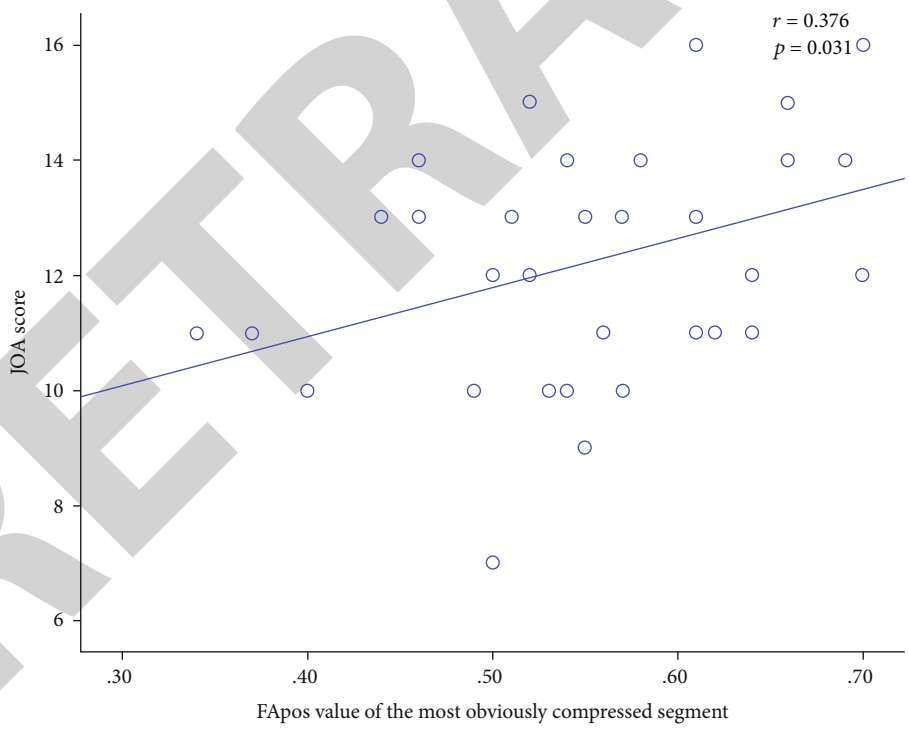

(d)

Figure 4: Continued.

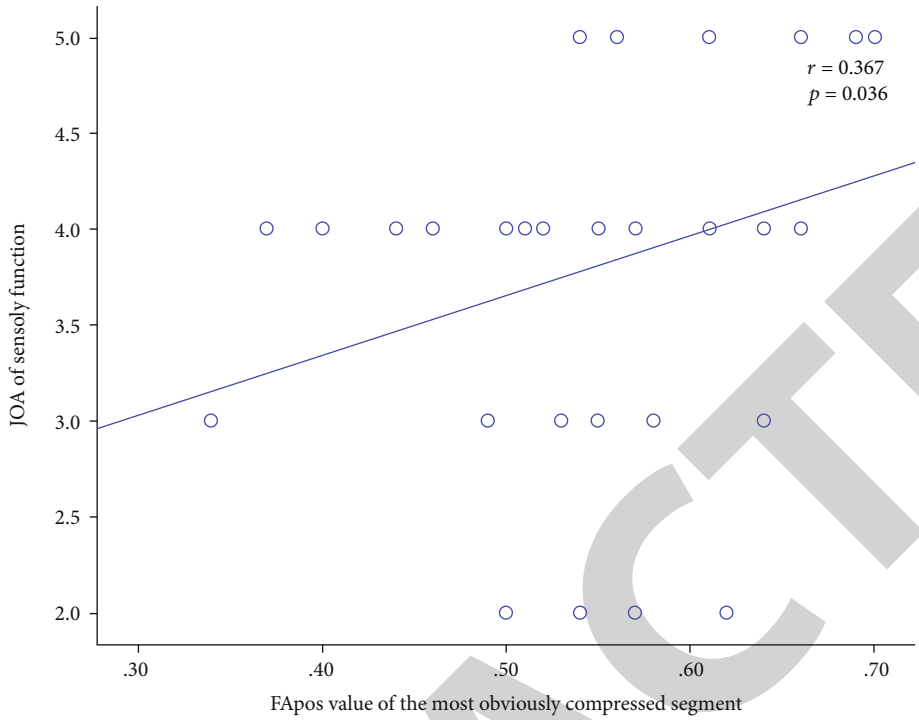

(e)

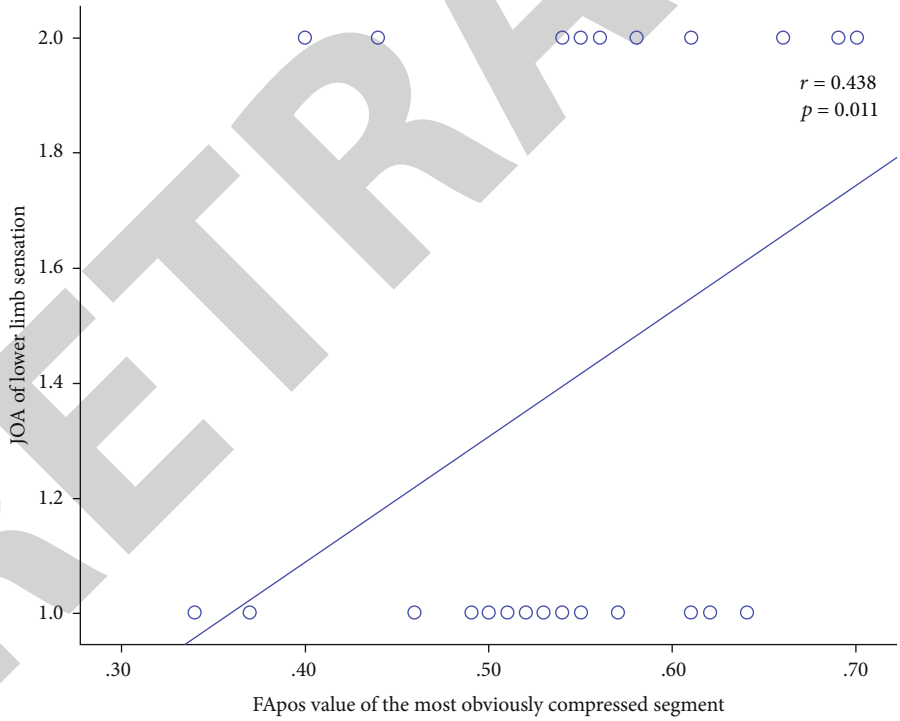

(f)

Figure 4: (a)–(c) Correlation analysis of mean ADC and FA value in the CSM group. The results showed that mean FA values of the cervical spinal cord in CSM patients were positively correlated with JOA scores, JOA scores of motor function and lower limb motor function. (d)–(f) Correlation analysis of ADC_{pos} and FA_{pos} value in the CSM group. The results showed that FA_{pos} values of bilateral posterior funiculus were positively correlated with JOA scores and JOA scores of sensory function and lower limb sensory function.

The S1 accepted the impulses from thalamus projection such as the contralateral sensation of pain, warmth, and touch. There were nociceptive neurons in S1, which encoded the nociceptive perception of pain, and its function was to feel and analyze sensory stimuli [27, 28]. Studies [29, 30] found that synaptic plasticity of S1 was altered after

Table 4: Correlation analysis between ADC and FA with clinical parameters in the CSM group (r/p).

	JOA	Motor function	Upper limb movement	Lower limb movement	Sensory function	Upper limb sensation	Lower limb sensation	Trunk sensation	NDI
ADC	0.144/ 0.423	0.132/ 0.464	0.095/ 0.598	0.095/ 0.598	0.156/ 0.386	0.244/ 0.172	-0.119/ 0.508	0.192/ 0.284	0.079/ 0.663
FA	0.345/ 0.049*	0.345/ 0.049*	0.260/ 0.144	0.374/ 0.032*	0.343/ 0.051	0.111/ 0.538	0.271/ 0.127	0.194/ 0.28	-0.202/ 0.259

Abbreviations: CSM: cervical spondylotic myelopathy; NDI: Neck Disability Index; JOA: Japanese Orthopedic Association; ADC: apparent diffusion coefficient; FA: fractional aniostropy; *the difference was statistically significant.

Table 5: Correlation analysis between ADC_{pos} and FA_{pos} with clinical parameters in the CSM group (r/p).

	JOA	Motor function	Upper limb movement	Lower limb movement	Sensory function	Upper limb sensation	Lower limb sensation	Trunk sensation	NDI
ADC_{pos}	-0.054/ 0.765	-0.178/ 0.321	-0.140/ 0.436	-0.208/ 0.245	0.136/ 0.45	0.312/ 0.077	-0.258/ 0.148	0.233/ 0.192	0.040/ 0.824
FA_{pos}	0.376/ 0.031*	0.311/ 0.079	0.318/ 0.071	0.281/ 0.113	0.367/ 0.036*	0.064/ 0.725	0.438/ 0.011*	0.078/ 0.666	-0.269/ 0.13

Abbreviations: CSM: cervical spondylotic myelopathy; NDI: Neck Disability Index; JOA: Japanese Orthopedic Association; ADC_{pos}: apparent diffusion coefficient of posterior funiculus; FA_{pos}: fractional anisotropy of posterior funiculus; *the difference was statistically significant.

peripheral nerve injury in neuropathic pain, which represented new synaptic connections. Some studies [31–33] believed that the sensorimotor network was composed of the primary sensorimotor area of cortex (SMC), premotor cortex (PMC), parietal cortex (PC), supplementary motor area (SMA), prefrontal cortex (PFC), insula, and cerebellum. In this study, we observed reduced FC between multiple sensory subareas of S1 and PC (including ANG and MTG), SMA (including SFG), and PFC (including SFG, SFGmed, and MFG). The ANG was located in the posterior part of the inferior parietal lobule. The posterior PC was an important associative cortical region that regulated sensory and motor functions as well as cognitive functions. The reduced FC between S1 and ANG could be related to sensory disorders in CSM. Therefore, we could infer that reduced proprioceptive and tactile afferent fibers might lead to reduced FC between the posterior parietal cortex and S1.

JOA score has been proven to be a reliable and effective functional measure in CSM [34–36]. JOA score included the assessment of upper and lower limb motor function, upper and lower limb sensory function, trunk sensory function, and bladder function. The lower the score was, the more severe the dysfunction was. NDI score included neck pain and related symptoms and the ability to perform daily living activities. Higher scores indicated higher levels of dysfunction. Our study showed that the FC value between the left $S1_{hand}$ and left ANG was negatively correlated with NDI score. Besides, the FC value between the left $S1_{hand}$ and left ITG was positively correlated with JOA score of upper limb sensation. These results were similar to previous reports [13]. This might be because the more severe spinal cord compression in CSM patients, the more obvious fiber bundle damage, resulting in the more serious brain function impairment, and thus the lower FC value.

Our results showed the ADC values increased, while FA values decreased from C2/3 to C6/7. This was fundamentally similar to previous studies but still existed partial differences [37, 38]. The difference might be caused by the different ROI selection ranges in the measurement of ADC and FA values. They measured the ADC values and FA values by the average values of gray and white matter, while the ROI selection of this study directly measured white matter rather than gray matter. Therefore, our method of measurement was more accurate. Compared with the HC group, the ADC values of the CSM group increased, while the FA values decreased, which was consistent with the previous studies [39–43]. We thought the chronic compression of the cervical spinal might lead to chronic ischemia hypoxia. Therefore, cell membrane permeability increased, part of the cell membranes and myelin was damaged, the number of fiber cells reduced, and the internal molecular outflowed from extracellular edema [44]. Besides, Jin et al. [45] compared the segmentation effect of FA and ADC and then found that the FA map was better for segmentation. Finally, the diffusion of water molecules along the direction of the nerve fiber bundle degree was reduced, and the spread of the perpendicular to the direction of the nerve fiber bundle degree increased. That is, the degree of anisotropy decreased, and the degree of isotropy increased.

The results showed that mean FA values of the cervical spinal cord in CSM patients were positively correlated with JOA scores, especially positively correlated with JOA scores of and lower limb motor function. This was consistent with previous studies [46–48]. The bilateral posterior funiculus only existed the ascending sensory fibers, namely, fasciculus gracilis and fasciculus cuneatus. However, the anterior and lateral funiculus not only existed the ascending sensory fibers but also descending motor fibers. Our study aimed at exploring sensory fibers, so that the ADC and FA values of bilateral posterior cord were separately extracted and correlated with clinical parameters for analysis. Consequently, the results showed that FA_{pos} values of bilateral posterior

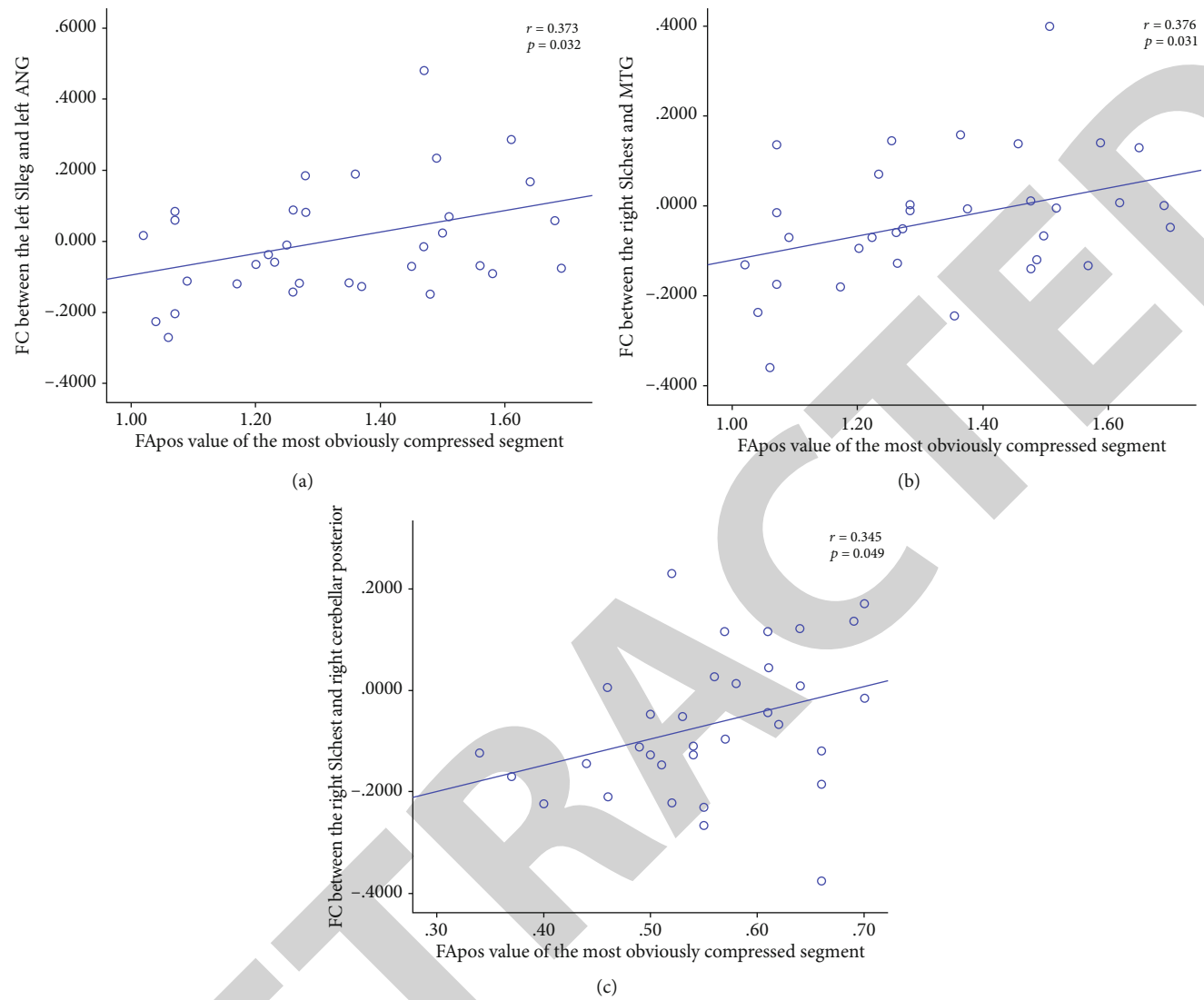

Figure 5: (a) ADC_{pos} value of bilateral posterior funiculus was positively correlated with the FC value between the left $S1_{leg}$ and left ANG. (b) ADC_{pos} value of bilateral posterior funiculus was positively correlated with the FC value between the right $S1_{chest}$ and MTG. (c) The FA_{pos} value of bilateral posterior funiculus was positively correlated with the FC value between the right $S1_{chest}$ and right cerebellar posterior lobe.

funiculus were positively correlated with JOA scores and JOA scores of sensory function and lower limb sensory function. This might indicate that the lower the FA value of the posterior funiculus, the more obviously the patient's dysfunction, especially sensory dysfunction. It might be related to the existence of ascending sensory fibers in the posterior funiculus.

Studies have shown that spinal cord injury was associated with decreased gray matter volume in the primary sensory cortex in patients with spinal cord injury, and the change of gray matter volume was significantly correlated with the degree of sensory impairment [21]. Our results showed that the ADC_{pos} values of bilateral posterior funiculus were positively correlated with the FC value between the left $S1_{leg}$ and left ANG and the FC value between the right $S1_{chest}$ and MTG. The FA_{pos} values of bilateral posterior funiculus were positively correlated with the FC value between the right $S1_{chest}$ and right cerebellar posterior lobe. The author believed that different degrees of spinal cord compression in CSM patients might lead to axon demyelination, and cerebral cortical nerve cells lacked nutrition leading to atrophy or apoptosis. The decrease of ascending afferent neurons leaded to decreased gray matter volume. Changes in the brain structure further leaded to brain functional changes. However, there was no significant correlation between the FC values and mean ADC values and mean FA values. This further illustrated the importance of extracting the posterior funiculus for separate analysis. And the results might suggest that chronic cervical spinal cord microstructural injury was synchronized with the compensatory recombination of cortical sensorimotor network in CSM patients. To some extent, the DTI parameters of the cervical spinal cord could objectively reflect the degree of impairment of cerebral cortex sensory network.

5. Limitations

There are several limitations in this current study. First, the sample size is relatively small in this study, and studies with a large number of participants are necessary in the future. Second, this is a cross-sectional study that reveals the correlation between FC of the primary somatosensory cortex and cervical spinal cord DTI in CSM patients. However, longitudinal studies are necessary to evaluate the effect of decompression surgery on alterations of dynamic connectomics of brain networks. Third, this study included all the CSM patients. However, the FC and DTI results of mild, moderate, and severe patients may be different. Finally, it is necessary to carry out the comparison of CSM patients before and after surgery and long-term follow-up after surgery.

6. Conclusion

Cervical spinal cord DTI parameters (ADC and FA) and rs-fMRI of CSM patients can evaluate the functional impairment after spinal cord injury. In CSM patients, chronic cervical spinal cord microstructural injury might be synchronized with the compensatory recombination of cerebral cortex sensory function, and DTI parameters of bilateral posterior funiculus could objectively reflect the degree of cerebral cortex sensory function impairment to a certain extent.

Data Availability

The patient data used to support the findings of this study are restricted by the Institutional Review Board of the First Affiliated Hospital of Nanchang University in order to protect patient privacy.

Conflicts of Interest

The authors have no conflicts of interest to declare.

Authors' Contributions

Guoshu Zhao and Chenlei Zhang contributed equally to this work and should be considered as co-first authors.

Acknowledgments

This work was supported by the National Natural Science Foundation of China (No. 81460329) and the National Natural Science Foundation of Jiangxi Province (No. 20192ACBL20039, 20181BAB205063).

Supplementary Materials

Supplemental materials contained SFigure 1-7 and Stable 1-3, which described the analysis of functional connectivity based on bilateral primary somatosensory cortex (S1), ADC and FA value of different levels of the cervical spinal cord in healthy controls, ADC and FA value from C2/3 to C6/7 of the cervical spinal cord in the HC group, comparison of ADC and FA value in the healthy control group, and comparison of ADC and FA value in the healthy control group. *(Supplementary Materials)*

References

[1] M. Lannon and E. Kachur, "Degenerative cervical myelopathy: clinical presentation, assessment, and natural history," *Journal of Clinical Medicine*, vol. 10, no. 16, p. 3626, 2021.

[2] D. Baptiste and M. G. Fehlings, "Pathophysiology of cervical myelopathy," *The Spine Journal: Official Journal of the North American Spine Society*, vol. 6, no. 6, pp. S190–S197, 2006.

[3] C. Wen, J. Cui, H. Liu et al., "Is diffusion anisotropy a biomarker for disease severity and surgical prognosis of cervical spondylotic myelopathy?," *Radiology*, vol. 270, no. 1, pp. 197–204, 2014.

[4] E. Lee, J. W. Lee, Y. J. Bae, H. J. Kim, Y. Kang, and J. M. Ahn, "Reliability of pre-operative diffusion tensor imaging parameter measurements of the cervical spine in patients with cervical spondylotic myelopathy," *Scientific Reports*, vol. 10, no. 1, p. 17410, 2020.

[5] S. Shabani, M. Kaushal, M. Budde, M. Wang, and S. Kurpad, "Diffusion tensor imaging in cervical spondylotic myelopathy: a review," *Journal of Neurosurgery. Spine*1–8.

[6] H. Zhang, L. Guan, Y. Hai, Y. Liu, H. Ding, and X. Chen, "Multi-shot echo-planar diffusion tensor imaging in cervical spondylotic myelopathy," *The Bone & Joint Journal*, vol. 102-B, no. 9, pp. 1210–1218, 2020.

[7] J. Leitch, C. R. Figley, and P. W. Stroman, "Applying functional MRI to the spinal cord and brainstem," *Magnetic Resonance Imaging*, vol. 28, no. 8, pp. 1225–1233, 2010.

[8] P. Freund, N. Weiskopf, J. Ashburner et al., "MRI investigation of the sensorimotor cortex and the corticospinal tract after acute spinal cord injury: a prospective longitudinal study," *The Lancet Neurology*, vol. 12, no. 9, pp. 873–881, 2013.

[9] A. Athanasiou, M. A. Klados, N. Pandria et al., "A Systematic Review of investigations into functional brain connectivity following spinal cord injury," *Frontiers in Human Neuroscience*, vol. 11, p. 517, 2017.

[10] N. Duggal, D. Rabin, R. Bartha et al., "Brain reorganization in patients with spinal cord compression evaluated using fMRI," *Neurology*, vol. 74, no. 13, pp. 1048–1054, 2010.

[11] A. Oni-Orisan, M. Kaushal, W. Li et al., "Alterations in cortical sensorimotor connectivity following complete cervical spinal cord injury: A Prospective resting-state fMRI study," *PLoS One*, vol. 11, no. 3, article e0150351, 2016.

[12] K. Ryan, S. Goncalves, R. Bartha, and N. Duggal, "Motor network recovery in patients with chronic spinal cord compression: a longitudinal study following decompression surgery," *Journal of Neurosurgery. Spine*, vol. 28, no. 4, pp. 379–388, 2018.

[13] F. Zhou, Y. M. Tan, L. Wu, Y. Zhuang, L. C. He, and H. H. Gong, "Intrinsic functional plasticity of the sensory-motor network in patients with cervical spondylotic myelopathy," *Scientific Reports*, vol. 5, no. 1, p. 9975.

[14] F. Zhou, H. Gong, X. Liu, L. Wu, K. D. K. Luk, and Y. Hu, "Increased low-frequency oscillation amplitude of sensorimotor cortex associated with the severity of structural impairment in cervical myelopathy," *PLoS One*, vol. 9, no. 8, article e104442, 2014.

[15] Y. Cao, Y. Zhan, M. du et al., "Disruption of human brain connectivity networks in patients with cervical spondylotic myelopathy," *Quantitative Imaging in Medicine and Surgery*, vol. 11, no. 8, pp. 3418–3430, 2021.

[16] J. Kim, M. Loggia, C. Cahalan et al., "The somatosensory link in fibromyalgia: functional connectivity of the primary somatosensory cortex is altered by sustained pain and is associated with clinical/autonomic dysfunction," *Arthritis & Rheumatology (Hoboken, NJ)*, vol. 67, no. 5, pp. 1395–1405, 2015.

[17] I. Strigo, G. H. Duncan, M. Boivin, and M. C. Bushnell, "Differentiation of visceral and cutaneous pain in the human brain," *Journal of Neurophysiology*, vol. 89, no. 6, pp. 3294–3303, 2003.

[18] V. Napadow, J. Liu, M. Li et al., "Somatosensory cortical plasticity in carpal tunnel syndrome treated by acupuncture," *Human Brain Mapping*, vol. 28, no. 3, pp. 159–171, 2007.

[19] E. Moulton, G. Pendse, S. Morris, M. Aiello-Lammens, L. Becerra, and D. Borsook, "Segmentally arranged somatotopy within the face representation of human primary somatosensory cortex," *Human Brain Mapping*, vol. 30, no. 3, pp. 757–765, 2009.

[20] F. D. V. Fallani, L. Astolfi, F. Cincotti et al., "Cortical functional connectivity networks in normal and spinal cord injured patients: evaluation by graph analysis," *Human Brain Mapping*, vol. 28, no. 12, pp. 1334–1346, 2007.

[21] L. Henderson, S. M. Gustin, P. M. Macey, P. J. Wrigley, and P. J. Siddall, "Functional reorganization of the brain in humans following spinal cord injury: evidence for underlying changes in cortical anatomy," *The Journal of Neuroscience: The Official Journal of the Society for Neuroscience*, vol. 31, no. 7, pp. 2630–2637, 2011.

[22] P. Wrigley, S. Press, S. Gustin et al., "Neuropathic pain and primary somatosensory cortex reorganization following spinal cord injury," *Pain*, vol. 141, no. 1, pp. 52–59, 2009.

[23] S. Emery, "Cervical spondylotic myelopathy: diagnosis and treatment," *The Journal of the American Academy of Orthopaedic Surgeons*, vol. 9, no. 6, pp. 376–388, 2001.

[24] H. Vernon, "The Neck Disability Index: state-of-the-art, 1991-2008," *Journal of Manipulative and Physiological Therapeutics*, vol. 31, no. 7, pp. 491–502, 2008.

[25] P. Azimi, H. R. Mohammadi, and A. Montazeri, "An outcome measure of functionality and pain in patients with lumbar disc herniation: a validation study of the Japanese Orthopedic Association (JOA) score," *Journal of Orthopaedic Science : Official Journal of the Japanese Orthopaedic Association*, vol. 17, no. 4, pp. 341–345, 2012.

[26] Y. Chao-Gan and Z. Yu-Feng, "DPARSF: a MATLAB Toolbox for "Pipeline" data analysis of resting-state fMRI," *Frontiers in Systems Neuroscience*, vol. 4, p. 13, 2010.

[27] E. Duerden and M. C. Albanese, "Localization of pain-related brain activation: a meta-analysis of neuroimaging data," *Human Brain Mapping*, vol. 34, no. 1, pp. 109–149, 2013.

[28] Y. Wang, X. Zhang, Q. Guan, L. Wan, Y. Yi, and C. Liu, "Altered regional homogeneity of spontaneous brain activity in idiopathic trigeminal neuralgia," *Neuropsychiatric Disease and Treatment*, vol. 11, pp. 2659–2666, 2015.

[29] S. Kim and J. Nabekura, "Rapid synaptic remodeling in the adult somatosensory cortex following peripheral nerve injury and its association with neuropathic pain," *The Journal of Neuroscience: The Official Journal of the Society for Neuroscience*, vol. 31, no. 14, pp. 5477–5482, 2011.

[30] S. Kim, H. Hayashi, T. Ishikawa et al., "Cortical astrocytes rewire somatosensory cortical circuits for peripheral neuropathic pain," *The Journal of Clinical Investigation*, vol. 126, no. 5, pp. 1983–1997, 2016.

[31] W. Shirer, S. Ryali, E. Rykhlevskaia, V. Menon, and M. D. Greicius, "Decoding subject-driven cognitive states with whole-brain connectivity patterns," *Cerebral Cortex*, vol. 22, no. 1, pp. 158–165, 2012.

[32] S. Kokkonen, J. Nikkinen, J. Remes et al., "Preoperative localization of the sensorimotor area using independent component analysis of resting-state fMRI," *Magnetic Resonance Imaging*, vol. 27, no. 6, pp. 733–740, 2009.

[33] V. van de Ven, E. Formisano, D. Prvulovic, C. H. Roeder, and D. E. J. Linden, "Functional connectivity as revealed by spatial independent component analysis of fMRI measurements during rest," *Human Brain Mapping*, vol. 22, no. 3, pp. 165–178, 2004.

[34] C. Chen, R. K. Lyu, S. T. Lee, Y. C. Wong, and L. J. Wang, "Intramedullary high signal intensity on T2-weighted MR images in cervical spondylotic myelopathy: prediction of prognosis with type of intensity," *Radiology*, vol. 221, no. 3, pp. 789–794, 2001.

[35] F. Salvi, J. C. Jones, and B. J. Weigert, "The assessment of cervical myelopathy," *The Spine Journal: Official Journal of the North American Spine Society*, vol. 6, no. 6, pp. S182–S189, 2006.

[36] Y. Aota, T. Niwa, M. Uesugi, T. Yamashita, T. Inoue, and T. Saito, "The correlation of diffusion-weighted magnetic resonance imaging in cervical compression myelopathy with neurologic and radiologic severity," *Spine*, vol. 33, no. 7, pp. 814–820, 2008.

[37] H. Mamata, F. A. Jolesz, and S. E. Maier, "Apparent diffusion coefficient and fractional anisotropy in spinal cord: age and cervical spondylosis-related changes," *Journal of Magnetic Resonance Imaging: JMRI*, vol. 22, no. 1, pp. 38–43, 2005.

[38] C. Wheeler-Kingshott, S. J. Hickman, G. J. M. Parker et al., "Investigating Cervical Spinal Cord Structure Using _Axial_ Diffusion Tensor Imaging," *NeuroImage*, vol. 16, no. 1, pp. 93–102, 2002.

[39] J. Renoux, D. Facon, P. Fillard, I. Huynh, P. Lasjaunias, and D. Ducreux, "MR diffusion tensor imaging and fiber tracking in inflammatory diseases of the spinal cord," *AJNR. American Journal of Neuroradiology*, vol. 27, no. 9, pp. 1947–1951, 2006.

[40] A. Martin, I. Aleksanderek, J. Cohen-Adad et al., "Translating state-of-the-art spinal cord MRI techniques to clinical use: a systematic review of clinical studies utilizing DTI, MT, MWF, MRS, and fMRI," *NeuroImage Clinical*, vol. 10, pp. 192–238, 2016.

[41] F. Dong, Y. Wu, P. Song et al., "A preliminary study of 3.0-T magnetic resonance diffusion tensor imaging in cervical spondylotic myelopathy," *European Spine Journal*, vol. 27, no. 8, pp. 1839–1845, 2018.

[42] K. Wang, O. Idowu, C. B. Thompson et al., "Tract-specific diffusion tensor imaging in cervical spondylotic myelopathy before and after decompressive spinal surgery: preliminary results," *Clinical Neuroradiology*, vol. 27, no. 1, pp. 61–69, 2017.

[43] L. Guan, X. Chen, Y. Hai et al., "High-resolution diffusion tensor imaging in cervical spondylotic myelopathy: a preliminary follow-up study," *NMR in Biomedicine*, vol. 30, no. 10, 2017.

Hindawi
Disease Markers
Volume 2022, Article ID 5389162, 6 pages
https://doi.org/10.1155/2022/5389162

Research Article

Decreased Adiponectin Levels Are a Risk Factor for Cognitive Decline in Spinal Cord Injury

Fan-jie Liu,[1] Hong-hao Xu,[2] Ying Yin,[3] Yuan-zhen Chen,[1] Liang-yu Xie,[1] Hua-zhong Li,[1] Dan-dan Wang,[1] and Bin Shi[1]

[1]*Bone Biomechanics Engineering Laboratory of Shandong Province, Shandong Medicinal Biotechnology Center (School of Biomedical Sciences), Neck-Shoulder and Lumbocrural Pain Hospital of Shandong First Medical University, Shandong First Medical University & Shandong Academy of Medical Sciences, Jinan, 250062 Shandong Province, China*
[2]*Department of Trauma Bone Surgery, The Affiliated Hospital of Shandong University of TCM, Jinan, 250014 Shandong Province, China*
[3]*Department of Acupuncture, The Affiliated Hospital of Shandong University of TCM, Jinan, 250014 Shandong Province, China*

Correspondence should be addressed to Dan-dan Wang; 158wdd@163.com and Bin Shi; sdyky-shibin@163.com

Received 16 December 2021; Revised 27 December 2021; Accepted 29 December 2021; Published 17 January 2022

Academic Editor: Wen-Qing Shi

Objective. Spinal cord injury (SCI) has become popular in recent years, and cognitive decline is a common complication. Adiponectin is a common protein hormone involved in the course of many diseases, but its relationship with SCI has not yet been elucidated. The purpose of our prospective study is to explore whether adiponectin can be used as a biomarker of cognitive decline in SCI. *Methods*. A total of 64 healthy volunteers and 92 patients with acute SCI were recruited by us. Serum adiponectin levels, demographic data (age and gender), lifestyle (smoking and drinking), medical history (diabetes and hypertension), and clinical baseline data (low-density lipoprotein, high-density lipoprotein, and fasting blood glucose) were recorded. Three months after enrollment, we used the Montreal Cognitive Assessment (MoCA) to evaluate cognitive function. Based on a quarter of the serum adiponectin levels, SCI patients were divided into 4 groups, and the differences in their MoCA scores were compared. In addition, we used multivariate linear regression to predict the risk factors of the MoCA score. *Results*. The serum adiponectin level ($6.1 \pm 1.1\,\mu$g/ml) of SCI patients was significantly lower than that of the healthy control group ($6.7 \pm 0.9\,\mu$g/ml), and there was a significant difference between the two ($p < 0.001$). The group with higher serum adiponectin levels after 3 months of spinal cord injury had higher MoCA scores. Multivariate regression analysis showed that serum adiponectin level is a protective factor for cognitive function after SCI ($\beta = 0.210$, $p = 0.043$). *Conclusions*. Serum adiponectin levels can be used as an independent predictor of cognitive function in patients with acute SCI.

1. Introduction

Spinal cord injury (SCI) has an epidemic trend worldwide, and the reported incidence is about 3-195 cases/million per year, and the average incidence in different regions is 1/1000 [1]. There are about 20,000 new SCI cases in the USA each year, and there is a lack of relevant data reports in China [2]. The average age of onset of SCI patients is 43 years old, and the most common causes are motor vehicle accidents and falls [3]. The per capita life-long economic burden of SCI patients ranges from US$1.5 million to US$3 million depending on the severity of the disease, and the annual socioeconomic burden of SCI is estimated to be US$2.67 billion [4]. Therefore, there is an urgent need to improve the health and quality of life of patients with SCI.

Adiponectin is a protein hormone derived from adipocytes, which can regulate the metabolism of glucose and fatty acids, and has a wide-ranging regulatory role in multisystem diseases such as endocrine system, musculoskeletal system, nervous system, and atherosclerosis [5]. Adiponectin is a 244-amino acid polypeptide composed of four different domains, and its structure is similar to complement 1Q and TNF-α factor [6, 7]. The human adiponectin gene is located on chromosome [8]. In serum, it has the following

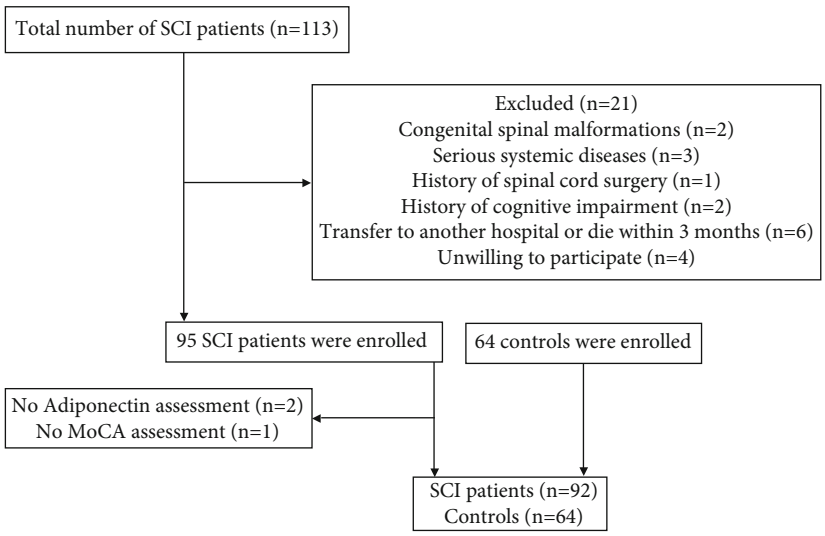

Figure 1: Flowchart of the study. SCI: spinal cord injury; MoCA: Montreal Cognitive Assessment.

three forms: trimers, hexamers, and high molecular weight polymers. Similarly, adiponectin also has three main receptors: AdipoR1 (highly expressed in skeletal muscle), AdipoR2, (highly expressed in the liver), and T-cadherin (highly expressed in vascular endothelial cells and smooth muscle) [9]. AdipoR1 and R2 can regulate inflammation and oxidative stress by acting on AMPK and (PPAR)-α pathways, while activating T-cadherin can attenuate oxidative stress, thereby protecting vascular endothelial cells from playing an antiatherosclerotic effect [7]. Compared with many other hormones, the concentration of adiponectin in plasma is relatively high, about 5-10 μg/ml [10], which makes it easy to detect and has the advantage of being a potential biomarker.

Cognitive impairment is one of the important complications of SCI, indicating that SCI may increase the risk of cognitive impairment after SCI [11]. Studies have shown that adiponectin and leptin can act synergistically to promote synaptic and memory functions in the brain, while lower levels of adiponectin can cause cognitive decline [12]. Whether adiponectin is related to cognitive impairment after SCI is the question that our study aims to solve. The clarification of the relationship between adiponectin and cognitive impairment is helpful for the diagnosis, treatment, and rehabilitation of SCI patients with cognitive impairment.

2. Methods

2.1. Study Population. The study included all patients with acute SCI who visited Neck-Shoulder and Lumbocrural Pain Hospital and the Affiliated Hospital of Shandong University of TCM between September 2018 and August 2021. The diagnosis of acute SCI is based on diagnosis and treatment guidelines [13, 14]. Exclusion criteria include the combined presence of congenital spinal malformations and serious systemic diseases, history of spinal cord surgery and cognitive impairment, transfer to other hospitals or death within 3 months, and unwilling to receive adiponectin testing or MoCA assessment. In addition, age- and gender-matched populations were recruited as controls. The flowchart is shown in Figure 1. The study strictly complied with the ethical requirements of the Declaration of Helsinki and was approved by the hospital ethics committee. All participants or family members agreed to participate in the study.

2.2. Baseline Data Collection. The baseline data we collected includes demographic data (age and gender), lifestyle (smoking and drinking), medical history (diabetes and hypertension), and clinical baseline data (low-density lipoprotein, high-density lipoprotein, and fasting blood glucose). The demographic data, lifestyle, and medical history are obtained by asking patients or family members and medical records. The clinical baseline data comes from routine inspections in the hospital. All data is archived by a dedicated person.

2.3. Cognitive Function Test. In this study, the currently popular MoCA scale was used to detect the cognitive function of patients with SCI after 3 months of onset. The MoCA scale began as a cognitive screening tool in 1996. It was created by Ziad Nasreddine in Montreal, so it was named after the place name. The subject was asked to answer 30 questions within 10 minutes, and each question was assigned 1 point, so the total score was 30 points. The average score of a normal person is 27.4, and a score of <26 is considered to have cognitive impairment. MoCA has been translated into 46 languages for free use by scientific researchers and clinicians all over the world [15].

2.4. Serum Adiponectin Detection. Blood samples of patients with acute SCI were collected immediately after admission, and the serum samples were stored in a refrigerator at -80°C and were frozen and thawed for use before analysis. Serum adiponectin levels use ELISA (Abcam, USA) reagents, and the operation process is carried out strictly in accordance with the instructions provided by the manufacturer.

Table 1: Baseline data and serum adiponectin levels of study population.

	Controls ($n = 64$)	SCI ($n = 92$)	p value
Age (years)	57.1 ± 6.3	57.6 ± 6.7	0.639
Gender (male/female)	50/14	76/16	0.485
Smoking, n (%)	34	51	0.776
Drinking, n (%)	42	59	0.848
Diabetes, n (%)	11	19	0.589
Hypertension, n (%)	15	26	0.679
LDL (mmol/l)	2.4 ± 0.8	2.5 ± 0.9	0.476
HDL (mmol/l)	1.2 ± 0.2	1.1 ± 0.3	0.021
FBG (mmol/l)	5.6 ± 0.7	5.8 ± 0.8	0.108
Adiponectin, (μg/ml)	6.7 ± 0.9	6.1 ± 1.1	<0.001
MoCA (points)	27.4 ± 1.3	23.3 ± 2.5	<0.001

LDL: low-density lipoprotein; HDL: high-density lipoprotein; FBG: fasting blood glucose; MoCA: Montreal Cognitive Assessment.

2.5. Statistical Analysis. The software used in the statistical analysis of this study is SPSS 22.00. n is used to record count data, and the mean ± standard deviation is used to represent continuous data. The chi-square test was used for the comparison of the two groups of count data, and the t-test was used for the comparison of the two groups of continuous data. The correlation analysis between serum adiponectin level (quartile) and MoCA score was performed by p for trend test. Multivariate linear regression analysis was used to finally determine the risk factors that affect the cognitive function of SCI patients. The statistical standards for all the above tests are two-tailed $p < 0.05$.

3. Results

3.1. Baseline Data. Based on the principle of voluntary participation, a total of 92 acute CI patients and 64 controls were included in the study after strict screening. The high-density lipoprotein levels of the control group and SCI group were 1.2 ± 0.2 mmol/l and 1.1 ± 0.3 mmol/l, respectively. The control group had a higher level of high-density lipoprotein ($p < 0.001$), and the results are shown in Table 1 and Figure 2(a). Except for high-density lipoprotein, the two groups had no differences in demographic data (age and gender), lifestyle (smoking and drinking), medical history (diabetes and hypertension), and clinical baseline data (low-density lipoprotein and fasting blood glucose) (statistically significant ($p > 0.05$)). The specific data information is shown in Table 1.

3.2. Serum Adiponectin Level and MoCA Score. The serum adiponectin levels of the control group and SCI group were 6.7 ± 0.9 μg/ml and 6.1 ± 1.1 μg/ml, respectively. There are significant differences between the groups ($p < 0.001$). The results are shown in Table 1 and Figure 2(b); the MoCA scores of the control group and SCI group are 27.4 ± 1.3 points and 23.3 ± 2.5 points, respectively. The MoCA score of the SCI group was significantly lower than that of the control group ($p < 0.001$). The results are shown in Table 1 and Figure 2(c).

3.3. Correlation between MoCA and Serum Adiponectin Levels. According to the serum adiponectin level, we divided patients with acute SCI into 4 groups, namely, $Q1$, $Q2$, $Q3$, and $Q4$ groups. We found that as the serum adiponectin level increased ($Q1$-$Q4$), the MoCA score also increased, and after statistical analysis, this correlation was significant ($p < 0.001$). The above relevant analysis results are shown in Table 2. Therefore, serum adiponectin may be a cognitive protective factor in SCI.

3.4. Multivariate Regression Analysis. In order to predict the risk factors affecting the cognitive function of SCI patients, we included serum adiponectin levels, age, gender, smoking, drinking, diabetes, hypertension, low-density lipoprotein, high-density lipoprotein, and fasting blood glucose into the regression model. The analysis results showed that after adjusting age, gender, smoking, drinking, diabetes, hypertension, low-density lipoprotein, high-density lipoprotein, and fasting blood glucose, the serum adiponectin level is still a significant factor affecting the cognitive function of SCI patients (Table 3). Therefore, the serum adiponectin level may be an independent protective factor for the cognitive function of patients with SCI ($\beta = 0.210$, $p = 0.043$).

4. Discussions

The main conclusions of our study are as follows: Compared with the control, the serum adiponectin level of SCI patients decreased significantly; higher quartile levels of serum adiponectin have higher MoCA scores, and this correlation is statistically significant. Further regression analysis suggested that the serum adiponectin level can independently predict the cognitive function of patients with SCI, and it may be a protective neurological factor. The advantage of our study is that we reported for the first time the correlation between serum adiponectin levels and short-term cognitive function (3 months) in patients with SCI.

The role of inflammation in SCI has been deeply studied. In the SCI animal model, the native microglia, as well as the macrophages, neutrophils, and lymphocytes recruited from the surroundings, are rapidly activated within a few minutes to a few days after SCI [16]. These activated cells release pro-inflammatory cytokines and chemokines, amplify the inflammatory response, and inhibit axon regeneration, thereby inducing secondary neuronal damage [17]. In the autopsy of humans, similar results were found in animal models, namely, the aggregation of inflammatory cells after SCI [18]. In a study on SCI biomarkers, researchers found that the level of inflammatory mediators in the blood is 10% of the concentration in CSF, and both can predict the prognosis of SCI [19]. In addition to acute SCI, persistent inflammation can also be found in chronic SCI. Functional genomics has studied the genome-wide changes of inflammation and other immune-related mediators in SCI and found that the significant reduction of natural killer (NK) cell genes and the upregulation of inflammatory genes

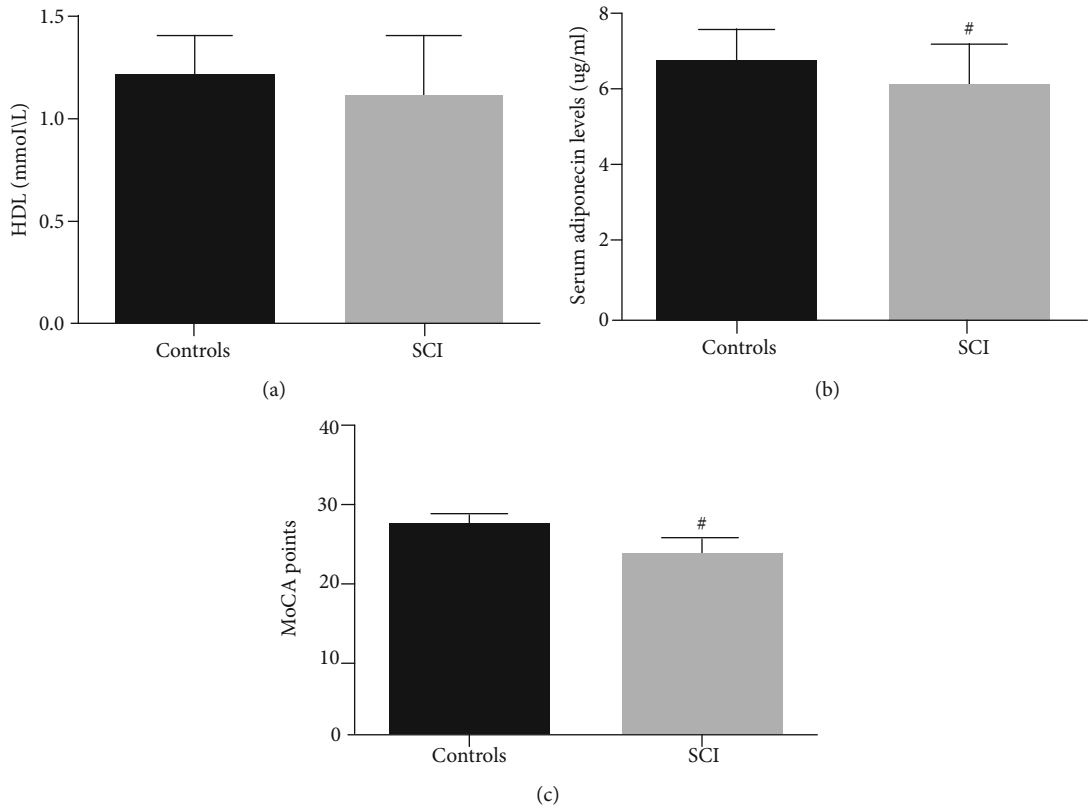

Figure 2: Comparison of HDL, MoCA, and serum adiponectin levels between the two groups. SCI: spinal cord injury; HDL: high-density lipoprotein; MoCA: Montreal Cognitive Assessment.

Table 2: Relationship between cognitive impairment and adiponectin levels.

Variable	*Q*1	*Q*2	*Q*3	*Q*4	*p* values
MoCA score	19.1 ± 1.8	21.3 ± 1.7	23.4 ± 2.1	24.8 ± 1.5	<0.001

MoCA: Montreal Cognitive Assessment.

Table 3: Analysis of multiple linear risk factors of cognitive impairment in SCI patients.

	Regression coefficient	95% confidence interval	*p* value
Age	0.236	0.204-1.027	0.164
Gender	0.195	0.168-1.053	0.256
Smoking	0.148	0.129-1.076	0.223
Drinking	0.179	0.145-1.098	0.152
Diabetes	0.204	0.187-1.105	0.105
Hypertension	0.183	0.162-1.081	0.203
LDL	0.137	0.110-1.049	0.261
HDL	0.162	0.131-1.024	0.097
FBG	0.221	0.186-1.132	0.238
Adiponectin	0.210	0.153-0.867	0.043

SCI: spinal cord injury; LDL: low-density lipoprotein; HDL: high-density lipoprotein; FBG: fasting blood glucose.

indicate that inflammation is involved in the course of chronic SCI [20, 21].

Recently, some studies have found that adiponectin may play a role in a series of inflammatory diseases. The study by Shore and his colleagues found in animal models that exogenous adiponectin can reduce allergen-induced airway hyperresponsiveness and attenuate inflammation [22]. In another study, an asthma model was constructed in adiponectin-deficient mice, and it was found that adiponectin-deficient mice had more severe pulmonary artery muscularization and pulmonary hypertension than normal mice [23]. This result further suggested that adiponectin plays a key role in chronic airway inflammation. Research by Frühbeck et al. found that the ratio of adiponectin/leptin in metabolic syndrome is low, leading to an increase in oxidative stress and inflammation. This ratio can be used as a biological marker of metabolic syndrome [24]. Chinese scholars have discovered that adiponectin plays a protective role in coronary heart disease by inhibiting

macrophages and reducing inflammation [25]. A study by the University of Tokyo found that adiponectin-deficient psoriasis mice showed increased infiltration of dermal IL-17-derived Vγ4+$\gamma\delta$-T cells, suggesting that adiponectin is involved in the regulation of skin inflammation [26]. Interestingly, recent studies have shown that recombinant adiponectin peptides can improve neurological damage caused by cerebral hemorrhage; the mechanism of which is through the inhibition of drp1/astrocyte-mediated inflammatory activation [27]. The role of adiponectin in more and more inflammatory diseases has been discovered, suggesting that treatment targeting adiponectin may be a new direction for immunotherapy.

However, the role of adiponectin in SCI has not been reported yet. Adiponectin receptor agonist AdipoRon can reduce astrocyte proliferation after SCI, thereby improving the prognosis, suggesting that activating adiponectin signaling is a potential treatment for SCI [28]. O'Brien and his colleagues found that adiponectin is closely related to the metabolic profile of SCI patients, and the mechanism may be that adiponectin can promote mitochondrial biogenesis [29]. Clinical studies have shown that circulating adiponectin may indeed be a potential biomarker for predicting the risk of osteoporosis and fracture in patients with SCI [30].

In addition, adiponectin is also believed to be involved in the maintenance of cognitive function. A study from Brazil suggests that patients with mild cognitive impairment and Alzheimer's disease have significantly lower serum adiponectin levels [31]. A Polish study showed that patients with diabetes and mild cognitive impairment have low serum adiponectin levels, suggesting that adiponectin may be involved in cognitive impairment [32]. Scholars in Pittsburgh found that adiponectin inhibits the activation of microglia in a PPAR γ-dependent manner to improve the cognitive function of vascular dementia [33]. However, the role of adiponectin in the cognitive maintenance of SCI patients has not been reported yet.

Our research has the following limitations: (1) no dynamic study of serum adiponectin levels in patients with SCI, (2) no relevant mechanism studies in animal and cell experiments, (3) no verification of our conclusions in more populations, and (4) the baseline data of SCI patients lack assessment of the severity of the disease, which may be an important factor affecting the prognosis. However, we are the first study to report the correlation between SCI cognitive impairment and adiponectin.

5. Conclusions

The level of serum adiponectin in patients with SCI is significantly reduced, and it is related to the decline of cognitive function. Serum adiponectin level is an independent predictor of cognitive decline in SCI patients. Our research is helpful for the development of targeted therapy for adiponectin in the future, thereby reducing the socioeconomic burden of the complications of cognitive impairment after SCI.

Data Availability

The study data presented may be made available from the corresponding authors upon reasonable request.

Conflicts of Interest

The authors report no conflict of interest.

Authors' Contributions

Fan-jie Liu and Hong-hao Xu are the co-first authors, and their contributions to this research are equal.

References

[1] R. Thietje and S. Hirschfeld, *Epidemiology of spinal cord injury*, Springer, In Neurological Aspects of Spinal Cord Injury, 2017.

[2] J. E. Koblinski, M. J. DeVivo, Y. Chen, and V. Nfonsam, "Colorectal cancer mortality after spinal cord injury," *The Journal of Spinal Cord Medicine*, pp. 1–6, 2020.

[3] O. Bloom, P. E. Herman, and A. M. Spungen, "Systemic inflammation in traumatic spinal cord injury," *Experimental Neurology*, vol. 325, article 113143, 2020.

[4] C. D. Cruz, A. Coelho, T. Antunes-Lopes, and F. Cruz, "Biomarkers of spinal cord injury and ensuing bladder dysfunction," *Advanced Drug Delivery Reviews*, vol. 82, pp. 153–159, 2015.

[5] J. Bloemer, P. D. Pinky, M. Govindarajulu et al., "Role of adiponectin in central nervous system disorders," *Neural Plasticity*, vol. 2018, 2018.

[6] J. H. Kim, J. M. Han, H. Kim et al., "Low serum adiponectin level is associated with better physical health-related quality of life in chronic kidney disease," *Scientific Reports*, vol. 11, pp. 1–8, 2021.

[7] M. Iwabu, M. Okada-Iwabu, T. Yamauchi, and T. Kadowaki, "Adiponectin/AdipoR research and its implications for lifestyle-related diseases," *Frontiers in Cardiovascular Medicine*, vol. 6, p. 116, 2019.

[8] C.-C. Chen, Y.-H. Wei, C.-C. Huang, S.-H. Hung, Z.-W. Wang, and R.-H. Wong, "Interaction of adiponectin genotypes and insulin resistance on the occurrence of Taiwanese metabolic syndrome," *BioMed Research International*, vol. 2021, Article ID 5570827, 9 pages, 2021.

[9] R. Polito, E. Nigro, A. Pecoraro et al., "Adiponectin receptors and pro-inflammatory cytokines are modulated in common variable immunodeficiency patients: correlation with Ig replacement therapy," *Frontiers in Immunology*, vol. 10, p. 2812, 2019.

[10] M. Chandran, S. A. Phillips, T. Ciaraldi, and R. R. Henry, "Adiponectin: more than just another fat cell hormone?," *Diabetes Care*, vol. 26, pp. 2442–2450, 2003.

[11] S. Sun, S. Sun, Y. Meng, B. Shi, and Y. Chen, "Elevated serum neuropeptide FF levels are associated with cognitive decline in patients with spinal cord injury," *Disease Markers*, vol. 2021, 2021.

[12] L. Forny-Germano and F. G. De Felice, "The role of leptin and adiponectin in obesity-associated cognitive decline and Alzheimer's disease," *Frontiers in Neuroscience*, vol. 12, 2019.

[13] M. G. Fehlings, L. A. Tetreault, J. R. Wilson et al., "A clinical practice guideline for the management of patients with acute

spinal cord injury and central cord syndrome: recommendations on the timing (≤24 hours versus>24 hours) of decompressive surgery," *Global Spine Journal*, vol. 7, 3_suppl, pp. 195S–202S, 2017.

[14] T. G. Hornby, D. S. Reisman, I. G. Ward et al., "Clinical practice guideline to improve locomotor function following chronic stroke, incomplete spinal cord injury, and brain injury," *Journal of Neurologic Physical Therapy*, vol. 44, no. 1, pp. 49–100, 2020.

[15] Q. Wang, K. Wang, Y. Ma, S. Li, and Y. Xu, "Serum galectin-3 as a potential predictive biomarker is associated with post-stroke cognitive impairment," *Oxidative Medicine and Cellular Longevity*, vol. 2021, 2021.

[16] V. Neirinckx, C. Coste, R. Franzen, A. Gothot, B. Rogister, and S. Wislet, "Neutrophil contribution to spinal cord injury and repair," *Journal of Neuroinflammation*, vol. 11, no. 1, p. 150, 2014.

[17] J. Ruschel, F. Hellal, K. C. Flynn et al., "Systemic administration of epothilone B promotes axon regeneration after spinal cord injury," *Science*, vol. 348, no. 6232, pp. 347–352, 2015.

[18] T. Zrzavy, C. Schwaiger, I. Wimmer et al., "Acute and non-resolving inflammation associate with oxidative injury after human spinal cord injury," *Brain: A Journal of Neurology*, vol. 144, pp. 144–161, 2021.

[19] M.-C. Tsai, C.-P. Wei, D.-Y. Lee et al., "Inflammatory mediators of cerebrospinal fluid from patients with spinal cord injury," *Surgical Neurology*, vol. 70, pp. S19–S24, 2008.

[20] J. Smith, J. R. Morgan, S. J. Zottoli, P. J. Smith, J. D. Buxbaum, and O. E. Bloom, "Regeneration in the era of functional genomics and gene network analysis," *The Biological Bulletin*, vol. 221, pp. 18–34, 2011.

[21] J.-C. Meunier, "Utilizing functional genomics to identify new pain treatments," *American Journal of Pharmacogenomics*, vol. 3, pp. 117–130, 2003.

[22] S. A. Shore, R. D. Terry, L. Flynt, A. Xu, and C. Hug, "Adiponectin attenuates allergen-induced airway inflammation and hyperresponsiveness in mice," *Journal of Allergy and Clinical Immunology*, vol. 118, pp. 389–395, 2006.

[23] B. D. Medoff, Y. Okamoto, P. Leyton et al., "Adiponectin deficiency increases allergic airway inflammation and pulmonary vascular remodeling," *American Journal of Respiratory Cell and Molecular Biology*, vol. 41, pp. 397–406, 2009.

[24] G. Frühbeck, V. Catalán, A. Rodríguez et al., "Involvement of the leptin-adiponectin axis in inflammation and oxidative stress in the metabolic syndrome," *Scientific Reports*, vol. 7, no. 1, p. 6619, 2017.

[25] Y. Zhou, Y. Wei, L. Wang et al., "Decreased adiponectin and increased inflammation expression in epicardial adipose tissue in coronary artery disease," *Cardiovascular Diabetology*, vol. 10, no. 1, 2011.

[26] S. Shibata, Y. Tada, C. S. Hau et al., "Adiponectin regulates psoriasiform skin inflammation by suppressing IL-17 production from $\gamma\delta$-T cells," *Nature Communications*, vol. 6, no. 1, p. 7687, 2015.

[27] X. Wu, J. Luo, H. Liu et al.et al., "Recombinant adiponectin peptide ameliorates brain injury following intracerebral hemorrhage by suppressing astrocyte-derived inflammation via the inhibition of Drp1-mediated mitochondrial fission," *Translational Stroke Research*, vol. 11, pp. 924–939, 2020.

[28] Q. Zhou, H. Xiang, A. Li et al., "Activating adiponectin signaling with exogenous AdipoRon reduces myelin lipid accumulation and suppresses macrophage recruitment after spinal cord injury," *Journal of Neurotrauma*, vol. 36, no. 6, pp. 903–918, 2019.

[29] L. C. O'Brien, Z. A. Graham, Q. Chen, E. J. Lesnefsky, C. Cardozo, and A. S. Gorgey, "Plasma adiponectin levels are correlated with body composition, metabolic profiles, and mitochondrial markers in individuals with chronic spinal cord injury," *Spinal Cord*, vol. 56, pp. 863–872, 2018.

[30] C. Tan, R. Battaglino, A. Doherty et al., "Adiponectin is associated with bone strength and fracture history in paralyzed men with spinal cord injury," *Osteoporosis International*, vol. 25, no. 11, pp. 2599–2607, 2014.

[31] A. L. Teixeira, B. S. Diniz, A. C. Campos et al., "Decreased levels of circulating adiponectin in mild cognitive impairment and Alzheimer's disease," *Neuromolecular Medicine*, vol. 15, pp. 115–121, 2013.

[32] M. Gorska-Ciebiada, M. Saryusz-Wolska, A. Borkowska, M. Ciebiada, and J. Loba, "Adiponectin, leptin and IL-1 β in elderly diabetic patients with mild cognitive impairment," *Metabolic Brain Disease*, vol. 31, pp. 257–266, 2016.

[33] W. Miao, L. Jiang, F. Xu et al., "Adiponectin ameliorates hypoperfusive cognitive deficits by boosting a neuroprotective microglial response," *Progress in Neurobiology*, vol. 205, article 102125, 2021.

Hindawi
Disease Markers
Volume 2022, Article ID 8705436, 6 pages
https://doi.org/10.1155/2022/8705436

Research Article

Evaluation of Meibomian Gland Function after Therapy of Eyelid Tumors at Palpebral Margin with Super Pulse CO_2 Laser

Songjiao Zhao,[1] **Jueni Duan**,[2] **Jing Zhang**,[3] **and Lan Gong**[1,3]

[1]*Department of Ophthalmology, Eye, Ear, Nose, & Throat Hospital of Fudan University, Shanghai 200031, China*
[2]*Department of Physical Examination, Shenzhen University General Hospital, China*
[3]*Department of Facial Plastic and Reconstructive Surgery, Eye, Ear, Nose, & Throat Hospital of Fudan University, Shanghai 200031, China*

Correspondence should be addressed to Jing Zhang; 13816653516@139.com and Lan Gong; 13501798683@139.com

Received 12 October 2021; Accepted 30 December 2021; Published 17 January 2022

Academic Editor: Ting Su

Purpose. To investigate the effect on meibomian gland function of super pulse carbon dioxide (CO_2) laser excision in the treatment of eyelid tumors at palpebral margin. *Methods*. 36 patients with 36 eyelid tumor size ≤ 1 cm and within 1 mm to palpebral margin were recruited in this study. Of which, 16 cases with tumors in the upper eyelid and 20 cases in the lower eyelid were involved. The eyelid tumors of all the patients were treated by super pulse CO_2 laser with its power density varied between 0.6 and 21.1 W/mm^2 and in repeat mode. The laser spot size ranged from 120 to 200 μm. Ocular surface parameters including tear film break-up time (BUT) and meibograde, meibum expressibility, and meibum quality were evaluated at pretherapy, 1 week, 1 month, and 3 months posttherapy in all 36 patients. *Result*. All the patients were satisfied with the therapy. No infective complications and recurrence occurred in any of the 36 patients at the following period. The eyelid wound recovered well with nearly normal appearing after 2 to 3 weeks. The morphology of limbi palpebralis, BUT, meibograde, meibum expressibility, and meibum quality of all the 36 patients showed no significant difference before and after the therapy. *Conclusions*. Super pulse CO_2 laser had no effect on meibomian gland function and morphology in the excision of tumors at palpebral margins, which was an efficacy and well-tolerated therapy with lower complications and recurrence.

1. Introduction

Eyelid benign tumors are common cosmetic concerns and traditionally treated by surgical excision in daily ophthalmology practice. However, specific surgical difficulties and complications such as eyelid deformity and scar formation following surgery should be considered in tumors located at palpebral margin. Laser therapy, for instance, carbon dioxide with infrared source (CO_2, 10600 nm) [1], erbium yttrium aluminum garnet laser (Er:YAG, 2790–2940 nm) [2], and argon laser (Ar, 488–514 nm) [3] has been widely used and demonstrated superior to traditional surgery in the treatment of eyelid tumor for the shorter operation time, less pain, no bleeding, mild postoperative reaction, no scar, satisfactory healing result, and good acceptable by patients. The application of CO_2 laser in a super pulse model has been proved effectively and predominantly in the treatment of eyelid benign tumors for the shortened exposure time and reduced thermal damage [1, 4–6].

Meibomian gland is a critical sebaceous gland that is located in the superior and inferior tarsal plates and opened at the palpebral margin. The meibum is delivered from the opening to the ocular surface to maintain the tear film stability and ocular surface homeostasis [7]. Hyposecretion or obstruction would affect meibomian gland function, even leading to meibomian gland dysfunction. Several iatrogenic conditions such as eyelid surgery and cosmetic procedures were identified and reduced the outflow of lipid secretion because of inadequate gland squeezing, inflammatory obstruction of the opening, and even complete loss of meibomian gland [8–10]. Although super pulse CO_2 laser has been demonstrated superior to other traditional lasers, it has been reported to form atrophic scarring at the treated lesion [4]. Furthermore, the safety and efficacy of super pulse

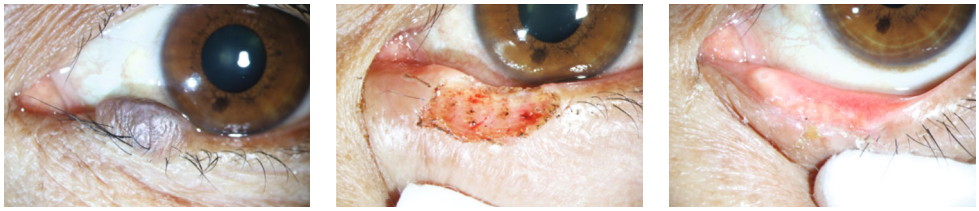

(a) (b) (c)

Figure 1: Pigmented nevus located at palpebral margin and close to the papilla: (a) before the laser therapy, (b) just after the laser therapy, and (c) 1 month after the laser therapy.

CO_2 laser in therapy of tumor at palpebral margin has not been investigated. Considering that eyelid tumor at palpebral margin is generally colocalized with the opening of meibomian gland, we wondered whether the inflammation or scar formation of palpebral margin following super pulse CO_2 laser excision would have effect on meibomian gland function.

In this study, we investigated the effect of super pulse CO_2 laser excision on meibomian gland function in the treatment of eyelid tumors at palpebral margin. The safety and cosmetic effect of super pulse CO_2 laser was also evaluated.

2. Methods

2.1. Patients. Thirty-six patients who underwent super pulse CO_2 laser-assisted benign eyelid tumor excision at the Eye, Ear, Nose and Throat Hospital of Fudan University, from May 2020 to March 2021, were recruited in this study. Written informed consent was obtained from all the participants. The exclusion criteria included premalignant lesions, large lesions (diameter > 1 cm), and blepharitis. The study conformed to the Declaration of Helsinki and was approved by the ethics committee of the Eye, Ear, Nose, and Throat Hospital of Fudan University (2016034).

2.2. Data Collection and Ocular Examination. General ophthalmologic examination including visual acuity, intraocular pressure, anterior segment and fundus, and eyelid examination was performed before treatment. Age, gender, operated eye and eyelid, the number of lesions, and the size of lesions were collected. All the patients received ocular surface examination including tear film break-up time (BUT), meibograde, and meibomian gland function before treatment and 1 week, 1 month, and 3 months after treatment. Intraoperative and postoperative complications or recurrence were also recorded.

2.3. Super Pulse CO_2 Laser-Assisted Eyelid Tumor Excision. All the patients underwent super pulse CO_2 laser-assisted eyelid tumor excision by the same senior oculoplastic surgeon (Jing Zhang) under topical anesthesia with 2% lidocaine. A corneal protection plate was used to prevent ocular injury. The lesion basement was excised using a CO_2 laser (wave length: 10600 nm; power density: 0.6-21.1 W/mm^2; exposure time: 0.05 seconds) with the help of a biopsy forceps. Then, a larger spot of CO_2 laser (150-200 μm) was used to photocoagulate the margin and bottom of the treated area to form a shallow pit. Histopathological examination was performed for the resected tumors with sufficient residual tissue. Topical chlortetracycline ointment was used immediately after the treatment. Patients were informed to keep the treated area dry until the crust desquamated and fell off. Figure 1 shows the picture of pigmented nevus before and after super pulse CO_2 laser treatment.

2.4. Tear Film Break-Up Time (BUT). A minimal volume fluorescein was instilled into the lower fornix of patients using the fluorescein strips (Jingming, Tianjing, China). The patients were requested to blink several times naturally and then look straight and keep eyes open, until the first dry spots on the cornea surface appeared under the cobalt blue light of the slit lamp. The time (seconds) from the last blink to the first appearance of dry spots was recorded as BUT. This procedure was repeated for three times.

2.5. Meibograde. Meibographies of the upper and lower eyelids were captured by the Oculus Keratograph 5 M (Wetzlar, Germany), and the meibomian gland dropout rate was analyzed qualitatively by ImageJ software (National Institutes of Health, USA). Meibograde of each eyelid was graded based on the meibomian gland dropout as 0-3: 0, no dropout of meibomian gland; 1, dropout was less than one third of the meibomian gland; 2, dropout was between one third and two thirds of the meibomian gland; and 3, dropout was over two thirds of the meibomian gland. Meibogrades of the upper and lower eyelid were summed to grade as 0-6 for each eye (Figure 2).

2.6. Meibomian Gland Function. The assessment of meibomian gland function was under slitlamp using a grade method considering meibomian gland expressibility, meibum quality, and lid margin changes. Over 8 meibomian glands of laser treated eyelid were digitally pressed, and the meibum expressibility was graded as 0-3: 1, light; 2, moderate; and 3, heavy pressure, as well as the quality of meibum was graded as 0-3: 0, clear; 1, cloudy; 2, granular; and 3, toothpaste. Based on the irregularity of the lid margin, telangiectasia, plugging of meibomian orifices, and replacement of the mucocutaneous junction, lid margin changes were graded as 0-4.

2.7. Statistical Analyses. Data analyses were performed using Graphpad Prism 9 software (USA). The results are expressed as the mean ± standard deviation. Chi square test was used

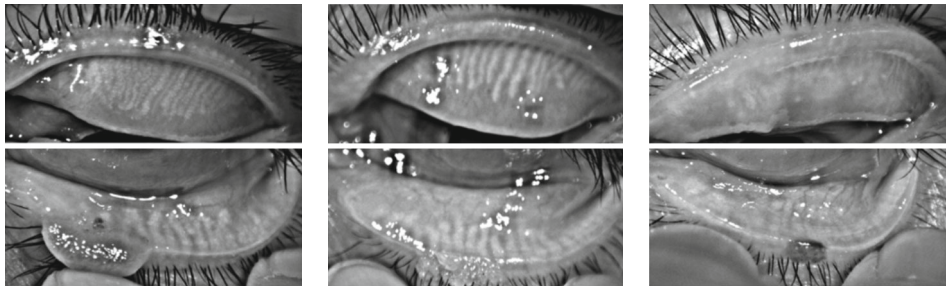

(a) (b) (c)

Figure 2: Meibographies of the upper and lower eyelids showing different meibomian gland dropouts: (a) less than one third at both upper and lower eyelids, (b) between one third and two thirds at both upper and lower eyelids, and (c) over two thirds at both upper and lower eyelids.

Table 1: Demographic and preoperative characteristics.

Characteristics	$n = 36$
Age (mean ± SD)	38.1 ± 15.3
Sex, n (%)	
Male	11 (30.6%)
Female	25 (69.4%)
Laterality, n (%)	
Left	20 (55.6%)
Right	16 (44.4%)
Eyelid, n (%)	
Upper	16 (44.4%)
Lower	20 (55.6%)
Size of lesions, n (%)	
≤5 mm	24 (64.8%)
5-10 mm	13 (35.2)
BUT (s, mean ± SD)	5.4 ± 2.8
Meibograde (mean ± SD)	2.9 ± 1.0
Meibum expressibility (mean ± SD)	1.9 ± 0.9
Meibum quality (mean ± SD)	1.6 ± 0.9

BUT: tear film break-up time

to compare BUT, meibograde, meibum expressibility, and meibum quality before and after treatment.

3. Results

A total of 36 patients (36 eyes with 36 eyelid tumors) that underwent super pulse CO_2 laser-assisted eyelid tumor excision were included, with 11 males and 25 females. The mean age at the time of therapy was 38.1 ± 15.3 years (range from 11 years to 65 years). The tumors were primarily located at the left eye ($n = 20$, 55.6%), and the lower eyelid was more involved ($n = 20$, 55.6%). The lesion size was 1 cm at most, including 24 lesions ≤ 5 mm and 13 lesions > 5 mm. Before the CO_2 laser treatment, the mean values of BUT, meibograde, meibum expressibility, and meibum quality in the treated eyes were 5.4 ± 2.8 s, 2.9 ± 1.0, 2.9 ± 1.0, and 1.6 ± 0.9, respectively (Table 1).

Table 2: The histopathological diagnosis of the benign eyelid lesions treated with CO_2 laser.

Histopathological diagnosis	$N = 32$ (100%)
Pigmented nevus	13 (40.6%)
Squamous papilloma	11 (34.4%)
Intradermal nevus	4 (12.5%)
Xanthelasma palpebrarum	2 (6.3%)
Viral wart	1 (3.1%)
Dermis collagen fiber hyperplasia	1 (3.1%)

Histopathological diagnosis was clarified in 32/36 patients (88.9%).

The wound healing was satisfactory in all the 36 patients without any infection. None of the patients were complicated by lid notching, entropion, or ectropion. Eyelash loss was occurred in 4 patients (11.1%) with lesions larger than 5 mm. Transient hypopigmentation was occurred in 3 patients (8.3%). No distinctive hyperpigmentation, scar hypertrophy, blistering, or swelling at the treated areas. No systematic complications or recurrence was observed in the following period or recurrence.

Histopathological diagnosis was clarified in 32 patients (88.9%). Pigmented nevus ($n = 13$, 40.6%) and squamous papilloma ($n = 11$, 34.4%) were the two primary types, followed by intradermal nevus ($n = 4$, 12.5%), xanthelasma palpebrarum ($n = 2$, 6.3%), viral wart ($n = 1$, 3.1%), and dermis collagen fiber hyperplasia ($n = 1$, 3.1%) (Table 2).

After the CO_2 laser treatment, BUT did not significantly changed in eyes with upper or lower eyelid tumors (Figure 3(a)). Compared with the meibograde and meibum expressibility from the pretreated values, no significant difference was found at any follow-up time in eyes with upper or lower eyelid tumors (Figures 3(b) and 3(c)). The lid margin changes showed an insignificant increase at 1 week posttherapy and returned to the basal level at 1 month posttherapy in eyes with lower eyelid tumors (Figure 3(d)). Although the score of meibum quality gently increased after the treatment, the changing trend was not statistically significant in eyes with both upper and lower eyelid tumors (Figure 3(e)). The super pulse CO_2 laser treatment in upper and lower eyelid tumors showed no significant difference.

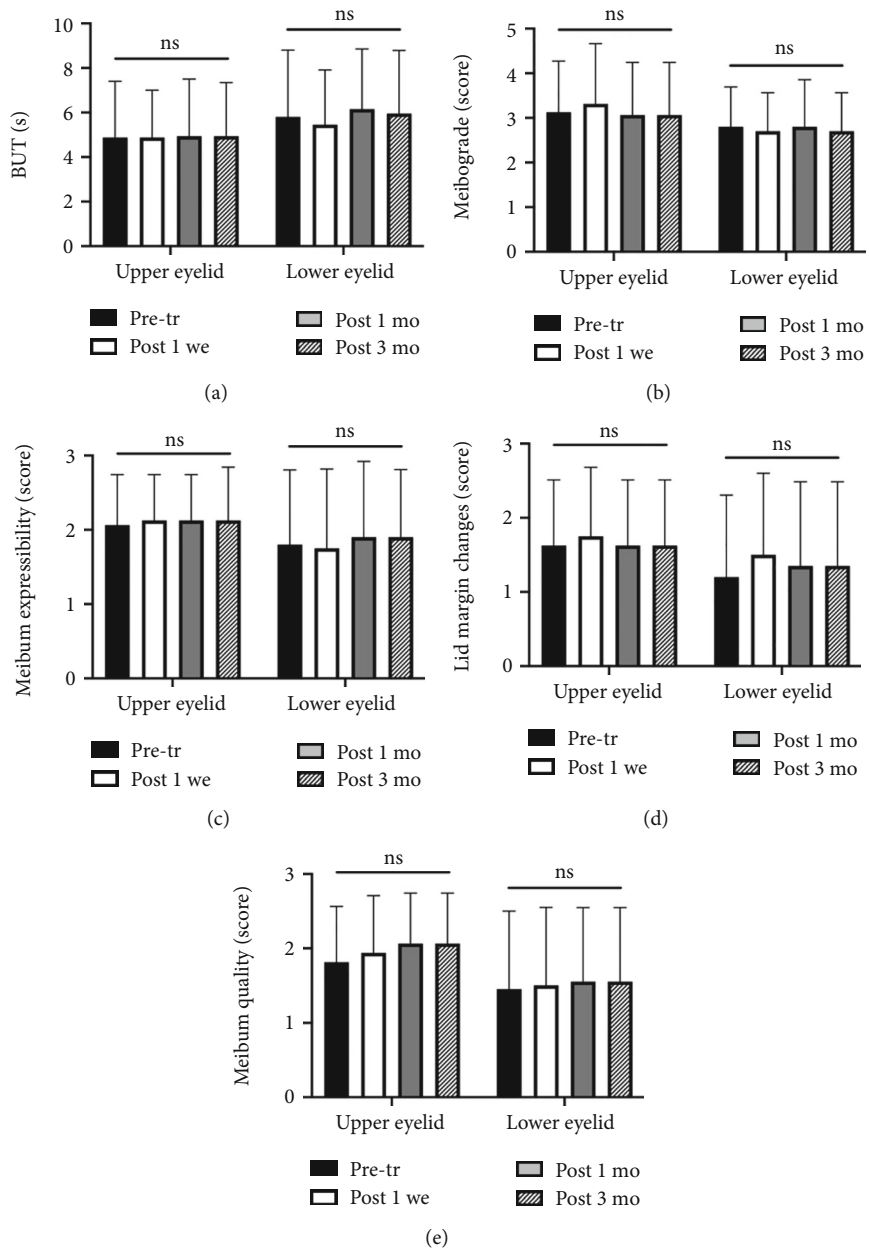

Figure 3: Changes in tear film parameter and meibomian gland function after super pulse CO_2 laser therapy. Evaluation of the BUT (a), meibograde (b), meibum expressibility (c), lid margin changes (d), and meibum quality (e) at pretherapy and posttherapy in the eyes with upper or lower eyelid tumors. No significant differences were found at any follow-up time compared to the pretreated values. The super pulse CO_2 laser therapy showed no significant difference between upper and lower eyelid tumors.

4. Discussion

This study demonstrated that super pulse CO_2 laser excision showed no significant effect on meibomian gland function in therapy of eyelid benign lesions at palpebral margin, serving as a safe and effective alternative therapeutic modality of traditional surgical excision.

Eyelid benign tumors accounted for nearly 80% of eyelid tumors, and not a few proportion was existed at palpebral margins in different types of pathology [11]. The palpebral margin is a complex structure with eyelash follicles and exocrine gland located such as meibomian gland and sebaceous gland. Traditional surgical excision of tumors at palpebral margins was a challenge because of the complications such as scar hypertrophy, eyelash loss, and angulation deformity, leading to patients' dissatisfaction.

Advancement of laser technology in recent two decades has increased options for eyelid benign tumor treatment, which achieved precise tissue damage by using appropriate wavelength and pulse duration of laser energy [12]. Comparing with other laser therapy, super pulse CO_2 lasers enables hemorrhage-free noncontact incisional excision and that producing superior tissue contraction and hemostasis, especially in the deeper lesion removal [2]. For tumors with

special location such as palpebral margins, CO_2 laser surgery keeps the margins in their anatomical position so that entropion or ectropion is not to be reckoned with, showing advantageous in preserving patients' appearance with complete morphology of palpebral margin [1, 5, 13].

Although CO_2 laser therapy exhibits more thermal necrosis and slower wound healing times that would be accompanied by the longer inflammatory reaction [12], the satisfactory therapeutic and cosmetic results with reduced complications and recurrence rate were confirmed by numerous studies in eyelid benign lesions [1, 4, 5, 14–17].

Consistent with our previous reports, this study also identified the good clinical response of super pulse CO_2 laser in excision of eyelid benign tumors without any recurrence in the follow-up period [1, 13]. Here, the original contribution was to further investigate the potential effects of super pulse CO_2 laser on the meibomian gland. Meibomian glands are distributed on the posterior edged of the palpebral margin, participating in the ocular surface homeostasis [7]. Persistent inflammation of eyelid margin or ocular surface might lead to the infiltration of inflammatory cells in the surrounding microenvironment that serves as an inflammatory form of meibomian gland dysfunction [18]. Ocular surgeries such as cosmetic blepharoplasty and cataract have been demonstrated to effect on meibomian gland function owing to direct damage or ocular surface inflammation [19, 20]. In the super pulse CO_2 laser therapy of eyelid benign tumors at palpebral margin, the intensive heat generated by CO_2 laser directly destroys the surrounding tissue of the lesions. The local and adjacent meibomian gland might be potentially affected due to the inflammatory cells infiltration or thermal injury of the opening at the margin, which at risk of hyperkeratinization of resulting in degenerative gland dilatation and atrophy [21]. Based on this, we investigate the changes of meibomian gland morphology and function after the super pulse CO_2 laser excision. To our amazement, except for those preoperative atrophy, neither meibomian gland function nor morphology was affected by the super pulse CO_2 laser in the following period. Furthermore, the tear film stability remains unchanged after the procedure. This might be contributed to the short pulse duration (microseconds) and narrower zone of coagulation of super pulse CO_2 laser. Comparing with traditional CO_2 laser, super pulse CO_2 laser provides a sufficient interval time to cool the surrounding tissue, limiting thermal damage and inflammatory infiltration [1, 22], which might have less thermal damage and functional effect of meibomian gland. To the best of our knowledge, this is the first study that identified the nonsignificant effect of super pulse CO_2 laser on meibomian gland.

There are several limitations of this study including the relative small subject number and follow-up period (3 months). Besides, no control group treated with traditional laser therapy or surgical excision was included in this study. Further study should be conducted with a longer follow-up time and a larger subject number, comparing with traditional treatment group, to make a more convincing report.

5. Conclusion

Our study identified that super pulse CO_2 laser had no effect on meibomian gland function and morphology in the excision of tumors at palpebral margins, which was an efficacy and well-tolerated therapy with lower complications and recurrence.

Data Availability

The datasets used and/or analyzed during the current study are available from the corresponding author on reasonable request.

Conflicts of Interest

The authors declare that the research was conducted in the absence of any commercial or financial relationships that could be construed as a potential conflict of interest.

Authors' Contributions

Songjiao Zhao and Jueni Duan have contributed equally to this work. Jing Zhang and Lan Gong have contributed equally to this work and share last authorship.

Acknowledgments

We would like to thank Xiaozhao Zhang for her help in data collection. This work was supported by the Natural Science Foundation of China (NSFC) (82070924).

References

[1] J. Zhang, J. Duan, and L. Gong, "Super pulse CO2laser therapy for benign eyelid tumors," *Journal of cosmetic dermatology*, vol. 17, no. 2, pp. 171–175, 2018.

[2] W. E. Lieb, T. Klink, and S. Münnich, "CO2 and erbium YAG laser in eyelid surgery. A comparison," *Der Ophthalmologe: Zeitschrift der Deutschen Ophthalmologischen Gesellschaft*, vol. 97, no. 12, pp. 835–841, 2000.

[3] Ş. Korkmaz, F. Ekici, and S. Sül, "Argon laser-assisted treatment of benign eyelid lesions," *Lasers in medical science*, vol. 30, no. 2, pp. 527–531, 2015.

[4] S. M. Esmat, A. Z. Elramly, D. M. Abdel Halim, H. I. Gawdat, and H. I. Taha, "Fractional CO_2 laser is an effective therapeutic modality for xanthelasma palpebrarum: a randomized clinical trial," *Dermatologic Surgery*, vol. 40, no. 12, pp. 1349–1355, 2014.

[5] A. Rentka, J. Grygar, Z. Nemes, and A. Kemeny-Beke, "Evaluation of carbon dioxide laser therapy for benign tumors of the eyelid margin," *Lasers in medical science*, vol. 32, no. 8, pp. 1901–1907, 2017.

[6] A. Vogel and V. Venugopalan, "Mechanisms of pulsed laser ablation of biological tissues," *Chemical Reviews*, vol. 103, no. 2, pp. 577–644, 2003.

[7] P. Chhadva, R. Goldhardt, and A. Galor, "Meibomian gland disease: the role of gland dysfunction in dry eye disease," *Ophthalmology*, vol. 124, no. 11s, pp. S20–Ss6, 2017.

[8] A. Klein-Theyer, J. Horwath-Winter, F. R. Dieter, E. M. Haller-Schober, R. Riedl, and I. Boldin, "Evaluation of ocular

surface and tear film function following modified Hughes tarsoconjunctival flap procedure," *Acta ophthalmologica*, vol. 92, no. 3, pp. 286–290, 2014.

[9] T. Wan, X. Jin, L. Lin, Y. Xu, and Y. Zhao, "Incomplete blinking may attribute to the development of Meibomian gland dysfunction," *Current eye research*, vol. 41, no. 2, pp. 179–185, 2016.

[10] J. A. Gomes, D. T. Azar, C. Baudouin et al., "TFOS DEWS II iatrogenic report," *The Ocular Surface*, vol. 15, no. 3, pp. 511–538, 2017.

[11] M. Deprez and S. Uffer, "Clinicopathological features of eyelid skin tumors. A retrospective study of 5504 cases and review of literature," *The American Journal of dermatopathology*, vol. 31, no. 3, pp. 256–262, 2009.

[12] B. Yates, S. K. Que, L. D'Souza, J. Suchecki, and J. J. Finch, "Laser treatment of periocular skin conditions," *Clinics in dermatology*, vol. 33, no. 2, pp. 197–206, 2015.

[13] N. Song, H. Tong, J. Ma, and J. Zhang, "Case series of laser therapy of eyelid peripunctal benign tumor," *Photobiomodulation, photomedicine, and laser surgery*, vol. 39, no. 10, pp. 661–664, 2021.

[14] S. B. Cho, H. J. Kim, S. Noh, S. J. Lee, Y. K. Kim, and J. H. Lee, "Treatment of syringoma using an ablative 10, 600-nm carbon dioxide fractional laser: a prospective analysis of 35 patients," *Dermatologic Surgery*, vol. 37, no. 4, pp. 433–438, 2011.

[15] N. Al-Hadithy, K. Al-Nakib, and A. Quaba, "Outcomes of 52 patients with congenital melanocytic naevi treated with ultra pulse carbon dioxide and frequency doubled Q-switched Nd-Yag laser," *Journal of plastic, reconstructive & aesthetic surgery: JPRAS*, vol. 65, no. 8, pp. 1019–1028, 2012.

[16] H. J. Park, D. Y. Lee, J. H. Lee, J. M. Yang, E. S. Lee, and W. S. Kim, "The treatment of syringomas by CO_2 laser using a multiple-drilling method," *Dermatologic surgery*, vol. 33, no. 3, pp. 310–313, 2007.

[17] J. Pozo, I. Castiñeiras, and B. Fernández-Jorge, "Variants of milia successfully treated with CO_2 laser vaporization," *Journal of Cosmetic and Laser Therapy*, vol. 12, no. 4, pp. 191–194, 2010.

[18] T. Suzuki, "Inflamed obstructive Meibomian gland dysfunction causes ocular surface inflammation," *Inflamed obstructive Meibomian gland dysfunction causes ocular surface inflammation*, vol. 59, no. 14, pp. DES94–DES101, 2018.

[19] Y. Park, H. B. Hwang, and H. S. Kim, "Observation of influence of cataract surgery on the ocular surface," *PloS one*, vol. 11, no. 10, article e0152460, 2016.

[20] S. Y. Zhang, Y. Yan, and Y. Fu, "Cosmetic blepharoplasty and dry eye disease: a review of the incidence, clinical manifestations, mechanisms and prevention," *International journal of ophthalmology*, vol. 13, no. 3, pp. 488–492, 2020.

[21] J. Bu, Y. Wu, X. Cai et al., "Hyperlipidemia induces meibomian gland dysfunction," *The ocular surface*, vol. 17, no. 4, pp. 777–786, 2019.

[22] G. Ben-Baruch, J. P. Fidler, T. Wessler, P. Bendick, and H. F. Schellhas, "Comparison of wound healing between chopped mode-superpulse mode CO_2 laser and steel knife incision," *Lasers in surgery and medicine*, vol. 8, no. 6, pp. 596–599, 1988.

Hindawi
Disease Markers
Volume 2022, Article ID 8086991, 23 pages
https://doi.org/10.1155/2022/8086991

Research Article

Identification of Hub Genes Associated with Immune Infiltration in Cardioembolic Stroke by Whole Blood Transcriptome Analysis

Qiaoqiao Li,[1,2,3] Xueping Gao,[4] Xueshan Luo,[1,2,3] Qingrui Wu,[1,2,3] Jintao He,[1,2,3] Yang Liu,[1,3] Yumei Xue,[1,3] Shulin Wu,[1,3] and Fang Rao[1,2,3]

[1]*Guangdong Cardiovascular Institute, Guangdong Provincial People's Hospital, Guangdong Academy of Medical Sciences, China*
[2]*Research Center of Medical Sciences, Guangdong Provincial People's Hospital, China*
[3]*Provincial Key Laboratory of Clinical Pharmacology, Guangdong Academy of Medical Sciences, Guangzhou 510080, China*
[4]*Department of Clinical Laboratory Medicine, Southwest Hospital, Third Military Medical University (Army Medical University), Chongqing 400038, China*

Correspondence should be addressed to Fang Rao; raofang@gdph.org.cn

Received 3 November 2021; Accepted 11 December 2021; Published 15 January 2022

Academic Editor: Ting Su

Cardioembolic stroke (CS) is the most common type of ischemic stroke in the clinic, leading to high morbidity and mortality worldwide. Although many studies have been conducted, the molecular mechanism underlying CS has not been fully grasped. This study was aimed at exploring the molecular mechanism of CS using comprehensive bioinformatics analysis and providing new insights into the pathophysiology of CS. We downloaded the public datasets GSE58294 and GSE16561. Differentially expressed genes (DEGs) were screened via the limma package using R software. CIBERSORT was used to estimate the proportions of 22 immune cells based on the gene expression profiling of CS patients. Using weighted gene correlation network analysis (WGCNA) to cluster the genes into different modules and detect relationships between modules and immune cell types, hub genes were identified based on the intersection of the protein-protein interaction (PPI) network analysis and WGCNA, and their clinical significance was then verified using another independent dataset GSE16561. Totally, 319 genes were identified as DEGs and 5413 genes were clustered into nine modules using WGCNA. The blue module, with the highest correlation coefficient, was identified as the key module associated with stroke, neutrophils, and B cells naïve. Based on the PPI analysis and WGCNA, five genes (*MCEMP1*, *CLEC4D*, *GPR97*, *TSPAN14*, and *FPR2*) were identified as hub genes. Correlation analysis indicated that hub genes had general association with infiltration-related immune cells. ROC analysis also showed they had potential clinical significance. The results were verified using another dataset, which were consistent with our analysis. Five crucial genes determined using integrative bioinformatics analysis might play significant roles in the pathophysiological mechanism in CS and be potential targets for pharmaceutic therapies.

1. Introduction

Stroke is a devastating cerebrovascular disease, containing two types: ischemic stroke (IS) and hemorrhagic stroke (HS). Accounting for approximately 80% of all cases, ischemic stroke is the most common subtype, which is triggered by arterial embolization or thromboembolism in the cerebrum [1]. A wide range of clinical manifestations of IS includes physical disability, impaired cognitive and emotional abilities [2].

Constituting about 20% of ischemic stroke, cardioembolic stroke (CS) was mainly caused by nonvalvular atrial fibrillation, myocardial infarction, and rheumatic heart disease [3, 4]. Atrial fibrillation is not only the most common sustained cardiac arrhythmia but also one of the most frequent risk factors that contribute to CS. Moreover, along

with fast economic development, social urbanization, aging of population, and changes of lifestyle, the prevalence of CS has increased dramatically, imposing a tremendous medical and social-economic burden on patients. Preventive strategies are generally recommended for all cardioembolic stroke patients, including universal elements of cardiovascular risk factor management such as treatment of diabetes mellitus, blood pressure control, alcohol and tobacco reduction, and antiplatelet medication [5]. Diagnosis of stroke was restricted to history, physical examination, and radiological imaging, which were with limited availability and higher cost. Furthermore, due to the lack of specific early diagnostic markers at the early onset of CS, missed diagnosis and misdiagnosis forces remain relatively common in patients. Thrombolytic therapies are currently the most effective treatment available after CS, regrettably, due to the main method for the treatment of cerebral infarction which is limited by a time window (about 3 h), which results in only around one-third of patients with diagnosed CS which are suitable for receiving these curative therapies [6]. Hence, identification of specific biomarkers for patients at the early onset of CS will prove beneficial. The mechanism of cardioembolic stroke (CS) is complex and involves a myriad of distinct pathogenic factors, consisting of inflammation, oxidative stress, excitotoxicity, apoptosis, excitotoxicity, ion imbalance, and neuroprotection [7]. Nevertheless, the detailed communicative regulatory mechanisms leading to CS remain incompletely understood. Increasing evidence indicates that immune cells play a considerable role in the pathogenesis of CS. Immune-mediated inflammatory markers such as CRP and IL-6 have been reported to be associated with CS [8]. However, the specific molecular mechanism underlying immune or inflammatory marker-mediated CS still needs further investigation.

Weighted gene correlation network analysis (WGCNA) is used to build a coexpression network, detect gene modules, and assess the relationships between gene modules and the biological phenotypes in order to screen the candidate diagnostic biomarkers or potential therapeutic targets.

In our study, we aimed to explore the association between immune cells and CS using integrated bioinformatics methods. CIBERSORT was applied to estimate the proportions of 22 immune cells based on the gene expression profiling of CS patients, and WGCNA was then used to identify the key module associated with CS and immune infiltration. Candidate hub genes were then identified within the key modules. Based on the protein-protein interaction (PPI) network, hub genes were identified. Potential clinical significance of the genes was then determined by using the receiver operating characteristic curve analysis. We hope that this research can offer new insights into significant diagnostic biomarker and potential therapeutic targets for treating CS.

2. Methods

2.1. Medical Ethics. The raw datasets were available from the NCBI Gene Expression Omnibus repository under accession number (GEO https://www.ncbi.nlm.nih.gov/geo/info/linking.html; GSE58294 and GSE16561). In our study, neither human trials nor animal experiments were applied.

2.2. Data Acquisition. We downloaded the corresponding datasets (GSE58294, GSE16561) available from the GEO database for further analysis. In the dataset of GSE58294 (GPL570), the expression matrix of a total of 92 individuals was acquired from the blood samples, including 69 cardioembolic stroke patients and 23 controls. Cardioembolic stroke subjects were analyzed at three time points: less than 3 hours, 5 hours, and 24 hours following the event. The GSE16561 dataset (GPL6883) contains 39 diagnosed with ischemic stroke, and 24 healthy control subjects. All samples were obtained from the blood of patients.

2.3. Data Preprocessing and Differentially Expressed Gene (DEG) Screening. The origin microarray data preprocessing, including normalization and background correction, was performed by using the "Affy" package in R; then, the gene expression profile was generated [9]. Principal component analysis was performed to distinguish the cardioembolic stroke and control samples. Differentially expressed genes (DEGs) between two groups were identified using the Bioconductor package Limma (linear models for microarray analysis) [10]. Genes with $|\log 2 \text{ fold-change (FC)}| > 1$ and adjust p value < 0.05 were regarded as statistically significant DEGs.

2.4. GO and KEGG Analyses. Gene Ontology (GO) analysis and a Kyoto Encyclopedia of Genes and Genomes (KEGG) term enrichment analysis were performed using ClusterProfiler software in R language, which showed the biological processes (BPs), cellular components (CCs), molecular functions (MFs), and pathways related to DEGs and genes in the key modules identified in the following. The enrichment significance threshold was set to an adjusted p value below 0.05 [11].

2.5. GSEA Analysis. Using the median expression level of Mast Cell Expressed Membrane Protein 1(MCEMP1) as cutoff, cardioembolic stroke samples were divided into low and high expression groups. Gene set enrichment analysis (GSEA) was conducted by the "gseaplot2" package to identify the differentially activated signaling pathways in the high MCEMP1 expression group. An $|\text{NES}| > 1$ and $\text{FDR} < 0.25$ were considered as statistically significant (NES: normalized enrichment score; FDR: false discovery rate) [10].

2.6. Immune Cell Infiltration Analysis. Normalized gene expression matrixes were utilized to estimate the relative proportions of 22 types of infiltrating immune cells using the CIBERSORT algorithm [12]. The correlation between immune cells was determined by Spearman's correlation and visualized by heatmap. Next, significant immune cells between cardioembolic stroke and control samples were screened with the threshold Wilcoxon test at p value < 0.05.

2.7. Weighted Gene Coexpression Network Analysis

2.7.1. Construction of Coexpression Network. The genes ranking in the top 25% of the median absolute deviation in the corresponding expression matrix were selected for

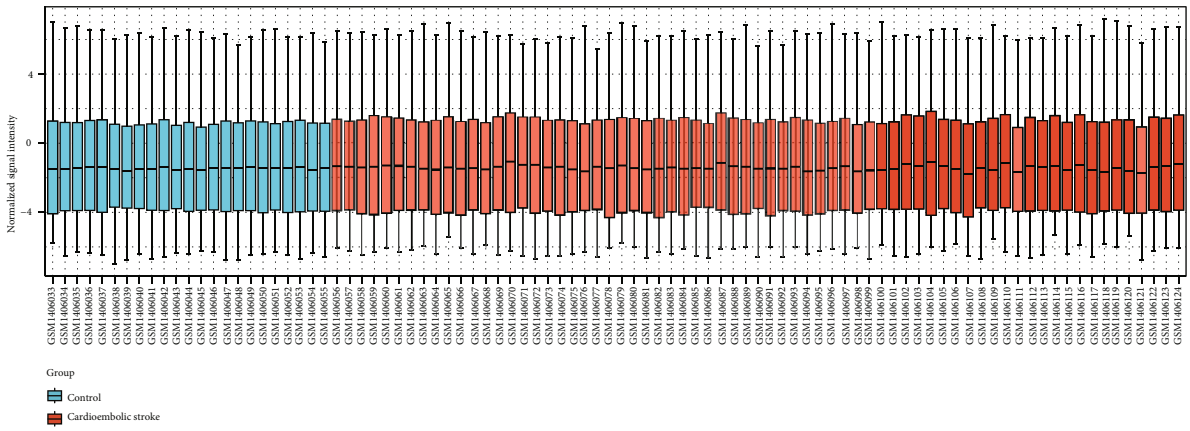

(a)

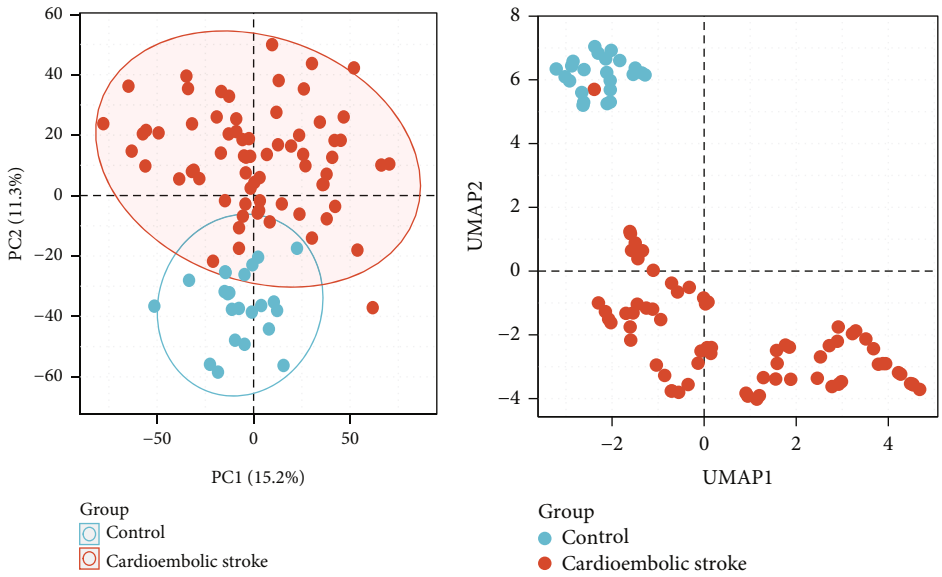

(b) (c)

Figure 1: Continued.

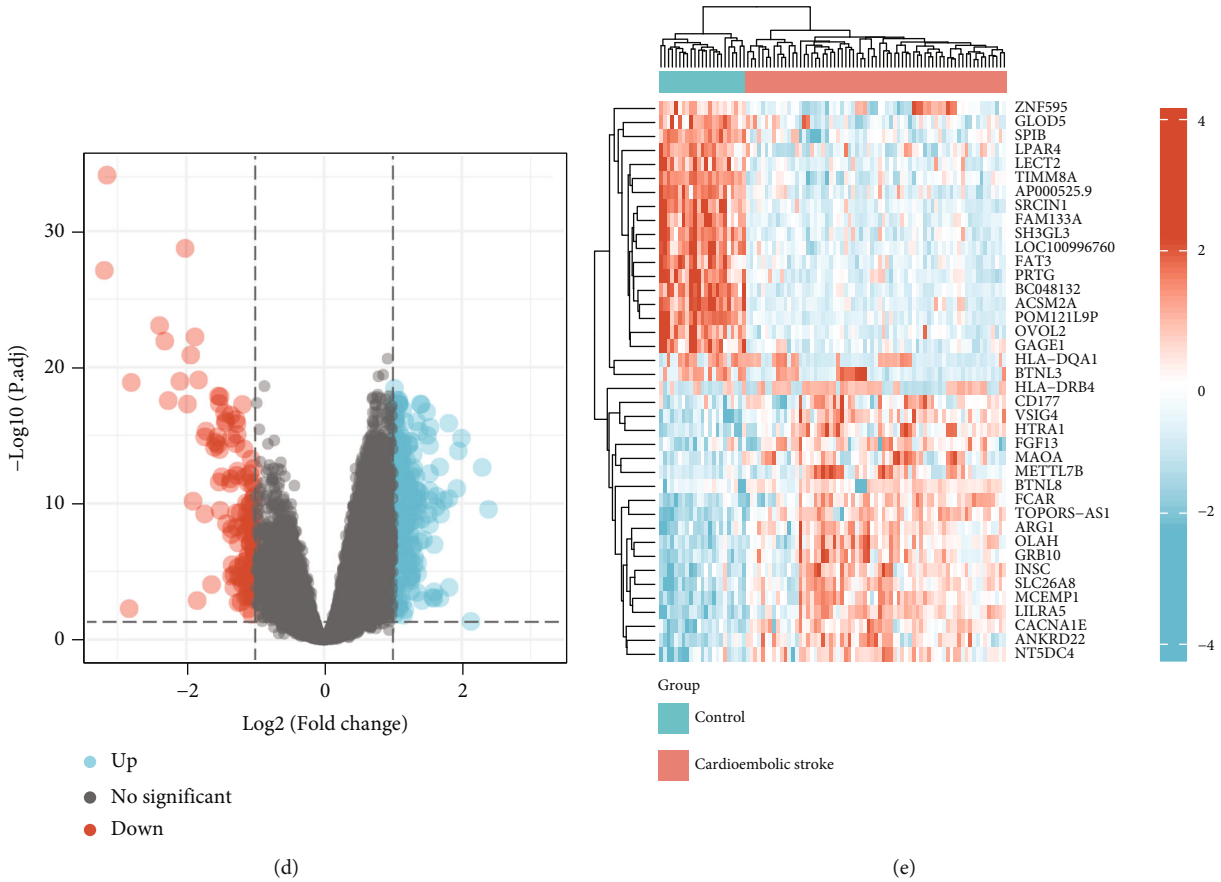

Figure 1: Data preprocessing and identification of DEGs. (a) Box plots after normalization of the raw data between cardioembolic stroke and healthy control samples. (b) PCA for cardioembolic stroke and healthy control samples. (c) UMAP analysis. (d) The volcano plot of DEGs. (e) The heatmap of top 40 DEGs. DEGs: differentially expressed genes; PCA: principal component analysis; UMAP: uniform manifold approximation and projection.

Weighted Gene Coexpression Network Analysis (WGCNA) by the "WGCNA" package in R [13]. Briefly, WGCNA was applied to construct a coexpression network based on the matrix of pairwise Pearson correlation coefficients. To satisfy the scale-free topology, an appropriate soft thresholding power β should be determined. Then, the genes can be clustered into different functional modules with different colors, which were clustered and classified by the dynamic tree cut algorithm with min. Module size was 50, and the minimum height for merging modules was 0.25. The grey module represented the genes that cannot be merged.

2.7.2. Correlation Analysis and Identification of Key Modules. Module eigengenes (MEs) were considered to be a representation of the corresponding gene expression profile in different modules. Stroke and immune cell infiltration levels were selected as the main clinical traits. The module membership (MM) was defined as the correlation of MEs with gene expression. Gene significance (GS) was defined as the correlation coefficient in the Spearman correlation between gene expression and clinical traits. Modules with the highest GS levels were regarded as key modules and selected for further analysis. Furthermore, genes with MM > 0.8 and GS > 0.5 were defined as hub genes [14].

2.8. Construction of PPI (Protein-Protein Interaction) Network. DEGs were imported to the search tool of the STRING database to generate the PPI network identifying the interactions between the hub genes with the threshold of interaction score > 0.9. The hub genes' expression pattern and biological function in the PPI network were visualized by "igraph" (version 1.2.6) and "ggraph" (version 1.0.1) packages in "R" [15, 16]. PPI networks of *MCEMP1* were calculated using the GeneMANIA algorithm [17].

2.9. Identification of Key Genes. To screen out the key genes in the development of cardioembolic stroke, we made intersection of hub genes in the WGCNA and PPI as candidate hub genes. Heatmaps of the candidate hub gene expression patterns were generated with the R package "ComplexHeatmap" (version 2.0.0) [18]. In order to ensure the accuracy and robustness of identification of key genes, CytoHubba, a plug-in Cytoscape software (version 3.6.7), was applied to screen the top 10 key genes in candidate hub genes' PPI networks via the degree methods [19]. The intersection of five algorithms in CytoHubba was employed to generate real key genes.

2.10. Correlation Analysis of Immune Cells and Key Genes. We investigated the relationship between key gene's expression and relative percentages of immune cells in

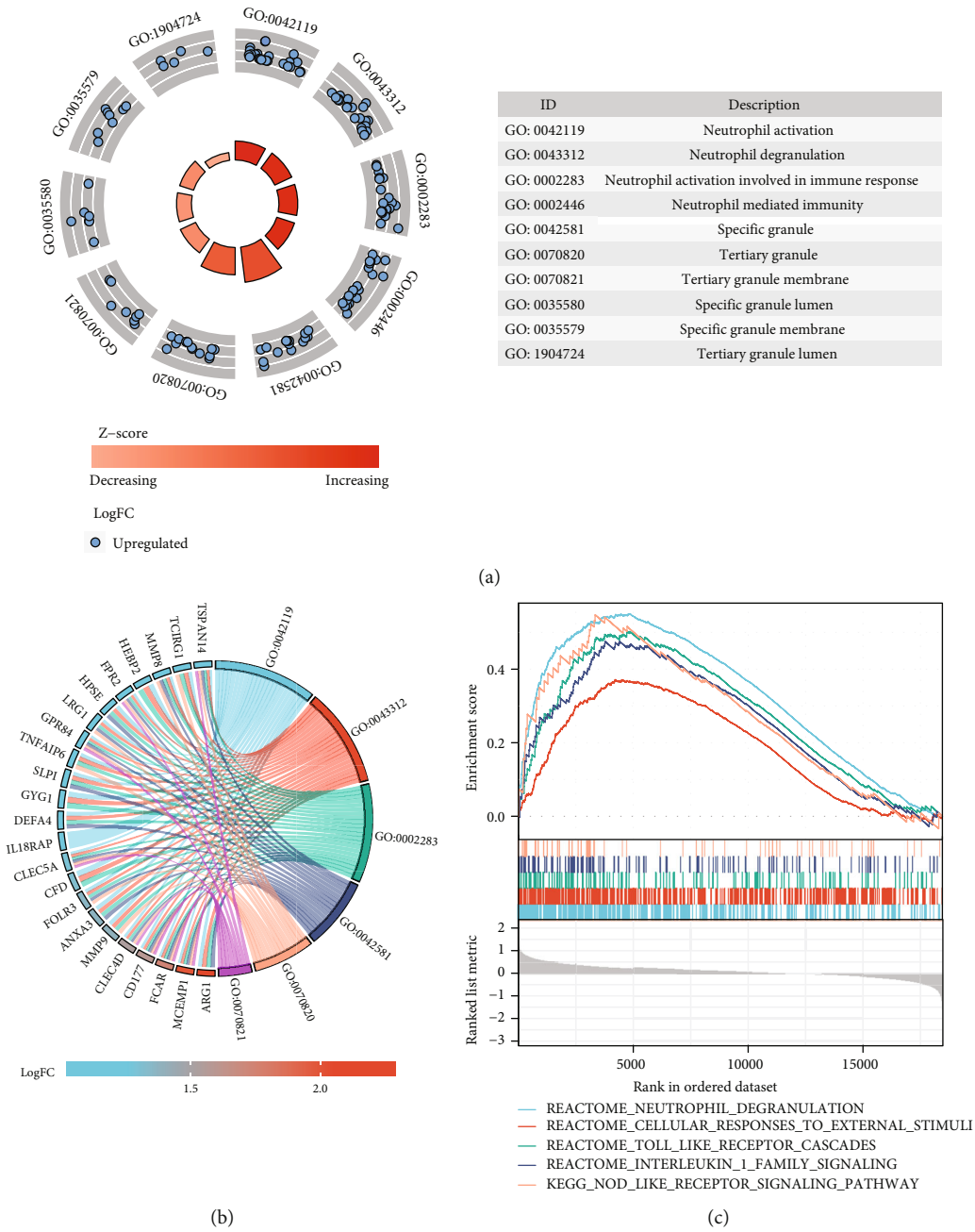

ID	Description
GO: 0042119	Neutrophil activation
GO: 0043312	Neutrophil degranulation
GO: 0002283	Neutrophil activation involved in immune response
GO: 0002446	Neutrophil mediated immunity
GO: 0042581	Specific granule
GO: 0070820	Tertiary granule
GO: 0070821	Tertiary granule membrane
GO: 0035580	Specific granule lumen
GO: 0035579	Specific granule membrane
GO: 1904724	Tertiary granule lumen

Figure 2: Functional enrichment analysis of DEGs. (a) GOCircle plot showing the top 10 of significantly changed functional terms of DEGs. The height of bars in the inner ring represented the -log 10 adjust P values of GO terms, with higher bars indicating higher significance of the GO category, and color corresponded to the z-score. The scatter plots in the out ring showed the expression levels of each gene (log fold change) in the corresponding GO terms. The description of GO categories was displayed in the table at the bottom. (b) GO chord plot showed genes linked by ribbons to their corresponding GO terms. Different colors represented different GO terms. (c) Results of gene set enrichment analysis in the cardioembolic stroke group.

cardioembolic stroke samples by using Spearman correlation test analysis. The results were visualized using the R package ggplot2 in R software [10]. $p < 0.05$ was considered statistically significant.

2.11. Receiver Operating Characteristic (ROC) Analysis. To identify the potential clinical significance of key genes, the diagnostic values of the key genes in GSE58294 were evaluated by applying "pROC" packages [20]. Another dataset (GSE16561) was used for independent verification.

2.12. Validation of the Key Gene Expression. We downloaded the validation datasets GSE58294 and GSE16561 from the GEO database (http://www.ncbi.nlm.nih.gov/geo/). All expression values of genes were normalized. A Wilcoxon rank-sum test was performed by comparing the key gene

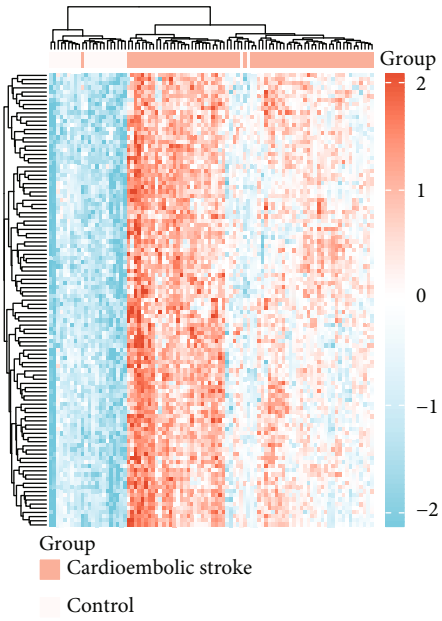

(a)

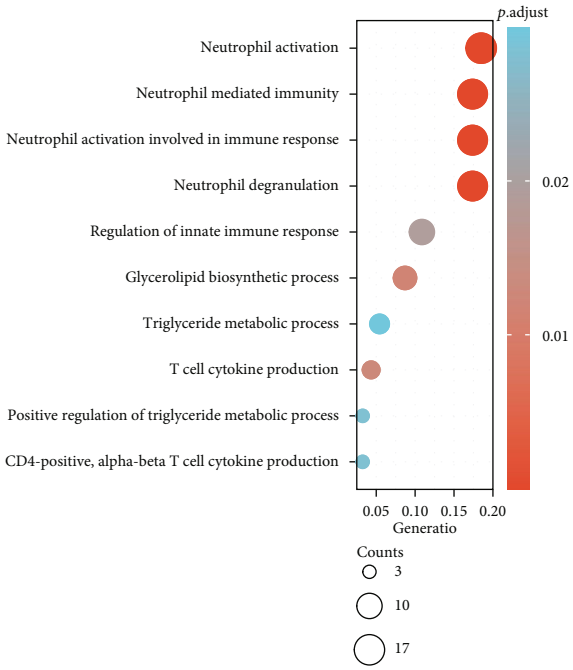

(b)

Figure 3: Continued.

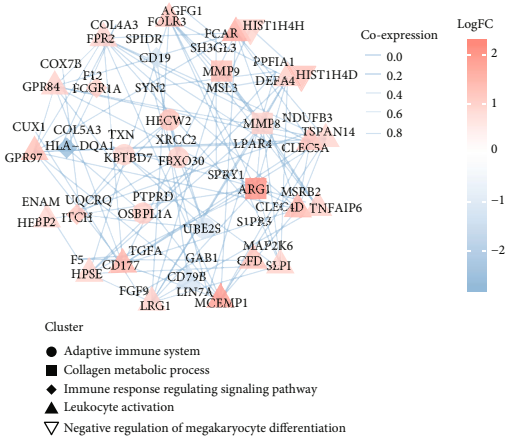

(c)

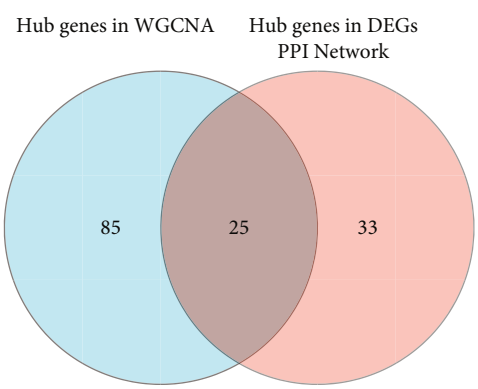

(d)

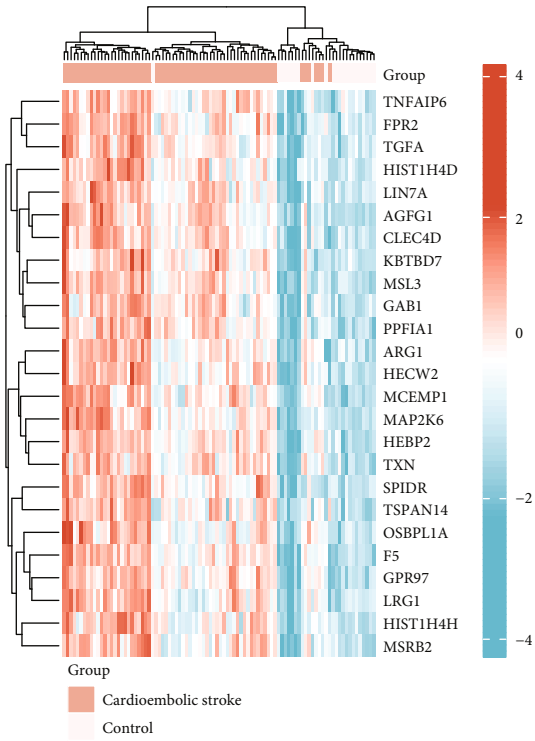

(e)

Figure 3: Continued.

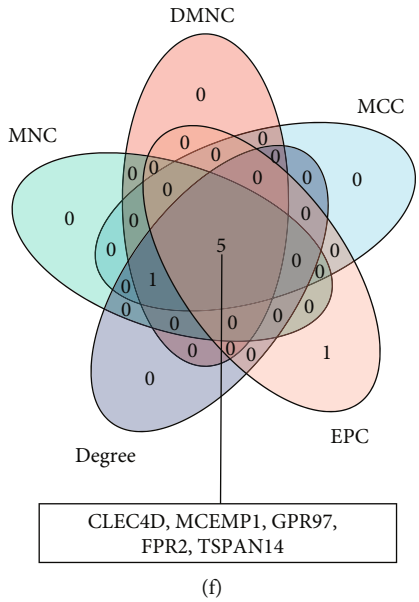

Figure 3: Identification of the key genes. (a) Heatmap of 110 hub genes in blue module. (b) GO analysis of 110 hub genes in blue module. (c) PPI network of 58 DEGs. The red color represented the upregulated genes while the blue color represented downregulated genes. DEGs were subsequently divided into different clusters based on their biological functions. The width of intergenic lines indicated the score of coexpression. (d) Venn plot of hub genes in WGCNA and DEGs. A total of 25 genes were identified as key genes. (e) Heatmap showing the expression profile of 25 key genes. (f) A Venn diagram between five algorithms of CytoHubba. CLEC4D, MCEMP1, GPR97, FPR2, and TSPAN14 were determined as the crucial genes in the cardioembolic stroke.

expression value between stroke and control using a p value < 0.05 to indicate statistical significance. Box plots of the expression of key genes were illustrated by the ggplot2 R package.

2.13. Statistical Analysis. All data analyses were performed in R v3.6.3. Details of these bioinformatics analyses were described in corresponding subsections. A p value < 0.05 was defined as statistically significant.

3. Results

3.1. Data Preprocessing and DEG Screening. Box plots after normalization of the raw data are illustrated in Figure 1(a). Principal component analysis (PCA) and uniform manifold approximation and projection (UMAP) analysis showed a good distinction between cardioembolic stroke and control samples (Figures 1(b) and 1(c)). Under the screening criteria of $p$adjust < 0.05 and $|\log 2$ fold-change (FC)$| > 1$, a total of 319 genes were identified as DEGs, of which 198 genes were upregulated and 121 genes were downregulated. The volcano plot of DEGs is displayed in Figure 1(d). DEGs in GSE58294 were arranged based on the fold change of expression values, the top 40 were illustrated by applying heatmap (Figure 1(e)).

3.2. Functional Enrichment Analyses. All DEGs were selected for function enrichment analysis; the top 10 most significant GO terms according to their adjust p values were displayed in GOCircle plots (Figure 2(a)). The majority of terms in the biological process category were associated with neutrophil activation (GO:0042119), neutrophil degranulation (GO:0043312), and neutrophil activation involved in immune response (GO:0002283). Genes involved in biological processes that were upregulated in cardioembolic stroke were shown using a chord plot (Figure 2(b)). We further explored our microarray data by using GSEA with the "ggplot2" package in R language; the results indicated that the cardioembolic stroke groups were mostly enriched in terms of neutrophil degranulation, cellular response to external stimuli, toll-like receptor cascades, interleukin-1 family signaling, and nod-like receptor signaling pathway (Figure 2(c)). Hub genes in key module were selected to perform GO enrichment analyses in order to investigate the biological function, as displayed in Figure 3(b).

3.3. Immune Cell Infiltration Analysis. Applying the CIBERSORT algorithm, we investigated the difference of immune infiltration among cardioembolic stroke and control samples in 22 subpopulations of immune cells (Figure 4(a)). Furthermore, the results of correlation analysis of infiltrated immune cells implied that T cells CD8 and B cells naïve, neutrophils, and macrophages M2 were positively correlated, and T cells CD8 and T cells CD4 naïve, neutrophils, and T cells CD8 were negatively correlated (Figure 4(b)). As shown in the heatmap and violin plot, compared with the control sample, T cells memory activated ($p < 0.001$), NK cells resting ($p = 0.003$), macrophages M0 ($p = 0.005$), macrophages M2 ($p = 0.003$), and neutrophils ($p = 0.001$) infiltrated more in the cardioembolic stroke group, while B cells naïve ($p < 0.001$), T cells CD8 ($p = 0.005$), and T cells CD memory resting ($p = 0.009$) showed the opposite results (Figures 4(c) and 4(d)).

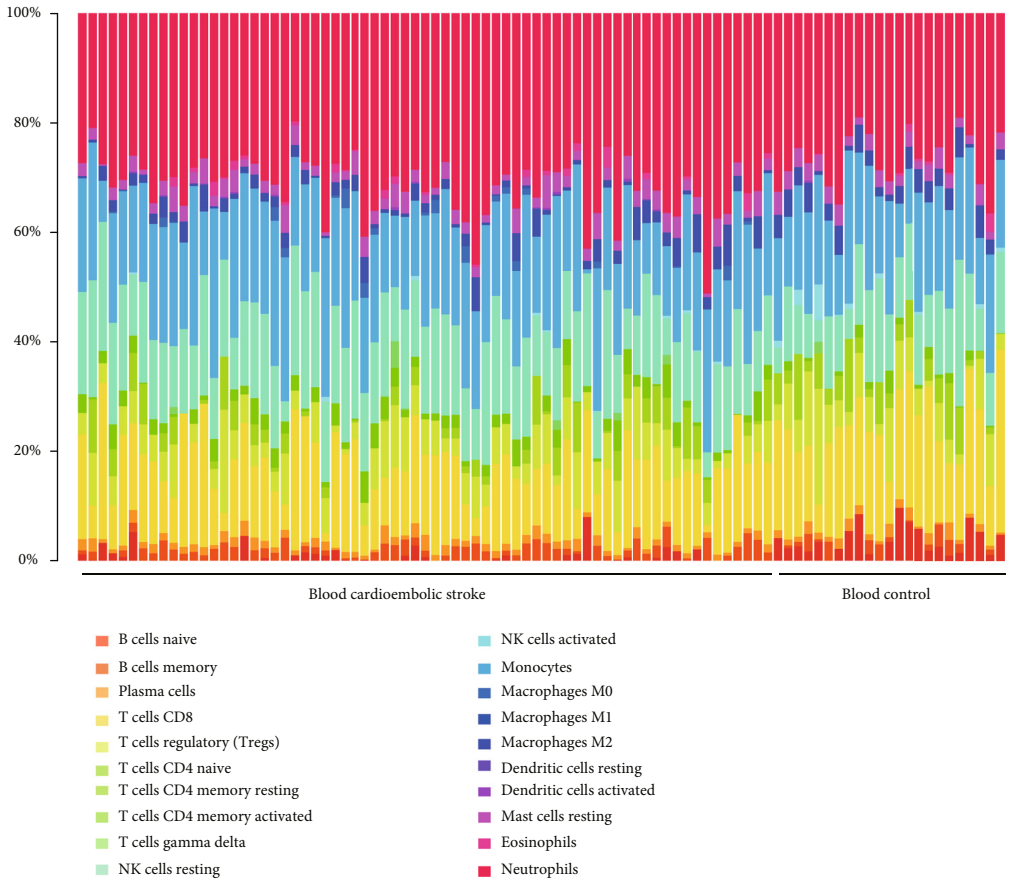

(a)

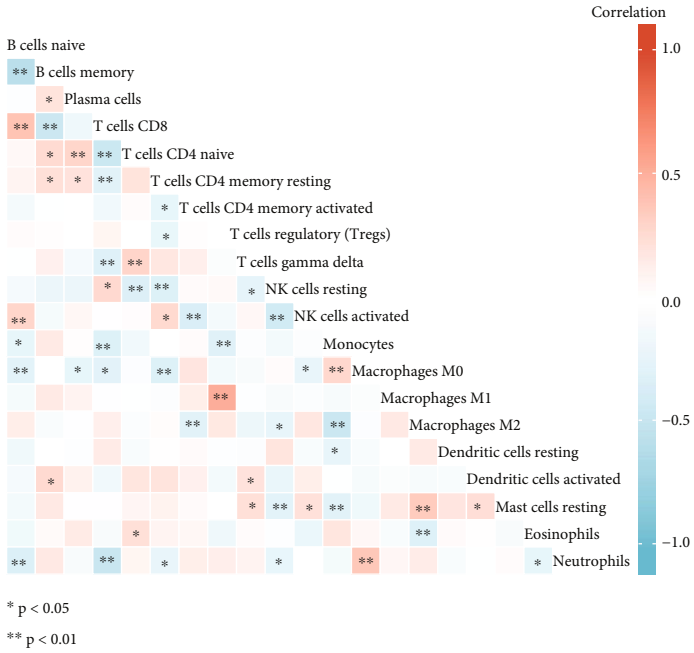

(b)

Figure 4: Continued.

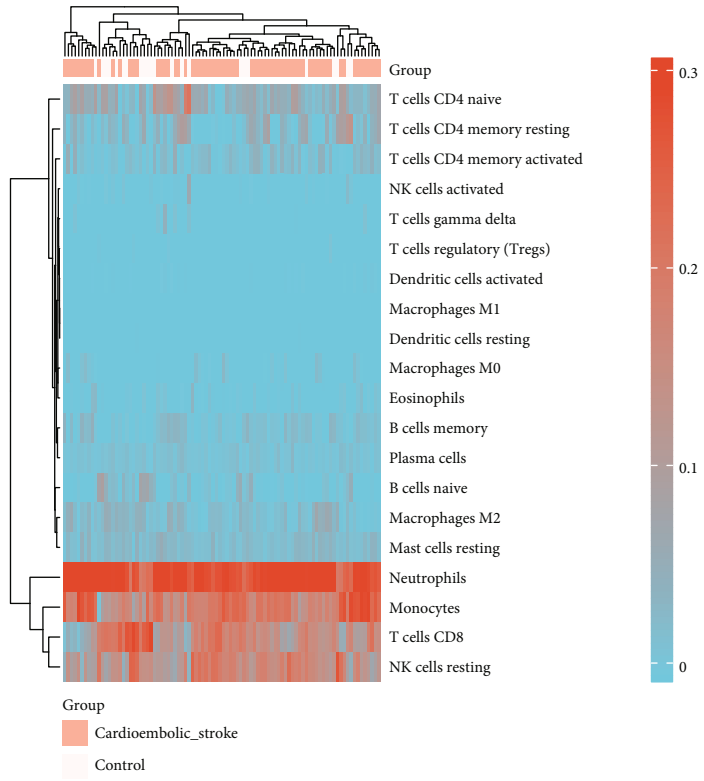

(c)

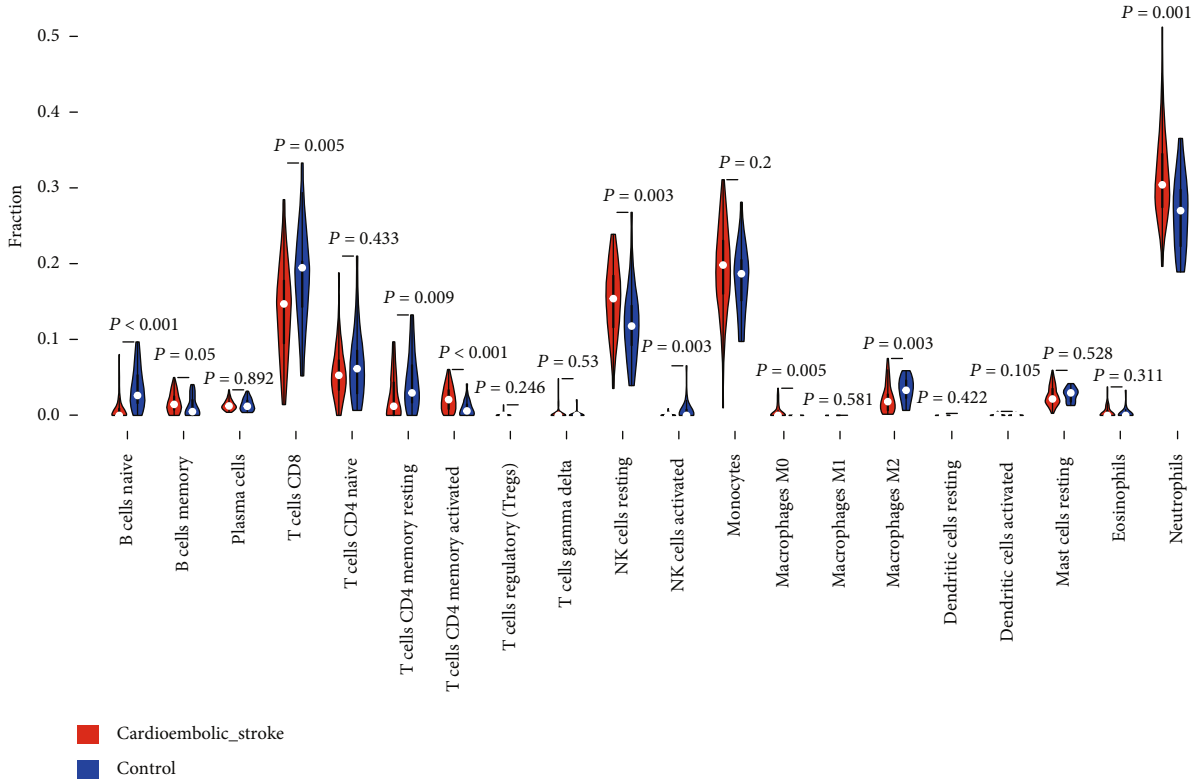

(d)

Figure 4: Immune cell infiltration analysis. (a) Relative proportions of 20 types of infiltrated immune cells between cardioembolic stroke and healthy control groups. (b) Correlation heatmap of all 20 immune infiltrated cells. (c) Heatmap of the 20 immune cell proportions in all samples in GSE58294. (d) Violin plot showing the significant changes of the immune infiltration level in cardioembolic stroke compared to the control group.

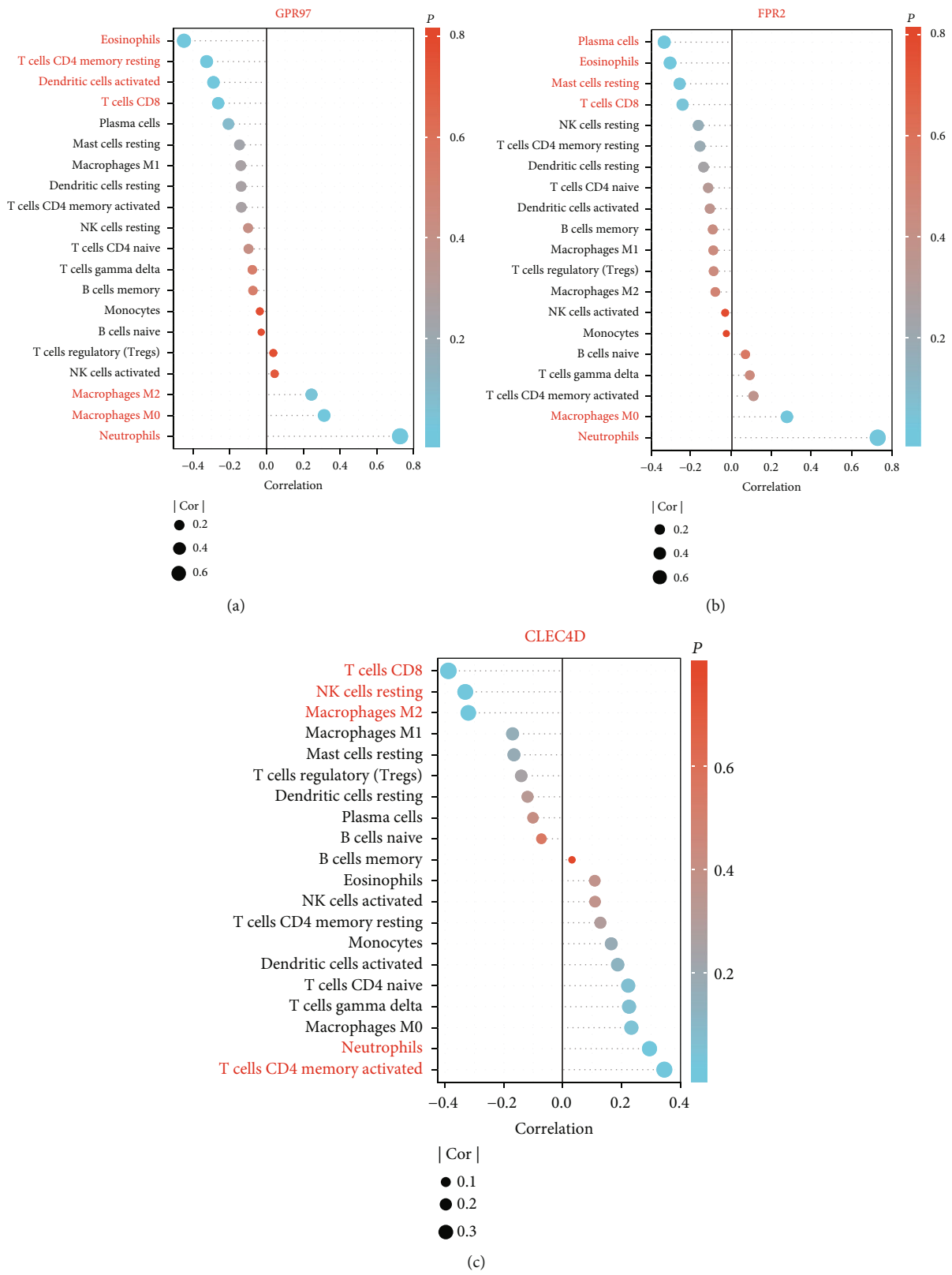

Figure 5: Continued.

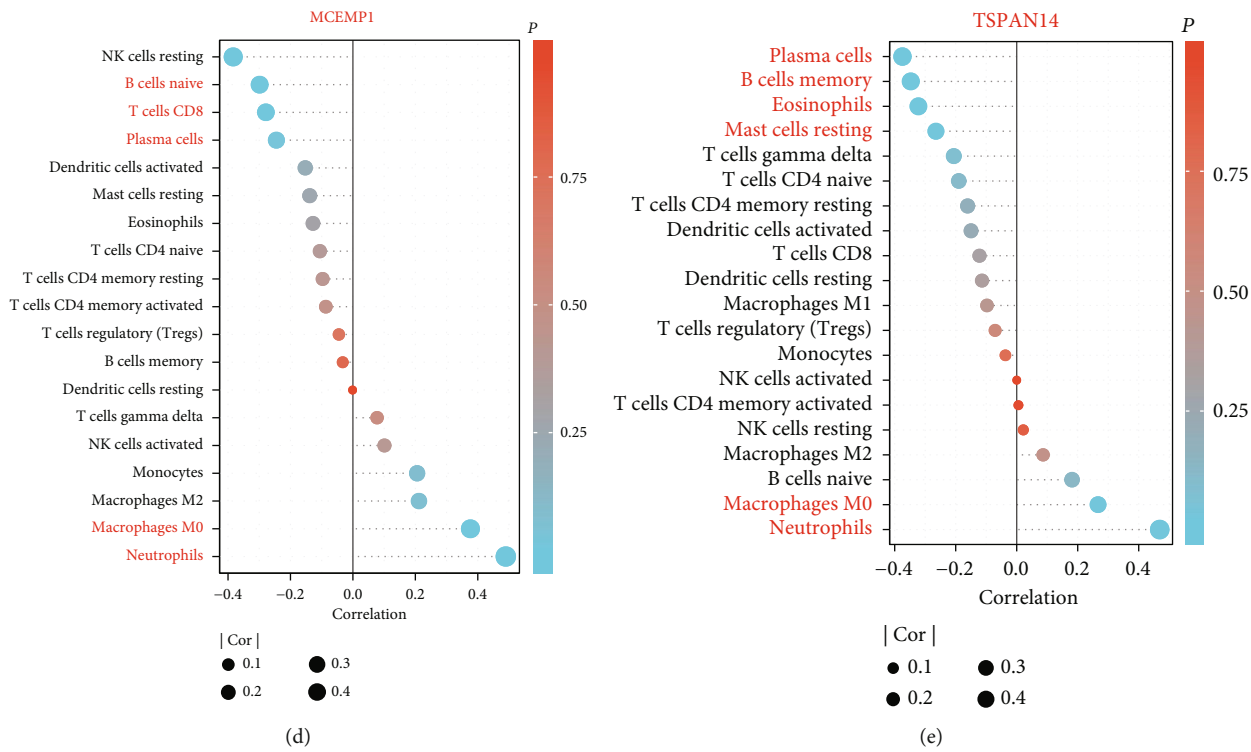

Figure 5: Correlation analysis between key gene expressions and the relative percentages of immune cells in the cardioembolic stroke group. (a–e) Lollipop plots illustrated the relationship between the relative proportions of infiltration-related immune cells and (a) GPR97, (b) FPR2, (c) CLEC4D, (d) MCEMP1, and (e) TSPAN14.

3.4. Correlation Analysis between Key Genes and Infiltration-Related Immune Cells. As implied from the correlation analysis, *MCEMP1* displayed a positive correlation with neutrophils ($r = 0.489$, $p < 0.001$) and macrophages M0 ($r = 0.376$, $p = 0.001$) and a negative correlation with NK cells resting ($r = -0.383$, $p = 0.001$). *FPR2* displayed a positive correlation with neutrophils ($r = 0.728$, $p = 1.26E - 12$) and a negative correlation with T cells CD8 ($r = -0.244$, $p = 0.042$). *TSPAN14* was positively correlated with neutrophils ($r = 0.468$, $p < 0.001$) and macrophages M0 ($r = 0.266$, $p = 0.0267$). *GPR97* positively correlated with neutrophils ($r = 0.726$, $p = 1.66E - 12$) and negatively correlated with T cells CD4 memory resting ($r = -0.325$, $p = 0.006$) and T cells CD8 ($r = -0.263$, $p = 0.029$). *CLEC4D* showed positively correlated with neutrophils ($r = 0.29$, $p = 0.014$) and negatively correlated with macrophages M2 ($r = -0.321$, $p = 0.007$), T cells CD8 ($r = -0.388$, $p < 0.001$), and NK cells resting ($r = -0.331$, $p = 0.005$) (Figures 5(a)–5(e)).

3.5. Construction of Coexpression Network. Based on the screening criteria above, a total of 5413 genes were subjected to WGCNA. To detect the possible outlier samples, a cluster tree including 92 samples, clinic traits, and infiltration-related immune cells was performed by applying average linkage methods. Results indicated that no outlier was found in the samples included in the WGCNA analysis (Figure 6(a)). We then established a scale-free (scale-free $R^2 = 0.90$) coexpression network with the soft-thresholding power $\beta = 3$ (Figures 6(b) and 6(c)). After merging the highly correlated modules by a clustering height cut-off of 0.25 (Figure 7(a)), nine modules were finally obtained for further analysis. Ultimately, initial modules and merged modules display under the clustering tree (Figure 7(b)). Then, the correlations between the modules were analyzed; there was no significant correlation between different modules (Figure 7(c)). The correlation analysis of transcripts was performed within the modules, and no significant correlation between different modules was detected, implying the reliability of the division of modules (Figure 7(d)).

3.6. Identification of the Clinically Significant Modules and Hub Genes. The association between the modules and clinical traits (disease status and infiltration-related immune cells) was explored by measuring the correlation between ME values and clinical features. The results indicated that blue module was positively correlated with cardioembolic stroke ($r = 0.86$, $p = 1e - 27$), neutrophils ($r = 0.64$, $p = 4e - 12$), and macrophages M0 ($r = 0.4$, $p = 8e - 05$), and negative correlations were observed between blue modules and B cells naive ($r = -0.58$, $p = 9e - 10$) and blue modules and T cells CD8 ($r = -0.45$, $p = 7e - 06$) (Figure 8(a)). Additionally, the module significance displayed in bar diagram showed the mean gene significance across whole genes of each module. Blue module was identified as the most clinically significant module (Figure 8(b)). Scatter plots of GS for stroke vs. MM (Figure 8(c)), GS for neutrophils vs. MM (Figure 8(d)), GS for B cells naive vs. MM (Figure 8(e)), and GS for T cells

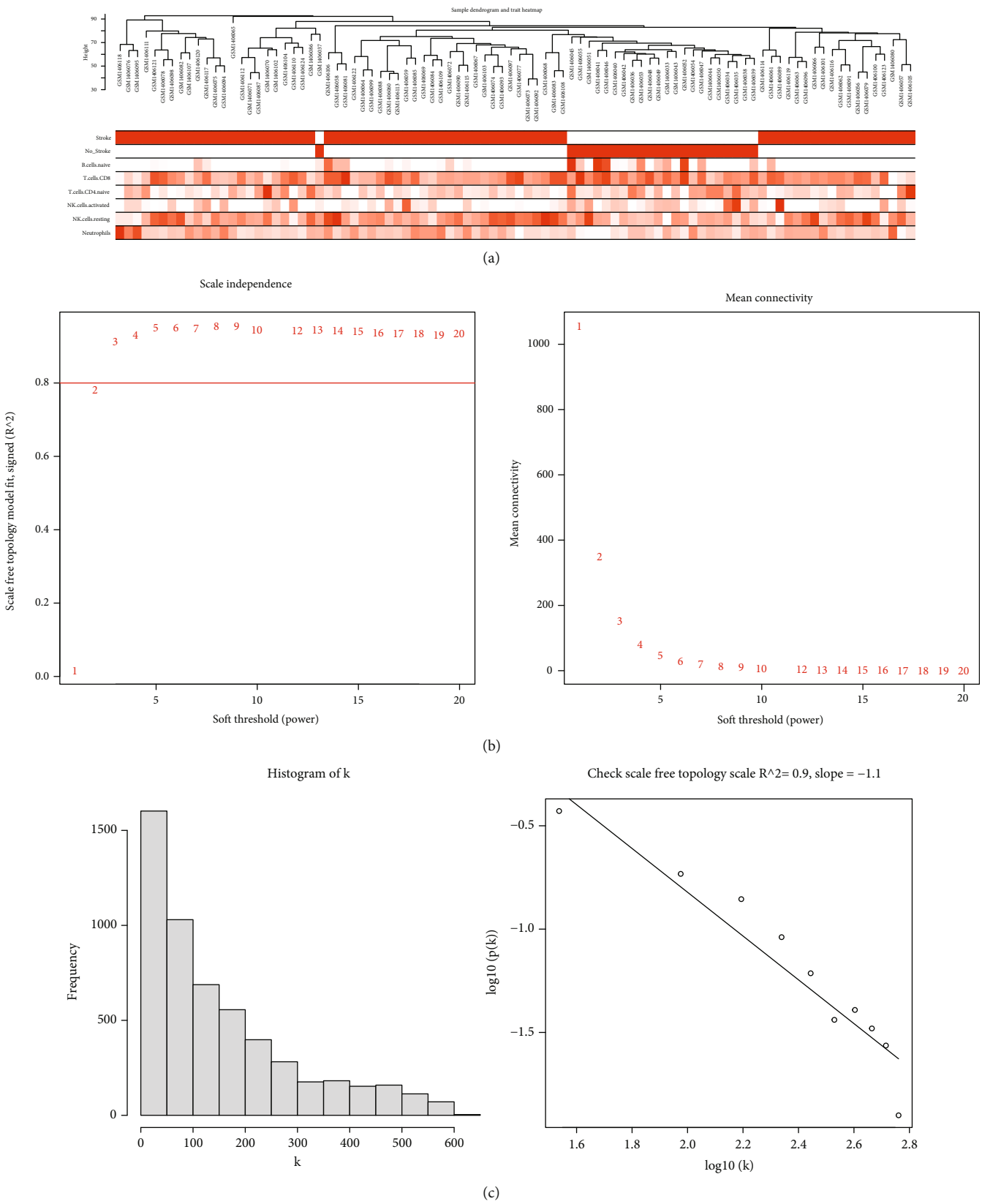

Figure 6: Clustering of samples and selection of the best fit soft-thresholding power. (a) Clustering according to the expression level of cardioembolic stroke patients. The color intensity was proportional to disease status (stroke, no stroke) and infiltration-related immune cells. (b) The cut-off for soft-thresholding power β was set to be 0.80, and β =3 was determined. (c) The coexpression network exhibits a scale-free topology.

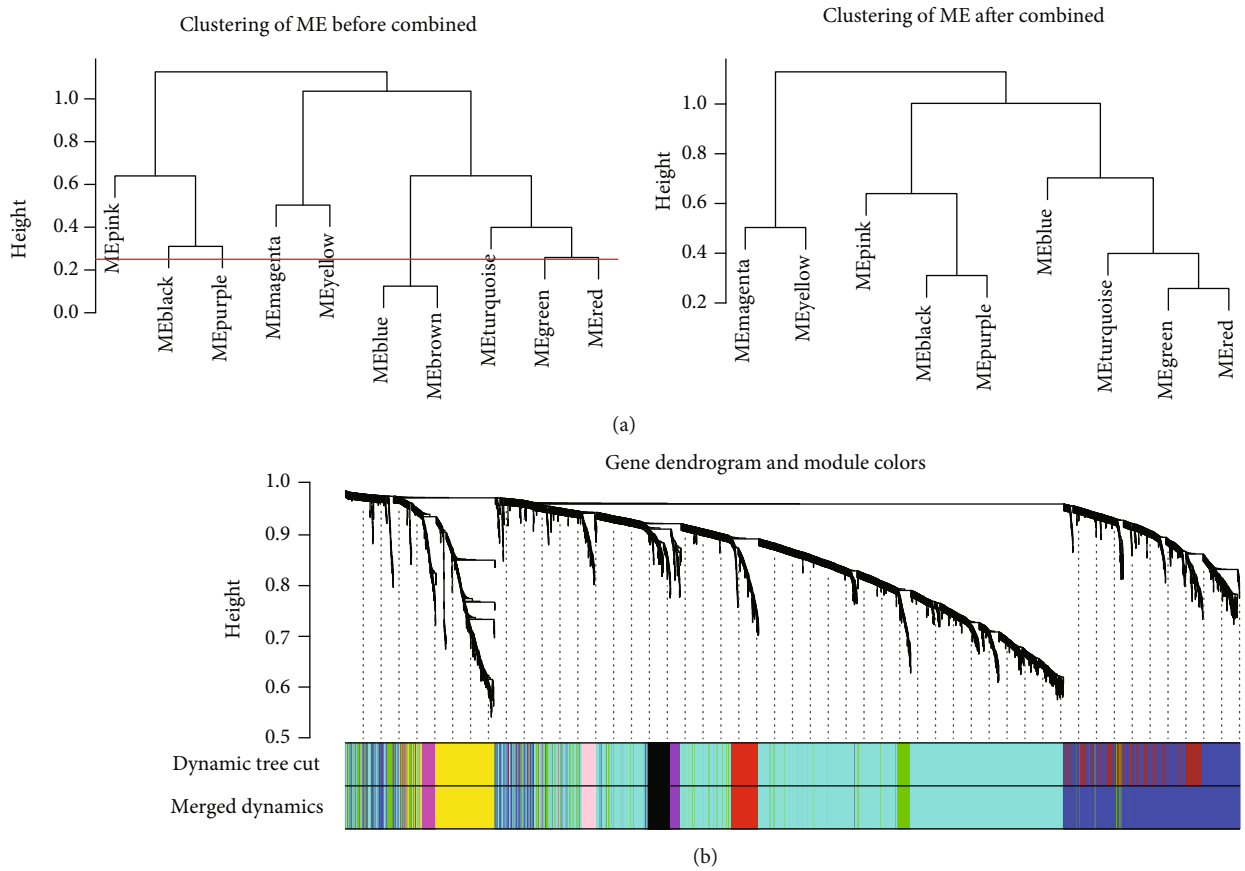

Figure 7: Continued.

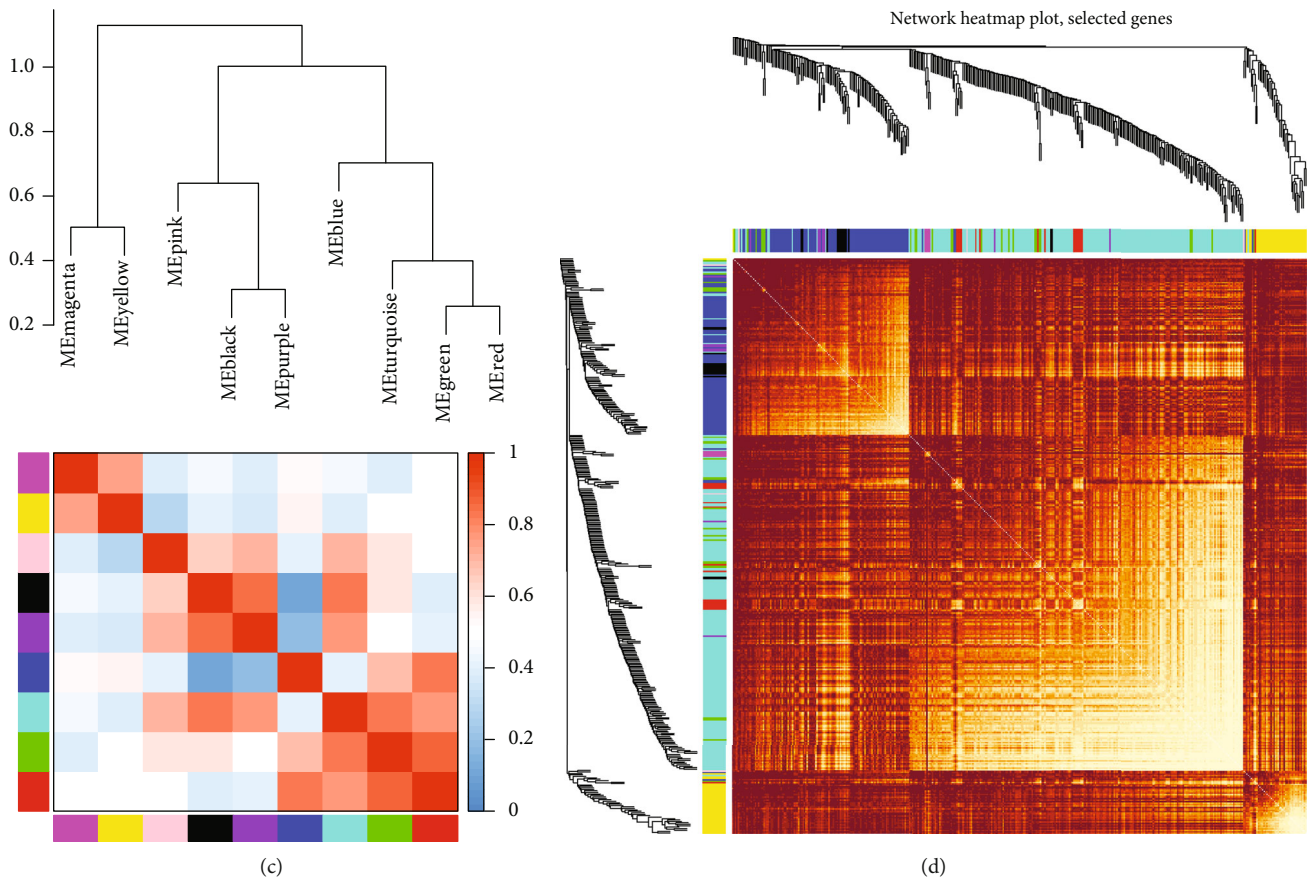

Figure 7: Construction of coexpression network. (a) Clustering dendrograms were cut at a height of 0.25 to detect and combine the similar modules. (b) Origin and merged modules displaying under the clustering tree. (c) Adjacency heatmap of module eigengenes. Red indicated high correlation, and blue represented the opposite results. (d) Clustering dendrogram of nine module eigengenes.

CD8 vs. MM (Figure 8(f)) in the blue module were plotted, respectively. The results indicated that blue module was highly correlated with stoke and immune infiltration. Under the screening criteria of $|MM| > 0.8$ and $|GS| > 0.5$, 110 highly connected hub genes were determined for further analyses.

3.7. Screening Key Genes by Integrating Multiple Analysis. Heatmap showed 110 hub genes in the blue module that were highly expressed in the cardioembolic stroke group (Figure 3(a)). To gain further insight into the biological functions of the hub genes in blue module, GO analyses were applied and results indicated they were mainly enriched in "neutrophil activation," "neutrophil-mediated immunity," "regulation of immune response," "T cell cytokine production," and "CD4 positive, alpha-beta T cell cytokine production" (Figure 3(b)). DEGs were imported into the online tool of the STRING database to generate the PPI network, and a total of 58 genes were identified as hub genes, and their expression pattern and biological functions are also visualized in Figure 3(c). The results implied that most of them were associated with immune response and collagen metabolic process. In addition, we used the Venn diagram to overlap the hub genes in the PPI network and blue module targets and found 25 overlapped DEGs (Figure 3(d)). As displayed in Figure 3(e), the 25 gene expression patterns between stroke and control were also visualized. Five algorithms of the CytoHubba, containing MCC, DMNC, MNC, EPC, and Degree, were then used to process the 25 DEG PPI network to screen the top ten genes. A Venn diagram (Figure 3(f)) was made to build the intersection of genes identified by five algorithms, and *CLEC4D*, *MCEMP1*, *GPR97*, *FPR2*, and *TSPAN14* were determined as key genes.

3.8. MCEMP1 and Its Associated Signal Pathways. We used the full information provided by the Gene-MANIA database to identify the 20 next neighboring proteins of the *MCEMP1*-related query genes; *CLEC4D* and *FPR2* were involved in this analysis. Networks were presented in Figure 9(a). To explore the potential biological functions of *MCEMP1* in CS, GSEA was applied to identify the differentially activated signaling pathways in the high MCEMP1 expression group. Results indicated that the term of neutrophil degranulation, NFKB pathway, inflammasomes, the NLRP3 inflammasome, and IL1R pathway was significantly enriched in the high expression group of *MCEMP1* (Figure 9(b)). Heatmap displayed the associated significantly enriched genes in the term of NLRP3

inflammasome (Figure 9(c)), and interleukin signal pathway (Figure 9(d)).

3.9. ROC Analysis of Key Genes. We performed receiver operating characteristic (ROC) analysis of *CLEC4D*, *MCEMP1*, *GPR97*, *FPR2*, and *TSPAN14* to further validate the diagnostic value of those key genes. The results indicated that all these crucial genes showed potential clinical significance at 3 h (Figure 10(a)), 5 h (Figure 10(b)), and 24 h (Figure 10(c)) following the cardioembolic stroke event. Furthermore, the validation dataset (GSE16561) confirmed the above-presented results: *CLEC4D* (AUC 0.913), *GPR97* (AUC 0.847), *MCEMP1* (AUC 0.796), and *TSPAN14* (AUC 0.718) (Figure 11(c)). To improve the efficiency in distinguishing the capacity of stroke, we constructed the combined diagnosis model of four crucial genes; the AUC value of the stroke reached to 0.946 (95% CI: 0.892–0.999) (Figure 11(b)). These results implied that all crucial genes played key roles in stroke.

3.10. Validation of Key Gene Expression. We further validated the expression of these key genes in two datasets. In dataset GSE16561, with the threshold of $p < 0.05$, *CLEC4D*, *GPR97*, *MCEMP1*, and *TSPAN14* were significantly upregulated in the stroke group (Figures 11(c) and 11(d)) (The platform GPL6883 did not explore *FPR2's* expression). In another dataset GSE58294, at 3 h, 5 h, and 24 h postonset, key genes (*CLEC4D*, *MCEMP1*, *GPR97*, *FPR2*, and *TSPAN14*) were significantly upregulated in the stroke group, as compared with those in the normal control (Figures 10(d)–10(g)).

4. Discussion

Cardioembolic stroke (CS) results in a high rate of disability, morbidity, and mortality, which is a common central nervous system disease with poor prognosis [21]. CS is a common and complex disease with multiple risk factors and causes, including atrial fibrillation, coronary heart disease, valvular heart disease, hypertension, obesity, and diabetes [21, 22]. Previous studies indicated that inflammation and immunity response were involved in the occurrence and development of CS [23]. Markus et al. have also reported potential cardioembolic stroke biomarkers in their study, including common inflammatory markers CRP, interleukin-6, interleukin-1β, and tumor necrosis factor-α [24], whereas, currently, there were no specific and highly sensitive biomarkers for distinguishing CS from large stroke cases. Therefore, it is imperative to find potential new candidate biomarkers in order to help physicians to develop a strategy for treating CS at early stages.

In this study, we downloaded the GSE58294 dataset from the available GEO database and estimated the composition of the immune cells using CIBERSORT algorithms based on the expression matrix, then employing WGCNA to determine the modules associated with the immune cell types. Totally, nine modules were screened; among them, blue module was the most significantly associated with CS, neutrophils, B cells naïve, and T cells CD8. To our knowledge, it is the first time to use WGCNA to explore the relationships between immune cell types and CS. We systematically analyzed the proportion of specific types of immune cells in CS patients. It may provide a novel insight into the strategies for diagnosis and immunotherapy of CS. Under the condition of MM > 0.8 and GS > 0.5, 110 candidate hub genes were then identified within the key modules. We then applied functional enrichment analysis on genes, and results indicated that genes were mainly enriched in neutrophil activation, neutrophil-mediated immunity, regulation of innate immune response, and T cell cytokine production. Additionally, DEGs between CS and control were also screened and used to construct the PPI network. Genes within the network were clustered into different subclades, including the adaptive immune system, collagen metabolic process, and immune response regulating signaling pathway. In order to find potential new biomarkers, we generated another new 25 hub genes by taking the intersection of hub genes in DEGs' PPI network and hub genes in key module. Based on the CytoHubba, five hub genes were determined, including *MCEMP1*, *CLEC4D*, *TSPAN14*, GPR97, and *FPR2*. The relationship between hub genes and immune cell was also determined, and results showed that genes were significantly positively correlated with neutrophils and macrophages M0 and negatively correlated with T cells CD8. Finally, by using the ROC analysis, we found that not only individual crucial genes but also the combined diagnosis model of them had potential diagnostic significance.

Mast cell expressed membrane protein 1, this gene encodes a single-pass transmembrane protein MCEMP1. Based on its expression pattern, it is thought to be involved in regulating mast cell differentiation or immune responses. Jian et al. have reported that MCEMP1 was found to be highly expressed in rats with cerebral ischemic stroke [25]. Furthermore, silencing MCEMP1 resulted in the upregulation of vascular endothelial growth factor (VEGF), while downregulation of Caspase3 led to the promotion of microvessel density (MVD) in rats with ischemic stroke [25]. Moreover, silencing of MCEMP1 could increase Ki67-positive cells and reduce terminal deoxynucleotidyl transferase-mediated d-UTP nick end labeling (TUNEL) positive cells in the marginal zone of cortical infarction in rats. Their study has proved that silenced MCEMP1 could suppress neuronal apoptosis and enhance angiogenesis in rats with cerebral ischemic stroke, emphasizing on that MCEMP1 silencing could serve as a therapeutic target for cerebral ischemic stroke treatment. Raman et al. implicated that peripheral blood expression of MCEMP1 within 1 month after stroke has been proposed as a diagnosis and prognostic biomarker for primary stroke [26]. With all this being taken into consideration, MCEMP1 is a key molecule in the regulation and maintenance of the cerebral ischemic stroke. However, the role of MCEMP1 in cardioembolic stroke (CS) and its underlying mechanisms remain poorly understood. Our study was first to associate the immune response and CS and prove that MCEMP1 was correlated with neutrophils, B cells naïve, and T cells CD8. Besides this, NLRP3 inflammasome and interleukin-1 signal pathway

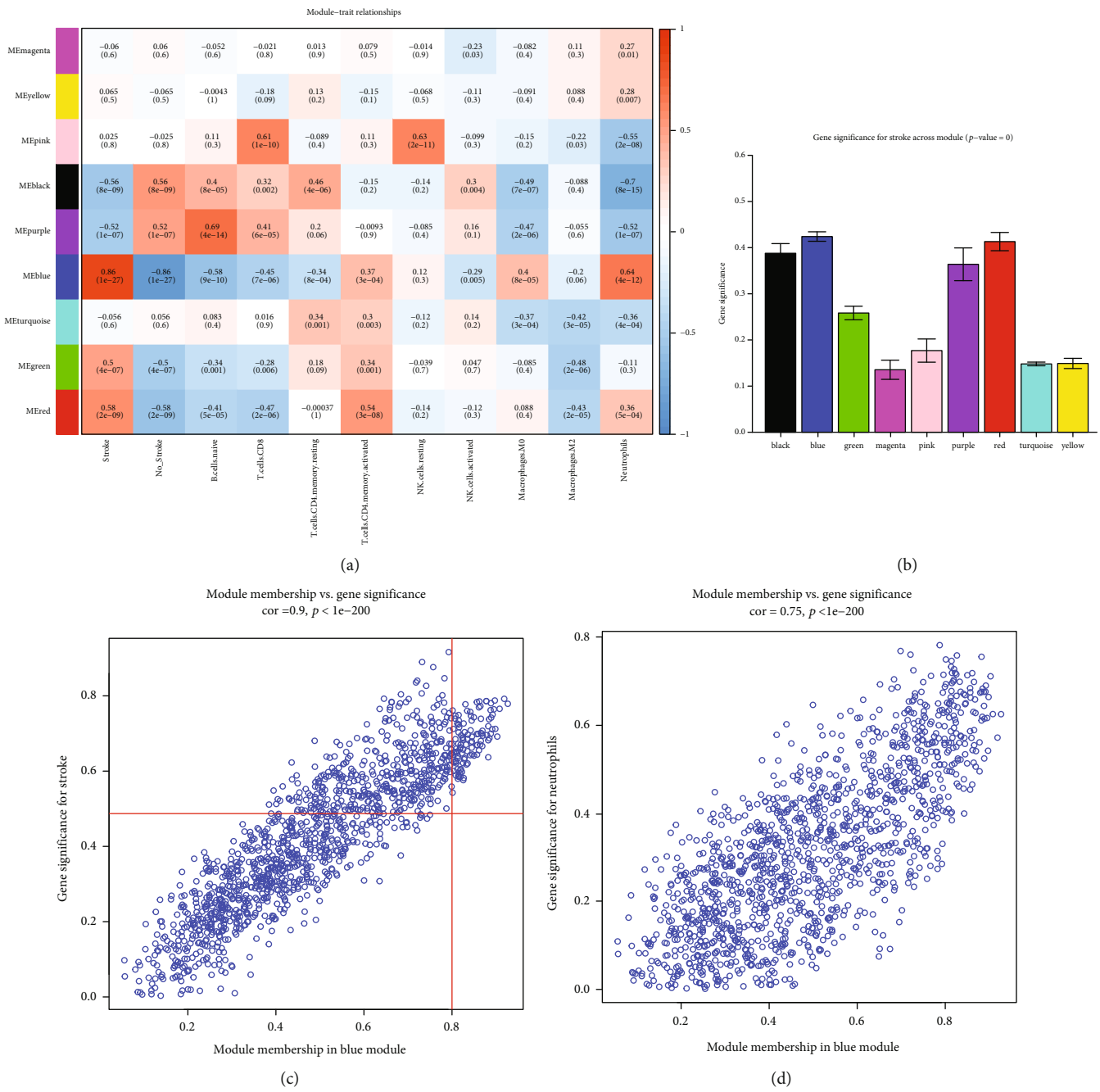

Figure 8: Continued.

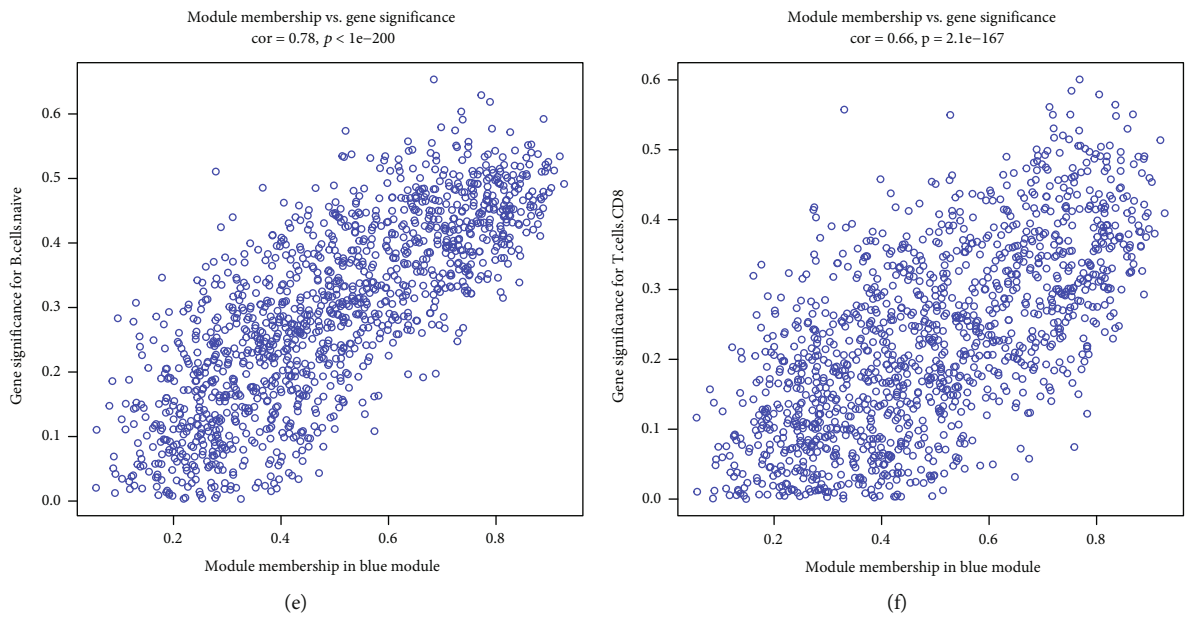

Figure 8: Screening of clinical related modules. (a) Heatmap of module-trait correlation. Red represented positive correlation and blue represented negative correlation. (b) Gene significance for stroke across all modules, the blue module was determined as clinical related module. (c–f) Scatter plot for correlation between the module membership (MM) and gene significance (GS) revised MM and GS (c) stroke, (d) neutrophils, (e) B cells naïve, and (f) T cells CD8.

were significantly enriched in the MCEMP1 high-expression group. Consequently, all of the results have suggested that the MCEMP1 was involved in the process of inflammatory and immune response and it was worthy of additional investigation and development.

CLEC4D (C-Type Lectin Domain Family 4 Member D), a member of the C-type lectin/C-type lectin-like domain (CTL/CTD) superfamily, acted as a pattern recognition receptor (PRR) of the innate immune system: recognized damage-associated molecular patterns (DAMPs) of pathogen-associated molecular patterns (PAMPs) of bacteria [27, 28]. CLEC4D played vital roles as regulators of cell adhesion, cell-cell signaling, inflammation, and immune response [29]. Moreover, studies have shown that the relative mRNA expression of CLEC4D in peripheral blood of patients suffering ischemic stroke within 24 h after onset was dramatically increased, compared with the normal control group, which was consistent with our analysis results [29]. Additionally, our study indicated that CLEC4D was positively correlated with neutrophils and T cells CD4 memory activated, while negatively associated with T cells CD8, which implied that CLEC4D might act through an inflammatory mechanism dependent upon immune effectors in cardioembolic stroke.

GPR97, also named as ADGRG3, is especially expressed in whole blood, particularly in neutrophils. GPR97 was a significant molecule that regulated the development of B cell and migration of lymphatic endothelial cells in vitro via the small GTPases RhoA and CDC42 [30]. Wang et. al have also verified that GPR97 regulated proinflammatory cytokine production in vitro culture assay and played an important role in the development of experimental autoimmune encephalomyelitis (EAE), which indicated that it may have a therapeutic potential for the treatment of CNS autoimmunity [31]. However, the role of GPR97 in CS is unclear and needs to be further explored.

Tetraspanin 14 (TSPAN14), expressed by many types of tissues, especially whole blood, was involved in neutrophil degranulation, positive regulation of notch signaling pathway, and protein maturation. A previous study has reported that TSPAN14 was correlated with periventricular white matter hyperintensities which was an indicator of a history of cerebrovascular disease [32]. Our results indicated that TSPAN14 was positively associated with macrophages M0 and neutrophils, which suggested TSPAN14 may contribute to CS by participating in immunity and inflammation.

Other genes with high degree in the crucial gene cluster, such as FPR2, also played vital roles in CS pathogenesis. FPR2 is preferentially expressed by monocytes, as previously discussed, and was found to be expressed mainly by mammalian phagocytic leukocytes and involved in inflammation and antibacterial host defense [33]. Vital et al. found that targeting the AnxA1/FPR2/ALX pathway represents an attractive therapeutic strategy for the treatment of thrombo-inflammation, counteracting, e.g., stroke in high-risk patient cohorts [34]. The findings of Gavins et al. implicated that FPR ligands, particularly in the brain, could be novel and exciting anti-inflammatory therapeutics for the treatment of a variety of clinical conditions, including stroke [35]. There are also several limitations still detected in our present study. First, the data we used was from public databases, which were limited in the sample size. Further research with larger sample sizes should be carried out to validate our results. Second, the functions and potential molecular mechanisms of genes are quite complicated, and further verification of cellular and animal experiments is required.

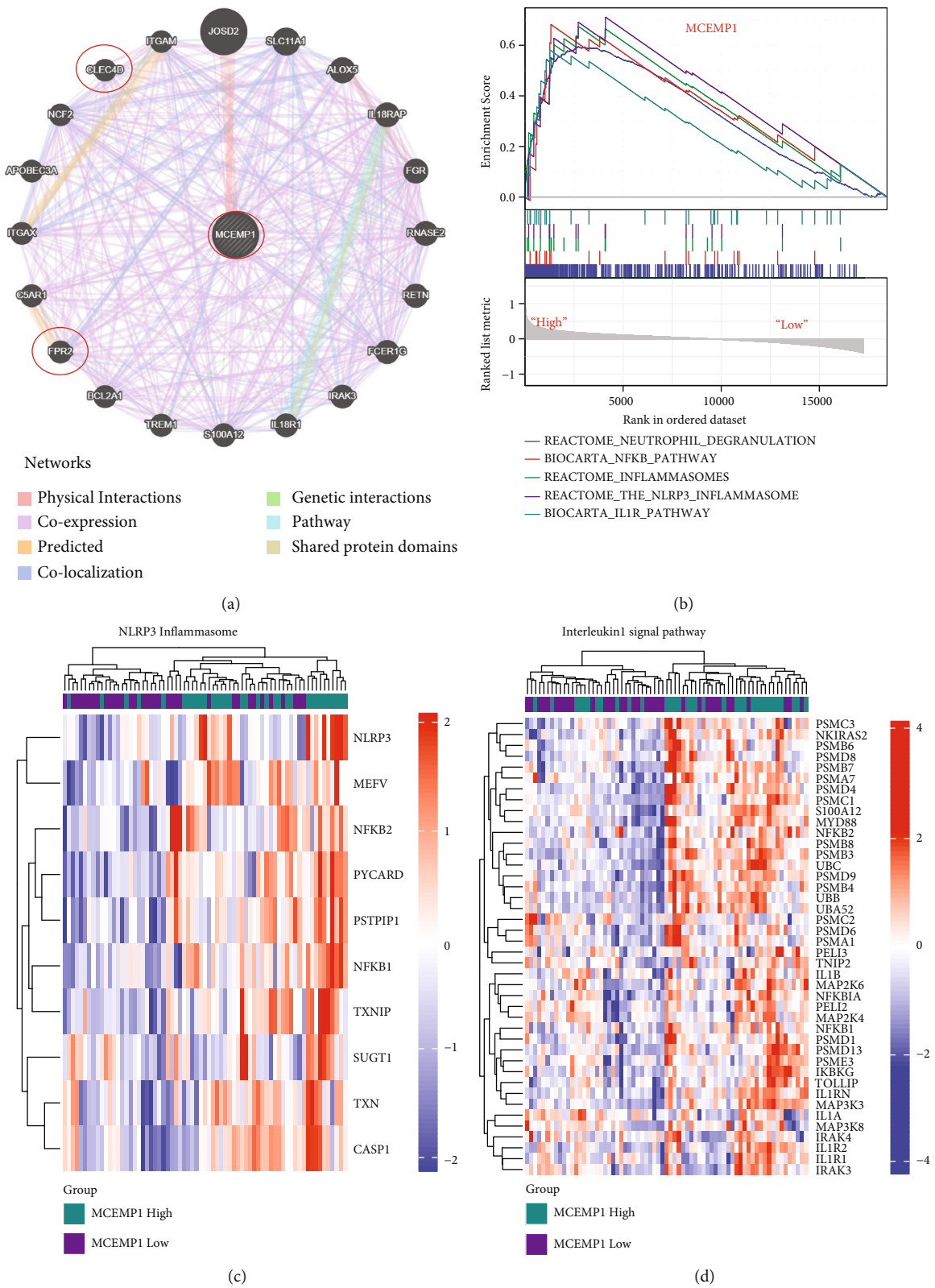

Figure 9: MCEMP1 and its associated signal pathways. (a) MCEMP1 and its coexpression network. (b) GSEA results. (c, d) NLRP3 inflammasome and interleukin-1 signal pathway were significantly enriched in the MECMP1 high group.

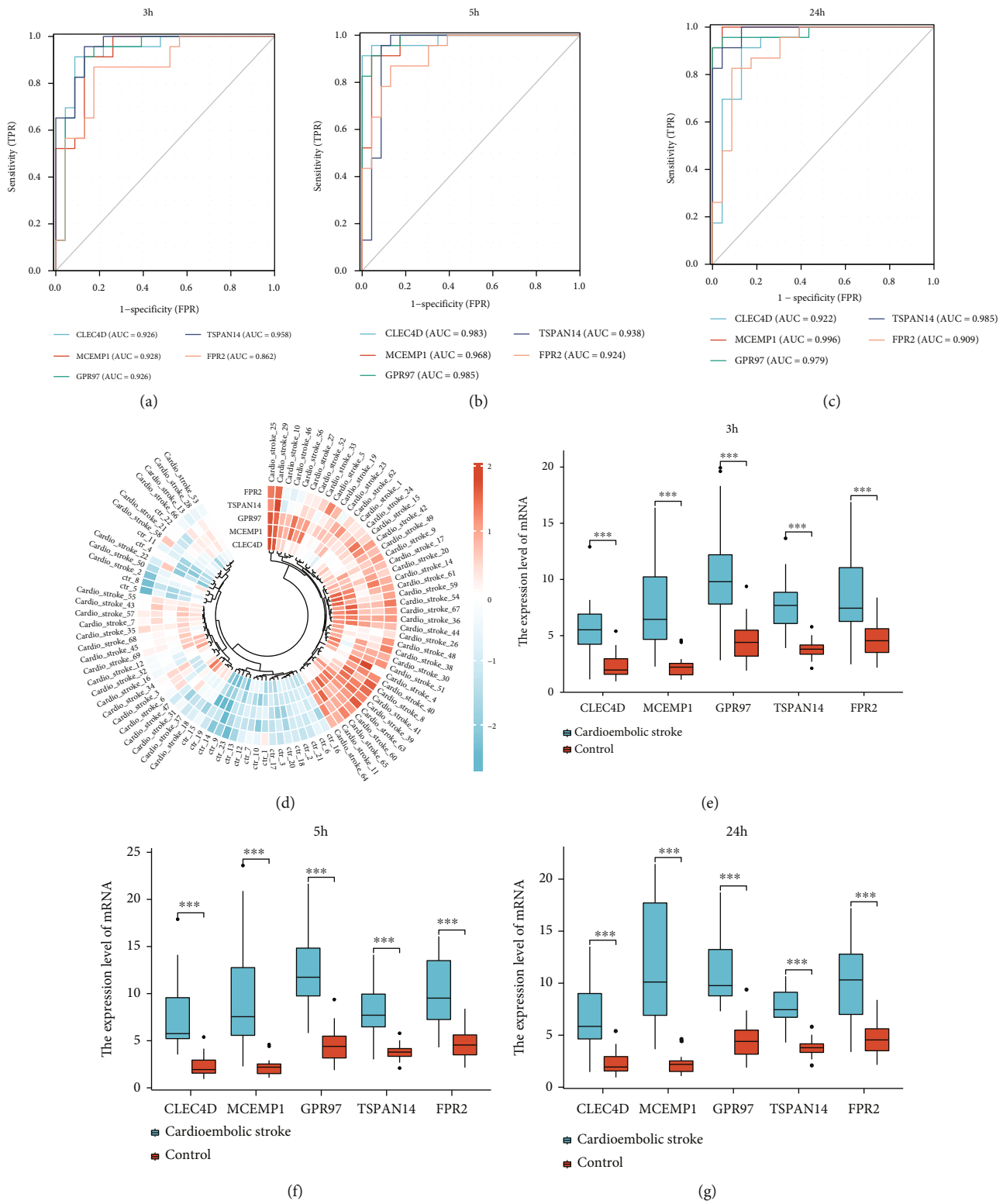

Figure 10: The potential clinical values and expression level of five key genes. (a-c) Applying ROC analysis of 5 key genes to discriminate between cardioembolic stroke and control group, (a) 3 hours, (b) 5 hours, and (c) 24 hours following cardioembolic stroke. (d) Annular heatmap showing the expression of hub genes in each sample. (e–g) Box plots displaying changes in expression levels of CLEC4D, MCEMP1, GPR97, TSPAN14, and FPR2 in 3 h, 5 h, and 24 h after cardioembolic stroke. All crucial genes were significantly increased in patients with cardioembolic stroke compared to normal individuals.

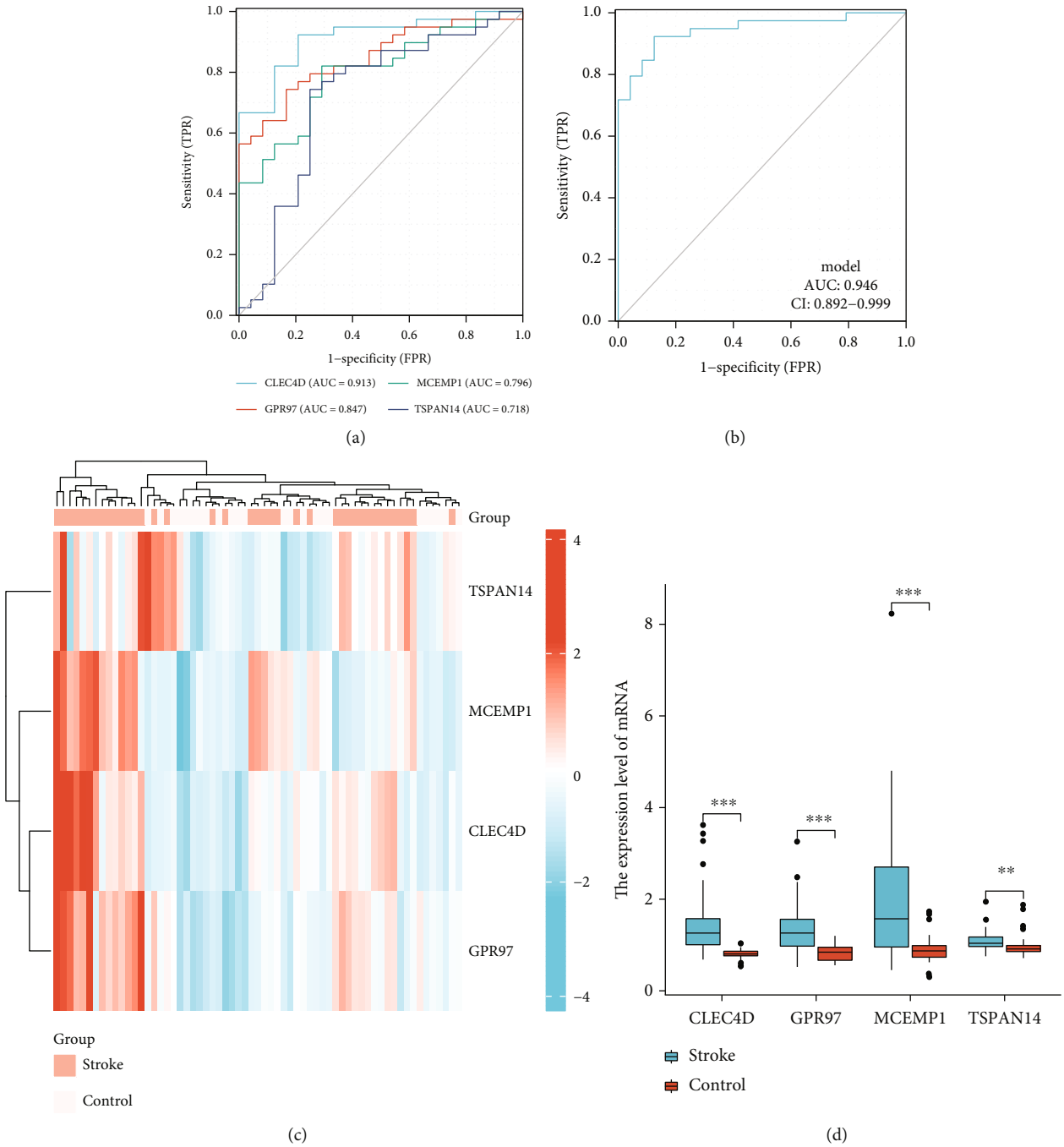

Figure 11: The verification of crucial genes as biomarkers for stroke in an independent dataset. (a) Receiver operating characteristic curves for individual CLEC4D, GPR97, MCEMP1, and TSPAN14 of stroke versus control. (b) Evaluation of clinical diagnostic efficacy of 4 key gene signatures (AUC = 0.946, 95% CI = 0.892–0.999) (Logistic regression model = -14.1075+ 7.9797∗CLEC4D+ 1.8645∗GPR97+ 1.8384∗MCEMP1+ 2.7048∗TSPAN14). (c) Heatmap showing the relative expression levels of CLEC4D, GPR97, MCEMP1, and TSPAN14 in each sample. (d) Box plot indicated the expression of 4 crucial genes following stroke were all significantly higher than healthy individuals.

5. Conclusion

In our study, we performed WGCNA to analyze the relationships between immune cell types and cardioembolic stroke (CS) for the first time. Five crucial genes (*MCEMP1*, *TSPAN14*, *CLEC4D*, *GPR97*, and *FPR2*) were identified. These five genes may therefore be potential in CS and are worthy of further investigation.

Data Availability

The datasets used in this study can be acquired in NCBI datasets (GEO https://www.ncbi.nlm.nih.gov/geo/info/linking.html; GSE58294; GSE16561).

Conflicts of Interest

The authors declare that they have no conflicts of interest.

Authors' Contributions

Qiaoqiao Li and Fang Rao designed the study, and Qiaoqiao Li, Xueping Gao, and Xueshan Luo conducted the literature search. Qingrui Wu and Jintao He analyzed the data and prepared figures and/or tables. Qiaoqiao Li and Yang Liu carried out the data analysis. Qiaoqiao Li and Xueping Gao wrote the paper. Yumei Xue, Shulin Wu, and Fang Rao performed editing and reviewing. All authors contributed ideas and comments, revised the paper, and approved the final version. Qiaoqiao Li, Xueping Gao, and Xueshan Luo contributed equally to this work.

Acknowledgments

This work was supported by grants from the Medical Science and Technology Foundation of Guangdong Province (2019B020230004), the National Natural Science Foundation of China (No. 81870254), and the High-Level Hospital Construction Plan (No. DFJH201808).

References

[1] Y. M. Qiu, C. L. Zhang, A. Q. Chen et al., "Immune cells in the BBB disruption after acute ischemic stroke: targets for immune therapy?," *Frontiers in Immunology*, vol. 12, 2021.

[2] J. Huang, F.-C. Zhou, B. Guan et al., "Predictors of remission of early-onset poststroke depression and the interaction between depression and cognition during follow-up," *Frontiers in Psychiatry*, vol. 9, 2019.

[3] Q. Xu, B. Zhao, Y. Ye et al., "Relevant mediators involved in and therapies targeting the inflammatory response induced by activation of the NLRP3 inflammasome in ischemic stroke," *Journal of Neuroinflammation*, vol. 18, no. 1, p. 123, 2021.

[4] H. Park, M. Han, Y. D. Kim et al., "Impact of the total number of carotid plaques on the outcome of ischemic stroke patients with atrial fibrillation," *Journal of Clinical Medicine*, vol. 8, no. 11, p. 1897, 2019.

[5] V. L. Feigin, B. Norrving, M. G. George, J. L. Foltz, G. A. Roth, and G. A. Mensah, "Prevention of stroke: a strategic global imperative," *Nature Reviews Neurology*, vol. 12, no. 9, pp. 501–512, 2016.

[6] D. Petrovic-Djergovic, S. N. Goonewardena, and D. J. Pinsky, "Inflammatory disequilibrium in stroke," *Circulation Research*, vol. 119, no. 1, pp. 142–158, 2016.

[7] C. Cheyuo, A. Jacob, R. Wu, M. Zhou, G. F. Coppa, and P. Wang, "The parasympathetic nervous system in the quest for stroke therapeutics," *Journal of Cerebral Blood Flow and Metabolism*, vol. 31, no. 5, pp. 1187–1195, 2011.

[8] B. M. Famakin, "The immune response to acute focal cerebral ischemia and associated post-stroke immunodepression: a focused review," *Aging and Disease*, vol. 5, no. 5, pp. 307–326, 2014.

[9] L. Gautier, L. Cope, B. M. Bolstad, and R. A. Irizarry, "Affy - analysis of Affymetrix GeneChip data at the probe level," *Bioinformatics*, vol. 20, no. 3, pp. 307–315, 2004.

[10] C. Ginestet, "ggplot2: elegant graphics for data analysis," *Journal of the Royal Statistical Society Series a-Statistics in Society*, vol. 174, no. 1, pp. 245-246, 2011.

[11] G. Yu, L.-G. Wang, Y. Han, and Q.-Y. He, "clusterProfiler: an R package for comparing biological themes among gene clusters," *Omics-a Journal of Integrative Biology*, vol. 16, no. 5, pp. 284–287, 2012.

[12] A. M. Newman, C. B. Steen, C. L. Liu et al., "Determining cell type abundance and expression from bulk tissues with digital cytometry," *Nature Biotechnology*, vol. 37, no. 7, pp. 773–782, 2019.

[13] P. Langfelder and S. Horvath, "WGCNA: an R package for weighted correlation network analysis," *BMC Bioinformatics*, vol. 9, no. 1, 2008.

[14] Y. Kong, Z.-C. Feng, Y.-L. Zhang et al., "Identification of immune-related genes contributing to the development of glioblastoma using weighted gene co-expression network analysis," *Frontiers in Immunology*, vol. 11, 2020.

[15] J. A. Gustavsen, S. Pai, R. Isserlin, B. Demchak, and A. R. Pico, "RCy3: network biology using Cytoscape from within R," *F1000Research*, vol. 8, pp. 1774–1774, 2019.

[16] E. T. Bullmore and O. Sporns, "Complex brain networks: graph theoretical analysis of structural and functional systems," *Nature Reviews Neuroscience*, vol. 10, no. 3, pp. 186–198, 2009.

[17] D. Warde-Farley, S. L. Donaldson, O. Comes et al., "The GeneMANIA prediction server: biological network integration for gene prioritization and predicting gene function," *Nucleic Acids Research*, vol. 38, suppl_2, pp. W214–W220, 2010.

[18] Z. Gu, R. Eils, and M. Schlesner, "Complex heatmaps reveal patterns and correlations in multidimensional genomic data," *Bioinformatics*, vol. 32, no. 18, pp. 2847–2849, 2016.

[19] P. Shannon, A. Markiel, O. Ozier et al., "Cytoscape: a software environment for integrated models of biomolecular interaction networks," *Genome Research*, vol. 13, no. 11, pp. 2498–2504, 2003.

[20] X. Robin, N. Turck, A. Hainard et al., "pROC: an open-source package for R and S+ to analyze and compare ROC curves," *BMC Bioinformatics*, vol. 12, no. 1, 2011.

[21] W. Liang, X. Huang, and W. Chen, "The effects of baicalin and baicalein on cerebral ischemia: a review," *Aging and Disease*, vol. 8, no. 6, pp. 850–867, 2017.

[22] S.-J. Hong, S. K. Kim, D. H. Yun, J. Chon, and H. J. Park, "Association between microRNA-4669 polymorphism and ischemic stroke in a Korean population," *Disease Markers*, vol. 2019, 9 pages, 2019.

[23] A. Drieu, D. Levard, D. Vivien, and M. Rubio, "Anti-inflammatory treatments for stroke: from bench to bedside," *Therapeutic Advances in Neurological Disorders*, vol. 11, p. 175628641878985, 2018.

[24] A. Markus, S. Valerie, and K. Mira, "Promising biomarker candidates for cardioembolic stroke etiology. A brief narrative review and current opinion," *Frontiers in Neurology*, vol. 12, 2021.

[25] R. Jian, M. Yang, and F. Xu, "Lentiviral-mediated silencing of mast cell-expressed membrane protein 1 promotes angiogenesis of rats with cerebral ischemic stroke," *Journal of Cellular Biochemistry*, vol. 120, no. 10, pp. 16786–16797, 2019.

[26] K. Raman, M. J. O'Donnell, A. Czlonkowska et al., "Peripheral BloodMCEMP1Gene expression as a biomarker for stroke prognosis," *Stroke*, vol. 47, no. 3, pp. 652–658, 2016.

[27] L.-L. Zhu, X.-Q. Zhao, C. Jiang et al., "C-Type Lectin Receptors Dectin-3 and Dectin-2 Form a Heterodimeric Pattern- Recognition Receptor for Host Defense against Fungal Infection," *Immunity*, vol. 39, no. 2, pp. 324–334, 2013.

[28] Y. Miyake, K. Toyonaga, D. Mori et al., "C-type lectin MCL is an FcR gamma-coupled receptor that mediates the adjuvanticity of mycobacterial cord factor," *Immunity*, vol. 38, pp. 1050–1062, 2013.

[29] L. M. Graham, V. Gupta, G. Schafer et al., "The C-type Lectin Receptor CLECSF8 (CLEC4D) Is Expressed by Myeloid Cells and Triggers Cellular Activation through Syk Kinase," *Journal of Biological Chemistry*, vol. 287, no. 31, pp. 25964–25974, 2012.

[30] N. Valtcheva, A. Primorac, G. Jurisic, M. Hollmen, and M. Detmar, "The Orphan Adhesion G Protein-coupled Receptor GPR97 Regulates Migration of Lymphatic Endothelial Cells via the Small GTPases RhoA and Cdc42," *Journal of Biological Chemistry*, vol. 288, no. 50, pp. 35736–35748, 2013.

[31] J. Wang, X. Wang, X. Chen et al., "Gpr97/Adgrg3 ameliorates experimental autoimmune encephalomyelitis by regulating cytokine expression," *Acta Biochimica et Biophysica Sinica*, vol. 50, no. 7, pp. 666–675, 2018.

[32] N. J. Armstrong, K. A. Mather, M. Sargurupremraj et al., "Common genetic variation indicates separate causes for periventricular and deep white matter hyperintensities," *Stroke*, vol. 51, no. 7, pp. 2111–2121, 2020.

[33] R. D. Ye, S. L. Cavanagh, O. Quehenberger, E. R. Prossnitz, and C. G. Cochrane, "Isolation of a cDNA that encodes a novel granulocyte N-formyl peptide receptor," *Biochemical and Biophysical Research Communications*, vol. 184, no. 2, pp. 582–589, 1992.

[34] S. A. Vital, E. Y. Senchenkova, J. Ansari, and F. N. E. Gavins, "Targeting AnxA1/formyl peptide receptor 2 pathway affords protection against pathological thrombo-inflammation," *Cell*, vol. 9, no. 11, p. 2473, 2020.

[35] F. N. E. Gavins, "Are formyl peptide receptors novel targets for therapeutic intervention in ischaemia-reperfusion injury?," *Trends in Pharmacological Sciences*, vol. 31, no. 6, pp. 266–276, 2010.

Hindawi
Disease Markers
Volume 2022, Article ID 5179247, 12 pages
https://doi.org/10.1155/2022/5179247

Research Article

Crosslinking-Induced Corneal Endothelium Dysfunction and Its Protection by Topical Ripasudil Treatment

Xuemei Wang,[1,2] Yanlin Zhong,[1,2] Minghui Liang,[1,2] Zhirong Lin,[1,2] Huping Wu,[1,2] and Cheng Li[1,2]

[1]*Eye Institute and Affiliated Xiamen Eye Center of Xiamen University, Xiamen, Fujian, China*
[2]*Fujian Provincial Key Laboratory of Ophthalmology and Visual Science & Ocular Surface and Corneal Diseases, Xiamen University, Xiamen, Fujian, China*

Correspondence should be addressed to Huping Wu; wuhuping123@163.com and Cheng Li; cheng-li@xmu.edu.cn

Received 19 October 2021; Accepted 16 December 2021; Published 13 January 2022

Academic Editor: Wen-Qing Shi

Purpose. To investigate the changes of corneal endothelium under different crosslinking conditions and the protective effect of ripasudil. *Methods*. Corneal crosslinking groups were infiltrated with riboflavin and subsequently irradiated with 0.54 J/cm^2 or 1.08 J/cm^2 UVA, while noncrosslinking groups included neither UVA nor riboflavin treatment, only 1.08 J/cm^2 UVA and only riboflavin treatment. Corneal opacity, variations in corneal endothelial cells, and corneal thickness of all groups were observed by slit lamp, *in vivo* confocal microscopy, and optical coherence tomography. Immunofluorescence staining and scanning electron microscopy were performed to evaluate changes in the structure and function of the corneal endothelium. The mice that received a corneal crosslinking dose of 1.08 J/cm^2 were instilled with ripasudil to explore its protective effect on the corneal endothelium. *Results*. Treatment with UVA and riboflavin caused an increase in corneal opacity and corneal thickness and decreased endothelial cell density. Furthermore, treatment with UVA and riboflavin caused endothelial cell DNA damage and destroyed the tight junction and pump function of the endothelium, while riboflavin or the same dose of UVA alone did not affect the endothelium. Ripasudil reduced DNA damage in endothelial cells, increased the density of cells, and protected the endothelium's integrity and function. *Conclusion*. Riboflavin combined with UVA can damage the corneal endothelium's normal functioning. The corneal endothelium's wound healing is dose-dependent, and the ROCK inhibitor ripasudil maintains the endothelium's pump and barrier functions.

1. Introduction

Corneal crosslinking (CXL) therapy has been introduced as a minimally invasive treatment to prevent the development of keratectasia, which has completely changed the treatment of keratoconus and other corneal ectasias such as pellucid marginal degeneration and iatrogenic ectasia. CXL has also been used in the treatment of other diseases, such as bullous keratopathy, infectious ulcers, ulcerative keratitis, and other causes of corneal edema [1].

The fundamentals of CXL and the molecular processes of photooxidative CXL are combined with riboflavin as a photosensitizer in this treatment. The intention of collagen CXL with riboflavin/UVA light is to artificially enhance crosslinking in the corneal stroma to restore mechanical stability [2]. The procedure damages cell membranes, causing keratocyte death, in addition to the positive tissue stiffening impact [3, 4]. Riboflavin is nontoxic and can be used as a biological drug or a coloring agent in food processing [2]. Riboflavin serves both as a photosensitizer to promote corneal stiffening (crosslinking) by UVA and as a shield to reduce the level of UVA to below the cytotoxic threshold [5].

Regarding the adverse reactions caused by CXL, some studies have reported damage or inflammation of the corneal endothelium following CXL [6]. According to the previous studies [7], the endothelial phototoxic level is 0.35 mW/cm^2, and a minimal corneal thickness of 400 μm is required to ensure safe riboflavin/UVA CXL using the typical 3 mW/cm^2 surface irradiance (5.4 J/cm^2 surface dose) [8]. Although some preventive measures have been taken,

postoperative corneal edema, suggestive of endothelial damage, has also been reported in thicker corneas [9]. Furthermore, despite some studies linking CXL to endothelial cell death, scientists have yet to definitively ascertain whether CXL alters the structure and function of the corneal endothelium in *vivo* models.

Since the use of a mouse model can increase knowledge regarding the basic cellular and molecular pathways activated by CXL therapy [10], studying different CXL protocols in mice is useful for understanding the physiological responses of different intensities of CXL and to determine the appropriate range of UVA fluence of CXL in mice. Previous studies have demonstrated that even when the UVA fluence is dropped to 0.09 J/cm^2, a considerable corneal stiffening impact is still generated, and a fluence between 1.62 and 2.7 J/cm^2 generates the least negative effects, such as scar formation and neovascularization [10, 11]. A CXL protocol for mice has previously been established [12]. Since the corneal thickness of mice differs from that of human, the treatment parameters were altered according to the Lambert-Beer law to make the relative UVA absorption of the mouse cornea equal to that of the human cornea in the Dresden protocol [13]. According to this calculation [14], when the radiation dosage to the mouse cornea is 1.53 J/cm^2, the corresponding radiation dose to the human cornea is 5.4 J/cm^2. However, white central scars in the cornea can even be found at a dose of 1.53 J/cm^2 [10]. Since a dose of 1.53 J/cm^2 may be a relatively high dose for mouse corneal crosslinking, we chose threshold UVA dosages below 1.53 J/cm^2 to investigate potential damage to the corneal endothelium by combined riboflavin/UVA therapy.

Previous pioneering studies have shown that inhibiting ROCK signaling promotes corneal endothelial cell adhesion, migration, proliferation, and wound healing [15–20]. In human keratinocytes, RhoA/ROCK signaling is one of the regulators involved in oxidative damage and apoptosis, and blockade of RhoA/ROCK with a ROCK inhibitor can reduce the levels of DNA damage [21]. After destroying the central endothelium via transcorneal freezing, individuals with Fuchs endothelial corneal dystrophy (FECD) were given eye drops containing a ROCK inhibitor, which reduced corneal edema and increased visual acuity [22, 23]. In individuals with bullous keratopathy, cell-based treatments also assisted the reformation of the corneal endothelium layer [24]. Ripasudil hydrochloride hydrate (K-115) is a ROCK inhibitor that selectively inhibits ROCK1 and ROCK2, and a dose of 0.4 percent ripasudil has been licensed in Japan for the treatment of glaucoma [25]. Ripasudil has been recommended as an effective medicine for adjuvant therapy in FECD patients [26, 27], as well as a prospective therapeutic agent for retinal hypoxia neovascular diseases [28].

In the present study, we exploited the transparent property of the cornea and created a model that provided direct visualization of the cellular behavior in response to CXL *in vivo*, as determined by *in vivo* confocal microscopy and optical coherence tomography (OCT), monitoring the swelling of the cornea as a result of endothelial cell function and morphology. Moreover, we found that riboflavin plays an important role in mediating corneal endothelial damage. Since ROCK inhibitors have been reported to suppress oxidative damage, we tested the effect of ripasudil on corneal endothelium changes in CXL-induced mice.

2. Materials and Methods

2.1. Animals. 58 SPF male C57/BL6 mice (6–8 weeks old) (Shanghai SLAC Experimental Animal Center, China) were utilized in this work. They were housed in a clean environment with a temperature of 24 ± 1°C, a relative humidity of 59 ± 9%, and a 12 h/12 h light/dark cycle. The Xiamen University Experimental Animal Ethics Committee authorized the research procedure, which complied with the ARVO Declaration on the Use of Animals in Ophthalmology and Visual Studies. The mice ($n = 58$) were randomly separated into two sets. For the first part of the study, 40 mice were divided into five groups: 1.08 J/cm^2 UVA only, riboflavin only, 0.54 J/cm^2 UVA plus riboflavin, 1.08 J/cm^2 UVA plus riboflavin, and neither UVA nor riboflavin, to investigate their effect of independent variables on endothelium layer integrity. In a second assessment using 6 mice from each group, for the control and Ripa group, mice received 1.08 J/cm^2 UVA plus riboflavin to examine ripasudil's pharmacological effectiveness in the mouse CXL model.

2.2. Corneal Crosslinking Procedure. Pentobarbital (40 mg/kg) was injected intraperitoneally for anesthesia, and proparacaine eye drops were given topically. Mechanical removal of corneal epithelium in the range of diameter 2 mm and 0.27% riboflavin solution diluted in sodium chloride (Avedro, USA) was applied to the deepithelialized corneas for 20 minutes. Subsequently, a UVA lamp would be used to irradiate the cornea at 365 nm with a fluence of 0.54 J/cm^2 (9 mW/cm^2 for 1 minute) or 1.08 J/cm^2 (9 mW/cm^2 for 2 minutes) (UVX 2000 system, IROC Innocross AG Co. Ltd., Switzerland). Following CXL, the corneal epithelial incision was treated with levofloxacin eye drops (Tobradex; Alcon Laboratories, Inc) three times a day until it healed.

2.3. Eye Drop Treatment. One drop of 0.4% ripasudil (Kowa Company, Tokyo, Japan) was topically instilled (2.5 μL) four times daily in both eyes of six mice; PBS was instilled in both eyes of six further mice as a control.

2.4. Assessment of the Ocular Surface. Having followed CXL, all the corneas were checked daily using a slit light (BQ900H Haag-Streit, Bern, Switzerland). Corneal opacity scores were made depending on the sum of the scores of the several stated measures employed for this aim at postoperative 36 h, 4 d, 7 d, and 14 d. Corneal opacity scores were calculated according to the degree of edema in the central and peripheral part of the cornea.

2.5. In Vivo Confocal Microscopy. The mice were used in our trial following the administration of pentobarbital (40 mg/kg). The central corneal structure was examined by confocal laser scanning microscopy using a Heidelberg Retina Scanner III/Rostock Corneal Module (Heidelberg Engineer GmbH, Heidelberg, Germany). One drop of carbomer gel (Alcon Laboratories, Fort Worth, TX) was utilized prior to observation.

By adjusting the controller, the cap center was extended to the center of the cornea, and the computer screen showed a digital image of the cornea. At least 10 images were photographed of each structure: the superficial epithelial layer, basal epithelial layer, stromal layer, and endothelial layer. All measurements were performed by a researcher who was blinded to the specific experimental conditions. The built-in software program was used to evaluate the density of endothelial cells.

2.6. Optical Coherence Tomography. Anterior segment images were taken using optical coherence tomography (OCT) (OPTOPROBE, England) at postoperative 36 h, 4 d, 7 d, and 14 d. The central corneal thickness was measured using inbuilt software.

2.7. Staining with Immunofluorescence. Frozen sections and corneal whole mounts were fixed with acetone at −20°C for 10 minutes and then incubated at 4°C overnight with primary antibodies for Texas Red–X phalloidin (1 : 150), anti-ZO-1 (1 : 150), anti-Na^+/K^+-ATPase (1 : 200), anti-γ-H2AX (1 : 400), and anti-8-OHdG (1 : 200). The next day, samples were incubated with Alexa Fluor 488-conjugated IgG (1 : 300) or Alexa Fluor 594-conjugated IgG (1 : 300) for 2 h at room temperature in the darkness. A laser confocal scanning microscope (Fluoview 1000, Olympus, Japan) had been used to investigate the immunofluorescence staining after three washes in PBS and counterstaining with DAPI (H-1200, Vector).

2.8. Ultrastructure of the Corneal Endothelium. The corneas of the 5 groups were fixed overnight in PBS (pH 7.4) containing 2.5% glutaraldehyde at 4°C, following which 4 mm × 2 mm pieces were produced without contact with the endothelium. Then, the ultrastructure of the corneal endothelium was observed by scanning electron microscope (SEM, JSM6390LV, JEOL, Tokyo, Japan) after dehydration, drying, and gold plating.

2.9. Statistical Analysis. Statistical analysis was performed by using the GraphPad Prism 8.0 program (GraphPad Software, Inc, San Diego, CA). Two-way ANOVA was used to compare symptoms at different time points. One-way ANOVA was used to compare multiple groups. The probability < 0.05 was considered statistically significant. All data is reported as mean ± SD.

3. Results

3.1. CXL Irradiation Causes Corneal Edema in Mice. Slit-lamp examination revealed visible edema in the cornea of each CXL-treated group at posttreatment 36 h, while in the U(-), R(-), U(++), R(-), and U(-), R(+) groups, corneal edema was not obvious. In the U(+), R(+) group, corneal transparency was restored after 14 days, while the corneas remained edematous in the U(++), R(+) group (Figure 1(a)). In comparison with the U(++), R(-), or U(-), R(+) groups, the corneal opacity scores of CXL group were significantly higher at 36 h after treatment. In the U(+), R(+) group, scores reversed to the baseline on the 14th day, but in the U(++), R(+) group, the values remained high (Figure 1(b)).

3.2. CXL Irradiation Causes Alterations in Mouse Corneal Endothelial Cell Morphology. Mouse corneal endothelial cell morphology and density were assessed by *in vivo* confocal microscopy at various time points after CXL. The corneal endothelium showed a characteristic hexagonal monolayer with a regular size and shape in the U(-), R(-), U(++), R(-), and U(-), R(+) groups. However, CXL mice showed exacerbated morphological changes, such as increased cell size and loss of discernible cell borders as compared with the other three groups at the same recovery time points (Figure 2(a)). Figure 2(b) depicts the variations in corneal endothelial cell density in each group over time. In the U(++), R(+) group, endothelial damage from 36 h to d14 persisted, and endothelial cell density was the lowest, being significantly less than that in the U(++), R(-), or U(-), R(+) groups.

3.3. CXL Irradiation Increases the Thickness of the Central Cornea by OCT. Corneal edema leads to an increase in central corneal thickness (CCT), which is a hallmark of endothelial cell functional impairment. In the U(++), R(-), and U(-), R(+) groups, the corneal thickness did not change significantly. OCT demonstrated that in the U(+), R(+), and U(++), R(+) groups, the corneal thickness was considerably higher than in the U(++), R(-), or U(-), R(+) groups at 36 h after CXL (Figures 3(a) and 3(b)). In the U(+), R(+) group, the thickness tended to be increased by 36 h, reaching significance but then returning to normal by day 14; however, the corneal thickness in the U(++), R(+) group did not recover even after 14 days (Figure 3(b)).

3.4. CXL Induces Na^+/K^+-ATPase Mislocalization and Disruption of Cytoskeletal Organization and Tight Junction Integrity. Ion transporter proteins including as bicarbonate transporters, monocarboxylate transporters (MCT), and aquaporin water channels assist the pump function, which is primarily maintained by Na^+/K^+-ATPase [29]. In the U(++), R(-), and U(-), R(+) groups on day 4, Na^+/K^+-ATPase was uniformly and consistently expressed at the cell membrane, while its localized expression was disrupted and dispersed in the CXL groups (Figure 4(a)). The U(+), R(+) group's Na^+/K^+-ATPase localization began to restore to its usual distribution after 14 days, but the U(++), R(+) group's recovery was only partially complete (Figure 4(b)).

In the typical corneal endothelium, F-actin was found at the apical cell borders, resulting in a double-banded appearance. In the CXL groups, the double-banded structure had vanished by day 4 and the F-actin expression pattern was diffused (Figure 4(a)). The F-actin distribution in the U(+), R(+) group almost recovered after 14 days, but the F-actin distribution in the U(++), R(+) group was only partially restored and the cytoskeleton was partially rearranged (Figure 4(b)).

The corneal endothelium's barrier integrity is supported by cell-to-cell connections such as adhesion and tight junctions, which are primarily formed by ZO-1. ZO-1 produced a consistent hexagonal pattern in the non-CXL groups' corneal endothelium and was continually expressed along the cell boundary. On day 4, ZO-1 expression at the cell boundary in the CXL groups turned partial and discontinuous

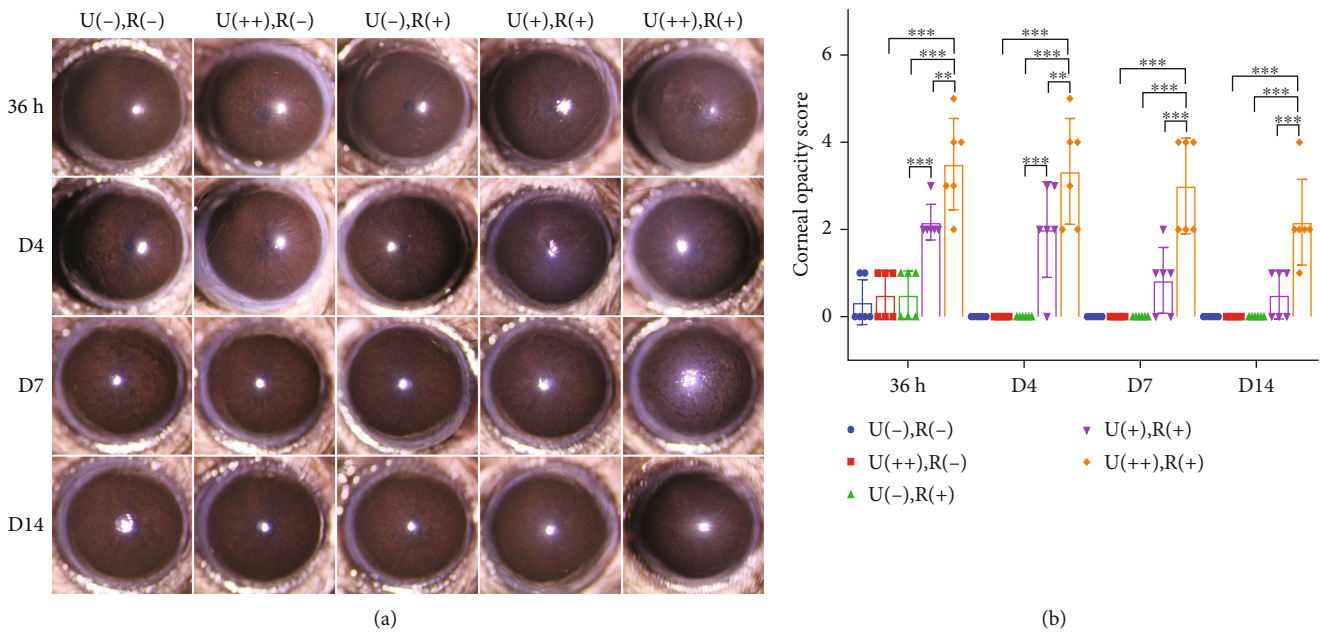

Figure 1: CXL irradiation causes corneal edema in mice. Representative slit-lamp images showing differences between the 5 different groups at time points corresponding to 36 h, 4 d, 7 d, and 14 d after CXL treatment. (a) Time-dependent changes in corneal opacity scores in the 5 groups. Data are expressed as the mean ± SD; $n = 6$. $^{**}P < 0.01$; $^{***}P < 0.001$. (b) U(-), R(-): neither UVA norriboflavin; U(++), R(+): 1.08 J/cm^2 UVA; U(-), R(+): riboflavin only; U(+), R(+): 0.54 J/cm^2 UVA plus riboflavin; U(++), R(+): 1.08 J/cm^2 UVA plus riboflavin.

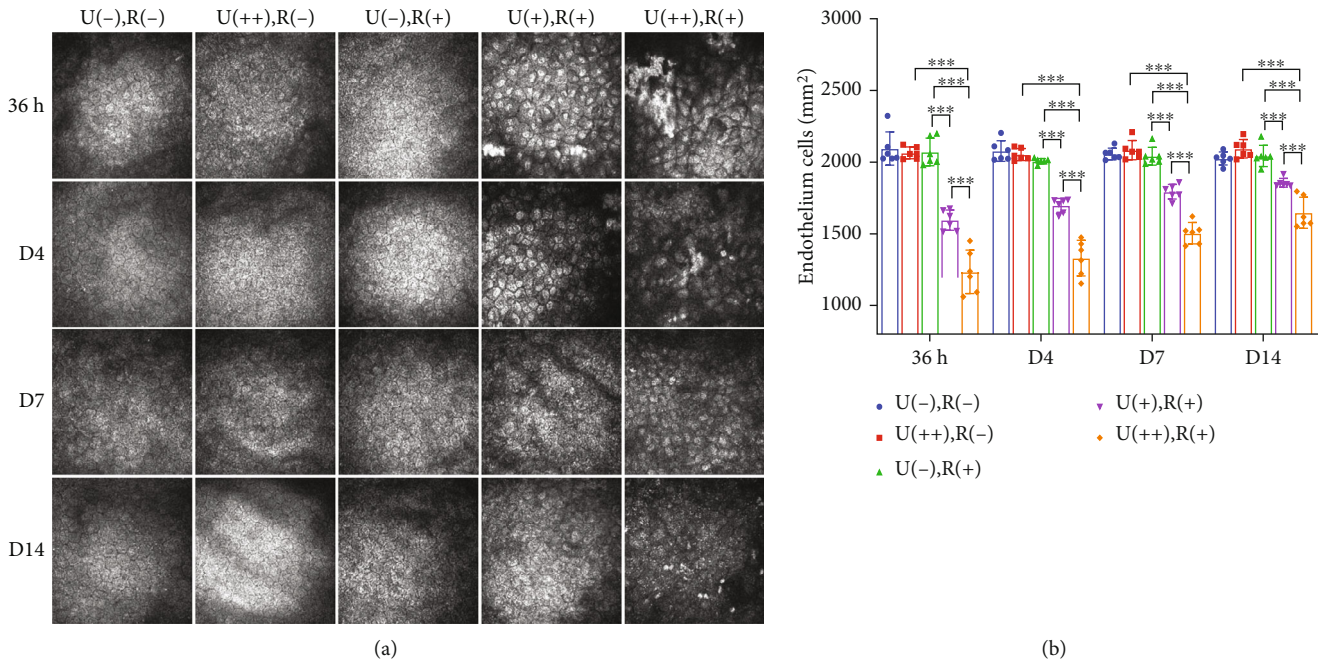

Figure 2: CXL irradiation causes morphological changes in mouse corneal endothelial cells and decreases cell density. (a) Representative confocal microscopy images showing differences in the endothelial cell layer between the 5 different groups at time points corresponding to 36 h, 4 d, 7 d, and 14 d after CXL treatment. (b) Cell density analysis of the 5 groups. Data are expressed as the mean ± SD; $n = 6$. $^{***}P < 0.001$.

(Figure 4(a)); however, 14 days later, the distribution of ZO-1 in the U(+), R(+) group was substantially restored, while the distribution of ZO-1 in the U(++), R(+) group had not recovered (Figure 4(b)).

3.5. CXL Disrupts the Fine Structure of the Mouse Corneal Endothelial Cells. To obtain a more comprehensive overview of the CXL-induced changes in corneal endothelial cells, the fine structure of the posterior cornea was evaluated by SEM.

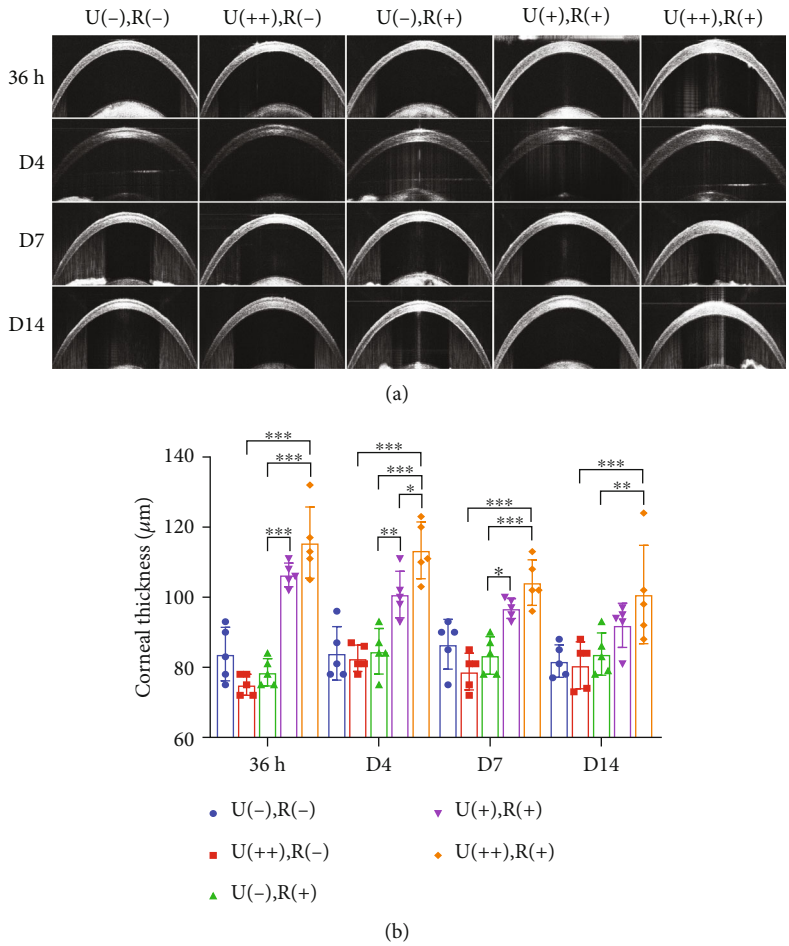

Figure 3: CXL irradiation modulates the thickness of the central cornea. (a) Representative OCT images of mouse corneas in the 5 different groups at time points corresponding to 36 h, 4 d, 7 d, and 14 d after CXL treatment. (b) Central corneal thickness analysis based on OCT images. Data are expressed as the mean ± SD; $n = 5$. $^{*}P < 0.05$; $^{**}P < 0.01$; $^{***}P < 0.001$.

In the U(-), R(-), U(++), R(-), and U(-), R(+) groups, the corneal endothelial cells appeared flat and hexagonal. In addition, sharply demarcated and interdigitating cellular borders, apical microvilli, and infrequent cilia were also observed. On day 14, the morphology of the corneal endothelial cells in the U(+), R(+) group had virtually recovered as compared to the U(-), R(+) group. The cell border between corneal endothelial cells became blurry in several locations in the U(++), R(+) group, indicating breakdown of cell-cell tight junctions (Figure 4(c), arrow).

3.6. CXL Induces DNA Damage in Mouse Corneal Endothelial Cells. Intense immunostaining with anti-8-OHdG (8-hydroxy-2′-deoxyguanosine), a biomarker of DNA oxidation [30] occurring when DNA is oxidatively modified by ROS, was detected in the corneal endothelium in the CXL groups after 36 h. There was a significant increase in CXL-induced nuclear 8-OHdG in comparison with the U (++), R(-) or U(-), R(+) group, especially in the U(++), R(+) group (Figure 5(a)). H2AX is found in the nucleosome as a histone variant. H2AX is quickly phosphorylated at Ser139 within 1–3 minutes after DNA double-strand breaks, and the relative amount of phosphorylated H2AX molecules rises linearly with the severity of DNA damage [31, 32]. In the endothelial monolayer of the CXL groups, nuclei with very intense staining were evident, indicating the presence of DNA damage. The amount of γ-H2AX expression in the CXL groups was considerably greater than in the U(++), R(-) or U(-), R(+) groups. The punctate staining pattern clearly implies that corneal endothelial cells respond to nuclear DNA damage by producing DNA damage foci, and positive nuclear staining for H2AX phosphorylated at Ser139 gives evidence that corneal endothelial cells are capable of detecting nuclear DNA damage (Figure 5(b)).

3.7. Ripasudil Reduces Corneal Edema in CXL Mice and Protects the Corneal Endothelium from CXL-Induced Injury. It was observed that multiple daily administrations of ripasudil eye drops in mouse eyes for 7 days improved corneal opacification as compared with the U(++), R(+), Ripa(-) group (control) (Figure 6(a)). On day 7, the corneal thickness of the U(++), R(+), Ripa(+) mice was considerably lower than that of the control group (Figures 6(b) and 6(d)).

In vivo confocal microscopy revealed relatively minor cell body expansion and loose intercellular connections in

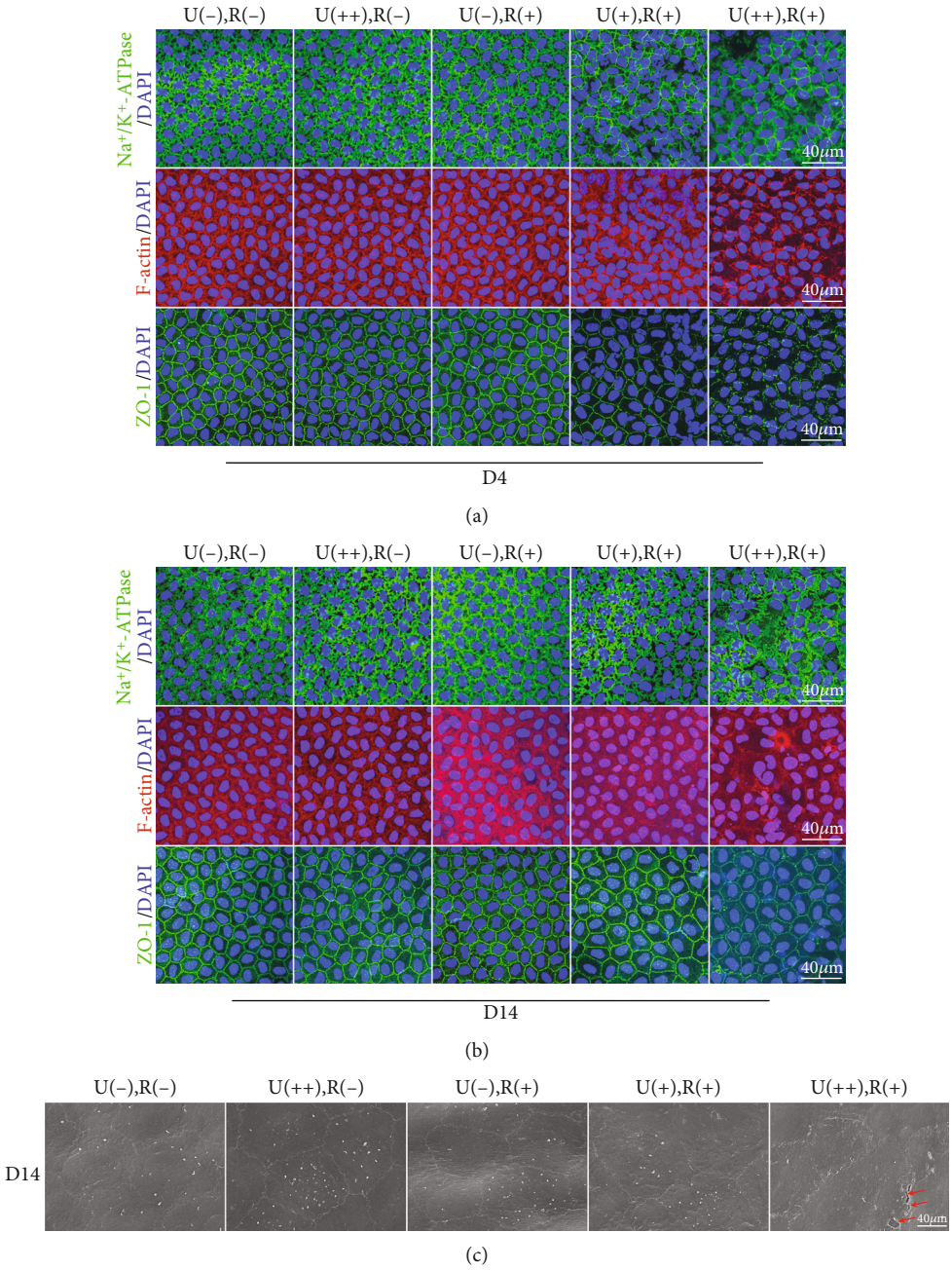

Figure 4: CXL irradiation destroys the integrity of tight junctions and disrupts the localization of Na^+/K^+-ATPase in corneal endothelial cells. (a, b) Representative confocal images of wholemount mouse central corneal endothelial cells detecting ZO-1, F-actin, and Na^+/K^+-ATPase localization on (a) day 4 and (b) day 14. On day 4, ZO-1, F-actin, and Na^+/K^+-ATPase staining of endothelial cells show a disrupted distribution of these markers in the U(+), R(+), and U(++), R(+) groups as compared with that in the other 3 groups. After 14 days, the normal distribution around the cell borders was restored in the U(+), R(+) group, but the recovery was still incomplete in the U(++), R(+) group. (c) Representative SEM images of the apical surface of central corneal endothelial cells on day 14. The microvilli on endothelial cells have almost disappeared, and the cell boundary between endothelial cells is discontinuous (arrows) in the U(++), R(+) group as compared with the U(++), R(-), or U(-), R(+) group.

the U(++), R(+), Ripa(+) group, in contrast to the loose and flaky shedding seen in the control group (Figure 6(c)). Ripa-treated corneal endothelial cells had a considerably higher density than those in the control group (Figure 6(e)). Wholemount immunofluorescence labeling of ZO-1, Na^+/K^+-ATPase, and -H2AX was done to further investigate the protective effect of ripasudil on corneal endothelial cells in CXL animals. The tight junction marker ZO-1 exhibited integrated structures with a defined boundary in the Ripa-treated group, but ZO-1 expression at the cell border was irregular, even absent, in the control group. Na^+/K^+-ATPase, a pump functional marker, exhibited regular and continuous expression around the cell border in the Ripa-treated group, which was similar to the non-CXL group. However, the

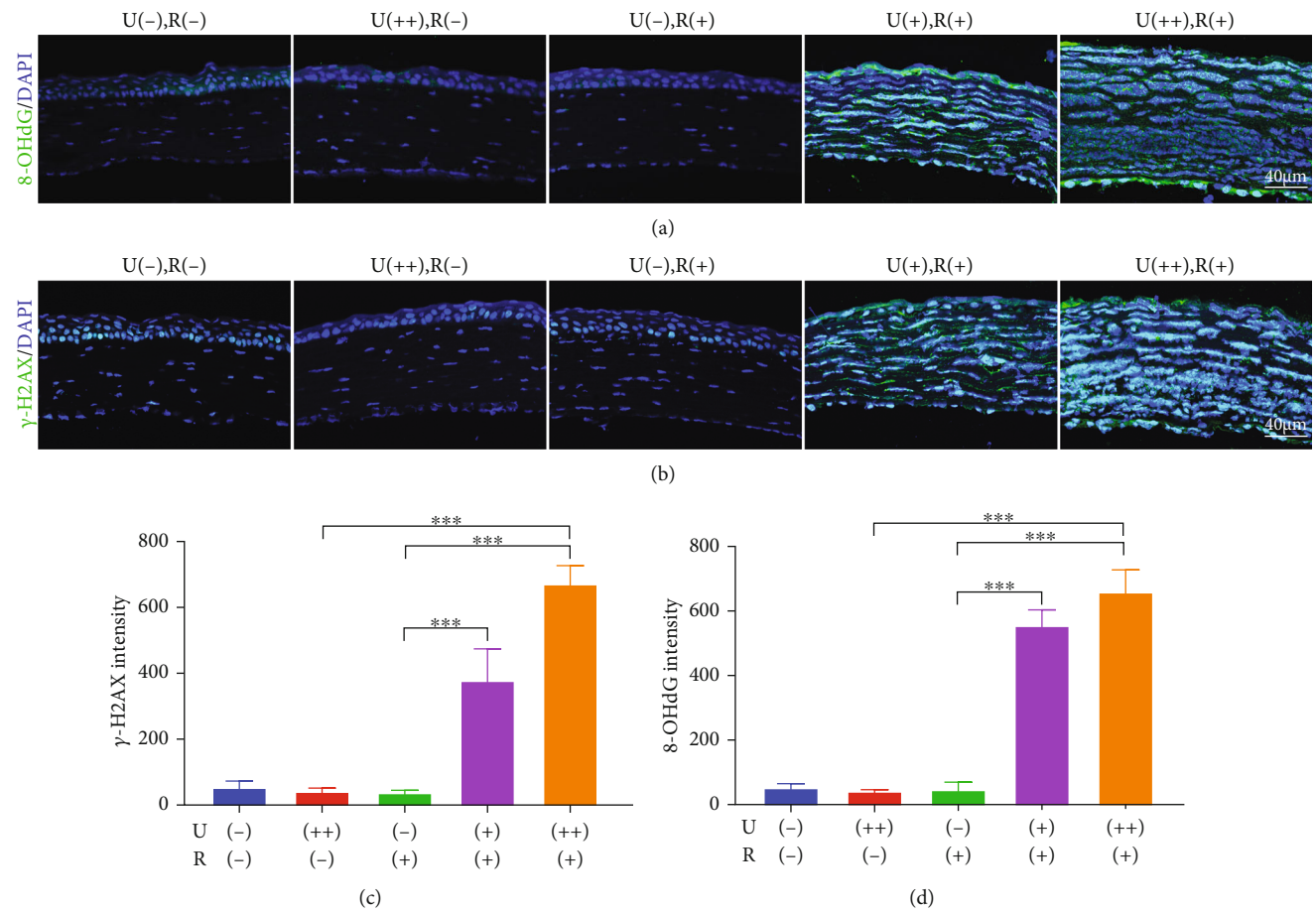

Figure 5: CXL irradiation causes DNA damage in corneal endothelial cells. (a) Representative confocal images of the mouse corneal endothelium with 8-OHdG staining at 36 h after CXL treatment. (b) Representative confocal images of the mouse corneal endothelium with γ-H2AX staining at 36 h after CXL treatment. (c) Mean immunofluorescence intensity of 8-OHdG in endothelial cells. (d) Mean immunofluorescence intensity of γ-H2AX in endothelial cells. Data are expressed as the mean ± SD; $n = 3$. $^{***}P < 0.001$.

expression of Na^+/K^+-ATPase became sparse and was absent in certain localized areas in the control group. γ-H2AX is an important marker of DNA damage. In the control group, some nuclei with intense staining were observed in the corneal endothelium on day 7; however, the Ripa-treated group showed no positive nuclei staining in the endothelium at the same time point (Figure 6(f)).

4. Discussion

CXL is a well-known therapy that is receiving increased popularity as a treatment choice for progressive keratoconus, especially considering its relatively low level of side effects. Despite the reported high safety profile, some reports indicate the possibility of corneal endothelial damage with obvious corneal edema after CXL treatment [33]. We used a mouse corneal crosslinking model to study endothelial cell changes caused by different crosslinking conditions, especially changes in function and morphology, in addition to studying the protective effect of ripasudil on endothelial injury to the cornea.

In the present study, we demonstrate that riboflavin, as a photosensitizer, damaged the corneal endothelium's integrity and function under UVA irradiation. The barrier integrity and pump efficiency of the corneal endothelium after combined riboflavin/UVA treatment were destroyed in comparison with the same dose of UVA treatment alone. The corneal endothelium's barrier and pump activities are critical for maintaining corneal transparency [34, 35]. Our results revealed a correlation between variations in these characteristics and CXL-induced edema. In the CXL-0.54 J/cm^2 group, the corneal endothelium's tight junction and pump activities were recovered to almost the same extent as those in the non-CXL groups, and the transparency of the cornea was also restored by day 14. This reversal indicates that the corneal endothelial function underwent time-dependent recovery. In contrast, the recovery of the CXL-1.08 J/cm^2 group was incomplete after 14 days. In a previous study, the cytotoxic radiation level following combined riboflavin/UVA treatment was approximately 10 times lower than that after UVA treatment alone since riboflavin enhances the cytotoxic effect caused by the oxidation of UVA light owing to the increase in UVA absorption [4]. After riboflavin treatment, the absorption of UVA in the cornea increased to 95%, while that without riboflavin reached only 25–35% [36]. Pitts et al. [37] discovered corneal endothelial cell injury in pigmented

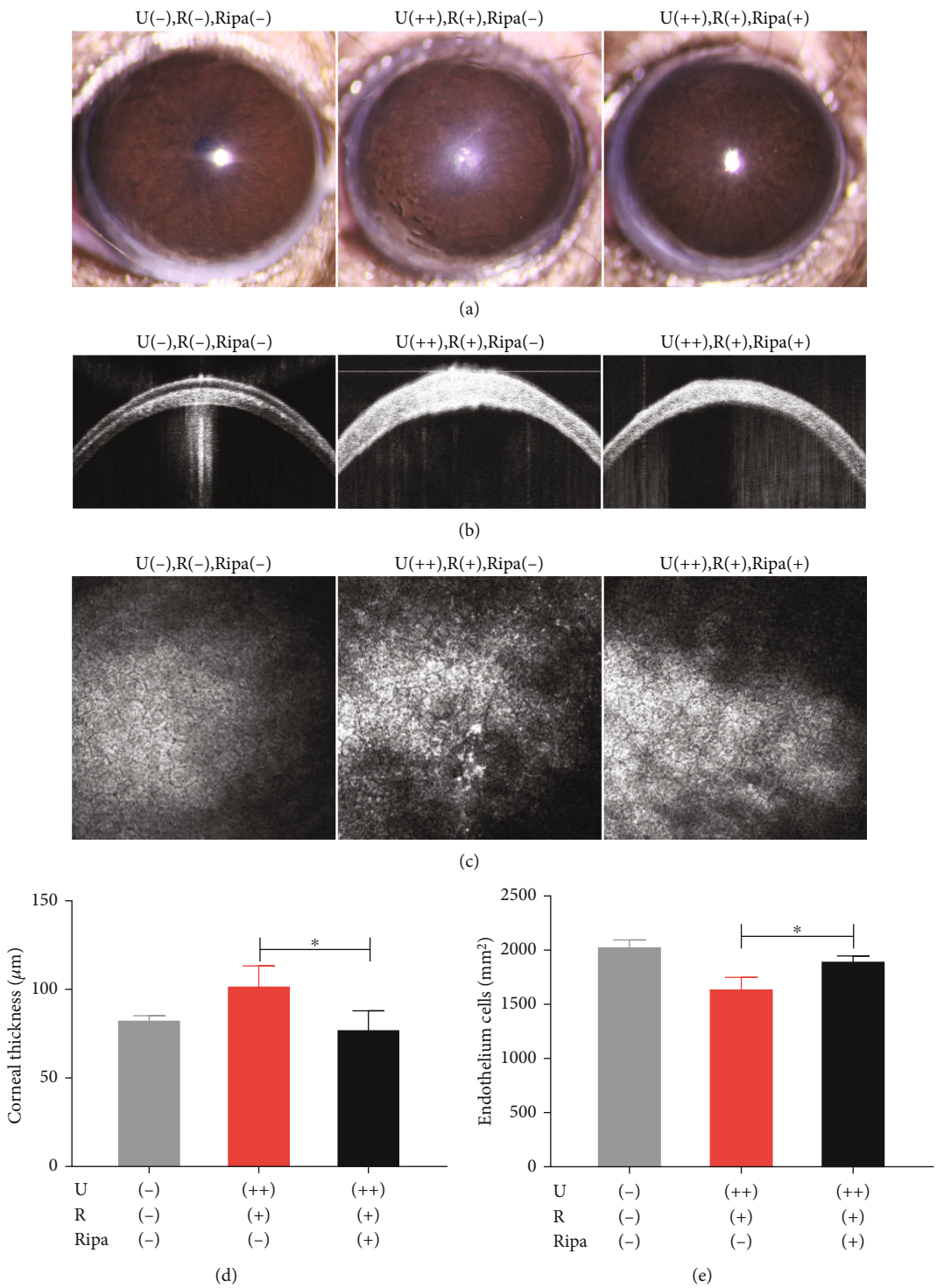

Figure 6: Continued.

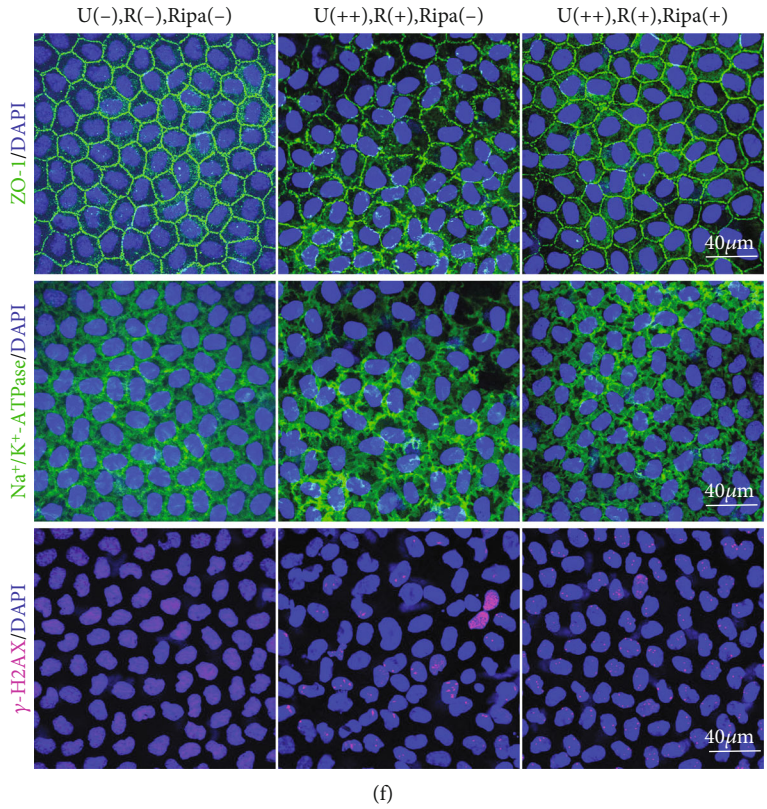

Figure 6: Ripasudil reduces corneal edema and exhibits protection of the corneal endothelium from CXL irradiation in mice. (a) Mouse corneal clarity was examined by slit-lamp microscopy with or without ripasudil treatment after 7 days of CXL treatment. (b) Representative OCT images of mouse corneas after 7 days of CXL treatment. (c) Representative *in vivo* confocal images of corneal endothelial cells after 7 days of CXL treatment. (d) Analysis of the corneal thickness based on the OCT image on day 7 after CXL irradiation. (e) Endothelial cell density analysis of corneas on day 7 after CXL irradiation. (f) Representative confocal images of wholemount mouse corneal endothelium with ZO-1, Na^+/K^+-ATPase, and γ-H2AX staining on day 7 after CXL irradiation. Data are expressed as the mean ± SD; $n = 4$. $^*P < 0.05$. U(-), R(-), Ripa(-): no UVA, riboflavin, or ripasudil treatment; U(++), R(+), Ripa(-): 1.08 J/cm^2 UVA plus riboflavin only; U(++), R(+), Ripa(+): 1.08 J/cm^2 UVA, riboflavin, and ripasudil treatment.

rabbits following a relatively high surface UVA dose of 42.5 J/cm^2 in the absence of a photosensitizing agent. Our relatively low cytotoxic UVA surface dose of 0.54 J/cm^2 can be paraphrased by the multiplying effect on UVA absorption by riboflavin [38]. However, UVB-induced endothelial cell loss can be found at a lower dosage level of 0.47 J/cm^2 in rabbit corneas due to the shorter wavelength of UVB and accordingly higher energy content [39].

We found that *in vivo* treatment with riboflavin and UVA caused oxidative DNA damage in endothelial cells. Riboflavin induced increased expression of γ-H2AX and 8-OHdG under UVA irradiation, the extent of which was dependent on the dose of UVA, but this upregulated expression did not occur following treatment with either riboflavin or UVA alone. Reactive oxygen species (ROS), for example, singlet oxygen produced by CXL, are biologically toxic [40]. Excessive ROS levels cause rapid oxidative damage to proteins, cell membranes, mitochondria, and/or nuclear DNA [41]; thus, this can explain why we found corneal endothelial cell DNA damage following combined treatment with riboflavin and UVA. In contrast, UVB is directly absorbed by DNA, especially aromatic heterocyclic bases, which absorb chromophores efficiently, with maximal absorption occurring between 260 and 280 nm [42]. The endothelial layer is more susceptible to the redox imbalance caused by UVA; therefore, changes in the macromolecules of endothelial cells during corneal crosslinking require further study. For example, oxidative damage to cellular components and modification of redox-active proteins are essential for understanding the molecular basis of the oxidative reaction of endothelial damage induced by corneal crosslinking. In comparison with the same dose of UVA or riboflavin treatment alone, UVA combined with riboflavin caused corneal endothelial cell DNA damage, disrupted the tight junction and pump functions of the endothelium, and further induced corneal edema and increased corneal thickness. This suggests that riboflavin is phototoxic to the endothelium during CXL treatment of thin corneas and loses its protective effect at the endothelial level; thus, new crosslinking agents with lower corneal toxicity are required.

We observed that the ROCK inhibitor, ripasudil, exhibited protective effects against damage caused by CXL in corneal endothelial cells. In previous studies, fasudil, which has a structure similar to that of ripasudil, had an indirect antioxidant effect in various disease models such as hypercholesterolemia, diabetes, and ischemia [43–45].

ROS can be generated during corneal crosslinking, which can cause corneal cell damage [46]. Researchers have reported that ripasudil can inhibit oxidative stress and the generation of ROS via the Rho/ROCK pathway in the neuroprotective treatment of glaucoma [47]; therefore, ripasudil may have similar antioxidant effects and thus protect endothelial cells in our CXL model. Our study demonstrates that ROCK inhibition by ripasudil can reduce DNA damage, decrease the destruction of connections between endothelial cells, increase endothelial cell density, and protect the pump and barrier functions of the corneal endothelium. In a previous study, exposure to UVB greatly increased the level of DNA damage, and the blockade of RhoA/ROCK with CT04 or Y27632 could completely inhibit UVB radiation-induced damage [21]. Here, we show that ripasudil can decrease the expression of γ-H2AX, which is regarded as a marker of DNA damage. Moreover, we found that ripasudil protected the key functional proteins involved in endothelial pump and barrier functions in the CXL model. Based on the present results, the ROCK inhibitor, ripasudil, decreases endothelial damage induced by corneal crosslinking, indicating mediation via the ROCK signaling pathway; however, the specific mechanism has yet to be elucidated.

There are limitations to this study. Although we found that the protective effect of ROCK inhibitor ripasudil on corneal crosslinking-induced endothelial injury was mediated by ROCK signaling pathway, the specific mechanism was not explained. This is the next step in the future. Secondly, the animal model used in this study is mice, so rabbits can be used for characterization and further study of mechanism to better simulate. There is also more evidence for clinical trials of drugs that are later extended to humans.

5. Conclusions

Riboflavin combined with UVA may cause oxidative damage to the corneal endothelium, and the repair of endothelial damage caused by corneal crosslinking is dose-dependent. The ROCK inhibitor, ripasudil, had a protective effect on endothelial cells during corneal crosslinking. These results provide a basis for further investigation into the specific mechanism and treatment of endothelial damage caused by crosslinking.

Data Availability

All data used to support the findings of this study are available from the corresponding author upon request.

Ethical Approval

The research protocol was approved by the Experimental Animal Ethics Committee of Xiamen University and met the standards in the ARVO Declaration on the Use of Animals in Ophthalmology and Visual Studies.

Disclosure

The authors are accountable for all aspects of the work in ensuring that questions related to the accuracy or integrity of any part of the work are appropriately investigated and resolved.

Conflicts of Interest

None of the authors have any ethical conflicts of interest.

Authors' Contributions

All of the listed authors have reviewed and approved the content before submission. Xuemei Wang and Yanlin Zhong contributed equally to this work and share the first authorship.

Acknowledgments

This study was supported in part by grants from the National Key R&D Program of China (grant numbers 2020YFA0908103 and 2018YFA0107301), the National Natural Science Foundation of China (grant numbers 82070931 and 81770891), and the Huaxia Translational Medicine Fund for Young Scholars (grant number 2017-A-001).

References

[1] N. Sorkin and D. Varssano, "Corneal collagen crosslinking: a systematic review," *Ophthalmologica*, vol. 232, no. 1, pp. 10–27, 2014.

[2] F. Raiskup and E. Spoerl, "Corneal crosslinking with riboflavin and ultraviolet a. part II. Clinical indications and results," *The Ocular Surface*, vol. 11, no. 2, pp. 93–108, 2013.

[3] G. Wollensak, E. Spoerl, M. Wilsch, and T. Seiler, "Keratocyte apoptosis after corneal collagen cross-linking using riboflavin/UVA treatment," *Cornea*, vol. 23, no. 1, pp. 43–49, 2004.

[4] G. Wollensak, E. Spoerl, F. Reber, and T. Seiler, "Keratocyte cytotoxicity of riboflavin/UVA-treatment _in vitro_," *Eye*, vol. 18, no. 7, pp. 718–722, 2004.

[5] D. M. Gore, A. Margineanu, P. French, D. O'Brart, C. Dunsby, and B. D. Allan, "Two-photon fluorescence microscopy of corneal riboflavin absorption," *Investigative Ophthalmology & Visual Science*, vol. 55, no. 4, pp. 2476–2481, 2014.

[6] T. G. Seiler, A. Batista, B. E. Frueh, and K. Koenig, "Riboflavin concentrations at the endothelium during corneal crosslinking in humans," *Investigative Ophthalmology & Visual Science*, vol. 60, no. 6, pp. 2140–2145, 2019.

[7] G. Wollensak, E. Sporl, F. Reber, L. Pillunat, and R. Funk, "Corneal endothelial cytotoxicity of riboflavin/UVA treatment in vitro," *Ophthalmic Research*, vol. 35, no. 6, pp. 324–328, 2003.

[8] G. Wollensak, E. Spoerl, M. Wilsch, and T. Seiler, "Endothelial cell damage after riboflavin-ultraviolet-A treatment in the rabbit," *Journal of Cataract and Refractive Surgery*, vol. 29, no. 9, pp. 1786–1790, 2003.

[9] N. S. Gokhale, "Corneal endothelial damage after collagen cross-linking treatment," *Cornea*, vol. 30, no. 12, pp. 1495–1498, 2011.

[10] S. Kling, A. Hammer, A. Conti, and F. Hafezi, "Corneal crosslinking with riboflavin and UV-A in the mouse cornea in vivo:

Morphological, Biochemical, and Physiological Analysis," *Translational Vision Science & Technology*, vol. 6, no. 1, p. 7, 2017.

[11] A. Hammer, S. Kling, M. O. Boldi et al., "Establishing corneal cross-linking with riboflavin and UV-A in the mouse cornea in vivo: biomechanical analysis," *Investigative Ophthalmology & Visual Science*, vol. 56, no. 11, pp. 6581–6590, 2015.

[12] I. M. Beshtawi, R. Akhtar, M. C. Hillarby et al., "Biomechanical changes after repeated collagen cross-linking on human corneas assessed in vitro using scanning acoustic microscopy," *Invest Ophth Vis Sci*, vol. 55, no. 3, pp. 1549–1554, 2014.

[13] G. Wollensak, E. Spoerl, and T. Seiler, "Riboflavin/ultraviolet-A-induced collagen crosslinking for the treatment of keratoconus," *American Journal of Ophthalmology*, vol. 135, no. 5, pp. 620–627, 2003.

[14] D. Tabibian, S. Kling, A. Hammer, O. Richoz, and F. Hafezi, "Repeated cross-linking after a short time does not provide any additional biomechanical stiffness in the mouse cornea in vivo," *Journal of Refractive Surgery*, vol. 33, no. 1, pp. 56–60, 2017.

[15] N. Okumura, N. Koizumi, M. Ueno et al., "Enhancement of corneal endothelium wound healing by Rho-associated kinase (ROCK) inhibitor eye drops," *British Journal of Ophthalmology*, vol. 95, no. 7, pp. 1006–1009, 2011.

[16] N. Okumura, Y. Okazaki, R. Inoue et al., "Effect of the Rho-associated kinase inhibitor eye drop (Ripasudil) on corneal endothelial wound healing," *Investigative Ophthalmology & Visual Science*, vol. 57, no. 3, pp. 1284–1292, 2016.

[17] A. Pipparelli, Y. Arsenijevic, G. Thuret, P. Gain, M. Nicolas, and F. Majo, "ROCK inhibitor enhances adhesion and wound healing of human corneal endothelial cells," *PLoS One*, vol. 8, no. 4, 2013.

[18] L. C. Meekins, N. Rosado-Adames, R. Maddala, J. J. Zhao, P. V. Rao, and N. A. Afshari, "Corneal endothelial cell migration and proliferation enhanced by Rho kinase (ROCK) inhibitors in in vitro and in vivo models," *Investigative Ophthalmology & Visual Science*, vol. 57, no. 15, pp. 6731–6738, 2016.

[19] A. S. Goldstein, B. T. Aldrich, J. M. Skeie et al., "Assessing the effects of Ripasudil, a novel Rho kinase inhibitor, on human corneal endothelial cell health," *Journal of Ocular Pharmacology and Therapeutics*, vol. 34, no. 10, pp. 692–699, 2018.

[20] S. Kassumeh, A. von Studnitz, S. G. Priglinger et al., "Ex vivoexcimer laser ablation of cornea guttata and ROCK inhibitor-aided endothelial recolonization of ablated central cornea," *Acta Ophthalmologica*, vol. 98, no. 6, pp. E773–E780, 2020.

[21] J. Q. Liang, X. W. Zeng, Y. Halifu et al., "Blocking RhoA/ROCK inhibits the pathogenesis of pemphigus vulgaris by suppressing oxidative stress and apoptosis through TAK1/NOD2-mediated NF-κB pathway," *Molecular and Cellular Biochemistry*, vol. 436, no. 1-2, pp. 151–158, 2017.

[22] N. Okumura, N. Koizumi, E. P. Kay et al., "The ROCK inhibitor eye drop accelerates corneal endothelium wound healing," *Investigative Ophthalmology & Visual Science*, vol. 54, no. 4, pp. 2493–2502, 2013.

[23] N. Koizumi, N. Okumura, M. Ueno, H. Nakagawa, J. Hamuro, and S. Kinoshita, "Rho-associated kinase inhibitor eye drop treatment as a possible medical treatment for Fuchs corneal dystrophy," *Cornea*, vol. 32, no. 8, pp. 1167–1170, 2013.

[24] S. Kinoshita, N. Koizumi, M. Ueno et al., "Injection of cultured cells with a ROCK inhibitor for bullous keratopathy," *New England Journal of Medicine*, vol. 378, no. 11, pp. 995–1003, 2018.

[25] G.-J. K. Ripasudil, "Ripasudil: First global approval," *Drugs*, vol. 74, no. 18, pp. 2211–2215, 2014.

[26] G. Moloney, C. Petsoglou, M. Ball et al., "Descemetorhexis without grafting for Fuchs endothelial dystrophy-supplementation with topical Ripasudil," *Cornea*, vol. 36, no. 6, pp. 642–648, 2017.

[27] M. S. Macsai and M. Shiloach, "Use of topical rho kinase inhibitors in the treatment of Fuchs dystrophy after Descemet stripping only," *Cornea*, vol. 38, no. 5, pp. 529–534, 2019.

[28] M. Yamaguchi, S. Nakao, R. Arita et al., "Vascular normalization by ROCK inhibitor: therapeutic potential of Ripasudil (K-115) eye drop in retinal angiogenesis and hypoxia," *Investigative Ophthalmology & Visual Science*, vol. 57, no. 4, pp. 2264–2276, 2016.

[29] J. A. Bonanno, "Molecular mechanisms underlying the corneal endothelial pump," *Experimental Eye Research*, vol. 95, no. 1, pp. 2–7, 2012.

[30] S. Melov, "Mitochondrial oxidative stress - physiologic consequences and potential for a role in aging," *Annals of the New York Academy of Sciences*, vol. 908, no. 1, pp. 219–225, 2000.

[31] E. P. Rogakou, D. R. Pilch, A. H. Orr, V. S. Ivanova, and W. M. Bonner, "DNA Double-stranded Breaks Induce Histone H2AX Phosphorylation on Serine 139," *The Journal of Biological Chemistry*, vol. 273, no. 10, pp. 5858–5868, 1998.

[32] T. T. Paull, E. P. Rogakou, V. Yamazaki, C. U. Kirchgessner, M. Gellert, and W. M. Bonner, "A critical role for histone H2AX in recruitment of repair factors to nuclear foci after DNA damage," *Current Biology*, vol. 10, no. 15, pp. 886–895, 2000.

[33] A. Sharma, J. M. Nottage, K. Mirchia, R. Sharma, K. Mohan, and V. S. Nirankari, "Persistent corneal edema after collagen cross-linking for keratoconus," *American Journal of Ophthalmology*, vol. 154, no. 6, pp. 922–926.e1, 2012.

[34] S. Dikstein and D. M. Maurice, "The metabolic basis to the fluid pump in the cornea," *The Journal of Physiology*, vol. 221, no. 1, pp. 29–41, 1972.

[35] J. Fischbarg and D. M. Maurice, "An update on corneal hydration control," *Experimental Eye Research*, vol. 78, no. 3, pp. 537–541, 2004.

[36] T. Tsubai and M. Matsuo, "Ultraviolet light-induced changes in the glucose-6-phosphate dehydrogenase activity of porcine corneas," *Cornea*, vol. 21, no. 5, pp. 495–500, 2002.

[37] D. G. Pitts, A. P. Cullen, and P. D. Hacker, "Ocular effects of ultraviolet radiation from 295 to 365 nm," *Investigative Ophthalmology & Visual Science*, vol. 16, pp. 932–939, 1977.

[38] K. S. Cho, E. H. Lee, J. S. Choi, and C. K. Joo, "Reactive oxygen species-induced apoptosis and necrosis in bovine corneal endothelial cells," *Investigative Ophthalmology & Visual Science*, vol. 40, pp. 911–919, 1999.

[39] A. Podskochy, L. Gan, and P. Fagerholm, "Apoptosis in UV-exposed rabbit corneas," *Cornea*, vol. 19, no. 1, pp. 99–103, 2000.

[40] G. Wollensak, "Crosslinking treatment of progressive keratoconus: new hope," *Current Opinion in Ophthalmology*, vol. 17, no. 4, pp. 356–360, 2006.

[41] C. Zinflou and P. J. Rochette, "Ultraviolet A-induced oxidation in cornea: characterization of the early oxidation-related events," *Free Radical Biology and Medicine*, vol. 108, pp. 118–128, 2017.

[42] A. Svobodova and J. Vostalova, "Solar radiation induced skin damage: review of protective and preventive options," *International Journal of Radiation Biology*, vol. 86, no. 12, pp. 999–1030, 2010.

[43] Z. Ma, J. Zhang, E. Ji, G. Cao, G. Li, and L. Chu, "Rho kinase inhibition by fasudil exerts antioxidant effects in hypercholesterolemic rats," *Clinical and Experimental Pharmacology & Physiology*, vol. 38, no. 10, pp. 688–694, 2011.

[44] R. Guo, B. X. Liu, S. P. Zhou, B. C. Zhang, and Y. W. Xu, "The protective effect of Fasudil on the structure and function of cardiac mitochondria from rats with type 2 diabetes induced by Streptozotocin with a high-fat diet is mediated by the attenuation of oxidative stress," *BioMed Research International*, vol. 2013, Article ID 430791, 9 pages, 2013.

[45] C. L. Gibson, K. Srivastava, N. Sprigg, P. M. W. Bath, and U. Bayraktutan, "Inhibition of Rho-kinase protects cerebral barrier from ischaemia-evoked injury through modulations of endothelial cell oxidative stress and tight junctions," *Journal of Neurochemistry*, vol. 129, no. 5, pp. 816–826, 2014.

[46] G. Wollensak, E. Iomdina, D. D. Dittert, and H. Herbst, "Wound healing in the rabbit cornea after corneal collagen cross-linking with riboflavin and UVA," *Cornea*, vol. 26, no. 5, pp. 600–605, 2007.

[47] K. Yamamoto, K. Maruyama, N. Himori et al., "The novel Rho kinase (ROCK) inhibitor K-115: a new candidate drug for neuroprotective treatment in glaucoma," *Investigative Ophthalmology & Visual Science*, vol. 55, no. 11, pp. 7126–7136, 2014.

Hindawi
Disease Markers
Volume 2022, Article ID 8631038, 12 pages
https://doi.org/10.1155/2022/8631038

Research Article

Hypochlorous Acid Can Be the Novel Option for the Meibomian Gland Dysfunction Dry Eye through Ultrasonic Atomization

Zhiyuan Li,[1,2] Haiyan Wang,[3] Mo Liang,[1,2] Zhenghua Li,[1,2] Yvliang Li,[1,2] Xiaoping Zhou,[1,2] and Guoping Kuang[1,2]

[1]*The Diagnosis and Treatment Technology Research and Development Centre for Dry Eye and Ocular Surface Disease of Chenzhou, Chenzhou, 423000 Hunan, China*
[2]*The Ophthalmology Department of the Affiliated Chenzhou Hospital, Hengyan Medical School, University of South China, Chenzhou, 423000 Hunan, China*
[3]*The Operation Department of the Affiliated Chenzhou Hospital, Hengyan Medical School, University of South China, Chenzhou, 423000 Hunan, China*

Correspondence should be addressed to Zhiyuan Li; tolizhiyuan01@163.com

Received 22 October 2021; Revised 11 December 2021; Accepted 17 December 2021; Published 5 January 2022

Academic Editor: Ting Su

Background. Dry eye is a multifactor disease which needs comprehensive treatments to keep the homeostasis of ocular surface. *Objective*. To explore the effect of hypochlorous acid on the meibomian gland dysfunction dry eye through ultrasonic atomization. *Methods*. We set this study of 0.01% HOCL and 0.1% hyaluronate by ultrasonic atomization. All the data was recorded at the 1st, 15th, 30th, and 55th days. The patients' complains, the meibum analysis, conjunctive congestion, corneal staining, Schirmer's I test, and NIBUT were recorded by K5M, the MMP-9, and IL-2 of tear by inflammation kit; the *Demodex* was recorded by microscopy. *Results*. 53 patients have joined this study. There is no statistic difference between them on OSDI (day 15: $p = 0.061$, 30: $p = 0.055$, 55: $p = 0.052$); results show the 10.57 ± 0.13 and 12.54 ± 0.17 reduction on OSDI; the differences of both treatments are significant ($^{**}p < 0.01$). Increased Schirmer's and TBUT are 3.27 ± 0.10 and 6.29 ± 0.10 ($^{**}p < 0.01$) or 7.32 ± 1.72 s and 9.22 ± 1.41 s ($^{*}p < 0.05$); the decreased conjunctive and corneal staining are 0.23 ± 0.07 and 0.45 ± 0.06 ($^{**}p < 0.01$) or 0.42 ± 0.03 and 0.37 ± 0.02 ($^{*}p < 0.05$) at both groups. The differences of MMP-9 and IL-2 negative rate are significant ($Z = 0.896$, $^{**}p = 0.002 < 0.01$; $Z = 0.659$, $^{**}p = 0.001 < 0.01$); the number of *Demodex* mites at first is 10 or 11, while the last is 2 or 6 ($Z = -4.642$, $^{**}p < 0.01$; $Z = 2.742$, $p > 0.05$). The *Demodex* count between them is significant ($Z = -2.310$, $^{*}p = 0.032 < 0.05$). The survival times (ST) of each stage at the HOCL are 110.75 (108.50 ± 24.50), 95.50 (90.25 ± 14.50), and 75.25 (73.48 ± 8.50) min which are shorter than those of control which are 155.50 (160.10 ± 21.50), 130.25 (128.25 ± 16.50), and 105.75 (102.50 ± 14.50) min ($^{**}p < 0.01$). The *Demodex* eradication rate of HOCL is statistic significant ($^{*}p15^{th}$ vs. 1^{st}day $= 0.028 < 0.05$; $^{**}p30^{th}$ vs. 1^{st}day $= 0.002 < 0.01$; $^{**}p55^{th}$ vs. 1^{st}day $= 0.0018 < 0.01$). *Conclusions*. 0.01% HOCL improves the *Demodex* eradication by shortening the survival time; the HOCL acts on the ocular surface by reducing the inflammation. The ultrasonic atomization helps for the drug usage.

1. Introduction

The Dry Eye Work Shop (DEWS) II (2017) report has rewritten the dry eye disease (DED) definition: "Dry eye is a multifactorial ocular surface disease characterized by loss of tear film homeostasis associated ocular symptoms, in which tear film instability and hyperosmolarity, inflammation and ocular surface lesions, as well as neurosensory abnormalities play etiologic roles" [1]. The major prevalence globally ranges from 5–7% of the USA to 40–70% of the Eastern Asian [2]. The most vulnerable age of the disease is middle and elderly people (age > 40 years), but the incidence is rising among the young [3, 4]. It is crucial for the public to realize the importance of DED by reliable therapy.

Meibomian gland dysfunction (MGD) is defined as a team of aberrant signs, acquired or congenital, implicated

by dysfunction of the eyelid meibomian glands. MGD leads to affecting tear film function, ocular discomfort, evaporative caused dry eye, or ocular surface problems [5]. The study of 619 randomly chosen participants from a population-based study in north China; 8.6% were symptomatic MGD while the asymptomatic MGD rate was 21.9% [6]. Many of these ocular clinical manifestations interweave with dry eye, and *Demodex* relative MGD is believed to be the key pathological factor to evaporative induced dry eye [7].

Kinds of means are used for the therapy of MGD-related DED, containing nondrug treatments such as Traditional Chinese Medicine (TCM), ultrasonic atomization (UA), intraductal eyelid meibomian gland probing, meibomian gland massage, optimized pulsed light therapy (OPT), and lipiflow. Consider these means are effect to a certain range; difficulties are the inappropriate usage, insignificant effects, high financial expenditure, and the secondary actions [8]. It is necessary for the invention of new proposal to improve the effect.

Hypochlorous acid (HOCL) has multifaceted applications in dermatology, wound healing, eye care, and dentistry. It is the ordinary disinfectant in industrial domestic and medical aspects and has the same active components of household bleach but with a different chemical composition [9]. HOCl is an attractive material for the nonsynthetic microbial toxic medium. Impurity-free HOCl originated from the products of the human immune response [10]. Across the oxidative reaction, highly activated molecules such as HOCl are stimulated from the leukocyte's action to external microorganisms [11]. Due to its quickly neutralized feature, HOCL is nontoxic to the ocular surface [12].

Ultrasonic atomization (UA) [13] is a procedure that damages liquid surface tension and atomizes drops into cute elements through ultrasonic vibration. It is the conventional ophthalmological choice in TCM for DED. This procedure of 20 min makes the droplets fully expose and permeate the ocular surface. Motivation of anatomized steam can accelerate body fluid circulation around eyelid and thus reinforce the release of meibomian gland secretions.

Anyway, concentrate on this earlier work to assess the particular therapeutic safety and effects of ultrasonic-atomizer HOCL for the remedy of MGD-related DED which is necessary. Until now, this is the premier double-blind, placebo-controlled randomized study for the hypothesis.

2. Participants and Evaluations

2.1. Study Design and Participants. A double-blind layout was designed in this clinical research. Thus, the 1 : 1 ratio of HOCL and placebo treatment groups was carried out to engender random codes using the statistics software SAS9.4 (SAS Institute Inc., Cary, NC, USA), under the block randomization modus. Observed were then followed a medication box labelled with a bunch of number which contained all medicaments. The clinical research group used market-oriented available HOCL 0.01% pH 5.4 (20 mL) (Avenova®, NovaBay Pharmaceuticals, Inc., Emeryville, California, USA) [14]. At the same time, the control was treated with a placebo material 0.1% Purified Sodium Hyaluronate (20 mL) (Santen Pharmaceutical Co. Ltd.) which is a 0.72% (g/mL) sodium chloride solution with the osmotic pressure of 235 mOsmol/kg and a pH value of 6.5. Patients were also treated with fixed bracket ultrasonic atomizer (product number: HL100A, Yuwell, Jiangsu, China). The medications in this study were atomized for 20 min per 5 days with the ultrasonic atomizer held before the patient's eye. All the patients were treated with meibomian gland massage once a week, 4 times altogether. The treatment duration was 55 days with check point time at the 1st day (baseline) and then the 15th day, 30th day, and 55th day; treatment safety and effectiveness evaluations were executed on-site during the follow-ups. All trails were done on the same instrument. The investigator and the statistician know nothing of patients' identity.

2.2. Inclusion and Exclusion Criteria. All the study subjects were enrolled during Jan 2020-June 2021 period who met the inclusion criteria and were of the same nationality (Han Chinese, aged from 20 to 70 years). Patients with MGD-DED were chosen from those subjects who visited the eye clinic for dry eye.

We excluded patients less than 20 or more than 70 years old; those who with the histories of ocular injury and surgery within 3 months; those with ocular problems such as ocular inflammation, allergy, and nasolacrimal sac problems; those who are using a punctual plug or contact lenses; or those are using eye drops including high-quality artificial tears drops within 24 hr before the examination. Anyone whose outcome results were hard to be confirmed was excluded.

2.3. Ethnic Achievement. This study followed the principium of the Declaration of Helsinki, and this protocol was approved by the institutional review board of the ethics committee of the Affiliated Chenzhou Hospital, Hengyan Medical School, University of South China (ID: 2020YJ03). Informed consent was achieved by the recruiters after a discussion of the purpose and probability on sequences of the clinic trail.

2.4. Dry Eye Diagnosis and Classification

(i) The standards for the general normal are as follows [15, 16]:

(1) Ocular surface disease index (OSDI) score of less than 12

(2) Without tear film outliers (tear film break-up time, TBUT > 5 seconds, and Schirmer's test value of >5 mm after 5 min)

(3) Lack of evidence of corneal or conjunctive epithelial erosion with fluorescent staining

(4) Normal lid margins or meibum

(ii) The criteria for the aqueous-deficient dry eye (ADDE) group are as follows [15, 16]:

(1) Presence of dry eye complains (OSDI ≥ 12)

(2) Poor tear production as defined by Schirmer's test I (≤5 mm) and tear film instability as named by the FBUT(≤5 seconds)

(3) The evidence of corneal or conjunctivae epithelial damage with a fluorescent staining score of ≥3

(iii) The criteria for the MGD group are as follows [15, 16]:

(1) Presence of symptoms (OSDI ≥ 12)

(2) At least one lid margin abnormality

(3) Poor meibomian gland expression (grade ≥ 1) or worse qualitative variety in meibum (meibum quality score ≥ 3).

(iv) The criteria for the ADDE/MGD-related dry eye group are as follows [15, 16]:

(1) Presence of dry eye complaints (OSDI ≥ 12)

(2) Poor tear production as recorded by Schirmer's test I (≤5 mm) and tear membrane film instability showed by the FBUT(≤5 seconds)

(3) The evidence of corneal or conjunctivae epithelial discontinue with a fluorescent staining score of ≥3

(4) Not only one lid margin abnormality

(5) Worse meibomian gland expression (grade ≥ 1) or poor quality changes in meibum (meibum qualitative score ≥ 3).

2.5. Ultrasonic Atomization Process [17]. Patients were also assembled with fixed wing ultrasonic nebulizers (product Number: HL100A, Yuwell, Jiangsu, China). The atomizing pipeline was placed 5–10 cm before the eyelid, and the patients open their eyes larger and stare in all orientations off and on to ensure that the ultrasonic atomizing fine droplets fully penetrate the conjunctive. Treatment fluid was used 20 mL HOCL or placebo each time. The body temperature of an ultrasonic-atomized aerosol is very close to the room environment; make the entire process arousing the least irritations. The therapy period was 55 days with check points at time day one (baseline) and then at the 15th day, 30th day, and 55th day; treatment safety and efficacy assessments were implemented on-site during these visits.

2.6. Clinic Assessment. One author of our team performed the experiments, and data were obtained from both eyes. In all the subjects, clinic results were taken sequentially as follows:

Subjective symptoms were graded on a serial scale from 0 to 4, according to the verified 12-item ocular surface disease index (OSDI) questionnaire. The total OSDI marks range from 0 to 100 and was calculated using the following equation: OSDI = (the summary of scores for every question answered × 100)/(overall number of answered questions × 4) [18].

The following are the objective data through Oculus K5M:

(1) Tear meniscus height (TMH) was recorded by Keratograph® 5M (K5M; Oculus, Optikgerate, Germany). The keratograph was set to "film (TF) scan-tear meniscus mode" to capture the image of the TMH of the ocular surface, following the manufacturer's synopsis, as previously reported [19, 20]

(2) Tear membrane film evaluation with the "TF-Scan, Non-Invasive Keratograph Break-Up Time (NI-KBUT) mode" was chosen when the subjects were asked to blink three to five times and then keep their eyes open. There is abnormality on the manifested destructive or break-up of the tear film; meanwhile, the picture was recorded. The equipment provided a representative of tear film break-up all the time, including a tear film topographic map showing the size and location of the tear discontinue regions, as well as the first break time (NIKBUT-first) and the average break-up time (NIKBUT-average; the meanings of all tear film break-up over the entire cornea), as previously described [21]

(3) Conjunctive and corneal staining was graded from 0 to 3 and corresponds to the National Eye Institute (NEI)/Industry Workshop scale [20] from 0 to 33 based on the type of fluorescent staining under the slit lamp

(4) Schirmer's examination I was performed without topical anaesthesia by placing Schirmer's strip in the1/3 middle lateral part of the lower fornix. The length of wetting was recorded after 5 min, and the patients were asked to make their eyes slightly closed during the test [22]

(5) The eyelid margins and meibomian glands were examined for lid margin anomalous, gland expression, and meibum amount and colour, as previously described [23, 24]. Lid margin anomalous were scored as 0 (absent) or 1 (present) for the following parameters: plugged meibomian gland orifices, vascular congestion, irregularity of the lid margin, and partly expressions of the mucocutaneous borderline [25, 26]. The extent of meibomian gland expression, using steady digital pressure applied on five glands of the middle third of the lower lid, was graded as such: grade 0, all five glands expressible; grade 1, three or four glands expressible; grade 2, one or two glands expressible; and grade 3, no glands expressible [27].

The meibum attribute on eight lower lid glands was graded as follows: grade 0, clear; grade 1, cloudy; grade 2, cloudy with granular particulates; and grade 3, thick, like toothpaste-like particulates. Each of the eight glands of the lower eyelid was graded on the scale from 0 to 3. The scores of the eight glands were summarized (range: 0–24) [28]

The following are the data from optical microscopy for *Demodex*:

(1) For *Demodex* count [29] on each eye, pluck out 3 upper and lower eyelashes. Try to select the eyelashes with sleeve-like scales at the roots. Clamp the eyelashes with tweezers, and rotate them slightly to loosen the eyelashes. After plucking, place them in parallel on the glass slide. Observe the amount and morphology of *Demodex* mites under the optical microscope. If the plucked eyelashes are accompanied by scales, add 100% alcohol or 0.25% fluorescent sodium solution and observe again. The *Demodex* count includes its life cycle

(2) For the survival time (ST) of *Demodex*, written informed protocols have been acquired from each patient before cilia have been removed. After eyelashes have been pulled out from the participants' eyelid in each group at room temperature, these eyelashes with *Demodex* mites were quickly fastened on the glass slide. HOCL and placebo eyelid patch extracts were then layered onto the glass slide with a micropipette individually. The original sample was treated as the blank origin group. As *Demodex* is more vulnerable at the young stage of life, only adult *Demodex* with four pairs of well-developed legs and a robust body were found [30]. After the cilia had been extracted from the eyelid, the activity of the *Demodex* body and legs was observed instantly and continuously under the ordinary optical microscope at the magnification of ×10 or ×40. The ST was named as the period from the time-point of eyelid patch extract trickled on the body to the cessation of activity

(3) In *Demodex* mite eradication, only the data of *Demodex* mites was ≥3; the patient was considered *Demodex*-positive [30]. Otherwise, "absolute *Demodex* eradication" was defined as complete *Demodex* eradication with the tissue reduced to zero [31]

2.7. Tear Film Protein Factors [32]. Tear specimens were obtained using a diagnostic test reagent strip in order to asses with inflammatory kits (Inflammation Dry® test; Rapid Pathogenesis Screening Inc., Sarasota, FL, USA) for each patient. Microbiological pieces were collected before and 20 minutes after implementation of the procedure.

2.8. Sample Size Calculation. There was not a previous study that has directly related studied the subjective complains and objective data with ocular eyelid ultrasonic atomization for disinfection. The arbitrary effect size of 1-β¼0.80 and 0.7 at α¼0.05 [33, 34] (a priori, two-tailed, matched-pair test) was selected to count the minimum sample for this study and was estimated to be 25.

2.9. Statistical Analyses. The main variables did not have a normal distribution; nonparametric tests were used. The clinical variables and ocular surface index were compared between the control and HOCL ultrasonic atomization using the Analysis of Variance (ANOVA) and for categorical variables using Fisher exact or chi-square test. A confrontation of clinical manifestations and ocular surface index is due to the presence of a simultaneous multiple tear membrane film break-up pattern and ocular surface index by the K5M; the observation index does not coincide with the normal distribution and is expressed as the median P50 (P25, P75). Statistical analyses were performed using SPSS (version 19.0; SPSS Inc., Chicago, IL, USA). A p values less than 0.05 was considered statistical significant.

3. Results and Analysis

3.1. The Clinic Trail Diagram for the Procedure for the Safety and Efficiency of HOCL and Placebo Drug Ultrasonic Atomization. These 64 recruited patients were randomly selected for double-blind treatments. Two persons in the HOCL and placebo group did not attend screen schedule; accordingly, 30 patients were analyzed in these groups separately. A total of 27 or 26 patients have finished all clinic visits, respectively; this shows that only 1 patient dropped out from each group for adverse events (transient conjunctive hyperaemia) (Figure 1).

3.2. Basic Clinical Information of Enrolled Patients. If the patient wore glasses, the best corrected visual acuity should be recorded, without recording the uncorrected visual acuity. If the patient wore no glasses, the uncorrected visual acuity was recorded. The data of subjects in the designated treatment and amount of subjects in the specified systematization of percentages were based on the number of subjects in the homeostasis treatment. The data in Table 1 show patient clinical idiographic at the beginning. These data show no differentiation in demographic distinctive between them. Results also show no statistic differences at baseline between them in signs of MGD and/or DED as well as in terms of ocular symptoms.

For persistent variables, p value was calculated using Analysis of Variance (ANOVA) and for categorical variables using a chi-square test/Fisher's exact test if cell frequency is <5.

3.3. The Variations of Tear Film Function at the Check Points between HOCL and Placebo Treatment Groups

3.3.1. Primary Outcomes of Ocular Complaint Scores Slowly Reduced in Both Groups in the following Three Visits (Table 2). There is no statistical significant differentiation between them in the symptom score reduction of the 15th day ($p = 0.061$) and 30th day ($p = 0.055$) and 55th days ($p = 0.052$); results reveal a 10.57 ± 0.13 ($^{**}p < 0.01$) and

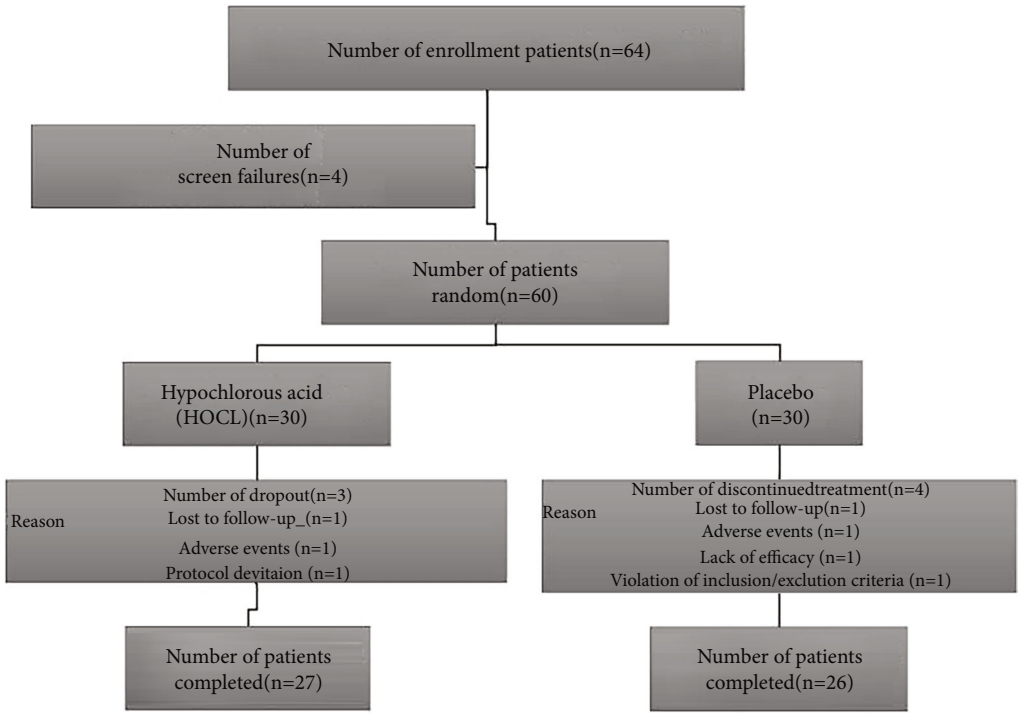

Figure 1: Subject flow chart.

12.54 ± 0.17 ($^{**}p < 0.01$) decrease in calculated symptom scores after 55 days of atomization management considering the beginnings in both groups, respectively; the difference between them is statistic significant ($^{**}p < 0.01$) (Table 2). Results for individual complaint score show that the HOCL brings more benefit than that of control.

3.3.2. Results Show That Both Schirmer's and TBUT Have Been Ameliorated in Both Groups (Table 2). Tear volume scores (Schirmer's) have increased after the treatment; these increases were 3.27 ± 0.10 and 6.29 ± 0.10 in the contrast and HOCL groups after 55 days of treatment. There are statistical differences between the HOCL and placebo groups in the increased value (Schirmer's) after 55 days of application ($^{**}p < 0.01$) (Table 1). The TBUT in the HOCL were always higher than those of the placebo after therapy over a treatment period. After 55 days of management, TBUT were 7.32 ± 1.72 s and 9.22 ± 1.41 s in the placebo and HOCL groups, separately. The alterations between both groups are statistical difference ($^{*}p < 0.05$).

3.3.3. Results Show That Conjunctive Congestion Has Been Alleviated by the Atomization Treatment. The decreased values on the conjunctive congestion of the both groups are 0.23 ± 0.07 and 0.45 ± 0.06 ($^{**}p < 0.01$) between the beginning and last interviews, respectively (Table 1). The corneal staining has also been decreased after therapy: decreased figures are 0.42 ± 0.03 and 0.37 ± 0.02 in the placebo contrast and HOCL groups ($^{*}p < 0.05$), respectively. There is a statistical difference in both groups at the final clinical assessment (corneal staining score > 1 at the beginning) (Table 1).

3.4. The Inflammation Factors of MMP-9 and IL-2 Represent the Ocular Surface Inflammation Reactions

3.4.1. MMP-9 and IL-2 Biomarker. MMP-9 and IL-2 levels were measured at the beginning and last of the study in the tears' components of the recruiter by the Inflammation Dry® test. 16 subjects out of 27 (59.26%) from the HOCL group and 16 subjects out of 26 (61.54%) from the placebo groups demonstrate MMP-9-positive results in the left eye at the 1st day. Three out of 27 (11.11%) from the HOCL group and 12 out of 26 (46.15%) subjects from the placebo contrast group displayed MMP-9-positive results in the left eye at the 55th day. The MMP-9 shows the inflammation difference between those groups is significant ($Z = 0.896$, $^{**}p = 0.002 < 0.01$); 15 individuals out of 27 (55.55%) from the HOCL group and 15 out of 26 (57.69%) from the placebo groups manifest IL-2-positive results in the left eye at the 1st day. Two out of 27 (7.41%) from the HOCL group and 10 out of 26 (38.46%) subjects from the placebo contrast group express IL-2-positive results in the left eye at the 55th day. The IL-2 shows the inflammation difference between them is significant ($Z = 0.659$, $^{**}p = 0.001 < 0.01$).

3.5. The Demodex Data. The *Demodex* detection and calculation through light microscopy between the first and the final examination.

3.5.1. Demodex Count. A total of 27 HOCL treatment patients (54 eyes, 18 females and 9 males, 37.84 ± 1.02 years) and 26 placebo individuals (52 eyes, 17 females and 9 males, 38.30 ± 1.24 years), matched by gender and age, were

Table 1: Characteristic of the patients at baseline.

Variables	Hypochlorous acid (HOCL, $N = 27$)	Placebo ($N = 26$)	Statistical	p value
Demographics				
Age (year)				
Mean ± SEM	37.84 ± 1.02	38.30 ± 1.24	$Z = 0.1921$	0.8343
Sex				
Male, n (%)	9 (32.29%)	9 (34.61%)		
Female, n (%)	18 (67.71%)	17 (65.38%)	$\chi^2 = 0.0583$	0.6743
Best corrected visual acuity				
Mean ± SEM	0.82 ± 0.04	0.83 ± 0.02	$Z = -0.6572$	0.5692
Eye symptom score				
Mean ± SEM	13.38 ± 0.32	14.17 ± 0.42	$Z = 0.2192$	0.6172
Meibum quality score				
0, n (%)	11 (40.83)	10 (38.46)	$Z = 0.4412$	0.5658
1, n (%)	9 (35.33)	8 (30.77)		
2, n (%)	5 (21.32)	6 (23.08)		
3, n (%)	2 (6.67)	2 (7.69)		
Eyelid edge change score				
Mean ± SEM	1.58 ± 0.06	1.71 ± 0.06	$Z = -0.0921$	0.4835
Meibum expression score				
Mean ± SEM	2.43 ± 0.18	2.65 ± 0.2	$Z = -0.7112$	0.5162
Conjunctive congestion score				
0, n (%)	7 (24.50)	6 (23.08)	$Z = 0.1031$	0.8917
1, n (%)	12 (48.00)	11 (42.31)		
2, n (%)	4 (14.81)	7 (17.28)		
3, n (%)	4 (14.81)	2 (7.69)		
Corneal labeling score				
Mean ± SEM	0.58 ± 0.07	0.60 ± 0.07	$Z = -0.4231$	0.7325
Schirmer's I test				
Mean ± SEM	5.57 ± 0.31	5.62 ± 0.18	$Z = -0.0347$	0.4372
None interfere tear breakup time(s)				
Mean ± SEM	4.23 ± 0.18	4.08 ± 0.20	$Z = 1.128$	0.2327

consecutively recruited for this study. The medium number of *Demodex* mites on three eyelashes per patient at the enrollment check of HOCL group for *Demodex* at the first day is 10, while the last data of HOCL group is 2 ($Z = -4.642$, $^{**}p < 0.01$). The medium figure of *Demodex* on three cilia per patient at the enrollment check of the placebo group for *Demodex* at the first day was 11, while the last result of placebo group is 6 ($Z = 2.742$, $p > 0.05$). When we analyze the data of both groups, the difference is statistically significant ($Z = -2.310$, $^{*}p = 0.032 < 0.05$).

3.5.2. The Survival Time (ST) of Demodex. The mean ST of *Demodex* mite in particular treatments are shown in Figure 2 (survival time of *Demodex*). The average ST at different check points in the HOCL group is 110.75 (108.50 ± 24.50) min, 95.50 (90.25 ± 14.50) min, and 75.25 (73.48 ± 8.50) min which are significantly lower than the average ST at different check points in the placebo group which are 155.50 (160.10 ± 21.50) min, 130.25 (128.25 ± 16.50) min, and 105.75 (102.50 ± 14.50) min ($^{**}p < 0.01$).

3.5.3. The Demodex Mite Eradication Rate. The *Demodex* counts and ocular parameters at each checkpoint of treatment were also compared (Figure 3 the *Demodex* mite eradication rate). The *Demodex* count in the HOCL group has been reduced by −2.25 ± 0.84 after the 15th day's management; meanwhile, the *Demodex* count in the placebo group has been downregulated by −0.74 ± 0.03 after the 15th day's therapy ($p = 0.056 > 0.05$). There is significant differentiation in the *Demodex* mite eradication rate between them at the 55th day ($^{**}p = 0.006 < 0.01$). Compared with that of the placebo, the *Demodex* mite eradication rate of HOCL is statistically significant at each checkpoint ($^{*}p15^{th}$ vs. 1st day $= 0.028 < 0.05$; $^{**}p30^{th}$ vs. 1st day $= 0.002 < 0.01$; $^{**}p55^{th}$ vs. 1st day $= 0.0018 < 0.01$).

Table 2: Summary of efficacy endpoints between hypochlorous acid (HOCL) and placebo groups.

Visit duration	HOCL ($n = 27$), mean ± SEM	Placebo ($n = 26$), mean ± SEM	p value by ANOVA for HOCL vs. placebo
(a) Ocular surface disease index (OSDI) scores			
1st day	18.65 ± 5.20	21.54 ± 4.98	0.058
15th day	14.25 ± 4.45	13.68 ± 5.02	0.061
30th day	11.14 ± 4.14	10.89 ± 4.98	0.055
55th day	8.08 ± 4.32	9.00 ± 6.68	0.052
(b) Schirmer's test average of both eyes			
1st day	7.09 ± 2.34	6.65 ± 1.82	0.411
15th day	9.22 ± 2.12	7.64 ± 2.04	0.053
30th day	12.28 ± 3.28	9.90 ± 4.21	<0.05*
55th day	13.38 ± 2.73	9.92 ± 2.12	<0.01**
(c) Tear film break-up time (TBUT) average of both eyes			
1st day	4.78 ± 1.12	4.86 ± 1.02	0.423
15th day	4.89 ± 1.56	4.97 ± 1.25	0.351
30th day	6.13 ± 1.13	6.09 ± 1.08	0.459
55th day	9.22 ± 1.41	7.32 ± 1.72	<0.05*
(d) Conjunctivae labeling average of both eyes			
1st day	0.86 ± 0.19	0.88 ± 0.20	0.677
55th day	0.41 ± 0.27	0.65 ± 0.25	<0.01**
(e) Corneal labeling average of both eyes			
1st day	1.05 ± 0.09	1.24 ± 0.12	0.406
55th day	0.68 ± 0.11	0.82 ± 0.09	<0.05*

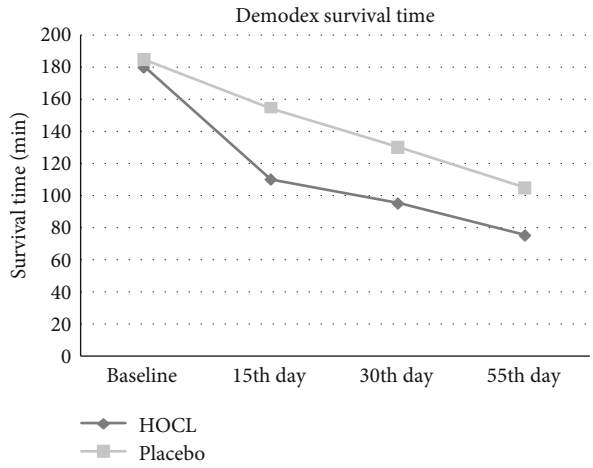

Figure 2: The survival time of *Demodex*.

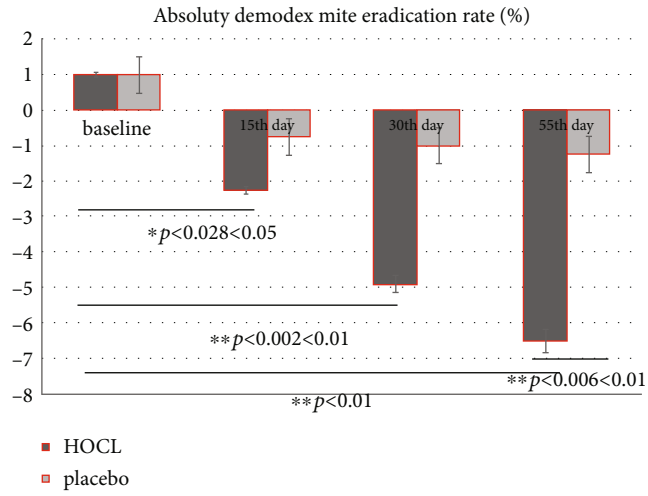

Figure 3: The *Demodex* mite eradication rate.

4. Discussion

4.1. The Inflammation of Dry Eye. Dry eye is a chronic recurrent ocular surface disease that most patients' complaints or signs of tear film homeostasis eruption with multiple pathological reactions and the disease or dysfunction of tears fluid producing cells/glands that result in the erratic tear film [35]. Tear eruption is accompanied by raising tear osmotic pressure (local or diffuse area) which induces stress signaling pathways in the ocular surface epithelium and resident immunologic cells and triggers the production of innate inflammatory molecules that arouse the vicious self-perpetuating circulation which leads to being further downregulated in tear film function and worse symptoms. Hyperosmolarity stress has been shown to trigger mitogen-activated protein kinase (MAPK) pathway and stimulate secretion of proinflammatory cytokines (e.g., IL-1β, IL-2,

IL-6, and TNF-α), chemokines, and matrix metalloproteinase such as MMP-3 and MMP-9 as well as cytokine apoptosis [36]. The connection of these inflammatory mediators is intricate which has been shown to affect themselves; the Meibomian gland dysfunction (MGD) "-Relative" dry eye is the leading one, thus amplifying the inflammatory cascade which leads to cornea epithelial barrier disruption, conjunctivae goblet cell loss, and meibomian glandular dysfunction [37]. This manifests the pathological closed loop making the treatment effects uncertain and disease recurrent.

4.2. The Natural of HOCL to the Ocular Diseases. Pure HOCl is released as the element of the human immune reaction [32]. During the "oxidative burst," small, highly reactive molecules, such as free HOCl, are generated as leukocyte responds to the pathogenesis of organisms [38]. This element is an oxidant that kills bacteria through the protein and lipid halogenations and/or per oxidation process [39], which has a diffuse spectrum of activity and exhibits rapid killing vitality [40]. The form of HOCL 0.01% (Avenova®, Nova Bay Pharmaceuticals, Inc., Emeryville, California, USA) is commercially formulated free of sodium hypochlorite with the pH of 3.5-6.0 which has been used in the ocular sickness that has been proved to be safe and effective: Yin et al. and Gold et al. [41, 42] found that 0.01% HOCL significantly reduced inflammation and was effective in killing >99.9% of tested pathogenesis microorganisms without side effect on the ocular surface; HOCL is a potent oxidizing ingredient effective against a wide spectrum of organisms, including the most common bacteria implicated in endophthalmitis after surgery or trauma [9, 32]. Ngo et al. [43] evaluated the comfort levels of several eyelid cleansing products in the treatment of blepharitis associated with *Demodex* folliculorum who have achieved the conclusion that the HOCL 0.01% has the highest degree of patients' comfort.

4.3. HOCL Can Alleviate the Inflammation Reaction of Ocular Surface. Ocular inflammations and hyperosmolarity stress are key components of the pathologic circle for the chronic dry eye. Our data show that the ocular inflammation factors between HOCL and placebo group are significantly different ($Z = 0.896$, $^{**}p = 0.002 < 0.01$; $Z = 0.659$, $^{**}p = 0.001 < 0.01$) at the end of experiment which confirms with the previous study that HOCL can reduce inflammatory factors, such as decreasing the activity of histamine and interleukin-2 (IL-2) and matrix metalloproteinase-9 (MMP-9) (Table 3) all of which are involved in the development of irritation and itching [44]. HOCL has been shown to have effect on controlling the biofilms and wound healing of ocular epithelium [45]. Some authors [43, 46] have reported the decreasing in the figure of *Demodex* mites by HOCL. These biological activities are largely due to the per oxidation reaction property. But the traditional use efficiency of HOCL to the ocular surface is limited for its instability inwardness.

4.4. The Mechanism of Ultrasonic Atomization Ocular Surface Device. Ultrasonic atomization moistening device is an extraordinary method for ocular surface which comprises a liquid box and a ventilation high-humidity transparent mirror room around the ocular surface. The atomization system is arranged inside the liquid box, and the atomization system is used for atomizing water in the liquid box. A second gas outlet hole is formed in the liquid box, the first gas inlet hole is formed in the mirror room, and the first gas inlet hole is mixed with the second gas. According to the ultrasonic atomization ocular surface eye moistening device, a high-humidity environment is formed around the ocular surface; the dry eye symptom can be alleviated by the time-depended highly concentrated drugs whose droplets continuously, uniformly, and comprehensively overlay the eyelid, conjunctiva, and cornea and maximize the contact area between the ocular tissue and liquid and there of accelerating drug utilization [47].

4.5. The Clinic Tear Film Data of Ocular Surface. A series of clinical researches have shown that the ultrasonic atomization distinguishing using kinds of liquids improves the meibum expression, increases tear fluid, remits the symptoms and signs of DED, and stabilizes the tear film (Table 2) [47–49]. The placebo contrast in this study was 0.1% Purified Sodium Hyaluronate. A public study showed that ultrasonic atomization with saline alone can also ameliorate the symptoms and signs (including Schirmer's I test, TBUT, and corneal fluorescent staining). Compared with the artificial tears (0.1% Purified Sodium Hyaluronate, Santen Pharmaceutical Co. Ltd.), the treatment effect of the placebo ultrasonic atomization group due to Schirmer's is significantly inferior than that of HOCL ($^{**}p < 0.01$). The causes for the difference are the chemical nature of HOCL which induces a strong per oxidation and/or halogenation reaction helps for the penetratation ability of eye droplets to the ocular surface. Therefore, in this study, there is statistical difference in the amelioration of TBUT at the endpoint of this trial ($^{*}p < 0.05$) which relates to the significant alleviation effect on the enhancement of oxidizing reactions through the ultrasonic atomization drug deliver system.

4.6. The Pathogenesis Mechanism and the Treatments of Demodex on the MGD-EDE. The *Demodex* blepharitis has been the hotspot issue by both ophthalmologists and dermatologist in the past decades. Several pathogenesis mechanisms of *Demodex* blepharitis have been elaborated in previous studies. First, *Demodex* mites can block the sebaceous ducts and hair follicles mechanically causing epithelial hyperplasia and keratinization, while debris or waste from *Demodex* mites could diminish innate immune response or the inflammatory reactions. Second, *Demodex* mites damage the habitat at which they live by persistent adjustment and invasions [50].

Since the *Demodex* mite is the pathogenesis for blepharitis and Meibomian gland dysfunction, there are kinds of treatments that have been explored. Different tea tree essential oil (TTO) products are now broadly introduced in *Demodex* blepharitis [51–53]. Liu et al. [50] reported that the okra eyelid dressing effectively eliminated *Demodex* mites both in vivo and in vitro, whose application was associated with the least ocular discomforts. Besides up-to-data

Table 3: Figures of subjects positive for inflammation biomarker between hypochlorous acid and placebo groups.

Biomarker variation	HOCL ($N = 27$), negative positive		Placebo ($N = 26$), negative positive		p value for HOCL vs. placebo Z-test
	N (%)	n (%)	n (%)	n (%)	
MMP-9					
1st day	11 (40.74)	16 (59.26)	10 (38.46)	16 (61.54)	
55th day	24 (88.88)	3 (11.11)	14 (53.84)	12 (46.15)	$Z = 0.896$, $^{**}p = 0.002$
IL-2					
1st day	12 (44.44)	15 (55.55)	11 (42.31)	15 (57.69)	
55th day	25 (92.59)	2 (7.41)	16 (61.54)	10 (38.46)	$Z = 0.659$, $^{**}p = 0.001$

N: number of subjects in designated treatment; n: number of subjects in special category; %n (number of subjects in special category)/N (number of subjects in designated treatment) × 100; $^{*}p < 0.05$ and $^{**}p < 0.01$.

drugs, a previous study also show that the eye care practitioners (ECPs) should additionally consider both HOCl-based and TTO cleansers as the first-line choice [53]. Murphy et al. [46] have reported a reduction in the amount of *Demodex* mites with treatment of HOCL which coincides with our study. The treatments for the ocular *Demodex* are such a hot issue that several clinic research protocols are undergoing; the pure HOCL shows amazing prospect.

In this study, the *Demodex* count data of the Table 4 has been decreased from 10 to 2 parasites per cilia at the HOCL group ($Z = -4.642$, $^{**}p < 0.01$), from 11 to 6 parasites per cilia at the placebo contrast group ($Z = 2.742$, $p > 0.05$) at the endpoint of this clinic trail that the difference between these groups of the variation is significant ($Z = -2.310$, $^{*}p = 0.032 < 0.05$) which have seemingly slight decrease when making the determination of the clinical improvements. The exact links between the clinical symptoms and parasite burden remain somehow elusive. Gao et al. [51] have introduced this method of *Demodex* counts with the account of mites recorded in our study, both at the start and at the end of trial. A weekly eyelid scrub with 50% TTO has been verified successful in killing ocular *Demodex* infestation, and counts as low as zero have been proved in a previous study after 4 weeks of treatments [52, 53]. This present study reflects that HOCL has the same effect with that of TTO in terms of *Demodex* eradication on the eyelid tissue; it significantly shortens the survival time of *Demodex* in vivo, the average ST at different check points in the HOCL group is 110.75 (108.50 ± 31.50) min, 95.50 (90.25 ± 14.50) min, and 75.25 (73.48 ± 8.50) min alone which are significantly shorter compared with the average ST in the placebo group which are 155.50 (160.10 ± 21.50) min, 130.25 (128.25 ± 16.50) min, and 105.75 (102.50 ± 14.50) min ($^{**}p < 0.01$) (Figure 2). Therefore, HOCL is proved to be a novel treatment for *Demodex* blepharitis by shortening the average survival time.

Additionally, compared with the traditional application of 50% TTO treatment for 3 months in a row, we found that there was no only obvious differentiation between them (*Demodex* mite eradication rate between the two groups at the 55th day) ($^{**}p = 0.006 < 0.01$) (Figure 3) with regard to the average *Demodex* figures, but the successful killing rate is higher at different check points of this clinic trail in HOCL groups than that of control ($^{*}p15^{th}$ vs. 1st day = 0.028 < 0.05; $^{**}p30^{th}$ vs. 1st day = 0.002 < 0.01; $^{**}p55^{th}$ vs. 1st day = 0.0018 < 0.01) (Figure 3). The HOCL is a natural immunity reaction of the human body; our data shows no discomforts which coincide with previous study [12, 14, 44, 51]. Otherwise, many discomforts such as allergic reactions, contact dermatitis, and ocular irritations are well-known adverse reactions of TTO proposal [54]. The lower incidence of adverse reactions will ensure higher quality treatment compliance of patient as the reliable choice for MGD-EDE patients.

Table 4: The *Demodex* count between HOCL and placebo groups [P50 (P25, P75)].

Groups	Cases	1st day	55th day	Z	p
HOCL	54	10 (7,15)	2 (0,4)	-4.642	<0.01
Placebo	52	11 (8,18)	6 (4,14)	2.742	>0.05
Z		-0.892	-2.310		
p		0.431	0.032<0.05		

Due to the limitations of the small quantity of recruit in the present study, the effect of HOCL through ultrasonic atomization for *Demodex* blepharitis/MGD-DED needs further confirmation in a larger cohort and the observation for the alleviation of MGD-DED symptoms needs a long period. The anti-inflammation effects of the pure HOCL in *Demodex* blepharitis are elaborated, the mechanisms of the acaricidal effects of HOCL remain to be fully expound. In order to make sure for the symptom alleviation during the chronic disease management process of dry eye, future studies are required to clarify the tenet of HOCL to cure the *Demodex* blepharitis as well as maintain the ocular surface tear bio film stability.

5. Conclusion

We summarized the clinic data that the pure HOCL can improve the eradication rate of the *Demodex* mite by shortening its average survival time.

The HOCL induces lipid per oxidation reaction to the ocular surface pathogenesis microorganisms that the ocular surface inflammation can be alleviated.

The ultrasonic atomization drug delivery system helps for the drug usage.

Data Availability

The data sets used and/or analyzed during the present study are available from the corresponding author on reasonable request.

Consent

Oral consent from the patient whose lid margin and *Demodex* photographs score are displayed in Table 1 was obtained prior to publication.

Conflicts of Interest

The authors declare that they have no competing interests.

Authors' Contributions

Zhiyuan Li participated in the project design, sample size calculation, and revision of the manuscript. Zhenghua Li was responsible for the enrolment and follow-up of patients and participated in performing the statistical analysis. Mo Liang, Haiyan Wang, and Yvlian Li performed the clinic treatment and chronic disease management. Xiaoping Zhou and Guoping Kuang also drafted the manuscript. All the authors confirm the authenticity of the raw data and read and approved the final manuscript.

Acknowledgments

The present study was sponsored by Chenzhou Science and Technology Bureau Fund (grant No. ZDYF-20200092); the hospital management fund by the University of South China (grant No. 2019YJGL04); and the Outstanding Youth Fund of the First People's Hospital of Chenzhou City (grant No. N2019-006). We thank the participants of the study. The authors acknowledge the guidance and support provided by Prof. Hua Wang from the Ophthalmology Department of Xiangya Hosptial, Central South University, Prof. Jundong Zhu from Aier Eye Group, Central South University, and Dr. Jin Liu, Independent Consultant, the Eye Institute of Xiamen University, for conducting this study.

References

[1] J. P. Craig, J. D. Nelson, D. T. Azar et al., "TFOS DEWS II report executive summary," *The Ocular Surface*, vol. 15, no. 4, pp. 802–812, 2017.

[2] F. Stapleton, M. Alves, V. Y. Bunya et al., "TFOS DEWS II epidemiology report," *The Ocular Surface*, vol. 15, no. 3, pp. 334–365, 2017.

[3] D. M. Radomska-Leśniewska, A. Osiecka-Iwan, A. Hyc, A. Góźdź, A. M. Dąbrowska, and P. Skopiński, "Therapeutic potential of curcumin in eye diseases," *Central European Journal of Immunology*, vol. 44, no. 2, pp. 181–189, 2019.

[4] P. K. Gupta, P. Asbell, and J. Sheppard, "Current and future pharmacological therapies for the management of dry eye," *Eye & Contact Lens*, vol. 46, no. 2, pp. S64–S69, 2020.

[5] S. Y. Moon, S. A. Han, H. J. Kwon et al., "Effects of lid debris debridement combined with meibomian gland expression on the ocular surface MMP-9 levels and clinical outcomes in moderate and severe meibomian gland dysfunction," *BMC Ophthalmology*, vol. 21, no. 1, p. 175, 2021.

[6] J. W. Hu, S. Y. Pan, H. Yang, and X. H. Xiao, "Prevalence and risk factors of dry eye disease in young and middle-aged office employee: a Xi'an study," *International Journal of Ophthalmology*, vol. 14, no. 4, pp. 567–573, 2021.

[7] J. Xiao, M. Y. Adil, X. Chen et al., "Functional and morphological evaluation of meibomian glands in the assessment of meibomian gland dysfunction subtype and severity," *American Journal of Ophthalmology*, vol. 209, pp. 160–167, 2020.

[8] L. Jie, O. Shang-Kun, L. Wei, L. Zu-Guo, and P. Qing-Hua, "Physical therapy modalities of Western medicine and traditional Chinese medicine for meibomian gland dysfunction," *Digital Chinese Medicine.*, vol. 3, no. 4, pp. 229–238, 2020.

[9] E. Romanowski, N. Stella, K. Yates, K. M. Brothers, R. P. Kowalski, and R. M. Q. Shanks, "In vitro evaluation of a hypochlorous acid hygiene solution on established biofilms," *Eye & Contact Lens*, vol. 44, no. 2, pp. S187–S191, 2018.

[10] I. A. Jones and L. T. Joshi, "Biocide use in the antimicrobial era: a review," *Molecules*, vol. 26, no. 8, p. 2276, 2021.

[11] A. Ulfig and L. I. Leichert, "The effects of neutrophil-generated hypochlorous acid and other hypohalous acids on host and pathogens," *Cellular and Molecular Life Sciences*, vol. 78, no. 2, pp. 385–414, 2021.

[12] W.-H. Chang, P.-Y. Liu, M.-H. Lin et al., "Applications of hyaluronic acid in ophthalmology and contact lenses," *Molecules*, vol. 26, no. 9, p. 2485, 2021.

[13] Z. Haoyan and Z. Tao, "Clinical observation of ultrasonic atomization of traditional Chinese medicine in treatment of dry eye in patients with type 2 diabetes mellitus," *Clinical Journal of Traditional Chinese Medicine*, vol. 4, pp. 743–747, 2020.

[14] A. Fam, P. T. Finger, A. S. Tomar, G. Garg, and K. J. Chin, "Hypochlorous acid antiseptic washout improves patient comfort after intravitreal injection: A patient reported outcomes study," *Indian Journal of Ophthalmology*, vol. 68, no. 11, pp. 2439–2444, 2020.

[15] R. Arita, N. Morishige, S. Koh et al., "Increased tear fluid production as a compensatory response to meibomian gland loss: a multicenter cross-sectional study," *Ophthalmology*, vol. 122, no. 5, pp. 925–933, 2015.

[16] J. W. Jung, J. Y. Kim, H. S. Chin, Y. J. Suh, T. I. Kim, and K. Y. Seo, "Assessment of meibomian glands and tear film in post-refractive surgery patients," *Clinical & Experimental Ophthalmology*, vol. 45, no. 9, pp. 857–866, 2017.

[17] Z. Liu, M. Jin, Y. Li et al., "Efficacy and safety of Houttuynia eye drops atomization treatment for meibomian gland dysfunction-related dry eye disease: a randomized, double-blinded, placebo-controlled clinical trial," *Journal of Clinical Medicine*, vol. 9, no. 12, p. 4022, 2020.

[18] R. M. Schiffman, M. D. Christianson, G. Jacobsen, J. D. Hirsch, and B. L. Reis, "Reliability and validity of the ocular surface disease index," *Archives of Ophthalmology*, vol. 118, no. 5, p. 615, 2000.

[19] P. Arriola-Villalobos, J. I. Fernández-Vigo, D. Díaz-Valle, J. E. Peraza-Nieves, C. Fernández-Pérez, and J. M. Benítez-del-

Castillo, "Assessment of lower tear meniscus measurements obtained with Keratograph and agreement with Fourier-domain optical-coherence tomography," *The British Journal of Ophthalmology*, vol. 99, no. 8, pp. 1120–1125, 2015.

[20] K. W. Lee, J. Y. Kim, H. S. Chin, K. Y. Seo, T. I. Kim, and J. W. Jung, "Assessment of the tear meniscus by strip meniscometry and keratograph in patients with dry eye disease according to the presence of meibomian gland dysfunction," *Cornea*, vol. 36, no. 2, pp. 189–195, 2017.

[21] J. Kim, J. Y. Kim, K. Y. Seo, H. S. Chin, J. W. Jung, and J. W. Jung, "Location and pattern of non-invasive keratographic tear film break-up according to dry eye disease subtypes," *Acta Ophthalmologica*, vol. 97, no. 8, pp. e1089–e1097, 2019.

[22] N. Li, X. G. Deng, and M. F. He, "Comparison of the Schirmer I test with and without topical anesthesia for diagnosing dry eye," *International Journal of Ophthalmology*, vol. 5, no. 4, pp. 478–481, 2012.

[23] S. C. Pflugfelder, S. C. Tseng, O. Sanabria et al., "Evaluation of subjective assessments and objective diagnostic tests for diagnosing tear-film disorders known to cause ocular irritation," *Cornea*, vol. 17, no. 1, pp. 38–56, 1998.

[24] C. H. Yeh, S. X. Yu, and M. C. Lin, "Meibography phenotyping and classification from unsupervised discriminative feature learning," *Translational Vision Science & Technology*, vol. 10, no. 2, p. 4, 2021.

[25] K. K. Nichols, G. N. Foulks, A. J. Bron et al., "The international workshop on meibomian gland dysfunction: executive summary," *Investigative Ophthalmology & Visual Science*, vol. 52, no. 4, pp. 1922–1929, 2011.

[26] J. E. Kim, N. R. Kim, H. S. Chin, K. Y. Seo, T. I. Kim, and J. W. Jung, "Factors associated with ocular surface epithelial damage in patients with primary Sjögren's syndrome," *BMC Ophthalmology*, vol. 21, no. 1, p. 114, 2021.

[27] S. Y. Lee, K. Lee, C. K. Park et al., "Meibomian gland dropout rate as a method to assess meibomian gland morphologic changes during use of preservative-containing or preservative-free topical prostaglandin analogues," *PLoS One*, vol. 14, no. 6, article e0218886, 2019.

[28] K. Y. Seo, S. M. Kang, D. Y. Ha, H. S. Chin, and J. W. Jung, "Long-term effects of intense pulsed light treatment on the ocular surface in patients with rosacea-associated meibomian gland dysfunction," *Contact Lens & Anterior Eye*, vol. 41, no. 5, pp. 430–435, 2018.

[29] Chinese branch of Asian dry eye association, ophthalmology group of ophthalmology committee of cross-strait medical exchange association, "Consensus of diagnosis and treatment experts on vermicoid mite blepharitis in China 2018," *Chinese Journal of Ophthalmology*, vol. 54, no. 7, pp. 491–495, 2018.

[30] Y. Y. Gao, M. A. di Pascuale, W. Li et al., "High prevalence of Demodex in eyelashes with cylindrical dandruff," *Investigative Ophthalmology & Visual Science*, vol. 46, no. 9, pp. 3089–3094, 2005.

[31] X. Zhang, N. Song, and L. Gong, "Therapeutic effect of intense pulsed light on ocular demodicosis," *Current Eye Research*, vol. 44, no. 3, pp. 250–256, 2019.

[32] D. W. Stroman, K. Mintun, A. B. Epstein et al., "Reduction in bacterial load using hypochlorous acid hygiene solution on ocular skin," *Clinical Ophthalmology*, vol. 11, no. 11, pp. 707–714, 2017.

[33] S. B. Hulley, S. R. Cummings, W. S. Browner, D. G. Grady, and T. B. Newman, *Designing Clinical Research: An Epidemiologic Approach*, Lippincott Williams& Wilkins, Philadelphia, PA, USA, 4th edition, 2013.

[34] F. Faul, E. Erdfelder, A. G. Lang, and A. Buchner, "G∗power 3: a flexible statistical power analysis program for the social, behavioral, and biomedical sciences," *Behavior Research Methods*, vol. 39, no. 2, pp. 175–191, 2007.

[35] P. Aragona, G. Giannaccare, R. Mencucci, P. Rubino, E. Cantera, and M. Rolando, "Modern approach to the treatment of dry eye, a complex multifactorial disease: a P.I.C.a.S.S.O. board review," *British Journal of Ophthalmology*, vol. 105, no. 4, pp. 446–453, 2021.

[36] S. C. Pflugfelder and C. S. de Paiva, "The pathophysiology of dry eye disease: what we know and future directions for research," *Ophthalmology*, vol. 124, no. 11, pp. S4–S13, 2017.

[37] T. Yamaguchi, "Inflammatory Response in Dry Eye," *Investigative Ophthalmology & Visual Science*, vol. 59, no. 14, p. DES192, 2018.

[38] M. Jaganjac, A. Cipak, R. J. Schaur, and N. Zarkovic, "Pathophysiology of neutrophil-mediated extracellular redox reactions," *Frontiers in Bioscience-Landmark.*, vol. 21, no. 4, pp. 839–855, 2016.

[39] M. J. Davies and C. L. Hawkins, "The role of Myeloperoxidase in biomolecule modification, chronic inflammation, and disease," *Antioxidants & Redox Signaling*, vol. 32, no. 13, pp. 957–981, 2020.

[40] T. Appiah, Y. D. Boakye, and C. Agyare, "Antimicrobial activities and time-kill kinetics of extracts of selected Ghanaian mushrooms," *Evidence-based Complementary and Alternative Medicine*, vol. 2017, Article ID 4534350, 15 pages, 2017.

[41] H. Y. Yin, S. Tighe, S. C. Tseng, and A. M. S. Cheng, "Successful management of chronic blepharo-rosacea associated demodex by lid scrub with terpinen-4-ol," *American Journal of Ophthalmology Case Reports*, vol. 23, article 101171, 2021.

[42] M. H. Gold, A. Andriessen, A. C. Bhatia et al., "Topical stabilized hypochlorous acid: the future gold standard for wound care and scar management in dermatologic and plastic surgery procedures," *Journal of Cosmetic Dermatology*, vol. 19, no. 2, pp. 270–277, 2020.

[43] W. Ngo, L. Jones, and E. Bitton, "Short-term comfort responses associated with the use of eyelid cleansing products to manage Demodex folliculorum," *Eye & Contact Lens*, vol. 44, no. 2, pp. S87–S92, 2018.

[44] J. Q. Del Rosso and N. Bhatia, "Status report on topical hypochlorous acid: clinical relevance of specific formulations, potential modes of action, and study outcomes," *The Journal of Clinical and Aesthetic Dermatology*, vol. 11, no. 11, pp. 36–39, 2018.

[45] M. M. Kiamco, H. M. Zmuda, A. Mohamed et al., "Hypochlorous-acid-generating electrochemical scaffold for treatment of wound biofilms," *Scientific Reports*, vol. 9, no. 1, p. 2683, 2019.

[46] O. Murphy, V. O'Dwyer, and A. Lloyd-McKernan, "The efficacy of tea tree face wash, 1, 2-Octanediol and microblepharoexfoliation in treating _Demodex folliculorum_ blepharitis," *Contact Lens & Anterior Eye*, vol. 41, no. 1, pp. 77–82, 2018.

[47] K. Ma, Q. S. Li, Z. Y. Zhang, M. H. Xiang, and Y. Q. Zhao, "Research progress in physical therapy for dry eye," *International Eye Science*, vol. 18, pp. 660–663, 2018.

[48] J. C. Yuqiu Xu, "Research progress of ultrasonic atomization treating dry eye," *Journal Traditional Chinese Medicine Ophthalmology*, vol. 30, pp. 367–370, 2020.

[49] Y. Zhou, "Clinical observation and analysis of dry eye after phacoemulsification and intraocular lens implantation with traditional Chinese medicine ultrasonic atomization," *Hunan University of Chinese Medicine*, vol. A01, pp. 45-46, 2018.

[50] W. Liu and L. Gong, "Anti-demodectic effects of okra eyelid patch inDemodexblepharitis compared with tea tree oil," *Experimental and Therapeutic Medicine*, vol. 21, no. 4, p. 338, 2021.

[51] Y. Y. Gao, M. A. Di Pascuale, A. Elizondo, and S. C. Tseng, "Clinical treatment of ocular demodecosis by lid scrub with tea tree oil," *Cornea*, vol. 26, no. 2, pp. 136–143, 2007.

[52] S. Tighe, Y. Y. Gao, and S. C. Tseng, "Terpinen-4-ol is the most active ingredient of tea tree oil to kill Demodex mites," *Translational Vision Science & Technology*, vol. 2, no. 7, p. 2, 2013.

[53] E. Bitton, *Treatment of Demodex with hypochlorous acid: case report consistent treatment with hypochlorous acid may improve symptoms for symptomatic dry eye patients. Dry eye patients report improvement in symptoms with hypochlorous acid use over 30 days. This abstract was presented at the 2019 ARVO annual meeting*, Vancouver, Canada, 2019.

[54] H. Koo, T. H. Kim, K. W. Kim, Y. S. Chun, J. C. Kim, and J. C. Kim, "Ocular surface discomfort and Demodex: effect of tea tree oil eyelid scrub in Demodex blepharitis," *Journal of Korean Medical Science*, vol. 27, no. 12, pp. 1574–1579, 2012.

Hindawi
Disease Markers
Volume 2021, Article ID 6575195, 8 pages
https://doi.org/10.1155/2021/6575195

Research Article

Outcomes of a Foldable Capsular Vitreous Body Implantation: A Retrospective Study

Xiangzhong Xu, Huimin Ge, Jiajun Li, Weihong Shang, Yuke Ji, Weihua Yang, and Keran Li

Department of Ophthalmology, The Affiliated Eye Hospital of Nanjing Medical University, Nanjing 210029, China

Correspondence should be addressed to Weihua Yang; benben0606@139.com and Keran Li; kathykeran860327@126.com

Received 12 November 2021; Revised 30 November 2021; Accepted 6 December 2021; Published 26 December 2021

Academic Editor: Ting Su

Background. The vitreous body is an important part of the ocular body fluid. A foldable capsular vitreous body (FCVB) is designed to treat chronic adverse complications in severe ocular trauma and silicone oil-dependent eyes. This study is aimed at investigating a method for implanting an FCVB, its postoperative efficacy, and clinical value. *Methods*. A retrospective analysis was performed on data from 18 patients who underwent vitrectomy and FCVB implantation for severe ocular trauma and silicone oil-dependent eyes between March 2019 and May 2020. All treated eyes underwent clinical examinations involving the best-corrected visual acuity, intraocular pressure, FCVB position, anterior segment photography, and wide-angle fundus photography regularly after surgery. *Results*. Eighteen eyes from 18 patients were enrolled in this study. A total of 2.00–4.20 (3.46 ± 0.78) ml of silicone oil were injected into the FCVB during surgery. The patients were followed up at 1, 2, and 4 weeks and 3, 6, and 12 months after surgery. Twelve months after surgery, visual acuity improved in 7 (38.89%) eyes. In contrast, 10 (55.56%) eyes showed no obvious improvement, and 1 (5.56%) eye had decreased vision. Intraocular pressure at 12 months was 10.13 ± 3.52 mmHg, which was comparable to that before the surgery ($t = 0.38$, $P = 0.71$). The anterior chamber depth examined by slit lamp was 2.00–3.00 cornea thickness (CT) in 7 eyes, 1.00–2.00 CT in 2 eyes, and <1.00 CT in one eye. The anterior chamber disappeared in eight eyes. There were eight eyes with clear cornea, four eyes with localized opacity, and two eyes with obvious gray-white opacity. There was no case of severe FCVB deflection, rupture, or exposure during the observation period. *Conclusion*. FCVB implantation is an effective and safe treatment for eyes with severe ocular trauma and silicone oil-dependent eyes. It may support retinal reattachment, slow down eyeball atrophy, reduce the risk of chronic adverse complications such as corneal endothelial decompensation, and maintain intraocular pressure and preoperative visual function.

1. Introduction

The vitreous body is an important part of the ocular body fluid, which supports the retina, supplies nutrition, stabilizes intraocular metabolism, and acts as a cell barrier and ocular refractive media [1]. Furthermore, the natural vitreous body is nonrenewable. Severe ocular trauma, complex retinal tears, and proliferative diabetic retinopathy can cause damage to intraocular tissues and reduce ocular function; common chronic complications include eyeball atrophy and corneal endothelial decompensation. In recent years, vitreoretinal surgery combined with vitreous tamponade, which includes sterile gas (air, expandable gas), liquid (balanced salt solution, silicone oil (SO), and perfluorocarbon liquid, among others), and polymer (hydrogel), has been used to replace the natural vitreous body with vitreous substitutes to support the retina, promote the anatomical reduction of the retina, and prevent eyeball atrophy. However, nearly 18% of patients remain at risk of ocular atrophy after SO removal [2]. In addition, long-term retention of SO in the eye can lead to secondary glaucoma, cataracts, keratopathy, anterior chamber oil emulsification, and other complications [3]. Some patients need to replace SO repeatedly, which results in severe physical and financial burdens. As a new

vitreous substitute product, a foldable capsular vitreous body (FCVB) has an anatomical structure comparable to that of the human vitreous cavity. It is mainly composed of three parts: the vitreous cavity, drainage tube, and drainage valve. The vitreous cavity is an elastic film formed by the polymerization of polyvinyl siloxane and polymethylhydrosiloxane by computer simulation, and the capsule wall is approximately 0.01 mm thick. The drainage valve is connected to the vitreous body through a drainage tube with a diameter of approximately 1.00 mm, which has excellent mechanical properties, optical properties, and biocompatibility that help support the retina [4]. Compared with other established vitreous substitutes used in the clinic, the FCVB remains stable in the eye for a long time, while avoiding serious complications caused by SO filling [4]. However, at present, FCVB has not been promoted in clinical application, and the number of cases in previous studies was also low. In addition, the clinical safety and efficacy of FCVB have not been verified yet. In this study, FCVB implantation, as a new method for treating severe ocular trauma or SO-dependent eyes, was performed in 18 patients to analyze the safety and effectiveness of the FCVB and to evaluate its clinical value.

2. Materials and Methods

2.1. Study Design. A retrospective study of 18 patients (17 male and 1 female) that underwent FCVB implantation between March 2019 and May 2020 was performed. The patients' average age was 50.61 ± 11.63 years (range, 34–70 years). Fourteen eyes with severe eyeball rupture were treated with phase I debridement and suturing, among which 10 eyes were treated with FCVB implantation within 5–14 (11.5 ± 5.21) days after the injury, and 4 eyes were treated with the same approach within 1.5–4 (2.88 ± 1.03) months after the injury. FCVB implantation was performed in the other four SO-dependent eyes due to vitrectomy and SO filling for severe ocular trauma.

The inclusion criteria were as follows: (1) severe ocular rupture with retinal and choroid injury, visual acuity below 0.05; (2) ocular trauma with mild ocular atrophy, ocular axis of 16.00–28.00 mm; (3) SO-dependent eye after vitrectomy, with secondary complications such as band-shaped degeneration of the cornea, glaucoma, or SO emulsification.

Exclusion criteria were as follows: (1) severe liver and kidney dysfunction, cardiovascular disease, nervous system disease and other systemic diseases, and inability to tolerate FCVB implantation; (2) single eye; (3) severe intraocular infections, uveitis, or intraorbital infections; (4) diseases affecting the development of the orbit in the contralateral eye; (5) allergies to silicone materials or scars; (6) ineligibility for FCVB implantation; (8) overall health unsuitable for participation in a clinical trial; (9) poor compliance and inability to complete the test process as required.

This study followed the principles of the Declaration of Helsinki and was approved by the Ethics Committee of the Affiliated Eye Hospital of Nanjing Medical University (20210015). All patients and their families were informed of the undertaken precautions and possible complications related to the surgery as well as the FCVB implant before the surgery, and an informed consent form was signed by each participant. The clinical trials strictly adhered to the principles of the World Medical Association's Declaration of Helsinki.

2.2. Surgical Technique. All operations were performed by the same surgeon. (1) A three-channel vitrectomy was conducted to remove the central and peripheral vitreous, SO, and vitreous hemorrhage, peeling off the surface or subretinal proliferative membrane. (2) An approximately 4 mm incision was performed on the sclera as FCVB implantation site at either the 4 or 8 o'clock position 5 mm away from the corneal limbus. (3) Perform gas-fluid exchange to lift the IOP over 50 mmHg and evaluate the state of retina and cornea. (4) A suitable type of capsule was prepared preoperatively according to the length of the patient's ocular axis, while the capsular integrity was checked and the scleral puncture port was enlarged to 4 mm. (5) An FCVB was properly folded and implanted into the eyeball cavity through the incision with a push injector. The lens surface of the FCVB was placed facing the lens. If there was any tilting, the position of the FCVB capsule was adjusted with an iris repositor. Subsequently, the SO was slowly injected into the capsule through the drainage valve with a syringe until the intraocular pressure (IOP) was moderate, while the conditions of the retina and color of the optic disc were observed with the aid of an optical fiber. (6) The scleral incision was sutured, and a drainage tube was ligated and fixed to the sclera (Figure 1).

After the surgery, patients were strictly instructed to lie in a prone position for 1 month. Standard postoperative medication: (1) systemic administration: antibiotics, dexamethasone, and hemostatic, followed by prednisone (0.6 mg/kg orally, decreasing weekly) for 8 weeks; (2) local medication: tobramycin and dexamethasone eye drops and ointment (2 months, according to the condition of the eye); cycloplegia; (3) the treatment time of severe eye trauma and children patients should be extended to 3-4 months; (4) avoid strenuous exercise and overuse of eyes.

2.3. Follow-Up Examinations. Measurement of best-corrected visual acuity and IOP (NIDEK, NT-5100), corneal endothelial cell test (NIDEK, CEM-530), UBM (SUOER, SW-3200L), ocular axis test (Optical Biometry, IOLMaster 700), B-ultrasound (Meda Co, ltd, ODM-2100S), anterior segment photography (cqsaikang, LS-6), fundus photography (Panoramic Ophthalmoscope-Daytona, A10600), facial photography (NICON, IXUS145), and orbital computed tomography examination (SomATom 90) were performed for all patients before surgery. Best-corrected visual acuity, intraocular pressure, FCVB position, anterior segment photography, and fundus photography were performed at 1, 2, and 4 weeks and 3, 6, and 12 months after the implantation.

2.4. Statistical Analysis. In this study, SPSS 23.0 statistical software was used for data analyses. Descriptive statistics were presented as frequencies and composition ratios, and measurement data were expressed as mean ± SD. The t-test was used for comparisons of normally distributed binocular

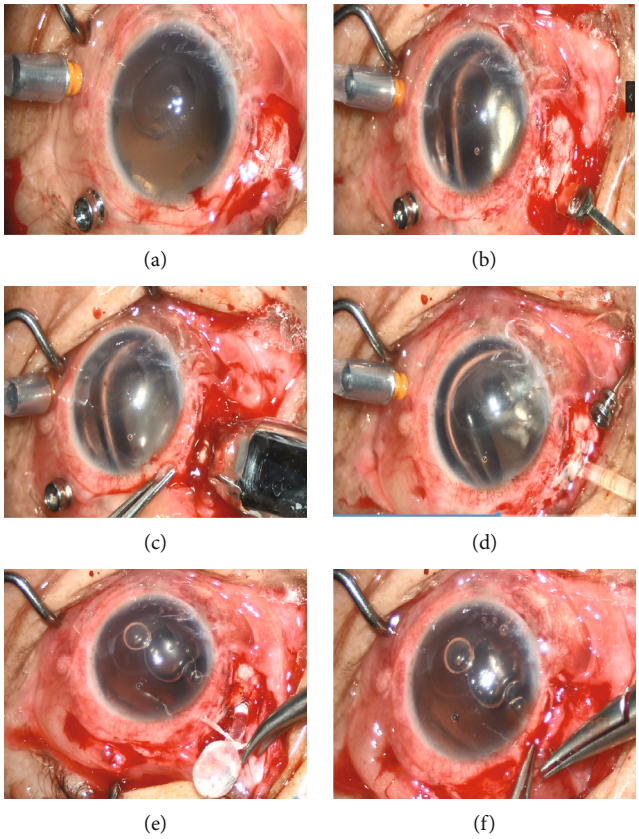

Figure 1: Surgical FCVB implantation. (1) A three-channel incision was made in the supranasal, supratemporal, and inferotemporal regions posterior to corneoscleral margin. (2) An L-shaped scleral incision of approximately 4 mm was made 5 mm posterior to the corneal limbus. (3) FCVB was folded and implanted into the eyeball cavity through the incision with a push injector, and the lens surface of the capsule was placed facing the lens. (4) SO was slowly injected into the capsule through the drainage valve with a syringe until the IOP was moderate. (5) The scleral incision was sutured, and the drainage tube was ligated and fixed in the sclera. (6) Contrapuntal suture of conjunctiva was performed.

parameters before and after surgery; the Wilcoxon matched-pair signed-rank test was used for the analysis of nonnormally distributed data. Count data were compared using the chi-square test. Statistical significance was set at P values of <0.05.

3. Results

3.1. General Condition. An FCVB was successfully implanted in 18 eyes of 18 patients in this study. The amount of SO injected into the FCVB was in the range of 2.00–4.20 (3.46 ± 0.78) ml. During the follow-up period, no FCVB rejection, displacement, rupture, exposure, sympathetic ophthalmitis, bullae keratopathy, or other serious surgical complications were observed in any patient. Postoperative findings are presented in Figures 2 and 3.

3.2. Vision. Twelve eyes (66.67%) had no light sensation before surgery, 3 (16.67%) eyes had preserved light sensation, and 3 (16.67%) eyes had manual sensation. Twelve months after the operation, 8 (44.44%) eyes had no light sensation, 3 (16.67%) eyes had preserved light sensation, and 7 (38.89%) eyes had manual sensation. Among them, there were 7 (38.89%) eyes with improved vision, 10 (55.56%) eyes without obvious improvement, and 1 (5.56%) eye with decreased vision.

3.3. Intraocular Pressure. Preoperative IOP was in the range of 3.00–30.00 (10.17 ± 6.82) mmHg in all subjects. The IOP was in the range of 3.00–26.00 (11.44 ± 6.24) mmHg 1 week after surgery, which represented a significant change from baseline ($t = -0.66$, $P = 0.52$). Twelve months after surgery, the mean IOP of the other 16 eyes was 10.13 ± 3.52 mmHg, except for two eyes in which IOP could not be measured due to corneal degeneration. The IOP of 6 eyes was of <8.00 mmHg and that of 12 eyes was in the normal range (8.00–21.00 mmHg). No patient had IOP of >22.00 mmHg, and these values did not change from baseline ($t = 0.38$, $P = 0.71$).

3.4. Conditions of Anterior Chamber and Capsule. Twelve months after surgery, 7, 2, 1, and 8 eyes had anterior chamber depth of 2.00–3.00 CT, 1.00–2.00 CT, <1.00 CT, and undetectable value, respectively. No patient had any obvious deviation in FCVB, with intact morphology and no capsular rupture or exposure. Thin exudate membranes were found on the anterior surface of the implanted capsule or pupil area in four eyes, and YAG laser resection was performed.

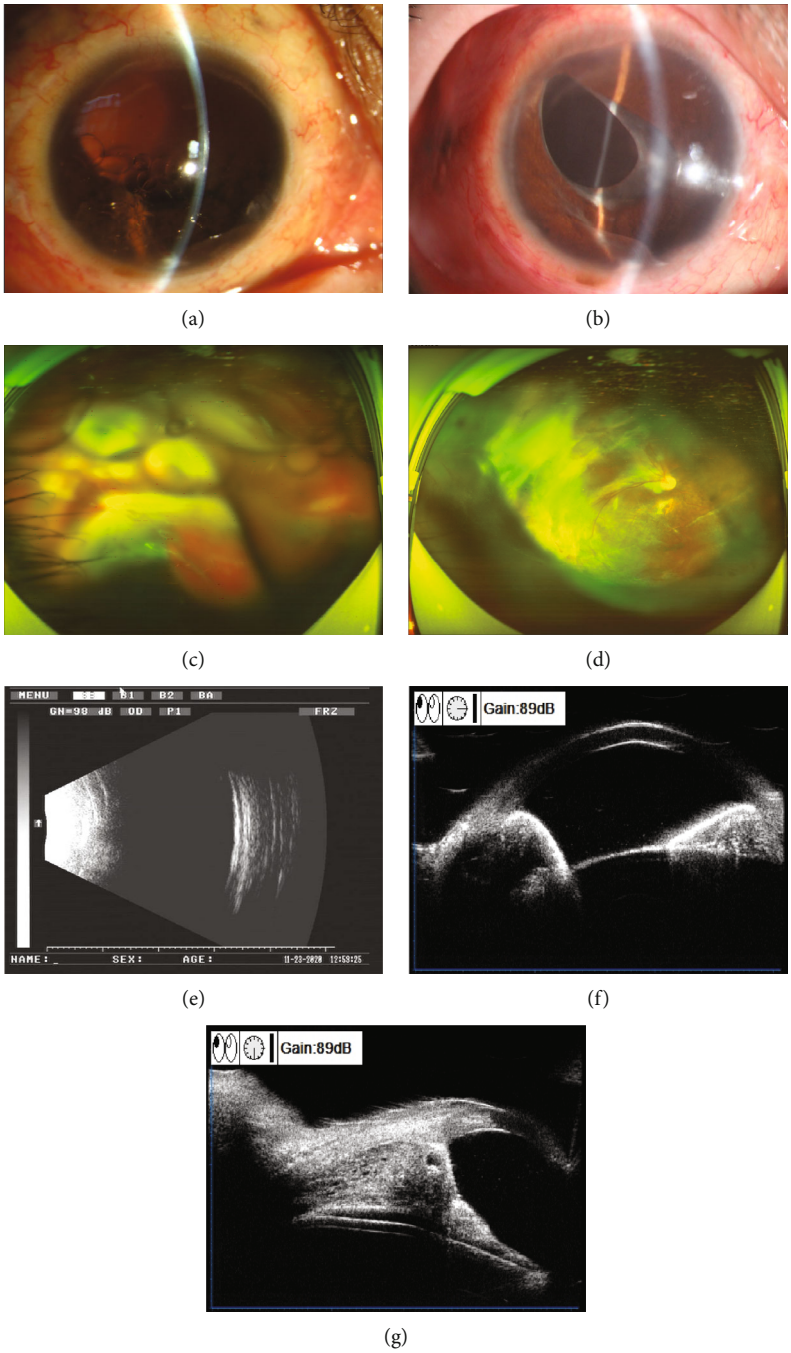

Figure 2: Examination results before and 12 months after FCVB implantation in stage II eyeball rupture. (a) Preoperative anterior segment photography revealed that the vitreous cavity was filled with SO, and the SO moved into the anterior chamber. The cornea was clear; most of the iris and crystal were absent. (b) Anterior segment photography at 12 months after surgery revealed that the cornea was clear, the anterior chamber was not shallow, part of the iris and the lens were absent, and FCVB was in place in the vitreous cavity. (c) Preoperative fundus photography showed retinal folds and extensive retinal detachment. (d) Fundus photography at 12 months after surgery displayed that the retina was flat. (e) B-ultrasound at 12 months after surgery showed the reflection of the posterior wall of the eyeball as smooth, and the FCVB shape as intact. (f, g) UBM at 12 months after surgery showed approximately normal anterior chamber depth, with opened chamber angle, and smooth front surface of FCVB.

3.5. Corneal Condition. All enrolled patients underwent the corneal endothelium count and corneal thickness assessment before surgery. Corneal endothelium and corneal thickness could not be assessed in 9 and 10 patients, respectively, due to a large amount of anterior chamber hematoma and corneal opacity before surgery. The corneal endothelium count of the remaining nine patients was in the range of 1554.00–2710.00 (2113.00 ± 443.09) CD/mm^2 and in the range of 2441.00–3046.00 (2690.22 ± 186.644) CD/mm^2 for contralateral eyes. This difference was statistically significant

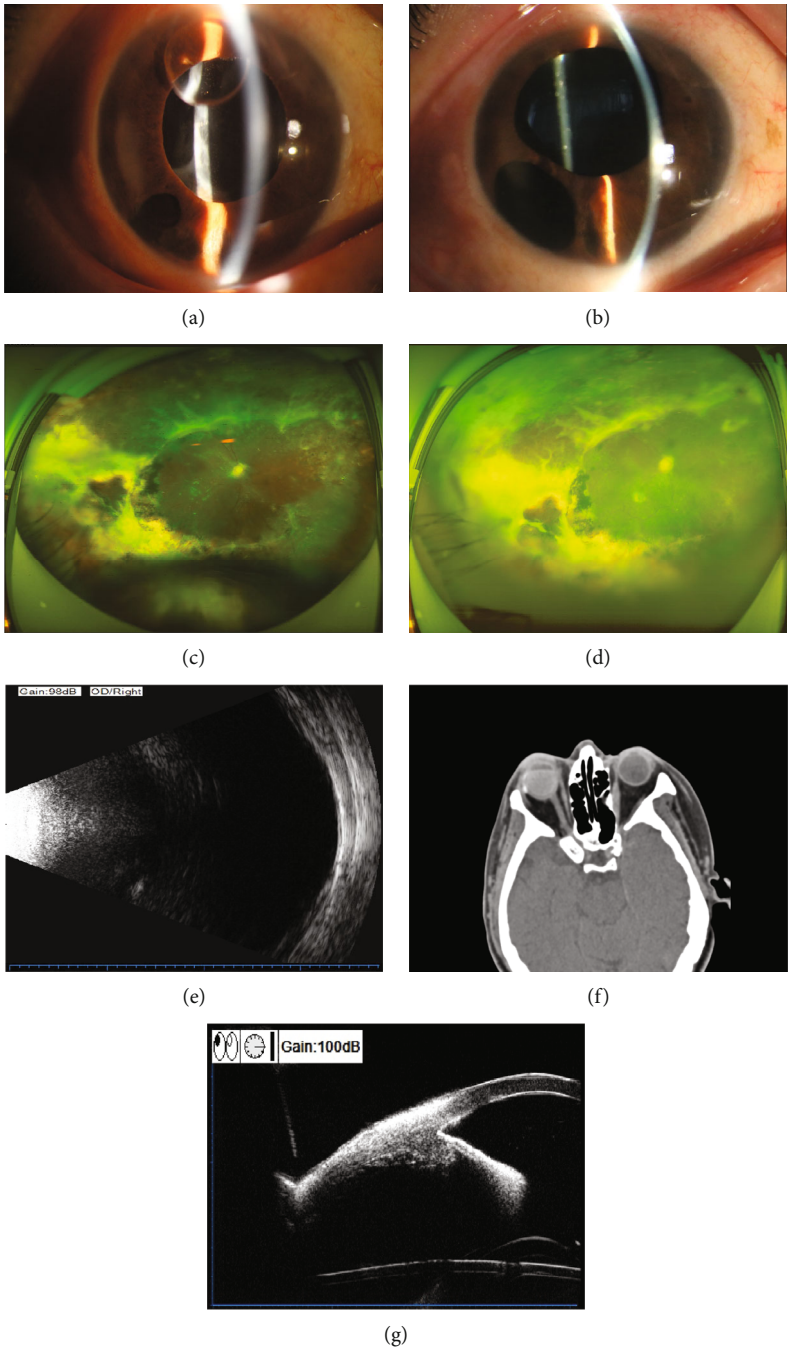

Figure 3: Examination results before and 12 months after FCVB implantation in the SO-dependent eye. (a) Preoperative anterior segment photography indicated that the vitreous cavity was filled with SO, and the SO was moved into the anterior chamber. The cornea was clear, the pupil was dilated but had upward deviation, and the lens was absent. (b) Anterior segment photography at 12 months after surgery revealed that the cornea was clear, the pupil was still round but with upward deviation, and iris root incision was unobstructed. (c) Preoperative fundus photography showed extensive degeneration, detachment, and proliferation of peripheral retina lesions. (d) Fundus photography 12 months after surgery indicated that the retina was flat. (e) B-ultrasound eye at 12 months after surgery showed the reflection of the posterior wall of the eyeball as smooth and the FCVB morphology as intact. (f) Postoperative orbital computed tomography displayed that the appearance of eyeball was normal, the FCVB position was correct, and the SO was filled in place. (g) UBM at 12 months after surgery showed approximately normal anterior chamber depth, with opened chamber angle and smooth front surface of FCVB.

($t = -3.77$, $P = 0.005$). The corneal thickness of eight eyes was in the range of 475.00–754.00 mm (627 ± 81.983) mm and in the range of 468.00–591.00 (534.5 ± 36.516) mm for the contralateral eyes. This difference was statistically significant ($t = 3.11$, $P = 0.02$). Table 1 shows the corneal opacity before and after FCVB implantation in 14 patients with

Table 1: Corneal opacity condition before and after FCVB implantation for ocular trauma.

Corneal condition	Before surgery			12 months after surgery		
	Phase I for FCVB implantation group	Phase II for FCVB implantation group	In total	Phase I for FCVB implantation group	Phase II for FCVB implantation group	In total
Still clear	6	2	8	6	2	8
Localized opacity	4	2	6	2	2	4
Total opacity	0	0	0	2	0	2

severe ocular rupture. Twelve months after the surgery, the cornea remained clear in eight eyes; among them, the FCVB was implanted in six eyes at stage I and two eyes at stage II post-injury. There were four eyes with localized corneal opacity, including two eyes with FCVB implantation in stage I and two eyes with FCVB implantation in stage II post-injury. There were two eyes with total corneal opacity (gray and white) with FCVB implantation in stage I post-injury (both patients had severe corneal injury, ciliary body injury, low intraocular pressure, and mild atrophy before surgery). The other four silicone oil-dependent eyes had no significant change in corneal opacity before and after FCVB implantation.

4. Discussion

The vitreous body helps maintain IOP, support normal anatomical structure of intraocular tissues, and stabilize intraocular metabolism. Severe ocular trauma is a kind of complex disease, often accompanied by cornea, sclera, iris, lens, vitreous body, retina, and choroid injury. Fiber blood vessels and complexity of glial hyperplasia caused low intraocular pressure after retinal detachment and ciliary body damage, leading to long-term chronic complications such as loss of vision, eyeball atrophy, and even enucleation of the eyeball. Therefore, vitrectomy is an effective way for the treatment of severe eye trauma. Currently, vitreous substitutes have some serious shortcomings, such as short duration of intraocular maintenance, high toxicity, and many complications. Precisely, there is no perfect material that has the ability to completely mimic the functions of natural vitreous body along [1, 4].

FCVB was designed to change the traditional supporting mode of the retina with a 360° arc solid pressure effect and isolated the SO with the capsule of FCVB, which is a brand-new therapy strategy. Since that, FCBV implantation has greatly reduced the incidence of complications. Furthermore, patients were no need to keep prone posture after surgery. Silicone oil can also be extracted through the drainage valve of the FCVB or injected with normal saline and silicone oil to regulate intraocular pressure [5, 6].

This study included 10 patients who underwent vitrectomy combined with FCVB implantation and SO injection at stage I (an average of 11.5 days) after debridement of severe eyeball rupture. Severe tissue damage such as massive hemorrhage of the vitreous body, total retinal detachment and defect, and choroidal detachment with cyclodialysis were observed during the surgery. Four patients underwent SO removal combined with FCVB implantation and SO reinjection at stage II (an average of 2.9 months) after debridement for severe ocular trauma. Mild retinal atrophy was observed before surgery, and severe retinal detachment occurred again after the removal of the emulsified SO during surgery. There were four cases of SO-dependent eyes, i.e., repeated silicone oil injection and removal, and the course of disease ranged from 8 months to 10 years. These cases may have become SO-dependent eyes, accompanied by different degrees of eyeball atrophy. Traditional SO filling has poor postoperative efficacy; therefore, FCVB combined with SO injection should be considered.

Twelve patients without light perception before surgery were enrolled in this study, while four patients had restored visual acuity including light perception or hand moving after the surgery, and more than 50% of the patients maintained preoperative visual acuity. Lin et al. found that FCVB implantation could not effectively improve postoperative visual acuity in patients with severe retinal detachment and severe macular scarring, choroid detachment, or other ocular tissue injuries before surgery but could maintain the preoperative visual acuity [5]. Meanwhile, FCVB implants had no significant effect on the diopter of the Gullstrand-Emsley model eyes before and after surgery [6, 7]. *In vivo* studies revealed that FCVB implantation could promote anatomical reduction of the detached retina, specifically, in patients whose lower retina could not be restored after SO filling [5]; it could also inhibit the migration of activated neurogliocytes, collagen fiber IV, and microglial cells into the vitreous cavity during retinal healing [8]. These studies indicate that FCVB implantation combined with SO filling can effectively restore the retina for a long time and promote partial recovery of visual function. For patients with severe ocular injury, preoperative visual function can be maintained even if postoperative visual acuity cannot be improved. However, one patient had no light sensation after surgery, which was thought to be associated with severe retinal detachment and scarring caused by acute retinal necrosis. Animal studies have shown that FCVB implantation can effectively simulate natural vitreous morphology and maintain normal IOP in the short and long term after surgery [7, 9]. At the last follow-up assessment, 14 (77.78%) eyes had an IOP of more than 10 mmHg; two patients could not be examined due to severe corneal degeneration. Measurements in the remaining 16 eyes showed no significant change from baseline values, indicating that FCVB

implantation could effectively control further ocular atrophy and this finding is consistent with that of a study by Yanni et al. [5, 10]. Moreover, FCVB implantation can prevent the displacement of SO in the vitreous cavity, reduce the occurrence of secondary ocular hypertension caused by obstruction of the anterior chamber angle or crystal turbidity expansion, promote the recovery of ciliary body function to maintain the stability of aqueous fluid circulation [11], and effectively delay the progression of ocular atrophy. However, some studies have shown that retinal structural disorders were found 180 days after FCVB filling [9], suggesting that we need to explore and find an ideal target intraocular pressure to alleviate the mechanical damage caused by long-term FCVB filling.

Chen et al. showed that anterior chamber depth did not change significantly 6 months after FCVB implantation compared with that before surgery [8]. However, anterior chamber disappearance occurred in eight patients during the follow-up period; meanwhile, no significant increase in IOP was observed in our studies, which may be associated with severe ocular trauma resulting in ciliary body detachment, ciliary body dysfunction, and decreased aqueous fluid secretion function [12]. In addition, some studies have shown that in FCVB implantation, ciliary body reduction and suturing are feasible for patients with ciliary body separation; for patients with traumatic aniridia, polypropylene suture can be used to intercept and suture the ciliary sulcus, which can effectively reduce the occurrence of postoperative superficial anterior chamber and corneal degeneration [13]. For patients with a shallow anterior chamber after surgery, a viscoelastic agent injection can effectively restore the position of iris-FCVB, slow down the drainage of the aqueous humor, and promote the formation of anterior chamber.

Overall, 11%–49% of patients experience SO displacement and nearly all patients experience SO emulsification 12 months after traditional vitrectomy, resulting in secondary glaucoma, corneal degeneration, and other serious complications [14]. In our studies, the corneas remained clear in eight eyes at 12 months of follow-up; however, the corneas were gray and white with obvious opacity in two eyes with severe ocular rupture and there was no significant change in this parameter compared with its preoperative values. These findings suggest that FCVB implantation effectively reduces the occurrence of corneal degeneration caused by long-term SO dependence. Early FCVB implantation reduces SO damage to the corneal endothelium. Nevertheless, due to persistent low IOP caused by early posttraumatic ciliary body hypofunction and intraocular inflammation, shallow anterior chamber and decompensation of the corneal endothelium are likely to occur. For the patients undergoing FCVB implantation in phase II, intraocular inflammation was effectively controlled, and no obvious eyeball atrophy was observed.

FCVB implantation combined with SO refilling can further promote the recovery of intraocular tissue structure and function [15]. In addition, it can be used as an intraocular drug sustained-release system (for drugs such as dexamethasone, levofloxacin, and 5-fluorouracil) in a time- and dose-dependent manner that directly acts on retinal tissues, improves drug bioavailability, increases drug action duration, and inhibits intraocular inflammation [16–18]. Therefore, FCVB implantation effectively reduces corneal endothelial decompensation, persistently low IOP, and helps prevent chronic complications such as progressive eyeball atrophy. However, it was not a comparative study and lack of long-term follow-up. To ensure the superiority and safety of FCVB among all the vitreous substitutes, it is certainly worth conducting large-scale comparative clinical trials in the future.

5. Conclusions

The present findings suggest that FCVB implantation can be effective for patients with severe ocular trauma and SO-dependent eyes. It can support the retina, maintain eyeball shape, and stabilize visual acuity, which may become a new carrier of intraocular fluid that integrates vitreous substitutes and drug sustained-release systems, providing a new direction for the treatment of traumatic and refractory vitreoretinal diseases. However, the cost of FCVB is expensive and longer follow-up periods of observation are deficient. Future studies should include larger samples and longer follow-up periods to validate the present findings.

Abbreviations

FCVB: Foldable capsular vitreous body
SO: Silicone oil
IOP: Intraocular pressure
CT: Cornea thickness.

Data Availability

All the data supporting our findings is contained within the manuscript and tables. The relevant raw data will be freely available from the Affiliated Eye Hospital of Nanjing Medical University by request.

Conflicts of Interest

We declare that they have no conflicts of interest.

Authors' Contributions

Xiang Zhong Xu and Huimin Ge are co-first authors.

Acknowledgments

The authors would like to thank the Affiliated Eye Hospital of Nanjing Medical University for supporting the research work. This study was supported by the National Natural Science Foundation of China (81700859) and the Natural Science Foundation of Jiangsu Province (BK20171065).

References

[1] I. Yadav, S. D. Purohit, H. Singh et al., "Vitreous substitutes: an overview of the properties, importance, and development,"

Journal of Biomedical Materials Research, Part B, Applied Biomaterials, vol. 109, no. 8, pp. 1156–1176, 2021.

[2] C.-F. Fan and X.-H. Zhu, "The therapeutic value of vitrectomy for early atrophy of eyeball after trauma," *Chinical Journary Practical Ophthalmology*, vol. 24, no. 1, pp. 94–97, 2006.

[3] M. Nicolai, N. Lassandro, A. Franceschi et al., "Intraocular pressure rise linked to silicone oil in retinal surgery: a review," *Vision*, vol. 4, no. 3, p. 36, 2020.

[4] Q.-Y. Gao, Y. Fu, and Y.-N. Hui, "Vitreous substitutes: challenges and directions," *International Journal of Ophthalmology*, vol. 8, no. 3, pp. 437–440, 2015.

[5] X. Lin, J. Ge, Q. Gao et al., "Evaluation of the flexibility, efficacy, and safety of a foldable capsular vitreous body in the treatment of severe retinal detachment," *Investigative Ophthalmology and Visual Science*, vol. 52, no. 1, pp. 374–381, 2011.

[6] Q. Gao, X. Chen, J. Ge et al., "Refractive shifts in four selected artificial vitreous substitutes based on Gullstrand-Emsley and Liou-Brennan schematic eyes," *Investigative Ophthalmology & Visual Science*, vol. 50, no. 7, pp. 3529–3534, 2009.

[7] J. Chen, Q. Gao, Y. Liu et al., "Clinical device-related article evaluation of morphology and functions of a foldable capsular vitreous body in the rabbit eye," *Journal of Biomedical Materials Research, Part B, Applied Biomaterials*, vol. 97B, no. 2, pp. 396–404, 2011.

[8] H. Chen, S. Feng, Y. Liu et al., "Functional evaluation of a novel vitreous substitute using polyethylene glycol sols injected into a foldable capsular vitreous body," *Journal of Biomedical Materials Research Part A*, vol. 101, no. 9, pp. 2538–2547, 2013.

[9] S. Feng, H. Chen, Y. Liu et al., "A novel vitreous substitute of using a foldable capsular vitreous body injected with polyvinylalcohol hydrogel," *Scientific Reports*, vol. 3, no. 1, 2013.

[10] Y. Yanni, T. Bei, L. Qian, and W. Wenbin, "Evaluation of the efficacy and safety of a foldable capsular vitreous body in the treatment of severe retinal detachment," *Chinese Journal of Ophthalmology*, vol. 55, no. 4, pp. 259–266, 2019.

[11] X. Zhang, X. Tian, B. Zhang, L. Guo, X. Li, and Y. Jia, "Study on the effectiveness and safety of foldable capsular vitreous body implantation," *BMC Ophthalmology*, vol. 19, no. 1, 2019.

[12] J. Jinchen, W. Xiaoxuan, X. Liuqing, H. Shaolei, and K. Huanjun, "Clinical observation and perception of foldable capsular vitreous body implantation in 73 cases," *International Eye Science*, vol. 20, no. 11, pp. 1975–1978, 2020.

[13] D. Wei, C. Fang, Z. Jun, and X. Zhenggao, "The use of silicone oil retention sutures in a traumatic aphakic eye with anitidia," *Chinical Journal Ocular Trauma and Occupational Eye Diseases*, vol. 40, no. 8, pp. 638–939, 2018.

[14] X. Lin, Z. Wang, Z. Jiang et al., "Preliminary efficacy and safety of a silicone oil-filled foldable capsular vitreous body in the treatment of severe retinal detachment," *Retina*, vol. 32, no. 4, pp. 729–741, 2012.

[15] S. Peng, K. Xiangbin, H. Yujuan, and L. Xin, "Clinical efficacy of foldable capsular vitreous body in traumatic silicon oil dependent eyes," *Practical Clinical Medicine*, vol. 20, no. 7, pp. 52–54, 2020.

[16] Y. Liu, Q. Ke, J. Chen et al., "Sustained mechanical release of dexamethasone sodium phosphate from a foldable capsular vitreous body," *Investigative Ophthalmology & Visual Science*, vol. 51, no. 3, pp. 1636–1642, 2010.

[17] Z. Jiang, T. Wang, B. Pan et al., "Evaluation of the levofloxacin release characters from a rabbit foldable capsular vitreous body," *International Journal of Nanomedicine*, vol. 7, pp. 1–10, 2011.

[18] H. Zheng, Z. Wang, P. Wang, Y. Liu, Z. Jiang, and Q. Gao, "Evaluation of 5-fluorouracil released from a foldable capsular vitreous body in vitro and in vivo," *Graefes Archive of Clinical and Experimental Ophthalmology*, vol. 250, no. 5, pp. 751–759, 2012.

Hindawi
Disease Markers
Volume 2021, Article ID 4933194, 14 pages
https://doi.org/10.1155/2021/4933194

Research Article

MiR-126-HMGB1-HIF-1 Axis Regulates Endothelial Cell Inflammation during Exposure to Hypoxia-Acidosis

Jinxue Liu,[1] Eileen Wei,[2] Jianqin Wei,[3] Wei Zhou,[4] Keith A. Webster,[5,6,7] Bin Zhang,[8] Dong Li,[9] Gaoxing Zhang,[8] Yidong Wei,[10] Yusheng Long,[11,12] Xiuyu Qi,[11,13] Qianhuan Zhang,[11] and Dingli Xu[1]

[1]*Department of Cardiology, Nanfang Hospital, Southern Medical University, Guangzhou 510515, China*
[2]*Gulliver High School, Miami, FL 33156, USA*
[3]*Department of Medicine Miller School of Medicine, University of Miami, Miami, FL 33136, USA*
[4]*Department of Ophthalmology, Jiangmen Central Hospital, Affiliated Jiangmen Hospital of Sun Yat-Sen University, Jiangmen 529030, China*
[5]*Integene International, LLC, Miami, FL 33137, USA*
[6]*Cullen Eye Institute, Department of Ophthalmology, Baylor College of Medicine, Houston, TX 77030, USA*
[7]*Everglades Biopharma, LLC, Houston, TX 77030, USA*
[8]*Department of Cardiology, Jiangmen Central Hospital, Affiliated Jiangmen Hospital of Sun Yat-Sen University, Jiangmen 529030, China*
[9]*Department of Intensive Care Unit and Clinical Experimental Center, Jiangmen Central Hospital, Affiliated Jiangmen Hospital of Sun Yat-Sen University, Jiangmen 529030, China*
[10]*Department of Surgery, Youjiang Medical University for Nationalities, Chengxiang Rd, Baise, Guangxi 533000, China*
[11]*Department of Cardiology, Guangdong Cardiovascular Institute, Guangzhou 510080, China*
[12]*Department of Cardiology, Guangdong Cardiovascular Institute and Second School of Clinical Medicine, Southern Medical University, Guangzhou 510515, China*
[13]*Department of Cardiology, Guangdong Cardiovascular Institute and Shantou University Medical College, Shantou 515041, China*

Correspondence should be addressed to Qianhuan Zhang; zhangqianhuan9@gmail.com and Dingli Xu; dinglixu@smu.edu.cn

Received 2 October 2021; Accepted 20 November 2021; Published 21 December 2021

Academic Editor: Ting Su

Crosstalk between molecular regulators miR-126, hypoxia-inducible factor 1-alpha (HIF-1-α), and high-mobility group box-1 (HMGB1) contributes to the regulation of inflammation and angiogenesis in multiple physiological and pathophysiological settings. Here, we present evidence of an overriding role for miR-126 in the regulation of HMGB1 and its downstream proinflammatory effectors in endothelial cells subjected to hypoxia with concurrent acidosis (H/A). *Methods*. Primary mouse endothelial cells (PMEC) were exposed to hypoxia or H/A to simulate short or chronic low-flow ischemia, respectively. RT-qPCR quantified mRNA transcripts, and proteins were measured by western blot. ROS were quantified by fluorogenic ELISA and luciferase reporter assays employed to confirm an active miR-126 target in the HMGB1 3′UTR. *Results*. Enhanced expression of miR-126 in PMECs cultured under neutral hypoxia was suppressed under H/A, whereas the HMGB1 expression increased sequentially under both conditions. Enhanced expression of HMGB1 and downstream inflammation markers was blocked by the premiR-126 overexpression and optimized by antagomiR. Compared with neutral hypoxia, H/A suppressed the HIF-1α expression independently of miR-126. The results show that HMGB1 and downstream effectors are optimally induced by H/A relative to neutral hypoxia via crosstalk between hypoxia signaling, miR-126, and HIF-1α, whereas B-cell lymphoma 2(Bcl2), a HIF-1α, and miR-126 regulated gene expressed optimally under neutral hypoxia. *Conclusion*. Inflammatory responses of ECs to H/A are dynamically regulated by the combined actions of hypoxia, miR-126, and HIF-1α on the master regulator HMGB1. The findings may be relevant to vascular diseases including atherosclerotic occlusion and interiors of plaque where coexisting hypoxia and acidosis promote inflammation as a defining etiology.

1. Introduction

As integral vasoregulators, endothelial cells (ECs) serve as multifunctional biosensors that coordinate vascular responses to environmental stress of which hypoxia, oxidative stress, acidosis, and inflammation are especially prominent in myocardial disease and cancer [1–5]. By regulating EC survival, senescence, growth, invasion, glucose metabolism, and multiple molecular signaling pathways, hypoxia and HIF factor signaling are central to vascular EC responses to conditions of ischemia and downstream consequences of endothelial dysfunction, remodeling, and vascular disease [6–10]. Acidosis, an obligatory component of chronic ischemia caused by vessel occlusion, and present inside atherosclerotic plaque [11], is primarily driven by increased glycolysis and buildup of extracellular waste metabolites. Acidosis when combined with hypoxia additionally regulates and/or accentuates multiple aspects of the responses of ECs to ischemia, including survival, inflammation, and vessel tone and integrity via stress kinase signaling, calcium, and NO pathways [12–15]. Multiple microRNAs are known to modulate endothelial inflammatory responses [16] and established roles for miR-126 in regulating vascular integrity, angiogenesis, atherogenesis, and vessel functions that have been described [17–21].

Although miR-126 has been widely studied in the context of cellular hypoxia [22–27], its role in ECs subjected to chronic ischemic and/or acidotic conditions is relatively unexplored. HIF-1α has been shown to induce the miR-126 expression in a number of cell types including cultured human umbilical vein endothelial cells, and other studies have described positive feedback loop regulation between HIF-1α and miR-126 [26, 28, 29]. Consequently, HIF-1/miR-126 signaling is implicated in vasculogenesis and vascular disease, including proliferation, differentiation, migration, atherogenesis, senescence, and programmed cell death of vascular cells [30]. Inflammation is a fundamental cellular component of innate and adaptive immunity that, when deregulated is implicated in multiple cardiovascular pathologies, notably those that involve atherosclerosis, diabetes, obesity, hypertension, and responses to ischemia-reperfusion and myocardial infarction [31–33]. Acidosis occurs most frequently in association with sustained ischemia, inflammation, and metabolic disease where under the most severe conditions of ischemia, affected tissue pH can fall below 6.5 [12] and significantly impact basic physiological processes including immune responses, cell viability, angiogenesis, and localized inflammation [34–37].

The high-mobility group box 1 protein (HMGB1) is a secreted cytokine immunomodulator with central roles in autoimmune, infectious, and inflammatory pathologies especially related to cancer and cardiovascular disease. HMGB1 has been linked with angiogenesis, endothelial dysfunction, inflammation, and atherosclerosis through its regulation of toll-like receptor 4 and inflammatory cytokine secretions [38–43]. HMGB1 is expressed in myocardial cells where it selectively binds chromatin and activates innate immune and inflammatory-related genes [44]. Recently, microRNAs including miR-126 have been shown to confer important regulation of HMGB1 [45–50]. Here, we identify a pH component in the regulation of HMGB1 with contextual targeting by miR-126 that constitutes a critical component of signal transmission in the EC response to conditions of chronic simulated ischemia and associated inflammation.

2. Materials and Methods

2.1. Reagents. Primary mouse aortic endothelial cells (PMEC) were from Cell Biologics. Antibodies were obtained from the following vendors: p-Akt, Akt, Bcl2, TNF-α, and NAPDH oxidase, from Cell Signaling Technology, and HMGB1 and NADPH from Abcam; human premicroRNA expression constructs, Lenti-PremiR-126 and Anti-miR-126 from System Bioscience LLC; OxiSelect ROS assay kit from Cell Biolabs; Lipofectamine 2000 reagent from Thermo Fisher Scientific; and Luc-Pair miR luciferase assay kit from GeneCopoeia.

2.2. Endothelial Cell Culture and Treatment. PMECs, plated at 1×10^6 cells per ml, were cultured in Dulbecco's Modified Eagle's Medium (DMEM) with 10% fetal bovine serum in a humidified atmosphere with 5% CO_2 at 37°C. Our conditions for exposure to hypoxia (0.5% O_2/5% CO_2) are described in detail elsewhere [51–53]. Media was titrated with lactic acid to achieve a starting pH of 7.4 ± 0.05 for hypoxia alone and 6.7 ± 0.05 for hypoxia-acidosis (H/A), a moderately acidic pH for ischemic tissues within the range that can be caused by severely occluded myocardial tissue or within a tumor environment in vivo [54, 55]. Our H/A conditions are designed to mimic chronic low-flow ischemia caused by such severe occlusion as well as ECs within an atherosclerotic lesion where oxygen and ionic exchanges between vessels and the blood are restricted. Media for the H/A condition was replaced daily, and cultures were exposed to hypoxia for 24 h and H/A for 72 h to more closely mimic chronic ischemia. Previous studies by others and ourselves have documented that most cells including primary ECs respond rapidly to hypoxia with activation of HIF-1α within 8-12 h of exposure and minimal additional change of HIF-1 responses between 24 and 72 h [56–62]. Under these conditions, we found that media pH under either condition did not change significantly over 24 h. Extended times are also appropriate to mimic metabolic adaptations to simulated ischemia because of the vastly larger extracellular space of cultured ECs versus vascular ECs in vivo. In some incubations, cells were subjected to lentivirus infection using Lipofectamine 2000 before exposure to conditions.

2.3. Western Blot. Our procedures for western blots are described in detail elsewhere [51, 52]. Briefly, 30 μg of total protein per lane in loading buffer was separated by 12% SDS-PAGE gel and proteins transferred onto membranes. After blocking, primary antibodies (1 : 500 dilution) were incubated overnight at 4°C, followed by room temperature exposure to secondary antibodies (1 : 4000 dilution). Reactive bands were revealed by chemiluminescence.

2.4. RNA Analysis. For RNA quantification, total RNA was isolated from cells using TRIzol Reagent and subjected to real-time PCR using TaqMan probes (Applied Biosystems) as described previously [63]. All values are expressed relative to a mean expression value for the 22,000+ transcripts on each microarray.

2.5. Measurement of ROS. ROS were measured using an Oxi-Select ROS assay kit, exactly as described by the manufacturer and as previously reported [64].

2.6. Luciferase Reporter Assay. Luciferase assays were performed on cell extracts as previously described [65] using a Luc-Pair miR luciferase assay kit (GeneCoepia). Relative luciferase activities are expressed as luminescence units normalized to Renilla luciferase activity. Luminescence was quantitated using a multimode microplate reader (BMG Labtech).

2.7. Quantitative RT-PCR. The MiR-126 expression was quantified using a quantitative real-time reverse transcription-PCR assay from Ambion described previously [66]. Briefly, PCR reactions were carried out in triplicate in a 25 μl volume using SYBR Green Assay Master Mix (Applied Biosystems) for 3 min at 95°C, followed by 40 cycles of 95°C for 15 s, 60°C for 30 s, and 72°C for 45 s in a Bio-Rad I Cycler (Bio-Rad Laboratories). Micro-RNA primers were used as follows: miR-126 forward, 5′-TATAAGATCTGAGGATAGGT GGGTTCCCGAGAACT-3′, reverse, 5′-ATATGAATTCTC TCAGGGCTATGCCGCCTAAGTAC-3′; HMGB1 forward, 5′-TATGGCAAAAGCGGACAAGG-3′, reverse, 5′-CTTCG CAACATCACCAATGGA-3′; GAPDH forward, 5′-ACA ACTTTGGTATCGTGGAAGG-3′, reverse, 5′-GCCATCAC GCCACAGTTTC-3′; U6 forward 5′-CTCGCTTCGGCAG-CACA-3′, reverse 5′-AACGCTTCACGAATTTGCGT-3′. The relative gene expression was quantified using the $2^{-\Delta\Delta Cq}$ method [67]. Three independent experiments were routinely performed for each assay.

2.8. Statistics. All data are expressed as mean ± S.E.M. Statistical comparisons were performed using Graphpad Prism software (GraphPad Software Inc.), and Student's *t*-test was used to compare differences.

3. Results

Suppression of hypoxia-induced miR-126 and HMGB1 by acidosis of PMECs: cultured PMECs were subjected to 24 h of hypoxia alone or 72 h hypoxia with concurrent acidosis and isolated RNAs and proteins quantified for expression of mir-126, HMGB1, and HIF-1α. As shown in Figure 1, hypoxia alone conferred increased expression of miR-126 and HMGB1-specific RNAs, respectively, by 12 ± 2 – fold and 2.1 ± 0.1 – fold (both $p < 0.01$ relative to aerobic controls) and proteins HMGB1 and HIF-1α, respectively, by 1.85 ± 0.1 – fold and 3.6 ± 0.2 – fold (both $p < 0.01$ relative to aerobic controls). When acidosis was present for 72 h with concurrent hypoxia, mir-126 levels were 4.1 ± 0.05 – fold relative to aerobic cells, a decline of 3-fold relative to hypoxia alone, whereas HMGB1 mRNA levels were further increased over pH neutral hypoxia to 3.2 ± 0.15 of aerobic cell, an increase of 50% over neutral hypoxia. At the protein level, HMGB1 protein increased in parallel with the mRNA also to 3.2 ± 0.1 – fold relative to aerobic cells, whereas HIF-1 protein under H/A was 1.8 ± 0.1 – fold of aerobic cells, a 50% decline relative to neutral hypoxia. As discussed in Methods, previous work by others and ourselves has shown that HIF-1α accumulates rapidly when primary ECs are exposed to hypoxia, maximally within 4-8 h with no significant change between 24 and 72 h in most cases [56, 57, 61]. The results indicate positive regulation of all 3 RNA/gene targets by hypoxia and quenching of miR-126 and HIF-1α by concurrent acidosis, but enhanced expression of HMGB1 by H/A.

3.1. Inflammatory Indicators, Increased under Hypoxia, Are Enhanced by HA. HMGB1 is a secreted immune-inflammatory protein expressed in many cell types, that acts as a damage-associated molecular pattern (DAMP) factor [68] and can induce signaling pathways by binding to immune modulators such as advanced glycation end products (RAGE) and toll-like receptors (TLRs) [69, 70], thereby stimulating inflammatory cascade. To investigate functional consequences of HMGB1 induction by hypoxia in the presence and absence of acidosis, we assayed putative downstream inflammatory effectors of HMGB1 including ROS, NADPH, and TNF-α, as well as survival signaling pathway intermediates p-Akt and Bcl-2. As shown in Figure 2, ROS production, TNF-α, and NAPDH expression were significantly increased by both hypoxia alone and hypoxia-acidosis ($p < 0.01$), in a manner that paralleled closely the expression patters of HMGB1. P-Akt, a marker of survival kinases, was also significantly induced by both experimental manipulations while prosurvival, antiapoptosis marker Bcl2 was increased by both hypoxia and hypoxia-acidosis but more markedly by the former (all $p < 0.01$). The results are consistent with positive and regulation of HMGB1 and its downstream inflammatory effectors by hypoxia that is incrementally enhanced by concurrent acidosis.

3.2. Contextual Regulation of the HMGB1 Expression by miR-126 Modulators. It was reported that the HMGB1 gene contains a 3′UTR target for miR-126 and that elevated miR-126 downregulated HMGB1 and suppressed inflammatory responses of ECs during exposure to hyperglycemia [50]. Because the actions of miR-126 are context-dependent and can mediate positive or negative actions on gene expression depending on the prevailing environments [21], we asked whether miR-126 contributes to the incremental regulation of HMGB1 gene expression by hypoxia-acidosis. To do this, PMECs were transfected with optimal doses of miR-126 pre-miR or antagomir RNAs and the expression of HMGB1 and HIF-1α measured after exposure to H/A for 72 h as described in Methods. As shown in Figure 3, ECs pretransfected with the miR-126 mimic displayed robust expression of miR-126 relative to controls, whereas the expression in antagomir-transfected cells was reduced by about 50% of control nontransfected cells (Figure 3(a)). Despite the high

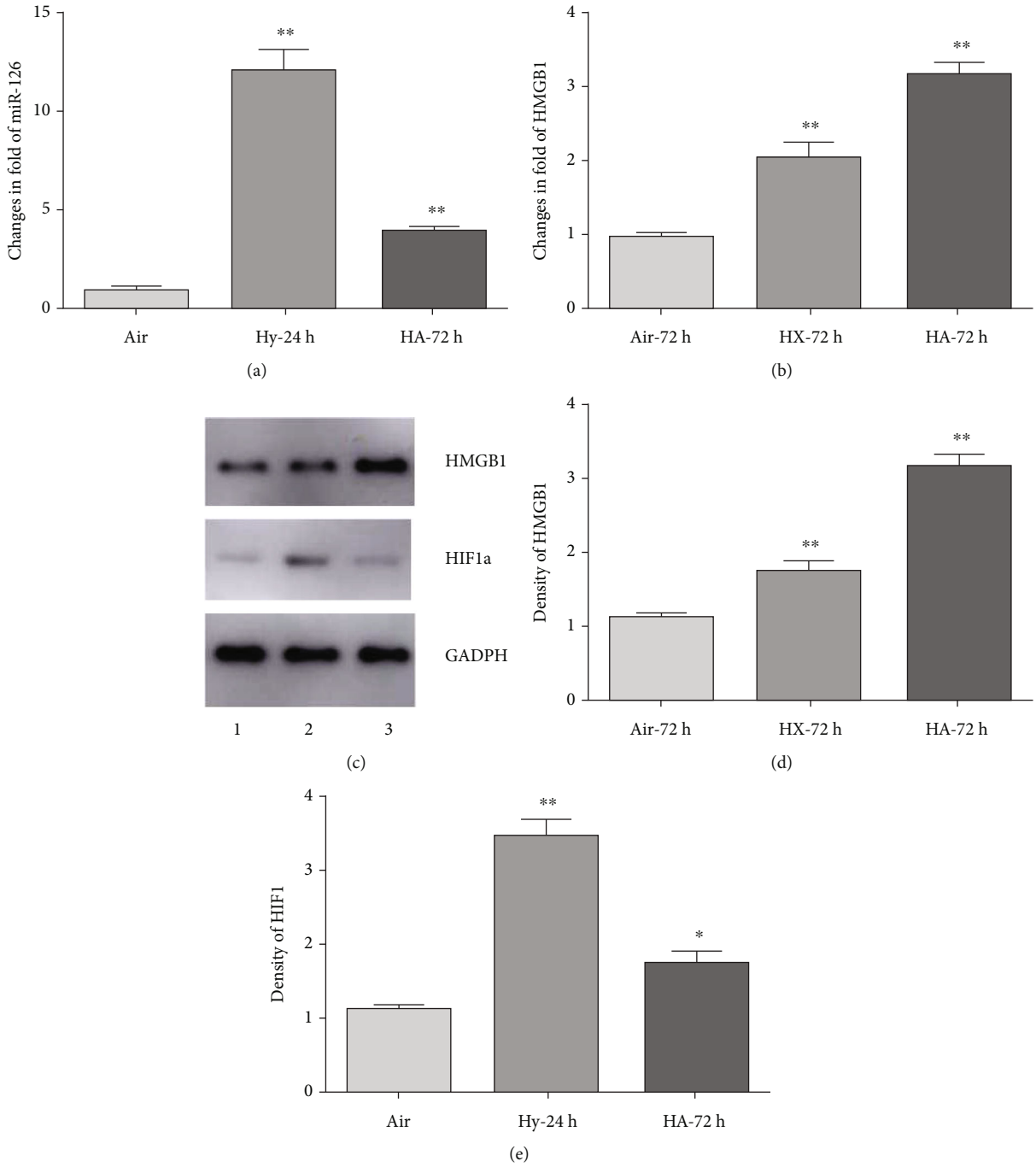

Figure 1: Quantification of responses of miR-126, HMGB1, and HIF-1α to hypoxia and H/A in PMECs. MiR-126 and HMGB1 RNAs were measured by RT-PCR (a, b) and Western blot (c)–(e). Results are expressed as mean ± SEM. $^{**}p < 0.01$, $^{*}p < 0.05$. Hy-24 h and HA-72 h: PMECs were exposed to hypoxia for 24 hours or H/A for 72 hours. Results are expressed as mean ± SEM. $^{**}p < 0.01$; $^{*}p < 0.05$; $n = 4$.

expression of apparent miR-126 conferred by overexpression of the mimic, levels of HMGB1 mRNA remained unchanged relative to nontransfected control cells; perhaps, an indication that elevated basal miR-126 under hypoxia-acidosis alone is sufficient to convey significant degradation of HMGB1 mRNA. Conversely, the overexpression of the antagomir conferred almost 6-fold increased expression of HMGB1 mRNA; again, consistent with the possibility that endogenous miR-126 actively promotes degradation of HMGB1 mRNA expression under hypoxia-acidosis. Protein expression analyses supported such an interpretation that miR-126 regulates the HMGB1 gene expression during exposure to hypoxia-acidosis by promoting mRNA degradation and suppressing translation. As shown in Figures 3(c) and 3(d), the overexpression of the miR-126 mimic significantly blocked HMGB1 protein expression ($p < 0.01$), whereas the antagomir overexpression conferred >10-fold increased protein expression relative to control conditions.

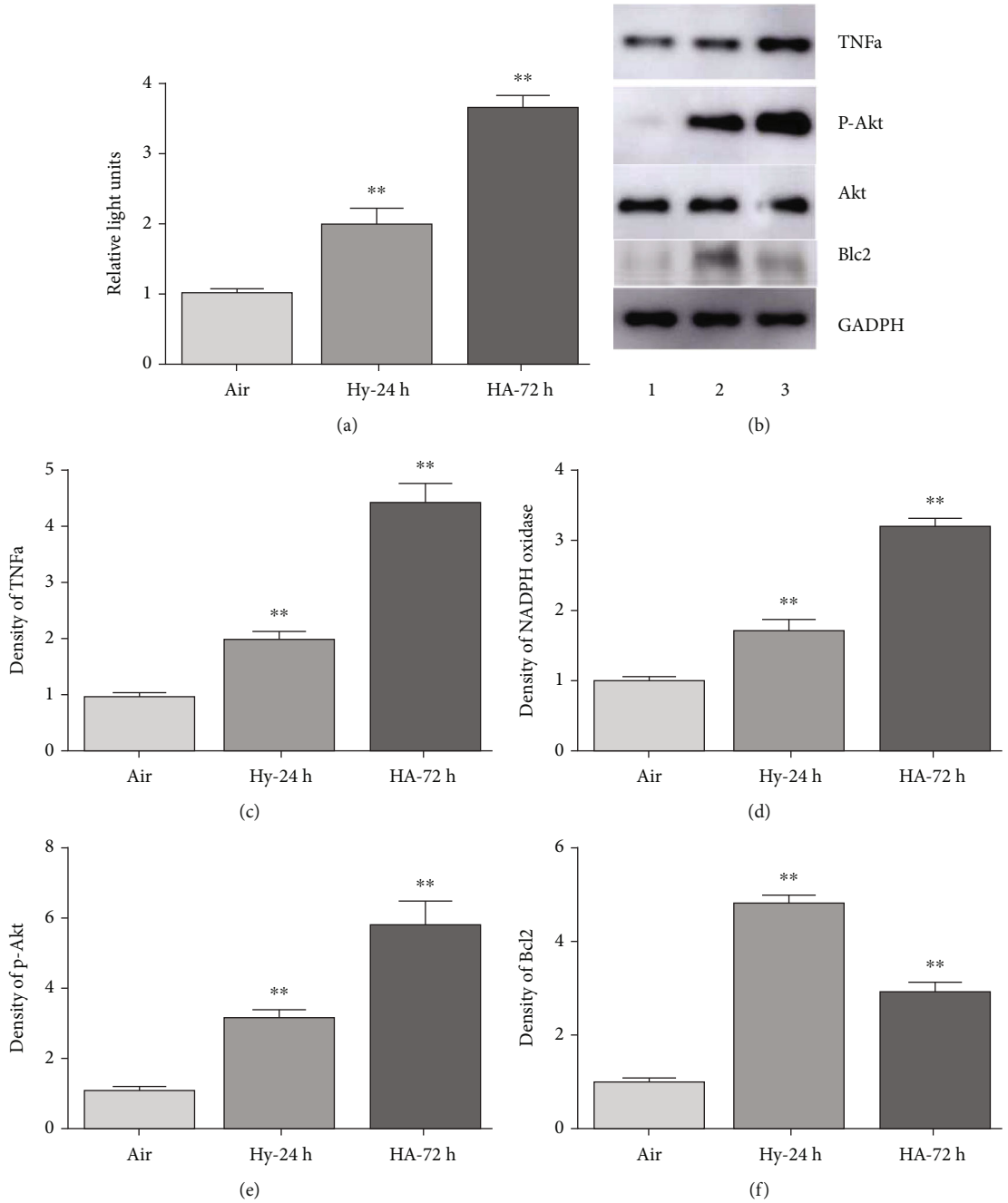

Figure 2: Responses of markers of inflammation, Akt, and Bcl2 during exposure of PMECs to 24 h hypoxia (Hy) and 72 h H/A. ECs were infected with premiR-126 or antagomiR-126 and cultured under the specified conditions. (a) ROS were quantified using an OxiSelect ROS assay kit. (b)–(f) Western blots quantified TNFα, p-Akt, and Bcl2. Results are expressed as mean ± SEM. $^{**}p < 0.01$; $^{*}p < 0.05$; $n = 4$.

As a control, and to ensure that the results are not influenced by an indirect interference of miR-126 on HIF-1α, we demonstrate in Figure 3(e) that HIF-1α protein levels, increased under hypoxia-acidosis, were not affected by miR-126 mimic or antagomir overexpression in these ECs. The results demonstrate that decreasing miR-126 levels by transfection of an antagomiR prior to exposure to hypoxia-acidosis conferred markedly increased expression of HMGB1 mRNA and protein consistent with a classical miR-mediated targeting of the HMGB1 gene to induce mRNA degradation and translational repression [71]. This interpretation is also supported by the effects of the overexpression of the miR-126 mimic, although relatively minor compared with the antagomir. Both effects suggest significant regulation of the HMGB1 gene expression by endogenous miR-126 under hypoxia-acidosis.

3.3. Confirmation of a Hypoxia-Acidosis Regulable miR-126 Target Site on the HMGB1 Gene 3′UTR. To confirm that miR-126 can directly regulate the HMGB1 gene expression, we synthesized oligonucleotides containing putative wild type and mutant HMGB1-miR-126 binding sites and

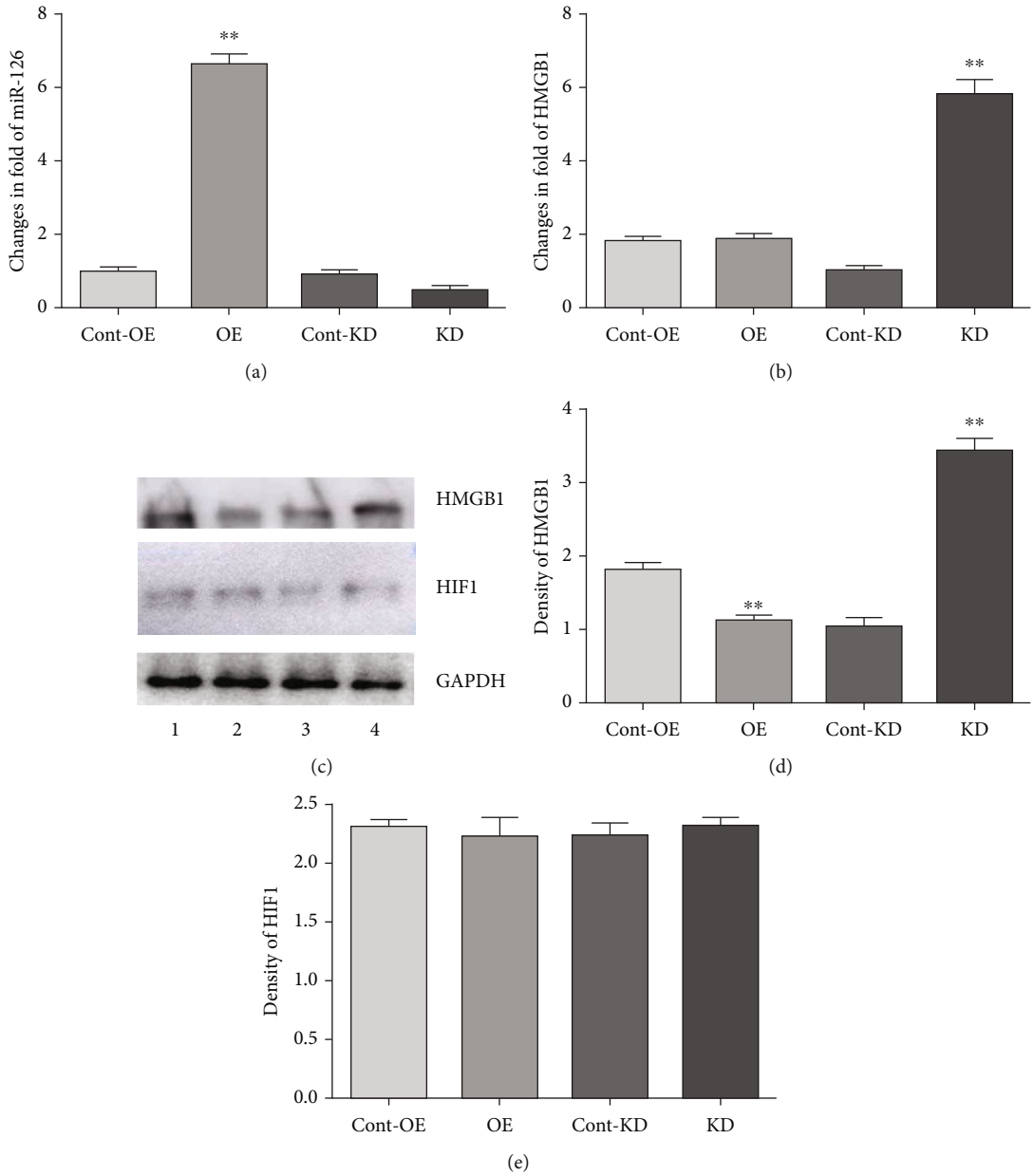

Figure 3: PremiR and antagomir regulation of miR-126 expression and downstream responses of HMGB1 and HIF-1α in PMECs during H/A culture. PMECs were infected with premiR-126 (OE) or anti-miR-126 (KD) and cultured under H/A. (a, b) miR-126 and HMGB1 RNAs were measured by RT-PCR. (c)–(e) western blots quantified and HIF-1α. Results are expressed as mean ± SEM. $^{**}p < 0.01$. Cont-OE and Cont-KD refer to control (empty) vectors for the respective experimental premiR and antagomir overexpression groups. Results are expressed as mean ± SEM. $^{**}p < 0.01$; $^{*}p < 0.01$; $n = 4$.

inserted them upstream of the Luciferase reporter gene as described in Methods (Figure 4(a)). Plasmids were transfected into PMECs with nontransfected cells as controls and subjected to conditions of hypoxia-acidosis (Figures 4(b) and 4(c)). We first confirmed that the overexpression of the premiR-126 conferred decreased expression of HMGB1, whereas knockdown by the antagomir conferred increased expression, as expected from results shown in Figures 1 and 3 (data not shown). Luciferase reporter gene assays revealed that luciferase activity was significantly decreased or enhanced, respectively, by premiR-126 or antagomiR-126, when compared with controls ($p < 0.01$). Importantly, the expression of an HMGB1 reporter plasmid that contained a mutated 3′UTR reporter gene was unaffected by either premiR-126 or antagomir ($p > 0.5$) (Figures 5(b) and 5(c)). These results confirm that miR-126 targets the HMGB1 gene expression through a 3′ UAAUAAUU target site and its regulation by H/A.

3.4. Predominant Role for miR-126 in the Regulation of Inflammation Markers by Hypoxia and H/A. To investigate possible individual roles of hypoxia, acidosis, HIF-1a, and

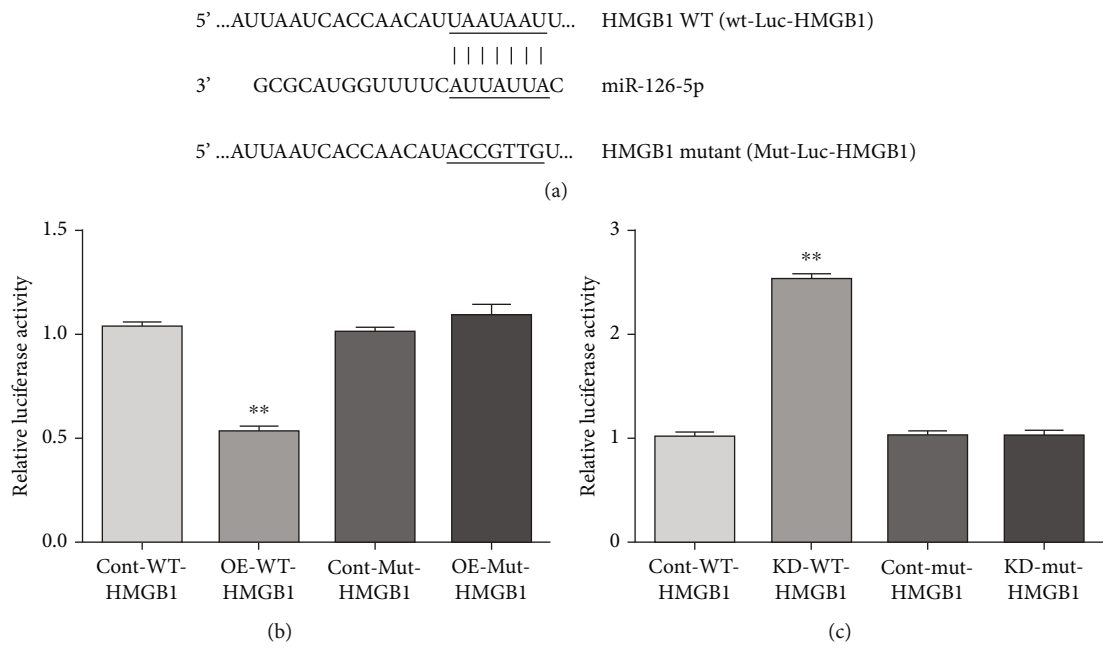

Figure 4: Context-dependent targeting of HMGB1 by miR-126. MirR-126 seed sequence and complementary binding site in the HMGB1 3′ UTR are highlighted (a). PMECs were untreated or transfected with premiR-126 or antagomiR-126. Luciferase activities were quantified after subjection of cultures to H/A. Results are expressed as mean ± SEM. $^{**}p < 0.01$; $n = 4$. Cont-WT-HMGB1: control (empty) vector for WT- HMGB1; OE-WT-HMGB1: overexpression of premiR-126 for WT HMGB1; Cont-Mut-HMGB1: control (empty) vector for mutant HMGB1; OE-Mut-HMGB1: overexpression of premiR-126 for mutant HMGB1; KD-WT-HMGB1: antagomiR-126 for WT-HMGB1; KD-Mut-HMGB1: antagomiR-126 for mutant HMGB1.

the apparent overriding actions of miR-126 in regulating the HMGB1-responsive inflammatroy cascade, MPECs were pretransfected with miR-126 premiR or antagomiR, subjected to conditions of hypoxia alone or H/A and expression of inflammatory and cell survival markers measured and compared with aerobic controls as described in Methods and Figure 3. Relative intracellular levels of miR-126 after transfection of antagomiR or antagomiR and subjection to conditions are shown in Figure 5(a). Compared with antagomiR-overexpressing control aerobic incubations, exposure of transfected cells to hypoxia conferred increased miR-126 of 5.3 ± 0.3 – fold, that decreased to 3.4 ± 0.02 – fold under H/A. In antagomiR-transfected cells, miR-126 levels under hypoxic incubations were increased by 2.5 ± 0.2 – fold over aerobic controls and by 1.6 ± 0.1 – fold under H/A. The expression of inflammation markers, ROS, NADPH oxidase, TNFα, and survival kinase p-Akt displayed trends that are consistent with the results of Figure 3 and supports a major role for miR-126 in suppression of the EC inflammatory response via HMGB1 under conditions of hypoxia and especially H/A. The expressed levels of all proteins from cells incubated under hypoxia alone or H/A were the lowest when miR-126 was induced (Figures 5(b) and 5(d)–5(f), OE columns 2-3), and, conversely, the highest when miR-126 was reduced (Figures 5(b) and 5(d)–5(f), KD columns 5-6) consistent with an overriding role for miR-126 in the regulation and suppression by acidosis as a major component of inflammatory pathway regulation during H/A. Levels of the antiapoptosis survival protein Bcl2, induced under hypoxia, were further induced by H/A in the presence of miR-129 KD and low miR-129, consistent with the suppressive role for the miR-126 in Bcl2 gene expression [72, 73]. In agreement with the results shown in Figures 1 and 3, HIF-1α induction by hypoxia was reduced under the H/A condition and unaffected by OE or KD of miR-126 premiR (OE) or antagomiR (KD).

4. Discussion

We provide novel evidence for a dominant role of the miR-126 suppression by acidosis in the regulation of the HMGB1 gene expression and its downstream inflammation mediators in endothelial cells subjected to simulated chronic ischemia. The regulation is transmitted via a contextually responsive miR-126 target in the HMGB1 3′UTR. We also describe enhanced activation of the prosurvival, antiapoptosis protein Bcl2 by H/A via a slightly divergent signaling pathway that involves a quantitative antagonism between miR-126 and HIF-1α, whereas previous reports have documented negative regulation of both HMGB1 and Bcl2 by miR-126, and the present study is the first to describe acidosis as a driving force behind such regulation in the context of ischemia. Our findings that miR-126 levels increased 12-fold under pH-neutral hypoxia in parallel with a 3.5-fold increase of HIF-1α (Figures 1(a) and 1(e)) are consistent with previous reports that miR-126 is positively regulated by HIF-1α [26, 28, 29]. Previous work has also shown that HIF-1α can regulate micro-RNAs directly by binding to HRE-motifs in the 5′ upstream sequences of host genes [74], or

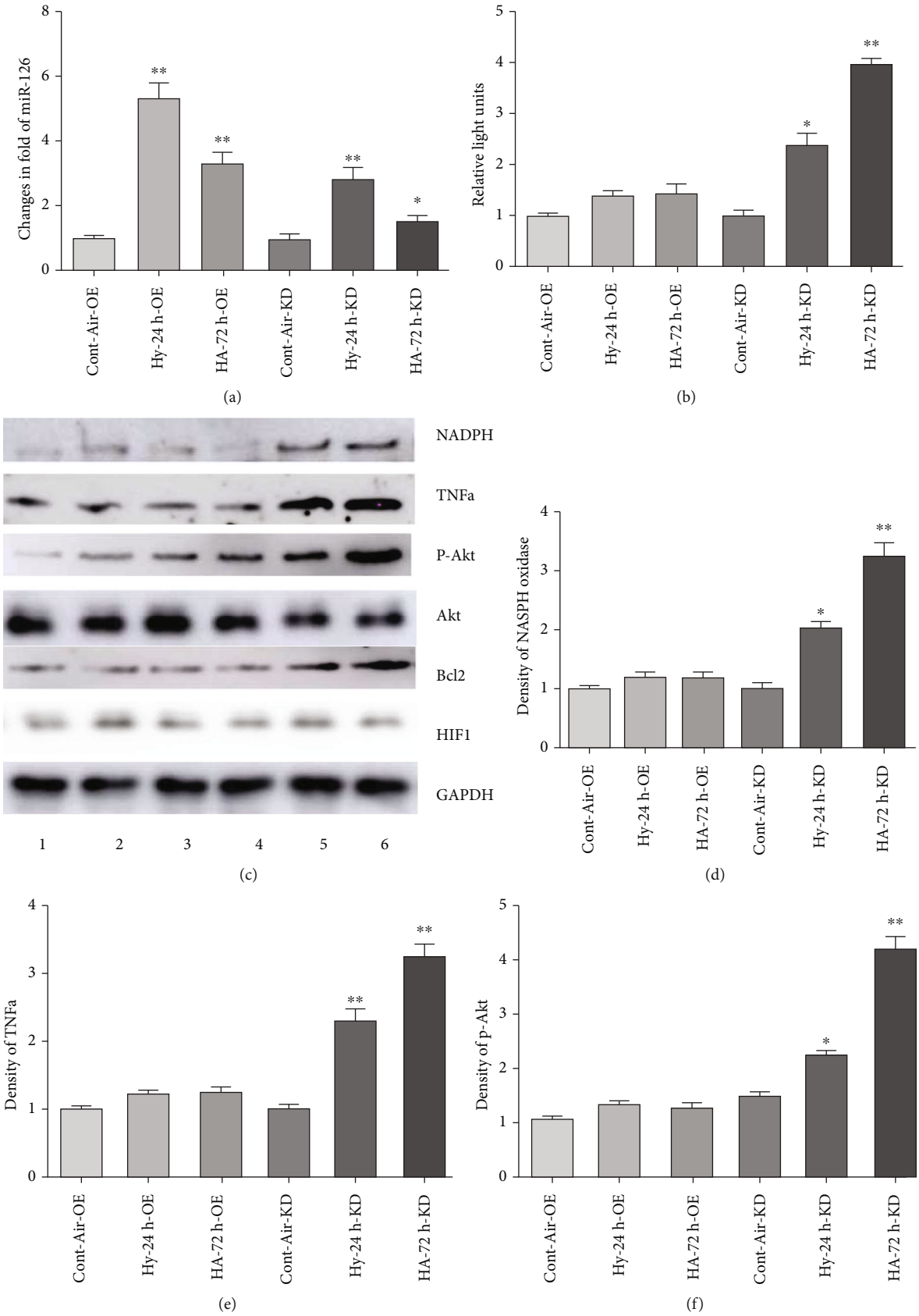

Figure 5: Continued.

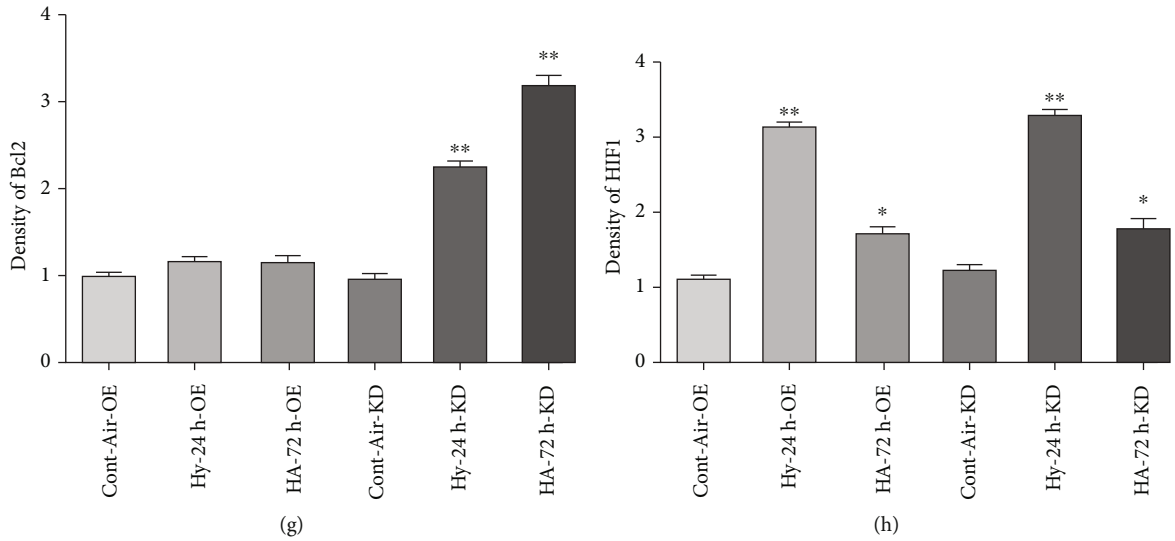

Figure 5: Attenuation of inflammatory markers in PMECs by miR-126 during H/A. ECs were infected with premiR-126 or antagomiR-126 and cultured under H/A. miR-126 RNA was measured using RT-PCR (a) ROS were measured using an OxiSelect ROS assay kit (b) Western blot analyses were performed to quantify TNFα, Akt, and Bcl2. (c)–(h) Results are expressed as mean ± SEM. $^{**}p < 0.01$, $^{*}p < 0.01$. Cont-Air-OE, Hy-24 h-OE, and HA-72 h-OE: ECs were transfected with empty vector or premiR-126 and treated aerobically. Hypoxia 24 h or H/A 72 h. Cont-Air-KD, Hy-24 h-KD, and HA-72 h-KD: ECs were transfected with control vector or antagomiR-126 and treated aerobically. Hypoxia 24 h and H/A 72 h.

indirectly by regulating the activities of associated signal intermediates, for example, c-Myc [75]. We found that the incremental increase of miR-126 supported by neutral hypoxia was reduced >70% under H/A, coincident with a similar >70% loss of the HIF1-α expression (Figures 1(a) and 1(e)), in parallel with a significant 50% augmentation of the HMGB1 expression under H/A relative to neutral hypoxia ($p < 0.01$). The results support an indirect role for HIF-1α in the regulation of HMBG1 via downregulation of miR-126. In contrast, the Bcl2 expression, optimally activated by neutral hypoxia, was reduced under H/A (Figures 1(a) and 2(f)), most likely due to the opposing effects of coincident downregulated HIF-1α and suppressed miR-126 under H/A (see illustration, Figure 6).

Results of premiR/antagomiR transfections confirmed the potent regulation of the HMGB1 gene expression by miR-126 during exposure to H/A (Figure 3). The HMBG1 expression was low in cells transfected with premiRs and maximally induced by antagomir (Figure 3(e) columns 2 and 4), whereas HIF-1α was unresponsive to premiR/anti-miR-modulated expression of miR-126 (Figure 3(e)). Cotransfection of PMECs with miR-126 premiR, antagomiR, and expression vectors directing expression of Luciferase by 5′ wild type or mutated miR-126 target sites confirmed an miR-126 target sequence in the HMGB1 3′ UTR, as previously reported [50] and its responsiveness to H/A. Luciferase activity was differentially regulated by a factor > 5 – fold by WT premiR over antagomiR in transfected cells exposed to H/A ($p < 0.01$), and the regulation was eliminated by mutation of the site (Figure 4(b)). These results confirm the presence of a pH-regulable miR-126 target on the HMGB1 3′UTR.

The expression levels of HMGB1-regulated inflammation markers in transfected cells subjected to conditions of hypoxia and H/A followed patterns that are consistent with positive and negative regulation by hypoxia and miR-126, respectively (Figures 4(b)–4(e)). The HMGB1 gene is positively regulated by hypoxia through PI3K and YAP/Hippo pathways, that are independent of HIF-1α, and HMGB1 positively regulates the expression of HIF-1α [76–81]. Consistent with this, the inflammatory marker expression was only partially eliminated by miR-126 premiR transfection (OE) of cells under neutral hypoxia, compared with aerobic cells (Figures 4(b)–4(e), columns 1, 2, and 4), and the highest levels of inflammatory marker expression were seen in antagomiR expressing cells under H/A, a condition that drives maximal suppression of miR-126, sustained hypoxia, and reduced HIF-1α. It is noteworthy that Bcl2 expression, dually regulated in an antagonistic manner by HIF-1α and miR-126, was increased under H/A compared with neutral hypoxia only in antagomir-transfected cells (compare Figures 2(f) and 4(g)), despite lower HIF-1α (Figure 4(h)), suggesting an overriding role for miR-126 vs. HIF-1α in Bcl2 regulation under these conditions of simulated ischemia.

Taken together, the results support the scheme depicted in Figure 6. Neutral hypoxia increases miR-126 by HIF-1α dependent and independent pathways, and this induction is largely reversed by H/A. HMGB1, its downstream inflammatory markers and Akt, induced by neutral hypoxia, is super induced by HA due to H/A suppression of inhibitory miR-126 and sustained regulation by hypoxia via YAP/Hippo signaling. Repression of HIF-1α activity by H/A may be partially alleviated in this condition via positive feedback regulation by HMGB1, as well as positive regulation by miR-126 under some circumstances. Survival, antiapoptosis factor Bcl2 is directly regulated by HIF-1α and negatively regulated by miR-126; therefore, the relative levels of these

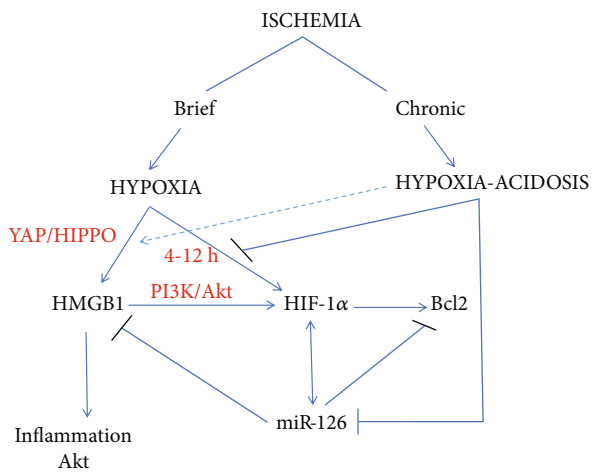

Figure 6: Schematic of crosstalk regulation of HMGB1, Akt, and Bcl2 expression and downstream inflammation mediators during exposure of PMECs to simulated ischemia. Acidosis is usually associated with severe, sustained ischemia when metabolic waste products including lactic acid accumulate within ischemic tissues. Hypoxia with or without acidosis rapidly activates HIF pathways, and miR-126 is induced in parallel with accumulated nuclear HIF-1α that increases the HMGB1 expression independently of HIF via YAP/HIPPO signaling, an effect that is retained under H/A (dashed line). By activating the PI3K/Akt pathway, HMGB1 also indirectly increases the HIF-1α expression in a hypoxia-HMGB1-HIF amplifying loop. HIF-1α directly and positively upregulates Bcl2, an effect that is countered via negative regulation by miR-126. During H/A, HIF-1a and miR-126 both decrease at least in part because acidosis blocks HIF-1α, the principal pathway for hypoxia-mediated transcriptional induction of miR-126. Reduced miR-126 during H/A relieves negative regulation on HMGB1 while the positive regulation by hypoxia is retained resulting in optimal activation of HMGB1 and its downstream inflammatory intermediates by H/A. In contrast because Bcl2 is positively regulated by HIF-1α and negatively regulated by miR-126, the optimal expression occurs under neutral hypoxia when HIF-1α is most active and predominates over miR-126.

regulators determine the Bcl2 expression. Consequently, neutral hypoxia conferred higher expression of Bcl2 than H/A, but H/A in the presence of miR-126 antagomiR conferred the greatest level of the Bcl2 expression.

The studies are relevant to inflammation involving the endothelium, especially during cardiovascular disease and rapidly growing tumors wherein microenvironments of hypoxia and acidosis are common [12–16, 82]. Previous work has also shown that proinflammatory factors are increased by an acidotic extracellular environment with or without hypoxia [83, 84]. Development of inflammation during sever chronic ischemia in both conditions is exacerbated by acidic pH as well as by the underlying hypoxia. Such changes interfere with a wide range of immunological functions conferring increased levels of inflammatory cytokines, interleukin IL-1β, IL-6, IL-8, IL-10, TNF-α, NADPH oxidase, and ROS [12, 82, 85].

In addition to targeting HMGB1, a key driver of inflammatory and immune responses in numerous disease settings [86–89], miR-126 can target multiple other disease-associated genes of relevance to this study, including angiogenesis-related vascular endothelial growth factor A, sprouty-related protein-1, phosphoinositidol-3 kinase regulatory subunit-2 1, and the adapter molecule crk [90–92]. Our discovery that acidosis exerts marked control over HMBG1 and Bcl2 expression as well as downstream inflammation responders and Akt, via miR-126 and HIF-1α (summarized in Figure 6), in the context of chronic ischemia is novel and represents important additions to our understanding of vascular inflammation and cell survival during ischemic disease, including atherosclerosis and vasculatures of solid tumors, wherein hypoxia and acidosis are integral disease components.

4.1. Study Limitations. Our results support an overriding role for miR-126 in optimally inducing expression of the HMGB1 gene and its downstream mediators of inflammation and oxidative stress during exposure to conditions of chronic simulated ischemia in cultured endothelial cells. The proposed mechanism involves acidosis-mediated suppression of HIF-1α activity and consequential blocking of hypoxia-induced transcription of the miR-126 host genes, thereby blocking HMGB1 suppression by mir-126. We acknowledge that the relation of HIF-1α with miR-126 is correlative, and we do not yet have a mechanism; however, the results are consistent with other reports that have described HIF-1α regulation of miR-126 in endothelial cells [26, 28, 29]. Also, we do not know the mechanism of acidosis regulation of HIF-1α; indeed, early literature has documented positive regulation of the HIF pathway by driving nuclear sequestration of the VLH factor [93]. Our unique conditions of chronic H/A may account for the differences. Finally, our use of a prolonged 72 h exposure time for H/A to more closely simulate chronic ischemia with acidosis introduces another variable. We contend that the comparison with 24 h neutral hypoxia is valid at least in part because previous reports by others and ourselves have shown that the HIF pathway of cultured endothelial cells responds rapidly to hypoxia, usually within 4-8 h, and is sustained without significant change during exposure times of 24 h through 72 h, and provided nutrients are replenished and media pH controlled, as is the case in our incubations [10, 56, 61, 62]. Except miRNA, other types of noncoding RNA may be associated with endothelial cell inflammation during exposure to H/A, including Piwi RNA [94] and circular RNA [95]. Further discussion is needed in future studies.

Data Availability

The datasets generated during and/or analyzed during the current study are available from the corresponding author on reasonable request.

Conflicts of Interest

There are no conflicts of interest.

Authors' Contributions

J.X.L, E.W, J.Q.W, Q.H.Z, and D.L.X contributed to the experiment design. J.X.L, E.W, J.Q.W, and Q.H.Z contributed to the experiment and performances. J.X.L, E.W, J.Q.W, W.Z., K.A.W, B.Z, D.L, G.X.Z, Y.D.W, Y.S.L, X.Y.Q, Q.H.Z, and D.L.X contributed to the data analysis, interpretation, and manuscript writing.

Funding

Supported by 2012A03220005 (JXL), R24EY028764 (Webster), and R43EY031238 (Webster).

References

[1] B. W. Wong, E. Marsch, L. Treps, M. Baes, and P. Carmeliet, "Endothelial cell metabolism in health and disease: impact of hypoxia," *The EMBO Journal*, vol. 36, no. 15, pp. 2187–2203, 2017.

[2] S. G. Eskin, C. L. Ives, L. V. McIntire, and L. T. Navarro, "Response of cultured endothelial cells to steady flow," *Microvascular Research*, vol. 28, no. 1, pp. 87–94, 1984.

[3] D. Bouis, Y. Kusumanto, C. Meijer, N. Mulder, and G. Hospers, "A review on pro- and anti-angiogenic factors as targets of clinical intervention," *Pharmacological Research*, vol. 53, no. 2, pp. 89–103, 2006.

[4] M. K. Reriani, L. O. Lerman, and A. Lerman, "Endothelial function as a functional expression of cardiovascular risk factors," *Biomarkers in Medicine*, vol. 4, no. 3, pp. 351–360, 2010.

[5] D. Vestweber, "How leukocytes cross the vascular endothelium," *Nature Reviews. Immunology*, vol. 15, no. 11, pp. 692–704, 2015.

[6] A. Janaszak-Jasiecka, A. Siekierzycka, A. Płoska, I. T. Dobrucki, and L. Kalinowski, "Endothelial dysfunction driven by hypoxia-the influence of oxygen deficiency on NO bioavailability," *Biomolecules*, vol. 11, no. 7, p. 982, 2021.

[7] K. Ullah and R. Wu, "Hypoxia-inducible factor regulates endothelial metabolism in cardiovascular disease," *Frontiers in Physiology*, vol. 12, article 670653, 2021.

[8] M. Meyer, G. Allenbach, M. Nicod Lalonde, N. Schaefer, J. O. Prior, and S. Gnesin, "Increased ^{18}F-FDG signal recovery from small physiological structures in digital PET/CT and application to the pituitary gland," *Scientific Reports*, vol. 10, no. 1, p. 368, 2020.

[9] L. Meyer, "Apartment clinics keep senior citizens in the community," *Hospitals*, vol. 50, no. 13, pp. 63-64, 1976.

[10] J. Hu, D. J. Discher, N. H. Bishopric, and K. A. Webster, "Hypoxia regulates expression of the endothelin-1 gene through a proximal hypoxia-inducible factor-1 binding site on the antisense strand," *Biochemical and Biophysical Research Communications*, vol. 245, no. 3, pp. 894–899, 1998.

[11] G. Ferns and L. Heikal, "Hypoxia in Atherogenesis," *Angiology*, vol. 68, no. 6, pp. 472–493, 2017.

[12] E. Crimi, F. S. Taccone, T. Infante, S. Scolletta, V. Crudele, and C. Napoli, "Effects of intracellular acidosis on endothelial function: An overview," *Journal of Critical Care*, vol. 27, no. 2, pp. 108–118, 2012.

[13] N. Rohwer and T. Cramer, "Hypoxia-mediated drug resistance: novel insights on the functional interaction of HIFs and cell death pathways," *Drug Resistance Updates*, vol. 14, no. 3, pp. 191–201, 2011.

[14] J. W. Thompson, R. M. Graham, and K. A. Webster, "DNase activation by hypoxia-acidosis parallels but is independent of programmed cell death," *Life Sciences*, vol. 91, no. 7-8, pp. 223–229, 2012.

[15] R. M. Graham, D. P. Frazier, J. W. Thompson et al., "A unique pathway of cardiac myocyte death caused by hypoxia–acidosis," *The Journal of Experimental Biology*, vol. 207, Part 18, pp. 3189–3200, 2004.

[16] L. Xiao, Y. Liu, and N. Wang, "New paradigms in inflammatory signaling in vascular endothelial cells," *American Journal of Physiology. Heart and Circulatory Physiology*, vol. 306, no. 3, pp. H317–H325, 2014.

[17] F. Kuhnert, M. R. Mancuso, J. Hampton et al., "Attribution of vascular phenotypes of the murineEgfl7locus to the microRNAmiR-126," *Development*, vol. 135, no. 24, pp. 3989–3993, 2008.

[18] S. Wang, A. B. Aurora, B. A. Johnson et al., "The endothelial-specific microRNA miR-126 governs vascular integrity and angiogenesis," *Developmental Cell*, vol. 15, no. 2, pp. 261–271, 2008.

[19] J. Agudo, A. Ruzo, N. Tung et al., "The miR-126-VEGFR2 axis controls the innate response to pathogen-associated nucleic acids," *Nature Immunology*, vol. 15, no. 1, pp. 54–62, 2014.

[20] A. Schober, M. Nazari-Jahantigh, Y. Wei et al., "MicroRNA-126-5p promotes endothelial proliferation and limits atherosclerosis by suppressing Dlk1," *Nature Medicine*, vol. 20, no. 4, pp. 368–376, 2014.

[21] P. Nammian, V. Razban, S. Tabei, and S. L. Asadi-Yousefabad, "MicroRNA-126: dual role in angiogenesis dependent Diseases," *Current Pharmaceutical Design*, vol. 26, no. 38, pp. 4883–4893, 2020.

[22] M. Alique, G. Bodega, C. Giannarelli, J. Carracedo, and R. Ramírez, "MicroRNA-126 regulates hypoxia-inducible factor-1α which inhibited migration, proliferation, and angiogenesis in replicative endothelial senescence," *Scientific Reports*, vol. 9, no. 1, p. 7381, 2019.

[23] Q. Pan, Y. Wang, Q. Lan et al., "Exosomes derived from mesenchymal stem cells ameliorate hypoxia/reoxygenation-injured ECs via transferring microRNA-126," *Stem Cells International*, vol. 2019, Article ID 2831756, 13 pages, 2019.

[24] H. H. Yang, Y. Chen, C. Y. Gao, Z. T. Cui, and J. M. Yao, "Protective effects of MicroRNA-126 on human cardiac microvascular endothelial cells against hypoxia/reoxygenation-induced injury and inflammatory response by activating PI3K/Akt/eNOS signaling pathway," *Cellular Physiology and Biochemistry*, vol. 42, no. 2, pp. 506–518, 2017.

[25] P. Ye, J. Liu, F. He, W. Xu, and K. Yao, "Hypoxia-induced deregulation of miR-126 and its regulative effect on VEGF and MMP-9 expression," *International Journal of Medical Sciences*, vol. 11, no. 1, pp. 17–23, 2014.

[26] W. Song, Q. Liang, M. Cai, and Z. Tian, "HIF-1α-induced upregulation of microRNA-126 contributes to the effectiveness of exercise training on myocardial angiogenesis in myocardial infarction rats," *Journal of Cellular and Molecular Medicine*, vol. 24, no. 22, pp. 12970–12979, 2020.

[27] Y. Ren, R. Bao, Z. Guo, J. Kai, C. G. Cai, and Z. Li, "miR-126-5p regulates H9c2 cell proliferation and apoptosis under hypoxic conditions by targeting IL-17A," *Experimental and Therapeutic Medicine*, vol. 21, no. 1, p. 67, 2021.

[28] W. Liu, L. Li, Y. Rong et al., "Hypoxic mesenchymal stem cell-derived exosomes promote bone fracture healing by the transfer of miR-126," *Acta Biomaterialia*, vol. 103, pp. 196–212, 2020.

[29] S. G. Ong, W. H. Lee, M. Huang et al., "Cross talk of combined gene and cell therapy in ischemic heart disease: role of exosomal microRNA transfer," *Circulation*, vol. 130, 11 Supplement 1, pp. S60–S69, 2014.

[30] D. A. Chistiakov, A. N. Orekhov, and Y. V. Bobryshev, "The role of miR-126 in embryonic angiogenesis, adult vascular homeostasis, and vascular repair and its alterations in atherosclerotic disease," *Journal of Molecular and Cellular Cardiology*, vol. 97, pp. 47–55, 2016.

[31] E. Elia, S. Ministrini, F. Carbone, and F. Montecucco, "Diabetic cardiomyopathy and inflammation: development of hostile microenvironment resulting in cardiac damage," *Minerva Cardioangiologica*, 2021.

[32] M. Wang, Y. Liu, Y. Liang, K. Naruse, and K. Takahashi, "Systematic understanding of pathophysiological mechanisms of oxidative stress-related conditions-diabetes mellitus, cardiovascular diseases, and ischemia-reperfusion injury," *Frontiers in Cardiovascular Medicine*, vol. 8, article 649785, 2021.

[33] D. L. Harrington, H. R. Barten, E. I. Audannio et al., "Genome sequences ofgordoniabacteriophages Jodelie19, BlingBling, and Burnsey," *Microbiology Resource Announcements*, vol. 10, no. 5, 2021.

[34] L. Dong, E. A. Krewson, and L. V. Yang, "Acidosis activates endoplasmic reticulum stress pathways through GPR4 in human vascular endothelial cells," *International Journal of Molecular Sciences*, vol. 18, no. 2, p. 278, 2017.

[35] A. Chen, L. Dong, N. R. Leffler, A. S. Asch, O. N. Witte, and L. V. Yang, "Activation of GPR4 by acidosis increases endothelial cell adhesion through the cAMP/Epac pathway," *PLoS One*, vol. 6, no. 11, article e27586, 2011.

[36] L. Dong, Z. Li, N. R. Leffler, A. S. Asch, J. T. Chi, and L. V. Yang, "Acidosis activation of the proton-sensing GPR4 receptor stimulates vascular endothelial cell inflammatory responses revealed by transcriptome analysis," *PLoS One*, vol. 8, no. 4, article e61991, 2013.

[37] B. K. Siesjö, K. I. Katsura, T. Kristián, P. A. Li, and P. Siesjö, "Molecular mechanisms of acidosis-mediated damage," *Acta Neurochirurgica. Supplement*, vol. 66, pp. 8–14, 1996.

[38] J. Yang, C. Huang, J. Yang, H. Jiang, and J. Ding, "Statins attenuate high mobility group box-1 protein induced vascular endothelial activation : a key role for TLR4/NF-κB signaling pathway," *Molecular and Cellular Biochemistry*, vol. 345, no. 1-2, pp. 189–195, 2010.

[39] Q. Lin, X. P. Yang, D. Fang et al., "High-mobility group box-1 mediates toll-like receptor 4-dependent angiogenesis," *Arteriosclerosis, Thrombosis, and Vascular Biology*, vol. 31, no. 5, pp. 1024–1032, 2011.

[40] E. M. Bauer, R. Shapiro, T. R. Billiar, and P. M. Bauer, "High mobility group box 1 inhibits human pulmonary artery endothelial cell migration via a toll-like receptor 4- and interferon response factor 3-dependent mechanism(s)," *The Journal of Biological Chemistry*, vol. 288, no. 2, pp. 1365–1373, 2013.

[41] S. Yang, L. Xu, T. Yang, and F. Wang, "High-mobility group box-1 and its role in angiogenesis," *Journal of Leukocyte Biology*, vol. 95, no. 4, pp. 563–574, 2014.

[42] H. Mudaliar, C. Pollock, J. Ma, H. Wu, S. Chadban, and U. Panchapakesan, "The role of TLR2 and 4-mediated inflammatory pathways in endothelial cells exposed to high glucose," *PLoS One*, vol. 9, no. 10, article e108844, 2014.

[43] J. Lan, H. Luo, R. Wu et al., "Internalization of HMGB1 (high mobility group box 1) promotes angiogenesis in endothelial cells," *Arteriosclerosis, Thrombosis, and Vascular Biology*, vol. 40, no. 12, pp. 2922–2940, 2020.

[44] A. Wahid, W. Chen, X. Wang, and X. Tang, "High-mobility group box 1 serves as an inflammation driver of cardiovascular disease," *Biomedicine & Pharmacotherapy*, vol. 139, article 111555, 2021.

[45] L. Liu, W. Ren, and K. Chen, "MiR-34a promotes apoptosis and inhibits autophagy by targeting HMGB1 in acute myeloid leukemia cells," *Cellular Physiology and Biochemistry*, vol. 41, no. 5, pp. 1981–1992, 2017.

[46] L. J. Coleman, J. Zou, and F. T. Crews, "Microglial-derived miRNA let-7 and HMGB1 contribute to ethanol-induced neurotoxicity via TLR7," *Journal of Neuroinflammation*, vol. 14, no. 1, p. 22, 2017.

[47] Y. Wang, S. Shen, Z. Li, W. Li, and X. Weng, "MIR-140-5p affects chondrocyte proliferation, apoptosis, and inflammation by targeting HMGB1 in osteoarthritis," *Inflammation Research*, vol. 69, no. 1, pp. 63–73, 2020.

[48] H. Ai, W. Zhou, Z. Wang, G. Qiong, Z. Chen, and S. Deng, "microRNAs-107 inhibited autophagy, proliferation, and migration of breast cancer cells by targeting HMGB1," *Journal of Cellular Biochemistry*, vol. 120, no. 5, pp. 8696–8705, 2018.

[49] W. Zhang, Y. Wang, and Y. Kong, "Exosomes derived from mesenchymal stem cells modulate miR-126 to ameliorate hyperglycemia-induced retinal inflammation via targeting HMGB1," *Investigative Ophthalmology & Visual Science*, vol. 60, no. 1, pp. 294–303, 2019.

[50] S. T. Tang, F. Wang, M. Shao, Y. Wang, and H. Q. Zhu, "MicroRNA-126 suppresses inflammation in endothelial cells under hyperglycemic condition by targeting HMGB1," *Vascular Pharmacology*, vol. 88, pp. 48–55, 2017.

[51] K. A. Webster, D. J. Discher, S. Kaiser, O. Hernandez, B. Sato, and N. H. Bishopric, "Hypoxia-activated apoptosis of cardiac myocytes requires reoxygenation or a pH shift and is independent of p53," *The Journal of Clinical Investigation*, vol. 104, no. 3, pp. 239–252, 1999.

[52] L. A. Kubasiak, O. M. Hernandez, N. H. Bishopric, and K. A. Webster, "Hypoxia and acidosis activate cardiac myocyte death through the Bcl-2 family protein BNIP3," *Proceedings of the National Academy of Sciences of the United States of America*, vol. 99, no. 20, pp. 12825–12830, 2002.

[53] K. A. Webster, D. J. Discher, O. M. Hernandez, K. Yamashita, and N. H. Bishopric, "A glycolytic pathway to apoptosis of hypoxic cardiac myocytes. Molecular pathways of increased acid production," *Advances in Experimental Medicine and Biology*, vol. 475, pp. 161–175, 2000.

[54] E. R. Swenson, "Hypoxia and its Acid-Base consequences: from mountains to malignancy," *Advances in Experimental Medicine and Biology*, vol. 903, pp. 301–323, 2016.

[55] P. Vaupel and G. Multhoff, "Hypoxia-/HIF-1α-driven factors of the tumor microenvironment impeding antitumor immune responses and promoting malignant progression," *Advances in Experimental Medicine and Biology*, vol. 1072, pp. 171–175, 2018.

[56] R. Bartoszewski, A. Moszyńska, M. Serocki et al., "Primary endothelial cell-specific regulation of hypoxia-inducible factor (HIF)-1 and HIF-2 and their target gene expression profiles

during hypoxia," *The FASEB Journal*, vol. 33, no. 7, pp. 7929–7941, 2019.

[57] M. L. Jin, Z. H. Zou, T. Tao et al., "Effect of the recombinant adenovirus-mediated HIF-1 alpha on the expression of VEGF in the hypoxic brain microvascular endothelial cells of Rats," *Neuropsychiatric Disease and Treatment*, vol. 16, pp. 397–406, 2020.

[58] N. Patel, C. S. Gonsalves, P. Malik, and V. K. Kalra, "Placenta growth factor augments endothelin-1 and endothelin-B receptor expression via hypoxia-inducible factor-1α," *Blood*, vol. 112, no. 3, pp. 856–865, 2008.

[59] B. Y. Kang, J. M. Kleinhenz, T. C. Murphy, and C. M. Hart, "The PPARγ ligand rosiglitazone attenuates hypoxia-induced endothelin signaling in vitro and in vivo," *American Journal of Physiology. Lung Cellular and Molecular Physiology*, vol. 301, no. 6, pp. L881–L891, 2011.

[60] S. Earley, L. D. Nelin, L. G. Chicoine, and B. R. Walker, "Hypoxia-induced pulmonary endothelin-1 expression is unaltered by nitric oxide," *Journal of Applied Physiology*, vol. 92, no. 3, pp. 1152–1158, 2002.

[61] J. Luo, J. Martinez, X. Yin, A. Sanchez, D. Tripathy, and P. Grammas, "Hypoxia induces angiogenic factors in brain microvascular endothelial cells," *Microvascular Research*, vol. 83, no. 2, pp. 138–145, 2012.

[62] K. Yamashita, D. J. Discher, J. Hu, N. H. Bishopric, and K. A. Webster, "Molecular regulation of the endothelin-1 gene by hypoxia:," *The Journal of Biological Chemistry*, vol. 276, no. 16, pp. 12645–12653, 2001.

[63] A. Wilson, L. A. Shehadeh, H. Yu, and K. A. Webster, "Age-related molecular genetic changes of murine bone marrow mesenchymal stem cells," *BMC Genomics*, vol. 11, no. 1, p. 229, 2010.

[64] B. Zhang, G. Zhang, T. Wei et al., "MicroRNA-25 protects smooth muscle cells against corticosterone-induced apoptosis," *Oxidative Medicine and Cellular Longevity*, vol. 2019, Article ID 2691514, 10 pages, 2019.

[65] S. Sharma, J. Liu, J. Wei, H. Yuan, T. Zhang, and N. H. Bishopric, "Repression of miR-142 by p300 and MAPK is required for survival signalling via gp130 during adaptive hypertrophy," *EMBO Molecular Medicine*, vol. 4, no. 7, pp. 617–632, 2012.

[66] H. Shi, L. Chen, H. Wang et al., "Synergistic induction of miR-126 by hypoxia and HDAC inhibitors in cardiac myocytes," *Biochemical and Biophysical Research Communications*, vol. 430, no. 2, pp. 827–832, 2013.

[67] S. Fang, X. Ma, S. Guo, and J. Lu, "MicroRNA-126 inhibits cell viability and invasion in a diabetic retinopathy model via targeting IRS-1," *Oncology Letters*, vol. 14, no. 4, pp. 4311–4318, 2017.

[68] M. E. Bianchi and A. A. Manfredi, "High-mobility group box 1 (HMGB1) protein at the crossroads between innate and adaptive immunity," *Immunological Reviews*, vol. 220, no. 1, pp. 35–46, 2007.

[69] H. E. Harris, U. Andersson, and D. S. Pisetsky, "HMGB1: a multifunctional alarmin driving autoimmune and inflammatory disease," *Nature Reviews Rheumatology*, vol. 8, no. 4, pp. 195–202, 2012.

[70] U. Andersson and H. E. Harris, "The role of HMGB1 in the pathogenesis of rheumatic disease," *Biochimica et Biophysica Acta*, vol. 1799, no. 1-2, pp. 141–148, 2010.

[71] D. P. Bartel, "Metazoan MicroRNAs," *Cell*, vol. 173, no. 1, pp. 20–51, 2018.

[72] C. Gong, J. Fang, G. Li, H. H. Liu, and Z. S. Liu, "Effects of microRNA-126 on cell proliferation, apoptosis and tumor angiogenesis via the down-regulating ERK signaling pathway by targeting EGFL7 in hepatocellular carcinoma," *Oncotarget*, vol. 8, no. 32, pp. 52527–52542, 2017.

[73] C. D. Yu, W. H. Miao, Y. Y. Zhang, M. J. Zou, and X. F. Yan, "Inhibition of miR-126 protects chondrocytes from IL-1β induced inflammation via upregulation of Bcl-2," *Bone and Joint Research*, vol. 7, no. 6, pp. 414–421, 2018.

[74] A. Madej, J. Popłoński, and E. Huszcza, "Improved oxidation of naringenin to carthamidin and isocarthamidin by Rhodotorula marina," *Applied Biochemistry and Biotechnology*, vol. 173, no. 1, pp. 67–73, 2014.

[75] M. He, Q. Y. Wang, Q. Q. Yin et al., "HIF-1 α downregulates miR-17/20a directly targeting p21 and STAT3: a role in myeloid leukemic cell differentiation," *Cell Death and Differentiation*, vol. 20, no. 3, pp. 408–418, 2013.

[76] M. Zhao, Y. Zhang, Y. Jiang et al., "YAP promotes autophagy and progression of gliomas via upregulating HMGB1," *Journal of Experimental & Clinical Cancer Research*, vol. 40, no. 1, p. 99, 2021.

[77] H. He, X. Wang, J. Chen, L. Sun, H. Sun, and K. Xie, "High-mobility group box 1 (HMGB1) promotes angiogenesis and tumor migration by regulating hypoxia-inducible factor 1 (HIF-1α) expression via the phosphatidylinositol 3-kinase (PI3K)/AKT signaling pathway in breast cancer cells," *Medical Science Monitor*, vol. 25, pp. 2352–2360, 2019.

[78] Y. F. Xu, Z. L. Liu, C. Pan et al., "HMGB1 correlates with angiogenesis and poor prognosis of perihilar cholangiocarcinoma via elevating VEGFR2 of vessel endothelium," *Oncogene*, vol. 38, no. 6, pp. 868–880, 2019.

[79] Z. Wang, N. K. Saadé, and P. A. Ariya, "Advances in ultra-trace analytical capability for micro/nanoplastics and water-soluble polymers in the environment: fresh falling urban snow," *Environmental Pollution*, vol. 276, article 116698, 2021.

[80] S. Y. Park, S. W. Lee, H. Y. Kim, W. S. Lee, K. W. Hong, and C. D. Kim, "HMGB1 induces angiogenesis in rheumatoid arthritis via HIF-1α activation," *European Journal of Immunology*, vol. 45, no. 4, pp. 1216–1227, 2015.

[81] H. C. Yao, M. Zhou, Y. H. Zhou et al., "Intravenous high mobility group box 1 upregulates the expression of HIF-1α in the myocardium via a protein kinase B-dependent pathway in rats following acute myocardial ischemia," *Molecular Medicine Reports*, vol. 13, no. 2, pp. 1211–1219, 2016.

[82] G. J. Casimir, N. Lefèvre, F. Corazza, J. Duchateau, and M. Chamekh, "The Acid-Base balance and gender in inflammation: a mini-review," *Frontiers in Immunology*, vol. 9, p. 475, 2018.

[83] J. Iijima, K. Konno, and N. Itano, "Inflammatory alterations of the extracellular matrix in the tumor microenvironment," *Cancers (Basel)*, vol. 3, no. 3, pp. 3189–3205, 2011.

[84] G. Landskron, M. de la Fuente, P. Thuwajit, C. Thuwajit, and M. A. Hermoso, "Chronic inflammation and cytokines in the tumor microenvironment," *Journal of Immunology Research*, vol. 2014, Article ID 149185, 19 pages, 2014.

[85] F. G. Zampieri, J. A. Kellum, M. Park et al., "Relationship between acid-base status and inflammation in the critically ill," *Critical Care*, vol. 18, no. 4, p. R154, 2014.

[86] C. Deng, L. Zhao, Z. Yang et al., "Targeting HMGB1 for the treatment of sepsis and sepsis-induced organ injury," *Acta Pharmacologica Sinica*, 2021.

[87] L. Qu, C. Chen, Y. Chen et al., "High-mobility group box 1 (HMGB1) and autophagy in acute lung injury (ALI): a review," *Medical Science Monitor*, vol. 25, pp. 1828–1837, 2019.

[88] Y. Liu, G. B. Zhuang, and X. Z. Zhou, "HMBG1 as a driver of inflammatory and immune processes in the pathogenesis of ocular diseases," *Journal of Ophthalmology*, vol. 2018, Article ID 5195290, 8 pages, 2018.

[89] C. Pilzweger and S. Holdenrieder, "Circulating HMGB1 and RAGE as clinical biomarkers in malignant and autoimmune diseases," *Diagnostics (Basel)*, vol. 5, no. 2, pp. 219–253, 2015.

[90] C. Fernández-Hernando and Y. Suárez, "MicroRNAs in endothelial cell homeostasis and vascular disease," *Current Opinion in Hematology*, vol. 25, no. 3, pp. 227–236, 2018.

[91] J. E. Fish, M. M. Santoro, S. U. Morton et al., "miR-126 regulates angiogenic signaling and vascular integrity," *Developmental Cell*, vol. 15, no. 2, pp. 272–284, 2008.

[92] P. Theofilis, M. Sagris, E. Oikonomou et al., "Inflammatory mechanisms contributing to endothelial dysfunction," *Biomedicine*, vol. 9, no. 7, p. 781, 2021.

[93] K. Mekhail, L. Gunaratnam, M. E. Bonicalzi, and S. Lee, "HIF activation by pH-dependent nucleolar sequestration of VHL," *Nature Cell Biology*, vol. 6, no. 7, pp. 642–647, 2004.

[94] S. Zheng, H. Zheng, A. Huang et al., "Piwi-interacting RNAs play a role in vitamin C-mediated effects on endothelial aging," *International Journal of Medical Sciences*, vol. 17, no. 7, pp. 946–952, 2020.

[95] A. Huang, H. Zheng, Z. Wu, M. Chen, and Y. Huang, "Circular RNA-protein interactions: functions, mechanisms, and identification," *Theranostics*, vol. 10, no. 8, pp. 3503–3517, 2020.

Hindawi
Disease Markers
Volume 2021, Article ID 4026604, 25 pages
https://doi.org/10.1155/2021/4026604

Research Article

Comprehensive Analysis to Identify Key Genes Involved in Advanced Atherosclerosis

Tian-ming Huo and Zhi-wei Wang

Department of Cardiovascular Surgery, Renmin Hospital of Wuhan University, Wuhan, 430060 Hubei Province, China

Correspondence should be addressed to Zhi-wei Wang; wangzhiwei@whu.edu.cn

Received 17 October 2021; Accepted 13 November 2021; Published 10 December 2021

Academic Editor: Wen-Qing Shi

Background. The study was aimed at finding accurate and effective therapeutic targets and deepening our understanding of the mechanisms of advanced atherosclerosis (AA). *Methods*. We downloaded the gene expression datasets GSE28829, GSE120521, and GSE43292 from Gene Expression Omnibus. Weighted gene coexpression network analysis (WGCNA) was performed for GSE28829, and functional enrichment analysis and protein–protein interaction network analysis were conducted on the key module. Significant genes in the key module were analyzed by molecular complex detection, and genes in the most important subnetwork were defined as hub genes. Multiple dataset analyses for hub genes were conducted. Genes that overlapped between hub genes and differentially expressed genes (DEGs) of GSE28829 and GSE120521 were defined as key genes. Further validation for key genes was performed using GSE28829 and GSE43292. Gene set enrichment analysis (GSEA) was applied to key genes. *Results*. A total of 77 significant genes in the key module of GSE28829 were screened out that were mainly associated with inflammation and immunity. The subnetwork was obtained from significant genes, and 18 genes in this module were defined as hub genes, which were related to immunity and expressed in multiple diseases, particularly systemic lupus erythematosus. Some hub genes were regulated by SPI1 and associated with the blood, spleen, and lung. After overlapping with DEGs of GSE28829 and GSE120521, a total of 10 genes (HCK, ITGAM, CTSS, TYROBP, LAPTM5, FCER1G, ITGB2, NCF2, AIF1, and CD86) were identified as key genes. All key genes were validated and evaluated successfully and were related to immune response pathways. *Conclusion*. Our study suggests that the key genes related to immune and inflammatory responses are involved in the development of AA. This may deepen our understanding of the mechanisms of and provide valuable therapeutic targets for AA.

1. Background

Cardiovascular disease (CVD) is one of the leading causes of death in the world, and approximately 17 million people die from it every year [1]. Atherosclerosis (AS) is the most frequent cause of CVD [2]. The main feature of AS is complex chronic inflammation. Its pathogenesis and molecular mechanisms are multifactorial and characterized by smooth muscle cell proliferation, endothelial damage, cell apoptosis, inflammatory cell activation, lipid accumulation, vascular matrix changes, and oxidative stress [3, 4]. As early atherosclerosis (EA) progresses to advanced atherosclerosis (AA), atherosclerotic plaques will gradually expand and rupture, leading to vascular stenosis or occlusion and causing myocardial infarction and ischemic stroke [5, 6]. Current treatment strategies for reversing advanced plaque formation are still limited, and the mechanisms of AA are not fully elucidated [7]. Thus, more comprehensive and in-depth investigations of AA are needed.

In recent years, high-throughput platforms for gene expression analysis, such as microarrays, have become effective tools for revealing the pathogenesis of CVD. With the help of this method, researchers have already discovered many biomarkers related to CVD and AS. By comparing the expression levels of lncRNA from peripheral blood mononuclear cells in patients with coronary artery disease and healthy people, researchers found that ENST0000 0444488.1 and uc010yfd.1 can better distinguish these two

groups [8]. NEDD4L, FBXO44, FBXO27, WSB1, FBXW8, UBE2F, and ASB1 have been reported as hub genes that help elucidate the pathogenesis and progression of AS [9]. Such studies have mainly been limited to plaque-related expression profiles, and only a few have addressed advanced plaque. Some scholars have found that the stability of atherosclerotic plaques is mainly affected by inflammation, matrix remodeling, and calcification, which are reflected in differentially expressed genes (DEGs) between stable plaque and unstable plaque [10]. By screening DEGs from stable and ruptured plaques, FABP4 and leptin have been shown to be involved in the process of atherosclerotic plaque rupture [11]. CCL4, CCL18, MMP9, and SPP1 are highly expressed in ruptured plaques and have been validated with experimental evidence [12].

However, some false positives may occur in these studies due to the limitation of the number of samples. While the hub genes are statistically significant, they are not functionally annotated in many cases, or they have important roles in the protein–protein interaction (PPI) network that is not statistically significant [13]. Also, because of the small rate of change or low abundance of some hub genes, information on those genes may have been missed.

Weighted gene coexpression network analysis (WGCNA) is a method that is mainly based on the network. Using this method, a scale-free network is constructed by analyzing all the expression profiles included in a study. WGCNA can identify gene coexpression network modules, determine the correlation between modules and phenotypes, and then discover important genes that regulate key biological processes [14]. This method has helped researchers achieve many remarkable results in numerous areas, including cancers [15], the nervous system [16], and the immune system [17].

In our study, we identified key modules and significant genes using WGCNA for GSE28829 and conducted a bioinformatic analysis for key module and hub genes to reveal potential functions. In order to avoid both false positive and false negative results, the DEGs of GSE28829 and GSE120521 were screened out to confirm some key genes. Finally, those key genes were validated in GSE28829 and GSE43292. We believe that this research can deepen our understanding of the mechanisms of AA and guide us in finding better treatment strategies.

2. Materials and Methods

2.1. Study Design. The raw data for GSE28829 and GSE43292 and the normalized data for GSE120521 were downloaded from the Gene Expression Omnibus (GEO) database. The overall research design flow chart is shown in Figure 1. First, gene expression profiles of plaques in GSE28829 and GSE120521 were used to identify DEGs in EA and AA. For WGCNA, the variances of every gene in all samples were calculated and sorted in descending order, and the top 25% of genes were selected as candidates. Then, we selected a significant coexpression module for further analysis. To reveal the potential functions of the genes in this module, we used the clusterProfiler package for functional enrichment analysis. Moreover, significant genes were screened from this module based on gene significance and module membership (MM) value. Next, we constructed the PPI network and performed molecular complex detection (MCODE) analysis using the Cytoscape software to obtain the important subnetworks of these genes. The hub genes from the most important subnetwork were further analyzed with the Metascape tool. In order to find the key genes, we simultaneously mapped the hub genes to DEGs of GSE28829 and GSE120521, and the overlapping genes were identified as key genes. All of the key genes were validated in dataset GSE43292 and evaluated in datasets GSE28829 and GSE43292. Finally, to obtain further insights into the functions of these key genes, we performed a gene set enrichment analysis (GSEA) for each key gene.

2.2. Data Preprocessing. The three datasets were downloaded from the GEO database. The data consisted of gene expression profiles with early and advanced samples of carotid atheroma plaque. Details are shown in Table 1.

All analyses using R packages were based on the R software (version 4.0.2). The raw data of GSE28829 [18] and GSE43292 [19] were read using the affy package [20]. In order to make the data better for analysis, the robust multi-array average (RMA) method was used to normalize the data, and batch effects were removed [21]. When the probe expression data were duplicated, their average value was used as the gene expression value. For GSE120521 [10], the processed gene expression data provided by GEO were used.

2.3. Identification of DEGs. The limma R package was used to screen DEGs [22]. To calculate the P values of the genes, an adjusted t-test was used. The false discovery rate (FDR) was calculated using the Benjamini and Hochberg method. Genes with an FDR lower than 0.05 and an absolute value of fold change (FC) higher than 2 were set as significant DEGs.

2.4. Construction of Coexpression Network. In order to avoid the background noise owning to the low expression levels of genes, variances of every gene in samples of both groups in GSE28829 were calculated. The results were sorted in descending order, and the genes with the top 25% variance were selected as candidate genes. The coexpression network of the candidate genes was constructed with the WGCNA package [23], with the minimum number of genes in a module set at 50. The maximum number of genes in a module was set as the number of all input genes. The cut height was set at 0.2 to merge possible similar modules.

2.5. Identification of Key Modules Related to AA. The module eigengene (ME) represents the gene expression levels in the module. The relationship between the module and AA can be determined by calculating the correlation between the ME and the clinical phenotype of AS, and the module with the highest absolute value of ME is the key module. Gene significance (GS) represents the correlation between a gene and a phenotype. In the module trait correlation analysis, genes with an MM higher than 0.9 and a GS higher than 0.4 in the key module were identified as significant genes.

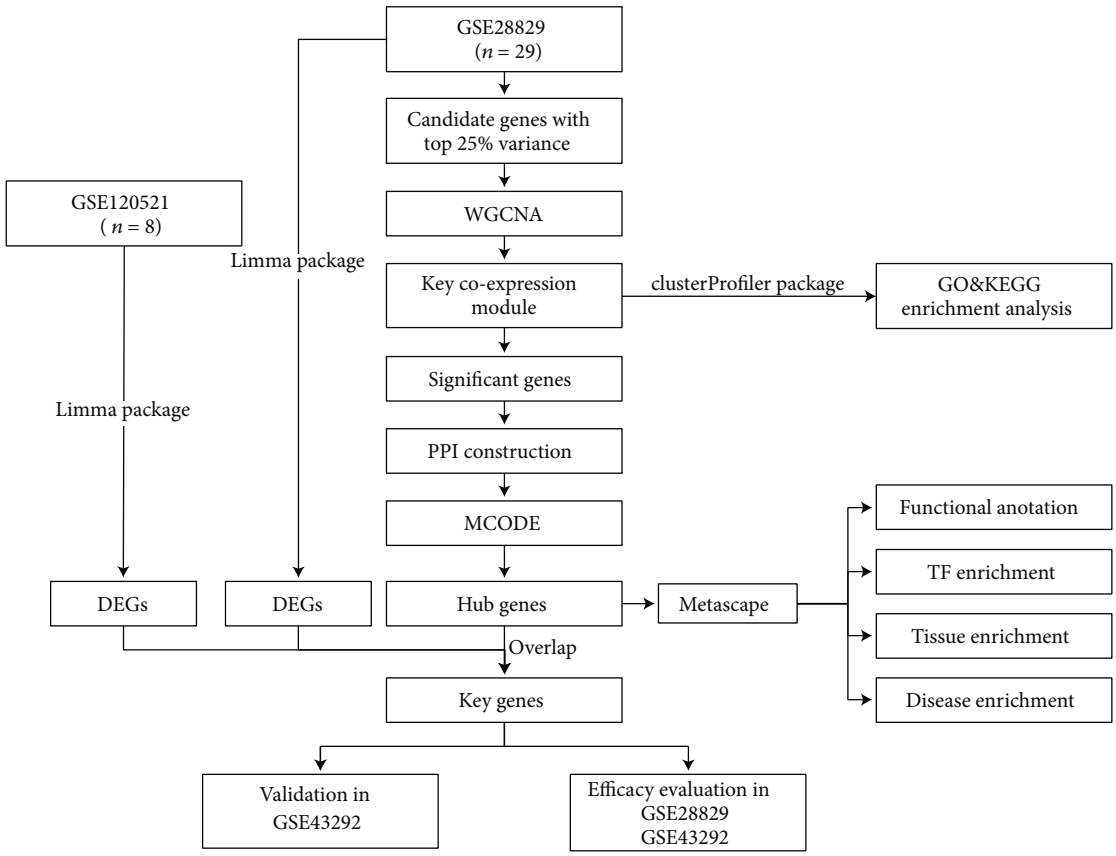

Figure 1: Research design flow chart.

Table 1: The summary of the datasets.

GEO ID	Platform	Tissue type	Sample size	Experiment type
GSE28829	GPL570	Advanced carotid atherosclerotic plaques and early carotid atherosclerotic plaques	16 vs. 13	Array
GSE120521	GPL16791	Unstable carotid atherosclerotic plaques and stable carotid atherosclerotic plaques	4 vs. 4	High-throughput sequencing
GSE43292	GPL6244	Advanced carotid atherosclerotic plaques and early carotid atherosclerotic plaques	32 vs. 32	Array

2.6. Functional Enrichment Analysis of the Key Module. In order to further understand the functions of the genes in the key module, the clusterProfiler package [24] was used to identify and visualize the gene ontology (GO) terms enriched by the genes in the key module. Significant enrichment was screened as a P value lower than 0.05.

2.7. PPI Network Construction of Significant Genes and Hub Gene Selection. The STRING database 11.5 was used to construct the PPI network of significant genes [25], and the combined score was chosen as greater than 0.4. The PPI network was visualized using the Cytoscape software (version 3.8.2) [26]. We screened the subnetworks of the PPI network using the MCODE plug-in [27]. The criteria used for cutoff were degree cutoff = 2, node score cutoff = 0.2, max depth = 100, and K − core = 2. The genes in the most significant subnetwork were defined as hub genes.

2.8. Multidatabase Analysis of Hub Genes. Metascape is a comprehensive portal containing 40 databases that integrate functions such as functional enrichment analysis, gene annotation, and interactive group analysis. Following the screening of the important subnetwork, the Metascape tool was used for further gene annotation analysis. Also, another three datasets, DisGeNET, PaGenBase, and TRRUST, were applied to identify the gene related disease, specific tissue, and transcription factor, respectively. The criteria for cutoff were set as P value < 0.01, enrichment factor > 1.5, and minimum count = 3.

2.9. Key Gene Selection and Validation. In order to avoid false positive rates in the results, hub genes were simultaneously mapped to DEGs of GSE28829 and GSE120521, and the overlapping genes were identified as key genes. All of the key genes were further validated in GSE28829 and

GSE43292 databases. The pROC package [28] was used to plot the ROC curve and calculate the area under curve (AUC). The ROC curve was used to evaluate whether the key genes can distinguish AA and EA plaques well.

2.10. GSEA for Key Genes. GSEA was performed based on the gene list obtained from each key gene using the GSEA function from the R package clusterProfiler [29]. The reference gene set was h.all.v7.4.entrez.gmt in the Molecular Signatures Database. The criterion for significance was set as an adjusted P value < 0.05.

3. Results

3.1. Data Preprocessing and Identification of DEGs. The gene expression distribution of samples in GSE28829 before data processing is shown in Figure 2(a). We could see that their median distribution was not on a straight line. After normalization, the median value of gene expression was basically at the same level (Figure 2(b)). After that, a total of 329 DEGs were distinguished from GSE28829. Among these, 270 upregulated genes and 59 downregulated genes were screened out. The expression of genes in GSE120521 was already normalized. Next, 539 upregulated genes and 557 downregulated genes were screened out from GSE120521. The DEGs of the two datasets are shown in Table S1 and Table S2.

3.2. Coexpression Network Selection and Identification of the Significant Module. A total of 5,044 genes out of 20,174 annotated genes were selected as candidates with the top 25% variance. In order to gain further insight into the biological functions of these genes in the progression of AA, we conducted the WGCNA analysis. The network was built using the WGCNA R package. After calculation, the best soft-thresholding power was set at 7, and the correlation coefficient threshold was set at 0.85 (Figure 3(a)). Several modules comprised most genes, which can be seen with the blue, brown, green, and yellow-green areas in Figure 3(b). The relationship between a module and a phenotype was analyzed, and multiple modules were related to AA (Figure 3(c)). The GS of all genes in each module is shown in Figure 3(d). We could intuitively see that the blue one is the module that has the most significant relationship with AA. Figure 3(e) provides the relationship between the MM and GS of each gene in the blue module. A total of 77 genes with a high GS for AA were selected as the hub genes.

3.3. Functional Enrichment Analysis of the Key Coexpression Module. The GO terms of the biological process (BP) analysis showed that the BPs of the blue module were mainly enriched in neutrophil activation, neutrophil activation involved in immune response, neutrophil-mediated immunity, neutrophil degranulation, and leukocyte migration, which are indicative of immune cell stimulation and migration in patients with AA (Figure 4(a)). The GO terms of the cellular component (CC) were mainly enriched in the secretory granule membrane, endocytic vesicle, secretory granule lumen, and vesicle lumen. The GO terms of molecular function (MF) were enriched in amide binding, peptide binding, immune receptor activity, cytokine binding, and amyloid beta binding. The Kyoto Encyclopedia of Genes and Genomes (KEGG) pathway is mainly involved in tuberculosis, phagosome, lysosome, neutrophil extracellular trap formation, osteoclast differentiation, rheumatoid arthritis, leishmaniasis, hematopoietic cell lineage, cell adhesion molecules, and systemic lupus erythematosus. In addition, these AA correlated pathways were related to immunity–inflammation responses (Figure 4(b)).

The relationship between those genes and BP terms indicated that many genes enriched in neutrophil activation are also related to other BP terms, such as immune response, leukocyte proliferation, leukocyte migration, and regulation of cell–cell adhesion, which indicates that those genes could be related to multiple biological pathways involved in the progression of AA (Figure 4(c)). Also, Figure 4(d) shows that many genes related to phagosome, tuberculosis, and *Staphylococcus aureus* infection are also enriched for other pathways, including leishmaniasis, rheumatoid arthritis, and osteoclast differentiation.

Overall, these findings demonstrate that genes in the blue module are involved in immune and inflammation-related functions.

3.4. PPI Construction and Multidatabase Analysis of Modules. The PPI network of the significant genes in the blue module (interaction score > 0.4) was constructed, and 61 nodes and 398 interaction pairs were identified from the network (Figure 5(a)). Two highly connected modules were harvested by the MCODE analysis, and only one module had a score greater than 10 (16.941) (Figure 5(b)). The module contained 18 nodes and 144 edges. The genes in the module 1 were identified as hub genes.

In order to fully understand the role hub genes play in the development of AA, we conducted a multidatabase analysis of these genes. Enrichment analysis of module 1 in the Metascape database indicated that the hub genes are mainly related to positive regulation of immune response, *Staphylococcus aureus* infection, myeloid leukocyte activation, osteoclast differentiation, positive regulation of cytokine production, IgG binding, negative regulation of the immune system process, natural killer cell mediated cytotoxicity, Rap1 signaling pathway, lytic vacuole, positive regulation of leukocyte proliferation, cytokine-mediated signaling pathway, and myeloid leukocyte differentiation (Figure 6(a)). Disease enrichment analysis in the DisGeNET database revealed that these genes were mainly related to lupus nephritis, nephritis, lupus vulgaris, and lupus erythematosus (Figure 6(b)). Tissue characteristic enrichment analysis in the PaGenBase database suggested that hub genes were enriched in the blood, spleen, and lung (Figure 6(c)). Transcription factors analysis in the TRRUST database showed that the hub genes were mainly regulated by SPI1 (Figure 6(d)).

3.5. Key Gene Selection and Validation. In order to find the key genes, the hub genes were mapped to the DEGs from GSE28829 and GSE120521 (Figure 7), and 10 genes were screened out: HCK, ITGAM, CTSS, TYROBP, LAPTM5, FCER1G, ITGB2, NCF2, AIF1, and CD86.

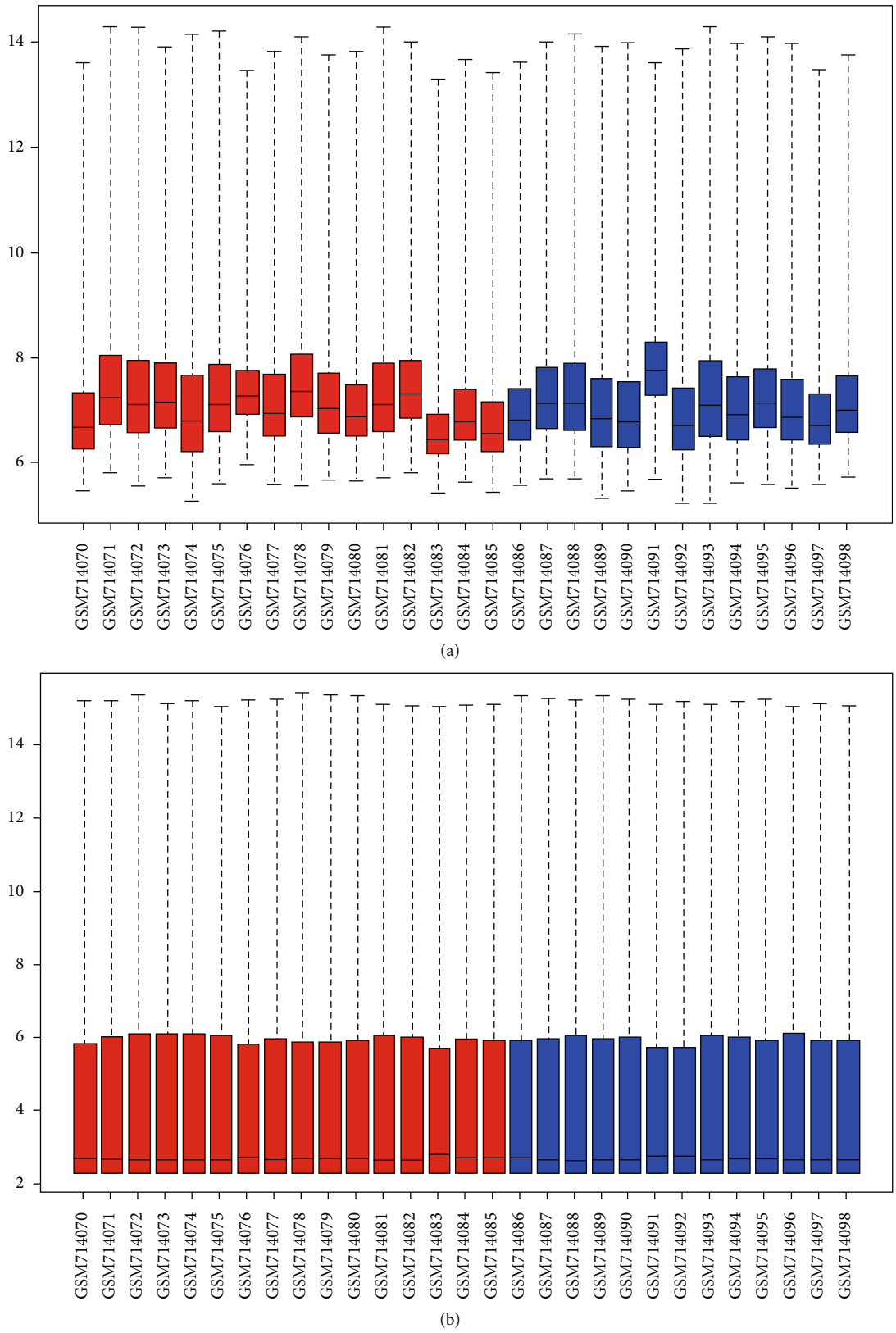

Figure 2: Box plots for the gene expression data. Red bars represent advanced atherosclerotic plaque samples, and blue bars represent early atherosclerotic plaque samples. The black lines in each box represent the median gene expression level. (a) The black lines of raw data are not at the same level. (b) After data processing, the black lines are almost at the same level.

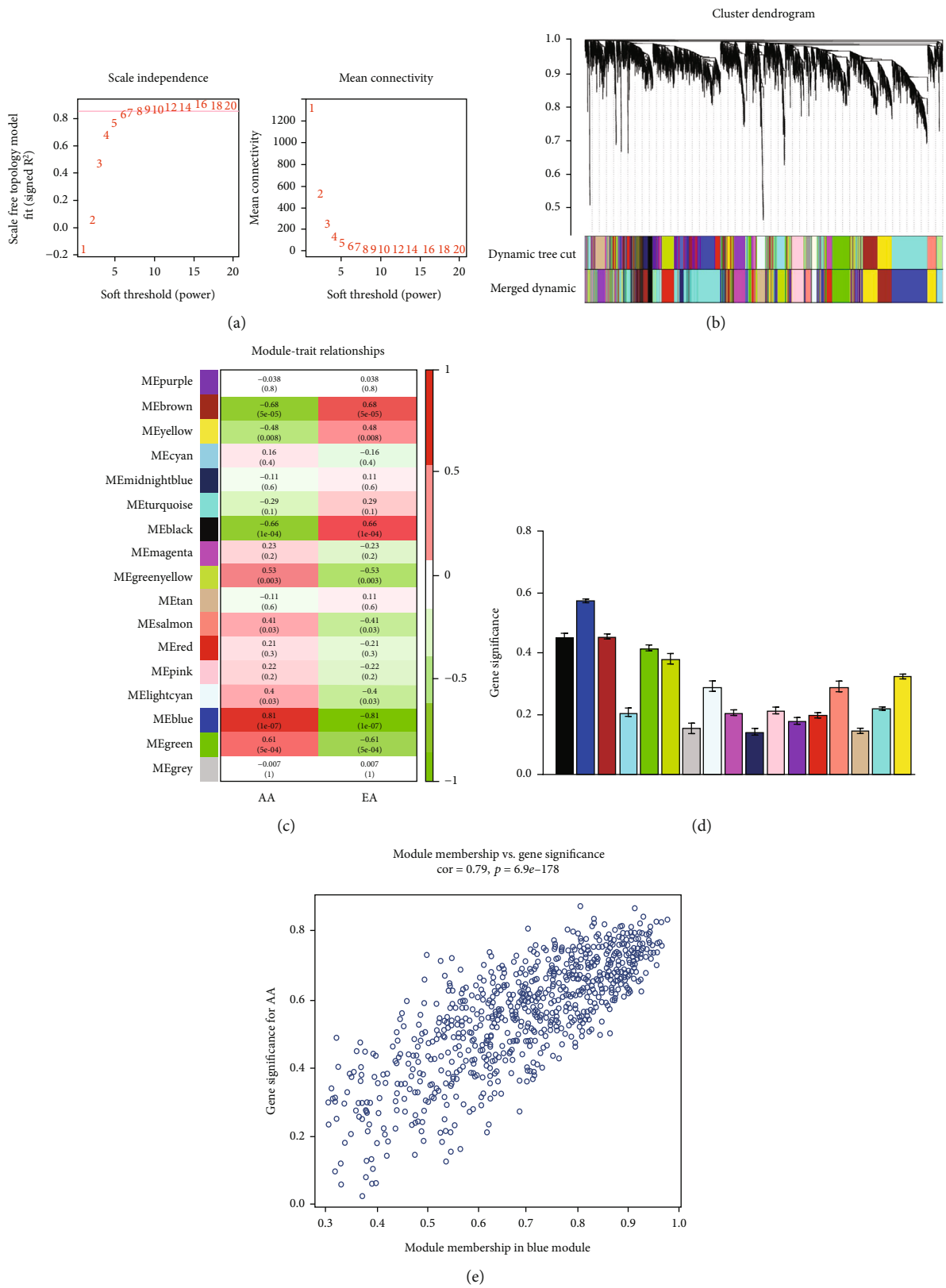

Figure 3: Gene coexpression networks in samples of GSE28829 and module trait correlation analysis of key coexpression network. (a) Analysis of the scale-free index for soft-thresholding powers and 0.85 were used as the correlation coefficient threshold, and the best soft-thresholding power was 7. (b) Gene dendrogram and modules colors of 29 samples in GSE28829. (c) Heatmap of the correlation between modules and AA and EA. (d) Module significance values of all the 17 coexpression modules associated with AA. (e) The gene significance for AA in the blue module.

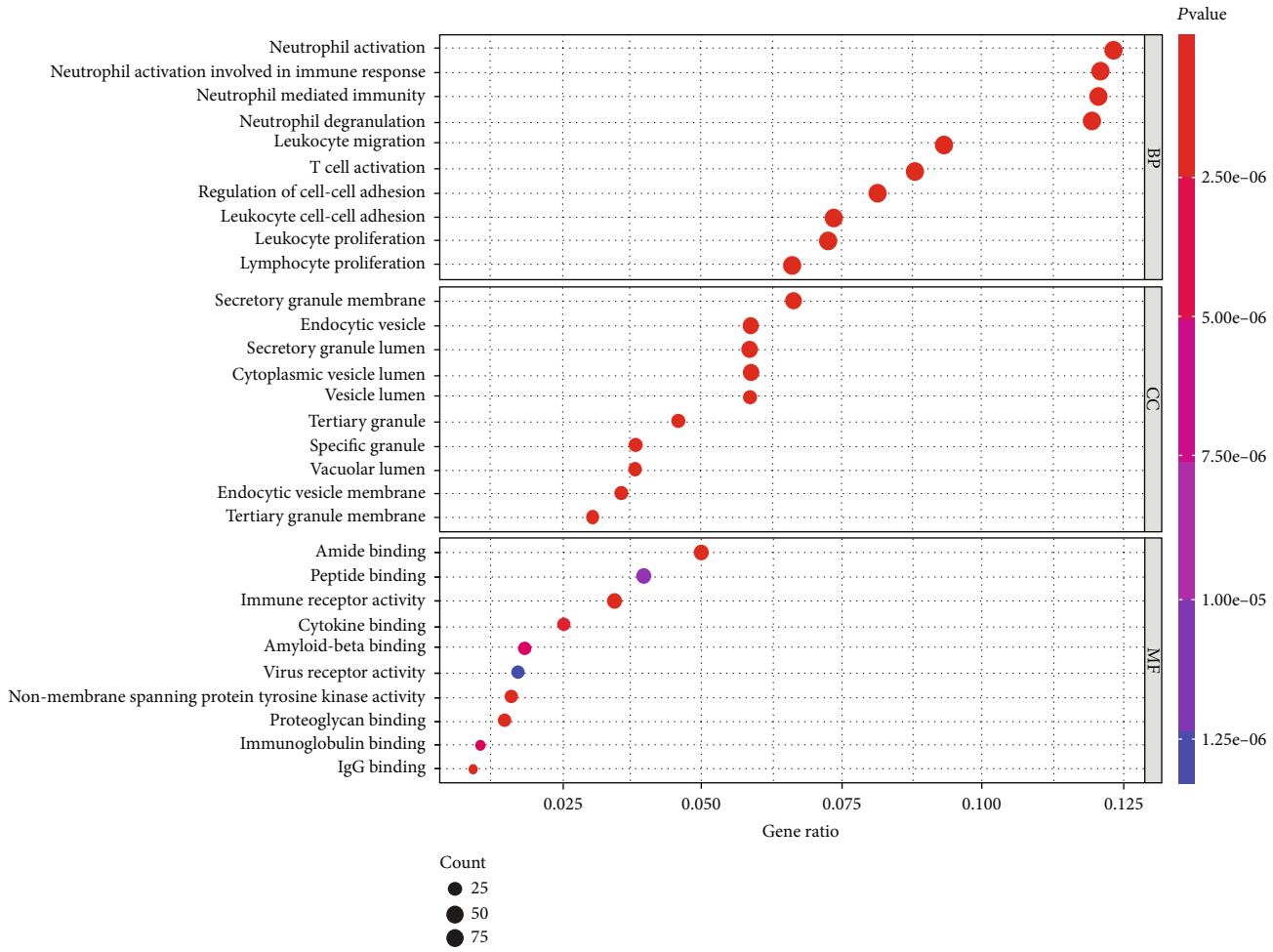

(a)

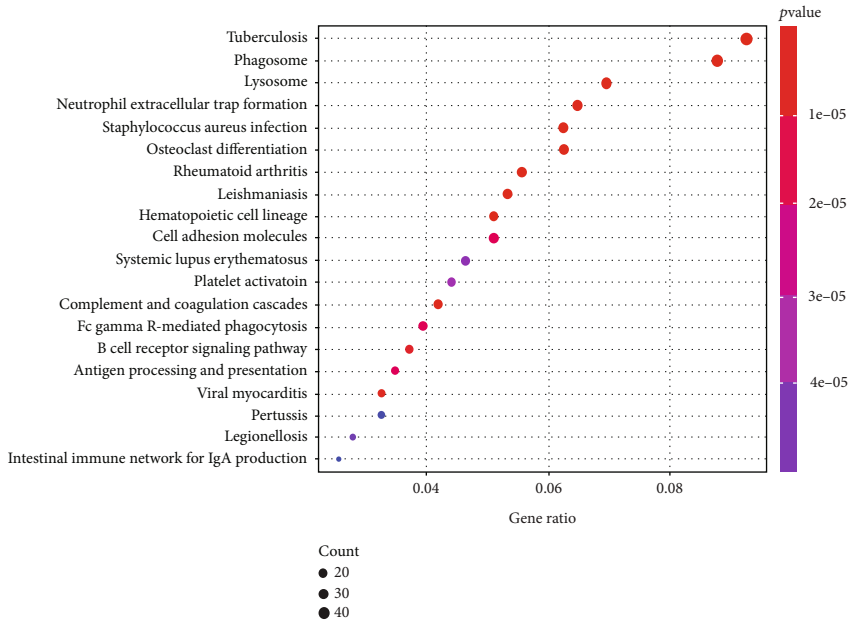

(b)

Figure 4: Continued.

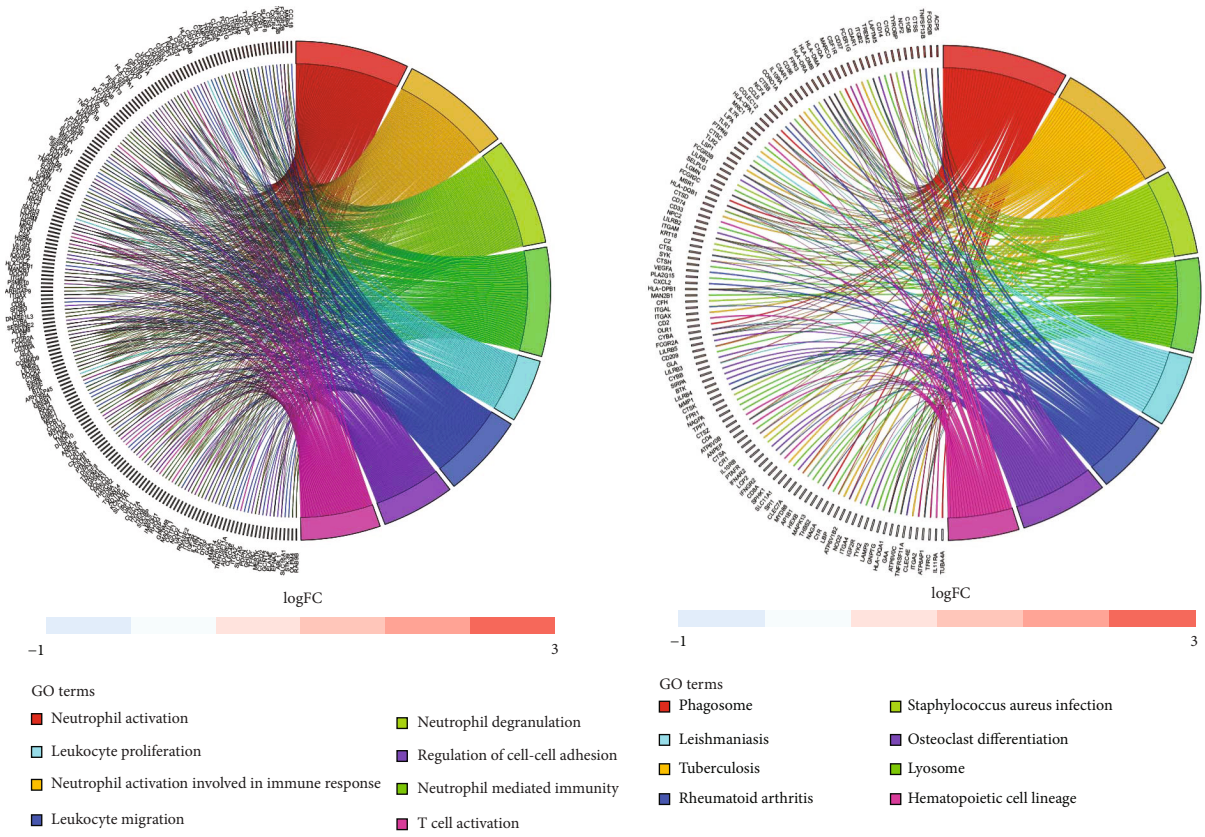

(c) (d)

Figure 4: Functional enrichment analysis for blue module of AA plaque. (a) Biological process, cellular component, and molecular function analysis. (b) KEGG pathway analysis. (c) The relationship between genes and GO terms. (d) The relationship between genes and KEGG terms.

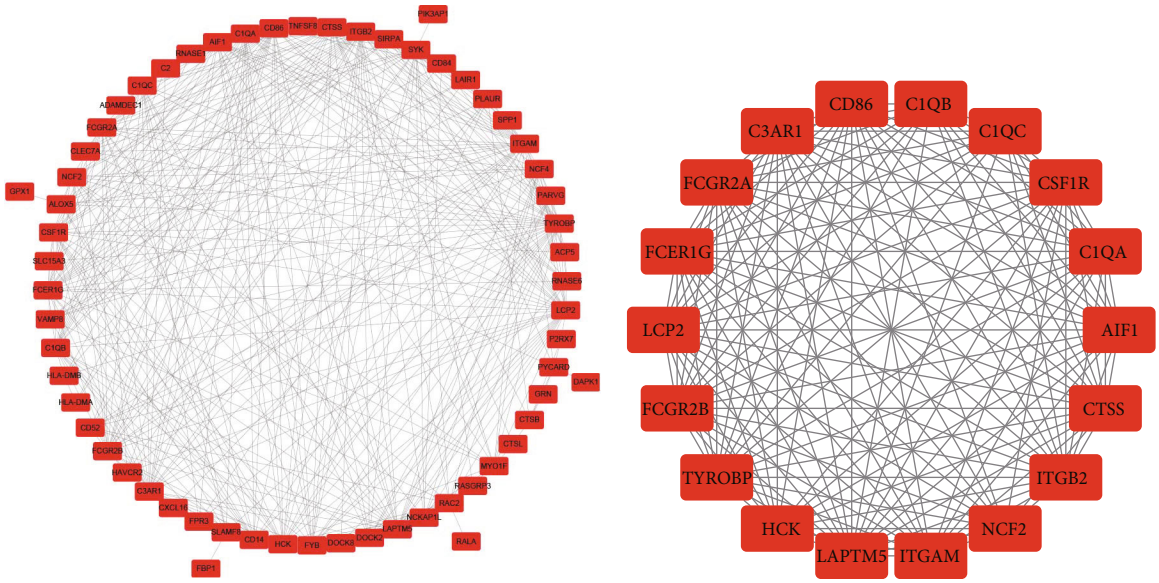

(a) (b)

Figure 5: The PPI network of blue module and significant subnetwork of network. (a) Protein-protein interaction (PPI) network of the significant genes in blue module after WGCNA. (b) Subnetwork of the module with highest scores in PPI network after MCODE.

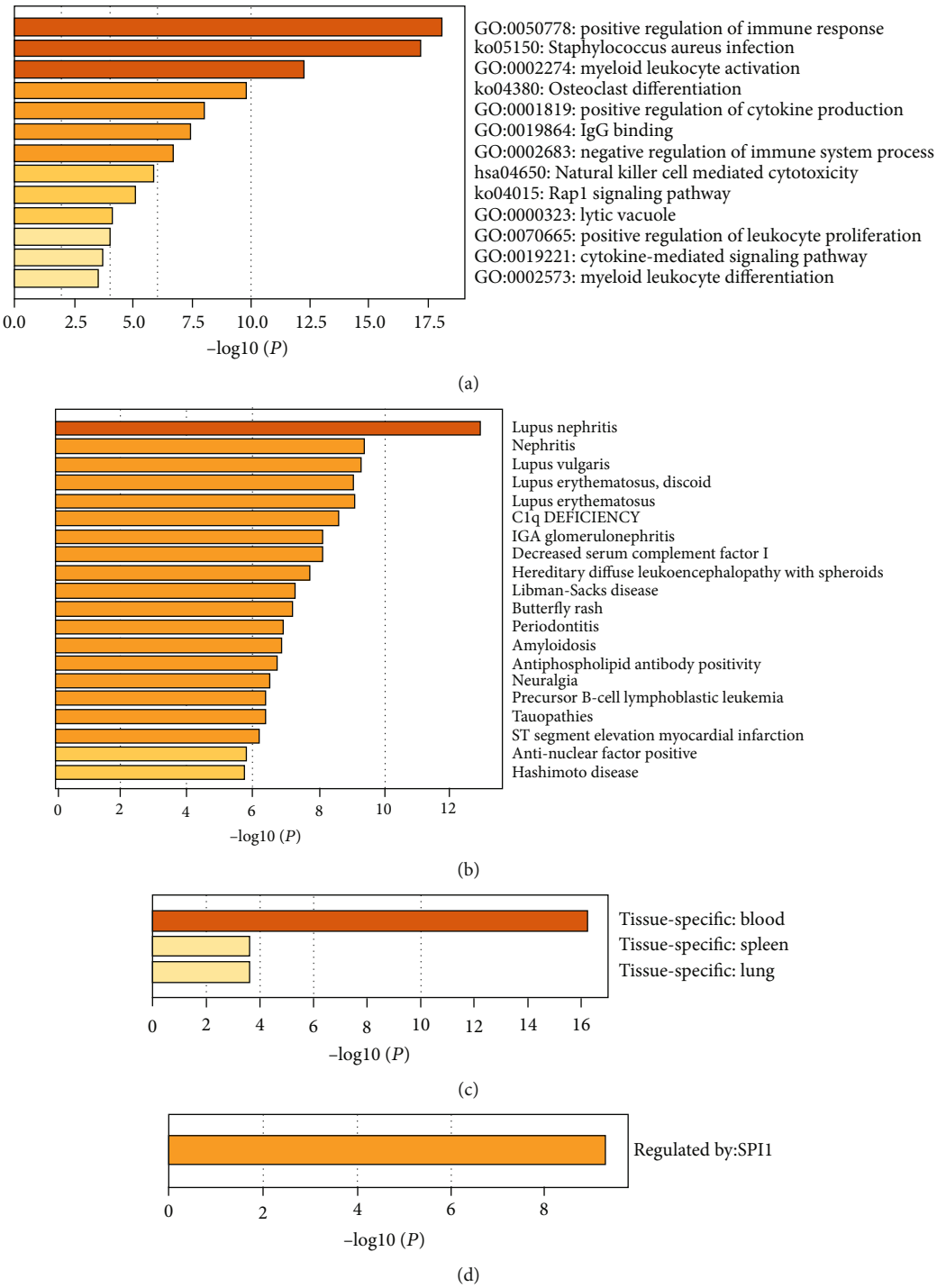

Figure 6: Multidatabase analysis of hub genes. (a) Biological functions of hub genes. (b) Disease enrichment related to hub genes involved in AA. (c) Enrichment of genes in specific tissues. (d) Enrichment of transcriptional regulators of hub genes.

The expression levels of all 10 of the key genes were tested in GSE43292. The results (Figure 8) showed that all of the key genes were highly expressed (all $P < 0.001$) in AA plaques as compared to EA in GSE43292. Furthermore, we plotted the ROC and calculated the AUCs for the key genes and found that all of the AUCs of key genes were greater than 0.8 in GSE28829 (Figure 9(a)) and GSE43292 (Figure 9(b)).

3.6. Gene Set Enrichment Analysis. The full list of gene sets enriched in AA plaques with those 10 key genes was highly expressed using GSEA (Figure 10). All of the gene sets were mainly related to immunity and inflammation. In addition, AIF1 (Figure 10(i)) was also related to oxidative phosphorylation and allograft rejection. The gene sets related to immunity and inflammation were selected to perform further analysis. The gene sets "complement," "inflammatory

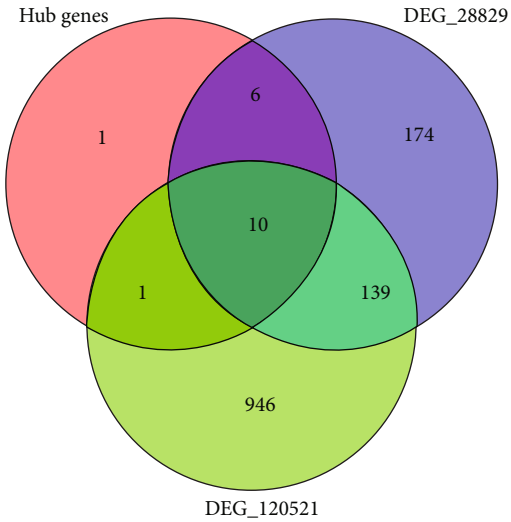

Figure 7: Key genes selection. A total of 10 common genes related to hub genes and DEGs of GSE28829 and GSE120521.

response," "interferon γ response," and "TNF-α signaling via NF-κB" were enriched in samples with high expression levels of HCK, ITGAM, CTSS, TYROBP, LAPTM5, FCER1G, ITGB2, NCF2, and CD86 (Figure 11). The samples with high AIF1 expression were mainly enriched in "complement," "inflammatory response," and "interferon γ response" (Figure 11(i)).

4. Discussion

Our study applied WGCNA to build the gene network related to AA and found some coexpression networks. Combined with PPI and MCODE plug-in analyses, several key genes associated with the pathogenesis of AA were identified. Our findings broaden the horizons of the mechanism of AS development from early to advanced stages.

In the present study, through the WGCNA analysis, 17 coexpression modules were determined. The blue module, containing 829 genes, was most significantly associated with AA. We performed an enrichment analysis on the genes in the blue module and found that the blue module was mainly enriched in immune and inflammatory pathways. In recent decades, a lot of research has been conducted to examine the immune and inflammatory mechanisms in AS. Researchers have found that inflammation is closely related to AS and plaque instability [30]. Monocyte-differentiated macrophages become foam cells after ingesting lipids, and foam cells can cause cell adhesion, matrix degradation, and inflammatory cell infiltration by secreting inflammatory factors, which can lead to plaque rupture [31]. The activation of neutrophils can be affected by oxidatively modified low-density lipoprotein (oxLDL), thereby enhancing the formation of a neutrophil extracellular trap (NET). After the formation of NET, the enzymes released by neutrophils can induce the oxidative modification and/or degradation of LDL, produce modified proinflammatory LDL, and promote the further activation of neutrophils [32]. NET can also aggravate endothelial dysfunction, causing plaque instability and weakening of the fibrous cap, leading to AS and thrombosis [33]. Th1 cells mainly promote inflammation, while Th2 cells show a dual role not only slightly promoting the occurrence of AS but also inhibiting the development of AS [34]. Regulatory T cells mainly inhibit the formation of AS [35, 36]. Therefore, our research also confirmed that immune cells are involved in the formation of AA plaques.

In order to find genes that are more closely related to AA in the key module, we selected 77 significant genes from the blue module for further analysis by setting the MM and GS values. By constructing the PPI network, we harvested the subnetwork with the highest score from significant genes, which had a total of 18 hub genes. We conducted a Metascape analysis, and the results showed that the genes are related to many biological functions, including positive regulation of immune response, *Staphylococcus aureus* infection, myeloid leukocyte activation, and osteoclast differentiation. These biological functions are also related to immune cells, which further confirms the role of immune response in AA. According to the results of the TRRUST database analysis, SPI1 is the main regulatory transcription factor for these genes. It has been reported that the expression of SPI1 increased during the differentiation process of myeloid cells, while the expression in differentiated mast cells, monocytes, B cells, and peripheral blood neutrophils maintained high levels [37]. The DisGeNET database analysis showed that these genes are closely related to systemic lupus erythematosus (SLE) and other diseases. The common point of SLE and AS is inflammation as the main feature, and the difference is that the inflammation of SLE is autoimmune, which impairs several organ systems, including the cerebrovascular and cardiovascular systems [38, 39]. The enhanced proinflammatory state and systemic inflammation play an important role during the formation of atherosclerotic thrombosis [38]. AS may also be accelerated by systemic inflammation. Therefore, the prevalence of AS in SLE patients is greater than that in the general population [40]. Tissue characteristic enrichment analysis indicated that these genes were enriched in the blood, spleen, and lung. It also revealed that the tissue distribution of genes has a strong correlation with immunity. The multidatabase analysis further confirmed that the hub gene related immune and inflammatory response plays an important role in AA and helped us to understand the pathogenesis of AA from more aspects.

We also incorporated the DEGs of GSE28829 and GSE120521 for combined analysis. Finally, we found 10 key genes: HCK, ITGAM, CTSS, TYROBP, LAPTM5, FCER1G, ITGB2, NCF2, AIF1, and CD86. ITGAM and ITGB2 encode the αM chain and β2 chain of integrin, respectively. Under the stimulation of inflammation and thrombus, the αM β2 integrin can mediate the adhesion of neutrophils and monocytes to endothelial cells [41]. HCK is a signal transduction protein that mainly transmits membrane receptor signals. It plays an important role in the innate immune response by regulating the phagocytosis of neutrophils and the proliferation and migration of macrophages [42]. It is reported that after knocking out HCK, the endothelial adhesion and migration in AS plaques will

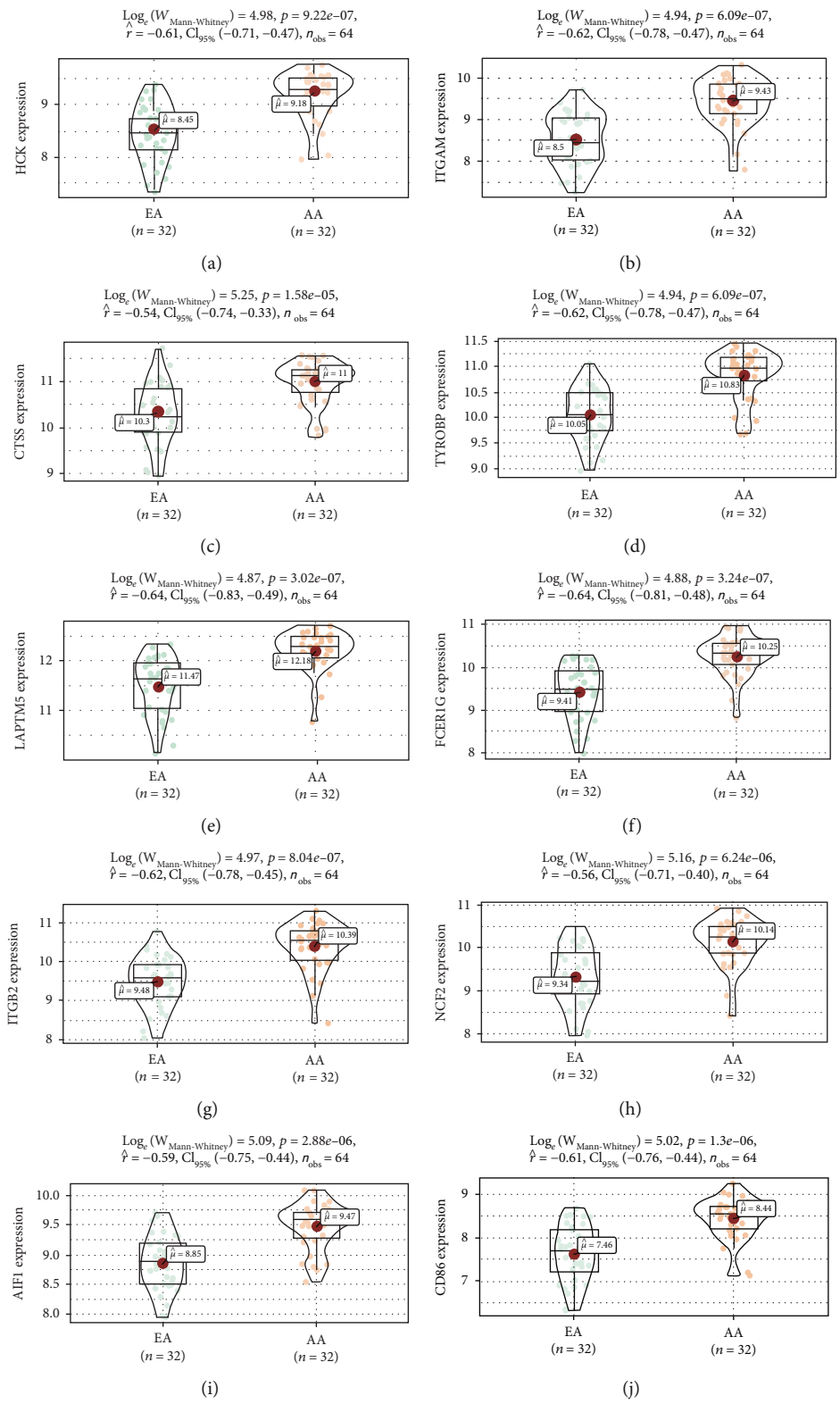

Figure 8: Validation of key genes in dataset GSE43292. (a) HCK. (b) ITGAM. (c) CTSS. (d) TYROBP. (e) LAPTM5. (f) FCER1G. (g) ITGB2. (h) NCF2. (i) AIF1. (j) CD86.

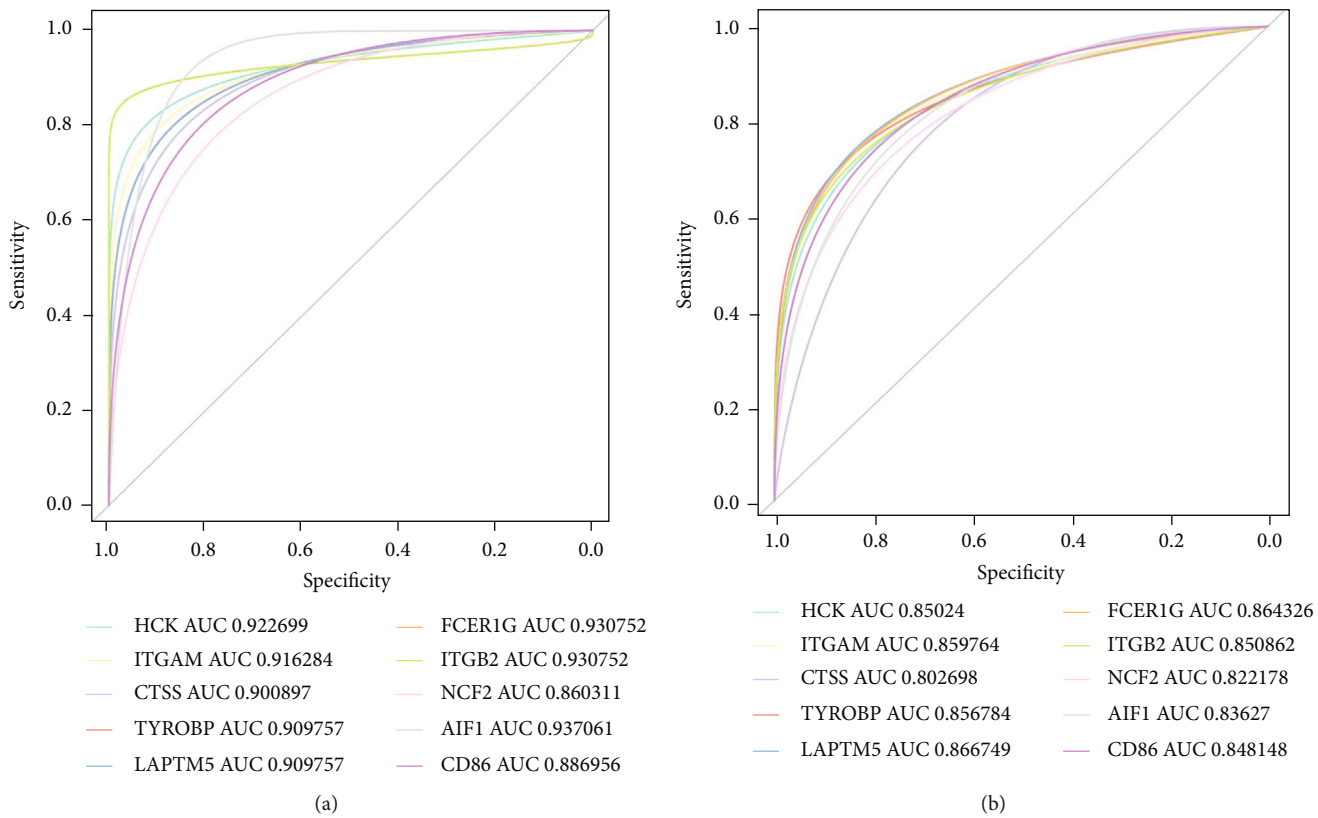

Figure 9: ROC curve of key genes. (a) ROC curve for GSE28829. (b) ROC curve for GSE43292.

be weakened, leading to decreases in plaque formation [43]. Interestingly, the same study found that after HCK knockout, monocytes had a subpopulation imbalance and accumulated under the endothelium, which increases the instability of the plaque. Our research showed that the high levels of HCK expression in AA are a risk factor for the further development of AS. We estimate that the different effects may be related to different stages of AS, such as the difference between AA and EA. Whether it protects or aggravates AS and what its mechanism needs to be further explored. TYROBP, also known as DAP12, is a transmembrane receptor widely found in neutrophils and monocytes/macrophages [44, 45]. Studies have found that DAP12 seems to be related to lipid deposition and plaque inflammation in the process of promoting AS [46]. CTSS can degrade antigen proteins into peptides and can also reshape the components of the extracellular matrix [47]. Previous studies have shown that CTSS is expressed by endometrial macrophages and smooth muscle cells and that it participates in the formation of AS, together with serine proteases and MMP [48]. NCF2 is a neutrophil solute factor that encodes a subunit of NADPH oxidase [49]. NADPH oxidase is the main source of reactive oxygen species (ROS), which mainly play the roles of antibacterial, anti-inflammatory, and redox signal transduction [50]. Researchers pointed out that NADPH oxidase and the ROS produced are significantly related to hypertension [51]. Oxidative stress is a risk factor for AS. Some studies have suggested that NADPH may be involved in the promotion of atherosclerotic inflammation [52]. However, there is no direct evidence that NCF2 is involved in the progression of AS. AIF1 is mainly expressed in cells of the monocyte lineage [53]. In vitro, AIF1 can enhance the phagocytosis and lipid uptake of macrophages [54] and can also increase the proliferation and migration of macrophages, inducing inflammation [55]. LAPTM5 positively regulates proinflammatory signaling pathways by promoting NF-κB and MAPK signaling and the production of proinflammatory cytokines in macrophages [56]. At present, FCER1G and CD86 are rarely studied in the cardiovascular system.

Our research showed that not only these key genes are significantly increased in AA plaques of GSE28829 but also, more importantly, their expression levels were verified in another dataset (GSE43292). We also found that these genes are mainly enriched in "complement," "inflammatory response," "interferon γ response," and "TNF-α signaling via NF-κB." In fact, the roles of the above pathways in AS have been frequently studied. For example, TNF-α can guide inflammatory cells to accumulate in atherosclerotic plaques, affect plaque stability, and cause thrombosis and cell necrosis [57, 58]. And the plaque stability affection of TNF-α underlines its role in promoting the formation of AA. IFNγ affects immune cells, endothelial cells, and smooth muscle cells in AS plaques [59, 60]. This also further confirms the connection between these genes and immune cells, which is consistent with existing research.

As a whole, some previous studies have resolved the relationship between key genes and AS/AA, while our research

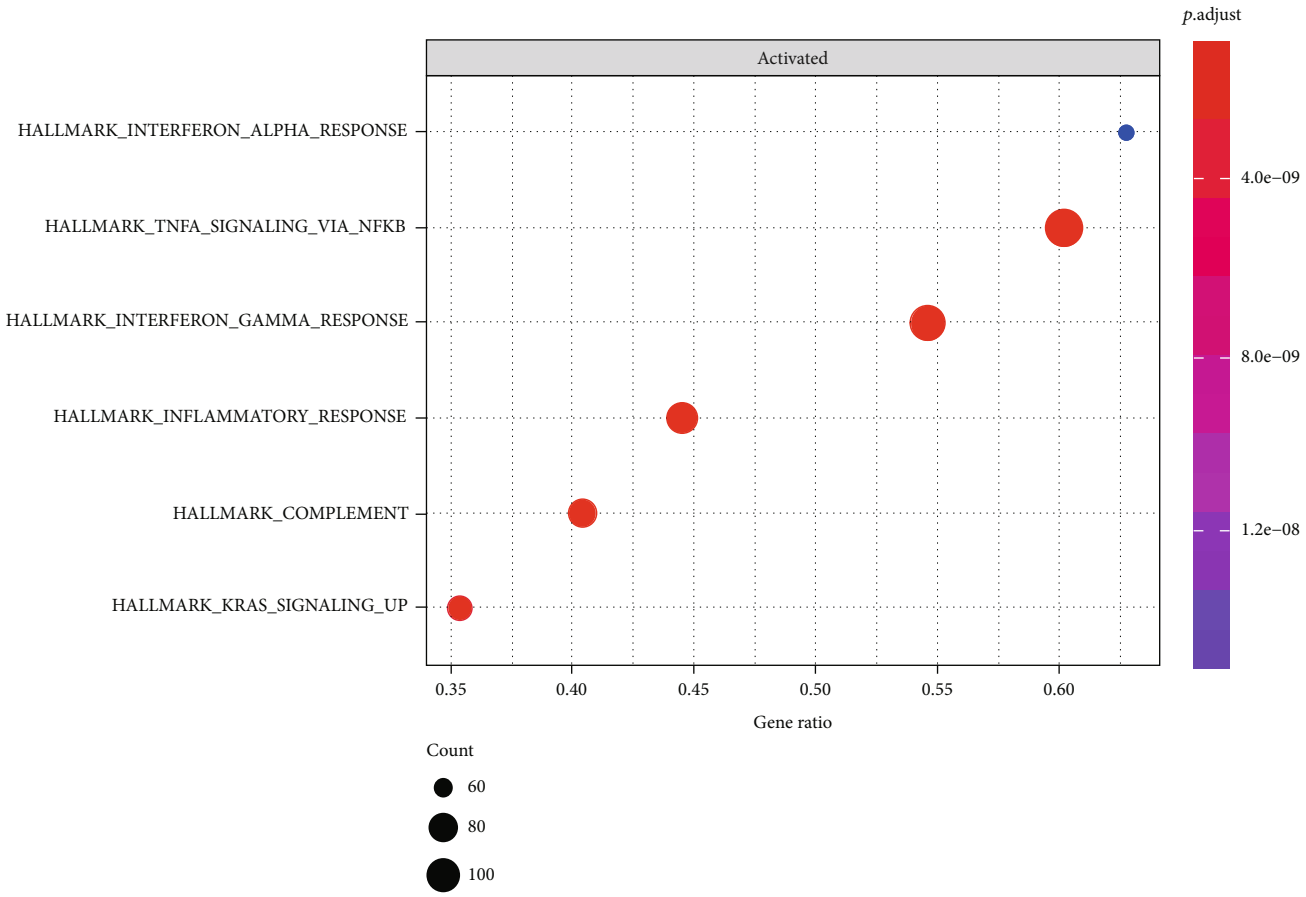

(a)

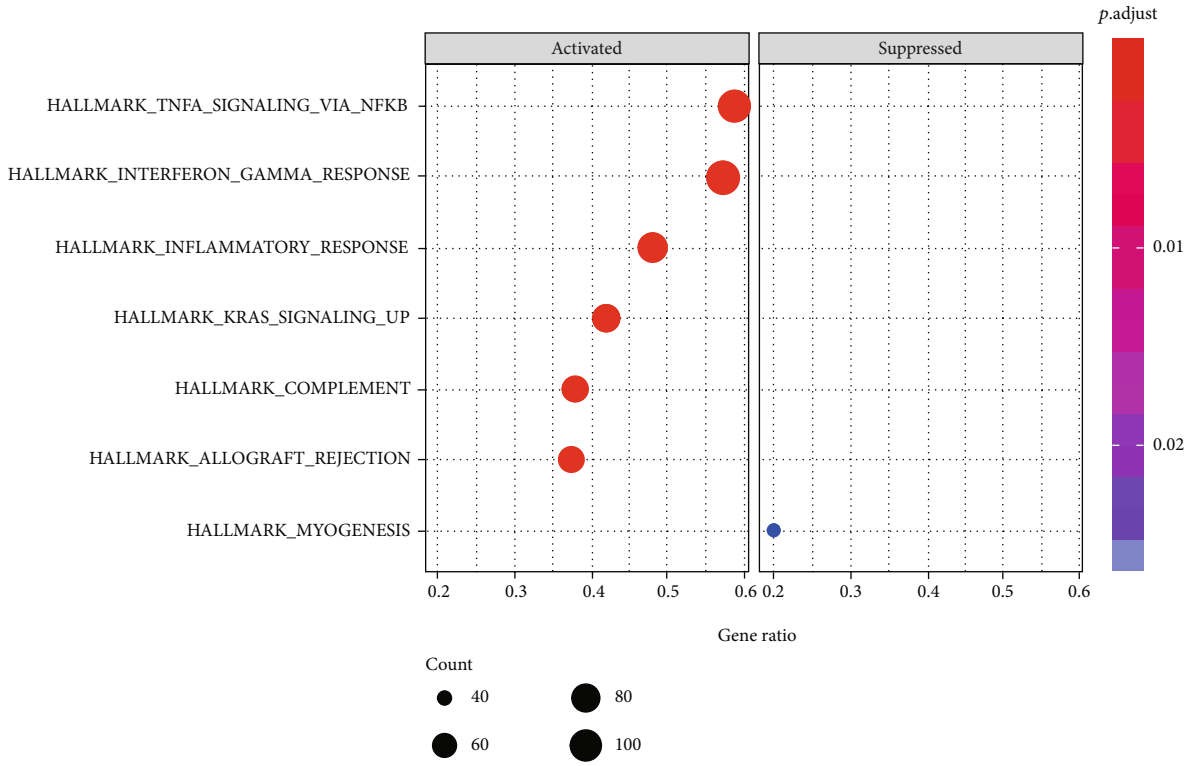

(b)

Figure 10: Continued.

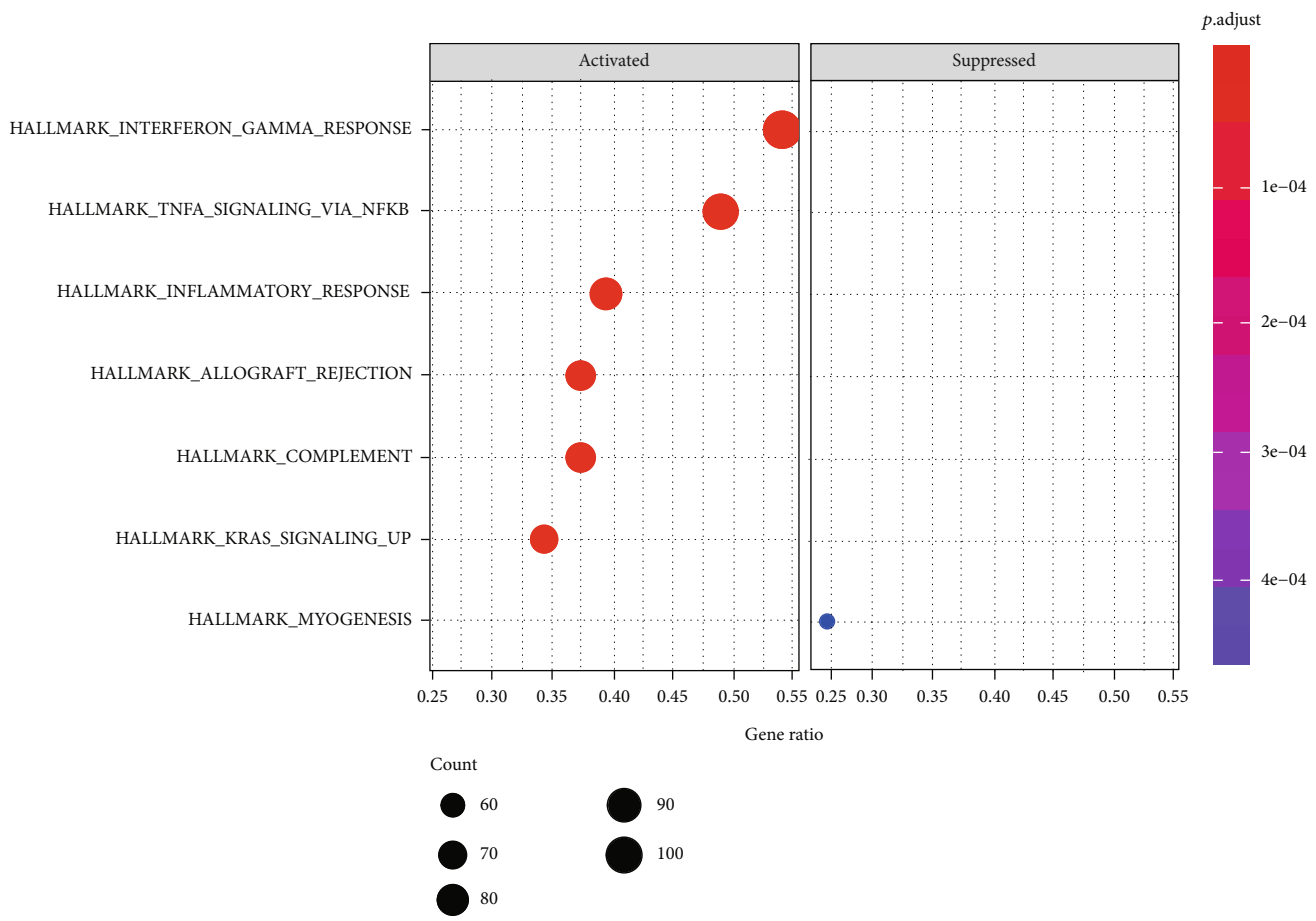

(c)

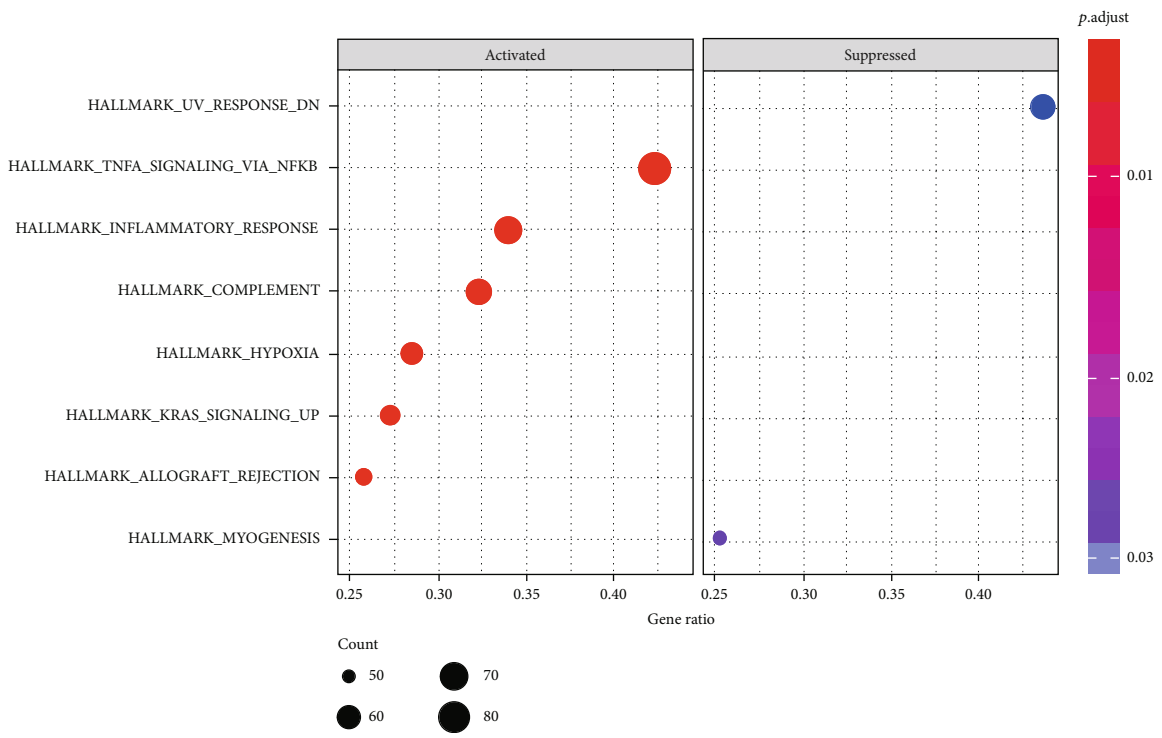

(d)

Figure 10: Continued.

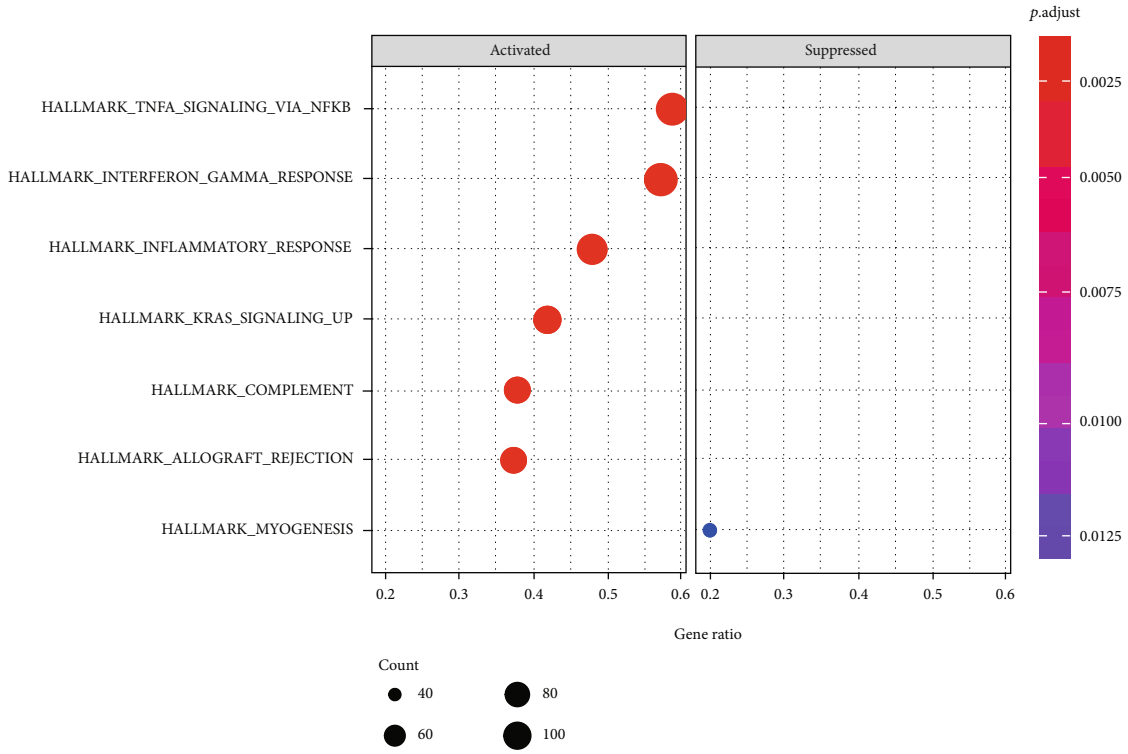

(e)

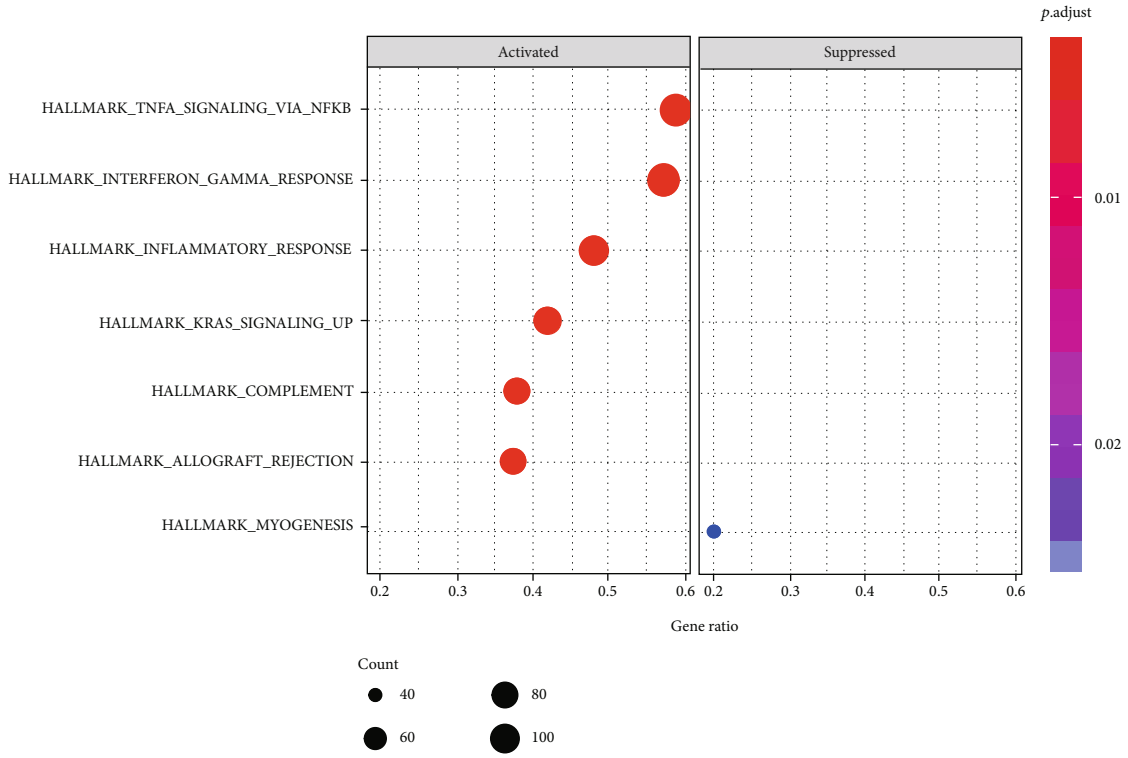

(f)

Figure 10: Continued.

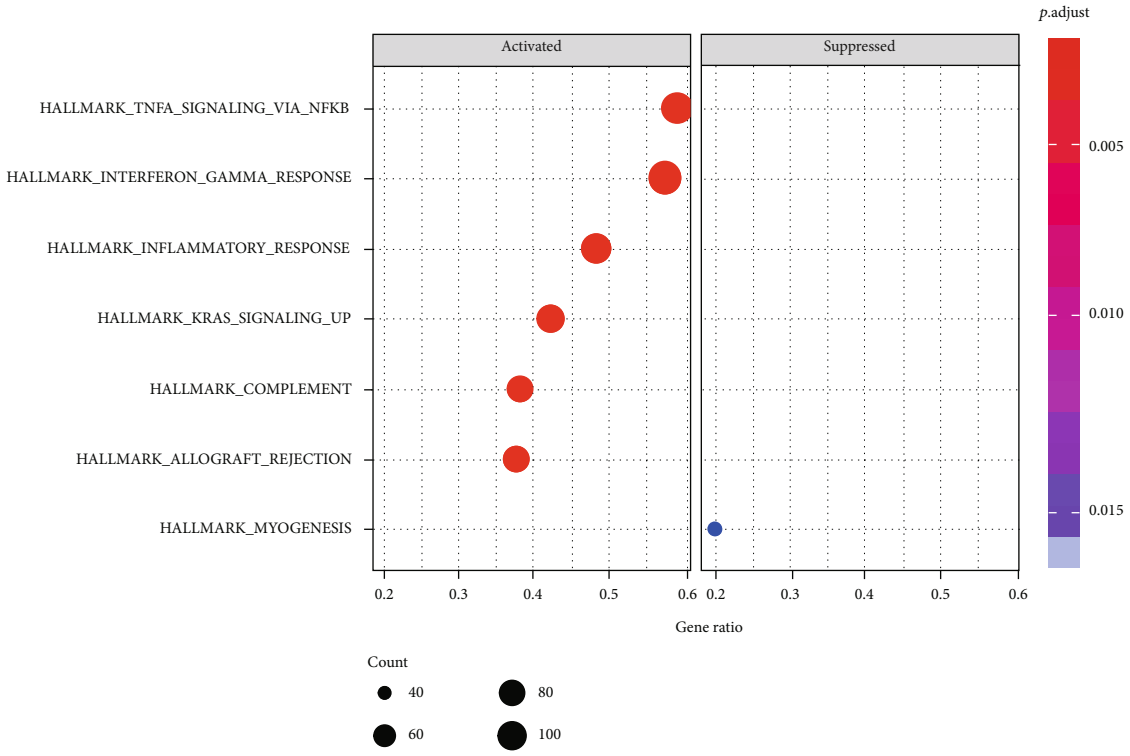

(g)

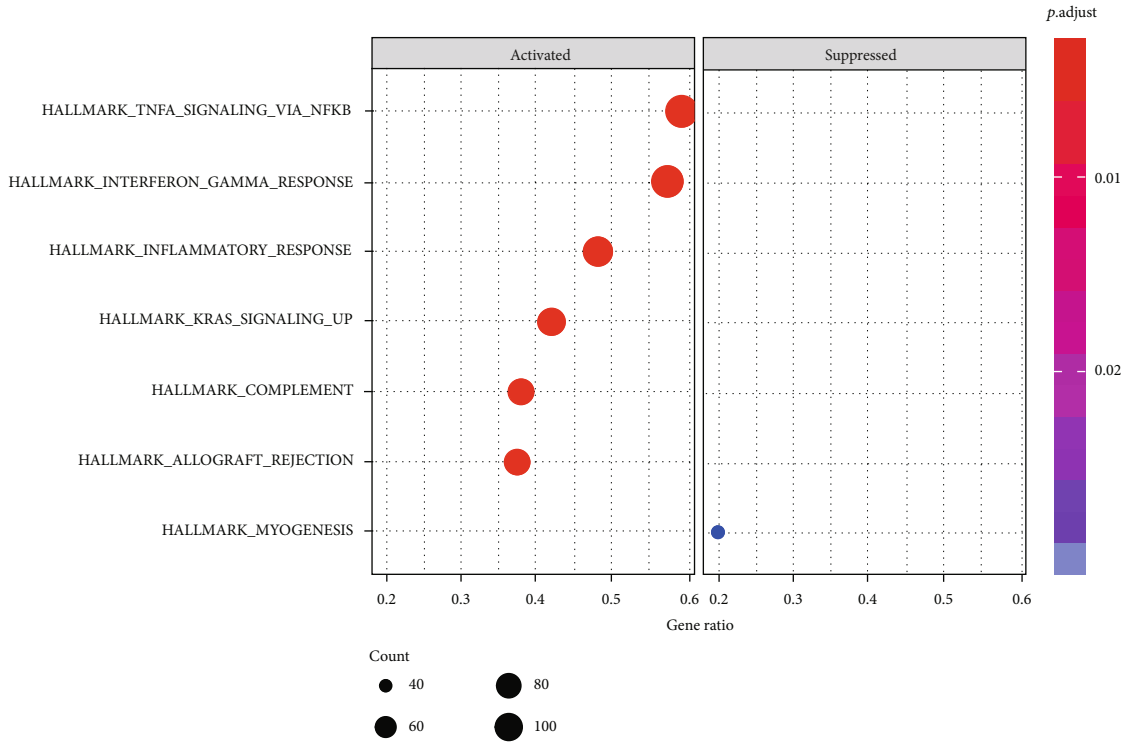

(h)

Figure 10: Continued.

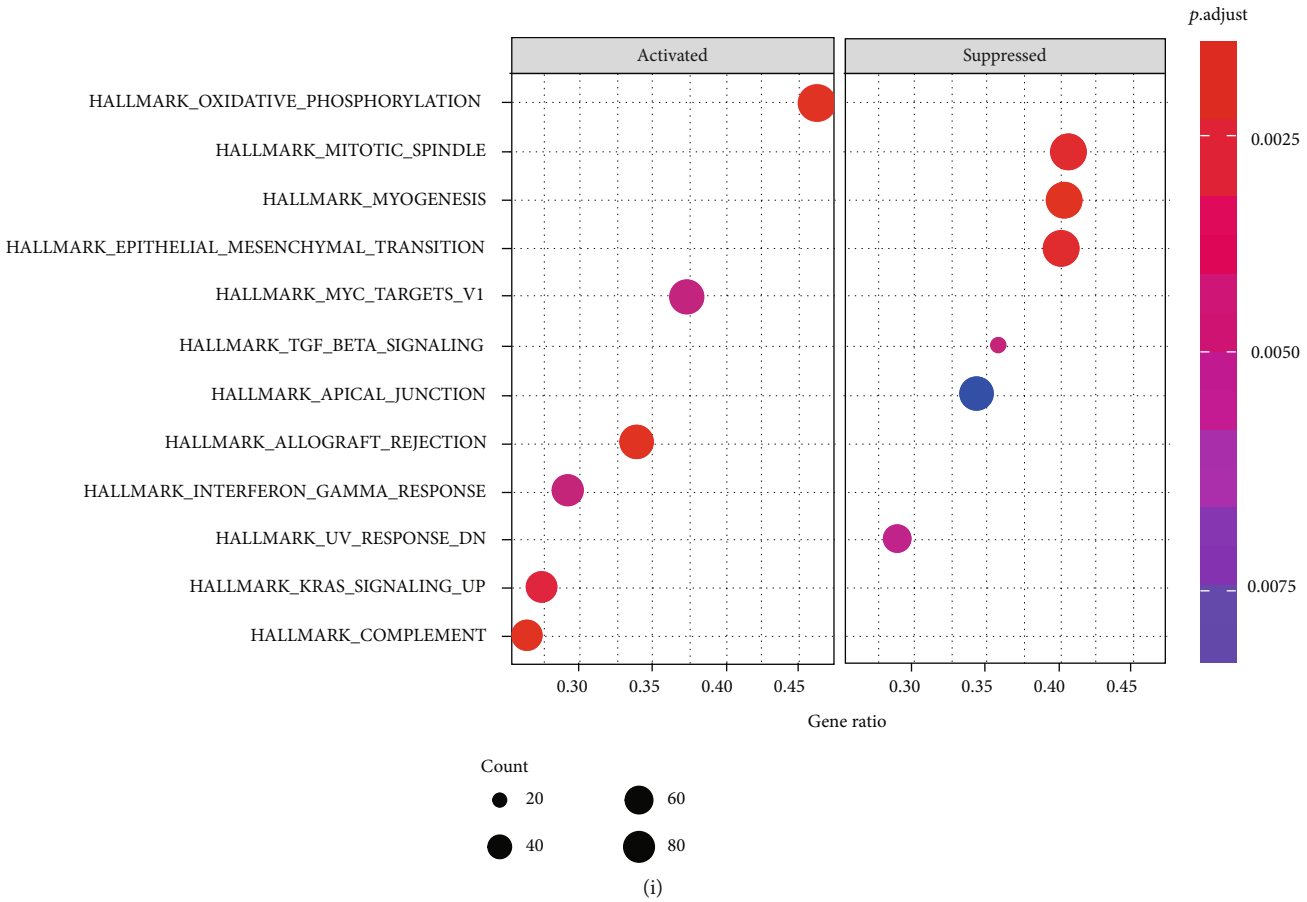

(i)

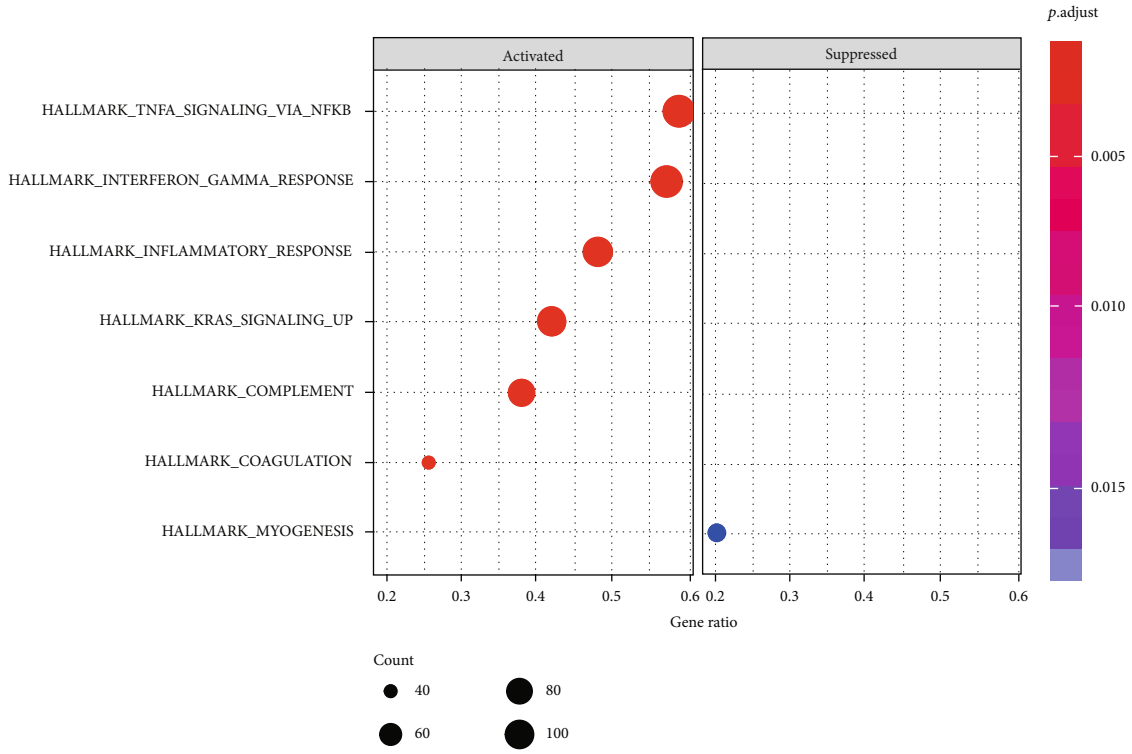

(j)

Figure 10: Gene set enrichment analysis for key genes. (a) HCK. (b) ITGAM. (c) CTSS. (d) TYROBP. (e) LAPTM5. (f) FCER1G. (g) ITGB2. (h) NCF2. (i) AIF1. (j) CD86.

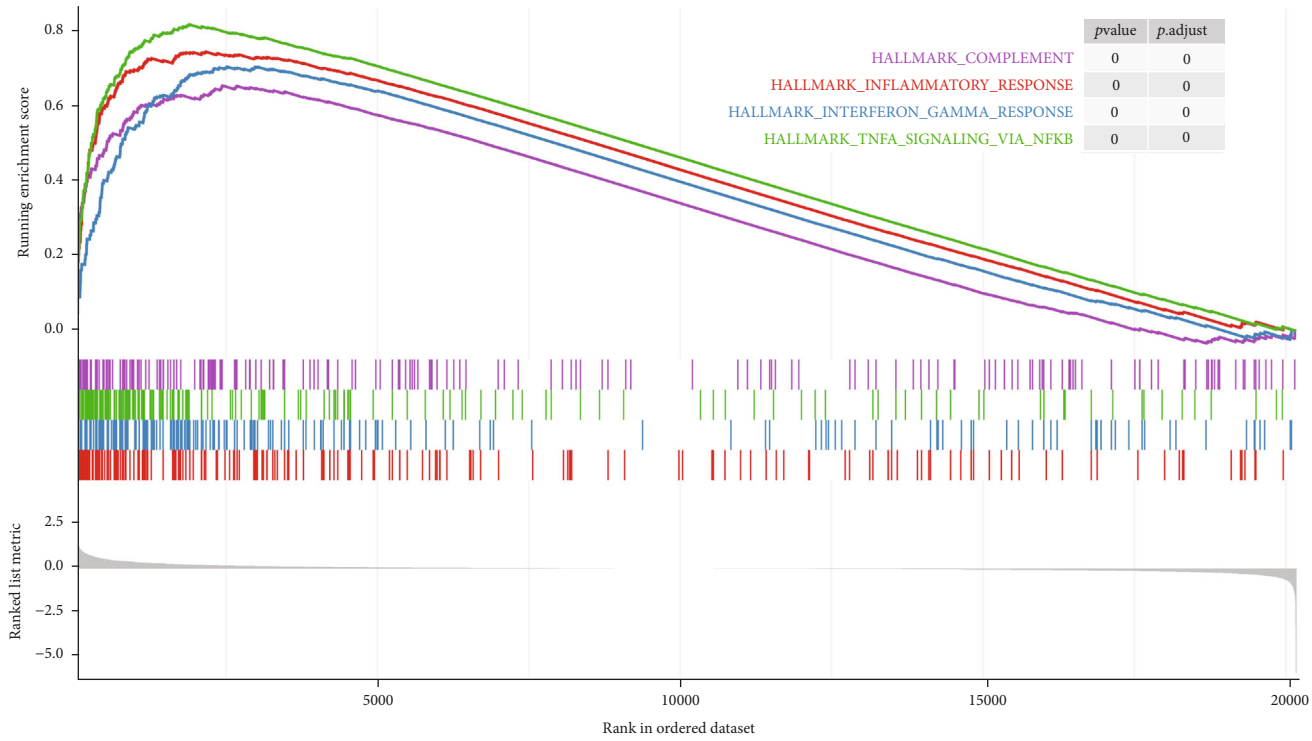

(a)

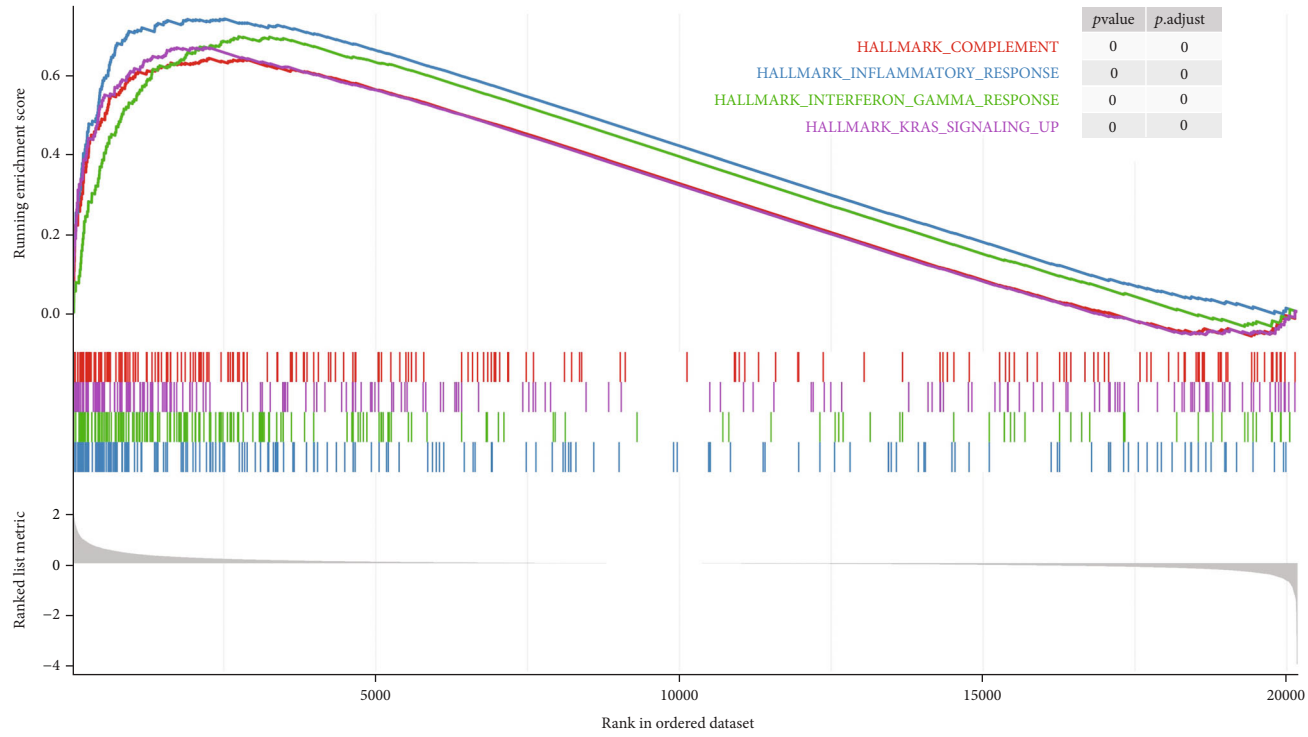

(b)

Figure 11: Continued.

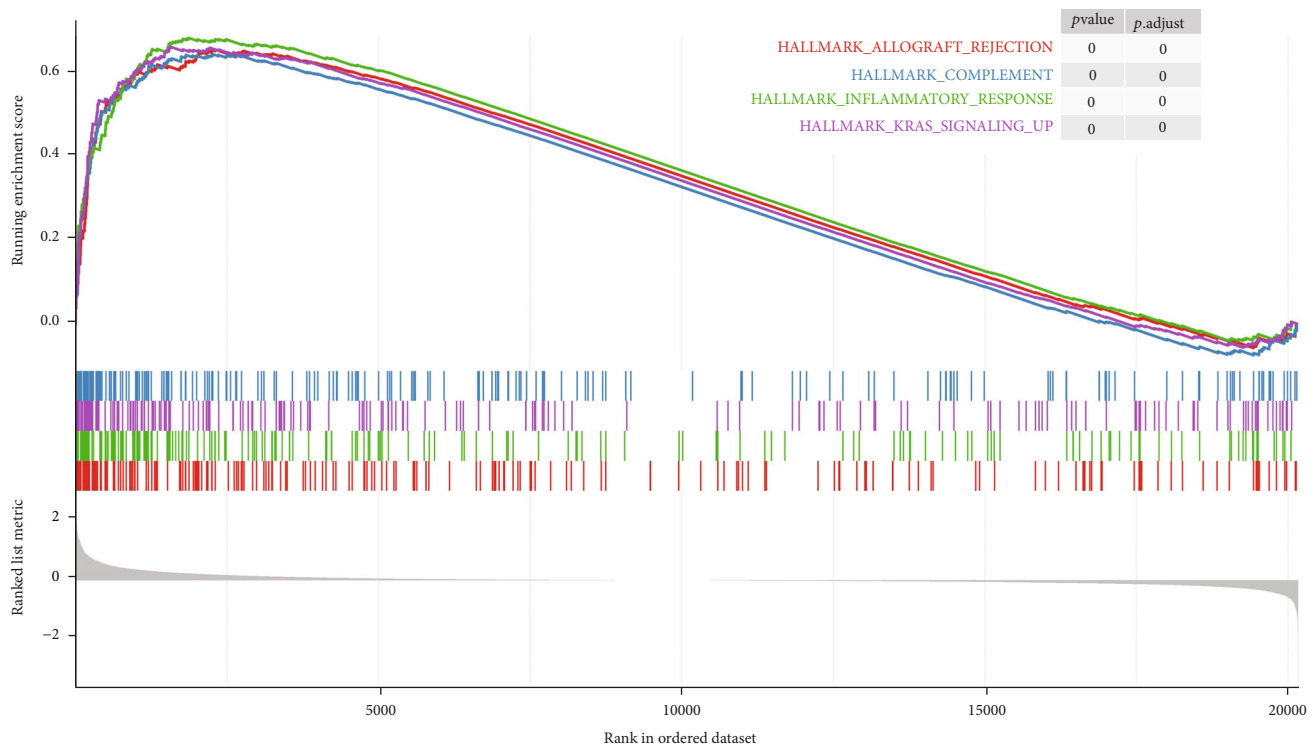

(c)

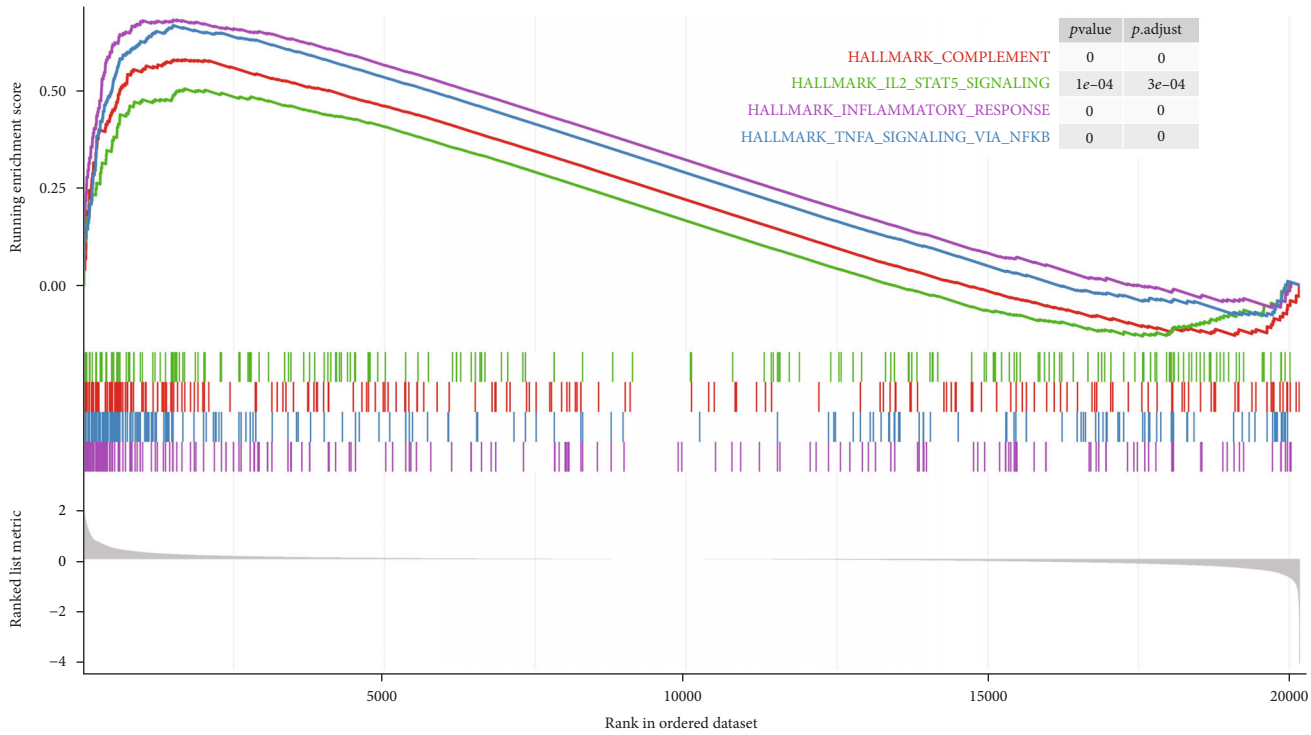

(d)

Figure 11: Continued.

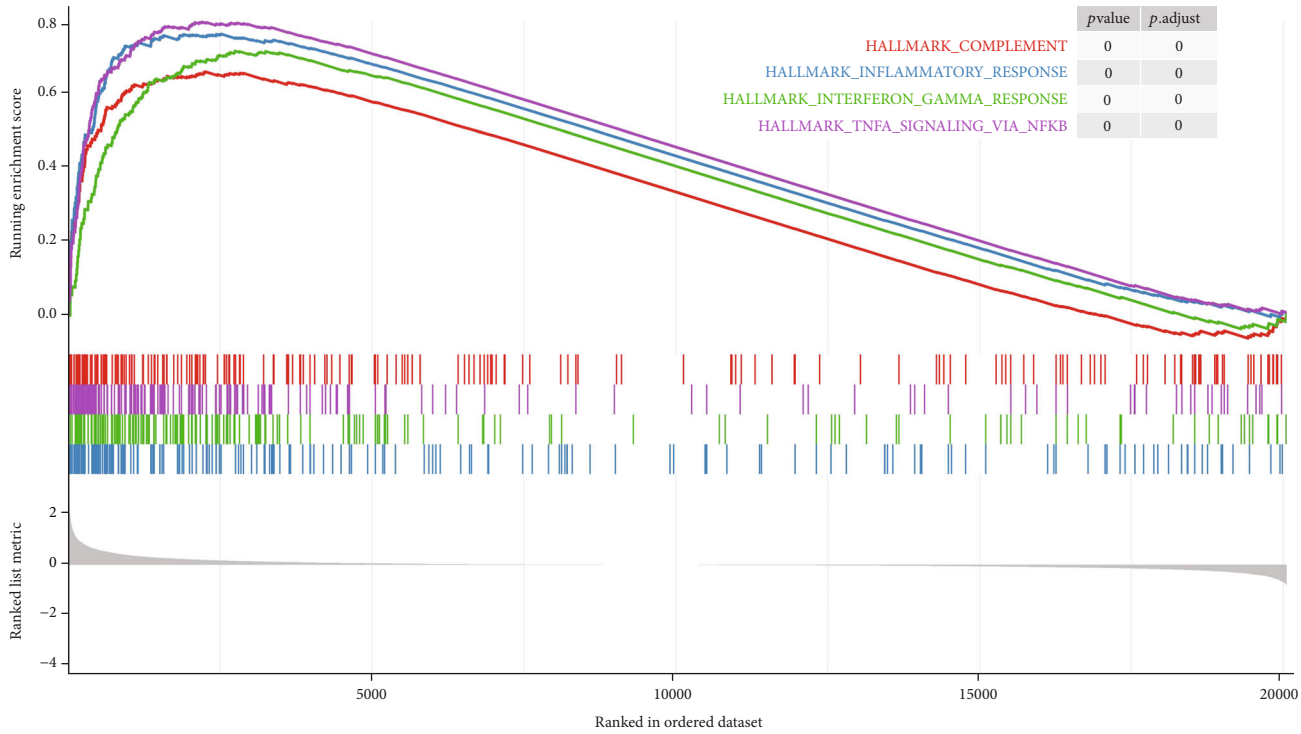

(e)

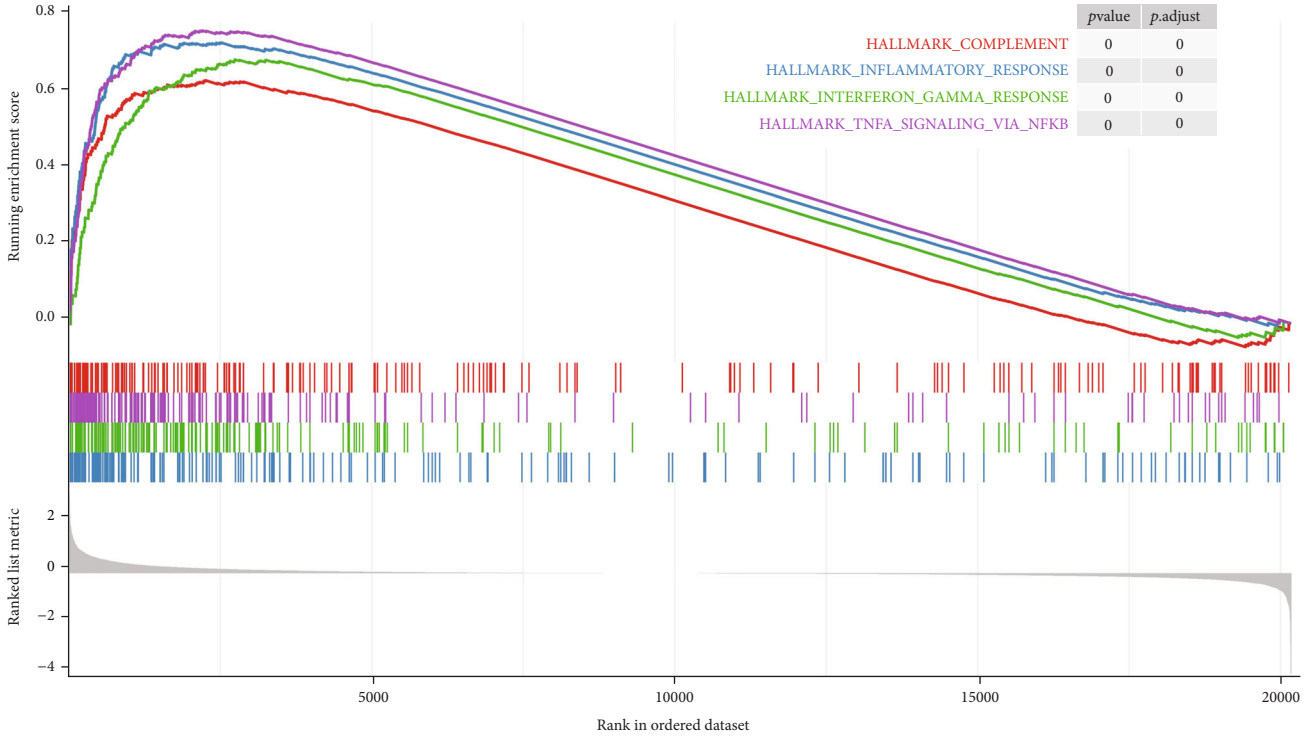

(f)

Figure 11: Continued.

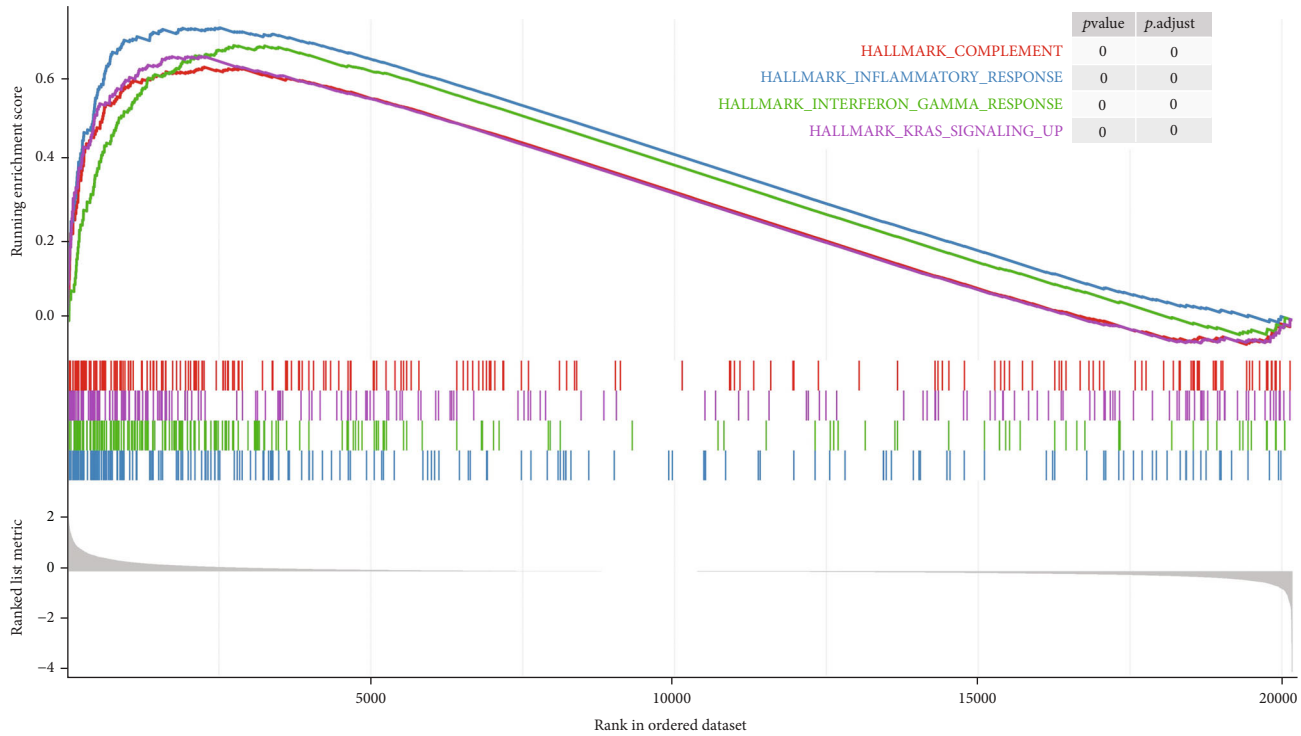

(g)

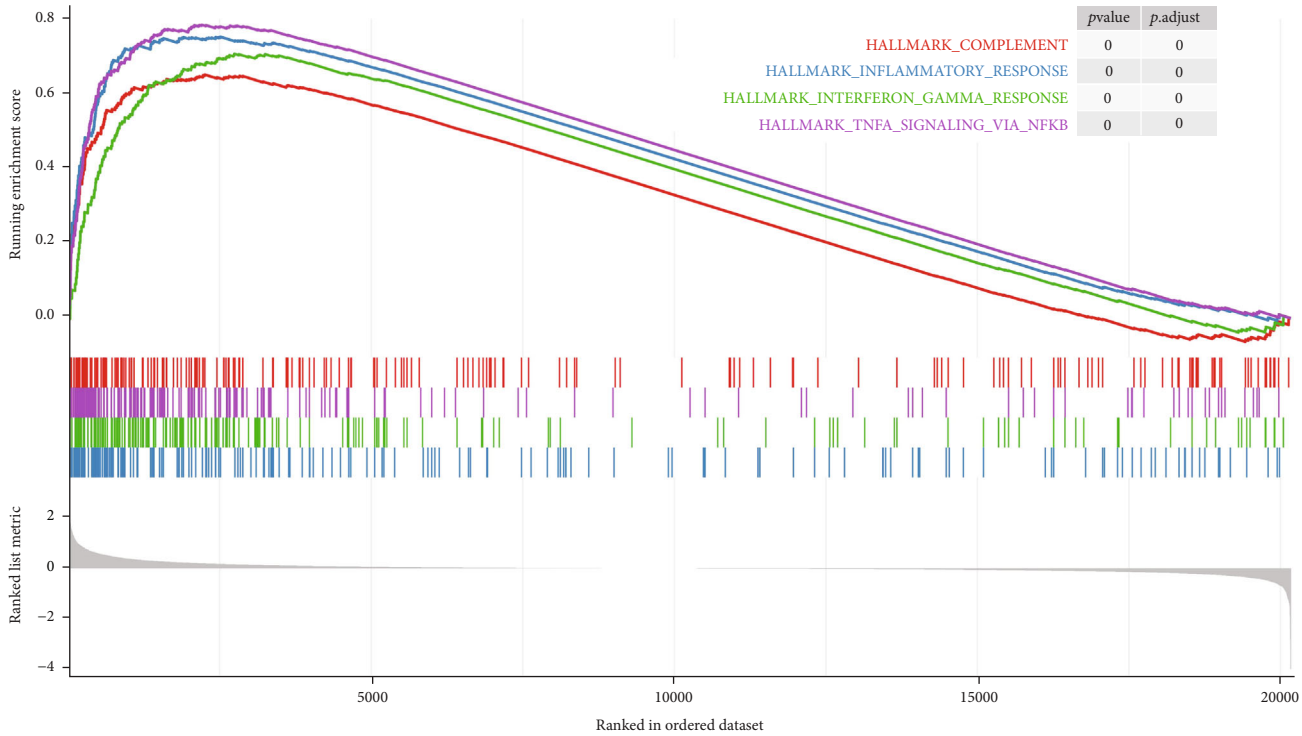

(h)

Figure 11: Continued.

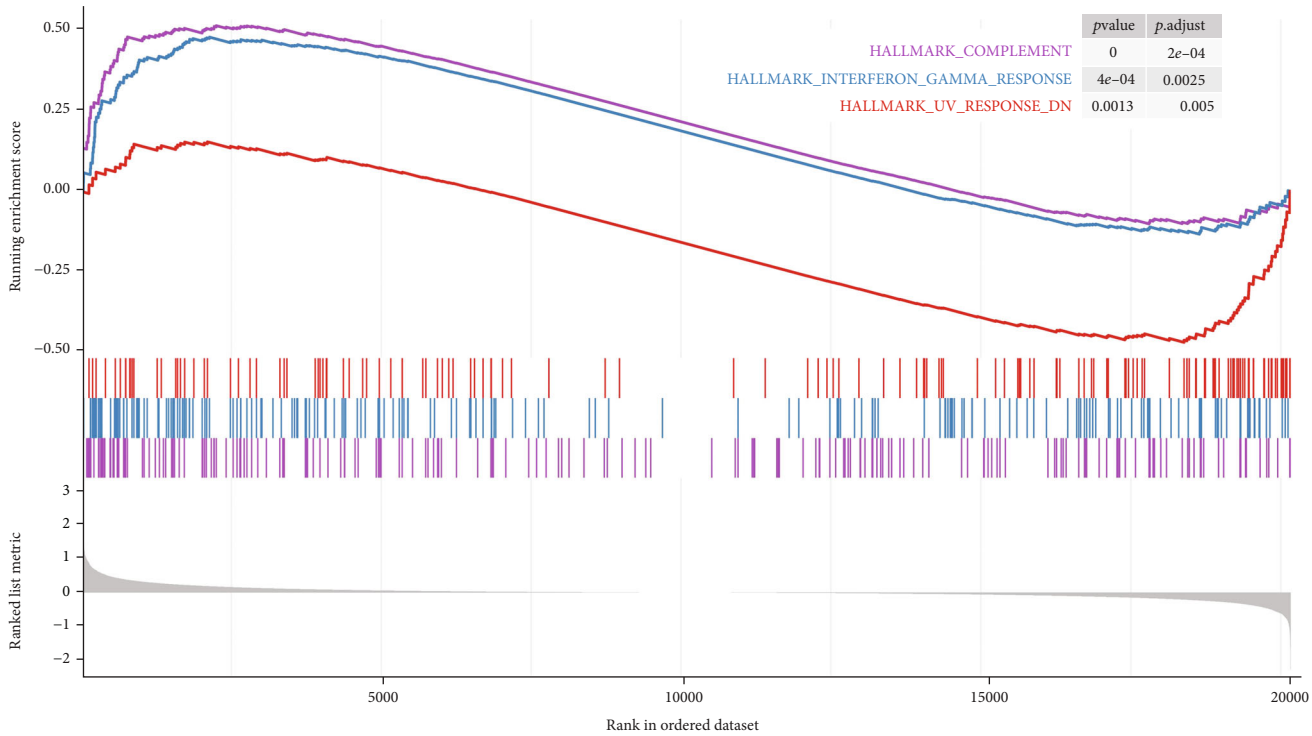

(i)

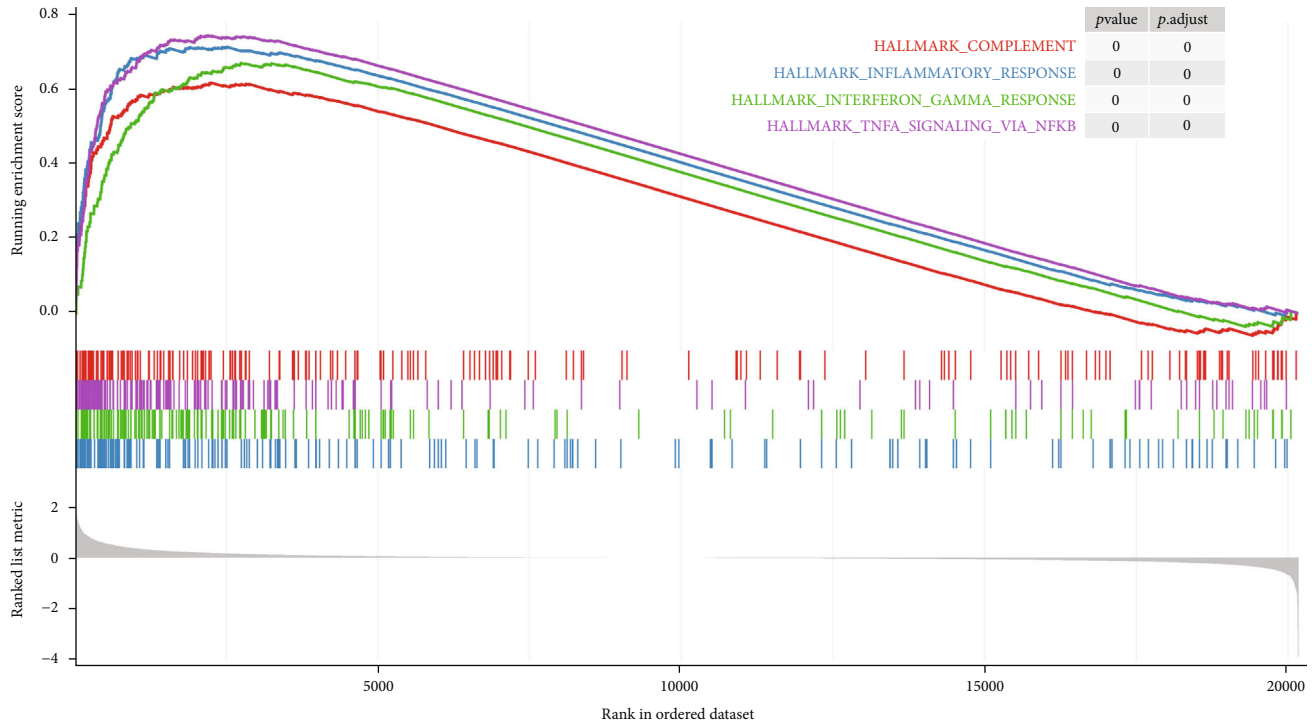

(j)

Figure 11: Gene sets related to immunity for key genes. (a) HCK. (b) ITGAM. (c) CTSS. (d) TYROBP. (e) LAPTM5. (f) FCER1G. (g) ITGB2. (h) NCF2. (i) AIF1. (j) CD86.

further emphasized the relationships of genes and immune responses with AA, but the mechanism behind their involvement is still unclear.

Although we tried to find key genes through multiple algorithms and increase the credibility of these genes by using multiple datasets, our research still has certain limitations. First, the key genes are based on studies of AS and normal groups in most existing studies. Therefore, if the comparison to the normal group can be added to our study, we may be able to dynamically understand the roles of these

genes in the whole process of AS, from initiation to development. In fact, we have tried to include samples of atherosclerosis at different stages in the study, but we did not find any suitable datasets. Also, we have not further studied the exact molecular mechanisms of key genes involved in AA. Furthermore, as mentioned above, immune response has become the main pathogenic factor of AA. The changes of immune cells at different stages of the disease and the relationship between immune cells and genes will become our research focus in the future.

5. Conclusion

In conclusion, we comprehensively discussed the cells and related factors involved in the development of AA. This further confirmed that, in AA, immune response has become the main pathogenic mechanism. It was also discovered that multiple key genes play an important role in the development of EA to AA. This deepens our understanding of the occurrence and development of AA and also provides a strong basis for us to find a treatment for the disease.

Data Availability

The data used to support the findings of this study are available from the corresponding author upon request.

Conflicts of Interest

The authors declare that they have no conflict of interest.

Authors' Contributions

Tian-ming Huo and Zhi-wei Wang conceived the idea, performed analysis, and drafted the manuscript; Tian-ming Huo performed data acquisition and figure preparations; Zhi-wei Wang interpreted the results and help to revise the manuscript. The authors read and approved the final manuscript.

Acknowledgments

This work was supported by grants from the National Natural Science Foundation of China (No. 82070481).

Supplementary Materials

Table S1: the DEGs of GSE28829. Table S2: the DEGs of GSE120521. *(Supplementary Materials)*

References

[1] E. J. Benjamin, P. Muntner, A. Alonso et al., "Heart Disease and Stroke Statistics-2019 update: a report from the American Heart Association," *Circulation*, vol. 139, no. 10, pp. e56–e528, 2019.

[2] K. K. Lee, D. Stelzle, R. Bing et al., "Global burden of atherosclerotic cardiovascular disease in people with hepatitis C virus infection: a systematic review, meta-analysis, and modelling study," *The Lancet Gastroenterology & Hepatology*, vol. 4, no. 10, pp. 794–804, 2019.

[3] C. Weber and H. Noels, "Atherosclerosis: current pathogenesis and therapeutic options," *Nature Medicine*, vol. 17, no. 11, pp. 1410–1422, 2011.

[4] R. B. Singh, S. A. Mengi, Y. J. Xu, A. S. Arneja, and N. S. Dhalla, "Pathogenesis of atherosclerosis: a multifactorial process," *Experimental and Clinical Cardiology*, vol. 7, no. 1, pp. 40–53, 2002.

[5] K. Sakakura, M. Nakano, F. Otsuka, E. Ladich, F. D. Kolodgie, and R. Virmani, "Pathophysiology of atherosclerosis plaque progression," *Heart, Lung & Circulation*, vol. 22, no. 6, pp. 399–411, 2013.

[6] L. G. Spagnoli, A. Mauriello, G. Sangiorgi et al., "Extracranial thrombotically active carotid plaque as a risk factor for ischemic stroke," *JAMA*, vol. 292, no. 15, pp. 1845–1852, 2004.

[7] C. Gaurav, B. Saurav, R. Goutam, and A. K. Goyal, "Nanosystems for advanced therapeutics and diagnosis of atherosclerosis," *Current Pharmaceutical Design*, vol. 21, no. 30, pp. 4498–4508, 2015.

[8] L. Li, L. Wang, H. Li et al., "Characterization of lncRNA expression profile and identification of novel lncRNA biomarkers to diagnose coronary artery disease," *Atherosclerosis*, vol. 275, pp. 359–367, 2018.

[9] Y. Gu, X. Ma, J. Li, Y. Ma, and Y. Zhang, "Identification of candidate targets for the diagnosis and treatment of atherosclerosis by bioinformatics analysis," *American Journal of Translational Research*, vol. 13, no. 5, pp. 4137–4151, 2021.

[10] A. D. Mahmoud, M. D. Ballantyne, V. Miscianinov et al., "The human-specific and smooth muscle cell-enriched lncRNA SMILR promotes proliferation by regulating mitotic CENPF mRNA and drives cell-cycle progression which can be targeted to limit vascular remodeling," *Circulation Research*, vol. 125, no. 5, pp. 535–551, 2019.

[11] K. Lee, M. Santibanez-Koref, T. Polvikoski, D. Birchall, A. D. Mendelow, and B. Keavney, "Increased expression of fatty acid binding protein 4 and leptin in resident macrophages characterises atherosclerotic plaque rupture," *Atherosclerosis*, vol. 226, no. 1, pp. 74–81, 2013.

[12] P. Chen, Y. Chen, W. Wu, L. Chen, X. Yang, and S. Zhang, "Identification and validation of four hub genes involved in the plaque deterioration of atherosclerosis," *Aging*, vol. 11, no. 16, pp. 6469–6489, 2019.

[13] W. Shi, R. Zou, M. Yang et al., "Analysis of genes involved in ulcerative colitis activity and tumorigenesis through systematic mining of gene co-expression networks," *Frontiers in Physiology*, vol. 10, p. 662, 2019.

[14] B. Zhang and S. Horvath, "A general framework for weighted gene co-expression network analysis," *Statistical Applications in Genetics and Molecular Biology*, vol. 4, no. 1, p. Article 17, 2005.

[15] Z. Wang, Z. Ren, R. Li et al., "Multi-omics integrative bioinformatics analyses reveal long non-coding RNA modulates genomic integrity via competing endogenous RNA mechanism and serves as novel biomarkers for overall survival in lung adenocarcinoma," *Frontiers in Cell and Development Biology*, vol. 9, p. 691540, 2021.

[16] E. F. Mendez, H. Wei, R. Hu et al., "Angiogenic gene networks are dysregulated in opioid use disorder: evidence from multiomics and imaging of postmortem human brain," *Molecular Psychiatry*, vol. 2021, 2021.

[17] M. Yao, C. Zhang, C. Gao et al., "Exploration of the shared gene signatures and molecular mechanisms between systemic

lupus erythematosus and pulmonary arterial hypertension: evidence from transcriptome data," *Frontiers in Immunology*, vol. 12, p. 658341, 2021.

[18] Y. Döring, H. D. Manthey, M. Drechsler et al., "Auto-antigenic protein-DNA complexes stimulate plasmacytoid dendritic cells to promote atherosclerosis," *Circulation*, vol. 125, no. 13, pp. 1673–1683, 2012.

[19] H. Ayari and G. Bricca, "Identification of two genes potentially associated in iron-heme homeostasis in human carotid plaque using microarray analysis," *Journal of Biosciences*, vol. 38, no. 2, pp. 311–315, 2013.

[20] L. Gautier, L. Cope, B. M. Bolstad, and R. A. Irizarry, "affy–analysis of Affymetrix GeneChip data at the probe level," *Bioinformatics*, vol. 20, no. 3, pp. 307–315, 2004.

[21] R. A. Irizarry, B. Hobbs, F. Collin et al., "Exploration, normalization, and summaries of high density oligonucleotide array probe level data," *Biostatistics*, vol. 4, no. 2, pp. 249–264, 2003.

[22] M. E. Ritchie, B. Phipson, D. Wu et al., "limma powers differential expression analyses for RNA-sequencing and microarray studies," *Nucleic Acids Research*, vol. 43, no. 7, article e47, 2015.

[23] P. Langfelder and S. Horvath, "WGCNA: an R package for weighted correlation network analysis," *BMC Bioinformatics*, vol. 9, no. 1, p. 559, 2008.

[24] G. Yu, L. G. Wang, Y. Han, and Q. Y. He, "clusterProfiler: an R package for comparing biological themes among gene clusters," *OMICS*, vol. 16, no. 5, pp. 284–287, 2012.

[25] D. Szklarczyk, A. L. Gable, D. Lyon et al., "STRING v11: protein-protein association networks with increased coverage, supporting functional discovery in genome-wide experimental datasets," *Nucleic Acids Research*, vol. 47, no. D1, pp. D607–D613, 2019.

[26] P. Shannon, A. Markiel, O. Ozier et al., "Cytoscape: a software environment for integrated models of biomolecular interaction networks," *Genome Research*, vol. 13, no. 11, pp. 2498–2504, 2003.

[27] G. D. Bader and C. W. Hogue, "An automated method for finding molecular complexes in large protein interaction networks," *BMC Bioinformatics*, vol. 4, no. 1, p. 2, 2003.

[28] T. Sing, O. Sander, N. Beerenwinkel, and T. Lengauer, "ROCR: visualizing classifier performance in R," *Bioinformatics*, vol. 21, no. 20, pp. 3940-3941, 2005.

[29] A. Subramanian, P. Tamayo, V. K. Mootha et al., "Gene set enrichment analysis: a knowledge-based approach for interpreting genome-wide expression profiles," *Proceedings of the National Academy of Sciences of the United States of America*, vol. 102, no. 43, pp. 15545–15550, 2005.

[30] P. Raggi, J. Genest, J. T. Giles et al., "Role of inflammation in the pathogenesis of atherosclerosis and therapeutic interventions," *Atherosclerosis*, vol. 276, pp. 98–108, 2018.

[31] C. K. Glass and J. L. Witztum, "Atherosclerosis: The Road Ahead," *Cell*, vol. 104, no. 4, pp. 503–516, 2001.

[32] T. Obama and H. Itabe, "Neutrophils as a novel target of modified low-density lipoproteins and an accelerator of cardiovascular diseases," *International Journal of Molecular Sciences*, vol. 21, no. 21, p. 8312, 2020.

[33] O. Soehnlein, "Multiple roles for neutrophils in atherosclerosis," *Circulation Research*, vol. 110, no. 6, pp. 875–888, 2012.

[34] A. Daugherty and D. L. Rateri, "T lymphocytes in atherosclerosis: the yin-yang of Th1 and Th2 influence on lesion formation," *Circulation Research*, vol. 90, no. 10, pp. 1039-1040, 2002.

[35] K. Ley, "Role of the adaptive immune system in atherosclerosis," *Biochemical Society Transactions*, vol. 48, no. 5, pp. 2273–2281, 2020.

[36] R. Saigusa, H. Winkels, and K. Ley, "T cell subsets and functions in atherosclerosis," *Nature Reviews. Cardiology*, vol. 17, no. 7, pp. 387–401, 2020.

[37] J. Wittwer, J. Marti-Jaun, and M. Hersberger, "Functional polymorphism in ALOX15 results in increased allele-specific transcription in macrophages through binding of the transcription factor SPI1," *Human Mutation*, vol. 27, no. 1, pp. 78–87, 2006.

[38] B. H. Hahn, "Systemic lupus erythematosus and accelerated atherosclerosis," *The New England Journal of Medicine*, vol. 349, no. 25, pp. 2379-2380, 2003.

[39] E. V. Arkema, E. Svenungsson, M. Von Euler, C. Sjowall, and J. F. Simard, "Stroke in systemic lupus erythematosus: a Swedish population-based cohort study," *Annals of the Rheumatic Diseases*, vol. 76, no. 9, pp. 1544–1549, 2017.

[40] M. J. Roman, B. A. Shanker, A. Davis et al., "Prevalence and correlates of accelerated atherosclerosis in systemic lupus erythematosus," *The New England Journal of Medicine*, vol. 349, no. 25, pp. 2399–2406, 2003.

[41] A. Mazzone, I. Mazzucchelli, G. Fossati et al., "Iloprost effects on phagocytes in patients suffering from ischaemic diseases: in vivo evidence for down-regulation of alpha M beta 2 integrin," *European Journal of Clinical Investigation*, vol. 26, no. 10, pp. 860–866, 1996.

[42] A. K. Roseweir, A. Powell, S. L. Horstman et al., "Src family kinases, HCK and FGR, associate with local inflammation and tumour progression in colorectal cancer," *Cellular Signalling*, vol. 56, pp. 15–22, 2019.

[43] I. Medina, C. Cougoule, M. Drechsler et al., "Hck/Fgr kinase deficiency reduces plaque growth and stability by blunting monocyte recruitment and intraplaque motility," *Circulation*, vol. 132, no. 6, pp. 490–501, 2015.

[44] M. Kobayashi, H. Konishi, T. Takai, and H. Kiyama, "A DAP12-dependent signal promotes pro-inflammatory polarization in microglia following nerve injury and exacerbates degeneration of injured neurons," *Glia*, vol. 63, no. 6, pp. 1073–1082, 2015.

[45] K. Otero, I. R. Turnbull, P. L. Poliani et al., "Macrophage colony-stimulating factor induces the proliferation and survival of macrophages via a pathway involving DAP12 and β-catenin," *Nature Immunology*, vol. 10, no. 7, pp. 734–743, 2009.

[46] H. M. Wang, J. H. Gao, and J. L. Lu, "Pravastatin improves atherosclerosis in mice with hyperlipidemia by inhibiting TREM-1/DAP12," *European Review for Medical and Pharmacological Sciences*, vol. 22, no. 15, pp. 4995–5003, 2018.

[47] R. I. Campden and Y. Zhang, "The role of lysosomal cysteine cathepsins in NLRP3 inflammasome activation," *Archives of Biochemistry and Biophysics*, vol. 670, pp. 32–42, 2019.

[48] G. K. Sukhova, Y. Zhang, J. H. Pan et al., "Deficiency of cathepsin S reduces atherosclerosis in LDL receptor-deficient mice," *The Journal of Clinical Investigation*, vol. 111, no. 6, pp. 897–906, 2003.

[49] R. T. Kenney and T. L. Leto, "A HindIII polymorphism in the human NCF2 gene," *Nucleic Acids Research*, vol. 18, no. 23, p. 7193, 1990.

[50] M. Breitenbach, M. Rinnerthaler, M. Weber et al., "The defense and signaling role of NADPH oxidases in eukaryotic cells: review," *Wiener Medizinische Wochenschrift (1946)*, vol. 168, no. 11-12, pp. 286–299, 2018.

[51] H. Li, X. Han, Z. Hu et al., "Associations of NADPH oxidase-related genes with blood pressure changes and incident hypertension: the GenSalt study," *Journal of Human Hypertension*, vol. 32, no. 4, pp. 287–293, 2018.

[52] J. Marques, A. Cortes, A. Pejenaute, and G. Zalba, "Implications of NADPH oxidase 5 in vascular diseases," *The International Journal of Biochemistry & Cell Biology*, vol. 128, article 105851, 2020.

[53] U. Utans, W. C. Quist, B. M. McManus et al., "Allograft inflammatory factory-1. A cytokine-responsive macrophage molecule expressed in transplanted human hearts," *Transplantation*, vol. 61, no. 9, pp. 1387–1392, 1996.

[54] T. Mishima, K. Iwabuchi, S. Fujii et al., "Allograft inflammatory factor-1 augments macrophage phagocytotic activity and accelerates the progression of atherosclerosis in ApoE-/- mice," *International Journal of Molecular Medicine*, vol. 21, no. 2, pp. 181–187, 2008.

[55] Z. F. Yang, D. W. Ho, C. K. Lau et al., "Allograft inflammatory factor-1 (AIF-1) is crucial for the survival and pro-inflammatory activity of macrophages," *International Immunology*, vol. 17, no. 11, pp. 1391–1397, 2005.

[56] W. K. Glowacka, P. Alberts, R. Ouchida, J. Y. Wang, and D. Rotin, "LAPTM5 Protein Is a Positive Regulator of Proinflammatory Signaling Pathways in Macrophages," *The Journal of Biological Chemistry*, vol. 287, no. 33, pp. 27691–27702, 2012.

[57] H. Koukkunen, K. Penttilä, A. Kemppainen et al., "C-reactive protein, fibrinogen, interleukin-6 and tumour necrosis factor-alpha in the prognostic classification of unstable angina pectoris," *Annals of Medicine*, vol. 33, no. 1, pp. 37–47, 2001.

[58] S. S. Wang, S. W. Hu, Q. H. Zhang, A. X. Xia, Z. X. Jiang, and X. M. Chen, "Mesenchymal stem cells stabilize atherosclerotic vulnerable plaque by anti-inflammatory properties," *PLoS One*, vol. 10, no. 8, article e0136026, 2015.

[59] J. E. McLaren and D. P. Ramji, "Interferon gamma: a master regulator of atherosclerosis," *Cytokine & Growth Factor Reviews*, vol. 20, no. 2, pp. 125–135, 2009.

[60] I. Tabas and A. H. Lichtman, "Monocyte-macrophages and T cells in atherosclerosis," *Immunity*, vol. 47, no. 4, pp. 621–634, 2017.

Hindawi
Disease Markers
Volume 2021, Article ID 4391133, 11 pages
https://doi.org/10.1155/2021/4391133

Research Article

Discovery and Validation of Novel Methylation Markers in *Helicobacter pylori*-Associated Gastric Cancer

Huan Wang,[1,2] **Nian-Shuang Li**,[1] **Cong He**,[1] **Chuan Xie**,[1] **Yin Zhu**,[1] **Nong-Hua Lu**,[1] **and Yi Hu**[1]

[1]*Department of Gastroenterology, The First Affiliated Hospital of Nanchang University, Nanchang, 330006 Jiangxi Province, China*
[2]*Medical College of Nanchang University, Nanchang, 330006 Jiangxi Province, China*

Correspondence should be addressed to Yi Hu; 360041934@qq.com

Received 11 August 2021; Revised 24 October 2021; Accepted 8 November 2021; Published 8 December 2021

Academic Editor: Ting Su

Previous studies have shown that abnormal methylation is an early key event in the pathogenesis of most human cancers, contributing to the development of tumors. However, little attention has been given to the potential of DNA methylation patterns as markers for *Helicobacter pylori*- (*H. pylori*-) associated gastric cancer (GC). In this study, an integrated analysis of DNA methylation and gene expression was conducted to identify some potential key epigenetic markers in *H. pylori*-associated GC. DNA methylation data of 28 H. *pylori*-positive and 168 H. *pylori*-negative GC samples were compared and analyzed. We also analyzed the gene expression data of 18 H. *pylori*-positive and 145 H. *pylori*-negative GC cases. Finally, the results were verified by *in vitro* and *in vivo* experiments. A total of 5609 differentially methylated regions associated with 2454 differentially methylated genes were identified. A total of 228 differentially expressed genes were identified from the gene expression data of *H. pylori*-positive and *H. pylori*-negative GC cases. The screened genes were analyzed for functional enrichment. Subsequently, we obtained 28 genes regulated by methylation through a Venn diagram, and we identified five genes (GSTO2, HUS1, INTS1, TMEM184A, and TMEM190) downregulated by hypermethylation. HUS1, GSTO2, and TMEM190 were expressed at lower levels in GC than in adjacent samples ($P < 0.05$). Moreover, *H. pylori* infection decreased HUS1, GSTO2, and TMEM190 expression *in vitro* and *in vivo*. Our study identified HUS1, GSTO2, and TMEM190 as novel methylation markers for *H. pylori*-associated GC.

1. Introduction

Helicobacter pylori (*H. pylori*) is a microaerophilic, spiral-shaped gram-negative bacterium that colonizes the stomach and adheres to the gastric mucosa [1]. *H. pylori* has been confirmed to have close relationships with gastritis, peptic ulcer, gastric cancer (GC), and mucosa-related lymphoid tissue lymphoma [2]. *H. pylori* infection is the most definite risk factor for GC [3]. Out of the 952,000 new cases of GC diagnosed worldwide every year, it is estimated that 753,000 (79%) of the recent cases are attributed to *H. pylori* infection [4]. Currently, the specific mechanism of *H. pylori*-induced GC is still unclear. Moreover, specific molecular markers to identify subjects at high risk of *H. pylori*-associated GC need to be explored.

One of the key regulators involved in the environmental response is the methylation of genomic regulatory regions. The methylation of CpG islands in gene promoters is involved in the regulation of gene expression. DNA methylation abnormalities are the main epigenetic mechanism related to gene silencing and play an important role in tumorigenesis [5, 6]. Overall hypomethylation of specific genes is related to genomic instability and the inactivation of tumor suppressor genes [7]. Several studies have indicated that *H. pylori* infection is related to hypermethylation of gene promoters [8]. However, at the whole-genome level, studies on the mechanism of abnormal DNA methylation involved in the carcinogenesis of *H. pylori*-associated GC are still scarce. Moreover, the molecular mechanism of the abnormal methylation of gene

regulatory regions involved in the generation and development of GC remains elusive.

This study is aimed at exploring the potential methylation-related gene markers in *H. pylori*-related GC by analyzing the methylation and gene expression data of The Cancer Genome Atlas (TCGA) database, combined with related experiments.

2. Materials and Methods

2.1. Data Sources. DNA methylation data from 397 samples (395 GC and 2 normal samples) were obtained from TCGA (https://cancergenome.nih.gov/). The RNA-Seq data and clinical information of 407 samples (375 tumor samples and 32 normal samples) were obtained from UCSC Xena (https://xenabrowser.net/datapages/). A flowchart of the process of data acquisition and the subsequent analysis is shown in Figure 1.

2.2. Screening of Differentially Methylated Genes. After screening, a total of 188 cases with *H. pylori* infection information (20 positive and 168 negative) were included and analyzed. The minfi package [9] was used to preprocess and normalize the DNA methylation data. Benjamini-Hochberg was used to correct the P value, and $|\log 2FC| > 1$, $P < 0.01$ were set as the thresholds to screen for differentially methylated sites.

2.3. Screening of Differentially Expressed Genes. The samples with clear clinical information of *H. pylori* infection were screened from the tumor samples. A total of 163 GC samples (18 with *H. pylori* and 145 without *H. pylori*) were included in the subsequent analysis. The analysis used the R language edge package [10] to analyze the difference between *H. pylori*-positive and -negative groups. The threshold of differential gene selection was set as $P < 0.01$. The results were visualized by volcano map.

2.4. Enrichment Analysis. The genes obtained from differential gene analysis and differential methylation analysis were enriched and analyzed with the R language cluster profiler package [11], and the top 10 genes were used for visualization.

2.5. Screening for Decreased Gene Expression due to Hypermethylation. The results of the intersection of the differentially expressed genes (DEGs) obtained from the differential gene analysis and the differentially methylated genes (DMGs) obtained from the differential methylation analysis were taken as the genes affected by the methylation of *H. pylori*-associated GC. In this analysis, the methylation sites of each gene in GC patients infected by *H. pylori* and those not infected by *H. pylori*, as well as the expression of each gene in the two groups, were visualized by box plots, and the Wilcoxon rank-sum test was performed. Ultimately, 5 genes with significantly upregulated methylation levels and significantly downregulated gene expression levels in the *H. pylori*-positive group were screened out.

2.6. Cell Culture and H. pylori Strains. AGS cells (human GC cells) were cultured in DMEM/F12 (Gibco, CA, USA) containing 10% fetal bovine serum (FBS) and 1% penicillin/streptomycin (Gibco) at 37°C in an atmosphere of 5% CO_2. *H. pylori* 7.13 (provided by Dr. Richard Peek from the Vanderbilt University Medical Center) was cultured on Campylobacter agar plates containing 10% sheep serum under microaerophilic conditions at 37°C. The concentration of the bacteria was determined by spectrophotometry (OD600 nm) after suspension in DMEM/F12. Subsequently, the cell culture medium was replaced with fresh medium without antibiotics, and the cells were cocultured with *H. pylori* at different times or multiplicities of infection (MOIs).

2.7. Western Blotting. The harvested cells were lysed with lysis buffer containing protease inhibitor cocktail (Roche, Amherst, CA, USA). Protein samples were separated by SDS–PAGE and transferred to nitrocellulose membranes. The blocking buffer was prepared with 5% nonfat dry milk in TBST buffer, and the membranes were blocked at room temperature for 1 hour and then incubated with primary antibodies in a shaker at 4°C overnight. Antibodies were anti-GSTO2 (Proteintech, 14562-1-AP), anti-HUS1 (Proteintech, 11223-1-AP), anti-INTS1 (Sigma–Aldrich, HPA021658), anti-TMEM184A (Proteintech, 25989-1-AP), anti-TMEM190 (Invitrogen, PA5-70986), and anti-Actin (TransGen Biotech, HC201-01). The membranes were incubated with the corresponding secondary antibodies (1 : 2000) for 1 hour at room temperature the next day, and finally, the proteins were visualized with chemiluminescence solution.

2.8. Patients and Tissue Specimens. Human gastric tissue samples (8 pairs of GC and adjacent samples, 11 *H. pylori*-positive, and 12 *H. pylori*-negative GC specimens) were collected from GC patients who underwent gastrectomy at the First Affiliated Hospital of Nanchang University. Gastric mucosal tissues of patients who underwent gastroscopic biopsy at the First Affiliated Hospital of Nanchang University (12 *H. pylori*-positive and 12 *H. pylori*-negative patients with gastritis) were collected. The diagnoses of GC and gastritis were confirmed based on histology, and the diagnosis of *H. pylori* infection was based on immunohistochemistry or culture results. All subjects provided informed consent for obtaining the study specimens. The study protocol was approved by the Clinical Research Ethics Committee of the First Affiliated Hospital of Nanchang University. The gastric mucosal tissues of the mice were derived from C57BL/6 mice infected with the *H. pylori* SS1 strain successfully constructed by our research group [12] (12 in the control group and 12 in the *H. pylori* infection group).

2.9. Real-Time Quantitative PCR Analysis. TRIzol (Invitrogen) was then used to extract total tissue RNA, after which SYBR® Premix Ex Taq (TaKaRa) was used for qRT–PCR. The primers used for the detection of human specimens: β-actin forward primer 5′-TGACGTGGACATCCGCAAAG-3′ and reverse primer 5′-CTGGAAGGTGGACA

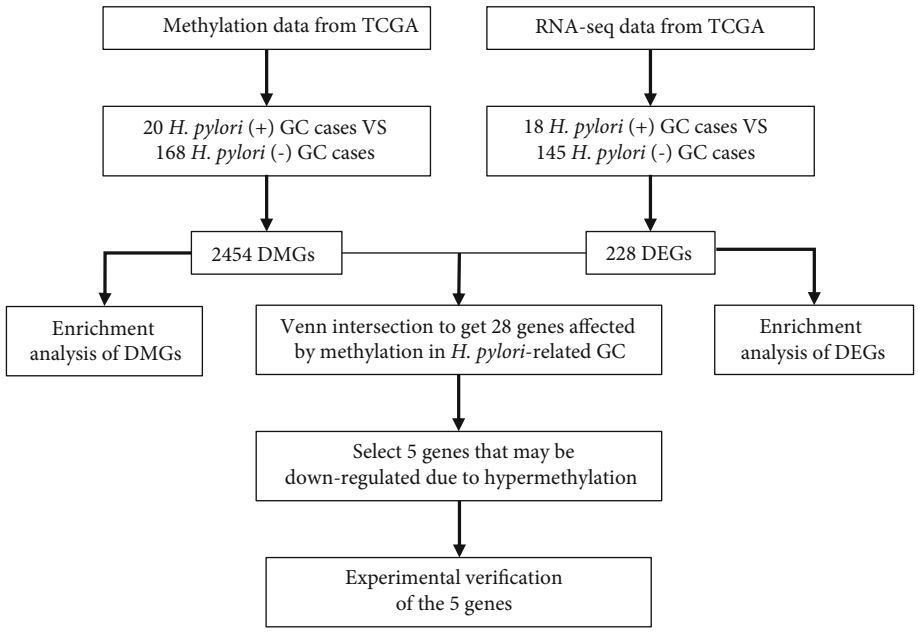

Figure 1: Flowchart of the data acquisition and analysis process. TCGA: The Cancer Genome Atlas (https://cancergenome.nih.gov/); DMGs: differentially methylated genes; DEGs: differentially expressed genes.

GCGAGG-3′; GSTO2 forward primer 5′-TGTGTATGGGA TACTGGACTGT-3′ and reverse primer 5′-AGGCATTAG GGTTGTTCTGAAAA-3′; HUS1 forward primer 5′-GAATGCCAGGGCTTTGAAAATC-3′ and reverse primer 5′- CACAATGCGGCTACTGCTTG-3′; INTS1 forward primer 5′-GTCAGGCCAATGAATCGAAAAC-3′ and reverse primer 5′-CGACGGAGAAATGGCTCGT-3′; TMEM184A forward primer 5′-CTACACCGTGCCACAG GAG-3′ and reverse primer 5′-CCGCACAGAGTCGAAG TAGA-3′; TMEM190 forward primer 5′-CCAGACGAA AACGTGCGGA-3′ and reverse primer 5′-GCGAGACGG ACTTGGACAT-3′.The primers used for the detection of mouse specimens: β-actin forward primer 5′-GGCTGT ATTCCCCTCCATCG-3′ and reverse primer 5′-TCGTCG GTCCTTAGACAGTGA-3′; GSTO2 forward primer 5′-AAAGCTGTTTCCGTATGACCC-3′ and reverse primer 5′-CGCTATCAGACATTCCTTGCTTA-3′; HUS1 forward primer 5′-AGCTGAACTTCATCCTTTGCG-3′ and reverse primer 5′-ACGGTAAGACAGGGAAAGTGTT-3′; INTS1 forward primer 5′-GTGAAGGCGCTTCCTCTAGG-3′ and reverse primer 5′-ACCCCAGAGCAATAAAGTCCC-3′; TMEM184A forward primer 5′-AGGCGTGTTTGTAT GGACTGC-3′ and reverse primer 5′-CGGGGCGGTAT AGGAACGTA-3′; TMEM190 forward primer 5′-CCTG TGGCAGCCTACTCTTC-3′ and reverse primer 5′-TCGT CGGTCCTTAGACAGTGA-3′.

2.10. Statistical Analysis. The Student's t-test was used for comparison between two groups. $P < 0.05$ was considered statistically significant.

3. Results

3.1. Identification of DMGs and Enrichment Analysis of the DMGs. The methylation data were normalized and standardized. As shown in Figure S1, the normalized methylation data were essentially at the same level, and the normalized data were analyzed for differential methylation. Principal component analysis (PCA) was performed on the selected samples based on the normalized M value. As shown in Figure 2(a), the *H. pylori*-positive and -negative samples were not well distinguished. This might be due to the small number of *H. pylori*-positive samples.

According to the screening threshold, a total of 5609 methylation results with significant differences were obtained. The results without corresponding genes and the results of one methylation corresponding to multiple genes were excluded. Finally, a one-to-one methylation-gene relationship was obtained, and a total of 3298 results were obtained for subsequent analysis. The repeated genes were removed, and 2454 DMGs remained (Figure 2(b)), of which 1679 were hypomethylated and 775 were hypermethylated. All 2454 DMGs were displayed in Supplementary Table 1.

The R package Cluster profiler was used for enrichment analysis to investigate the functions of the DMGs. As shown in Figure 2(c), these genes were enriched in the biological process (BP) categories (axonogenesis, embryonic organ development, etc.). The top significant cellular compartment (CC) categories were presynapse, cell-substrate junction, and cell-substrate adherens junction. Kyoto Encyclopedia of Genes and Genomes (KEGG) pathway analysis revealed that the main enrichments were in the MAPK signaling pathway, the Hippo signaling pathway, and the TGF-beta signaling pathway.

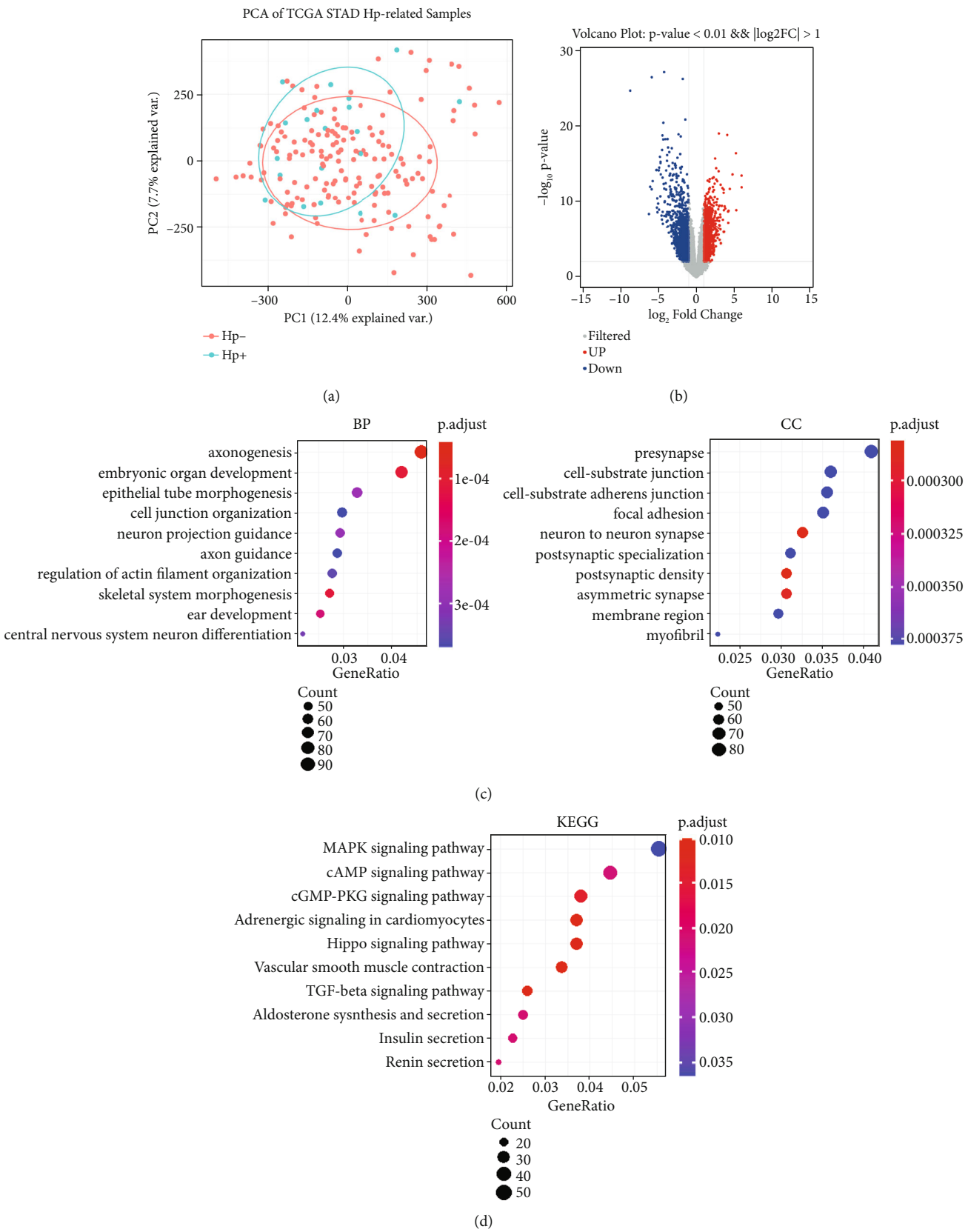

Figure 2: Identification of DMGs and enrichment analysis of the DMGs. (a) PCA of *H. pylori*-positive GC and *H. pylori*-negative GC samples. (b) Volcano map of methylation results in 188 GC samples. Red represents hypermethylation, and blue represents hypomethylation. (c) Top 10 genes from the GO analysis of 2454 DMGs. BP: biological process; CC: cellular component. (d) Top 10 genes from the KEGG analysis. KEGG: Kyoto Encyclopedia of Genes and Genomes.

3.2. Identification of DEGs and Enrichment Analysis of the DEGs. PCA results of gene expression were consistent with the methylated PCA results, and the *H. pylori*-positive and *H. pylori*-negative samples were not clearly divided into two clusters (Figure 3(a)). As described in the Methods section, a differential analysis was performed on all mRNA expression levels in the selected samples. According to the screening threshold, a volcano map of the difference analysis results is shown in Figure 3(b), and a total of 228 DEGs (112 upregulated genes and 116 downregulated genes) were obtained. The entire list of 228 DEGs is presented in Supplementary Table 2. Next, we conducted an enrichment analysis on the 228 DEGs, and GO analysis did not obtain statistically significant results, though these genes were mainly enriched in chromatin separation in the BP category and microtubules in the CC category. KEGG pathway enrichment results were mainly related to the immune system, the immune response, and complement pathways (Figure 3(c)).

3.3. Screening for Genes with Reduced Expression Caused by Hypermethylation. To obtain genes affected by methylation, we took the intersection of 2454 DMGs and 228 DEGs, as shown in Figure 4(a). A total of 28 genes were identified, and the functions of these 28 genes are shown in Supplementary Table 3. Furthermore, the methylation sites and the expression of the 28 genes in different groups (*H. pylori*-positive and *H. pylori*-negative) were visualized. Finally, five genes with reduced expression that may be caused by hypermethylation were obtained, namely, GSTO2 (cg10122050, cg19917656, and cg23659134), HUS1 (cg10190813), INTS1 (cg07005770), TMEM184A (cg10633906), and TMEM190 (cg08133641, cg04264070, and cg04800569) (Figures 4(b)–4(f)).

3.4. Experimental Verification of the Five Genes. The above five genes were selected by comparing the *H. pylori*-positive GC and *H. pylori*-negative GC samples. To confirm the above findings, we cocultured the *H. pylori* 7.13 strain with AGS cells and found that *H. pylori* infection significantly downregulated the expression levels of HUS1, GSTO2, TMEM190, and INTS1 but not TMEM184A (Figures 5(a)–5(e)). This is consistent with the previous analysis results.

We also examined the expression levels of these five genes in eight pairs of GC and adjacent samples and found that the HUS1, GSTO2, TMEM184A, and TMEM190 mRNA levels in GC samples were significantly lower than those in adjacent samples ($P < 0.05$). We collected *H. pylori*-positive and *H. pylori*-negative chronic nonatrophic gastritis (CNAG) and GC specimens and found that HUS1 and GSTO2 were significantly downregulated ($P < 0.05$) in the *H. pylori*-positive group of CNAG samples and GC samples. The mRNA level of TMEM190 was also downregulated in the *H. pylori*-positive group ($P < 0.05$), even though the difference was not statistically significant in the GC samples. In addition, we verified these genes at the animal level and found that the mRNA levels of GSTO2 and TMEM190 were significantly downregulated in the gastric mucosa of *H. pylori*-infected mice ($P < 0.05$) (Figures 6(a)–6(e)).

4. Discussion

Abnormal DNA methylation in the gene promoter region is believed to play a crucial role in GC tumorigenesis [13, 14]. The pathogen *H. pylori* is known to be closely related to GC. *H. pylori* may promote carcinogenesis by inducing abnormal methylation of gastric epithelial cells [15]. However, it is necessary to conduct further research to clarify the detailed molecular mechanism of the abnormal promoter methylation caused by infection with this pathogen.

This study comprehensively analyzed the DNA methylation and RNA-seq data of *H. pylori*-positive and -negative GC samples to investigate the changes in DNA methylation patterns present in *H. pylori*-associated GC. A total of 2454 DMGs and 228 DEGs were identified in this study. To study the roles of epigenetic DNA changes in pathways, the DMGs and DEGs were comprehensively analyzed. The enrichment results of DEG functions and pathways were mainly related to the immune system, the immune response, and the complement pathway. It is known that immunity is involved in the generation and development of GC [16]. The enrichment results of gene functions and pathways corresponding to DMGs were mainly concentrated in various signal transduction pathways, such as the Hippo signaling pathway and the MAPK signaling pathway. The Hippo signaling pathway is considered to regulate cell proliferation, programmed death, and cancer formation [17]. Previous research has shown that epigenetic changes induced by *H. pylori* in GC contain abnormal methylation of components of the MAPK signaling pathway [15]. These results suggest that abnormally methylated genes may lead to the destruction of core cancer signaling pathways and play significant roles in the occurrence and development of *H. pylori*-associated GC.

Five genes that may be downregulated by hypermethylation were identified as GSTO2 (cg10122050, cg19917656, and cg23659134), HUS1 (cg10190813), INTS1 (cg07005770), TMEM184A (cg10633906), and TMEM190 (cg08133641, cg04264070, and cg04800569). Studies have shown that the HUS1 gene is involved in DNA damage repair and apoptosis and has a clear relationship with the occurrence and development of tumors [18]. In our study, it was also found that *H. pylori* infection can significantly downregulate the expression of HUS1. The expression level of HUS1 in GC tissues was significantly lower than that in adjacent tissues. Studies have shown that *H. pylori* infection decreases the expression of GST. The mechanism may be due to the deletion of the GST gene caused by *H. pylori* infection or one of the pathogenic factors inhibiting the activation of the active site of GST, thereby weakening the protective effect of GST on the gastric mucosa [19, 20]. The genetic polymorphism of GSTO2 is closely related to the risk of GC [21]. Similarly, this study also found that *H. pylori* infection downregulated the expression of GSTO2, and the expression of GSTO2 in GC tissues was also significantly lower than that in adjacent tissues. This is consistent with current studies. In recent years, it has been reported that INTS1 plays important roles in the DNA damage response, perinuclear dynein recruitment, adipocyte differentiation and maturation, hematopoiesis, primary cilia formation, tumor development, and virus

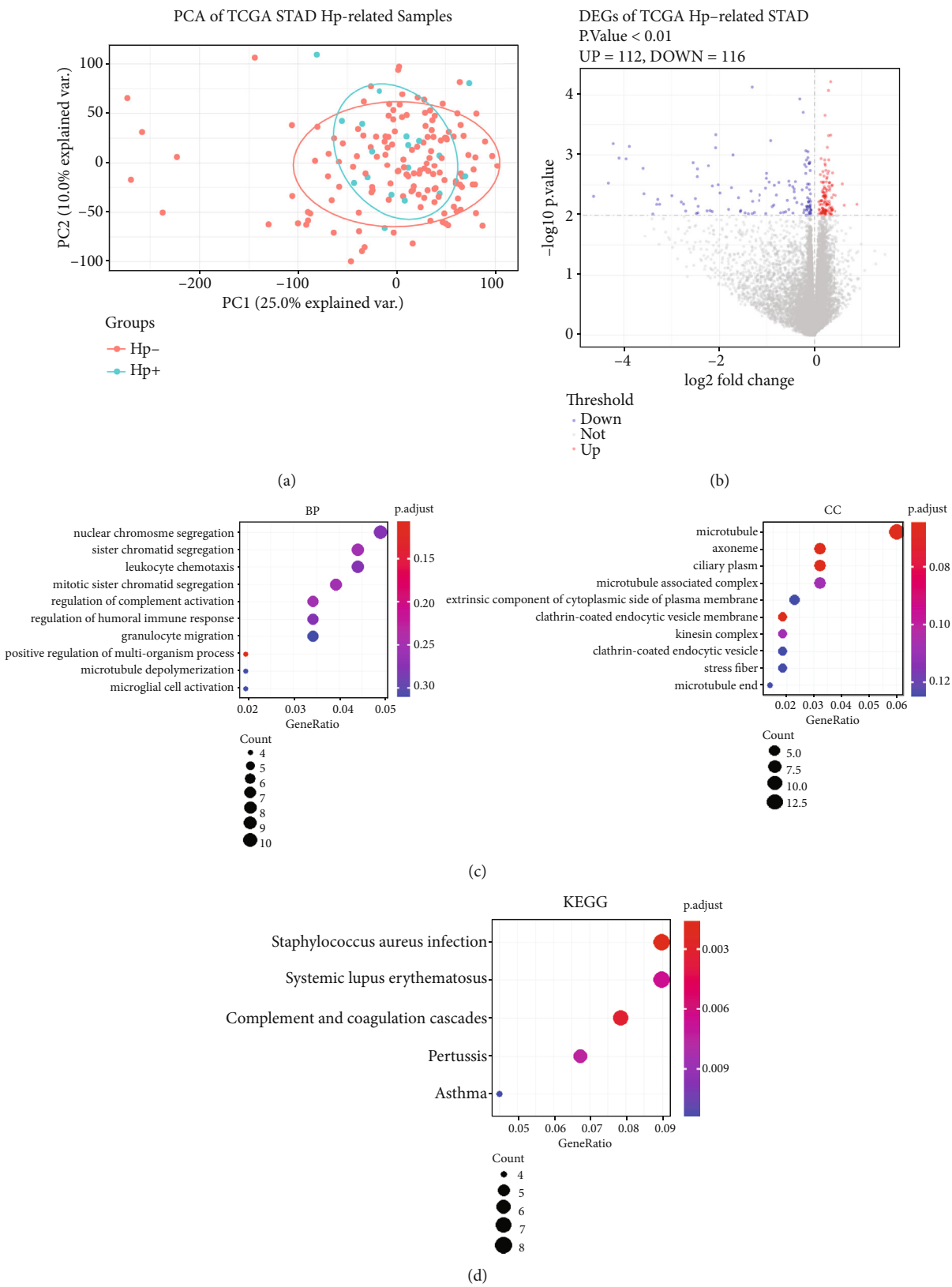

Figure 3: Identification and enrichment analysis of DEGs. (a) PCA of *H. pylori*-positive GC and *H. pylori*-negative GC samples. (b) Volcano map of the difference analysis. The differential gene screening threshold is $P < 0.01$. Red indicates the upregulated DGEs ($n = 112$), and blue represents the downregulated DEGs ($n = 116$). (c) GO analysis of 228 DEGs. BP: biological process; CC: cellular component. (d) KEGG analysis. KEGG: Kyoto Encyclopedia of Genes and Genomes.

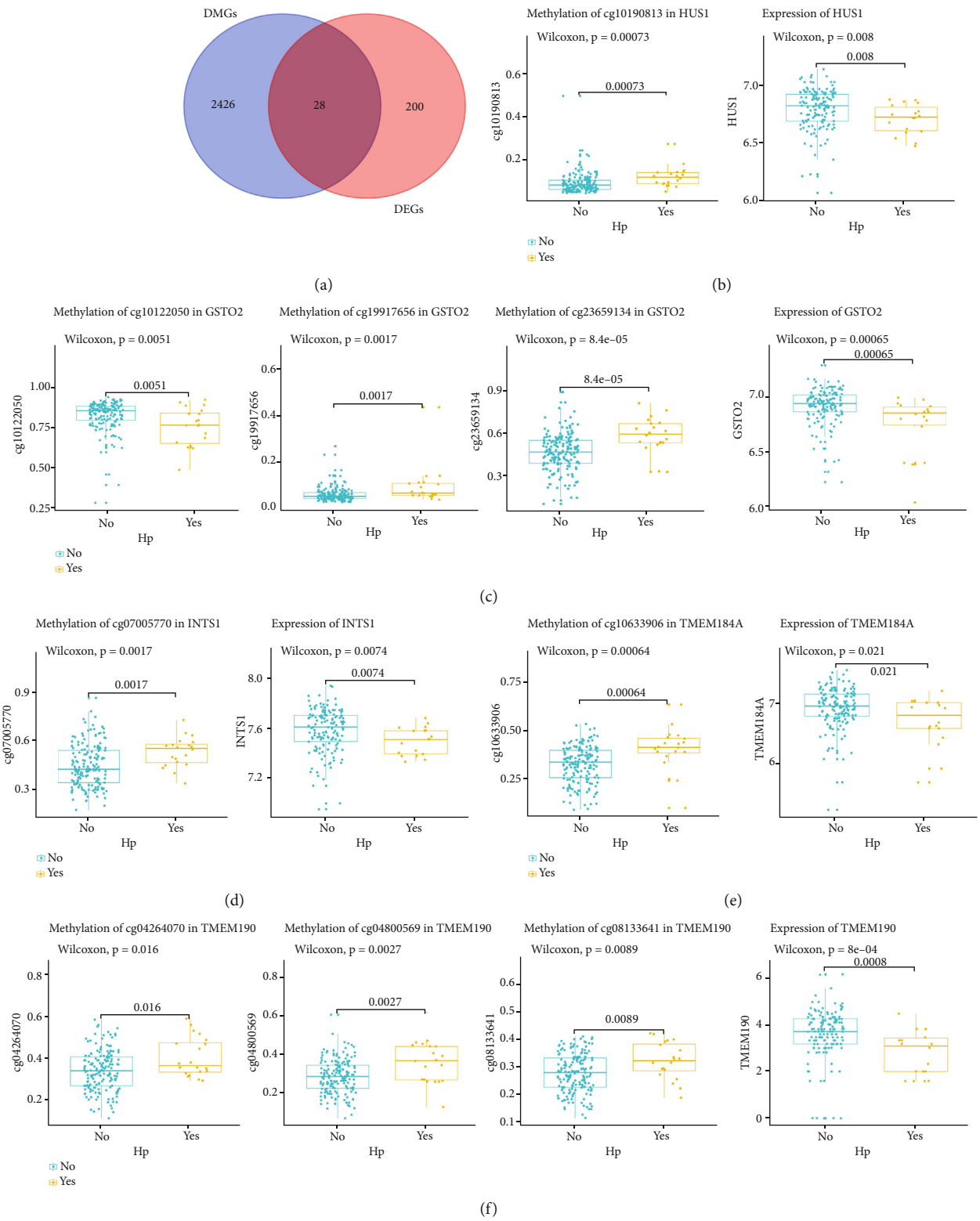

Figure 4: Screening for genes with reduced expression caused by hypermethylation. (a) Venn diagram of the intersection of 2454 DMGs and 228 DEGs. (b)–(f) Genes with reduced expression may be caused by hypermethylation. Box plots of methylation levels and gene expression levels of the five genes (GSTO2, HUS1, INTS1, TMEM184A, and TMEM190) in the two groups are shown. Blue represents the *H. pylori*-positive group, and yellow represents the *H. pylori*-negative group.

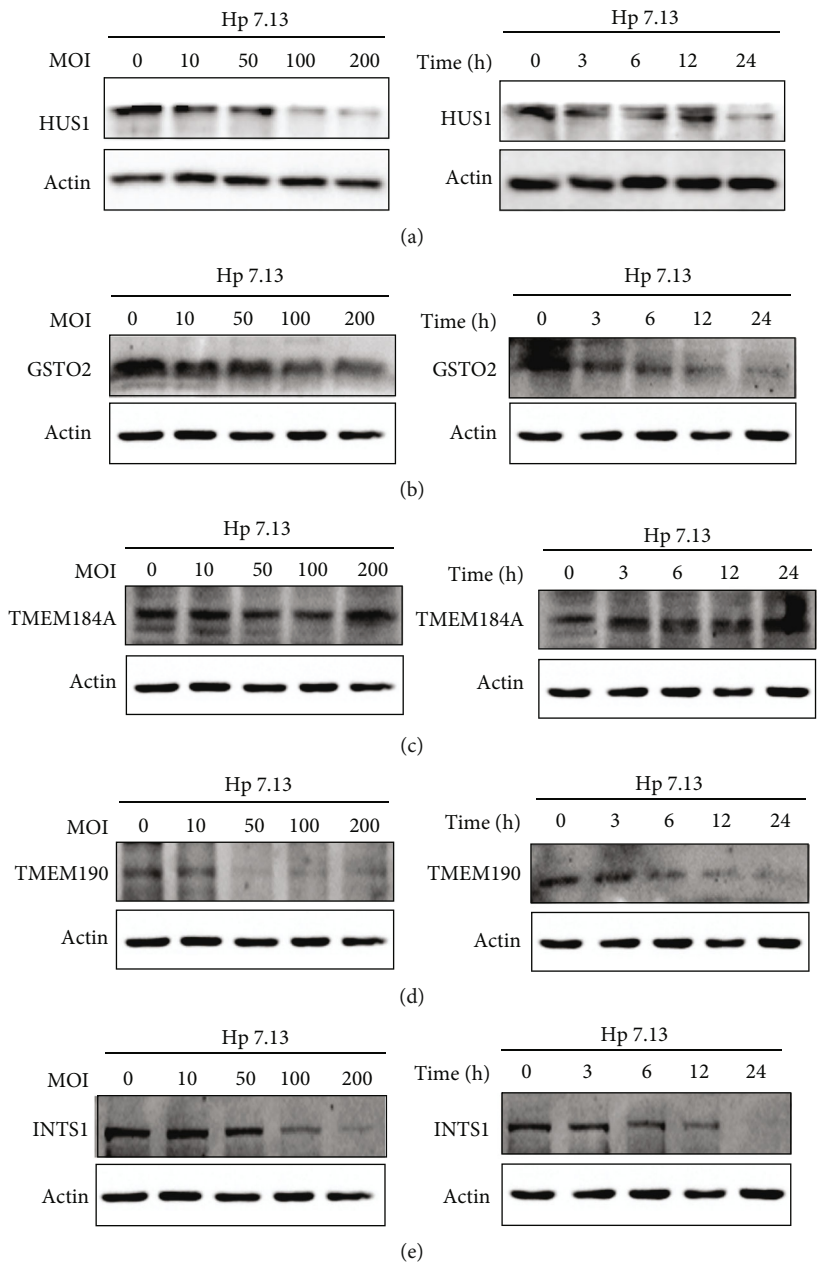

Figure 5: *In vitro* experimental verification of the five genes. (a)–(e) Western blots of the five genes (GSTO2, HUS1, INTS1, TMEM184A, and TMEM190) in AGS cells with *H. pylori* 7.13 infection at different MOIs or at different time points; $^{*}P < .05$, $^{**}P < .01$, $^{***}P < .001$.

microRNA formation [22], while its role in the pathogenesis of *H. pylori* infection has not yet been reported. In our study, *H. pylori* infection significantly downregulated its expression. However, no significant difference was detected in the expression levels in GC and adjacent tissues, which may be due to the small sample size. As a result, further experiments are needed to explore its role in *H. pylori* carcinogenesis. TMEM184A is a conserved transmembrane protein that is related to the sex determination of germ cells and the interaction between germ cells and somatic cells and participates in the anti-inflammatory response [23]. This study shows that its expression in GC is significantly lower than that in adjacent tissues. However, its relationship with *H. pylori* infection needs to be further verified. TMEM190 is a small transmembrane protein containing a trefoil domain that was previously discovered through proteomic analysis of mouse sperm. However, the biological significance of the molecule is still unclear [24]. This study found, for the first time, that *H. pylori* infection can downregulate the expression of TMEM190, and the expression of this gene in GC was significantly lower than that in adjacent tissues.

In the process of cancer occurrence and development, DNA methylation changes may be detected earlier than other types of prognostic markers, with higher clinical sensitivity and dynamic range. Therefore, the combination of

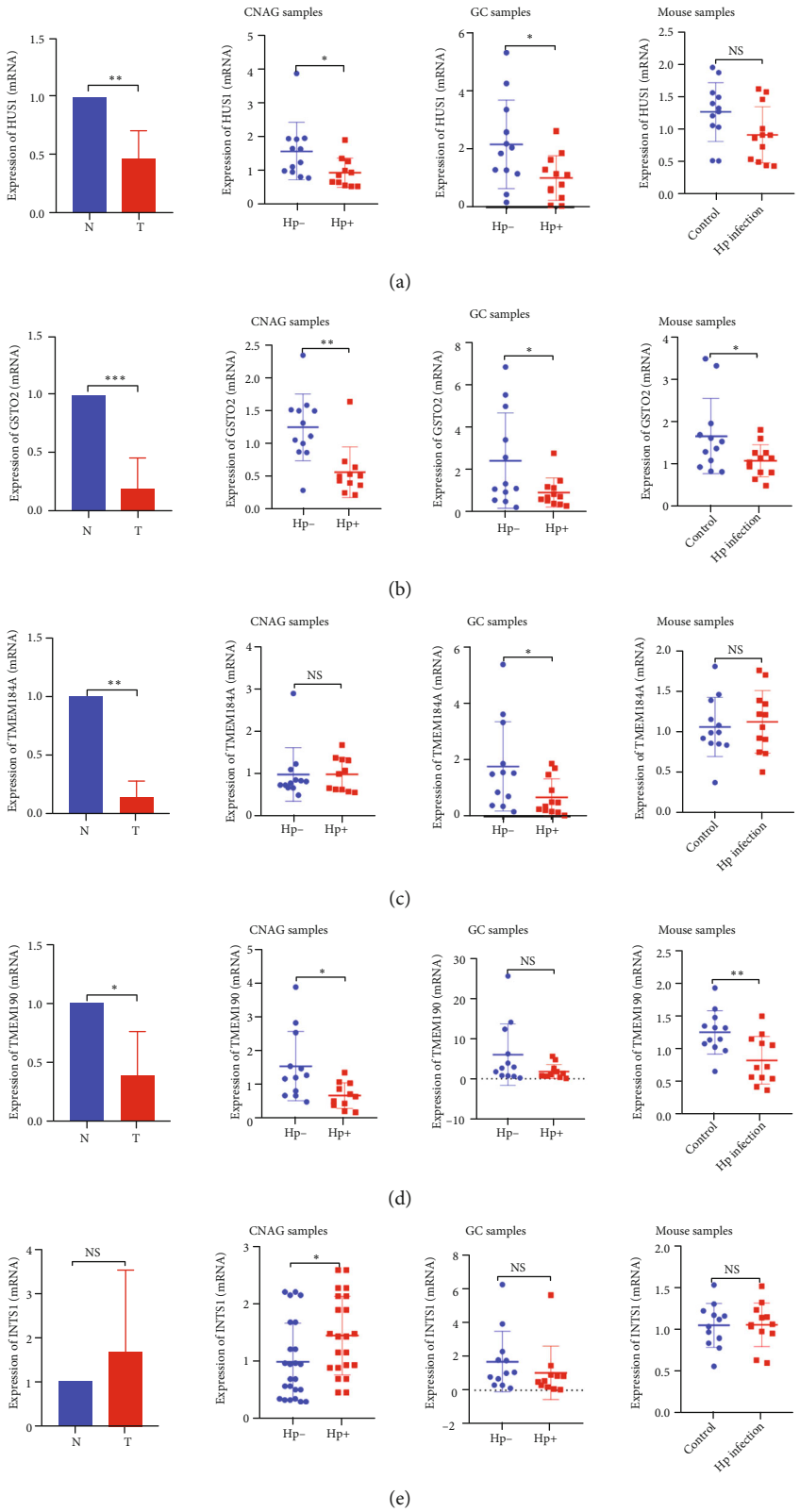

Figure 6: *In vivo* experimental verification of the five genes. (a)–(e) Expression of the five genes in GC and adjacent samples ($n = 8$), *H. pylori*-positive ($n = 11$) and *H. pylori*-negative ($n = 12$) CNAG samples, *H. pylori*-positive ($n = 12$) and *H. pylori*-negative ($n = 12$) GC samples, and *H. pylori*-infected ($n = 12$) and uninfected ($n = 12$) mouse samples. Hp-: *H. pylori*-negative; Hp+: *H. pylori*-positive. $^{*}P < .05$, $^{**}P < .01$, $^{***}P < .001$.

these candidate genes with other genetic and transcriptional events of *H. pylori*-associated GC will help to improve the accuracy of prognosis prediction. However, this study has some limitations. First, more independent datasets are required to further validate the prognostic value of the genes. Second, additional experimental studies are needed to understand their functional effects.

5. Conclusion

In conclusion, our study reveals five genes affected by methylation using public expression and epigenetic datasets. We further found that HUS1, GSTO2, and TMEM190 can be downregulated by *H. pylori* infection, and that their expression levels were lower in GC. We demonstrated that HUS1, GSTO2, and TMEM190 may play an important role in the pathogenesis and carcinogenesis of *H. pylori* infection and may be related to the methylation process. This study not only increases the understanding of the potential molecular mechanism of *H. pylori*-associated GC but also proves the role of abnormal DNA methylation in *H. pylori*-associated GC.

Data Availability

The original data used in this study were all from the TCGA database (https://cancergenome.nih.gov/).

Conflicts of Interest

The authors declare that there are no conflicts of interest.

Authors' Contributions

Wang H and Hu Y performed this study and wrote the manuscript; Li NS, He C, and Xie C revised the manuscript; Lu NH and Zhu Y designed this study and edited the manuscript.

Acknowledgments

This study was supported by the National Natural Science Foundation of China (no. 82000531); the Project for Academic and Technical Leaders of Major Disciplines in Jiangxi Province, Grant/Award number: 20194BCJ22016; the Youth Project of the Jiangxi Natural Science Foundation (20202BABL216006); the Key Fund of the Jiangxi Education Department (GJJ190007); the Scientific Research of Health Commission of Jiangxi Province (20213019); Scientific Research of Traditional Chinese Medicine of Jiangxi Province (2020A0047); the Young Teachers' Scientific Research and Cultivation Fund of the Medical Department of Nanchang University (PY201919).

Supplementary Materials

Figure S1: normalization and standardization of methylation data. (a) Unnormalized TCGA GC methylation data. (b) Normalized TCGA GC methylation data. Supplementary Table 1: list of 2454 DMGs. Supplementary Table 2: list of 228 DEGs. Supplementary Table 3: functional roles of the 28 genes. *(Supplementary Materials)*

References

[1] S. E. Crowe, "Helicobacter pylori infection," *The New England Journal of Medicine*, vol. 380, no. 12, pp. 1158–1165, 2019.

[2] J. Hooi, W. Y. Lai, W. K. Ng et al., "Global prevalence of _Helicobacter pylori_ infection: systematic review and meta-analysis," *Gastroenterology*, vol. 153, no. 2, pp. 420–429, 2017.

[3] I. J. Choi, C. G. Kim, J. Y. Lee et al., "Family history of gastric cancer and Helicobacter pylori treatment," *The New England Journal of Medicine*, vol. 382, no. 5, pp. 427–436, 2020.

[4] M. Plummer, C. de Martel, J. Vignat, J. Ferlay, F. Bray, and S. Franceschi, "Global burden of cancers attributable to infections in 2012: a synthetic analysis," *The Lancet Global Health*, vol. 4, no. 9, pp. e609–e616, 2016.

[5] K. Skvortsova, C. Stirzaker, and P. Taberlay, "The DNA methylation landscape in cancer," *Essays in Biochemistry*, vol. 63, no. 6, pp. 797–811, 2019.

[6] F. Kohler and M. Rodriguez-Paredes, "DNA methylation in epidermal differentiation, aging, and cancer," *The Journal of Investigative Dermatology*, vol. 140, no. 1, pp. 38–47, 2020.

[7] V. Ebrahimi, A. Soleimanian, T. Ebrahimi et al., "Epigenetic modifications in gastric cancer: focus on DNA methylation," *Gene*, vol. 742, article 144577, 2020.

[8] J. S. Muhammad, E. Ma, and G. Khoder, "Helicobacter pylori-induced DNA methylation as an epigenetic modulator of gastric cancer: recent outcomes and future direction," *Pathogens*, vol. 8, no. 1, p. 23, 2019.

[9] M. J. Aryee, A. E. Jaffe, H. Corrada-Bravo et al., "Minfi: a flexible and comprehensive Bioconductor package for the analysis of Infinium DNA methylation microarrays," *Bioinformatics*, vol. 30, no. 10, pp. 1363–1369, 2014.

[10] M. D. Robinson, D. J. McCarthy, and G. K. Smyth, "edgeR: a Bioconductor package for differential expression analysis of digital gene expression data," *Bioinformatics*, vol. 26, no. 1, pp. 139-140, 2010.

[11] G. Yu, L. G. Wang, Y. Han, and Q. Y. He, "clusterProfiler: an R package for comparing biological themes among gene clusters," *OMICS*, vol. 16, no. 5, pp. 284–287, 2012.

[12] C. Xie, N. Li, H. Wang et al., "Inhibition of autophagy aggravates DNA damage response and gastric tumorigenesis via Rad51 ubiquitination in response toH. pyloriinfection," *Gut Microbes*, vol. 11, no. 6, pp. 1567–1589, 2020.

[13] S. Yamashita, T. Kishino, T. Takahashi et al., "Genetic and epigenetic alterations in normal tissues have differential impacts on cancer risk among tissues," *Proceedings of the National Academy of Sciences of the United States of America*, vol. 115, no. 6, pp. 1328–1333, 2018.

[14] W. M. Grady, M. Yu, and S. D. Markowitz, "Epigenetic alterations in the gastrointestinal tract: current and emerging use for biomarkers of cancer," *Gastroenterology*, vol. 160, no. 3, pp. 690–709, 2021.

[15] B. Yousefi, M. Mohammadlou, M. Abdollahi et al., "Epigenetic changes in gastric cancer induction by Helicobacter pylori," *Journal of Cellular Physiology*, vol. 234, no. 12, pp. 21770–21784, 2019.

[16] D. C. Lazar, M. F. Avram, I. Romosan, M. Cornianu, S. Taban, and A. Goldis, "Prognostic significance of tumor immune microenvironment and immunotherapy: novel insights and future perspectives in gastric cancer," *World Journal of Gastroenterology*, vol. 24, no. 32, pp. 3583–3616, 2018.

[17] N. Li, N. Lu, and C. Xie, "The Hippo and Wnt signalling pathways: crosstalk during neoplastic progression in gastrointestinal tissue," *The FEBS Journal*, vol. 286, no. 19, pp. 3745–3756, 2019.

[18] A. M. Lyndaker, P. X. Lim, J. M. Mleczko et al., "Conditional inactivation of the DNA damage response gene Hus1 in mouse testis reveals separable roles for components of the RAD9-RAD1-HUS1 complex in meiotic chromosome maintenance," *PLoS Genetics*, vol. 9, no. 2, article e1003320, 2013.

[19] H. S. Kim, S. J. Kwack, and B. M. Lee, "Alteration of cytochrome P-450 and glutathione S-transferase activity in normal and malignant human stomach," *Journal of Toxicology and Environmental Health. Part A*, vol. 68, no. 19, pp. 1611–1620, 2005.

[20] B. L. Green, J. D. Lindy, M. C. Grace, and A. C. Leonard, "Chronic posttraumatic stress disorder and diagnostic comorbidity in a disaster sample," *The Journal of Nervous and Mental Disease*, vol. 180, no. 12, pp. 760–766, 1992.

[21] M. Masoudi, I. Saadat, S. Omidvari, and M. Saadat, "Genetic polymorphisms of GSTO2, GSTM1, and GSTT1 and risk of gastric cancer," *Molecular Biology Reports*, vol. 36, no. 4, pp. 781–784, 2009.

[22] R. Oegema, D. Baillat, R. Schot et al., "Human mutations in integrator complex subunits link transcriptome integrity to brain development," *PLoS Genetics*, vol. 13, no. 5, article e1006809, 2017.

[23] S. L. Farwell, D. Kanyi, M. Hamel et al., "Heparin decreases in tumor necrosis factor α (TNFα)-induced endothelial stress responses require transmembrane protein 184A and induction of dual specificity phosphatase 1," *The Journal of Biological Chemistry*, vol. 291, no. 10, pp. 5342–5354, 2016.

[24] H. Nishimura, S. Gupta, D. G. Myles, and P. Primakoff, "Characterization of mouse sperm TMEM190, a small transmembrane protein with the trefoil domain: evidence for colocalization with IZUMO1 and complex formation with other sperm proteins," *Reproduction*, vol. 141, no. 4, pp. 437–451, 2011.

Hindawi
Disease Markers
Volume 2021, Article ID 8668978, 9 pages
https://doi.org/10.1155/2021/8668978

Research Article

Septicemic Melioidosis Detection Using Support Vector Machine with Five Immune Cell Types

Ke Xu,[1] Fang Lian,[2] Yunfan Quan,[1] Jun Liu,[3] Li Yin,[1] Xuexia Li,[1] Shen Tian,[1] Hua Pei,[2] and Qianfeng Xia[1,2]

[1]*Key Laboratory of Tropical Translational Medicine of Ministry of Education and School of Tropical Medicine and Laboratory Medicine, Hainan Medical University, Haikou, Hainan, China*
[2]*Department of Clinical Laboratory, The Second Affiliated Hospital, Hainan Medical University, Haikou, China*
[3]*School of Basic Medicine and Life Sciences, Hainan Medical University, Haikou, Hainan, China*

Correspondence should be addressed to Hua Pei; phzmh61@aliyun.com and Qianfeng Xia; xiaqianfeng@hainmc.edu.cn

Received 26 September 2021; Accepted 17 November 2021; Published 6 December 2021

Academic Editor: Ting Su

Melioidosis, caused by *Burkholderia pseudomallei* (*B. pseudomallei*), predominantly occurs in the tropical regions. Of various types of melioidosis, septicemic melioidosis is the most lethal one with a mortality rate of 40%. Early detection of the disease is paramount for the better chances of cure. In this study, we developed a novel approach for septicemic melioidosis detection, using a machine learning technique—support vector machine (SVM). Several SVM models were built, and 19 features characterized by the corresponding immune cell types were generated by Cell type Identification Estimating Relative Subsets Of RNA Transcripts (CIBERSORT). Using these features, we trained a binomial SVM model on the training set and evaluated it on the independent testing set. Our findings indicated that this model performed well with means of sensitivity and specificity up to 0.962 and 0.979, respectively. Meanwhile, the receiver operating characteristic (ROC) curve analysis gave area under curves (AUCs) ranging from 0.952 to 1.000. Furthermore, we found that a concise SVM model, built upon a combination of CD8+ T cells, resting CD4+ memory T cells, monocytes, M2 macrophages, and activated mast cells, worked perfectly on the detection of septicemic melioidosis. Our data showed that its mean of sensitivity was up to 0.976 while that of specificity up to 0.993. In addition, the ROC curve analysis gave AUC close to 1.000. Taken together, this SVM model is a robust classification tool and may serve as a complementary diagnostic technique to septicemic melioidosis.

1. Introduction

Melioidosis is a serious tropical infectious disease that frequently outbreaks in Southeast Asia and northern Australia. The disease is caused by the gram-negative bacillus *Burkholderia pseudomallei* (*B. pseudomallei*), which inhabits in soil and surface water [1]. In endemic regions, melioidosis is a main cause of lethal community-acquired septicemia and pneumonia in adults [2, 3], and mortality rates range from10 to 50% [4]. Biologically, *B. pseudomallei* first invades epithelial cells of the mucosal surface or broken skin, is expanded intracellularly, and then disseminates to a variety of cell types, resulting in bacteremia and sapremia [5]. Basically, the *B. pseudomallei* infection leads to two types of melioidosis, acute melioidosis and chronic melioidosis. Of note, nearly 85% of melioidosis cases are of acute type, and patients with acute melioidosis develop sepsis rapidly, namely, septicemic melioidosis. This condition is a life-threatening with a mortality rate of 40% [6].

High mortality rate of patients with acute melioidosis is attributed to limitations on early clinical diagnosis. A case in point is that the bacterial blood culture remains the mainstay of melioidosis diagnosis. In fact, *B. pseudomallei* can grow on the culture media, but its growth is extremely slower than other microbes. In some cases, it takes up to more than four days for the establishment of bacterial colonies. That may miss out the best time for melioidosis treatment, as Tiangpitayakorn et al. reported that 35% of melioidosis patients died within 2 days of admission [7]. The mortality rate of the patients treated with melioidosis-

appropriate drug regimens within two days of admission was decreased by 30% [8]. These findings suggest that early detection for melioidosis is fundamental for the better chances of cure and has been recognized by many researchers as a focus of research in melioidosis. As a result, a variety of detection approaches have been developed based upon different theories. Nevertheless, these approaches, which are either performed poorly or costly, are not able to be implemented in the clinical settings [9–11]. This prompts us to search for a new detection approach with fast, accurate, yet inexpensive advantages.

Many patients with melioidosis have abnormal immune conditions, suggesting that the onset and development of the disease are mainly determined by the host's immune status [12–14]. This has been exemplified by twofold. On the one hand, most of immunocompetent individuals can clear the *B. pseudomallei* infection, leaving no clinical symptom [15]. On the other hand, individuals with long-term use of steroid, which leads to the induction and maintenance of immunosuppression, are susceptible to *B. pseudomallei* infection [15]. In addition, upon the bacterial invasion, neutrophils and macrophages were recruited at the site of infection, and neutrophils directly led to the bacterial containment [16]. Also, the T cell-mediated immune response is essential for the prevention of the active infection [17]. Jenjaroen et al. showed that the patients with melioidosis displayed the increased levels of CD4+ and CD8+ T cells, and the levels of these cells were decreased with increased mortality [18]. These abovementioned evidence supports the roles played by neutrophil macrophages and lymphocytes in the onset and development of melioidosis. The changes in the levels of these immune cells reflect the disease status. Thus, a key question is whether the immune cells serving as a unique pattern can be used for the detection of melioidosis.

Peripheral blood is an accessible source of immune cells and reflects the real immune status of individuals. Previous studies have provided useful insight based upon peripheral blood samples subjected to microarray-based profiling and analysis, suggesting that it is an instrumental approach to investigate melioidosis [19].

Computer-aided diagnosis, which are designed to help improve the accuracy of disease diagnosis [20], has been recognized by the World Health Organization (WHO) [21]. Recently, a number of computer-aided diagnoses were performed with the supervised machine learning (SML). Briefly, SML learns known data to build a mathematical model and predicts unknown data [22]. The key process incorporates multiple different statistical, probabilistic, and optimization techniques. Among a variety of learning models, the support vector machine (SVM) is a very powerful and versatile machine learning model, capable of performing linear or nonlinear classification. More importantly, SVMs are particularly well suited for classification of complex but small- or medium-sized datasets [23, 24]. Since the high-throughput microarray gene expression data was available in the early 2000s, researchers have implemented SVM on disease classification. First trial was conducted with an SVM to classify two different types of leukemia using gene expression microarray dataset in 1999 [25]. Since then, a series of breakthroughs have been achieved in clinical diagnoses [26, 27]. In this study, we employed the algorithm "Cell type Identification By Estimating Relative Subsets Of RNA Transcripts (CIBERSORT)," which has been deemed to be the most accurate method available [28]. This algorithm allows us to generate a dataset of 22 immune cell types. This dataset was then input into the training models, and a series of good classifications were made. With a series of feature selections, we found that a novel SVM model, trained by a combination of CD8+ T cells, resting CD4+ memory T cells, monocytes, M2 macrophages, and activated mast cells, is able to achieve accurate detection of septicemic melioidosis.

2. Material and Methods

2.1. Dataset Collection. The human peripheral blood microarray data were obtained from NCBI GEO datasets, the accession numbers were GSE13015 and GSE69528. In this study, 36 healthy donors (health), 39 patients with type 2 diabetes (type 2 diabetes), and 9 patients who had recovered from melioidosis (recovery), 69 patients with septicemic melioidosis (B.pseudomallei) were grouped. In addition, 91 patients with sepsis due to other organisms (other infections) were grouped, respectively, including 3 Aeromonas spp., 2 Acinetobacter lwoffii, 3 Acinetobacter baumannii, 1 Bacillus spp., Micrococcus spp., 1 Citrobacter freundii, 7 Corynebacterium spp., 1 Cryptococcus neoformans, 4 Enterococcus spp., 16 E. coli, 1 Escherichia coli, Viridans streptococcus, 1 Klebsiella pneumoniae, Viridans streptococci, 1 Klebsiella spp., Pseudomonas aeruginosa, 6 Klebsiella pneumonia, 4 Micrococcus spp., 4 Salmonella, 1 Salmonella gr. C, 1 Sphingobacterium spp., 1 Sphingomonas spp., 9 Staphylococcus aureus, 1 Streptococcus suis, 3 Streptococcus pyogenes, 4 Viridans streptococci, 1 Acinetobacter baumannii, 4 C. albicans, 1 Enterococcus faecium, 1 S. pneumoniae, 1 Salmonella serotype B, 6 Staphylococcus coagulase negative, and 2 Streptococcus non A, B.

2.2. CIBERSORT Analysis. CIBERSORT, as an instrumental tool, can precisely measure the relative levels of distinct immune cell types. It can characterize each immune cell type with a bulk gene expression signature consisting of 500 genes or so. The original CIBERSORT gene signature file LM22, defining 22 immune cell types, was applied for analyzing the dataset from the septicemic melioidosis. CIBERSORT metrics with pearson correlation coefficient, CIBERSORT p value, and root mean squared error (RMSE) were measured for each sample [28].

2.3. Training and Testing Set. Features and corresponding labels determining septicemic melioidosis status (positive for septicemic melioidosis and negative for no septicemic melioidosis) across all the samples were integrated into a data frame. The data frame was then randomly split into two data sets, the training and testing ones, according to a ratio of seven to three.

2.4. Support Vector Machine. We utilized an SVM framework provided by the python package scikit-learn to build

our binomial (septicemic melioidosis and no septicemic melioidosis) classifier. As the support vector machine is sensitive to feature scales, our classifier was actually designed to incorporate a two-step framework: the first step was a standardized scaler provided by StandardScaler class of sklearn for feature normalization, and the second step was a support vector machine classifier. A radial basis function (rbf) kernel of SVM was prioritized, and hyperparameters, gamma, and C were fine-tuned on training dataset using grid search paired with threefold cross validation, which was carried out using GridSearchCV function of sklearn. The hyperparameter set yielding the greatest average score through cross-validation was selected. The SVM framework with optimized hyperparameters was then implemented on the independent testing set for final validation.

2.5. Feature Selection. We conducted three feature selection methods in our framework. These feature selection techniques include filter-based method (select K Best (SKB)), wrapped method (recursive feature elimination), and embedded-based method (select from model (SM)). The latter two require estimators that have important features or coefficient properties. Random forest was intentionally employed as estimator, as it is eligible and can be manipulated easily.

3. Results

3.1. Principal Component Analysis Exhibited the Model Data Distributions. Having conducted CIBERSORT analysis, we obtained a large table with 22 immune cell types. The values of follicular T helper cell, dendritic resting cell, and eosinophil in more than 80% samples are zero, which is empirically useless for analysis. We therefore removed the three cell types. Principal component analysis (PCA) is by far the most popular dimensionality reduction algorithm. It identifies the right hyperplane that lies closest to the data, and the data were then projected onto it. In order to get an intuitive sense of the model data distribution, we conducted the principal component analysis. In Figure 1, the result of the projection of our dataset onto the two dimensional space was displayed. As you viewed that majority of healthy donor (health) instances were aggregated tightly on the middle right area, while the remaining spread far apart over a wide area on the left. These instances were overlapped with those of a small portion of patients with type 2 diabetes (type 2 diabetes) as well as with those of all the patients who had recovered from melioidosis (recovery). We first intended to separate patients with septicemic melioidosis (B. pseudomallei) from health, type 2 diabetes, and recovery. It seems likely that the data is nonlinearly separable since several outliers were located on the opposite side, making it impossible to find a line for separation. To address this challenge, it is preferable to select a more flexible model. Another issue was that parts of instances of B. pseudomallei and patients with sepsis due to other organisms (other infections) were massively overlapped. Tackling this issue might require to add new features (dimensionality increase) using some specialized functions or to remove some outliers.

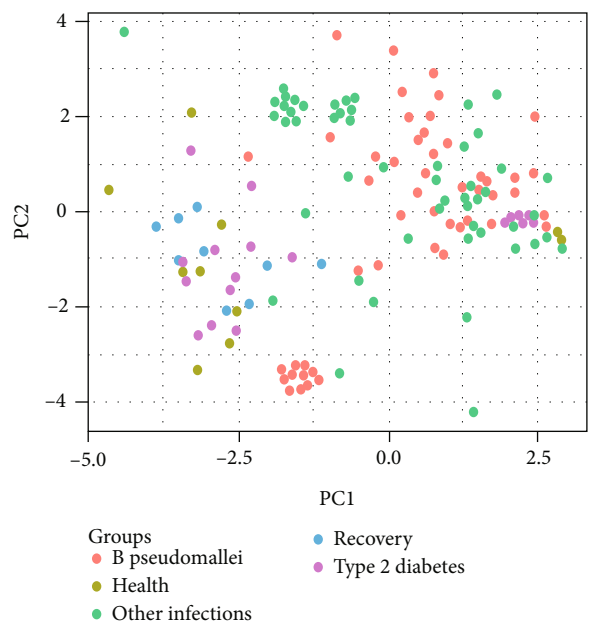

Figure 1: Principal component analysis depicting the model data distributions. B. pseudomallei denotes patients with septicemic melioidosis. Health denotes healthy donors. Type 2 diabetes denotes individuals with type 2 diabetes mellitus but have no *B. pseudomallei* infection. Recover denotes individuals recovering from septicemic melioidosis. Other infections denotes those infected with other bacterial pathogens.

3.2. Performance of Support Vector Machine on the Health, Type 2 Diabetes, and Recovery Dataset. 153 instances including 36 health, 39 type 2 diabetes, 69 B. pseudomallei, and 9 recovery, with 19 features, were randomly split into two datasets, the training and testing using 7 : 3 ratio. Accordingly, the training set incorporated 107 instances, and the testing set contained 46 instances. SVM classifier with a radical basis function (rbf) kernel in concert with default hyperparameters was implemented on the training set. After that, the trained model was performed on the testing dataset. This process was repeated four times, in order to obtain a reliable evaluation for the model. As predicted, B. pseudomallei and a mixed group including health, type 2 diabetes, and recovery were well separated (Figure 2). The means of sensitivity and specificity reach up to 0.988 and 1.000, respectively.

3.3. Performance of Support Vector Machine on the Other Infection Dataset. 160 instances (69 B. pseudomallei and 91 other infections) with 19 features were randomly split into two datasets: training and testing using 7 : 3 ratio. Accordingly, the training set incorporated 112 instances, and the testing set contained 48 instances. An SVM model with an rbf kernel and default hyperparameters were implemented on the training set. After that, the trained model was performed on the testing dataset. This process was repeated four times, in order to obtain a reliable evaluation for the model. As shown in Figure 3, classifying B. pseudomallei from other infections was difficult. The values of sensitivity ranged from 0.857 to 1.000 and those of specificity from

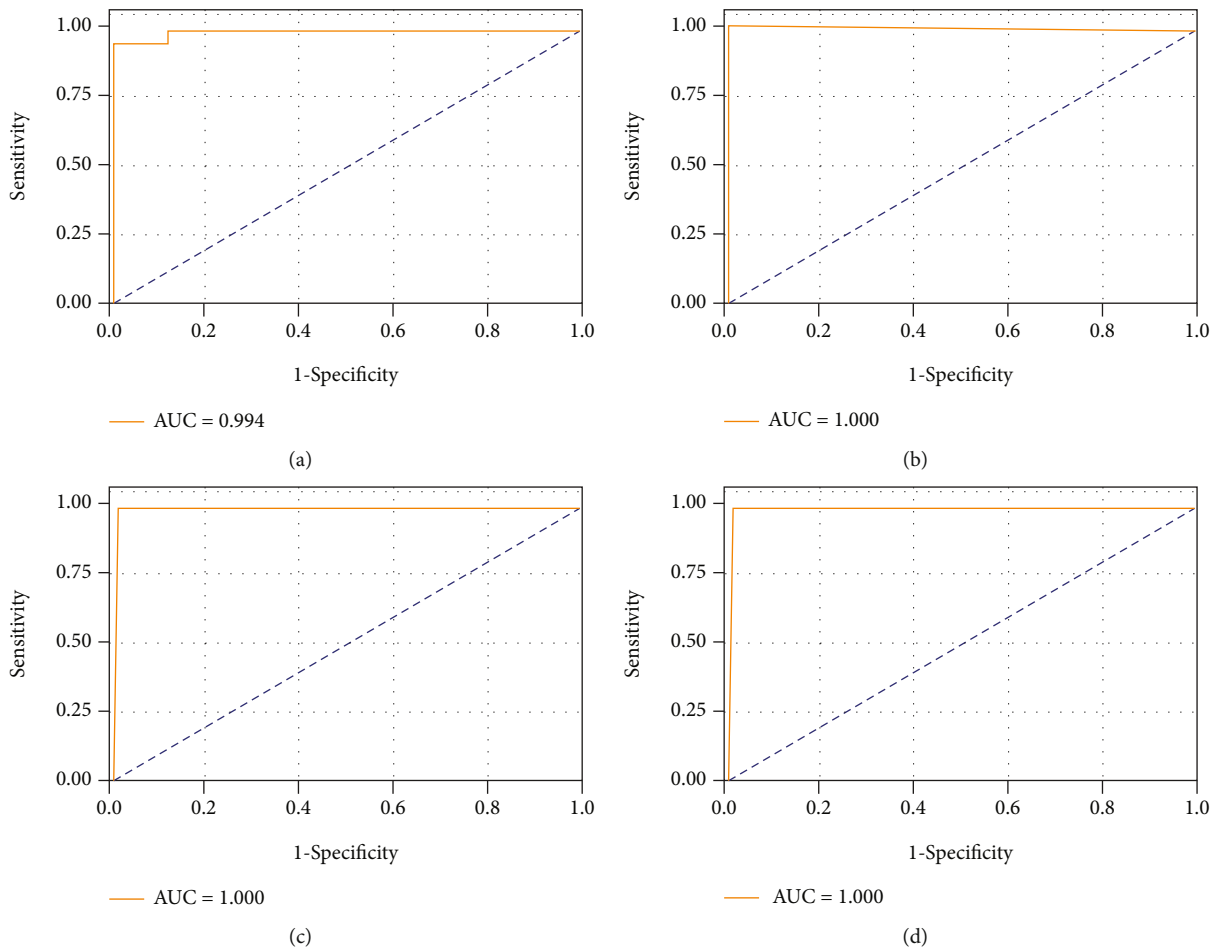

Figure 2: Receiver operating characteristic curves depicting SVM classification between patients with septicemic melioidosis and a mixed group including healthy donors, individuals with type 2 diabetes mellitus, and individuals recovering from septicemic melioidosis on testing dataset. Four subplots represent randomly resampling four times. AUC: area under the curve. Sensitivity and specificity were shown in the following brackets: (a) (0.994, 0.952, 1.000); (b) (1.000, 1.000, 1.000); (c) (1.000, 1.000, 1.000); (d) (1.000, 1.000, 1.000).

0.889 to 1.000. Since kernel selection is very important for the SVM performance and regularization (namely, tuning of hyperparameters) of the model is likely to further improve its performance, it is possible that a proper manipulation of the model selection and regularization might achieve a better performance. Therefore, we tested whether a particular set of model and hyperparameters could be selected. However, any attempt to improve the SVM performance failed, suggesting that the dataset per se may be inseparable. We reasoned that removal of some outliers from the dataset might be a better way to improve the model performance. Therefore, some combinations of 29 elements from other infections were generated, and removal of Corynebacterium spp., Enterococcus spp., E.coli, Salmonella, Staphylococcus aureus, Acinetobacter baumannii, C. albicans, Staphylococcus coagulase negative, Streptococcus non A,B, Enterococcus faecium, S. pneumoniae, and Salmonella serotype B indeed improved the model performance according to the model performance score (data not shown). The trimmed dataset was integrated into those of B. pseudomallei, health, type 2 diabetes, and recovery. An SVM model with an rbf kernel was applied on this new table. The data of Figure 4 showed that this SVM model worked perfectly. It achieved the mean of sensitivity of 0.962 and that of specificity of 0.979.

3.4. Feature Selections. One intention of our work was to provide useful guidance for the clinical diagnosis of melioidosis. Using flow cytometry to examine 19 immune cell types across the samples is laborious, costly, time-consuming, and, more importantly, infeasible. Besides, some features may be redundant or irrelevant, and they harm the performance of the model. Therefore, it is required to conduct feature selection to remove those redundant and irrelevant. Here, three feature selection techniques including filter-based method (select K Best (SKB)), wrapped method (recursive feature elimination), and embedded-based method (select from model (SM)) were employed. As a result, three sets of features were selected ((1) naïve B cells, plasma cells, gamma delta T cells, resting NK cells, activated NK cells, M0 macrophages, activated dendritic cells, activated mast cells, and neutrophils; (2) naïve B. cells, plasma cells, CD8+ T cells, naïve CD4+ T cells, gamma delta T cells, resting NK cells, activated NK cells, monocytes,. M0 macrophages, activated dendritic cells, activated mast cells, and neutrophils; and (3)

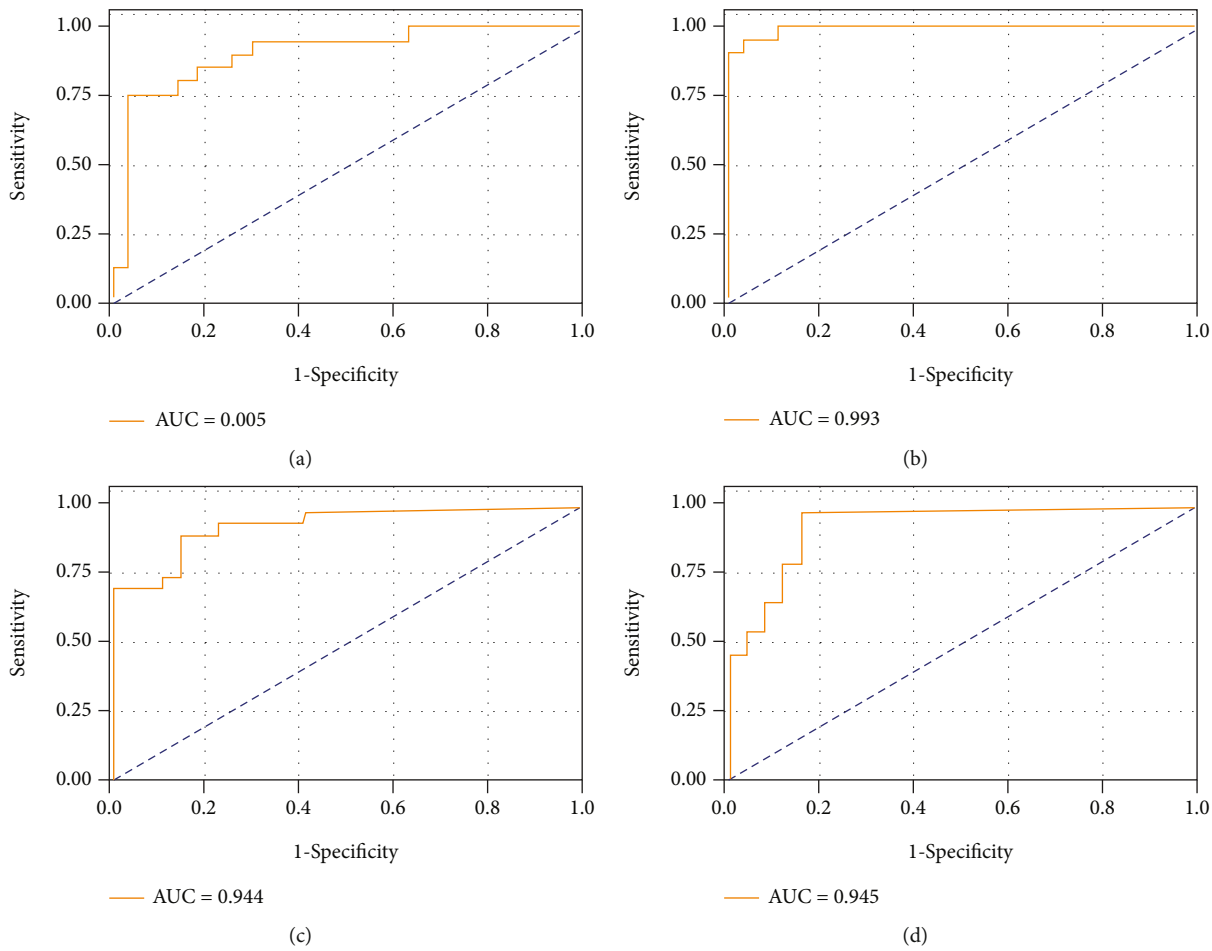

Figure 3: Receiver operating characteristic curves depicting SVM classification between patients with septicemic melioidosis and other infections on testing dataset. Four subplots represent randomly resampling four times. AUC: area under the curve. Sensitivity and specificity were shown in the following brackets: (a) (0.905, 0.857, 0.889); (b) (0.993, 1.000, 1.000); (c) (0.944, 0.905, 1.000); (d) (0.945, 0.905, 1.000).

naïve B cells, plasma cells, naïve CD4+ T cells, resting CD4+ memory T cells, regulatory T cells, activated NK cells, M0 macrophages, M2 macrophages, activated dendritic cells, resting mast cells, and activated mast cells). The three sets of features were pooled, generating a set of 16 features. We next screened all possible combinations of the 16 features. The entire process was evaluated by the model performance score, and our ultimate goal was to search for an excellent combination with fewer elements. Our findings indicated that CD8+ T cells, resting CD4+ memory T cells, monocytes, M2 macrophages, and activated mast cells were relevant features. Only when these five features worked together could we improve the SVM model (rbf kernel) performance, with means of sensitivity and specificity up to 0.976 and 0.993, respectively. These findings indicated that merely five features are able to help classify B. pseudomallei from the other groups.

4. Discussion

Bacterial blood culture is the gold standard for melioidosis diagnosis, but it has low sensitivity and takes more than four days to make definitive conclusion. That may cause the patients to miss out the best time for melioidosis treatment, according to previous studies showing that 35% of melioidosis patients died within 2 days of admission [7]. The mortality rate of the patients treated with melioidosis-appropriate drug regimens within two days of admission was decreased by 30% [8]. These results suggest that incompetent early detection is a main cause of high mortality rate. To address this challenge, researchers have developed a variety of early detection approaches. But these existing techniques have their own limitations. For instance, many serological diagnostic assays have been developed for detecting specific antibodies produced in response to *B. pseudomallei* infection. But most of them are based on poorly characterized antigens and have never been subjected to large-scale critical evaluation. Of these assays, indirect haemagglutination test is the most commonly utilized. This assay on admission has a sensitivity of only 56% in Australia [29] and 73% in Thailand [10]. Moreover, 68% of the patients with test negative on admission subsequently showed seroconversion [29]. The indirect haemagglutination test fails probably because the healthy population in the endemic regions are usually

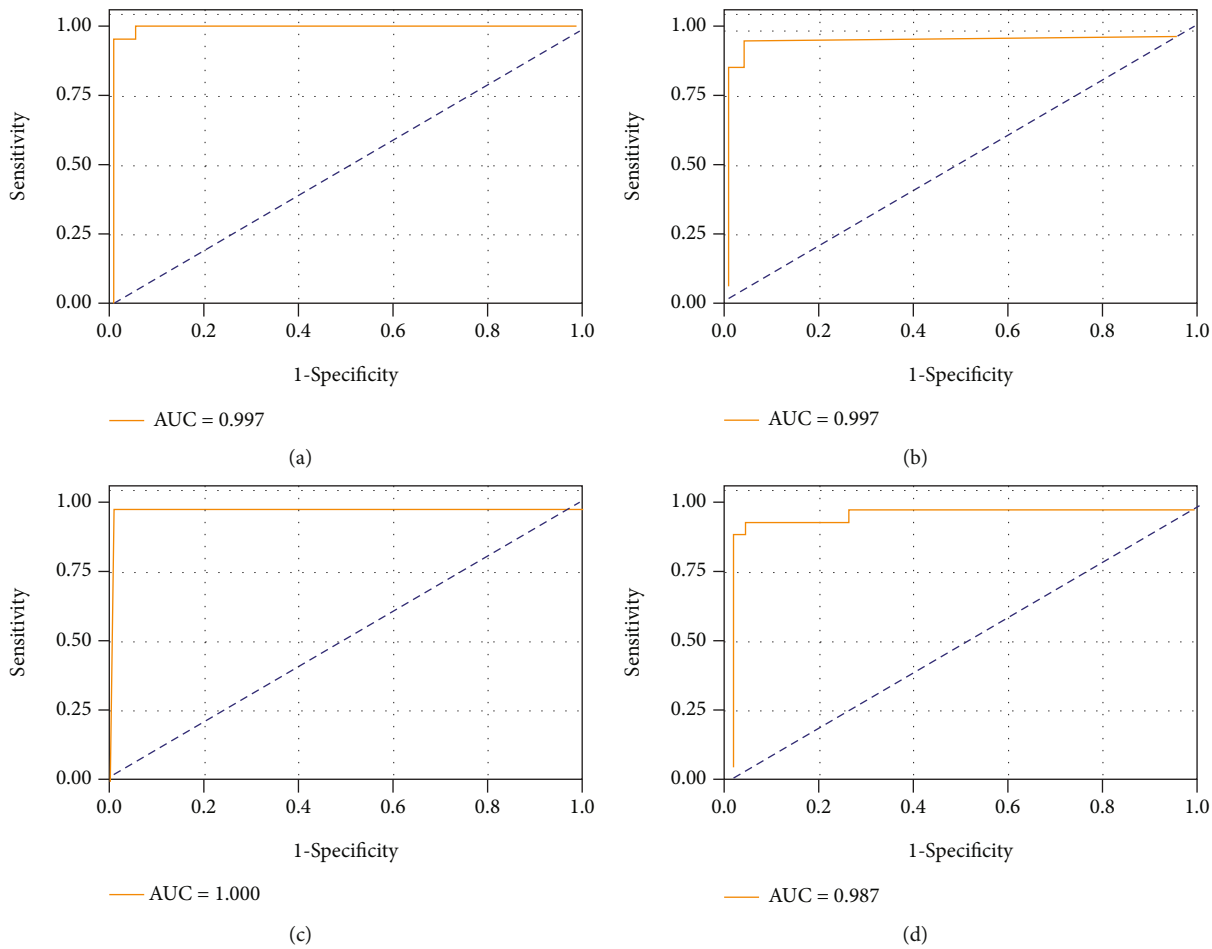

Figure 4: Receiver operating characteristic curves depicting SVM classification between patients with septicemic melioidosis and a mixed group including healthy donors, individuals with type 2 diabetes mellitus, individuals recovering from septicemic melioidosis, and part of other infections on testing dataset. Four subplots represent randomly resampling four times. AUC: area under the curve. Sensitivity and specificity were shown in the following brackets: (a) (0.997, 0.952, 1.000); (b) (0.997, 0.952, 0.972); (c) (1.000, 1.000, 0.972); (d) (0.987, 0.952, 0.972).

exposed to *B. pseudomallei* [2, 10]. The specific antibodies against *B. pseudomallei* are generated and become detectable in the blood. As a result, a number of patients with fever are misdiagnosed with melioidosis. Conversely, some patients with melioidosis who are supposed to produce the antibodies do not otherwise mount an adequate humoral immune response. Of note, our approach is not dependent upon the performance of humoral immune response. Removal of B cells and plasma cells did not harm the SVM model accuracy but rather improved its performance (Figure 5). Another popular serological assay is serum IgG ELISAs [30, 31]. This assay shows 72% to 83% sensitivity and greater than 95% specificity, but it is impossible to separate recovered patients from those with active infections [11, 30]. In contrast, our approach is fully capable of addressing this challenge and offers perfect sensitivity and specificity (0.988 and 1.000) (Figure 2). Lastly, it should be noted that a protein microarray using both recombinant and purified B. pseudomallei proteins for serum IgG capture shows greater than 80% sensitivity and 97% specificity [32]. Obviously, it is outperformed by our approach. Apart from the detection performance, the protein microarray-based approach is unlikely to be inexpensive in the short run.

Our findings indicated that five immune cell types (CD8 + T cells, resting CD4+ memory T cells, monocytes, M2 macrophages, and activated mast cells) were relevant to detection of septicemic melioidosis, suggesting that these cell types might be implicated in the onset and development of the disease. Similarly, in the C57BL/6 mice cell model, PECM (peritoneal exudate cells macrophage identified by nonspecific esterase) and NAPEC (nonadherent peritoneal exudate cells that were believed to be full of lymphocytes) cultures exhibited remarkably lower microbicidal activity against *B. pseudomallei*, when compared to PEC (peritoneal exudate cells) suggesting that lymphocyte, in concert with macrophages, may promote killing of *B. pseudomallei* [33]. Jenjaroen et al. found that the patients with acute melioidosis survived, with a significant change in the levels of CD4 + and CD8 + T cells, when compared to those dead [18]. Due to the technical limitations, these studies have necessarily been limited to a very narrow view of the immune response, only investigating a handful of immune cells.

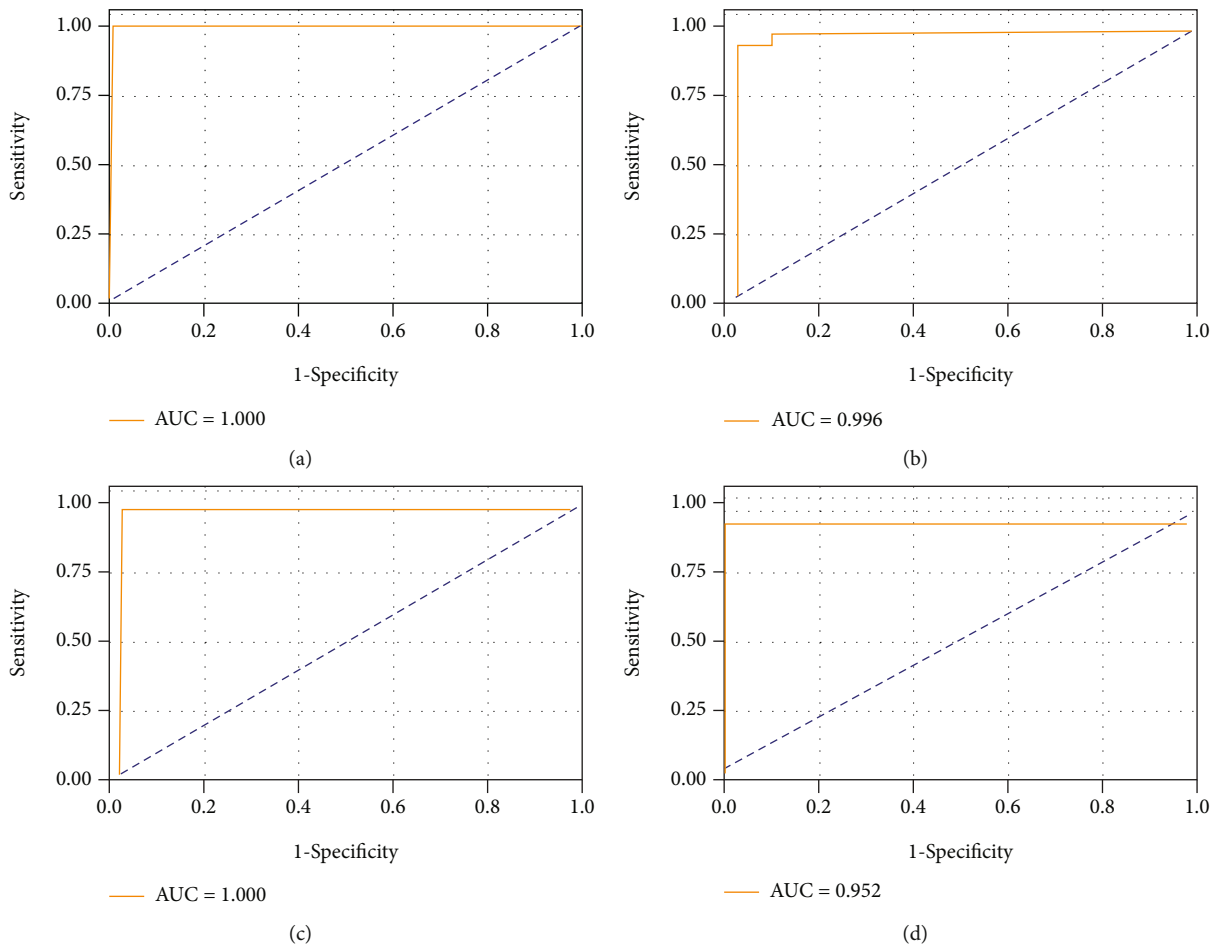

Figure 5: Receiver operating characteristic curves depicting SVM classification between patients with septicemic melioidosis and a mixed group including healthy donors, individuals with type 2 diabetes mellitus, individuals recovering from septicemic melioidosis, and part of other infections on testing dataset, using merely five immune cell types. Four subplots represent randomly resampling four times. AUC: area under the curve. Sensitivity and specificity were shown in the following brackets: (a) (1.000, 1.000, 1.000); (b) (0.996, 0.952, 1.000); (c) (1.000, 1.000, 0.972); (d) (0.952, 0.952, 1.000).

Moreover, they do not specify which T cell subsets play important roles in melioidosis. According to the data of CIBERSORT and SVM analysis, we propose that CD8+ T cells and resting CD4+ memory T cells may be relevant to septicemic melioidosis. In our future investigations, we will confirm the functional contributions of the two T cell subsets during septicemic melioidosis.

Macrophages present in several forms, including proinflammatory (M1), nonactivated (M0), or anti-inflammatory (M2) that play distinct roles in the initiation and development of inflammation. In melioidosis, little is known about M2 macrophages. But there are several studies of macrophage forms on the other intracellular bacterial pathogens (IBPs). For instance, M2 macrophages were a comfortable replication niche for *Salmonella* and *Brucella* strains [34, 35]. And these cells favor expansion of *Chlamydia pneumoniae* [36]. In this study, M2 macrophage was selected from 22 immune cell types, suggesting that M2 macrophage may be relevant to septicemic melioidosis. The specific role of M2 macrophage is needed to be further investigated.

Monocytes are a type of leukocyte or white blood cell. They are the largest type of leukocyte and can differentiate into macrophages and myeloid lineage dendritic cells. It was found that monocytes of patients with melioidosis well suited for *B. pseudomallei* survival and expansion, when compared to those from healthy donors [37]. In the C57BL/6 melioidosis mouse model, the role of monocyte has been elucidated. Briefly, microabscesses developed secondary to primary foci via hematogenous routes, and *B. pseudomallei* was steadily harbored inside monocytes [38, 39] located in the inflamed liver and spleen during early infection. Subsequently, the bacterium was released into the blood by the infected monocyte-derived Kupffer cells. Once bacteremia recurred or persisted, *B. pseudomallei* invaded differentiated monocytes. During late infection, the circulating monocytes harboring *B. pseudomallei* were expanded [40]. Consistent with these findings, our results revealed that monocyte was one of the most important immune cell types during septicemic melioidosis. Unexpectedly, neutrophil is not in our shortlist, while activated mast

cells were included. These findings are needed to be further confirmed with experiments in the near future. Meanwhile, considering that the role of mast cell in melioidosis remains unclear, we presume that it might be a reasonable direction to investigate melioidosis.

In conclusion, the results of the present study indicate that an SVM model with five features including CD8+ T cells, resting CD4+ memory T cells, monocytes, M2 macrophages, and activated mast cells is a robust detection tool for septicemic melioidosis. As a promising diagnostic approach, it may serve as a complementary to improve detection and diagnosis of this disease.

5. Conclusion

It has been reported that 35% of melioidosis patients died within 2 days of admission. However, the bacterial blood culture, which is the gold standard for melioidosis diagnosis, take more than four days, along with low sensitivity, and patients could miss out the best time for melioidosis treatment. Therefore, more and more techniques for the early detection of melioidosis have been developed. However, these techniques are either costly, time-consuming, or poor performance with low sensitivity and specificity. Here, we developed a novel early detection of melioidosis, based upon the support vector machine algorithms and peripheral blood microarray data. This technique gave an excellent detection outcome with high sensitivity and specificity over other existing counterparts. More importantly, it triangulated the five immune cell types, and these cell types might be unitized to develop low-cost fast detection techniques in the near future.

Data Availability

The datasets in this study can be obtained in NCBI datasets. The accession numbers can be found in this paper.

Ethical Approval

Ethical approval is not required.

Conflicts of Interest

The authors declare that they have no conflicts of interest.

Authors' Contributions

QX and HP designed the study. JL, LY, XL, and ST carried out the literature search. HP, YQ, and JL collected the data. KX and FL carried out the data analysis. KX wrote the paper with QX, and HP reviewed and edited. All authors contributed ideas and comments, revised the paper, and approved the final version. Ke Xu and Fang Lian contributed equally to this work.

Acknowledgments

We gratefully acknowledge project supported by the Hainan Province Clinical Medical Center. This study was funded by Major Science and Technology Program of Hainan Province (ZDKJ202003), the National Natural Science Foundation of China (grant nos. 81960002, 81660502, and 81860002), the Hainan Natural Science Foundation (No. 820MS051), and the Top Experts Program of Hainan Province (2019RC381).

References

[1] W. J. Wiersinga, B. J. Currie, and S. J. Peacock, "Melioidosis," *New England Journal of Medicine*, vol. 367, no. 11, pp. 1035–1044, 2012.

[2] W. Chaowagul, N. J. White, D. A. Dance et al., "Melioidosis: a major cause of community-acquired septicemia in northeastern Thailand," *Journal of Infectious Diseases*, vol. 159, no. 5, pp. 890–899, 1989.

[3] D. Limmathurotsakul, N. Golding, D. A. Dance et al., "Predicted global distribution of Burkholderia pseudomallei and burden of melioidosis," *Nature Microbiology*, vol. 1, no. 1, article 15008, 2016.

[4] A. C. Cheng and B. J. Currie, "Melioidosis: epidemiology, pathophysiology, and management," *Clinical Microbiology Reviews*, vol. 18, no. 2, pp. 383–416, 2005.

[5] D. Limmathurotsakul, M. Kanoksil, V. Wuthiekanun et al., "Activities of daily living associated with acquisition of melioidosis in northeast Thailand: a matched case-control study," *PLoS Neglected Tropical Diseases*, vol. 7, no. 2, article e2072, 2013.

[6] N. White, "Melioidosis," *The Lancet*, vol. 361, no. 9370, pp. 1715–1722, 2003.

[7] S. Songsivilai, C. Tiangpitayakorn, N. Piyasangthong, and T. Dharakul, "Speed of detection of Burkholderia pseudomallei in blood cultures and its correlation with the clinical outcome," *The American Journal of Tropical Medicine and Hygiene*, vol. 57, no. 1, pp. 96–99, 1997.

[8] O. Sangwichian, T. Whistler, A. Nithichanon et al., "Adapting microarray gene expression signatures for early melioidosis diagnosis," *Journal of Clinical Microbiology*, vol. 58, no. 7, 2020.

[9] D. Limmathurotsakul, K. Jamsen, A. Arayawichanont et al., "Defining the true sensitivity of culture for the diagnosis of melioidosis using Bayesian latent class models," *PLoS One*, vol. 5, no. 8, article e12485, 2010.

[10] A. C. Cheng, S. J. Peacock, D. Limmathurotsakul et al., "Prospective evaluation of a rapid immunochromogenic cassette test for the diagnosis of melioidosis in northeast Thailand," *Transactions of the Royal Society of Tropical Medicine and Hygiene*, vol. 100, no. 1, pp. 64–67, 2006.

[11] V. Suttisunhakul, V. Wuthiekanun, P. J. Brett et al., "Development of rapid enzyme-linked immunosorbent assays for detection of antibodies to Burkholderia pseudomallei," *Journal of Clinical Microbiology*, vol. 54, no. 5, pp. 1259–1268, 2016.

[12] B. J. Currie, "Melioidosis: evolving concepts in epidemiology, pathogenesis, and treatment," *Seminars in Respiratory and Critical Care Medicine*, vol. 36, no. 1, pp. 111–125, 2015.

[13] Y.-H. Gan, "Interaction between Burkholderia pseudomallei and the Host Immune Response: Sleeping with the Enemy?," *The Journal of Infectious Diseases*, vol. 192, no. 10, pp. 1845–1850, 2005.

[14] K. Xu, D. Xu, H. Pei et al., "Whole blood transcriptome analysis reveals the correlation between specific immune cells and

septicemic melioidosis," *Disease Markers*, vol. 2021, 13 pages, 2021.

[15] Z. Chagla, N. Aleksova, J. Quirt, J. Emery, C. Kraeker, and S. Haider, "Melioidosis in a returned traveller," *Canadian Journal of Infectious Diseases and Medical Microbiology*, vol. 25, no. 4, 226 pages, 2014.

[16] A. Easton, A. Haque, K. Chu, R. Lukaszewski, and G. J. Bancroft, "A critical role for neutrophils in resistance to experimental infection with Burkholderia pseudomallei," *The Journal of Infectious Diseases*, vol. 195, no. 1, pp. 99–107, 2007.

[17] J. Barnes, J. Warner, W. Melrose et al., "Adaptive immunity in melioidosis: a possible role for T cells in determining outcome of infection with _Burkholderia pseudomallei_," *Clinical Immunology*, vol. 113, no. 1, pp. 22–28, 2004.

[18] K. Jenjaroen, S. Chumseng, M. Sumonwiriya et al., "T-cell responses are associated with survival in acute melioidosis patients," *PLoS Neglected Tropical Diseases*, vol. 9, no. 10, article e0004152, 2015.

[19] R. Pankla, S. Buddhisa, M. Berry et al., "Genomic transcriptional profiling identifies a candidate blood biomarker signature for the diagnosis of septicemic melioidosis," *Genome Biology*, vol. 10, no. 11, p. R127, 2009.

[20] A. Tartar, N. Kilic, and A. Akan, "Classification of pulmonary nodules by using hybrid features," *Computational and Mathematical Methods in Medicine*, vol. 2013, 11 pages, 2013.

[21] W. Gulbinat, "What is the role of WHO as an intergovernmental organisation," in *The coordination of telematics in healthcare*, World Health Organisation Geneva, Switzerland, 1997, http://www.hon.ch/libraray/papers/gulbinat.html.

[22] J. A. Cruz and D. S. Wishart, "Applications of machine learning in cancer prediction and prognosis," *Cancer Informatics*, vol. 2, article 117693510600200, 2006.

[23] H.-Y. Wang, B.-Y. Sun, Z.-H. Zhu et al., "Eight-signature classifier for prediction of nasopharyngeal carcinoma survival," *Journal of Clinical Oncology*, vol. 29, no. 34, pp. 4516–4525, 2011.

[24] Y. Jiang, W. Liu, T. Li et al., "Prognostic and predictive value of p21-activated kinase 6 associated support vector machine classifier in gastric cancer treated by 5-fluorouracil/oxaliplatin chemotherapy," *eBioMedicine*, vol. 22, pp. 78–88, 2017.

[25] T. R. Golub, D. K. Slonim, P. Tamayo et al., "Molecular classification of cancer: class discovery and class prediction by gene expression monitoring," *Science*, vol. 286, no. 5439, pp. 531–537, 1999.

[26] A. Statnikov, C. F. Aliferis, I. Tsamardinos, D. Hardin, and S. Levy, "A comprehensive evaluation of multicategory classification methods for microarray gene expression cancer diagnosis," *Bioinformatics*, vol. 21, no. 5, pp. 631–643, 2005.

[27] R. Zhang, G.-B. Huang, N. Sundararajan, and P. Saratchandran, "Multicategory classification using an extreme learning machine for microarray gene expression cancer diagnosis," *IEEE/ACM Transactions on Computational Biology and Bioinformatics*, vol. 4, no. 3, pp. 485–495, 2007.

[28] A. M. Newman, C. L. Liu, M. R. Green et al., "Robust enumeration of cell subsets from tissue expression profiles," *Nature Methods*, vol. 12, no. 5, pp. 453–457, 2015.

[29] G. Lum, K. Freeman, B. Currie, M. O'brien, and A. Cheng, "Indirect hemagglutination assay in patients with melioidosis in northern Australia," *The American Journal of Tropical Medicine and Hygiene*, vol. 74, no. 2, pp. 330–334, 2006.

[30] A. Pumpuang, S. J. Dunachie, P. Phokrai et al., "Comparison of O-polysaccharide and hemolysin co-regulated protein as target antigens for serodiagnosis of melioidosis," *PLoS Neglected Tropical Diseases*, vol. 11, no. 3, article e0005499, 2017.

[31] Y. Hara, C.-Y. Chin, R. Mohamed, S. D. Puthucheary, and S. Nathan, "Multiple-antigen ELISA for melioidosis - a novel approach to the improved serodiagnosis of melioidosis," *BMC Infectious Diseases*, vol. 13, no. 1, p. 165, 2013.

[32] C. Kohler, S. J. Dunachie, E. Müller et al., "Rapid and sensitive multiplex detection of Burkholderia pseudomallei-specific antibodies in melioidosis patients based on a protein microarray approach," *PLoS Neglected Tropical Diseases*, vol. 10, no. 7, article e0004847, 2016.

[33] G. C. Ulett, N. Ketheesan, and R. G. Hirst, "Macrophage-lymphocyte interactions mediate anti-Burkholderia pseudomallei activity," *FEMS Immunology & Medical Microbiology*, vol. 21, no. 4, pp. 283–286, 1998.

[34] N. A. Eisele, T. Ruby, A. Jacobson et al., "Salmonella Require the Fatty Acid Regulator PPAR δ for the Establishment of a Metabolic Environment Essential for Long-Term Persistence," *Cell Host & Microbe*, vol. 14, no. 2, pp. 171–182, 2013.

[35] M. N. Xavier, M. G. Winter, A. M. Spees et al., "PPARγ-Mediated Increase in Glucose Availability Sustains Chronic Brucella abortus Infection in Alternatively Activated Macrophages," *Cell Host & Microbe*, vol. 14, no. 2, pp. 159–170, 2013.

[36] T. Buchacher, A. Ohradanova-Repic, H. Stockinger, M. B. Fischer, and V. Weber, "M2 polarization of human macrophages favors survival of the intracellular pathogen Chlamydia pneumoniae," *PLoS One*, vol. 10, no. 11, article e0143593, 2015.

[37] S. Puthucheary and S. Nathan, "Comparison by electron microscopy of intracellular events and survival of Burkholderia pseudomallei in monocytes from normal subjects and patients with melioidosis," *Singapore Medical Journal*, vol. 47, no. 8, pp. 697–703, 2006.

[38] P.-J. Liu, Y.-S. Chen, H.-H. Lin et al., "Induction of mouse melioidosis with meningitis by CD11b+ phagocytic cells harboring intracellular B. pseudomallei as a Trojan horse," *PLoS Neglected Tropical Diseases*, vol. 7, no. 8, article e2363, 2013.

[39] S. R. Zaki, Y. L. Chen, P. W. Greer et al., "Alteration of the phenotypic and pathogenic patterns of Burkholderia pseudomallei that persist in a soil environment," *The American Journal of Tropical Medicine and Hygiene*, vol. 90, no. 3, pp. 469–479, 2014.

[40] Y.-S. Chen, H.-H. Lin, P.-T. Hsueh et al., "Involvement of L-selectin expression in Burkholderia pseudomallei-infected monocytes invading the brain during murine melioidosis," *Virulence*, vol. 8, no. 6, pp. 751–766, 2017.

Hindawi
Disease Markers
Volume 2021, Article ID 7879508, 10 pages
https://doi.org/10.1155/2021/7879508

Research Article

A Novel Predictive Nomogram including Serum Lipoprotein a Level for Nonsentinel Lymph Node Metastases in Chinese Breast Cancer Patients with Positive Sentinel Lymph Node Metastases

Zeng Fang,[1] Ruizhi Wang,[2] Ciqiu Yang,[3] Dong Wang,[2] Wanna Chen,[1] Bo Lin,[1] Dongsheng Gong,[2] Songqi Li,[1] Jiadong Liang,[1] Xiaoli Liang,[1] Chunxian Zeng,[4] Jie Li,[1] Kun Wang,[3] and Weiming Lv[1]

[1]*Department of Breast and Thyroid Surgery, First Affiliated Hospital, Sun Yat-sen University, China*
[2]*Department of Laboratory Medicine, First Affiliated Hospital, Sun Yat-sen University, China*
[3]*Department of Breast Surgery, Guangdong Provincial People's Hospital, Guangdong Academy of Medical Science, China*
[4]*Shenzhen Key Laboratory of Viral Oncology, Clinical Innovation & Research Center, Shenzhen Hospital, Southern Medical University, China*

Correspondence should be addressed to Jie Li; lijie78@mail.sysu.edu.cn, Kun Wang; gzwangkun@126.com, and Weiming Lv; lvwm@mail.sysu.edu.cn

Received 12 August 2021; Accepted 26 October 2021; Published 22 November 2021

Academic Editor: Yi Shao

Background. We developed a new nomogram combining serum biomarkers with clinicopathological features to improve the accuracy of prediction of nonsentinel lymph node (SLN) metastases in Chinese breast cancer patients. *Methods*. We enrolled 209 patients with breast cancer who underwent SLN biopsy and axillary lymph node dissection. We evaluated the relationships between non-SLN metastases and clinicopathologic features, as well as preoperative routine tests of blood indexes, tumor markers, and serum lipids, including lipoprotein a (Lp(a)). Risk factors for non-SLN metastases were identified by logistic regression analysis. The nomogram was created using the R program to predict the risk of non-SLN metastases in the training set. Receiver operating characteristic (ROC) analysis was applied to assess the predictive value of the nomogram model in the validation set. *Results*. Lp(a) was significantly associated with non-SLN metastasis status. Compared with the MSKCC model, the predictive ability of our new nomogram that combined Lp(a) level and clinical variables (pathologic tumor size, lymphovascular invasion, multifocality, and positive/negative SLN numbers) was significantly greater (AUC: 0.732, 95% CI: 0.643–0.821) (C-index: 0.703, 95% CI: 0.656–0.791) in the training cohorts and also performed well in the validation cohorts (C-index: 0.773, 95% CI: 0.681–0.865). Moreover, the new nomogram with Lp(a) improved the accuracy (12.10%) of identification of patients with non-SLN metastases (NRI: 0.121; 95% CI: 0.081–0.202; $P = 0.011$). *Conclusions*. This novel nomogram based on preoperative serum indexes combined with clinicopathologic features facilitates accurate prediction of risk of non-SLN metastases in Chinese patients with breast cancer.

1. Introduction

The sentinel lymph node (SLN) is the first organ reached by metastasizing cancer cells. At present, the SLN biopsy procedure is used to assess regional lymph node involvement in patients with breast cancer. The standard treatment for breast cancer patients with SLN metastases is complete axillary lymph node dissection (ALND) [1, 2]. However, approximately 50% of patients with positive SLN do not have additional nodal metastases after ALND [3]. Therefore, many patients undergo unnecessary ALND, with no additional therapeutic benefit or further staging information

provided. Thus, the need for complete ALND in patients with SLN metastases and at low risk of lymph node metastases is controversial [4, 5].

New models for accurate prediction of the status of non-SLN metastasis in patients with metastasis-positive SLN and to distinguish patients with low risk of lymph node metastasis are urgently required to avoid unnecessary ALND. Currently, a prediction model designed by the Memorial Sloan Kettering Cancer Center (MSKCC) is widely used in clinical practice [6]. This model is user-friendly and provides precise and individualized estimate advantages; however, it has been reported that the MSKCC nomogram, which is based on samples from Western countries (reported AUC: 0.77), is unsatisfactory for prediction in Chinese populations (tested AUC: from 0.683 to 0.700) [7, 8].

Previous studies and MSKCC models have suggested that clinicopathologic features, such as pathologic size, lymphovascular invasion, multifocality, and positive/negative SLN numbers, are independent risk factors for non-SLN metastases [6–8]. However, the correlation between preoperative blood indexes and non-SLN metastases in patients with positive SLN biopsies remains to be determined. Furthermore, no predictive nomogram for the risk of non-SLN metastases in patients with a positive SLN biopsy based on clinicopathologic features and preoperative serum markers has yet been developed. Therefore, in this study, we aimed to identify some markers in blood as risk factors for non-SLN metastases and to construct a novel nomogram combined with MSKCC model factors and blood markers for the prediction of non-SLN metastases in Chinese patients with positive SLN metastasis to guide treatment.

2. Materials and Methods

2.1. Patients. This retrospective study was approved by the Ethics Committee of the First Affiliated Hospital, Sun Yat-sen University and Guangdong Provincial People's Hospital (China). Data were retrieved from the medical records of patients who underwent surgery for breast cancer at the First Affiliated Hospital, Sun Yat-sen University and Guangdong Provincial People's Hospital. Patient records were anonymized and deidentified prior to analysis, and the requirement to obtain written informed consent from patients was waived by the committee approval because of the retrospective study design.

A total of 209 patients with metastasis-positive SLNs who underwent ALND between January 2014 and July 2019 were retrospectively enrolled in this study. The following inclusion criteria were applied: (1) histologically confirmed primary breast cancer before surgery, (2) no preoperative distant metastases, and (3) clinicopathologic features and data for serum markers including routine blood test indexes (white blood cell (WBC), Neu (neutrophil), Lym (lymphocyte), platelet (PLT), neutrophil to lymphocyte ratio (NLR), and platelet to lymphocyte ratio (PLR)), tumor markers (carcinoembryonic antigen (CEA), carbohydrate antigen 153 (CA153), and carbohydrate antigen 125

Table 1: Descriptive characteristics of the primary cohort and validation cohort.

	Primary cohort ($n = 116$)		Validation cohort ($n = 93$)		P
	n	%	n	%	
Age (year)					
≤50	66	56.9	49	52.7	0.607
>50	50	43.1	44	47.3	
Pathologic size (cm)					
≤0.5	7	6.0	2	2.2	
0.6-1.0	19	16.4	9	9.7	
1.1-2.0	59	50.9	29	31.2	0.103
2.1-3.0	26	22.4	31	33.3	
3.1-4.0	2	1.7	15	16.1	
4.1-5.0	2	1.7	5	5.4	
≥5.1	1	0.9	2	2.1	
Tumor type					
Ductal	114	98.3	92	98.9	0.976
Lobular	2	1.7	1	1.1	
Lymphovascular invasion					
No	94	81.0	81	87.1	0.339
Yes	22	19.0	12	12.9	
Multifocality					
No	112	96.6	88	94.6	0.900
Yes	4	3.4	5	5.4	
Estrogen-receptor status					
Negative	17	14.7	12	12.9	0.718
Positive	99	85.3	81	87.1	
No. of positive SLN					
1	57	49.1	48	51.6	
2	27	23.3	20	21.5	
3	16	13.8	13	14.0	0.255
4	9	7.8	3	3.2	
5	4	3.4	4	4.3	
6	1	0.9	2	2.2	
7	2	1.7	3	3.3	
No. of negative SLN					
0	20	17.2	14	15.1	
1	20	17.2	9	9.7	
2	26	22.4	18	19.4	
3	16	13.8	18	19.4	0.314
4	13	11.2	16	17.2	
5	6	5.2	7	7.5	
6	9	7.8	5	7.2	
7	6	5.2	5	7.2	
Non-SLN metastases					
Yes	58	50.0	52	55.9	0.397
No	58	50.0	41	54.1	

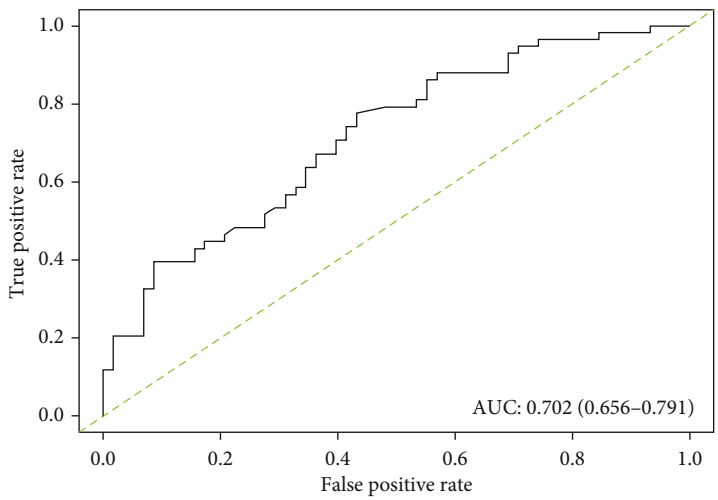

Figure 1: A receiver operating characteristic (ROC) curve of the MSKCC model illustrated an AUC of 0.702 (95% CI: 0.656-0.791), which revealed a worse ability to estimate the status of non-SLN metastasis in Chinese patients.

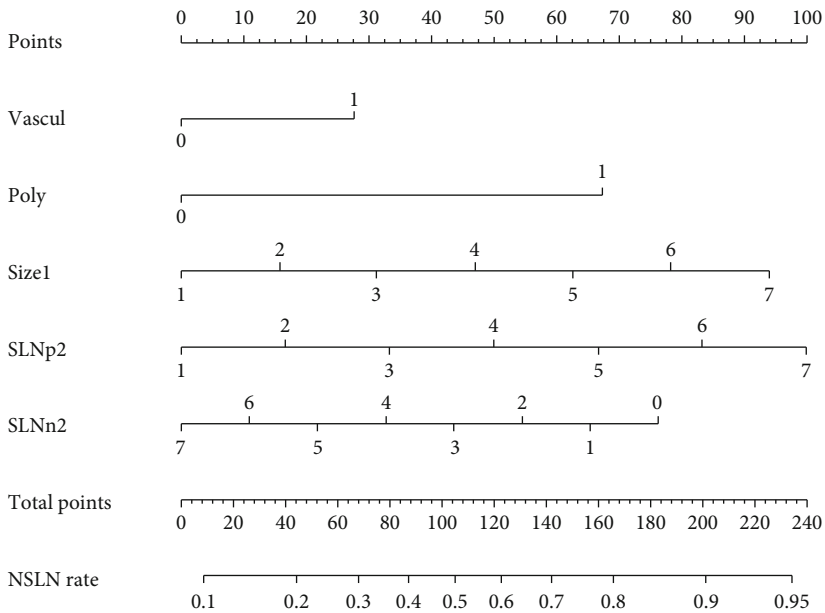

Figure 2: A nomogram composed of clinical-related factors from the MSKCC model in primary cohort. The risk value of lymph node metastasis was calculated by drawing a vertical line to the point on the axis for each of the factors. The points for each factor were summed and located on the total point line. And then, the bottom line corresponding vertically to the above total line illustrated the individual predictive value for lymph node metastasis.

(CA125)), and serum lipids (cholesterol (Chol), triglyceride (TG), low-density lipoprotein cholesterol (LDL-c), high-density lipoprotein cholesterol (HDL-c), apolipoprotein A (ApoA), apolipoprotein B (ApoB), apolipoprotein E (ApoE), and Lp(a)) were clearly recorded. The exclusion criteria were as follows: (1) prior history of SLN biopsy, (2) any preoperative chemotherapy or radiotherapy, (3) with another malignancy or life-threatening disease diagnosed during the three years prior to surgery, and (4) death in hospital due to postoperative complications. Of the enrolled patients, 116 were assigned to the training set and 93 were assigned to the validation set.

2.2. Identification of Combined Serum Markers and Clinicopathologic Features. Preoperative data for serum markers, including routine blood indexes (WBC, Neu, Lym, PLT, NLR, and PLR), tumor markers (CEA, CA153, and CA125), and lipids (Chol, TG, LDL-c, HDL-c, ApoA, ApoB, ApoE, and Lp(a)) were standardized by measurement using the same tests and reported using consistent units. The clinicopathologic features of age, pathologic tumor size, tumor type (ductal vs. lobular), lymphovascular invasion (yes vs. no), multifocality (yes vs. no), estrogen-receptor status (yes vs. no), histological grade (I/II vs. III), and positive and negative SLN numbers were analyzed. The presence

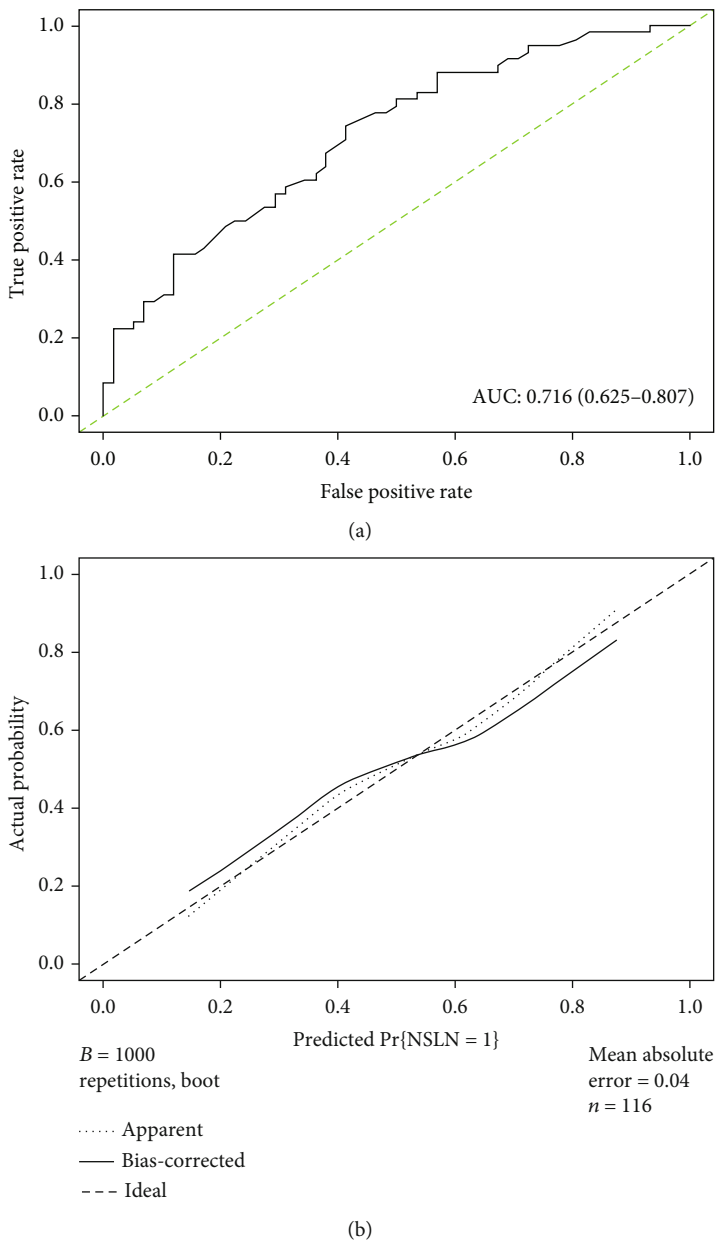

Figure 3: ROC curve and calibration plot of nomogram in primary cohort. (a) ROC curve of the model illustrated an AUC of 0.716 (95% CI: 0.625-0.807), which revealed a better ability to estimate the status of non-SLN metastasis in Chinese patients. (b) Calibration plot of a nomogram.

and absence of SLN metastases were diagnosed histologically and defined as non-SLN(+) and non-SLN(-), respectively.

2.3. Statistical Analysis and Nomogram Construction. All statistical analyses were performed using SPSS version 19.0 and R (version3.1.2 URL http://www.R-project.org/). Unordered categorical variables were analyzed using the Chi-squared test. Logistic regression analysis was used to analyze risk factors for non-SLN metastases. A nomogram was used as a model to evaluate the value of factors for predicting the risk of non-SLN metastases in patients. The predictive accuracy of the nomogram was then validated by ROC analysis and quantified by calculation of the area under the ROC curve (AUC). An AUC of 0.5 indicates no relationship while an AUC of 1.0 indicates perfect concordance. Moreover, the nomogram was subjected to 1,000 bootstrap resamples for reduction of overfit bias and for internal validation with a logistic calibration plot. A two-sided P value < 0.05 was considered to indicate statistical significance. Net reclassification improvement (NRI) was determined using R software to evaluate the improvement of the nomogram compared with the MSKCC nomogram.

3. Results

3.1. Clinical Characteristics. In total, 209 breast cancer patients who underwent ALND were enrolled in this study.

The average age of the patients was 41 years (range, 21–79 years). Of these patients, 116 (58 non-SLN(-) and 58 non-SLN(+))were allocated to the training cohort and 93 (41 non-SLN(-) and 52 non-SLN(+)) were allocated to the validation cohort. The baseline clinical and pathological characteristics of all the study participants are listed in Table 1. The baseline clinicopathologic factors were similar in the two cohorts. The rates of non-SLN(+) were 50.0% and 55.9% in the training and validation cohorts, respectively.

3.2. Nomogram Based on Clinical Factors from the MSKCC Model and Predictive Ability of the MSKCC Model in Chinese Patients. Using the MSKCC model, a score was assigned to each patient in the training cohort. The total score calculated using the nomogram corresponded to a predictive value for the risk of non-SLN metastasis. A ROC curve was generated to validate the predictive accuracy of the nomogram; the AUC was 0.702 (95% CI: 0.656–0.791) (Figure 1).

We then constructed a nomogram based on the clinical factors from the MSKCC model to predict the risk of non-SLN metastasis for patients in the training primary cohort (Figure 2). A ROC curve and calibration plot were generated to validate the predictive accuracy of this nomogram model (Figure 3). The AUC of the ROC curve for this model was 0.716 (95% CI: 0.625–0.807).

These results confirmed the inferior ability of the nomogram for predicting the status of lymph node involvement in Chinese patients compared with previous reports in Western patients (reported AUC: 0.77) [6].

3.3. Identification of Risk Factors and Multivariate Analysis for Prediction of Risk of Non-SLN Metastasis. Logistic regression analysis was performed to determine the risk factors for non-SLN metastasis (Table 2). In the univariate analysis, clinicopathologic features, such as age, pathologic tumor size, lymphovascular invasion, multifocality, estrogen-receptor status, numbers of positive and negative SLNs, CEA, CA125, LDL-c, HDL-c, and Lp(a), were found to be significantly associated with non-SLN metastasis. In the multivariate analysis, pathologic tumor size, numbers of positive and negative SLNs, and Lp(a) were identified as independent risk factors for non-SLN metastasis.

3.4. Nomogram Combining Lp(a) and Clinical-Related Factors from the MSKCC Model Predicts Non-SLN Metastasis. A new nomogram was constructed to predict the risk of non-SLN metastasis for patients based on the combination of Lp(a), a novel independent risk factor identified in the training set, and clinical factors from the MSKCC model (Figure 4). For each patient, points were assigned for each of the clinicopathologic risk factors. A total score was calculated from the nomogram to predict the risk of non-SLN metastasis. A ROC curve and calibration plot were generated to validate the predictive accuracy of this nomogram model (Figure 5). The AUC of the ROC curve for this model was 0.732 (95% CI: 0.643-0.821), which revealed good concordance and a reliable ability to estimate the status of lymph node involvement.

Table 2: Univariable and multivariable logistic regression analysis of factors associated with the incidence of non-SLN metastases.

Clinical variables	*P*
Univariable analysis	
Age	0.072
Pathologic size	0.083
Tumor type (ductal vs. lobular)	0.999
Lymphovascular invasion (yes vs. no)	0.160
Multifocality (yes vs. no)	0.332
Estrogen-receptor status (yes vs. no)	0.195
Grade (I/II vs. III)	0.521
No. of positive SLN	0.015
No. of negative SLN	0.008
WBC	0.743
Neu	0.781
Lym	0.995
PLT	0.896
NLR	0.690
PLR	0.804
CEA	0.152
CA125	0.115
CA153	0.547
Chol	0.857
TG	0.404
LDL-c	0.325
HDL-c	0.303
ApoA	0.909
ApoB	0.628
ApoE	0.950
Lp(a)	0.130
Multivariable analysis	
No. of positive SLN	0.009
No. of negative SLN	0.009
Pathologic size	0.038
Lp(a)	0.028

To assess the validity of this model and evaluate the level of improvement in accuracy gained by using the selected clinicopathologic features and biomarkers in this new nomogram, we calculated the NRI between the new nomogram with Lp(a) and the nomogram without Lp(a). A shown in Table 3, the new nomogram with Lp(a) provides a 12.10% improvement in the accuracy of the model for identification of patients with non-SLN metastasis compared with the old nomogram (NRI: 0.121; 95% CI: 0.081–0.202; $P = 0.011$).

Having developed a novel and promising nomogram model to predict the risk of non-SLN metastasis in patients with a positive SLN biopsy, we then examined its predictive ability in our validation cohort. The favorable calibration of the new nomogram was confirmed with the validation cohort, with a C-index of 0.773 (95% CI: 0.681-0.865) for the estimation of the risk of non-SLN metastasis (Figure 6).

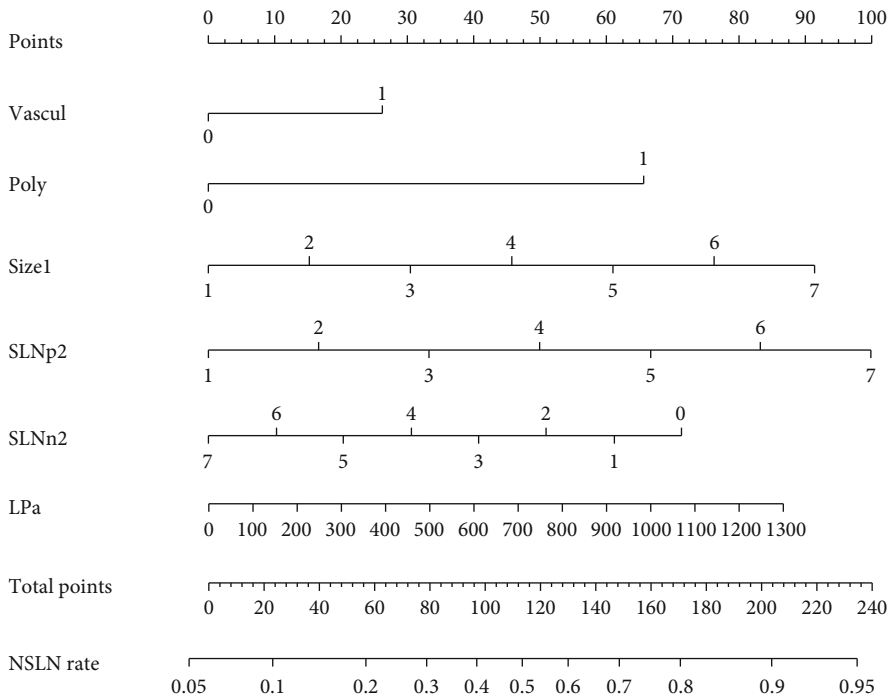

Figure 4: A nomogram composed of Lp(a) and clinical-related factors from the MSKCC model in primary cohort. Constructed Lp(a) nomogram to predict non-SLN metastasis for Chinese patients, with the pathologic size, tumor type (ductal vs. lobular), lymphovascular invasion (yes vs. no), multifocality (yes vs. no), estrogen-receptor status (yes vs. no), No. of positive SLN, No. of negative SLN, and Lp(a) level.

4. Discussion

An effective method to improve the accuracy of predicting the risk of non-SLN metastasis in patients with a positive SLN biopsy is urgently needed in the era of precision medicine. In this study, we first analyzed common blood indexes to identify differential biomarkers in the training cohort and found that Lp(a) was found to be significantly associated with the risk of non-SLN metastasis. We next constructed a new nomogram based on the combination of clinicopathologic features from the MSKCC model and Lp(a) levels using the training cohort. The performance of this new nomogram for prediction of the risk of non-SLN metastasis was verified in the validation cohort. The subgroup of patients identified with a very low risk of non-SLN metastasis using this nomogram might be candidates for observation rather than immediate ALND, which is recommended for the patients identified with a high risk of non-SLN metastasis. Thus, our nomogram may improve the prediction of non-SLN metastasis status and guide individualized therapies for patients with a positive SLN biopsy.

Accumulating evidence shows a close relationship between the level of blood lipids and the occurrence and development of tumors, including breast cancer [9–13]. However, the mechanism underlying this correlation is not completely clear, and the data are inconsistent [14–18]. For example, in a study of 2,724 patients with breast cancer conducted in Sweden over a period of four years, Olsson reported a positive correlation with breast cancer in individuals with hypolipidemia and diabetes, which is inconsistent with the results obtained in studies in China [13]. Serum lipids represent a group of indicators with a variety of functions. In accordance with these characteristics, different, and even directly conflicting, conclusions on the relationships between these factors and breast cancer have been reported. Studies have shown that cholesterol metabolites (27-hydroxycholesterol) in humans have estrogenic functions and bind to estrogen receptors in breast tumor cells, thus promoting the proliferation of breast tumor cells [19]. These results highlight the potential of statins or dietary management to reduce the risk of the occurrence, progression, and recurrence of breast cancer. However, some studies have shown that cholesterol metabolites inhibit the occurrence and development of breast cancer. Dendrogenin A, a metabolite produced by cholesterol and histamine metabolism, has been shown to stimulate breast cancer cell redifferentiation both in vitro and in vivo [20]. In addition, new data have shown that the incidence, recurrence rate, and mortality of breast cancer are positively correlated with the intake of high-fat dairy products [21].

Lp(a) is a cholesterol-rich macromolecular lipoprotein [22] that exists at relatively stable concentrations in serum. LP(a) levels are determined mainly by genetic factors and are largely unaffected by statins, age, sex, smoking, diet, environment, lipid metabolism, and other factors [23–25]. This suggests the potential value of serum LP(a) as a predictive biomarker. Lp(a) is an independent risk factor for cardiovascular diseases such as coronary artery

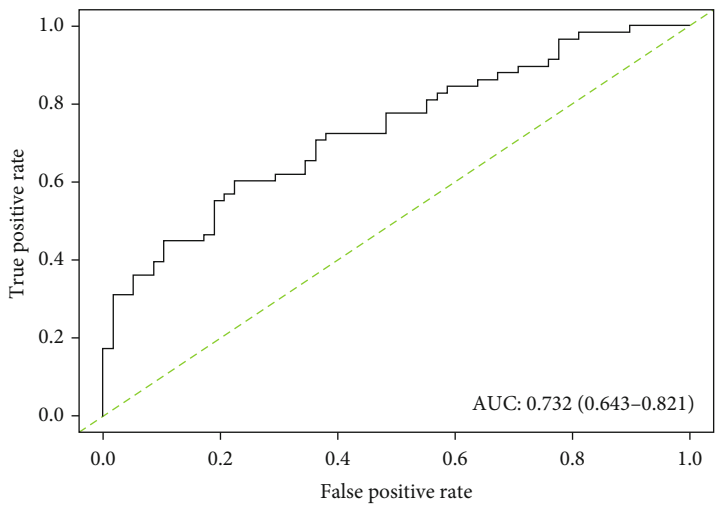

(a)

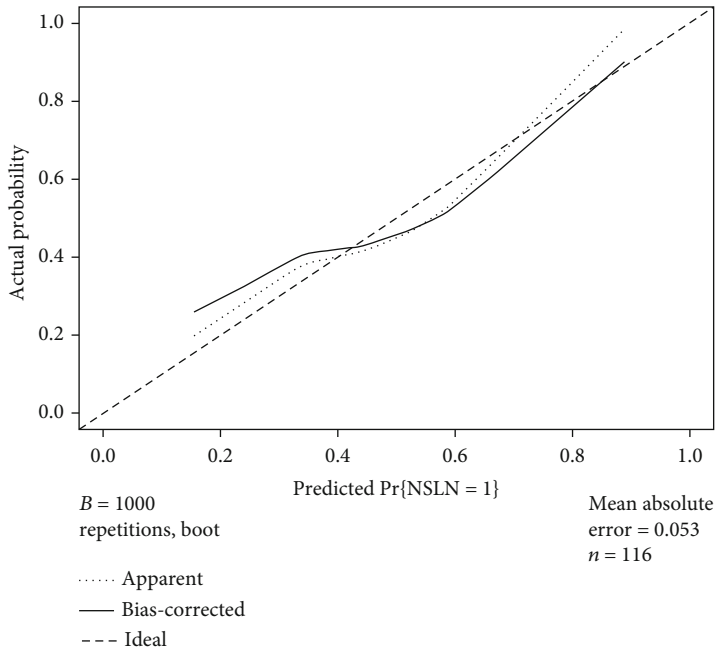

(b)

Figure 5: ROC curve and calibration plot of new nomogram in primary cohort. (a) ROC curve of the model illustrated an AUC of 0.732 (95% CI: 0.643-0.821), which revealed a good concordance and a reliable ability to estimate the status of non-SLN metastasis in Chinese patients. (b) Calibration plot of a new nomogram.

Table 3: Improved predictive ability of new nomogram compared to the MSKCC model in Chinese patients by NRI.

	Improved ability (95% CI)	*P* value
NRI	0.121 (0.081-0.202)	0.011

disease, peripheral vascular disease, and calcified aortic valve disease [26–30]. However, our study is the first to provide evidence of the relationship between Lp(a) and breast cancer.

Previous studies have evaluated the risk of non-SLN metastasis in patients with a positive SLN biopsy based on a combination of clinicopathologic features and a micro-RNA-based signature or one-step nucleic acid amplification [30, 31]. Although these studies showed high accuracy for the prediction in non-SLN metastasis, such approaches are inconvenient in clinical practice. Therefore, we evaluated the potential of blood biomarkers as an effective approach for the prediction of non-SLN metastasis in patients with a positive SLN biopsy. Our results suggest that the evaluation of serum Lp(a) levels could be an important tool for the management of patients with positive SLN, assisting in the stratification of patients that may harbor non-SLN metastases, aiding in therapy planning and patient staging, and ultimately contributing to an improvement in quality of life and survival rates.

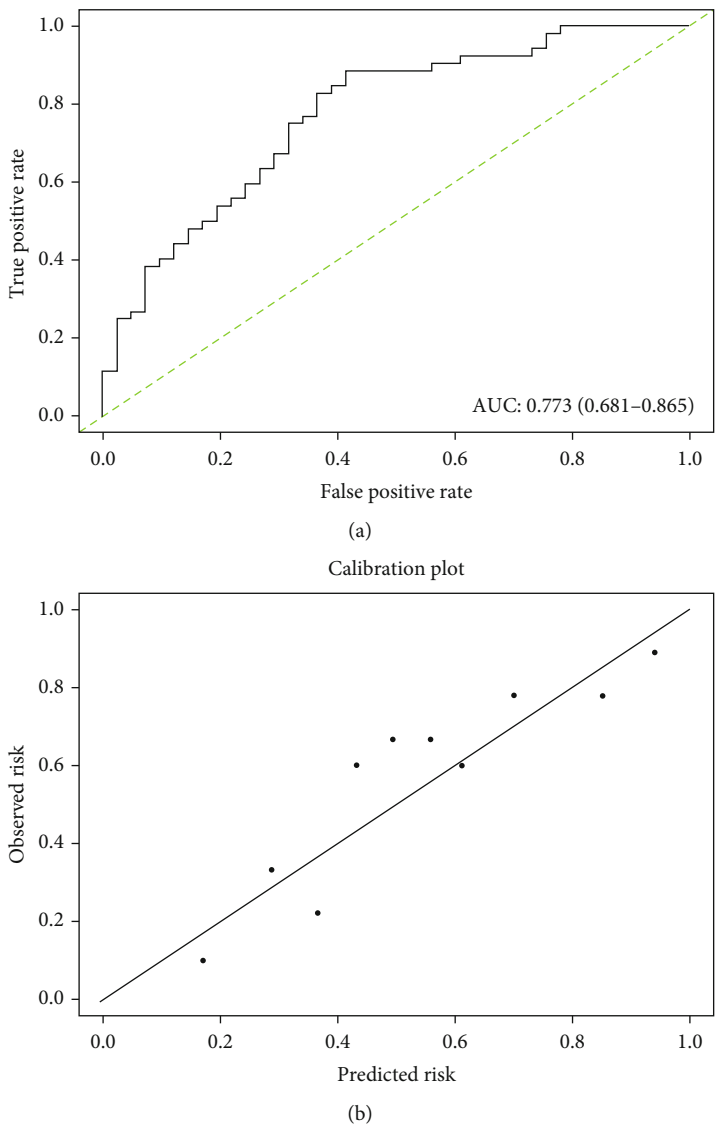

Figure 6: ROC curve and calibration plot of a new nomogram in validation cohort. (a) ROC curve of the model illustrated an AUC of 0.773 (95% CI: 0.681-0.865), which revealed a good concordance and a reliable ability to estimate the status of non-SLN metastasis in Chinese patients. (b) Calibration plot of a new nomogram.

Several limitations of our study should be noted. First, the results could be influenced by inherent biases and variation associated with a retrospective study design. Second, the model was established and validated in cohorts from the same ethnic group (Chinese). As breast cancer patients in China are often younger than in those in other countries, our prediction model may not be directly applicable in non-Asian patients. Fourth, only a relatively small number of patients were enrolled in our study; therefore, our results required confirmation in large-scale, multiethnic, and multicenter clinical trials.

5. Conclusions

In this study, we evaluated the value of serum biomarkers for accurate prediction of non-SLN metastasis in patients with a positive SLN biopsy and revealed an association between serum Lp(a) levels and lymph node metastases in breast cancer. Our results suggest that serum Lp(a) levels, which can be conveniently obtained prior to surgery, can be combined with clinicopathologic features (pathologic tumor size, lymphovascular invasion, multifocality, and positive and negative SLN numbers) to accurately predict the risk of non-SLN metastases. This novel nomogram model has the potential for convenient use to optimize current treatment strategies by avoiding unnecessary ALND procedures.

Data Availability

Data are available on request. Our data are available on request through contacting the corresponding author (lvwm@mail.sysu.edu.cn).

Additional Points

Highlights. (i) Lp(a) is an independent risk factor for non-SLN metastases. (ii) We constructed a new nomogram combining clinicopathologic features and Lp(a). (iii) Our nomogram accurately predicted non-SLN metastasis in clinical practice

Conflicts of Interest

The authors declare that they have no conflicts of interest.

Authors' Contributions

Zeng Fang, Ruizhi Wang, and Ciqiu Yang contributed equally to this work.

Acknowledgments

The study is supported by the Natural Science Foundation of Guangdong Province (2018A0303130241) and Shenzhen Key Laboratory of Viral Oncology (ZDSYS201707311140430) to Chunxian Zeng and China Postdoctoral Science Foundation (2020M672985) to Zeng Fang.

References

[1] G. H. Lyman, M. R. Somerfield, L. D. Bosserman, C. L. Perkins, D. L. Weaver, and A. E. Giuliano, "Sentinel lymph node biopsy for patients with early-stage breast cancer: American Society of Clinical Oncology clinical practice guideline update," *Journal of Clinical Oncology*, vol. 35, no. 5, pp. 561–564, 2017.

[2] G. H. Lyman, S. Temin, S. B. Edge et al., "Sentinel lymph node biopsy for patients with early-stage breast cancer: American Society of Clinical Oncology clinical practice guideline update," *Journal of Clinical Oncology*, vol. 32, no. 13, pp. 1365–1383, 2014.

[3] I. Jatoi, J. R. Benson, and M. Toi, "De-escalation of axillary surgery in early breast cancer," *The Lancet Oncology*, vol. 17, no. 10, pp. e430–e441, 2016.

[4] K. U. Chu, R. R. Turner, N. M. Hansen, M. B. Brennan, A. Bilchik, and A. E. Giuliano, "Do all patients with sentinel node metastasis from breast carcinoma need complete axillary node dissection?," *Annals of Surgery*, vol. 229, no. 4, pp. 536–541, 1999.

[5] V. J. Kamath, R. Giuliano, E. L. Dauway et al., "Characteristics of the sentinel lymph node in breast cancer predict further involvement of higher-echelon nodes in the axilla," *Archives of Surgery*, vol. 136, no. 6, pp. 688–692, 2001.

[6] K. J. van Zee, D.-M. E. Manasseh, J. L. B. Bevilacqua et al., "A nomogram for predicting the likelihood of additional nodal metastases in breast cancer patients with a positive sentinel node biopsy," *Annals of Surgical Oncology*, vol. 10, no. 10, pp. 1140–1151, 2003.

[7] L. U. Jianwei and W. U. Peiqi, "Validation of the non-sentinel lymph node metastasis prediction models in Chinese breast cancer population and the construction of a new model," *Journal of Fen Zi Ying Xiang*, vol. 41, no. 2, pp. 212–218, 2018.

[8] A. Lombardi, S. Maggi, M. L. Russo et al., "Non-sentinel lymph node metastases in breast cancer patients with a positive sentinel lymph node: validation of five nomograms and development of a new predictive model," *Tumori*, vol. 97, no. 6, pp. 749–755, 2011.

[9] J. C. Melvin, L. Holmberg, S. Rohrmann, M. Loda, and M. van Hemelrijck, "Serum lipid profiles and cancer risk in the context of obesity: four meta-analyses," *Journal of Cancer Epidemiology*, vol. 2013, 12 pages, 2013.

[10] H. Usman, R. Rashid, F. Ameer et al., "Revisiting the dyslipidemia associated with acute leukemia," *Clinica Chimica Acta*, vol. 444, pp. 43–49, 2015.

[11] M. N. Mieno, M. Sawabe, N. Tanaka et al., "Significant association between hypolipoproteinemia(a) and lifetime risk of cancer: an autopsy study from a community-based Geriatric Hospital," *Cancer Epidemiology*, vol. 38, no. 5, pp. 550–555, 2014.

[12] A. K. Win, R. J. MacInnis, J. L. Hopper, and M. A. Jenkins, "Risk prediction models for colorectal cancer: a review," *Cancer Epidemiology, Biomarkers & Prevention*, vol. 21, no. 3, pp. 398–410, 2012.

[13] C. S. Liu, H. S. Hsu, C. I. Li et al., "Central obesity and atherogenic dyslipidemia in metabolic syndrome are associated with increased risk for colorectal adenoma in a Chinese population," *BMC Gastroenterology*, vol. 10, no. 1, 2010.

[14] C. DeSantis, J. Ma, L. Bryan, and A. Jemal, "Breast cancer statistics, 2013," *CA: a Cancer Journal for Clinicians*, vol. 64, no. 1, pp. 52–62, 2014.

[15] P. J. Goodwin, N. F. Boyd, W. Hanna et al., "Elevated levels of plasma triglycerides are associated with histologically defined premenopausal breast cancer risk," *Nutrition and Cancer*, vol. 27, no. 3, pp. 284–292, 1997.

[16] A. G. Renehan, M. Tyson, M. Egger, R. F. Heller, and M. Zwahlen, "Body-mass index and incidence of cancer: a systematic review and meta-analysis of prospective observational studies," *The Lancet*, vol. 371, no. 9612, pp. 569–578, 2008.

[17] Y. Kim, S. K. Park, W. Han et al., "Serum high-density lipoprotein cholesterol and breast cancer risk by menopausal status, body mass index, and hormonal receptor in Korea," *Cancer Epidemiology, Biomarkers & Prevention*, vol. 18, no. 2, pp. 508–515, 2009.

[18] A. S. Furberg, M. B. Veierod, T. Wilsgaard, L. Bernstein, and I. Thune, "Serum high-density lipoprotein cholesterol, metabolic profile, and breast cancer risk," *Journal of the National Cancer Institute*, vol. 96, no. 15, pp. 1152–1160, 2004.

[19] E. R. Nelson, C. Y. Chang, and D. P. McDonnell, "Cholesterol and breast cancer pathophysiology," *Trends in Endocrinology and Metabolism*, vol. 25, no. 12, pp. 649–655, 2014.

[20] P. de Medina, M. R. Paillasse, G. Segala et al., "Dendrogenin A arises from cholesterol and histamine metabolism and shows cell differentiation and anti-tumour properties," *Nature Communications*, vol. 4, no. 1, 2013.

[21] J. S. Davis, S. Y. Jung, and S. Chang, "High- and low-fat dairy intake, recurrence, and mortality after breast cancer diagnosis:," *Breast Diseases: A Year Book Quarterly*, vol. 24, no. 4, pp. 326-327, 2013.

[22] K. Berg, "A new serum type system in man—the Lp system," *Acta Pathologica et Microbiologica Scandinavica*, vol. 59, pp. 369–382, 1963.

[23] C. A. Emdin, A. V. Khera, P. Natarajan et al., "Phenotypic characterization of genetically lowered human lipoprotein(a) levels," *Journal of the American College of Cardiology*, vol. 68, no. 25, pp. 2761–2772, 2016.

[24] J. W. McLean, J. E. Tomlinson, W. J. Kuang et al., "cDNA sequence of human apolipoprotein(a) is homologous to plasminogen," *Nature*, vol. 330, no. 6144, pp. 132–137, 1987.

[25] S. M. Marcovina and J. J. Albers, "Lipoprotein (a) measurements for clinical application," *Journal of Lipid Research*, vol. 57, no. 4, pp. 526–537, 2016.

[26] Emerging Risk Factors Collaboration, "Lipoprotein(a) concentration and the risk of coronary heart disease, stroke, and nonvascular mortality," *JAMA*, vol. 302, no. 4, pp. 412–423, 2009.

[27] P. R. Kamstrup, A. Tybjærg-Hansen, and B. G. Nordestgaard, "Extreme lipoprotein(a) levels and improved cardiovascular risk prediction," *Journal of the American College of Cardiology*, vol. 61, no. 11, pp. 1146–1156, 2013.

[28] U. Kassner, T. Schlabs, A. Rosada, and E. Steinhagen-Thiessen, "Lipoprotein(a) - an independent causal risk factor for cardiovascular disease and current therapeutic options," *Atherosclerosis. Supplements*, vol. 18, pp. 263–267, 2015.

[29] F. Kronenberg, "Human genetics and the causal role of lipoprotein (a) for various diseases," *Cardiovascular Drugs and Therapy*, vol. 30, no. 1, pp. 87–100, 2016.

[30] X. Xie, W. Tan, B. Chen et al., "Preoperative prediction nomogram based on primary tumor miRNAs signature and clinical-related features for axillary lymph node metastasis in early-stage invasive breast cancer," *International Journal of Cancer*, vol. 142, no. 9, pp. 1901–1910, 2018.

[31] K. Shimazu, N. Sato, A. Ogiya et al., "Intraoperative nomograms, based on one-step nucleic acid amplification, for prediction of non-sentinel node metastasis and four or more axillary node metastases in breast cancer patients with sentinel node metastasis," *Annals of Surgical Oncology*, vol. 25, no. 9, pp. 2603–2611, 2018.

Hindawi
Disease Markers
Volume 2021, Article ID 3514827, 10 pages
https://doi.org/10.1155/2021/3514827

Research Article

The Prognostic Value of the Albumin to Gamma-Glutamyltransferase Ratio in Patients with Hepatocellular Carcinoma Undergoing Radiofrequency Ablation

Wenfeng Liu,[1,2] **Feng Zhang**,[1,2] **Bing Quan**,[1,2] **Miao Li**,[1,2] **Shenxin Lu**,[1,2] **Jinghuan Li**,[1,2] **Rongxin Chen**,[1,2] **and Xin Yin**[1,2]

[1]*Liver Cancer Institute, Zhongshan Hospital, Fudan University, Shanghai 200032, China*
[2]*National Clinical Research Center for Interventional Medicine, Shanghai 200032, China*

Correspondence should be addressed to Xin Yin; yin.xin@zs-hospital.sh.cn

Received 3 September 2021; Accepted 26 October 2021; Published 19 November 2021

Academic Editor: Ting Su

Albumin to gamma-glutamyltransferase ratio (AGR) is a newly developed biomarker for the prediction of patients' prognosis in solid tumors. The purpose of the study was to establish a novel AGR-based nomogram to predict tumor prognosis in patients with early-stage HCC undergoing radiofrequency ablation (RFA). 394 hepatocellular carcinoma (HCC) patients who had received RFA as initial treatment were classified into the training cohort and validation cohort. Independent prognostic factors were identified by univariate and multivariate analyses. The value of AGR was evaluated by the concordance index (*C*-index), receiver operating characteristic (ROC) curves, and likelihood ratio tests (LAT). Logistic regression and nomogram were performed to establish the pretreatment scoring model based on the clinical variables. As a result, AGR = 0.63 was identified as the best cutoff value to predict overall survival (OS) in the training cohort. According to the results of multivariate analysis, AGR was an independent indicator for OS and recurrence-free survival (RFS). In both training cohort and validation cohort, the high-AGR group showed better RFS and OS than the low-AGR group. What is more, the *C*-index, area under the ROC curves, and LAT χ^2 values suggested that AGR outperformed the Child-Pugh (CP) grade and albumin-bilirubin (ALBI) grade in terms of predicting OS. The AGR, AKP, and tumor size were used to establish the OS nomogram. Besides, the results of Hosmer-Lemeshow test and calibration curve analysis displayed that both nomograms in the training and validation cohorts performed well in terms of calibration. Therefore, the AGR-based nomogram can predict the postoperative prognosis of early HCC patients undergoing RFA.

1. Introduction

Primary liver cancer can be divided into three types: hepatocellular carcinoma (HCC), intrahepatic cholangiocarcinoma, and combined hepatocellular and cholangiocarcinoma [1]. HCC is one of the most common malignancies in humans and the second leading cause of cancer-related deaths in men in developing countries [2, 3]. The high incidence of HCC in Asia is closely related to hepatitis B virus (HBV), with more than 5 percent of people being chronically infected [4], whereas alcoholism and hepatitis C virus (HCV) infection are more closely related to HCC in Western countries [5].

Tumor ablation is a widely accepted treatment choice for patients with early stage HCC. Ablation induces tumor necrosis through temperature changes or injection of chemical reagents such as ethanol. Among them, radiofrequency ablation (RFA) is the preferred ablation technique because it provides better disease control than percutaneous ethanol injection [6]. This difference is particularly pronounced in tumor nodules with a diameter of more than 2 cm. In HCC patients with Child-Pugh (CP) A, the survival rate after ablation is similar to those undergoing surgical resection [7]. In addition, previous studies have proved that the long-term therapeutic effect of RFA for patients with small HCC is equivalent to liver resection and liver transplantation [8, 9].

The prognostic prediction of tumors is particularly important and meaningful. Tumor-Node-Metastasis (TNM) system and CP classification are widely used to assess the clinical prognosis of HCC patients. However, it has been recognized that there are differences in the prognosis of patients with the same TNM stage and CP grade [10]. Other pathological features and tumor markers such as tumor differentiation, tumor size, and AFP level are also used in the survival assessment of HCC patients. However, it is generally believed that not only the characteristics of the tumor itself are closely connected with the prognosis of patients, but also host-related factors are closely related to the prognosis of the tumor. Thus, the above indicators lack a certain degree of sensitivity and specificity, nor do they consider the patient's nutritional status, inflammation, and other related factors.

Previous studies have shown that inflammation can promote the malignant biological behavior of liver cancer cells and is related to the prognosis of patients [11]. In recent years, several commonly used clinical indicators of inflammation have shown their potential as predictors of prognosis in various kinds of tumors. Neutrophil to lymphocyte ratio (NLR) is an indicator of systemic inflammation of humans, which might be related to the prognosis of many tumor patients including liver cancer [12]. Previous studies displayed that NLR is associated with prognosis of liver cancer patients undergoing radical resection [13] and radiofrequency ablation [14]. Besides, an increasing number of studies evaluated the value of platelet to lymphocyte ratio (PLR) and monocyte to lymphocyte ratio (MLR) in HCC and other tumors [15–17]. Therefore, it is reasonable to predict the prognosis of HCC patients using different inflammation indicators.

Albumin (ALB) and gamma-glutamyltransferase (GGT) are indicators of liver function and inflammation, respectively. New evidence suggested that serum ALB was an independent prognostic factor for several malignancies [18]. GGT is an essential enzyme that plays a role in the metabolism of glutathione. Numerous studies have shown that elevated GGT level was correlated with high carcinogenesis risk and poor outcome [19]. In fact, a researcher first proposed the concept of albumin to gamma-glutamyltransferase ratio (AGR) in 2017 and showed that AGR is a predictor of the prognosis of patients with intrahepatic cholangiocarcinoma [20]. Based on previous research, we thus reasonably hypothesized that the AGR might be a potential prognostic indicator for HCC patients receiving RFA.

Till now, no studies have proven the prognostic value of AGR in HCC patients undergoing RFA. Therefore, we sought to evaluate the significance of AGR in HCC and constructed an AGR-based nomogram to predict prognosis for HCC patients undergoing RFA as initial treatment.

2. Materials and Methods

2.1. Patients. From 2010 to 2018, 394 early-stage HCC patients who received RFA as initial treatment were retrospectively recruited in Zhongshan Hospital of Fudan University. The inclusion criteria of patients were as follows: (1) diagnosed with HCC according to the American Association for the Study of Liver Diseases (AASLD) criteria [21]; (2) CP grade A or B; (3) solitary nodule < 5 cm or ≤3 nodule and none >3 cm; (4) no evidence of vascular invasion, lymph node involvement, or extrahepatic metastasis; (5) there were preoperative laboratory data and complete follow-up data.

The exclusion criteria were as follows: (1) patients undergoing other antitumor treatments before RFA; (2) patients undergoing incomplete ablation confirmed by contrast-enhanced computed tomography (CT) or magnetic resonance imaging (MRI) scan 4 weeks after RFA; (3) patients with other malignant tumors at the same time; and (4) patients with chronic kidney disease stage ≥ III and heart failure with New York Heart Association class ≥ III. Subsequently, 394 HCC patients were randomly allocated into a training cohort ($n = 279$) and verification cohort ($n = 115$) at a ratio of 7 : 3. Patient clinical characteristics, including age, gender, etiology, presence or absence of liver cirrhosis, laboratory results, and tumor-related characteristics before initial RFA treatment, were collected. The AGR was calculated by the ratio of serum ALB (g/L) to GGT (U/L).

The present study got ethics approval from the Medical Ethics Committee of Zhongshan Hospital of Fudan University and complies with the Declaration of Helsinki.

2.2. Treatment and Follow-Up. The surgical procedure has been described in a previous study [22]. All patients were followed up one month after the initial RFA and every two or three months thereafter. A physical examination, blood routine examination, liver function examination, tumor maker examination, and abdominal ultrasound examination were performed. Contrast-enhanced CT or MRI was immediately performed on patients whose test results indicate tumor recurrence.

2.3. Statistical Analysis. Continuous variables were expressed in mean ± standard deviation (SD), and the Student t-test was used for comparison. Categorical variables were described by percentages and compared using Pearson χ^2 analysis or Fisher's exact test. X-tile statistical software (version 3.6.1, Yale University, New Haven, CT, USA) was applied to determine the optimal threshold of AGR for OS. According to the defined cutoff value, patients were divided into a low-AGR group and high-AGR group. The survival curve was estimated by the Kaplan-Meier method, and the survival difference was estimated by the log-rank test. We also used univariate analysis to identify significant variables related to OS. We selected variables with P value less than 0.1 in multivariate Cox proportional hazards regression model. Concordance index (C-index), area under the curve (AUC), and likelihood ratio test (LAT) were used to compare the prediction effects of AGR, CP classification, and albumin-bilirubin (ALBI) classification. Combined with the results of multivariate analysis, an AGR-based nomograph of 3-year and 5-year OS proportion was constructed. The Hosmer-Lemeshow test (H-L test) and calibration curve were used to evaluate the degree of consistency between

Table 1: Demographics and clinical characteristics of patients in the training and validation cohorts.

	Total ($n = 394$)	Training cohort ($n = 279$)	Validation cohort ($n = 115$)	P value*
Gender				0.538
Male	306	219	87	
Female	88	60	28	
Age	58.71 ± 11.33	58.58 ± 11.27	59.02 ± 11.52	0.726
TB (μmol/L)	14.23 ± 7.81	13.88 ± 7.83	15.05 ± 7.75	0.173
ALT (U/L)	46.96 ± 61.28	43.01 ± 46.45	56.50 ± 86.82	0.117
PT	12.89 ± 2.17	12.85 ± 2.13	12.99 ± 2.28	0.564
ALB	39.48 ± 6.26	39.43 ± 5.00	39.61 ± 8.59	0.793
AFP	328.78 ± 1164.07	274.61 ± 816.44	460.20 ± 1738.18	0.275
γ-GT (U/L)	76.25 ± 95.40	74.64 ± 95.98	80.08 ± 94.03	0.363
Etiology				0.544
HBV infection	311	224	87	
HCV infection	13	8	5	
Other	70	47	23	
Liver cirrhosis				0.743
Yes	259	182	77	
No	135	97	38	
AKP (U/L)	94.54 ± 52.08	92.18 ± 44.41	100.27 ± 67.06	0.236
AGR	0.99 ± 0.74	1.00 ± 0.73	0.98 ± 0.77	0.806
CP grade				0.874
A	394	277	114	
B	3	2	1	
AGR				0.403
1	232	168	64	
2	162	111	51	
γ-GT (U/L)				0.719
≤50	195	140	55	
>50	199	139	60	
Tumor size (cm)				0.253
≤3	322	232	90	
3-5	72	47	25	
Tumor number				0.397
Single	315	220	95	
Multiple	79	59	20	
AJCC TNM-8				0.137
Ia	180	133	47	
Ib	135	87	48	
II	79	59	20	
ALBI				0.264
1	225	166	59	
2	164	109	55	
3	5	4	1	

Abbreviations: AGR: albumin to gamma-glutamyltransferase ratio; TB: total bilirubin; ALT: alanine aminotransferase; PT: prothrombin time; ALB: albumin; AFP: alfa-fetoprotein; γ-GT: γ-glutamyl transpeptidase; HBV: hepatitis B virus; HCV: hepatitis C virus; AKP: alkaline phosphatase; CP grade: Child-Pugh grade; AJCC TNM-8: the 8th edition of American Joint Committee on Cancer TNM staging system; ALBI grade: albumin-bilirubin grade. *Statistically significant.

Table 2: Associations between AGR and other characteristics.

	Total ($n = 279$)	AGR > 0.63 ($n = 168$)	AGR ≤ 0.63 ($n = 111$)	P value*
Gender				0.737
Male	219	133	86	
Female	60	35	25	
Age	58.58 ± 11.27	57.76 ± 11.42	59.82 ± 10.97	0.136
TB (μmol/L)	13.88 ± 7.83	13.25 ± 8.19	14.84 ± 7.17	0.098
ALT (U/L)	43.01 ± 46.45	40.46 ± 45.34	46.98 ± 45.94	0.301
PT	12.85 ± 2.13	12.79 ± 1.75	12.96 ± 2.60	0.501
ALB	39.43 ± 5.00	40.68 ± 4.52	37.52 ± 5.11	<0.001*
AFP	274.61 ± 816.44	316.25 ± 882.14	211.58 ± 704.68	0.295
γ-GT (U/L)	73.44 ± 95.98	34.48 ± 13.69	132.41 ± 131.04	<0.001*
Etiology				0.272
HBV infection	224	139	86	
HCV infection	8	6	2	
Other	47	24	23	
Liver cirrhosis				0.916
Yes	182	110	72	
No	97	58	39	
AKP (U/L)	92.18 ± 44.41	80.42 ± 27.57	109.99 ± 57.44	<0.001*
AGR	1.00 ± 0.73	1.41 ± 0.67	0.38 ± 0.15	<0.001*
CP grade				0.081
A	277	168	109	
B	2	0	2	
γ-GT (U/L)				<0.001*
≤50	140	139	1	
>50	139	29	110	
Tumor size (cm)				0.281
≤3	232	143	89	
3-5	47	25	22	
Tumor number				0.175
Single	220	137	83	
Multiple	59	31	28	
AJCC TNM-8				0.200
Ia	133	87	46	
Ib	87	50	37	
II	59	31	28	
ALBI				<0.001*
1	166	115	51	
2	109	53	56	
3	4	0	4	

Abbreviations: AGR: albumin to gamma-glutamyltransferase ratio; TB: total bilirubin; ALT: alanine aminotransferase; PT: prothrombin time; ALB: albumin; AFP: alfa-fetoprotein; γ-GT: γ-glutamyl transpeptidase; HBV: hepatitis B virus; HCV: hepatitis C virus; AKP: alkaline phosphatase; CP grade: Child-Pugh grade; AJCC TNM-8: the 8th edition of American Joint Committee on Cancer TNM staging system; ALBI grade: albumin-bilirubin grade. *Statistically significant.

the predicted risk of the model and the actual risk. Stata software (version 15.1, StataCorp, College Station, TX) and R software (version 3.5.1) were utilized for analysis. $P < 0.05$ was thought as statistically significant.

3. Results

3.1. Demographics and Clinical Characteristics. Table 1 displays the main characteristics of the training cohort and

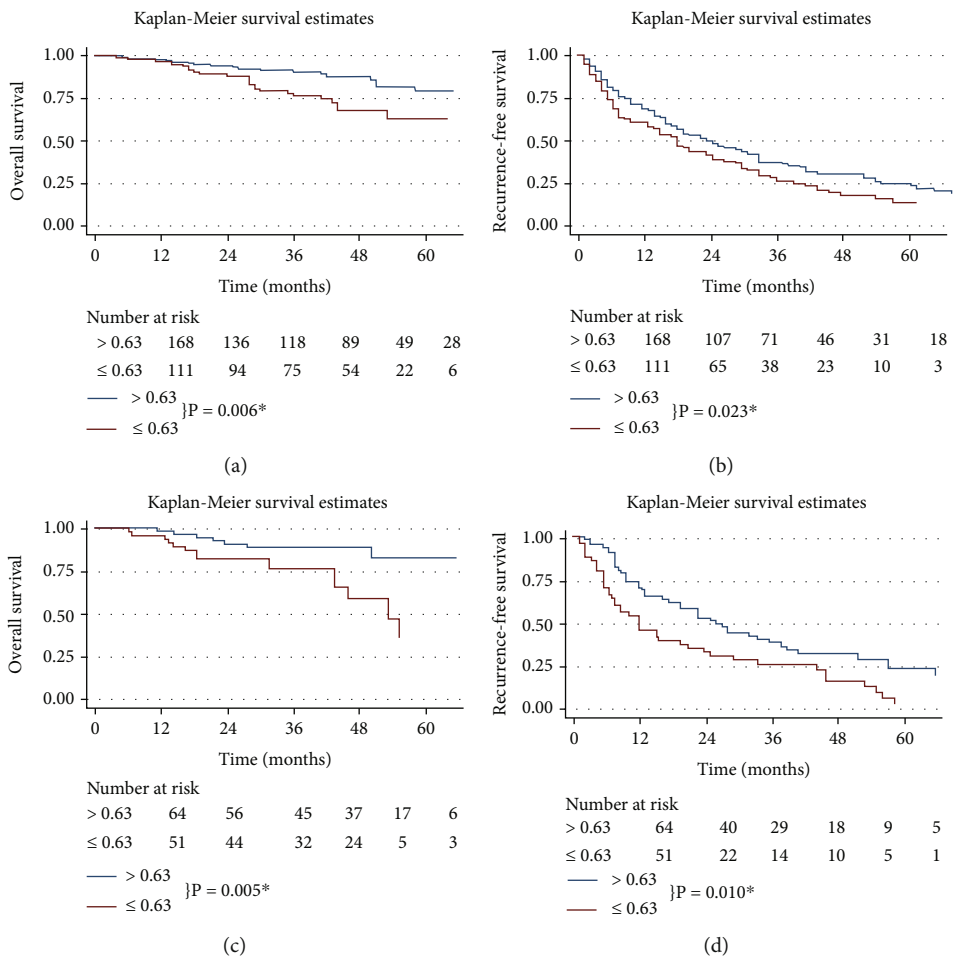

Figure 1: Kaplan–Meier survival curves of different groups divided by AGR. OS according to AGR values in the training cohort and validation cohort (a, c). RFS according to AGR values in the training cohort and validation cohort (b, d) *Statistically significant. Abbreviations: AGR: albumin to gamma-glutamyltransferase ratio; OS: overall survival; RFS: recurrence-free survival.

validation cohort. In the training cohort, there were 219 males (78.5%) and 60 females (21.5%), with an average age of 58.58 ± 11.27 years. 224 patients (80.3%) had hepatitis B virus (HBV) infection background. There were 182 cases (65.2%) with liver cirrhosis and 277 cases (99.3%) with CP A grade. The laboratory results showed that the average levels of ALB and γ-GT were 39.43 ± 5.00 g/L and 74.64 ± 95.98 U/L, respectively. In terms of tumor characteristics, 47 cases (16.8%) had tumors larger than 3 cm in diameter, and 59 cases (21.1%) had multiple tumors. In the American Joint Committee on Cancer TNM staging system (AJCC-TNM) Ia, Ib, and II, there were 133 cases (47.7%), 87 cases (31.2%), 59 cases (21.1%), respectively.

In the validation cohort, there were 87 males (75.7%) and 28 females (24.3%), with an average age of 59.02 ± 11.52 years. 87 patients (75.7%) had hepatitis B virus (HBV) infection background. There were 77 cases (70.0%) with liver cirrhosis and 114 cases (99.1%) with CP A grade. The laboratory results showed that the average levels of ALB and γ-GT were 39.61 ± 8.59 g/L and 80.08 ± 94.03 U/L, respectively. In terms of tumor characteristics, 25 cases (21.7%) had tumors larger than 3 cm in diameter, and 20 cases (17.4%) had multiple tumors. In the AJCC-TNM Ia, Ib, and II, there were 47 cases (40.9%), 48 cases (41.7%), and 20 cases (17.4%), respectively. In a word, no statistical difference was found between the training cohort and validation cohort regarding demographics and clinical characteristics.

3.2. Clinicopathological Characteristics of the Low-AGR Group and High-AGR Group. By analyzing the data of the training cohort using X-tile, the optimal threshold of AGR was determined to be 0.63. Then, the patients were divided into the low-AGR group (AGR ≤ 0.63, $n = 111$) and high-AGR group (AGR > 0.63, $n = 168$). The correlation between AGR and other characteristics is shown in Table 2. Generally, patients with low AGR levels have poorer liver function (ALBI stages 2 and 3) and have higher levels of AKP ($P < 0.05$).

3.3. Survival Analysis. The mean follow-up time was 39.1 months (range: 1-140 months). At the end of the follow-up, 68 patients (17.3%) died and 296 patients (75.1%) had tumor recurrence. In the training cohort, the 3-year and 5-year overall survival (OS) rates were 84.9% and 72.6%, respectively. In the validation cohort, the 3-year, and 5-

Table 3: Univariate and multivariate analyses for overall survival in the training cohort and validation cohort.

Variable	Training cohort			Validation cohort		
	Univariate analysis *P* value	Multivariate analysis HR (95% CI)	*P* value	Univariate analysis *P* value	Multivariate analysis HR (95% CI)	*P* value
Age (>65)	0.298			0.781		
Gender (female/male)	0.370			0.451		
HBV infection (presence)	0.875			0.389		
HCV infection (presence)	0.274			0.253		
Liver cirrhosis (no/yes)	0.234			0.631		
AGR stage	0.012*	2.295 (1.248-4.221)	0.008*	0.024*	3.327 (1.349-8.206)	0.009*
AKP (U/L) (>135)	0.031*	3.299 (1.458-7.467)	0.004*	0.039*	3.409 (1.317-8.825)	0.012*
CP grade (A vs. B)	0.024*			0.245		
Tumor number (single, multiple)	0.485			0.466		
Tumor size (cm) (≤3, 3–5)	0.044*	2.002 (1.108-3.974)	0.047*	0.021*	2.090 (1.223-3.573)	0.007*
TB (μmol/L) (≥34)	0.952			0.441		
ALT (U/L) (>40)	0.364			0.682		
AFP (ng/mL) (>400)	0.624			0.570		
ALBI grade (1/2/3)	0.017*			0.111		
AJCC TNM-8 (Ia, Ib, II)	0.945			0.307		

Abbreviations: HR: hazard ratio; HBV: hepatitis B virus; HCV: hepatitis C virus; AGR: albumin to gamma-glutamyltransferase ratio; AKP: alkaline phosphatase; CP grade: Child-Pugh grade; TB: total bilirubin; ALT: alanine aminotransferase; AFP: alfa-fetoprotein; ALBI grade: albumin-bilirubin grade; AJCC TNM-8: the 8th edition of American Joint Committee on Cancer TNM staging system. *Statistically significant.

Table 4: Comparison of predictive efficacy among different liver function-related indices.

	Training cohort				Validation cohort			
	C-index	AUC (95% CI) 3-year OS	AUC (95% CI) 5-year OS	LAT χ^2	*C*-index	AUC (95% CI) 3-year OS	AUC (95% CI) 5-year OS	LAT χ^2
AGR	0.64 (0.49-0.78)	0.63 (0.48-0.76)	0.65 (0.52-0.78)	11.2	0.62 (0.50-0.74)	0.59 (0.50-0.69)	0.63 (0.52-0.73)	6.7
ALBI grade	0.61 (0.48-0.76)	0.61 (0.46-0.76)	0.63 (0.50-0.77)	4.9	0.52 (0.42-0.64)	0.51 (0.41-0.61)	0.53 (0.43-0.64)	3.1
CP grade	0.52 (0.37-0.68)	0.52 (0.36-0.67)	0.53 (0.38-0.68)	2.2	0.50 (0.38-0.62)	0.49 (0.38-0.57)	0.52 (0.40-0.63)	0.7

Abbreviations: AUC: area under the curve; LAT χ^2; likelihood ratio test χ^2; OS: overall survival; AGR: albumin to gamma-glutamyltransferase ratio; ALBI grade: albumin-bilirubin grade; CP grade: Child-Pugh grade. *Statistically significant.

year OS rates were 83.3% and 62.9%, respectively. Regarding RFS, the 3-year and 5-year recurrence-free survival (RFS) rates of patients in the training cohort were 31.4% and 17.4%, respectively, while the 3-year and 5-year RFS rates were 30.7% and 13.0% in the validation cohort. What is more, there was no statistical difference in survival time between the two groups ($P = 0.310$ for OS and $P = 0.356$ for RFS).

As shown in Figure 1, the survival rate of patients with low AGR levels was significantly lower than that of patients with high AGR levels. The 3-year and 5-year OS rates were 90.6% and 79.4% in the high-AGR group, and 76.7% and 63.3% in the high-AGR group, respectively. The 3-year and 5-year RFS rates were 35.0% and 20.5% in the high-AGR group and 26.1% and 13.5% in the high-AGR group, respectively. In addition, the above findings have been verified in the verification cohort.

3.4. Univariate and Multivariate Analysis. In the training cohort, the outputs of univariate analysis showed that AGR, AKP, and tumor size were significantly associated with OS. Through further multivariate analysis, the above factors were all important independent factors affecting prognosis. In the validation cohort, univariate and multivariate analyses confirmed that AGR, AKP, and tumor size are index of OS in HCC patients. The details are illustrated in Table 3.

3.5. Comparing the Prognostic Performance of AGR with Different Liver Function Assessment Methods. The prognostic prediction effects of AGR, AGR grade, and CP classification were evaluated by *C*-index, AUCs, and LAT χ^2 values. In the training cohort, the *C*-index values of AGR, CP classification, and ALBI grade were 0.64 (95% CI: 0.49-0.78), 0.61 (95% CI: 0.48-0.76), and 0.52 (95% CI: 0.37-0.68), while in the validation cohort, the corresponding *C*-index values were 0.62 (95% CI: 0.50-0.74), 0.52 (95% CI: 0.42-0.64), and 0.50 (95% CI: 0.38-0.62), respectively. We have also noticed that the 3-year and 5-year AUCs and LAT χ^2 of AGR were higher than those of ALBI and CP in both the training cohort and validation cohort. All these results indicated that AGR can be used as a superior predictor for

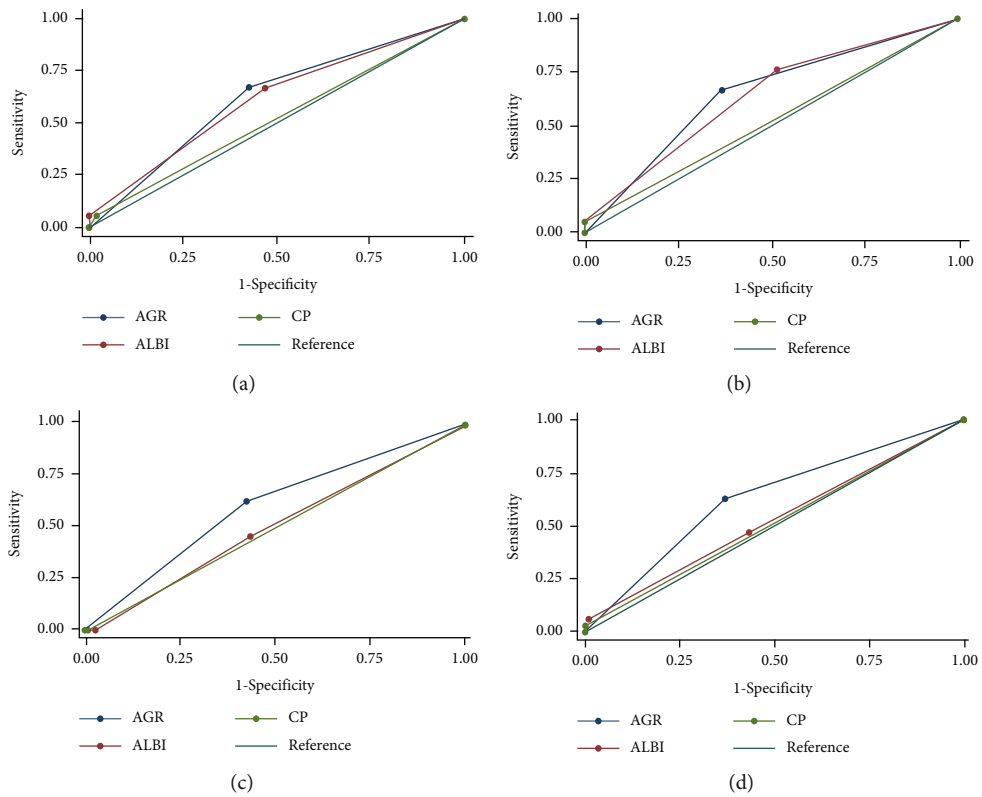

Figure 2: ROC curves of AGR, ALBI grade, and CP grade: (a, b) ROC curves for predicting the 3-year and 5-year OS in the training cohort; (c, d) ROC curves for predicting the 3-year and 5-year OS in the validation cohort. Abbreviations: ROC: receiver operating characteristic; AGR: albumin to gamma-glutamyltransferase ratio; ALBI: albumin-bilirubin; CP: Child-Pugh; OS: overall survival.

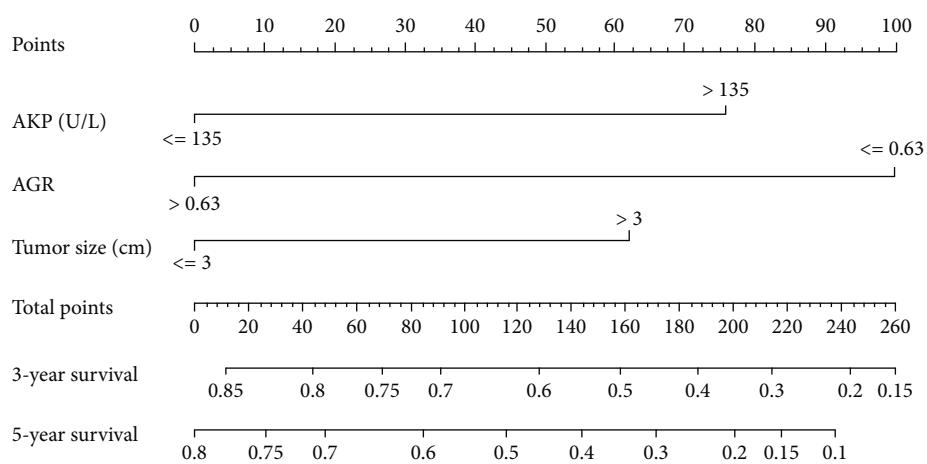

Figure 3: The AGR-based nomogram for forecasting the 3-year and 5-year survival probabilities of HCC after RFA. Abbreviations: AGR: albumin to gamma-glutamyltransferase ratio; HCC: hepatocellular carcinoma; RFA: radiofrequency ablation.

prognosis in HCC patients undergoing RFA. More details are demonstrated in Table 4 and Figure 2.

3.6. Development and Validation of AGR-Based Nomogram Model. Through the multivariate Cox proportional hazards model, three variables including AGR, AKP, and tumor size were determined as independent prognostic factors. Based on those factors, we constructed the 3- and 5-year OS forecast nomogram model, shown in Figure 3.

In addition, we performed the H-L test and calibration curves to verify the value of the AGR-based nomogram. The P values of the H-L test for 3-year and 5-year OS in the training cohort were 0.837 and 0.963, respectively. In the validation cohort, the corresponding P values were 0.630 and 0.942. All P values were above 0.05, indicating a good fit of the AGR-based nomogram. Besides, the calibration curves showed that the predicted probabilities of 3-year and 5-year OS of the AGR-based nomogram were close

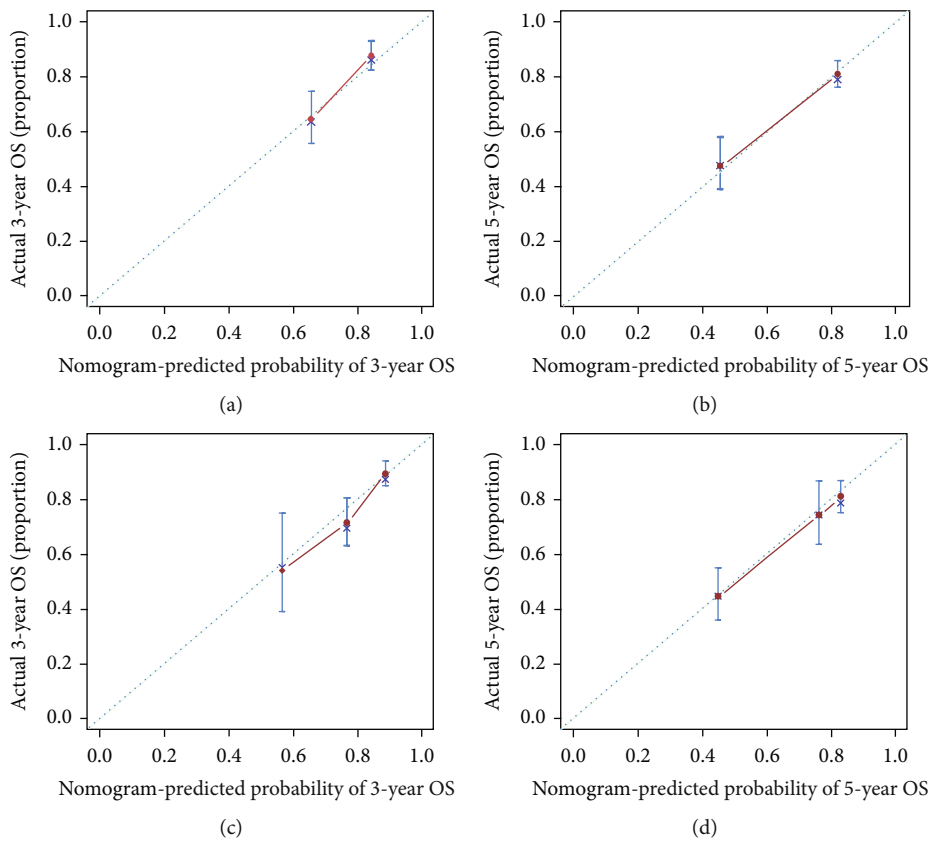

Figure 4: Calibration curves for predicting the 3-year and 5-year OS of HCC patients receiving RFA. Calibration curves for predicting the 3-year and 5-year OS in the training cohort (a, b) and validation cohort (c, d). Abbreviations: HCC: hepatocellular carcinoma; RFA: radiofrequency ablation; OS: overall survival.

to the actual probabilities, suggesting AGR-based nomogram had an excellent predictive value in the training or validation cohort (Figure 4).

4. Discussion

HCC is one of the common malignant tumors of the digestive system that seriously endanger human health. The incidence and mortality of primary liver cancer in Asian population are higher than those in other populations [23]. RFA is an effective method for the management of small liver cancer. Evaluating the survival time of HCC patients after treatment is of great significance for formulating reasonable treatment plans and improving the quality of life of patients with HCC.

In the present study, we first confirmed the prognostic value of AGR in HCC patients receiving RFA as the initial treatment. The AGR of 0.63 was determined as the best cut-off value in the present study. Patients with low levels of AGR are significantly detrimental to OS and RFS in the training and validation group. In addition, our results comprehensively indicate that preoperative AGR is an important prognostic indicator of HCC undergoing RFA.

Chronic inflammation is one of the main factors that promote the occurrence or development of tumors. It is believed about twenty percent of malignant tumors develop from inflammation [24]. Once inflammation is triggered, inflammatory cells will secrete a large number of inflammatory factors in the process of migrating, causing damage to DNA and destroying the stability of proliferating cells' genes. Finally, under the repeated stimulation of inflammatory factors, the genes of the cells change and unrestricted proliferation occurs. And the upregulated cytokine can further promote angiogenesis and tumor metastasis [25]. After liver cells are damaged, the cell membrane ruptures or increases in permeability, causing liver enzymes to escape into the blood. Peripheral blood liver enzymes, such as GGT, are the final manifestation of liver inflammation in the peripheral blood, which can better reflect the symptoms of hepatitis. A comprehensive analysis of inflammation-related cells or liver enzyme indicators in peripheral blood should be able to reflect the liver inflammation more objectively and accurately, so as to judge the prognosis of liver cancer.

There is no doubt that liver function is a key factor in the prognosis of systemic diseases. In detail, ALB is a kind of protein synthesized by the liver cells, reflecting the nutritional status of patients. When the patient's body is stimulated by tumor cells and inflammatory factors, the ability of the liver to synthesize albumin is significantly reduced, and the content of serum albumin will be significantly reduced. Thus, as an important liver function index, ALB is one of the indexes of CP classification system. Studies have

shown that ALB was related to the prognosis of various malignant tumors, such as gastric cancer, colon cancer, liver cancer, and glioblastoma [26, 27].

Based on the above, AGR is not just a combination of liver function parameters; it is more a reflection of the internal inflammation state and seems to help assess the survival of cancer patients. In fact, Jing et al. [20] analyzed the AGR levels of 206 patients with intrahepatic cholangiocarcinoma for the first time. They calculated that the optimal cutoff value of AGR for patients with cholangiocarcinoma was 0.6. Recently, AGR was also used to forecast the prognosis of gallbladder cancer [28]. By analyzing the preoperative AGR levels of 140 patients with gallbladder cancer, researchers established and verified the prediction nomograms of 1-, 3-, and 5-year survival probability. In terms of consistency, identification, and net benefits, AGR-based nomograms achieved considerable prognostic performance. AGR also showed a good predictive value in pancreatic ductal adenocarcinoma [29]. In the current study, we firstly verified that AGR might be an indicator for forecasting the prognosis of HCC patients with RFA as initial treatment.

As far as we know, CP classification and ALBI grade are common tools for the assessment of liver function and patients' prognosis [30, 31]. However, CP classification was originally established on the basis of predicting the prognosis of esophageal gastric varix devascularization in patients with cirrhosis and portal hypertension [32]. CP classification includes serum albumin, bilirubin, and prothrombin time but also includes the presence of hepatic encephalopathy and ascites, so the results obtained by CP classification contain a certain degree of subjectivity. Therefore, the application of CP classification to assess liver function in patients with HCC has always been controversial. ALBI grade is developed on the basis of a large number of cohort studies of HCC patients and is a more objective method for evaluating liver function [33]. Unlike other malignant tumors, most primary liver cancer in China is caused by chronic liver disease and hepatitis B virus infection. What is more, a previous study found that the level of serum GGT had a potential to predict the outcome of primary liver cancer patients after RFA [34]. Therefore, we selected AGR, an indicator of liver function and inflammation, to try to predict the prognosis of HCC patients receiving RFA as the initial treatment. Unfortunately, based on multivariate analysis, neither CP grade nor ALBI grade in HCC showed good prognostic significance. In contrast, AGR was determined as an independent prognostic factor for both the training group and validation cohort. In addition, the C-index, AUC, and LAT χ^2 values proved that AGR was more discriminatory compared with the CP grade and ALBI grade in HCC. Based on the results of univariate and multivariate analyses, we further established an AGR-based prognostic nomogram, which might be helpful for clinical decision making. Moreover, we further evaluated the predictive performance of the nomogram. The results of the calibration curves suggested that the nomogram had good predictive performance in both the training cohort and validation cohort.

However, there are some limitations in the current study. Firstly, the current study is a retrospective research. Besides, the sample size is relatively limited. And there are many factors that affect AGR. Therefore, strict control of bias and more detailed stratification are needed. Moreover, more patients and multicenter study are needed to verify our conclusions and obtain more reliable results.

To sum up, we found that HCC patients undergoing RFA as initial treatment with $AGR \geq 0.63$ have a better prognosis than those with $AGR < 0.63$. The AGR-based nomogram model can effectively predict prognosis of early HCC patients undergoing RFA.

Data Availability

All data is available on request.

Conflicts of Interest

The authors report no conflicts of interest in this work.

Acknowledgments

This study was supported by the National Natural Science Foundation of China (No. 81972889) and Exploratory Clinical Research Projects of National Clinical Research Center for Interventional Medicine (2021-001).

References

[1] J. C. Mejia and J. Pasko, "Primary liver cancers: intrahepatic cholangiocarcinoma and hepatocellular carcinoma," *The Surgical Clinics of North America*, vol. 100, no. 3, pp. 535–549, 2020.

[2] G. Giannelli and S. Antonaci, "Novel concepts in hepatocellular carcinoma: from molecular research to clinical practice," *Journal of Clinical Gastroenterology*, vol. 40, no. 9, pp. 842–846, 2006.

[3] L. Kulik and H. B. El-Serag, "Epidemiology and management of hepatocellular carcinoma," *Gastroenterology*, vol. 156, no. 2, pp. 477–491.e1, 2019.

[4] M. J. Goh, D. H. Sinn, S. Kim et al., "Statin use and the risk of hepatocellular carcinoma in patients with chronic hepatitis B," *Hepatology*, vol. 71, no. 6, pp. 2023–2032, 2020.

[5] J. D. Yang, P. Hainaut, G. J. Gores, A. Amadou, A. Plymoth, and L. R. Roberts, "A global view of hepatocellular carcinoma: trends, risk, prevention and management," *Nature Reviews Gastroenterology & Hepatology*, vol. 16, no. 10, pp. 589–604, 2019.

[6] D. Ansari and R. Andersson, "Radiofrequency ablation or percutaneous ethanol injection for the treatment of liver tumors," *World Journal of Gastroenterology*, vol. 18, no. 10, pp. 1003–1008, 2012.

[7] G. Germani, M. Pleguezuelo, K. Gurusamy, T. Meyer, G. Isgrò, and A. K. Burroughs, "Clinical outcomes of radiofrequency ablation, percutaneous alcohol and acetic acid injection for hepatocelullar carcinoma: a meta-analysis," *Journal of Hepatology*, vol. 52, no. 3, pp. 380–388, 2010.

[8] K. Hasegawa, N. Kokudo, M. Makuuchi et al., "Comparison of resection and ablation for hepatocellular carcinoma: a cohort

study based on a Japanese nationwide survey," *Journal of Hepatology*, vol. 58, no. 4, pp. 724–729, 2013.

[9] M. Kudo, "Radiofrequency ablation for hepatocellular carcinoma: updated review in 2010," *Oncology*, vol. 78, no. 1, pp. 113–124, 2010.

[10] L. F. Shen, S. H. Zhou, and Q. Yu, "Predicting response to radiotherapy in tumors with PET/CT: when and how?," *Translational Cancer Research*, vol. 9, no. 4, pp. 2972–2981, 2020.

[11] Y. M. Yang, S. Y. Kim, and E. Seki, "Inflammation and liver cancer: molecular mechanisms and therapeutic targets," *Seminars in Liver Disease*, vol. 39, no. 1, pp. 026–042, 2019.

[12] Y. Mano, K. Shirabe, Y. Yamashita et al., "Preoperative neutrophil-to-lymphocyte ratio is a predictor of survival after hepatectomy for hepatocellular Carcinoma," *Annals of Surgery*, vol. 258, no. 2, pp. 301–305, 2013.

[13] Y. Okamura, T. Sugiura, T. Ito et al., "Neutrophil to lymphocyte ratio as an indicator of the malignant behaviour of hepatocellular carcinoma," *The British Journal of Surgery*, vol. 103, no. 7, pp. 891–898, 2016.

[14] K. Tajiri, H. Baba, K. Kawai et al., "Neutrophil-to-lymphocyte ratio predicts recurrence after radiofrequency ablation in hepatitis B virus infection," *Journal of Gastroenterology and Hepatology*, vol. 31, no. 7, pp. 1291–1299, 2016.

[15] B. Li, P. Zhou, Y. Liu et al., "Platelet-to-lymphocyte ratio in advanced cancer: review and meta-analysis," *Clinica Chimica Acta*, vol. 483, pp. 48–56, 2018.

[16] Z. Zhu, L. Xu, L. Zhuang et al., "Role of monocyte-to-lymphocyte ratio in predicting sorafenib response in patients with advanced hepatocellular carcinoma," *Oncotargets and Therapy*, vol. 11, no. 11, pp. 6731–6740, 2018.

[17] Y. Ha, M. A. Mohamed Ali, M. M. Petersen et al., "Lymphocyte to monocyte ratio-based nomogram for predicting outcomes of hepatocellular carcinoma treated with sorafenib," *Hepatology International*, vol. 14, no. 5, pp. 776–787, 2020.

[18] D. Gupta and C. G. Lis, "Pretreatment serum albumin as a predictor of cancer survival: a systematic review of the epidemiological literature," *Nutrition Journal*, vol. 9, no. 1, p. 69, 2010.

[19] S. K. Kunutsor, T. A. Apekey, M. Van Hemelrijck, G. Calori, and G. Perseghin, "Gamma glutamyltransferase, alanine aminotransferase and risk of cancer: systematic review and meta-analysis," *International Journal of Cancer*, vol. 136, no. 5, pp. 1162–1170, 2015.

[20] C. Y. Jing, Y. P. Fu, H. J. Shen et al., "Albumin to gamma-glutamyltransferase ratio as a prognostic indicator in intrahepatic cholangiocarcinoma after curative resection," *Oncotarget*, vol. 8, no. 8, pp. 13293–13303, 2017.

[21] M. G. Silveira, E. M. Brunt, J. Heathcote, G. J. Gores, K. D. Lindor, and M. J. Mayo, "American Association for the Study of Liver Diseases endpoints conference: design and endpoints for clinical trials in primary biliary cirrhosis," *Hepatology*, vol. 52, no. 1, pp. 349–359, 2010.

[22] X. Yin, L. Zhang, Y. H. Wang et al., "Transcatheter arterial chemoembolization combined with radiofrequency ablation delays tumor progression and prolongs overall survival in patients with intermediate (BCLC B) hepatocellular carcinoma," *BMC Cancer*, vol. 14, no. 1, p. 849, 2014.

[23] M. C. S. Wong, J. L. W. Huang, J. George et al., "The changing epidemiology of liver diseases in the Asia-Pacific region," *Nature Reviews Gastroenterology & Hepatology*, vol. 16, no. 1, pp. 57–73, 2019.

[24] J. Marx, "Inflammation and cancer: the link grows stronger," *Science*, vol. 306, no. 5698, pp. 966–968, 2004.

[25] T. O. Adekoya and R. M. Richardson, "Cytokines and chemokines as mediators of prostate cancer metastasis," *International Journal of Molecular Sciences*, vol. 21, no. 12, p. 4449, 2020.

[26] X. Wang, M. Li, J. Wang, and Y. Cao, "The effect of nano-albumin paclitaxel on the early postoperative recurrence of primary liver cancer," *Journal of Nanoscience and Nanotechnology*, vol. 20, no. 12, pp. 7283–7288, 2020.

[27] C. Liu and X. Li, "Stage-dependent changes in albumin, NLR, PLR, and AFR are correlated with shorter survival in patients with gastric cancer," *Clinical Laboratory*, vol. 65, 2019.

[28] L. Sun, X. Ke, D. Wang et al., "Prognostic value of the albumin-to-γ-glutamyltransferase ratio for gallbladder cancer patients and establishing a nomogram for overall survival," *Journal of Cancer*, vol. 12, no. 14, pp. 4172–4182, 2021.

[29] S. Li, H. Xu, C. Wu et al., "Prognostic value of γ-glutamyltransferase-to-albumin ratio in patients with pancreatic ductal adenocarcinoma following radical surgery," *Cancer Medicine*, vol. 8, no. 2, pp. 572–584, 2019.

[30] X. Wen, M. Yao, Y. Lu et al., "Integration of prealbumin into Child-Pugh classification improves prognosis predicting accuracy in HCC patients considering curative surgery," *Journal of Clinical and Translational Hepatology*, vol. 6, pp. 1–8, 2018.

[31] A. Hiraoka, T. Kumada, K. Michitaka, and M. Kudo, "Newly Proposed ALBI Grade and ALBI-T score as tools for assessment of hepatic function and prognosis in hepatocellular carcinoma patients," *Liver Cancer*, vol. 8, no. 5, pp. 312–325, 2019.

[32] T. Körner, J. Kropf, B. Kosche, H. Kristahl, D. Jaspersen, and A. M. Gressner, "Improvement of prognostic power of the Child-Pugh classification of liver cirrhosis by hyaluronan," *Journal of Hepatology*, vol. 39, no. 6, pp. 947–953, 2003.

[33] S. K. Na, S. Y. Yim, S. J. Suh et al., "ALBI versus Child-Pugh grading systems for liver function in patients with hepatocellular carcinoma," *Journal of Surgical Oncology*, vol. 117, no. 5, pp. 912–921, 2018.

[34] H. Ma, L. Zhang, B. Tang et al., "γ-Glutamyltranspeptidase is a prognostic marker of survival and recurrence in radiofrequency-ablation treatment of hepatocellular carcinoma," *Annals of Surgical Oncology*, vol. 21, no. 9, pp. 3084–3089, 2014.

Hindawi
Disease Markers
Volume 2021, Article ID 1602797, 10 pages
https://doi.org/10.1155/2021/1602797

Research Article

PKM2 Is a Potential Diagnostic and Therapeutic Target for Retinitis Pigmentosa

Peiwen Zhu, Qian Yang, Gang Li, and Qing Chang

Department of Ophthalmology and Vision Science, Eye and Ear, Nose and Throat Hospital of Fudan University, Shanghai 200031, China

Correspondence should be addressed to Qing Chang; dr_changqing@126.com

Received 17 September 2021; Accepted 26 October 2021; Published 11 November 2021

Academic Editor: Ting Su

Retinitis pigmentosa (RP) is a major cause of blindness that is difficult to diagnose and treat. PKM2, a subtype of pyruvate kinase, is strongly associated with oxidative stress and is expressed in photoreceptors. We investigated whether PKM2 reduces photoreceptor cell apoptosis and evaluated possible antiapoptotic mechanisms in RP. We established RP models by exposing 661W cells to blue light and modulated PKM2 activity using a PKM2 inhibitor. We measured the apoptosis rates using calcein-acetoxymethyl ester/propidium iodide double staining and Cell Counting Kit-8, the oxidative stress levels using a reactive oxygen species assay, and the changes in protein expression by western blotting. Photodamage increased PKM2 expression, cellular oxidative stress, and apoptosis of 661W cells. PKM2 inhibition significantly reduced the levels of apoptosis and oxidative stress induced by photodamage. Our data suggest that PKM2 is a potential disease marker and therapeutic target for RP.

1. Introduction

Retinitis pigmentosa (RP) is a set of inherited retinal diseases manifested by progressive photoreceptor cell degeneration, with an incidence of approximately 1 in 4000 [1]. The etiology and pathogenesis of RP are unknown, hindering its diagnosis [2]. Clinically, RP is mainly diagnosed by visual field imaging and electroretinography, based on highly subjective assessments, resulting in poor accuracy and reproducibility, and these factors also make it difficult to diagnosis RP at an early stage [3]. The treatment of RP has also progressed slowly due to the difficulties in diagnosis and unclear pathogenesis. Numerous studies of RP have focused on gene therapy, and many breakthroughs have been achieved in recent years. However, there is extensive genetic heterogeneity in RP, with dozens of gene mutations accompanied by X-linked inheritance and autosomal recessive genes, which make it difficult to apply gene therapy universally in the clinic [2]. Thus, finding alternative diagnostic and treatment targets for RP lesions is of particular clinical importance.

The clinical manifestations of RP include night blindness in adolescence, followed by progressive visual field constriction, and loss of visual acuity in both eyes, and ultimately blindness because the lesions in rod cells usually precede those in cone cells [4, 5]. Although the pathogenesis of RP is not well defined, apoptosis of photoreceptor cells appears to be a common feature of this group of diseases [6], and it may be accelerated by oxidative stress and light exposure [4, 5]. The retina consumes a large amount of oxygen and produces high levels of reactive oxygen species (ROS), particularly in photoreceptors, which are highly susceptible to ROS-induced apoptosis [7]. Understanding the mechanisms involved in photoreceptor cell death is crucial to identify and develop appropriate therapeutic strategies to preserve photoreceptors by inhibiting specific steps in these pathways.

Pyruvate kinase (PK), the rate-limiting enzyme in the glycolytic system, converts phosphoenolpyruvate to pyruvate. There are four isoforms of PK, namely, PKL, PKR, PKM1, and PKM2, which are differentially expressed in human tissues [8]. PKM2 is distributed in tissues such as the brain, liver, retina, and tumors and is the predominant isoform in tumors and the retina [9]. Researchers have long noted that in tumors and the retina, pyruvate is converted in large amounts to lactate despite the presence of oxygen, a

process termed "aerobic glycolysis" or the "Warburg effect" that is closely related to PKM2 [9]. Many studies have confirmed that the regulation of PKM2 in tumor cells can protect against oxidative stress [10, 11]. Like tumor tissue, the retina has high rates of aerobic glycolysis with abundant PKM2 expression [12]. Therefore, regulation of PKM2 may also protect against antioxidative stress in the retina.

In this study, we investigated the effect of modulating PKM2 activity on light-induced cellular oxidative stress using a photoreceptor cell line *in vitro* as a model of RP to reveal the potential role of PKM2 in the photoreceptors of patients with RP.

2. Materials and Methods

2.1. Cell Culture. The mouse retinal cone cell line 661W was provided by Dr. Muayyad R. Al-Ubaidi (University of Oklahoma Health Sciences Center, Oklahoma City, OK, USA). The cells were incubated in Dulbecco's modified Eagle's medium (DMEM; Sigma-Aldrich, USA) containing 10% fetal bovine serum (FBS; Gibco, USA), 100 U/mL penicillin (Gibco, USA), and 100 μg/mL streptomycin (Gibco, USA). The cultures were maintained at 37°C in a humidified atmosphere of 95% air and 5% CO_2 and passaged by trypsinization (0.25% Trypsin-ethylenediaminetetraacetic acid; Gibco) every 2 or 3 days.

2.2. Light-Induced Cellular Oxidative Stress Damage in 661W Cells. The 661W cells were seeded at 1×10^4 cells/well in 96-well plates and incubated for 24 h. The entire medium was then replaced with fresh medium containing 2% FBS. PKM2 inhibitor shikonin (Selleck, USA) or its solvent, dimethyl sulfoxide (DMSO; Beyotime, China), were added to the culture medium and incubated for 2 h. The final concentration of DMSO was not more than 0.1%. The cells were exposed to 6000 lux of blue light (wavelength~450 nm) for 3 h at 37°C to induce photodamage. The luminance was measured using a light meter (PP710, SanLiang, China). Calcein-acetoxymethyl ester (AM)/propidium iodide (PI) double staining, ROS assays, Cell Counting Kit-8 (CCK8) assays, and western blotting were performed after photodamage.

2.3. Calcein-AM/PI Double Staining. Calcein-AM/PI double staining was performed according to the manufacturer's instructions (Dojindo, Japan). At 24 h after light-induced damage, the cells were gently washed three times with PBS to remove any active esterases present in the culture medium. Then, the dye solution (50 μL) was added to each well. The dye solution was prepared by adding PI solution (15 μL) and calcein-AM solution (10 μL) to PBS (5 mL), resulting in calcein-AM and PI concentrations of 2 and 4.5 μM, respectively. After incubation at 37°C, the fluorescence of each well was measured using a fluorescence microplate reader.

2.4. Cell Viability Assay. A CCK8 assay kit (Dojindo, Japan) was used to measure cell viability before light-induced damage, immediately after light exposure, and at 24 h and 48 h after light exposure. The relative cell viability was calculated based on the optical density (OD) according to

$$\text{Cell viability (\%)} = \frac{\text{OD value of the experimental group} - \text{OD value of the blank group}}{\text{OD value of the control group} - \text{OD value of the blank group}} \times 100\%. \quad (1)$$

Equation (1) shows the relative cell viability calculation, where OD is the optical density.

2.5. ROS Assays. The intracellular ROS levels were measured using a ROS assay kit (Dojindo, Japan). The kit contains highly sensitive 2′,7′-dichlorofluorescein diacetate (DCFH-DA), which is more susceptible to oxidation to fluorescent dichlorofluorescein (DCF) by intracellular ROS than normal DCFH-DA. Thus, the ROS level can be quantified by the fluorescence of DCF. At 24 h after light exposure, the cells were incubated with highly sensitive DCFH-DA for 20 min at 37°C and observed by fluorescence microscopy or measured at 488 nm excitation and 525 nm emission using a fluorescence microplate reader.

2.6. Western Blotting. The cells were washed twice with cold PBS and lysed for 30 min on ice with RIPA lysis buffer (Beyotime, China). The lysates were centrifuged at 12,000 g for 15 min, and the supernatants were collected. After measuring the protein concentration using a bicinchoninic acid assay (Beyotime, China), the supernatants were mixed with loading buffer (4 : 1; Beyotime, China) and heated at 100°C for 10 min. Samples (total protein: 10 μg) were electrophoretically resolved on 12%–20% gradient Tris-glycine sodium dodecyl sulfate–polyacrylamide gels and transferred to polyvinylidene difluoride membranes using a Trans-Blot Turbo Transfer System (Bio-Rad, USA). The membranes were then blocked with 5% skim milk in Tris-buffered saline containing Tween for 1 h and incubated with the following antibodies: anti-nuclear factor erythroid 2-related factor 2 (NRF2; 1 : 1000; Proteintech, USA), anti-PKM2 (1 : 1,000; Abcam, USA), anti-PKM1 (1 : 1,000; Abcam, USA), anti-B-cell lymphoma-2 (BCL2; 1 : 1,000; Proteintech, USA), anti-BCL2-associated X (BAX; 1 : 5,000; Proteintech, USA), and β-actin (1 : 10,000, Abcam, USA). The antigen–primary antibody complexes were detected with horseradish peroxidase-conjugated secondary antibodies and developed using a chemiluminescent reagent (SuperSignal West Femto, Thermo Fisher Scientific, USA). The expression of β-actin was used as control. Densitometric analysis of the bands was performed with the ImageJ ver. 1.51 (National Institutes of Health, USA).

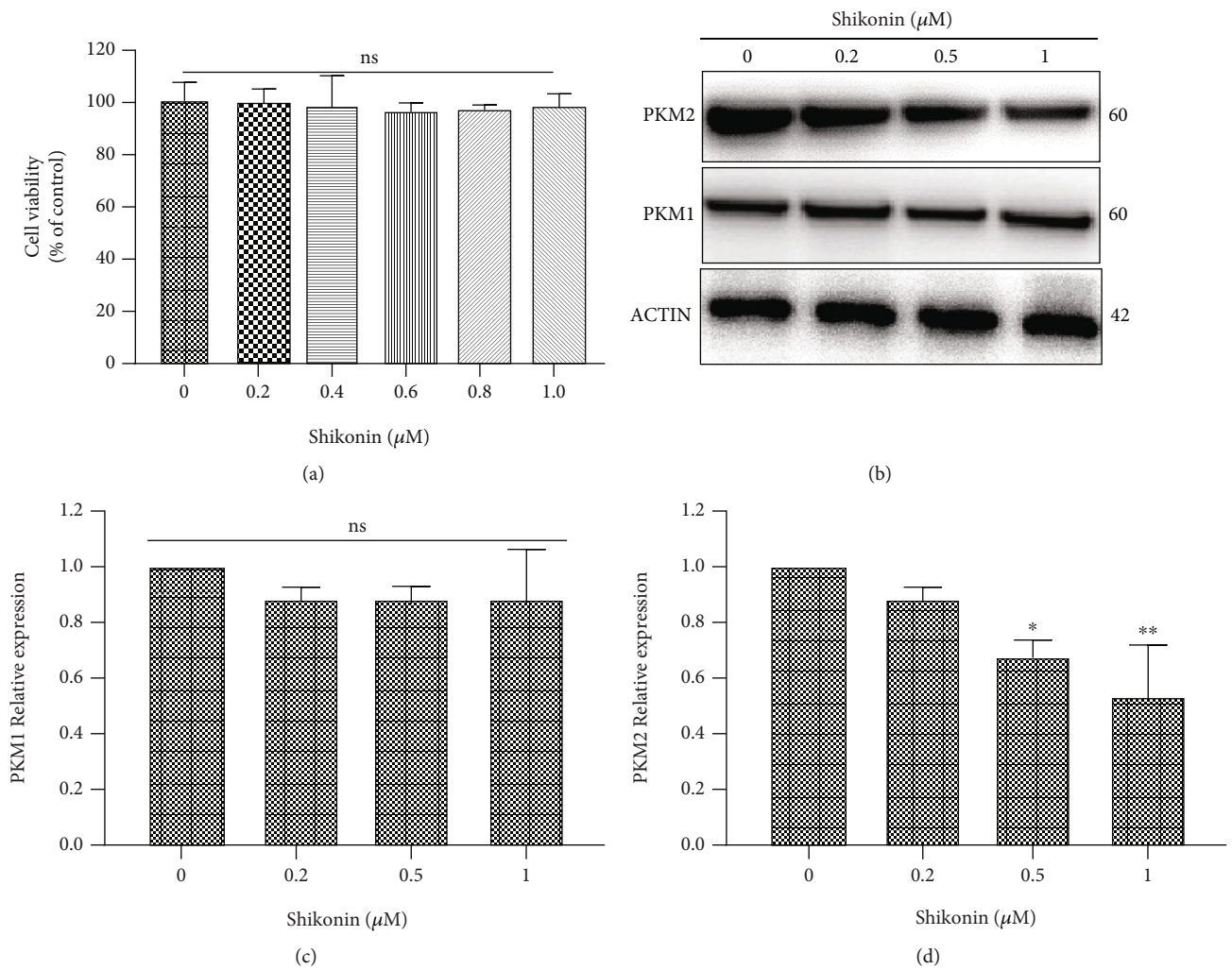

Figure 1: Effects of shikonin on 661W cells. (a) CCK8 assay results showing that PKM2 inhibition did not inhibit cell viability at 48 h. (b, c) Western blotting showing that shikonin did not inhibit the expression of PKM1, another PK subtype, in 661W cells. (b, d) Western blotting showing that shikonin significantly inhibited the expression of PKM2 in a dose-dependent manner in 661W cells. Notes: data from three separate experiments ($N = 3$) were averaged and analyzed by one-way ANOVA with post hoc LSD correction. ns: not significant. $^{*}P < 0.05$ and $^{**}P < 0.01$ versus the control group (0 μM shikonin).

2.7. Statistics. Results are expressed as mean ± standard deviation or 95% confidence interval. Comparisons were made using significant differences between 2 groups were analyzed using the 2-tailed independent samples t-test. Analyses with multiple comparisons were carried out via 1-way ANOVA with a post hoc LSD correction. $P < 0.05$ was considered statistically significant. All statistical analyses were performed using SPSS version 20 (IBM Corp., USA).

3. Results

3.1. PKM2 Inhibition Did Not Inhibit the Viability of 661W Cells. To evaluate whether shikonin may have cytotoxic effects on photoreceptor cells, we treated the 661W cells with different concentrations of shikonin for 24 h. To avoid solvent effects, the volume of DMSO administered was the same in each group and matched the volume used in the negative control group treated with DMSO alone. The results of the CCK8 assay confirmed that shikonin did not affect cell viability at any of the doses tested, and the viability of cells was equivalent to that of the negative control group (Figure 1(a)).

3.2. Shikonin Specifically Decreased PKM2 Expression in 661W Cells. 661W cells were treated with different concentrations of shikonin for 24 h to determine its effects on the expression of PKM1 and PKM2. Western blotting showed that shikonin significantly inhibited the expression of PKM2 in a dose-dependent manner but did not inhibit the expression of another PK subtype in photoreceptors (Figures 1(b)–1(d)).

3.3. Blue Light-Induced Apoptosis in 661W Cells. After exposure to blue light (6000 lux for 3 h), the 661W cells were returned to their normal culture environment for a further 24 or 48 h, at which times the extent of apoptosis was measured. The percentage of apoptotic cells was 27.82% at 24 h (95% confidence interval (CI): 25.32%–30.29%;

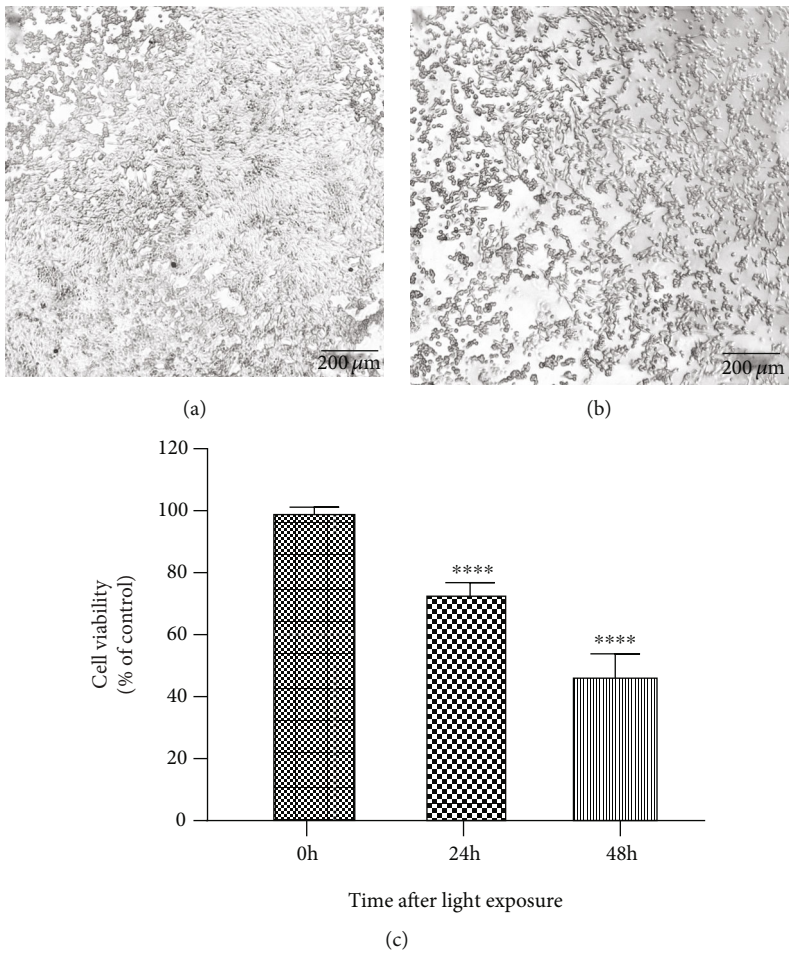

Figure 2: Blue light induces apoptosis in 661W cells. (a, b) Apoptosis at 24 h (a) and 48 h (b) after the 661W cells were returned to their normal culture environment following exposure to blue light. (c) Quantification of 661W cell apoptosis. Notes: data from three separate experiments ($N = 3$) were averaged and analyzed by one-way ANOVA with post hoc LSD correction. $^{****}P < 0.0001$ versus the control group (0 h, before light exposure).

Figures 2(a) and 2(c)) and 55.56% at 48 h (95% CI 63.43%–47.69%; Figures 2(b) and 2(c)) after light exposure.

Western blotting also confirmed that exposure to blue light-induced apoptosis in 661W cells with downregulation of BCL2 at 12, 24, 48, and 72 h and upregulation of BAX (Figure 3). At 72 h after light exposure, the relative expression levels of BCL2 and BAX were 0.16-fold (95% CI 0.04–0.27) and 1.51-fold (95% CI 1.22–1.75) the preexposure levels, respectively.

3.4. Blue Light Exposure Upregulated PKM2 in 661W Cells. Western blotting showed an increase in PKM2 expression over time following blue light exposure, consistent with the trend observed for BAX, whereas BCL2 and NRF2 expression levels decreased over time (Figure 3). At 72 h after blue light exposure, the relative expression levels of PKM2 and NRF2 were 2.64-fold (95% CI 2.67–3.00) and 0.19-fold (95% CI 0.16–0.22) the corresponding levels preexposure. Although there were fluctuations in PKM1 expression levels after light exposure, the changes were not statistically significant.

3.5. PKM2 Inhibition Reduced Apoptosis in 661W Cells following Blue Light Exposure. The 661W cells were pretreated with different concentrations of shikonin before light exposure to explore the effects of modulating PKM2 activity on apoptosis. The CCK8 assay revealed no difference in cell viability among the groups before photodamage (Figure 4(a)). Pretreatment with shikonin at concentrations of 0.1–0.5 μM reduced the level of apoptosis at 24 and 48 h after light exposure (Figures 4(b) and 4(c)), with the greatest antiapoptotic effect at a concentration of 0.3 μM. At this concentration, the cell viabilities at 24 and 48 h were 165.54% (95% CI 157.89–173.19) and 221.06% (95% CI 199.79–242.33), respectively, relative to the control group.

Consistent with the results of the CCK8 assay, the calcein-AM/PI double staining revealed that the number of apoptotic cells was lowest in cells treated with 0.3 μM shikonin (Figures 5(a) and 5(b)) at 48 h after light exposure. Western blotting revealed that 0.3 μM shikonin upregulated BCL expression by 1.87-fold (95% CI 1.63–2.13) and downregulated BAX expression by 0.49-fold (95% CI 0.38–0.61) (Figures 5(c) and 5(d)).

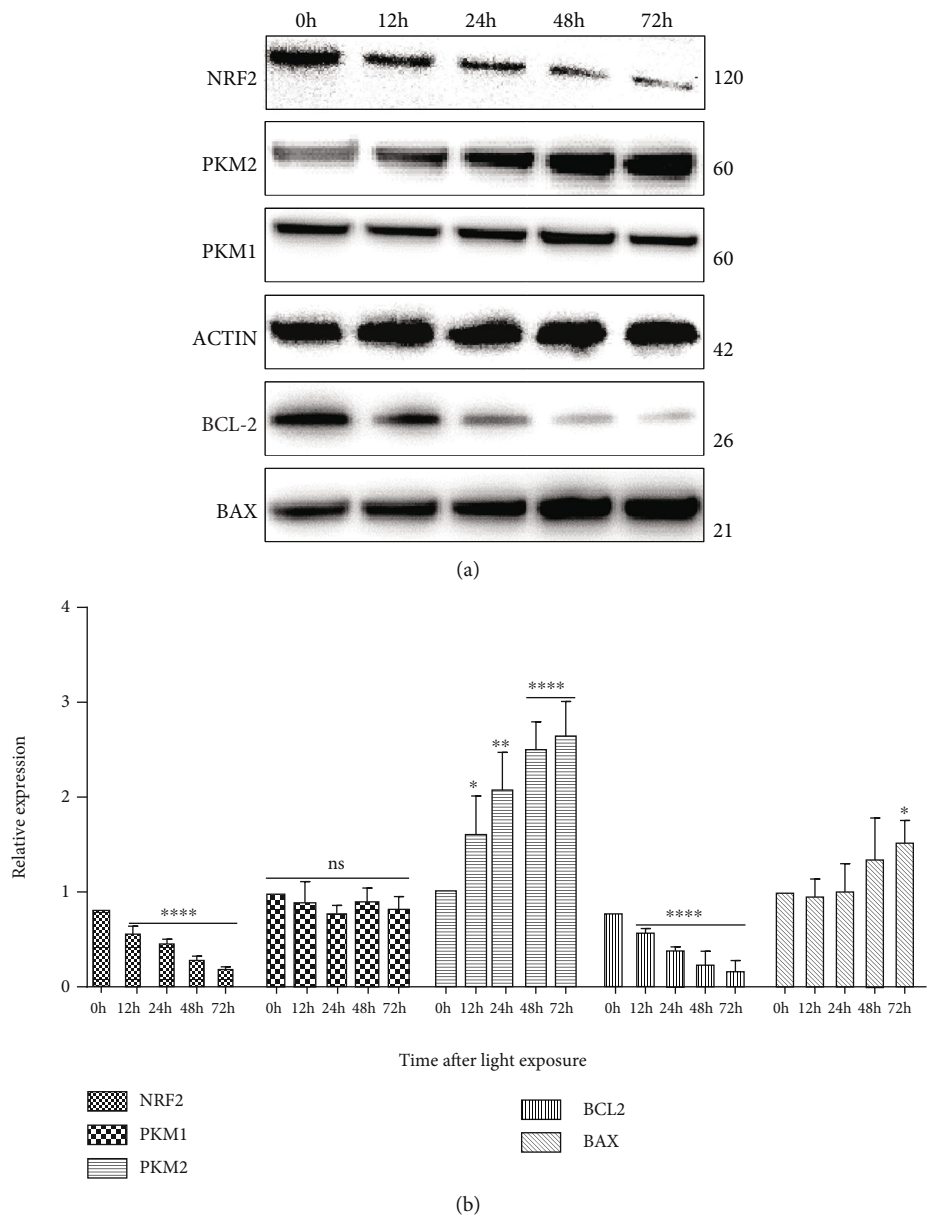

Figure 3: Effects of blue light exposure on protein expression in 661W cells. (a, b) Western blot analyses of NRF2, PKM1, PKM2, BCL2, and BAX expression levels in 661W cells exposed to blue light. Notes: data from three separate experiments ($N = 3$) were averaged and analyzed by one-way ANOVA with post hoc LSD correction. $^{*}P < 0.05$, $^{**}P < 0.01$, and $^{****}P < 0.0001$ versus the control group (0 h).

3.6. PKM2 Inhibition Relieves Oxidative Stress in 661W Cells. Qualitative and quantitative detection of ROS showed that 0.3 μM shikonin reduced the level of oxidative stress by 10.29% (95% CI 0–45.11) relative to the positive control group at 24 h after light exposure (Figures 6(a)–6(d) and 6(f)). Western blotting showed that 0.3 μM shikonin downregulated the PKM2 expression by 0.63-fold (95% CI 0.61–0.66) and upregulated NRF2 expression by 1.50-fold (95% CI 1.21–1.80) at 24 h after light exposure (Figures 6(e) and 6(g)).

4. Discussion

RP is difficult to diagnose, especially at an early stage. RP lesions affect the retinal blood vessels, photoreceptor cells, retinal pigment epithelium, and choroid, culminating in photoreceptor apoptosis [6]. In this study, we found that PKM2 expression was upregulated during apoptosis of 661W cells. PKM2 has previously been studied as a potential diagnostic or prognostic marker for various diseases [13, 14]. Our findings imply that PKM2 may serve as a disease marker and therapeutic target for RP.

Apoptosis of rod cells precedes that of cone cells in RP [15]. The apoptosis of rod cells leads to night blindness, whereas apoptosis of cone cells leads to progressive narrowing of the central visual field and ultimately blindness. This suggests that the vision and quality of life of patients with advanced RP are highly dependent on the rate of cone cell loss. Light exposure and oxidative stress are key factors that

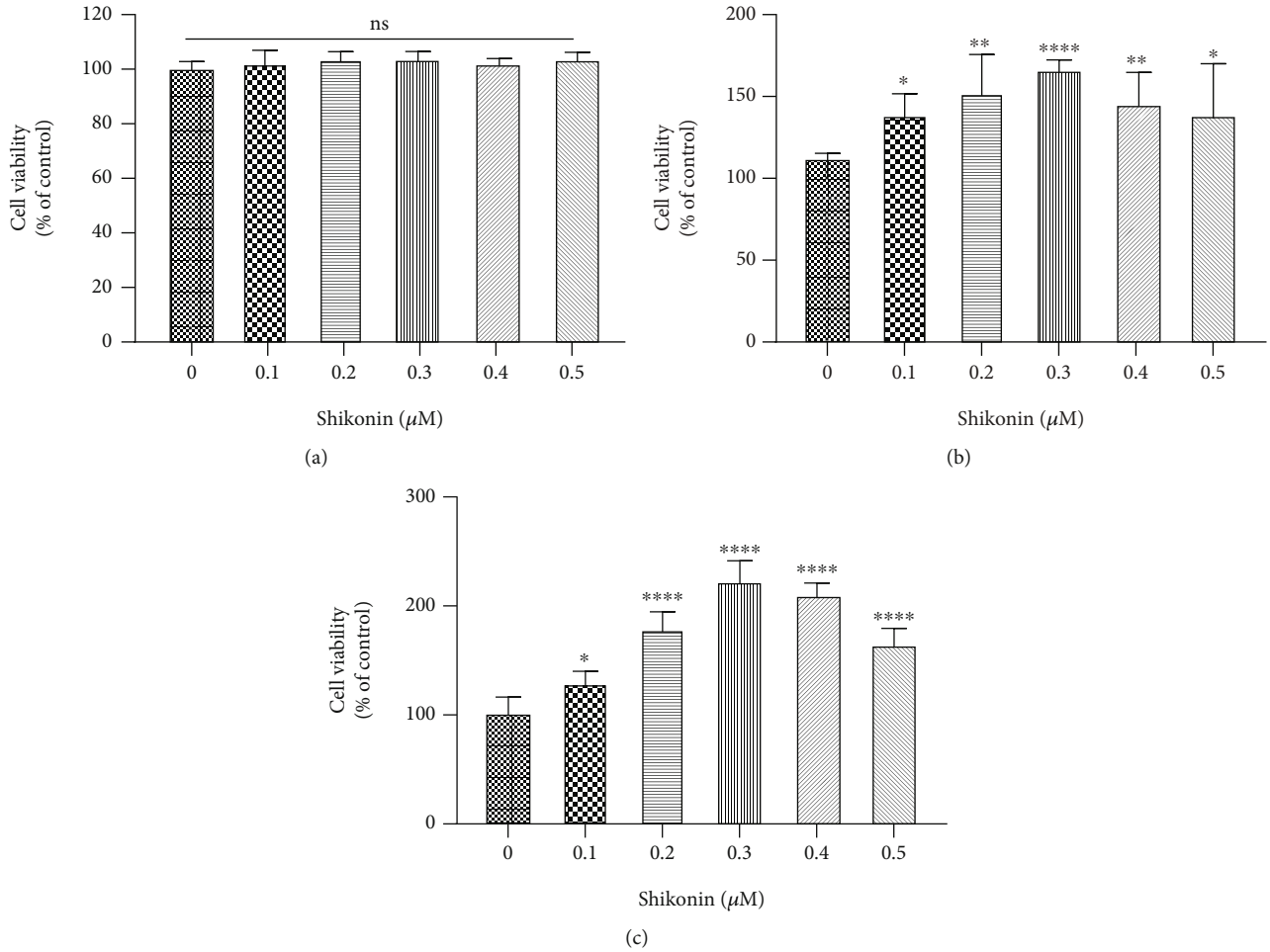

Figure 4: PKM2 inhibition enhances cell viability in 661W cells. (a) Effects of shikonin on the viability of 661W cells before light exposure. (b, c) Effects of pretreatment with shikonin on the viability of 661W cells at 24 h (b) and 48 h (c) after light exposure. Notes: data from three separate experiments ($N = 3$) were averaged and analyzed by one-way ANOVA with *post hoc* LSD correction. ns: not significant. $^{*}P < 0.05$, $^{**}P < 0.01$, and $^{****}P < 0.0001$ versus the control group (0 μM shikonin).

contribute to the progression of RP. Thus, protecting cone cells from photodamage versus oxidative stress is important for preserving vision and quality of life in patients with RP [4].

661W cells are the most commonly used cell line to study RP [16]. Thus, we used this cell line to establish a model of light exposure and oxidative stress that mimics the apoptosis of cone cells in patients with advanced RP. In this cell model, apoptosis continued and the oxidative stress persisted for some time after light exposure. We found that PKM2 expression was consistently upregulated and oxidative stress was exacerbated concomitant with the apoptosis of 661W cells. Because the respiratory chain substrate end of the inner mitochondrial membrane is a major source of ROS, it is unsurprising that the flow of glucose to aerobic respiration directly increases ROS production [17]. It was previously reported that enhanced aerobic respiration promotes apoptosis of cone cells [18]. Considering these earlier findings together with our results, we suggest that the elevated expression of PKM2 promotes intracellular ROS production, which in turn induces apoptosis in cone cells. The changes in the expression of BCL2 and BAX support our theory.

PKM2 modulates intracellular oxidative stress and increases nicotinamide adenine dinucleotide phosphate (NADPH) production, in addition to reducing ROS generation by regulating glucose metabolism pathways [10, 11]. The activity of PKM2 is modified by succinylation, phosphorylation, and acetylation [9]. Inhibition of PKM2 leads to the accumulation of glycolytic intermediates, which prevent complete oxidative decomposition of glucose and instead redirect it to the pentose phosphate pathway (PPP). This contributes to the synthesis of NADPH and nonessential amino acids and promotes cell biosynthesis [19]. NADPH, generated by the PPP, is a component of multiple antioxidant stress systems and provides them with reducing equivalents [20, 21]. For example, the thioredoxin (TRX) system, which consists of NADPH, TRX reductase, and TRX, is a key antioxidant system involved in the defense against oxidative stress by regulating the protein dithiol/disulfide balance through its disulfide reductase activity [21]. The TRX system donates electrons to thiol-dependent

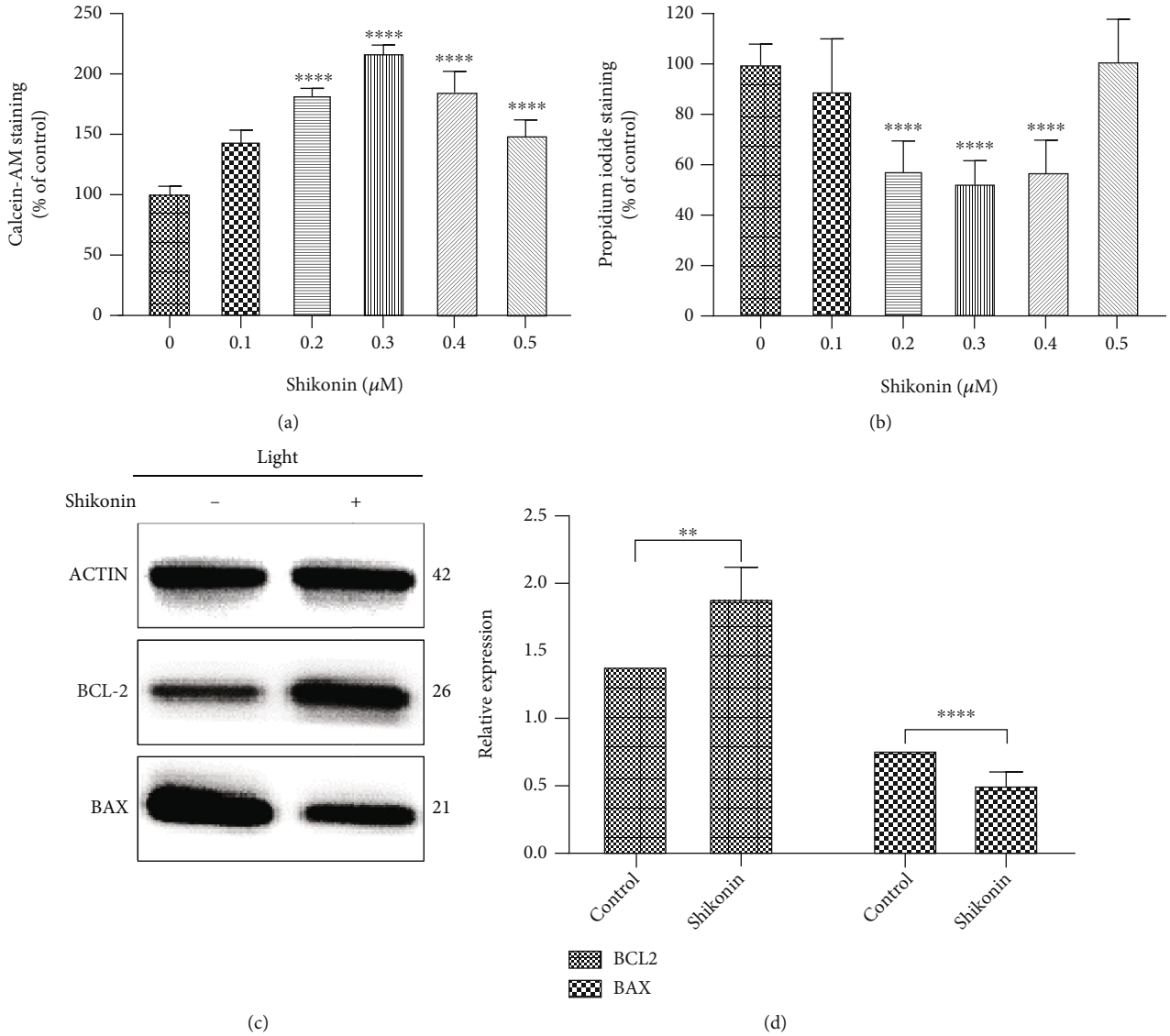

Figure 5: Inhibition of PKM2 reduces apoptosis induced by blue light exposure in 661W cells. (a, b) Dose-dependent effects of shikonin on apoptosis, determined by calcein-AM/PI double staining, of 661W cells at 48 h after light exposure. (c, d) Western blotting showing the effects of shikonin on BCL2 and BAX expression levels in 661W cells after light exposure. Notes: data from three separate experiments ($N = 3$) were averaged and analyzed by one-way ANOVA with post hoc LSD correction. ns: not significant. $^{**}P < 0.01$ and $^{****}P < 0.0001$ versus the relevant control groups (0 μM shikonin).

peroxidases for the rapid removal of reactive oxygen and nitrogen species [21]. The TRX system also exerts antioxidative activity via DNA and protein repair by reducing the activities of ribonucleotide reductase and methionine sulfoxide reductase and by regulating a number of redox-sensitive transcription factors [21]. Similarly, the constitutive glutaredoxin (GRX) system, which comprises GRX, a protein with similar structure to TRX, is an important intracellular resistance system against ROS. The GRX system comprises systemic NADPH as well as glutathione (GSH), GSH reductase, and GRX and removes ROS via a similar mechanism to the TRX system [20]. In addition, reduced GSH can convert peroxides to water in a process catalyzed by GSH peroxidase, while NADPH reduces the oxidized form of GSH (GSSG) to GSH, and acts as an antioxidant [22]. The conversion of GSSG to GSH is an important mechanism in the retina countering oxidative stress and highlights the important role of NADPH in retinal cells [23].

PKM2 inhibition helps cells mitigate oxidative stress by activating PPP, while alleviating chronic intracellular oxidative stress by promoting the accumulation of the glycolytic intermediate, 3-phosphoglycerate [24]. 3-Phosphoglycerate can be diverted to the phosphoserine pathway for de novo synthesis of serine, which plays a crucial role in the antioxidant defense system as a precursor for GSH synthesis [25], and can also be used as a raw material for the synthesis of proteins, nucleic acids, and lipids involved in repairing oxidative stress damage [24].

In photoreceptor cells, all-*trans*-retinal is reduced to all-*trans*-retinol by retinol dehydrogenase to maintain visual

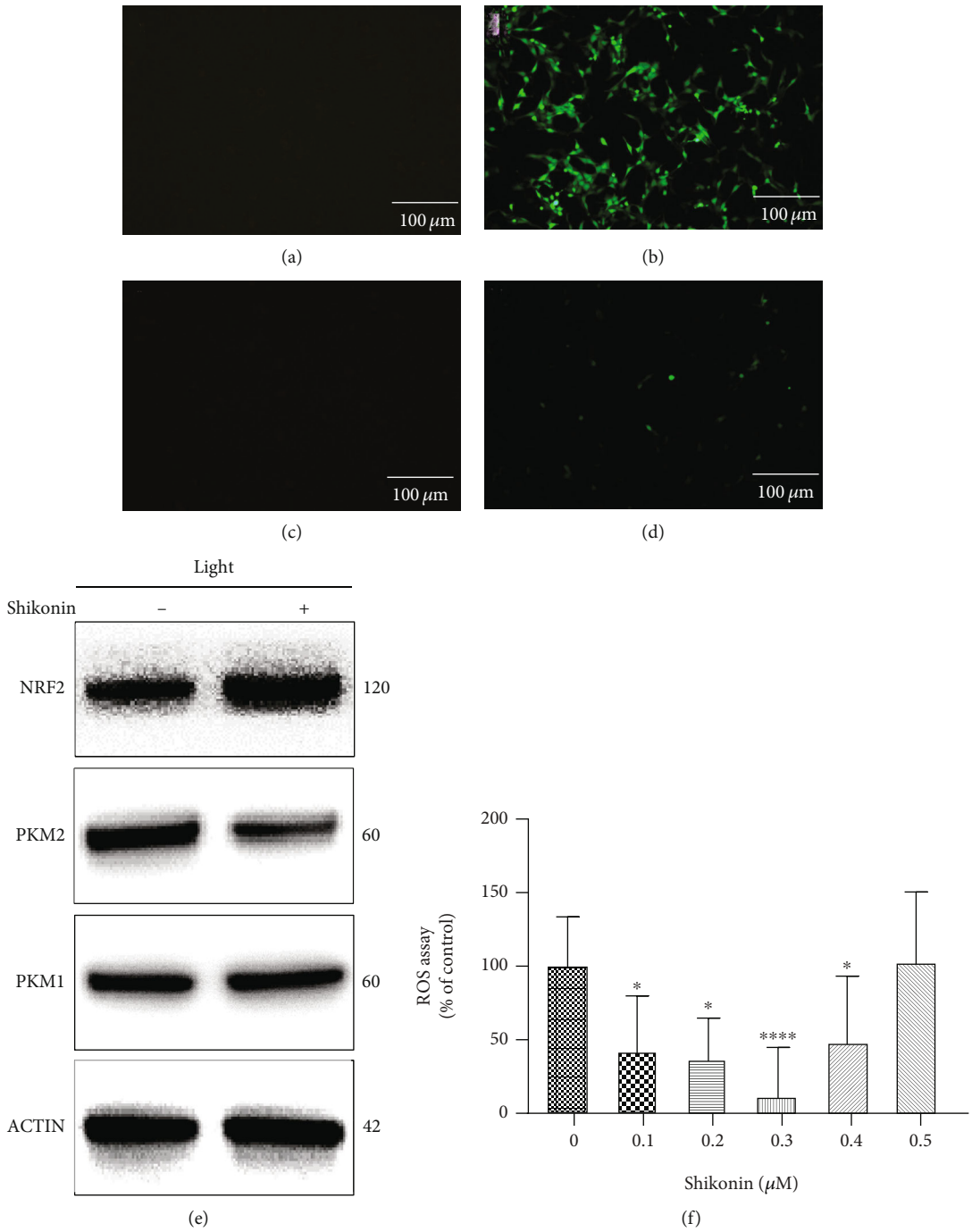

Figure 6: Continued.

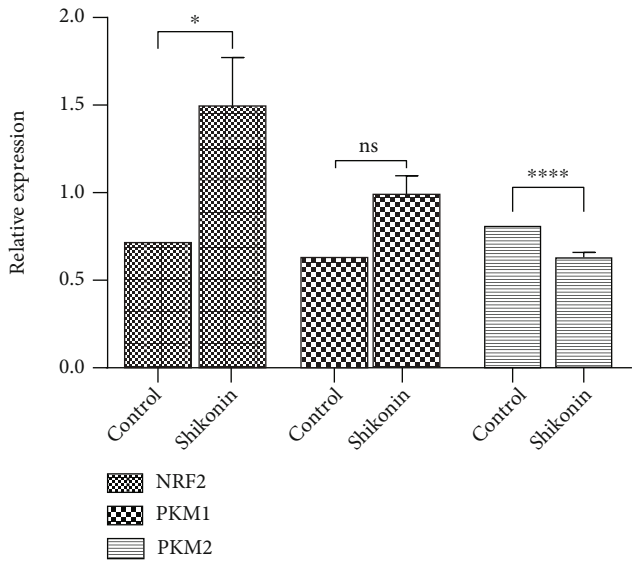

(g)

Figure 6: PKM2 inhibition relieves oxidative stress in 661W cells. (a–d) ROS fluorescence staining of 661W cells before blue light exposure (a), 661W cells treated with shikonin before light exposure (b), 661W cells exposed to blue light (c), and 661W cells treated with shikonin and exposed to blue light (d). (f) Quantitative analysis of ROS in 661W cells treated with different concentrations of shikonin and exposed to blue light. (e, g) Western blotting of NRF2, PKM1, and PKM2 protein expression levels in 661W cells treated with shikonin and exposed to blue light. Notes: data from three separate experiments ($N = 3$) were averaged and analyzed by one-way ANOVA with *post hoc* LSD correction. ns: not significant. $^{*}P < 0.05$, $^{***}P < 0.001$, and $^{****}P < 0.0001$ versus the relevant control group (0 μM shikonin).

sensitivity, a step that requires the reduction of NADPH [26]. Thus, NADPH appears to be vital for maintaining retinal visual sensitivity, maintaining retinal redox homeostasis, and providing reducing equivalents for lipid and protein synthesis [23, 26, 27]. Activation of the PPP pathway can also promote the synthetic repair of proteins, nucleic acids, and lipids that are damaged by oxidative stress [24]. In our study, treatment with a PKM2 inhibitor significantly reduced light-induced apoptosis of 661W cells and reduced the intracellular oxidative stress level, which was accompanied by upregulation of intracellular antiapoptotic proteins and downregulation of proapoptotic proteins. Therefore, PKM2 seems to be an important therapeutic target for retinal diseases, such as RP.

Overall, these findings support the development of PKM2 inhibitors as a promising therapeutic target for retinal diseases, such as RP. Indeed, Rajala et al. reported that the visual acuity of rod *PKM2*-knockout mice was not affected at 5 months [28]. Our experiments also showed that the moderate inhibition of PKM2 activity did not affect the viability of 661W cells, but the function of PKM2 was not restricted to glycolysis. More research is still needed before we can use PKM2 expression and inhibition for the diagnosis and treatment of RP.

5. Conclusions

We found that PKM2 is a key factor in RP and that regulation of PKM2 can reduce RP oxidative stress and protect photoreceptor cells. We believe that PKM2 is a potential diagnostic marker and therapeutic target for RP.

Data Availability

All data are available from the corresponding author by request.

Conflicts of Interest

The authors declare no conflict of interest.

Authors' Contributions

Peiwen Zhu and Qian Yang have contributed equally to this work.

Acknowledgments

This work was supported by the National Natural Science Foundation of China (Grant Nos. 81870670 and 82171078) and Shanghai clinical three-year action plan major clinical research project (Grant Nos. SHDC2020CR2041B and SHDC2020CR5014).

References

[1] S. K. Verbakel, R. A. C. van Huet, C. J. F. Boon et al., "Non-syndromic retinitis pigmentosa," *Progress in Retinal and Eye Research*, vol. 66, pp. 157–186, 2018.

[2] A. Berger, S. Lorain, C. Joséphine et al., "Repair of Rhodopsin mRNA by Spliceosome-Mediated RNA *Trans* -Splicing: A New Approach for Autosomal Dominant Retinitis Pigmentosa," *Molecular Therapy*, vol. 23, no. 5, pp. 918–930, 2015.

[3] A. Fahim, "Retinitis pigmentosa," *Current Opinion in Pediatrics*, vol. 30, no. 6, pp. 725–733, 2018.

[4] K. Tsuruma, Y. Tanaka, M. Shimazawa, Y. Mashima, and H. Hara, "Unoprostone reduces oxidative stress- and light-induced retinal cell death, and phagocytotic dysfunction, by activating BK channels," *Molecular Vision*, vol. 17, pp. 3556–3565, 2011.

[5] A. I. Arroba, D. Wallace, A. Mackey, E. J. De La Rosa, and T. G. Cotter, "IGF-I maintains calpastatin expression and attenuates apoptosis in several models of photoreceptor cell death," *European Journal of Neuroscience*, vol. 30, no. 6, pp. 975–986, 2009.

[6] M. F. Dias, K. Joo, J. A. Kemp et al., "Molecular genetics and emerging therapies for retinitis pigmentosa: basic research and clinical perspectives," *Progress in Retinal and Eye Research*, vol. 63, pp. 107–131, 2018.

[7] Y. Du, A. Veenstra, K. Palczewski, and T. S. Kern, "Photoreceptor cells are major contributors to diabetes-induced oxidative stress and local inflammation in the retina," *Proceedings of the National Academy of Sciences of the United States of America*, vol. 110, no. 41, pp. 16586–16591, 2013.

[8] W. J. Israelsen, T. L. Dayton, S. M. Davidson et al., "PKM2 isoform-specific deletion reveals a differential requirement for pyruvate kinase in tumor cells," *Cell*, vol. 155, no. 2, pp. 397–409, 2013.

[9] W. J. Israelsen and M. G. Vander Heiden, "Pyruvate kinase: function, regulation and role in cancer," *Seminars in Cell and Developmental Biology*, vol. 43, pp. 43–51, 2015.

[10] D. Anastasiou, G. Poulogiannis, J. M. Asara et al., "Inhibition of pyruvate kinase M2 by reactive oxygen species contributes to cellular antioxidant responses," *Science*, vol. 334, no. 6060, pp. 1278–1283, 2011.

[11] M. Siragusa, J. Thöle, S. I. Bibli et al., "Nitric oxide maintains endothelial redox homeostasis throughPKM2 inhibition," *The EMBO Journal*, vol. 38, no. 17, 2019.

[12] R. V. S. Rajala, "Aerobic glycolysis in the retina: functional roles of pyruvate kinase isoforms," *Frontiers in Cell and Developmental Biology*, vol. 8, 2020.

[13] Y. Wang, Y. Li, L. Jiang, X. Ren, B. Cheng, and J. Xia, "Prognostic value of glycolysis markers in head and neck squamous cell carcinoma: a meta-analysis," *Aging*, vol. 13, no. 5, pp. 7284–7299, 2021.

[14] H. Jiang, Y. Zou, J. Zhao et al., "Pyruvate kinase M2 mediates glycolysis in the lymphatic endothelial cells and promotes the progression of lymphatic malformations," *American Journal of Pathology*, vol. 191, no. 1, pp. 204–215, 2021.

[15] C. Hamel, "Retinitis pigmentosa," *Orphanet Journal of Rare Diseases*, vol. 1, no. 1, 2006.

[16] G. Wheway, L. Nazlamova, D. Turner, and S. Cross, "661W photoreceptor cell line as a cell model for studying retinal ciliopathies," *Frontiers in genetics*, vol. 10, 2019.

[17] V. Larosaand and C. Remacle, "Insights into the respiratory chain and oxidative stress," *Bioscience Reports*, vol. 38, no. 5, 2018.

[18] J. Shen, X. Yang, A. Dong et al., "Oxidative damage is a potential cause of cone cell death in retinitis pigmentosa," *Journal of Cellular Physiology*, vol. 203, no. 3, pp. 457–464, 2005.

[19] F. Wang, K. Wang, W. Xu et al., "SIRT5 desuccinylates and activates pyruvate kinase M2 to block macrophage IL-1β production and to prevent DSS-induced colitis in mice," *Cell Reports*, vol. 19, no. 11, pp. 2331–2344, 2017.

[20] H. Sies, C. Berndt, and D. P. Jones, "Oxidative stress," *Annual Review of Biochemistry*, vol. 86, no. 1, pp. 715–748, 2017.

[21] J. Luand and A. Holmgren, "The thioredoxin antioxidant system," *Free Radical Biology and Medicine*, vol. 66, pp. 75–87, 2014.

[22] R. Margis, C. Dunand, F. K. Teixeira, and M. Margis-Pinheiro, "Glutathione peroxidase family - an evolutionary overview," *FEBS Journal*, vol. 275, no. 15, pp. 3959–3970, 2008.

[23] P. A. Campochiaroand and T. A. Mir, "The mechanism of cone cell death in retinitis pigmentosa," *Progress in Retinal and Eye Research*, vol. 62, pp. 24–37, 2018.

[24] E. Mullarkyand and L. C. Cantley, *Diverting glycolysis to combat oxidative stress*, Innovative Medicine: Springer Japan, 2015.

[25] E. Mullarky, K. R. Mattaini, M. G. Vander Heiden, L. C. Cantley, and J. W. Locasale, "PHGDH amplification and altered glucose metabolism in human melanoma," *Pigment Cell & Melanoma Research*, vol. 24, no. 6, pp. 1112–1115, 2011.

[26] M. Tsacopoulos, C. L. Poitry-Yamate, P. R. Macleish, and S. Poitry, "Trafficking of molecules and metabolic signals in the retina," *Progress in Retinal and Eye Research*, vol. 17, no. 3, pp. 429–442, 1998.

[27] R. B. Hamanakaand and N. S. Chandel, "Warburg effect and redox balance," *Science*, vol. 334, no. 6060, pp. 1219-1220, 2011.

[28] A. Rajala, Y. Wang, R. S. Brush et al., "Pyruvate kinase M2 regulates photoreceptor structure, function, and viability," *Cell Death & Disease*, vol. 9, no. 2, 2018.

Hindawi
Disease Markers
Volume 2021, Article ID 5390195, 6 pages
https://doi.org/10.1155/2021/5390195

Research Article

The Ocular Surface Characteristics in Prostate Cancer Patients Treated with Androgen Deprivation Therapy

Weina Li,[1,2,3] Xiaofeng Li,[1] Feilun Cui,[4] Zhipeng Xu,[4] Nuo Dong,[1,2] and Cheng Li[1,2]

[1]*Eye Institute & Affiliated Xiamen Eye Center, School of Medicine, Xiamen University, Xiamen, China*
[2]*Fujian Provincial Key Laboratory of Ophthalmology and Visual Science & Ocular Surface and Corneal Diseases, Xiamen, China*
[3]*Department of Ophthalmology, Changhai Hospital, Shanghai, China*
[4]*Department of Urology, Zhenjiang First People's Hospital, Zhenjiang, China*

Correspondence should be addressed to Nuo Dong; profeye@163.com and Cheng Li; cheng-li@xmu.edu.cn

Weina Li and Xiaofeng Li contributed equally to this work.

Received 8 September 2021; Accepted 22 October 2021; Published 9 November 2021

Academic Editor: Wen-Qing Shi

Background.To investigate the association of long-term androgen deprivation therapy (ADT) with ocular surface characteristics in prostate cancer patients. *Methods*. A total of 30 male prostate cancer patients who received ADT were selected. All candidates were scored using the Ocular Surface Disease Index (OSDI) and subsequently divided into two groups containing 9 symptomatic patients (scores >12) and 21 asymptomatic patients (scores ≤ 12). Another 20 healthy age-matched males were selected as the control group. Each candidate was assessed with respect to eyelid margin abnormality, tear film break-up time (NI-BUT), tear meniscus height (TMH), meiboscore, meibum expressibility, and demodex infection. *Results*. The NI-BUT in the ADT group was significantly shorter than that in the control group. The scores for OSDI, eyelid margin abnormality, meibum expressibility, and meiboscores were significantly higher in the ADT group ($P < 0.05$). Moreover, the NI-BUT in the symptomatic ADT group was significantly shorter than that in the asymptomatic ADT group ($P < 0.05$). The meiboscores and meibum expressibility score in the symptomatic ADT group were significantly higher than those in the asymptomatic ADT group ($P < 0.05$). The presence of demodex in the symptomatic ADT group was also higher than that in the asymptomatic ADT group ($P < 0.05$).The length of time that patients had been taking ADT was positively correlated with meiboscores and negatively correlated with NI-BUT. *Conclusion*. Androgen levels were associated with significant changes in relative meibomian gland function. Subjective symptoms, such as dryness and foreign body sensation, were more obvious in prostate cancer patients receiving ADT, which may be caused by MGD and demodex infection. It's recommended that more attention be paid to the ocular surface in prostate cancer patients taking ADT by performing examination of NI-BUT and meibomian gland morphology and function with a view to providing more comprehensive prevention and treatment protocols.

1. Introduction

Prostate cancer is the most common malignant tumor in men, and its incidence is gradually increasing annually. As early as 1941, Huggins and Hodges proposed androgen deprivation as an effective treatment for prostate cancer [1]. Nowadays, androgen deprivation therapy (ADT) is the mainstay of treatment for locally recurrent or advanced prostate cancer [2]. Although ADT is customized based on individual disease characteristics, side effects of these drugs are inevitable due to the long-term lack of androgen regulation. The effect of meibomian gland damage on the development of dry eye after long-term ADT has rarely been evaluated.

The meibomian glands can synthesize and secrete lipids to form the superficial tear film layer. Meibomian gland dysfunction (MGD) is a chronic diffuse abnormality of the meibomian glands, characterized by terminal duct obstruction and/or qualitative/quantitative changes in glandular secretion [3]. MGD is thought to be caused by abnormal lipid excretion that results in increased evaporation, leading to

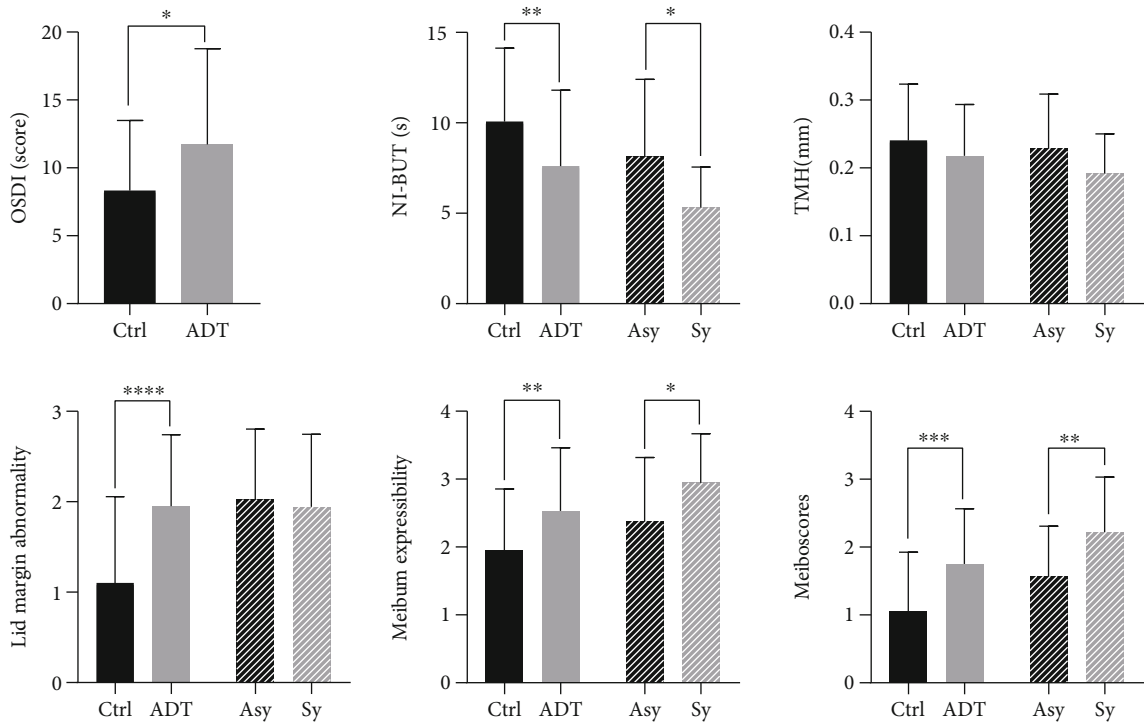

Figure 1: Mann–Whitney U test of each examined item between prostate cancer patients receiving ADT and the control group, as well as between the asymptomatic and symptomatic ADT groups ($^{***}P < 0.001$, $^{**}P < 0.01$, $^{*}P < 0.05$).

evaporative dry eye disease (DED). Previous studies have shown that androgens can exert a protective function on the ocular surface [4].

The meibomian glands are an androgen target. They express androgen receptor proteins in acinar epithelial cell nuclei [5], in addition to mRNAs for type 1 and/or type 2 5α-reductase, which convert testosterone to the very potent dihydrotestosterone [6].

Androgens play a key role in meibomian gland physiology, stimulating function and suppressing keratinization [7]. Schirra et al. [8] demonstrated that androgens regulate the expression of more than 1590 genes involved mainly in lipid metabolism in the mouse meibomian gland. Moreover, androgen deficiency is a risk factor for MGD and evaporative DED [7, 9]. MGD and DED have been reported to be associated with age and gender, the prevalence of which is higher in the elderly and in women [7, 10]. Although there is some evidence supporting the ability of chronic androgen deficiency to alter lipid secretion in meibomian glands, leading to MGD and DED [11], there is no clinical confirmation of their relationship with symptoms of dry eye or treatment time in patients taking androgen deprivation drugs.

To date, there have been only limited investigations regarding the possible association between androgens and meibomian glands. Given this background, we predict that androgen deficiency will influence meibomian gland function, alter meibum secretion, and decrease tear film stability, and that abnormality of the ocular surface in prostate cancer patients is related to the length of time taking ADT. To test this hypothesis, we sought to determine the effects of androgen deficiency on the ocular surface and meibomian glands by comparing prostate cancer patients receiving long-term ADT with age-matched male controls.

2. Materials and Methods

The study sample comprised 30 male prostate cancer patients (74.77 ± 8.62 years old, $n = 60$) receiving long-term ADT and 20 age-matched male controls (72.30 ± 6.19 years old, $n = 40$) who had not received ADT. The average duration of ADT in prostate cancer patients was 15.06 months (range 3–60 months). For the ADT group, prostate cancer patients receiving ADT was the sole inclusion criterion. The exclusion criteria were infectious keratitis or conjunctivitis, continuous eye drop use, history of eye surgery, and serious systematic disease. All participants were recruited from Zhenjiang First People's Hospital between June 2018 and December 2019.

2.1. Symptom Assessment. Dry eye symptoms were assessed using the OSDI Questionnaire, which comprises 12 questions regarding the frequency of ocular discomfort, visual problems interfering with daily activity, and ocular discomfort caused by environmental factors [12]. Total OSDI was calculated using the following formula: OSDI = [(sum of all answered questions) × 100]/[total number of answered questions) × 4]. Total scores were expressed on a scale of 0 to 100, with higher scores representing a greater disability [13]. Subjects with a score > 12 were placed into the symptomatic group, and the rest were placed into the asymptomatic group.

Table 1: Ocular surface assessment and statistical results among the groups. Data are shown as the mean ± SD. *P* value was calculated using the Mann–Whitney *U* test.

	Ctrl	ADT	*P*	Asymptomatic ADT group	Symptomatic ADT group	*P*
Age	72.30 ± 6.19	74.77 ± 8.62	0.276	72.22 ± 7.88	75.61 ± 8.97	0.418
OSDI	8.31 ± 1.15	11.72 ± 1.28	0.04	-	-	-
NI-BUT (s)	10.07 ± 4.05	7.60 ± 4.20	0.006	8.13 ± 4.27	5.32 ± 2.23	0.033
TMH(mm)	0.24 ± 0.08	0.21 ± 0.07	0.134	0.22 ± 0.07	0.19 ± 0.05	0.085
Lid margin abnormality score	1.10 ± 0.95	1.95 ± 0.79	≤0.001	2.02 ± 0.78	1.94 ± 0.80	0.666
Meibum expressibility	1.95 ± 0.90	2.53 ± 0.92	0.007	2.38 ± 0.93	2.94 ± 0.72	0.013
Meiboscores	1.05 ± 0.87	1.75 ± 0.81	≤0.001	1.57 ± 0.73	2.22 ± 0.80	0.005

Table 2: Demodex infection rate among the groups.

	Ctrl	ADT	Symptomatic ADT group	Asymptomatic ADT group
Demodex infection rate (%)	60.00%	70.00%	100%	57.14%
X^2	0.53		—	
P	0.46[a]		0.029[b]	

2.2. Noninvasive Tear Film Break-Up Time. All subjects underwent imaging with a Keratograph (Oculus, Wetzlar, Germany) that measured the noninvasive tear film breakup time (NI-BUT). Subjects focused on the central target, and a Placido disc pattern comprising 22 illuminated rings was projected onto the corneal surface. Subjects were asked to blink twice and keeped their eyes open until the next eye blink or the sampling procedure ended. Then, the first NI-BUT was recorded.

2.3. Tear Meniscus Height. The tear meniscus height (TMH) was evaluated using a Keratograph that had four infrared diodes under deactivation of red ring illumination and measured perpendicular to the eyelid margin at the 6 o'clock position of the corneal midline [14]. All examinations were performed three times.

2.4. Meibographic Evaluation. Meibography was accomplished using the infrared camera system of the oculus Keratograph. The meibomian glands were visualized by everting the eyelid. Areas of meibomian gland dropout and total tarsal plate were measured to calculate the percentage of meibomian gland dropout. Meiboscores were assessed according to the grading scale as described by Arita et al. [15]: grade 0, no loss of meibomian glands; grade 1, area loss < 33% of the total meibomian gland area; grade 2, area loss between 33% and 67% of the total meibomian gland area; and grade 3, area loss > 67% of the total meibomian gland area.

2.5. Eyelid Margin Abnormality. Under a slit lamp microscope, eyelid margin abnormality was quantitated as the total score of the following 4 parameters: plugged meibomian gland orifices, eyelid margin irregularity, eyelid margin vascular engorgement, and mucocutaneous junction displacement. The score ranged from 0 to 4 depending on the number of abnormalities present [16].

2.6. Examination of Demodex Infection. A total of 4 eyelashes from each eyelid were removed using fine forceps and placed on a glass slide. A drop of 70% glycerinum was added to the lashes before a coverslip was mounted. Under a light microscope, demodex was identified based on morphology and movement.

2.7. Meiboscores. After placing a hot compress on the eyelid for 10 minutes, pressure was applied to the upper and lower eyelid using two cotton buds to encourage the meibomian glands to secrete lipids. Characteristics of the meibum were graded on a numerical scale of 0–3 as follows [17]: grade 0, clear fluid; grade 1, cloudy fluid; grade 2, cloudy fluid with granular debris; and grade 3, thick toothpaste-like fluid. The higher the meiboscore, the cloudier and more viscous the meibum.

2.8. Statistical Analysis. The data were analyzed using SPSS 26.0 (Inc, Chicago, Illinois, USA) and are expressed as the mean ± standard deviation. Comparison of clinical parameters between the ADT and control groups was performed using the Mann–Whitney *U* test, X^2 test, and Fisher's exact probability test. Correlations between clinical parameters in the ADT group were evaluated by Spearman's correlation. $P < 0.05$ was considered statistically significant.

3. Results

A total of 100 eyes (ADT group, 60; control group, 40) were evaluated. Subjects in both groups were age-matched elderly males. The reference value for serum testosterone in healthy men was 1.75–7.81 ng/mg. This study selected prostate cancer patients whose serum testosterone value was 0.10 ± 0.13 ng/mg, which is significantly below normal.

The dry eye symptoms in prostate cancer patients receiving long-term ADT were more severe than those in control individuals (Figure 1). In comparison with the control group, the ADT group exhibited a significantly shorter NI-BUT ($P = 0.004$; Table 1). The OSDI, eyelid margin abnormality

Table 3: Correlation between the duration of ADT and each ocular test. P value was calculated using Spearman's correlation test. $P < 0.05$ was considered statistically significant.

	NI-BUT (s)	TMH (mm)	Lid margin abnormality score	Meibum expressibility	Meiboscores	Time and ADT
NI-BUT (s)	RA					
TMH(mm)	$R = -0.144$ $P = 0.274$	RA				
Lid margin abnormality score	$R = 0.076$ $P = 0.565$	$R = -0.048$ $P = 0.713$	RA			
Meibum expressibility	$R = 0.02$ $P = 0.882$	$R = 0.067$ $P = 0.611$	$R = 0.157$ $P = 0.23$	RA		
Meiboscores	$R = -0.116$ $P = 0.377$	$R = 0.144$ $P = 0.272$	$R = -0.016$ $P = 0.901$	$R = 0.390^{**}$ $P = 0.002$	RA	
Time and ADT	$R = -0.563^{**}$ $P \leq 0.001$	$R = 0.161$ $P = 0.22$	$R = -0.006$ $P = 0.963$	$R = 0.304^{*}$ $P = 0.018$	$R = 0.132$ $P = 0.316$	RA

score, and mean meiboscores as well as meibum expressibility scores in the ADT group were significantly higher than those in the control group (all, $P < 0.05$; Table 1); however, there was no significant difference in TMH between the two groups.

According to the OSDI scores, prostate cancer patients were divided into the symptomatic ADT group (scores > 12) containing 9 patients and the asymptomatic ADT group (scores ≤ 12) containing 21 patients. Following subgroup analysis of patients with established dry eye symptoms and those without, we found that the NI-BUT in the symptomatic ADT group was significantly shorter than that in the asymptomatic ADT group ($P < 0.05$). The mean meiboscores and meibum expressibility scores in the symptomatic ADT group were significantly higher than those in the asymptomatic ADT group ($P < 0.05$). Ocular surface discomfort was associated with a decrease in NI-BUT. There were no significant differences in the eyelid margin abnormality score or TMH between the symptomatic and asymptomatic ADT groups according to the completion of a questionnaire designed to assess dry eye symptoms.

Previous research has shown that demodex infestation is closely related to meibomian gland dysfunction and ocular surface inflammation [18]. In the present research, the percentage of demodex infection was 60.0% and 70.0% in the ADT and control group, respectively. There was no significant difference in demodex infection rate between these two groups ($P > 0.05$; Table 2). However, following grouping of the prostate cancer patients based on OSDI score, all 9 symptomatic patients had demodex infection. For the symptomatic and asymptomatic groups, the demodex infection rate was 100% and 57.14%, respectively. The difference was statistically significant ($P < 0.05$; Table 2).

MGD is a common and chronic progressive disease that has an adverse impact on the ocular surface. The duration of ADT as a time-dependent variable was examined for its association with MGD. In the present study, correlation analysis between clinical parameters in the ADT group (Table 3) revealed that the treatment time was positively correlated with the meiboscores and negatively correlated with the NI-BUT.

4. Discussion

Androgens are known to induce the proliferation and differentiation of sebaceous glands throughout the body [19]. Given that the meibomian glands are large sebaceous glands that express androgen receptors, androgens also play an important role in meibomian gland development. However, long-term ADT suppresses androgen levels, which can slow or stop the growth of prostate cancer, but this leads to physiological changes in the ocular surface. The present study investigated the changes in the structure and function of the ocular surface in prostate cancer patients taking ADT. These patients experienced a greater frequency of tear film debris, irregular eyelid margins, atrophy and orifice metaplasia of the meibomian glands, and a marked decrease in the quality of meibomian gland secretions than age-matched controls.

Dry eye syndrome is a relatively common. Analysis of the OSDI scores results indicated that ADT group did have a higher frequency of dry eye syndrome. Tear film stability is evaluated by measuring the NI-BUT. There was a significant decrease in NI-BUT values in the ADT group as compared with those in the control group, demonstrating a decrease in tear film stability. The eyelid margin abnormality, meibum expressibility, and meiboscores were higher than those in the control group, indicating changes in the morphology and function of meibomian glands in patients taking ADT. Androgens have been shown to significantly affect lipid metabolic pathways [20], and the synthesis and/or elaboration of lipids by the meibomian glands is thought to be regulated by androgens [5]. A previous study showed that ADT can exert a significant and consistent influence on the mass/charge ratios of neutral lipid fraction of meibomian gland secretions [21]. Moreover, Jennifer et al. [22] reported that androgen insensitivity can cause

meibomian gland dysfunction and significantly increase dry eye signs and symptoms in patients with complete androgen insensitivity syndrome (CAIS). Androgens can also modulate the morphology, physiology, molecular biology, immunology, and secretion of the lacrimal gland [23]. Interestingly, Sullivan et al. [24] demonstrated that ADT has no influence on the level of tear secretion in humans. Similarly, no significant difference in TMH between the two groups was found in the present study. Androgen deficiency appears to cause the development of meibomian gland dysfunction and evaporative dry eye.

Prostate cancer can be aggressive and metastasize to the bones and regional lymph nodes. There are no reports of metastasis to the eye; therefore, prostate cancer itself does not cause tear function-related damage to the ocular surface. To further investigate the reasons for dry eye in prostate cancer patients treated with ADT, we divided these patients into symptomatic and asymptomatic subgroups based on the OSDI score. Our results indicate that the NI-BUT was shorter in the symptomatic ADT group than that in the asymptomatic ADT group. A significant difference was noted in meibum expressibility scores and meiboscores between these two groups ($P < 0.05$ for each), indicating that the tear film stability was worse in the symptomatic ADT group. Meibomian glands secrete lipids into the tear film, forming a superficial lipid layer that can maintain tear film stability. It can be concluded that the reason for tear film instability in the ADT group, especially in those with dry eye symptoms, may be abnormalities in the meibomian glands.

Demodex mites are a potential cause of MGD [25]. The demodex infestation rate was significantly higher in the symptomatic ADT group (9/9, 100.00%, Table 2) than that in the asymptomatic ADT group, indicating that the ocular discomfort experienced by prostate cancer patients was related to ocular demodex infestation. Franz et al. [26] reported that the prevalence of demodex in patients with ocular discomfort was high. Moreover, Lee et al. [27] showed that the number of demodex mites was proportional to the OSDI score and the severity of ocular discomfort. Taken together, this evidence implies that demodex infestation can cause an increase in the subjective symptoms of ocular surface damage. Thus, eradication of demodex may be beneficial in relieving ocular surface discomfort related to MGD.

MGD has many underlying causative factors such as age, gender, and hormones. Aging may impact atrophy of meibomian gland acini epithelial cells and reduce the quality of meibomian gland secretions [28]. Decreased sex hormone levels, especially androgens, which are correlated with advancing age, may contribute to meibomian gland loss [24], leading to increased viscosity of the meibum, hyperkeratinization of the meibomian gland orifices, and meibomian gland obstruction [29]. MGD due to androgen deficiency has been demonstrated in prostate cancer patients receiving ADT [11]; however, no studies to date have reported an association of ADT duration with changes in the ocular surface. In the present study, the duration of ADT was positively associated with the meibomian gland dropout score in the ADT group but negatively correlated with the NI-BUT. This indicates that a longer duration of ADT was associated with poorer tear function and a larger meibomian gland dropout area. Similarly, decreased sebaceous gland function and secretion are correlated with both an atrophy of acinar cells and a reduction in serum androgen levels [30]. Meibomian gland atrophy tends to increase with age, and a significant correlation between age and loss of meibomian gland area was observed by infrared meibography in a previous study [14]. In short, the androgen level is associated with meibomian gland alterations. Thus, we speculated that androgens may stimulate meibomian gland function, enhancing tear film stability and decreasing tear film evaporation and consequently ameliorating dry eye symptoms. A longer duration of ADT can lead to a significant increase in the risk of MGD.

To the best of our knowledge, this is the first study to investigate the association between long-term ADT and the risk of MGD in an Asian population. Our study focused on the relationship between androgens and the ocular surface and found that androgen deficiency was related to ocular discomfort, eyelid margin abnormality, and meibomian gland loss. In conclusion, we demonstrate that long-term ADT in prostate cancer patients increases the risk of MGD. Moreover, demodex infection can aggravate ocular surface discomfort. Monitoring ocular surface health and treating demodex are crucial in prostate cancer patients taking ADT.

Data Availability

All data used to support the findings of this study is available on request.

Conflicts of Interest

The authors declare that there is no potential conflict of interest relevant to the publication of this article.

Authors' Contributions

Weina Li and Xiaofeng Li contributed equally to this study.

Acknowledgments

This study was supported in part by grants from The National Key R&D Program of China (2020YFA0908100), the National Natural Science Foundation of China (NSFC Nos. 81970771, 82070931, 81770891, 81672955), the Health Research Talent Training Program of Fujian PRC (2016-ZQN-90), Xiamen Key Medical and Health Project (No. 3502Z20191101), Zhenjiang Science Technology Planning Project (No. SH2019033), and the Huaxia Translational Medicine Fund for Young Scholars (Nos. 2017-A-001, 2017-A-002).

References

[1] C. Huggins and C. V. Hodges, "Studies on prostatic cancer. I. The effect of castration, of estrogen and androgen injection on serum phosphatases in metastatic carcinoma of the prostate," *CA: a Cancer Journal for Clinicians*, vol. 22, no. 4, pp. 232–240, 1972.

[2] E. M. Bolton and T. Lynch, "Are all gonadotrophin-releasing hormone agonists equivalent for the treatment of prostate

cancer? A systematic review," *BJU International*, vol. 122, no. 3, pp. 371–383, 2018.

[3] J. D. Nelson, J. Shimazaki, J. M. Benitez-del-Castillo et al., "The international workshop on meibomian gland dysfunction: report of the definition and classification subcommittee," *Investigative Opthalmology & Visual Science*, vol. 52, no. 4, pp. 1930–1937, 2011.

[4] D. A. Sullivan, B. D. Sullivan, J. E. Evans et al., "Androgen deficiency, meibomian gland dysfunction, and evaporative dry eye," *Annals of the New York Academy of Sciences*, vol. 966, no. 1, pp. 211–222, 2002.

[5] D. A. Sullivan, B. D. Sullivan, M. D. Ullman et al., "Androgen influence on the meibomian gland," *Investigative Ophthalmology & Visual Science*, vol. 41, no. 12, pp. 3732–3742, 2000.

[6] E. M. Rocha, L. A. Wickham, L. A. da Silveira et al., "Identification of androgen receptor protein and 5alpha-reductase mRNA in human ocular tissues," *British Journal of Ophthalmology*, vol. 84, no. 1, pp. 76–84, 2000.

[7] D. A. Schaumberg, J. J. Nichols, E. B. Papas, L. Tong, M. Uchino, and K. K. Nichols, "The international workshop on meibomian gland dysfunction: report of the subcommittee on the epidemiology of, and associated risk factors for, MGD," *Investigative Ophthalmology & Visual Science*, vol. 52, no. 4, pp. 1994–2005, 2011.

[8] F. Schirra, T. Suzuki, S. M. Richards et al., "Androgen control of gene expression in the mouse meibomian gland," *Investigative Ophthalmology & Visual Science*, vol. 46, no. 10, pp. 3666–3675, 2005.

[9] D. A. Sullivan, A. Bélanger, J. M. Cermak et al., "Are women with Sjögren's syndrome androgen-deficient?," *The Journal of Rheumatology*, vol. 30, no. 11, pp. 2413–2419, 2003.

[10] J. A. Smith, J. Albeitz, C. Begley et al., "The Epidemiology of Dry Eye Disease: Report of the Epidemiology Subcommittee of the International Dry Eye WorkShop (2007)," *The Ocular Surface*, vol. 5, no. 2, pp. 93–107, 2007.

[11] K. L. Krenzer, M. R. Dana, M. D. Ullman et al., "Effect of androgen deficiency on the human meibomian gland and ocular surface," *The Journal of Clinical Endocrinology and Metabolism*, vol. 85, no. 12, pp. 4874–4882, 2000.

[12] B. E. Dougherty, J. J. Nichols, and K. K. Nichols, "Rasch analysis of the Ocular Surface Disease Index (OSDI)," *Investigative Ophthalmology & Visual Science*, vol. 52, no. 12, pp. 8630–8635, 2011.

[13] R. M. Schiffman, M. D. Christianson, G. Jacobsen, J. D. Hirsch, and B. L. Reis, "Reliability and validity of the Ocular Surface Disease Index," *Archives of Ophthalmology*, vol. 118, no. 5, pp. 615–621, 2000.

[14] R. Arita, K. Itoh, K. Inoue, and S. Amano, "Noncontact infrared meibography to document age-related changes of the meibomian glands in a normal population," *Ophthalmology*, vol. 115, no. 5, pp. 911–915, 2008.

[15] R. Arita, K. Itoh, S. Maeda et al., "Proposed diagnostic criteria for obstructive meibomian gland dysfunction," *Ophthalmology*, vol. 116, no. 11, pp. 2058–2063.e1, 2009.

[16] H. Lee, K. Min, E. K. Kim, and T. I. Kim, "Minocycline controls clinical outcomes and inflammatory cytokines in moderate and severe meibomian gland dysfunction," *American Journal of Ophthalmology*, vol. 154, no. 6, pp. 949–957.e1, 2012.

[17] A. J. Bron, L. Benjamin, and G. R. Snibson, "Meibomian gland disease. Classification and grading of lid changes," *Eye*, vol. 5, no. 4, pp. 395–411, 1991.

[18] X. Luo, J. Li, C. Chen, S. Tseng, and L. Liang, "Ocular demodicosis as a potential cause of ocular surface inflammation," *Cornea*, vol. 36, no. 1, pp. S9–S14, 2017.

[19] A. Azmahani, Y. Nakamura, K. M. McNamara, and H. Sasano, "The role of androgen under normal and pathological conditions in sebaceous glands: the possibility of target therapy," *Current Molecular Pharmacology*, vol. 9, no. 4, pp. 311–319, 2016.

[20] D. M. Kelly and T. H. Jones, "Testosterone: a metabolic hormone in health and disease," *The Journal of Endocrinology*, vol. 217, no. 3, pp. R25–R45, 2013.

[21] B. D. Sullivan, J. E. Evans, K. L. Krenzer, M. Reza Dana, and D. A. Sullivan, "Impact of antiandrogen treatment on the fatty acid profile of neutral lipids in human meibomian gland secretions," *The Journal of Clinical Endocrinology and Metabolism*, vol. 85, no. 12, pp. 4866–4873, 2000.

[22] J. M. Cermak, K. L. Krenzer, R. M. Sullivan, M. R. Dana, and D. A. Sullivan, "Is complete androgen insensitivity syndrome associated with alterations in the meibomian gland and ocular surface?," *Cornea*, vol. 22, no. 6, pp. 516–521, 2003.

[23] H. Wagner, B. A. Fink, and K. Zadnik, "Sex- and gender-based differences in healthy and diseased eyes," *Optometry*, vol. 79, no. 11, pp. 636–652, 2008.

[24] D. A. Sullivan, K. L. Krenzer, B. D. Sullivan, D. B. Tolls, I. Toda, and M. R. Dana, "Does androgen insufficiency cause lacrimal gland inflammation and aqueous tear deficiency?," *Investigative Ophthalmology & Visual Science*, vol. 40, no. 6, pp. 1261–1265, 1999.

[25] Y. Y. Gao, M. A. di Pascuale, A. Elizondo, and et al.S. C. G. Tseng, "Clinical Treatment of Ocular Demodecosis by Lid Scrub With Tea Tree Oil," *Cornea*, vol. 26, no. 2, pp. 136–143, 2007.

[26] D. F. Rabensteiner, H. Aminfar, I. Boldin et al., "Demodex mite infestation and its associations with tear film and ocular surface parameters in patients with ocular discomfort," *American Journal of Ophthalmology*, vol. 204, pp. 7–12, 2019.

[27] S. H. Lee, Y. S. Chun, J. H. Kim, E. S. Kim, and J. C. Kim, "The relationship betweenDemodexand ocular discomfort," *Investigative Ophthalmology & Visual Science*, vol. 51, no. 6, pp. 2906–2911, 2010.

[28] B. D. Sullivan, J. E. Evans, M. R. Dana, and D. A. Sullivan, "Influence of aging on the polar and neutral lipid profiles in human meibomian gland secretions," *Archives of Ophthalmology*, vol. 124, no. 9, pp. 1286–1292, 2006.

[29] E. Knop, N. Knop, T. Millar, H. Obata, and D. A. Sullivan, "The international workshop on meibomian gland dysfunction: report of the subcommittee on anatomy, physiology, and pathophysiology of the meibomian gland," *Investigative Ophthalmology & Visual Science*, vol. 52, no. 4, pp. 1938–1978, 2011.

[30] J. L. Bolognia, "Aging skin," *The American Journal of Medicine*, vol. 98, no. 1, pp. S99–S103, 1995.

Hindawi
Disease Markers
Volume 2021, Article ID 2821673, 11 pages
https://doi.org/10.1155/2021/2821673

Research Article

The Roles of Liver Inflammation and the Insulin Signaling Pathway in PM2.5 Instillation-Induced Insulin Resistance in Wistar Rats

Zhihua Zhang,[1] Shujun Hu,[2] Ping Fan,[2] Ling Li,[3] Shanshan Feng,[2] Huabing Xiao,[2] and Lingyan Zhu[2,4]

[1]*Queen Mary School, Nanchang University, Nanchang 330006, China*
[2]*Department of Endocrinology, The First Affiliated Hospital of Nanchang University, Nanchang 330006, China*
[3]*Department of Endocrinology and Metabolism, Tongji Hospital, School of Medicine, Tongji University, Shanghai 200065, China*
[4]*The People's Hospital of Yudu County, Yudu 342300, China*

Correspondence should be addressed to Ling Li; dalingll@126.com and Lingyan Zhu; zly982387@126.com

Received 18 August 2021; Accepted 29 September 2021; Published 29 October 2021

Academic Editor: Ting Su

To elucidate the mechanism of how the liver participates in PM2.5-caused insulin resistance. A novel Wistar rat model was developed in this study by instilling a suspension of lyophilized PM2.5 sample (2.5 mg/kg, 5 mg/kg, or 10 mg/kg) collected from the atmosphere. Systemic insulin resistance indicators, including serum fasting blood glucose (FBG), fasting insulin (FINS), Homeostatic Model Assessment for Insulin Resistance (HOMA-IR), and hemoglobin A1 (HbA1), were upregulated by the PM2.5 instillation. The area under the curve (AUC_{glu}) calculated by intraperitoneal glucose tolerance testing (IPGTT) was also significantly greater in the PM2.5 instillation groups. Additionally, PM2.5 instillation was found to cause liver damage and inflammation. The serum levels of aspartate aminotransferase (AST), alanine aminotransferase (ALT), total bilirubin (TBIL), tumor necrosis factor-α (TNF-α), and interleukin-6 (IL-6) were significantly elevated by PM2.5 instillation. PM2.5 also triggered IL-6 and TNF-α transcription but inhibited mRNA synthesis and suppressed signaling activation of the insulin-phosphoinositide 3-kinase- (PI3K-) Akt-glucose transporter 2 (GLUT2) pathway in the rat liver by reducing the ratio of phosphorylated Akt to phosphorylated insulin receptor substrate 1 (IRS-1). Thus, PM2.5-induced inflammation activation and insulin signaling inhibition in the rat liver contribute to the development of systemic insulin resistance.

1. Introduction

According to the World Health Organization, the global prevalence of diabetes in adults over 18 years old increased from 4.7% in 1980 to 8.5% in 2014, while the prevalence of diabetes in China had already reached 9.7% in 2010 [1]. Diabetes can lead to blindness, renal failure, cardiovascular disease, and reduced limb amputation; therefore, the burden caused by diabetes to families is tremendous. Large numbers of related studies have shown that the main mechanism involved in the development and progression of type 2 diabetes is insulin resistance, which implies a significant reduction in the physiological effects of uptake and utilization of glucose [2]. Thus, there is an urgent need to better understand the underlying mechanism in order to design efficient insulin resistance prevention strategies. On the other hand, with the development of modern industries and urbanization, air pollution has become an issue throughout the world [3]. Meanwhile, more and more studies have demonstrated the adverse effects of ambient air pollutants such as particulate matter with a diameter less than 2.5 μm (PM2.5) on human health. A strong association between PM2.5 exposure and diabetes prevalence has been established, suggesting that ambient air pollution may contribute to the increased prevalence of diabetes in the adult U.S. and Asian populations [4, 5]. Moreover, animal experimental studies

Table 1: PCR primers.

Primers	Sequences	Product size
β-Actin-F β-Actin-R	5′-CACGATGGAGGGGCCGGACTCATC-3′ 5′-TAAAGACCTCTATGCCAACACAGT-3′	240 bp
AKT1-F AKT1-R	5′-GCTCTTCTTCCACCTGTCTCG-3′ 5′-CACAGCCCGAAGTCCGTTA-3′	186 bp
PI3K-F PI3K-R	5′-GACAGGCACAACGACAAC-3′ 5′-AAGCCCTAACGCAGACAT-3′	214 bp
INSR-F INSR-R	5′-AATGAGGAATGTGGGGACGT-3′ 5′-GTTCTGAACAGTTGCCCAGG-3′	202 bp
IRS1-F IRS1-R	5′-GTCCAGACTCCTCCAACCTC-3′ 5′-AGACCCACCTCCAATGTCAG-3′	239 bp
GLUT2-F GLUT2-R	5′-AGTCACACCAGCACATACGA-3′ 5′-TGGCTTTGATCCTTCCGAGT-3′	170 bp
IL-6-F IL-6-R	5′-GTTGCCTTCTTGGGACTGATG-3′ 5′-TACTGGTCTGTTGTGGGTGGT-3′	102 bp
TNF-α-F TNF-α-R	5′-GAAACAGTCTGCGAGGTGTG-3′ 5′-TTCTTCTTGCAGCCACACAC-3′	158 bp

have shown that PM2.5 exposure leads to systemic inflammation and insulin resistance [6–8], but the roles of target organs besides the pancreas, including the liver, adipose tissue, and skeletal muscle, on PM2.5-induced insulin resistance still remain controversial. The liver is one of the most important organs involved in insulin resistance, and some studies have shown that PM2.5 exposure induces liver damage [8, 9]; however, another study has found no significant effect of PM2.5 on the liver [10]. To systematically analyze the hepatic mechanism involved in the development of systemic insulin resistance, we performed PM2.5 instillation (0, 0.75, 2.5, 5, or 10 mg/kg) in Wistar rats for 8 weeks. Systemic insulin resistance indicators, including serum fasting blood glucose (FBG), fasting insulin (FINS), Homeostatic Model Assessment for Insulin Resistance (HOMA-IR), and hemoglobin A1 (HbA1), were examined. The area under the curve (AUC_{glu}) calculated by intraperitoneal glucose tolerance testing (IPGTT) in the different PM2.5 instillation groups was also measured. In addition, the serum levels of aspartate aminotransferase (AST), alanine aminotransferase (ALT), total bilirubin (TBIL), tumor necrosis factor-α (TNF-α), and interleukin-6 (IL-6) as well as the hepatic mRNA expression of IL-6 and TNF-α were determined. Furthermore, the impact of PM2.5 exposure on the synthesis of insulin-phosphoinositide 3-kinase (PI3K-) Akt-glucose transporter 2 (GLUT2) signaling pathway molecules in the rat liver at the mRNA level was analyzed. Finally, the PM2.5-induced phosphorylation of Akt and insulin receptor substrate 1 (IRS-1) in the rat liver was evaluated and compared by western blotting.

2. Materials and Methods

2.1. PM2.5 Collection and Suspension Preparation. The PM2.5 samples were collected from December 2016 to March 2017 at Xinxiang Medical College, which is located close to the center of Xinxiang City (Xinxiang, Henan, China). The sampling site is surrounded by residential areas and is far away from major roads and factories. After sampling, the filter of the PM2.5 high-volume air sampler (Tisch Environmental, USA) was cut off and sonicated in sterile double-distilled water using a UC-6B ultrasonicator (Shanghai, China) for 3×15 min. The PM2.5 eluted from the filter was then lyophilized, weighed, and stored at −20°C until further use. Scanning electron microscopy was also conducted to confirm that the particulate matter collected had a diameter of no more than 2.5 μm.

2.2. Animal Models. Sixty healthy Wistar rats, weighing 180–220 g, were purchased from Charles River, China. To avoid sex-dependent differences, only male mice were included in the study. All experiments described in the experimental protocol were approved by the Institutional Review Committee for Animal Care and Use at Xinxiang Medical College (Xinxiang, Henan, China), and all experimental procedures were performed to minimize animal suffering. The health and behavior of the animals were checked daily. The rats were housed together and acclimatized in a freestanding clean room for 1 week (22–28°C, 60% humidity, *ad libitum* access to filtered water and food, 12 h light/12 h dark cycle). Sixty rats were then randomly allocated into five groups (12

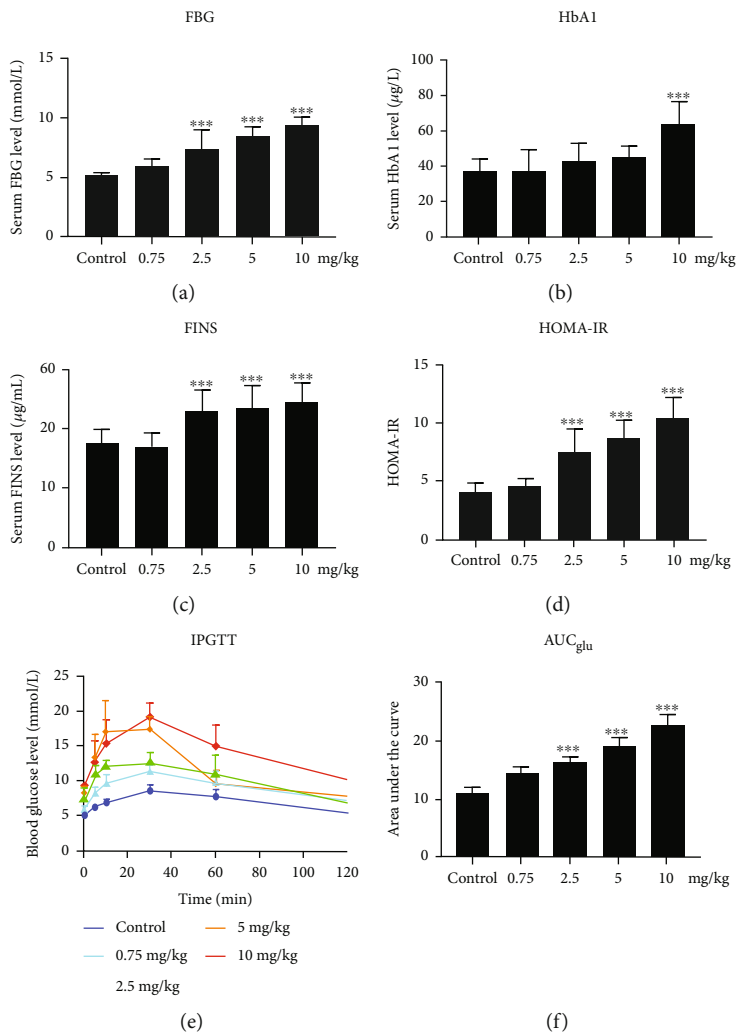

Figure 1: Effect of PM2.5 exposure on systemic insulin resistance indicators in Wistar rats. Experiments were performed after PM2.5 instillation at different dosages or saline instillation (control) for 8 weeks. Values are shown as the mean ± standard error of 12 rats/group. $^{*}p < 0.05$, and $^{**}p < 0.01$. (a) Fasting blood glucose (FBG), (b) fasting insulin (FINS), (c) hemoglobin A1c (HbA1c), (d) Homeostatic Model Assessment for Insulin Resistance (HOMA-IR), and (e) intraperitoneal glucose tolerance testing (IPGTT) curves. (f) The area under the curve (AUC_{glu}).

rats/group), including control, 0.75 mg/kg, 2.5 mg/kg, 5 mg/kg, and 10 mg/kg PM2.5 instillation groups. Before exposure, the PM2.5 lyophilized powder taken from a refrigerator was weighed, and the corresponding concentration of PM2.5 was resuspended in saline. To avoid aggregation, particle suspensions were always sonicated for 3×15 min and vortexed. By using noninvasive inhalation tracheal instillation, the rats in each dosage group were infused with PM2.5 three times a week for 8 weeks [10]. The rats in the control group were given the same volume of normal saline via tracheal instillation. No rats died during this experiment.

2.3. IPGTT and Sample Collection. After PM2.5 instillation, IPGTT of rats was performed in each group, and the AUC_{glu} was calculated [11]. Venous blood from rats that had fasted for 4.5 h was obtained from a small tail clip, and the fasting glucose level (0 min) measurements were conducted with an ACCU-CHEK glucometer (Roche, Shanghai, China). After 50% glucose solution (2 g/kg body weight) was injected intraperitoneally, the blood glucose values were measured at 5, 10, 30, 60, and 120 min postadministration. The AUC_{glu} was calculated using the following formula: $AUC_{glu} = (0\ \text{min} + 5\ \text{min})/24 + (5\ \text{min} + 10\ \text{min})/24 + (10\ \text{min} + 30\ \text{min})/6 + (30\ \text{min} + 60\ \text{min})/4 + (60\ \text{min} + 120\ \text{min})/2$. After IPGTT, the animals were anesthetized with ether and sacrificed by femoral artery terminal exsanguination. The blood was collected for serum isolation and stored at −70°C until use. At the same time, the liver was removed and spliced into two equal parts. After weighing, one part was fixed in 4% buffered paraformaldehyde, and the other part was frozen at −70°C.

2.4. Hematoxylin and Eosin (HE) Staining. Briefly, rat liver samples fixed in 4% buffered paraformaldehyde were dehydrated in a series of ethanol solutions, cleared in xylene, and embedded in paraffin. The paraffin-embedded tissues were sectioned into 4 μm thick slices using a rotary microtome (Leica RM 2016, Wetzlar, Germany) and subjected to

Table 2

(a) Serum concentrations of FBG, HbA1c, INS, and HOMA-IR in rats ($\bar{x} \pm s$)

	FBG (mmol/L)	HbA1 (μg/mL)	INS (ng/mL)	HOMA-IR
Control group	5.20 ± 0.29	37.02 ± 7.35	17.74 ± 2.38	4.119 ± 0.748
0.75 mg/kg PM2.5 group	6.02 ± 0.48	37.93 ± 11.32	17.39 ± 2.13	4.651 ± 0.623
2.5 mg/kg PM2.5 group	7.46 ± 1.48^{ab}	43.05 ± 9.51	23.04 ± 3.50^{ab}	7.632 ± 1.860^{ab}
5 mg/kg PM2.5 group	8.54 ± 0.68^{abc}	44.86 ± 6.67	23.61 ± 3.63^{ab}	8.925 ± 1.316^{ab}
10 mg/kg PM2.5 group	9.54 ± 0.47^{abc}	64.45 ± 11.98^{abcd}	24.80 ± 3.04^{ab}	10.556 ± 1.699^{abc}
F	24.556	6.708	6.774	21.053
p	<0.001	<0.001	<0.001	<0.001

Note: compared to the control group, $^{a}p < 0.05$; compared to the 0.75 mg/kg PM2.5 group, $^{b}p < 0.05$; compared to the 2.5 mg/kg PM2.5 group, $^{c}p < 0.05$; compared to the 5 mg/kg PM2.5 group, $^{d}p < 0.05$.

(b) Intraperitoneal glucose tolerance test in rats (IPGTT) ($\bar{x} \pm s$)

	Blood glucose (mmol/L)						AUC_{glu}
	0′	5′	10′	30′	60′	120′	
A	5.2 ± 0.3	6.3 ± 0.4	6.9 ± 0.5	8.6 ± 0.9	7.8 ± 1.0	5.5 ± 0.3	11.1 ± 0.9
B	6.0 ± 0.5	8.4 ± 0.7	9.8 ± 1.1	11.4 ± 0.9	9.8 ± 1.7	7.4 ± 1.6	14.5 ± 1.2^{a}
C	7.5 ± 1.5^{ab}	11.2 ± 1.0^{ab}	12.2 ± 0.7^{a}	12.7 ± 1.4^{a}	11.1 ± 2.6^{ab}	7.1 ± 0.7^{a}	16.4 ± 0.9^{ab}
D	8.5 ± 0.7^{abc}	13.5 ± 3.1^{ab}	17.1 ± 4.4^{abc}	17.5 ± 1.8^{abc}	9.7 ± 1.7^{ab}	7.8 ± 2.2^{a}	19.1 ± 1.4^{abc}
E	9.5 ± 0.5^{abc}	12.8 ± 2.9^{ab}	15.4 ± 3.4^{ab}	19.2 ± 2.0^{abc}	15.0 ± 2.9^{abc}	10.3 ± 0.7^{abcd}	22.8 ± 1.8^{abcd}
F	24.56	11.78	12.95	43.22	8.21	9.16	60.61
p	<0.001	<0.001	<0.001	<0.001	<0.001	<0.001	<0.001

Note: A: control group; B: 0.75 mg/kg PM2.5 group; C: 2.5 mg/kg PM2.5 group; D: 5 mg/kg PM2.5 group; E: 10 mg/kg PM2.5 group; AUC_{glu}: area under the curve; F: F value; p: p value. Compared to the control group, $^{a}p < 0.05$; compared to the 0.75 mg/kg PM2.5 group, $^{b}p < 0.05$; compared to the 2.5 mg/kg PM2.5 group, $^{c}p < 0.05$; compared to the 5 mg/kg PM2.5 group, $^{d}p < 0.05$.

HE staining with hematoxylin for 5–7 min at room temperature. After rinsing, the slices were stained with eosin for 2 min at room temperature. Micrographs under 200x magnification were randomly selected and captured using a light microscope.

2.5. Circulating Inflammation-Related and Biochemical Biomarker Measurements. The FBG, ALT, AST, and TBIL levels were determined by Chemoray (Rayto, Shenzhen, China). The FINS, IL-6, and TNG-α levels were measured by enzyme-linked immunosorbent assay (ELISA) kits, according to the manufacturer's instructions (Elabscience Biotechnology, Wuhan, China). The HbA1c level was determined by ELISA, according to the manufacturer's instructions (USCN Business, Wuhan, China). The HOMA-IR was calculated by the following formula: HOMA-IR = FBG × FINS/22.5 [12].

2.6. Quantitative Polymerase Chain Reaction (qPCR). Total RNA was isolated from whole liver lysates by TRIzol, according to the manufacturer's instructions (TRIzol, Aidlab, Beijing). RNA was reverse-transcribed using the reverse transcriptase M-MLV (RNase H) (FulenGen, Guangzhou, China). The synthesized cDNA was subjected to qPCR using 2x All-in-One qPCR Mix (Vazyme, Nanjing, China) in triplicate, according to the manufacturer's instructions. The β-actin gene was used as an internal control to normalize the expression of target genes, and the specific primers are listed in Table 1. The melting curves and the $E = 2^{-\triangle\triangle C}t$ algorithm were analyzed by LightCycler software (Roche Diagnostics).

2.7. Western Blot Analysis. Total protein of rat liver tissue in each group was extracted using radioimmunoprecipitation assay lysis buffer. The protein concentration was determined using a bicinchoninic acid protein concentration quantification kit (Beyotime Biotechnology, Shanghai, China). Denatured proteins were separated by sodium dodecyl sulfate-polyacrylamide gel electrophoresis and transferred to a polyvinylidene difluoride membrane. The membranes were blocked with 5% nonfat dry milk in tris-buffered saline containing 0.05% Tween 20 or 1–3% bovine serum albumin and probed with primary antibodies overnight at 4°C. The primary antibodies used included IRS-1, Akt (1 : 1000 dilution, Proteintech Inc., Wuhan, China), p-IRS-1 (1 : 1000 dilution, Cell Signaling, USA), p-Akt^{Ser473} (1 : 2000 dilution, Abcam, USA), and β-actin (1 : 200 dilution, Boster Biological Technology Co. Ltd., Wuhan, China). Following washing, the membranes were incubated with goat horseradish peroxidase-conjugated secondary antibodies (1 : 50,000 dilution, Boster Biological Technology Co. Ltd., Wuhan, China). The reactions were detected by using an Enhanced

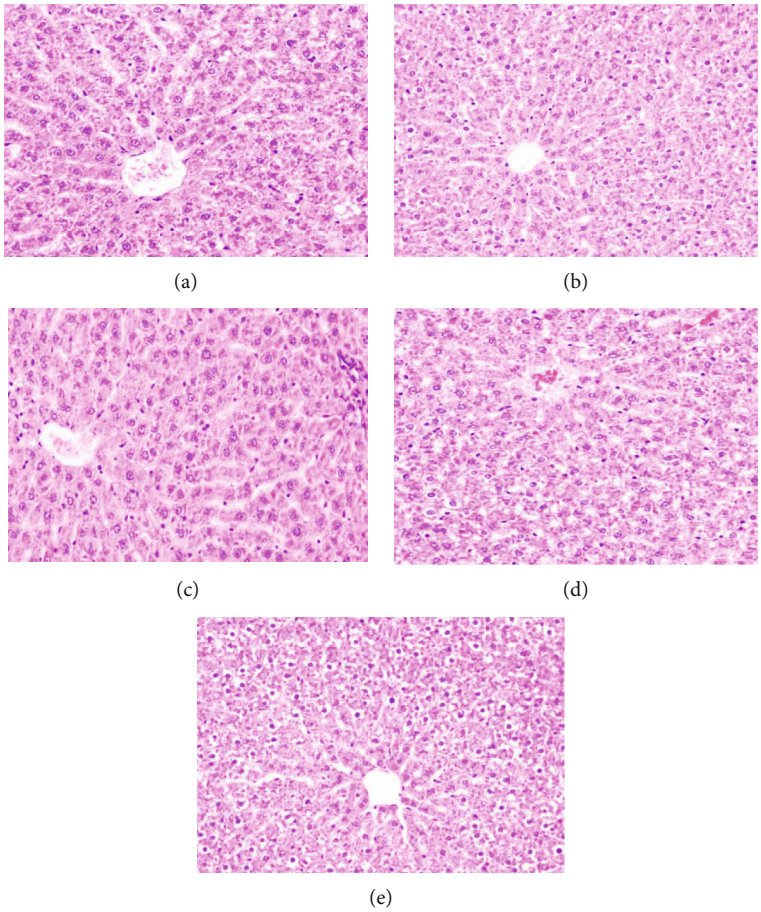

Figure 2: Effect of PM2.5 exposure on liver damage. (a–e) Representative images of liver hematoxylin and eosin staining in the control group (a), 0.75 mg/kg PM2.5 group (b), 2.5 mg/kg PM2.5 group (c), 5 mg/kg PM2.5 group (d), and 10 mg/kg PM2.5 group (e). Original magnification, 200x.

Chemiluminescence Western Blot detection kit (Thermo Fisher, USA), and the detected bands were visualized via exposure to an X-ray beam in a dark room.

2.8. Statistical Analysis. Data were analyzed by SPSS20.0 (IBM Corp., Armonk, NY, USA). For the normally distributed measurement data, the results were presented as the mean ± standard error, and the Levene test was used for the homogeneity of variance. One-way analysis of variance was used for multiple group comparisons, and the least significant difference test was used for pairwise comparisons between groups. Nonparametric tests were used for measurement data that did not meet the assumptions of equal variance. $p < 0.05$ was set to indicate a significant difference.

3. Results

3.1. PM2.5 Instillation-Induced Insulin Resistance in Rats. To study the effect of PM2.5 instillation on systemic insulin resistance in rats, the levels of FBG, FINS, HbA1c, and HOMA-IR were examined in all five groups (Figures 1(a)–1(d) and Table 2(a)). Compared to the control group, the levels of FBG, FINS, and HOMA-IR started to be significantly higher in the 2.5 mg/kg PM2.5 group and continued to the 10 mg/kg PM2.5 group ($p < 0.05$). Compared to the 0.75 mg/kg PM2.5 group, the FBG, FINS, and HOMA-IR levels in the 2.5, 5, and 10 mg/kg PM2.5 groups were all significantly elevated ($p < 0.05$). The FINS and HOMA-IR levels in the 5 mg/kg PM2.5 group were significantly higher ($p < 0.05$) than those in the 2.5 mg/kg PM2.5 group. The FBG and HOMA-IR but not the FINS level in the 10 mg/kg PM2.5 group were significantly elevated compared to those in the 2.5 mg/kg PM2.5 group. There were no significant differences in the FBG, FINS, and HOMA-IR levels between the 5 and 10 mg/kg PM2.5 groups. Only the HbA1c level in the 10 mg/kg PM2.5 group was significantly increased when compared to each of the other four groups ($p < 0.05$). Next, we performed IPGTT and calculated the AUC_{glu} for the rats in each group administered with different dosages of PM2.5 instillation (Figures 1(e) and 1(f) and Table 2(b)). Compared to the control group, the glucose levels in the 2.5, 5, and 10 mg/kg PM2.5 groups at each time point were all significantly elevated ($p < 0.05$). Similarly, the AUC_{glu} in the 2.5, 5, and 10 PM2.5 groups were also significantly higher than that of the control group ($p < 0.05$). Thus, PM2.5 instillation in rats induced insulin resistance in a dose-dependent manner.

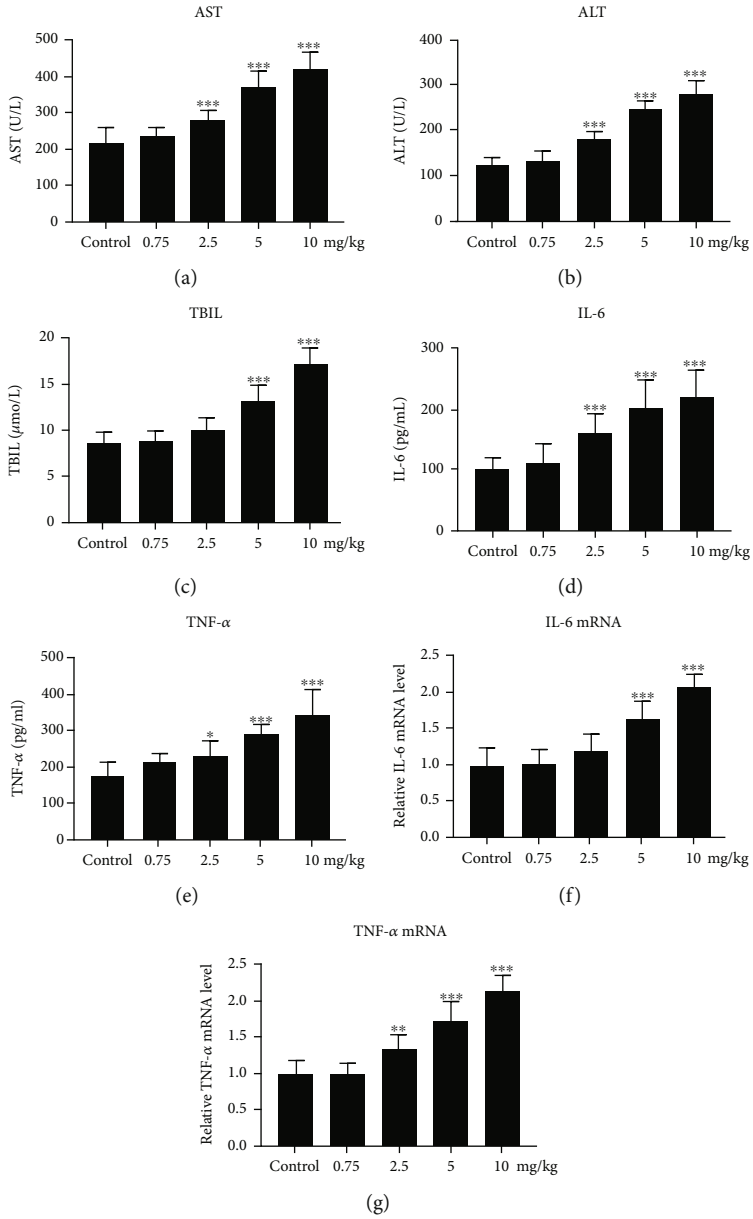

Figure 3: Effect of PM2.5 exposure on the expression of liver injury and inflammation-related biomarkers. (a–e) The circulating concentrations of AST (a), ALT (b), TBIL (c), IL-6 (d), and TNF-α (e) in response to PM2.5 exposure. (f, g) PM2.5-induced cytokine mRNA expression of IL-6 (f) and TNF-α (g) in the rat liver. Values are shown as the mean ± standard error of 12 rats/group. $^{*}p < 0.05$, and $^{**}p < 0.01$.

3.2. PM2.5 Instillation Induced Liver Injury and Inflammation in Rats. At first, we found that PM2.5 instillation induced liver damage in a dose-dependent manner according to the pathological analysis with HE staining of the liver sections (Figures 2(a)–2(e)). Compared to the control group, as the dose of PM2.5 instillation increased, the amounts of inflammatory cell infiltration and ballooning of hepatocytes increased. Next, we examined the serum level changes of the liver injury and inflammation-related biomarkers, including AST, ALT, TBIL, IL-6, and TNF-α (Figures 3(a)–3(e) and Table 3(a)). Compared to the control group, the ALT, AST, IL-6, and TNF-α serum levels were significantly elevated ($p < 0.05$), starting from 2.5 mg/kg PM2.5 instillation. The serum level of TBIL started to be significantly increased with 5 mg/kg PM2.5 instillation ($p < 0.05$). Compared to the 0.75 mg/kg PM2.5 group, the ALT and IL-6 serum levels started to be significantly higher with 2.5 mg/kg PM2.5 instillation ($p < 0.05$), while the serum levels of AST, TBIL, and TNF-α started to be significantly elevated with 5 mg/kg PM2.5 instillation ($p < 0.05$). Compared to the 2.5 mg/kg group, the ALT, AST, TBIL, and TNF-α levels in the 5 and 10 mg/kg PM2.5 groups were all significantly higher ($p < 0.05$), whereas the serum level of IL-6 was only significantly increased in the 10 mg/kg PM2.5 group ($p < 0.05$).

To confirm the protein level changes of the proinflammatory cytokines in PM2.5-instilled rats, we further examined the mRNA expression of IL-6 and TNF-α in the rat liver of each

Table 3

(a) Serum concentrations of ALT, AST, TBIL, IL-6, and TNF-α in rats ($\bar{x} \pm s$)

	ALT (U/L)	AST (U/L)	TBIL (μmol/L)	IL-6 (pg/mL)	TNF-α (pg/mL)
Control group	126.1 ± 13.9	218.7 ± 39.1	8.77 ± 1.05	104.1 ± 15.5	177.7 ± 31.7
0.75 mg/kg PM2.5 group	136.9 ± 18.4	237.2 ± 23.4	9.02 ± 0.92	110.8 ± 30.1	211.5 ± 24.5
2.5 mg/kg PM2.5 group	182.2 ± 17.3^{ab}	282.7 ± 23.3^{a}	10.14 ± 1.18	163.4 ± 29.5^{ab}	232.1 ± 38.4^{a}
5 mg/kg PM2.5 group	250.0 ± 18.1^{abc}	374.4 ± 38.6^{abc}	13.22 ± 1.70^{abc}	202.5 ± 44.9^{ab}	290.0 ± 27.4^{abc}
10 mg/kg PM2.5 group	281.8 ± 29.4^{abcd}	422.3 ± 43.6^{abcd}	17.36 ± 1.49^{abcd}	222.6 ± 40.8^{abc}	347.3 ± 61.5^{abcd}
F	58.359	32.314	38.886	12.346	14.832
p	<0.001	<0.001	<0.05	<0.05	<0.001

Note: compared to the control group, $^{a}p < 0.05$; compared to the 0.75 mg/kg PM2.5 group, $^{b}p < 0.05$; compared to the 2.5 mg/kg PM2.5 group, $^{c}p < 0.05$; compared to the 5 mg/kg PM2.5 group, $^{d}p < 0.05$.

(b) Changes in liver IL-6 and TNF-α gene expression in rats ($\bar{x} \pm s$)

	IL-6	TNF-α
Control group	0.982 ± 0.231	1.009 ± 0.158
0.75 mg/kg PM2.5 group	1.009 ± 0.202	0.986 ± 0.166
2.5 mg/kg PM2.5 group	1.185 ± 0.243	1.333 ± 0.208^{ab}
5 mg/kg PM2.5 group	1.641 ± 0.207^{abc}	1.714 ± 0.259^{abc}
10 mg/kg PM2.5 group	2.048 ± 0.172^{abcd}	2.128 ± 0.199^{abcd}
F	23.527	29.364
p	<0.001	<0.001

Note: compared to the control group, $^{a}p < 0.05$; compared to the 0.75 mg/kg PM2.5 group, $^{b}p < 0.05$; compared to the 2.5 mg/kg PM2.5 group, $^{c}p < 0.05$; compared to the 5 mg/kg PM2.5 group, $^{d}p < 0.05$.

group by qPCR (Figures 3(f) and 3(g) and Table 3(b)). Compared to the control and 0.75 mg/kg PM2.5 groups, IL-6 mRNA expression was significantly increased in the 5 and 10 mg/kg PM2.5 groups ($p < 0.05$); TNF-α mRNA expression was significantly higher in the 2.5, 5, and 10 mg/kg PM2.5 groups ($p < 0.05$). Compared to the 2.5 mg/kg group, IL-6 and TNF-α mRNA expressions were both significantly elevated in the 5 and 10 mg/kg PM2.5 groups ($p < 0.05$). There was also an elevation in the IL-6 and TNF-α mRNA expression in the 10 mg/kg PM2.5 group, compared to the 5 mg/kg PM2.5 group ($p < 0.05$), indicating that PM2.5 induced proinflammatory cytokine transcription in the rat liver.

3.3. PM2.5 Instillation Inhibited the Synthesis of Hepatic Insulin Signaling Pathway Molecules. Inhibition of the insulin-PI3K-Akt-GLUT2 signaling pathway has been reported to be associated with insulin resistance [13–16]. To further investigate the mechanism underlying PM2.5 instillation-induced insulin resistance in the rat liver, the mRNA expression of the insulin-PI3K-Akt-GLUT2 signaling pathway molecules was examined by qPCR (Figures 4(a)–4(e) and Table 4). Compared to the control group, the GLUT2 mRNA level was significantly lower in the 2.5, 5, and 10 mg/kg PM2.5 groups ($p < 0.05$), while the insulin receptor (INSR), IRS-1, PI3K, and Akt mRNA levels were significantly lower in the 5 and 10 mg/kg PM2.5 groups ($p < 0.05$). Compared to the 0.75 mg/kg PM2.5 group, the INSR, IRS-1, Akt, and GLUT2 mRNA levels in the 5 and 10 mg/kg PM2.5 groups were significantly decreased ($p < 0.05$), while the PI3K mRNA level was significantly decreased in the 10 mg/kg PM2.5 group ($p < 0.05$). Compared to the 2.5 mg/kg PM2.5 group, the INSR, IRS-1, and Akt mRNA expression levels in the 5 and 10 mg/kg PM2.5 groups were significantly lower, while the PI3K and GLUT2 mRNA levels were significantly lower in the 10 mg/kg PM2.5 group ($p < 0.05$). Compared to the 5 mg/kg PM2.5 group, there was no significant difference in the INSR, IRS-1, PI3K, Akt, or GLUT2 mRNA level in the 10 mg/kg PM2.5 group. Decreased expression of these molecules at the mRNA level revealed that PM2.5 instillation may induce insulin resistance by inhibiting the transcription of insulin-PI3K-Akt-GLUT2 signaling pathway molecules.

3.4. PM2.5 Instillation Induced Phosphorylation of Insulin Signaling Pathway Proteins. Phosphorylation of key serine residues is another indicator of insulin-PI3K-Akt-GLUT2 signaling pathway function. For example, serine phosphorylation of Akt is accompanied by insulin receptor activation. In contrast, serine phosphorylation of IRS proteins can decrease their capacity to attract downstream PI3K, resulting in signaling inhibition [13–16]. Thus, we next examined the changes in IRS-1, p-IRS-1, Akt, and p-Akt protein expression by western blot analysis (Figures 5(a)–5(d)). The ratio of p-IRS-1/ISR-1 increased, while the ratio of p-Akt/Akt decreased as the PM2.5 instillation dose increased (Figure 5(e) and Table 5). Compared to the control group,

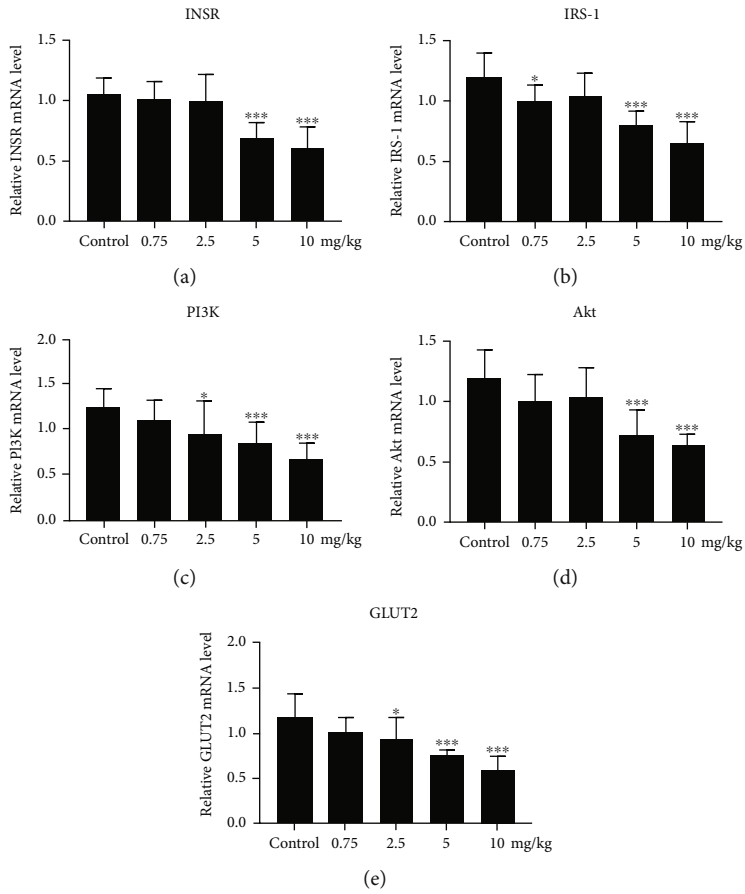

Figure 4: Effect of PM2.5 exposure on the expression of insulin-PI3K-Akt-GLUT2 signaling pathway molecules. (a–e) PM2.5-induced mRNA expression changes of INSR (a), IRS-1 (b), PI3K (c), Akt (d), and GLUT2 (e). Values are shown as the mean ± standard error of 12 rats/group. $^{*}p < 0.05$, and $^{**}p < 0.01$.

Table 4: Changes in liver expression of INSR, IRS-1, PI3K, AKT, and GLUT2 in rats ($\bar{x} \pm s$).

	INSR	IRS-1	PI3K	AKT	GLUT2
Control group	1.053 ± 0.135	1.193 ± 0.201	1.254 ± 0.186	1.195 ± 0.231	1.185 ± 0.247
0.75 mg/kg PM2.5 group	1.014 ± 0.146	1.000 ± 0.134	1.117 ± 0.196	1.021 ± 0.198	1.009 ± 0.159
2.5 mg/kg PM2.5 group	0.997 ± 0.217	1.043 ± 0.185	0.967 ± 0.333	1.051 ± 0.226	0.938 ± 0.243[a]
5 mg/kg PM2.5 group	0.691 ± 0.124[abc]	0.798 ± 0.111[abc]	0.855 ± 0.227[a]	0.723 ± 0.206[abc]	0.763 ± 0.050[ab]
10 mg/kg PM2.5 group	0.605 ± 0.172[abc]	0.651 ± 0.171[abc]	0.685 ± 0.150[ab]	0.645 ± 0.087[abc]	0.599 ± 0.143[abc]
F	8.210	8.434	4.753	7.026	7.571
p	<0.001	<0.001	<0.001	<0.001	<0.001

Note: compared to the control group, [a]$p < 0.05$; compared to the 0.75 mg/kg PM2.5 group, [b]$p < 0.05$; compared to the 2.5 mg/kg PM2.5 group, [c]$p < 0.05$; compared to the 5 mg/kg PM2.5 group, [d]$p < 0.05$.

the p-IRS-1/ISR-1 ratios were significantly higher in all study groups ($p < 0.05$), while the p-Akt/Akt ratio started to be significantly decreased in the 2.5 mg/kg PM2.5 group ($p < 0.05$). Compared to the 0.75 mg/kg PM2.5 group, the ratios of p-IRS-1/ISR-1 and p-Akt/Akt in the 2.5, 5, and 10 mg/kg PM2.5 groups were all significantly different ($p < 0.05$). Compared to the 2.5 mg/kg PM2.5 group, the ratios of p-IRS-1/ISR-1 and p-Akt/Akt in the 5 and 10 mg/kg PM2.5 groups were all significantly different ($p < 0.05$). There was also a significant difference in the ratios of both p-IRS-1/ISR-1 and p-Akt/Akt between the 5 and 10 mg/kg PM2.5 groups ($p < 0.05$). Collectively, our results indicate that the phosphorylation of insulin signaling pathway proteins induced by PM2.5 instillation contributed to insulin resistance in the rat liver.

4. Discussion

Increasing numbers of experimental animal research studies have demonstrated the impact of PM2.5 inhalation on the

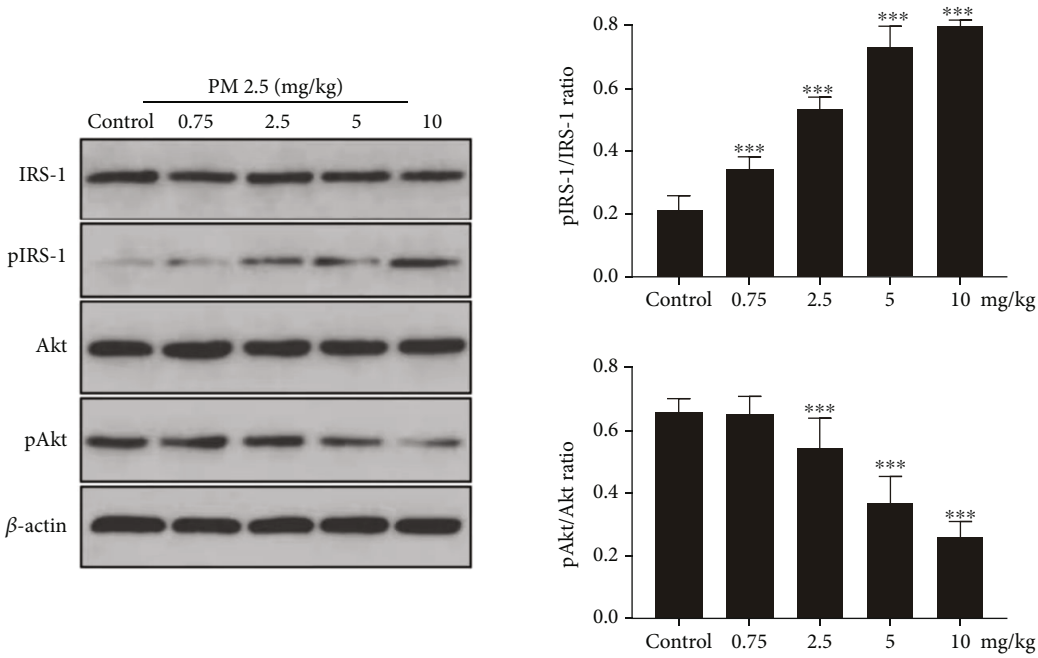

Figure 5: Effect of PM2.5 exposure on the phosphorylated and total protein expression changes in the rat liver. (a–d) Representative western blotting bands of IRS-1 (a), p-IRS-1 (b), Akt (c), and p-Akt (d) proteins. (e) Statistical analysis. Values are shown as the mean ± standard error of 12 rats/group. $^{*}p < 0.05$, and $^{**}p < 0.01$.

Table 5: Changes in the p-IRS-1/IRS-1 and p-AKT/AKT ratios in the rat liver ($\bar{x} \pm s$).

	p-IRS-1/IRS-1	p-AKT/AKT
Control group	0.215 ± 0.041	0.661 ± 0.041
0.75 mg/kg PM2.5 group	0.344 ± 0.038[a]	0.653 ± 0.056
2.5 mg/kg PM2.5 group	0.536 ± 0.036[ab]	0.544 ± 0.098[ab]
5 mg/kg PM2.5 group	0.724 ± 0.076[abc]	0.370 ± 0.083[abc]
10 mg/kg PM2.5 group	0.800 ± 0.018[abcd]	0.261 ± 0.046[abcd]
F	144.861	33.347
p	<0.001	<0.001

Note: compared to the control group, [a]$p < 0.05$; compared to the 0.75 mg/kg PM2.5 group, [b]$p < 0.05$; compared to the 2.5 mg/kg PM2.5 group, [c]$p < 0.05$; compared to the 5 mg/kg PM2.5 group, [d]$p < 0.05$.

development of insulin resistance and diabetes [17]. For example, long-term exposure to PM2.5 in C57BL/6 mice resulted in impaired glucose tolerance and resistance to insulin [8]. In a Sprague-Dawley rat model, exposure to PM2.5 significantly activated the oxidative response and inflammation in the pancreas, leading to reduced levels of GLUT2 [18]. In the present study, for the first time, PM2.5-induced insulin resistance was established in a Wistar rat model. In animal models, intratracheal inhalation and instillation are the main techniques of PM2.5 exposure [17]. Inhalation exposure is a physiological method that requires both an expensive exposure chamber and technical expertise. In contrast, intratracheal instillation includes direct application of the material to the trachea. It enables more control over the concentration and location of the material, and it is cheaper. The disadvantages of intratracheal instillation include its invasive and nonphysiological features. To overcome these drawbacks, in this study, a noninvasive intratracheal instillation method was used. This method caused less stress to the animals as it is not invasive; therefore, it is more reliable and the effectiveness was proved by our consistent results. The PM2.5-induced systemic insulin resistance was initially observed after exposure for 8 weeks. Systemic insulin resistance indicators, including FBG, FINS, HOMA-IR, and HbA1, were upregulated as the PM2.5 instillation concentration was increased. At the same time, the AUC_{glu} calculated by IPGTT with different dosages of PM2.5 instillation was also significantly greater than that of the control group.

The liver is one of the most important organs involved in insulin resistance, and the inhibition or defects of the insulin-PI3K-Akt signaling pathway in the liver may be the underlying mechanism [13–16]. Once activated by an insulin signal, the main downstream effector Akt enters into the cytoplasm, where glycogen synthase kinase 3 (GSK3) is phosphorylated and inactivated, which in turn promotes glycogen synthesis. In addition, inactivation of GSK3 by Akt results in the dephosphorylation of eukaryotic translation initiation factor 2 subunit beta and the storage of amino acids. PI3K and Akt are also known to play a role in insulin-induced glucose uptake into cells by translocation of the glucose transporter GLUT2. In line with these findings, in our study, the hepatic insulin-PI3K-Akt-GLUT2 signaling pathway was found to be consistently inactivated at both the mRNA expression and protein phosphorylation levels by PM2.5.

It has become increasingly evident that insulin resistance is often associated with the proinflammatory cytokine response in insulin-sensitive tissues including the liver, which may lead to a decreased insulin sensitivity [19–21]. For instance, TNF-α stimulation leads to serine phosphorylation of IRS-1, which attenuates its ability to transduce insulin-mediated cellular events [22]. Furthermore, mice genetically deficient in TNF-α or the TNF receptor 1 gene do not develop insulin resistance, even under elevated fatty or obese circumstances [23]. Treatment of cultured 3T3-L1 adipocytes with TNF-α also led to reduced expression of the INSR, IRS-1, and GLUT2 genes as well as decreased insulin-stimulated glucose uptake [24]. Here, we found that after 8 weeks of PM2.5 instillation, the rat liver developed inflammation, as shown by the HE staining experiments. The extent of the injury and inflammation increased as the dose of the PM2.5 instillation increased. The liver damage markers ALT, AST, and TIBL also increased, which further indicated liver injury. In addition to liver injury, there was also systemic as well as liver inflammation, with an increase of IL-6 and TNF-α at both the protein and mRNA levels. These observations are consistent with some previous studies, in which IL-6 has been reported to be elevated after PM2.5 exposure [7]. Future studies are warranted to determine the acute effect of PM2.5 on the interaction between inflammation and the insulin signaling pathway. At the same time, other insulin-sensitive tissues, such as adipose tissue and skeletal muscle, should also be further evaluated using the same model.

However, our study had several limitations. For example, due to the constraints of their availability, more advanced methods, such as a versatile aerosol concentration enrichment system, were not used. Furthermore, we did not perform *in vitro* cell biology experiments to observe and study the effect of PM2.5 on the insulin signaling pathway in human liver cells to determine if the results from our rat study are consistent or to clarify its potential clinical significance. Nevertheless, to the best of our knowledge, this is the first systematic study investigating the impact of PM2.5 on insulin resistance-related hepatic inflammation and the insulin signaling pathway in a rat model. Our findings also suggest a link between air pollution and hepatic metabolic abnormalities, which is important information for public health agencies to assess risk to humans.

Data Availability

The data used to support the findings of this study are available from the corresponding author upon request.

Conflicts of Interest

All of the authors declare that they have no conflicts of interest.

Authors' Contributions

Lingyan Zhu is responsible for project guidance, funding, laboratory scheduling, and critical revision of this manuscript. Zhihua Zhang and Lingyan Zhu designed the study and wrote the manuscript based on data interpretation. Zhihua Zhang made major contributions to the experimental operation, with collaborations from Shujun Hu, Ping Fan, Ling Li, Shanshan Feng, and Huabing Xiao. Ling Li and Shujun Hu contributed mainly to the animal model and data analysis, with the assistance of Ping Fan, Shanshan Feng, and Huabing Xiao. All authors read and approved the final manuscript. All authors also agreed to be accountable for all aspects of the work and ensured that questions related to the accuracy or integrity of any part of the work were appropriately investigated and resolved.

Acknowledgments

This work was supported by grants from the National Natural Science Foundation of China (Nos. 82160155, 81860153, and 81500589), the China Traditional Chinese and Western Medicine Committee Hehuang Scientific Research Fund (No. 2019005), the Key Project of the Natural Science Foundation of Jiangxi Province (No. 20202ACBL216007), the Education and Teaching Program of Nanchang University (Nos. NCUYJSJG-2021-068 and 20190054), and the Science and Technology Plan of Health Commission of Jiangxi Province (No. 20203106).

References

[1] W. Yang, J. Lu, J. Weng et al., "Prevalence of diabetes among men and women in China," *The New England Journal of Medicine*, vol. 362, no. 12, pp. 1090–1101, 2010.

[2] A. Festa, A. J. Hanley, R. P. Tracy, R. D'Agostino Jr., and S. M. Haffner, "Inflammation in the prediabetic state is related to increased insulin resistance rather than decreased insulin secretion," *Circulation*, vol. 108, no. 15, pp. 1822–1830, 2003.

[3] W. Yang and S. T. Omaye, "Air pollutants, oxidative stress and human health," *Mutation Research*, vol. 674, no. 1-2, pp. 45–54, 2009.

[4] J. F. Pearson, C. Bachireddy, S. Shyamprasad, A. B. Goldfine, and J. S. Brownstein, "Association between fine particulate matter and diabetes prevalence in the U.S," *Diabetes Care*, vol. 33, no. 10, pp. 2196–2201, 2010.

[5] X. Q. Lao, C. Guo, L. Y. Chang et al., "Long-term exposure to ambient fine particulate matter (PM2.5) and incident type 2 diabetes: a longitudinal cohort study," *Diabetologia*, vol. 62, no. 5, pp. 759–769, 2019.

[6] C. Liu, X. Xu, Y. Bai et al., "Air pollution-mediated susceptibility to inflammation and insulin resistance: influence of CCR2 pathways in mice," *Environmental Health Perspectives*, vol. 122, no. 1, pp. 17–26, 2014.

[7] Y. H. Yan, C. C. K. Chou, J. S. Wang et al., "Subchronic effects of inhaled ambient particulate matter on glucose homeostasis and target organ damage in a type 1 diabetic rat model," *Toxicology and Applied Pharmacology*, vol. 281, no. 2, pp. 211–220, 2014.

[8] X. Xu, C. Liu, Z. Xu et al., "Long-term exposure to ambient fine particulate pollution induces insulin resistance and mitochondrial alteration in adipose tissue," *Toxicological Sciences*, vol. 124, no. 1, pp. 88–98, 2011.

[9] S. A. Meo, A. N. Memon, S. A. Sheikh et al., "Effect of environmental air pollution on type 2 diabetes mellitus," *European Review for Medical and Pharmacological Sciences*, vol. 19, no. 1, pp. 123–128, 2015.

[10] Y. F. Jin, W. D. Wu, and Q. Zhang, "Establishment of an inhalable intratracheal instillation," *Journal of Zhengzhou University*, vol. 1, no. 21, pp. 1671–6825, 2015.

[11] W. Wang, J. Zhou, M. Chen et al., "Exposure to concentrated ambient PM2.5 alters the composition of gut microbiota in a murine model," *Particle and Fibre Toxicology*, vol. 15, no. 1, 2018.

[12] M. Albareda, J. Rodriguez-Espinosa, M. Murugo, A. de Leiva, and R. Corcoy, "Assessment of insulin sensitivity and beta-cell function from measurements in the fasting state and during an oral glucose tolerance test," *Diabetologia*, vol. 43, no. 12, pp. 1507–1511, 2000.

[13] X. Huang, G. Liu, J. Guo, and Z. Su, "The PI3K/AKT pathway in obesity and type 2 diabetes," *International Journal of Biological Sciences*, vol. 14, no. 11, pp. 1483–1496, 2018.

[14] P. Yang, Y. Liang, Y. Luo et al., " Liraglutide ameliorates nonalcoholic fatty liver disease in diabetic mice via the IRS2/PI3K/Akt signaling pathway ," *Diabetes, Metabolic Syndrome and Obesity: Targets and Therapy*, vol. Volume 12, pp. 1013–1021, 2019.

[15] L. Ren, X. Zhou, X. Huang, C. Wang, and Y. Li, "The IRS/PI3-K/Akt signaling pathway mediates olanzapine-induced hepatic insulin resistance in male rats," *Life Sciences*, vol. 217, pp. 229–236, 2019.

[16] Y. Zhang, J. Hai, M. Cao et al., "Silibinin ameliorates steatosis and insulin resistance during non-alcoholic fatty liver disease development partly through targeting IRS-1/PI3K/Akt pathway," *International Immunopharmacology*, vol. 17, no. 3, pp. 714–720, 2013.

[17] C. C. Cho, W. Y. Hsieh, C. H. Tsai, C. Y. Chen, H. F. Chang, and C. S. Lin, "In vitro and in vivo experimental studies of PM2.5 on disease progression," *International Journal of Environmental Research and Public Health*, vol. 15, no. 7, p. 1380, 2018.

[18] L. Yi, C. Wei, and W. Fan, "Fine-particulate matter (PM2.5), a risk factor for rat gestational diabetes with altered blood glucose and pancreatic GLUT2 expression," *Gynecological Endocrinology*, vol. 33, no. 8, pp. 611–616, 2017.

[19] P. Haberzettl, T. E. O'Toole, A. Bhatnagar, and D. J. Conklin, "Exposure to fine particulate air pollution causes vascular insulin resistance by inducing pulmonary oxidative stress," *Environmental Health Perspectives*, vol. 124, no. 12, pp. 1830–1839, 2016.

[20] G. S. Hotamisligil, "Inflammation and metabolic disorders," *Nature*, vol. 444, no. 7121, pp. 860–867, 2006.

[21] C. de Luca and J. M. Olefsky, "Inflammation and insulin resistance," *FEBS Letters*, vol. 582, no. 1, pp. 97–105, 2008.

[22] G. S. Hotamisligil, P. Peraldi, A. Budavari, R. Ellis, M. F. White, and B. M. Spiegelman, "IRS-1-mediated inhibition of insulin receptor tyrosine kinase activity in TNF-alpha- and obesity-induced insulin resistance," *Science*, vol. 271, no. 5249, pp. 665–670, 1996.

[23] K. T. Uysal, S. M. Wiesbrock, M. W. Marino, and G. S. Hotamisligil, "Protection from obesity-induced insulin resistance in mice lacking TNF-α function," *Nature*, vol. 389, no. 6651, pp. 610–614, 1997.

[24] J. M. Stephens, J. Lee, and P. F. Pilch, "Tumor Necrosis Factor-α-induced Insulin Resistance in 3T3-L1 Adipocytes Is Accompanied by a Loss of Insulin Receptor Substrate-1 and GLUT4 Expression without a Loss of Insulin Receptor-mediated Signal Transduction," *The Journal of Biological Chemistry*, vol. 272, no. 2, pp. 971–976, 1997.

Hindawi
Disease Markers
Volume 2021, Article ID 7155772, 9 pages
https://doi.org/10.1155/2021/7155772

Research Article

The Metabolome of Carbapenem-Resistant Klebsiella pneumoniae Infection in Plasma

Zhongwei Wen, Mei Liu, Dong Rui, Xiaoxiao Liao, Rui Su, Zhenming Tang, Zhineng Wen, and Zhougui Ling

Department of Respiratory and Critical Care Medicine, The Fourth Affiliated Hospital of Guangxi Medical University, No. 156 Heping Road, Liuzhou 545005, Guangxi Province, China

Correspondence should be addressed to Zhougui Ling; lzhougui@gmail.com

Received 17 August 2021; Revised 13 September 2021; Accepted 12 October 2021; Published 22 October 2021

Academic Editor: Wen-Qing Shi

Aim. Carbapenem-resistant *Klebsiella pneumoniae*- (CR-Kp-) mediated infections represent a challenge for clinical practitioners due to their expanding prevalence in hospital environments and antibiotic resistance. However, few studies have shown metabolic changes of carbapenem-resistant *Klebsiella pneumoniae* and CR-Kp-negative patients, and relevant studies are urgently needed. *Methods*. In this study, we comprehensively profile the metabolites of 20 CR-Kp-positive and 18 CR-Kp-negative patients in plasma by using 2D gas chromatography–time-of-flight mass spectrometry (GC×GC-TOFMS). *Results*. We identified 58 metabolites that were carbapenem-resistant *Klebsiella pneumoniae*-associated. N-Acetyl glucosamine, butanedioic acid, and myoinositol play a significant character in CR-Kp infection. *Conclusions*. Our study provides valuable data to serve as potential targets for developing therapies against CR-Kp infection.

1. Introduction

Klebsiella pneumoniae (K. pneumoniae), a Gram-negative bacterium, is an essential member of the *Klebsiella* genus of *Enterobacterales*. *K. pneumoniae* infections constitute a significant cause of morbidity and mortality globally. These infections generally start elsewhere, typically the lungs, genitourinary tract, or gastrointestinal tract [1, 2].

Carbapenem-resistant *K. pneumoniae* (CR-Kp) is a multidrug-resistant pathogen, which affects people worldwide, prevalent in low, middle, and upper-income countries [3]. The primary mechanism mediates resistance to carbapenems: CR-Kp can produce β-lactamases with the ability to hydrolyze cephalosporins and reduce membrane permeability in the cell wall [4, 5]. CR-Kp infections have provided enhanced mortality and many costs for health care systems. Moreover, the pathogen's multidrug resistance to newly expanded antibiotics causes the therapy of *K. pneumoniae* infections much more challenging [6]. Hence, it is urgent to develop and increase our understanding of how host defenses limit CR-Kp diffusion and pathogenesis and produce innovative therapeutic procedures.

Metabolomics (or metabolome) is a rapidly developing method that is aimed at identifying and quantifying the fluctuations in the concentrations of metabolites in a biological sample, such as blood, urine, or saliva [7]. Metabolomics studies are routinely conducted using analytical instrumentation like liquid or gas chromatography-mass spectrometry (LC-MS and GC–MS, respectively) and nuclear magnetic resonance (NMR) to draw a metabolic atlas by detecting metabolites [8, 9, 10, 11]. And this method has been widely used in many studies of Klebsiella pneumonia in the past [12]. Nevertheless, there are few studies on the metabolome of *CR-Kp*-infected patients.

This study is aimed at providing the first comprehensive analysis of the metabolome of CR-Kp-infected patients.

Table 1: Demographic and clinical characteristics of patients with carbapenem-resistant K. pneumoniae (CR-Kp) bloodstream infections compared with CR-Kp-negative patients.

Characteristic	CR-kp positive ($n = 20$)	CR-kp negative ($n = 18$)
Age (median, range) (yr)	58 (41-70)	58 (40-70)
Sex		
Male	13	12
Female	7	6
Hospital	20	18
Comorbidity		
Diabetes	6	1
Malignancy	2	0
Chronic kidney disease	2	3
Chronic pulmonary disease	1	1
Antibiotic		
Use of any antibiotic	20	18
β-Lactam/β-lactamase inhibitor combinations	15	2
Cephalosporins, second generation	2	2
Cephalosporins, third and fourth generations	16	18
Carbapenems	2	10
Mechanical ventilation	5	0
Infection related		
ESBL production*	7	8
VIM-1 production	5	4
MIC of carbapenems**		
>4 μg/mL	5	3
≤4 μg/mL	15	15
Final death	5	0

**ESBL: extended spectrum beta-lactamase; **the MICs of both imipenem and meropenem were >4 μg/mL.

Through metabolome analysis of the plasma of infected patients, we can better understand the metabolic changes of CR-Kp infection and discover feasible targets for future treatment.

2. Methods

2.1. Clinical Samples. Blood samples were collected from 38 patients, which included 20 patients infected by carbapenem-resistant *K. pneumoniae* (CR-Kp) in the Fourth Affiliated Hospital of Guangxi Medical University from March 2016 to July 2020 (Table 1). Blood cultures were performed by automated systems (BacTAlert®, USA). *K. pneumoniae* isolate identity and antimicrobial susceptibility testing (AST) used the Vitek 2 System (bioMérieux, USA). Eighteen adult patients with blood cultures negative for CR-Kp were classified as the CR-Kp-negative group (Table 1). Informed written consent was obtained from each patient. Plasma samples were collected within 24 h after admission. Blood samples were centrifuged at 3,000 × g for 15 minutes at 4°C for plasma collection and deposited at -80°C.

2.2. Metabolomics. GC×GC-TOFMS (LECO, USA) sample preparation, derivatization, and spectral acquisition were prepared according to published methods [13]. Briefly, 50 μL of plasma and 300 μL of mixed solvent (methanol : chloroform = 3 : 1, Thermo Fisher, USA) were added into a 1.5 mL centrifuge tube and vortexed for 30 s. Leave the hybrid solution in the refrigerator at −20°C for 10 minutes. After centrifugation at 1000 RPM for ten minutes, transfer 300 μL of the supernatant to the vial and add 10 μL of 0.1 mg mL^{-1} chlorobenzene (Thermo Fisher, USA), alanine (Sigma-Aldrich, USA), and 1 mg mL^{-1} heptadecanoic acid. After the sample was freeze-dried, 80 μL of 15 mg mL^{-1} pyridine (Sigma-Aldrich, USA) dissolved methoxamine and 50 μL BSTFA (1%TMCS, Sigma-Aldrich, USA) were added, respectively. The mixed sample was at 70°C for 60 minutes and then cooled down before injection.

2.3. Statistical Analysis. All results are shown as the mean ± SEM. Statistical analysis was conducted using unpaired Student's t-tests for two groups and one-way analysis of variance (ANOVA) or two-way ANOVA for multiple groups. Missing values were imputed by MetImp 1.2 [14]. Feature selection and modeling were performed by Random forest, owing to its advantages in small sample sizes, complicated data structure, and high-dimensional feature space. Random forests were implemented using the "randomForest" R

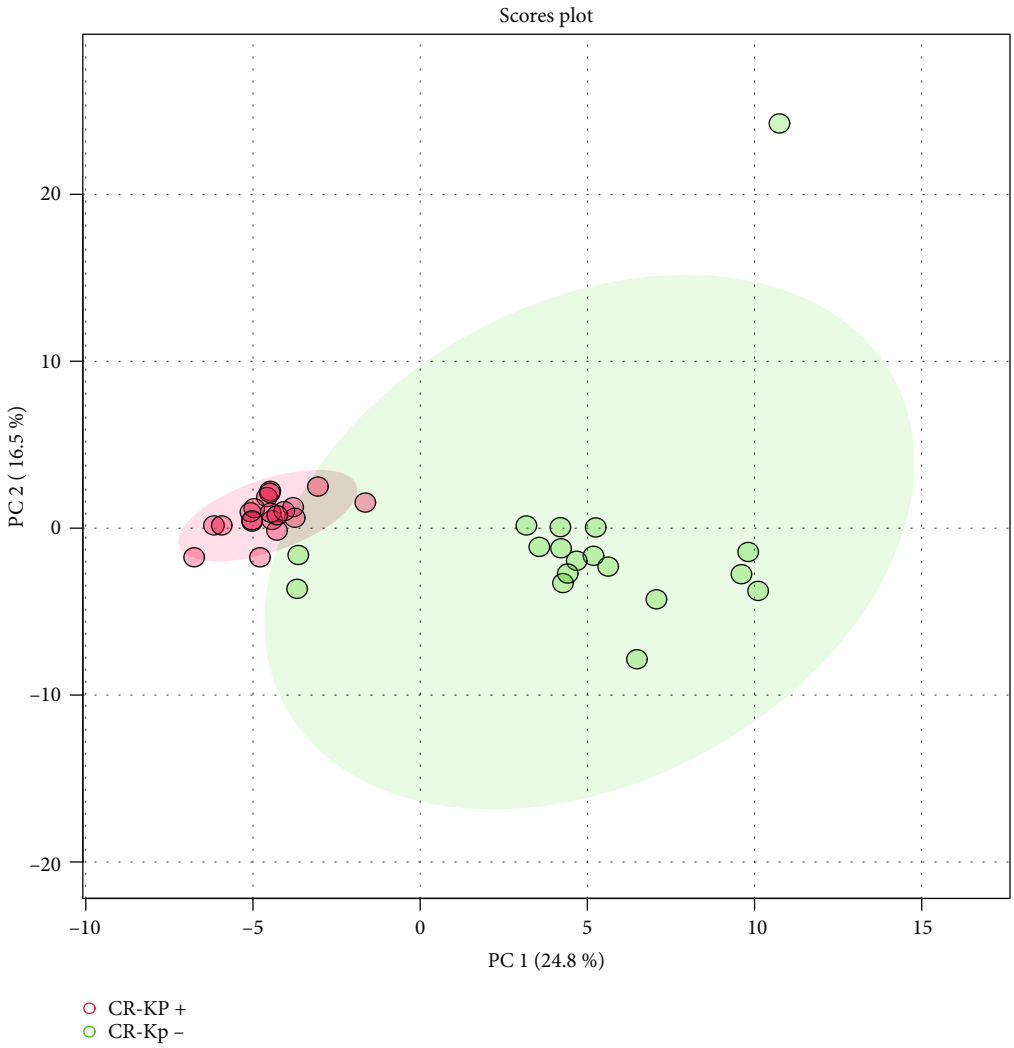

(a)

Figure 1: Continued.

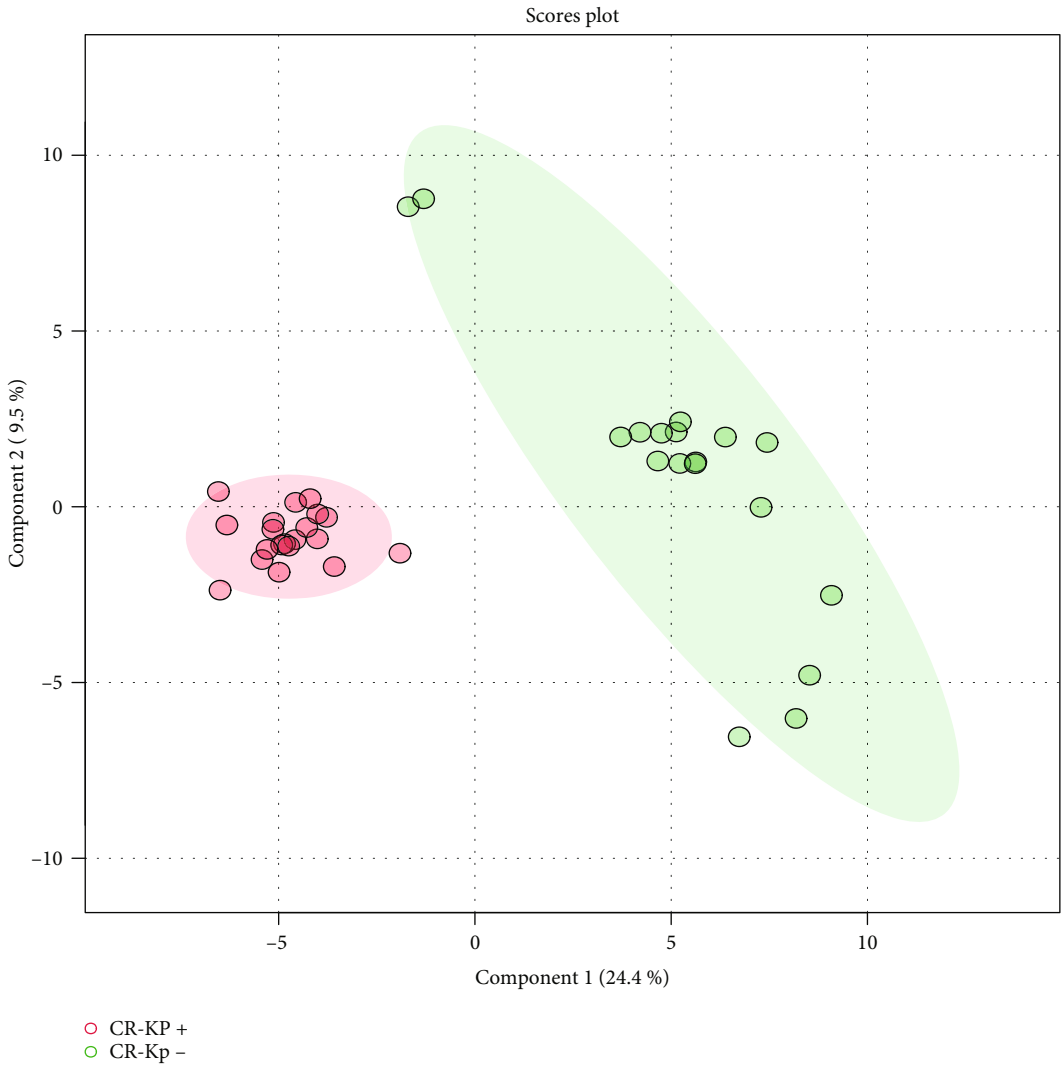

(b)

Figure 1: PCA and PLS-DA plot. Based on the metabolic profiling of carbapenem-resistant *K. pneumoniae*- (*CR-Kp*-) infected and CR-Kp-negative patients in plasma.

package. All analyses were performed using R software (version 4.0.2).

3. Results

3.1. Metabolic Profiling of Plasma. Principal component analysis (PCA) and partial least squares-discriminant analysis (PLS-DA) analytical procedures were implemented in this investigation to distinguish significantly changed metabolites induced by CR-Kp infection. Figure 1 shows that the CR-Kp-positive and CR-Kp-negative groups separate in the PCA and PLS-DS plots. This suggests that the significant metabolite variation between the two groups can be identified.

A total of 58 significantly changed metabolites ($P < 0.05$) were detected (Supplementary Table 1). Carbohydrates, organic acids, fatty acids, and amino acids were significantly altered in the CR-Kp-positive group. Moreover, the volcano plot (Figure 2(a)) indicates differentially expressed metabolites ($P < 0.05$ and $|\log(\text{fold change})| > 0.5$). In detail, all selected meaningful metabolites are shown in the heat map (Figure 2(b)).

3.2. Key Metabolites Identified by Random Forest. Random forest (RF) was utilized on the dataset for the two comparative cases. The model was built based on 58 significantly changed metabolites. Figure 3(a) shows the separation between the CR-Kp-negative group and the positive group. RF yielded 98.37% classification accuracy with 100 trees (Figure 3(b)). The variable number dependence section evaluates whether and how much RF performance depends on the number of variables included. This section assesses its capability on an important variable (key metabolites) preference. Figure 3(c) displays the top 15 metabolites' mean decrease accuracy, revealing how much the model loses by excluding each variable. The more

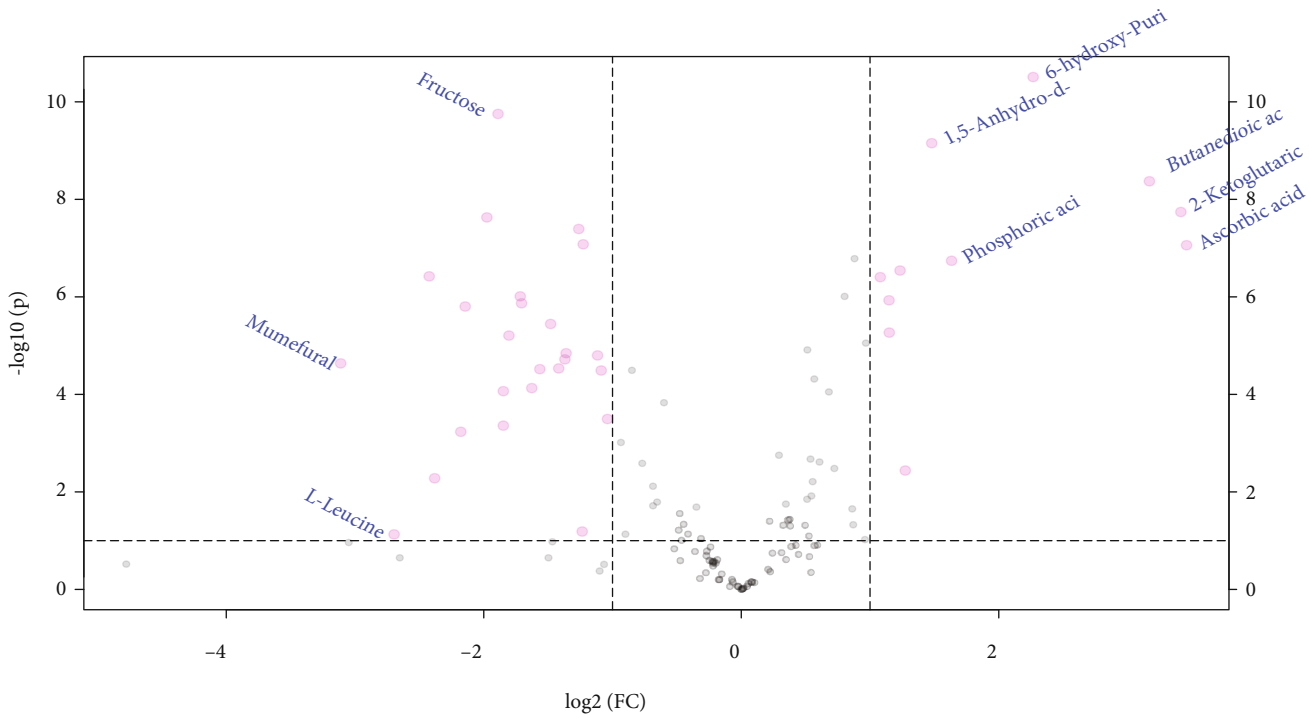

(a)

Figure 2: Continued.

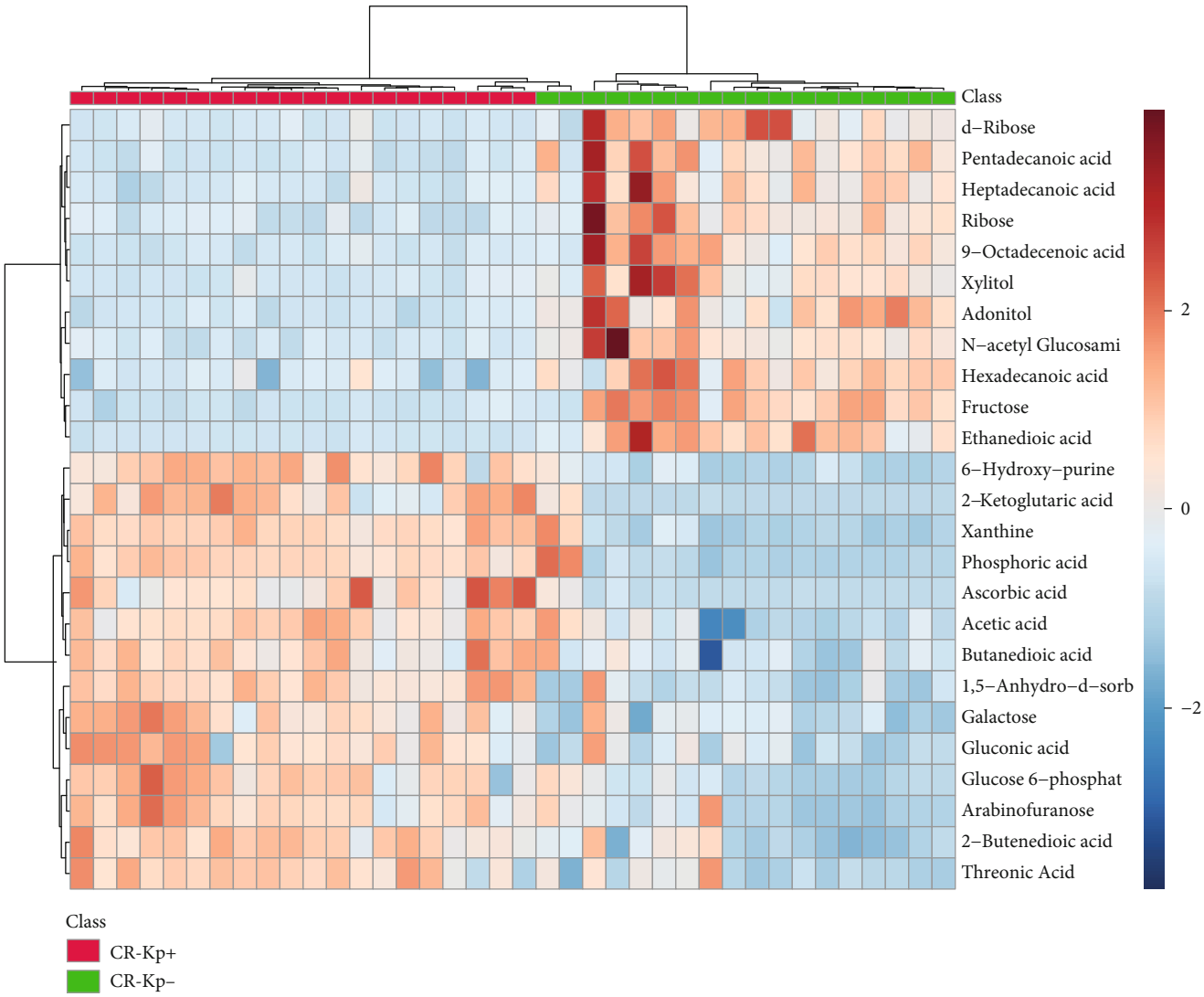

(b)

Figure 2: Differential expressed metabolites: (a) volcano plot and (b) heat map of the metabolites in plasma. The outcomes were selected by a threshold of $P < 0.05$.

the accuracy endures, the more influential the variable is for the successful classification. The variables are shown with descending importance. N-Acetyl glucosamine, butanedioic acid, and myoinositol are the most significant metabolites with the differential infected and control groups.

3.3. Key Metabolite's Function Analysis. Differentially expressed metabolite correlation analysis was applied to analyze the consistency of metabolite trends (Supplementary Figure S1). The metabolite's interrelation was assessed by Pearson correlation, and the results reveal significant metabolite-metabolite correlations. All differential metabolites were mapped to terms in the KEGG database and GO pathway to understand the functions of differential metabolites and the biological processes related to *CR-Kp* infection. The KEGG and GO enrichment analysis showing the top 25 enriched functions is shown in Supplementary Figure S2. Pathway analysis revealed neomycin, kanamycin, and gentamicin biosynthesis as the top canonical pathways (Supplementary Figure S2A). Similarly, the differential metabolites also could be enriched in ammonia recycling, urea cycle, and glutamate metabolism (Supplementary Figure S2B).

4. Discussion

Pneumonia remains a preeminent cause of death and hospitalization worldwide, particularly between teenagers and aging individuals [15, 16]. *K. pneumoniae* is one of the most generally isolated pathogens in pneumonia, leading to sepsis [17]. Still, *K. pneumoniae* is a severe threat, and increasing antimicrobial resistance exacerbates this problem [18]. Although diverse *K. pneumoniae* isolates may differ in their resistome, according to geographic area, cultural community switch, and antibiotic stewardship, this species exhibits an

The OOB error is 0.0263

	CR-Kp +	CR-Kp −	Class.error
Control	20	0	0
Infected	1	17	0.0556

(a)

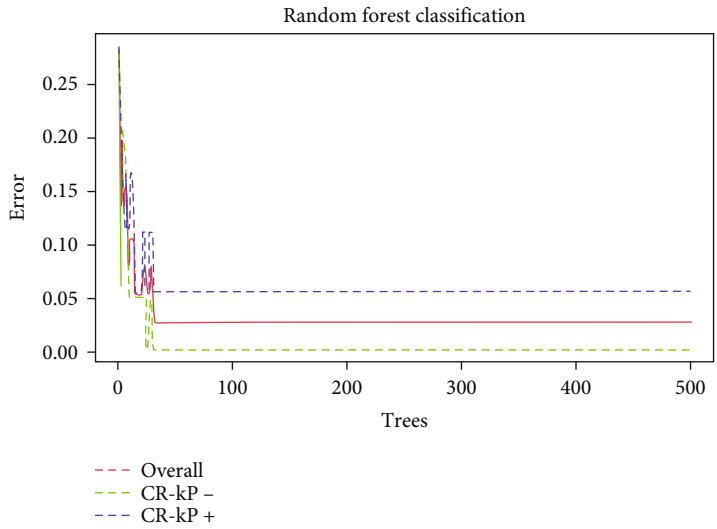

(b)

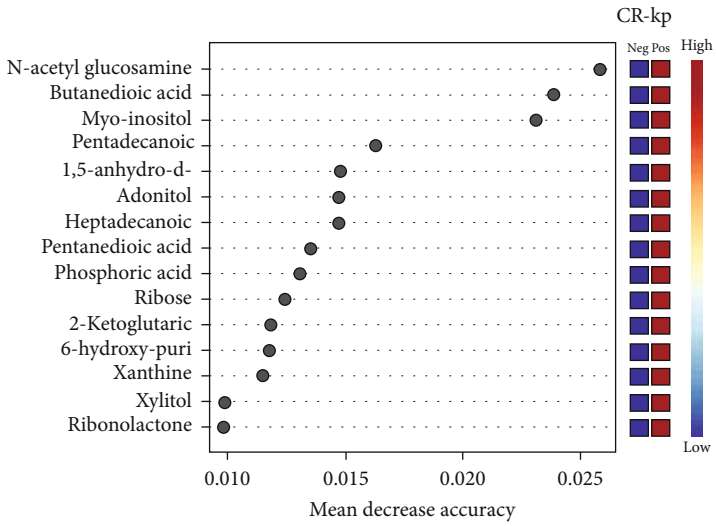

(c)

Figure 3: Key metabolites selection: (a) confusion matrix of Random forest classifier; (b) Random forest classification; (c) Random forest variable importance plot. Mean decrease accuracy is the measure of the performance of the model without each metabolite. A higher value indicates the importance of that metabolite in the predicting group (*CR-Kp*-positive vs. CR-Kp negative).

amenable ability to concentrate and rearrange resistances [19]. Future metabolic and translational studies must be needed to decipher specific targets to design targeted prevention and treatment.

This study serves the first use of GC×GC-TOFMS for the analysis of the metabolomics profiling of CR-Kp-infected patients in plasma. We found that 58 metabolites were differentially expressed in CR-Kp-positive infected patients' plasma but not the negative ones. Focusing on these metabolites, PCA showed good separation between the samples from both groups. Our study showed that patients infected with CR-Kp had significantly altered metabolic profiles of carbohydrates, organic acids, fatty acids, and amino acids. Notably, N-acetyl glucosamine, butanedioic acid, and myo-inositol are the most significantly changed metabolites between the two groups. Research shows that N-acetyl glucosamine (GlcNAc) sugar residues within the core LPS in several species of Gram-negative bacteria play a vital role in targeting the DC-SIGN receptor. DC-SIGN is an innate immune receptor, and the interaction of bacterial core LPS and DC-SIGN may represent an ancient interaction between Gram-negative bacteria and host phagocytic cells [20]. Butanedioic acid (succinic acid) is a dicarboxylic acid in the TCA cycle. Moreover, succinic acid is a microbial metabolite produced by *Escherichia coli*, *Pseudomonas aeruginosa*, and *K. pneumoniae* [21]. Study shows that *K. pneumoniae* utilizes glycerol as the carbon source to produce succinic acid [22]. Blocking the production of succinic acid may be a potential target for inhibiting CR-Kp. Additionally, myoinositol is rarely reported as a newly discovered metabolite in *K. pneumoniae* infection, which may also be a potential growth inhibitory target. The neomycin, kanamycin, and

gentamicin biosynthesis pathways were significantly changed in the CR-Kp-positive group. We infer that it is related to the use of β-lactam/β-lactamase inhibitor combinations.

In conclusion, this study identifies 58 significant CR-Kp-associated molecules in GC×GC-TOFMS. Myoinositol changes significantly in the CR-Kp-positive and CR-Kp-negative groups and can be used as a potential target for treating CR-Kp infection. Future studies are required to better explore those metabolites as a potential therapeutic target.

5. Limitations

Our study has some notable limitations. To our knowledge, our study is the first metabolome study of carbapenem-resistant *Klebsiella pneumoniae*. However, it cannot be used by the clinicians directly. Further, the infected patient sample size was limited, and further study is warranted to confirm our findings.

Data Availability

Data is available on request. The original contributions presented in the study are included in the article/Supplementary Material. Further inquiries can be directed to the corresponding authors.

Conflicts of Interest

The authors report no conflict of interest.

Authors' Contributions

Zhougui Ling had the idea and launched the study. Zhongwei Wen and Mei Liu had full access to all data in the study and take responsibility for the integrity of the data and the accuracy of the data analysis. All authors reviewed the manuscript and approved the version for publication. Zhongwei Wen and Mei Liu contributed equally to this work.

Supplementary Materials

Supplementary Figure S1: Spearman correlation coefficient analysis. The value > 0 indicates a positive correlation, while a value < 0 indicates a negative correlation. Supplementary Figure S2: function enrichment analysis. A, KEGG pathway analysis; B, GO pathway enrichment. Supplementary Table 1: carbapenem-resistant Klebsiella pneumoniae infection-associated metabolites. *(Supplementary Materials)*

References

[1] R.-W. Tsay, L. K. Siu, C.-P. Fung, and F.-Y. Chang, "Characteristics of bacteremia between community-acquired and nosocomial Klebsiella pneumoniae infection: risk factor for mortality and the impact of capsular serotypes as a herald for community-acquired infection," vol. 162, pp. 1021–1027, 2002.

[2] M. N. Al-Hasan, B. D. Lahr, J. E. Eckel-Passow, and L. M. Baddour, "Epidemiology and outcome of Klebsiella species bloodstream infection: a population-based study," *Mayo Clinic Proceedings*, vol. 85, no. 2, pp. 139–144, 2010.

[3] E. A. Neuner, J. Y. Yeh, G. S. Hall et al., "Treatment and outcomes in carbapenem-resistant Klebsiella pneumoniae bloodstream infections," *Diagnostic microbiology and infectious disease*, vol. 69, pp. 357–362, 2011.

[4] A. Leavitt, I. Chmelnitsky, R. Colodner, I. Ofek, Y. Carmeli, and S. Navon-Venezia, "Ertapenem resistance among extended-spectrum-β-lactamase-producing Klebsiella pneumoniae isolates," *Journal of clinical microbiology*, vol. 47, pp. 969–974, 2009.

[5] J.-J. Wu, L.-R. Wang, Y.-F. Liu, H.-M. Chen, and J. J. Yan, "Prevalence and characteristics of ertapenem-resistant Klebsiella pneumoniae isolates in a Taiwanese university hospital," vol. 17, pp. 259–266, 2011.

[6] M. Shanthi and U. Sekar, "Extended spectrum beta lactamase producing Escherichia coli and Klebsiella pneumoniae: risk factors for infection and impact of resistance on outcomes," *Journal of the Association of Physicians of India*, vol. 58, pp. S41–S44, 2010.

[7] X. Liu and J. W. Locasale, "Metabolomics: a primer," vol. 42, pp. 274–284, 2017.

[8] A.-H. Emwas, R. Roy, R. T. McKay et al., "NMR spectroscopy for metabolomics research," *Metabolites*, vol. 9, p. 123, 2019.

[9] R. Chaleckis, I. Meister, P. Zhang, and C. E. Wheelock, "Wheelock, Challenges, progress and promises of metabolite annotation for LC–MS-based metabolomics," *Current opinion in biotechnology*, vol. 55, pp. 44–50, 2019.

[10] D. J. Beale, F. R. Pinu, K. A. Kouremenos et al., "Review of recent developments in GC–MS approaches to metabolomics-based research," *Metabolomics*, vol. 14, pp. 1–31, 2018.

[11] S. Shoja, M. Ansari, F. Faridi et al., "Identification of carbapenem-resistant Klebsiella pneumoniae with emphasis on New Delhi metallo-beta-lactamase-1 (bla NDM-1) in Bandar Abbas, South of Iran," *Microbial Drug Resistance*, vol. 24, pp. 447–454, 2018.

[12] C. A. Rees, A. Smolinska, and J. E. Hill, "The volatile metabolome of Klebsiella pneumoniae in human blood," *Journal of breath research*, vol. 10, article 027101, 2016.

[13] X. Zheng, K. Zhou, Y. Zhang et al., "Food withdrawal alters the gut microbiota and metabolome in mice," *The FASEB Journal*, vol. 32, pp. 4878–4888, 2018.

[14] R. Wei, J. Wang, M. Su et al., "Missing value imputation approach for mass spectrometry-based metabolomics data," *Scientific reports*, vol. 8, pp. 1–10, 2018.

[15] J. P. Janssens and K. H. Krause, "Pneumonia in the very old," *The Lancet infectious diseases*, vol. 4, pp. 112–124, 2004.

[16] K. McIntosh, "Community-acquired pneumonia in children," *New England Journal of Medicine*, vol. 346, pp. 429–437, 2002.

[17] C. I. Kang, J. H. Song, D. R. Chung et al., "Risk factors and pathogenic significance of severe sepsis and septic shock in 2286 patients with gram-negative bacteremia," *Journal of Infection*, vol. 62, pp. 26–33, 2011.

[18] C. J. Norsigian, H. Attia, R. Szubin et al., "Comparative genome-scale metabolic modeling of metallo-beta-lactamase–producing multidrug-resistant Klebsiella pneumoniae clinical isolates," *Frontiers in cellular and infection microbiology*, vol. 9, p. 161, 2019.

[19] S. Navon-Venezia, K. Kondratyeva, and A. Carattoli, "Klebsiella pneumoniae: a major worldwide source and shuttle for

antibiotic resistance," *FEMS microbiology reviews*, vol. 41, pp. 252–275, 2017.

[20] P. Zhang, S. Snyder, P. Feng et al., "Role of N-acetylglucosamine within core lipopolysaccharide of several species of gram-negative bacteria in targeting the DC-SIGN (CD209)," *The Journal of Immunology*, vol. 177, pp. 4002–4011, 2006.

[21] A. Gupta, M. Dwivedi, A. A. Mahdi, C. L. Khetrapal, and M. Bhandari, "Broad identification of bacterial type in urinary tract infection using 1H NMR spectroscopy," vol. 11, pp. 1844–1854, 2012.

[22] V. Kumar and S. Park, "Potential and limitations of Klebsiella pneumoniae as a microbial cell factory utilizing glycerol as the carbon source," *Biotechnology advances*, vol. 36, pp. 150–167, 2018.

Hindawi
Disease Markers
Volume 2021, Article ID 6166492, 13 pages
https://doi.org/10.1155/2021/6166492

Research Article

Whole Blood Transcriptome Analysis Reveals the Correlation between Specific Immune Cells and Septicemic Melioidosis

Ke Xu,[1] Dahua Xu,[2] Hua Pei,[3] Yunfan Quan,[1] Jun Liu,[4] Li Yin,[1] Xuexia Li,[1] ShenTian,[1] Kongning Li,[2] and Qianfeng Xia[1]

[1]*Key Laboratory of Tropical Translational Medicine of Ministry of Education and School of Tropical Medicine and Laboratory Medicine, Hainan Medical University, Haikou, Hainan, China*
[2]*Key Laboratory of Tropical Translational Medicine of Ministry of Education and College of Biomedical Information and Engineering, Hainan Medical University, Haikou 571199, China*
[3]*Department of Clinical Laboratory, The Second Affiliated Hospital, Hainan Medical University, Haikou, China*
[4]*School of Basic Medicine and Life Sciences, Hainan Medical University, Haikou, Hainan, China*

Correspondence should be addressed to Kongning Li; likongning@hainmc.edu.cn and Qianfeng Xia; xiaqianfeng@hainmc.edu.cn

Received 6 August 2021; Revised 4 September 2021; Accepted 24 September 2021; Published 13 October 2021

Academic Editor: Ting Su

Melioidosis is a serious infectious disease caused by the environmental Gram-negative bacillus *Burkholderia pseudomallei*. It has been shown that the host immune system, mainly comprising various types of immune cells, fights against the disease. The present study was to specify correlation between septicemic melioidosis and the levels of multiple immune cells. First, the genes with differential expression patterns between patients with septicemic melioidosis (*B. pseudomallei*) and health donors (control/healthy) were identified. These genes being related to cytokine binding, cell adhesion molecule binding, and MHC relevant proteins may influence immune response. The Kyoto Encyclopedia of Genes and Genomes (KEGG) analysis revealed 23 enriched immune response pathways. We further leveraged the microarray data to investigate the relationship between immune response and septicemic melioidosis, using the CIBERSORT analysis. Comparison of the percentages of 22 immune cell types in *B. pseudomallei* vs. control/healthy revealed that those of CD4 memory resting cells, CD8+ T cells, B memory cells, and CD4 memory activated cells were low, whereas those of M0 macrophages, neutrophils, and gamma delta T cells were high. The multivariate logistic regression analysis further revealed that CD8+ T cells, M0 macrophages, neutrophils, and naive CD4+ cells were strongly associated with the onset of septicemic melioidosis, and M2 macrophages and neutrophils were associated with the survival in septicemic melioidosis. Taken together, these data point to a complex role of immune cells on the development and progression of melioidosis.

1. Introduction

Melioidosis, a serious tropical infectious disease, frequently outbreaks in Southeast Asia and northern Australia. It is caused by the Gram-negative bacillus *Burkholderia pseudomallei* (*B. pseudomallei*), which inhabits in soil and surface water [1]. In some endemic areas, melioidosis is a major cause of pneumonia in adults [2] and lethal septicemia, and case fatality rates range from 10 to 50% [3]. Naturally acquired disease in human species is the result of *B. pseudomallei*-induced infection due to the pathogenic bacteria entry through broken skin, inhalation, or ingestion [4]. Certain environmental conditions (tropical storms, rainy season, etc.) and certain occupations (rice farming [5]) are known to the risk factors of the infection [3]. In addition, several internal risk factors cannot be overnighted. For instance, diabetes mellitus, type 2 diabetes in particular, is a common risk factor predisposing individuals to melioidosis with more than 50% patients with melioidosis having type 2 diabetes [6]. Also, immunosuppression appears to

be another important risk factor, as 60–90% of patients with melioidosis had the history of immunosuppressive treatments [3]. Like other infection diseases, there are of acute (caused by infections from recent bacterial exposure) and chronic types. Nearly 85% of melioidosis cases are of acute type, and patients with acute melioidosis develop sepsis rapidly, namely, septicemic melioidosis. This condition is a life-threatening one with a death rate of 40% [1].

The immune system is a host defense system consisting of a variety of immune cells, organs, proteins, and tissues that protects against disease. As the immune system meets a pathogen, it primarily invokes the two immune responses with the involvements of T cell and B cell in the adaptive immune response as well as neutrophils and macrophages in the innate immune response. In melioidosis, the immune responses play a big part as well. Epidemiologically, immunosuppression is believed to predispose individuals to *B. pseudomallei* infection [7, 8]. The weight of evidence is that in the most cases, *B. pseudomallei* infection merely leads to subclinical condition as most of immunocompetent individuals can remove the infection without any medical intervention [9]. In the C57BL/6 mice cell model, the microbicidal activity against *B. pseudomallei* was significantly lower in PECM (peritoneal exudate cells macrophage identified by nonspecific esterase) and NAPEC (nonadherent peritoneal exudate cells that were assumed to be full of lymphocytes) cultures when compared to peritoneal exudate cell (PEC) cultures, suggesting that macrophage-lymphocyte interactions promoted the killing of *B. pseudomallei* [10]. In agreement with this finding, patients with acute melioidosis come through with elevated levels of and CD8+ and CD4+ T cells, whereas those dead were with decreased levels of these cells [11]. Nevertheless, the immune response is also likely to be destructive as exemplified excessive recruitment of neutrophils causing tissue damage [12]. It is highly likely that multiple immune cells are engaged in melioidosis. However, due to technical limitations, the previous studies are unable to fully investigate the multiple immune cells, with only a small bunch of selected immune cells or mixed ones without proper identifications being explored. Therefore, it is required to investigate multiple immune cells in melioidosis with new technique.

The whole blood can recapitulate the real immune status of individuals. Previous studies have shown that the whole blood samples collected from melioidosis patients being subjected to microarray-based profiling had been proved to be an instrumental approach to investigate the onset and development of melioidosis [13]. More importantly, Conejero et al. reanalyzed the above whole blood transcriptional microarray data and provided useful insight into melioidosis [14]. Thus, in the current study, we reanalyzed the whole blood transcriptional microarray data in an effort to determine whether immune cells, the key players in the core immune network, play a big part in septicemic melioidosis. Accordingly, to better understand multiple immune cells contributing to the immune response to the disease, an established computational approach (CIBERSORT), which is capable of evaluating 22 immune cell types, was employed. This study was to more thoroughly investigate the specific roles of the immune cells in septicemic melioidosis.

2. Material and Methods

2.1. Patients' Characteristics and Dataset Collection. The human whole blood microarray and the clinical data were obtained from NCBI GEO datasets, and the accession number was GSE13015. In the current study were 8 healthy donors (control/healthy), 12 patients with type 2 diabetes (type 2 diabetes), 9 patients recovering from melioidosis (control/recovery), and 40 patients with septicemic melioidosis (*B. pseudomallei*). In addition, 37 patients with sepsis caused by other organisms (1 *Acinetobactor baumannii*, 1 *Aeromonas hydrophila*, 4 *C. albicans*, 3 *Corynebacterium* spp., 8 *E. coli*, 1 *Enterococcus faecium*, 2 *Enterococcus* spp., 1 *K. pneumoniae*, 1 *S. pneumoniae*, 1 *Salmonella serotype* B, 2 *Salmonella* spp., 4 *Staphylococcus aureus*, 6 *Staphylococcus coagulase* negative, and 2 *Streptococcus* non A, B.) were included. With the limma package in R, differentially expressed genes were identified with absolute cutoff log2 fold change value greater than or equal to 0.9. The clinical data were shown in a previous research [13].

2.2. Enrichment Analysis of the Gene Ontology (GO) Function and Kyoto Encyclopedia of Genes and Genomes (KEGG) Pathway. The package of http://org.Hs.eg.db in R was used to convert the gene name to Entirez IDs. ClusterProfiler package was then used to enrich the network with GO enrichment and KEGG enrichment pathways [15]. The results with p values less than 0.05 were considered statistically significant.

2.3. CIBERSORT Analysis. CIBERSORT, as an instrumental tool, can precisely measure the relative levels of distinct immune cell types. It can characterize each immune cell type with a bulk gene expression signature consisting of around 500 genes. Here, the original CIBERSORT gene signature file LM22, defining 22 immune cell types, was applied for analyzing the dataset from the septicemic melioidosis. CIBERSORT metrics with Pearson correlation coefficient, CIBERSORT p value, and root mean squared error (RMSE) were measured for each sample [16].

2.4. Statistical Analysis. Difference between immune cell types was determined by Mann-Whitney U-test. Correlations among immune cell types and clinical features were determined by Spearman's rank correlation. A value of $p < 0.05$ was considered significant. The relevant parameters with spearman absolute r value > 0.5 were selected. The multivariate logistic regression analyses [17] were performed to identify potential risk factors for septicemic melioidosis. In order to clear the impact of multicollinearity of the covariates in the multivariate regression model [18], the Akaike information criterion (AIC) was therefore used for the further selection of parameters. Only those noncorrelated parameters (with AIC < 10) were included in the multivariate logistic regression analysis. The receiver-operating characteristic (ROC) curve was plotted [19] with the true-positive fraction (sensitivity) versus the false-positive (1-specificity). A value of the area under the curve (AUC) equal to 0.9–1.0 is regarded as a perfect prediction, while a value of 0.5 is equivalent to a random. An AUC value between 0.7

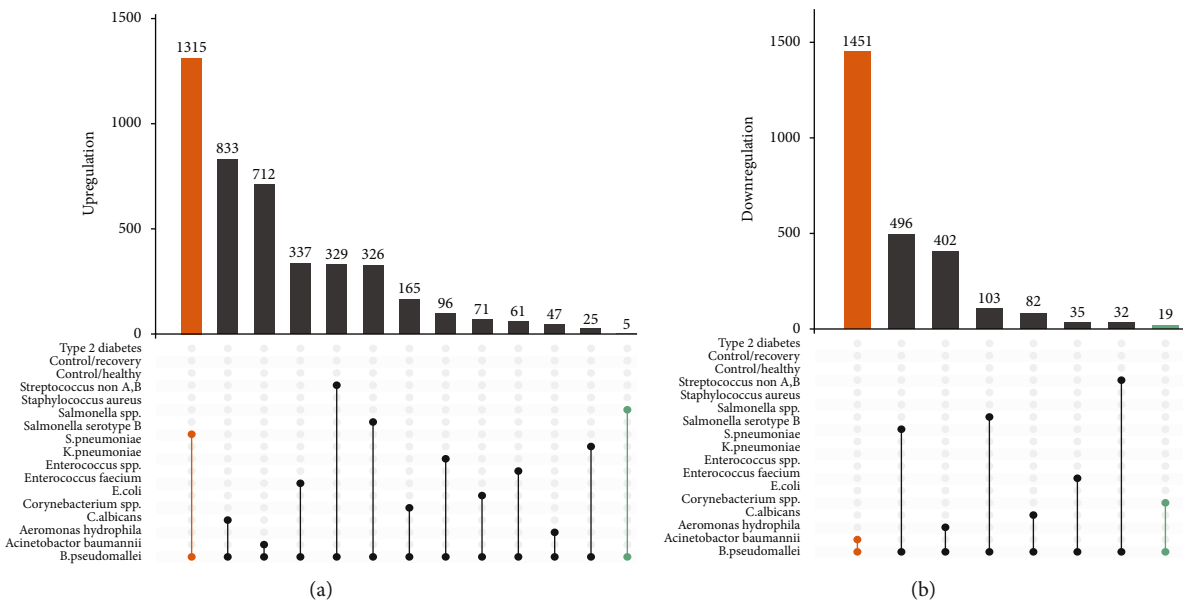

Figure 1: Upset plot depicting the numbers of the genes considered differentially expressed. (a) The upregulation of differentially expressed genes. There are multiple groups for comparison. (b) The downregulation of differentially expressed genes. The numbers of differentially expressed genes are indicated above. Type 2 diabetes vs. control/recovery, control/recovery vs. control/healthy, *B. pseudomallei* vs. *Acinetobactor baumannii*, *B. pseudomallei* vs. *Aeromonas hydrophila*, *B. pseudomallei* vs. *C. albicans*, *B. pseudomallei* vs. *Corynebacterium* spp., *B. pseudomallei* vs. *E. coli*, *B. pseudomallei* vs. *Enterococcus faecilum*, *B. pseudomallei* vs. *Enterococcus* spp., *B. pseudomallei* vs. *K. pneumoniae*, *B. pseudomallei* vs. *S. pneumoniae*, *B. pseudomallei* vs. *Salmonella serotype* B, *B. pseudomallei* vs. *Salmonella* spp., *B. pseudomallei* vs. *Staphylococcus aureus*, *B. pseudomallei* vs. *Staphylococcus coagulase* negative. Note: when the number of the differentially expressed genes was zero, it was remove from the plot. For instance, the results of *B. pseudomallei* vs. *Staphylococcus coagulase* negative, control/recovery vs. control/healthy, and type 2 diabetes vs. control/healthy were null.

and 0.9 indicated a good prediction, whereas an AUC value between 0.5 and 0.7 indicates a bad prediction.

3. Results

3.1. Transcriptomic Analysis of Human Whole Blood. As diabetes mellitus, type II diabetes in particular, is believed to be a general risk factor predisposing individuals to melioidosis, and this allows us to hypothesized that differentially expressed genes might be present among healthy donors (control/healthy), patients with type 2 diabetes (type 2 diabetes), and patients who had recovered from melioidosis (control/recovery). It is extremely important as the differentially expressed genes can constitute a promising gene signature with which to alert individuals who are susceptible to *B. pseudomallei* infection. Our findings, however, showed no significant differential expression between control/healthy and type 2 diabetes, as well as between control/healthy and control/recovery (Figure 1). This corroborates previous findings, in which control/healthy dataset cannot be separated from type 2 diabetes counterpart according to unsupervised clustering analysis [13], suggesting that background type II diabetes predisposing individuals to melioidosis may not map to significant transcriptional changes. Despite this, type 2 diabetes and control/recovery datasets were intended not to be integrated into the control/healthy counterpart for the subsequent analysis, as doing so could allow potential confounders to obscure the "real" effect. It has been documented that patients with septicemic melioidosis has a higher mortality rate as compared to the other pathogen-caused diseases [1]. We first determined whether there were distinct genes being differently expressed between the patients with septicemic melioidosis (designated as *B. pseudomallei*) and patients with other infections. As shown in Figure 1, a series of differential expression patterns were displayed. Of note, no significant differential expression between *B. pseudomallei* and *Staphylococcus coagulase* negative was found. Five genes were upregulated, and no gene downregulated in *B. pseudomallei* vs. *Staphylococcus aureus*. It appears that no overlap between genes that are differentially expressed between *B. pseudomallei* vs. other infections could be found. More importantly, no significant overlap between genes that are differentially expressed between *B. pseudomallei* and other infections was found, even when *Staphylococcus aureus* and *Staphylococcus coagulase* negative were removed. Analogue to our findings, Sangwichian et al. found that two other bacterial infections were falsely identified as *B. pseudomallei* by real-time PCR, suggesting that it is difficult to differentiate melioidosis from other pathogenic infections by transcriptional analysis [20].

3.2. Enrichment Analysis of the GO Function and KEGG Pathway. A total of 3593 genes, of which 2149 were upregulated and 1444 downregulated, that were differentially expressed between *B. pseudomallei* and control/healthy were identified. Functional enrichment of Gene Ontology (GO) biological process annotations were identified among differentially expressed genes. They were mainly related to

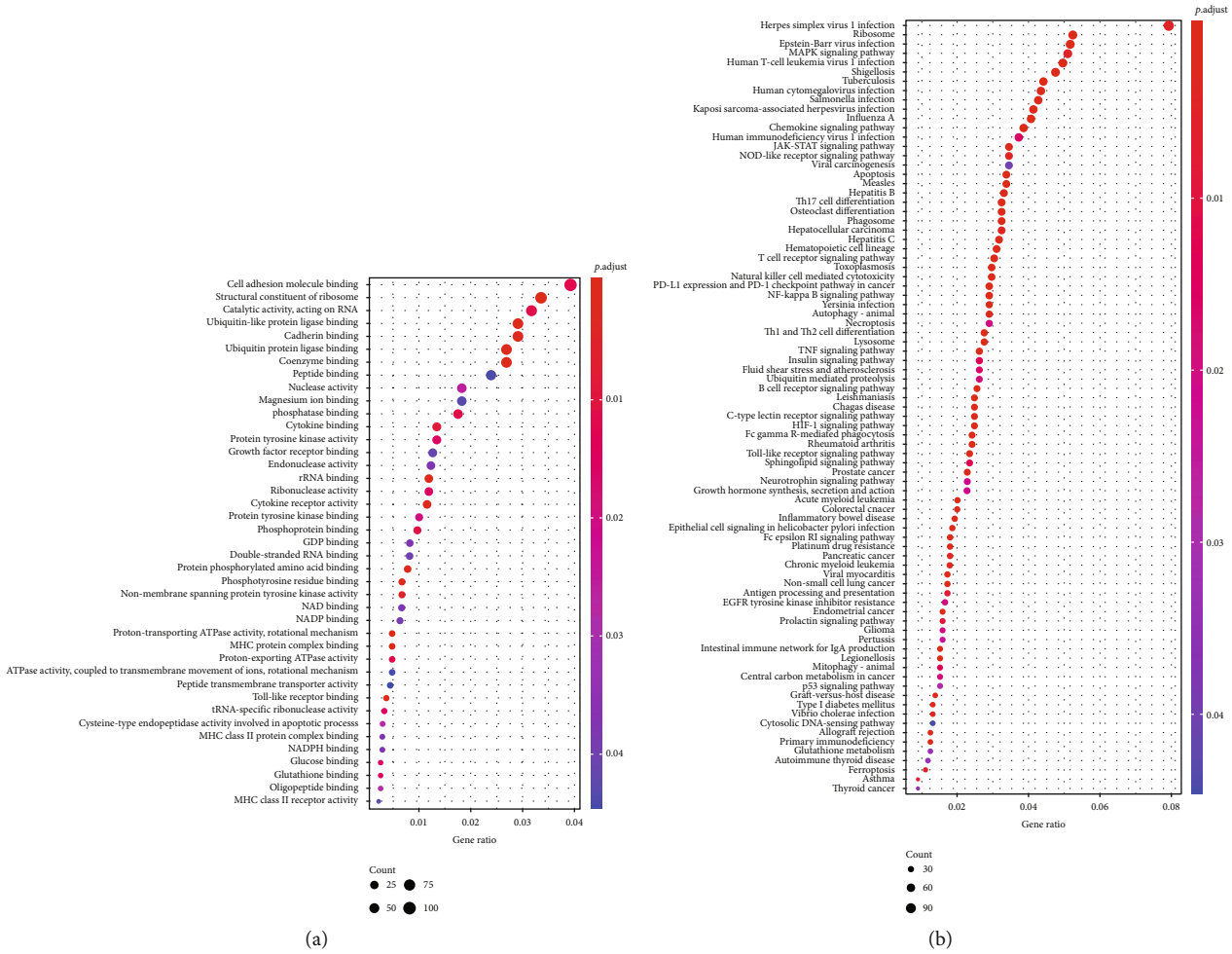

Figure 2: Analysis of gene enrichments. (a) Enriched Gene Ontology (GO) biological process identified by analyzing the differentially expressed genes in *B. pseudomallei* vs. control/healthy. Those with *p*.adjust.value < 0.05 were included. (b) Enriched KEGG pathways identified by analyzing the differentially expressed genes in B. *pseudomallei* vs. control/healthy.

cytokine binding, cell adhesion molecule binding, Toll-like receptor binding, and MHC relevant proteins (Figure 2(a)). This suggests that multiple genes relevant to immune response were involved. We then reasoned that the biological pathways related to immune response may take a big part. Biological pathway analysis by Kyoto Encyclopedia of Genes and Genomes (KEGG) was performed. The results with an adjusted p value < 0.05 are shown in Figure 2(b). Apparently, the most genes were enriched on the pathways related to immunology, such as Human T-cell leukemia virus 1 infection, chemokine signaling pathway, human immunodeficiency virus 1 infection, JAK-STAT signaling pathway, Th17 cell differentiation, T cell receptor signaling pathway, natural killer cell-mediated cytotoxicity, PD-L1expression and PD-1 checkpoint pathway in cancer, NF-kappa B signaling pathway, Th1 and Th2 cell differentiation, TNF signaling pathway, B cell receptor signaling pathway, rheumatoid arthritis (type III hypersensitivity), Fc gamma R-mediated phagocytosis, Toll-like receptor signaling pathway, acute myeloid leukemia, inflammatory bowel disease, chronic myeloid leukemia, antigen processing and presentation, graft-versus-host disease, allograft rejection, primary immunodeficiency, and autoimmune thyroid disease. These findings suggest that the immune response may stand to influence *B. pseudomallei* infection.

3.3. Distribution of Immune Cells in the Septicemic Melioidosis. Since immune cells are essential players in the immune response, our focus was primarily on them [21], the CIBERSORT was employed for exploring the proportion of each immune cell type between *B. pseudomallei* and control/healthy. The distribution of cell fractions was illustrated in Figure 3(a). In order to determine whether certain cell types were associated with septicemic melioidosis, the Mann-Whitney U-test was used to measure significant difference in the proportions of the immune cells between *B. pseudomallei* and control/healthy. Among the 22 immune cell types, those with p less than 0.05 were plotted. As expected, the proportion of neutrophils was high in *B. pseudomallei*, when compared with control/healthy, coinciding with the previous result that excessive neutrophils play a damaging role in the patients with melioidosis [12]. In

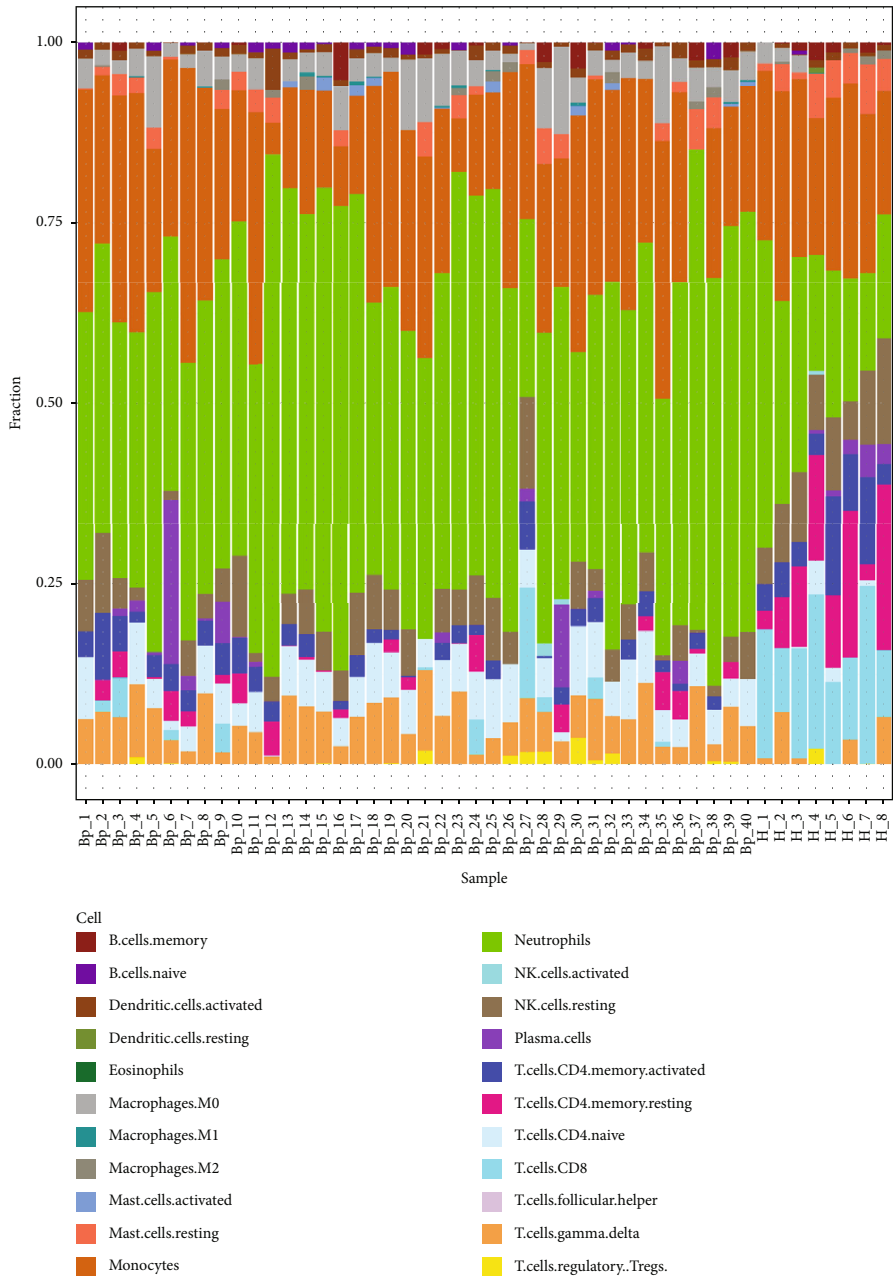

(a)

Figure 3: Continued.

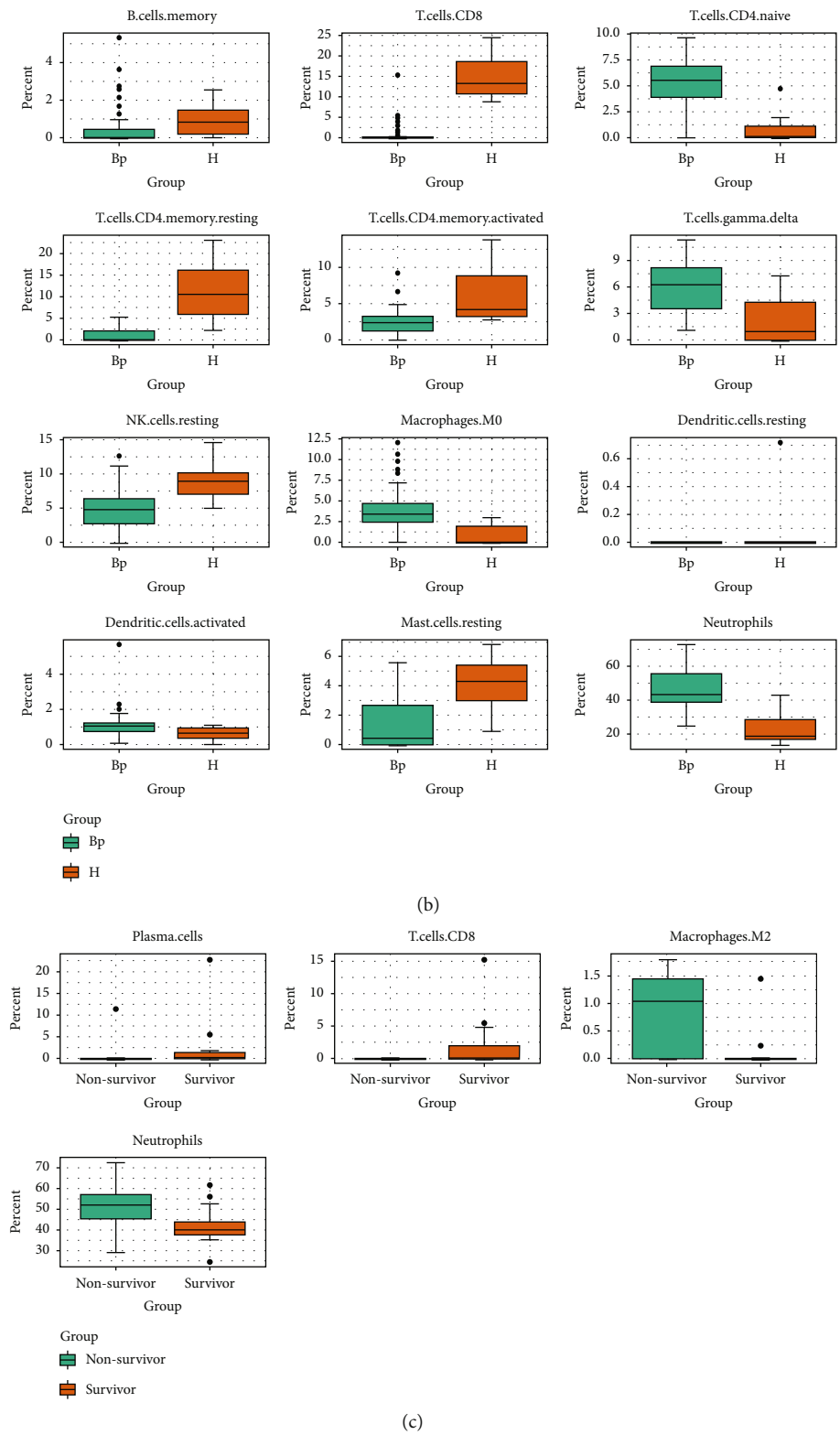

Figure 3: Correlation between the immune cells and the onset and development of septicemic melioidosis. (a) Stacked bar plot describing in immune cell compositions of patients with septicemic melioidosis and healthy control, derived using the CIBERSORT analysis, was carried out. Each bar represents percent fractions for the cell types, with colors representing the different cell types. (b) Boxplots depicting proportions of relevant immune cell types between patients with melioidosis and healthy control. Mann-Whitney U-test was performed, and $p < 0.05$ was allowed to be plotted. (c) Boxplots depicting proportions of relevant immune cell types between survivors and nonsurvivors with melioidosis. Mann-Whitney U-test was performed, and $p < 0.05$ was allowed to be plotted.

contrast to control/healthy, the proportion of CD8+ T cells was markedly low in *B. pseudomallei*, which is analogue to the findings published by Jenjaroen et al. that a lower CD8 + T cell level was observed in the worsen outcomes caused by *B. pseudomallei* infection [11]. The proportion of naive CD4+ T cells, a quiescent T cell subpopulation, was high in *B. pseudomallei* when compared with control/healthy, whereas that of CD4 memory resting cells and CD4 memory activated cells were low in *B. pseudomallei*. In addition, the proportion of B memory cells in *B. pseudomallei* was low too. These findings suggest that adaptive immune response is likely to be suppressed in patients with septicemic melioidosis. We also observed that the proportions of M0 macrophages, resting macrophage, and gamma delta T cells, an unconventional T cell subpopulations that are the key components of innate immune response, were high in *B. pseudomallei*, whereas that of NK resting cells was low, suggesting the interplay between *B. pseudomallei* infection and innate immune response was complicated (Figure 3(b)).

Since the immune cells were implicated in septicemic melioidosis, we then investigated whether the immune cell types were associated survival in septicemic melioidosis. As shown in Figure 3(c), only four immune cell types were selected. As expected, the proportion of neutrophils was high in nonsurvivors, when compared with survivors. The higher proportion of M2, an immune suppressor cell subpopulation, was present in nonsurvivors, whereas the proportions of plasma cells and CD8+ T cells were lower. These findings suggest that the adaptive immune response was overwhelmingly suppressed in severe septicemic melioidosis.

3.4. Correlation between the Immune Cells and the Onset of Septicemic Melioidosis. We next investigated the correlations between the selected immune cells and several clinical features, of which all serve as parameters for correlation analysis. Those selected parameters (with absolute r value > 0.5 highlighted with color round marks) were included in the multivariate logistic regression analysis. As shown in Figure 4(a), the neutrophils, M0, and naive CD4+ T cells were positively correlated with melioidosis, while the resting CD4+ T cells and CD8+ T cells were negatively correlated with melioidosis. The other immune cell types, along with age and gender were not correlated with melioidosis (Figure 4(a)). Therefore, the neutrophils, M0, naive CD4+ T cells, resting CD4+ T cells, and CD8+ T cells were selected for multivariate logistic regression. Multiple parameter models were then generated based on the full combinations of these selected parameters. The models with at least one parameter's p value < 0.05 were allowed to be proceeded with ROC curve analysis, and the results were illustrated in Figure 4(b). The ROC curve analysis gave AUCs from 0.91 to 0.99. It is safe to say that each model was promising, as each of AUC values is greater than 0.7. Top 5 AUC values were given 0.98 from CD8+ T cells + M0 macrophages, 0.98 from CD8+ T cells + M0 macrophages, 0.98 from CD8+ T cells, 0.98 from CD8+ T cells+ neutrophils, and 0.99 from naive CD4+ cells + neutrophils, respectively. Of note, the two-parameter models of naive CD4+ cells + neutrophils increased the AUC marginally from 0.91 (one parameter model of naive CD4+ cells) and 0.99. All the more than two parameter models but CD8+ T cells + M0 macrophages + neutrophils had been excluded presumably because of multicollinearity. These findings suggest that several models are able to predict the onset of septicemic melioidosis.

3.5. Correlation between the Immune Cells and Survival of Patients with Septicemic Melioidosis. As several immune cells were associated with the development of melioidosis, we then asked whether most of these immune cells were implicated in the survival of patients with septicemic melioidosis. The correlation analysis was carried out as described above. Surprisingly, type II diabetes was not relevant to the patient survival, with very low absolute r value (r value = -0.1) (Figure 5(a)). Only M2 was eligible for the following the logistic regression analysis. Because the absolute correlation score of neutrophils was marginally less than 0.5, and neutrophils were reckoned as a relevant parameter. Thus, neutrophils was added to the logistic regression analysis, regardless of its correlation result. ROC curve analysis gave AUCs from 0.74–0.82. The two-parameter model of M2 macrophages + neutrophils largely improved the one parameter model of M2 macrophages (Figure 5(b)).

4. Discussion

This study was to establish correlation between septicemic melioidosis and the levels of multiple immune cells. First, the genes that were differentially expressed between patients with septicemic melioidosis (*B. pseudomallei*) and health donors (control/healthy) were identified. These genes were linked to cytokine binding, cell adhesion molecule binding, and relevant MHC functions. The Kyoto Encyclopedia of Genes and Genomes (KEGG) pathway findings revealed 23 enriched immune response pathways. We further leveraged the microarray data to investigate the relationship between immune response and melioidosis. CIBERSORT analysis was performed. Comparison of the levels of 22 immune cell types in *B. pseudomallei* vs. control/healthy revealed that the levels of CD8+ T cells, CD4 memory resting cells, CD4 memory activated cells, and B memory cells were low, whereas those of M0 macrophages, gamma delta T cells, and neutrophils were high. The multivariate logistic regression analysis further revealed that CD8+ T cells, M0 macrophages, neutrophils, and naive CD4+ cells were strongly associated with septicemic melioidosis, and M2 macrophages and neutrophils were associated with severe septicemic melioidosis. Together, these data point to a complex interplay of mechanisms underlying the effects of specific immune cells on the onset and development of septicemic melioidosis.

In melioidosis, *B. pseudomallei* can multiply within macrophages without activating a bactericidal response [22]. On the other hand, activated macrophages by inflammatory cytokines display improved killing of *B. pseudomallei* [23]. Although increasing evidence favors the important roles played by macrophages in melioidosis, the roles of specific macrophage subsets in the disease remain unclear. In general, macrophages are classified into nonactivated (M0),

(a)

Figure 4: Continued.

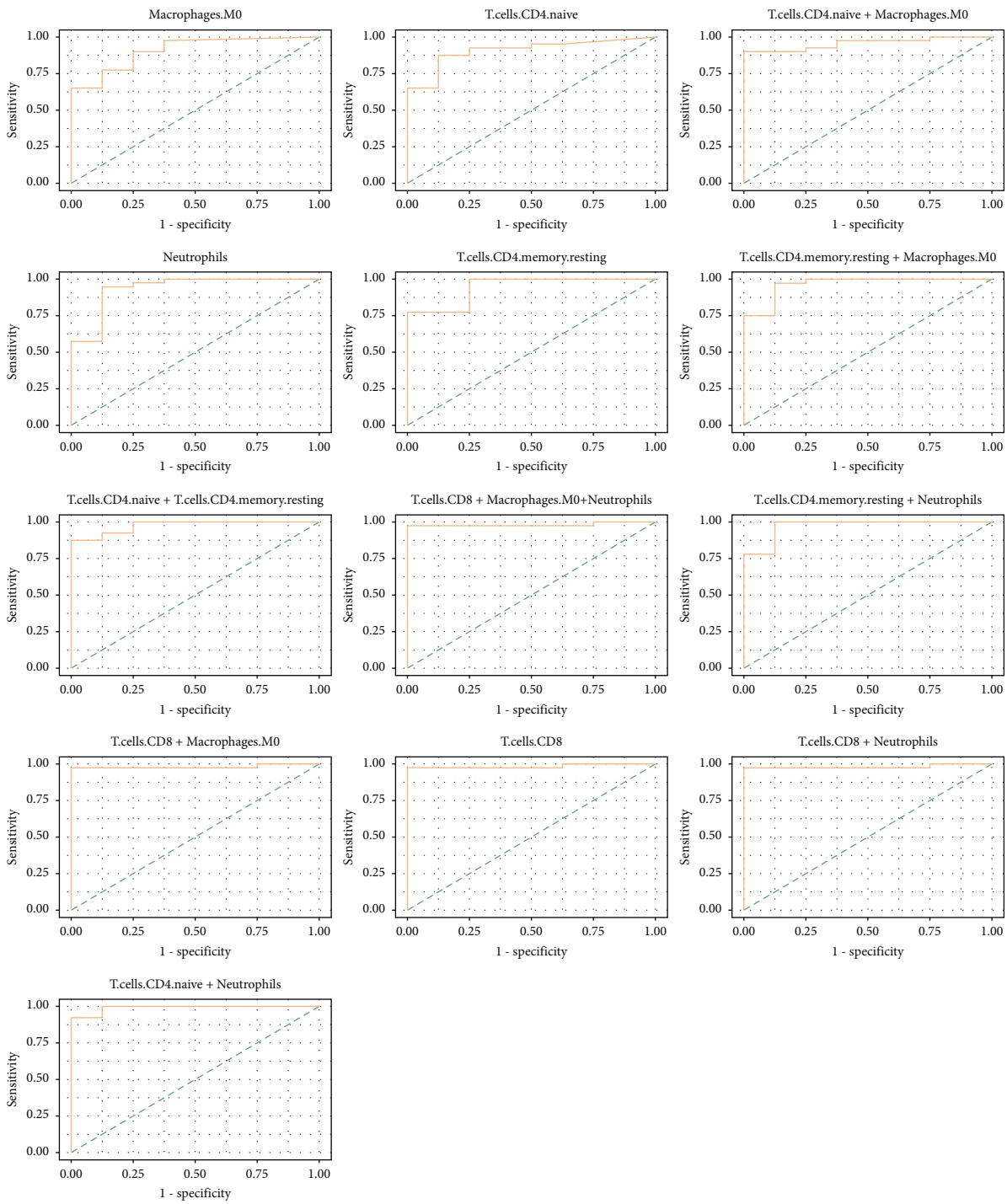

(b)

Figure 4: Further confirmation of the correlation between selected immune cell types and the onset of septicemic melioidosis. (a) Heatmap depicting correlation among selected immune cell types and several clinical features in the patients with melioidosis, with absolute r value > 0.5 highlighted with color round marks. (b) Receiver-operating characteristic curves depicting the combinations of selected immune cell types between patients with melioidosis and healthy control. The curves with at least one immune cell type's p value less than 0.05 were allowed to be plotted. AUC (area under the curve), specificity, and sensitivity were shown in the following brackets. M0 macrophages (0.91, 1.00, 0.65); naive CD4+ cells (0.91, 0.88, 0.88); naive CD4+ cells + M0 macrophages (0.96, 1.00, 0.9); neutrophils (0.94, 0.88, 0.95); resting CD4 memory T cells (0.94, 1.00, 0.78); resting CD4 memory T cells + M0 macrophages (0.97, 0.88, 0.98); naive CD4+ cells + resting CD4 memory T cells (0.98, 1.00, 0.88); CD8+ T cells + M0 macrophages + neutrophils (0.98, 1.00, 0.98); resting CD4 memory T cells + neutrophils (0.97, 0.88, 1.00); CD8+ T cells + M0 macrophages (0.98, 1.00, 0.98); CD8+ T cells (0.98, 1.00, 0.98); CD8+ T cells + neutrophils (0.98, 1.00, 0.97); naive CD4+ cells + neutrophils (0.99, 1.00, 0.93).

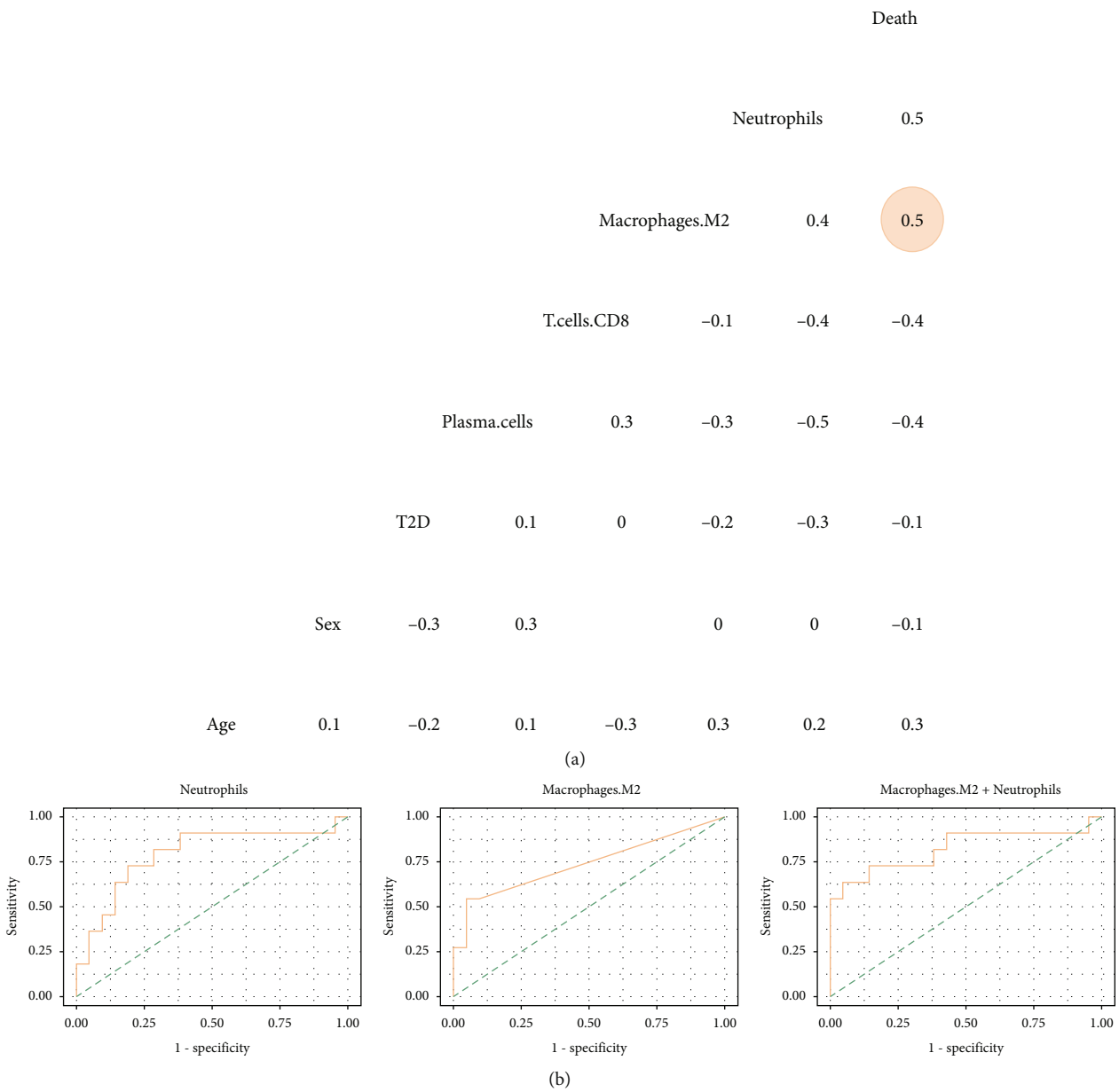

Figure 5: Further confirmation of the correlation between selected immune cell types and the development of septicemic melioidosis. (a) Heatmap depicting correlation among selected immune cell types and several clinical features in the patients with melioidosis, with absolute r value > 0.5 highlighted with color round marks. (b) Receiver-operating characteristic curves depicting the combinations of selected immune cell types between survivors and nonsurvivors with melioidosis. The curves with at least one immune cell type's p value less than 0.05 were allowed to be plotted. AUC (area under the curve), specificity, and sensitivity were shown in the following brackets. Neutrophils (0.79, 0.81, 0.73); M2 macrophages (0.74, 0.95, 0.55); M2 macrophages + neutrophils (0.82, 0.95, 0.64).

proinflammatory (M1), and anti-inflammatory (M2) subsets, each of which plays a distinctive role in the inflammation. We demonstrated that the level of M0 macrophages was high in patients with melioidosis, and the greater level of M2 macrophages was biased towards severe septicemic melioidosis. Our results suggest that conversion from M0 to M2 macrophages may simply reflect the onset and development of septicemic melioidosis (Figures 4 and 5). To the best of our knowledge, this result represents a novel and striking example in which shifts between macrophage subsets are correlated with the development and progression of melioidosis. In agreement with our finding, the previous studies of macrophage subsets on the other intracellular bacterial pathogens (IBPs) demonstrated that M2 macrophages were a comfortable replication niche for *Salmonella* and *Brucella* strains [24, 25]. M2 macrophages also favored replication of *Chlamydia pneumoniae* [26]. The results of the present study, as well as those of other researchers, support the view that M2 macrophages are favorable to IBP infections. Intriguingly, increasing level of M2 macrophages was

associated with worse survival in lung cancer [27]. Therefore, further exploration of M2 macrophages may help improve the treatment for melioidosis.

We observed that patients with septicemic melioidosis exhibited the extremely low level of CD8+ T cells, when compared with healthy donors. And CD8+ T cells alone were able to predict the onset of septicemic melioidosis (Figure 4(b)). Moreover, an extreme level of CD8+ T cells was present in nonsurvivors with septicemic melioidosis. Our findings suggest that a low level of CD8+ are associated not only with the onset of septicemic melioidosis but also with death caused by septicemic melioidosis. Analogue to these, a decreased level of CD8+ T cells was found to be correlated with greater mortality [11]. This finding experimentally confirms the role played by CD8+ T cells in the disease as well. Jenjaroen et al. also found that the level of CD4+ T cells was elevated in survivors of melioidosis vs. nonsurvivors. This observation was not found in this study. Perhaps, the conflicting observations can be explained by difference in methodological approaches or the subsets of the patients. It should be noted that several T cell subsets were implicated in the onset of melioidosis, as measured by CIBERSORT, an algorithm that allows us to profile 22 immune cell types. In *B. pseudomallei* vs. control/healthy, the levels of CD4 memory resting cells, CD4 memory activated cells, CD8+ T cells, and B memory cells were elevated, whereas the level of naive CD4+ T cells was decreased (Figure 3(b)). More importantly, the levels of plasma cells and CD8+ T cells were lower in nonsurvivors with septicemic melioidosis than those in survivors (Figure 3(c)). These findings suggest that the adaptive immune response is likely to be suppressed in patients with septicemic melioidosis, and deteriorating adaptive immune response might lead to poor survival.

Immune checkpoint molecules are inhibitory receptors expressed on immune cells that result in immunosuppressive signaling pathways. These molecules are key for modulating the duration and magnitude of immune responses [28, 29]. Signaling through these molecules can deplete immune cells, especially T cells. T cell exhaustion is reflected by expression of immune checkpoint molecules, such as the expressions of programmed cell death protein 1(PD1) and cytotoxic T lymphocyte antigen 4 (CTLA4). Blockade of PD1 and CTLA4 favored T cell-mediated immune response. It has been well documented that several pathogens (such as genus *Plasmodium vivax*) and cancers lead to inhibitions on the immune cells via immune checkpoint proteins [30–32]. The data of Figure 2(b) showed that PDL1/PD-1 checkpoint pathway is involved in septicemic melioidosis, suggesting that, at minimum, significant change in gene expression levels of either PDL1 or PD-1 could be found. However, no change in the two genes' levels was significant. Of note, in addition to PDL1 and PD-1, there are other major immune checkpoint elements, such as LAG3, TIM3, TIGIT, CD96, BTLA, TNF5F14, GITR, and VISTA [33]. Among these major immune checkpoint elements, we found that LAG3, CD96, and BTLA were strongly overexpressed in patients with septicemic melioidosis (data not shown), suggesting that the depletion of the T cell subsets in septicemic melioidosis might be the result of overexpression of LAG3, CD96, and BTLA. Blockade of these elements might be promising and novel strategy for the treatment of septicemic melioidosis. Moreover, LAG3 was commonly coexpressed with PD1 [34]. Dual blockade of BTLA and PD1 improves antitumor immunity [35]. Blockade of CD96 and PD1-PDL1 was able to improve tumor control [36]. These lines of evidence suggest PD1 and PDL1 should still be taken into account in the future studies. The exclusion of the two genes in this study might be due to the cut-off fold change setting.

Apart from immune response, multiple differentially expressed genes had functions relating to glucose metabolism such as NAD binding, NADP binding, glucose binding, glutathione binding, and GDP binding (Figure 2(a)). In addition, the glutathione metabolism was identified in the KEGG analysis (Figure 2(b)). Although the role of glucose metabolism in melioidosis remains unclear, it has been found in other intracellular pathogenic bacteria. When growth factors are available, the growth factor-stimulated, proliferating immune cells take up glucose by several glucose transporters (GLUTs) to produce larger quantities of intermediary metabolites and NADPH. These molecules are brought into glutathione production and launch the aerobic glycosis, which is a metabolic hallmark for many fast proliferating cancers. Moreover, HIF-1 enhances transcription of GLUTs and most enzymes of the glycolytic pathway. P53 activated glutaminase 2 (GLS2) and this enzyme catalyzes glutamine. These above-mentioned might explain why many cancer-related pathways are implicated in septicemic melioidosis [37].

5. Conclusion

In conclusion, the findings of present study indicate the relationship between the specific immune cell types and onset and development of septicemic melioidosis. These findings broaden our view on the complex interplay between immune cells and *B. pseudomallei* infection and offer novel insights into the roles of immune cell types in septicemic melioidosis.

Data Availability

The datasets in this study can be obtained in NCBI datasets. The accession number(s) can be found in this paper.

Conflicts of Interest

The authors declare that they have no conflicts of interest.

Authors' Contributions

KL and QX designed the study, and JL, LY, XL, and ST conducted the literature search. HP, YQ, and JL collected the data. KX and DX carried out the data analysis. KX wrote the paper with DX, QX, and KL editing and reviewing. All authors contributed ideas and comments, revised the paper, and approved the final version. Ke Xu and Dahua Xu contributed equally to this work.

Acknowledgments

This study was funded by the Major Science and Technology Program of Hainan Province (ZDKJ202003), the Hainan Natural Science Foundation (No. 820MS051), and the National Natural Science Foundation of China (grant nos. 81660502 and 81860002).

References

[1] N. White, "Melioidosis," *The Lancet*, vol. 361, no. 9370, pp. 1715–1722, 2003.

[2] D. Limmathurotsakul, N. Golding, D. A. B. Dance et al., "Predicted global distribution of _Burkholderia pseudomallei_ and burden of melioidosis," *Nature Microbiology*, vol. 1, no. 1, p. 15008, 2016.

[3] A. C. Cheng and B. J. Currie, "Melioidosis: epidemiology, pathophysiology, and management," *Clinical Microbiology Reviews*, vol. 18, no. 2, pp. 383–416, 2005.

[4] D. Limmathurotsakul, M. Kanoksil, V. Wuthiekanun et al., "Activities of daily living associated with acquisition of melioidosis in Northeast Thailand: a matched case-control study," *PLoS Neglected Tropical Diseases*, vol. 7, no. 2, article e2072, 2013.

[5] Y. Lin, Q. Wu, X. Liu et al., "Molecular tracking investigation of melioidosis cases reveals regional endemicity in Hainan, China," *Biomedical Reports*, vol. 5, no. 6, pp. 766–770, 2016.

[6] S. Wongratanacheewin, N. P. J. Day, N. Teerawattanasook et al., "Increasing incidence of human melioidosis in Northeast Thailand," *The American Journal of Tropical Medicine and Hygiene*, vol. 82, no. 6, pp. 1113–1117, 2010.

[7] C. McLeod, P. S. Morris, P. A. Bauert et al., "Clinical presentation and medical management of melioidosis in children: a 24-year prospective study in the Northern Territory of Australia and review of the literature," *Clinical Infectious Diseases*, vol. 60, no. 1, pp. 21–26, 2015.

[8] P. Turner, S. Kloprogge, T. Miliya et al., "A retrospective analysis of melioidosis in Cambodian children, 2009–2013," *BMC Infectious Diseases*, vol. 16, no. 1, p. 688, 2016.

[9] Z. Chagla, N. Aleksova, J. Quirt, J. Emery, C. Kraeker, and S. Haider, "Melioidosis in a Returned Traveller," *Canadian Journal of Infectious Diseases and Medical Microbiology*, vol. 25, 226 pages, 2014.

[10] G. C. Ulett, N. Ketheesan, and R. G. Hirst, "Macrophage-lymphocyte interactions mediate anti-Burkholderia pseudomalleiactivity," *FEMS Immunology & Medical Microbiology*, vol. 21, no. 4, pp. 283–286, 1998.

[11] K. Jenjaroen, S. Chumseng, M. Sumonwiriya et al., "T-cell responses are associated with survival in acute melioidosis patients," *PLoS Neglected Tropical Diseases*, vol. 9, no. 10, article e0004152, 2015.

[12] I. Ceballos-Olvera, M. Sahoo, M. A. Miller, L. . Barrio, and F. Re, "Inflammasome-dependent pyroptosis and IL-18 protect against Burkholderia pseudomallei lung infection while IL-1β is deleterious," *PLoS Pathogens*, vol. 7, no. 12, article e1002452, 2011.

[13] R. Pankla, S. Buddhisa, M. Berry et al., "Genomic transcriptional profiling identifies a candidate blood biomarker signature for the diagnosis of septicemic melioidosis," *Genome Biology*, vol. 10, no. 11, p. R127, 2009.

[14] L. Conejero, K. Potempa, C. M. Graham et al., "The blood transcriptome of experimental melioidosis reflects disease severity and shows considerable similarity with the human disease," *The Journal of Immunology*, vol. 195, no. 7, pp. 3248–3261, 2015.

[15] G. Yu, L.-G. Wang, Y. Han, and Q. Y. He, "clusterProfiler: an R package for comparing biological themes among gene clusters," *Omics: a journal of integrative biology*, vol. 16, no. 5, pp. 284–287, 2012.

[16] N. Rohr-Udilova, F. Klinglmüller, R. Schulte-Hermann et al., "Deviations of the immune cell landscape between healthy liver and hepatocellular carcinoma," *Scientific Reports*, vol. 8, no. 1, pp. 1–11, 2018.

[17] X. Liang, J. A. Bradley, D. Zheng et al., "Prognostic factors of radiation dermatitis following passive-scattering proton therapy for breast cancer," *Radiation Oncology*, vol. 13, no. 1, p. 72, 2018.

[18] B. R. Kirkwood and J. A. Sterne, *Essential medical statistics [M]*, John Wiley & Sons, 2010.

[19] J. A. Hanley and B. J. Mcneil, "The meaning and use of the area under a receiver operating characteristic (ROC) curve," *Radiology*, vol. 143, no. 1, pp. 29–36, 1982.

[20] O. Sangwichian, T. Whistler, A. Nithichanon et al., "Adapting microarray gene expression signatures for early melioidosis diagnosis," *Journal of Clinical Microbiology*, vol. 58, no. 7, 2020.

[21] R. R. Rich, T. A. Fleisher, W. T. Shearer, H. W. Schroeder Jr., A. J. Frew, and C. M. Weyand, *Clinical Immunology E-Book: Principles and Practice [M]*, Elsevier Health Sciences, 2012.

[22] A. L. Jones, T. J. Beveridge, and D. E. Woods, "Intracellular survival of Burkholderia pseudomallei," *Infection and Immunity*, vol. 64, no. 3, pp. 782–790, 1996.

[23] K. MIYAGI, K. KAWAKAMI, and A. SAITO, "Role of reactive nitrogen and oxygen intermediates in gamma interferon-stimulated murine macrophage bactericidal activity against Burkholderia pseudomallei," *Infection and Immunity*, vol. 65, no. 10, pp. 4108–4113, 1997.

[24] N. A. Eisele, T. Ruby, A. Jacobson et al., "Salmonella Require the Fatty Acid Regulator PPAR δ for the Establishment of a Metabolic Environment Essential for Long-Term Persistence," *Cell Host & Microbe*, vol. 14, no. 2, pp. 171–182, 2013.

[25] M. N. Xavier, M. G. Winter, A. M. Spees et al., "PPARγ-Mediated Increase in Glucose Availability Sustains Chronic _Brucella abortus_ Infection in Alternatively Activated Macrophages," *Cell Host & Microbe*, vol. 14, no. 2, pp. 159–170, 2013.

[26] T. Buchacher, A. Ohradanova-Repic, H. Stockinger, M. B. Fischer, and V. Weber, "M2 polarization of human macrophages favors survival of the intracellular pathogen Chlamydia pneumoniae," *PLoS One*, vol. 10, no. 11, article e0143593, 2015.

[27] J. E. Beane, S. A. Mazzilli, J. D. Campbell et al., "Molecular subtyping reveals immune alterations associated with progression of bronchial premalignant lesions," *Nature Communications*, vol. 10, no. 1, pp. 1–13, 2019.

[28] S. H. Baumeister, G. J. Freeman, G. Dranoff, and A. H. Sharpe, "Coinhibitory pathways in immunotherapy for cancer," *Annual review of immunology*, vol. 34, no. 1, pp. 539–573, 2016.

[29] D. M. Pardoll, "The blockade of immune checkpoints in cancer immunotherapy," *Nature Reviews Cancer*, vol. 12, no. 4, pp. 252–264, 2012.

[30] J. M. Horne-Debets, R. Faleiro, D. S. Karunarathne et al., "PD-1 Dependent Exhaustion of $CD8^+$ T Cells Drives Chronic Malaria," *Cell Reports*, vol. 5, no. 5, pp. 1204–1213, 2013.

[31] X. Tian, A. Zhang, C. Qiu et al., "The upregulation of LAG-3 on T cells defines a subpopulation with functional exhaustion and correlates with disease progression in HIV-infected subjects," *The Journal of Immunology*, vol. 194, no. 8, pp. 3873–3882, 2015.

[32] D. Sauce, J. R. Almeida, M. Larsen et al., "PD-1 expression on human CD8 T cells depends on both state of differentiation and activation status," *AIDS*, vol. 21, no. 15, pp. 2005–2013, 2007.

[33] F. Anzengruber, D. Ignatova, T. Schlaepfer et al., "Divergent LAG-3 versus BTLA, TIGIT, and FCRL3 expression in Sézary syndrome," *Leukemia & Lymphoma*, vol. 60, no. 8, pp. 1899–1907, 2019.

[34] S. R. Woo, M. E. Turnis, M. V. Goldberg et al., "Immune inhibitory molecules LAG-3 and PD-1 synergistically regulate T-cell function to promote tumoral immune escape," *Cancer Research*, vol. 72, no. 4, pp. 917–927, 2012.

[35] J. Fourcade, Z. Sun, O. Pagliano et al., "CD8+T cells specific for tumor antigens can be rendered dysfunctional by the tumor microenvironment through upregulation of the inhibitory receptors BTLA and PD-1," *Cancer Research*, vol. 72, no. 4, pp. 887–896, 2012.

[36] S. J. Blake, W. C. Dougall, J. J. Miles, M. W. L. Teng, and M. J. Smyth, "Molecular pathways: targeting CD96 and TIGIT for cancer immunotherapy," *Clinical Cancer Research*, vol. 22, no. 21, pp. 5183–5188, 2016.

[37] W. Eisenreich, T. Rudel, J. Heesemann, and W. Goebel, "To eat and to be eaten: mutual metabolic adaptations of immune cells and intracellular bacterial pathogens upon infection," *Frontiers in cellular and infection microbiology*, vol. 7, p. 316, 2017.

Hindawi
Disease Markers
Volume 2021, Article ID 9711179, 13 pages
https://doi.org/10.1155/2021/9711179

Research Article

OATP1B1 Plays an Important Role in the Transport and Treatment Efficacy of Sorafenib in Hepatocellular Carcinoma

Jinhua Wen[1] **and Menghua Zhao**[2]

[1]*Department of GCP, the First Affiliated Hospital of Nanchang University, Nanchang 330006, China*
[2]*School of Pharmacy, Nanchang University, Nanchang 330006, China*

Correspondence should be addressed to Jinhua Wen; wenjh8606@163.com

Received 13 August 2021; Accepted 8 September 2021; Published 26 September 2021

Academic Editor: Wen-Qing Shi

Background. Sorafenib is an anticancer drug used in the treatment of unresectable hepatocellular carcinoma and advanced renal cell carcinoma. It is a substrate for the human OATP1B1. This study is aimed at assessing the role of OATP1B1 in transportation and uptake of sorafenib in hepatocellular carcinoma and how OATP1B1 affects the pharmacodynamics of sorafenib in vitro and in vivo. *Methods*. Sorafenib transport was measured in HepG2, HepG2-OATP1B1∗1a, HepG2-OATP1B1∗1b, HepG2-OATP1B1∗15, LO2, LO2-OATP1B1∗1a, LO2-OATP1B1∗1b, and LO2-OATP1B1∗15 cells, as well as in HepG2 cells transfected with miR-148a mimics. The viability and apoptosis rate of cells treated with sorafenib were evaluated. A liver cancer rat model was established to explore the pharmacokinetics and pharmacodynamics of sorafenib after overexpression of Oatp2. *Results*. Changes in expression and genetic mutations of OATP1B1 significantly affected the uptake of sorafenib in HepG2 and LO2 transgenic cells, and the uptake of sorafenib was higher in HepG2 than LO2. Genetic mutations of OATP1B1 significantly affected the cell viability and apoptosis rate of HepG2 cells after sorafenib treatment. Compared to control group, the uptake of sorafenib in miR-148a mimic-transfected HepG2 cells was decreased, and the cell viability was increased. PCN significantly increased the expression of Oatp2 and affected the pharmacokinetics of sorafenib. Vascular endothelial growth factor levels and microvascular density in tumor-adjacent tissues decreased significantly, suggesting that increased Oatp2 expression improves the treatment effect of sorafenib in a rat model of liver cancer. *Conclusions*. OATP1B1 plays an important role in the pharmacokinetics and pharmacodynamics of sorafenib in hepatocellular carcinoma.

1. Background

Sorafenib is approved by the United States Food and Drug Administration for the treatment of unresectable hepatocellular carcinoma and advanced renal cell carcinoma. Sorafenib inhibits tumor growth and angiogenesis by targeting both the RAF/MEK/ERK pathway and receptor tyrosine kinases [1]. In humans, sorafenib is administered in tablet form, and the majority (77%) of the sorafenib dose is either unabsorbed or eliminated through the hepatobiliary route (50% unchanged), and 19% of the dose (mostly glucuronides) is excreted in urine [2]. The liver is the main target organ of sorafenib. A study using a HEK293 cell model demonstrated that sorafenib was a substrate for the human organic anion transport polypeptide 1B1 (OATP1B1) and caused a dramatic increase in plasma levels of sorafenib-glucuronide [3]. However, the sorafenib transportation mediated by OATP1B1 and its effect on cancer are not clear. The expression and function of OATPs also change under conditions of liver cancer. OATP1B1 (also known as OATP-C or LST-1 and coded by the gene *SLCO1B1*) is an uptake transporter expressed in the basolateral (sinusoidal) membrane of hepatocytes and plays an important role in the transport of endogenous substances and a variety of clinical drugs [4]. It has 2 single nucleotide polymorphisms: 388 A > G (63% mutation frequency in Asian populations) and 521 T > C (16% mutation frequency in Asian populations) [5], which form four haplotypes: OATP1B1∗1a (c.388APc.521 T), OATP1B1∗1b (c.388GPc.521 T), OABP1B1∗5 (c.388APc.521 C), and OATP1B1∗15

(c.388GPc.521 C). Many studies have revealed that genetic mutations affected OATP1B1 transporter activity and exert a significant effect on drug transport [6]. Genetic polymorphisms could also significantly alter the transporting activities of OATP1B1 [7]. Therefore, OATP1B1 plays an important role in drug transport and clinical treatment. However, its expression, function, and effect on drug treatment in hepatocellular carcinoma tissue are not known. It is also unclear whether genetic mutations of OATP1B1 have different effects on OATP1B1-mediated drug transport or cell viability in HepG2 cells. This study is the first to explore the effects of OATP1B1 mutation on drug transportation and its effects on tumor suppression. It has been reported that miR-148a can regulate the expression of OATP1B1 meditated by PXR [8], which played a key role in regulating the expression of some metabolic enzymes and relevant drug transporters [9]. Therefore, we also investigated the effects of miR-148a mimics on the expression of the OATP1B1 gene in HepG2 cells, as well as the functions of OATP1B1 in tumor treatment. Finally, we upregulated the expression of Oatp2 in a rat model of hepatocellular carcinoma to explore the changes in drug pharmacokinetics and the therapeutic effects of Oatp2 on hepatocellular carcinoma. Our experiments are aimed at elucidating the role of OATP1B1 in the pharmacokinetics of sorafenib treatment in hepatocellular carcinoma.

2. Experimental Materials and Methods

2.1. Materials and Main Instruments. The reagents used were as follows: HepG2, LO2, and lentivirus are purchased from Hangzhou Hibio (Hangzhou, China); sorafenib (>99% purity), China Science & Technology Co., Ltd. (Hangzhou, China); Pregnenolone-16α-carbonitrile (PCN), Cayman Chemical (Ann Arbor, MI, USA); OATP1B1 antibody, Abcam (Cambridge, UK); goat anti-mouse IgG (GAM007), goat anti-rabbit IgG (GAR007), and glyceraldehyde-3-phosphate dehydrogenase (GAPDH), Allied biology; GAPDH (Mab5465), Lianke Biology, China; miR-148a mimics, Ribobio, Guangzhou, China; methanol and acetonitrile (chromatographic purity), Sigma-Aldrich (St. Louis, MO, USA); high purity RNA rapid extraction kit, fetal bovine serum, and BCA protein assay kit, Thermo Fisher Scientific Co., Ltd. (Massachusetts, USA); Hiscript II Q RT SuperMix for qPCR and ChamQ SYBR color qPCR master mix, Vazyme Biotech Co., Ltd. (Nanjing, China); SuperSignal West Dura, Thermo Fisher Scientific (Waltham, MA, USA); PrimeScript™ RT reagent kit, Takara Bio Inc. (Kusatsu, Shiga, Japan); and TransIntro™ EL Transfection Reagent, Transcript First-strand cDNA synthesis superMix, and TransStart™ Green qPCRSuperMix from TransGen (Beijing, China). The following instruments were also used: Mini-PROTEAN Tetra electrophoresis system and the ChemiDoc XRS+ gel imaging system, Bio-Rad (Hercules, CA, USA); a low-light spectrophotometer, Merinton Company (Beijing, China); flow cytometer, Becton, Dickinson and Company (Franklin Lakes, NJ, USA); cell incubator, Thermo Fisher Scientific; inverted microscope, Olympus (Shinjuku City, Tokyo, Japan); low-speed desktop centrifuge, Shanghai Medical Equipment Co., Ltd. (Shanghai, China); full-wavelength microplate reader, Molecular Devices, (SpectraMax i3x, Silicon Valley, USA); desktop high-speed refrigerated centrifuge, Xiangyi Instrument Co. Ltd. (Hunan, China); and high-performance liquid chromatography (HPLC) system, Shimadzu (LC-20AT, Shimadzu, Kyoto, Japan).

2.2. Animals. Male Sprague-Dawley rats (Shanghai slake experimental animal Co., Ltd., 20170005034834) aged approximately 100 days and weighing 250 ± 20 g were used in the experiments. Animal dosing procedures were performed in accordance with the ethical guidelines described in the Principles of Laboratory Animal Care (HB2019000003022).

2.3. Method

2.3.1. Effect of OATP1B1 Genetic Mutations on Drug Transport and Treatment Effects in HepG2 and LO2 Cells

(1) Cell Culture of HepG2 and LO2 Cells. Based on the culture conditions and methods followed in previous studies, the hepatoma cell line HepG2 and the normal human hepatocyte cell line LO2 were cultured in an incubator (37°C, 5% CO_2, and saturated humidity) in minimal essential medium containing 10% fetal bovine serum.

(2) Establishment of HepG2-OATP1B1 and LO2-OATP1B1 Transgenic Cell Models. In order to construct the plasmid target gene, the target genes of OATP1B1∗1a, OATP1B1∗1b, and OATP1B1∗15 were obtained using the following forward (F) and reverse (R) primers: OATP1B1∗1a, 5′-GGGGTACCATCATGGACCAAAATCAAC-3′ (F) and 5′-CTCGAGTGGAAACACAGAAGCAGAAG-3′ (R); OATP1B1∗1b, 5′-CTAAAGAAACTAATATCGATTCATCAGAAAATTC-3′ (F) and 5′-GAATTTTCTGATGAATCGATATTAGTTTCTTTAG-3′ (R); and OATP1B1∗15, 5′-CATGTGGATATATGCGTTCATGGGTAATATGC-3′ (F) and 5′-GCATATTACCCATGAACGCATATATCCACATG-3′ (R). HepG2 and LO2 transgenic cells expressing OATP1B1∗1a, OATP1B1∗1b, and OATP1B1∗15 genotypes were constructed using lentivirus technology. The pGC-FU GFP lentiviral vector transfer system was used as the gene transmission medium to construct the recombinant lentiviral vectors of OATP1B1∗1a, OATP1B1∗1b, and OATP1B1∗15-GFP fusion genes. Gene expression was detected using RT-qPCR testing and Western Blotting. Cell extracts were prepared in lysis buffer. The cell debris was removed by centrifugation at 12,000 × g at 4°C for 15 min, and the total protein concentration was measured using a BCA protein assay kit. Protein samples (50 μg) were subjected to sodium dodecyl sulfate polyacrylamide gel electrophoresis (SDS-PAGE) and electrophoretically transferred to polyvinylidene difluoride (PVDF) membranes. Immunoblots were probed using the rabbit polyclonal OATP1B1 antibody (diluted 1 : 2000) with mouse polyclonal anti-β-actin (diluted 1 : 5000) antibody as the loading control. After incubation with horseradish peroxidase- (HRP-) conjugated secondary antibody, signals were detected by SuperSignal West Dura using a Bio-Rad ChemiDoc XRS imaging system,

and densitometry analysis was performed using the Image Lab Software (Bio-Rad).

(3) Uptake of Sorafenib in HepG2-OATP1B1 and LO2-OATP1B1 Cells. The effect of OATP1B1 gene mutations on the transport of sorafenib in hepatoma cells was evaluated as follows: HepG2, LO-2, and corresponding virus-infected cells in the logarithmic growth phase were collected and diluted with culture medium to a concentration of 1.0×10^6 cells/mL, added to a 12-well culture plate (0.5 mL per well), and cultured for 3 days. Two hours before the experiment, the old culture medium was slowly removed, and the cells were washed thrice using preheated uptake buffer solution. Following the final incubation at 37°C for 10 min, the uptake buffer was slowly removed at regular intervals, and uptake buffers containing different sorafenib concentrations (5, 10, and 15 μM) were added. The cells were incubated at 37°C for 10 min, and the upper layer of the cells was slowly removed. After washing four times using 4°C uptake buffer, 0.2 mL sterile water was added for 3 freeze-thaw cycles in a -80°C ultralow temperature refrigerator. The cell lysate was transferred to an Eppendorf tube and centrifuged at 15,000 rpm for 10 min. The sorafenib content of cells was determined using high performance liquid chromatography (HPLC), and the protein content was determined through the Coomassie brilliant blue staining method. The cells in the experiments were divided into the following groups: HepG2 (control), HepG2-OATP1B1∗1a, HepG2-OATP1B1∗1b, HepG2-OATP1B1∗15, LO2 (control), LO2-OATP1B1∗1a, LO2-OATP1B1∗1b, and LO2-OATP1B1∗15.

(4) Determination of Sorafenib Concentration. HPLC-UV was used to determine the concentration of sorafenib. The mobile phase was acetonitrile/water/0.1% trifluoroacetic acid (45/35/20, *v*/*v*); flow rate, 1.0 mL/mL/min; column temperature, 35°C; UV detection wavelength, 266 nm; and injection volume, 20 μL. The samples were extracted using acetonitrile.

(5) Effect of OATP1B1 Genetic Mutation on Treatment Effect in HepG2 Cells. To evaluate the effect of different OATP1B1 genotypes on tumor inhibition by sorafenib, the cell counting kit- (CCK-) 8 method was used to detect the proliferation of HepG2 cells, while flow cytometry was used to detect apoptosis in HepG2, HepG2-OATP1B1∗1a, HepG2-OATP1B1∗1b, and HepG2-OATP1B1∗15 cells.

2.3.2. Effect of Regulating OATP1B1 Expression on the Viability and Apoptosis Rate of HepG2 Cell

(1) Regulating OATP1B1 Expression in HepG2 Cells. To investigate the effect of miR-148a on pregnane X receptor (PXR) and OATP1B1 expression, after miR-148a mimics were transfected into HepG2 cells with the TransIntro™ ELTransfection Reagent, mRNA expression levels of PXR and OATP1B1 were detected by Real-Time Quantitative reverse transcription PCR (RT-qPCR) testing and Western Blotting, respectively. Total RNA was extracted using an RNA extraction kit as per the manufacturer's instructions. RNA (2.0 μg) was first reverse-transcribed to cDNA using the Transcriptor First-strand cDNA Synthesis Kit, and RT-qPCR was performed using TransStart™ Green qPCR SuperMix as per the manufacturer's instructions. The following primers were used: OATP1B1, 5′-AACTCCTACTGATTCTCGATGGG-3′ (F) and 5′-GTTTCCAGCACATGCAAAGAC-3′ (R); PXR, 5′-TTGCCCATCGAGGACCAGAT-3′ (F) and 5′-GTCTCCGCGTTGAACACTGT-3′ (R); and GAPDH, 5′-AGAAGGCTGGGGCTCATTTG-3′ (F) and 5′-AGGGGCCATCCACAGTCTTC-3′ (R). For Western Blotting, as previously reported [10], the total protein was first lysed with radio-immunoprecipitation assay buffer, and then, the protein concentrations were quantified using a BCA protein assay kit. Next, the protein samples (40 μg) were separated using 10% SDS-PAGE and transferred onto a PVDF membrane. Subsequently, the PVDF membranes were blocked for 2 h with 5% skimmed milk and then incubated overnight at 4°C with specific primary antibodies. Following incubation, the membranes were washed in tris-buffered saline (TBS), incubated with secondary HRP-conjugated anti-rabbit IgG antibody for 1 h with 5% skimmed milk, and again washed in TBS at room temperature. Immune complexes were detected using a Bio-Rad ChemiDoc XRS system, and the protein expression was normalized to glyceraldehyde 3 phosphate dehydrogenase (GAPDH) expression levels.

(2) Uptake of Sorafenib in HepG2 Cells Transfected with miR-148a Mimics and Control HepG2 Cells. The effects of incubation time (0.5-2 h) and drug concentration (5, 10, and 15 μmol/L) on sorafenib uptake by transgenic and control HepG2 cells were investigated. Uptake kinetics experiments were conducted as mentioned above.

(3) Effect of Regulating OATP1B1 Expression on the Viability and Apoptosis Rate of HepG2 Cells. The CCK-8 method was used to measure cell viability. After drug treatment at different time points, 400 μL of 10% CCK-8 solution was added to each well, and the reaction was conducted at 37°C for 1 h. The optical density (OD) of each well was read at 450 nm and 650 nm, and the final OD value was measured as OD_{450}-OD_{650}. The experimental results were calculated as follows: Cell survival rate (%) = experimental group $(OD_{450} - OD_{650}) \times 100$/control group $(OD_{450} - OD_{650})$. To study the effect of a PXR inducer on the cell viability of the control and miR-148a mimic-transfected HepG2 cells, the cells were incubated with or without 5 μmol/L rifampicin for 24 h. Following this, sorafenib was added, and the cells were further incubated for approximately 24 h. The CCK-8 method was used to measure cell viability. The half-maximal inhibitory concentration (IC_{50}) was calculated after incubation for 24 h at 37°C and 5% CO2. To study the effects of sorafenib on the cell cycle of transgenic HepG2 cells, we used flow cytometry for different cycles after the cells had been incubated for approximately 36 h.

2.3.3. Pharmacokinetic Changes of Sorafenib after PXR Regulation of Oatp2 Expression and Its Effect on the Therapeutic Effect of Liver Cancer in Rats

(1) Establishment of PXR-Activated Liver Cancer Rat Model. The Solt-Farber method of cancer induction was applied to promote diethylnitrosamine- (DEN-) induced liver cancer in rats. The rats were intraperitoneally injected with 200 mg/kg DEN solution at one time and then fed with a diet

containing 0.02% 2-acetaminofluorene for 14 days after 2 weeks. For most of the rats, liver resections were performed in the third week, and normal diet resumed in the fourth week. After 4 weeks, the pathological sections were observed to detect liver cancer foci in the rat liver. Following this, the PCN activation method was used to construct the rat model. Rats in the experimental group were intraperitoneally injected with PCN (75 mg/kg) for 4 consecutive days, whereas those in the control group were intraperitoneally injected with a similar volume of normal saline. The rats were killed 24 h after the last administration, and the Oatp2 expression was detected by RT-qPCR testing and Western Blotting.

(3) Pharmacokinetic Analysis ($n = 5$). Ten rats with liver cancer were divided into two groups: the experimental group ($n = 5$, the rats were intraperitoneally injected with PCN (75 mg/kg) for 4 consecutive days) and the control group ($n = 5$, not treated with PCN). All rats in the two groups received gavage administrations of sorafenib (50 mg/kg). Before 0 and at 0.5, 1, 1.5, 2, 3, 4, 6, 8, 12, 24, 48, 72, and 96 h after sorafenib administration, 0.2 mL blood was collected from the caudal vein. All blood samples were centrifuged at 3,000 × g for 5 min, and the plasma was separated and stored at -80°C until analysis.

(4) Evaluation of Treatment Efficacy ($n = 10$). Twenty rats with liver cancer were divided into two groups: the experimental group ($n = 10$, the rats were intraperitoneally injected with PCN (75 mg/kg) for 4 consecutive days) and the control group ($n = 10$, not treated with PCN). All the rats in the two groups were administered sorafenib (50 mg/kg/d for 20 days) by gavage. Following this, the serum aspartate aminotransferase (AST), alanine aminotransferase (ALT), and total bilirubin (TB) levels in rats were measured. The peritumoral tissues were pathologically examined, and the microvascular density (MVD) and levels of vascular endothelial growth factor (VEGF) were measured ($n = 5$). The main procedures of immunohistochemistry were as follows: xylene dewaxing, gradient alcohol rehydration; blocking and inactivating endogenous peroxidase; antigen repair; primary antibody were added and incubated overnight in a refrigerator at 4°C, and then, the temperature was turned to room temperature for equilibrium for 30 min, and PBS was rinsed for 3 × 5 min; the secondary antibody was added and then incubated at 37°C for 30 min and rinsed with PBS for 3 × 5 min; DAB staining, reaction progress was observed under a microscope, and the reaction was thoroughly rinsed with tap water; lignin redyeing, drying, sealing, and photographing; VEGF positive rate and MVD count. Survival time and survival rate of the sorafenib-treated and control groups were observed for 60 days ($n = 5$).

2.4. Statistical Analysis. All data are presented as the mean ± SE. Statistical analysis was performed using GraphPad Prism 5.0 (GraphPad Software Inc., San Diego, CA, USA). All t-tests were two-tailed, and $P < 0.05$ was considered statistically significant. To determine the pharmacokinetics of sorafenib, the concentration-time data were analyzed using the Drug and Statistics software (DAS version 2.0, Center of Institute of Clinical Pharmacology, Nanchang University, Nanchang, Jiangxi, China).

3. Results

3.1. Effect of OATP1B1 Genetic Mutations on Drug Transport and Treatment Effect in HepG2 and LO2 Cells. We successfully established transgenic cell models of OATP1B1∗1a-HepG2, OATP1B1∗1b-HepG2, OATP1B1∗15-HepG2, OATP1B1∗1a-LO2, OATP1B1∗1b-LO2, and OATP1B1∗15-LO2. OATP1B1 was highly expressed in these HepG2 and LO2 cells after being transfected with the OATP1B1-lentivirus plasmid. Western Blot and RT-qPCR test results indicated that the expression of OATP1B1∗15 was higher in OATP1B1∗15-HepG2 cells than in OATP1B1∗1a-HepG2 cells (Figure 1). RT-qPCR test results show higher mRNA expression in transgenic HepG2 cells than in control cells (0.00 ± 0.00 vs. 1.13 ± 0.42 vs. 1.29 ± 0.22 vs. 1.00 ± 0.081, respectively). Compared to control GFP-LO2 cells, OATP1B1 expression increases to approximately 32.93%, 45.12%, and 35.37% in OATP1B1∗1a-GFP-LO2, OATP1B1∗1b-GFP-LO2, and OATP1B1∗15-GFP-LO2 cells, respectively. RT-qPCR test results also show higher mRNA expression in transgenic LO2 cells than in control cells (0.00 ± 0.00 vs. 1.25 ± 0.43 vs. 1.80 ± 0.48 vs. 0.73 ± 0.32, respectively). OATP1B1 expression in HepG2 cells is higher than in LO2 cells but showed no significantly difference.

We initially studied the uptake pharmacokinetics features of OATP1B1-mediated transport of sorafenib by measuring cellular intake in OATP1B1-overexpressing HepG2 and LO2 cells. As shown in Figures 2(a) and 2(b), overexpression of OATP1B1 could significantly increases the uptake of sorafenib in transgenic cells of HepG2 and LO2. The intake of sorafenib in OATP1B1∗1a-HepG2 was significantly higher than HepG2 cells and increased by about 49.64, 50.00, and 136.16%, respectively, when the concentrations of sorafenib were 5, 10, and 15 μmol/L. The same results also showed in OATP1B1∗1a-LO2 cells and increased by about 56.25, 292.55, and 223.97%. Among the different gene types, OATP1B1∗1a-HepG2 and OATP1B1∗1a-LO2 cells showed the highest uptake (more than 1.5-fold that observed in control cells). Notably, OATP1B1 gene mutations affected the uptake of sorafenib. Compared to OATP1B1∗1a, both OATP1B1∗1b and OATP1B1∗15 reduced the uptake of sorafenib in HepG2 and LO2 transgenic cells. Simultaneously, we found that the uptake of sorafenib in HepG2 was obviously higher than in LO2 cells and increased by about 117.19, 200.00, and 182.19%, respectively, when the concentrations of sorafenib were 5, 10, and 15 μmol/L. The same results could also see in transgenic cells of HepG2. As the mRNA and protein level of OATP1B1 in HepG2 than LO2 cells was not obvious difference, therefore, the reason for this uptake difference may be related with the function change of OATP1B1 in HepG2.

After sorafenib treatment, the rate of apoptosis increased significantly in OATP1B1-HepG2 cells compared to that in the control group (Figure 3(a)). When the concentrations of sorafenib were 5, 10, and 15 μmol/L, the rate of apoptosis in OATP1B1∗1a-HepG2 increased by about 78.04, 92.63, and 50.95% compared with HepG2 cells. Gene mutations also affected the rate of apoptosis of HepG2 cells; for

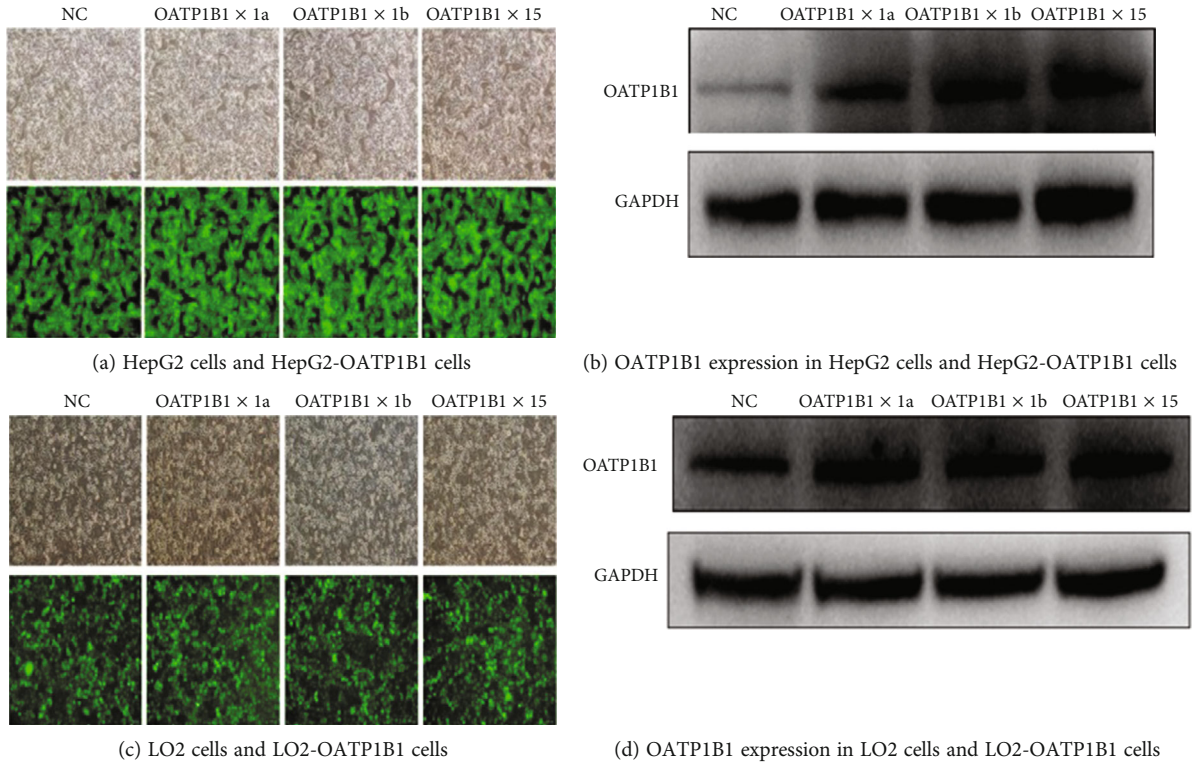

(a) HepG2 cells and HepG2-OATP1B1 cells

(b) OATP1B1 expression in HepG2 cells and HepG2-OATP1B1 cells

(c) LO2 cells and LO2-OATP1B1 cells

(d) OATP1B1 expression in LO2 cells and LO2-OATP1B1 cells

Figure 1: OATP1B1 expression in control and transgenic HepG2 and LO2 cells. The fluorescent photos show HepG2 and LO2 control cells and the cells after being transfected with lentivirus containing pGC-FU-OATP1B1∗1a, pGC-FU-OATP1B1∗1b, and pGC-FU-OATP1B1∗15 (a, c). OATP1B1 expression is detected by Western Blotting and RT-qPCR. Compared to control GFP-HepG2 cells, OATP1B1 expression increases to approximately 110.41%, 147.92%, and 193.75% in OATP1B1∗1a-GFP-HepG2, OATP1B1∗1b-GFP-HepG2, and OATP1B1∗15-GFP-HepG2 cells, respectively (b). Compared to control GFP-LO2 cells, OATP1B1 expression increases to approximately 32.93%, 45.12%, and 35.37% in OATP1B1∗1a-GFP-LO2, OATP1B1∗1b-GFP-LO2, and OATP1B1∗15-GFP-LO2 cells, respectively (d). Protein level of OATP1B1 in HepG2 than LO2 cells was not obvious difference. NC: control.

instance, the rate of apoptosis in OATP1B1∗1b and OATP1B1∗15-HepG2 cells was lower than that of OATP1B1∗1a-HepG2 cells (Figure 3(a)). Correspondingly, cell viability in OATP1B1∗1a-HepG2 was decreased about 12.62, 12.67, and 21.97% compared with HepG2 cells, and we found that the cell viability was higher in OATP1B1∗1b and OATP1B1∗15-HepG2 cells than in OATP1B1∗1a-HepG2 cells after sorafenib treatments (5-15 μmol/L) (Figure 3(b)).

3.2. Effect of Regulating OATP1B1 Expression on the Viability and Apoptosis Rate of HepG2 Cells. When miR-148a mimics were transfected into HepG2 cell lines, OATP1B1 and PXR expression levels decreased significantly (Figure 4), indicating that miR-148a inhibits the expression of these proteins. Simultaneously, miR-148a affected the uptake of sorafenib in HepG2 cells incubated for different time (30-120 min) with varying concentrations of sorafenib (5-15 μmol/L) (Figure 5). As shown in Figure 5, when the cells were incubated approximately 30 min, intracellular sorafenib accumulation was reduced by 46.1%, 28.5%, and 52.5% in cells overexpressing miR-148a after addition of 5, 10, and 15 μmol/L of sorafenib, respectively. Correspondingly, the viability of HepG2 cells increased by about 8.2%, 12.1%, and 19.9%.

Interestingly, after transfection with miR-148a mimics, the HepG2 cell survival rates increased by about 8.20%, 12.08%, and 19.90% when the concentrations of sorafenib were 5, 10, and 15 μmol/L (Figure 6(a)). The results mean that drug's inhibitory effect on cell growth may weaken in transfected cells compared to that in the control cells. Therefore, these results confirmed that miR-148a mimics significantly affected the function of OATP1B1 in HepG2 cells; in other words, they may decrease the cancer suppression effect of sorafenib. On adding the PXR inducer rifampicin, sorafenib significantly decreased the vitality of HepG2. This phenomenon was observed in both HepG2 cell lines and HepG2 cell transfected with miR-148a mimics. Rifampicin, acts as activation of receptor, the activation of PXR may increase the expression of OATP1B1, leading to an increase in sorafenib uptake which resulting in a decline in cell vitality. Because miR-148a mimics could decrease the expression of OATP1B1, we could note that the cell viability be higher in transfected HepG2 cells than in the control group of HepG2 cells after sorafenib being added with or without rifampicin. The IC_{50} values for sorafenib in HepG2 and miR-148a mimic-transfected HepG2 cells at the experiment condition with or without rifampicin were calculated as follows (shown in Figure 6(b)): HepG2 cells without rifampicin, 14.66 ± 2.35 μmol/L; HepG2 with rifampicin,

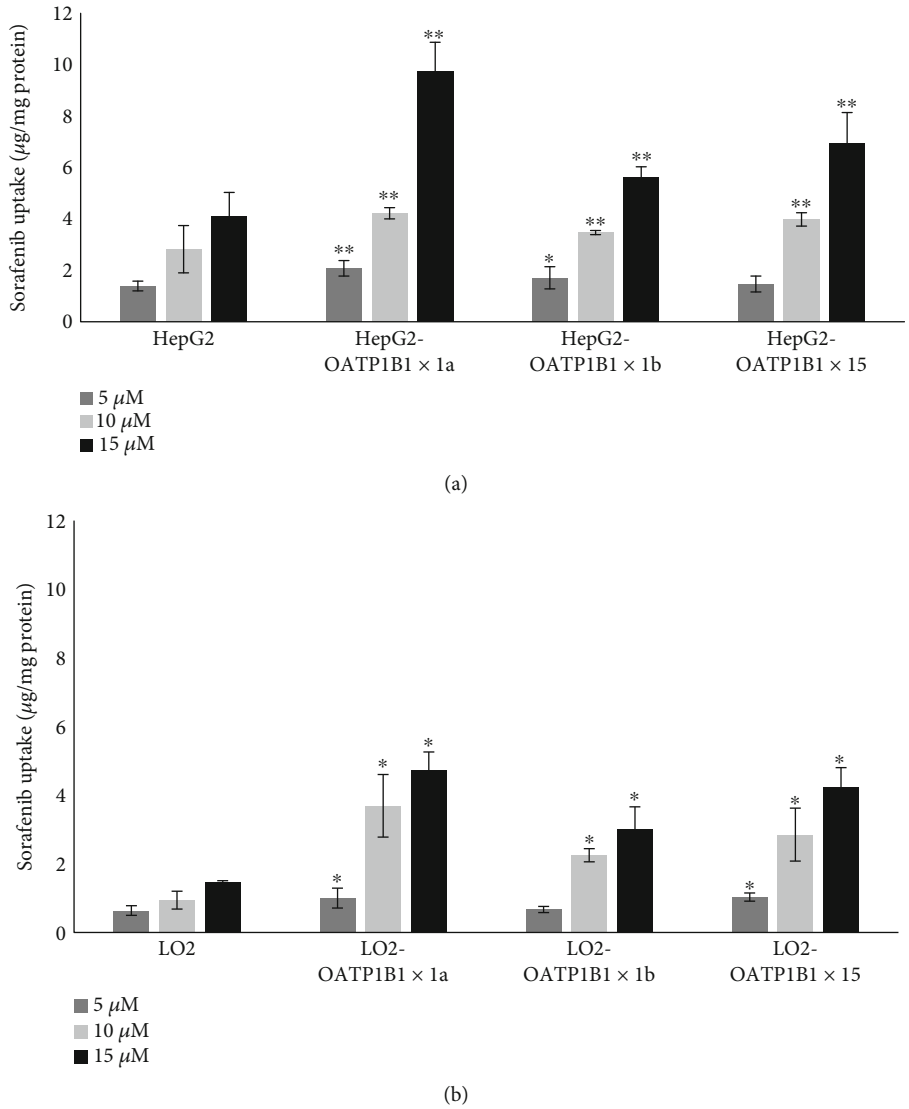

Figure 2: Uptake of sorafenib in control and transgenic HepG2 and LO2 cells. HepG2, OATP1B1-HepG2, LO2, and OATP1B1-LO2 cells were incubated with different concentrations of sorafenib (5, 10, and 15 μM) for 10 min (a, b). Overexpression of OATP1B1 in HepG2 cells significantly increases the uptake of sorafenib compared with control of HepG2 cells (a). Gene mutations significantly decrease the intake of sorafenib in OATP1B1∗1b-HepG2 cells (decrease by about 17.77% and 28.47%) and OATP1B1∗15-HepG2 cells (decrease by about 42.24% and 28.47%) compared to those of OATP1B1∗1a-GFP-HepG2 cells when treated with sorafenib concentrations of 10 and 15 μM, respectively (a). Similar to the patterns in OATP1B1-HepG2 cells, OATP1B1 overexpression in LO2 cells significantly increases sorafenib uptake of sorafenib compared with control of LO2 cells (b). Gene mutations also decrease the intake of sorafenib in OATP1B1∗1b-GFP-LO2 cells (decrease by about 39.02% and 22.76%) and OATP1B1∗15-GFP-LO2 cells (decrease by about 35.94% and 10.57%) compared to those of OATP1B1∗1a-LO2 cells when treated with sorafenib. Concentrations of 10 and 15 μM, respectively (b). Interestingly, sorafenib uptake in HepG2 and OATP1B1-HepG2 cells are all significantly higher than in LO2 and OATP1B1∗1a-LO2 cells (a, b). $^{*}P < 0.05$; $^{**}P < 0.01$.

11.6 ± 1.69 μmol/L; HepG2 cells transfected with miR-148a mimics without rifampicin, 16.13 ± 3.05 μmol/L; and HepG2 cells transfected with miR-148a mimics with rifampicin, 14.04 ± 2.42 μmol/L.

HepG2 cell cycle results showed that with increasing sorafenib concentration, the proportion of G0/G1 phase cells increased significantly; however, the number of cells in the S phase decreased significantly, and there was no significant trend in the number of G2/M phase cells (Table 1). This indicated that sorafenib has an inhibitory effect on the cell cycle and increasing drug concentration enhanced G0/G1 phase arrest. After transfection with miR-148a mimics, the proportion of HepG2 cells in G0/G1 phases decreased significantly; however, the number of cells in the S phase increased significantly, indicating that interference with the Oatp2 expression may affect the therapeutic effect of sorafenib.

3.3. Pharmacokinetic Changes of Sorafenib after PXR Regulation of Oatp2 Expression and Its Effect on the Therapeutic Effect of Liver Cancer in Rats. We successfully established a rat model of hepatocellular carcinoma and

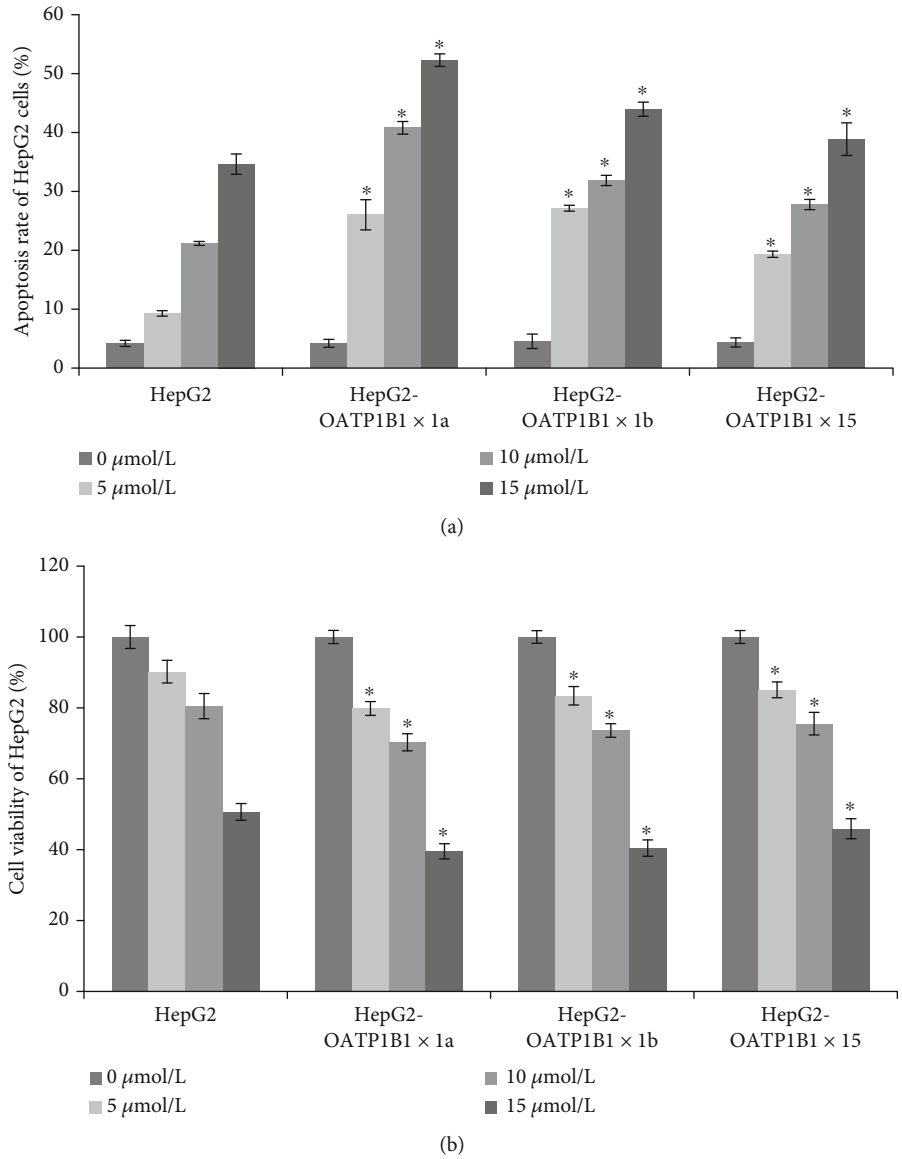

Figure 3: (a) Apoptosis rate of HepG2, HepG2-OATP1B1∗1a, HepG2-OATP1B1∗1b, and HepG2-OATP1B1∗15 cells incubated with sorafenib (0-15 μM). After sorafenib treatment, the rate of apoptosis increased significantly in OATP1B1-HepG2 cells compared to that in the control group. Gene mutations also affected the rate of apoptosis of HepG2 cells. (b) Cell viability of HepG2, HepG2-OATP1B1∗1a, HepG2-OATP1B1∗1b, and HepG2-OATP1B1∗15 cells incubated with sorafenib (0-15 μM). Cell viability in HepG2-OATP1B1∗1a, HepG2-OATP1B1∗1b, and HepG2-OATP1B1∗15 cells was significantly decreased compared with HepG2 cells ($P < 0.05$), and we found that the cell viability was higher in OATP1B1∗1b or ∗15-HepG2 cells than in OATP1B1∗1a-HepG2 cells after sorafenib treatments. $^{*}P < 0.05$.

found that protein or mRNA expression of both Oatp2 and PXR in the liver increased significantly after the rats being intraperitoneally injected with PCN (75 mg/kg) for 4 consecutive days (Figures 7(a)–7(d)). The blood concentration of sorafenib was determined by HPLC. Pharmacokinetic parameters were significantly different between the experimental and control groups (Figure 8, Table 2). PCN significantly affected the pharmacokinetics of sorafenib and increased its concentration in the blood and liver. Elimination half-life and the area under the concentration-time curve were significantly higher in the experimental group than in the control group and increased by about 76.28 and 73.04%, respectively. However, there was no difference in the values of ALT (U/L) (1.94 ± 0.24 vs. 1.98 ± 0.36), AST (U/L) (1000 ± 139 vs. 967 ± 150), and TB (μmol/L) (2061 ± 283 vs. 2017 ± 296) in rats after oral administration of sorafenib with or without treatment with PCN. With increasing Oatp2 expression, the histopathological observations of peritumoral tissues and the degree of necrosis and degeneration of surrounding normal hepatocytes were significantly improved compared to those of the control group. VEGF positive rate and MVD count in tumor-adjacent tissues were also significantly decreased in the experimental group ($6.36 \pm 2.29\%$ vs. $18.36 \pm 5.65\%$, 27.50 ± 11.56 vs. 53.10 ± 24.74, respectively, $P < 0.05$) (Figure 9). Finally, the survival time and survival rate of the sorafenib treatment

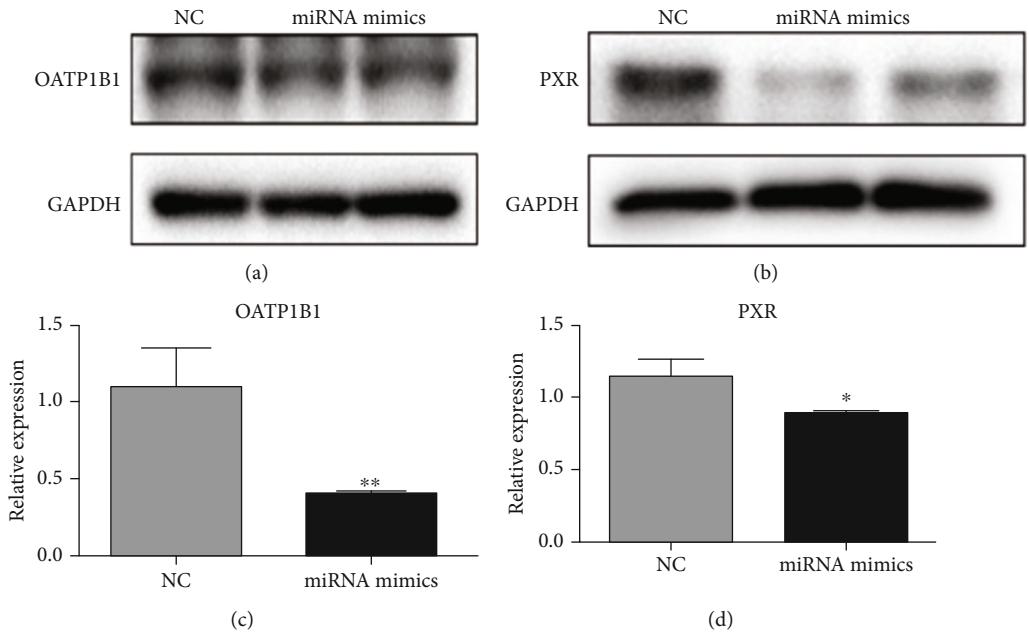

Figure 4: Protein and mRNA expression levels of OATP1B1 and PXR in HepG2 cells following transfection with miR-148a mimics. Compared to control cells, OATP1B1 expression is significantly lower in transfected cells (0.90 ± 0.02 vs. 0.81 ± 0.06) (a). Similar to protein expression, mRNA levels of OATP1B1 are significantly lower in transfected cells (1.10 ± 0.26 vs. 0.41 ± 0.01) (c). Expression of PXR proteins in HepG2 cells is significantly lower after transfection with miR-148a mimics (0.84 ± 0.13 vs. 0.32 ± 0.08) (b). mRNA levels of PXR are also significantly lower than in control cells (1.15 ± 0.12 vs. 0.90 ± 0.01) (d). NC: control. $^{*}P < 0.05$; $^{**}P < 0.01$.

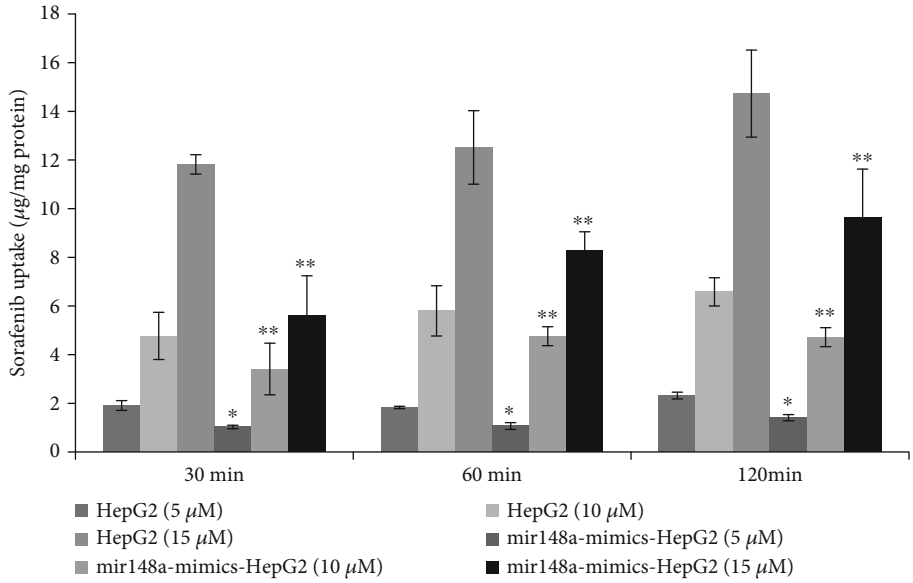

Figure 5: miR-148a affected the uptake of sorafenib in HepG2 cells incubated for different time (30-120 min) with varying concentrations of sorafenib (5-15 μmol/L). Bars represent the mean ± SE ($n = 3$) of sorafenib uptake in control and transfected HepG2 cells incubated with different concentrations of sorafenib (5, 10, and 15 μM) for 30, 60, and 120 min, respectively. Intake of sorafenib increased significantly with concentration increasing in both groups of cells. Transfection with miR-148a mimics significantly affects the uptake of sorafenib in HepG2 cells ($^{*}P < 0.05$; $^{**}P < 0.01$). However, incubation time has no apparent effect on the uptake of sorafenib in control and transfected HepG2 cells. $^{*}P < 0.05$; $^{**}P < 0.01$.

group and control group were observed for 60 days. The results showed that survival-related traits improved after the Oatp2 expression being increased due to the PCN-mediated activation of PXR (survival rate 90% vs. 80%).

4. Discussion

In this study, we demonstrated that sorafenib was a substrate for the human OATP1B1 transporter. Using HepG2 and

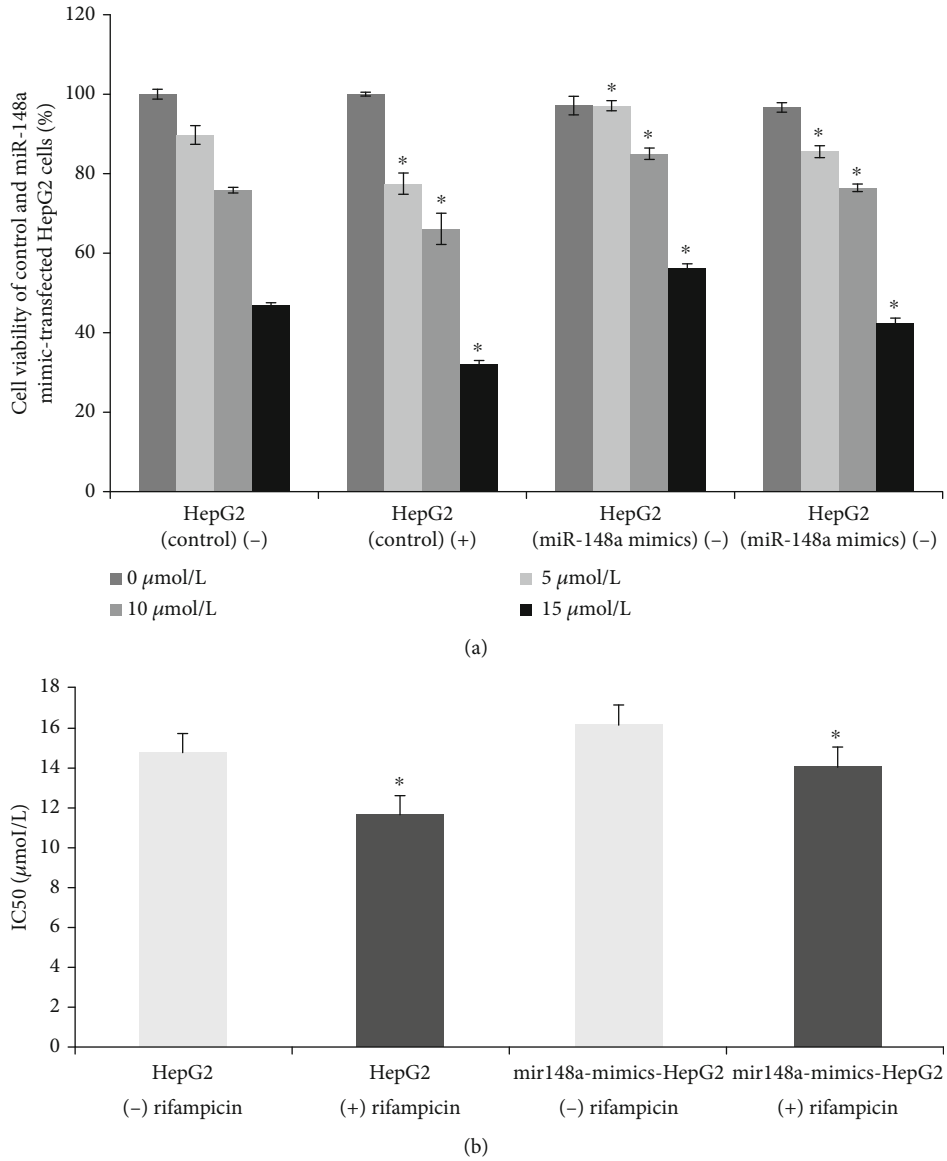

Figure 6: (a) Cell viability of HepG2 (control) and miR-148a mimic-transfected HepG2 cells after incubation with sorafenib (0-15 μM) followed by or not by rifampicin (5 μmol/L). The cell viability was significantly decreased in miR-148a mimic-transfected HepG2 cells compared with the HepG2 cells ($^*P < 0.05$). On adding the PXR inducer rifampicin, sorafenib significantly decreased the vitality both in HepG2 cell lines and HepG2 cell transfected with miR-148a mimics ($^*P < 0.05$). (b) The IC_{50} values for sorafenib in HepG2 and miR-148a mimic-transfected HepG2 cells at the experiment condition with or without rifampicin were calculated. Rifampicin is an inducer of PXR; (–) not treat with rifampicin; (+) treat with rifampicin. ($^*P < 0.05$).

Table 1: Effect of different concentrations of sorafenib (0-15 μM) treatment on cell cycles of miR-148a mimic-transfected and control HepG2 cells.

Cycles	Cells	0 μmol/L	5 μmol/L	10 μmol/L	15 μmol/L
G1	HepG2	56.27 ± 0.25	58.57 ± 1.01	62.83 ± 0.57	67.20 ± 0.46
	HepG2 (miR-148a)	54.67 ± 0.78	54.87 ± 0.35	60.77 ± 0.68	62.93 ± 0.93
S	HepG2	31.70 ± 0.50	26.57 ± 3.80	24.50 ± 3.80	21.13 ± 0.96
	HepG2 (miR-148a)	31.57 ± 1.51	33.00 ± 0.44	26.90 ± 2.03	24.03 ± 1.65
G2	HepG2	10.46 ± 0.66	12.43 ± 2.07	13.26 ± 4.53	11.70 ± 0.98
	HepG2 (miR-148a)	9.36 ± 1.78	10.26 ± 0.43	13.37 ± 1.96	11.23 ± 0.68

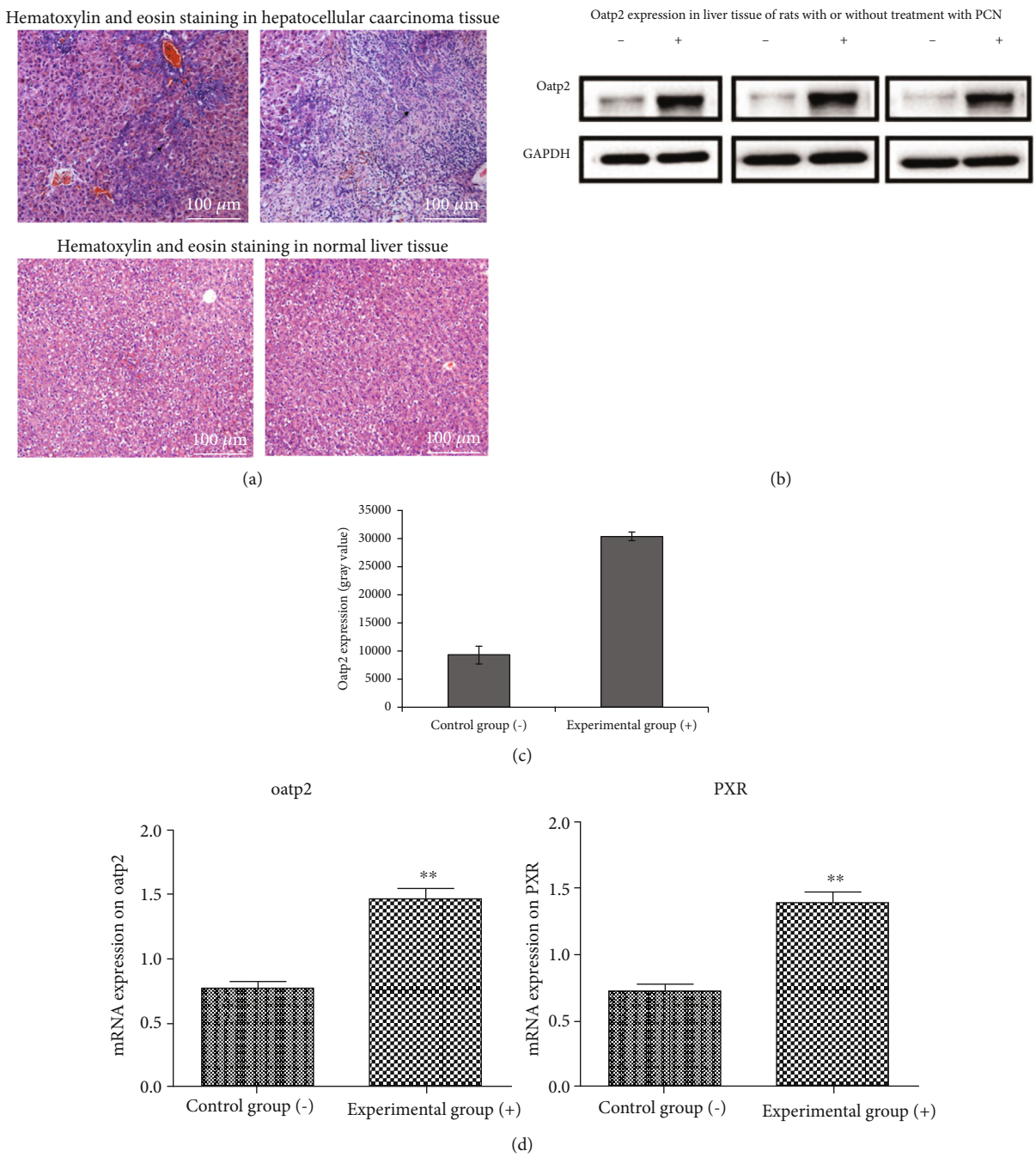

Figure 7: (a) Compared with hematoxylin and eosin staining in normal liver tissue, hematoxylin and eosin staining showing severe congestion in hepatocellular carcinoma tissue, scattered inflammatory cells, nuclear pyknosis in most liver nuclei, and obvious mitosis. The black arrow indicates the mitotic image. (b) OATP2 expression in liver tissue of rats with or without treatment with PCN. Liver tissues were collected and washed with ice-cold PBS 3 times and lysed with lysis buffer. Lysis buffer was collected and centrifuged at 1.4×10^4 rpm for 20 min, and supernatants were used to analyze OATP2 levels by Western Blotting. Compared to the control rats, OATP2 expression is significantly increased in rats treated with PCN. (c) Western Blot bands show that OATP2 expression increases to approximately 227.7% of that in control rats. (d) mRNA expression of OATP2 and PXR in the experimental group is also significantly higher than in the control group. Symbols indicate rat models of hepatocellular carcinoma untreated (-) or treated (+) with PCN. $^{*}P < 0.05$; $^{**}P < 0.01$.

LO2 cell models overexpressing the OATP1B1-type proteins, we determined that sorafenib was incorporated into cells in a concentration-dependent manner and found that the cell intakes in HepG2 were significantly higher than in LO2. Furthermore, sorafenib transport was lower in cells expressing the naturally occurring OATP1B1 variants (OATP1B1∗1b and OATP1B1∗15) compared with wild type of OATP1B1∗1a, thus, exhibiting reduced transport

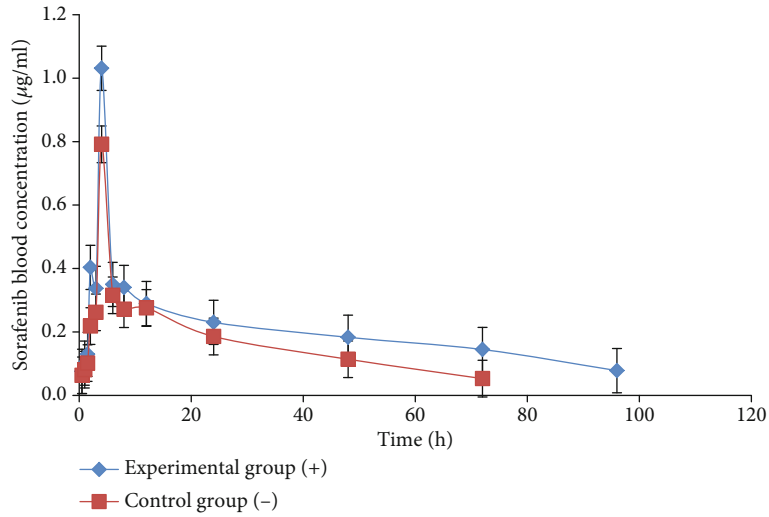

Figure 8: Influence of PCN (and increased OATP2 expression) on sorafenib pharmacokinetics ($n = 5$). The pharmacokinetic profiles of sorafenib in rats after oral administration of 50 mg/kg sorafenib with or without treatment with PCN (75 mg/kg) for 4 days. PCN significantly affects the pharmacokinetics of sorafenib. Symbols indicate rat models of hepatocellular carcinoma untreated (-) or treated (+) with PCN.

Table 2: Pharmacokinetic parameters of sorafenib in rats after oral administration of sorafenib with or without PCN.

Parameters	(-) PCN treatment	(+) PCN treatment
Kα (h^{-1})	0.98 ± 0.17	0.79 ± 0.11
α (h^{-1})	0.67 ± 0.15	0.78 ± 0.14
β (h^{-1})	0.026 ± 0.013	0.016 ± 0.003
Tka (h)	0.69 ± 0.15	0.88 ± 1.12
Tα (h)	1.03 ± 0.35	0.89 ± 0.16
Tβ (h)	27.07 ± 4.38	47.72 ± 4.61*
AUC (μg/mL/h)	125.55 ± 11.11	217.26 ± 26.42*

(+) PCN treatment: sorafenib (50 mg/kg) was administered orally with PCN treatment (75 mg/kg); (-) PCN treatment: sorafenib (50 mg/kg) was administered orally without PCN treatment (75 mg/kg); Kα (h^{-1}): absorption rate constant; α (h^{-1}): distribution rate constant; β (h^{-1}): elimination rate constant; Tka (h): absorption half-life; Tα: distribution half-life; Tβ (h): elimination half-life; AUC (μg/mL/h): area under concentration-time curve. (*$P < 0.05$ compared with (-) PCN treatment).

function. Polymorphisms of OATP1B1 could significantly affect the uptake kinetics of sorafenib both in HepG2 and LO2 cell.

Overexpression of OATP1B1 in HepG2 also affecting the pharmacological effect of sorafenib, which showed that the rate of apoptosis increased significantly in OATP1B1-HepG2 cells compared to that in the control group, correspondingly, cell viability was significantly reduced. Interesting, the rate of apoptosis of HepG2-OATP1B1∗1a cells was significantly higher than those of HepG2-OATP1B1∗1b and HepG2-OATP1B1∗15 cells when the concentrations of sorafenib were 10 and 15 μM. Polymorphisms of OATP1B1 significantly affected the treatment effect of sorafenib in hepatocellular carcinoma, consistent with the notion that certain reduced function variants of *SLCO1B1* (the gene encoding OATP1B1) were associated with an increased risk of sorafenib-associated toxicity [11]. These results suggest that OATP1B1 may play an important role in pharmacodynamics of sorafenib.

We also found that miR-148a mimics reduced the protein and mRNA expression levels of OATP1B1 and PXR in HepG2 cells. Simultaneously, after being incubated about 30 min, intracellular sorafenib accumulation was reduced by 46.1%, 28.5%, and 52.5% in cells overexpressing miR-148a after the addition of 5, 10, and 15 μmol/L of sorafenib, respectively. Correspondingly, the viability of HepG2 cells increased by about 8.2%, 12.1%, and 19.9%. Simultaneously, when the PXR activator rifampicin was added, the viability of both HepG2 and miR-148a mimic-transfected HepG2 cells was decreased; however, the cell viability of the transfected cells was still higher than that of HepG2 cells. The activation of PXR may increase the expression of OATP1B1, leading to an increase in sorafenib uptake.

A previous study showed that PCN increased the expression of both Mdr1a/1b mRNA and P-gp protein in the intestine and brain. PCN also increases the expression of Mdr1a/1b mRNA in the liver [12]. Another in vivo study showed that in rats pretreated with verapamil, the C_{max} of sorafenib increased by about 57.40% from 55.73 ng/mL to 87.72 ng/mL, and the area under the curve (AUC) $_{(0\text{-}t)}$ increased by approximately 58.2% when sorafenib was coadministered with verapamil. These results indicate that P-gp is involved in the transport of sorafenib, and verapamil acts as a P-gp inhibitor that could increase its absorption [13]. Therefore, when the PCN is combined with sorafenib, the absorption of sorafenib may decrease. However, the results of our study are contrary to this hypothesis. Our results showed that when the rats were pretreated with PCN, the plasma concentration of sorafenib was significantly increased. Compared to that in the control rats, Oatp2

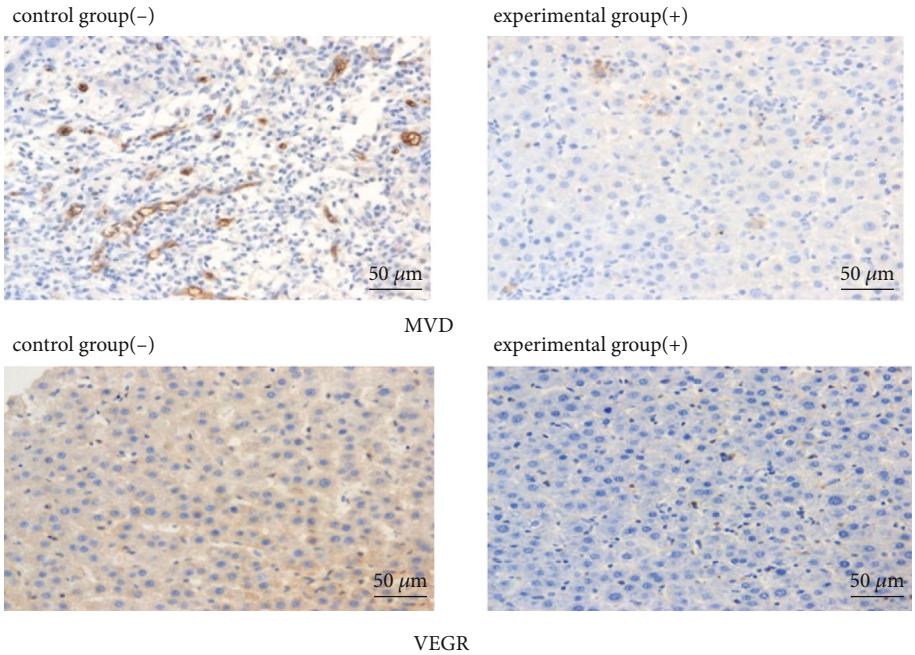

Figure 9: Histopathological observations of peritumoral tissues. Vascular endothelial growth factor (VEGF) levels and microvessel density (MVD) in peritumoral tissues of rats in the control and experimental groups after immunohistological staining and treatment with 50 mg/kg sorafenib for 20 days. VEGF expression and MVD counts in the experimental group were significantly lower than those in the control group (not treated with PCN). VEGF positive rate and MVD count in tumor-adjacent tissues were also significantly decreased in the experimental group ($6.36 \pm 2.29\%$ vs. $18.36 \pm 5.65\%$, 27.50 ± 11.56 vs. 53.10 ± 24.74, respectively). Symbols represent rat models of hepatocellular carcinoma untreated (-) or treated (+) with PCN.

protein expression was significantly higher after the hepatoma mice were treated with PCN for 4 days. We hypothesize that after pretreatment with PCN, a significant increase in the OATP2 expression in liver tissue or the intestine would increase the uptake of sorafenib, which is beyond the P-gp-mediated efflux; this is a noteworthy and important finding. Previous research has shown that there were minimal differences in peak plasma concentration and plasma AUC for sorafenib, sorafenib N-oxide, and total active compounds (sorafenib + sorafenib N-oxide) between OATP1b2(-/-) and wild-type mice after a single oral sorafenib dose of 10 mg/kg [3]. However, the results of our study are contrary to the findings of this study. This may be due to differences in the expression of OATPs in hepatocellular carcinoma rats and mice, which may result in changes in the expression and function of OATPs under conditions of liver cancer. Although the survival rate of hepatocellular carcinoma rats improved after the Oatp2 expression being increased, this result showed no statistical difference, and larger sample sizes of liver cancer rats are needed to explore whether survival can be improved.

Sorafenib is also reported to be metabolized by CYP3A4 in the liver; a study showed that triptolide might also cause a higher C_{max} and lower oral clearance rate of sorafenib by inhibiting CYP3A-mediated metabolism [14]. Further research is needed to elucidate whether PCN changes the expression and function of CYP3A4 in a rat model of liver cancer and whether it affects the pharmacokinetics and pharmacodynamics of sorafenib.

5. Conclusions

OATP1B1 plays an important role in the pharmacokinetics and pharmacodynamics of sorafenib. Changes in the expression and function of OATP1B1 would significantly affect the uptake of sorafenib in HepG2 and LO2 transgenic cells. The uptake of sorafenib by HepG2 cells was higher than that by LO2 cells. Simultaneously, the uptake of sorafenib in HepG2 was significantly higher than in miR-148a mimic-transfected HepG2 cells. These results confirmed that miR-148a mimics would significantly affect the function of OATP1B1 in HepG2 cells; in other words, they may decrease the cancer suppression effect of sorafenib. PCN could significantly increase the expression of Oatp2 and affect the pharmacokinetics of sorafenib. At the same time, VEGF levels and MVD in tumor-adjacent tissues decreased significantly, suggesting that increased Oatp2 expression improves the treatment effect of sorafenib in a rat model of liver cancer [15].

Abbreviations

ALT: Alanine aminotransferase
AST: Aspartate aminotransferase
GAPDH: Glyceraldehyde 3 phosphate dehydrogenase
HPLC: High performance liquid chromatography
MVD: Microvascular density
OATP1B1: Organic anion transport polypeptide 1B1
PCN: Pregnenolone-16α-carbonitrile
PVDF: Polyvinylidene difluoride

PXR: Pregnane X receptor
RT-qPCR: Real-Time Quantitative reverse transcription PCR
SDS-PAGE: Sodium dodecyl sulfate polyacrylamide gel electrophoresis
TB: Total bilirubin
VEGF: Vascular endothelial growth factor.

Data Availability

The data used during the study are available online https://osf.io/z3aq4/?view_only=a1f302519f8647509a658d114f292364. The authors can also make data available on request through an email to the corresponding author, wenjh8606@163.com, Prof. Dr. Wen.

Ethical Approval

All animal experiments were carried out in accordance with the protocol approved by the First Affiliated Hospital of Nanchang University, which complies with international rules and policies for laboratory animal use and care as founded in the European Community guidelines (EEC Directive of 1986; 86/609/EEC).

Consent

No consent was necessary.

Disclosure

This paper has been presented preprint in Research Square according to the following link: https://www.researchsquare.com/article/rs-130868/v1.

Conflicts of Interest

We declare that they have no conflicts of interest.

Authors' Contributions

Jinhua Wen and Menghua Zhao did most of experiments and wrote the original draft. All authors read and approved the final manuscript.

Acknowledgments

This study was supported by the National Natural Science Foundation of China (81660620, 81860661) and the Department of Science and Technology of Jiangxi Province (20171ACB21059, 20192BCBL23018).

References

[1] A. A. Abdelgalil, H. M. Alkahtani, and F. I. Al-Jenoobi, "Sorafenib," *Profiles Drug SubstExcip Relat Methodol*, vol. 44, pp. 239–266, 2019.

[2] X. Wang, X. Zhang, F. Liu, M. Wang, and S. Qin, "The effects of triptolide on the pharmacokinetics of sorafenib in rats and its potential mechanism," *Pharmaceutical Biology*, vol. 55, no. 1, pp. 1863–1867, 2017.

[3] E. I. Zimmerman, S. Hu, J. L. Roberts et al., "Contribution of OATP1B1 and OATP1B3 to the disposition of sorafenib and sorafenib-glucuronide," *Clinical Cancer Research*, vol. 19, no. 6, pp. 1458–1466, 2013.

[4] H. H. Lee and R. H. Ho, "Interindividual and interethnic variability in drug disposition: polymorphisms in organic anion transporting polypeptide 1B1 (OATP1B1; SLCO1B1)," *British Journal of Clinical Pharmacology*, vol. 83, no. 6, pp. 1176–1184, 2017.

[5] M. Niemi, E. Schaeffeler, T. Lang et al., "High plasma pravastatin concentrations are associated with single nucleotide polymorphisms and haplotypes of organic anion transporting polypeptide-C (OATP-C, SLCO1B1)," *Pharmacogenetics*, vol. 14, no. 7, pp. 429–440, 2004.

[6] L. Zhu, F. R. Yu, Y. Wang, B. Ning, and T. Tang, "CYP2C9 and OATP1B1 genetic polymorphisms affect the metabolism and transport of glimepiride and gliclazide," *SciRep*, vol. 8, p. 10994, 2018.

[7] T. Nozawa, M. Nakajima, I. Tamai et al., "Genetic polymorphisms of human organic anion transporters OATP-C (SLC21A6) and OATP-B (SLC21A9): allele frequencies in the Japanese population and functional analysis," *The Journal of Pharmacology and Experimental Therapeutics*, vol. 302, no. 2, pp. 804–813, 2002.

[8] Y. Rao, G. F. Jin, M. Y. Liu et al., "Effect and mechanism of miR-206/miR-613 on expression of OATP1B1," *Yao Xue Xue Bao*, vol. 51, no. 12, pp. 1858–1863, 2016.

[9] W. Jinhua, Z. Ying, and L. Yuhua, "PXR-ABC drug transporters/CYP-mediated ursolic acid transport and metabolism in vitro and vivo," *Arch Pharm (Weinheim) Actions*, vol. 353, no. 9, p. 2000082, 2020.

[10] Y. Xu, J. Hu, Y. Zhang et al., "LncRNA HOTAIR modulates the expression of OATP1B1 in HepG2 cells by sponging miR-206/miR-613," *Xenobiotica*, vol. 50, no. 12, pp. 1494–1500, 2020.

[11] S. Bins, A. Lenting, S. el Bouazzaoui et al., "Polymorphisms in SLCO1B1 and UGT1A1 are associated with sorafenib-induced toxicity," *Pharmacogenomics*, vol. 17, no. 14, pp. 1483–1490, 2016.

[12] R. I. R. Macias, A. Sánchez-Martín, G. Rodríguez-Macías et al., "Role of drug transporters in the sensitivity of acute myeloid leukemia to sorafenib," *Oncotarget*, vol. 9, no. 47, pp. 28474–28485, 2018.

[13] X. Wang, X. Zhang, X. Huang, Y. Li, M. Wu, and J. Liu, "The drug–drug interaction of sorafenib mediated by P-glycoprotein and CYP3A4," *Xenobiotica*, vol. 46, no. 7, pp. 651–658, 2016.

[14] X. Ma, X. Qin, X. Shang, M. Liu, and X. Wang, "Organic anion transport polypeptide 1b2 selectively affects the pharmacokinetic interaction between paclitaxel and sorafenib in rats," *Biochem Pharmacol*, vol. 169, no. 7, p. 113612, 2019.

[15] J. H. Wen and M. Zhao, "OATP1B1 plays an important role in the transport and treatment efficacy of sorafenib in hepatocellular carcinoma," *Research Square*, pp. 1–17, 2021.